WOODHEAD PUBLISHING IN MATERIALS

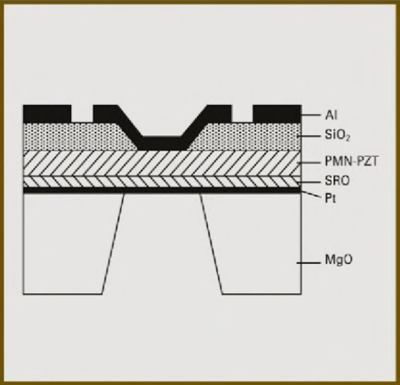
Al
SiO2
PMN-PZT
SRO
Pt
MgO

Advanced piezoelectric materials

Science and technology

Edited by Kenji Uchino

WP
WOODHEAD
PUBLISHING

VISIT…

LANZAROTE Caliente.COM

Advanced piezoelectric materials

Related titles:

Handbook of advanced dielectric, piezoelectric and ferroelectric materials: Synthesis, properties and applications
(ISBN 978-1-84569-186-8)
This comprehensive book covers the latest developments in advanced dielectric, piezoelectric and ferroelectric materials. It presents current research from leading innovators in the field. Sections cover topics under the general headings: High strain high performance piezo- and ferroelectric single crystals; Electric field-induced effects and domain engineering; Morphotropic phase boundary related materials and phenomena; High power piezoelectric and microwave dielectric materials; Nanoscale piezo-and ferroelectrics; Piezo- and ferroelectric films; Novel processing, new materials and properties.

Advanced adhesives in electronics: Materials, properties and applications
(ISBN 978-1-84569-576-7)
Adhesives are widely used in the manufacture of electronic devices to act as passive and active components. Recently there has been considerable interest, both industrially and academically, in thermally and electrically conductive adhesives. *Advanced adhesives in electronics* reviews the latest research in adhesives in electronics, with particular focus on conductive adhesives. Chapters discuss specific applications, such as the use of adhesives in flip-chip assembly and photonics. The reliability and failure of joints are discussed with chapters on diffusion, thermal stress and environmental reliability. Process development of adhesive joints in electronic products and the modelling of conductive adhesive joints are also reviewed.

Microjoining and nanojoining
(ISBN 978-1-84569-179-0)
Many recent advances in technology have been associated with nanotechnology and the miniaturisation of components, devices and systems of electronic, precision and medical products. Among the key technical prerequisites, effective microjoining plays an essential role. Microjoining, having been closely associated with the evolution of microelectronic packaging, covers a much broader area, and is essential for manufacturing many electronic, precision and medical products. Part I of the book reviews the basics of microjoining and Part II covers microjoining processes. A third group of chapters discusses microjoining of materials and a final group of chapters analyses the applications of microjoining.

Details of these and other Woodhead Publishing materials books can be obtained by:

- visiting our web site at www.woodheadpublishing.com
- contacting Customer Services (e-mail: sales@woodheadpublishing.com; fax: +44 (0) 1223 893694; tel.: +44 (0) 1223 891358 ext. 130; address: Woodhead Publishing Limited, Abington Hall, Granta Park, Great Abington, Cambridge CB21 6AH, UK)

If you would like to receive information on forthcoming titles, please send your address details to: Francis Dodds (address, tel. and fax as above; e-mail: francis.dodds@woodheadpublishing.com). Please confirm which subject areas you are interested in.

Advanced piezoelectric materials

Science and technology

Edited by
Kenji Uchino

WOODHEAD PUBLISHING

Oxford Cambridge Philadelphia New Delhi

Published by Woodhead Publishing Limited, Abington Hall, Granta Park,
Great Abington, Cambridge CB21 6AH, UK
www.woodheadpublishing.com

Woodhead Publishing, 525 South 4th Street #241, Philadelphia, PA 19147, USA

Woodhead Publishing India Private Limited, G-2, Vardaan House, 7/28 Ansari Road,
Daryaganj, New Delhi – 110002, India
www.woodheadpublishingindia.com

First published 2010, Woodhead Publishing Limited
© Woodhead Publishing Limited, 2010
The authors have asserted their moral rights.

This book contains information obtained from authentic and highly regarded sources. Reprinted material is quoted with permission, and sources are indicated. Reasonable efforts have been made to publish reliable data and information, but the author and the publisher cannot assume responsibility for the validity of all materials. Neither the author nor the publisher, nor anyone else associated with this publication, shall be liable for any loss, damage or liability directly or indirectly caused or alleged to be caused by this book.

Neither this book nor any part may be reproduced or transmitted in any form or by any means, electronic or mechanical, including photocopying, microfilming and recording, or by any information storage or retrieval system, without permission in writing from Woodhead Publishing Limited.

The consent of Woodhead Publishing Limited does not extend to copying for general distribution, for promotion, for creating new works, or for resale. Specific permission must be obtained in writing from Woodhead Publishing Limited for such copying.

Trademark notice: Product or corporate names may be trademarks or registered trademarks, and are used only for identification and explanation, without intent to infringe.

British Library Cataloguing in Publication Data
A catalogue record for this book is available from the British Library.

ISBN 978-1-84569-534-7 (print)
ISBN 978-1-84569-975-8 (online)

The publisher's policy is to use permanent paper from mills that operate a sustainable forestry policy, and which has been manufactured from pulp which is processed using acid-free and elemental chlorine-free practices. Furthermore, the publisher ensure's that the text paper and cover board used have met acceptable environmental accreditation standards.

Typeset by Replika Press Pvt Ltd, India
Printed by TJI Digital, Padstow, Cornwall, UK

Contents

Contributor contact details *xi*

Preface *xv*

1 The development of piezoelectric materials and the new perspective 1
K. Uchino, The Pennsylvania State University, USA

1.1 The history of piezoelectrics 1
1.2 Piezoelectric materials: present status 21
1.3 Piezoelectric devices: brief review of applications 44
1.4 References 82

Part I Piezoelectric materials

2 Lead zirconate titanate-based piezo-ceramics 89
M. Kimura, A. Ando and Y. Sakabe, Murata Manufacturing Co., Ltd, Japan

2.1 Introduction 89
2.2 Crystalline structure and phase relations 91
2.3 Compositional modifications 94
2.4 Shaping approach and application trend 100
2.5 Low temperature sintering 104
2.6 Summary and future trends 107
2.7 References 107

3 Relaxor ferroelectric-based ceramics 111
K. Uchino, The Pennsylvania State University, USA

3.1 Introduction 111
3.2 Crystal structures of relaxor ferroelectrics 114
3.3 Dielectric properties of relaxor ferroelectrics 115
3.4 Electrostriction in relaxor ferroelectrics 125

3.5 Electrooptic effect 127
3.6 Conclusions 128
3.7 References 128

4 Lead-free piezo-ceramics 130
T. Takenaka, Tokyo University of Science, Japan

4.1 Introduction 131
4.2 Barium titanate ($BaTiO_3$) [BT]-based ceramics 132
4.3 Potassium niobate ($KNbO_3$) [KN]–sodium niobate ($NaNbO_3$) [NN]–lithium niobate ($LiNbO_3$) [LN] system 132
4.4 Potassium niobate ($KNbO_3$) [KN]-based ceramics 133
4.5 Bismuth sodium titanate $(Bi_{1/2}Na_{1/2})TiO_3$ [BNT]-based ceramics 140
4.6 Bismuth sodium titanate $(Bi_{1/2}Na_{1/2})$ TiO_3 [BNT]–bismuth potassium titanate $(Bi_{1/2}K_{1/2})TiO_3$ [BKT]–barium titanate ($BaTiO_3$) [BT] system 144
4.7 Bismuth sodium titanate $(Bi_{1/2}Na_{1/2})TiO_3$ [BNT]–bismuth lithium titanate $(Bi_{1/2}Li_{1/2})TiO_3$ [BLT]–bismuth potassium titanate $(Bi_{1/2}$ $K_{1/2})$ TiO_3 [BKT] system 148
4.8 Bismuth potassium titanate $(Bi_{1/2}$ $K_{1/2})TiO_3$ [BKT]-based ceramics 158
4.9 Conclusions 163
4.10 Acknowledgements 165
4.11 References 165

5 Quartz-based piezoelectric materials 171
Y. Saigusa, River Eletec, Japan

5.1 Piezoelectricity of quartz crystal 171
5.2 Production of artificial quartz crystal 181
5.3 Cutting angles and their vibration mode 184
5.4 Applications of resonator, oscillator and filter 194
5.5 Acknowledgements 203
5.6 References 203

6 Lithium niobate and lithium tantalate-based piezoelectric materials 204
V. Ya. Shur, Ural State University, Russia

6.1 Introduction 204
6.2 Piezoelectric properties of lithium niobate and lithium tantalate 206
6.3 The advantages of single crystal ferroelectrics for piezoelectric applications 212

6.4 The influence of the periodic domain structure on piezoelectric and acoustic properties 213
6.5 Nano- and micro-domain engineering in lithium niobate and lithium tantalate crystals 217
6.6 Applications of domain engineered lithium niobate and lithium tantalate crystals for light frequency conversion 226
6.7 Generation of terahertz radiation in periodically poled lithium niobate crystal 228
6.8 Conclusions and future trends 231
6.9 References 233

7 Single crystal PZN–PT, PMN–PT, PSN–PT and PIN–PT-based piezoelectric materials 239
L. Luo, X. Zhao and H. Luo Shanghai Institute of Ceramics, China

7.1 Introduction 239
7.2 The history of relaxor ferroelectrics 240
7.3 PZN–PT crystal 242
7.4 PMN–PT crystal 251
7.5 PSN–PT crystal 264
7.6 PIN–PT crystal 269
7.7 Theoretical models for relaxor-based crystals 272
7.8 Application in piezoelectric actuators and medical transducers 276
7.9 Conclusion and future trends 278
7.10 References 280

8 Electroactive polymers as actuators 287
Y. Bar-Cohen, Jet Propulsion Lab, USA

8.1 Introduction 287
8.2 Historical review 288
8.3 The two electroactive polymers (EAP) groups 289
8.4 Current and under consideration applications 303
8.5 The armwrestling challenge – as a state-of-the-art indicator 306
8.6 Challenges, trends and potential developments 309
8.7 Conclusions 310
8.8 Acknowledgements 313
8.9 References 313

9 Piezoelectric composite materials 318
K. Uchino, The Pennsylvania State University, USA

9.1 Introduction 318

9.2 Connectivity 319
9.3 Composite effects 319
9.4 PZT:polymer composites 323
9.5 Composite dampers and energy harvesters 333
9.6 Magnetoelectric sensors 343
9.7 References 345

Part II Preparation methods and applications

10 Manufacturing methods for piezoelectric ceramic materials 349
K. Uchino, The Pennsylvania State University USA

10.1 Material designing 349
10.2 Fabrication processes of ceramics 359
10.3 Device designing 367
10.4 Size effect on ferroelectricity 378
10.5 References 385

11 Multilayer technologies for piezo-ceramic materials 387
K. Uchino, The Pennsylvania State University, USA

11.1 Introduction 387
11.2 Multilayer (ML) manufacturing processes 388
11.3 Internal electrode design 391
11.4 Electrode materials 399
11.5 Innovative multilayer (ML) structures 406
11.6 Reliability/lifetime of multilayer (ML) actuators 406
11.7 References 411

12 Single crystal preparation techniques for manufacturing piezoelectric materials 412
L.-C. Lim, National University of Singapore, Singapore

12.1 Introduction 412
12.2 Flux growth of PZN–PT single crystals (i.e. relaxor-PT crystals of low PT contents) 414
12.3 Flux growth of PMN–PT single crystals (i.e. relaxor-PT crystals of high PT contents) 421
12.4 Other commonly encountered phenomena 426
12.5 Conclusions 430
12.6 Acknowledgements 431
12.7 References 432

13 Thin film technologies for manufacturing piezoelectric materials 441
K. Wasa, Kyoto University, Japan

13.1 Introduction: bulk and thin film materials 441
13.2 Fundamentals of thin film deposition 443
13.3 Deposition of PZT-based thin films 453
13.4 Dielectric and piezoelectric properties of PZT-based thin films 458
13.5 PZT-based thin films for micro-electromechanical systems (MEMS) 466
13.6 PZT-based thin film micro-electromechanical systems (MEMS) 476
13.7 Conclusions 487
13.8 Acknowledgements 487
13.9 References 488

14 Aerosol techniques for manufacturing piezoelectric materials 493
J. Akedo, National Institute of Advanced Industrial Science and Technology, Japan

14.1 Introduction 493
14.2 Aerosol deposition process 495
14.3 Room temperature impact consolidation (RTIC) 497
14.4 Deposition properties and film patterning 504
14.5 Electrical properties of aerosol deposition (AD) films and improvements by heat treatment 508
14.6 Piezoelectric device applications 522
14.7 Conclusions 531
14.8 References 533

15 Manufacturing technologies for piezoelectric transducers 539
K. Uchino, The Pennsylvania State University, USA

15.1 Introduction 539
15.2 Transducer designs 539
15.3 Acoustic lens and horn 547
15.4 Acoustic impedance matching 550
15.5 Ultrasonic imaging application 551
15.6 Sono-chemistry 554
15.7 Acknowledgements 554
15.8 References 557

Part III Application oriented materials development

16 High power piezoelectric materials 561
K. Uchino, The Pennsylvania State University, USA

16.1 Introduction 561
16.2 General consideration of loss and hysteresis in piezoelectrics 563
16.3 Heat generation in piezoelectrics 578
16.4 Loss mechanisms in piezoelectrics 580
16.5 High power piezoelectric ceramics 587
16.6 High power piezoelectric components 592
16.7 Summary and conclusions 594
16.8 Acknowledgement 597
16.9 References 597

17 Photostrictive actuators using piezoelectric materials 599
K. Uchino, The Pennsylvania State University, USA

17.1 Introduction 599
17.2 Photovoltaic effect 600
17.3 Photostrictive effect 612
17.4 Photostrictive device applications 619
17.5 Conclusions 624
17.6 References 626

18 The performance of piezoelectric materials under stress 628
C. S. Lynch, University of California, Los Angeles, USA

18.1 Introduction 628
18.2 The unit cell, ferroelectricity, and ferroelasticity 630
18.3 Driving forces for polarization reorientation 635
18.4 Polarization as an order parameter 638
18.5 Groups of unit cells, defects, and domains 641
18.6 The large field behavior of relaxor single crystals 643
18.7 Calculation of 'domain engineered' properties 645
18.8 Field driven phase transformations 648
18.9 The large filed behavior of ferroelectric ceramics 651
18.10 Preisach modelling 652
18.11 Future trends 655
18.12 References 656

Index 660

Contributor contact details

(* = main contact)

Editor and Chapters 1, 3, 9, 10, 11, 15, 16 and 17

Kenji Uchino
International Center for Actuators and Transducers
The Pennsylvania State University
University Park
PA 16802
USA

E-mail: kenjiuchino@psu.edu

and

Micromechatronics Inc.
State College
PA 16801
USA

Chapter 2

Masahiko Kimura, Akira Ando and Yukio Sakabe*
Murata Manufacturing Co., Ltd
10-1 Higashikotari 1-chome
Nagaokakyo-shi
Kyoto 617-8555
Japan

E-mail: 725223ys@murata.co.jp

Chapter 4

Tadashi Takenaka
Faculty of Science and Technology
Tokyo University of Science
2641 Yamazaki
Noda
Chiba-ken 278-8510
Japan

E-mail: tadashi@ee.noda.tus.ac.jp

Chapter 5

Yasutaka Saigusa
Director, R&D Department
River Eletec Corporation
2-1-11, Fujimigaoka
Nirasaki
Yamanashi 407-8502
Japan

E-mail: Y-SAIGUSA@river-ele.co.jp
ysaigusa@kch.biglobe.ne.jp

Chapter 6

Vladimir Ya. Shur
Institute of Physics and Applied Mathematics
Ural State University
51 Lenin Ave
Ekaterinburg
Russia

E-mail: vladimir.shur@usu.ru

Chapter 7

Laihui Luo
Department of Physics
Ningbo Universtity
Ningbo 315211
China

and

Shanghai Institute of Ceramics
215 Chenbei Road Jiading
Shanghai, 201800
China

E-mail: llhsic@126.com

Xiangyong Zhao, Haosu Luo*
Shanghai Institute of Ceramics
215 Chenbei Road Jiading
Shanghai, 201800
China

E-mail: hsluo@mail.sic.ac.cn

Chapter 8

Yoseph Bar-Cohen
Jet Propulsion Laboratory (JPL)
California Institute of Technology
4800 Oak Grove Drive
M/S 67-119
Pasadena, CA 91109
USA

E-mail: yosi@jpl.nasa.gov

Chapter 12

Leong-Chew Lim
Department of Mechanical Engineering
National University of Singapore
9 Engineering Drive 1
Block EA, 07–08
Singapore 117576

E-mail: mpelimlc@nus.edu.sg

and

Microfine Materials Technologies Pte Ltd
10 Bukit Batok Crescent,
06–02 The Spire
Singapore 658079
Singapore

Chapter 13

Kiyotaka Wasa
Kyoto University
Sakyo-ku
Kyoto 606-8502
Japan

E-mail: kiyotkw@hi-ho.ne.jp

Chapter 14

Jun Akedo
National Institute of Advanced Industrial Science and Technology
Tsukuba
Ibaraki 305-8561
Japan

E-mail: akedo-j@aist.go.jp

Chapter 18

Christopher S. Lynch
University of California Los Angeles
Box 951597
46-147G Eng IV
Los Angeles, CA 90095-1597
USA

E-mail: cslynch@seas.ucla.edu

Preface

Research and development (R&D) trends go in cycles, rather, like 'history repeating itself'. Booms in materials (metal, ceramic, or polymer) tend to have a cycle of 25–30 years, close to one human generation, with some time lags like a three-phase alternating current. When I was a child, we had a 'New Steel Age' for constructing ships, buildings, and power plants following World War II. Synthetic polymers exemplified by nylon were popular for use in stockings, clothes, etc., creating a 'polymer boom' in the 1960s, which pushed forward Japanese economic power in the world. The 'New Stone Age', that is, silicon devices and 'fine ceramics' (including lead zirconate titanate, PZT) came in the 1970s. US economic power declined during that period, after the collapse of the Bretton Woods agreement. An improved metal age arrived in the 1980s, exemplified by 'amorphous' and 'whiskers' (micro size single crystals). This led to the gradual collapse of old fashioned steel companies such as US Steel and Nippon Steel. The second cycle 'polymer boom' started in the 1990s, coupled with micro/nano technologies. The leading media include flexible substrates/boards for silicon chips, functional polymers such as photo, electro, stress, temperature active polymers, and bio/medical applications of very thin films based on Langmuir-Blodgett (LB) technologies. We started the twenty-first century by hybridizing all; that is, composites, based on fine fabrication technologies.

Piezoelectricity was discovered by Pierre Curie in 1880. We needed to wait for about 30 years until World War I for its practical application in underwater detecting sonars. Then, after another 30 years, barium titanate (BT) was discovered during World War II, followed by the discovery of PZT, the present key composition, in 1954. At the end of the 'polymer boom', polyvinylidene-difluoride was discovered. Ecological restrictions may terminate the usage of the present Pb-containing piezo-ceramics in the 2010s. As can be seen from this quick overview of the technology history of materials, the R&D trend has been influenced significantly by so-called 'external environmental forces'. These forces can be summarized in the acronym 'STEP': social, technological, economic and political forces.

The editorial philosophy of this book is, therefore: '*Learning the history and forecasting the future*'. This philosophy is based on the following:

- A new product 'you believe' has been tried one generation back.
- Once the development fails, a period of one generation (25 years) is required to restart a similar development.
- Development starts from the application, then moves back to the fundamental research. In most cases, actual applications pull the development of suitable materials (needs-pull model).
- No research will die. It revives after a generation.
- Political/legal forces are stronger than technological ones.

This book is *not* intended to be just an omnibus of review papers, each of which includes primarily each group's own research content. Rather, this book is intended to make a comprehensive textbook for graduate students and junior researchers of piezoelectric materials by *transferring historical aspects comprehensively and correctly, and suggesting future directions*. Of course, it would be difficult to accomplish this desire. So, first, the editor carefully selected authorities in each sub-area of piezoelectric materials and, second, specially asked them to draft their manuscripts according to the editorial philosophy. I also asked my graduate students to evaluate the manuscript quality as a graduate-level textbook, and these comments were fed back to the contributors. Thus each draft has been modified and revised several times.

Acknowledgements

I would like to express my sincere appreciation to the following authorities for their cooperation with this project:

- Drs Yukio Sakabe, Akira Ando and Masahiko Kimura, Murata Mnfg. Co. – PZT-ceramics.
- Prof. Tadashi Takenaka, Tokyo University of Science – Pb-free piezoceramics.
- Mr Yasutaka Saigusa, River Eletec – Quartz.
- Prof. Vladimir Ya. Shur, Ural State University – Lithium niobate, tantalate.
- Profs Haosu Luo, Laihui Luo and Xiangyong Zhao, Shanghai Institute of Ceramics – Single crystals.
- Dr Yoseph Bar-Cohen, Jet Propulsion Lab – Electroactive polymers.
- Prof. Leong Chew Lim, National University of Singapore – Single crystal preparation.
- Prof. Kiyotaka Wasa, Kyoto University – Thin film technologies.
- Dr Jun Akedo, National Institute of Advanced Industrial Science and Technology – Aerosol technique.

- Prof. Christopher S. Lynch, University of California LA – Piezoelectricity under stress.

Chapter 1 is devoted to an overview of piezoelectric materials history, each section of which corresponds to the summaries in the subsequent chapters. Chapter 1 also provides the fundamentals of piezoelectricity, necessary terminologies and equations/formulas, followed by overall applications of piezoelectrics. Part I, Piezoelectric materials, includes Chapter 2 on PZT-based ceramics, Chapter 3 on relaxor ferroelectric ceramics, which are widely used at present, and Chapter 4 on Lead-free piezo-ceramics, which may represent the future, replacing the Pb-containing materials in the next 10 years. Chapter 5 on quartz and Chapter 6 on lithium niobate/tantalate treat traditional single crystals, and explain the present status and future prospects in the twenty-first century communication age. Chapter 7 on single crystal PZN-PT, PMN-PT discusses superior piezoelectricity, i.e., high electromechanical coupling factors, including medical applications. Chapter 8 on electroactive polymers is an exceptional part of this book, treating polymers rather than ceramics. The reader will learn what differentiates them from the piezo-ceramics. The final chapter in Part I, Chapter 9 on piezoelectric composite materials, introduces special features, which are introduced by coupling piezo-ceramics and polymers, starting from the basic principles of composite designing. Manufacturing techniques are also included in this chapter.

Part II, Preparation methods and applications, will answer the practical design and fabrication issues related to piezo-materials. Chapter 10 on piezo-ceramic manufacturing methods covers recent practical manufacturing methods. Chapter 11 describes multilayer technologies, particularly important for manufacturing actuators and transformers. Chapter 12 deals with how to prepare piezoelectric single crystals in general, focusing in particular on PNZ-PT and PMN-PT. In contrast, ‘thin film’ manufacturing technologies are introduced in Chapter 13. Chapter 14 introduces a recent popular ‘thick film’ technology, developed in Asian research groups. Chapter 15 introduces transducer designing and manufacturing technologies.

Part III, Application oriented materials development, includes Chapter 16 on high power piezoelectrics, Chapter 17 on photostrictive actuators, and Chapter 18 on piezoelectric performance under mechanical stress. High power drive generates significant heat generation, while the hysteresis of piezoelectrics is enhanced significantly under high mechanical stress. How to escape from these performance degradation and ageing are discussed in Part III. Photostrictor may be a future material useful in the optical communication age, which is basically originated from a coupling of photovoltaic and piezoelectric effects.

Thanks to the contributing authorities’ sincere efforts, the editor believes that this book covers most of the fundamentals, history and future trends relating to piezoelectric materials. I hope this book will become a standard textbook on advanced piezoelectric materials in most of the related universities and institutes.

Kenji Uchino
Director, International Center for Actuators & Transducers
Professor, Electrical Engineering
The Pennsylvania State University
and
Senior Vice President & CTO
Micromechatronics, Inc.

1

The development of piezoelectric materials and the new perspective

K. UCHINO, The Pennsylvania State University, USA

Abstract: Certain materials produce electric charges on their surfaces as a consequence of applying mechanical stress. The induced charges are proportional to the mechanical stress. This is called the *direct piezoelectric effect* and was discovered in quartz by Pierre and Jacques Curie in 1880. Materials showing this phenomenon also conversely have a geometric strain proportional to an applied electric field. This is the *converse piezoelectric effect*, discovered by Gabriel Lippmann in 1881. This article first reviews the historical episodes of piezoelectric materials in the sequence of quartz, Rochelle salt, barium titanate, PZT, lithium niobate/tantalate, relaxor ferroelectrics, PVDF, Pb-free piezoelectrics, and composites. Then, the detailed performances are described in the following section, which serves as the introduction to each chapter in this book. Third, since piezoelectricity is utilized extensively in the fabrication of various devices such as transducers, sensors, actuators, surface acoustic wave devices, frequency control, etc., applications of piezoelectric materials are introduced briefly in conjunction with materials. The author hopes that the reader can 'learn the history aiming at creating a new perspective for the future of piezoelectric materials'.

Key words: piezoelectric material, quartz, Rochelle salt, barium titanate, lead zirconate titanate, relaxor ferroelectrics, Pb-free piezoelectrics, electromechanical coupling factor.

1.1 The history of piezoelectrics

Any material or product has a lifecycle, which is determined by various 'external' environmental forces, which can be summarized under the acronym STEP (**S**ocial/cultural, **T**echnological, **E**conomic, and **P**olitical).[1] We will observe first how these forces encouraged/discouraged the development of piezoelectric materials.

1.1.1 The dawn of piezoelectrics

The Curie brothers (Pierre and Jacques Curie) discovered the *direct piezoelectric effect* in single crystal quartz in 1880. Under pressure, quartz generated an electrical charge/voltage from quartz and other materials. The root of the word 'piezo' means 'pressure' in Greek; hence the original meaning of the word piezoelectricity implied 'pressure electricity'. Materials showing this phenomenon also conversely have a geometric strain proportional to an applied electric field. This is the *converse piezoelectric effect*, discovered by Gabriel Lippmann in 1881. Recognizing the connection between the two phenomena helped Pierre Curie to develop pioneering ideas about the fundamental role of symmetry in the laws of physics. Meanwhile, the Curie brothers put their discovery to practical use by devising the piezoelectric quartz electrometer, which could measure faint electric currents, and helped Pierre's wife, Marie Curie, 20 years later in her early research.

It was at 11.45 pm on 10 April 1912 that the tragedy of the sinking of the *Titanic* happened (see Fig. 1.1). As the reader knows well, this was caused by an iceberg hidden in the sea. If the ultrasonic sonar system had been developed, it would not have happened. Owing to this tragic incident (social force), ultrasonic technology development was motivated, using piezoelectricity.

1.1.2 World War I: underwater acoustic devices with quartz and Rochelle salt

The outbreak of World War I in 1914 led to real investment to accelerate the development of ultrasonic technology in order to search for German U-Boats

1.1 The sinking of the *Titanic* was caused by an iceberg in the sea.

under the sea. The strongest forces both in these developments were social and political. Dr Paul Langevin, a professor at the Industrial College of Physics and Chemistry in Paris, who had a wide circle of friends including Drs Albert Einstein, Pierre Curie, Ernest Rutherford, among others, started experiments on ultrasonic signal transmission into the sea, in collaboration with the French Navy. Langevin succeeded in transmitting an ultrasonic pulse into the sea off the coast of southern France in 1917. We can learn most of the practical development approaches from this original transducer design (Fig. 1.2). First, 40 kHz was chosen for the sound wave frequency. Increasing the frequency (shorter wavelength) leads to the better monitoring resolution of the objective; however, it also leads to a rapid decrease in the reachable distance. Notice that quartz and Rochelle salt single crystals were the only available piezoelectric materials in the early twentieth century. Since the sound velocity in quartz is about 5 km/s, 40 kHz corresponds to the wavelength of 12.5 cm in quartz. If we use a mechanical resonance in the piezoelectric material, a 12.5/2 = 6.25 cm thick quartz single crystal piece is required. However, in that period, it was not possible to produce such large high-quality single crystals.[2]

In order to overcome this dilemma, Langevin invented a new transducer construction; small quartz crystals arranged in a mosaic were sandwiched by two steel plates. Since the sound velocity in steel is in a similar range to quartz, taking 6.25 cm in total thickness, he succeeded to set the thickness resonance frequency around 40 kHz. This sandwich structure is called

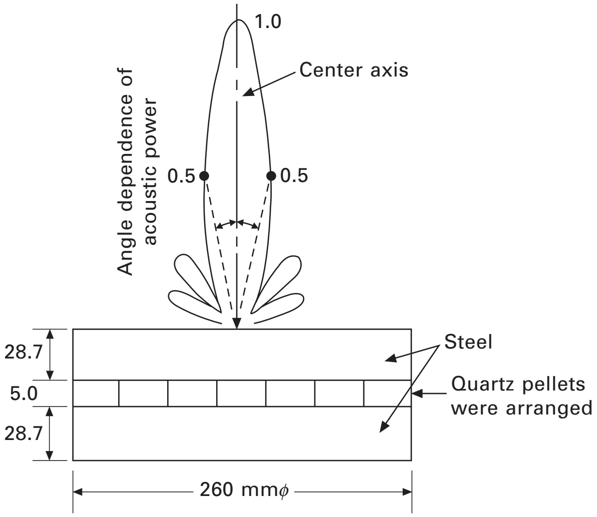
1.0
Center axis
Angle dependence of acoustic power
0.5
0.5
28.7
5.0
28.7
Steel
Quartz pellets were arranged
260 mmϕ

1.2 Original design of the Langevin underwater transducer and its acoustic power directivity.

'***Langevin type***' and remains popular even today. Notice that quartz is located at the center, which corresponds to the nodal plane of the thickness vibration mode, where the maximum stress/strain (or the minimum displacement) is generated.

Further, in order to provide a sharp directivity for the sound wave, Langevin used a sound radiation surface with a diameter of 26 cm (more than double that of the wavelength). Since the half maximum power angle ϕ can be evaluated as

$$\phi = 30 \times (\lambda/2a) \text{ [degree]}, \tag{1.1}$$

where λ is the wavelength in the transmission medium (not in steel) and a is the radiation surface radius, if we use λ = 1500 m/s/40 kHz = 3.75 cm, a = 13 cm, we obtain ϕ = 4.3° for this original design. He succeeded in practice in detecting the U-Boat 3000 m away. Moreover, Langevin also observed many bubbles generated during his experiments, which seems to be the 'cavitation' effect, which was utilized for ultrasonic cleaning systems some 60 years later.

Though the mechanical quality factor is significantly high (i.e., low loss) in quartz, its major problems for this transducer application include its low electromechanical coupling k, resulting in (1) low mechanical underwater transmitting power and receiving capability, and (2) narrow frequency bandwidth, in addition to the practical fact that only Brazil produced natural quartz crystals at that time. Thus, US researchers used Rochelle salt single crystals, which have a superior electromechanical coupling factor (k is close to 100% at 24 °C!) with a simple synthesizing process. Nicholson,[3] Anderson, and Cady undertook research on the piezoelectric underwater transducers during World War I. General Electric Laboratory (Moore[4]) and Brush Company produced large quantities of crystals in the early 1920s. The detailed history of Rochelle salt can be found in Ref. 5.

Rochelle salt is sodium potassium tartrate [$NaKC_4H_4O_6 \cdot 4H_2O$], and has two Curie temperatures at –18 °C and 24 °C with a narrow operating temperature range for exhibiting ferroelectricity, leading to high electromechanical coupling at 24 °C, on the other hand, rather large temperature dependence of the performance. It was used worldwide for underwater transducer applications until barium titanate and lead zirconate titanate (PZT) were discovered. Since this crystal is water-soluble, it is inevitable that it is degraded by humidity. However, the most delicate problem is its weakness to dryness. Thus, no researcher was able to invent the best coating technology for the Rochelle salt devices to achieve the required lifetime.

Many efforts to discover alternative piezoelectrics to Rochelle salt with better stability/reliability continued after World War I. Potassium di-hydrogen phosphase (KH_2PO_4 or KDP) was discovered by Georg Busch in 1935.[6] Knowing the ferroelectricity of Rochelle salt, and guessing the origin to be from the hydrogen bonds in the crystal, Busch searched hydrogen-bond crystals systematically and found KDP as a new ferroelectric/piezoelectric. Though many piezoelectric materials (such as Rochelle salt, barium titanate, and PVDF) were discovered by chance, KDP is an exceptional example of a discovery created by a perfectly planned systematic approach. Following KDP, ADP, EDT and DKT, amongst others, were discovered and examined. However, most of the water-soluble single crystal materials have been forgotten because of the performance and preparation improvements in synthetic quartz and perovskite ceramics (BT, PZT).

1.1.3 World War II: discovery of barium titanate

Barium titanate ($BaTiO_3$, BT) ceramics were discovered independently by three countries: US, Japan and Russia during World War II: E. Wainer and N. Salomon[7] in 1942, T. Ogawa[8] in 1944, and B. M. Vul[9] in 1944. Compact radar system development required compact high capacitance ‘condensers’ (the term ‘condenser’, rather than ‘capacitor’ was used at that time). Based on the widely used ‘Tita-Con’ (titania condenser) composed of TiO_2-MgO, researchers doped various oxides to find higher permittivity materials. According to the memorial article authored by Ogawa and Waku,[10] they investigated three dopants, CaO, SrO, and BaO in a wide fraction range. They found a maximum permittivity around the composition $CaTiO_3$, $SrTiO_3$ and $BaTiO_3$ (all were identified as perovskite structures). In particular, the permittivity, higher than 1000, in $BaTiO_3$ was enormous (10 times higher than that in Tita-Con) at that time, as illustrated in Fig. 1.3.

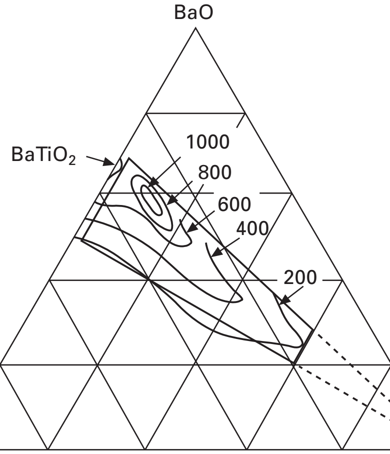

1.3 Permittivity contour map on the MgO-TiO_2-BaO system, and the patent coverage composition range (dashed line).[10]

It should be pointed out that the original discovery of $BaTiO_3$ was not related to piezoelectric properties. Equally important are the independent discoveries by R. B. Gray at Erie Resister (patent applied for in 1946)[11] and by Shepard Roberts at MIT (published in 1947)[12] that the electrically-poled BT exhibited ‘piezoelectricity’ owing to the domain re-alignment. At that time, researchers were arguing that the randomly-oriented ‘polycrystalline’ sample should not exhibit ‘piezoelectricity’, but the secondary effect, ‘electrostriction’. In this sense, Gray is the ‘father of piezoceramics’, by being first to verify that the polycrystalline BT exhibited piezoelectricity once it was electrically poled.

The ease in composition selection and in manufacturability of BT ceramics prompted W. P. Mason[13] and others to study the transducer applications using these electro-ceramics. Piezoelectric BT ceramics had reasonably high coupling coefficient and non-water solubility, but the bottlenecks were (1) a large temperature coefficient of electromechanical parameters because of the second phase transition (from tetragonal to rhombohedral) around room temperature or operating temperature, and (2) aging effect due to the low Curie temperature (phase transition from cubic to tetragonal) around only 120 °C. In order to increase the Curie temperature higher than 120 °C, and to decrease the second transition temperature below –20 °C, various ion replacements, such as Pb and Ca, were studied. From these trials, a new system PZT was discovered.

By the way, it is worth noting that the first multilayer capacitor was invented by Sandia Research Laboratory engineers under the Manhattan Project with the coating/pasting method for the switch of the Hiroshima nuclear bomb (private communication with Dr Kikuo Wakino, Murata Mnfg).

1.1.4 The discovery of lead zirconate titanate (PZT)

PZT

Following the methodology taken for the BT discovery, the perovskite isomorphic oxides such as $PbTiO_3$, $PbZrO_3$, and $SrTiO_3$ and their solid solutions were intensively studied. In particular, the discovery of ‘antiferroelectricity’ in lead zirconate[14] and the determination of the $Pb(Zr,Ti)O_3$ system phase diagram[15] by the Japanese group, E. Sawaguchi, G. Shirane and Y. Takagi are noteworthy. Figure 1.4 shows the phase diagram of the $Pb(Zr,Ti)O_3$ solid solution system reported by E. Sawaguchi, which was read and cited worldwide, and triggered the PZT era.

A similar discovery history to that of barium titanate was repeated for the lead zirconate titanate system. The material was discovered by the Japanese researcher group, but the discovery of its superior piezoelectricity was conducted by a US researcher Bernard Jaffe in 1954. B. Jaffe worked

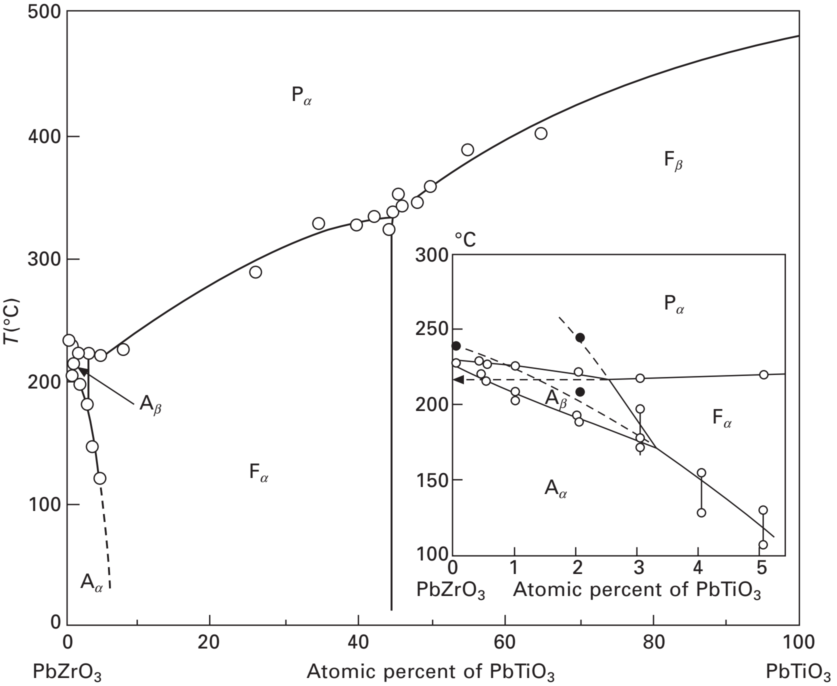

1.4 Phase diagram for the $Pb(Zr,Ti)O_3$ solid solution system proposed by E. Sawaguchi.[15] We now know another ferroelectric phase below the F_α phase.

at the National Bureau of Standards at that time. He knew well the Japanese group's serial studies on the PZT system, and focused on the piezoelectric measurement around the so-called MPB (morphotropic phase boundary) between the tetragonal and rhombodedral phases, and found enormous electromechanical coupling around that composition range.[16] His patent had a significant effect on the future development strategies of Japanese electroceramic industries. It is important to remember two important notions for realizing superior piezoelectricity: (1) Pb-included ceramics, and (2) MBP compositions.

Clevite corporation

As mentioned above, Brush Development Company manufactured Rochelle salt single crystals and their bimorph components for phonograph applications in the 1930s, and in the 1940s they commercialized piezoelectric quartz crystals by using a hydrothermal process. There was a big piezoelectric group in Brush lead by Hans Jaffe. However, in 1952 the Clevite Corporation was formed by merging the Cleveland Graphite Bronze Corporation and Brush, and H. Jaffe welcomed B. Jaffe from NBS to Clevite and accelerated the PZT business. Their contribution to developing varieties of PZTs (i.e., hard and soft PZTs) by doping acceptor (Mn) and donor (Nb) ions is noteworthy. By the way, 'PZT' was the trademark of Clevite and had not been used by other companies previously, and Hans Jaffe and Bernard Jaffe were not related at all (just by chance having the same last name). These episodes are described in their famous book *Piezoelectric Ceramics*.[11]

Clevite first concentrated on high quality military and commercial piezoelectric filters. In the mid 1960s, they tried to develop consumer filters for AM radios, especially automobile radios, but this was not commercially viable initially. However, after 1967, they successfully started mass production of 10.7 MHz ceramic filters for FM automobile radios, and delivered them to Philco-Ford. Clevite was bought by Gould Inc. in 1969, and resold to Vernitron in 1970. These drastic business actions terminated the promising piezoelectric filter program initiated by Clevite.

Murata Manufacturing Company

The Murata Manufacturing Co. Ltd was founded by A. Murata in 1944. He learned ceramic technology from his father who was the Chairman of the former Murata Pottery Manufacturing Co. Murata Manufacturing Company was started with 10 employees to produce electro-ceramic components. After World War II, under the guidance of Prof. Tetsuro Tanaka, who was one of the promoters of the Barium Titanate Study Committee during World War II, Murata started intensive studies on devices based on barium titanate ceramics. The first products with barium titanate ceramics were 50 kHz Langevin-type underwater transducers for fish-finders in Japan.[17] The second products were mechanical filters.[18]

In 1960, Murata decided to introduce PZT ceramics by paying a royalty to Clevite Corporation. As already mentioned in the previous section, because of the disappearance of Clevite from the filter business, Murata increased their worldwide share in the ceramic filter products market.

Ternary system

Since PZT was protected by Clevite's US patent subsequently, ternary solid solutions based on PZT with another perovskite phase were investigated intensively by Japanese ceramic companies in the 1960s. Examples of these ternary compositions are: PZTs in solid solution with $Pb(Mg_{1/3}Nb_{2/3})O_3$ (Matsushita-Panasonic), $Pb(Zn_{1/3}Nb_{2/3})O_3$ (Toshiba), $Pb(Mn_{1/3}Sb_{2/3})O_3$, $Pb(Co_{1/3}Nb_{2/3})O_3$, $Pb(Mn_{1/3}Nb_{2/3})O_3$, $Pb(Ni_{1/3}Nb_{2/3})O_3$ (NEC), $Pb(Sb_{1/2}Sn_{1/2})O_3$, $Pb(Co_{1/2}W_{1/2})O_3$, $Pb(Mg_{1/2}W_{1/2})O_3$ (Du Pont), all of which were patented by different companies (almost all composition patents have already expired). The ternary systems with more material designing flexibility exhibited in general better performance than the binary PZT system, which created advantages for Japanese manufacturers over Clevite and other US companies.

1.1.5 Lithium niobate/tantalate

Lithium niobate and tantalate have the same chemical formula ABO_3 as $BaTiO_3$ and $Pb(Zr,Ti)O_3$. However, the crystal structure is not perovskite, but ilmenite. Ferroelectricity in single crystals of $LiNbO_3$ (LN) and $LiTaO_3$ (LT) was discovered in 1949 by two researchers in Bell Telephone Laboratories, B. T. Matthias and J. P. Remeika.[19] Since the Curie temperatures in these materials are high (1140 °C and 600 °C for LN and LT, respectively), perfect linear characteristics can be observed in electrooptic, piezoelectric and other effects at room temperature. Though fundamental studies had been conducted, particularly into their electrooptic and piezoelectric properties, commercialization was not accelerated initially because the figure of merit was not very attractive in comparison with perovskite ceramic competitors. (Cb (columbium) was the former name of the chemical element 'niobium' in the 1950s.)

Since Toshiba, Japan, started mass production of LN single crystals after the 1980s, dramatic production cost reductions were achieved. Murata commercialized filters, so-called 'SAW filters', by using surface acoustic wave mode on the LN single crystal. Recent developments in electrooptic light valves, switches, and photorefractive memories, which are encouraged by optical communication technologies, can be found in Ref. 20.

1.1.6 Relaxor ferroelectrics: ceramics and single crystals

After the discovery of barium titanate and PZT, in parallel to the PZT-based ternary solid solutions, complex perovskite structure materials were intensively synthesized and investigated in the 1950s. In particular, the contributions by the Russian research group led by G. A. Smolenskii were enormous. Among them, huge dielectric permittivity was reported in $Pb(Mg_{1/3}Nb_{2/3})O_3$ (PMN)[21] and $Pb(Zn_{1/3}Nb_{2/3})O_3$ (PZN).[22] PMN-based ceramics became major compositions for high *k* (10,000) capacitors in the 1980s.

It is noteworthy to introduce two epoch-making discoveries in the late 1970s and early 1980s, relating to electromechanical couplings in the relaxor ferroelectrics: electrostrictive actuator materials and high *k* (95%) piezoelectric single crystals.

Cross *et al.* reported extraordinarily large secondary electromechanical coupling, i.e., 'electrostrictive' effect, with the strain level higher than 0.1% at room temperature, exhibiting negligible hysteresis during rising and falling electric field, in a composition 0.9 PMN–0.1 $PbTiO_3$ (See Fig. 1.5).[23] Every phenomenon has primary and secondary effects, which are sometimes recognized as linear and quadratic phenomena, respectively. In actuator materials, these correspond to the 'piezoelectric' and 'electrostrictive' effects.

When the author started actuator research in the middle of the 1970s, precise 'displacement transducers' (we initially used this terminology) were required in the Space Shuttle program, particularly for 'deformable mirrors', for controlling the optical pathlengths over several wavelengths (1 micron). Conventional piezoelectric PZT ceramics were plagued by hysteresis and aging effects under large electric fields; this was a serious problem for an optical positioner. Electrostriction, which is the secondary electromechanical coupling observed in centro-symmetric crystals, is not affected by hysteresis or aging.[20] Piezoelectricity is a primary (linear) effect, where the strain is generated in proportion to the applied electric field, while the electrostriction is a secondary (quadratic) effect, where the strain is in proportion to the square of the electric field (parabolic strain curve). Their response should be much faster than the time required for domain reorientation in piezoelectrics/ferroelectrics. In addition, electric poling is not required. However, at that time, most people believed that the secondary effect would be minor, and could not provide a larger contribution than the primary effect. Of course, this may be true in most cases, but the author's group actually discovered that relaxor ferroelectrics, such as the lead magnesium niobate-based solid

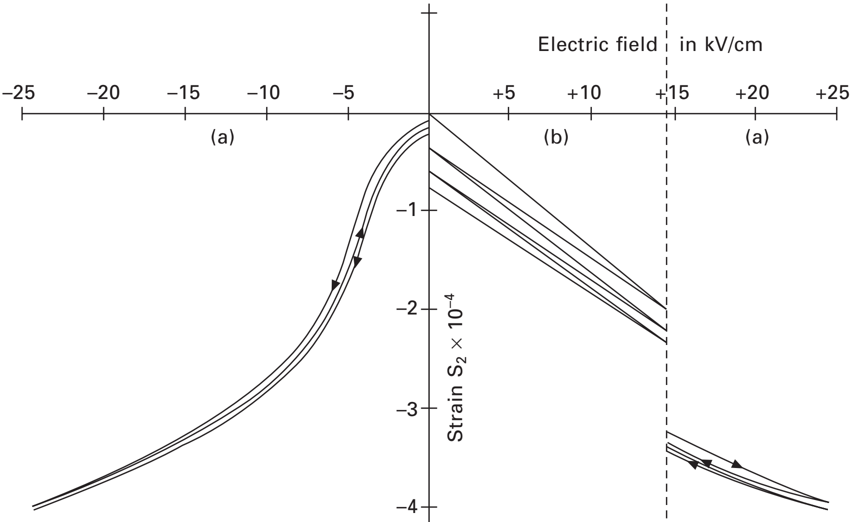

1.5 Transverse strain in ceramic specimens of 0.9PMN–0.1PT (a) and a typical hard PZT 8 piezoceramic (b) under varying electric fields.[23]

solutions exhibit enormous electrostriction. This discovery, in conjunction with the author's multilayer actuator invention (1978), accelerated the development of piezoelectric actuators after the 1980s.

Prof. S. Nomura's group was interested in making single crystals of PZT in the 1970s, in order to clarify the crystal orientation dependence of piezoelectricity. However, it was difficult to prepare large single crystals around the morphotropic phase boundary compositions (52/48). Thus, we focused on the $Pb(Zn_{1/3}Nb_{2/3})O_3$–$PbTiO_3$ solid solution system, which has a phase diagram similar to the PZT system, but large single crystals are more easily prepared. See the MPB between the rhombohedral and tetragonal phases in Fig. 1.6, in comparison with Fig. 1.4.[24] Figure 1.7 shows changes of electromechanical coupling factors with mole fraction of PT in the $Pb(Zn_{1/3}Nb_{2/3})O_3$–$PbTiO_3$ solid solution system, reported by J. Kuwata, K. Uchino and S. Nomura in 1982,[25] which was best cited in 1998. Note that the MPB composition, 0.91 PZN–0.09 PT, exhibited the maximum for all parameters, as expected, but the highest values in electromechanical coupling factor k_{33}* and the piezoelectric constant d_{33}* reached 95% and 1600 pC/N. When a young Ph.D. student, J. Kuwata, first reported these results to the author, even I myself could not believe these large numbers. Thus, we worked together to re-examine the experiments. When I saw the antiresonance frequency almost twice the resonance frequency, I needed to believe the incredibly high k value. The author still remembers that the first submission of our manuscript was rejected because the referee could not

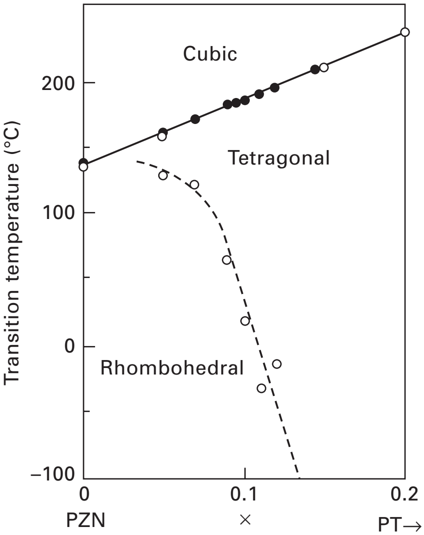

1.6 Phase diagram for the Pb $(Zn_{1/3}Nb_{2/3})O_3$–$PbTiO_3$ solid solution system.

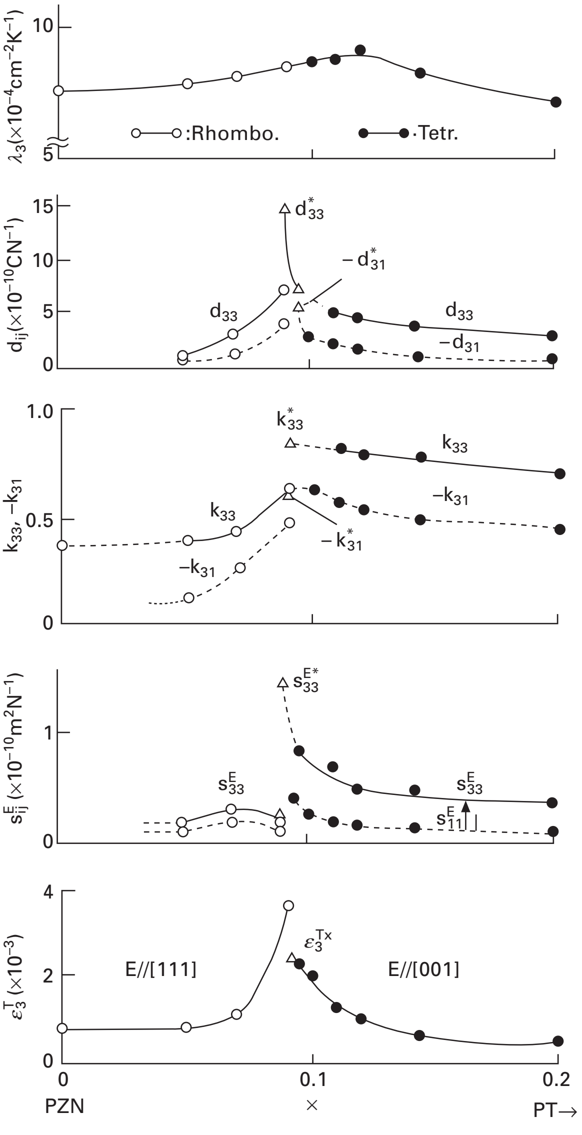

1.7 Changes of electromechanical coupling factors with mole fraction of PT in the Pb $(Zn_{1/3}Nb_{2/3})O_3$–$PbTiO_3$ solid solution system.

'believe this large value'. The maximum k_{33} in 1980 was about 72% in PZT-based ceramics. The paper was published after a year-long communication by sending the raw admittance curves, etc. However, our original discovery was not believed or not required for applications until the middle of the 1990s.

Economic recession and an aging demographic (the average life expectancy reached close to 85 years old) in Japan accelerated medical technologies, and high *k* piezoelectric materials have been paid attention in medical acoustics since the middle of the 1990s. Toshiba started re-investigation of PZN-PT single crystals, with a strong crystal manufacturing background of lithium niobate in the 1980s. The data reported 15 years earlier have been reconfirmed, and improved data were obtained, aiming at medical acoustic applications.[26] In parallel, S. E. Park and T. R. Shrout at The Pennsylvania State University demonstrated strains as large as 1.7% induced practically for the PZN-PT solid solution single crystals.[27] There is considerable interest at present in the application of these single crystals, sponsored by the US Navy. The single crystal relaxor ferroelectric is one of the rare examples where interest has been revived 15 years after the original discovery.

It is notable that the highest values are observed for a rhombohedral composition only when the single crystal is poled along the perovskite [001] axis, not along the [111] spontaneous polarization axis. Figure 1.8 illustrates an intuitive principle model in understanding this piezoelectricity enhancement depending on the crystal orientation in perovskite ferroelectrics. The key is the largest electromechanical coupling for the d_{15} shear mode in perovskite structures, because of the easy rotation of the oxygen octahedron, in comparison with the squeeze deformation of the octahedron. The reader can refer to the theoretical paper (Ref. 28) authored by X. H. Du, U. Belegundu and K. Uchino, which was also one of the most cited papers in 1998.

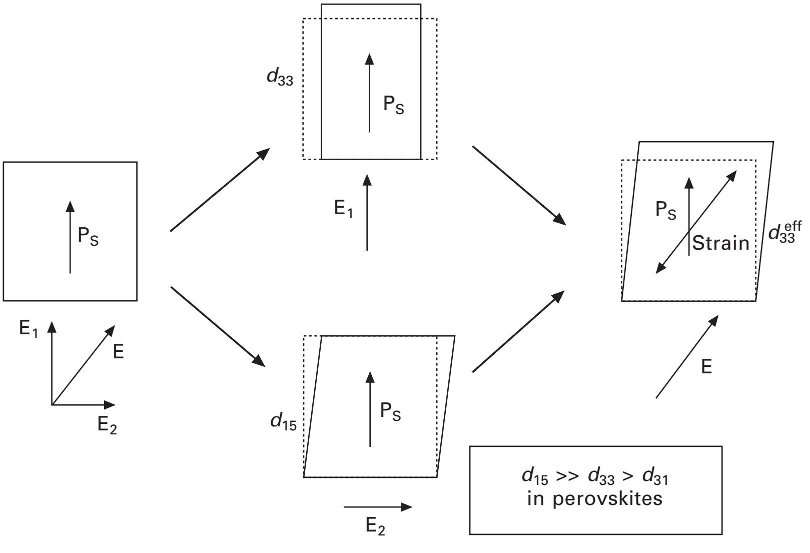

1.8 The intuitive principle model in understanding the piezoelectricity enhancement depending on the crystal orientation in perovskite ferroelectrics.

1.1.7 Piezoelectricity of polyvinylidene difluoride (PVDF)

In 1969, the piezoelectricity of polyvinylidene difluoride, PVDF, was discovered by H. Kawai at Kureha.[29] The piezoelectric coefficients of poled thin films of the material were reported to be as large as 6–7 pCN^{-1}, 10 times larger than that observed in any other polymer.

PVDF has a glass transition temperature (T_g) of about –35 °C and is typically 50–60% crystalline. To give the material its piezoelectric properties, it is mechanically stretched to orient the molecular chains and then poled under tension. Unlike other popular piezoelectric materials, such as PZT, PVDF has a negative d_{33} value. Physically, this means that PVDF will compress instead of expand or vice versa when exposed to the same electric field. PVDF-trifluoroethylene (PVDF-TrFE) copolymer is a well-known piezoelectric, which has been popularly used in sensor applications such as keyboards.

Bharti *et al.* reported that the field induced strain level can be significantly enhanced up to 5% by using a high-energy electron irradiation onto the PVDF films.[30]

1.1.8 Pb-free piezoelectrics

The twenty-first century has been called ‘the century of environmental management’. We are facing serious global problems such as the accumulation of toxic wastes, the *greenhouse effect*, contamination of rivers and seas, lack of energy resources, oil, natural gas, etc. In 2006, the European Community started RoHS (Restrictions on the use of certain Hazardous Substances), which explicitly limits the usage of lead (Pb) in electronic equipment. The net result is that we may need to regulate the usage of lead zirconate titanate (PZT), the most famous piezoelectric ceramic, in the future. Governmental regulation on PZT usage may be introduced in Japan and Europe in the next 10 years. RoHS seems to be a significant threat to piezoelectric companies who have only PZT piezo-ceramics. However, this also represents an opportunity for companies which are preparing alternative piezoceramics for the piezoelectric device market.

Pb (lead)-free piezoceramics started to be developed after 1999. Figure 1.9 shows statistics of various lead-free piezoelectric ceramics. The share of the papers and patents for bismuth compounds (bismuth layered type and $(Bi,Na)TiO_3$ type) exceeds 61%. This is because bismuth compounds are easily fabricated in comparison with other compounds. Figure 1.10 shows the current best data reported by Toyota Central Research Lab, where strain curves for oriented and unoriented (K, Na, Li) $(Nb, Ta, Sb)O_3$ ceramics are shown.[31] Note that the maximum strain reaches up to 1500×10^{-6}, which is equivalent to the PZT strain.

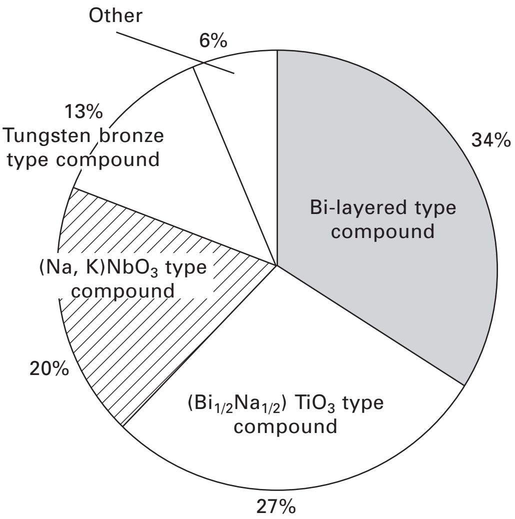

1.9 Patent disclosure statistics for lead-free piezoelectric ceramics (total number of patents and papers is 102).

1.1.9 Composites

Composite effects

T. Kitayama and S. Sugawara, Nippon Telegraph and Telephone, reported on piezoceramic–polymer composites at the Japan IEEE Conference in 1972, which would appear to be the first paper on piezoelectric-based composites.[32] As shown in Fig. 1.11, their paper dealt with the hot-rolled composites made from PZT powder and PVDF, and reported on the piezoelectric and pyroelectric characteristics. Flexibility similar to PVDF, but higher piezoelectric performance than PVDF was obtained.

Robert E. Newnham's contribution to establishing the composite connectivity concept, and the summary of sum, combination, and product effects promoted the systematic studies in the piezo-composite field.[33] In certain cases, the averaged value of the output of a composite does exceed both outputs of Phase 1 and Phase 2. Let us consider two different outputs, Y and Z, for two phases (i.e., Y_1, Z_1; Y_2, Z_2). When a *figure of merit* (FOM) for an effect is provided by the fraction (Y/Z), we may expect an extraordinary effect. Suppose that Y and Z follow the convex and concave type sum effects, respectively, as illustrated in Fig. 1.12, the combination value Y/Z will exhibit a maximum at an intermediate ratio of phases; that is, the average FOM is higher than either end member FOMs (Y_1/Z_1 or Y_2/Z_2). This was called a '*combination effect*'. Newnham's group studied various connectivity piezoceramic/polymer composites, which exhibited a combination property of g (the *piezoelectric voltage constant*) which is provided by $d/\varepsilon_0\varepsilon$ (d: piezoelectric strain constant,

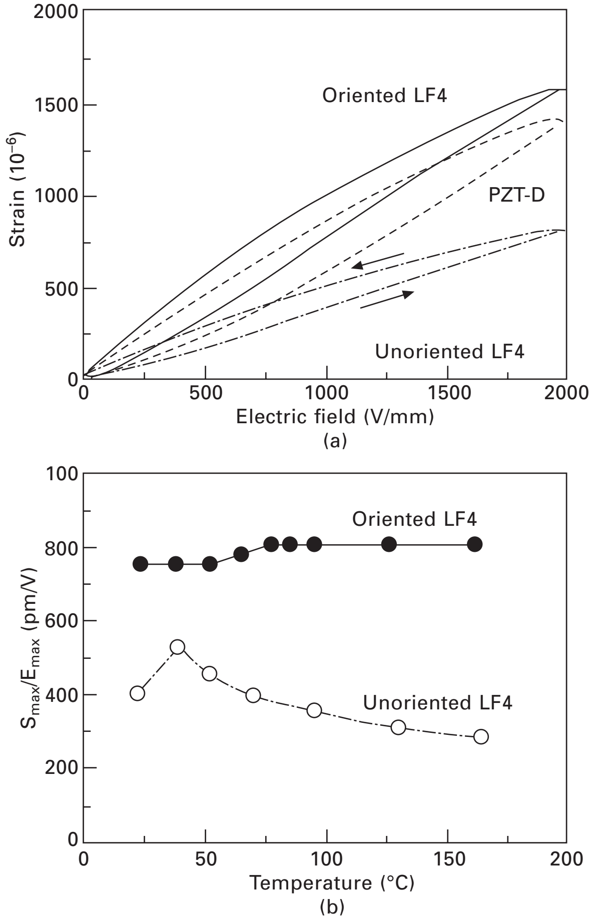

(a)

(b)

1.10 Strain curves for oriented and unoriented (K, Na, Li) (Nb, Ta, Sb) O_3 ceramics.[31]

and ε: relative permittivity), where *d* and ε follow the convex and concave type sum effects.

Magnetoelectric composites

When Phase 1 exhibits an output *Y* with an input *X*, and Phase 2 exhibits an output *Z* with an input *Y*, we can expect a composite which exhibits an output *Z* with an input *X*. A completely new function is created for the composite structure, called a '*product effect*'.

Philips developed a magnetoelectric material based on the product effect concept,[34] which exhibits electric voltage under the magnetic field application, aiming at magnetic field sensor. This material was composed

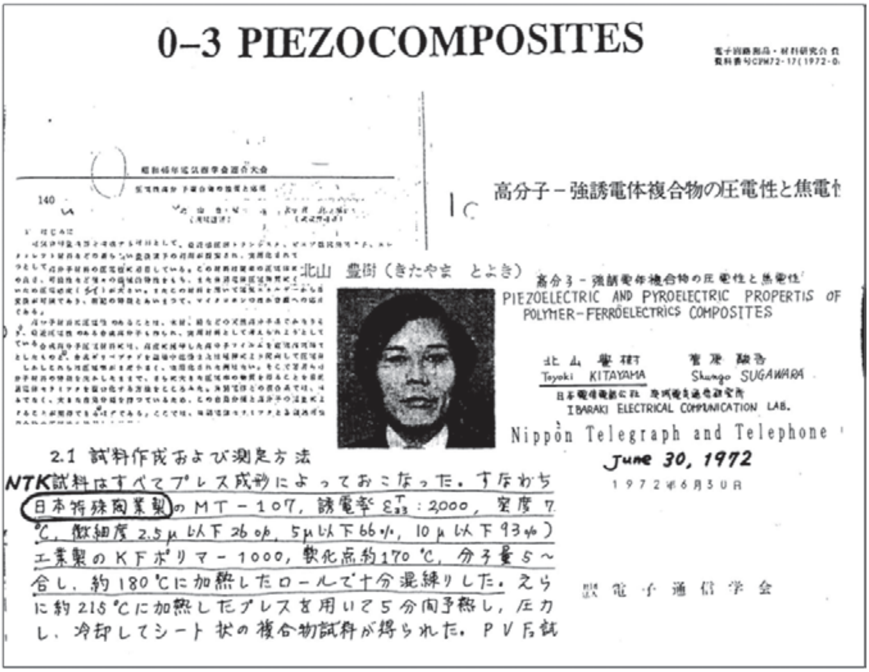

0–3 PIEZOCOMPOSITES

140

1c 高分子－強誘電体複合物の圧電性と焦電

北山 豊樹（きたやま とよき）

高分子－強誘電体複合物の圧電性と焦電性
PIEZOELECTRIC AND PYROELECTRIC PROPERTIS OF
POLYMER-FERROELECTRICS COMPOSITES

北山 豊樹　菅原 駿吾
Toyoki KITAYAMA　Shungo SUGAWARA
日本電信電話公社 茨城電気通信研究所
IBARAKI ELECTRICAL COMMUNICATION LAB.

Nippon Telegraph and Telephone

June 30, 1972

1972年6月30日

電子通信学会

2.1 試料作成および測定方法

NTK試料はすべてプレス成形によっておこなった。すなわち
日本特殊陶業製のMT－107，誘電率 ε_{33}^{T}：2000，密度7.
℃，微細度2.5μ以下26%，5μ以下66%，10μ以下93%）
工業製のKFポリマー－1000，軟化点約170℃，分子量5～
合し，約180℃に加熱したロールで十分混練りした。さら
に約215℃に加熱したプレスを用いて5分間予熱し，圧力
し，冷却してシート状の複合物試料が得られた。PVF$_2$試

1.11 The first report on piezoelectric composites by Kitayama and Sugawara in 1972.

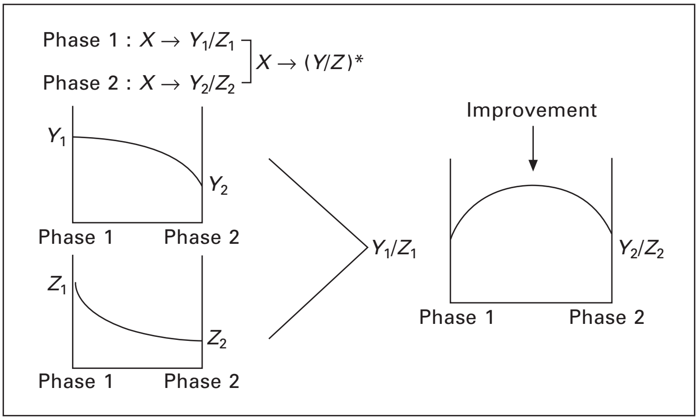
Phase 1 : $X \rightarrow Y_1/Z_1$
Phase 2 : $X \rightarrow Y_2/Z_2$
$X \rightarrow (Y/Z)^*$
Y_1
Y_2
Phase 1
Phase 2
Z_1
Z_2
Phase 1
Phase 2
Y_1/Z_1
Improvement
Y_2/Z_2
Phase 1
Phase 2

1.12 Basic concept of the performance improvement in a composite via a combination effect.

of magnetostrictive $CoFe_2O_4$ and piezoelectric $BaTiO_3$ mixed and sintered together. Figure 1.13(a) shows a micrograph of a transverse section of a unidirectionally solidified rod of the materials with an excess of TiO_2. Four finned spinel dendrites $CoFe_2O_4$ are observed in $BaTiO_3$ bulky whitish matrix. Figure

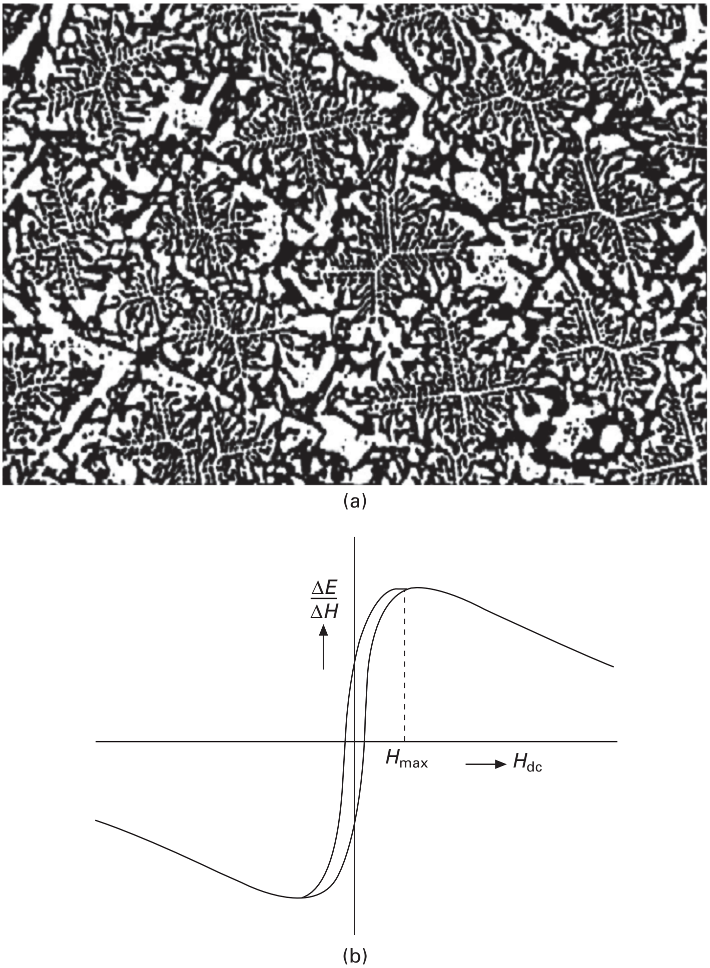

1.13 (a) Micrograph of a transverse section of a uni-directionally solidified rod of mixture of magnetostrictive $CoFe_2O_4$ and piezoelectric $BaTiO_3$, with an excess of TiO_2. (b) Magnetic field dependence of the magnetoelectric effect in a $CoFe_2O_4$–$BaTiO_3$ composite (at room temperature).

1.13(b) shows the magnetic field dependence of the magnetoelectric effect in an arbitrary unit measured at room temperature. When a magnetic field is applied on this composite, cobalt ferrite generates magnetostriction, which is transferred to barium titanate as stress, finally leading to the generation of a charge/voltage via the piezoelectric effect in $BaTiO_3$.

J. Ryu *et al*. extended the magnetoelectric composite idea into a laminate structure.[35] They used Terfenol-D and high *g* soft PZT layers, which are much superior to the performances of cobalt ferrite and BT, respectively.

However, due to the difficulty in co-firing these two materials, they invented the laminated structure. This idea now forms the basis of the magnetoelectric sensor designs in the microelectro-mechanical systems (MEMS) area.

Piezoelectric dampers

An intriguing application of PZT composites is as a passive mechanical damper. Consider a piezoelectric material attached to an object whose vibration is to be damped. When vibration is transmitted to the piezoelectric material, the vibration energy is converted into electrical energy by the piezoelectric effect, and an a.c. voltage is generated. If a proper resistor is connected, however, the energy converted into electricity is consumed in Joule heating of the resistor, and the amount of energy converted back into mechanical energy is reduced, so that the vibration can be rapidly damped. Taking the series resistance as R, the capacitance of the piezoelectric material as C, the vibration frequency as f, damping takes place most rapidly when the series resistor is selected in such a manner that the *impedance matching* condition, $R = 1/2\pi f C$, is satisfied.[36]

Being brittle and hard, ceramics are difficult to assemble directly into a mechanical system. Hence, flexible composites can be useful in practice. When a composite of polymer, piezoceramic powder and carbon black is fabricated (Fig. 1.14), the electrical conductivity of the composite is greatly changed by the addition of small amounts of carbon black.[37] By properly selecting the electrical conductivity of the composite (i.e., electrical impedance matching), the ceramic powder effectively forms a series circuit with the carbon black, so that the vibration energy is dissipated effectively. The conductivity of the composite changes by more than 10 orders of magnitude around a certain carbon fraction called the 'percolation threshold', where the carbon powder link starts to be generated. This eliminates the use of external resistors.

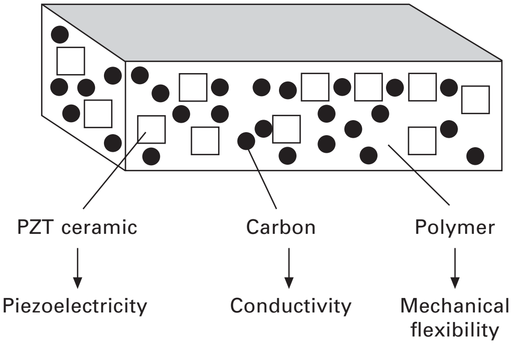

1.14 Piezoceramic–polymer–carbon black composite for vibration damping.

Note that the damper material exhibits a selective damping performance for a certain vibration frequency, depending on the selected resistivity of the composite, which can be derived from the electrical impedance matching between the permittivity and resistivity.

1.1.10 Other piezoelectric-related materials

Photostrictive materials

The phtostriction phenomenon was discovered by Dr P. S. Brody and the author independently almost at the same time in 1981.[38,39] In principle, the photostrictive effect arises from a superposition of the 'bulk' photovoltaic effect, i.e., generation of large voltage from the irradiation of light, and the converse-piezoelectric effect, i.e., expansion or contraction under the voltage applied.[39] In certain ferroelectrics, a constant electromotive force is generated with exposure to light, and a photostrictive strain results from the coupling of this bulk photovoltaic effect to inverse piezoelectricity. A bimorph unit has been made from PLZT 3/52/48 ceramic doped with slight addition of tungsten.[40] The remnant polarization of one PLZT layer is parallel to the plate and in the direction opposite to that of the other plate. When a violet light is irradiated to one side of the PLZT bimorph, a photovoltage of 1 kV/mm is generated, causing a bending motion. The tip displacement of a 20 mm bimorph 0.4 mm in thickness was 150 μm, with a response time of 1 sec.

A photo-driven micro walking device, designed to begin moving by light illumination, has been developed.[41] As shown in Fig. 1.15, it is simple in structure, having neither lead wires nor electric circuitry, with two bimorph legs fixed to a plastic board. When the legs are irradiated alternately with light, the device moves like an inchworm with a speed of 100 μm/min. In pursuit of thick film type photostrictive actuators for space structure applications, in collaboration with Jet Propulsion Laboratory, Penn State investigated the optimal range of sample thickness and surface roughness dependence of photostriction. 30 μm thick PLZT films exhibit the maximum photovoltaic phenomenon.[42]

Monomorphs

The 'monomorph' is defined as a single uniform material which can bend under an electric field. A semiconductive piezoelectric plate can generate this intriguing bending phenomenon, discovered by K. Uchino's group.[43] When attending a conference of the Physical Society of Japan, the author learned about a surface layer generated on a ferroelectric single crystal due to formation of a Schottky barrier. It was not difficult to replace some of the

PENNSTATE
University Park
Campus
1 8 5

1.15 Photo-driven walking machine.

technical terminologies with our words. First polycrystalline piezoelectric samples were used, with reduction processes to expand the Schottky barrier thickness. We succeeded in developing a monolithic bending actuator. A monomorph device has been developed to replace the conventional bimorphs, with simpler structure and manufacturing process. A monomorph plate with 30 mm in length and 0.5 mm in thickness can generate 200 μm tip displacement, in equal magnitude to that of the conventional bimorphs. The 'rainbow' actuator by Aura Ceramics[44] is a modification of the above-mentioned semiconductive piezoelectric monomorphs, where half of the piezoelectric plate is reduced so as to make a thick semiconductive electrode to cause a bend.

1.2 Piezoelectric materials: present status

In the following sections, the author provides the reader with the necessary fundamental knowledge on piezoelectricity, and the present status of materials.

1.2.1 Piezoelectric figures of merit

There are five important figures of merit in piezoelectrics: the *piezoelectric strain constant d*, the *piezoelectric voltage constant g*, the *electromechanical coupling factor k*, the *mechanical quality factor* Q_m, and the *acoustic impedance Z.*

Piezoelectric strain constant d

The magnitude of the induced strain x by an external electric field E is represented by this figure of merit (an important figure of merit for actuator applications):

$$x = dE \tag{1.2}$$

Piezoelectric voltage constant g

The induced electric field E is related to an external stress X through the piezoelectric voltage constant g (an important figure of merit for sensor applications):

$$E = gX. \tag{1.3}$$

Taking into account the relation, $P = dX$, we obtain an important relation between g and d:

$$g = d/\varepsilon_0\varepsilon \quad (\varepsilon\text{: relative permittivity}) \tag{1.4}$$

Electromechanical coupling factor k

The terms, *electromechanical coupling factor*, *energy transmission coefficient*, and *efficiency* are sometimes confused.[45] All are related to the conversion rate between electrical energy and mechanical energy, but their definitions are different.[46]

The electromechanical coupling factor k

$$k^2 = \frac{\text{Stored mechanical energy}}{\text{Input electrical energy}} \tag{1.5}$$

or

$$k^2 = \frac{\text{Stored electrical energy}}{\text{Input mechanical energy}} \tag{1.6}$$

Let us calculate Eq. (1.5), when an electric field E is applied to a piezoelectric material (See Fig. 1.16(a)). Since the input electrical energy is $(1/2)\varepsilon_0\varepsilon E^2$ per unit volume and the stored mechanical energy per unit volume under zero external stress is given by $(1/2)\ x^2/s = (1/2)\ (dE)^2/s$, k^2 can be calculated as

$$\begin{aligned} k^2 &= [(1/2)\ (dE)^2/s]/[(1/2)\ \varepsilon_0\varepsilon\ E^2] \\ &= \mathrm{d}^2/\varepsilon_0\varepsilon \cdot s \end{aligned} \tag{1.7}$$

The energy transmission coefficient λ_{max}

Not all the stored energy can actually be used, and the actual work done depends on the mechanical load. With zero mechanical load or a complete clamp (no strain), no output work is done. The energy transmission coefficient is defined by

$$\lambda_{max} = \frac{\text{Output mechanical energy}}{\text{Input electrical energy}_{max}} \tag{1.8}$$

or equivalently,

$$\lambda_{max} = \frac{\text{Output electrical energy}}{\text{Input mechanical energy}_{max}} \tag{1.9}$$

The difference between the above and Eqs. (1.5) and (1.6) is ‘stored’ or ‘spent’.

Let us consider the case where an electric field E is applied to a piezoelectric under constant external stress X (< 0, because a compressive stress is necessary to work to the outside). This corresponds to the situation where a mass is put suddenly on the actuator, as shown in Fig. 1.16(a). Figure 1.16(b) shows two electric field versus induced strain curves, corresponding to two conditions: under the mass load and no mass. Because the area on the electric field-strain domain does not mean the energy, we should use the stress-strain and electric field-polarization domains in order to discuss the mechanical and electrical energy, respectively. Figure 1.16(c) illustrates how to calculate the mechanical energy. Note that the mass shrinks the actuator first by sX (s: piezo-material’s compliance, and $X < 0$). This mechanical energy sX^2 is a sort of ‘loan’ to the actuator credited from the mass, which should be subtracted later. This energy corresponds to the hatched area in Fig. 1.16(c). By applying the step electric field, the actuator expands by the strain level dE under a constant stress condition. This is the mechanical energy provided from the actuator to the mass, which corresponds to $|dEX|$. Like paying back the initial ‘loan’, the output work (from the actuator to the mass) can be calculated as the area subtraction (shown by the dotted area in Fig. 1.16(c)):

$$\int (-x)\,\mathrm{d}x = -(dE + sX)X \tag{1.10}$$

Figure 1.16(d) illustrates how to calculate the electrical energy. The mass load X generates the ‘loan’ electrical energy by inducing $P = dX$ (see the hatched area in Fig. 1.16(d)). By applying a sudden electric field E, the actuator (like a capacitor) receives the electrical energy of $\varepsilon_0\varepsilon E^2$. Thus, the

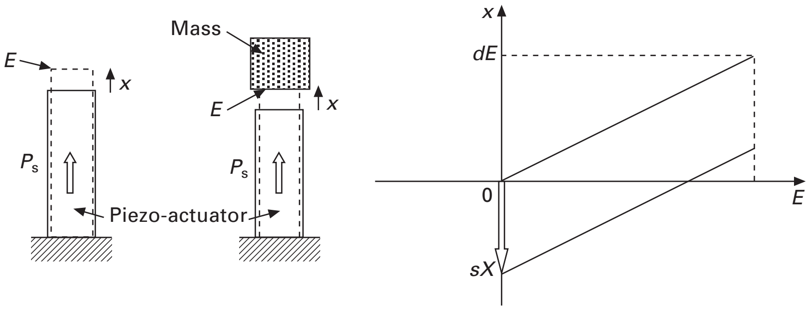
Mass
E
x
E
x
P_s
P_s
Piezo-actuator
x
dE
0
E
sX

(a) Mass load model

(b) Field vs strain

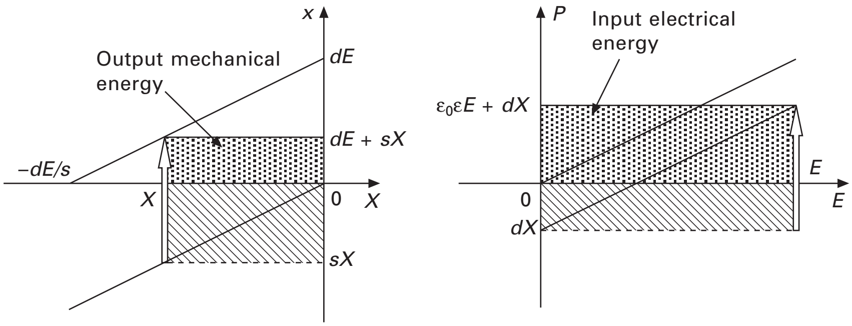
x
Output mechanical energy
dE
dE + sX
−dE/s
X
0
X
sX
P
Input electrical energy
$\varepsilon_0\varepsilon E + dX$
E
0
E
dX

(c) Stress vs. strain

(d) Field vs. polarization

1.16 Calculation of the input electrical and output mechanical energy: (a) load mass model for the calculation, (b) electric field versus induced strain curve, (c) stress versus strain curve, and (d) electric field versus polarization curve.

total energy is given by the area subtraction (shown by the dotted area in Fig. 1.16(d)):

$$\int (E)\,\mathrm{d}P = -(\varepsilon_0\varepsilon E + dX)E \tag{1.11}$$

We need to choose a proper load to maximize the *energy transmission coefficient*. From the maximum condition of

$$\lambda = -\,(dE + sX)\,X/(\varepsilon_0\varepsilon\,E + dX)\,E \tag{1.12}$$

we can obtain

$$\lambda_{\max} = \left[(1/k) - \sqrt{\left(\frac{1}{k^2}\right) - 1}\,\right]^2 = \left[(1/k) + \sqrt{\left(\frac{1}{k^2}\right) - 1}\,\right]^{-2} \tag{1.13}$$

See Ref. 45 for the detailed derivation process. Notice that

$$k^2/4 < \lambda_{\max} < k^2/2 \tag{1.14}$$

depending on the *k* value. For a small *k*, $\lambda_{max} = k^2/4$, and for a large *k*, $\lambda_{max} = k^2/2$.

It is also worth noting that the maximum condition stated above does not agree with the condition which provides the maximum output mechanical energy. The maximum output energy can be obtained when the dotted area in Fig. 1.16(c) becomes maximum under the constraint of the rectangular corner point tracing on the line (from dE on the vertical axis to $-dE/s$ on the horizontal axis). Therefore, the load should be half of the maximum generative stress and the mechanical energy: $-[dE - s(dE/2s)](-dE/2s) = (dE)^2/4s$. In this case, since the input electrical energy is given by $[\varepsilon_0\varepsilon E + d(-dE/2s)]E$

$$\lambda = 1/2[(2/k^2) - 1] \qquad 1.15$$

which is close to the value λ_{max} when *k* is small, but has a different value when *k* is large, which is predicted theoretically.

The efficiency η

$$\eta = \frac{\text{Output mechanical energy}}{\text{Consumed electrical energy}} \qquad 1.16$$

or

$$\eta = \frac{\text{Output electrical energy}}{\text{Consumed mechanical energy}} \qquad 1.17$$

The difference in the efficiency definition from Eqs. (1.8) and (1.9) is ‘input’ energy and ‘consumed’ energy in the denominators. In a work cycle (e.g., an electric field cycle), the input electrical energy is transformed partially into mechanical energy and the remainder is stored as electrical energy (electrostatic energy like a capacitor) in an actuator. In this way, the ineffective electrostatic energy can be returned to the power source, leading to near 100% efficiency, if the loss is small. Typical values of dielectric loss in PZT are about 1–3%.

Mechanical quality factor Q_M

The mechanical quality factor, Q_M, is a parameter that characterizes the sharpness of the electromechanical resonance spectrum. When the motional admittance Y_m is plotted around the resonance frequency ω_0, the mechanical quality factor Q_M is defined with respect to the full width $[2\Delta\omega]$ at $Y_m/\sqrt{2}$ as:

$$Q_M = \omega_0/2\Delta\omega \qquad 1.18$$

Also note that Q_M^{-1} is equal to the mechanical loss ($\tan \delta_m$). When we define a complex elastic compliance, $s^E = s^{E'} - js^{E''}$, the mechanical loss tangent is provided by $\tan \delta_m = s^{E''}/s^{E'}$. The Q_M value is very important in evaluating the magnitude of the resonant displacement and strain. The vibration amplitude at an off-resonance frequency ($dE \cdot L$, L: length of the sample) is amplified by a factor proportional to Q_M at the resonance frequency. For example, a longitudinally vibrating rectangular plate through the transverse piezoelectric effect d_{31} generates the maximum displacement given by $(8/\pi^2)\ Q_M\ d_{31}EL$. See Ref. 45 for the detailed derivation process. Another important note: Q_M^{-1} (= $\tan \delta_m$) generates the heat in the piezo-sample when driven at its resonance mode.

Acoustic impedance Z

The acoustic impedance Z is a parameter used for evaluating the acoustic energy transfer between two materials. It is defined, in general, by

$$Z^2 = \frac{\text{Pressure}}{\text{Volume velocity}} \tag{1.19}$$

In a solid material,

$$Z = \sqrt{\rho c} \tag{1.20}$$

where ρ is the density and c is the elastic stiffness of the material.

In more advanced discussions, there are three kinds of impedance: specific acoustic impedance (pressure/particle speed), acoustic impedance (pressure/volume speed) and radiation impedance (force/speed). (See Ref. 47 for details.)

1.2.2 Piezoelectric resonance[20]

The piezoelectric equations

When an electric field is applied to a piezoelectric material, deformation (ΔL) or strain ($\Delta L/L$) arises. When the field is alternating, mechanical vibration is caused, and if the drive frequency is adjusted to a mechanical resonance frequency of the device, a large resonating strain is generated. This phenomenon can be understood as a strain amplification due to accumulating input energy with time (amplification in terms of time), and is called *piezoelectric resonance*. The amplification factor is proportional to the mechanical quality factor Q_M. Piezoelectric resonance is very useful for realizing energy trap devices, actuators, etc. The theoretical treatment is as follows.

If the applied electric field and the generated stress are not large, the stress

X and the dielectric displacement D can be represented by the following equations:

$$x_i = s^E_{ij} X_j + d_{mi} E_m \quad (i, j = 1, 2, \ldots , 6; m, k = 1, 2, 3) \qquad 1.21$$

$$D_m = d_{mi} X_i + \varepsilon^X_{mk} E_k \qquad 1.22$$

These are called the *piezoelectric equations*. The number of independent parameters for the lowest symmetry trigonal crystal are 21 for s^E_{ij}, 18 for d_{mi} and 6 for ε^X_{mk}. The number of independent parameters decreases with increasing crystallographic symmetry. Concerning the polycrystalline ceramics, the poled axis is usually denoted as the z-axis and the ceramic is isotropic with respect to this z-axis (Curie group $C_{\infty v}$ (∞m)). The number of non-zero matrix elements in this case is 10 (s^E_{11}, s^E_{12}, s^E_{13}, s^E_{33}, s^E_{44}, d_{31}, d_{33}, d_{15}, ε^X_{11}, and ε^X_{33}).

Electromechanical coupling factor

Next, let us introduce the *electromechanical coupling factor k*, which corresponds to the rate of electromechanical transduction. The internal energy U of a piezoelectric vibrator is given by summation of the mechanical energy $U_M\left(= \int x\,dX\right)$ and the electrical energy $U_E\left(= \int D\,dE\right)$. U is calculated as follows, when linear relations Eqs. (1.21) and (1.22) are applicable:

$$\begin{aligned}
U &= U_M + U_E \\
&= \left[(1/2) \sum_{i,j} s^E_{ij} X_j X_1 + (1/2) \sum_{m,i} d_{mi} E_m X_1\right] \\
&\quad + \left[(1/2) \sum_{m,i} d_{mi} X_i E_m + (1/2) \sum_{k,m} \varepsilon^X_{mk} E_k E_m\right] \\
&= U_{MM} + 2U_{ME} + U_{EE} \\
&= (1/2) \sum_{i,j} s^E_{ij} X_j X_1 + 2 \cdot (1/2) \sum_{m,i} d_{mi} E_m X_1 + (1/2) \sum_{k,m} \varepsilon^X_{mk} E_k E_m
\end{aligned}$$

1.23

The s and ε terms represent purely mechanical and electrical energies (U_{MM} and U_{EE}), respectively, and the d term denotes the energy transduced from electrical to mechanical energy, or vice versa, through the piezoelectric effect (U_{ME}). The electromechanical coupling factor k is defined by:

$$k = U_{ME} / \sqrt{U_{MM} \cdot U_{EE}} \qquad 1.24$$

Note that this definition is equivalent to the definition provided in Section 1.11:

$$k^2 = \frac{U_{\mathrm{ME}}}{U_{\mathrm{E}}} = \frac{\text{Stored mechanical energy}}{\text{Input electrical energy}}$$

or

$$k^2 = \frac{U_{\mathrm{ME}}}{U_{\mathrm{M}}} = \frac{\text{Stored electrical energy}}{\text{Input mechanical energy}}$$

The k value varies with the vibration mode (even in the same ceramic sample), and can have a positive or negative value (see Table 1.1). From Table 1.1, it can be seen that k_{31}/k_{33} ratio around 0.47 originates from the d_{31}/d_{33} ratio around 0.43. The k value is governed primarily by the contributing piezoelectric d constant for that vibration mode.

Longitudinal vibration mode

Let us consider the longitudinal mechanical vibration of a piezoceramic plate through the transverse piezoelectric effect (d_{31}), as shown in Fig. 1.17. If the polarization is in the z-direction and x-y planes are the planes of the electrodes, the extensional vibration in the x direction is represented by the following dynamic equation (when the length L is more than 4–6 times the width w or the thickness b, we can neglect the coupling modes with width or thickness vibrations):

$$(\partial^2 u/\partial t^2) = F = (\partial X_{11}/\partial x) + (\partial X_{12}/\partial y) + (\partial X_{13}/\partial z) \qquad 1.25$$

where u is the displacement of the small volume element in the ceramic plate in the x-direction. The relations between stress, electric field (only E_z exists) and the induced strain are given by:

$$\begin{aligned}
x_1 &= s^E_{11} X_1 + s^E_{12} X_2 + s^E_{13} X_3 + d_{31} E_3 \\
x_2 &= s^E_{12} X_1 + s^E_{11} X_2 + s^E_{13} X_3 + d_{31} E_3 \\
x_3 &= s^E_{13} X_1 + s^E_{13} X_2 + s^E_{33} X_3 + d_{33} E_3 \qquad 1.26 \\
x_4 &= s^E_{44} X_4 \\
x_5 &= s^E_{44} X_5 \\
x_6 &= 2(s^E_{11} - s^E_{12}) X_6
\end{aligned}$$

When the plate is very long and thin, X_2 and X_3 may be set equal to zero through the plate. Since shear stress will not be generated by the electric field E_z (= E_3), Eq. (1.26) is reduced to only one equation:

$$X_1 = x_1/s^E_{11} - (d_{31}/s^E_{11}) E_z \qquad 1.27$$

Table 1.1 Several shapes of the piezoelectric resonator and their electromechanical coupling factors

	Coupling factor	Elastic boundary conditions	Resonator shape	Definition
a	k_{31}	$X_1 \neq 0,\ X_2 = X_3 = 0$ $x_1 \neq 0,\ x_2 \neq 0,\ x_3 = 0$	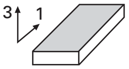	$\frac{d_{31}}{\sqrt{s_{11}^E \varepsilon_{33}^X}}$
b	k_{33}	$X_1 = X_2 = 0,\ X_3 \neq 0$ $x_1 = x_2 \neq 0,\ x_3 \neq 0$	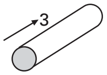 Fundamental mode	$\frac{d_{33}}{\sqrt{s_{33}^E \varepsilon_{33}^X}}$
c	k_p	$X_1 = X_2 \neq 0,\ X_3 = 0$ $x_1 = x_2 \neq 0,\ x_3 \neq 0$	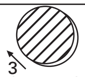 Fundamental mode	$k_{31}\sqrt{\frac{2}{1-\sigma}}$
d	k_t	$X_1 = X_2 \neq 0,\ X_3 \neq 0$ $x_1 = x_2 = 0,\ x_3 \neq 0$	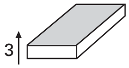 Thickness mode	$k_{33}\sqrt{\frac{\varepsilon_{33}^X}{c_{33}^D}}$
e	k_p'	$X_1 = X_2 \neq 0,\ X_3 \neq 0$ $x_1 = x_2 \neq 0,\ x_3 = 0$	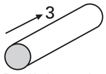 Radial mode	$\frac{k_p - Ak_{33}}{\sqrt{1-A^2}\sqrt{1-k_{33}^2}}$
f	k_{31}'	$X_1 \neq 0,\ X_2 \neq 0,\ X_3 = 0$ $x_1 \neq 0,\ x_2 = 0,\ x_3 \neq 0$	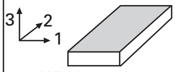 Width mode	$\frac{k_{31}}{\sqrt{1-k_{31}^2}}\sqrt{\frac{1+\sigma}{1-\sigma}}$
g	k_{31}''	$X_1 \neq 0,\ X_2 = 0,\ X_3 \neq 0$ $x_1 \neq 0,\ x_2 \neq 0,\ x_3 \neq 0$	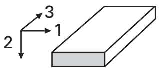 Width mode	$\frac{k_{31} - Bk_{33}}{\sqrt{1-k_{33}^2}}$
h	k_{33}'''	$X_1 \neq 0,\ X_2 \neq 0,\ X_3 \neq 0$ $x_1 \neq 0,\ x_2 = 0,\ x_3 = 0$	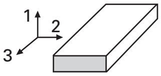 Width mode	$\frac{\sqrt{\frac{(k_p - Ak_{33})^2}{1-A^2} - (k_{31} - Bk_{33})^2}}{1 - k_{33}^2 - (k_{31} - Bk_{33})^2}$
i	k_{33}'	$X_1 \neq 0,\ X_2 = 0,\ X_3 \neq 0$ $x_1 = 0,\ x_2 \neq 0,\ x_3 \neq 0$	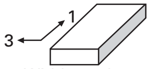 Width mode	$\frac{k_{33} - Bk_{31}}{\sqrt{(1-B^2)(1-k_{31}^2)}}$
j	$k_{24} = k_{15}$	$X_1 = X_2 = X_3 = 0,\ X_4 \neq 0$ $x_1 = x_2 = x_3 = 0,\ x_4 \neq 0$		$\frac{d_{15}}{\sqrt{\varepsilon_{11}^X s_{44}^E}}$

Here: $A = \frac{\sqrt{2}\, s_{13}^E}{\sqrt{s_{33}^E\,(s_{11}^E + s_{12}^E)}}$, $B = \frac{s_{13}^E}{\sqrt{s_{11}^E s_{33}^E}}$

Introducing Eq. (1.27) into Eq. (1.25), and allowing for $x_1 = \partial u/\partial x$ (non-suffix x corresponds to the Cartesian coordinate, and x_1 is the strain along the 1 (x) direction) and $\partial E_z/\partial x = 0$ (due to the equal potential on each electrode), leads to a harmonic vibration equation:

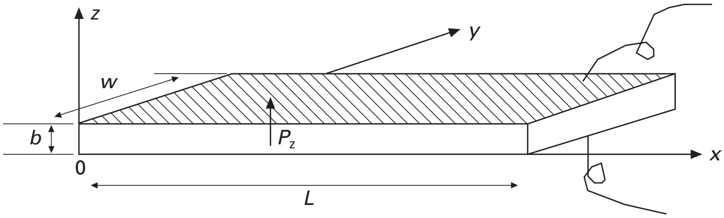

1.17 Longitudinal vibration through the transverse piezoelectric effect (d_{31}) in a rectangular plate.

$$-\omega^2 \rho s^E_{11} u = \partial^2 u/\partial x^2 \qquad 1.28$$

Here, ω is the angular frequency of the drive field, and ρ is the density. Substituting a general solution $u = u_1(x)e^{j\omega t} + u_2(x)e^{-j\omega t}$ into Eq. (1.27), and with the boundary condition $X_1 = 0$ at $x = 0$ and L (sample length) (due to the mechanically-free condition at the plate end), the following solution can be obtained:

$$\partial u/\partial x = x_1 = d_{31} E_z [\sin\omega(L - x)/v + \sin(\omega x/v)]/\sin(\omega L/v)$$

$$= d_{31}E_z \left(\frac{\cos\left[\dfrac{\omega(L-2x)}{2v}\right]}{\cos\left(\dfrac{\omega L}{2v}\right)} \right) \qquad 1.29$$

Here, v is the *sound velocity* in the piezoceramic which is given by

$$v = 1/\sqrt{\rho s^E_{11}} \qquad 1.30$$

When the specimen is utilized as an electrical component such as a filter or a vibrator, the electrical impedance [(applied voltage/induced current) ratio] plays an important role. The current flow into the specimen is described by the surface charge increment, $\partial D_3/\partial t$, and the total current is given by:

$$i = j\omega w \int_0^L D_3 \mathrm{d}x = j\omega w \int_0^L (d_{31}X_1 + \varepsilon^X_{33}E_z)\mathrm{d}x$$

$$= j\omega w \int_0^L \left[\mathrm{d}_{31}\left\{ \frac{\mathrm{x}_1}{\mathrm{s}^E_{11}} - \left(\frac{\mathrm{d}_{31}}{\mathrm{s}^E_{11}}\right)\mathrm{E}_z \right\} + \varepsilon^x_{33}\mathrm{E}_z \right]\mathrm{dx} \qquad 1.31$$

Using Eq. (1.29), the admittance for the mechanically free sample is calculated to be:

$$(1/Z) = (i/V) = (i/E_z\, t)$$

$$= (j\omega wL/E_z t)\int_0^L \left[\begin{array}{c}\left(\dfrac{d_{31}^2}{s_{11}^E}\right)\left(\dfrac{\cos\left[\dfrac{\omega(L-2x)}{2v}\right]}{\cos\left(\dfrac{\omega L}{2v}\right)}\right)E_z \\ +\left[\varepsilon_{33}^X - \left(\dfrac{d_{31}^2}{s_{11}^E}\right)\right]E_z\end{array}\right]dx$$

$$= (j\omega wL/t)\,\varepsilon_{33}^{LC}[1 + (d_{31}^2/\varepsilon_{33}^{LC}s_{11}^E)(\tan(\omega L/2v)/(\omega L/2v)] \qquad 1.32$$

where w is the width, L the length, t the thickness of the rectangular piezo-sample, and V is the applied voltage. ε_{33}^{LC} is the permittivity in a longitudinally clamped sample, which is given by

$$\varepsilon_{33}^{LC} = \varepsilon_{33}^X - \left(\frac{d_{31}^2}{s_{11}^E}\right) \qquad 1.33$$

The piezoelectric resonance is achieved where the admittance becomes infinite or the impedance is zero. The resonance frequency f_R is calculated from Eq. (1.32) (by putting $\omega L/2v = \pi/2$), and the fundamental frequency is given by

$$f_R = \omega_R/2\pi = v/2L = 1/(2L\sqrt{\rho s_{11}^E}) \qquad 1.34$$

On the other hand, the antiresonance state is generated for zero admittance or infinite impedance:

$$(\omega_A L/2v)\cot(\omega_A L/2v) = -d_{31}^2/\varepsilon_{33}^{LC}\, s_{11}^E = -k_{31}^2/(1-k_{31}^2) \qquad 1.35$$

The final transformation is provided by the definition,

$$k_{31} = d_{31}/\sqrt{s_{11}^E \cdot \varepsilon_{33}^X} \qquad 1.36$$

The resonance and antiresonance states are both mechanical resonance states with amplified strain/displacement states, but they are very different from the driving viewpoints. The mode difference is described by the following intuitive model.[20] In a high electromechanical coupling material with k almost equal to 1, the resonance or antiresonance states appear for $\tan(\omega L/2v) = \infty$ or 0 [i.e., $\omega L/2v = (m-1/2)\pi$ or $m\pi$ (m: integer)], respectively. The strain amplitude x_1 distribution for each state (calculated using Eq. (1.29)) is illustrated in Fig. 1.18. In the resonance state, large strain amplitudes and large capacitance changes (called *motional capacitance*) are induced, and the current can easily flow into the device. In contrast, at the antiresonance, the strain induced in the device compensates completely, resulting in no

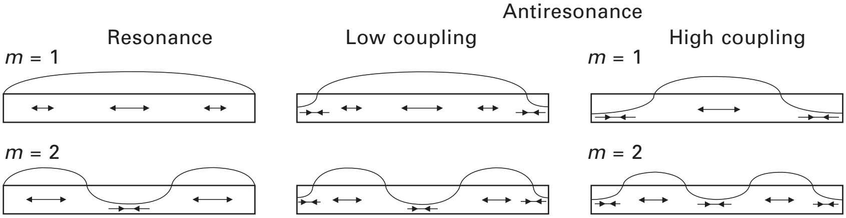

1.18 Strain distribution in the resonant or antiresonant state.

capacitance change, and the current cannot flow easily into the sample. Thus, for a high k material the first antiresonance frequency f_A should be twice as large as the first resonance frequency f_R.

It is notable that both resonance and antiresonance states are in the mechanical resonance, which can create large strain in the sample under minimum input electrical energy. The stress X_1 at the plate ends ($x = 0$ and L) is supposed to be zero in both cases. However, though the strain x_1 at the plate ends is zero for the resonance, the strain x_1 is not zero (actually the maximum) for the antiresonance. This means that there is only one vibration node at the plate center for the resonance (top-left in Fig. 1.18), and there are an additional two nodes at both plate ends for the antiresonance (top-right in Fig. 1.18). The reason is from the antiresonance drive, i.e., high voltage/low current (minimum power) drive due to the high impedance. The converse piezo-effect strain under E directly via d_{31} (uniform strain in the sample) superposes on the mechanical resonance strain distribution (distributed strain with nodes in the sample), two strains of which have exactly the same level theoretically at the antiresonance for $k_{31} = 1$.

In a typical case, where $k_{31} = 0.3$, the antiresonance state varies from the previously mentioned mode and becomes closer to the resonance mode (top-center in Fig. 1.18). The low-coupling material exhibits an antiresonance mode where the capacitance change due to the size change (*motional capacitance*) is compensated completely by the current required to charge up the static capacitance (called *damped capacitance*). Thus, the antiresonance frequency f_A will approach the resonance frequency f_R.

The general procedure for calculating the electromechanical parameters (k_{31}, d_{31}, s^E_{11}, and ε^X_{33}) from the impedance spectrum measurement is described below:

1. The sound velocity v in the specimen is obtained from the resonance frequency f_R (see Fig. 1.17), using Eq. (1.34): $f_R = v/2L$.
2. Knowing the density ρ, the elastic compliance s^E_{11} can be calculated from the sound velocity v:

$$v = 1/\sqrt{\rho s^E_{11}}$$

3. The electromechanical coupling factor k_{31} is calculated from the v value and the antiresonance frequency f_A through Eq. (1.35). Especially in low-coupling piezoelectric materials, the following approximate equation is useful:

$$k_{31}^2/(1 - k_{31}^2) = (\pi^2/4)\ (\Delta f/f_R) \cdot (\Delta f = f_A - f_R) \qquad 1.37$$

4. Knowing the permittivity ε_{33}^X from the independent measurement under an off-resonance condition, the d_{31} is calculated from k_{31} through Eq. (1.36): $k_{31} = d_{31}/\sqrt{s_{11}^E \cdot \varepsilon_{33}^X}$

Figures 1.19(a) and 1.19(b) compare observed impedance curves of rod-shaped samples for a typical k material (PZT 5H, $k_{33} = 0.70$) and a high k material (PZN-PT single crystal, $k_{33} = 0.90$). Note a large separation between the resonance and antiresonance peaks in the high k material, leading to the condition almost $f_A = 2f_R$. In contrast, a regular PZT sample exhibits $f_A = 1.3\ f_R$. The bandwidth of the piezo-transducer is defined by $\Delta f/f_R$, leading to 100% for the PZN-PT sample and only 30% for PZT 5H.

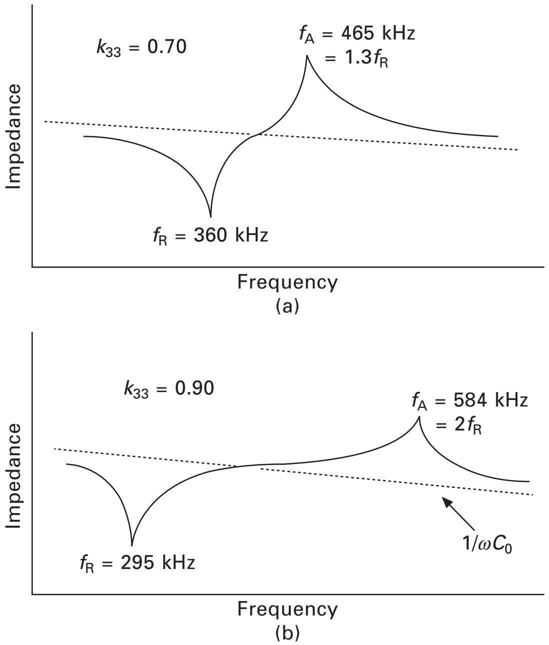

1.19 (a) Impedance curves for a reasonable k material (PZT 5H, k_{33} = 0.70), and (b) a high k material (PZN-PT single crystal, k_{33} = 0.90).

1.2.3 Overview of piezoelectric materials[48]

This section summarizes the current status of piezoelectric materials: single-crystal materials, piezo-ceramics, piezo-polymers, composites, and piezo-films. Table 1.2 shows the piezoelectric material parameters.[49] Quartz with the highest mechanical quality factor is used for low loss transducers. The PZT family shows high *d* and *k* suitable for high power transducers. Sm-doped lead titanates exhibit extremely high mechanical coupling anisotropy k_t/k_p, suitable for medical transducers. Piezo-polymer PVDF has small permittivity, leading to high piezo *g* constant, in addition to mechanical flexibility, suitable for pressure/stress sensor applications.

Single crystals

Although piezoelectric ceramics are widely used for a large number of applications, single crystal materials retain their utility, being essential for applications such as frequency stabilized oscillators and surface acoustic devices. The most popular single-crystal piezoelectric materials are quartz, lithium niobate ($LiNbO_3$), and lithium tantalate ($LiTaO_3$). The single crystals are anisotropic, exhibiting different material properties depending on the cut of the materials and the direction of bulk or surface wave propagation.

Quartz is a well-known piezoelectric material. α-quartz belongs to the triclinic crystal system with point group 32 and has a phase transition at 537 °C to its β-form which is not piezoelectric. Quartz has a cut with a zero temperature coefficient. For instance, quartz oscillators, operated in the thickness shear mode of the AT-cut, are used extensively for clock sources in computers, frequency stabilized ones in TVs and VCRs. On the other hand, an ST-cut quartz substrate with X-propagation has a zero temperature coefficient for surface acoustic wave, and so is used for SAW devices with high stabilized frequencies. Another distinguishing characteristic of quartz is an extremely high mechanical quality factor $Q_M > 10^5$.

Lithium niobate and lithium tantalate belong to an isomorphous crystal system and are composed of oxygen octahedron. The Curie temperatures of

Table 1.2 Piezoelectric properties of representative piezoelectric materials

Parameter	Quartz	$BaTiO_3$	PZT 4	PZT 5H	$(Pb,Sm)TiO_3$	PVDF-TrFE
d_{33} (pC/N)	2.3	190	289	593	65	33
g_{33} (10^{-3}Vm/N)	57.8	12.6	26.1	19.7	42	380
k_t	0.09	0.38	0.51	0.50	0.50	0.30
k_p		0.33	0.58	0.65	0.03	
$\varepsilon^X_3/\varepsilon_0$	5	1700	1300	3400	175	6
Q_M	$> 10^5$		500	65	900	3–10
T_C (°C)		120	328	193	355	

$LiNbO_3$ and $LiTaO_3$ are 1210 and 660 °C, respectively. The crystal symmetry of the ferroelectric phase of these single crystals is 3 m, and the polarization direction is along the c-axis. These materials have high electromechanical coupling coefficients for surface acoustic wave. In addition, large single crystals can easily be obtained from their melt using the conventional Czochralski technique. Thus, both materials occupy very important positions in the SAW device application field.

Single crystals of $Pb(Mg_{1/3}Nb_{2/3})O_3$ (PMN), $Pb(Zn_{1/3}Nb_{2/3})O_3$ (PZN) and their binary systems with $PbTiO_3$ (PMN-PT and PZN-PT) with extremely large electromechanical coupling factors are discussed in the following section.

Polycrystalline materials

Barium titanate (BT) $BaTiO_3$ is one of the most thoroughly studied and most widely used ferroelectric materials. Just below the Curie temperature (130 °C), the vector of the spontaneous polarization points in the [001] direction (tetragonal phase), below 5 °C it reorients in the [011] (orthorhombic phase) and below –90 °C in the [111] direction (rhombohedral phase). The dielectric and piezoelectric properties of ferroelectric ceramic $BaTiO_3$ can be affected by its own stoichiometry, microstructure, and by dopants entering onto the A or B site in solid solution. Modified ceramic $BaTiO_3$ with dopants such as Pb or Ca ions have been developed to stabilize the tetragonal phase over a wider temperature range and have been used as commercial piezoelectric materials. After the discovery of PZT, BT's role in piezoelectric devices faded out, and is primarily as capacitors at present. However, in the next 10 years, once Pb usage has been strictly regulated, interest in BT-based piezoceramics may revive.

Piezoelectric $Pb(Ti,Zr)O_3$ solid solutions (PZT) ceramics that were discovered in the 1950s are widely used nowadays because of their superior piezoelectric properties. The phase diagram for the PZT system ($PbZr_xTi_{1-x}O_3$) is shown in Fig. 1.20. The crystalline symmetry of this solid-solution system is determined by the Zr content. Lead titanate also has a tetragonal ferroelectric phase of perovskite structure. With increasing Zr content, x, the tetragonal distortion decreases and at $x > 0.52$ the structure changes from the tetragonal 4 mm phase to another ferroelectric phase of rhombohedral 3 m symmetry. The line dividing these two phases is called the morphotropic phase boundary (MPB). The boundary composition is considered to have both tetragonal and rhombohedral phases coexisting together. Figure 1.21 shows the dependence of several piezoelectric d constants on composition near the morphotropic phase boundary. The d constants have their highest values near the MPB. This enhancement in piezoelectric effect is attributed to the increased ease of reorientation of the polarization under an applied electric field.

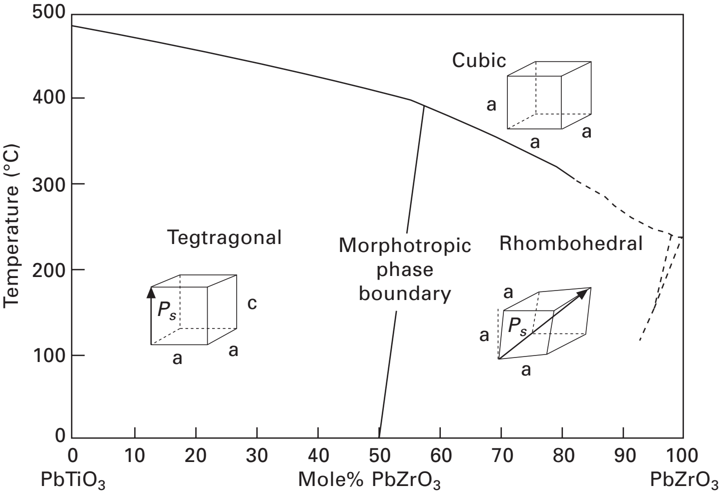

1.20 Phase diagram of lead zirconate titanate (PZT).

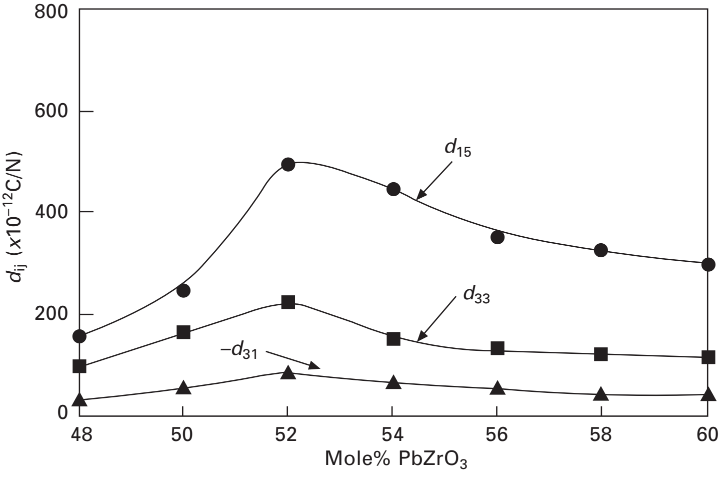

1.21 Dependence of several *d* constants on composition near the morphotropic phase boundary in the PZT system.

Doping the PZT material with *donor* or *acceptor* ions changes its properties dramatically. Donor doping with ions such as Nb^{5+} or Ta^{5+} provides 'soft' PZTs, such as PZT-5, because of the facility of domain motion due to the resulting Pb vacancies. On the other hand, acceptor doping with Fe^{3+} or Sc^{3+} leads to 'hard' PZTs, such as PZT-8, because the oxygen vacancies will pin the domain wall motion.

PZT in ternary solid solution with another perovskite phase has been investigated intensively by Japanese ceramics companies. Examples of these ternary compositions are: PZTs in solid solution with $Pb(Mg_{1/3}Nb_{2/3})O_3$ (Panasonic), $Pb(Zn_{1/3}Nb_{2/3})O_3$ (Toshiba), $Pb(Mn_{1/3}Sb_{2/3})O_3$, $Pb(Co_{1/3}Nb_{2/3})O_3$, $Pb(Mn_{1/3}Nb_{2/3})O_3$, $Pb(Ni_{1/3}Nb_{2/3})O_3$ (NEC), $Pb(Sb_{1/2}Sn_{1/2})O_3$, $Pb(Co_{1/2}W_{1/2})O_3$, $Pb(Mg_{1/2}W_{1/2})O_3$ (Du Pont), all of which were patented by different companies (almost all composition patents have already expired).

Table 1.3 summarizes piezoelectric, dielectric and elastic properties of typical PZTs: soft PZT-5H, semi-hard PZT-4, and hard PZT-8. Note that soft PZTs exhibit high k, high d, high ε, in comparison with Hard PZTs, while Q_M is quite high in hard PZTs. Thus, soft PZTs should be used for off-resonance applications, while hard PZTs are suitable for resonance applications.

Table 1.3 Piezoelectric, dielectric, and elastic properties of typical PZTs

	Soft PZT-5H	Semi-hard PZT-4	Hard PZT-8
EM coupling factor			
k_p	0.65	0.58	0.51
k_{31}	0.39	0.33	0.30
k_{33}	0.75	0.70	0.64
k_{15}	0.68	0.71	0.55
Piezoelectric coefficient			
d_{31} (10^{-12}m/V)	–274	–122	–97
d_{33}	593	285	225
d_{15}	741	495	330
g_{31} (10^{-3} Vm/N)	–9.1	–10.6	–11.0
g_{33}	19.7	24.9	25.4
g_{15}	26.8	38.0	28.9
Permittivity			
$\varepsilon_{33}^X/\varepsilon_0$	3400	1300	1000
$\varepsilon_{11}^X/\varepsilon_0$	3130	1475	1290
Dielectric loss (tan δ) (%)	2.00	0.40	0.40
Elastic compliance			
s_{11}^E (10^{-12} m^2/N)	16.4	12.2	11.5
s_{12}^E	–4.7	–4.1	–3.7
s_{13}^E	–7.2	–5.3	–4.8
s_{33}^E	20.8	15.2	13.5
s_{44}^E	43.5	38.5	32.3
Mechanical Q_M	65	500	1000
Density ρ (10^3 kg/mm^3)	7.5	7.5	7.6
Curie temperature(°C)	193	325	300

The end member of PZT, lead titanate has a large crystal distortion. $PbTiO_3$ has a tetragonal structure at room temperature with its tetragonality $c/a = 1.063$. The Curie temperature is 490 °C. Densely sintered $PbTiO_3$ ceramics cannot be obtained easily, because they break up into a powder when cooled through the Curie temperature due to the large spontaneous strain. Lead titanate ceramics modified by adding a small amount of additives exhibit a high piezoelectric anisotropy. Either $(Pb,Sm)TiO_3$[50] or $(Pb,Ca)TiO_3$[51] exhibits an extremely low planar coupling, that is, a large k_t/k_p ratio. Here, k_t and k_p are thickness extensional and planar electromechanical coupling factors, respectively. Since these transducers can generate purely longitudinal waves through k_t associated with no transverse waves through k_{31}, clear ultrasonic imaging is expected without 'ghost' caused by the transverse wave. $(Pb,Nd)(Ti,Mn,In)O_3$ ceramics with a zero temperature coefficient of surface acoustic wave delay have been developed as superior substrate materials for SAW device applications.[52]

Relaxor ferroelectrics

Relaxor ferroelectrics can be prepared either in polycrystalline form or as single crystals. They differ from the previously mentioned normal ferroelectrics in that they exhibit a broad phase transition from the paraelectric to ferroelectric state, a strong frequency dependence of the dielectric constant (i.e., dielectric relaxation) and a weak remanent polarization. Lead-based relaxor materials have complex disordered perovskite structures.

Relaxor-type electrostrictive materials, such as those from the lead magnesium niobate–lead titanate, $Pb(Mg_{1/3}Nb_{2/3})O_3–PbTiO_3$ (or PMN-PT), solid solution are highly suitable for actuator applications. This relaxor ferroelectric also exhibits an induced piezoelectric effect. That is, the electromechanical coupling factor k_t varies with the applied d.c. bias field. As the d.c. bias field increases, the coupling increases and saturates. Since this behavior is reproducible (no hysteresis), these materials can be applied as ultrasonic transducers which are tunable by the bias field.[53]

Single-crystal relaxor ferroelectrics with the MPB composition show tremendous promise as ultrasonic transducers and electromechanical actuators. Single crystals of $Pb(Mg_{1/3}Nb_{2/3})O_3$ (PMN), $Pb(Zn_{1/3}Nb_{2/3})O_3$ (PZN) and binary systems of these materials combined with $PbTiO_3$ (PMN-PT and PZN-PT) exhibit extremely large electromechanical coupling factors.[25,54] Large coupling coefficients and large piezoelectric constants have been found for crystals from the MPBs of these solid solutions. PZN-8%PT single crystals were found to possess a high k_{33} value of 0.94 for the (001) crystal cuts; this is very high compared to the k_{33} of conventional PZT ceramics of around 0.70–0.80.

Polymers

Polyvinylidene difluoride, PVDF or PVF2, is piezoelectric when stretched during fabrication. Thin sheets of the cast polymer are then drawn and stretched in the plane of the sheet, in at least one direction, and frequently also in the perpendicular direction, to transform the material to its microscopically polar phase. Crystallization from the melt forms the non-polar α-phase, which can be converted into the polar β-phase by a uni-axial or bi-axial drawing operation; the resulting dipoles are then reoriented through electric poling (see Fig. 1.22).

Large sheets can be manufactured and thermally formed into complex shapes. The copolymerization of vinilydene difluoride with trifluoroethylene (TrFE) results in a random copolymer (PVDF-TrFE) with a stable, polar β-phase. This polymer need not be stretched; it can be poled directly as formed. A thickness-mode coupling coefficient of 0.30 has been reported. Piezoelectric polymers have the following characteristics:

- small piezoelectric *d* constants (for actuators) and large *g* constants (for sensors), due to small permittivity,
- light weight and soft elasticity, leading to good acoustic impedance matching with water or the human body,
- a low mechanical quality factor Q_M, allowing for a broad resonance band width.
- Such piezoelectric polymers are used for directional microphones and ultrasonic hydrophones.

Composites

Piezo-composites comprising piezoelectric ceramic and polymer phases are promising materials because of their excellent and readily tailored properties. The geometry for two-phase composites can be classified according to the dimensional connectivity of each phase into 10 structures; 0-0, 0-1, 0-2, 0-3, 1-1, 1-2, 1-3, 2-2, 2-3, and 3-3.[33] A 1-3 piezo-composite, such as the

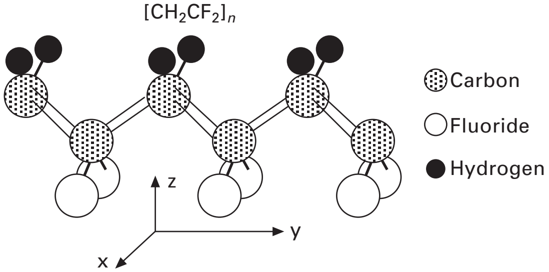

1.22 Structure of polyvinylidene diflouride (PVDF).

PZT-rod/polymer composite is one of the most promising configurations. The advantages of this composite are high coupling factors, low acoustic impedance, good matching to water or human tissue, mechanical flexibility, broad bandwidth in combination with a low mechanical quality factor and the possibility of making undiced arrays by structuring the electrodes. The thickness-mode electromechanical coupling of the composite can exceed the k_t (0.40–0.50) of the constituent ceramic, approaching almost the value of the rod-mode electromechanical coupling, k_{33} (0.70–0.80) of that ceramic.[55] The electromechanical coupling factor of the composites is much superior to the polymer piezoelectrics. Acoustic impedance is the square root of the product of its density and elastic stiffness. The acoustic match to tissue or water (1.5 Mrayls) of the typical piezo-ceramics (20–30 Mrayls) is significantly improved by forming a composite structure, that is, by replacing some of the heavy, stiff ceramic with a light, soft polymer. Piezoelectric composite materials are especially useful for underwater sonar and medical diagnostic ultrasonic transducer applications.

1.2.4 Thin films

Both zinc oxide (ZnO) and aluminum nitride (AlN) are simple binary compounds with a Wurtzite-type structure, which can be sputter-deposited as a c-axis oriented thin film on a variety of substrates. Since ZnO has reasonable piezoelectric coupling, thin films of this material are widely used in bulk acoustic and surface acoustic wave devices. The fabrication of highly oriented (along c) ZnO films have been studied and developed extensively. However, the performance of ZnO devices is limited, due to their low piezoelectric coupling (20–30%). PZT thin films are expected to exhibit higher piezoelectric properties. At present the development of PZT thin films is being carried out for use in micro-transducers and micro-actuators.

Thin film preparation technique

Techniques for fabrication of oxide thin films are classified into physical and chemical processes:

- Physical processes
  - Electron beam evaporation
  - RF sputtering, DC sputtering
  - Ion beam sputtering
  - Ion plating
- Chemical processes
  - Sol-gel method (dipping, spin coating, etc.)
  - Chemical vapor deposition (CVD)

- MOCVD
- Liquid phase epitaxy, melting epitaxy, capillary epitaxy, etc.

Sputtering has been most commonly used for ferroelectric thin films such as $LiNbO_3$, PLZT, and $PbTiO_3$. Figure 1.23 shows the principle of a magnetron sputtering apparatus. Heavy Ar plasma ions bombard the cathode (target) and eject its atoms. These atoms are deposited uniformly on the substrate in an evacuated enclosure. Choosing a suitable substrate and deposition condition, single crystal-like epitaxially deposited films can be obtained. The sol-gel technique has also been employed for processing PZT films. Applications of thin film ferroelectrics include memories, surface acoustic wave devices, piezo sensors and micro-mechatronic or MEMS (micro electro-mechanical system) devices.

As was discussed with regard to Fig. 1.8 (001) epitaxially-oriented PZT rhombohedral composition films are most suitable from the application viewpoint.[28] Kalpat *et al.* demonstrated (001) and (111) oriented films on the same Pt-coated Si substrate by changing the rapid thermal annealing profile.[56] Figures 1.24(a) and (b) show the PZT (70/30) films with (001) and (111) orientations.

MEMS application

The micromachining process used to fabricate the PZT micropump is illustrated in Fig. 1.25. The etching process for the silicon:PZT unit is shown on the

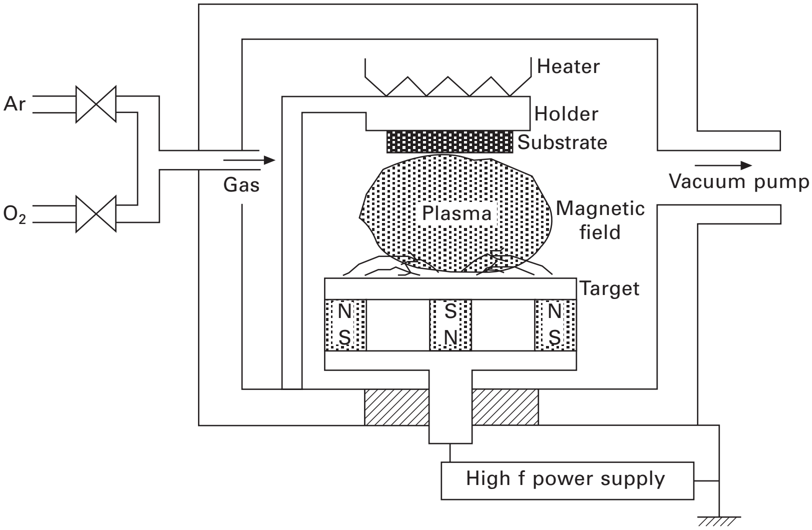

1.23 Principle of a magnetron sputtering apparatus.

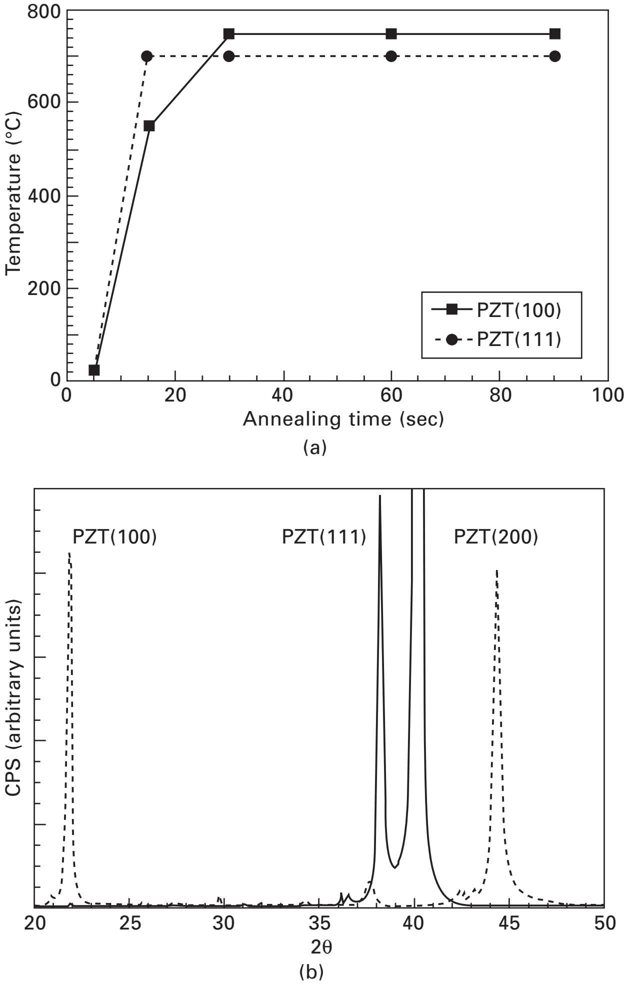

1.24 Epitaxially grown rhombohedral (70/30) PZT films with (001) and (111) orientations: (a) optimum rapid thermal annealing profiles, and (b) x-ray diffraction patterns for films grown according to these profiles.[56]

left-hand side of the figure and that for the glass plate on the right-hand side. A schematic of the micropump for a blood tester is shown in Fig. 1.26.[56] The blood sample and test chemicals enter the system through the two inlets, shown in Fig. 1.26, are mixed in the central cavity, and finally are passed through the outlet for analysis. The movement of the liquids through the system occurs through the bulk bending of the PZT diaphragm in response to the drive potential provided by the interdigital surface electrodes.

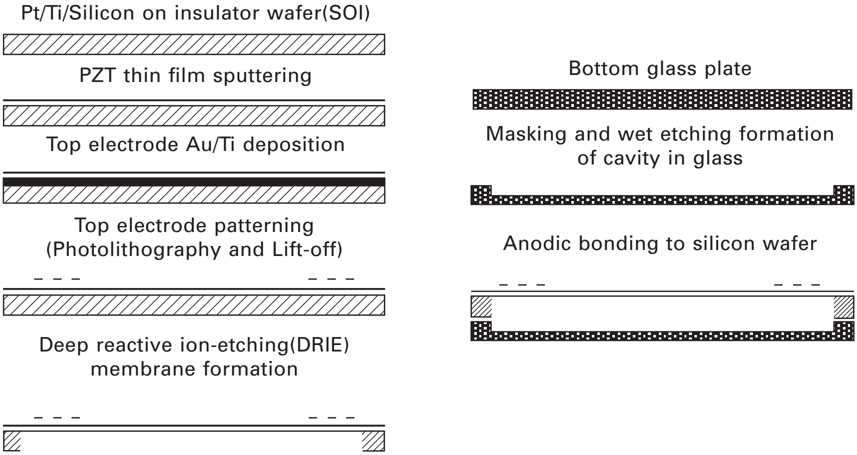
Pt/Ti/Silicon on insulator wafer(SOI)
PZT thin film sputtering
Top electrode Au/Ti deposition
Top electrode patterning (Photolithography and Lift-off)
Deep reactive ion-etching(DRIE) membrane formation
Bottom glass plate
Masking and wet etching formation of cavity in glass
Anodic bonding to silicon wafer

1.25 The micromachining process used to fabricate a PZT micropump.[56]

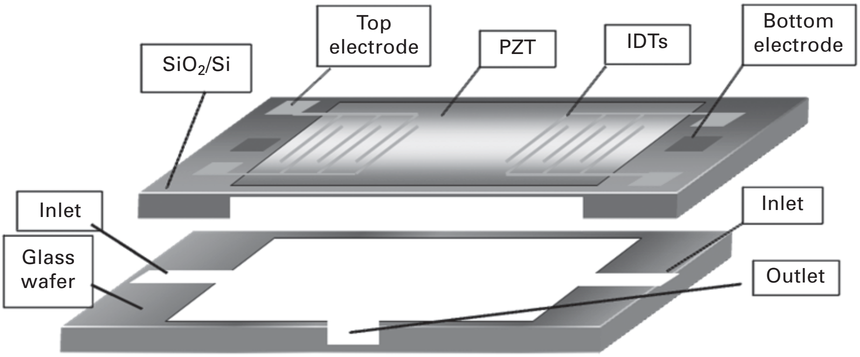
SiO2/Si
Top electrode
PZT
IDTs
Bottom electrode
Inlet
Glass wafer
Inlet
Outlet

1.26 A schematic diagram of the structure of a PZT micropump.[56] Actual size: 4.5 mm × 4.5 mm × 2 mm.

Constraints in thin/thick films

The thin film structure is inevitably affected by four significant parameters:

1. *Size constraints*: Similar to a powder sample, there may exist a critical film thickness below which the ferroelectricity would disappear.[57]
2. *Stress from the substrate*: Tensile or compressive stress is generated due to thermal expansion mismatch between the film and the substrate, leading sometimes to a higher coercive field for domain reorientation. The Curie temperature is also modified at a rate of 50 °C per 1 GPa.
3. *Epitaxial growth*: Crystal orientation dependence should be also

considered, similar to the case in single crystals. An example can be found in a rhombohedral composition PZT, which is supposed to exhibit the maximum performance when the P_s direction is arranged 57° cant from the film normal direction (i.e., (001) crystallographic orientation).[28]

4. *Preparation constraint*: Si substrate requires low sintering temperature of the PZT film. Typically 800 °C for a short period is the maximum for preparing the PZT, which may limit the crystallization of the film, leading to a reduction in the properties. A metal electrode on a Si wafer such as Pt also limits the crystallinity of the PZT film.

1.3 Piezoelectric devices: brief review of applications

1.3.1 Pressure sensors/accelerometers/gyroscopes

One of the basic applications of piezoelectric ceramics is as a gas igniter. The very high voltage generated in a piezoelectric ceramic under applied mechanical stress can cause sparking and ignite the gas. There are two means to apply the mechanical force, either by a rapid, pulsed application or by a more gradual, continuous increase.

Piezoelectric ceramics can be employed as stress sensors and acceleration sensors, because of the *direct piezoelectric effect*. Figure 1.27 shows a 3D stress sensor designed by Kistler. By combining an appropriate number of quartz crystal plates (extensional and shear types), the multilayer device can detect three-dimensional stresses.[58]

Figure 1.28 shows a cylindrical gyroscope manufactured by NEC-Tokin (Japan).[59] The cylinder has six divided electrodes, one pair of which are used to excite the fundamental bending vibration mode, while the other two pairs are used to detect the acceleration. When the rotational acceleration is applied about the axis of this gyro, the voltage generated on the electrodes is modulated by the Coriolis force. By subtracting the signals between the two sensor electrode pairs, a voltage directly proportional to the acceleration can be obtained.

1.3.2 Piezoelectric vibrators/ultrasonic transducers

Piezoelectric vibrators

In the use of mechanical vibration devices such as filters or oscillators, the size and shape of a device are very important, and both the vibrational mode and the ceramic material must be considered. The resonance frequency of the bending mode in a centimeter-size sample ranges from 100 to 1000 Hz, which is much lower than that of the thickness mode (100 kHz). For these vibrator applications the piezoceramic should have a high mechanical quality

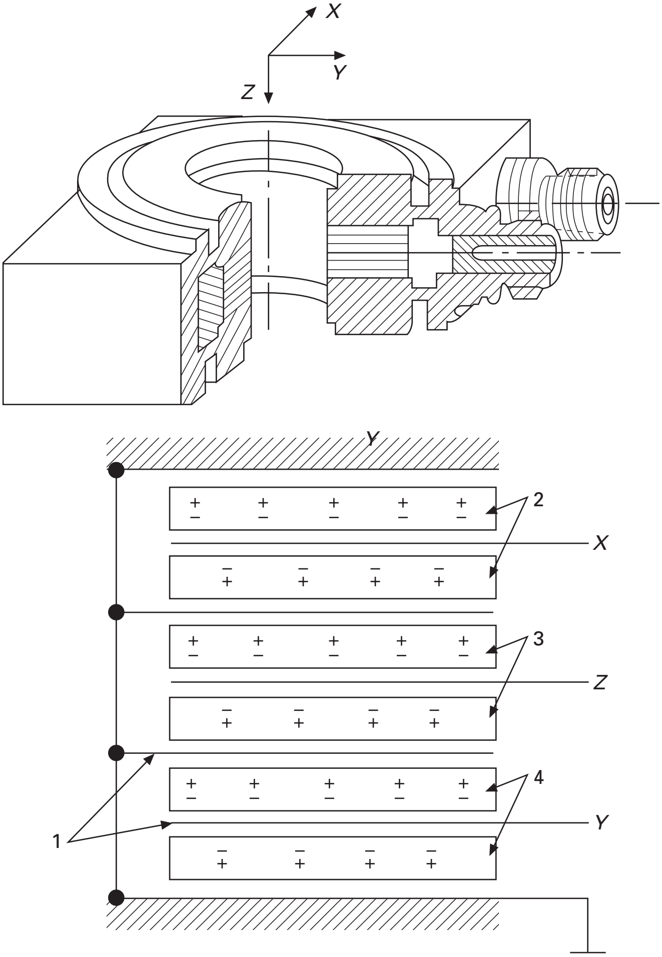

1.27 Three-dimensional stress sensor (by Kistler).[58]

factor (Q_M) rather than a large piezoelectric coefficient d; that is, hard piezoelectric ceramics are preferable.

For speakers or buzzers, audible by humans, devices with a rather low resonance frequency are used (100Hz–2kHz range). Examples are a unimorph consisting of one piezoceramic plate bonded with a metallic shim, a bimorph consisting of two piezoceramic plates bonded together, and a piezoelectric fork consisting of a piezo-device and a metal fork. A piezoelectric buzzer design has merits such as high electric power efficiency, compact size and long life. A state-of-the-art speaker has been reported with only 0.7 mm ultra-thin thickness and 0.4 g weight.[60] The power consumption is only 1/5–2/3 compared to electromagnetic types. The piezo-speaker has a wide

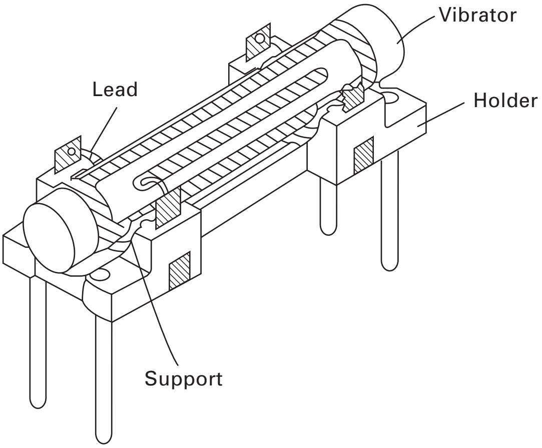

1.28 Cylindrical gyroscope (by NEC-Tokin).[59]

frequency range and high sound pressure, and in particular, no interference with credit cards, which is important nowadays.

Ultrasonic transducers

Ultrasonic waves are now used in various fields. The sound source is made from piezoelectric ceramics, as well as magnetostrictive materials. Piezoceramics are generally superior in efficiency and in size to magnetostrictive materials. In particular, hard piezoelectric materials with a high Q_M are preferable because of high power generation without heat generation. A liquid medium is usually used for sound energy transfer. Ultrasonic washers, ultrasonic microphones and sonars for short-distance remote control, underwater detection, and fish finding, and non-destructive testers are typical applications. Ultrasonic scanning detectors are useful in medical electronics for clinical applications ranging from diagnosis to therapy and surgery.

Ultrasonic imaging

One of the most important applications is based on the ultrasonic echo field.[61,62] Ultrasonic transducers convert electrical energy into mechanical form when generating an acoustic pulse and convert mechanical energy into an electrical signal when detecting its echo. The transmitted waves propagate into a body and echoes are generated which travel back to be received by the same transducer. These echoes vary in intensity according to the type of tissue or body structure, thereby creating images. An ultrasonic image represents the mechanical properties of the tissue, such as *density* and *elasticity*. We can recognize anatomical structures in an ultrasonic image since the organ boundaries and fluid-to-tissue interfaces are easily discerned. The ultrasonic imaging process can also be carried out in real time. This means we can follow rapidly moving structures such as the heart without motion distortion. In addition, ultrasound is one of the safest diagnostic imaging techniques. It does not use ionizing radiation like x-rays and thus is routinely used for fetal and obstetrical imaging. Useful areas for ultrasonic imaging include cardiac structures, the vascular systems, the fetus and abdominal organs such as liver and kidney. In brief, it is possible to see inside the human body without breaking the skin by using a beam of ultrasound.

Figure 1.29 shows the basic ultrasonic transducer geometry. The transducer is composed mainly of matching piezoelectric material and backing layers.[63] One or more matching layers are used to increase sound transmissions into tissues. The backing is added to the rear of the transducer in order to dampen the acoustic backwave and to reduce the pulse duration. Piezoelectric materials are used to generate and detect ultrasound. In general, broadband transducers should be used for medical ultrasonic imaging. The broad bandwidth response corresponds to a short pulse length, resulting in better axial resolution. Three factors are important in designing broad bandwidth transducers: *acoustic impedance matching*, a *high electromechanical coupling coefficient* of the transducer, and *electrical impedance matching*. These pulse echo transducers operate based on thickness mode resonance of the piezoelectric thin plate. Further, a low planar mode coupling coefficient, k_p, is beneficial for limiting energies being expended in non-productive lateral mode. A large dielectric constant is necessary to enable a good electrical impedance match to the system, especially with tiny piezoelectric sizes.

There are various types of transducers used in ultrasonic imaging. Mechanical sector transducers consist of single, relatively large resonators

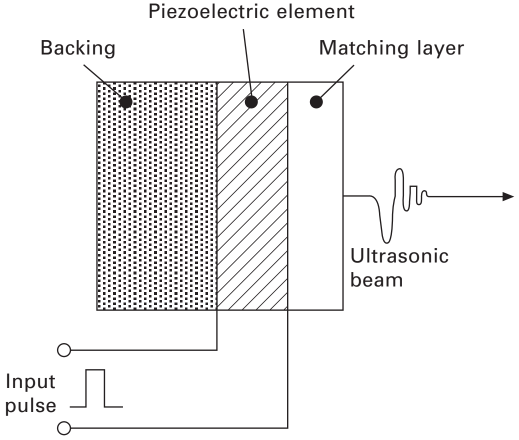

1.29 Basic transducer geometry for acoustic imaging applications.

and can provide images by mechanical scanning such as wobbling. Multiple element array transducers permit discrete elements to be individually accessed by the imaging system and enable electronic focusing in the scanning plane to various adjustable penetration depths through the use of phase delays. Two basic types of array transducers are linear and phased (or sector). A linear array is a collection of elements arranged in one direction, producing a rectangular display (see Fig. 1.30). A curved linear (or convex) array is a modified linear array whose elements are arranged along an arc to permit an enlarged trapezoidal field of view. The elements of these linear type array transducers are excited sequentially group by group with the sweep of the beam in one direction. These linear array transducers are used for radiological and obstetrical examinations. On the other hand, in a phased array transducer the acoustic beam is steered by signals that are applied to the elements with delays, creating a sector display. This transducer is useful for cardiology applications where positioning between the ribs is necessary.

Figure 1.31 demonstrates the superiority of the PZN-PT single crystal to the PZT ceramic for medical imaging transducer applications, developed by Toshiba Corporation.[64] Conventionally, the doctor needs to use two different

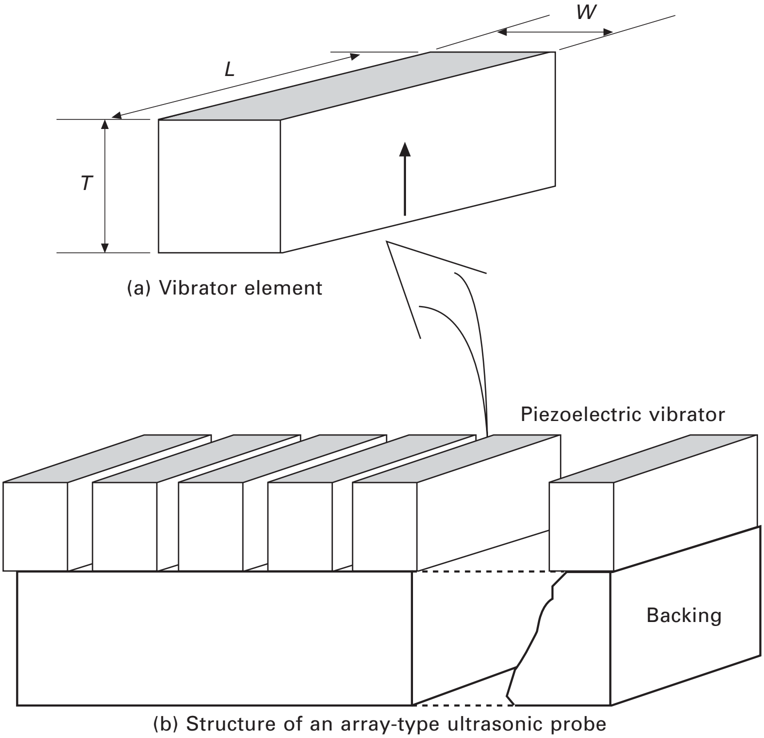

1.30 Linear array type ultrasonic probe.

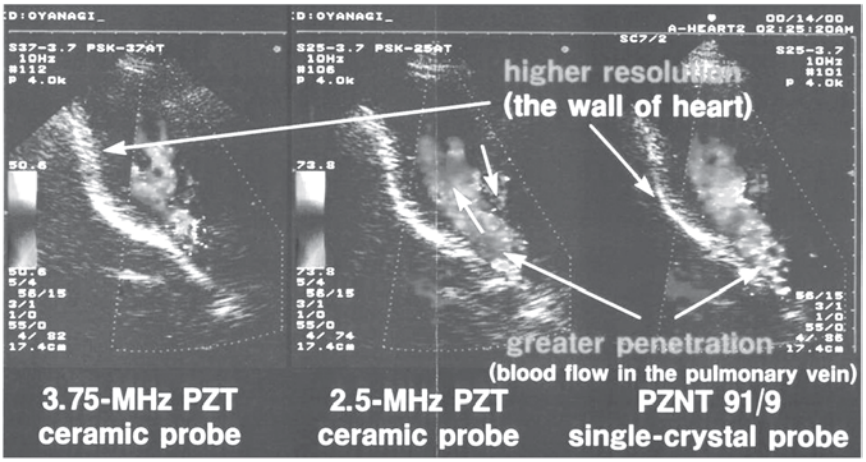
D:OYANAGI_
D:OYANAGI_
00/14/00
A-HEART2 02:25:20AM
SC7/2
S37-3.7 PSK-37AT
10Hz
#112
P 4.0k
S25-3.7 PSK-25AT
10Hz
#106
P 4.0k
S25-3.7
10Hz
#101
P 4.0K
higher resolution
(the wall of heart)
50.6
73.8
5/4
56/15
3/1
1/0
55/0
4/ 82
4/ 74
4/ 86
17.4cm
greater penetration
(blood flow in the pulmonary vein)
3.75-MHz PZT ceramic probe
2.5-MHz PZT ceramic probe
PZNT 91/9 single-crystal probe

1.31 Ultrasonic imaging with the two PZT ceramic probes (Left) and with the PZN-PT single crystal probe (Right). (Courtesy of Toshiba).

frequency PZT probes, one (2.5 MHz) for checking wider and deeper areas, and the other (3.75 MHz) for monitoring the specified area with a better resolution. The PZN-PT single crystal (with very high k_{33} and k_t) probe provides two additional advantages: (1) wide bandwidth – without changing the probe, the doctor can just switch the drive frequency from 2.5 to 3.75 MHz, (2) strong signal – because of the high electromechanical coupling, the receiving signal level is enhanced more than double compared with the PZT probe.

Sono-chemistry

Fundamental research on ‘Sono-chemistry’ is now very rapidly ongoing. Using the ‘cavitation’ effect, toxic materials such as dioxin and trichloroethylene can be easily transformed into innocuous materials at room temperature. Ultrasonic distillation is also possible at room temperature for obtaining highly concentrated Japanese ‘Sake’. Unlike the regular boiling distillation, this new method makes ‘Sake’ of much higher alcoholic concentration, while keeping the gorgeous taste and fragrance. Figure 1.32(a) shows the alcoholic concentration in the base solution and mist. This high-quality Sake product is now commercially available.[65]

High power ultrasonics is also applicable to transdermal drug delivery. The Penn State researchers are working on the commercialization of a ‘needle-free’ injection system of insulin by using cymbal piezo-actuators (see Fig. 1.32(b)).[66]

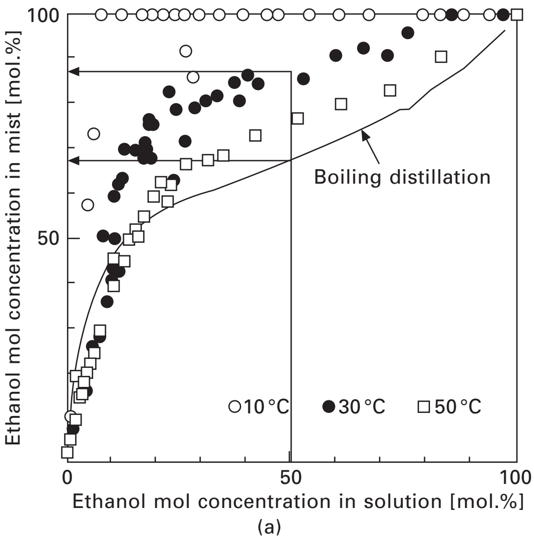

(a)

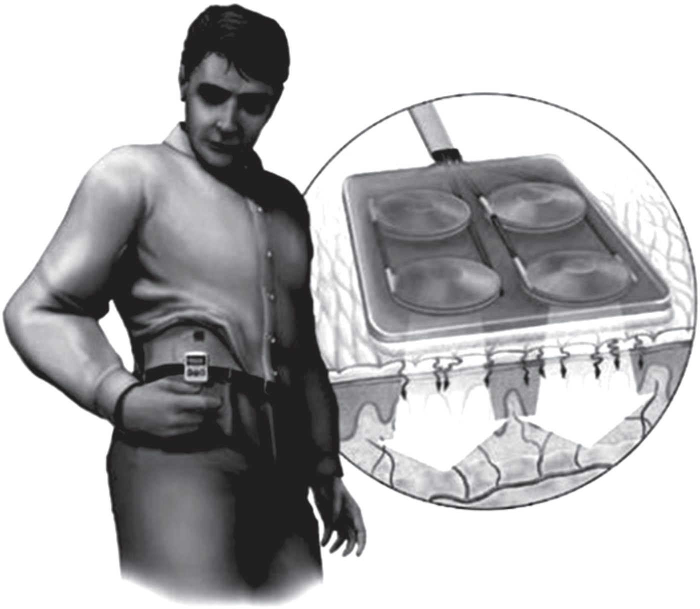

(b)

1.32 (a) Room temperature distillation with high power ultrasonic (courtesy of Matsuura Brewer), and (b) transdermal insulin drug delivery system using cymbal transducers[66] (illustration by Paul Perreault).

Resonators/filters

When a piezoelectric body vibrates at its resonant frequency it absorbs considerably more energy than at other frequencies resulting in a dramatic decrease in the impedance. This phenomenon enables piezoelectric materials to be used as a wave filter. A filter is required to pass a certain selected frequency band or to block a given band. The bandwidth of a filter fabricated from a piezoelectric material is determined by the square of the coupling coefficient k, that is, it is nearly proportional to k^2. The background is from the relation: $k_{31}^2/(1-k_{31}^2) = (\pi^2/4)(\Delta f/f_R)$, where $\Delta f = f_A - f_R$, and the bandwidth is provided by Δf. Quartz crystals with a very low k value of about 0.1 can pass very narrow frequency bands of approximately 1% of the center resonance frequency. On the other hand, PZT ceramics with a planar coupling coefficient of about 0.5 can easily pass a band of 10% of the center resonance frequency. The sharpness of the pass-band is dependent on the mechanical quality factor Q_M of the materials. Quartz also has a very high Q_M of about 10^6 which results in a sharp cut-off to the pass-band and a well-defined oscillation frequency.

A simple resonator is a thin disc type, electroded on its plane faces and vibrating radially, for filter applications with a center frequency ranging from 200 kHz to 1 MHz and with a bandwidth of several percent of the center frequency. For a frequency of 455 kHz the disc diameter needs to be about 5.6 mm. However, if the required frequency is higher than 10 MHz, other modes of vibration such as the thickness extensional mode are exploited, because of its smaller size. The trapped-energy type filters made from PZT ceramics have been widely used in the intermediate frequency range for applications such as the 10.7 MHz FM radio receiver and transmitter. When the trapped-energy phenomena are utilized, the overtone frequencies are suppressed. The plate is partly covered with electrodes of a specific area and thickness. The fundamental frequency of the thickness mode of the ceramic beneath the electrode is less than that of the unelectroded portion, because of the extra inertia of the electrode mass. The lower frequency wave of the electroded region cannot propagate into the unelectroded region. The higher frequency overtones, however, can propagate away into the unelectroded region. This is called the *trapped-energy principle*. Figure 1.33 shows a schematic drawing of a *trapped-energy filter*. In this structure the top electrode is split so that coupling between the two parts will only be efficient at resonance. More stable filters suitable for telecommunication systems have been made from single crystals such as quartz or $LiTaO_3$.

1.3.3 Surface acoustic wave devices

A *surface acoustic wave* (SAW), also called a *Rayleigh wave*, is essentially a coupling between longitudinal and shear waves. The energy carried by the

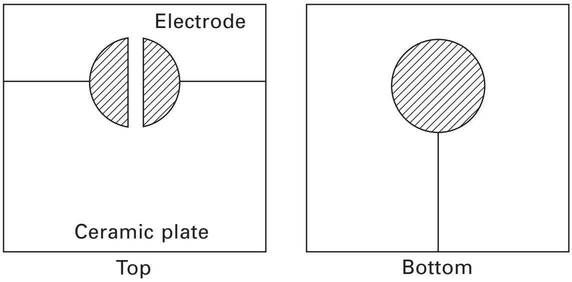

1.33 Schematic drawing of a trapped-energy filter.

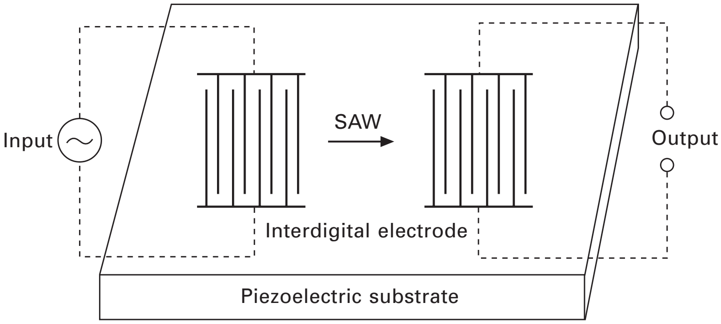

1.34 Fundamental structure of a surface acoustic wave device.

SAW is confined near the surface. An associated electrostatic wave exists for a SAW on a piezoelectric substrate, which allows electro-acoustic coupling via a transducer. The advantages of SAW technology are:[67,68]

- The wave can be electro-acoustically accessed and tapped at the substrate surface and its velocity is approximately 10^4 times slower than an electromagnetic wave.
- The SAW wavelength is on the same order of magnitude as line dimensions produced by photolithography and the lengths for both short and long delays are achievable on reasonably sized substrates.

There is a very broad range of commercial system applications which include front-end and IF (intermediate frequency) filters, CATV (community antenna television) and VCR (video cassette recorder) components, synthesizers, analyzers and navigators. In SAW transducers, finger (interdigital) electrodes provide the ability to sample or tap the wave and the electrode gap gives the relative delay. A SAW filter is composed of a minimum of two transducers. A schematic of a simple SAW bi-directional filter is shown in Fig. 1.34. A bi-directional transducer radiates energy equally from each side of the transducer. Energy that is not associated with the received signal is absorbed to eliminate spurious reflection.

Various materials are currently being used for SAW devices. The most popular single-crystal SAW materials are lithium niobate and lithium tantalate. The materials have different properties depending on the cut of the material and the direction of propagation. The fundamental parameters considered when choosing a material for given device applications are SAW velocity, temperature coefficients of delay (TCD), electromechanical coupling factor and propagation loss. Surface acoustic waves can be generated and detected by spatially periodic, interdigital electrodes on the plane surface of a piezoelectric plate. A periodic electric field is produced when an RF source is connected to the electrode, thus permitting piezoelectric coupling to a traveling surface wave. If an RF source with a frequency, f, is applied to the electrode having periodicity, d, energy conversion from an electrical to mechanical form will be maximum when

$$f = f_0 = v_s/d \qquad 1.38$$

where v_s is the SAW velocity and f_0 is the center frequency of the device. The SAW velocity is an important parameter determining the center frequency. Another important parameter for many applications is temperature sensitivity. For example, the temperature stability of the center frequency of SAW band-pass filters is a direct function of the temperature coefficient for the velocity and the delay for the material used. The first-order temperature coefficient of delay is given by:

$$(1/\tau)\cdot(d\tau/dT) = (1/L)\cdot(dL/dT) - (1/v_s)\cdot(dv_s/dT) \qquad 1.39$$

where $\tau = L/v_s$ is the delay time and L is the SAW propagation length. The surface wave coupling factor, k^2_s, is defined in terms of the change in SAW velocity which occurs when the wave passes across a surface coated with a thin massless conductor, so that the piezoelectric field associated with the wave is effectively short-circuited. The coupling factor, k^2_s, is expressed by:

$$k^2_s = 2\,(v_f - v_m)/v_f \qquad 1.40$$

where v_f is the free surface wave velocity and v_m the velocity on the metallized surface. In actual SAW applications, the value of k^2_s relates to the maximum bandwidth obtainable and the amount of signal loss between input and output, which determines the fractional bandwidth as a function of minimum insertion loss for a given material and filter. Propagation loss is one of the major factors that determines the insertion loss of a device and is caused by wave scattering at crystalline defects and surface irregularities. Materials which show high electromechanical coupling factors combined with small temperature coefficients of delay are generally preferred. The free surface velocity, v_f, of the material is a function of cut angle and propagation direction. The TCD is an indication of the frequency shift expected for a transducer due to a temperature change and is also a function of cut angle and propagation direction. The substrate is chosen based on the device design specifications which include operating temperature, fractional bandwidth, and insertion loss.

Piezoelectric single crystals such as 128°Y-X (128°-rotated-Y-cut and X-propagation) – $LiNbO_3$ and X-112°Y (X-cut and 112°-rotated-Y-propagation) – $LiTaO_3$ have been extensively employed as SAW substrates for applications in VIF filters. A c-axis oriented ZnO thin film deposited on a fused quartz, glass or sapphire substrate has also been commercialized for SAW devices. Table 1.4 summarizes some important material parameters for these SAW materials.

A delay line can be formed from a slice of glass such as PbO or K_2O doped SiO_2 glass in which the velocity of sound is nearly independent of temperature. PZT ceramic transducers are soldered on two metallized edges of the slice of glass. The input transducer converts the electrical signal to a shear acoustic wave which travels through the slice. At the output transducer the wave is reconverted into an electrical signal delayed by the length of time taken to travel around the slice. Such delay lines are used in color TV sets to introduce a delay of approximately 64 μsec and are also employed in videotape recorders.

Recent development on SAW actuator applications is interesting. A liquid transportation system was developed by using a standing-wave type SAW device.[69] A liquid droplet can be transported by controlling the SAW wave.

1.3.4 Micro-mass sensor

Bio-sensor

Quartz is not only for timers in clocks, but is also used for various micro-mass sensors. Because the mechanical quality factor Q_M is very large (= 10^6), the monitoring resolution of the resonance frequency reaches

Table 1.4 SAW material properties

	Material	Cut-propagation direction	k^2 (%)	TCD (ppm/C)	V_0 (m/s)	ε_r
Single crystal	Quartz	ST-X	0.16	0	3158	4.5
	$LiNb\ O_3$	128°Y-X	5.5	–74	3960	35
	$LiTaO_3$	X112°-Y	0.75	–18	3290	42
	$Li_2B_4O_7$	(110)-<001>	0.8	0	3467	9.5
Ceramic	PZT-$In(Li_{3/5}W_{2/5})O_3$		1.0	10	2270	690
	$(Pb,Nd)(Ti,Mn,In)O_3$		2.6	< 1	2554	225
Thin film	ZnO/glass		0.64	–15	3150	8.5
	ZnO/sapphire		1.0	–30	5000	8.5

$\Delta f_R/f_R = 10^{-6}$. Thus, even a small mass change on the quartz surface can be finely detected through the resonance frequency shift.

This micro-mass sensor can be utilized for a bio-sensor for detecting bacteria, such as *E. coli* and *Salmonella*. Levels as low as 10^4–10^7 cells per ml are already critical to humans in the case of *Salmonella*. Quartz oscillators can be used to detect this small amount of salmonella bacteria. Figure 1.35(a) shows the principle of this bio-sensor, where antibody/phage is coated on a single crystal quartz oscillator. Once particular bacteria are captured selectively by the antibodies, the surface mass of the oscillator is increased (see te SEM photo of captured bacteria in Fig. 1.35(b)). A sensitivity of 10^4 cells per ml can be obtained.[70]

Viscosity sensor

Several companies, including Stanford Research Systems, and Ulvac, Japan, commercialized a micro-balance to measure the viscosity of liquid. They

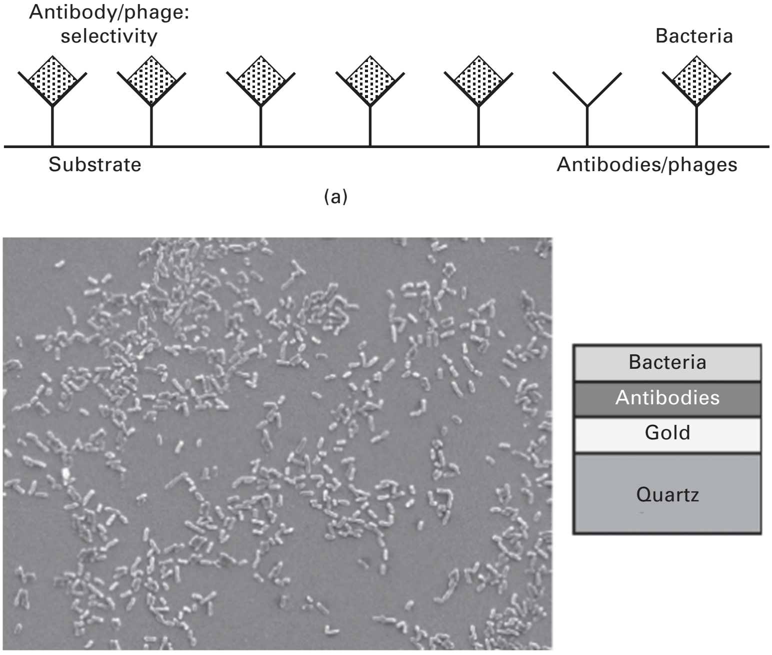

(a)

(b)

1.35 (a) Principle of a bio-sensor, where antibody/phage is coated on a single crystal quartz oscillator. Once particular bacteria are captured selectively by the antibodies (b), the surface mass of the oscillator is increased.

used a thickness-shear mode of the AT-cut quartz for intentionally enhancing the resonance frequency shift by the viscosity.[71]

1.3.5 Piezoelectric transformers

When input and output terminals are fabricated on a piezo-device and input/output voltage is changed through the vibration energy transfer, the device is called a *piezoelectric transformer*. Piezoelectric transformers were used in color TVs in the early 1970s, because of their compact size in comparison with the conventional electromagnetic coil-type transformers. Since serious problems were found initially in terms of mechanical strength (collapse occurred at the nodal point!) and in heat generation, the development approach was the same as that used for fabricating ceramic actuators. Recent lap-top computers with a liquid crystal display require a very thin, no electromagnetic-noise transformer to start the glow of a fluorescent back-lamp. This application has accelerated the development of the piezo-transformer, and the previous problems (mechanical strength and heat generation) have been almost overcome.

Since the original piezo-transformer was proposed by C. A. Rosen[72] a variety of such transformers have been investigated. Figure 1.36 shows a fundamental structure where two differently-poled parts coexist in one piezoelectric plate. A standing wave with a wavelength equal to the sample length is excited, a half wavelength existing on both the input (L_1) and output (L_2) parts. The voltage rise ratio r (step-up ratio) is given for the unloaded condition by:

$$r = (4/\pi^2)\, k_{31} k_{33} Q_{\mathrm{M}} (L_2/t) \left[2\sqrt{\frac{s_{33}^{\mathrm{E}}}{s_{11}^{\mathrm{E}}}} \right] \Bigg/ \left[\left(1 + \sqrt{\frac{s_{33}^{\mathrm{D}}}{s_{11}^{\mathrm{E}}}} \right) \right] \qquad 1.41$$

The r ratio is increased with increasing (L_2/t), where t is the thickness.

NEC proposed a multilayer type transformer (Fig. 1.37) in order to increase the voltage rise ratio.[73] Usage of the third-order longitudinal mode is another idea to distribute the stress concentration.

Step-down transformers for adaptor applications for portable equipment such as laptop computers and mobile phones have also been developed.

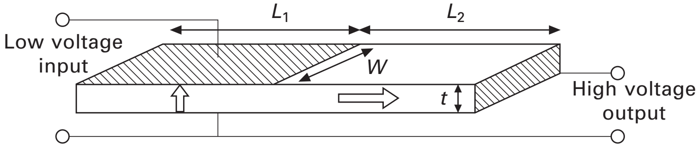

1.36 Piezoelectric transformer proposed by Rosen.[72]

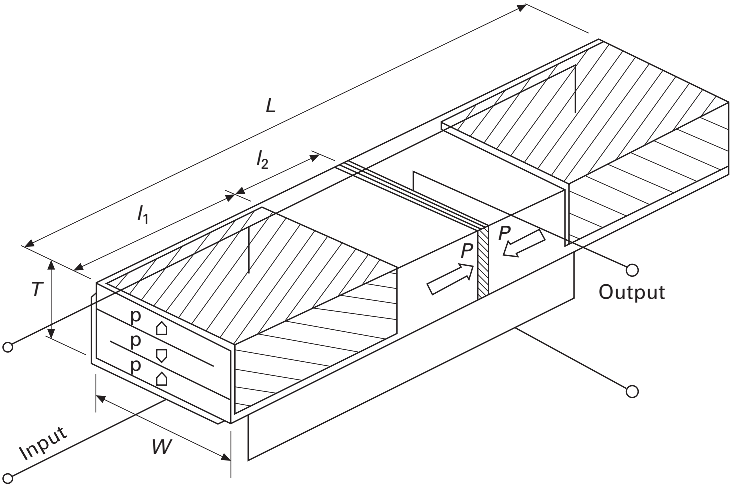

1.37 Multilayer type transformer by NEC.[73]

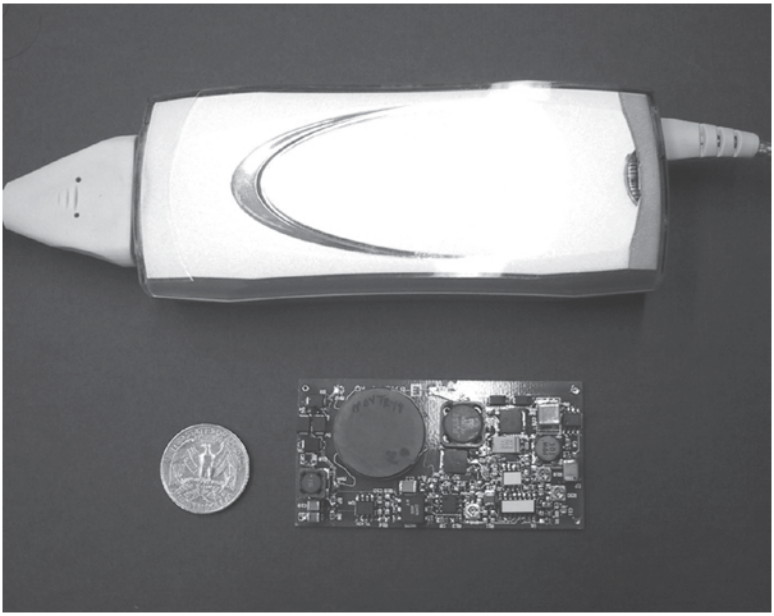

1.38 Credit-card size laptop computer adaptor (35 W) using a piezoelectric step-down transformer (below), in comparison with a commercial adaptor with an electromagnetic transformer (top).

Figure 1.38 shows a credit-card size 35 W adaptor for a laptop computer, developed by Face Electronics, Taiheiyo Cement, in collaboration with The Penn State University.[74]

1.3.6 Piezoelectric actuators

Piezoelectric and electrostrictive devices have become key components in smart actuator systems such as precision positioners, miniature ultrasonic motors and adaptive mechanical dampers. This section reviews the developments of piezoelectric and related ceramic actuators with particular focus on the improvement of actuator materials, device designs, and applications of the actuators.

Piezoelectric actuators are forming a new field between electronic and structural ceramics.[75–78] Application fields are classified into three categories: positioners, motors, and vibration suppressors. The manufacturing precision of optical instruments such as lasers and cameras, and the positioning accuracy for fabricating semiconductor chips, which must be adjusted using solid-state actuators, are generally on the order of 0.1 μm. Regarding conventional electromagnetic motors, tiny motors smaller than 1 cm are often required in office or factory automation equipment and are rather difficult to produce with sufficient energy efficiency. Ultrasonic motors, whose efficiency is insensitive to size, are considered superior in the mini-motor area. Vibration suppression in space structures and military vehicles using piezoelectric actuators is another promising field of application.

New solid-state displacement transducers controlled by temperature (shape memory alloy) or magnetic field (magnetostrictive alloy) have been proposed, but are generally inferior to the piezoelectric/electrostrictive ceramic actuators because of current technological trends aimed at reduced driving power and miniaturization.[78] The shape memory actuator is too slow in response with a very low energy efficiency, while the magnetostrictor requires a driving coil which is very bulky and generates magnetic noise.

Actuator designs

Two of the most popular actuator designs are the multilayers[79] and bimorphs (see Fig. 1.39). The multilayer, in which roughly 100 thin piezoelectric ceramic sheets are stacked together, has the advantages of low driving voltage (100 V), quick response (10 μs), high generative force (1 kN), and high electromechanical coupling. But the displacement, on the order of 10 μm, is not sufficient for some applications. This contrasts with the characteristics of the bimorph which consists of multiple piezoelectric and elastic plates bonded together to generate a large bending displacement of several hundred μm, but has relatively low response time (1 ms) and generative force (1 N).

A 3D positioning actuator with a stacked structure as pictured in Fig. 1.39 was proposed by a German company, where shear strain was utilized to generate the x and y displacements.[80] Polymer-packed PZT bimorphs have

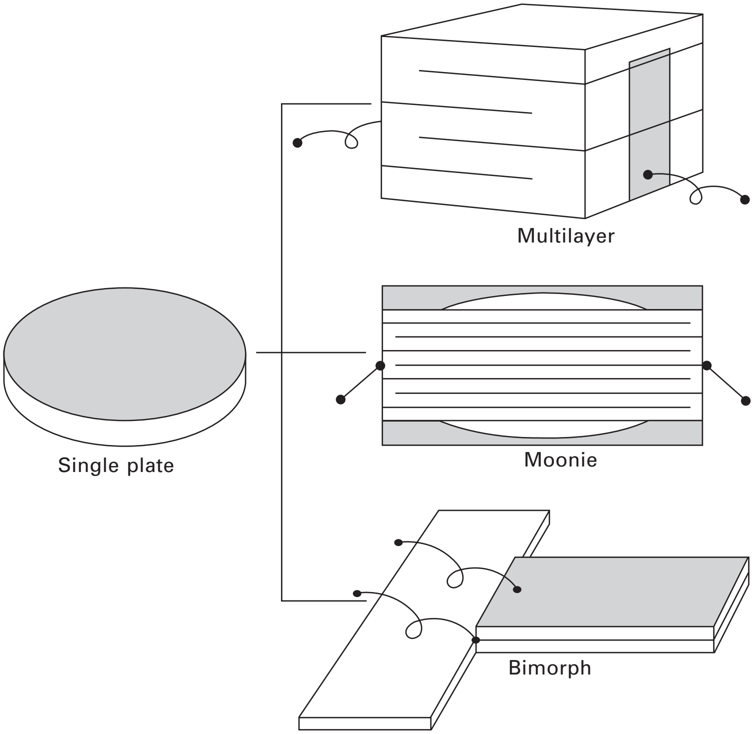

1.39 Typical designs for ceramic actuators: multilayer, moonie, and bimorph.

been commercialized by ACX for vibration reduction/control applications in smart structures.[81]

Market research conducted in 1998 by Japan Technology Transfer Association clarified that the actual demands on the actuators are as follows: 100 μm displacement, 100 N force, and 100 μsec response. Because neither the multilayer nor the bimorph can satisfy the actual demand, composite actuator structures called ‘moonie’ and ‘cymbal’ have been developed to provide characteristics intermediate between the multilayer and bimorph actuators; this transducer exhibits an order of magnitude larger displacement than the multilayer, and much larger generative force with quicker response than the bimorph.[82] The device consists of a thin multilayer piezoelectric element and two metal plates with a narrow moon-shaped or cymbal-shaped cavity bonded together as shown in Fig. 1.39. The moonie with a size of $5 \times 5 \times 2.5$ mm^3 can generate a 20 μm displacement under 60 V, eight times larger than the generative displacement produced by a multilayer of the same size.[83] This new compact actuator has been utilized in a miniaturized laser beam scanner.

Drive/control techniques

Piezoelectric/electrostrictive actuators may be classified into two categories, based on the type of driving voltage applied to the device and the nature of the strain induced by the voltage (Fig. 1.40): (1) rigid displacement devices for which the strain is induced uni-directionally along the direction of the applied d.c. field, and (2) resonating displacement devices for which the alternating strain is excited by an a.c. field at the mechanical resonance frequency (ultrasonic motors). The first can be further divided into two types: servo displacement transducers (positioners) controlled by a feedback system through a position-detection signal, and pulse drive motors operated in a simple on/off switching mode, exemplified by inkjet printers.

The material requirements for these classes of devices are somewhat different, and certain compounds will be better suited to particular applications. The ultrasonic motor, for instance, requires a very hard piezoelectric with a high mechanical quality factor Q_M, to suppress heat generation. Note that the resonating strain/displacement is amplified by a factor of Q_M, in comparison with the off-resonance strain/displacement (i.e., $dE \cdot L$).[84] Driving the motor at the antiresonance frequency, rather than at resonance, is also an intriguing technique to reduce the load on the piezoceramic and the power supply.[85] The servo displacement transducer suffers most from strain hysteresis and, therefore, a PMN electrostrictor is used for this purpose. The pulse drive motor requires a low permittivity material aimed at quick response with a certain power supply (a high power supply is expensive from the practical device application viewpoint!) rather than a small hysteresis, so soft PZT

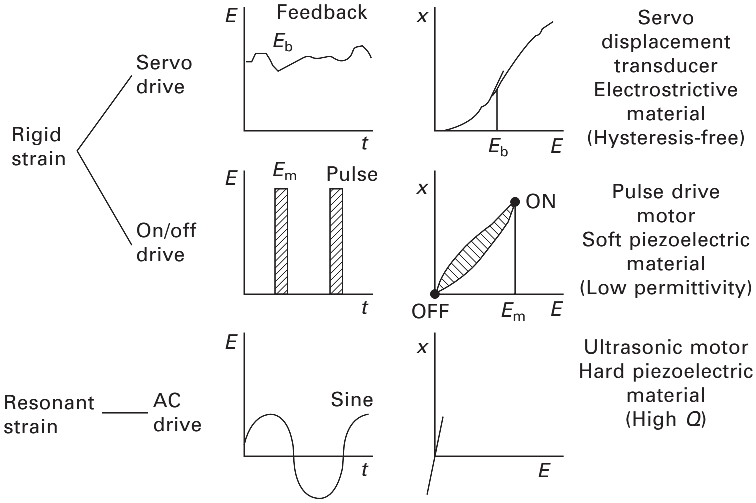
Rigid strain
Servo drive
On/off drive
Resonant strain
AC drive
E
Feedback
E_b
t
E
E_m
Pulse
t
E
Sine
t
x
E_b
E
x
ON
OFF
E_m
E
x
E
Servo displacement transducer Electrostrictive material (Hysteresis-free)
Pulse drive motor Soft piezoelectric material (Low permittivity)
Ultrasonic motor Hard piezoelectric material (High Q)

1.40 Classification of piezoelectric/electrostrictive actuators.

piezoelectrics are preferred rather than the high permittivity PMN for this application.

Pulse drive techniques for ceramic actuators are very important for improving the response of the device.[86,87] Figure 1.41 shows transient vibrations of a bimorph excited after a pseudo-step voltage is applied. The rise time is varied around the resonance period (n is the time scale with a unit of $T_0/2$, where T_0 stands for the resonance period). It is concluded that the overshoot and ringing of the tip displacement is completely suppressed when the rise time is precisely adjusted to the resonance period of the piezo-device (i.e., for $n = 2$).[86] A flight actuator was developed using a pulse-drive piezoelectric element and a steel ball. A 5 μm rapid displacement induced in a multilayer actuator can hit a 2 mm steel ball up to 20 mm in height. A dot-matrix printer head has been developed using a flight actuator.[88] By changing the drive voltage pulse width, the movement of the armature was easily controlled to realize no vibrational ringing or double hitting.

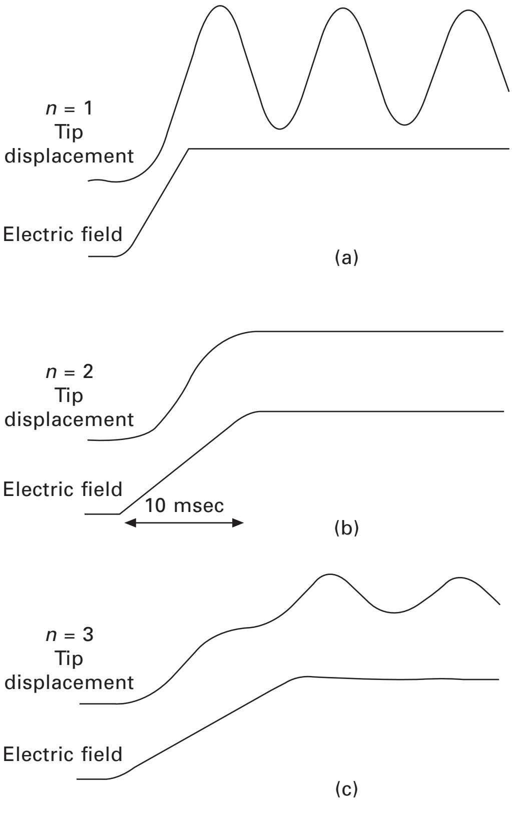

1.41 Transient vibration of a bimorph excited after a pseudo-step voltage applied. Here, n is a time scale with a unit of 1/2 of the resonance period (i.e., $2n$ = the resonance period).

Servo displacement transducers

A typical example of a servo displacement transducer is found in a space truss structure proposed by the Jet Propulsion Laboratory.[89] A stacked PMN actuator was installed at each truss nodal point and operated so that unnecessary mechanical vibration was suppressed immediately. A 'hubble' telescope has also been proposed using multilayer PMN electrostrictive actuators to control the phase of the incident light wave in the field of optical information processing (Fig. 1.42).[90] The PMN electrostrictor provided superior adjustment of the telescope image because of negligible strain hysteresis.

The US Army is interested in developing a rotor control system in helicopters. Figure 1.43 shows a bearingless rotor flexbeam with attached piezoelectric strips.[91] Various types of PZT-sandwiched beam structures have been investigated for such a flexbeam application and for active vibration control.[92]

Pulse drive motors

A dot matrix printer was the first widely commercialized product using ceramic actuators. Each character formed by such a printer was originally composed of a 24 × 24 dot matrix. A printing ribbon is subsequently impacted by a multi-wire array. A sketch of the printer head appears in Fig. 1.44(a).[93] The printing element is composed of a multilayer piezoelectric device, in which 100 thin ceramic sheets 100 μm in thickness were stacked, together with a sophisticated magnification mechanism (Fig. 1.44(b)). The magnification unit is based on a monolithic hinge lever with a magnification of 30×, resulting in an amplified displacement of 0.5 mm and energy transfer efficiency greater than 50%.

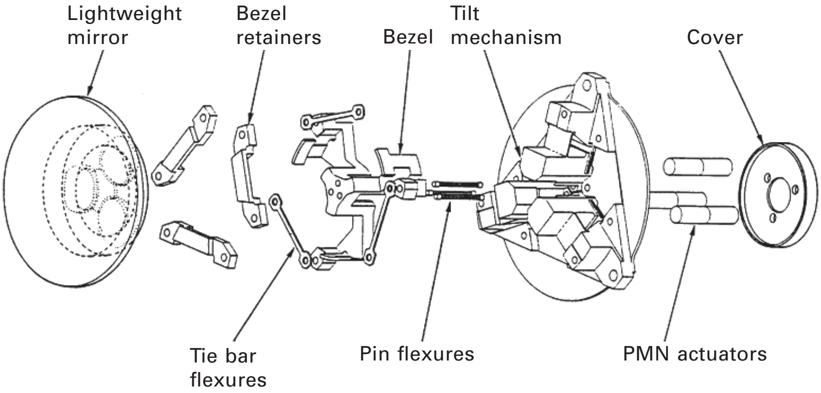

1.42 'Hubble' telescope using three PMN electrostrictive multilayer actuators for optical image correction.

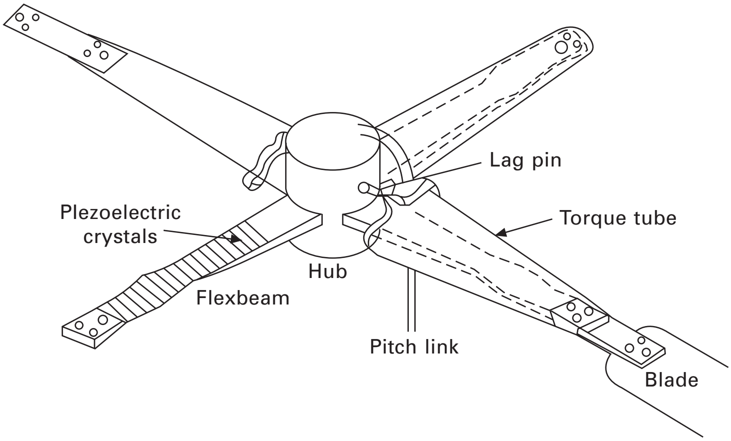
Lag pin
Plezoelectric crystals
Torque tube
Hub
Flexbeam
Pitch link
Blade

1.43 Bearingless rotor flexbeam with attached piezoelectric strips. A slight change in the blade angle provides for enhanced controllability.

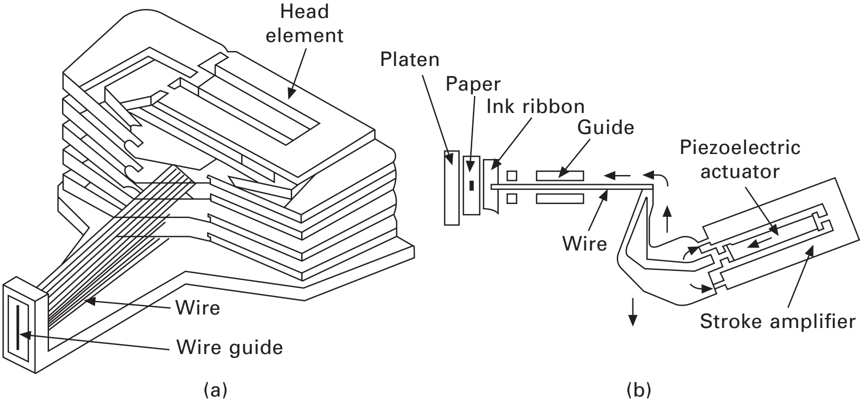
Head element
Wire
Wire guide
(a)
Platen
Paper
Ink ribbon
Guide
Piezoelectric actuator
Wire
Stroke amplifier
(b)

1.44 (a) Structure of a dot-matrix printer head (NEC), and (b) a differential-type piezoelectric printer-head element. A sophisticated monolithic hinge lever mechanism amplifies the actuator displacement by 30 times.

Figure 1.45 illustrates the recent inkjet printer produced by Seiko Epson,[94] in which PZT thin plates were laminated with vibration, chamber and communication plates to create a unimorph actuation mechanism. Using the cofiring technique with PZT and ZrO_2 elastic parts to manufacture this ML Chips head (MACH), Epson achieved superior stability in the ink chamber vibration and for various inks. In addition, more importantly, the manufacturing cost reduced dramatically by adopting this cofiring technique.

Toyota developed a Piezo TEMS (Toyota electronic modulated suspension),

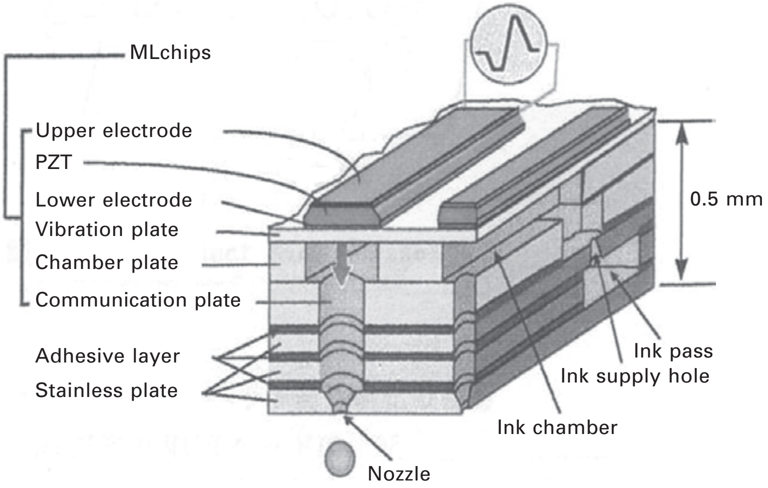

1.45 ACH inkjet printer head developed by Seiko Epson.

which is responsive to each protrusion on the road in adjusting the damping condition, and installed it on a 'Celcio' (equivalent to Lexus, internationally) in 1989.[95] In general, as the damping force of a shock absorber in an automobile is increased (i.e., 'hard' damper), the controllability and stability of a vehicle are improved. However, comfort is sacrificed because the road roughness is easily transferred to the passengers. The purpose of the electronically controlled shock absorber is to obtain both controllability and comfort simultaneously. Usually the system is set to provide a low damping force ('soft') so as to improve comfort, and the damping force is changed to a high position according to the road condition and the car speed to improve the controllability. In order to respond to a road protrusion, a very high response of the sensor and actuator combination is required.

Figure 1.46 shows the structure of the electronically controlled shock absorber. The sensor is composed of 5 layers of 0.5 mm thick PZT disks. The detecting speed of the road roughness is about 2 msec and the resolution of the up-down deviation is 2 mm. The actuator is made of 88 layers of 0.5 mm thick disks. Applying 500 V generates a displacement of about 50 μm, which is magnified by 40 times through a piston and plunger pin combination. This stroke pushes the change valve of the damping force down, then opens the bypass oil route, leading to the decrease of the flow resistance (i.e., 'soft'). The up-down acceleration and pitching rate were monitored when the vehicle was driven on a rough road. When the TEMS system was used, the up-down acceleration was suppressed to as small as the condition fixed at 'soft', providing comfort. At the same time, the pitching rate was also suppressed to as small as the condition fixed at 'hard', leading to better controllability.

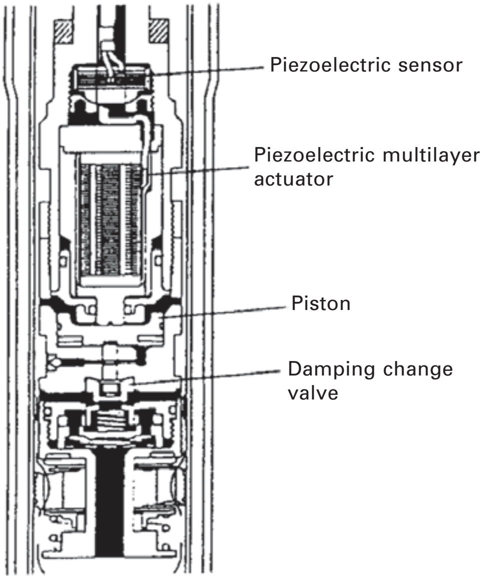

1.46 Toyota electronic modulated suspension (TEMS) with a multilayer piezoelectric actuator and a sensor.

In order to increase the diesel engine efficiency, high pressure fuel and quick injection control are required. For this purpose, piezoelectric actuators, specifically ML types, were adopted. The highest reliability of these devices at an elevated temperature (150 °C) for a long period (10 years) has been achieved. So-called common-rail type injection valves have been widely commercialized by Siemens, Bosch and Denso Corp. (Fig. 1.47).[96]

Figure 1.48 shows a walking piezo motor with four multilayer actuators developed by Philips.[97] Two shorter actuators function as clamps and the longer two provide the movement by an inchworm mechanism. A major drawback of this inchworm design is the mechanical noise created by the on-off drive (audible frequency due to the requirement lower than the mechanical resonance of the system).

1.3.7 Ultrasonic motors (USM)

The ultrasonic motor (USM) is one of the piezoelectric actuator categories. However, since it has been maturing as an industry already, the author uses a separate section for its discussion.

Electromagnetic motors were invented more than 100 years ago. While these motors still dominate the industry, a drastic improvement cannot be expected except through new discoveries in magnetic or superconducting

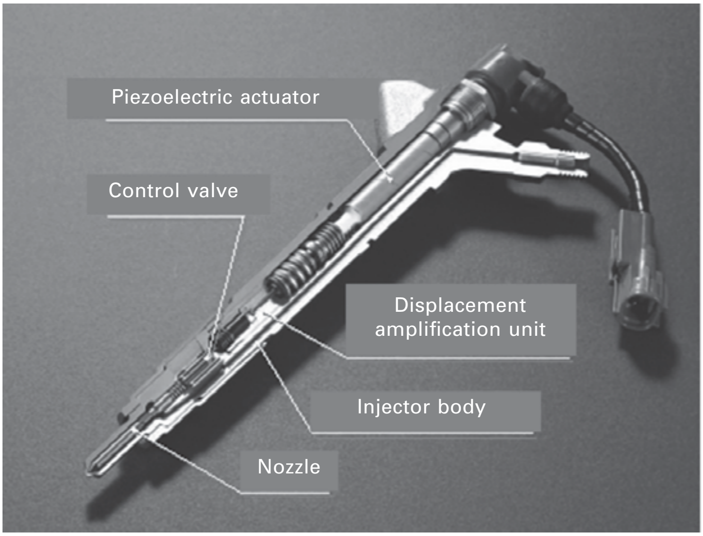
Piezoelectric actuator
Control valve
Displacement amplification unit
Injector body
Nozzle

1.47 Common rail type diesel injector with a piezoelectric multilayer actuator (Courtesy of Denso Corp.).

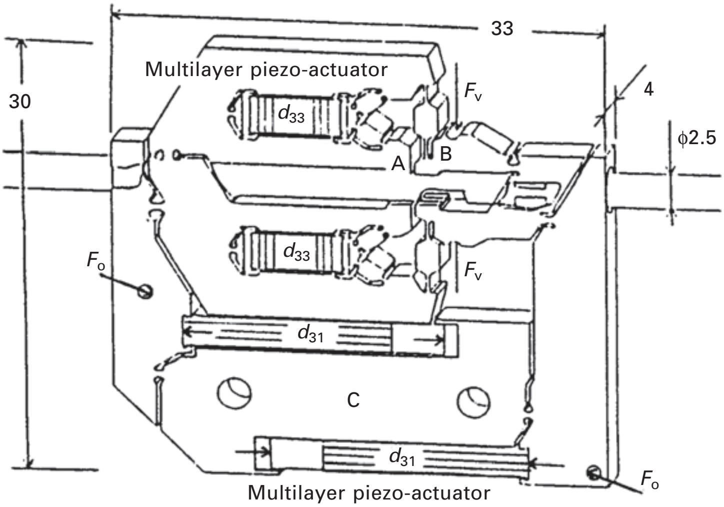
33
30
4
ϕ2.5
Multilayer piezo-actuator
F_v
d_{33}
A
B
F_o
d_{33}
F_v
d_{31}
C
d_{31}
F_o
Multilayer piezo-actuator

1.48 Walking piezo motor using an inchworm mechanism with four multilayer piezoelectric actuators by Philips.

materials. Regarding conventional electromagnetic motors, tiny motors smaller than 1 cm are rather difficult to produce with sufficient energy efficiency (more than 90% input electrical energy is spent for heat generation in a wristwatch motor at present!). Therefore, a new class of motors using high power ultrasonic energy, i.e., the ultrasonic motor, is gaining widespread attention. Ultrasonic motors made with piezoceramic whose efficiency is insensitive to size are superior in the mini-motor area. Figure 1.49 shows the basic construction of most ultrasonic motors, which consist of a high frequency power supply, a vibrator and a slider. The vibrator is composed of a piezoelectric driving component and an elastic vibratory part, and the slider is composed of an elastic moving part and a friction coat.

Although there had been some earlier attempts, the first practical ultrasonic motor was proposed by H. V. Barth of IBM in 1973.[98] Various mechanisms based on virtually the same principle were proposed by V. V. Lavrinenko *et al.*[99] and P. E. Vasiliev[100] in the former USSR. Because of the difficulty in maintaining constant vibration amplitude with temperature rise, wear and tear, the motors were not of much practical use at that time.

In the 1980s, with increasing chip pattern density, the semiconductor industry began to demand much more precise and sophisticated positioners which would not generate magnetic field noise. This urgent need accelerated the development of ultrasonic motors. Another advantage of ultrasonic motors over conventional electromagnetic motors with expensive copper coils is the improved availability of piezoelectric ceramics at reasonable cost. Japanese manufacturers are currently producing piezoelectric buzzers at about 30–40 cents per unit.

Let us summarize the advantages and disadvantages of the ultrasonic motor. The advantages are:

- Low speed and high torque
  - Direct drive

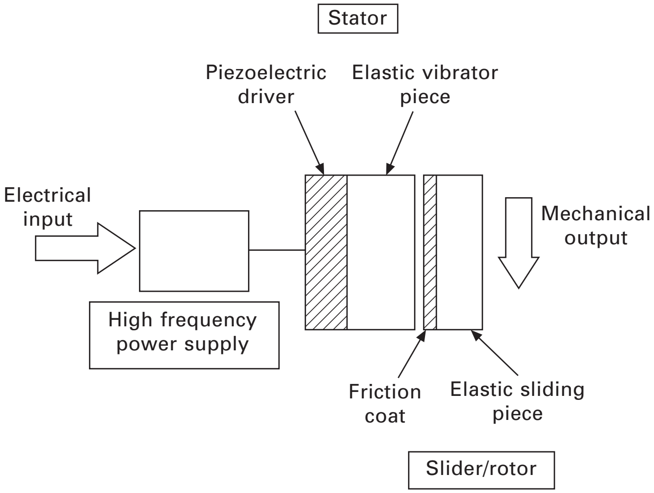

1.49 Fundamental construction of an ultrasonic motor.

- Quick response, wide velocity range, hard brake and no backlash
  - Excellent controllability
  - Fine position resolution
- High power/weight ratio and high efficiency
- Quiet drive (driven at an inaudible frequency for humans)
- Compact size and light weight
- Simple structure and easy production process
- Negligible effect from external magnetic or radioactive fields, and also no generation of these fields.

The disadvantages are:

- Necessity for a high frequency power supply
- Less durability due to frictional drive
- Drooping torque vs. speed characteristics.

Classification and principles of ultrasonic motors

The *standing-wave type* is sometimes referred to as a vibratory-coupler type or a 'woodpecker' type, where a vibratory piece is connected to a piezoelectric driver and the tip portion generates an elliptical movement. Figure 1.50 shows a simple model proposed by T. Sashida.[101] A vibratory piece is attached to a rotor or a slider with a slight cant angle θ. Take the x-y coordinate so that the x-axis is normal to the rotor face. When a vibration displacement,

$$u_x = u_0 \sin(\omega t + \alpha) \tag{1.42}$$

is excited at the piezoelectric vibrator, the vibratory piece generates bending because of restriction by the rotor, so that the tip moves along the rotor face between A → B, and freely between B → A. If the vibratory piece and the piezo-vibrator are tuned properly, they form a resonating structure, and if the bending deformation is sufficiently small compared with the length, the tip locus during the free vibration (B → A) is represented by

$$\begin{aligned} x &= u_0 \sin(\omega t + \alpha) \\ y &= u_1 \sin(\omega t + \beta) \end{aligned} \tag{1.43}$$

which composes an elliptical locus. Therefore, only the duration A → B provides a unidirectional force to the rotor through friction, and, therefore, an intermittent rotational torque or thrust. However, because of the inertia of the rotor, the rotation speed ripple is not observed to be large. The standing-wave type, in general, is low in cost (one vibration source) and has high efficiency (up to 98% theoretically), but lacks control in both the clockwise and counterclockwise directions, in general.

By comparison, the *propagating-wave type* (a surface-wave or 'surfing'

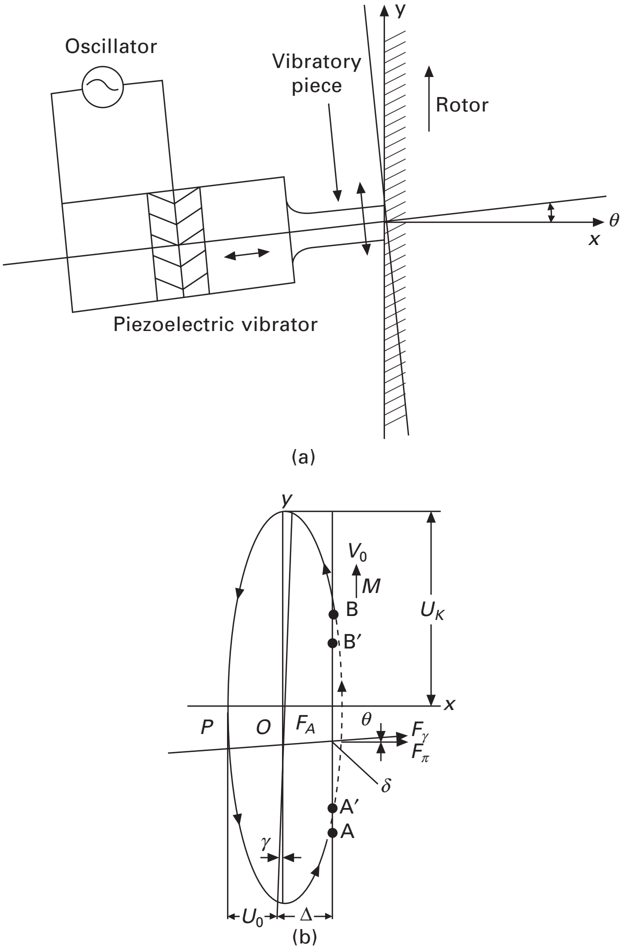
Oscillator
Vibratory piece
Rotor
y
θ
x
Piezoelectric vibrator
(a)
y
V_0
M
B
B′
U_K
x
P
O
F_A
θ
F_γ
F_π
δ
A′
A
γ
U_0
Δ
(b)

1.50 Vibratory coupler type motor (a) and its tip locus (b).

type) combines two standing waves with a 90° phase difference both in time and in space. The principle is illustrated in Fig. 1.51. A surface particle of the elastic body draws an elliptical locus due to the coupling of longitudinal and transverse waves. This type requires, in general, two vibration sources to generate one propagating wave, leading to low efficiency (not more than 50%), but it is controllable in both rotational directions.

Standing-wave type motors

T. Sashida developed a rotary type motor similar to the fundamental structure in Fig. 7.50.[101] Four vibratory pieces were installed on the edge face of a

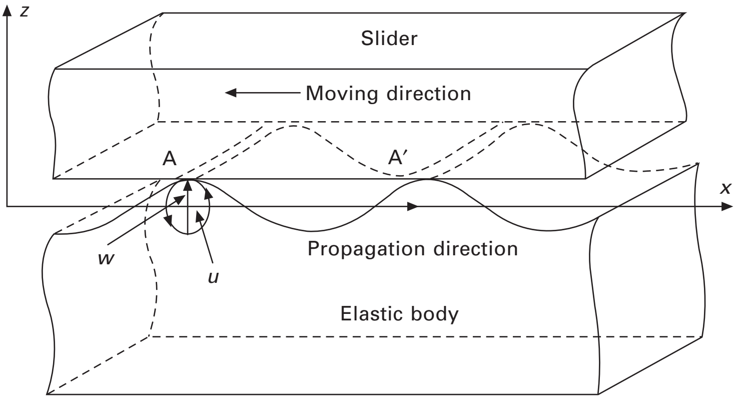

1.51 Principle of the propagating wave type motor.

cylindrical vibrator and pressed onto the rotor. This is one of the prototypes which triggered the present active development of ultrasonic motors. A rotation speed of 1500 rpm, torque of 0.08 N·m and an output of 12 W (efficiency 40%) were obtained under an input of 30 W at 35 kHz. This type of ultrasonic motor can provide a speed much higher than the inchworm types because of its high operating frequency and amplified vibration displacement at the resonance frequency.

Hitachi Maxel significantly improved the torque and efficiency by using a torsion coupler replacing Sashida's vibratory pieces (Fig. 1.52), and by increasing the pressing force with a bolt.[102] The torsion coupler looks like an old-fashioned TV channel knob, consisting of two legs which transform longitudinal vibration generated by the Langevin vibrator to a bending mode of the knob disk and a vibratory extruder. Notice that this extruder is aligned with a certain cant angle to the legs, which transforms the bending to a torsion vibration. This transverse moment coupled with the bending up-down motion leads to an elliptical rotation on the tip portion, as illustrated in Fig. 1.52(b). The optimum pressing force to get the maximum thrust is obtained when the ellipse locus is deformed roughly by half. A motor 30 mm × 60 mm in size and with a 20–30° cant angle between leg and vibratory piece can generate torques as high as 1.3 N·m with an efficiency of 80%. However, this type provides only unidirectional rotation. Note also that even though the drive of the motor is intermittent, the output rotation becomes very smooth because of the inertia of the rotor.

In collaboration with Samsung Electromechanics, Korea, The Penn State University developed a zoom mechanism with two micro rotary motors.[103–105] A micro motor called a 'metal tube type' consisting of a metal hollow cylinder and two PZT rectangular plates was used as basic micro actuators (see Fig. 1.53(a)). When we drive one of the PZT plates, Plate X, a bending vibration

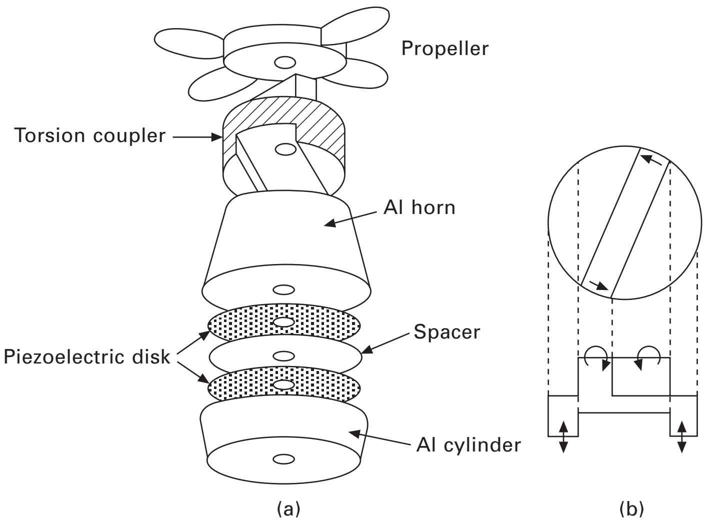

1.52 A mixed-mode ultrasonic motor incorporating a torsion coupler: (a) structure of the entire motor, and (b) motion of the torsion coupler.

is excited basically along the x′ axis. However, because of an asymmetric mass (Plate Y), another hybridized bending mode is excited with some phase lag along the y′ axis, leading to an elliptical locus in a clockwise direction, like a hula-hoop motion. In order to obtain a counter-clockwise rotation, one Plate Y is now driven. The rotor of this motor is a cylindrical rod with a pair of stainless ferrules pressed with a spring. The assembly is shown in Fig. 1.53(b). The metal cylinder motor 2.4 mm in diameter and 12 mm in length was driven at 62.1 kHz in both rotation directions. A no-load speed of 1800 rpm and an output torque up to 1.8 mN·m were obtained for rotation in both directions under an applied root mean square (rms) voltage of 80 V. A quite high maximum efficiency of about 28% for this small motor is a noteworthy feature.

The world's smallest camera with both optical zooming and auto focusing mechanisms for a cellular phone application developed in 2003 is shown in Fig. 1.54.[105] Two micro ultrasonic motors of 2.4 mm diameter and 14 mm length were installed to control zooming and focusing lenses independently in conjunction with screw mechanisms.

Nakamura *et al.* proposed a two-vibration-mode coupled type motor (Fig. 1.55), that is, a torsion Langevin vibrator was combined with three multilayer actuators to generate larger longitudinal and transverse surface displacements of the stator, as well as to control their phase difference.[106] The phase change can change the rotation direction.

Uchino *et al.* invented a π-shaped linear motor.[107] This linear motor is

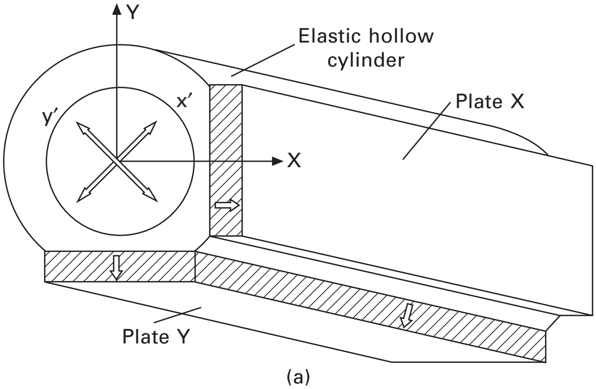

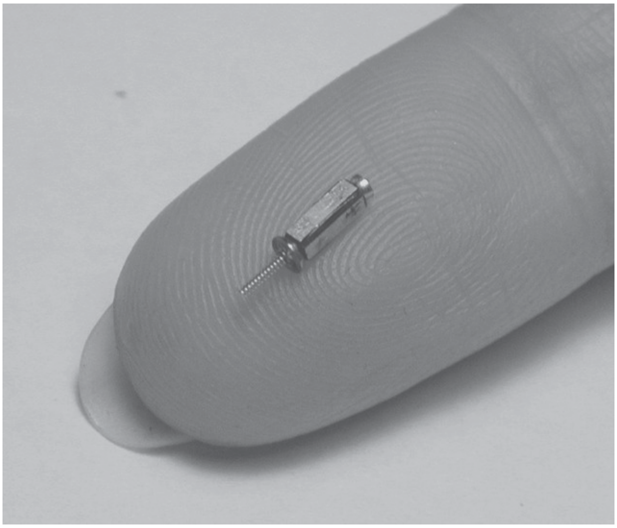
(b)

1.53 'Metal tube motor' using a metal tube and two rectangular PZT plates. (a) Schematic structure, and (b) photo of the world's smallest motor (1.5 mmf).

equipped with a multilayer piezoelectric actuator and fork-shaped metallic legs as shown in Fig. 1.56. Since there is a slight difference in the mechanical resonance frequency between the two legs, the phase difference between the bending vibrations of both legs can be controlled by changing the drive frequency. The walking slider moves in a way similar to a horse using its fore and hind legs when trotting. A test motor, 20 × 20 × 5 mm^3 in dimension, exhibits a maximum speed of 20 cm/s and a maximum thrust of 0.2 kgf (= 2 N) with a maximum efficiency of 20%, when driven at 98 kHz at 6 V (actual power = 0.7 W). This motor has been employed in a precision X-Y stage.

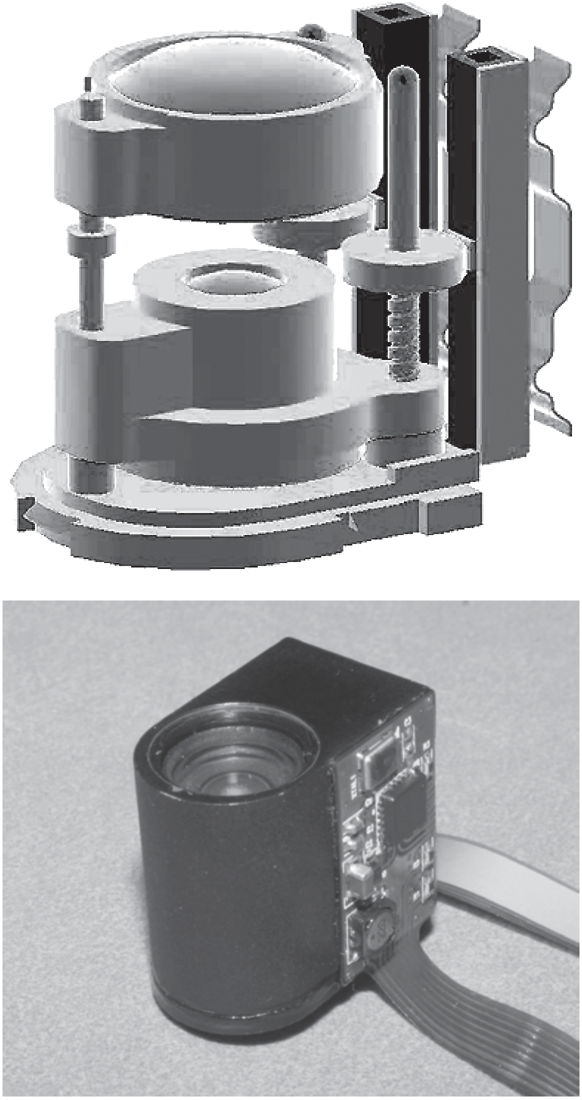

1.54 Camera auto zooming/focusing mechanism with two metal tube USMs in a Samsung cellular phone.

Propagating-wave type motors

Sashida and Ueha *et al*. manufactured a linear motor as illustrated in Fig. 1.57.[108,109] Two piezoelectric vibrators installed at both ends of a steel transmission rod excite and receive the traveling transverse wave (antisymmetric fundamental lambda wave mode). Adjusting a load resistance

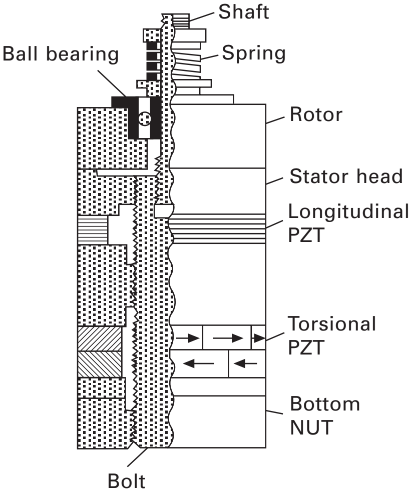
Shaft
Spring
Ball bearing
Rotor
Stator head
Longitudinal PZT
Torsional PZT
Bottom NUT
Bolt

1.55 Two-vibration-mode coupled type motor.

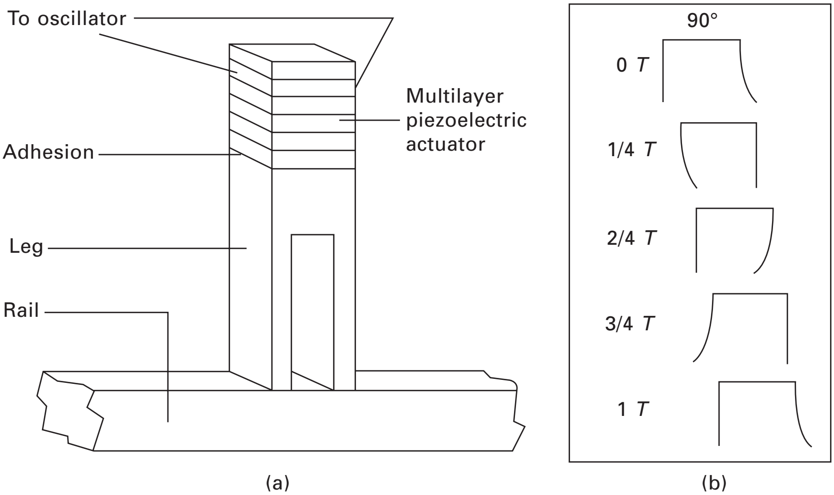
To oscillator
Multilayer piezoelectric actuator
Adhesion
Leg
Rail
90°
0 T
1/4 T
2/4 T
3/4 T
1 T

(a) (b)

1.56 p-shaped linear ultrasonic motor. (a) construction and (b) walking principle. Note the 90° phase difference of two legs similar to that associated with human walking.

in the receiving vibrator leads to a perfect traveling wave. Exchanging the roles of the transmitting and receiving piezo-components results in a reversal of the movement.

Using the bending vibration, the wavelength λ can be chosen as short as several mm to satisfy a stable surface contact with the slider by changing the cross-section area or the moment of inertia of the transmission rod. In the

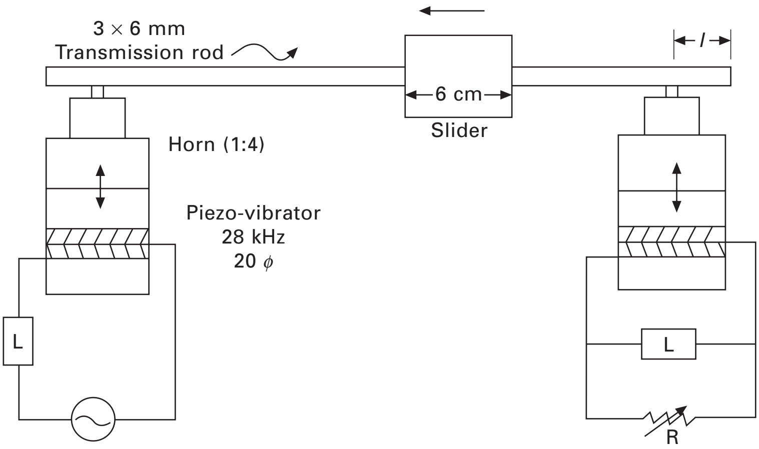

1.57 Linear motor using a bending vibration.

case of Fig. 1.57, λ = 26.8 mm. A slider, the contact face of which is coated with rubber or vinyl resin, clamps the transmission rod with an appropriate force. The transmission efficiency is strongly affected by the vibration source position on the rod, and shows a periodic variation with the distance from the free end of the rod to the position of the vibrator. Taking into account the wave phase, the vibration source should be fixed at a distance corresponding to one wavelength λ (i.e., 26.8 mm) from the rod end.

The slider, made of a steel clamper 60 mm in length, which theoretically covers two waves, was driven at a speed of 20 cm/s with a thrust of 50 N at 28 kHz. A major problem with this type of motor is its low efficiency (around 3%), because the whole rod must be excited even when only a small portion is utilized for the output. To overcome this dilemma, ring type motors were invented, where the whole rod can be utilized, because the lengths of the stator and rotor are the same.

When we deform the rod discussed in the previous section to make a ring by connecting the two ends topologically, we can make a rotary type motor using a bending vibration. Two types of ‘ring’ motor design are possible: the bending mode type and the extensional mode type.[110] Although the principle is similar to the linear type, more sophisticated structures are employed with respect to the ceramic poling and the mechanical support mechanism.

In general, when a vibration source drives one position of a closed ring (circular or square) at a frequency corresponding to the resonance of this ring, only a standing wave is excited, because the vibration propagates in two directions symmetrically from the vibration source and interference occurs. When multiple vibration sources are installed on the ring, displacements can be obtained by superimposing all the waves (two waves from each vibration source). Using the superimposition principle, we can generate a traveling-like wave in the closed ring with the profile of the original stationary wave.

Figure 1.58 shows the famous Sashida motor.[111] By means of the traveling elastic wave (up-down motion) induced by a thin piezoelectric ring (i.e., unimorph type), a ring-type slider in contact with the 'rippled' surface of the elastic body bonded onto the piezoelectric is driven in both directions by exchanging the sine and cosine voltage inputs. Another advantage is its thin design, which makes it suitable for installation in cameras as an automatic focusing device. Eighty percent of the exchange lenses in Canon's 'EOS' camera series have already been replaced by the ultrasonic motor mechanism.

The PZT piezoelectric ring is divided into 16 positively and negatively poled regions and two asymmetric electrode gap regions so as to generate a ninth-mode propagating wave at 44 kHz. A prototype was composed of a brass ring of 60 mm in outer diameter, 45 mm in inner diameter and 2.5 mm in thickness, bonded onto a PZT ceramic ring of 0.5 mm in thickness with divided electrodes on the back. The rotor was made of polymer coated with hard rubber or polyurethane.

Canon utilized Sashida's 'surfing' motor for a camera automatic focusing mechanism, installing the ring motor compactly in the lens frame. It is noteworthy that the stator elastic ring has many teeth, which can magnify the transverse elliptical displacement and improve the speed. The lens position can be shifted back and forth with a screw mechanism. The advantages of this motor over the conventional electromagnetic motor are:

- Silent drive due to the ultrasonic frequency drive and no gear mechanism (i.e., more suitable for video cameras with microphones).
- Thin motor design and no speed reduction mechanism such as gears, leading to space saving.
- Energy saving.

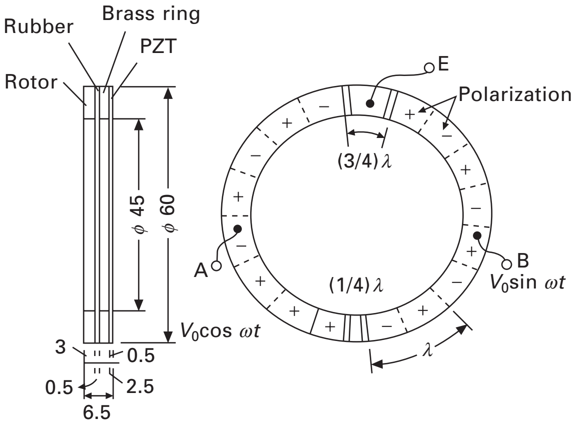

1.58 Stator structure of Sashida's motor.[111]

A general problem encountered for these traveling wave type motors is the support mechanism of the stator. In the case of a standing wave motor, the nodal points or lines are generally supported; this causes minimum effects on the resonance vibration. A traveling wave, however, does not have such steady nodal points or lines. Thus, special considerations are necessary. Matsushita Electric proposed a nodal line support method using a higher order vibration mode, where a wide ring is supported at the nodal circular line and 'teeth' are arranged on the maximum amplitude circle to get larger revolution.[112]

Seiko Instruments miniaturized the ultrasonic motor to dimensions of 10 mm and 4 mm in diameter using basically the same principle.[113] A driving voltage of 3 V and a current of 60 mA produces 6000 rev/min (no-load) with a torque of 0.1 mN·m. A 10 mm motor has been installed in a wristwatch for silent alarm function, while a 4 mm motor is used for perpetual function (i.e., date plate change). AlliedSignal developed ultrasonic motors similar to Shinsei's, which are utilized as mechanical switches for launching missiles.[114]

Smooth impact drive mechanism (SIDM)

Though the principle is different from the ultrasonic motor, a competitive technology is an impulse motor. Konika-Minolta developed a smooth impact drive mechanism (SIDM) using a ML piezo-element.[115] The idea comes from the 'stick & slick' condition of the ring object attached on a drive rod in Fig. 1.59(a). By applying a saw shape voltage to a multilayer actuator, alternating slow expansion and quick shrinkage are excited on a drive friction rod (see Fig. 1.59(b)). A ring slider placed on the drive rod will stick on the rod due to friction during a slow expansion period, while it will slide during a quick shrinkage period, so that the slider moves from the bottom to the top. A lens is attached to this slider. In order to obtain the opposite motion, the voltage saw shape is reversed. Compared to the USMs, the impulse motor is simpler, but the 1/10 smaller holding force may be a problem. The drive frequency can be much higher than the inchworm type, close up to the resonance frequency (i.e., the frequency inaudible to the human ear).

1.3.8 Piezoelectric energy harvesting

Piezoelectric passive damping to energy harvesting

Piezoelectric dampers were developed by the author's group in the 1980s. In order to suppress mechanical noise vibration, Uchino *et al.* used a piezoelectric, which could convert the vibration energy to electric

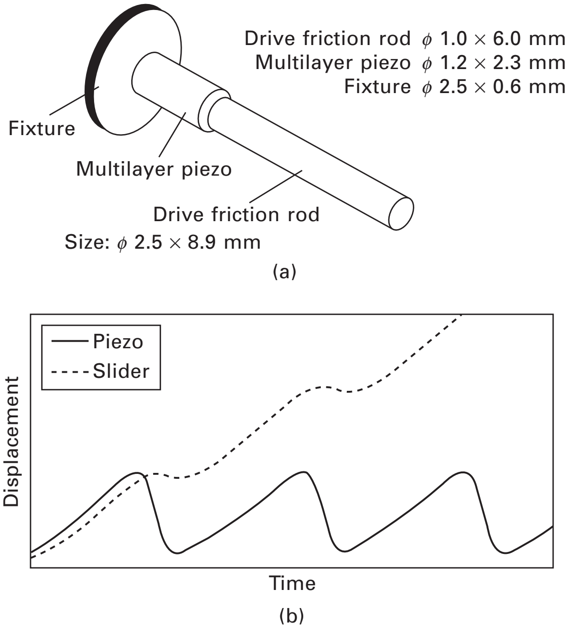
Drive friction rod ϕ 1.0 × 6.0 mm
Multilayer piezo ϕ 1.2 × 2.3 mm
Fixture ϕ 2.5 × 0.6 mm
Fixture
Multilayer piezo
Drive friction rod
Size: ϕ 2.5 × 8.9 mm
(a)
Piezo
Slider
Displacement
Time
(b)

1.59 (a) Illustration of the SIDM developed by Konica-Minolta for phone camera zooming applications. (b) Displacements of the piezo-element and the slider to show the 'stick & slick' motion.[115]

energy. The resistive shunt method was patented for consuming the converted electric energy in Joule heat, so that the mechanical vibration was dramatically damped. A piezoceramic patch was bonded on an elastic plate with its fundamental resonance frequency around 200 Hz. Figure 1.60 shows that there is an optimal resistance 6.6 kΩ to be connected to the piezoelectric damping device in order to obtain the quickest damping; that is, the resistance should be chosen equal to the piezo-damper impedance $Z = 1/\omega C$ (impedance matching).[36] The piezo-shunt methodologies have now been extended to a combination of resistive, capacitive, and inductive components.

Consuming the converted electric energy in Joule heat seemed to be useless. Thus, Uchino *et al.* started to accumulate the electric energy in batteries in the 1990s. Unused power exists in various forms such as vibrations, water flow, wind, human motion, and shock waves. In recent years, industrial and academic research units have focused attention on harvesting energy from vibrations using piezoelectric transducers. These efforts have provided the initial research guidelines and have brought to light the problems and limitations of implementing the piezoelectric transducer. There are three major steps associated with piezoelectric energy harvesting:[116]

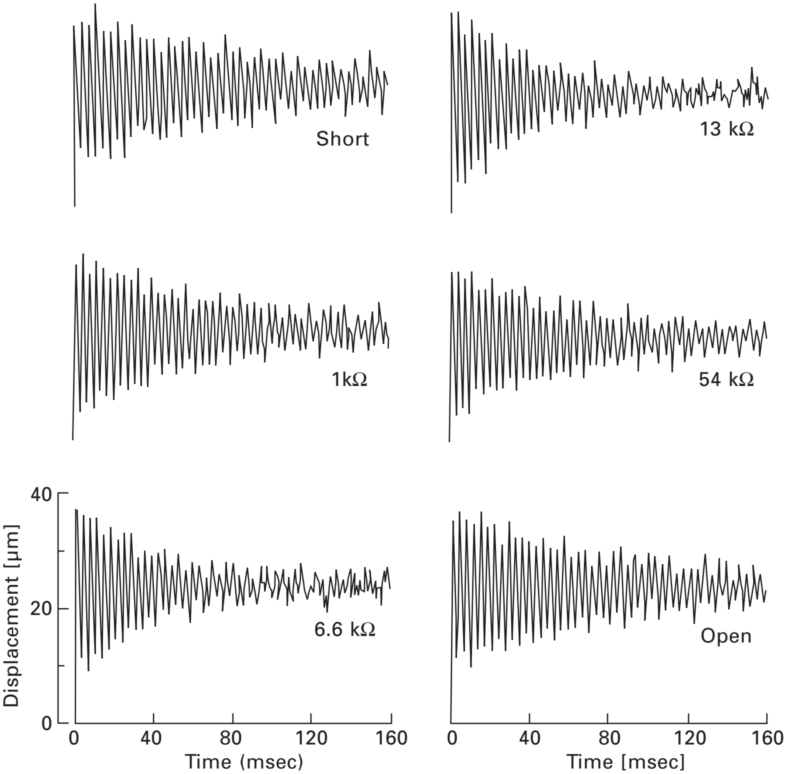

1.60 Resistive shunt piezoelectric patch for vibration damping test. The fundamental resonance frequency of this vibration system is around 200 Hz. Note that the resistance 6.6 kΩ exhibits the quickest damping.

1. *Mechanical-mechanical energy transfer*: This includes mechanical stability of the piezoelectric transducer under large stresses, and mechanical impedance matching.
2. *Mechanical-electrical energy transduction*: This relates with the electromechanical coupling factor in the composite transducer structure.
3. *Electrical-electrical energy transfer*: This includes electrical impedance matching, a d.c./d.c. converter to accumulate the energy into a capacitor or a rechargeable battery.

High energy harvesting (~W)

Periodic vibrations generated from rotating machines or engines are one of the most promising sources for recovering energy. Kim *et al.* investigated first the capability of harvesting the electrical energy from mechanical vibrations in a dynamic environment, such as an automobile engine through a 'cymbal' piezoelectric transducer.[117,118] The targeted mechanical vibration from an engine lies in the range of 50–150 Hz with force amplitude of the order of 1kN. It was found that under such severe stress conditions the metal-ceramic composite transducer 'cymbal' is a promising rigid structure, keeping a relatively high electromechanical transduction rate. The metal cap enhances the endurance of the ceramic to sustain high loads along with stress amplification. In our study, the experiments were performed under a force of 7–70 N at a frequency of 100 Hz on a cymbal of 29 mm diameter and 1 mm thickness. At this frequency and force level, 60 mW power was generated from a cymbal measured across a 400 kΩ resistor. Figure 1.61 illustrates the final cymbal energy harvesting composites, in which three cymbals are embedded in a triangular shaped rubber sheet. These composite sheets are inserted as mats below the engine. Since each cymbal can generate close to 100 mW continuously, 1 W can be obtained in total. Note that the optimal conditions for obtaining the maximum vibration damping and the maximum energy harvesting are exactly the same; that is, we can chase two 'rabbits' at the same time.

Usually the output impedance of the harvested electrical energy with a piezoelectric transducer is extremely high, so that the electrical impedance mismatch provides significant reduction of efficiency for accumulating the electric charge into a rechargeable battery, which has typically low impedance around 10–100 Ω. To overcome this problem, so-called switch-shunt is most popularly used for energy harvesting purposes. A d.c.-d.c. buck-converter was designed for the above cymbal system which allows transfer of 50 mW power out of 60 mW from the cymbal (82% efficiency) to a low impedance load of 5 kΩ with a 2% duty cycle and at a switching frequency of 1 kHz.[119]

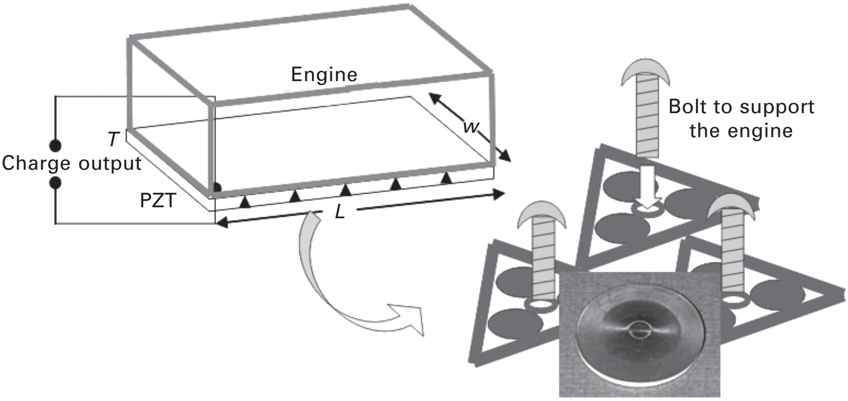

1.61 High power energy harvesting (1 W at 100 Hz) with 'cymbal' piezoelectric flexible composites.

Another unique circuit design may be with a piezoelectric transformer. The piezoelectric transformer used in the circuit has low output impedance around 50 Ω, and the efficiency of the piezoelectric transformer in the resonance is over 95%. This low output impedance is suitable for an impedance matching to the load (rechargeable battery).[120]

Low energy harvesting (~mW)

Another promising vibration source is human motion. Uchino *et al.* are developing intelligent clothing (IC) with piezoelectric energy harvesting system of flexible piezoelectric textiles, aiming at a general power source for charging portable equipment such as cellular phones, health monitoring units or medical drug delivery devices. The macro fiber composite (MFC) is an actuator that offers high performance and flexibility in a cost-competitive device (Smart Material Corp.). The MFC consists of rectangular piezoceramic rods sandwiched between layers of adhesive and electroded polyimide film. This film contains interdigitated electrodes that transfer the applied voltage directly to and from the ribbon shaped rods. This assembly enables in-plane poling, actuation, and sensing in a sealed, durable, ready-to-use package. When embedded in a surface or attached to flexible structures, the MFC actuator provides distributed solid-state deflection and vibration control (see Fig. 1.62). The MFC composites can generate power at the mW level.[120]

Remote electric switches developed by Face/PulseSwitch Systems, LC, VA are one of the successful products using a unimorph type (Thunder) piezo-device.[121] Lightning switch wireless transmitters (the switch controls)

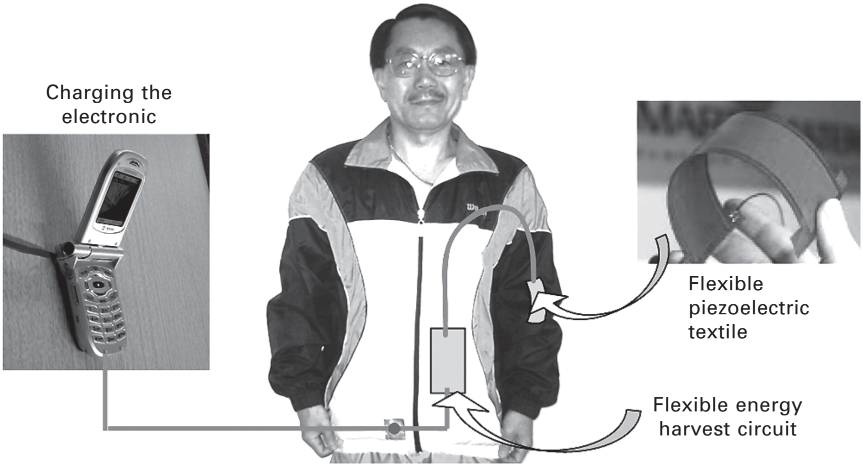
Charging the electronic
Flexible piezoelectric textile
Flexible energy harvest circuit

1.62 Intelligent clothing (IC) energy harvesting system with macro fiber composites.

use NASA space technology to generate their own electricity whenever the transmitter button is pushed mechanically through the piezoelectricity. Their radio signals travel 40 to more than 100 feet right through walls, floors, and ceilings.

1.4 References

1. K. Uchino: *Entrepreneurship for Engineers*, CRC Press, New York (2009).
2. K. Honda: *Ultrasonic World*, NHK Books No. 710, Tokyo, Japan (1994).
3. A. M. Nicholson: *Piezophony*, US Patent 1,495,429 (filed April 10, 1918: patented May 10, 1924).
4. E. W. Moore: *J. Amer. Chem. Soc.* **41**, 1060–1066 (1919).
5. G. Busch: *Condensed Matter News* **1**(2), 20–29 (1991).
6. G. Busch and P. Scherrer: *Naturwiss.* **23**, 737 (1935).
7. E. Wainer and N. Salomon: *Trans. Electrochem. Soc.* **89** (1946).
8. T. Ogawa: *Busseiron Kenkyu*, No. 6, pp. 1–27 (1947) (in Japanese).
9. B. M. Vul, *Electrichestvo*, No. 3 (1946) (in Russian).
10. T. Ogawa and S. Waku: *Splendid Tita-Bari*, Maruzen, Tokyo (1990) (in Japanese).
11. B. Jaffe, W. Cook and H. Jaffe: *Piezoelectric Ceramics*, Academic Press, London (1971).
12. S. Roberts: *Phys. Rev.* **71**, 890–895 (1947).
13. W. P. Mason: *Phys. Rev.* **73**, 1398–1399 (1948).
14. E. Sawaguchi, G. Shirane and Y. Takagi: *J. Phys. Soc. Japan* **6**, 333–339 (1951).
15. E. Sawaguchi: *J. Phys. Soc. Japan* **8**, 615–629 (1953).
16. B. Jaffe: US Patent 2,708,244, May (1955).
17. K. Abe, T. Tanaka, S. Miura and K. Okazaki: *Bull. Inst. Chem. Res., Kyoto Univ.* **31**, 295–304 (1953).
18. T. Tanaka: *Bull. Inst. Chem. Res., Kyoto Univ.* **32**, 43–53 (1954).
19. B. T. Matthias and J. P. Remeika: *Phys. Rev.* **76**, 1886–1887 (1949).
20. K. Uchino: *Ferroelectric Devices* 2nd edn, CRC Press, New York (2009).
21. G. A. Smolenskii and A. I Agranovskaya: *Sov. Phys., Solid State* **1**, 1429 (1960).
22. V. A. Bokov and I. E. Myl'nikova: *Sov. Phys., Solid State* **2**, 2428 (1961).
23. L. E. Cross, S. J. Jang, R. E. Newnham, S. Nomura and K. Uchino: *Ferroelectrics* **23**(3), 187 (1980).
24. J. Kuwata, K. Uchino and S. Nomura: *Ferroelectrics* **37**, 579 (1981).
25. J. Kuwata, K. Uchino and S. Nomura: *Jpn J. Appl. Phys.* **21**, 1298 (1982).
26. K. Yanagiwawa, H. Kanai and Y. Yamashita: *Jpn J. Appl. Phys.* **34**, 536 (1995).
27. S. E. Park and T. R. Shrout: *Mat. Res. Innovt.* **1**, 20 (1997).
28. X. H. Du, U. Belegundu and K. Uchino: *Jpn J. Appl. Phys.* **36** (9A), 5580–5587 (1997).
29. H. Kawai: *Jpn J. Appl. Phys* **8**, 975 (1969).
30. V. Bharti, H. S. Xu, G. Shanti, Q. M. Zhang and K. Liang: *J. Appl. Phys.* **87**, 452 (2000).
31. Y. Saito: *Jpn J. Appl. Phys.* **35**, 5168–73 (1996).

32. T. Kitayama and S. Sugawara: *Proc. Study Comm. Electronic Circuit Components & Mater.*, CPM72-17 (1972-0) (1972).
33. R. E. Newnham, D. P. Skinner and L. E. Cross: *Mater. Res. Bull.* **13**, 525 (1978).
34. J. Van Suchtelene: *Philips Res. Rep.* **27**, 28 (1972).
35. J. Ryu, A. Vazquez Carazo, K. Uchino and H.-E. Kim: *Jpn J. Appl. Phys.* **40**, 4948–4951 (2001).
36. K. Uchino and T. Ishii: *J. Ceram. Soc. Jpn* **96**, 863 (1988).
37. Y. Suzuki, K. Uchino, H. Gouda, M. Sumita, R. E. Newnham and A. R. Ramachandran: *J. Ceram. Soc. Jpn., Int'l Edition* **99**, 1096 (1991).
38. P. S. Brody: *Ferroelectrics* **50**, 27 (1983).
39. K. Uchino and M. Aizawa: *Jpn J. Appl. Phys. Suppl.* **24**, 139–141 (1985).
40. M. Tanimura and K. Uchino: *Sensors and Materials*, **1**, 47–56 (1988).
41. K. Uchino: *J. Rob. Mech.* **124**, 44–47 (1989).
42. S. Thakoor, J. M. Morookian and J. A. Cutts: *Conf. Proc. 10th IEEE Int'l Symp. on Appl. Ferroelectrics* **1**, 205–211 (1996).
43. K. Uchino, M. Yoshizaki, K. Kasai, H. Yamamura, N. Sakai and H. Asakura: *Jpn J. Appl. Phys.* **26**(7), 1046 (1987).
44. Aura Ceramics, Inc., Catalogue 'Rainbow'.
45. K. Uchino: *Micromechatronics*, CRC/Dekker, New York (2003).
46. T. Ikeda: *Fundamentals of Piezoelectric Materials Science*, Ohm Publishing Co., Tokyo (1984).
47. L. E. Kinsler, A. R. Frey, A. B. Coppens and J. V. Sanders: *Fundamentals of Acoustics*, John Wiley & Sons, New York, (1982).
48. Y. Ito and K. Uchino: Piezoelectricity, *Wiley Encyclopedia of Electrical and Electronics Engineering*, Vol. **16**, p. 479, John Wiley & Sons, Now York (1999).
49. W. A. Smith: *Proc. SPIE – The Int'l Society for Optical Engineering* 1733 (1992).
50. H. Takeuchi, S. Jyomura, E. Yamamoto and Y. Ito: *J. Acoust. Soc. Am.* **74**, 1114 (1982).
51. Y. Yamashita, K. Yokoyama, H. Honda and T. Takahashi: *Jpn J. Appl. Phys.* **20**, Suppl. 20–4, 183 (1981).
52. Y. Ito, H. Takeuchi, S. Jyomura, K. Nagatsuma and S. Ashida: *Appl. Phys. Lett.* **35**, 595 (1979).
53. H. Takeuchi, H. Masuzawa, C. Nakaya and Y. Ito: *Proc. IEEE 1990 Ultrasonics Symposium*, 697 (1990).
54. T. R. Shrout, Z. P. Chang, N. Kim and S. Markgraf: *Ferroelectric Lett.* **12**, 63 (1990).
55. W. A. Smith: *Proc. 1989 IEEE Ultrasonic Symposium*, 755 (1989).
56. S. Kalpat, X. Du, I. R. Abothu, A. Akiba, H. Goto and K. Uchino: *Jpn J. Appl. Phys.* **40**, 158 (2001).
57. K. Uchino, E. Sadanaga and T. Hirose, *J. Amer. Ceram. Soc.* **72**(8), 1555–1558 (1989).
58. Kistler, Stress Sensor, Production Catalog, Switzerland.
59. Tokin, Gyroscope, Production Catalog, Japan.
60. Y. Watabe: *Bull. Ceramic Soc. Japan* **42**(5), 396 (2007).
61. B. A. Auld: *Acoustic Fields and Waves in Solids*, 2nd edn, Robert E. Krieger, Melbourne (1990).

62. G. S. Kino: *Acoustic Waves: Device Imaging and Analog Signal Processing*, Prentice-Hall, Englewood Cliffs, NJ (1987).
63. C. S. Desilets, J. D. Fraser and G. S. Kino: *IEEE Trans. Sonics Ultrason.*, SU-25, 115 (1978).
64. S. Saitoh, T. Takeuchi, T. Kobayashi, K. Harada, S. Shimanuki and Y. Yamashita: *Jpn J. Appl. Phys.* **38**(5B), 3380–3384 (1999).
65. http://www.shumurie.co.jp
66. *Popular Mechanics* **180**(3), 20 (2003).
67. C. Campbell: *Surface Acoustic Wave Devices and Their Signal Processing Applications*, Academic Press, San Diego, CA (1989).
68. H. Matthews: *Surface Wave Filters*, Wiley Interscience, New York (1977).
69. A. Yamamoto and T. Higuchi: Japanese Patent Disclosure, P2004-190537A (2004).
70. Z.-Y. Cheng: private communication, Auburn University (2003).
71. http://www.thinksrs.com/products/QCM200.htm
72. C. A. Rosen: *Proc. Electronic Component Symp.*, 205 (1957).
73. S. Kawashima, O. Ohnishi, H. Hakamata, S. Tagami, A. Fukuoka, T. Inoue and S. Hirose: *Proc. IEEE Int'l Ustrasonic Symp. '94*, France (Nov. 1994).
74. K. Uchino: *Proc. Actuator 2006*, p. 48, Bremen Messe, Bremen, Germany, June 14–16 (2006).
75. K. Uchino: *Bull. Am. Ceram. Soc.* **65**(4), 647 (1986).
76. K. Uchino: *MRS Bull.* **18**(4), 42 (1993).
77. K. Uchino (ed.): *Handbook on New Actuators for Precision Position Control*, Fuji Technosystem, Tokyo (1994).
78. K. Uchino: *Proc. Workshop on Microsystem Technologies in the USA and Canada*, Germany, mst news, special issue, VDI/VDE, 28–36 (1996).
79. S. Takahashi, A. Ochi, M. Yonezawa, T. Yano, T. Hamatsuki and I. Fujui: *Ferroelectrics* **50**, 181 (1993).
80. A. Bauer and F. Moller: *Proc. 4th Int'l Conf. New Actuators, Germany*, p. 128 (1994).
81. Active Control Experts, Inc. Catalogue 'PZT Quick Pack' (1996).
82. Y. Sugawara, K. Onitsuka, S. Yoshikawa, Q. C. Xu, R. E. Newnham and K. Uchino: *J. Am. Ceram. Soc.* **75**(4), 996 (1992).
83. H. Goto, K. Imanaka and K. Uchino: *Ultrasonic Techno* **5**, 48 (1992).
84. K. Uchino and S. Hirose: *IEEE UFFC Transactions*, **48**, 307–321 (2001).
85. N. Kanbe, M. Aoyagi, S. Hirose and Y. Tomikawa: *J. Acoust. Soc. Jpn* (E) **14**(4), 235 (1993).
86. S. Sugiyama and K. Uchino: *Proc. Int'l. Symp. Appl. Ferroelectrics '86*, IEEE, p. 637 (1986).
87. C. Kusakabe, Y. Tomikawa and T. Takano: *IEEE Trans. UFFC* **37**(6), 551 (1990).
88. T. Ota, T. Uchikawa and T. Mizutani: *Jpn J. Appl Phys.* **24**, Suppl. 24–3, 193 (1985).
89. J. T. Dorsey, T. R. Sutter and K. C. Wu: *Proc. 3rd Int'l Conf. Adaptive Structures*, p. 352 (1992).
90. B. Wada: JPL Document D-10659, p. 23 (1993).
91. F. K. Straub: *Smart Mater. Struct.* **5**, 1 (1996).
92. P. C. Chen and I. Chopra: *Smart Mater. Struct.* **5**, 35 (1996).
93. T. Yano, E. Sato, I. Fukui and S. Hori: *Proc. Int'l Symp. Soc. Information Display*, p. 180 (1989).

94. N. Kurashima: *Proc. Machine Tech. Inst. Seminar*, MITI, Tsukuba, Japan (1999).
95. Y. Yokoya: *Electronic Ceramics* **22**(111), 55 (1991).
96. A. Fujii: *Proc. JTTAS Meeting*, Dec. 2, Tokyo (2005).
97. M. P. Koster: *Proc. 4th Int'l Conf. New Actuators*, Germany, p. 144 (1994).
98. H. V. Barth: *IBM Technical Disclosure Bull.* **16**, 2263 (1973).
99. V. V. Lavrinenko, S. S. Vishnevski and I. K. Kartashev: Izvestiya Vysshikh Uchebnykh Zavedenii, *Radioelektronica* **13**, 57 (1976).
100. P. E. Vasiliev *et al.*: UK Patent Application GB 2020857 A (1979).
101. T. Sashida: *Oyo Butsuri* **51**, 713 (1982).
102. A. Kumada: *Jpn J. Appl. Phys.* **24**, Suppl. 24–2, 739 (1985).
103. B. Koc, S. Cagatay and K. Uchino: *IEEE Ultrasonic, Ferroelectric, Frequency Control Trans.* **49**(4), 495–500 (2002).
104. S. Cagatay, B. Koc and K. Uchino: *IEEE Trans. UFFC* **50**(7), 782–786 (2003).
105. K. Uchino: *Proc. New Actuator 2004* (Bremen, June 14–16), p. 127 (2004).
106. K. Nakamura, M. Kurosawa and S. Ueha: *Proc. Jpn Acoustic Soc.* No. 1-1-18, p. 917 (Oct., 1993).
107. K. Uchino, K. Kato and M. Tohda: *Ferroelectrics* **87**, 331 (1988).
108. S. Ueha and Y. Tomikawa: *Ultrasonic Motors*, Monographs in Electr. & Electron. Engin. **29**, Oxford Science Publishers, Oxford (1993).
109. *Nikkei Mechanical*, Feb. 28, p. 44 (1983).
110. M. Kurosawa, S. Ueha and E. Mori: *J. Acoust. Soc. Amer.* **77**, 1431 (1985).
111. T. Sashida: *Mech. Automation of Jpn* **15**(2), 31 (1983).
112. K. Ise: *J. Acoust. Soc. Jpn* **43**, 184 (1987).
113. M. Kasuga, T. Satoh, N. Tsukada, T. Yamazaki, F. Ogawa, M. Suzuki, I. Horikoshi and T. Itoh: *J. Soc. Precision Eng.* **57**, 63 (1991).
114. J. Cummings and D. Stutts: *Amer. Ceram. Soc. Trans. 'Design for Manufacturability of Ceramic Components'*, p. 147 (1994).
115. Y. Okamoto, R. Yoshida and H. Sueyoshi: *Konica Minolta Tech. Report* **1** 23 (2004).
116. K. Uchino: *Proceedings of 5th Int'l Workshop on Piezoelectric Mater. & Appl.*, State College, PA, Oct. 6–10 (2008).
117. H. W. Kim, S. Priya, K. Uchino and R. E. Newnham: *J. Electroceramics* **15**, 27–34 (2005).
118. H. W. Kim, S. Priya and K. Uchino: *Japan J. Appl. Phys.* **45**(7), 5836–5840 (2006).
119. H. W. Kim, S. Priya, H. Stephanau and K. Uchino: *IEEE Trans. UFFC*, **54**(9), 1851–1859 (2007).
120. K. Uchino and A. Vazquez Carazo: *Proc. 11th Int'l Conf. New Actuators*, Bremen, Germany, June 9–11, 2008, A3.7, pp. 137–140 (2008).
121. http://www.lightningswitch.com/

Part I

Piezoelectric materials

2

Lead zirconate titanate-based piezo-ceramics

M. KIMURA, A. ANDO and Y. SAKABE,
Murata Manufacturing Co., Ltd, Japan

Abstract: Lead zirconate titanate (PZT) is the most common piezoelectric ceramic and exhibits excellent properties as is well known. In this chapter, basic knowledge of PZT, including its crystal structure and phase relations, is presented at the beginning. Compositional design and shaping approach to highlight the excellent performance characteristics are also described, including recent advances; in particular, multilayer structure and low temperature sintering have become important in PZT applications. Future trends are discussed briefly at the end.

Key words: lead zirconate titanate (PZT), perovskite structure, morphotropic phase boundary (MPB), multilayer ceramics, low temperature sintering.

2.1 Introduction

Piezoelectric ceramics were first put to practical use around 1950,[1] and have been actively used in a wide range of industries since then. Various applications have been devised using their electromechanical transducer ability, including communication circuit components, ultrasonic transducers, sensors and actuators. Such a wide application area is one characteristic of piezoelectric ceramics compared to other electro-ceramics. Many materials have been studied as possible candidate as practical piezoelectric ceramics over the years. In particular, lead-free materials are being actively surveyed because of increasing awareness of environmental issues at present, and several materials of interest have been discovered.[2] However, most practical materials on the market are still based on lead zirconate titanate ($Pb(Zr,Ti)O_3$: PZT), which is a solid solution of $PbZrO_3$ and $PbTiO_3$. The solid solutions were first studied by G. Shirane and co-workers in 1952,[3–5] and the phase diagram was reported by E. Sawaguchi in 1953.[6] Furthermore, the piezoelectricity was revealed by B. Jaffe *et al*. in 1955.[7] Since then, this material has seen enormously developments by many research teams as a representative electronic material to date. PZT-based ceramics realize the necessary high performance characteristics for various usages at a relatively low cost, and it is the so-called ‘king of piezoelectric materials’.

A distinctive feature of PZT is its large piezoelectricity. PZT has a perovskite-type crystalline structure, which is represented by the compositional formula ABO_3, and the structure is suitable to achieve large piezoelectricity, especially when the A site is filled by Pb. Moreover, the feature can be enhanced by compositional optimization. The piezoelectricity intensifies on a composition of phase boundary between rhombohedral and tetragonal phases in the solid solution. The phase boundary is better known as morphotropic phase boundary (MPB). In Section 2.2, the relationship between PZT's crystalline structure and the excellent piezoelectric properties, containing MPB, are discussed.

On the other hand, some electrical properties required for practical usages are not necessarily highest on the MPB. For example, tetragonal phase PZT generally indicates higher heat-proof characteristics, and it is often chosen for applications requiring high temperature reliability. Tetragonal, rhombohedral and the MPB compositions are appropriately chosen to suit the demands of each application in this way. The phases of PZT are easily controlled by the compositional change of the zirconate and titanate ratio in several situations. Also, various doping elements change PZT's properties drastically by substituting on the cation sites. Doping with low-valent elements generally improves the mechanical quality factor Q_m of PZT; while high-valent elements often increase the piezoelectric d constant. These kinds of compositional modifications are commonly used on the material design of PZT. A wide variety of electrical properties is often more important than large piezoelectricity for practical applications, and this can easily be realized by compositional modifications. In Section 2.3, these compositional modification techniques are described.

Moreover, PZT has the advantage of good shaping flexibility. Piezoelectric devices utilize the mechanical displacement or vibration, and therefore the performance is greatly influenced by a device shape also in the case of non-resonant devices. Structural innovations have been extensively studied to obtain higher performance. Ceramics have good forming flexibility, and in addition PZT has good workability. As is well known, there are other piezoelectric materials with superior piezoelectricity, for example, piezoelectric single crystals. However, their shaping flexibility is inferior to that of PZT ceramics, and unlike PZT they do not have a wide range of applications.

One of the most important shaping technologies is the multilayer technique. Ceramic components co-fired with multiple inner electrodes are often used in PZT applications, because of their high displacement, high reliability and low production cost. Noble metals with high melting point were generally used initially as an inner electrode material for the co-fired multilayer component. However, base metals or base metal alloys, whose melting points are generally lower than those of noble metals, are preferable for the inner electrode material on the cost front. Therefore, sintering temperature reduction of piezoelectric ceramics is decisively important, and has been actively studied. In Sections 2.4 and 2.5, recent trends in piezoelectric ceramic applications are briefly introduced, and the shaping techniques of PZT are discussed with a main focus on the multilayer technique. Then, sintering temperature reduction techniques in PZT are also described.

PZT-based ceramics are expected to be used in a wide range of applications at least for the forseeable future, because of their high performance and good industrial usability. Creation of new markets is also anticipated for PZT. At the end of the chapter, remaining research challenges and future trends in applications are briefly described.

2.2 Crystalline structure and phase relations

PZT is a solid solution of lead zirconate ($PbZrO_3$) and lead titanate ($PbTiO_3$), and has perovskite crystalline structure, the same as the two compositional end members. Perovskite-structured materials indicate excellent properties as functional materials on dielectric, piezoelectric, electro-optic, semi-conducting or superconducting fields.[8] They play major role in modern electronics, and are indispensable for the forseeable future.

The perovskite ABO_3 structure of PZT is shown in Fig. 2.1(a). A-site cations build a cuboid box, and an oxygen octahedron falls within the box. A B-site cation is placed around the center of the oxygen octahedron. In the case of PZT, the A-site is filled by Pb ions, and the B-site is randomly

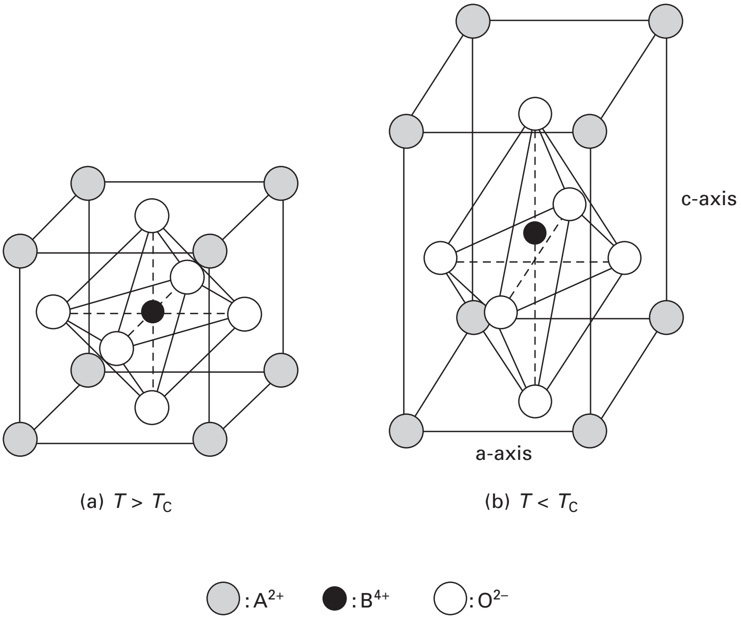

(a) $T > T_C$ (b) $T < T_C$

2.1 Schematic diagram of perovskite ABO_3 structure.

filled by Zr or Ti ions. The oxygen octahedron is sifted off the center of the cuboid box formed with Pb ions, and the B-site cations are also sifted from the center of the oxygen octahedron in the ferroelectric state of PZT as shown in Fig. 2.1(b). The spontaneous polarization is formed between those cations and the oxygen octahedron.

Cohen and Krakauer calculated the electron density distribution of perovskite barium titanate ($BaTiO_3$) using first principle computer simulation in 1990,[9] and suggested that the large spontaneous polarization of $BaTiO_3$ is strongly affected by the covalent bonding between the Ti and O ions. $BaTiO_3$ is essentially an ionic binding crystal, however their calculation results indicated that covalent bonding certainly existed between the Ti 3d and O 2p states. The covalent bonding probably induces large crystalline distortion and an electric dipole. Therefore, the large spontaneous polarization of $BaTiO_3$ is possibly due to the covalent bounding. Piezoelectric strain of ferroelectric materials S is roughly expressed by Eq. (2.1) with electrostriction coefficient Q, spontaneous polarization P_s, dielectric permittivity ε and induced electric field E, and large spontaneous polarization leads to large piezoelectricity

$$S = 2QP_s\varepsilon E. \qquad 2.1$$

From these findings, the perovskite structure is suitable to achieve large piezoelectricity.

On the other hand, the electronic states belonging to the Ba ion did not contribute to the covalent bonding and only played the role of a 'spacer grid' in the $BaTiO_3$ crystal in these studies. However, it was reported in another paper by Cohen[10] that the Pb 6s state contributed to the covalent bonding between the Ti and O ions in the case of $PbTiO_3$, and the contribution possibly strongly enhanced the crystal distortion. Spontaneous polarization of $PbTiO_3$ is three times larger than that of $BaTiO_3$. Cohen proposed that this large spontaneous polarization is due to the Pb 6s electrons hybridized with the covalent bonding between the Ti and O ions, and this is the reason why $PbTiO_3$ indicates larger piezoelectricity than $BaTiO_3$. This Pb 6s contribution was confirmed also by X-ray diffraction MEM (maximum entropy method) analysis.[11] These discussions lead to the conclusion that the PZT perovskite structure is very suitable for high performance piezoelectric materials.

Additionally, the piezoelectric properties of electromechanical coupling coefficient or piezoelectric constant drastically increase on a composition of phase boundary between the rhombohedral and tetragonal phases in PZT solid solution. The phase boundary was named the morphotropic phase boundary (MPB) by Jaffe. The phase diagram of PZT is shown in Fig. 2.2.[6] The phase boundary between the rhombohedral and tetragonal phases is confirmed to be vertically elongated around the composition with the Zr/Ti ratio of 53/47, and the crystal phase is sensitive to changes in the Zr/Ti ratio around the MPB. The relationship between piezoelectric properties and the Zr/Ti ratio

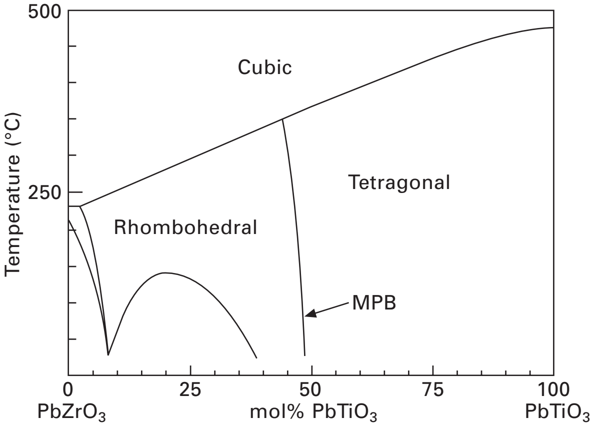

2.2 Phase diagram of $PbZrO_3$-$PbTiO_3$ solid solutions.

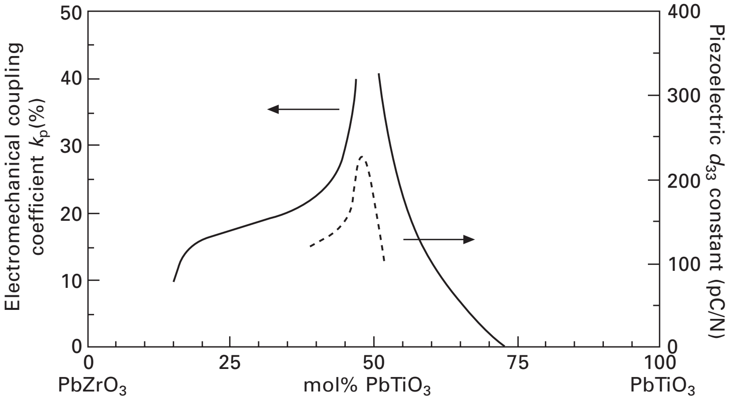

2.3 Relationship between piezoelectric properties, electromechanical coupling coefficient and piezoelectric *d* constant, and Zr/Ti ratio of PZT.

of PZT are shown in Fig. 2.3.[7] The highest properties are observed on the MPB, and the composition near the MPB is usually chosen for applications requiring high electromechanical transducer efficiency or large piezoelectric displacement. However, the reason for this enhanced piezoelectricity has not been significantly clarified.

Ishibashi and Iwata studied the origin of large piezoelectricity near the MPB by phenomenological theory.[12,13] The phase diagram in the vicinity of the MPB was schematically expressed by a simple Landau-type free energy in terms of the triaxial polarization components. The vertical boundary between the rhombohedral and tetragonal phases can be presented only by symmetric consistency of the polarization components. It was also indicated that the dielectric susceptibility increases dramatically, and the elastic stiffness constant decreases near the MPB by increasing equivalence of the triaxial polarization components. The large piezoelectric constants and high coupling coefficients are produced by the extremely large susceptibility and the small elastic constant of the MPB, respectively. They concluded that increasing the polarization equivalence and the crystallographic free energy isotropy produces the excellent piezoelectricity near the MPB, and the explanation facilitates our macroscopic understanding of the phenomena. However, phenomenological theory does not explain the physical mechanism in principle.

On the other hand, Noheda and his co-workers recently investigated the crystalline structure of MPB composition PZT using high-resolution synchrotron x-ray powder diffraction, which indicated the existence of a monoclinic ferroelectric phase on the MPB.[14,15] Subsequently several related studies have supported Noheda's research.[16–18] These studies suggested that the existence of a monoclinic phase could accelerate the switching between rhombohedral and tetragonal phases when an electric field is induced on MPB composition PZT, and the flexible phase switching could cause the large piezoelectricity. However, there is a counterargument to their interpretation,[19] and it has not perfectly resolved. Research is continuing in an attempt to clarify the MPB phenomena.

2.3 Compositional modifications

Another notable feature of PZT is its broad range of applications. A wide variety of piezoelectric properties can be realized using several compositional modification techniques, and an extraordinary variety of applications has become possible. The required characteristics of piezoelectric materials varies greatly depending on the application. For example, in the case of commonly used non-resonant actuator applications, a large piezoelectric d constant is strongly required and mechanical quality factor Q_m should be optimally small. In contrast, high mechanical quality factor Q_m is needed in ultrasonic motor applications, because the resonant displacement is proportional to the Q_m value. On the other hand, electromechanical coupling coefficient should be small for oscillator applications, because a large coupling coefficient results in decreasing frequency accuracy. Namely, a large value is required in some cases, and a small value is preferred in other cases for the same property. Major piezoelectric applications using PZT and their typical required properties are shown in Table 2.1.

Three typical methods of compositional modification are well known to realize the wide variety in PZT. One is modification of the Zr/Ti ratio. Zr or Ti-rich PZT indicates rhombohedral or tetragonal crystalline phases in the solid solution, respectively, as shown in Fig. 2.2. MPB composition

Table 2.1 Major piezoelectric applications and their required material properties

Application	Required material characteristics
Inkjet actuator	Large *d* constant, low dielectric permittivity, high mechanical strength
Fuel injection actuator	Large *d* constant, high Curie temperature, high mechanical strength
Buzzer, loudspeaker	Large *d* constant, low dielectric constant, high mechanical strength
Shock sensor	Large *d* constant, large *g* constant
Ultrasonic motor	High Q_m, large coupling coefficient, high mechanical strength
Piezo gyroscope	High Q_m, large coupling coefficient, high mechanical strength
Resonator	Temperature stability, high Q_m, low aging
Filter	Temperature stability, large coupling coefficient, low aging

has large piezoelectricity, and indicates a large piezoelectric constant and electromechanical coupling coefficient. However, stabilities of piezoelectric properties against external conditions such as heat or pressure change are inferior due to the phase transition. If these instabilities need to be avoided, composition distant from the MPB should be chosen. Tetragonal PZT has good temperature stability, because it is distant from the MPB and also has high Curie temperature. Therefore, it is usually used for applications requiring a high stability against several external conditions. On the other hand, rhombohedral PZT has a large piezoelectric constant compared to tetragonal PZT. Meanwhile, a temperature variation ratio of resonance frequency generally becomes smaller at two compositional points. One is around the MPB and the other is in the tetragonal phase,[20] and these compositions are important for communication circuit components. Recently, the importance of stability against external fluctuations has been relatively higher for many piezoelectric applications; therefore, tetragonal PZT has become popular on PZT compositional designs, and usage of rombohedral PZT is limited.

The second compositional modification is acceptor or donor ion doping in PZT cation sites. Doping changes the piezoelectric properties dramatically by affecting the ferroelectric domain configurations within the ceramics.[21,22] It is well known that piezoelectric ceramic properties are strongly dominated by the domain behavior, which is discussed before going on to discuss acceptor and donor doping on PZT. Electric field E dependence on polarization P and strain S of typical piezoelectric ceramics, including PZT, are schematically indicated in relation to the domain behavior. The correlation between electric field E and polarization P is shown in Fig. 2.4. Ferroelectric domains firstly orientate randomly within the ceramics just after sintering, and the

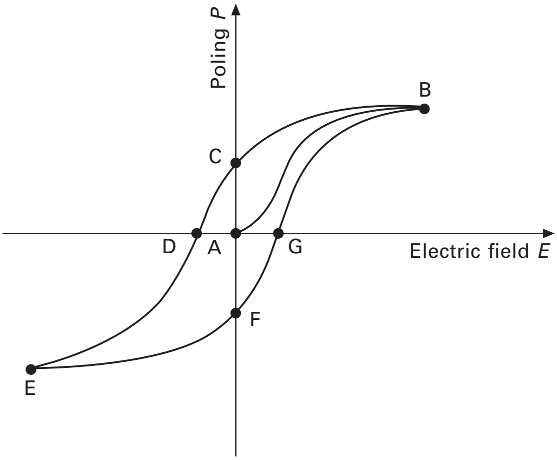

2.4 Schematic diagram of correlation between electric field *E* and polarization *P* in typical piezoelectric materials.

polarization value is zero at that time (point A). Polarization increases with application of an electric field along the route A to B, and the polarization growth is due to intrinsic crystal lattice strain, 180° domain switching and non-180° domain rotation. The domains gradually orientate themselves with 180° domain switching and non-180° domain rotation until the orientation reaches saturation. This process from A to B corresponds to 'poling' for piezoelectric ceramics. If the electric field is reduced from the point B, the domain orientation will return to the random state and the polarization also decreases. However, several parts of the domain cannot return to their initial state due to mechanical stress within the ceramics, and a certain polarization value remains even at a zero electric field (point C). This remaining polarization is called 'remanent polarization P_r'. A negative electric field must be induced to turn the polarization value back to zero, and the necessary electric field value is called the 'cohesive field E_c' (point D). By further increasing the negative electric field, polarization reversal arises until it is saturated again along the route D to E. Then, if the electric field is reversed again at point E, the polarization returns to zero along the route E–F–G. This hysteric *PE* curve is called the 'ferroelectric *PE* hysteresis curve'.[23]

Similar behavior can be seen in the relationship between induced electric field *E* and strain *S*, and this is called the 'butterfly curve' because of its appearance.[24] The schematic diagram is shown in Fig. 2.5. A non-polarization ceramic just after sintering also has no strain (point A). Strain *S* arises with intrinsic crystal lattice strain and the domain orientation by applying an electric field along the route A to B. Then, the strain decreases with decreasing the electric field along the route B to C, and the strain remaining by mechanical stress at point C is called 'remanent strain S_r'. Moreover, the electric field

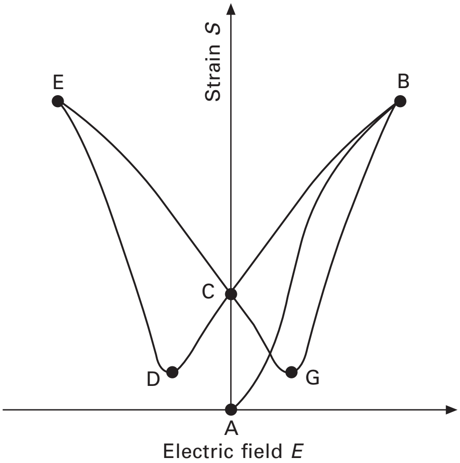

2.5 Schematic diagram of correlation between electric field *E* and strain *S* in typical piezoelectric materials.

value of point D, at which the strain also returns to its minimum value, indicates the cohesive field E_c. Piezoelectric ceramics are generally used from the state at point C, and driven by the loading an electric field. The piezoelectric *d* constant as a material constant is indicated by slope of tangent at a zero induced field (point C). Larger strain is obtained with increasing the electric field along the route C to B, and the strain is stronger due to the non-180° domain rotation. However, strain inflection and hysteresis also arise with increasing electric field due to the non-180° domain rotation.

Now let us return to the discussion of acceptor and donor doping. Lower valence element doping of the cation site, for example K^{1+} replacing Pb^{2+} site or Fe^{3+} replacing Ti^{4+}/Zr^{4+} site, is called 'accepter doping'. In this case, the ion replacement induces oxygen vacancies within the crystalline structure with following formulas:

$$(\mathrm{Pb}_{1-x}\mathrm{K}_x)(\mathrm{Ti,Zr})(\mathrm{O}_{3-x/2}\mathrm{V}_{\mathrm{O}x/2}), \qquad 2.2$$

$$\mathrm{Pb}\{(\mathrm{Ti,Zr})_{1-y}\mathrm{Fe}_y\}(\mathrm{O}_{3-3y/4}\mathrm{V}_{\mathrm{O}3y/4}), \qquad 2.3$$

where x and y indicate the substitution amount, and V_O is an arisen oxygen vacancy. The oxygen vacancies, which have a positive electric charge within the crystalline structure, are thought to couple to the doped acceptor ions with a negative electron charge, and form electric dipoles. It is commonly believed that the electric dipoles aggregate along the domain boundary, and restrict the non-180° domain rotation.[25] Therefore, the non-180° domain rotation requires a large amount of energy in acceptor-doped PZT, and the cohesive field, remanent polarization and remanent strain are generally larger than those of the non-doped PZT. The *PE* hysteresis shows rectangular type appearance compared to non-doped PZT, and the butterfly curve is horizontally elongated as shown in Fig. 2.6. The dielectric permittivity and piezoelectric *d* constant typically become smaller, because the slopes of tangent at a zero electric field in *PE* hysteresis and butterfly curve become smaller, on the other hand, the strain inflection and hysteresis are suppressed. Mechanical loss while driving also decreases due to the domain rotation restriction, and the mechanical quality factor Q_m becomes higher. Adding these piezoelectric property changes, the acceptor PZT typically possesses a strong internal field. This internal field is thought to stabilize the polarization orientation, and might affect the suppression of the strain inflection against an electric field. Moreover, it is noted that the temperature dependence of resonance frequency is generally improved by acceptor doping,[26] however the reason is not fully understood.

Higher valence element doping, for example La^{3+} replacing Pb^{2+} site or Nb^{5+} replacing Ti^{4+}/Zr^{4+} site, is called 'donor doping'. Non-doped PZT originally has Pb vacancies within the crystalline structure because of PbO vapor evaporation in the sintering process as indicated by following formula:

$$(Pb_{1-z}V_{Pbz})(Ti,Zr)(O_{3-z}V_{Oz}), \qquad 2.4$$

where V_{Pb} indicates a Pb vacancy, and z is the vacancy amount. Therefore, non-doped PZT usually exhibits p-type semi-conductivity. The doped donor ion provides the semi-conductivity, and the electric resistivity decreases in donor-doped PZT. On the other hand, the cohesive field, remanent polarization and remanent strain become smaller compared to acceptor-doped PZT. The *PE* hysteresis shows slender appearance, and the butterfly curve shows a vertically long shape as shown in Fig. 2.6. The dielectric permittivity and piezoelectric *d* constant become larger. The strain inflection and hysteresis are enhanced. The mechanical quality factor Q_m becomes lower. It is believed that these effects upon the piezoelectric properties are caused by acceleration of non-180° domain rotation with donor doping. The doped donor ion probably depresses the restrictive effect on the non-180° domain rotation of the oxygen vacancy.[25]

Acceptor and donor-doped PZT are called 'hard' and 'soft' PZT, respectively, corresponding to their electrically and mechanically rigid or adaptive behaviors. Hard PZT is used mainly for applications using the resonance because of the high Q_m and stable piezoelectric properties. On the other hand, soft PZT is popularly used for non-resonant sensor or actuator applications because of the large piezoelectric constant.

The third typical compositional modification is solid solution with other perovskite, particularly with compounds called 'complex perovskite'.[27] This is called the PZT ternary system, and is often used in combination with the two other methods mentioned above. It is noted that solid solutions with

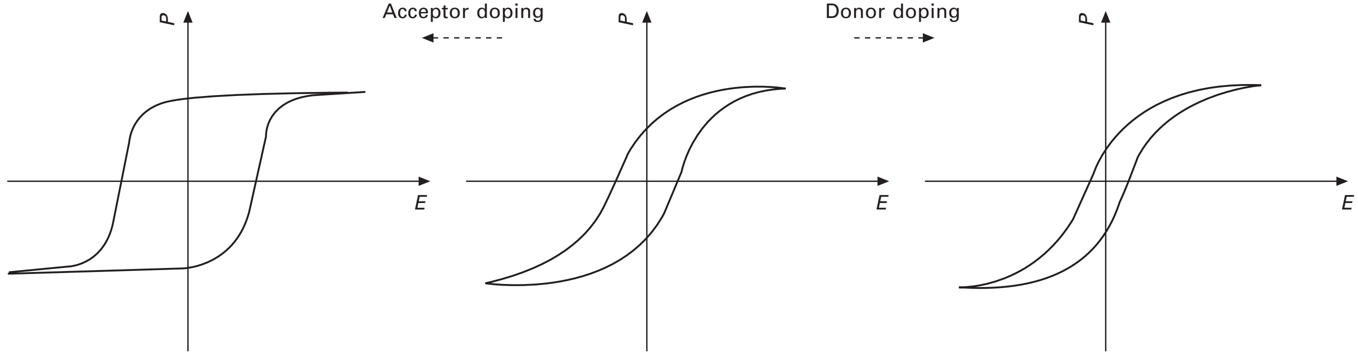

(a) *PE* hysteresis curve

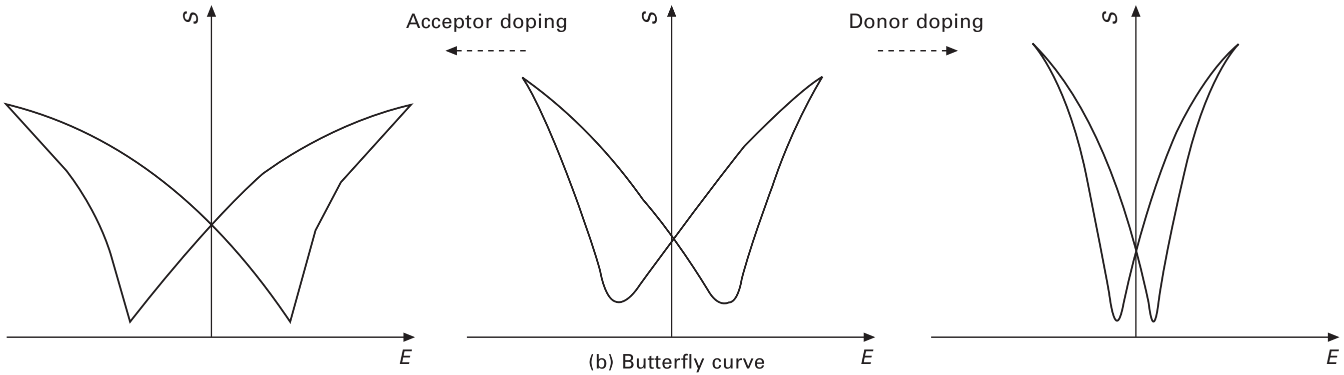

(b) Butterfly curve

2.6 PE hysteresis and butterfly curve of acceptor or donor doped PZT.

several complex perovskites improve the piezoelectric properties. For example, $Pb(Sb_{1/2}Nb_{1/2})O_3$ PZT[28] shows good temperature stability, and is used for communication circuit components. On the other hand, $Pb(Mn_{1/3}Sb_{2/3})O_3$ PZT[29] indicates high mechanical quality factor, and is used for electromechanical transducer applications.

$Pb(Ni_{1/2}Nb_{1/2})O_3$ PZT realizes extremely large piezoelectric *d* constant and is applied in some kinds of actuator applications. Also, the ternary compositions are often used for low temperature sintering with further modifications, which will be discussed in Section 2.5. Typical complex perovskite compounds for the PZT ternary system are shown in Table 2.2.

2.4 Shaping approach and application trend

The performance of piezoelectric devices is strongly influenced by their shape and dimensions as is well known. Therefore, structural innovations have been continuously studied in order to obtain higher performance. Ceramics have originally good forming flexibility, and various forming procedures including press molding, extrusion, injection molding and tape molding are available. Also, PZT ceramics has a good mechanical workability because of the ductility of lead-containing ceramics. Such a good shaping ability, as compared to other piezoelectric materials, can be said to be one of the main reasons for the widespread utilization of PZT.

Piezoelectric applications are classified into the following three categories from a functional point of view:[30] Electronic circuit components, sensors, and mechanical power sources. For electronic circuit components, piezoelectric resonance is used and the typical applications are filters and resonators as communication circuit components. Mechanical-to-electrical conversion is used for sensors, and the main applications include ultrasonic sensors, knocking sensors, shock sensors and acceleration sensors. Electrical-to-mechanical conversion is used for mechanical power sources, and the applications include actuator, speaker or ultrasonic cleaner. Piezoelectric

Table 2.2 Typical complex perovskite compounds for PZT ternary system

Compound	Curie temp. (°C)	Characteristics of the ternary system
$Pb(Mn_{1/3}Sb_{2/3})O_3$	–	High Q_m, large coupling coefficient
$Pb(Sn_{1/3}Sb_{2/3})O_3$	–	High Q_m, large coupling coefficient
$Pb(Mg_{1/3}Nb_{2/3})O_3$	–8	High Q_m, temperature stability, high mechanical strength
$Pb(Sb_{1/2}Nb_{1/2})O_3$	–	Temperature stability, low aging
$Pb(Ni_{1/3}Nb_{2/3})O_3$	–120	Large *d* constant, low sintering temperature
$Pb(Zn_{1/3}Nb_{2/3})O_3$	140	Large *d* constant, large permittivity
$Pb(Mn_{1/3}Nb_{2/3})O_3$	–	High Q_m, temperature stability

ceramics was first used as a pick-up device for a record player in 1948, and it was realized using $BaTiO_3$ ceramics. Then, PZT was launched as a piezoelectric ceramic with higher properties, and became very popular for use as a communication circuit component. Sensor applications increased from around 1980, and are now widely used in our daily lives. On the other hand, mechanical power source applications have rapidly increased with market growth of small and/or thin electromechanical devices in recent years, and will become an even more important application into the future. High speed and highly accurate displacement can be realized with low dissipation power using PZT components. Some intriguing examples of the applications are shown in Fig. 2.7. Inkjet actuators, camera module actuators, audio playback speakers or fuel injection actuators are attracting particular attention as new piezoelectric applications. Large displacement is one of the most important demands for the mechanical power source devices, and effective designs have been investigated. Bimorph, multilayer,[31] and moonie[32] are well-known typical designs to enhance the displacement, and these structure are shown in Fig. 2.8. Multilayer is the most popular among these structures, and has recently been successfully used in inkjet actuators, audio playback speakers and fuel injection actuators.

Ceramic multilayer technology has been greatly developed in the field of multilayer ceramic capacitor (MLCC).[33] High capacitance condensers consisting of several hundred thin dielectric layers with a thickness of about 1 μm have been put to practical usage. In the case of PZT, dozens of layers with several tens of micrometers thick are usually stacked. These multilayer ceramics are generally obtained by firing a laminated body consisted of pre-sintered tape compacts and printed inner electrodes. This process can realize high interface reliability and relatively low production cost in mass production. PZT without a compositional modification is sintered at about 1200 °C; therefore, the inner electrode metal needs to be insoluble at 1200 °C. Noble metal or alloys with a high content of noble metals is necessary in these cases, and Ag–Pd alloy with high Pd content was usually used for PZT in the early years. However, noble metals such as Pd are expensive and have price volatility risks. Therefore, base metal or alloys with lower noble metal content is preferable as the inner electrode metal from an industrial viewpoint. Low temperature sintering of the piezoelectric ceramics is necessary for using the electrode materials that have low melting point. The sintering temperature should be reduced to at least 960 °C, which is the melting point of Ag, to use pure Ag metal as the inner electrode, and has to be reduced to under 1000 °C when cost reasonable Ag–Pd alloys with low Pd content are used. Several methods have been proposed to reduce the sintering temperature of PZT, including compositional modification or process development, and PZT base compositions sintered at 900 or 1000 °C have been developed recently. Low temperature sintering was

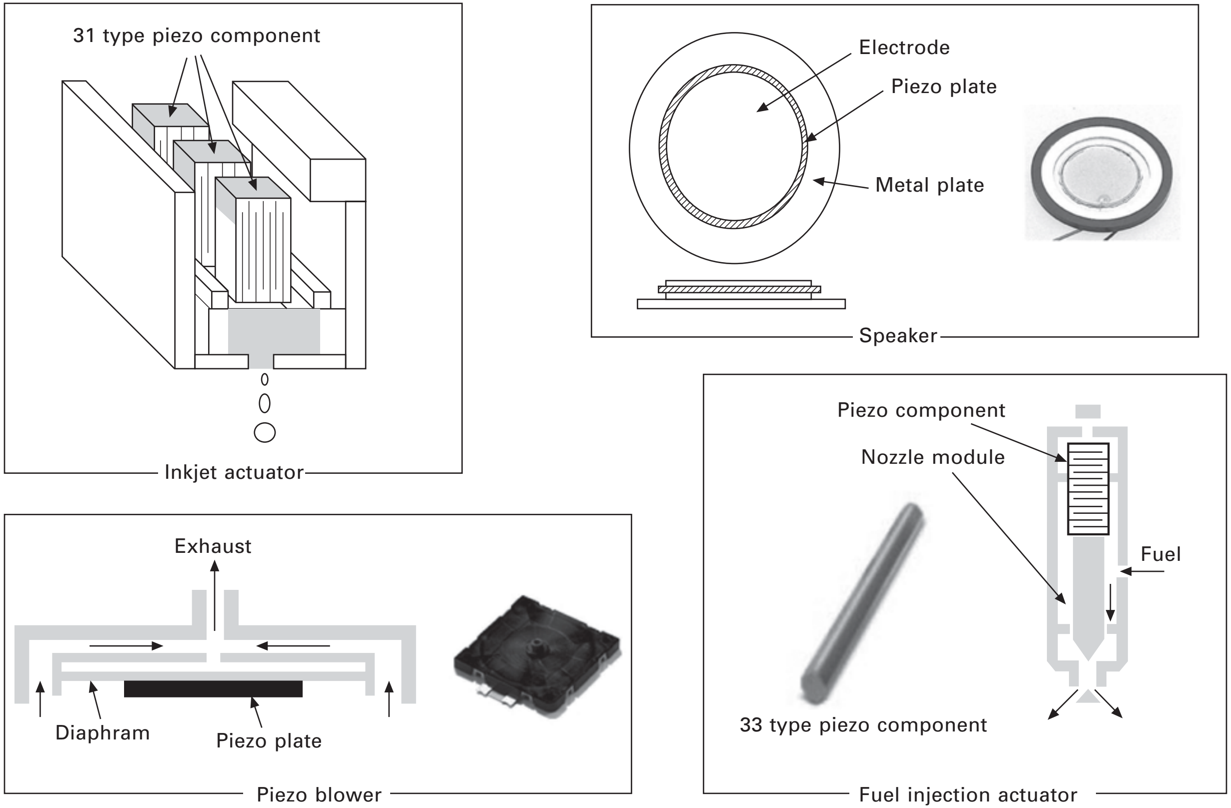
31 type piezo component
Inkjet actuator
Electrode
Piezo plate
Metal plate
Speaker
Exhaust
Diaphram
Piezo plate
Piezo blower
Piezo component
Nozzle module
Fuel
33 type piezo component
Fuel injection actuator

2.7 Typical mechanical power source applications.

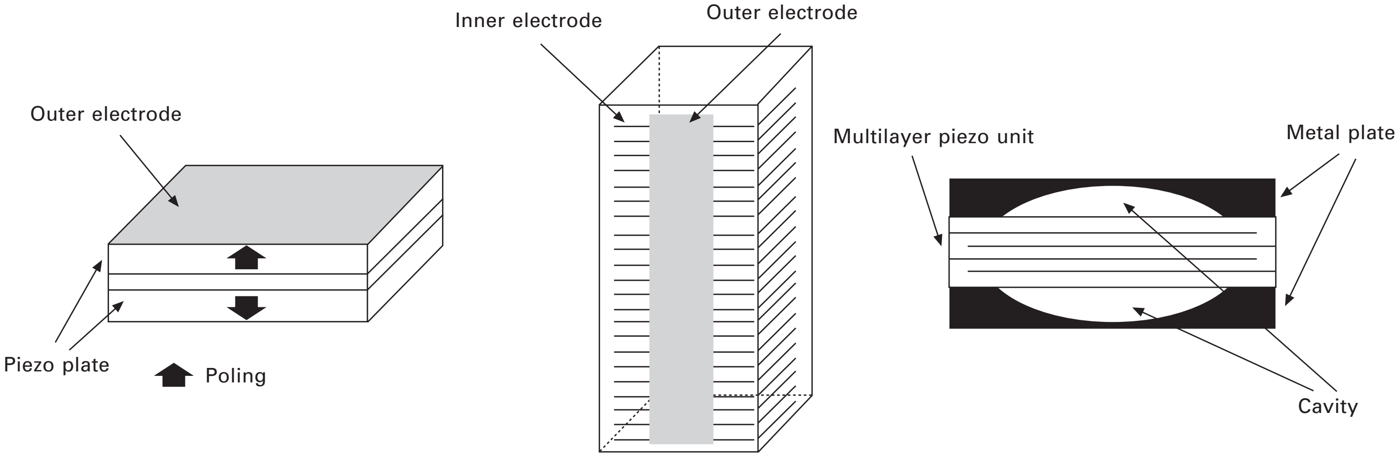
Outer electrode
Piezo plate
Poling
Inner electrode
Outer electrode
Multilayer piezo unit
Metal plate
Cavity

Bimorph

Multilayer

Moonie

2.8 Bimorph, moonie, and multilayer structure.

the most important technical interest in PZT in previous decades, and still remains a focus today.

2.5 Low temperature sintering

Low temperature sintering was mainly studied for co-firing PZT with inner electrode metals in multilayer ceramics as noted above. On the other hand, the reduction effects on energy consumption and CO_2 emission are also important from the viewpoint of environmental protection. Typical methods of low temperature sintering in PZT are classified into ceramic powder process, sintering process and compositional modification.

Mechanical pulverizing of the calcined powder and chemical powder synthesis are known as the temperature reduction technique on ceramic powder processing. Fine powder can be obtained by these methods, and high surface activity of the fine powder is applied for low temperature sintering. Mechanical pulverizing is the most common method in PZT low temperature sintering. It is generally effective to reduce the temperature by around 100 °C,[34] and relatively easy-to-use in ordinary ceramic processing. The method has been popularly used in practical mass production. Also, high performance pulverizing machines such as ‘bead mill’ or ‘wet jet mill’ have been actively developed. However, it is difficult to pulverize the powder into under 0.1 μm by these machines and to achieve the low temperature sintering below 1000 °C in PZT. Therefore, this process is often used together with other methods.

The buildup approach using chemical powder synthesis is also effective in obtaining fine powder, and an average diameter of under 0.1 μm can be achieved in practice. The great temperature reduction is realized using these methods. Low temperature sintering below 1000 °C was reported using the hydrothermal[35] or sol-gel synthesis[36] in PZT. However, these methods have not been widely used in practice because of high cost or production instability at this time. These processes are expected to be expanded gradually in PZT industrial processing with the demand for a decrease in sintering temperature or micro-structural homogeneity.

Spark plasma sintering,[37] microwave sintering[38] and hot isostatic pressing[39] are methods of sintering processing. Temperature reduction effects of several hundred degrees were reported by these processes or by the combination with other methods. However, it is difficult to realize high structural accuracy, especially on complex device shapes, and micro-structural homogeneity using these processes. Therefore, they are not suitable for the fabrication of multilayer ceramics with thin layers.

On the other hand, aerosol deposition (AD)[40] has recently attracted much attention as low temperature ceramic processing for PZT multilayer. This is a method to prepare a ceramic thick film by crashing the fine powder accelerated by high-velocity gas fluid onto a substrate. It has been reported that PZT thick film heat-treated at around 1000 °C after the deposition indicated relatively high piezoelectric properties.[41] The products using PZT thick films prepared by AD have been used for electric field probe, and PZT multilayer ceramics have also been studied.

Low temperature sintering using compositional modification is typically classified into the following two categories: addition of low melting point materials, and a compositional technique effected on the sinterability of PZT itself. Low melting point additives of Li_2CO_3,[42] $LiBiO_2$,[43] $Ba(Cu_{0.5}W_{0.5})O_3$[44] and $Pb_5Ge_3O_{11}$[43,45] have been reported to reduce the sintering temperature. These materials are considered to induce a liquid phase on their own or in combination with other constituent elements of PZT, and a tiny amount of the additives often produces the large effect of low temperature sintering. Low temperature sintering below 800 °C is probably possible in PZT using these methods. However, secondary phase occasionally arises on the grain boundary, and the piezoelectric properties are considerably inhibited by the secondary phase in these methods. Also, inhomogeneity sometimes arises on the microstructure. Careful control of the shrinking behavior is also necessary during the sintering process to obtain the high accuracy of shape and dimension of the ceramic body.

It is known that PZT ternary systems often have a lower sintering temperature than normal PZT compositions, and the dramatic reduction of sintering temperature was reported on the ternary system with further compositional modifications. In this case, the compositional technique is considered to affect the sinterability of the PZT matrix itself, and there is less problem of secondary phase or microstructure inhomogeneity unlike the low melting point additives method. $Pb(Zn_{1/3}Nb_{2/3})O_3$–PZT compositions achieved high piezoelectric properties by sintering around 900 °C.[46] Also, $Pb(Ni_{1/3}Nb_{2/3})O_3$–PZT with excess PbO was successfully fabricated by sintering at 900 °C.[47] Furthermore, Shiratsuyu *et al.* reported that sufficient density and relatively high piezoelectric properties were obtained for $Pb(Ni_{1/3}Nb_{2/3})O_3$–PZT composition with excess NiO.[48] The sintering temperature dependence on density is shown in Fig. 2.9. The filled and open circles indicate the densities of Ni excess and the stoichiometric specimens, whose compositions are indicated by the following chemical formulas:

$$0.6\text{PZT–}0.4\text{Pb}(\text{Ni}_{1.5/3}\text{Nb}_{2/3})\text{O}_3, \qquad 2.5$$

$$0.6\text{PZT–}0.4\text{Pb}(\text{Ni}_{1/3}\text{Nb}_{2/3})\text{O}_3, \qquad 2.6$$

respectively. The stoichiometric specimen was not densified at a sintering temperature less than 1100 °C. On the other hand, the saturated densities were obtained for the Ni excess specimens sintered in the temperature range higher than 800 °C. The sintering temperature dependence on electromechanical coupling coefficients k_p is shown in Fig. 2.10. A relatively high value was

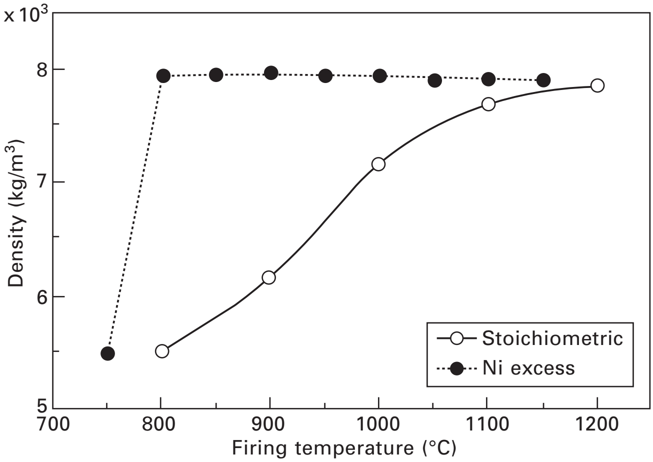

2.9 Sintering temperature dependence on density for Pb($Ni_{1/3}Nb_{2/3}$) O_3–PZT ceramics with excess NiO.

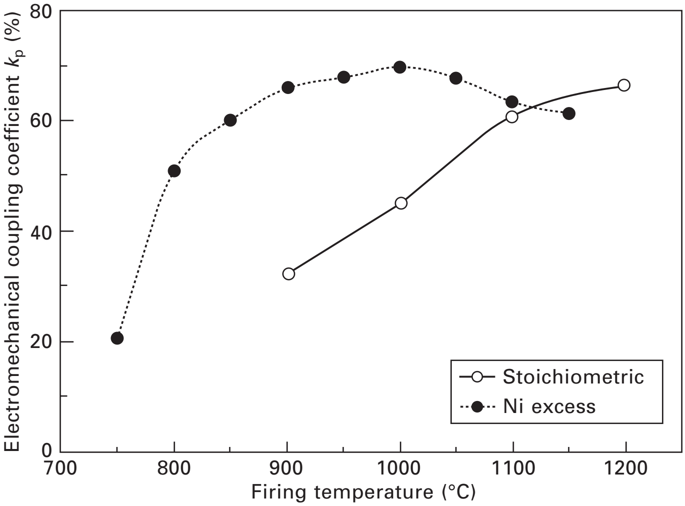

2.10 Sintering temperature dependence on electromechanical coupling coefficient k_p for Pb ($Ni_{1/3}Nb_{2/3}$) O_3-PZT ceramics with excess NiO.

also obtained for the specimen sintered at 800 °C for the Ni excess specimen. Although the low temperature sintering mechanism was not clarified, they proposed that inhibition of pyrochlore secondary phase generation by excess Ni strongly affected this low temperature sintering effect. Thus composition ceramics can be sintered with pure Ag inner electrode, and a good multilayer structure is possible.

2.6 Summary and future trends

More than 50 years have passed since PZT was first put into the market, and now it has become a standard electric functional material. PZT certainly has the highest piezoelectric properties compared to any other piezoelectric materials. However, the authors consider that the main reason for such a wide range of uses in various application fields is rather its easy-to-use characteristics. In this chapter, the cause of the excellent piezoelectric properties was first introduced in terms of the crystalline structure and phase relations. Then, PZT's fundamental composition designs enabling its wide usability, including Zr/Ti ratio control, acceptor/donor doping and the ternary system were discussed. Further, multilayer technology and the low temperature sintering techniques involved, which are probably the most important developments of recent years for PZT, were discussed. Commercial interest will continue to be centered on the multilayer technology. Study of the Cu inner electrode, which is expected to realize low production cost and high reliability, is also important as an alternative to the Ag or Ag–Pd inner electrode.[49,50] Scientific interest in PZT will be focused on MPB problems. The reason for the anomalous high piezoelectric properties in the MPB has not been perfectly established, as described in Section 2.2. The technology of crystalline structural analysis using transmission electron microscopy or powder diffraction is constantly advancing, and the reason will be clearly revealed in the near future. A thorough understanding of the MPB will be useful for new designs of PZT-type materials, and also for development of high performance lead-free piezoelectric ceramics.

Future new markets for PZT are expected especially in the fields of energy harvesting[51–53] and ultrasonic motor application.[54,55] The energy harvesting market is expected to develop in the next few years. Small-scale power generators for vibration monitoring or small lighting are major interests, and may be first put into practical usage in energy harvesting applications. Power generators for commercial power supply systems have also been studied using piezoelectric ceramics. However, their potential is as yet unclear. Meanwhile, ultrasonic motors have been studied since the 1970s, and have found practical usage in wristwatches and high-quality cameras. However, their use cannot be said to be widespread. Their smallsize, high energy efficiency and quietness are recently being re-evaluated, and they may find possible uses in mobile applications requiring high portability and low energy consumption.

2.7 References

1. http://www.murata.com/corporate/history/index.html
2. T. Takenaka and H. Nagata, 'Current status and prospects of lead-free piezoelectric ceramics', *J. Euro. Ceram. Soc.* **25**, 2693–2700 (2005).

3. G. Shirane and A. Takeda, ‘Phase transitions in solid solutions of $PbZrO_3$ and $PbTiO_3$ (I) small concentrations of $PbTiO_3$’, *J. Phys. Soc. Jpn* **7**, 5–11 (1952).
4. G. Shirane, K. Suzuki and A. Takeda, ‘Phase transitions in solid solutions of $PbZrO_3$ and $PbTiO_3$ (II) X-ray study’, *J. Phys. Soc. Jpn* **7**, 12–17 (1952).
5. G. Shirane and K. Suzuki, ‘Crystal structure of $Pb(Zr\text{-}Ti)O_3$’, *J. Phys. Soc. Jpn* **7**, 333 (1952).
6. E. Sawaguchi, ‘Ferroelectricity versus antiferroelectricity in the solid solutions of $PbZrO_3$ and $PbTiO_3$’, *J. Phys. Soc.* **8** 615–629 (1953).
7. B. Jaffe, R. S. Roth and S. Marzull, ‘Piezoelectric properties of lead zirconate-lead titanate solid solution ceramics’, *J. Appl. Phys.* **25**, 809–810 (1954).
8. A. S. Bhalla, R. Guo and R. Roy, ‘The perovskite structure – a review of its role in ceramic science and technology’, *Mat. Res. Innovations* **4**, 3–26 (2000).
9. R. E. Cohen and H. Krakauer, ‘Lattice dynamics and origin of ferroelectricity in $BaTiO_3$: linearized-augmented-plane-wave total-energy calculations’, *Phys. Rev. B* **42**, 6416–6423 (1990).
10. R. E. Cohen, ‘Origin of ferroelectricity in perovskite oxides’, *Nature* **358**, 136–138 (1992).
11. Y. Kuroiwa, S. Aoyagi, A. Sawada, J. Harada, E. Nishibori, M. Takata and M. Sakata, ‘Evidence for Pb-O covalency in tetragonal $PbTiO_3$’, *Phys. Rev. Lett.* **87**, 217601 (2001).
12. Y. Ishibashi and M. Iwata, ‘A theory of morphotropic phase boundary in solid-solution systems of perovskite-type oxide ferroelectrics’, *Jpn J. Appl. Phys.* **38**, 800–804 (1999).
13. Y. Ishibashi and M. Iwata, ‘Theory of morphotropic phase boundary in solid-solution systems of perovskite-type oxide ferroelectrics: elastic properties’, *Jpn J. Appl. Phys.* **38**, 1454–1458 (1999).
14. B. Noheda, D. E. Cox, G. Shirane, J. A. Gonzalo, L. E. Cross and S.-E. Park, ‘A monoclinic ferroelectric phase in the $Pb(Zr_{1-x}Ti_x)O_3$ solid solution’, *Appl. Phys. Lett.* **74**, 2059–2061 (1999).
15. B. Noheda, J. A. Gonzalo, R. Guo, S.–E. Park, L. E. Cross, D. E. Cox and G. Shirane, ‘The monoclinic phase in PZT: new light on morphotropic phase boundaries’, in R.E. Cohen (ed.), *Fundamental Physics of Ferroelectrics*, AIP, New York, pp. 304–313 (2000).
16. H. Lemmens and G. V. Tendeloo, ‘Evidence for another low-temperature phase transition in tetragonal $Pb(Zr_xTi_{1-x})O_3$ ($x = 0.515, 0.520$)’, *Phys. Rev.* **B 64**, 054101 (2001).
17. R. Ranjan, Ragini, S. K. Mishra, D. Pandey and B. J. Kennedy, ‘Antiferrodistortive phase transition in $Pb(Ti_{0.48}Zr_{0.52})O_3$: a powder neutron diffraction study’, *Phys. Rev.* **B 65**, 060102 (2002).
18. D. M. Hatch, H. T. Stokes, R. Ranjan, Ragini, S. K. Mishra, D. Pandey and B. J. Kennedy, ‘Antiferrodistortive phase transition in $Pb(Ti_{0.48}Zr_{0.52})O_3$: space group of the lowest temperature monoclinic phase’, *Phys. Rev.* **B 65**, 212101 (2002).
19. K. A. Schönau, L. A. Schmitt, M. Knapp, H. Fuess, R.-A. Eichel, H. Kungland M. J. Hoffmann, ‘Nanodomain structure of $Pb[Zr_{1-x}Ti_x]O_3$ at its morphotropic phase boundary: investigations from local to average structure’, *Phys. Rev.* **B 75**, 184117 (2007).
20. M. Boudys and K. Nejezchleb, ‘Temperature dependence of resonant frequency in piezoelectric ceramics’, *Tesla Electronics* **3**, 81–86 (1980).
21. M. Takahashi, ‘Space charge effect in lead zirconate titanate ceramics caused by the addition of impurities’, *Jpn J. Appl. Phys.* **9**, 1236–1246 (1970).

22. A. Hagimura and K. Uchino, 'Impurity doping effect on electrostrictive properties of (Pb,Ba)(Zr,Ti)O_3', *Ferroelectrics* **93**, 373–378 (1989).
23. B. Matthias and A. von Hippel, 'Domain structure and dielectric response of barium titanate single crystals', *Phys. Rev.* **73**, 1378–1384 (1948).
24. M. E. Caspari and W. J. Merz, 'The electromechanical behavior of $BaTiO_3$ single domain crystal', *Phys. Rev.* **80**, 1082–1089 (1950).
25. K. Uchino, *Ferroelectric Devices,* 2nd edn, CRC Press, New York (2009).
26. C. I. Cheon and H. G. Lee, 'The piezoelectric properties and the stability of the resonant frequency in Mn-Cr Co-doped PSZT ceramics', *J. Mat. Sci.: Mat. Electronics* **10**, 81–84 (1999).
27. G. A. Smolenskii and A. I. Agranovskaya, 'Dielectric polarization of a number of complex compounds', *Soviet Phys. Solid State* **1**, 1429–1437 (1960).
28. Y. Kawamura and H. Ohuchi, 'Electric properties of $Pb(Sb_{1/2}Nb_{1/2})O_3$–$PbTiO_3$–$PbZrO_3$ ceramics', *Jpn J. Appl. Phys.* **33**, 5332–5335 (1994).
29. S. Takahashi, Y. Sasaki, S. Hirose and K. Uchino, 'Stability of $PbZrO_3$–$PbTiO_3$–$Pb(Mn_{1/3}Sb_{2/3})O_3$ piezoelectric ceramics under vibration-level change', *Jpn J. Appl. Phys.* **34**, 5328–5331 (1995).
30. T. Shiosaki, 'Recent development in piezoelectric materials', *Ferroelectrics* **91**, 39–51 (1989).
31. S. Takahashi, A. Ochi, M. Yonezawa, T. Yano, T. Hamatsuki and I. Fukui, 'Internal electrode piezoelectric ceramic actuator', *Ferroelectrics* **50**, 181–190 (1983).
32. Y. Sugawara, K. Onitsuka, S. Yoshikawa, Q. Xu, R. E. Newnham and K. Uchino, 'Metal-ceramic composite actuators', *J. Am. Ceram. Soc.* **75**, 996–998 (1992).
33. Y. Sakabe, 'Multilayer ceramic capacitors', *Curr. Op. Solid State Mater. Sci.* **2**, 584–587 (1997).
34. K. Takahashi, M. Nishida, S. Kawashima and K. Kugimiya, 'Piezoelectric properties of nanostructure-controlled lead-perovskite-based ceramics', *Jpn J. Appl. Phys.*, **33**, 5313–5316 (1994).
35. M. Traianidis, C. Courtois, A. Leriche and B. Thierry, 'Hydrothermal synthesis of lead zirconium titanate (PZT) powders and their characteristics', *J. Eur. Ceram. Soc.* **19**, 1023–1026 (1999).
36. M. Dong and R. A. Gerhardt, 'Electrical characterization of sol-gel derived Pb(Zr,Ti)O_3 ceramics', in K. M. Nair and A. S. Bhalla (eds), *Dielectric Ceramic Materials*, American Ceramic Society, Westerville, OH, pp. 367–376 (1998).
37. Z. Wang, J. Qiu, J. Tani, Z. Sun, T. Iijima and T. Abe, 'Properties of PZT ceramics made by spark plasma sintering', *Dynamics & Design Conference, 1999 B*, 500–501 (1999).
38. P. K. Sharma, Z. Ounaies, V. V. Varadan and V. K. Varafdan, 'Dielectric and piezoelectric properties of microwave sintered PZT', *Smart Mater. Structure.* **10**, 878–883 (2001).
39. J.-F. Li, S. Wang, K. Wakabayashi, M. Esashi and R. Watanabe, 'Properties of modified lead zirconate titanate ceramics prepared at low temperature (800 °C) by hot isostatic pressing', *J. Am. Ceram. Soc.* **83**, 955–957 (2009).
40. J. Akedo, N. Minami, K. Fukuda, M. Ichiki and R. Maeda, 'Electrical properties of direct deposited piezoelectric thick film formed by gas deposition method: annealing effect of the deposited films', *Ferroelectrics* **231**, 285–292 (1999).
41. T. Miyoshi, 'Evaluation of Pb(Zr,Ti)O_3 ceramics prepared by aerosol deposition', *Jpn J. Appl. Phys.* **46**, 7018–7023 (2007).
42. N. J. Donnelly, T. R. Shrout and C. A. Randall, 'Properties of (1-x)PZT-xSKN

ceramics sintered at low temperature using Li_2CO_3', *J. Am. Ceram. Soc.* **91**, 2182–2188 (2008).

43. T. Hayashi, T. Inoue and Y. Akiyama, 'Low-temperature sintering and properties of $(Pb,Ba,Sr)(Zr,Ti,Sb)O_3$ piezoelectric ceramics using sintering aids', *Jpn J. Appl. Phys.* **38**, 5549–5552 (1999).
44. K. Murakami, D. Mabuchi, T. Kurita, Y. Niwa and S. Kaneko, 'Effect of adding various metal oxides on low-temperature sintering $Pb(Zr, Ti)O_3$ ceramics', *Jpn J. Appl. Phys.* **35**, 5188–5191 (1996).
45. T. Hayashi, T. Inoue and Y. Akiyama, 'Low temperature sintering of PZT powders coated with $Pb_5Ge_3O_{11}$ by sol-gel Method', *J. Eur. Ceram. Soc.* **19**, 999–1002 (1999).
46. S.-B. Seo, S.-H. Lee, C.-B. Yoon, G.-T. Park and H.-E. Kim, 'Low-temperature sintering and piezoelectric properties of $0.6Pb(Zr_{0.47}Ti_{0.53})O_3$–$0.4Pb(Zn_{1/3}Nb_{2/3})O_3$ ceramics', *J. Am. Ceram. Soc.* **87**, 1238–1243 (2004).
47. M. Kondo, M. Hida, K. Omote, O. Taniguchi, T. Mita, S. Umemiya and K. Kurihara, 'Preparation of $PbNi_{1/3}Nb_{2/3}O_3$-$PbTiO_3$-$PbZrO_3$ ceramics multilayer actuator with silver internal electrodes', *Sensors and Actuators A* **109**, 143–148 (2003).
48. K. Shiratsuyu, K. Hayashi, A. Ando and Y. Sakabe, 'Piezoelectric characterization of low-temperature-fired $Pb(Zr,Ti)O_3$-$Pb(Ni,Nb)O_3$ ceramics', *Jpn J. Appl. Phys.* **39**, 5609–5612 (2000).
49. C. A. Randall, A. Kelnberger, G. Y. Yang, R. E. Eitel and T. R. Shrout, 'High strain piezoelectric multilayer actuators – a material science and engineering challenge', *J. Electroceramics* **14**, 177–191 (2005).
50. N. Sakamoto, K. Iezumi, J. Yamazaki and M. Nanao, 'Diffused Cu effect in multilayer PZT elements with internal Cu electrodes on electrical performance and microstructure', 13th US–Japan Seminar on Dielectric and Piezoelectric Ceramics Ext. Abst., 77–80 (2007).
51. M. Umeda, K. Nakamura and S. Ueha, 'Analysis of the transformation of mechanical impact energy to electric energy using piezoelectric vibrator', *Jpn J. Appl. Phys.* **35**, 3267–3273 (1996).
52. C.-N. Xu, M. Akiyama, K. Nonaka and T. Watanabe, 'Electrical power generation characteristics of PZT piezoelectricceramics', *Ultrasonics, Ferroelectrics and Frequency Control, IEEE Trans.* **45**, 1065–1070 (1998).
53. S. P. Beeby, M. J. Tudor and N. White, 'Energy harvesting vibration sources for microsystems applications', *Measurement Sci. and Tech.* **17**, R175–R195 (2006).
54. K. Uchino, 'Piezoelectric actuators 2006', *J. Electroceramics* **20**, 301–311 (2007).
55. T. Kanda, A. Makino, T. Ono, K. Suzumori, T. Morita and M. K. Kurosawa, 'A micro ultrasonic motor using a micro-machined cylindrical bulk PZT transducer', *Sensors and Actuators* **A 127**, 131–138 (2006).

3

Relaxor ferroelectric-based ceramics

K. UCHINO, The Pennsylvania State University, USA

Abstract: Ferroelectric relaxor characteristics are discussed in conjunction with the disordered arrangement of the constituent ions. Dielectric properties are characterized by giant and temperature-insensitive dielectric constants and large frequency dependence (referred to as dielectric relaxation). These properties are consistently explainable by the dynamic response of very small spindle-like domains. Superior characteristics in electrostriction and electrooptic effects are also discussed.

Key words: ferroelectric relaxor, disordered perovskite, dielectric relaxation, diffuse phase transition, PMN, PZN, giant electrostriction, short-range ionic ordering, skanavi-type relaxation.

3.1 Introduction

After Smolensky discovered that the ferroelectric phase transition of Ba(Ti,Sn)O_3 becomes diffused drastically with increasing $BaSnO_3$ content,[1] the phenomena of diffused phase transition have been investigated intensively. Figure 3.1 demonstrates the phase transition diffuseness in the permittivity curve in the Ba(Ti,Sn)O_3 system. At a temperature several tens of degrees centigrade above the permittivity peak, where the phase is supposed to be paraelectric and non-piezoelectric, the solid solution specimen was found to exhibit piezoelectric resonance.[2]

Other than these solid solution systems, very similar diffused phase transition can be observed in complex perovskite oxides such as $Pb(Mg_{1/3}Nb_{2/3})O_3$ (PMN) and $Pb(Zn_{1/3}Nb_{2/3})O_3$ (PZN), where two kinds of ions share B sites randomly.[3] Figure 3.2 shows the temperature dependence of the spontaneous polarization in $Pb(Zn_{1/3}Nb_{2/3})O_3$.[4,5] It is remarkable that the spontaneous polarization remains further above the permittivity-peak temperature (140 °C). A similar trailing phenomenon is also observed in an electrooptic effect.[5] Temperature dependence of the permittivity of $Pb(Mg_{1/3}Nb_{2/3})O_3$ is plotted in Fig. 3.3, which obeys a special quadratic law[6,7]

$$1/\varepsilon \propto (T - T_0)^2, \qquad 3.1$$

instead of the normal ferroelectric Curie-Weiss law

$$1/\varepsilon \propto (T - T_0). \qquad 3.2$$

Relaxor ferroelectrics have been utilized for very compact chip capacitors.

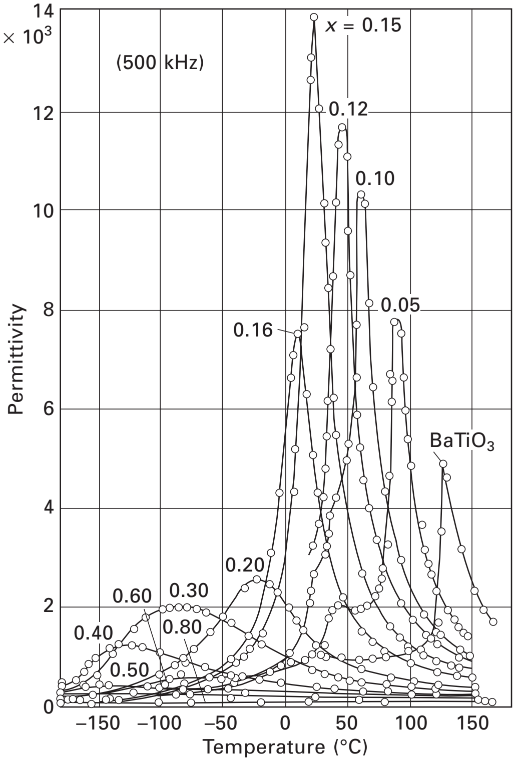

3.1 Temperature dependence of permittivity in (1-x)BaTiO$_3$-xBaSnO$_3$.

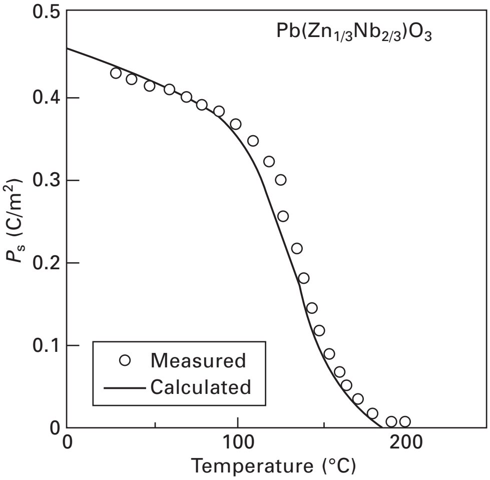

3.2 Temperature dependence of the spontaneous polarization measured in a <111> single crystal of Pb (Zn$_{1/3}$Nb$_{2/3}$)O$_3$.

The reasons why these complex perovskites have been investigated intensively for capacitor applications are their very high permittivity, and their temperature-insensitive characteristics (i.e., diffuse phase transition) in comparison with the normal ferroelectric perovskite solid solutions. However, the relaxors exhibit a problem, that is, *dielectric relaxation* (i.e., frequency dependence of permittivity), a characteristic highlighted by their name.

It is noteworthy to introduce two epoch-making discoveries in the late 1970s and early 1980s, relating with electromechanical couplings in the relaxor ferroelectrics: electrostrictive actuator materials, and high *k* (95%) piezoelectric single crystals.

PMN-based relaxor ferroelectrics were found to be promising transducer materials.[8] These ceramics are dominantly in the paraelectric phase at room temperature, and dimension control is obtained through the high intrinsic quadratic electrostrictive effect. Since stable ferroelectric domain structures do not occur, the problems of dimensional creep and non-reproducibility (aging and de-aging effect) of the conventional poled piezoelectric ceramic are largely eliminated. The PMN-$PbTiO_3$ family gives electrostrictions comparable to conventional piezoelectric PZT ceramics. The PMN-based electrostrictive materials have already been utilized for the 'Hubble' telescope actuators by NASA.[9]

In this chapter, we will discuss the crystallographic, dielectric and electromechanical performance of relaxor ferroelectrics compared with those of normal ferroelectrics. Single crystal performances are not included in this chapter, since they are discussed in detail in Chapter 7.

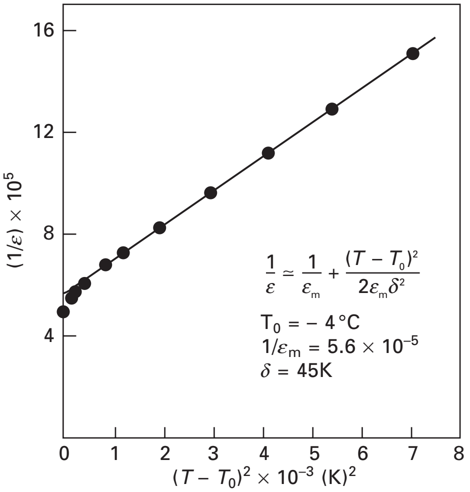

3.3 Dependence of the reciprocal permittivity on the square of temperature measured in a Pb $(Mg_{1/3}Nb_{2/3})O_3$ single crystal.

3.2 Crystal structures of relaxor ferroelectrics

Relaxor ferroelectrics contain three categories of crystal structure:

1 solid solutions with a non-polar component ($BaTiO_3$-$BaSnO_3$),
2 atomic deficiencies by a dopant ($(Pb^{2+}_{1-x}La^{3+}_{x}(Zr,Ti)_{1-x/4}\square_{x/4}O_3)$), and
3 complex perovskites with a combination of different valence ions ($(A^{2+}(B^{2+}_{1/2}B^{6+}_{1/2})O_3$, $A^{2+}(B^{3+}_{1/2}B^{5+}_{1/2})O_3$, $A^{2+}(B^{2+}_{1/3}B^{5+}_{2/3})O_3)$).

It is worth noting that the amount of the atomic vacancy or the molar ratio of the B-site ions is definitely fixed so as to neutralize the valence charge.

Let us take some examples of complex perovskites: $Pb(Mg_{1/3}Nb_{2/3})O_3$, $Pb(Mg_{1/2}W_{1/2})O_3$, $Ba(Mg_{1/3}Ta_{2/3})O_3$. First, $Pb(Mg_{1/3}Nb_{2/3})O_3$ exhibits random arrangement of Mg^{2+} and Nb^{5+} ions on the B-sites, and is called a disordered perovskite (Fig. 3.4(a)). Second, $Pb(Mg_{1/2}W_{1/2})O_3$ shows an ordered arrangement of Mg^{2+} and W^{6+} in an NaCl-type as shown in Fig. 3.4(b) (1:1 order). Third, the cation ordering is also found in $Ba(Mg_{1/3}Ta_{2/3})O_3$, where Mg^{2+} and Ta^{5+} are arranged in the sequence of Mg-Ta-Ta in the <111> direction (1:2 order, Fig. 3.4(c)).[10] The degree of the ionic ordering in complex perovskites depends basically on the difference in the valence charge or in the ionic radius.

The ordering of the ionic arrangement gives a significant effect on ferroelectricity. Simple perovskites exhibit either ferroelectricity ($BaTiO_3$, $PbTiO_3$) or antiferroelectricity ($PbZrO_3$, $PbHfO_3$). On the other hand, the 1:1 ordered complex perovskites tend to be antiferroelectric ($Pb(Mg_{1/2}W_{1/2})O_3$, $Pb(Co_{1/2}W_{1/2})O_3$), and disordered perovskites tend to be ferroelectric ($Pb(Mg_{1/3}Nb_{2/3})O_3$, $Pb(Fe_{1/2}Ta_{1/2})O_3$). In addition, the phase transition of the disordered perovskite is rather diffused and the crystal structure in the low temperature phase is rhombohedral.

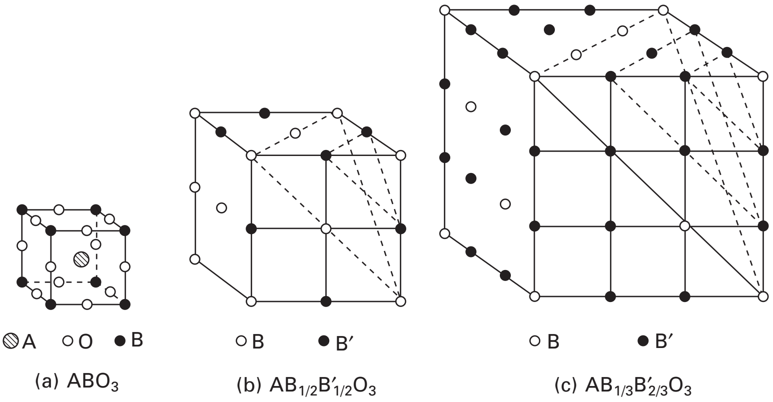

(a) ABO_3 (b) $AB_{1/2}B'_{1/2}O_3$ (c) $AB_{1/3}B'_{2/3}O_3$

3.4 Ordered arrangements of B-site ions in complex perovskites: (a) simple type, (b) 1:1 order type, and (c) 1:2 order type.

The close relationship between dielectric and crystallographic properties is suggestively exemplified in the previous work on $Pb(Sc_{1/2}Ta_{1/2})O_3$.[11] The degree of cation ordering (Sc^{3+}, Ta^{5+}) is easily changeable by simple thermal annealing without any compositional change. Figure 3.5 shows the differences in the dielectric constant (a), and the spontaneous polarization (b). The disordered sample (ordering parameter $S = 0.35$) exhibits a 'diffuse' transition from a ferroelectric to a paraelectric phase. By increasing the ordering ($S = 0.80$), the phase transition becomes 'sharp' and occurs at a higher temperature. Moreover, the P-E curve at a temperature just below the transition shows a double hysteresis, indicating a field-induced antiferro-to-ferroelectric transition.

It is interesting to note that the materials with the 1:2 cation order are usually non-polar, and often applicable to microwave dielectrics.[12]

3.3 Dielectric properties of relaxor ferroelectrics

As mentioned above, relaxor ferroelectrics have been investigated intensively for capacitor application because of their high permittivity and temperature-insensitive characteristics (i.e., diffuse phase transition), in comparison with normal perovskite solid solutions, and these are discussed in the following sections.

3.3.1 Origin of giant permittivity

An intuitive crystallographic model (*rattling ion model*) has been proposed to explain the very high permittivity of the disordered perovskites.[13] Figures 3.6(a) and (b) show the ordered and disordered structures for an $A(B_{I,1/2}B_{II,1/2})O_3$ perovskite crystal. Assuming a rigid ion model, a large 'rattling' space is expected for the smaller B ions in the disordered structure Fig. 3.6(b) because the large B ions prop open the lattice framework. Much less 'rattling' space is expected in the ordered arrangement (Fig. 3.6(a)) where neighboring atoms collapse systematically around the small B ions. The densely-packed structure in (Fig. 3.6(a)) has been observed for $Pb(Mg_{1/2}W_{1/2})O_3$-based ceramics.[14]

When an electric field is applied to a disordered perovskite, the B ions (usually high valence ions) with a large rattling space can shift easily without distorting the oxygen framework. Larger polarization can be expected for unit magnitude of electric field; in other words, larger dielectric constants and larger Curie–Weiss constants should be typical in this case. On the other hand, in ordered perovskites with a very small rattling space, the B ions cannot move easily without distorting the octahedron. A smaller permittivity and a smaller Curie–Weiss constant are expected.

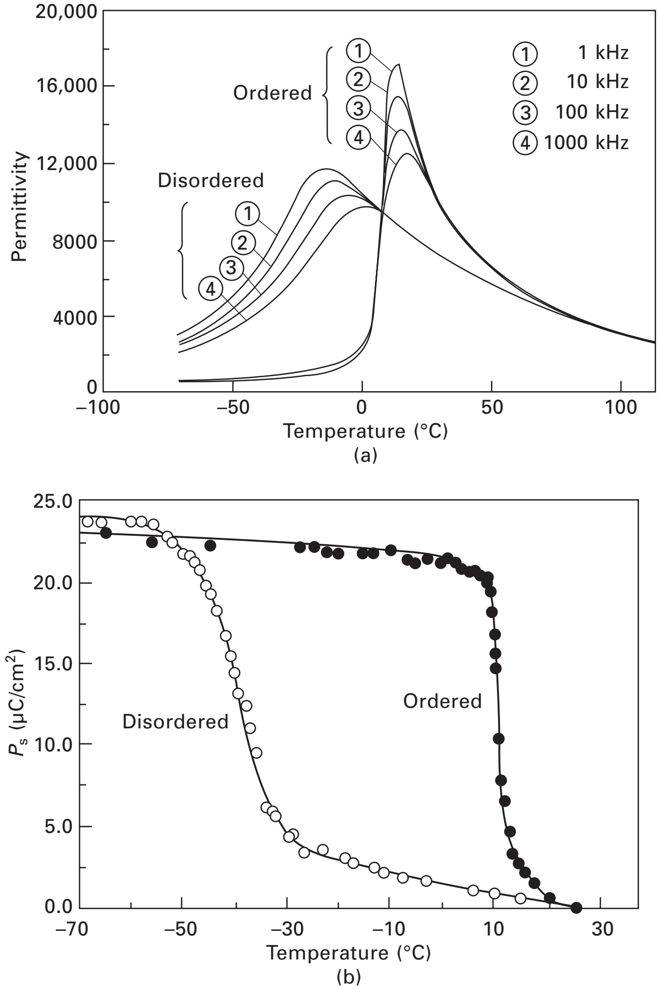

3.5 Dielectric properties of single crystals of $Pb(Sc_{1/2}Ta_{1/2})O_3$ with cation-ordering (S = 0.80) and without ordering (S = 0.35): (a) permittivity and (b) spontaneous polarization.

3.3.2 Diffuse phase transition

The exact reason why the phase transition is diffuse in the relaxor ferroelectrics has not yet been clarified. We introduce here the 'microscopic composition fluctuation' model which is one of the most widely accepted models for relaxor ferroelectrics.[15–20] Within a single *Känzig region* (the minimum polar region size in which cooperative polarization (ferroelectricity) can occur), typically on the order of 10–100 nm,[20] the model applied to a $Pb(B_{I,1/3}B_{II,2/3})O_3$ relaxor assumes a local composition fluctuation of the B_I^{2+} and B_{II}^{5+} ions.

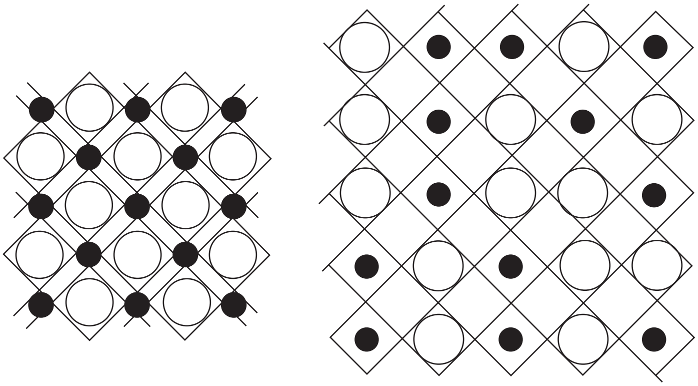

3.6 Crystal structure models of the $A(B_{I,\,1/2}B_{II,1/2})O_3$-type perovskite: (a) the ordered structure with a small rattling space and (b) the disordered structure with a large rattling space (○ = B_I (lower valence cation) and ● = B_{II} (higher valence cation)).

Figure 3.7 shows a computer simulation of the composition fluctuation in an $A(B_{I,1/2}B_{II,1/2})O_3$-type crystal calculated for various degrees of ionic ordering. The fluctuation of the B_I/B_{II} fraction x obeys a Gaussian error distribution.[19] The nearest coupling effect (a solid circle ion tends to occupy the nearest neighbor of an open circle ion) was taken into account for realizing the ordered clusters in the center figure of Fig. 3.7. Krause *et al.* have reported the short-range ionic ordering of $Pb(Mg_{1/3}Nb_{2/3})O_3$ observed by electron microscopy.[21] The high resolution image in Fig. 3.8 reveals somewhat ordered islands in the range of 2–5 nm, each of which may have a slightly different transition temperature. Compare the similarity between Fig. 3.8 and the center part of Fig. 3.7.

According to Rolov[16] we assume that physical properties in a local Känzig region may not change dramatically due to the composition fluctuation, but that only the local Curie temperature θ should be changed in proportion to the fluctuation Δx ($= x - x_{av}$), i.e.,

$$r = (\theta - \theta_{av})/(x - x_{av}), \tag{3.3}$$

where θ_{av} is an average Curie temperature and r is a constant. Then the distribution of the local Cuie temperature is given by

$$f(\theta) = (1/\sqrt{2\pi\sigma^2})\ \exp\left[-(\theta - \theta_{av})^2/2\sigma^2\right], \tag{3.4}$$

where σ is the standard deviation.

Based on this statistical distribution of the Curie temperature and the ferroelectric phenomenology, physical properties can be estimated theoretically.

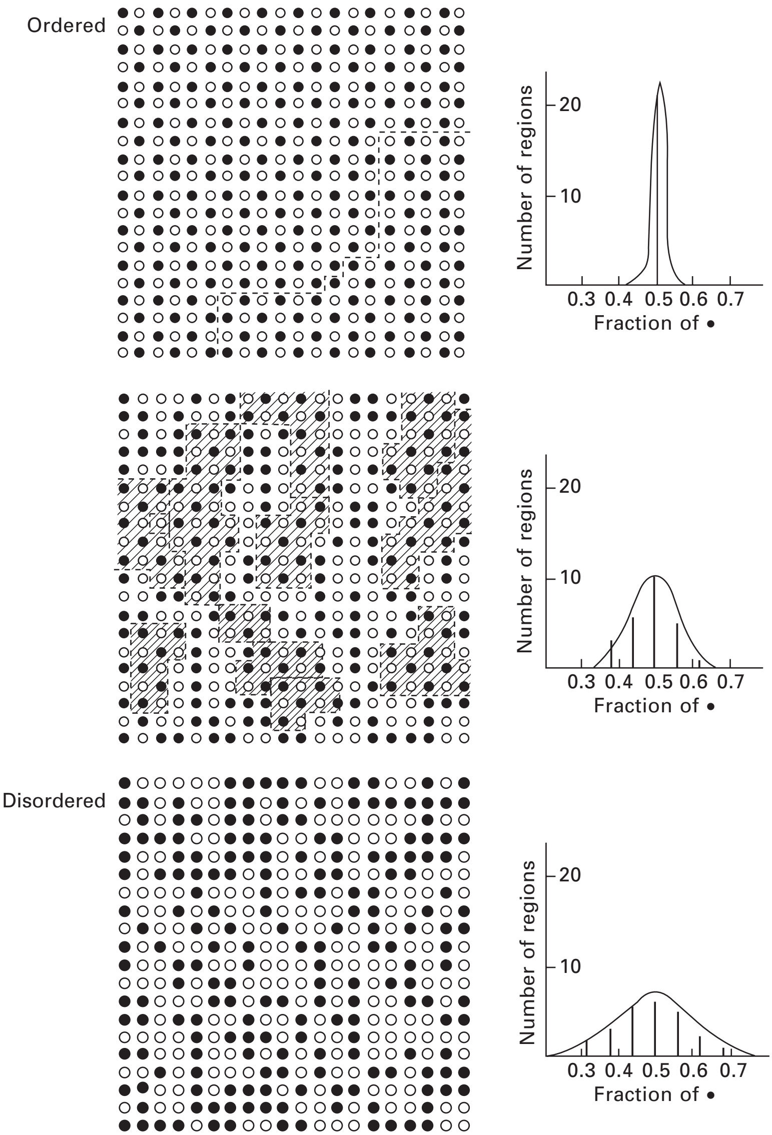

3.7 Computer simulation of the composition fluctuation in the $A(B_{I,1/2}B_{II,1/2})O_3$-type crystal calculated for various degrees of ionic ordering (Känzig region size: 4 × 4).

If the fluctuation of the local composition (not a semi-macroscopic compositional inhomogeneity!) is large enough to provide $\sigma >> 10\,°C$, the normal Curie–Weiss law

$$1/\varepsilon = (T - T_0)/C \qquad 3.5$$

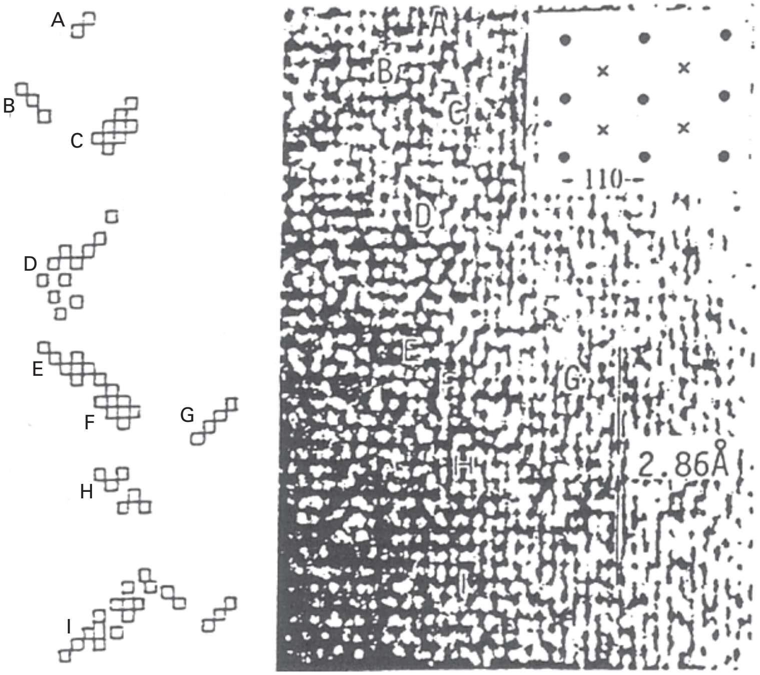

3.8 High resolution electron-microscope image of a $Pb(Mg_{1/3}Nb_{2/3})O_3$ single crystal sample with (110) plane. Note ion-ordered islands in the range of 2–5 nm.

(where T_0: Curie–Weiss temperature, C: Curie–Weiss constant), is transformed into

$$\begin{aligned} 1/\varepsilon &= (1/\varepsilon_m)\exp[-(T-\theta_{av})^2/2\sigma^2] \\ &= (1/\varepsilon_m)\,[1 + (T-\theta_{av})^2/2\sigma^2 + (T-\theta_{av})^4/8\sigma^4 + \ldots], \end{aligned} \qquad 3.6$$

where ε_m is the maximum permittivity at $T = \theta_{av}$. Equation (3.6) corresponds reasonably to an experimental result of Eq. (3.1) in the diffused phase transition.

As discussed above, we obtain a rather broad permittivity peak, which provides more stable temperature change. Thus, sometimes the 'Curie range' is specified rather than the 'Curie point'. In order to improve the temperature coefficient of permittivity (i.e., temperature stability) by promoting a more diffused phase transition, the following techniques are applied:[19]

- Ion-disordered crystals produced by
  - adding a non-ferroelectric component (e.g., $(Pb,Ba)(Zr,Ti)O_3$ where $BaZrO_3$ is a non-polar material)
  - generating lattice vacancies (e.g., (Pb,La, □)$(Zr,Ti)O_3$).

- Short-range ordering within the crystal due to the generation of cation-ordered clusters (e.g., $Pb(Mg_{1/3}Nb_{2/3},Ti)O_3$ and $Pb(Mg_{1/2}W_{1/2},Ti)O3$ (PMW-PT)).

Improvement of the temperature coefficient of permittivity by means of short-range ordering within the crystal is exemplified by the solid solution PMN-PT incorporating PMW or $Ba(Zn_{1/3}Nb_{2/3})O_3$ (BZN). The addition of PMW tends to generate microclusters of the 1:1 ordered type, and BZN clusters of the 1:2 ordered type.

3.3.3 Dielectric relaxation

Another significant characteristic of these 'relaxor' ferroelectrics is *dielectric relaxation* (frequency dependence of the permittivity) from which their name is derived. The temperature dependence of the permittivity for $Pb(Mg_{1/3}Nb_{2/3})O_3$ is plotted in Fig. 3.9 at various measuring frequencies.[3] With increasing measuring frequency, the permittivity in the low temperature (ferroelectric)

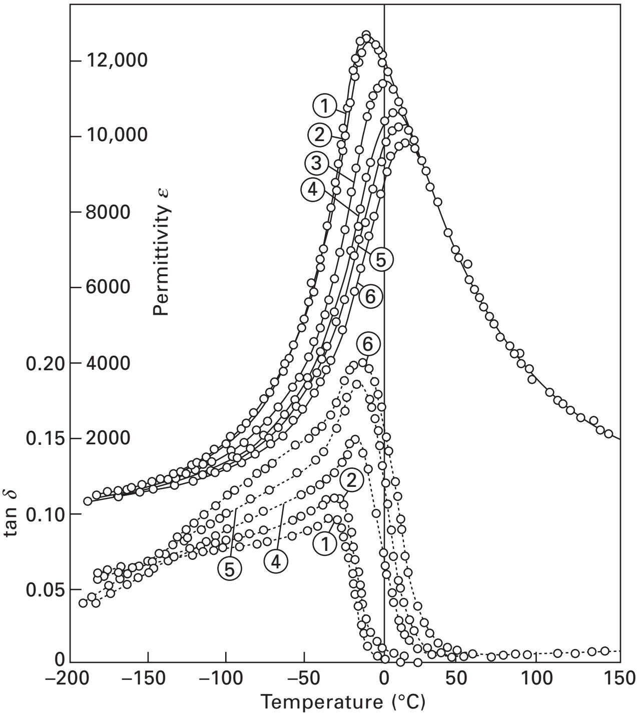

3.9 Temperature dependence of the permittivity and tan δ in $Pb(Mg_{1/3}Nb_{2/3})O_3$ for various measuring frequencies (kHz): (1) 0.4, (2) 1, (3) 45, (4) 450, (5) 1500, (6) 4500.

phase decreases and the peak temperature near 0 °C shifts towards higher temperature; this is contrasted with the behavior of normal ferroelectrics such as $BaTiO_3$, where the peak temperature changes little with the frequency.

Dielectric relaxation similar in origin to the above-mentioned $Pb(Mg_{1/3}Nb_{2/3})O_3$ can also be observed in non-polar disordered perovskites. Figure 3.10 shows the permittivity (real and imaginary parts)–temperature curves of the $(K_{3/4}Bi_{1/4})(Zn_{1/6}Nb_{5/6})O_3$ single crystal.[22] The permittivity peak is not associated with the phase transition, and the cubic crystal structure is maintained through the measuring temperature. When we make a Cole–Cole plot of the real and imaginary parts of the permittivity (Fig. 3.10(b)), multi-dispersive characteristics can be observed especially in a low temperature range. This is probably caused by shallow multi-potential wells in a locally distorted perovskite cell due to the disordered ionic arrangement (*Skanavi-type dielectric relaxation*).[23] The ferroelectric relaxor may include a coupled phenomenon of a Skanavi-type relaxation and a ferroelectric phase transition.

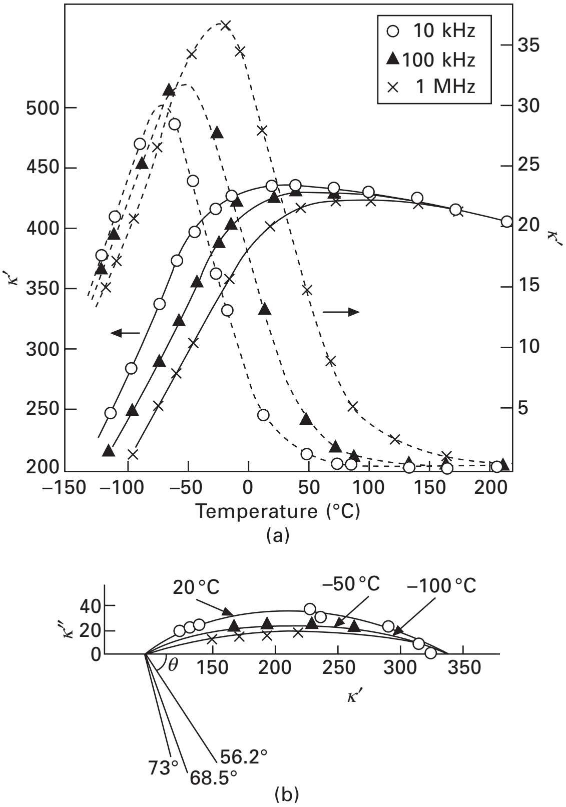

3.10 (a) Permittivity vs. temperature curves of the $(K_{3/4}Bi_{1/4})(Zn_{1/6}Nb_{5/6})O_3$ single crystal. (b) Cole–Cole plot.

Figure 3.11 illustrates the model proposed by the author's group. The Skanavi-type provides local dipoles and exhibits an 'electret'-like property. Of course, when no electric field is applied initially, no charge or polarization is expected because of no cooperative coupling in the crystal. When a long-range cooperative phenomenon, that is, dipole coupling (ferroelectricity), is superposed (indicated by the springs connecting the constituent ions), the net polarization appears.

It is notable that there is an alternative explanation for the dielectric relaxation, which has been proposed by Mulvihill *et al.* for $Pb(Zn_{1/3}Nb_{2/3})O_3$ single crystals.[24] Figures 3.12(a) and 3.12(b) show the dielectric constant and loss versus temperature for an unpoled and a poled PZN single crystal sample, respectively. The domain configurations are also pictured. The macroscopic domains were not observed in an unpoled sample even at room temperature (Fig. 3.12(a) right), only in that state large dielectric relaxation and loss were observed below the Curie temperature range. Once the macro-domains were induced by an external electric field (notice the spindle-like domains in Fig. 3.12(b) right), the dielectric dispersion disappeared and the loss became very small (that is, the dielectric behavior became rather normal!) below 100 °C. As the temperature is increased, the macroscopic spindle-like domains disappear in the poled sample at 100 °C, then immediately above this temperature both large dielectric dispersion and loss appear (Fig. 3.12(b) left). Therefore, the dielectric relaxation appears to be associated with the micro-domains generated in this material. This model suggests the relaxation origin from the micro-domain clusters, rather than each lattice dipole fluctuation. Mathematical treatment of the relaxor behavior originating from the presence of micro-domains has not yet been conducted.

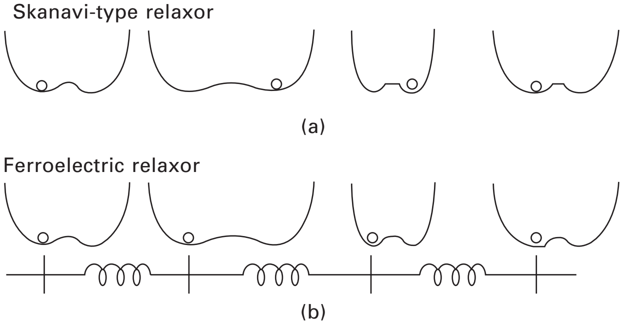

3.11 Multi-potential well model for (a) the Skanavi-type and (b) the ferroelectric relaxors. Note the difference in the cooperative phenomenon, represented by springs.

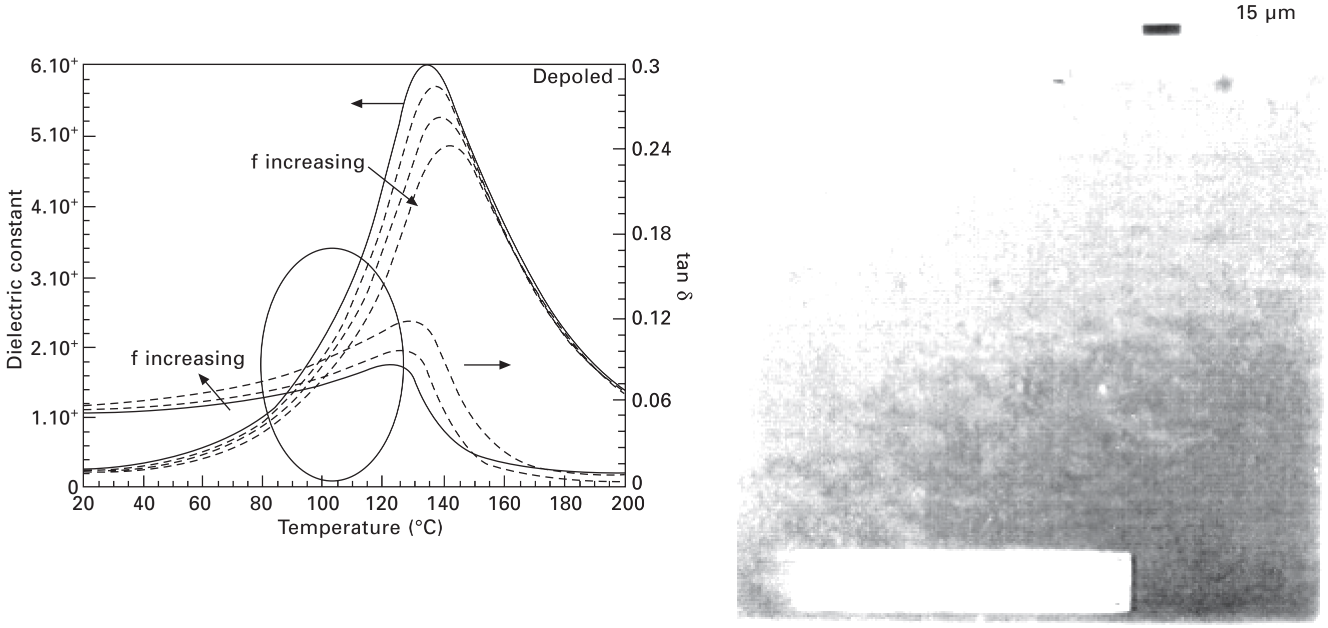

(a)

3.12 Dielectric constant and loss versus temperature measured for (a) an unpoled $Pb(Zn_{1/3}Nb_{2/3})O_3$ single crystal measured on the <111>, and (b) a poled PZN single crystal (rhombohedral (111) plates). The domain configurations are also pictured on the right-hand side. Once the macro-domains (spindle-like) were induced by an external electric field, the dielectric dispersion disappeared and the loss became very small.

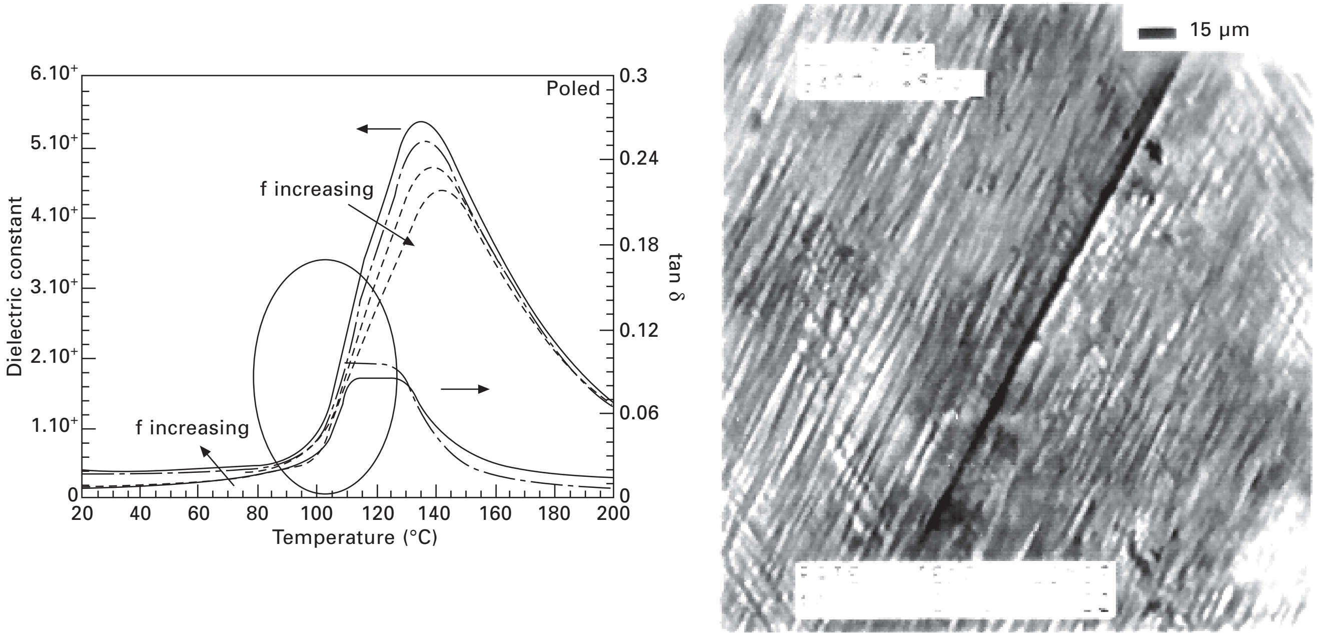

(b)

3.12 Continued

3.4 Electrostriction in relaxor ferroelectrics

There were two major discoveries made by the author's group in the late 1970s and early 1980s, relating to electromechanical couplings in the relaxor ferroelectrics: electrostrictive actuator materials, and high *k* (95%) piezoelectric single crystals. Cross *et al.* reported extraordinarily large secondary electromechanical coupling, i.e., 'electrostrictive' effect, with a strain level higher than 0.1% at room temperature, exhibiting negligible hysteresis during rising and falling electric field, in a composition 0.9 PMN–0.1 $PbTiO_3$.[8] High *k* studies are considered in Chapter 7.

Since the cation-disordered complex perovskite exhibits a diffused phase transition, the crystal is electrically poled easily when an electric field is applied around the transition temperature, and subsequently depoled completely without any remanent polarization because the domain is separated into micro-domains when the field is removed. This results in rather large apparent secondary effects in physical properties.

Concerning electric-field induced strains, $Pb(Mg_{1/3}Nb_{2/3})O_3$ for example, exhibits a large electrostriction (i.e., a second-order electromechanical property where strain is induced in proportion to the square of the applied field; $x = ME^2$, M is called an electrostrictive coefficient) at room temperature in the small electric-field range. Figure 3.13 shows the strain curve of the transversely induced electrostriction in $0.9Pb(Mg_{1/3}\text{-}Nb_{2/3})O_3$–$0.1PbTiO_3$.[8,25,26] The relaxor ceramics are anhysteretic, and retrace the same curve with rising and falling fields. For comparison, the piezoelectric strain (i.e., strain induced in proportion to the applied field; $x = dE$, d is called a piezoelectric

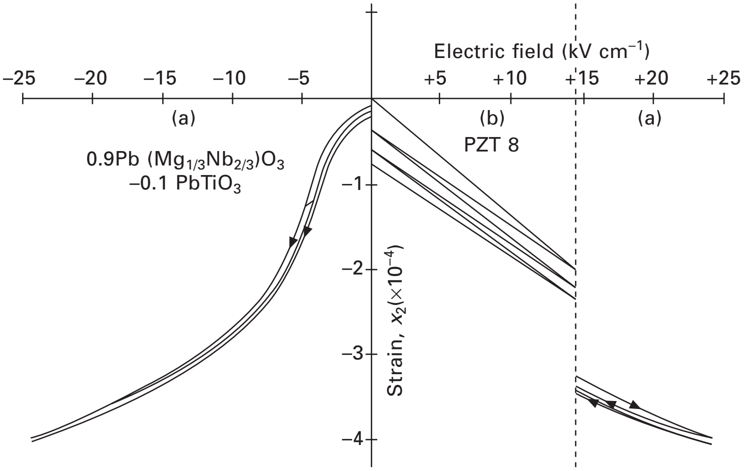

3.13 Transverse strain in ceramic specimens of 0.9PMN–0.1PT (a) and a typical hard PZT 8 piezoceramic (b) under varying electric fields.

coefficient) of a hard PZT 8 under a cyclic field is also plotted in Fig. 3.13. This material has often been used in the fabrication of multi-dither mirrors and other active optical components. Note that the electrostriction is comparable to or larger than the magnitude of the typical piezoelectric strain induced in $Pb(Zr,Ti)O_3$-based ceramics and far more reproducible under cyclic drive conditions.

Another interesting property of relaxor ferroelectrics is the very small thermal expansion effect throughout the Curie range. Figure 3.14 shows the thermal strain of $0.9Pb(Mg_{1/3}Nb_{2/3})O_3$–$0.1PbTiO_3$ plotted as a function of temperature.[8] In the temperature range –100 °C to +100 °C, the thermal expansion coefficient is less than $1 \times 10^{-6}\ K^{-1}$, comparable to the best low-expansion ceramics or fused silica. The thermal strains are far smaller than the electrostrictive strains, which is extremely advantageous for micropositioner applications.

When the author started actuator research in the mid 1970s, precise positioners were required in the Space Shuttle program, particularly for ‘deformable mirrors’, for controlling the optical pathlengths over several wavelengths (1 micron). Conventional piezoelectric PZT ceramics were plagued by hysteresis and aging effects under large electric fields; this was a serious problem for an optical positioner. Electrostriction, which is the secondary electromechanical coupling observed in centro-symmetric crystals, is not affected by hysteresis or aging. In addition, electric poling is not required. This discovery, in conjunction with the multilayer actuator invention (1978), accelerated the development of piezoelectric actuators after the 1980s.

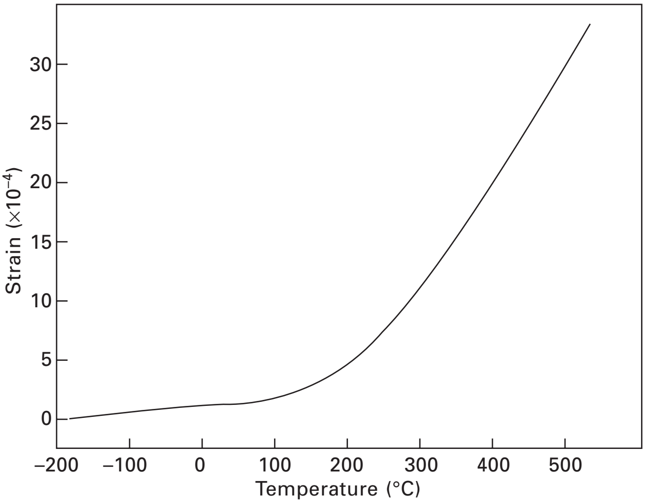

3.14 Thermal expansion in polycrystalline $0.9Pb(Mg_{1/3}Nb_{2/3})O_3$–$0.1PbTiO_3$.

Figure 3.15 shows the Hubble telescope proposed by the Jet Propulsion Laboratory, NASA, using six multilayer PMN electrostrictive actuators to control the phase of the incident light wave in the field of optical information processing.[9]

3.5 Electrooptic effect

Relaxor ferroelectrics are also utilized in non-linear optic applications because an extraordinarily large electrooptic Kerr effect can be observed even in the so-called paraelectric state. Figure 3.16 shows the birefringence versus electric field relation of $Pb(Zn_{1/3}Nb_{2/3})O_3$ in the paraelectric phase.[5] The parabolic curve in the low field region tends to approach a straight line in the high field region. This peculiar phenomenon is analyzed on the basis of the model that the crystal is composed of the ferroelectric and paraelectric phases mixed together. Suppose that the volume fraction of the paraelectric phase $x(T)$ is given by the accumulated Gaussian distribution (see Eq. (3.4)). The birefringence is estimated by the summation of linear and quadratic electrooptic effects:[18]

$$\Delta n = [1 - x(T)]\, n^3(r_{33} - r_{13})\, E/2 + x(T)\, n^3 g_{44}\, P^2/2, \qquad 3.7$$

where r and g represent electrooptic Pockels and Kerr coefficients, respectively.

Well-known electrooptic transparent ceramics PLZT, i.e., $(Pb_{1-x}La_x)(Zr_y\,Ti_z)_{1-x/4}O_3$, are examples of relaxors that have large electrooptic effect and are applicable to light valves, displays, etc. Transparent ceramics of $Pb(Mg_{1/3}–Nb_{2/3})O_3–PbTiO_3$ prepared by hot-pressing have been discovered to exhibit a giant electrooptic coefficient larger than the PLZT.[27]

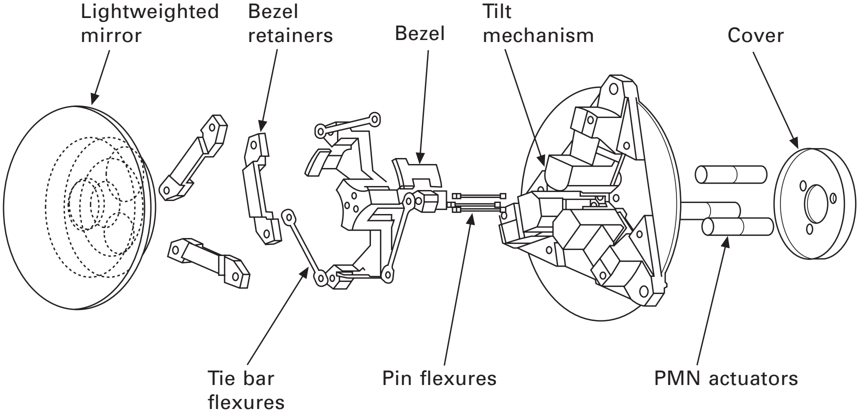

3.15 Hubble telescope using three $0.9Pb(Mg_{1/3}Nb_{2/3})O_3–0.1PbTiO_3$ electrostrictive actuators for optical image correction.

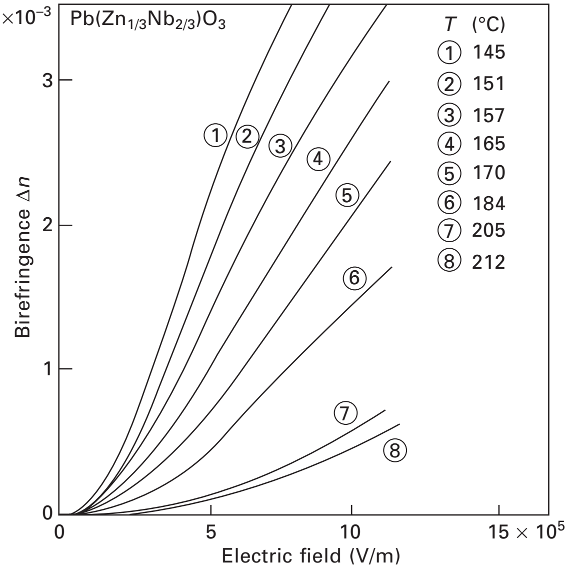

3.16 Birefringence vs. electric field relation of $Pb(Zn_{1/3}Nb_{2/3})O_3$ in the paraelectric phase.

3.6 Conclusions

Ferroelectric relaxor characteristics are closely related with the disordered arrangement of the constituent ions. Dielectric properties are characterized by giant and temperature-insensitive dielectric constants and large frequency dependence (i.e., dielectric relaxation). These properties are consistently explainable by the dynamic response of micro and spindle-like macro-domains. Superior characteristics in electrostriction and electrooptic effects are also attributed to the easy poling of the ferroelectric micro-domains.

3.7 References

1. G. A. Smolensky: *J. Phys. Soc. Jpn.* **28**, Suppl., 26 (1970).
2. G. A. Smolensky and V. A. Isupov: *Zh. Tech. Fiz.* **24**, 1375 (1954).
3. G. A. Smonlensky, V. A. Isupov, A. I. Agranovskaya and S. N. Popov: *Sov. Phys.–Solid State*, **2**, 2584 (1961).
4. S. Nomura, M. Abe, F. Kojima and K. Uchino: Jpn. *J. Appl. Phys.* **14**, 1881 (1975).
5. F. Kojima, J. Kuwata and S. Nomura: *Proc. 1st Mtg. Ferroelectric Mater. & Appl.* (Kyoto, 1977) p. 155.
6. V. V. Kirillov and V. A. Isupov: *Ferroelectrics* **5**, 3 (1973).
7. K. Uchino, S. Nomura, L. E. Cross, S. J. Japan and R. E. Newnham: *J. Appl. Phys.* **51**, 1142 (1980).

8. L. E. Cross, S. J. Jang, R. E. Newnham, S. Nomura and K. Uchino: *Ferroelectrics*, **23**(3), 187 (1980).
9. B. Wada: JPL Document D-10659, P.23 (1993).
10. G. Blasse and A. F. Corsmit: *J. Sol. State Chem.* **6**, 513 (1973).
11. N. Setter and L. E. Cross: *J. Appl. Phys.* **51**, 4356 (1980).
12. S. Nomura, K. Toyama and K. Kaneta: *Jpn. J. Appl. Phys.* **21**, L624 (1982).
13. K. Uchino, L. E. Cross, R. E. Newnham and S. Nomura: *J. Phase Transition* **1**, 333 (1980).
14. A. Amin, R. E. Newnham, L. E. Cross, S. Nomura and D. E. Cox: *J. Sol. State Chem.* **35**, 267–71 (1980).
15. V. A. Isupov: *Zh. Tech. Fiz.* **26**, 1912 (1956).
16. B. N. Rolov: *Fiz. Tverdogo Tela* **6**, 2128 (1963).
17. V. A. Isupov: *Izv. Akad. Nauk SSSR, Ser. Fiz.* **28**, 653 (1964).
18. J. Kuwata, K. Uchino and S. Nomura: *Ferroelectrics* **22**, 863 (1979).
19. K. Uchino, J. Kuwata, S. Nomura, L. E. Cross and R. E. Newnham: *Jpn. J. Appl. Phys.* **20**, Suppl. 4, 171 (1981).
20. W. Känzig: *Helv. Phys. Acta* **24**, 175 (1951).
21. H. B. Krause, J. M. Cowley and J. Wheatley: *Acta Cryst.* **A35**, 1015 (1979).
22. S. Nomura and F. Kojima: *Jpn. J. Appl. Phys.* **12**, 205 (1973).
23. G. I. Skanavi, I. M. Ksendzov, V. A. Trigubenko and V. G. Prokhvatilov: *Sov. Phys.-JETP* **6**, 250 (1958).
24. M. L. Mulvihill, L. E. Cross and K. Uchino: *Proc. 8th European Mtg. Ferroelectricity*, Nijmegen (1995).
25. K. Uchino, S. Nomura, L. E. Cross, R. E. Newnham and S. J. Jang: *J. Mater. Sci.* **16**, 569 (1981).
26. K. Uchino: *J. Ceram. Soc. Japan* **99**(10), 829–835 (1991).
27. K. Ohmura, Y. Murai, K. Uchino and J. Giniewicz: *Proc. Int'l Display Research Conf.*, IEEE, p. 137 (1988).

4
Lead-free piezo-ceramics

T. TAKENAKA, Tokyo University of Science, Japan

Abstract: Dielectric, ferroelectric and piezoelectric properties of perovskite lead-free ferroelectric ceramics such as $BaTiO_3$ [BT], $KNbO_3$ [KN], $(Bi_{1/2}Na_{1/2})$ TiO_3 [BNT] and $(Bi_{1/2}K_{1/2})$ TiO_3 [BKT]-based ceramics and their solid solutions are described as superior candidates for lead-free piezoelectric ceramics to reduce environmental damage to the earth. Perovskite-type ceramics seem to be suitable for actuator and high power applications that require a large piezoelectric constant, d_{33} and a high Curie temperature, T_c, or a depolarization temperature, T_d.

The electromechanical coupling factor, $k_{15} = 0.55$, and the piezoelectric strain constant, $d_{15} = 207$ pC/N, are obtained at Mn-doped KN–Mn0.1 wt%. In the case of the BNT-based solid solution, $x(Bi_{1/2}Na_{1/2})TiO_3$-$y(Bi_{1/2}K_{1/2})$ TiO_3-$zBaTiO_3$, [$x + y + z = 1$, $y{:}z = 2{:}1$, BNBK2:1(x)], the d_{33} values are 126, 181 and 80 pC/N for $x = 0.78$, 0.88 and 0.98, respectively. The depolarization temperature T_d, rhombohedral-tetragonal phase transition temperature $T_{R\text{-}T}$ and the temperature T_m of the maximum dielectric constant were determined from the temperature dependence of the dielectric and piezoelectric properties. The three component solid solution, $a(Bi_{1/2}Na_{1/2})$ TiO_3-$b(Bi_{1/2}Li_{1/2})TiO_3$- $c(Bi_{1/2}K_{1/2})TiO_3$ [$a + b + c = 1$] (BNLKT100b-100c) has the morphotropic phase boundary (MPB) between rhombohedral and tetragonal phases at approximately $c = 0.20$. The piezoelectric properties are at maximum and the T_d values show minimum near the MPB. The k_{33}, d_{33} and T_d of BNLKT4-20 and BNLKT8-20 were 0.603, 176 pC/N and 171 °C, and 0.590, 190 pC/N and 115 °C, respectively. On the other hand, the d_{33} and T_d of BNLKT4-28 were 135 pC/N and 218 °C, respectively. Considering both high T_d and high d_{33}, the tetragonal compositions of BNLKT4-100z are thought to be a superior candidate. The high-power characteristics of BNLKT4-8Mn0.6 were superior to those of hard PZT at a vibration velocity $v_{0\text{-}p} > 0.6$ m/s.

The solid solution, $(1\text{-}x)(Bi_{1/2}K_{1/2})TiO_3$–$xBaTiO_3$ [BKT-BT100x], seems to be lead-free piezoelectric ceramics with wide operating temperatures. The BKT-BT100x ceramics ($x = 0$–0.4) indicated high depolarization temperatures, T_d, around 300 °C. From these results, the BKT-BT system is a superior candidate as lead-free piezoelectric material for high power and/or high temperature applications.

Key words: ferroelectric properties, piezoelectric properties, perovskites, solid solution, lead-free piezoelectric ceramics, morphotropic phase boundary, depolarization temperature, $BaTiO_3$, $(Bi_{1/2}Na_{1/2})TiO_3$, $(Bi_{1/2}K_{1/2})$ TiO_3, $(K,Na)NbO_3$, $KNbO_3$, mechanical quality factor, Mn-doping, high-power characteristics.

4.1 Introduction

Piezoelectric materials play an important role in electronic devices such as actuators, sensors, accelerators, ultrasonic motors, transducers, filters and resonators and micro-electromechanical systems (MEMS). The most widely used piezoelectric materials are $PbTiO_3$-$PbZrO_3$ (PZT)-based multi-component systems (PZT systems)[1–4] because of their excellent piezoelectric properties. However, it has recently become desirable to use lead-free materials for environmental protection during the waste disposal of products. For example, legislation has been enforced in the EU in the form of the draft Directives on Waste from Electrical and Electronic Equipment (WEEE) since January 1, 2004, Restriction of Hazardous Substances (RoHS) since July 1, 2006 and End-of-Life Vehicles (ELV) since July 1, 2003. Therefore, lead-free piezoelectric materials have been attracting attention worldwide[5–7] in the search for new materials to replace PZT-based piezoelectric ceramics.

Lead-free piezoelectric materials, such as piezoelectric single crystals, e.g. langasite,[8] and ferroelectric ceramics with a perovskite structure,[9–60] a tungsten bronze structure,[61,62] and bismuth layer-structured ferroelectrics (BLSF),[63–69] have been extensively reported for mainly the past 10 years. Recently, various perovskite-structured ferroelectrics such as $BaTiO_3$ [BT], $(Bi_{1/2}Na_{1/2})TiO_3$ [BNT], $(Bi_{1/2}K_{1/2})TiO_3$ [BKT], $KNbO_3$ [KN], $(K,Na)NbO_3$ [KNN] and their solid solutions have been actively studied[17–60] as candidates for lead-free piezoelectric ceramics. These ceramics have been widely studied and their use is expected in actuator and high-power applications because of their relatively large piezoelectric constants, d, among lead-free piezoelectrics. However, there are some problems such as low Curie temperatures, T_c, or low depolarization temperatures, T_d, difficulties in poling treatments and/or low relative densities. Ferroelectric perovskite-structured ABO_3 type oxides are classified by their ionic valences: 2+:4+ type, $PbTiO_3$ [PT], 1+:5+ type, $KNbO_3$ [KN] and 3+:3+ type, $BiFeO_3$ [BF]. However, with the exception of PT, none of them exhibit superior ferroelectricity to that of PZT. Or, no lead-free materials display more excellent piezoelectric properties than those of PZT-based systems. To replace PZT-based systems, it is necessary that the required piezoelectric properties for various applications are classified and developed for each application. For example, the perovskite-type ceramics seem to be suitable for actuator and high-power applications. On the other hand, BLSF ceramics seem to be candidate materials for ceramic resonator applications.

In this chapter, a brief survey of non-lead based piezoelectric ceramics is given and dielectric, ferroelectric and piezoelectric properties of typical lead-free perovskite ferroelectric ceramics, such as $BaTiO_3$ [BT], $Bi_{1/2}Na_{1/2}TiO_3$ [BNT], $Bi_{1/2}K_{1/2}TiO_3$ [BKT] and $KNbO_3$ [KN]-based systems for actuator and high power applications, are described as superior candidates for environmental friendly lead-free piezoelectric materials to reduce some of the damage to earth.

4.2 Barium titanate ($BaTiO_3$) [BT]-based ceramics

Barium titanate, $BaTiO_3$ [BT],[9,10] was the first ferroelectric oxide with a perovskite structure to be discovered. This ceramic has a relatively high electromechanical coupling factor, k_{33} (~0.50), and piezoelectric strain constant, d_{33} (~190 pC/N), and has been used in piezoelectric applications such as sonars. However, the working temperature range of BT is too narrow for actual piezoelectric applications because BT has a low Curie temperature, (T_c = 120–135 °C).[9,10,55,56] On the other hand, bismuth potassium titanate, $(Bi_{1/2}K_{1/2})TiO_3$ [BKT], is a typical lead-free ferrolectric with a perovskite structure of tetragonal symmetry at room temperature and a relatively higher T_c of 380 °C.[14] Hiruma *et al.*[43] reported the electrical properties of BKT ceramics prepared by the hot-pressing (HP) method. To expand the working temperature range, that is, to elevate the T_c of the BT ceramic, dielectric and piezoelectric properties of $(1\text{-}x)$BT–xBKT solid solution (BT–BKT100x) system were also investigated.[40,70]. The T_c increased linearly with increasing BKT content (x) and the T_c of BT–BKT20 ($x = 0.2$) was higher than 200 °C.

Recently, large piezoelectric strain constants (d_{33} = 350 pC/N and d_{33} = 450 pC/N), of BT ceramics were reported, respectively, in the microwave sintered BT by using hydrothermally prepared fine particles[55] and in the BT prepared by the two-step sintering method.[56] These large d_{33}s may be caused by the elevated very high relative free permittivity ($\varepsilon_{33}{}^T/\varepsilon_0$), higher than 5000.

4.3 Potassium niobate ($KNbO_3$) [KN]–sodium niobate ($NaNbO_3$) [NN]– lithium niobate ($LiNbO_3$) [LN] system

Potassium niobate, $KNbO_3$ [KN], ceramics have attracted much attention as a candidate material for lead-free piezoelectric applications, because the single-crystal KN has a large piezoelectricity and a high Curie point.[11, 31, 33] KN has an orthorhombic symmetry at room temperature, and has phase transitions at −10, 225 and 425 °C corresponding to rhombohedral → orthorhombic → tetragonal → cubic, respectively. The electromechanical coupling factor of the thickness-extensional mode, k_t, in a KN crystal reaches as high as 0.69 for the 49.5 ° rotated X-cut about the Y-axis, which is the highest among current lead-free piezoelectrics.[50] KN single crystals are known to have high piezoelectric activities. However, it is difficult to obtain a dense ceramic body of KN by the ordinary firing process. To obtain the dense KN-based ceramic, the hot-press (HP) method or liquid phase sintering by additional dopants were investigated.[32,34] On the other hand, electrical properties of potassium–sodium niobates, $KNbO_3$–$NaNbO_3$ [KNN] system, were reported by Egerton *et al.*[12,15] Their work on ceramics in the system indicated that relatively low dielectric constants and high electromechanical coupling factors could be obtained over a wide range of compositions. However, it is difficult to realize the desired structure in a ceramic form because the sintering of these materials in air requires long soaking periods to achieve sufficient densification. There have been many reports on KN solid-solution systems such as $KNbO_3$–$NaNbO_3$ [KNN]. Good piezoelectric properties, such as a large planar coupling factor, $k_p = 0.56$, and a large remanent polarization, P_r up to 30 μC/cm^2, have been observed for KNN ceramics.[12] An excellent piezoelectric property of 416 pC/N in textured $(K_{0.5}Na_{0.5})NbO_3$-based ceramics has recently been reported by Saito *et al.*[36] Figure 4.1 shows (a) the piezoelectric strain constant, d_{31}, as a function of the content of Ta and Li ions and (b) the d_{33} as a function of the Curie temperature.[36] Table 4.1 summarizes piezoelectric properties of the textured LF4T compared with those of PZT4.[36]

Recently Guo *et al.*[37] also reported that $(1–x)(K,Na)NbO_3–xLiNbO_3$ solid solution [$(1–x)$KNN-xLN] shows the MPB composition between the orthorhombic and the tetragonal symmetries near $0.05 < x < 0.07$ with the higher Curie temperature of 450 °C and the higher d_{33} of 240 pC/N (Figs 4.2 and 4.3).

4.4 Potassium niotate ($KNbO_3$) [KN]-based ceramics

In terms of $KNbO_3$ [KN] ceramic, there are few papers and a limited number of reports on its electrical properties because of its deliquescent behavior and its poor sinterability by the conventional fabrication process in air. Recently, the dense KN-based ceramics have been obtained by using the modified conventional ceramic firing technique with good dielectric, ferroelectric, and piezoelectric properties.[45–47] A developed preparation procedure has been proposed to improve the deliquescence and sinterability behavior of KN-based ceramics such as $KNbO_3$ [KN] and $KNbO_3$+$MnCO_3$ x wt% [KN-Mn x]. To fix the problems of deliquescence and poor sinterability behavior, two conditions were optimized in whole sample preparation process. The first one is a calcination process for improvement of the deliquescence behavior, and the second one is a milling process for achieving fine KN powders and finally dense KN-based ceramic bodies.

Figure 4.4 shows the temperature dependences of the dielectric constant ε_s and the loss tangent tan δ of the KN ceramic calcined at (a) 1000 and (b) 600 °C. The Curie temperature T_c of the KN ceramic calcined at 1000 °C was 424 °C and the phase transition temperature T_2 from an orthorhombic

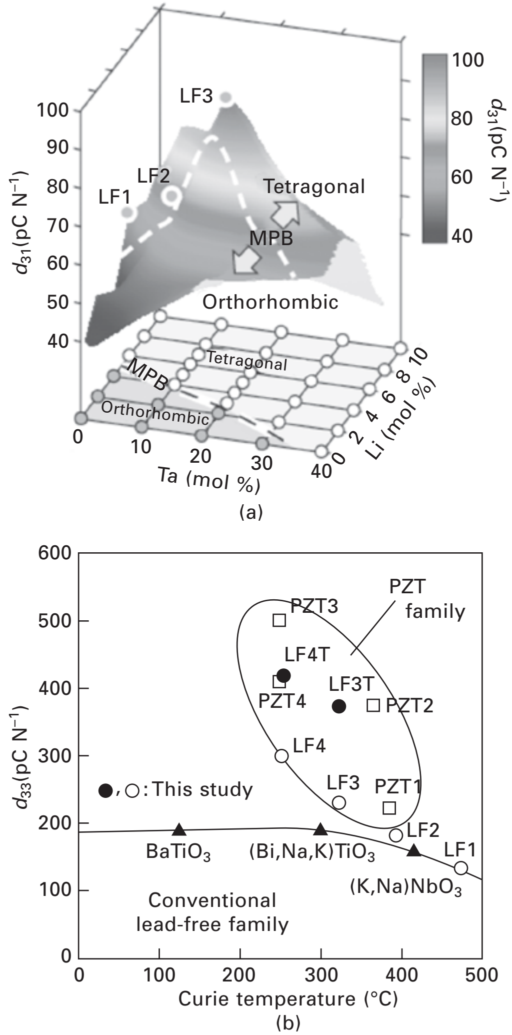

4.1 (a) The piezoelectric strain constant, d_{31}, as a function of the content of Ta and Li ions and (b) the d_{33} as a function of the Curie temperature.[36]

symmetry to a tetragonal symmetry was approximately 230 °C. There were no significant changes in T_c or T_2 for either of the two ceramics.

The KN samples for piezoelectric properties were poled at 5 kV/mm for 2–5 min at 150 °C. Note that the sample in the (33) mode was approximately in the full-poling state as judged from the maximum phase, $\theta_{max} = 87.4°$, of impedance in the inductance region between the resonance and antiresonance frequencies with the electromechanical coupling factor, $k_{33} = 0.492$, the

Table 4.1 Piezoelectric properties of the textured LF4T compared with those of PZT4[36]

Piezoelectric property		LF4T	PZT4
Curie temperature	T_c(°C)	253	250
Piezoelectric coupling constant	K_p	0.61	0.60
Piezoelectric charge sensor constant	d_{31}(pC N^{-1})	152	170
	d_{33}(pC N^{-1})	416	410
Piezoelectric voltage constant	g_{31}(10^{-3}Vm N^{-1})	11.0	8.3
	g_{33}(10^{-3}Vm N^{-1})	29.9	20.2
Dielectric constant	$\varepsilon^T_{33}/\varepsilon_0$	1570	2300
Normalized strain	S_{max}/E_{max} (pm V^{-1})	750	700

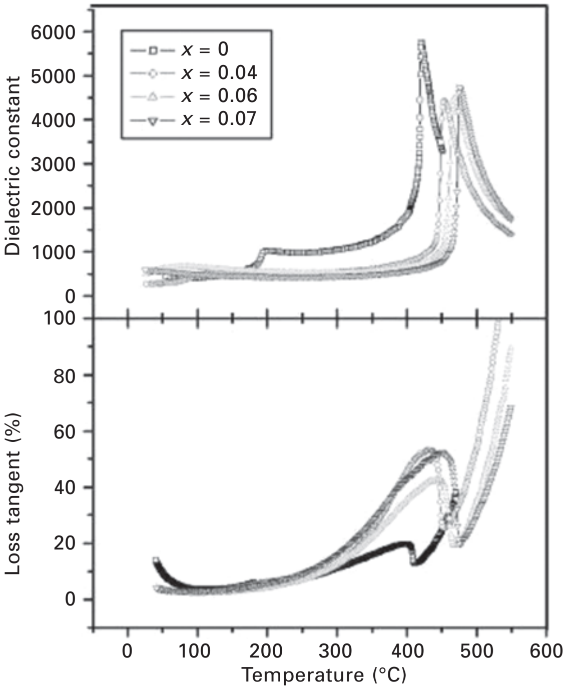

4.2 Temperature dependence of dielectric constant and loss tangent, tan δ, of (1-*x*)(K,Na)NbO$_3$–*x*LiNbO$_3$.[37]

piezoelectric constant, d_{33} = 91.7 pC/N and the mechanical quality factor, Q_m = 325, respectively. Figure 4.5 shows the temperature dependences of d_{33} and k_{33} for the KN ceramic as determined by the resonance-antiresonance method. The piezoelectric response disappeared above 430 °C, which corresponded to T_c. The k_{33} values in the orthorhombic region from RT to 225 °C were almost stable at approximately 0.5. Above the phase transition temperature, T_2, the k_{33} slightly decreased to approximately 0.35. The d_{33} was constant

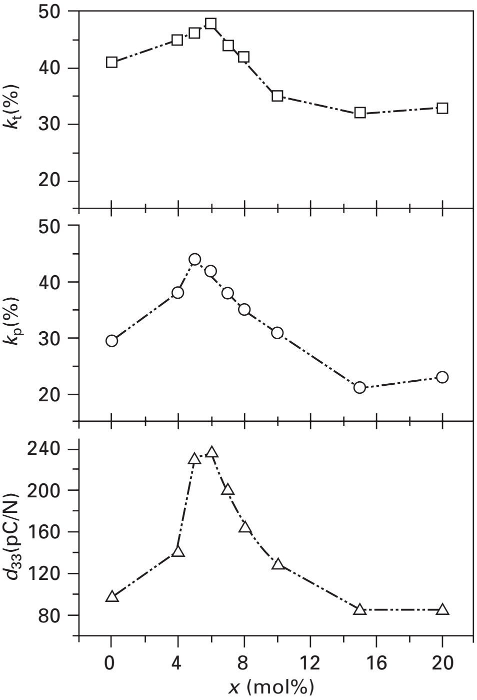

4.3 Electromechanical coupling factors, k_t and k_p, and the piezoelectric strain constant, d_{33} as a function of the content (*x*) of Li ion in (1-*x*)(K,Na)NbO$_3$–*x*LiNbO$_3$.[37]

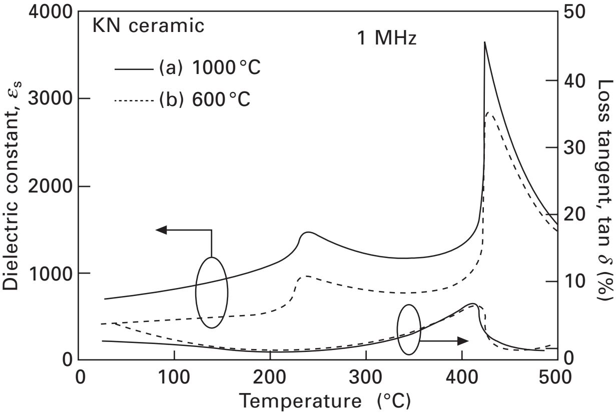

4.4 Temperature dependences of dielectric constant ε_s and loss tangent tan δ for KN ceramic calcined at (a) 1000 and (b) 600 °C.

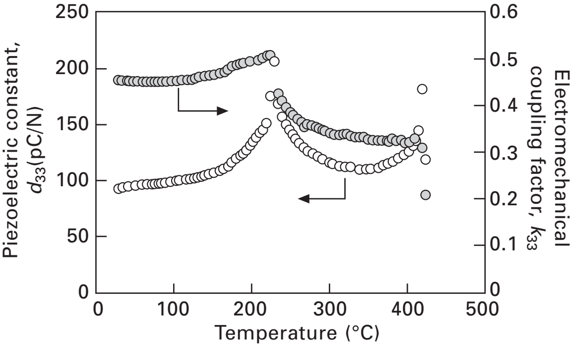

4.5 Temperature dependences of piezoelectric constant d_{33} and electromechanical coupling factor k_{33} for KN ceramic.

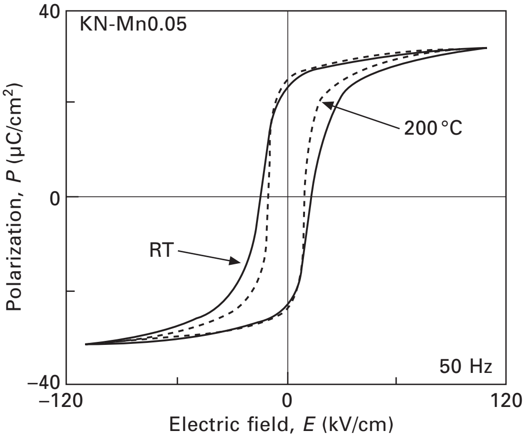

4.6 P–E hysteresis loops of KN–Mn0.05 at RT and 200 °C.

at about 100 pC/N below 200 °C and showed a maximum larger than 200 pC/N at T_2 of 225 °C.

The sintering temperatures of Mn-doped KN ceramics shift to lower temperatures and the sintering temperature range gradually becomes wide with increasing $MnCO_3$ content. The milled powders had fine particles as well as sub micron-sized ones. The preparation of a fine particle powder is one of the key points to obtaining dense KN-based ceramics as reported by Birol *et al.*[41] The crystal structures of KN and KN–Mn x (x = 0.05–1.6) were determined by the X-ray diffraction patterns. All sintered ceramics had a single-phase of perovskite structure with orthorhombic symmetry.

Figure 4.6 shows the *P–E* hysteresis loops of KN–Mn0.05 ceramics at RT and 200 °C with well-saturated loops. The remanent polarization, P_r, was 23 μC/cm^2 and the coercive field, E_c, was 13 kV/cm at RT. This result indicates that Mn doping for KN is effective in obtaining high-resistance specimens under high electric fields and high temperatures.

The coupling factor, k_{33}, of $KNbO_3$+$MnCO_3$ x wt% [KN–Mn x] decreased with increasing the amount of doped Mn ions. This tendency is similar to the relative density behavior as a function of Mn content. Figure 4.7 shows the frequency dependence of impedance on the (33), (31) and (p)-modes for the KN–Mn0.1. This sample was poled under 5 kV/mm at 150 °C. The phase, θ, in the impedance for the (33) mode reversed very well from the capacitive to the inductive region, and the maximum phase, θ_{max}, reached 88.1° which is very close to 90°. The electromechanical coupling factor, k_{33}, was 0.51. The k_{33} values of KN single crystals are 0.61 and 0.56, reported by Wada *et al.*[33] and Zgonik *et al.*,[48] respectively. The k_{33} value of the KN-Mn0.1 ceramic is about 84–91% that of the single crystal, which is reasonable for the full poling state of randomly oriented ceramics with orthorhombic symmetry. In the case of the (31) mode, the θ_{max} was 77.0°. It is not high enough to say that the specimen was poled fully. This is probably due to insufficiency of the applied electric field, E_a, in the poling treatment. At present, we cannot apply higher E_a without a surface discharge and breakdown of the specimen. The k_{31} reached 0.19, which is lower than expected from the single crystal. This is also probably due to the difficulty in poling.

On the other hand, the piezoelectric properties for the thickness-shear mode have not been sufficiently investigated in the ceramic form, even though the KN single crystal shows large shear mode piezoelectric properties such as k_{24} and d_{24}.[33] This is due to a problem of spurious peaks in the resonance and antiresonance characteristics. Therefore it has been difficult to estimate piezoelectric properties of (15) mode for the KN-based ceramic and thus has not been reported sufficiently so far. Figure 4.8 shows frequency dependence of impedance, Z, in the (15) mode for KN-Mn0.1 with wide frequency range. The fundamental frequency, $f^{(1)}$, third and fifth harmonics, $f^{(3)}$ and $f^{(5)}$ can be clearly observed. The k_{15} values[49] from $f^{(3)}/f^{(1)}$ and $f^{(5)}/f^{(3)}$ were 0.48 and 0.50, respectively, which were almost consistent with those calculated using the resonance and antiresonance methods.

To minimize the influence of spurious peaks, we prepared the sample with a larger aspect ratio by decreasing the sample thickness to 0.2 mm. Figure 4.9 shows the frequency dependence of impedance, Z, in the (15) mode for the KN–Mn0.1 with a sample size of $0.2 \times 2 \times 8$ mm^3. It is easy for the $k_{15} = 0.55$ in Fig. 4.9 to be calculated using the resonance and the antiresonance frequencies. The k_{15} value of the ceramic KN seems to be reasonable compared with those of the k_{15} (0.44) and the k_{24} (0.88) from the KN single crystal.[33,50]

Table 4.2 summarizes the piezoelectric properties of KN–Mn0.1 ceramic. The relative free permittivity, $\varepsilon_{11}^{T}/\varepsilon_0$, was 611. Piezoelectric strain constant, d_{15}, reached 207 pC/N which was large because of large k_{15} (=0.55), $\varepsilon_{11}^{T}/\varepsilon_0$

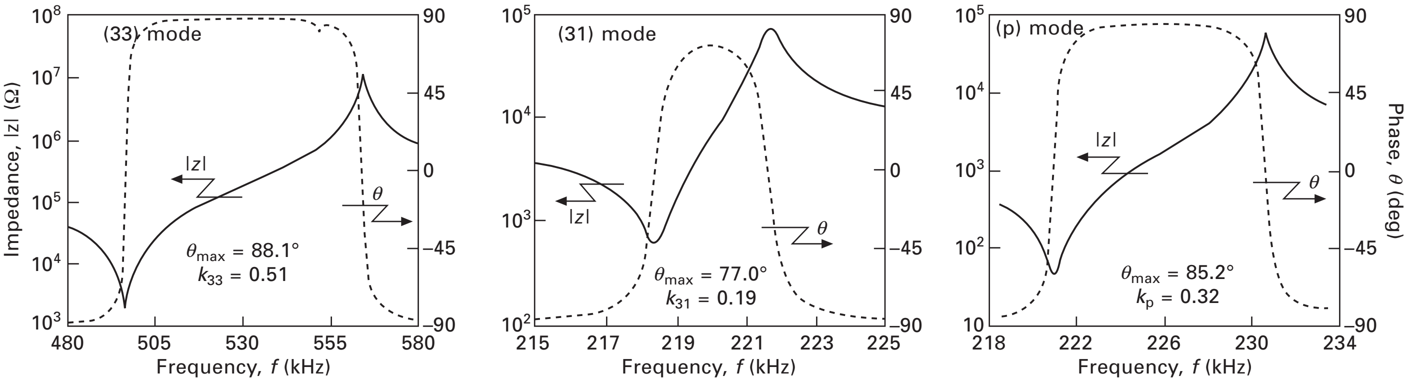

(a) (b) (c)

4.7 Frequency dependences of impedance, *Z*, in (33), (31) and (p) modes for KN–Mn0.1.

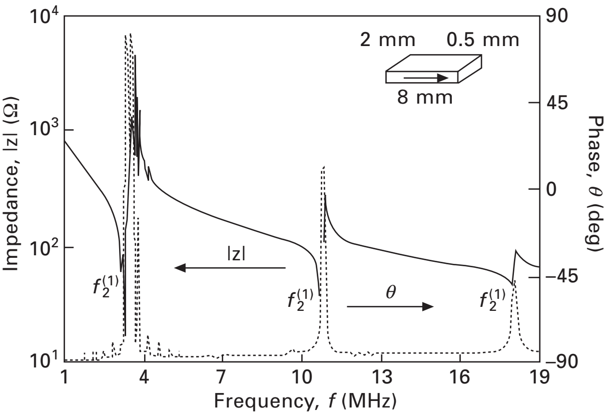

4.8 Wide range frequency dependence of impedance, *Z*, in the (15) mode for KN-Mn0.1 with a sample size of $0.5 \times 3 \times 8$ mm^3.

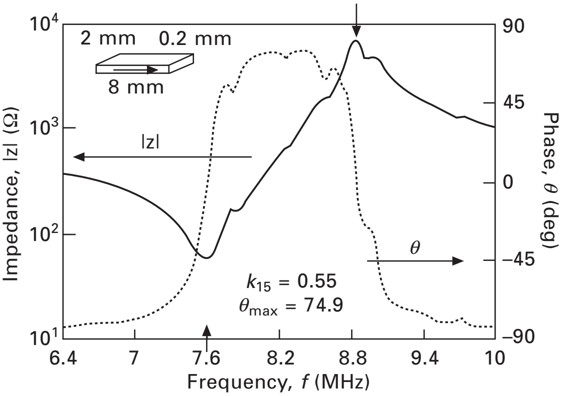

4.9 Frequency dependence of impedance, *Z*, in the (15) mode for KN–Mn0.1 with a sample size of $0.2 \times 2 \times 8$ mm^3.

(= 611) and s_{55}^{E} (= 25.7 pm^2/N). It indicated the possibility that larger d_{15} could be obtained as the poling state was further enhanced. The shear mode vibration of KN–Mn0.1 ceramic seems to be a very promising candidate for actuator and high power applications.

4.5 Bismuth sodium titanate $(Bi_{1/2}Na_{1/2})TiO_3$ [BNT]-based ceramics

Bismuth sodium titanate, $(Bi_{1/2}Na_{1/2})TiO_3$ [BNT],[13,14,17,44,71–73] is a perovskite-structured ferroelectric with rhombohedral symmetry (*R*3*C*) at room temperature (RT) and their phase transitions are complicated. The

Table 4.2 Piezoelectric properties in various vibration mode of KN–Mn0.1 ceramic

Relative free permittivity		Piezoelectric strain constant	
$\varepsilon^T_{33}/\varepsilon_0$	291	d_{33}	80.8
$\varepsilon^T_{11}/\varepsilon_0$	611	d_{31} (pC/N)	–29.7
		d_{15}	207
Electromechanical coupling factor			
k_{33}	0.51	Piezoelectric voltage constant	
k_{31}	0.19	g_{33}	31.4
k_{15}	0.55	g_{31} (× 10^3 V m/N)	–11.5
k_p	0.32	g_{15}	34.2
k_t	0.37	Elastic compliance constant	
		s^E_{33}	9.74
Frequency constant		s^E_{11} (pm^2/N)	7.54
N_{33}	2822	s^E_{55}	25.8
N_{31}	2730		
N_{15} (Hz m)	1798	Mechanical quality factor	
N_p	3535	$Q_m(33)$	391
N_t	3093	$Q_m(15)$	132

phase transition temperatures, $T_{R\text{-}T}$, from rhombohedral to tetragonal (the temperature T_m of the maximum dielectric constant), and $T_{T\text{-}C}$, from tetragonal to cubic (Curie temperature, T_C), are approximately 340 °C and 540 °C on heating, respectively, for BNT single crystals.[72–74]

The BNT ceramic shows the strong ferroelectric properties of a large remanent polarization, $P_r = 38$ μC/cm^2, and relatively high piezoelectric properties compared with other lead-free piezoelectric ceramics. Therefore, BNT is considered to be an excellent candidate as a key material in lead-free piezoelectric ceramics. However, data on piezoelectric properties of the BNT ceramic are scarce because it is difficult to pole this ceramic due to a large coercive field ($E_c = 73$ kV/cm) except in specialized work.[44] In the last two decades, BNT-based solid solutions[16–30] and A-site substituted BNT[75–77] that can be poled easily have been studied. The electromechanical coupling factor, k_{33}, of the BNT ceramic as the end-member of solid solutions varies from 0.25 to 0.40 because of the difference in the sintering conditions. The BNT ceramic needs a high sintering temperature of more than 1200 °C to obtain a dense body. It is thought that vaporization of Bi ions occurs during the sintering process at temperatures higher than 1200 °C, resulting in the poor poling treatment because of low resistivity. From the thermograph (TG, weight loss) measurement, the weight loss caused by the Bi vaporization was carried out at over 1130 °C. Various processes and methods are thought to prevent Bi vaporization and to obtain stoichiometric BNT ceramic. Thus, the BNT ceramic should be sintered at 1100 °C and lower.

Two approaches were attempted to sinter the BNT ceramic with higher density and higher resistivity as follows:[44]

1. the addition of Bi_2O_3 to the BNT ceramic (BNT+Bi_2O_3 x wt% [BNT-x])

sintered at 1225 °C for 5 min–10 h to compensate for the insufficiency of Bi ions and
2. the low sintering temperature process with a long soaking time of 30–100 h in the ordinary firing method and the hot-pressing (HP) method to suppress the Bi vaporization.

The excess Bi_2O_3-add BNT ceramics, BNT+Bi_2O_3 x wt% [BNT-x] (x = 0–2.0), including no excess Bi_2O_3 (BNT-0) were sintered at 1225 °C for 5 min–10 h to compensate for the insufficiency of Bi ions. The measured density ratio to the theoretical density as a function of the sintering temperature on the BNT-0 ceramic becomes higher as the sintering temperature increases. The highest density ratio of 98.0% was obtained at 1225 °C for 2 h. At temperatures higher than 1225 °C, the specimen was partially melted. From this result, the optimum sintering temperature was determined to be 1225 °C so as to obtain the highest relative density. The weight loss profile on the BNT-0 ceramic from the measurement of the TG analysis shows the weight loss occurring at temperatures higher than approximately 1130 °C. Therefore, when BNT samples were sintered at 1225 °C, it is assumed that some components evaporated into the air during the sintering process. It is thought that the evaporated component is mainly Bi ions. Therefore, the BNT ceramic sintered at 1225 °C is the Bi-poor composition as compared to the stoichiometric one. From these results, it is believed that the Bi_2O_3 addition and low sintering processes are effective for making the stoichiometric BNT ceramic.

X-ray diffraction patterns for BNT-x (x = 0, 0.1, 0.2, 0.3, 0.4, 0.5, 1.0 and 2.0) sintered at 1225 °C show a single phase of a perovskite structure with a rhombohedral symmetry. Lattice parameters, a, of BNT-x ceramics are almost constant (a = 3.87). The colors of the BNT-0 and BNT-0.3, –0.5 ceramics are white and those of BNT-1.0 and –2.0 ceramics become yellow with increasing Bi_2O_3 content. This result indicates that BNT-1.0 and –2.0 ceramics have excess Bi ions. It is very easy to obtain dense ceramics with high density ratios of higher than 95% on BNT-x ceramics.

Figure 4.10 shows the resistivity, ρ, of BNT-x as a function of excess Bi_2O_3 content (x). The ρ reaches its largest value of about 10^{14} Ω cm at x = 0.3. It is clear that the ρ is improved by adding the excess Bi_2O_3 and the optimum charge neutrality was observed for the BNT-0.3. Therefore, the BNT-0.3 seems to be a stoichiometic neutral state of BNT.

Two approaches under the low sintering temperature were tried to increase the density. The first is to keep the longer soaking time at the low temperature during the ordinary sintering process, and the other is to utilize the HP method to prepare the BNT ceramic with high density. The relative density ratio of the BNT-0 with no excess Bi_2O_3 increases with increasing the soaking time in the ordinary firing process at 1100 °C. The highest density ratio of

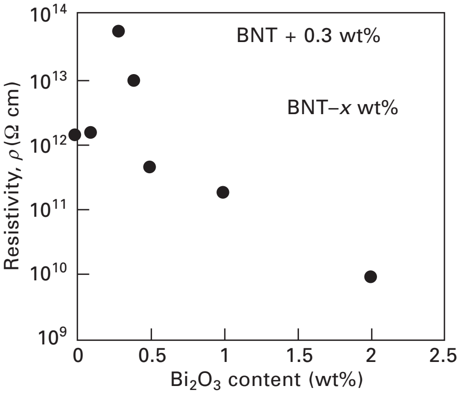

4.10 Resistivity, ρ, of BNT-x ceramics as a function of excess Bi_2O_3 content (x).[44]

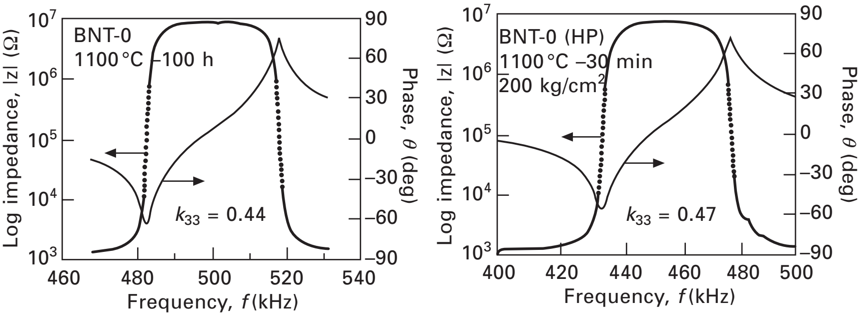

4.11 Frequency characteristics of the impedance, Z, for BNT-0 and HP-BNT-0 ceramics.[44]

96% was obtained at 100 h. On the other hand, densities of the hot-pressed BNT-0 (HP-BNT-0) ceramics under some conditions were higher than those of the non-hot pressed one. The HP-BNT-0 ceramic pressed at 200 kg/cm^2 under 1100 °C for 30 min showed a highest density ratio of more than 98%, and might be expected to have excellent piezoelectric properties.

Figure 4.11 shows the frequency characteristics of the impedance, Z, for BNT-0 and HP-BNT-0 ceramics both with clear resonance and antiresonance profiles. The k_{33} of the BNT-0 sintered at 1100 °C for 100 h and the HP-BNT-0 by the HP method at 1100 °C for 30 min were 0.44 and 0.48, respectively.

Table 4.3 summarizes the dielectric and piezoelectric properties of BNT-0.3 and HP-BNT-0 ceramics. The BNT ceramic is superior as a key material for some lead-free piezoelectric applications because of the relatively high electromechanical coupling factor, k_{33}, and the relatively high piezoelectric strain constant, d_{33}. The k_{33} and the d_{33} of the BNT-0.3 sintered at 1225 °C

Table 4.3 Dielectric and piezoelectric properties of BNT-0.3 and HP-BNT-0 ceramics.[44]

	BNT-0.3 1225 °C-30 min	BNT-0 (HP) 1100 °C-30 min
Curie temperature, T_c(°C)	337	–
Density, ρ_0 (g/cm^3)	5.91	5.96
Dielecgtric constant, $\varepsilon_{33}^T/\varepsilon_0$	406	422
Coupling factor, k_{33}	0.47	0.48
Mechanical qualiyy factor, Q_m	85	80
Elastic constant, s_{33}^E(pm^2/N)	10.5	10.0
Piezoelectric constant, d_{33}(pC/N)	92	93

for 30 min and the HP-BNT-0 by hot-pressing at 1100 °C for 30 min were 0.47 and 92 pC/N; and 0.48 and 93 pC/N, respectively.

4.6 Bismuth sodium titanate $(Bi_{1/2}Na_{1/2})TiO_3$ [BNT]–bismuth potassium titanate $(Bi_{1/2}K_{1/2})TiO_3$ [BKT]–barium titanate ($BaTiO_3$) [BT] system

The important feature is that the BNT forms a morphotropic phase boundary (MPB) with other perovskites having a tetragonal symmetry, such as $PbTiO_3$ [PT], $BaTiO_3$ [BT] and $(Bi_{1/2}K_{1/2})TiO_3$ [BKT], and these MPB compositions exhibit excellent piezoelectric properties.[21,30,35,52,54,57,78,79] Therefore, BNT-based solid solutions have attracted considerable attention as lead-free piezoelectric materials because of the existence of the MPB. Also easy preparation of the dense BNT-based ceramics is an advantage in manufacture.

Two solid solution systems, that is, (1-*x*)BNT–*x*BT (BNBT100*x*) and (1-*y*) BNT–*y*BKT (BNKT100*y*) have already been reported by Takenaka *et al.*[21] and Sasaki *et al.*,[30] respectively. It is reported that the MPB existed at x = 0.06–0.07 for BNBT100*x* and y = 0.16–0.20 for BNKT100*y*, respectively. Then, the dielectric and piezoelectric properties of the ternary-component system, $a(Bi_{1/2}Na_{1/2})TiO_3$–$b(Bi_{1/2}K_{1/2})TiO_3$–$cBaTiO_3$ (BNBK), were investigated,[35,42,52,53] focusing on the MPB compositions. Figure 4.12 shows the phase relation of the BNBK system around the MPB area. The MPBs of both BNBT6 and BNKT16 exist on the rhombohedral side, and the MPBs of both BNBT7 and BNKT20 exist on the tetragonal side around the MPB region, respectively. It was found by X-ray diffraction that the MPB between the rhombohedral and tetragonal phases exists between the two systems of BNBK1 [*a*(BNBT6)–(1-*a*)(BNKT16)] and BNBK2 [*a*(BNBT7)–(1-*a*)(BNKT20)] (a = 0, 0.2, 0.4, 0.6, 0.8, and 1, for each system).

Figure 4.13 shows the compositional dependence of the piezoelectric constant, d_{33}, for BNBK2:1(*x*), where *x*BNT–*y*BKT–*z*BT, [$x + y + z = 1$,

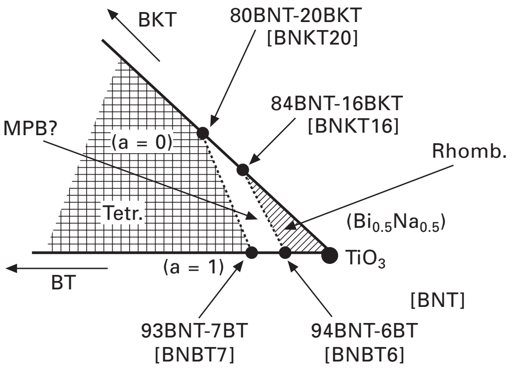

4.12 Phase relation of the $(Bi_{1/2}Na_{1/2})TiO_3$ (BNT)–$(Bi_{1/2}K_{1/2})TiO_3$ (BKT)–$BaTiO_3$ (BT) system around the MPBs.

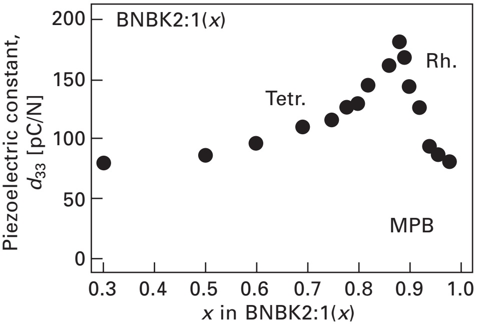

4.13 Compositional dependence of the piezoelectric constant, d_{33}, for BNBK2:1(*x*) as a function of the BNT content (*x*).

y:z = 2:1], as a function of the content (x) of BNT. High d_{33} values were obtained near the MPB composition being highest just on the tetragonal side. A maximum d_{33} value of 181 pC/N was obtained in BNBK2:1(0.88). On the tetragonal side, the d_{33} decreased because both the k_{33} and the free permittivity, ε_{33}^{T}, decreased. The d_{33} values of BNBK2:1(0.98) and BNBK2:1(0.30) were found to be 80.3 and 79.9 pC/N, respectively.

It is important for BNT-based solid solutions to investigate the actual working temperature for use in practical applications. For that reason, the depolarization temperature, T_d, was accurately determined from the temperature dependence of piezoelectric properties.[52–54] The temperature dependence of k_{33} is shown in Fig. 4.14 for (a) the rhombohedral side of x = 0.92–0.98, (b) the MPB composition of x = 0.88–0.90, and (c) the tetragonal side of x = 0.30–0.84 in BNBK2:1(x), respectively. It is recognized that the rhombohedral and tetragonal sides exhibit more stable k_{33} values with temperature than that for compositions around the MPB. The T_d and the temperature, T_m, with the maximum dielectric constant in the temperature dependence of BNBK2:1(x)

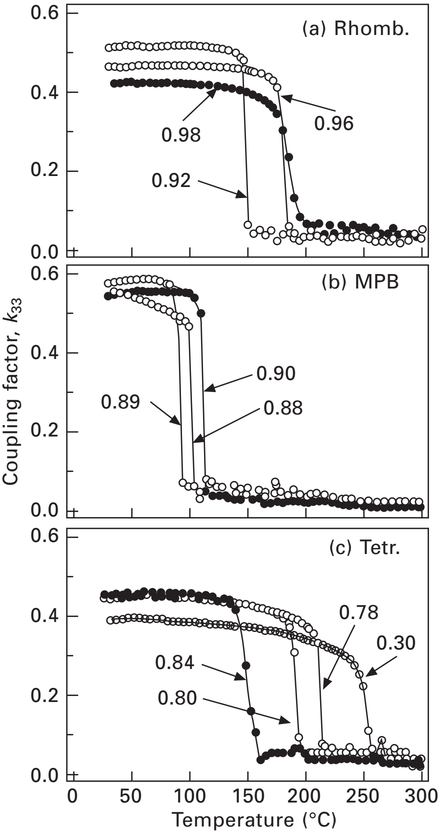

4.14 Temperature dependence of electromechanical coupling factor, k_{33}, of (a) rhombohedral side of x = 0.92–0.98, (b) MPB composition of x = 0.88–0.90, and (c) tetragonal side of x = 0.30–0.84 in BNBK2:1(x).

is summarized in Fig. 4.15. The T_m was determined by the temperature of the maximum ε_r in the temperature dependence of dielectric constant, ε_r. The T_m of BNBK2:1(x) was approximately the same at 300 °C; however, the T_d was largely decreasing near the MPB composition and increased with decreasing BNT content (x). These results indicate that the T_d is dependent on lattice anisotropy (tetragonality), c/a. Figure 4.16 demonstrates the relationship between the T_d and the d_{33} of the tetragonal and rhombohedral sides. It is necessary for actual applications to obtain the value in the upper right corner (high d_{33} and high T_d) of this figure. However, the d_{33} and the T_d indicate a trade-off relationship. The d_{33} as a function of the T_d on the tetragonal side is higher than that on the rhombohedral side.

Figure 4.17 shows the strain, S, of BNBK2:1(0.88), BNBK2:1(0.78) and BNBK2:1(0.98) as a function of the applied electric field, E_a, measured at

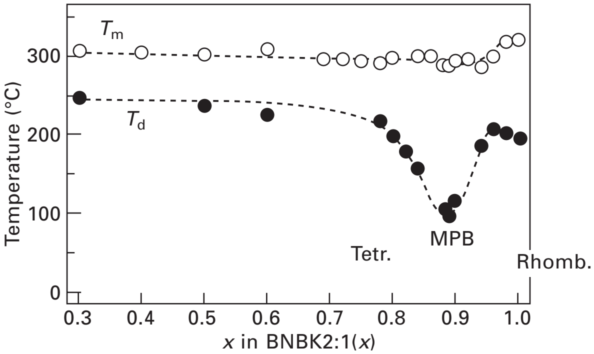

4.15 The depolarization temperature, T_d and the T_m, determined by the maximum dielectric constant, ε_r, from the measurement of temperature dependence of ε_r.

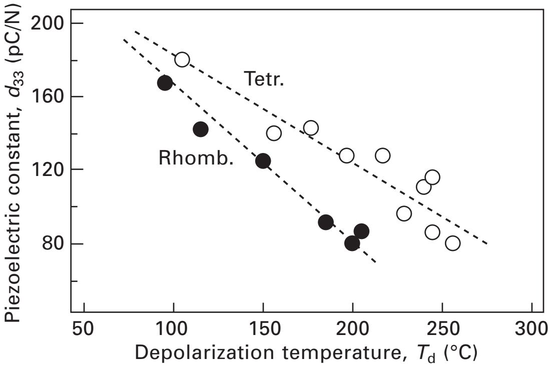

4.16 The relationship between the T_d and the d_{33} of the tetragonal side (Tetr.) and the rhombohedral side (Rhomb.).

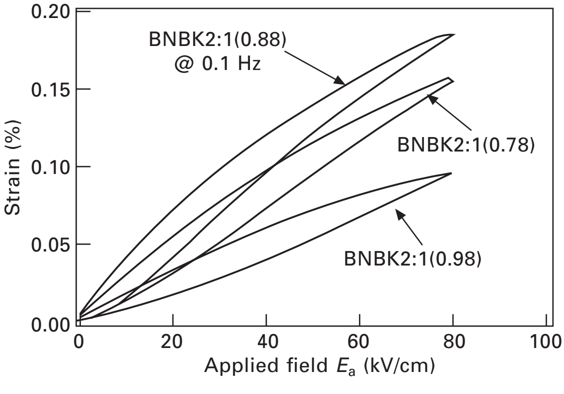

4.17 Strain of BNBK2:1(0.88), BNBK2:1(0.78) and BNBK2:1(0.98) as a function of the applied electric field, E_a.

0.1 Hz.[7] The magnitudes of their strains, S, are S (MPB) > S (tetragonal) > S (rhombohedral) for their compositions. Table 4.4 summarizes the piezoelectric properties of BNBK2:1(x) ($x = 0.78$, 0.88 and 0.98) including the d^* and the S obtained from the results of Fig. 4.17.[7] The d_{33}^* defined by the equation:

$$d_{33}^* \text{ [pm/V]} = \frac{Strain,\ S}{E_a\text{[kV/mm]}} \times 10^6, \tag{4.1}$$

for example, is 188 pm/V with relatively high T_d (206 °C) in the tetragonal composition ($x = 0.78$). Finally, Table 4.5 summarizes the depolarization temperatures, T_d, piezoelectric properties of rhombohedral, MPB, and tetragonal compositions of the BNBK2:1(x) ternary system.

4.7 Bismuth sodium titanate $(Bi_{1/2}Na_{1/2})TiO_3$ [BNT]–bismuth lithium titanate $(Bi_{1/2}Li_{1/2})TiO_3$ [BLT]–bismuth potassium titanate $(Bi_{1/2}K_{1/2})TiO_3$ [BKT] system

BNT has a low depolarization temperature T_d of 185 °C, and the MPBs of BNT-based solid solutions have a particularly low T_d of approximately

Table 4.4 Piezoelectric properties of BNBK2:1(x) (x = 0.78, 0.88 and 0.98)

x in BNBK2:1(x)		T_d(°C)	k_{33}	d_{33}(pC/N)	d_{33}^* (pm/V) at E_a = 80 kV/cm	Strain (%) at 80 kV/cm
0.98	Rhombohedral	200	0.42	80	121	0.097
0.88	MPB	113	0.56	181	240	0.183
0.78	Tetragonal	206	0.45	126	188	0.150

Table 4.5 The depolarization temperature, T_d, piezoelectric properties of rhombohedral, MPB, and tetragonal compositions of BNBK2:1(x) ternary system

	Rhombohedral		MPB		Tetragonal			
Comp. (x)	0.94	0.90	0.89	0.88	0.84	0.82	0.80	0.78
T_d(°C)	185	115	95	113	144	169	182	206
ε_s	844	1668	1698	1786	1617	1627	1058	879
$\varepsilon_{33}^T/\varepsilon_0$	493	756	778	999	1118	1081	993	883
$\varepsilon_{11}^T/\varepsilon_0$	652	900	1010	–	–	1078	–	–
k_{33}	0.476	0.543	0.579	0.560	0.455	0.473	0.455	0.452
k_{31}	0.153	0.207	0.222	0.217	0.094	0.098	0.097	0.100
k_t	0.443	0.499	0.510	0.501	0.474	0.445	0.450	0.417
k_p	0.253	0.340	0.361	0.319	0.156	0.159	0.170	0.162
k_{15}	0.330	0.449	0.459	–	–	0.316	–	–
d_{33}	91.6	142	168	181	140	144	128	126
d_{31}(pC/N)	–28.5	–48.0	–54.3	–59.2	–27.7	–28.2	–26.8	–26.3
d_{15}	109	184	212	–	–	139	–	–

100 °C,[52,54,57,80] even though the MPBs have excellent piezoelectric properties. For example, while the BNT–BKT–BT system shows a high electromechanical coupling factor, k_{33}, of 0.56 and a high piezoelectric constant, d_{33}, of 181 pC/N at the MPB, the T_d is as low as 113 °C.[52] The piezoelectric working temperature range is limited to below the T_d because piezoelectric properties disappear at the T_d and higher temperatures. Therefore, it is important to increase the T_d of the MPB composition to enable its practical use in piezoelectric applications. In order to increase the T_d, it is important to clarify the behavior of the phase transition temperatures, such as T_d, $T_{R\text{-}T}$ and T_C of BNT-based solid solutions. The T_d is thought to be the phase transition temperature from ferroelectric to antiferroelectric,[16] however, the nature of this phase transition is not yet clear until now. Similarly, it is not obvious whether the T_m is a phase transition temperature or not. The ferroelectric properties of the intermediate phase between T_d and $T_{R\text{-}T}$ and that at the temperatures higher than $T_{R\text{-}T}$ also have not yet been clarified due to the high conductivities at those higher temperatures. Although the detailed studies on the phase transition temperatures have been carried out for BNT single crystals, there are very few studies on the phase transition temperatures of BNT-based solid solutions, because of their low tetragonality ($c/a < 1.002$) at the tetragonal region.

Recently, we have investigated the variation in phase transition temperatures, such as the T_d, rhombohedral–tetragonal phase transition temperature, $T_{R\text{-}T}$, and the maximum dielectric temperature, T_m, of a BNT-based solid solution to increase the T_d of BNT. As a result, we have clarified that by substituting small amounts of Li^{1+} and K^{1+} in the A-site of BNT, it is possible to increase the T_d to 199 and 209 °C, respectively. Moreover, in order to co-substitute Li^{1+} and K^{1+} into the A-site of BNT, the T_d can be increased to 221 °C at the rhombohedral composition.

To clarify the details of the behavior of phase transition temperatures, the relationship between phase transition temperatures and electrical properties of BNT solid solutions substituted by monovalent (Li^+ and K^+) ions were investigated in detail. Two solid solutions, $(1\text{-}x)(Bi_{1/2}Na_{1/2})TiO_3–x(Bi_{1/2}K_{1/2})TiO_3$ [BNKT100x] and $(1\text{-}x)(Bi_{1/2}Na_{1/2})TiO_3–x(Bi_{1/2}Li_{1/2})TiO_3$ [BNLT100x] ceramics[81] were prepared by conventional ceramic fabrication. X-ray powder diffraction patterns of BNKT100x and BNLT100x (x = 0–0.24) indicated a single-phase of perovskite structure and a few secondary phases for BNLT28. Therefore, the solubility of Li (x) in the A-site of BNLT100x was limited to 0–0.24 at atmospheric pressure because of its small ionic radius. The lattice constants a and c, rhombohedrality 90°-α and tetragonality c/a of BNKT100x show an MPB between rhombohedral and tetragonal phases at x = 0.18–0.2. The 90°-α of BNKT100x was highest at $x = 0.1$, and then decreased with increasing x. In addition, the tetragonality c/a increased with x at $x > 0.20$. Phase transition temperatures, T_d, $T_{R\text{-}T}$ and T_m, are summarized in Fig. 4.18.

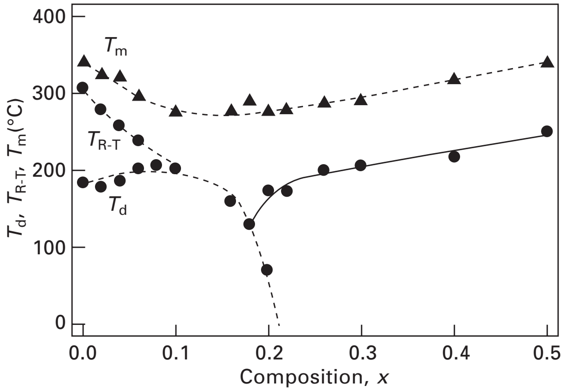

4.18 Phase transition temperatures T_d, T_{R-T} and T_m as a function of the content (x) of BKT for BNKT100x ceramics.

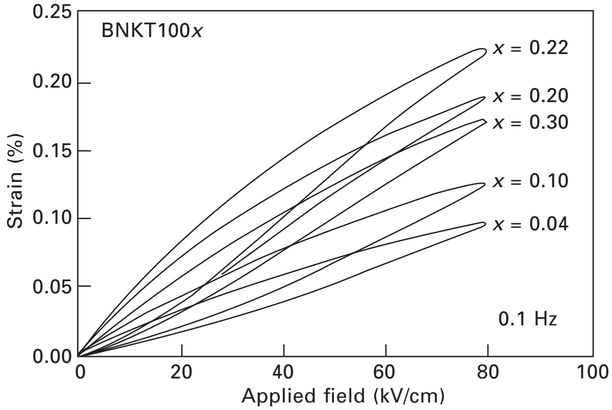

4.19 Field-induced strains of BNKT100x (x = 0.04, 0.10, 0.20, 0.22 and 0.30) under unipolar driving at 0.1 Hz.

Field-induced strains of BNKT100x under unipolar driving at 0.1 Hz are shown in Fig. 4.19, and the piezoelectric constant, d_{33}, and the normalized strain, d_{33}* (= S_{max}/E_{max}), at 80 kV/cm are summarized in Fig. 4.20. The d_{33}* was higher than the d_{33}, because the d_{33}* includes the domain contribution due to the high applied voltage and the low measuring frequency.[82] The highest value was obtained near the MPB composition for BNKT100x. Moreover, the ratios of the d_{33}* to the d_{33} are larger for the tetragonal compositions than for the rhombohedral compositions due to the difference in the domain structures.

The typical D–E hysteresis loops of a ferroelectric were obtained at room temperature for BNKT100x (x = 0, 0.18 and 0.22). The variation of the D–E hysteresis loops for BNKT100x in the temperature range between 80 and

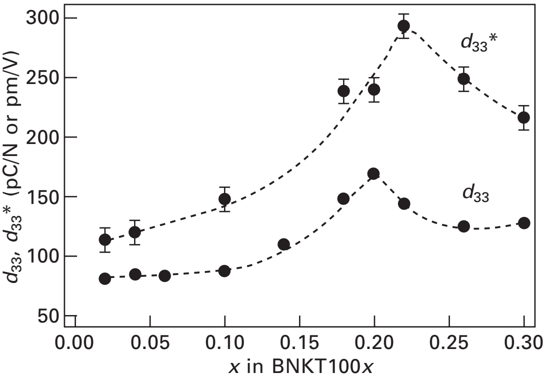

4.20 Compositional dependence of the piezoelectric constant d_{33} and the normalized strain, d_{33}*, for BNKT100*x*.

260 °C is shown in Fig. 4.21. Double-like hysteresis loops were observed at approximately the T_d to 180 °C for BNKT18 and BNKT22. It is considered that a double-like hysteresis loop is caused by mixture phases because of the existence of the intermediate phase near the MPB.[50] On the other hand, weak ferroelectric hysteresis loops were observed at 200 °C for BNKT18 and 220 °C for BNKT22. There is no discussion about ferroelectricity of the middle phase of $T_{R\text{-}T}$–T_m ($T_{R\text{-}T} > T_d$) and T_d–T_m ($T_{R\text{-}T} < T_d$) for BNT-based solid solutions. However, the results of this study indicate that those regions are probably very weakly ferroelectric.

Recently, an excellent piezoelectric constant d_{33} (d_{33} meter value) of 231 pC/N was obtained at the MPB composition of $(Bi_{1/2}Na_{1/2})TiO_3$–$(Bi_{1/2}Li_{1/2})TiO_3$–$(Bi_{1/2}K_{1/2})TiO_3$ [BNT–BLT–BKT] ternary systems.[79] However, the relationship between T_d and d_{33} has not been clarified. From the effects of Li and K substitution on the T_d in the A-site of BNT,[54] it is seen that the T_d of BNT increases when small amounts of Li and K are substituted. Thus, it is thought that co-substitution of Li and K is effective in increasing the T_d of BNT-based solid solutions. Therefore, this section describes the phase transition temperatures and the relationship between the T_d and the d_{33}, and also the piezoelectric properties of $x(Bi_{1/2}Na_{1/2})TiO_3$–$y(Bi_{1/2}Li_{1/2})TiO_3$–$z(Bi_{1/2}K_{1/2})TiO_3$ ($x + y + z = 1$) (abbreviated to BNLKT100y-100*z*) three component system.[58,83] In order to increase the T_d, a small amount of Li substitution is probably optimal. In addition, it is important to use the MPB composition to enhance the piezoelectric properties. Thus, BNLKT4-100*z* and BNLKT8-100*z* have been studied to clarify the effects of Li and K concentrations. Figure 4.22 shows the phase relation of the *x*BNT–*y*BLT–*z*BKT system including BNLT100*y* (BNT–BLT) and BNKT100*z* (BNT–BKT).

The ratios of the measured density to the theoretical density of sintered ceramics were all higher than 96%. BNLKT0-100*z* (z = 0–0.26), BNLKT4-

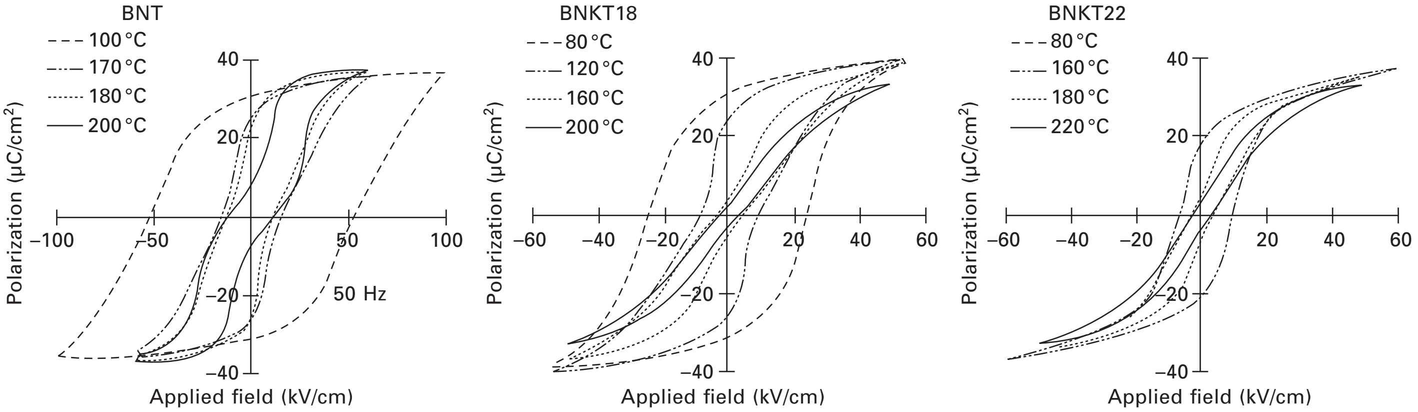

(a) (b) (c)

4.21 Temperature dependences of *D–E* hysteresis loops for (a) BNT, (b) BNKT18 and (c) BNKT22.

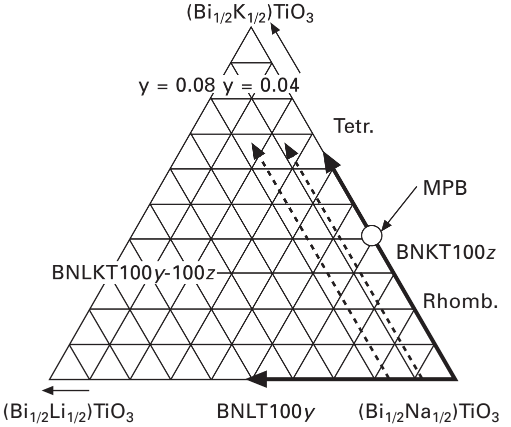

4.22 The phase relation of $(Bi_{1/2}Na_{1/2})TiO_3$ [BNT]–$(Bi_{1/2}Li_{1/2})TiO_3$ [BLT]–$(Bi_{1/2}K_{1/2})TiO_3$ [BKT] system.

100*z* (*z* = 0–0.28), and BNLKT8-100*z* (*z* = 0–0.28) all showed single phases of perovskite structure. X-ray powder diffraction patterns displayed the co-existence of rhombohedral and tetragonal phases at *z* = 0.18–0.20 for BNLKT4–100*z* and at *z* = 0.18–0.22 for BNLKT8-100*z*. Therefore, the MPBs exist in these compositions. The rhombohedrality, 90°-*α* and the tetragonality, *c*/*a* of BNLKT4-100*z* and BNLKT8-100*z* indicate that the 90°-*α* of BNLKT4-100*z* is larger than that of BNLKT8-100*z* and the 90°-*α* reached the maximum at *z* = 0.08 and showed the lowest at the MPB. However, the *c*/*a* increased significantly near the MPB composition with increasing *z*, which tendency is similar to the MPB of PZT.[1]

Figure 4.23 shows the variation in the depolarization temperature, T_d, as a function of the content (*z*) of BKT, for BNLKT0-100*z*, BNLKT4-100*z* and BNLKT8-100*z*. In order to determine the T_d accurately, it was measured from the temperature dependence of piezoelectric properties using fully poled 33-mode specimens and dielectric loss tangent, tan *δ*, using fully poled specimens.[54] The T_d of BNLKT4-100*z* was higher than those of BNLKT0-100*z* and BNLKT8-100z. On the rhombohedral side ($0 < z < 0.16$), the T_d was highest (221 °C) at *z* = 0.08. Then the T_d decreased with increasing *z* and the lowest value of T_d was approximately 160 °C for *y* = 0.04 at around the MPB composition of *z* = 0.16–0.18. On the tetragonal side ($0.2 < z < 0.28$), the T_d increased with increasing *z*, and that of BNLKT4-28 was 218 °C. The T_d of BNLKT0-0, (BNT), BNLKT4-0 and BNLKT8-0 were 185, 196 and 170 °C, respectively. This result indicates that a small amount of Li substitution is effective in increasing T_d of BNT-based solid solution. In addition, T_d of BNLKT4-100*z* and BNLKT8-100*z* showed a maximum at *z* = 0.08 at the rhombohedral side, the same as BNLKT0-100*z*. Although very few data on increased T_d have been reported previously at the rhombohedral composition

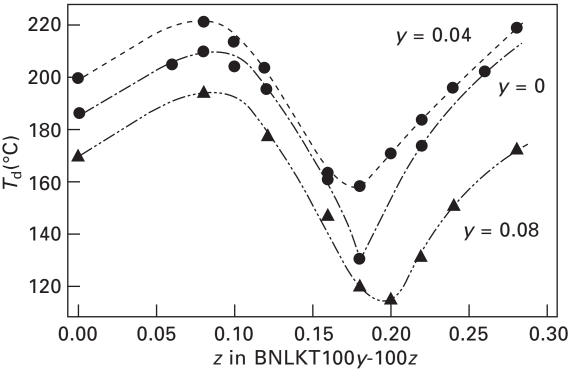

4.23 Depolarization temperature, T_d, of BNLKT100y-100z (y = 0, 0.04 and 0.08) as a function of the content (z) of BKT.

of BNT-based solid solutions,[60] the T_d could be increased up to 221 °C for BNLKT4-8.

Recently, piezoelectric ceramics have attracted much attention for high-power devices, such as ultrasonic motors and transducers.[84–87] These devices were mainly composed of Pb(Zr,Ti)O_3 (PZT)-based piezoelectric ceramics with a high mechanical quality factor Q_m, which is called hard PZT. However, the resonant vibration of hard PZT becomes unstable at a vibration velocity of approximately 1.0 m/s, resulting in Q_m markedly decreasing and vibration velocity not increasing. Moreover, PZT contains a large amount of PbO; therefore, recently, there has been much interest in lead-free piezoelectric ceramics as a material for replacing PZT-based ceramics. As materials for lead-free high-power applications, $SrBi_2Nb_2O_9$ and $(Sr,Ca)_2NaNb_5O_{15}$ have been reported.[61,88–89]

The relationship between the T_d and the d_{33}, and also the piezoelectric properties of the BNLKT100y-100z system indicate that it has a good possibility of use in high-power applications. Therefore, in this section, we would like to compare the properties of the rhombohedral and tetragonal sides of MPB composition in the T_d vs Q_m, and to discuss the optimum composition for high-power applications. In addition, we clarified the effect of Mn doping on the variations in T_d and piezoelectric properties with high-power characteristics of BNLKT100y-100z including w wt% $MnCO_3$-doped BNLKT100y-100z (abbreviated to BNLKT100y-100zMnw).

Figure 4.24 shows the piezoelectric strain constant, d_{33}, and the mechanical quality factor, Q_m(33), in the 33-mode, of BNLKT4-100z as a function of the content (z) of BKT. The d_{33} reaches about 180 pC/N at the MPB composition (z = 0.20). On the other hand, the Q_m(33) reached its highest value of approximately 200 at $z \leq 0.08$ and decreased to below 90 at $z \geq$ 0.18.

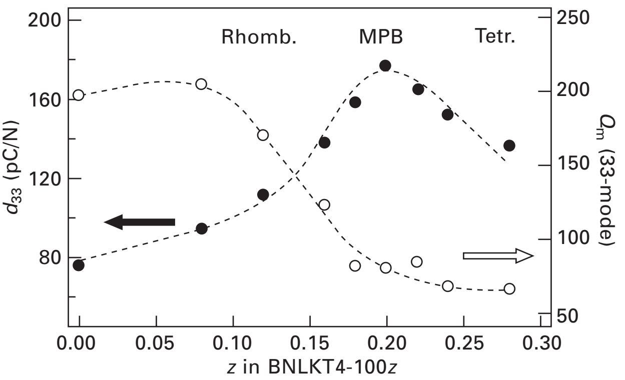

4.24 Piezoelectric strain constant, d_{33}, and the mechanical quality factor, $Q_m(33)$, in (33) mode, of BNLKT4-100*z* as a function of the content (*z*) of BKT.

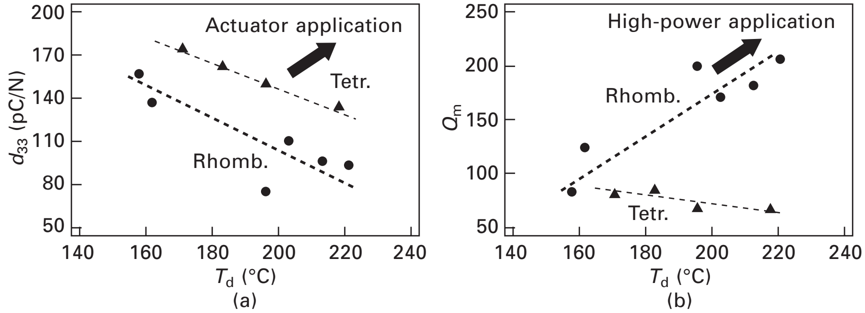

4.25 Relationship of the depolarization temperature, T_d, between (a) the d_{33} and (b) the $Q_m(33)$ for rhombohedral (*Rhomb.*) and tetragonal (*Tetr.*) sides.

Figure 4.25 shows the relationships between the T_d and (a) the d_{33} and (b) the Q_m on the rhombohedral and tetragonal sides. As has already been described, the tetragonal side of the MPB is considered to be an excellent candidate composition for actuator applications with high T_d and high d_{33} compared with the rhombohedral side and the MPB composition. On the other hand, it was found that the relationship between the T_d and the $Q_m(33)$ on the rhombohedral side is higher than those on the tetragonal side and the MPB composition. This indicates that the rhombohedral side is a suitable composition for high-power applications.

$MnCO_3$ was doped into BNLKT4-8 because this seems to be the optimum composition for high-power applications having both a high T_d and a high Q_m. BNLKT4-8Mn*w* (w = 0–0.6) showed high density ratios of more than 97% without any secondary phases. The resistivity, ρ, of these ceramics was higher than the order of 10^{12} Ω cm. The temperature dependences of the dielectric constant, ε_s, and the loss tangent, tan δ, of BNLKT4-8Mn*w* (*w* = 0–0.6) show that the maximum dielectric constant, ε_{max}, and tan δ decrease with increasing Mn (*w*). On the other hand, the dielectric maximum temperature, T_m, was almost constant at approximately 272 °C.

Figure 4.26 shows the variations of the k_{31} and the k_p, and the Q_m(31) and Q_m(p) in the (31) and the planar (p) modes of BNLKT4-8 as a function of the Mn concentration (*w*). Although the k_{31} and the k_p slightly decreased with increasing Mn concentration (*w*), the Q_m(31) and the Q_m(p) markedly increased with increasing *w*. The Q_m(31) and the Q_m(p) values were approximately 300 and 400 for BNLKT4-8 (*w* = 0), and 730 and 720 for BNLKT4-8Mn0.6, respectively. On the other hand, the d_{33} gradually decreased with increasing Mn concentration (*w*), and the d_{33} values of BNLKT4-8 and BNLKT4-8Mn0.6 were 94 and 85 pC/N, respectively.

Figure 4.27 (a) shows the temperature dependence of the k_{33} for BNLKT4-8Mn*w* (*w* = 0 and 0.6). It is found that the k_{33} is almost constant up to the T_d. Moreover, the T_d gradually decreases with increasing Mn concentration (*w*), as shown in Fig. 4.27 (b), with T_d = 204 °C for BNLKT4-8Mn0.6.

The decrease in the T_d with increasing the Mn content (*w*) indicates that the Mn ion substituted into either the A-site or B-site of BNLKT4-8. According to previous reports, both ε_{max} and T_m decrease with increasing amount of Mn in BNT and BNT–BT.[90,91] In BNLKT4-8Mn*w*, although the temperature dependence of dielectric constant showed that the ε_{max} decreased with increasing *w*, the T_m was almost constant at 272 °C.[83]

Considering the valence state of Mn ions in BNT, the Mn^{4+} substitution into the B-site probably decrease T_m because the ionic radius of Mn^{4+} is 0.530 Å which is similar to that of Al^{3+}. In contrast, the substitution of Mn^{2+} and Mn^{3+} into the A-site or B-site of BNT should increase the T_m of

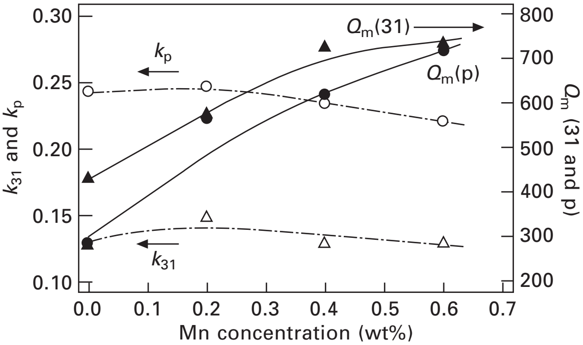

4.26 Coupling factors, *k*, and mechanical quality factors, Q_m, in the (31) and the planar (p) modes as a function of the Mn concentration (*w*).

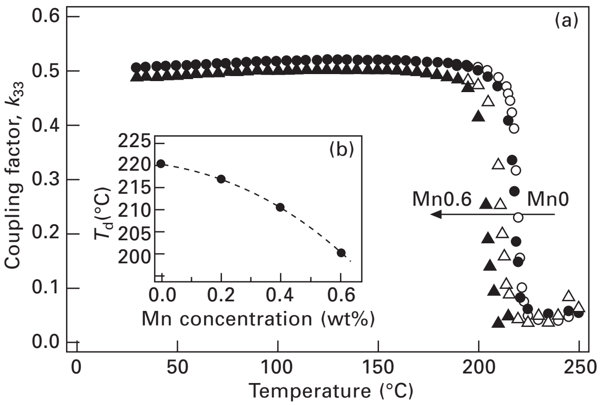

4.27 (a) Temperature dependence of the coupling factor, k_{33}, for BNLKT4-8Mn*w* ($w = 0$ and 0.6) and (b) the T_d as a function of *w*.

BNT. Therefore, the decay of T_d and the lack of variation in T_m indicate that Mn ions exist in BNLKT4-8, in the mixed state of Mn^{2+} or Mn^{3+}, and Mn^{4+}. The resistivity was maximum at $w = 0.2$, and then decreased with increasing Mn concentration *w*. The vaporization of A-site ions such as Bi, Na, and K occurs during sintering. Therefore, the very small amount of Mn probably compensates for the A-site vacancies as a donor, resulting in an increase in resistivity.[90,91] In contrast, Mn^{2+} or Mn^{3+} in the B-site works as an acceptor; therefore, resistivity decreases at $w > 0.2$. Generally, acceptor ions associate with oxygen vacancies, and cause domain pinning, thereby increasing in $Q_{m.}$.[92–94] Therefore, the Q_m of BNLKT4-8Mn*w* increases with increasing *w*.

The high-power characteristics of BNLKT4-8, BNLKT4-8Mn0.6, and PZT-H were evaluated by the high-power charcteristic measurement.[87] The small amplitude $Q_m(31)$ values of BNLKT4-8, BNLKT4-8Mn0.6, and PZT-H are 440, 740, and 1770, respectively. Figure 4.28 shows the variation in $Q_m(31)$ as a function of the vibration velocity $v_{0\text{-p}}$. It is found that the $Q_m(31)$ values of BNLKT4-8 and BNLKT4-8Mn0.6 decrease slower than that of PZT-H. Although the small amplitude $Q_m(31)$ of PZT-H was twice that of BNLKT4-8Mn0.6, that of BNLKT4-8Mn0.6 was larger than that of PZT-H at $v_{0\text{-p}} > 0.6$ m/s. Moreover, the $Q_m(31)$ of BNLKT4-8Mn0.6 was higher than 400 even at $v_{0\text{-p}} = 1.5$ m/s.

It is considered that the small decay of $Q_m(31)$ under a high amplitude vibration for BNLKT4-8 and BNLKT4-8Mn0.6 are attributed to the high coercive field E_c. It is known that the E_c at the rhombohedral composition is larger than that at the MPB and on the tetragonal side for BNT-based solid solutions.[52] The BNLKT4-8 has high E_c of 60 kV/cm, which is 4 times larger than that of PZT-H. Moreover, domain wall motion is suppressed by

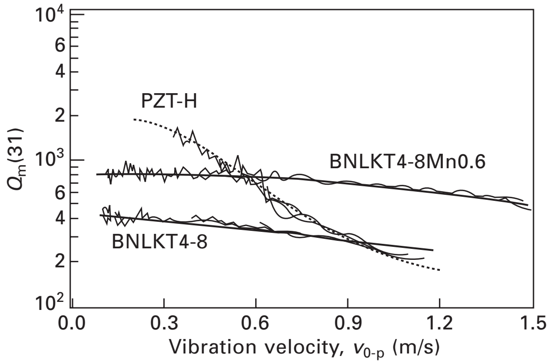

4.28 Variations in $Q_m(31)$ as a function of the vibration velocity $v_{0\text{-p}}$ for BNLKT4-8, BNLKT4-8Mn0.6, and PZT-H.

oxygen vacancies associated with the doping of acceptor ions.[84] Therefore, the acceptor-ion-doped rhombohedral composition of BNT-based solid solutions is stable even at vibration velocity higher than PZT-H.

4.8 Bismuth potassium titanate $(Bi_{1/2}K_{1/2})TiO_3$ [BKT]-based ceramics

Bismuth potassium titanate, $(Bi_{1/2}K_{1/2})TiO_3$ [BKT], is a typical lead-free ferroelectric with a perovskite structure of tetragonal symmetry at room temperature and has a relatively high Curie temperature, T_c, of 380 °C.[14] This indicates that BKT has a certain promise as a candidate for lead-free piezoelectrics in a wide working temperature range. However, with the exception of the author's groups reports,[43,95] there are few reports about this material owing to its poor sinterability. This problem has restricted extensive activities of researchers in investigations of BKT-based solid solution systems.

Recently, Hiruma *et al.*[43,95] reported the electrical properties of BKT ceramics prepared by the hot-pressing (HP) method. The optimum sintering temperature seems to be 1060–1080 °C. Figure 4.29 shows the temperature dependences of dielectric constants, ε_s, and dielectric loss tangents, tan δ, for BKT-HP1060 °C and BKT-HP1080 °C, in the temperature range from room temperature to 600 °C, measured at frequencies of 10 kHz, 100 kHz, and 1 MHz. The tan δ curves in Fig. 4.28 show two peaks. High-temperature peaks show frequency dispersions; therefore, it is thought that these peaks are related to the T_c. On the other hand, low-temperature peaks are almost independent of frequency; therefore, they are considered to indicate the second phase transition, T_2, between tetragonal and pseudo-cubic symmetries, whose temperatures of BKT-HP1060 °C and BKT-HP1080 °C are about 340

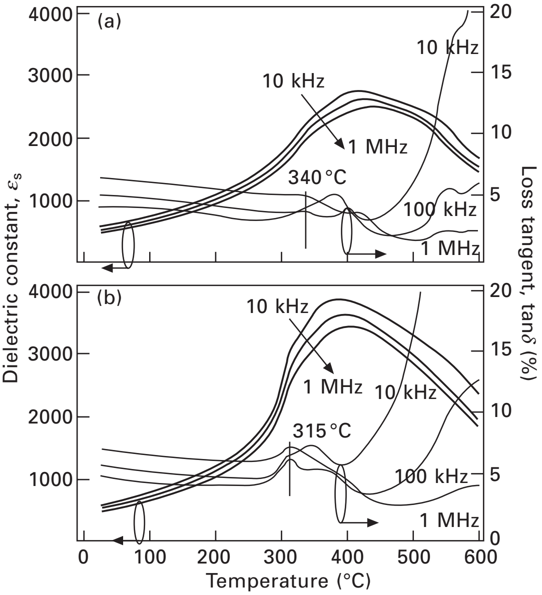

4.29 Temperature dependences of dielectric constant ε_s and dielectric loss tangent tan δ for the hot-pressed BKT ceramics sintered at (a) 1060 °C and (b) 1080 °C.

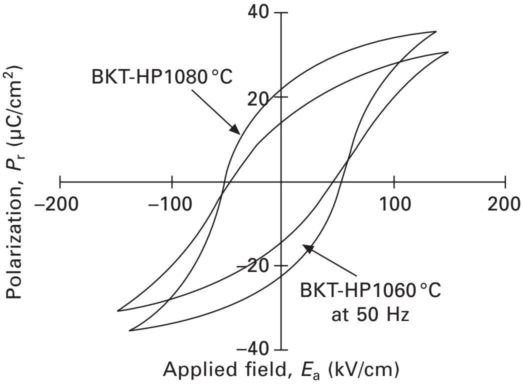

4.30 D–E hysteresis loops of the HP-BKT at 1060 °C and 1080 °C.

and 315 °C, respectively. The T_c of Bi_2O_3, La_2O_3 and $MnCO_3$-doped BKT ceramics showed a tendency to decrease with increasing dopant contents.

Figure 4.30 shows *D-E* hysteresis loops of BKT-HP1060 °C and BKT-HP1080 °C. Well-saturated *D-E* hysteresis loops with low leakage current were obtained for all specimens at room temperature. The P_r and the coercive fields E_c were 22.2 μC/cm^2 and 52.5 kV/cm for BKT-HP1080 °C, and

14.2 μC/cm^2 and 47.3 kV/cm for BKT-HP1060 °C, respectively. The different tendencies seem to be the difference in grain size, 0.2 μm for BKT-HP1060 °C and 0.4 μm for BKT-HP1080 °C.

A solid solution system, $(1\text{-}x)(\mathrm{Bi}_{1/2}\mathrm{K}_{1/2})\mathrm{TiO}_3$–x$\mathrm{BaTiO}_3$ [BKT–BT100x][7,96,97] was investigated to evaluate its characteristics and electrical properties by using randomly oriented and grain-oriented samples. In particular, attention was focused on the compositions near the BKT ($x = 0$–0.4), as the lead-free piezoelectric ceramics with the widest working temperature. X-ray diffraction patterns of BKT–BT100x ceramics with $0 < x < 1$ show a single phase of perovskite structure with tetragonal symmetry at room temperature. The sintered ceramics of BKT–BT indicated higher relative densities than 95%, even in the compositions of the BKT side as shown in Table 4.6.

Figure 4.31 shows the temperature dependence of electromechanical coupling factor, k_{33}, and the phase, θ, in the impedance-frequency characteristics of the (33)-mode for BKT[43] ceramic. This figure indicates that the BKT and BKT–BT ceramics seem to be attractive for higher temperature applications compared with the BT ceramic.

Figure 4.32 shows lattice constants, a and c, and lattice anisotropy, c/a, as a function of the amount (x) of BT in BKT–BT100x ceramics. Both BKT ($x = 0$) and BT ($x = 1$) have the same crystal structure of tetragonal symmetry; however, the c/a indicated nonlinear tendency. The c/a reaches a maximum (~1.025) at the composition around $x = 0.2$, which is very large among the lead-free piezoelectric materials. This result corresponds almost to that shown in Buhrer's report.[14]

From temperature dependences of dielectric constant, ε_r and loss tangent, tan δ, for the BKT–BT100x ceramics, the Curie temperature, T_c, linearly shifted to lower temperatures with increasing BT content (x), as shown in

Table 4.6 Physical and piezoelectric properties for non-oriented (OF) and grain-oriented (RTGG) BKT–BT10, 20 and 30 prepared by ordinary firing (OF) and RTGG methods[98]

	BKT-BT10		BKT-BT20		BKT-BT30	
	OF	RTGG	OF	RTGG	OF	RTGG
ρ_o/ρ_x(%)	98.5	97.8	99.3	95.4	98.0	94.3
F(%)	–	35	–	72	–	61
k_{33}	0.35	0.37	0.36	0.33	0.38	0.38
$\varepsilon_{33}^T/\varepsilon_0$	602	560	532	501	461	426
s_{33}^E(pm^2/N)	8.2	10.5	8.2	10.1	7.8	13.0
d_{33}(pC/N)	73.4	84.5	69.3	70.7	67.6	83.3
d_{33}* (pm/V)	103	168	116	143	103	134

ρ_o/ρ_x: relative density ratio, F: orientation factor, k_{33}: electromechanical coupling factor, ε_{33}^T: free permittivity, s_{33}^E: elastic constant, d_{33}: piezoelectric strain constant, d_{33}*: calculated from Eq. 4.1.

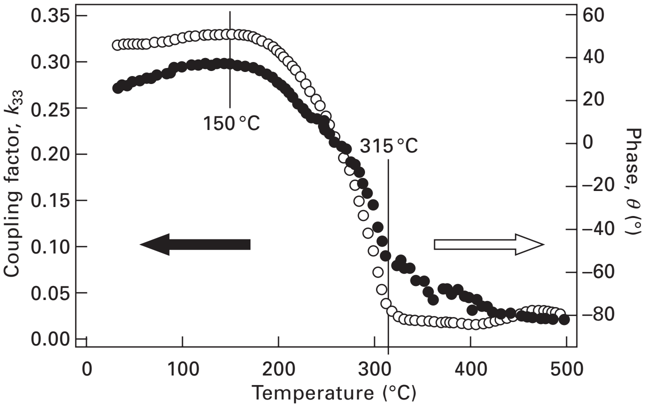

4.31 Temperature dependence of electromechanical coupling factor, k_{33}, and the phase, θ, in the impedance-frequency characteristics of the (33)-mode for BKT ceramic.[43]

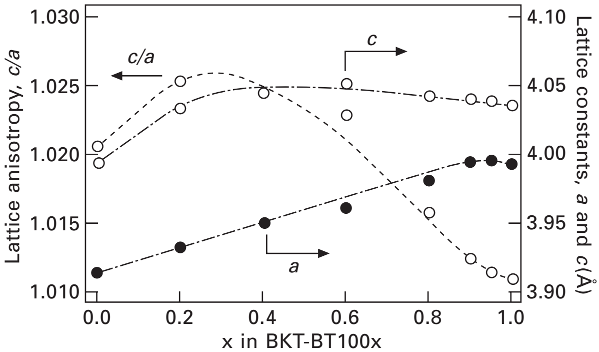

4.32 Lattice anisotropy, *c*/*a* and lattice constants, *a* and *c*, as a function of the amount (*x*) of BT in BKT–BT100*x* ceramics.

Fig. 4.33. The T_c of BKT–BT80 ($x = 0.8$) still shows a higher temperature than 200 °C. However, both the ε_r at room temperature and at the T_c decrease with increasing x. The T_2 in Fig. 4.34 shows the second-phase transition temperature from tetragonal to pseudo-cubic phases existing near 270 °C in BKT. The T_2 of BKT ceramic was reported by Ivanova *et al.*[70]

Figure 4.34 shows temperature dependences of the coupling factor, k_{33}, and the resonance frequency, f_r, for BKT–BT40. The k_{33} (= 0.35) at room temperature maintained the same value up to around 250 °C and then almost disappeared at about 300 °C. Also, the temperature dependence of the f_r showed the minimum at 305 °C. This temperature is not equal to the T_c of BKT–BT40. From this result, we determined the depolarization temperature, T_d, which corresponds to the secondary phase transition temperature, T_2,

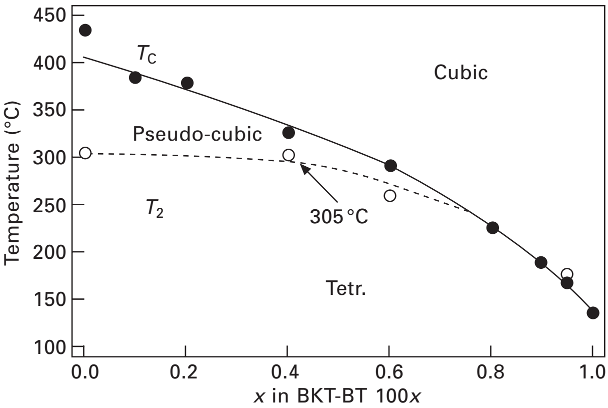

4.33 Curie temperature, T_c, and secondary phase transition temperature, T_2, of BKT–BT100x ceramics, as a function of the amount (x) of BT, measure at 1 MHz.

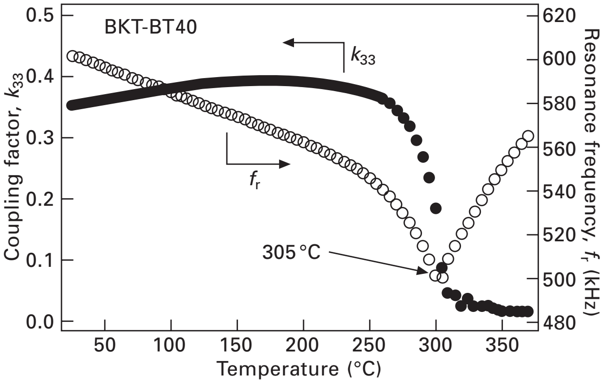

4.34 Temperature dependences of the coupling factor, k_{33} and the resonance frequency, f_r, for the BKT-BT40.

from the tetragonal to the pseudo-cubic phases, as shown in Fig. 4.33. The BKT–BT100x ceramics (x = 0–0.4) indicated high T_d temperatures around 300 °C.

Furthermore, grain orientation effects for piezoelectric properties were investigated in BKT–BT100x using a reactive template grain growth (RTGG) method.[98] Piezoelectric strain constant, d_{33}, for randomly oriented BKT–BT10, 20, and 30 are 73.4, 69.1, and 67.6 pC/N, respectively. These values are relatively small for practical use as actuators. So, we tried to prepare the textured samples by the RTGG method to enhance their piezoelectric properties. Textured specimens were prepared using the RTGG method with matrix and templates of plate-like $Bi_4Ti_3O_{12}$ (BIT) particles for BKT–BT. Calcination and sintering temperatures were 900–1000 °C and 1100–1400 °C, respectively. The piezoelectric properties of the textured and non-textured BKT–BT10, 20, and 30 are summarized in Table 4.6. The measured direction of textured specimens is parallel (//) to the tape stacking direction. The d_{33} in textured specimens were improved as compared with those of non-textured specimens. For example, the d_{33} in BKT–BT10 was improved from 73.4 to 84.5 pC/N. However, the increment was relatively small because the orientation factor, F, was still low at about 35%. Further systematic studies for improving the F may be necessary as a future work. From these results, the BKT–BT system seems to be a superior candidate for lead-free piezoelectric materials in high temperature applications.

4.9 Conclusions

The dielectric, ferroelectric, and piezoelectric properties of lead-free perovskite-type ceramics were investigated as possible candidates for lead-free piezoelectric materials to reduce environmental damage during the waste disposal of piezoelectric products. Perovskite ferroelectric ceramics seem to be suitable for high-power applications such as piezoelectric actuators requiring large piezoelectric constants, d_{33}, and high Curie temperatures, T_c, or high depolarization temperatures, T_d.

The dense KN-based ceramics, $KNbO_3$+$MnCO_3$ x wt% [KN–Mn x], can be obtained by using the modified conventional ceramic firing technique with good dielectric, ferroelectric, and piezoelectric properties. The electromechanical coupling factor, $k_{15} = 0.55$, and the piezoelectric strain constant, $d_{15} = 207$ pC/N, are obtained at Mn-doped KN–Mn0.1. The Bi-excess bismuth sodium titanate, $(Bi_{1/2}Na_{1/2})TiO_3$ (BNT)+Bi_2O_3 x wt% [BNT-x] and hot-pressing BNT [HP-BNT] ceramics were prepared and their piezoelectric properties were investigated. All the BNT-x ceramics sintered at 1225 °C showed a high density ratio of more than 97% to the theoretical density. The BNT-0.3 seems to be a stoichiometry because of the measurement results from the resistivity, ρ, Curie temperature, T_c, and microstructure. BNT-0.3 ceramic showed a relatively large electromechanical coupling factor ($k_{33} = 0.47$) and piezoelectric constant ($d_{33} = 93$ pC/N). The large piezoelectricity ($k_{33} = 0.48$) and d_{33} (= 98 pC/N), with the high density ratio (98%), could be obtained for the first time on the HP-BNT ceramic sintered at 1100 °C for 30 min and pressed at 200 kg/cm^2 as lead-free piezoelectric materials.

In the case of the ternary system $x(Bi_{1/2}Na_{1/2})TiO_3$–$y(Bi_{1/2}K_{1/2})TiO_3$–$zBaTiO_3$ ($x + y + z = 1$), [BNBKy:z (x)], enhanced piezoelectric properties were obtained near the MPB composition, and the highest electromechanical coupling factor, k_{33}, and d_{33} were 0.58 for BNBK2:1(0.89) and 181 pC/N for BNBK2:1(0.88). Nevertheless, the T_d shift to lower temperatures (about

100 °C) around the MPB compositions correspond to BNBK2:1(0.88–0.90). On the tetragonal side, T_d shifts to a value higher than 200 °C for $x < 0.78$, with $k_{33} = 0.452$ and $d_{33} = 126$ pC/N for BNBK2:1(0.78). This ternary system shows high potential (with properties such as large $d_{33} > 250$ pC/N and high $T_d > 250$ °C) for actuator applications.

A detailed study of the phase transition temperatures, such as T_d, $T_{R\text{-}T}$, and T_d, and the piezoelectric properties of $x(Bi_{1/2}Na_{1/2})TiO_3–y(Bi_{1/2}Li_{1/2})TiO_3–z(Bi_{1/2}K_{1/2})TiO_3$ ($x + y + z = 1$) (BNLKT100y-100z) three-component system were carried out. The T_d is related to the variation of lattice distortion, such as rhombohedrality 90°-α and tetragonality c/a. A small amount of Li substitution was very effective for increasing T_d, and that of BNLKT4-100z increased from 185 °C to 221 °C at the rhombohedral composition. Although excess Li substitution enhanced the piezoelectric properties, T_d drastically decreased with increasing Li substitution. Considering both high T_d and high d_{33}, the tetragonal composition of BNLKT4-100z is optimal for piezoelectric actuator applications.

The piezoelectric properties on rhombohedral and tetragonal sides of the MPB compositions were compared. It is clarified that the rhombohedral composition of BNLKT4-8 seems to be suitable for high-power application. In addition, a small amount of Mn doping is very effective for improving Q_m. The high-power characteristics of BNLKT4-8Mn0.6 is superior to those of PZT-H at approximately $v_{0\text{-}p} > 0.6$ m/s. Therefore, a Mn-doped BNT-based solid solution with rhombohedral symmetry is a promising candidate for lead-free high-power applications.

The $(1\text{-}x)(Bi_{1/2}K_{1/2})TiO_3–xBaTiO_3$ [BKT–BT100x] system was selected to elevate the T_c of BT to higher temperatures than 200 °C. The T_c of BKT–BT80 was about 230 °C. From these results, the BKT–BT system is a superior candidate for lead-free piezoelectric materials for use in high temperature applications. The piezoelectric properties of the textured and non-textured BKT–BT10, 20, and 30 have been studied. The d_{33} in a textured specimen of BKT–BT10 was improved as compared with that of a non-textured specimen, from 73.4 to 84.5 pC/N.

To replace PZT-based systems, it is necessary for special features of each lead-free material to correspond to the required piezoelectric properties for each application. Future trends in the research and development of lead-free piezoelectric ceramics seem to be focused on textured grain orientations realized using the templated grain growth (TGG) and seeded polycrystal conversion (SPC) methods. Also domain controls including engineered domain of lead-free ferroelectric ceramics will be very important to enhance the piezoelectric activities. The trend towards thick and thin films with lead-free piezoelectrics seems to be necessary for FBAW and MEMS applications.

4.10 Acknowledgements

The authors would like to thank Toho Titanium Co., Ltd., for providing high-purity titanium oxide (TiO_2) powder. This work was partially supported by Grants-in-Aid for Scientific Research (B) (Nos. 11555168 13555176, 15360352, 17360327, and 19360302) from the Japan Society for the Promotion of Science.

4.11 References

1. E. Sawaguchi, 'Ferroelectricity versus antiferroelectricity in the solid solutions of $PbZrO_3$ and $PbTiO_3$', *J. Phys. Soc. Jpn.*, **8**, 615–629, 1953.
2. B. Jaffe, R. S. Roth, and S. Marzullo, 'Piezoelectric properties of lead zirconate-lead titanate solid-solution ceramics', *J. Appl. Phys.*, **25**, 809, 1954.
3. B. Jaffe, W. R. Cook, and H. Jaffe, *Piezoelectric Ceramics*, New York: Academic Press, p. 142, 1971.
4. T. Yamamoto, 'Ferroelectric properties of the $PbZrO_3$-$PbTiO_3$ system', *Jpn. J. Appl. Phys.*, **35**(9B), 5104–5108, 1996.
5. T. Takenaka, 'Piezoelectric properties of some lead-free ferroelectric ceramics', *Ferroelectrics*, **230**, 87–98, 1999.
6. T. Takenaka and H. Nagata, 'Current status and prospects of lead-free piezoelectric ceramics', *J. European Cer. Soc.*, **25**(12), 2693–2700, 2005.
7. T. Takenaka, H. Nagata and Y. Hiruma, 'Current developments and prospective of lead-free piezoelectric ceramics', *Jpn. J. Appl. Phys.*, **47**, 3787–3801, 2008.
8. K. Shimamura, H. Takeda, T. Kohno and T. Fukuda, 'Growth and characterization of Lanthanum gallium silicate $La_3Ga_5SiO_{14}$ single crystals for piezoelectric applications', *J. Cryst. Growth*, **163**, 388–392, 1996.
9. A. Von Hippel, *J. Ind. Eng. Chem.*, **28**, 1097, 1946.
10. S. Robert, 'Dielectric and piezoelectric properties of barium titanate', *Phys. Rev.*, **71**, 890, 1947.
11. B. T. Mathias and J. P. Remeika, 'Dielectric properties of sodium and potassium niobates', *Phys. Rev.*, **82**, 727, 1951.
12. L. Egerton and D. M. Dillon, 'Piezoelectric and dielectric properties of ceramics in the system potassium-sodium niobate', *J. Am. Ceram. Soc.*, **42**, 438–442, 1959.
13. G. A. Smolensky, V. A. Isupov, A. I. Agranovskaya and N. N. Krainic, 'New ferroelectrics of complex composition. IV', *Soviet. Physics. Solid State*, **2**(11), 2651–2654, 1961.
14. C. F. Buhrer, 'Some properties of bismuth perovskites', *J. Chem. Phys.*, **36**(3), 798–803, 1962.
15. R. E. Jaeger and L. Egerton, 'Hot pressing of potassium-sodium niobates', *J. Am. Ceram. Soc.*, **45**(5), 209–213, 1962.
16. K. Sakata and Y. Masuda, 'Ferroelectric and antiferroelectric properties of $(Bi_{1/2}Na_{1/2})TiO_3$-$SrTiO_3$ solid solution ceramics', *Ferroelectrics*, **7**, 347–349, 1974.
17. J. Suchanicz, K. Roleder, A. Kania and J. Handerek, 'Electrostrictive strain and Pyroeffect in the region of phase co-existence in $Na_{0.5}Bi_{0.5}TiO_3$', *Ferroelectrics,* **77**, 107, 1988.
18. T. Takenaka and K. Sakata, 'New piezo- and pyroelectric sensor materials of $(BiNa)_{1/2}TiO_3$-based ceramics', *Sensors and Materials*, **1**, 123–131, 1988.

19. T. Takenaka and K. Sakata, ‘Dielectric, piezoelectric and pyroelectric properties of $(BiNa)_{1/2}TiO_3$-based ceramics’, *Ferroelectrics* , **95**, 153–156, 1989.
20. T. Takenaka, K. Sakata, and K. Toda, ‘Piezoelectric properties of $(Bi_{1/2}Na_{1/2})TiO_3$-based ceramics’, *Ferroelectrics*, **106**, 375–380, 1990.
21. T. Takenaka, K. Maruyama, and K. Sakata, ‘(Bi, Na)TiO_3-$BaTiO_3$ system for lead-free piezoelectric ceramics’, *Jpn. J. Appl. Phys.*, **30**(9B), 2236–2239, 1991.
22. T. Takenaka, A. Hozumi, T. Hata, and K. Sakata, ‘Mechanical properties of $(Bi_{1/2}Na_{1/2})$ TiO_3-based piezoelectric ceramics’, *Silicates Industries – Ceramic Science and Technology*, **58**(7–8), 136–142, 1993.
23. H. Nagata and T. Takenaka, ‘Lead-free piezoelectric ceramics of $(Bi_{1/2}Na_{1/2})$ TiO_3–1/2(Bi_2O_3·Sc_2O_3) system’, *Jpn. J. Appl. Phys.*, **36**, 6055–6057, 1997.
24. T. Takenaka, T. Okuda, and K. Takegahara, ‘Lead-free piezoelectric ceramics based on $(Bi_{1/2}Na_{1/2})TiO_3$-$NaNbO_3$’, *Ferroelectrics*, **196**, 175–178, 1997.
25. Y.-M. Chiang, G. W. Farrey, and A. N. Soukhojak, ‘Lead-free high-strain single-crystal piezoelectrics in the alkaline bismuth-titanate perovskite family’, *Appl. Phys. Lett.*, **73**, 3683, 1998.
26. H. Nagata and T. Takenaka, ‘Lead-free piezoelectric ceramics of $(Bi_{1/2}Na_{1/2})TiO_3$-$KNbO_3$-1/2(Bi_2O_3·Sc_2O_3) system’, *Jpn. J. Appl. Phys.*, **37**, 5311–5314, 1998.
27. H. Nagata and T. Takenaka, ‘$(Bi_{1/2}Na_{1/2})TiO_3$-based non-lead piezoelectric ceramics’, *J. Korean Phys. Soc.*, **32**, S1298–S1300, 1998.
28. T. Takenaka and H. Nagata, ‘Ferroelectric and piezoelectric properties of lead-free $(Bi_{1/2}Na_{1/2})TiO_3$-$KNbO_{3\text{-}1/2}$(Bi_2O_3·Sc_2O_3) ceramics’, *Proc. the 11th IEEE International Symposium on the Applications of Ferroelectrics (ISAF XI ’98)* (IEEE Catalog No. 98CH36245), pp. 559–562, 1999.
29. H. Nagata, N. Koizumi, and T. Takenaka, ‘Lead-free piezoelectric ceramics of $(Bi_{1/2}Na_{1/2})TiO_3$-$BaTiO_3$-$BiFeO_3$ system’, *Ferroelectrics*, **229**, 273–278, 1999.
30. A. Sasaki, T. Chiba, Y. Mamiya, and E. Otsuki, ‘Dielectric and piezoelectric properties of (Bi, Na)TiO_3–(Bi, K)TiO_3 systems’, *Jpn. J. Appl. Phys.*, **38**(9B), 5564–5567, 1999.
31. K. Nakamura and Y. Kawamura, ‘Orientation dependence of electromechanical coupling factors in $KNbO_3$’, *IEEE Trans. Ultrason. Ferroelect. Freq. Contr.*, **47**, 750, 2000.
32. H. Ishii, H. Nagata, and T. Takenaka, ‘Morphotropic phase boundary and electrical properties of bismuth sodium titanate-potassium niobate solid-solution ceramics’, *Jpn. J. Appl. Phys.*, **40**(9B), 5660–5663, 2001.
33. S. Wada, A. Seike, and T. Tsurumi, ‘Poling treatment and piezoelectric properties of potassium niobate ferroelectric single crystals’, *Jpn. J. Appl. Phys.*, **40**, 5690–5697, 2001.
34. K. Kakimoto, I. Masuda, and H. Osato, ‘Ferroelectric and piezoelectric properties of $KNbO_3$ ceramics containing small amounts of $LaFeO_3$’, *Jpn. J. Appl. Phys.*, **42**, 6102, 2003.
35. H. Nagata, M. Yoshida, Y. Makiuchi, and T. Takenaka, ‘Large piezoelectric constant and high Curie temperature of lead-free piezoelectric ceramic ternary system based on bismuth sodium titanate-bismuth potassium titanate-barium titanate near the morphotropic phase boundary’, *Jpn. J. Appl Phys.*, **42**(12), 7401–7403, 2003.
36. Y. Saito, H. Takao, T. Tani, T. Nonoyama, K. Takatori, T. Homma, T. Nagaya, and M. Nakamura, ‘Lead free piezoceramics,’ *Nature*, **42**, pp. 84–87, 2004.
37. Y. P. Guo, K. Kakimoto, and H. Ohsato, ‘Phase transitional behavior and piezoelectric properties of NKN-LN ceramics’, *Appl. Phys. Lett.*, **85**(18), 4121–4123, 2004.

38. Y. Guo, K. Kakimoto, and H. Ohsato, 'Structure and electrical properties of lead-free $(Na_{0.5}K_{0.5})NbO_3$-$BaTiO_3$ ceramics', *Jpn. J. Appl. Phys.*, **43**(9B), 6662–6666, 2004.
39. K. Kakimoto, I. Masuda, and H. Osato, 'Solid-solution structure and piezoelectric property of $KNbO_3$ ceramics doped with small amounts of elements', *Jpn. J. Appl. Phys.*, **43**, 6706, 2004.
40. Y. Hiruma, R. Aoyagi, H. Nagata, and T. Takenka, 'Piezoelectric properties of $BaTiO_3$-$(Bi_{1/2}K_{1/2})TiO_3$ ferroelectric ceramics', *Jpn. J. Appl. Phys.*, **43**(11A), 7556–7559, 2004.
41. H. Birol, D. Damjanovic, and N. Setter, 'Preparation and characterization of $KNbO_3$ ceramic', *J. Am. Ceram. Soc.* **88**, 1754, 2005.
42. Y. Makiuchi, R. Aoyagi, Y. Hiruma, H. Nagata, and T. Takenaka, '$(Bi_{1/2}Na_{1/2})TiO_3$-$(Bi_{1/2}K_{1/2})TiO_3$-$BaTiO_3$-based lead-free piezoelectric ceramics', *Jpn. J. Appl. Phys.*, **44**(6B), 4350–4353, 2005.
43. Y. Hiruma, R. Aoyagi, H. Nagata, and T. Takenaka, 'Ferroelectric and piezoelectric properties of $(Bi_{1/2}K_{1/2})TiO_3$ ceramics', *Jpn. J. Appl. Phys.,* **44**(7A), 5040–5044, 2005.
44. H. Nagata, T. Shinya, Y. Hiruma, T. Takenaka, I. Sakaguchi, and H. Haneda, 'Piezoelectric properties of bismuth sodium titanate ceramics', *Ceram. Trans.*, **167**, 213–222, 2005.
45. T. Yoshida, Y. Hiruma, R. Aoyagi, H. Nagata, and T. Takenaka, 'Processing and electrical properties of $KNbO_3$ ferroelectric dense ceramics added with small amount of Bi_2O_3 and $MnCO_3$', *Key Eng. Materials,* **301**, 19–22, 2005.
46. K. Matsumoto, Y. Hiruma, H. Nagata and T. Takenaka, 'Piezoelectric properties of pure and Mn-doped potassium niobate ferroelectric ceramics', *Jpn. J. Appl. Phys.*, **45**(5B), 4479–4483, 2006.
47. H. Nagata, K. Matsumoto, T. Hirosue, Y. Hiruma, and T. Takenaka, 'Fabrication and electrical properties of potassium niobate ferroelectric ceramics', *Jpn. J. Appl. Phys.,* **46**(10B), 7084–7088, 2007.
48. M. Zgonik, R. Schlesser, I. Biaggio, E. Voit, J. Tscheny, and P. Gunter, *J. Appl. Phys.*, **74**(2), 1287, 1993.
49. M. Onoe, H. F. Tiersten, and A. H. Meitzler, *J. Acoust. Soe. Amer.,* **35**, 36, 1963.
50. K. Nakamura, T. Tokiwa, and Y. Kawamura, *J. Appl. Phys.*, **91**, 9272, 2002.
51. K. Yoshii, Y. Hiruma, H. Nagata, and T. Takenaka, 'Electrical properties and depolarization temperature of $(Bi_{1/2}Na_{1/2})TiO_3$-$(Bi_{1/2}K_{1/2})TiO_3$ lead-free piezoelectric ceramics', *Jpn. J. Appl. Phys.,* **45**(5B), 4493–4496, 2006.
52. Y. Hiruma, Y. Makiuchi, R. Aoyagi, H. Nagata, and T. Takenaka, 'Lead-free piezoelectric ceramics based on $(Bi_{1/2}Na_{1/2})TiO_3$-$(Bi_{1/2}K_{1/2})TiO_3$-$BaTiO_3$ solid solution', *Ceram. Trans.*, **174**, 139–146, 2005.
53. Y. Hiruma, K. Yoshii, R. Aoyagi, H. Nagata, and T. Takenaka, 'Piezoelectric properties and depolarization temperatures of $(Bi_{1/2}Na_{1/2})TiO_3$-$(Bi_{1/2}K_{1/2})TiO_3$-$BaTiO_3$ lead-free piezoelectric ceramics', *Key Eng. Materials,* **320**, 23–26, 2006.
54. Y. Hiruma, H. Nagata, and T. Takenaka, 'Phase transition temperatures and piezoelectric properties of $(Bi_{1/2}Na_{1/2})TiO_3$-$(Bi_{1/2}K_{1/2})TiO_3$-$BaTiO_3$ lead-free piezoelectric ceramics', *Jpn. J. Appl. Phys.*, **45**(9B), 7409–7412, 2006.
55. H. Takahashi, Y. Numamoto, J. Tani, and S. Tsurekawa, 'Piezoelectric properties of $BaTiO_3$ ceramics with high performance fabricated by microwave sintering', *Jpn. J. Appl. Phys.*, **45**(9B), 7405–7408, 2006.
56. T. Karaki, K. Yan, T. Miyamoto, and M. Adachi, 'Lead-free piezoelectric ceramics

with large dielectric and piezoelectric constants manufactured from $BaTiO_3$ nano-powder', *Jpn. J. Appl. Phys.*, **46**(4), L97–L98, 2007.

57. S. Zhang, T. R. Shrout, H. Nagata, Y. Hiruma, and T. Takenaka, 'Piezoelectric properties in $(K_{0.5}Bi_{0.5})TiO_3$-$(Na_{0.5}Bi_{0.5})TiO_3$-$BaTiO_3$ lead-free ceramics', *IEEE Trans. Ultrason., Ferroelect., Freq. Contr.*, **54**(5), 910–917, 2007.
58. Y. Hiruma, H. Nagata, and T. Takenaka, 'Phase-transition temperatures and piezoelectric properties of $(Bi_{1/2}Na_{1/2})TiO_3$-$(Bi_{1/2}Li_{1/2})TiO_3$-$(Bi_{1/2}K_{1/2})TiO_3$ lead-free ferroelectric ceramics', *IEEE Trans. Ultrason., Ferroelect., Freq. Contr.,* **54**(12), 2493–2499, 2007.
59. T. Takenaka, H. Nagata, Y. Hiruma, K. Yoshii, and K. Matsumoto, 'Lead-free piezoelectric ceramics based on perovskite structures', *J. Electroceramics,* **19**, 259–265, 2007.
60. Y. Hiruma, Y. Watanabe, H. Nagata, and T. Takenaka, 'Phase transition temperatures of divalent and trivalent ions substituted $(Bi_{1/2}Na_{1/2})TiO_3$ ceramics', *Key Eng. Materials*, **350**, 93–96, 2007.
61. M. Kimura, T. Minamikawa, A. Ando, and Y. Sakabe, 'Temperature characteristics of $(Ba_{1-x}Sr_x)_2NaNb_5O_{15}$ ceramics', *Jpn. J. Appl. Phys.,* **36**, 6051–6054, 1997.
62. Y. Doshida, S. Kishimoto, K. Ishii, H. Kishi, H. Tamura, Y. Tomikawa, and S. Hirose, 'Miniature cantilever-type ultrasonic motor using Pb-free multilayer piezoelectric ceramics', *Jpn. J. Appl. Phys.* **46**, 4921, 2007.
63. S. Ikegami and I. Ueda, 'Piezoelectricity in ceramics of ferroelectric bismuth compound with layer structure', *Jpn. J. Appl. Phys.,* **13**(10), 1572–1579, 1974
64. T. Takenaka and K. Sakata, 'Grain orientation and electrical properties of hot-forged $Bi_4Ti_3O_{12}$ Ceramics', *Jpn. J. Appl. Phys.*, **19**(1), pp. 31–39, 1980.
65. T. Takenaka and K. Sakata, 'Grain orientation effects on electrical properties of bismuth layer-structured ferroelectric $Pb_{(1-x)}(NaCe)_{x/2}Bi_4Ti_4O_{15}$ solid solution', *J. Appl. Phys.,* **55**(4), 1092–1099, 1984.
66. T. Takenaka and K. Sakata, 'Piezoelectric and pyroelectric properties of calcium-modified and grain-oriented $(NaBi)_{1/2}Bi_4Ti_4O_{15}$ ceramics', *Ferroelectrics*, **94**, 175–181, 1989.
67. T. Takenaka, 'Grain orientation effects on electrical properties of bismuth layer-structured ferroelectric ceramics', *J. Ceramic Soc. Jpn.*, **110**(4), 215–224, 2002.
68. T. Takenaka and H. Nagata, 'Grain orientation and electrical properties of some bismuth layer-structured ferroelectrics for lead-free piezoelectric applications', *Ferroelectrics*, **336**, 119–136, 2006.
69. T. Takenaka, 'Grain orientation and electrical properties of bismuth layer-structure ferroelectrics'. In Z.-G. Ye (ed), '*Handbook of Advanced Dielectric, Piezoelectric and Ferroelectric Materials*', pp. 818–851, Woodhead Publishing Limited, Cambridge, 2008.
70. V. V. Ivanova, A. G. Kapyshev. Y. N. Veenevtsev, and G. S. Zhdanov, *Akad. Nauk. SSSR*, **26**, 354, 1962.
71. S.-E. Park and S.-J. Chung, 'Nonstoichiometry and the long-range cation ordering in crystals of $(Bi_{1/2}Na_{1/2})TiO_3$', *J. Amer. Cer. Soc.*, **77**(10), 2641–2647, 1994.
72. I. P. Pronin, P. P. Syrnikov, V. A. Isupov, V. M. Egorov, N. V. Zaitseva, and A. F. Ioffe, 'Peculiarities of phase transitions in sodium-bismuth titanate', *Ferroelectrics*, **25**, 395–397, 1980.
73. J. A. Zvirgzds, P. P. Kapostis, and J. V. Zvirgzde, 'X-ray study of phase transition in ferroelectric $(Bi_{0.5}Na_{0.5})TiO_3$', *Ferroelectrics*, **40**, 75–77, 1982.
74. I. G. Siny, C.-S. Tu, and V. H. Schmidt, 'Critical acoustic behaviour of the relaxor

ferroelectrics $Na_{1/2}Bi_{1/2}TiO_3$ in the intertransition region', *Phys. Rev. B*, **51**, 5659, 1995.

75. J. Y. Yi, J.-K. Lee, and K.-S. Hong, 'Dependence of the microstructure and the electrical properties of lanthanum-substituted $(Bi_{1/2}Na_{1/2})TiO_3$ on cation vacancies', *J. Amer. Cer. Soc.*, **85**(12), 3004–3010, 2003.
76. A. Herabut and A. Safari, 'Processing and electrochemical properties of $(Bi_{1/2}Na_{1/2})_{1-1.5x}La_xTiO_3$ ceramics', *J. Amer. Cer. Soc.*, **80**(11), 2954–2958, 1997.
77. Y. Watanabe, Y. Hiruma, H. Nagata, and T. Takenaka, 'Phase transition temperatures and electrical properties of divalent ions (Ca^{2+}, Sr^{2+} and Ba^{2+}) substituted $(Bi_{1/2}Na_{1/2})$ TiO_3 ceramics', *Ceramics International*, **34**(4), 761–764, 2008.
78. X. X. Wang, X. G. Tang, and H. L. W. Chan, "Electromechanical and ferroelectric properties of $(Bi_{1/2}Na_{1/2})TiO_3$–$(Bi_{1/2}K_{1/2})TiO_3$–$BaTiO_3$ lead-free piezoelectric ceramics', *Appl. Phys. Lett.*, **85**(1), 91–93, 2004.
79. D. Lin, D. Xiao, J. Zhu, and P. Yu, 'Piezoelectric and ferroelectric properties of $[Bi_{0.5}(Na_{1-x-y}K_xLi_y)_{0.5}]TiO_3$ lead free piezoelectric ceramics', *Appl. Phys. Lett.*, **88**(6), 062901–062903, 2006.
80. Y. Hiruma, K. Yoshii, H. Nagata, and T. Takenaka, 'Investigation of phase transition temperatures on $(Bi_{1/2}Na_{1/2})TiO_3$–$(Bi_{1/2}K_{1/2})TiO_3$ and $(Bi_{1/2}Na_{1/2})TiO_3$–$BaTiO_3$ lead-free piezoelectric ceramics by electrical measurements', *Ferroelectrics*, **346**, 114–119, 2007.
81. Y. Hiruma, K. Yoshii, H. Nagata, and T. Takenaka, 'Phase transition temperature and electrical properties of $(Bi_{1/2}Na_{1/2})TiO_3$–$(Bi_{1/2}A_{1/2})TiO_3$ (A = Li and K) lead-free ferroelectric ceramics', *J. Appl. Phys.,* **103**, 084121–1~7, 2008.
82. T. Tsurumi, T. Sasaki, H. Kakemoto, T. Harigai and S. Wada, 'Domain contribution to direct and converse piezoelectric effects of PZT ceramics', *Jpn. J. Appl. Phys.*, **43**, 7618, 2004.
83. Y. Hiruma, T. Watanabe, H. Nagata, and T. Takenaka: 'Piezoelectric properties of $(Bi_{1/2}Na_{1/2})TiO_3$-based solid solution for lead-free high-power applications', *Jpn. J. Appl. Phys.,* **47**(9B), 7659–7663 , 2008.
84. S. Takahashi and S. Hirose, 'Vibration-level characteristics of lead-zirconate-titanate ceramics', *Jpn. J. Appl. Phys.*, **31**, 3055, 1992.
85. S. Hirose, N. Magami, and S. Takahashi, 'Piezoelectric ceramic transformer using piezoelecric lateral effect on input and on output', *Jpn. J. Appl. Phys.*, **35**, 3038, 1996.
86. S. Tashiro, M. Ikehiro, and H. Igarashi, 'Influence of temperature rise and vibration level on electromechanical properties of high-power piezoelectric ceramics', *Jpn. J. Appl. Phys.*, **36**, 3004, 1997.
87. M. Umeda, K. Nakamura, and S. Ueha, 'The measurement of high-power characteristics for a piezoelectric transducer based on the electrical transient response', *Jpn. J. Appl. Phys.*, **37**, 5322, 1998.
88. S. Kawada, H. Ogawa, M. Kimura, K. Shiratsuyu, and H. Niimi, 'High-power piezoelectric vibration characteristics of textured $SrBi_2Nb_2O_9$ ceramics', *Jpn. J. Appl. Phys.*, **45**, 7455, 2006.
89. S. Kawada, H. Ogawa, M. Kimura, K. Shiratsuyu, and Y. Higuchi, 'Relationship between vibration direction and high-power characteristics of <001> textured $SrBi_2Nb_2O_9$ ceramics', *Jpn. J. Appl. Phys.*, **46**, 7079, 2007.
90. H. Nagata and T. Takenaka, 'Effects of substitution on electrical properties of $(Bi_{1/2}Na_{1/2})TiO_3$-based lead-free ferroelectrics', *Proc. the 12th IEEE International Symposium on the Applications of Ferroelectrics (ISAF XII 2000)* (IEEE Catalog No.00CH37076), pp. 45–51, 2001.

91. M. Zhu, L. Liu, Y. Hou, H. Wang, and H. Yan, 'Microstructure and electrical properties of MnO-doped $(Na_{0.5}Bi_{0.5})_{0.92}Ba_{0.08}TiO_3$ lead-free piezoceramics *J. Am. Ceram. Soc.*, **90**, 120, 2007.
92. P. Gerthsen, K. H. Härdtl, and N. A. Schmidt, 'Correlation of mechanical and electrical losses in ferroelectric ceramics', *J. Appl. Phys.*, **51**, 1131, 1980.
93. S. Takahashi, 'Effects of impurity doping in lead zirconate-titanate ceramics', *Ferroelectrics* **41**, 143, 1982.
94. K. Hayashi, A. Ando, Y. Hamaji, and Y. Sakabe, 'Study of the valence stake of the manganese lons in $PbTiO_3$ ceramics by means of ESR', *Jpn. J. Appl. Phys.*, **37**, 5237, 1998.
95. Y. Hiruma, H. Nagata and T. Takenaka, 'Grain-size effect on electrical properties of $(Bi_{1/2}K_{1/2})TiO_3$ ceramics', *Jpn. J. Appl. Phys.,* **46**, 1081–1084, 2007.
96. Y. Hiruma, H. Nagata, and T. Takenaka, 'Dielectric, ferroelectric and piezoelectric properties of barium titanate and bismuth potassium titanate solid-solution ceramics', *J. Ceramic Soc. Jpn.,* Supplement, **112**(5), S1125–1128, 2004.
97. T. Takenaka, Y. Hiruma, M. Nemoto, and H. Nagata, 'Piezoelectric properties of $(Bi_{1/2}K_{1/2})TiO_3$–$BaTiO_3$ ceramics with wide working temperatures', *Extended Abstract of the 17th International Symposium on the Applications of Ferroelectrics (ISAF 2008)*, PL002, 2008.
98. M. Nemoto, Y. Hiruma, H. Nagata, and T. Takenaka, 'Fabrication and piezoelectric properties of grain-oriented $(Bi_{1/2}K_{1/2})TiO_3$-$BaTiO_3$ ceramics', *Jpn. J. Appl. Phys.*, **47**, 3829–3832, 2008.

5

Quartz-based piezoelectric materials

Y. SAIGUSA, River Eletec, Japan

Abstract: This chapter examines the piezoelectric characteristics and common applications of quartz crystal. Section 5.1 covers the discovery of quartz crystal piezoelectricity including its structure and its differences from other piezoelectric materials. Section 5.2 compares natural quartz crystal with artificial quartz crystal and explains the methods and specifications for artificial quartz crystal growth. Section 5.3 introduces typically applied quartz crystal plates for vibrators and shows actual cutting angles. These vibrators include the most popular AT-cut thickness share mode and the tuning fork bending mode, and their characteristics such as frequency and temperature are explained in detail. This section also shows examples of quartz crystal miniaturization using another cutting method developed by the River Eletec Corporation. Section 5.4 demonstrates applications and standards for the quartz crystal vibrators and oscillators described throughout the chapter.

Key words: artificial quartz crystal, piezoelectricity, zero temperature coefficient, thirty-two (32) point groups, single crystal, vibration mode, resonator, oscillator, filter.

5.1 Piezoelectricity of quartz crystal

5.1.1 Discovery of Piezoelectricity

Today, most electronic instruments use quartz crystal devices. When stress is applied to piezoelectric materials such as quartz crystal, PZT, and $LiNbO_3$, electric polarization is created. This polarization phenomenon was first discovered by the Curie brothers in 1880.

Figure 5.1 shows the typical external form of natural quartz crystal and its axis. Figure 5.2 illustrates its cross section to the Z-axis and the cutting angle of the crystal plate.

The Curie brothers used a plate that was perpendicular to the X-axis (called the X-cut) for their piezoelectric experiment. They found that when they compressed or pulled on this plate, electric polarization was created in the direction of its thickness. This is called direct piezoelectricity. In opposition to this, they found that when an electric field is added to the X-direction, there is either expansion or contraction in the X or Y-axis directions. This phenomenon (called inverse piezoelectricity) was hypothesized by G. Lippmann, and later confirmed by the Curie brothers.

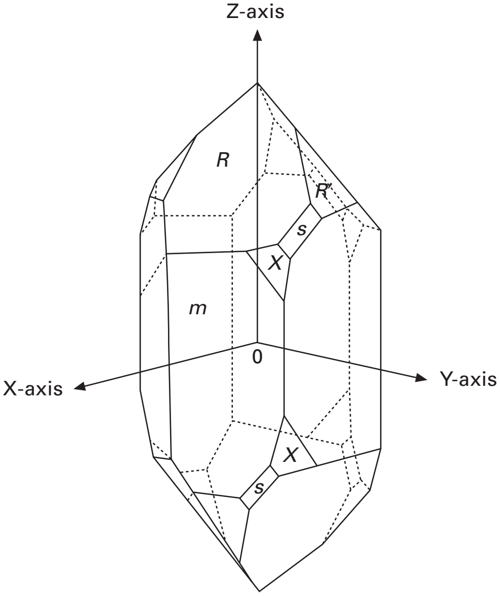
Z-axis
R
R′
s
X
m
0
X-axis
Y-axis
X
s

5.1 The typical external form of natural quartz crystal with its axis.

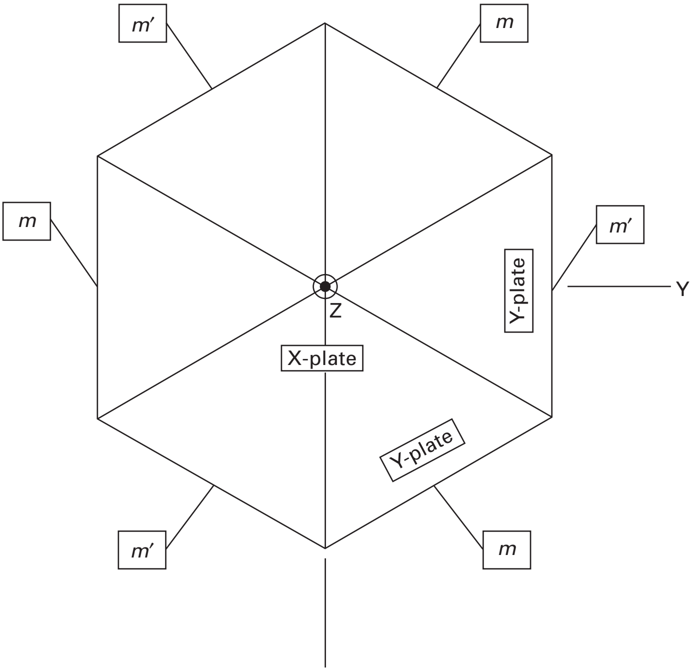
m′
m
m
m′
Y-plate
Y
Z
X-plate
Y-plate
m′
m

5.2 Cross section to Z-axis and cutting angle of crystal plate.

Professor W. G. Cady was one of the pioneers of the quartz crystal resonator. Cady made the X-plate (called the Langevin vibrator) where the Y dimension is longer than the Z dimension, and drove it by an alternative electric field shown in Fig. 5.3. He swept the frequency of alternative electric fields and found that there exists a resonant point unique to the dimension of the X-plate.

Professor Pierce had first published the quartz crystal oscillation circuit using a vacuum tube. This circuit is shown in Fig. 5.4. This circuit is the most basic quartz crystal oscillation circuit and is called the Pierce circuit. Compared with the previous LC oscillation circuit, the Pierce oscillation circuit provided a much more stable frequency. With the improvements

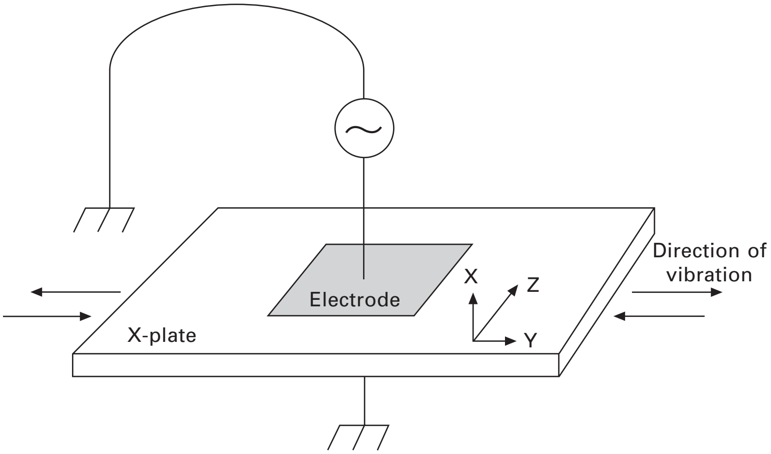

5.3 Experimental device by W. G. Cady.

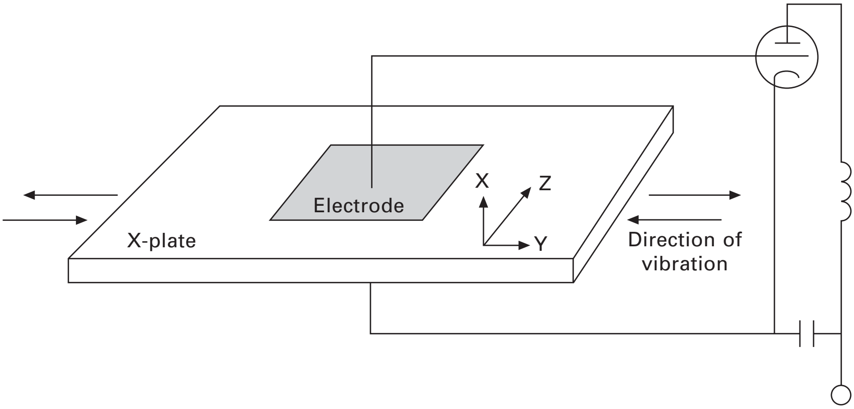

5.4 Pierce circuit.

of radio frequency (RF) communication technology, changes in the stable frequency oscillation and temperature adjustments have been required.

At one point, the Curie brothers had missed their cutting angle and made a Y-cut vibrator. Its frequency temperature characteristic showed the opposite curve to the X-cut. As a result of the X-cut vibrator and the Y-cut vibrator having an opposite frequency temperature curve, many people tried to find the zero temperature coefficient between these cuts. However, since the vibration mode of the X-cut and the Y-cut is different, there is not necessarily a zero temperature coefficient(s) that exists between these two cutting angles.

In 1932, Doctor Koga discovered that there exists a zero temperature coefficient with the plate at 35°15′ rotating the Y-plate from the Z-axis.[1] He named this cutting angle the 'R1-cut'. A similar discovery had been made by R. Bechmann and the Bell Laboratory. The Bell Laboratory named this cutting angle the 'AT-cut'. After these publications, other rotated Y-cuts had been discovered and named 'BT-cut,' 'CT-cut,' and 'DT-cut' successively (see Fig. 5.14).[2]

5.1.2 Symmetry of quartz crystal and its axis

In crystallography, there are 32 point groups and seven crystal systems. Quartz crystal belongs to the three-two point group of the trigonal crystal system. It has one axis of three-fold symmetry and three axes of two-fold symmetry. As shown in Fig. 5.2, the Z-axis (optic axis) is the three-fold symmetry axis and when the crystal is rotated 120/240 degrees around it, the characteristics are the same as the original position.[3] The X-axis (electric axis) and Y-axis (mechanical axis) are the two-fold symmetry axis and each pair of $X_1 - Y_1$, $X_2 - Y_2$ and $X_3 - Y_3$ axes have the same characteristics and relationships to each other (Fig. 5.5). These properties are used to investigate and determine constants of quartz crystal presented by tensor. When the quartz crystal is cut with a specified angle(s), these constants are transformed to the new axis of coordinates.

Figure 5.6 shows the unit cell of α-quartz. Small black circles show the Si atom and the large white circles show the O atom. Figure 5.7 shows the arrangement of these Si atoms and O atoms in the α-quartz viewed from the Z-axis. Si atoms and O atoms make a spiral structure toward the Z-axis. It is easily understood that the electrical center is located at the origin of the Z-Y plane.

To simplify, one unit of Si and O atoms are shown in Fig. 5.8 as viewed from the Z-axis. This shows that there is no stress added to the quartz crystal, and the electrical center of three Si and O atoms is agreed with the original point of the X-Y plane.

Figure 5.9 shows that there is a mechanical pressing stress being added toward the X-axis. The electrical center of three Si and O atoms is disagreed

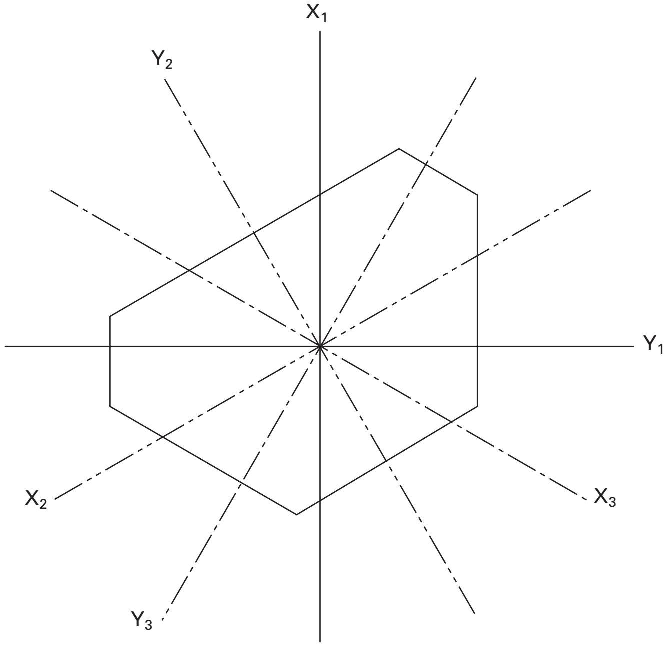
X_1
Y_2
Y_1
X_2
X_3
Y_3

5.5 X-axis (electric axis) and Y-axis (mechanical axis) are the two-fold symmetry axis.

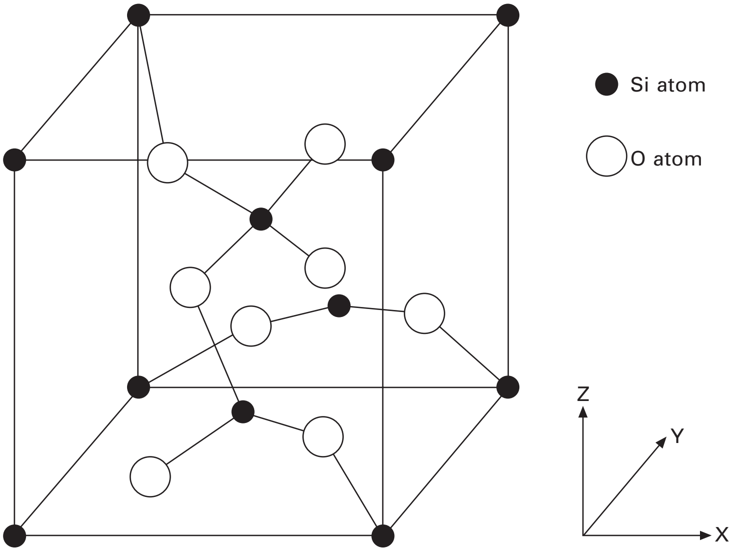
Si atom
O atom
Z
Y
X

5.6 Unit cell of α-quartz.

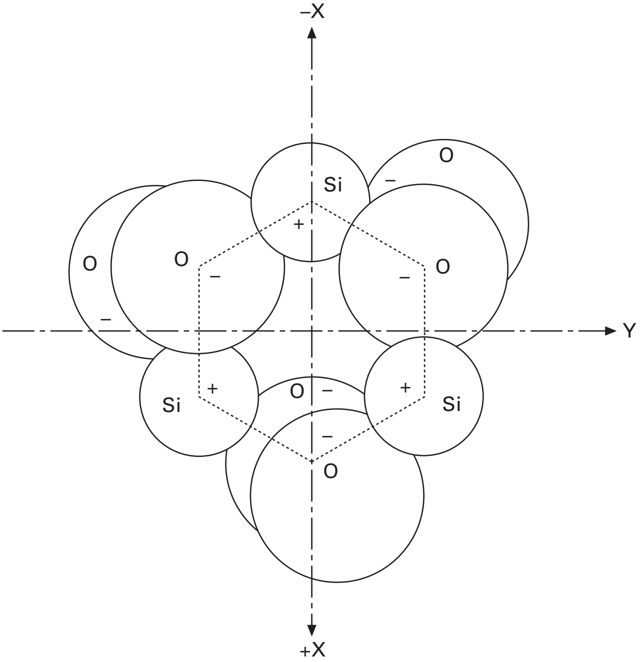
–X
Si
+
O
–
O
–
O
–
O
–
O
–
Y
Si
+
O
–
+
Si
–
O
+X

5.7 Arrangement of Si atoms and O atoms in the α-quartz viewed from Z-axis.

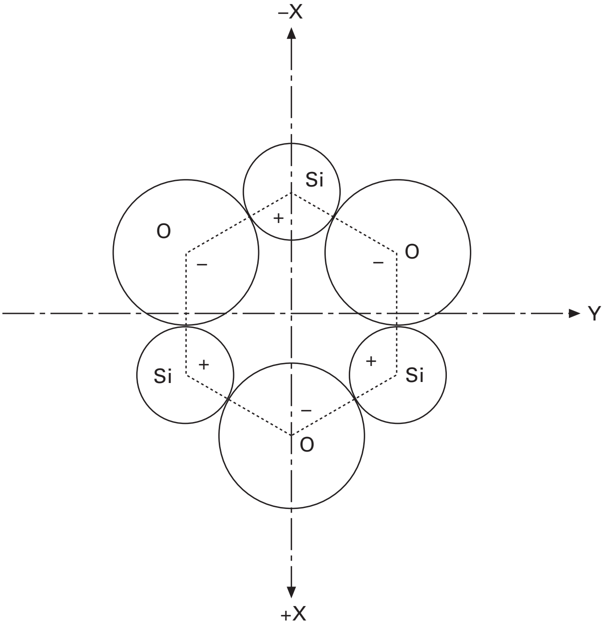
–X
Si
+
O
–
O
–
Y
Si
+
+
Si
–
O
+X

5.8 One unit of Si and O atoms in the α-quartz viewed from Z-axis.

and polarization toward the X-axis occurs. On the other hand, when pulling stress is added toward the X-axis, the opposite polarization occurs. Furthermore, when electrodes are placed on both the X plane and adding an AC electric field between these electrodes, mechanical vibrating displacement occurs in the direction of X. When the mechanical resonance is agreed to the AC frequency and phase, the resonance of the quartz crystal plate occurs. This behavior, as shown in Fig. 5.9, is called the longitudinal piezoelectricity.

Figure 5.10, shows the perpendicular piezoelectricity compared with the longitudinal piezoelectricity explained above. When mechanical stress is applied to the Y direction, polarization occurs toward the X direction. When the AC electric field along the Y direction is applied, vibration occurs to the X direction. Piezoelectricity and inverse piezoelectricity are explained as above.

Figure 5.11 shows that when you apply compress displacement to the X-axis and extensional displacement to the Y-axis at the same time, the electric field to the X direction appears. This is called inverse piezoelectricity. Even if these stresses were applied to the Z direction, no polarization would occur.

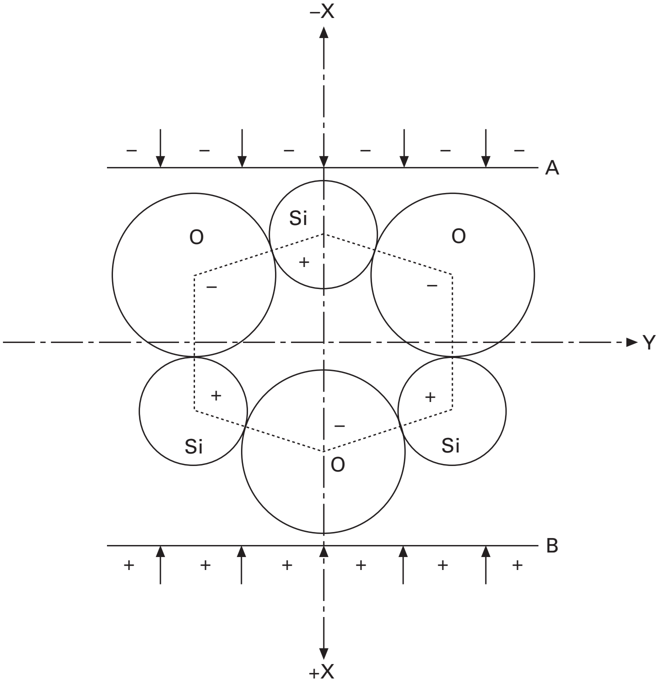

5.9 Direct longitudinal piezoelectricity.

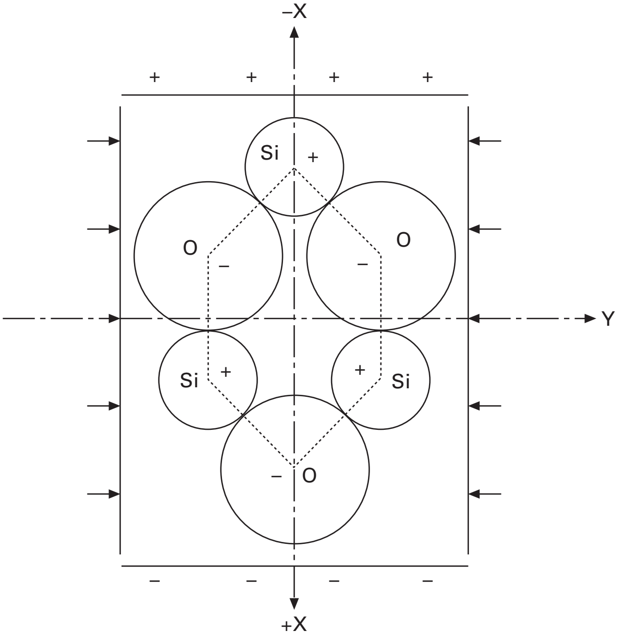
–X
+
+
+
+
Si
+
O
–
O
–
Y
Si
+
+
Si
–
O
–
–
–
–
+X

5.10 Direct perpendicular piezoelectricity.

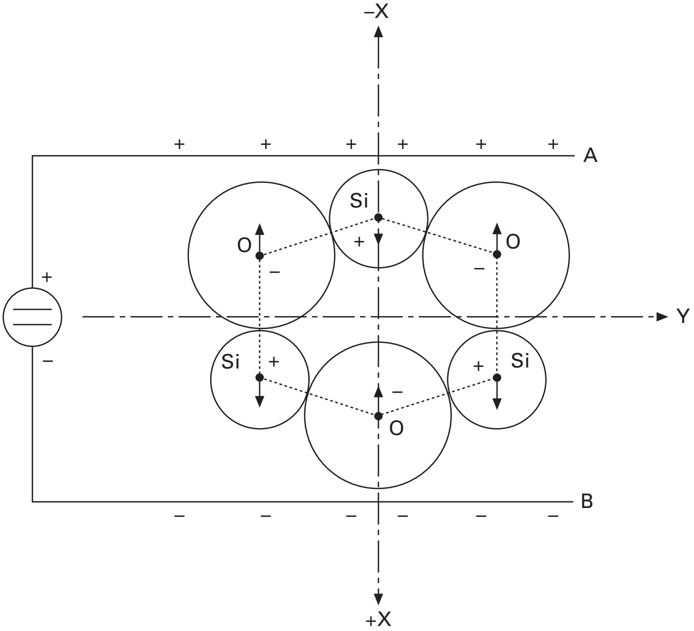
–X
+
+
+
+
+
+
A
Si
O
+
O
–
–
+
–
Y
Si
+
Si
+
–
O
B
–
–
–
–
–
–
+X

5.11 Inverse piezoelectricity.

5.1.3 Differences among other piezoelectric materials

There are many materials that have piezoelectricity aside from quartz crystal. These are classified as single crystals and polycrystals. Generally, single crystals like SiO_2, $LiNbO_3$, $LiTaO_3$ and $La_3Ga_5SiO_{14}$, etc., have a steady construction of elements so that their characteristics are stable. On the other hand, polycrystals such as $Pb(Zr.Ti)O_3$, $BaTiO_3$, and $PbTiO_3$, etc., have many rates of the elements so they have many characteristics.

All these piezoelectric materials have a relationship between their geometrical element arrangements and characteristics. The designer has to choose suitable material(s) when considering their process and purpose.[4]

Piezoelectric materials are used when electric energy is changed to mechanical energy or in reverse of the energy change. It is very important for a device designer to choose the material with characteristic(s) that suit their purpose. Table 5.1 shows the required characteristics for typical piezoelectric devices. The suitable material(s) have to be chosen based on these characteristics. For example, in designing timing devices, the designer has to regard frequency stability as the most important characteristic. The primary factors are:

- excellent frequency stability
- negligible deviation of equivalent circuit constants for aging
- stable oscillator.

Table 5.1 The energy change and required characteristics for typical piezoelectric devices

Typical piezoelectric devices	Energy transduction	Requirement	
Actuator Buzzer Ultrasonic cleaner Ultrasonic motor Speaker	Electrical to mechanical	Piezoelectric constant, *d*: Permittivity, ε: Quality factor, *Q*:	large high small
Acceleration sensor Microphone Ignitor	Mechanical to electrical	Piezoelectric constant, *g*: Permittivity, ε:	large high
Sonar Flaw detector Tuning fork vibrator	Electrical to mechanical	Electromechanical coupling factor, *k*: Quality factor, *Q*:	large large
Resonator, Oscillator Ceramic filter	Electrical to mechanical to electrical	Frequency-to-temperature coefficient, α: Change in frequency with time, Δf: Electromechanical coupling factor, *k*:	approximately 0 small large

Regarding the first factor, it is possible to get a device that has a zero temperature coefficient by choosing a suitable cut angle such as the AT-cut quartz crystal resonator. Its frequency stability is excellent under a wide range of temperatures compared with other resonators using other materials.

Regarding the second factor of having little or no deviation of equivalent circuits, the quartz crystal resonator has excellent aging stability because it is a very stable material from the viewpoint of chemical and physical aspects compared with other piezoelectric materials. Generally, polarization is necessary for polycrystals like PZT in order to unidirectionally polarize them by an external electric field. At this point, their piezoelectric characteristics are influenced not only by the polarization condition but also by the microscopic state of the material (grain size, grain boundaries, porosity, etc.). And the reliability (aging rate, performance change by temperature, etc.) is also influenced by the polarization condition. Compared with these polycrystalline materials, quartz crystal is one of the single crystal forms, and its composition is extremely stable. Therefore, the piezoelectric device that is made from it shows very stable reliability during aging.

Regarding the final factor, the Q-value of the quartz crystal resonator is so high that the oscillation stability is not particularly influenced by the element characteristics of the electric circuit. This leads to excellent frequency stability of the quartz crystal oscillator.

Table 5.2 shows various constants of piezoelectric single and polycrystal ($Pb(Zr,Ti)O_3$). Since the constants of ($Pb(Zr,Ti)O_3$) change with its composition of $(Zr,Ti)O_3$, they may be recognized as typical values. Electromechanical coupling factors of quartz crystal are small, but it has many superior points when compared with other piezoelectric materials as described above. Therefore it is one of the indispensable materials in frequency control devices today.

Table 5.2 Various constants of piezoelectric single crystal and polycrystal $Pb\ (Zr,Ti)\ O_3$

Materials	Specific permittivities ε	Piezoelectric constants, $d/10^{-12}CN^{-1}$
Quartz crystal (SiO_2)	$\varepsilon^T_{11}/\varepsilon_0 = 4.52$, $\varepsilon^T_{33}/\varepsilon_0 = 4.68$	$d_{11} = 2.31$, $d_{14} = 0.727$
Lithium niobate ($LiNbO_3$) crystal	$\varepsilon^T_{11}/\varepsilon_0 = 84$ $\varepsilon^T_{33}/\varepsilon_0 = 30$	$d_{15} = 68$, $d_{22} = 21$ $d_{31} = -1$, $d_{33} = 6$
Lithium tantalate ($LiTaO_3$) crystal	$\varepsilon^T_{11}/\varepsilon_0 = 51$ $\varepsilon^T_{33}/\varepsilon_0 = 45$	$d_{15} = 26$, $d_{22} = 7$ $d_{31} = -2$, $d_{33} = 8$
Lead zirconate titanate ($Pb(Zr,Ti)O_3$) ceramics	$\varepsilon^T_{11}/\varepsilon_0$ = from 1500 to 1700 $\varepsilon^T_{33}/\varepsilon_0$ = from 1300 to 1700	d_{15} = from 500 to 580, d_{31} = from −170 to −125 d_{33} = from 290 to 370

5.2 Production of artificial quartz crystal

5.2.1 The relationship between natural and artificial quartz crystal

Since its discovery, natural quartz crystal has been valued for its mysterious properties. People would admire it and use it for religious ceremonies and fortune-telling among other things. More recently, we can see quartz crystal has been used as jewelry and applied in other fine arts. From the standpoint of fascination, natural quartz crystal has much more value when compared with artificial quartz crystal.

The quartz crystal used for piezoelectric devices requires the following:

- no twin in a crystal
- the crystal should be either right-hand or left-hand coordinated
- less inclusion(s) and less dislocation
- fine production yields.

When comparing natural and artificial quartz crystal under these requirements, artificial quartz crystal has an advantage over natural quartz crystal. Therefore, 100% of piezoelectric devices are made from artificial quartz crystals today.

Artificial quartz crystals are produced by the hydrothermal process. They are grown in the autoclave as shown in Fig. 5.12.[5] The autoclave is divided into two zones by the baffle that controls the convection of the autoclave. The upper zone is the crystal growth zone and the lower zone is the raw material zone. Seed crystals are set in the growth zone and raw quartz called 'lasca' is set in the raw material zone. Generally, Y-bar and/or Z-plate are used for the seeds. Under high pressure and high temperature quartz crystal is soluble in alkaline solutions like Na_2CO_3 or NaOH, and this alkaline solution is put in the autoclave. The autoclave is then sealed and heated. Generally, the temperature of the growth zone and the material zone are kept around 300 °C and 400 °C, respectively. Then the pressure of the autoclave becomes about 400 MPa and convection begins. At this time, solution quartz convection contributes to quartz crystal growth on the seeds. The growth speed is different for each crystal axis and is shown as below.

Growth speeds: $Z > +X > -X > Y =$ approximately 0

The shapes of grown artificial quartz crystals are shown in Fig. 5.13. Compared with natural quartz crystal shown in Fig. 5.1, we can see the difference between them lies not only in their shape but also their axis. Artificial quartz crystal that has been grown is ground into lumbered quartz.

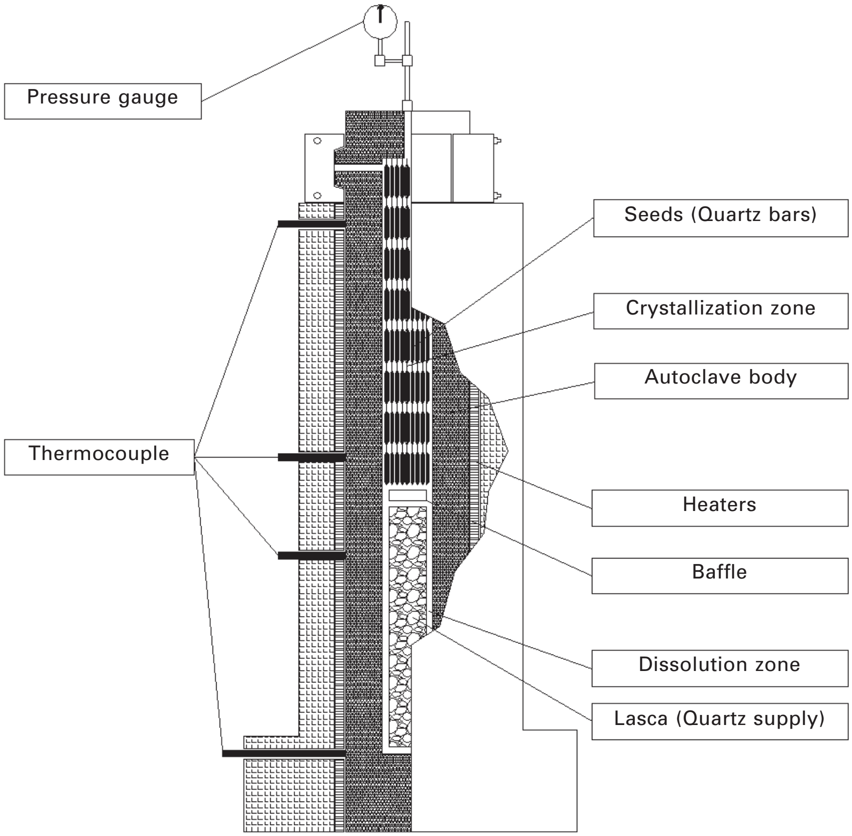
Pressure gauge
Seeds (Quartz bars)
Crystallization zone
Autoclave body
Thermocouple
Heaters
Baffle
Dissolution zone
Lasca (Quartz supply)

5.12 The cross section of the autoclave.

5.2.2 Specifications of artificial quartz crystal

The evaluation of artificial quartz crystal quality is specified in IEC 60758. Its leading terms are inclusion density, etch channel (dislocation) density and infrared absorption constant α. Usually, the inclusions contain Fe radical, Al radical, etc. Dislocations are evaluated for the quartz crystal element(s)/wafer(s) by etching it with HF, etc. If there is no dislocation, there is no strain, and the energy density of the quartz crystal lattice is uniform. However, if there is any dislocation, the energy density of that point has higher energy compared with other parts of quartz crystal, and will be selectively etched. We can then find the dislocation as an etch channel.

When we present an infrared beam to the quartz crystal, absorption occurs at the specified wavelength. The absorption has a relationship to the *Q* (quality factor) value of quartz crystal. This technique is used as a non-destruction evaluation of the quartz crystal quality. Before 1987, the evaluation of

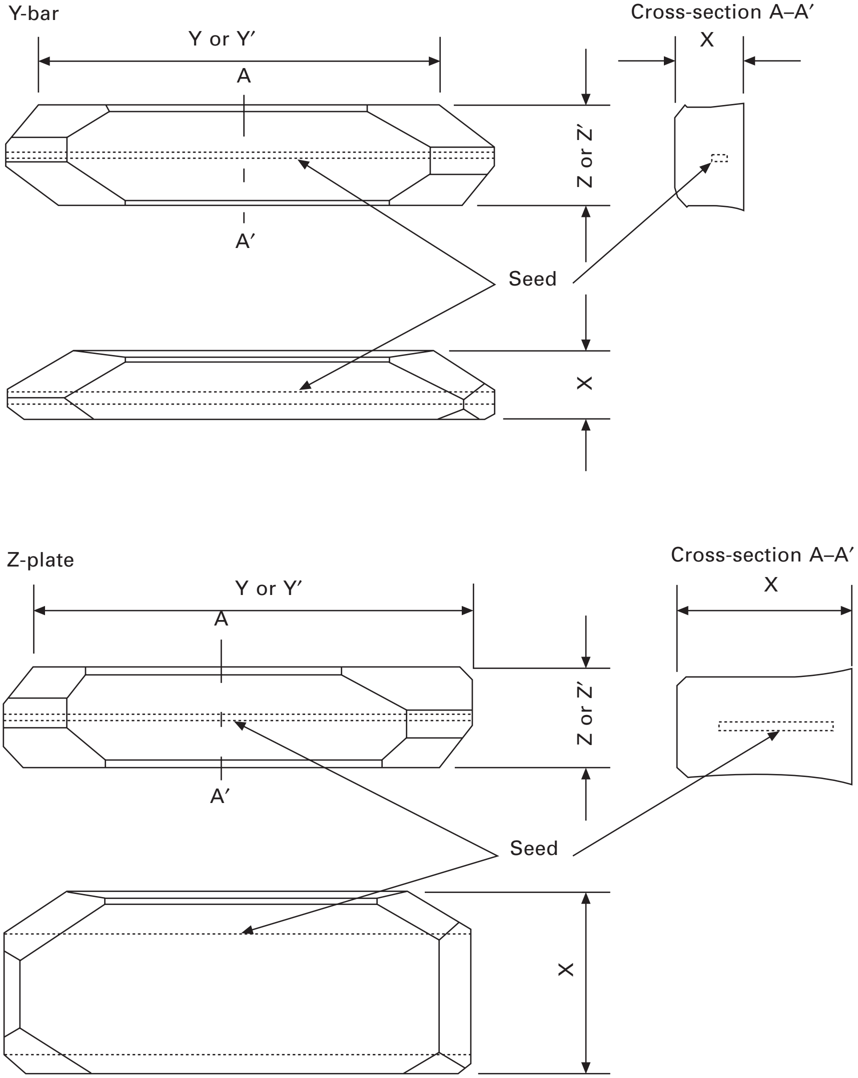
Y-bar
Cross-section A–A′
Y or Y′
X
A
Z or Z′
A′
Seed
X
Z-plate
Cross-section A–A′
Y or Y′
X
A
Z or Z′
A′
Seed
X

5.13 The shapes of grown artificial quartz crystal.

quartz crystal had been carried out by making an actual crystal vibrator, and measuring its Q value directory. This method can cause a process deviation and can create a small error in calculating the Q value of the quartz crystal. For these reasons, the infrared absorption method is used to evaluate the quality of quartz crystal. This direct measured Q value is used as a reference value today.

Tables 5.3–5.5 show the grade of quartz crystal and its required values as specified in JIS C6704.

Table 5.3 The grade of inclusion density in JIS C6704

Grade	Quantity of inclusions according to dimensions, pcs/cm^2			
	10–30 μm	30–70 μm	70–100 μm	> 100 μm
Ia	2	1	0	0
Ib	3	2	1	1
I	6	4	2	2
II	9	5	4	3
III	12	8	6	4

Table 5.4 The grade of infrared absorption constant α in JIS C6704

Grade	Limit for average α			Q/10^6
	α_{3500}	α_{3585}	α_{3410}	
Aa	0.026	0.015	0.075	3.8
A	0.033	0.024	0.082	3.0
B	0.045	0.050	0.100	2.4
C	0.060	0.069	0.114	1.8
D	0.080	0.100	0.145	1.4
E	0.120	0.160	0.190	1.0

Table 5.5 The grade of etch channel (dislocation) density ρ in JIS C6704

Grade	Maximum etch channel density, ρ/cm^2
1	10
2	30
3	100
4	300
5	600

5.3 Cutting angles and their vibration mode

5.3.1 Examples of typical cutting angles and their vibration mode and characteristics

Figure 5.14 shows some of the cutting angles of quartz crystal vibrators.[6,7] There are many kinds of vibration modes on quartz crystal resulting from its symmetry and its piezoelectric characteristics. Among these vibration modes, there are some modes that have first-degree zero temperature coefficient α. These cutting angles have excellent frequency stability against the temperature. The cutting angles shown in Fig. 5.14 are typical cutting angles for quartz crystal vibrators applied bulk waves.

Figure 5.15 shows examples of quartz crystal vibrators' frequency temperature characteristics that have zero temperature coefficient shown in Fig. 5.14.[6]

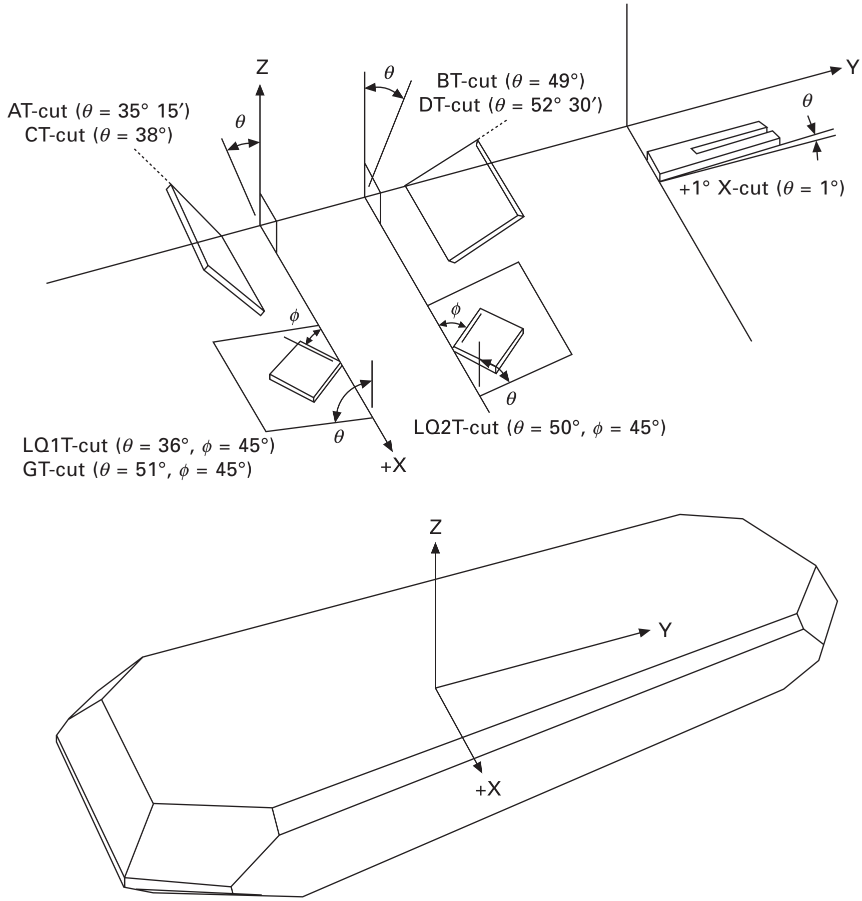
Z
θ
AT-cut (θ = 35° 15′)
CT-cut (θ = 38°)
θ
BT-cut (θ = 49°)
DT-cut (θ = 52° 30′)
Y
θ
+1° X-cut (θ = 1°)
ϕ
ϕ
θ
θ
LQ2T-cut (θ = 50°, ϕ = 45°)
LQ1T-cut (θ = 36°, ϕ = 45°)
GT-cut (θ = 51°, ϕ = 45°)
+X
Z
Y
+X

5.14 Cutting angles of typical quartz crystal vibrators.

Generally, using third-degree Taylor expansion, the frequency deviation of quartz crystal $\Delta f/f$ is shown by the following equation.

$$\Delta f/f = \alpha(t - t_0) + \beta(t - t_0)^2 + \gamma(t - t_0)^3$$

where t_0 is the Taylor expansion temperature.

The first-degree temperature coefficient α's of each quartz crystal vibrators shown in Fig. 5.14 become zero at 25 °C, and their temperature characteristics are determined by second-degree temperature coefficients β.

Table 5.6 also shows the value of second- and third-degree temperature coefficients of quartz crystal vibrators having zero temperature coefficient α. For example, +1°. X cut tuning fork quartz crystal vibrator, which is used in time clock bases, has a comparatively large value for the second-degree temperature coefficient β. The temperature coefficient is around – 3.5

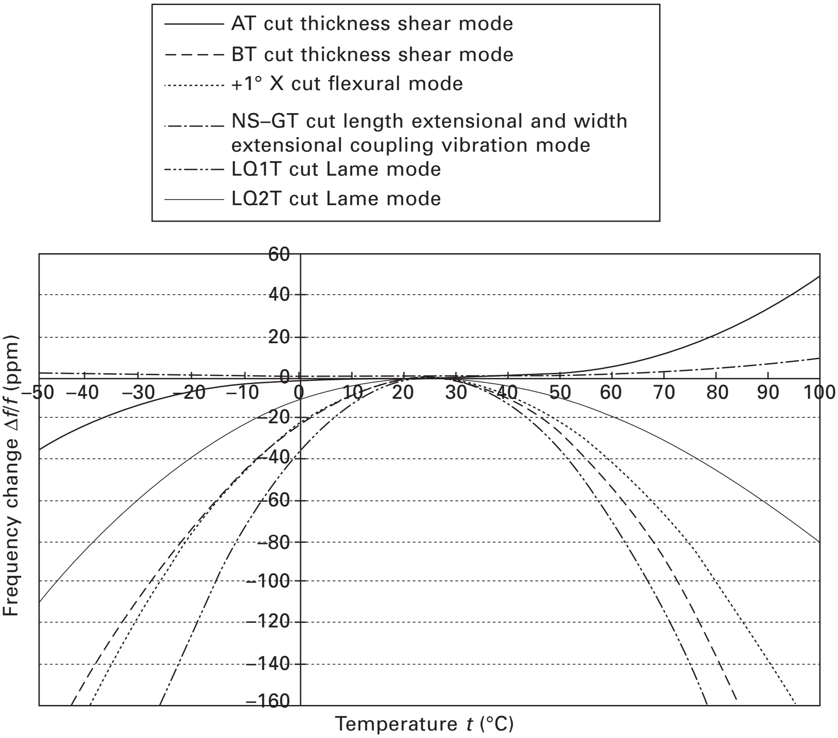

5.15 Examples of temperature frequency characteristics of quartz crystals vibrators.

$\times 10^{-8}/°C^2$, and its frequency deviation vs. temperature curve becomes a quadratic function curve in the operating temperature range shown in Fig. 5.15.

For the AT-cut to be used mainly in the MHz frequency range, which vibrates with the thickness share mode, the value of the second-degree temperature coefficient β is around $0.12 \times 10^{-8}/°C^2$, and could be negligible. Therefore, its frequency deviation vs. temperature curve becomes a cubic function curve also shown in Fig. 5.15.[8,9]

The quartz crystal vibrator that has the smallest frequency deviation within the operating temperature range is the NS-GT cut vibrator. Among the vibrators shown in Fig. 5.15, only the NS-GT cut vibrator works with coupled vibration mode. Other vibrators work with single vibration modes. Therefore, we can control the inflection point by designing the coupling condition, and create the NS-GT quartz crystal vibrator that has an extremely small frequency deviation.

Figure 5.16 shows the typical vibration mode of quartz crystal vibrators that have a zero temperature coefficient. There are other vibration modes, but they have not been applied at present, because:

Table 5.6 Resonant frequency temperature coefficients of crystal resonator with zero temperature coefficient

	α	$\beta/10^{-8}/(°C)^2$	$\gamma/10^{-10}/(°C)^3$
+1 °X cut			
Flexural mode (tuning fork)	0	–3.5	+0.37
AT cut			
Thickness shear mode	0	+0.12	+1.0
BT cut			
Thickness shear mode	0	–4.0	–0.95
CT cut			
Contour shear mode	0	–5.8	+0.21
DT cut			
Contour shear mode	0	–1.8	+0.40
NS-GT cut			
Length extensional and width extensional coupling vibration mode	0	–0.05–+0.05	–0.03–+0.03
LQ1T cut			
Lame mode	0	–5.8	+0.2
LQ2T cut			
Lame mode	0	–1.5	+0.3
TT(X1) cut			
Torsional mode	0	–1.5	+0.41
Z cut			
Length extensional mode	0	–3.2	+0.35

- they do not have zero temperature coefficients,
- it is difficult to hold the specimen without interference to the vibration part of element, etc.

It is known that, with the exception of the thickness shear mode, the other six modes shown in Fig. 5.16 have difficulty in holding the specimen. In order to solve this problem, the vibrating part and holding part are unified into one piece. It is very difficult to place the through holes on the vibrating element shown in Fig. 5.17 using only the machinery process. In this case, photolithography technology is used, with fluoride hydrogen as the etchant of quartz crystals.

5.3.2 Major cutting angles (AT-cut and +1°-X-cut) and their vibration

AT-cut thickness shear mode quartz crystal vibrator

Consider the infinite Y-plate (perpendicular to the Y-axis), and determine its thickness $2y_0$, with consistency ρ. Then we can determine its resonant frequency f as below.

$$f = \frac{m}{2(2y_0)}\sqrt{\frac{c'^{D}_{66}}{\rho}} \qquad 5.1$$

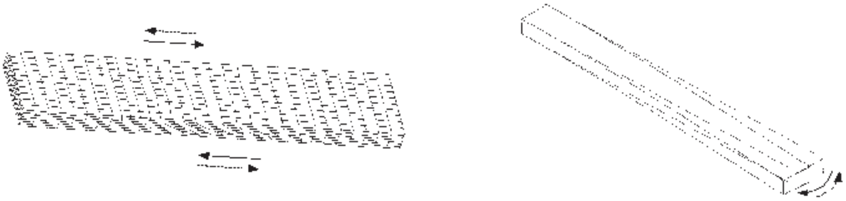

1. Thickness shear mode

2. Flexural mode

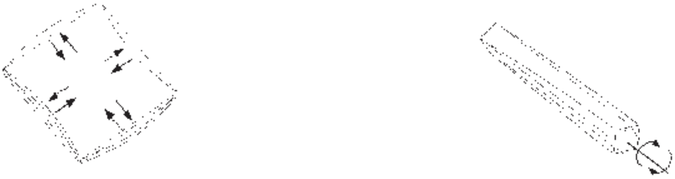

3. Lame mode

4. Torsional mode

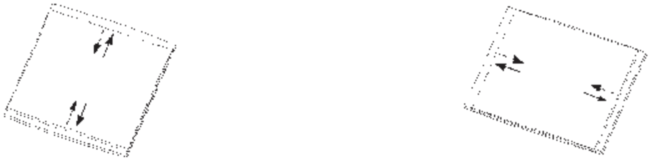

Width-extensional mode
(primary vibrational mode)

Length-extensional mode
(subvibrational mode)

5. Coupling mode which vibrates in the coupled with width-extensional mode and length-extensional mode

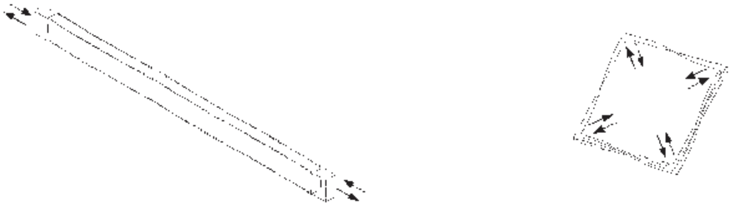

6. Length-extensional mode

7. Face shear mode

5.16 Typical vibration modes of quartz crystal vibrators.

where $$c'^{D}_{66} = c'^{E}_{66} + \frac{e^2_{26}}{\varepsilon'^{S}_{22}}$$

$$c'^{E}_{66} = c^{E}_{66} \cos^2 \theta + c^{E}_{44} \sin^2 \theta + 2c^{E}_{14} \cos\theta \sin\theta$$

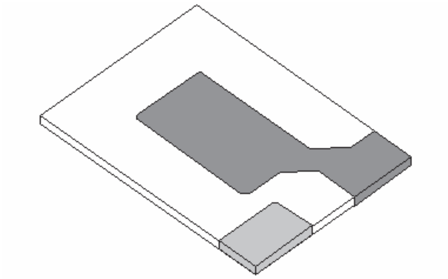

1. Shape of AT (BT) cut thickness shear mode quartz crystal

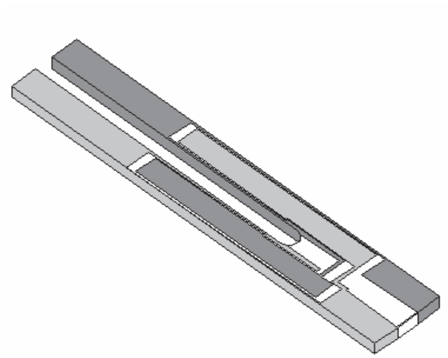

2. Shape of +1° X cut flexural mode quartz crystal

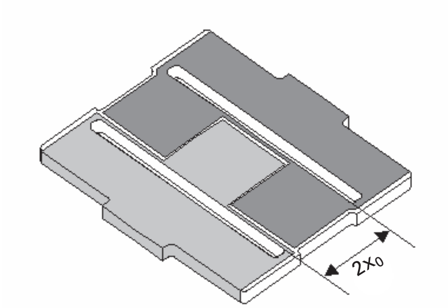

3. Shape of LQ1T (LQ2T) cut Lame mode quartz crystal

5.17 Examples of the shapes of quartz crystal vibrators and their electrodes.

$$e_{26} = -(e_{11}\cos^2\theta + e_{14}\cos\theta\,\sin\theta)$$
$$\varepsilon'^{S}_{22} = \varepsilon^{S}_{11}\cos^2\theta + \varepsilon^{S}_{33}\sin^2\theta$$

θ : Y-plate rotated angle around X-axis
c^E_{66}, c^E_{44}, c^E_{14}: elastic stiffness (under the static electric field)
e_{11}, e_{14}: piezoelectric constants
ε^S_{11}, ε^S_{33}: dielectric constants
m: the constant determined by electrical boundary condition

Therefore, when the angle is rotated $\theta = 35°15'$, the first-order temperature coefficient α becomes zero. This cutting is called the AT-cut, and it has excellent frequency temperature characteristics. It is obvious from Eq. 5.1 that when the cutting angle θ is designed, the resonant frequency is automatically determined by its thickness ($2y_0$) and they are inversely proportional to each other. Equation 5.1 can be approximately written as:

$$f = \frac{c}{2y_0}$$

The frequency of the AT-cut quartz crystal resonator partially depends on the thickness of the electrode. However, this proportional constant c has a value range from 1640 to 1680 MHz · µm. From the calculation above, the AT-cut resonator frequency range is practical from several MHz to over 100 MHz with fundamental vibration.

+1°-X-cut tuning fork quartz crystal vibrator (cantilever, tuning fork)

The resonant frequency of the flexural mode cantilever crystal vibrator with length $2y_0$ along the Y-axis, width $2x_0$ along the X-axis and its consistency ρ, can be written as:

$$f = \frac{m^2}{2\pi \cdot 2\sqrt{3}} \cdot \frac{2x_0}{(2y_0)^2} \cdot \sqrt{\frac{c'_{22}}{\rho}} \qquad 5.2$$

where c'_{22} is elastic stiffness, and m is constant of vibration determined by the boundary condition.

From Eq. 5.2, it is obvious that resonant frequency is determined by the length and width of the cantilever crystal vibrator. For the fundamental vibration, the value of m will be approximately 1.875. Equation 5.2 then becomes:

$$f = c\,\frac{2x_0}{(2y_0)^2}$$

For the +1°-X-cut cantilever crystal vibrator, the value of c (partially depends on mass of electrode) will range between 900 and 950 KHz · mm. The actual resonant frequency of the tuning fork crystal vibrator meets the calculated resonant frequency that uses the length of $2y_0$ when the width of the tuning fork base part is added.

The quartz crystal vibrator plays a very important part in providing a stable frequency. The relationship between the seven vibrating modes shown in Fig. 5.16 and their frequency is described below. In order to understand this relationship, we have to consider the construction of the quartz crystal vibrator. The vibrating crystal element has to be held in midair. Furthermore, the inside of the package sometimes needs to be kept in a vacuum and at other times filled with N_2, etc. Therefore, the package has to be designed with hermetic sealing technology.

From the examples, thickness shear mode and flexural mode crystal vibrators described above, it is clear that the frequency range of these vibrators are determined by the package sizes they use. Thus, we have to design the package size for the required frequency, and the reliability of the vibrator(s). On the other hand, we can choose a suitable vibration mode for the required frequency.

5.3.3 Other cutting angles developed by River Eletec Corporation

Generally, the AT-cut crystal vibrator is applied for the MHz range frequency control and its vibration mode is thickness sheare mode. To miniaturize the vibrators, it is also necessary to miniaturize the vibrating crystal elements. Recently, the typical ceramic package sizes for the surface mounting devices (SMD) are 5.0 × 3.2 mm and/or 3.2 × 2.5 mm. As shown in Section 5.3.2, the resonant frequency of an AT-cut vibrator is determined by its thickness. For example, the thickness of a 4 MHz AT-cut crystal vibrator will be around 0.42 mm, and when we design the 3.2 × 2.5 mm AT-cut SMD vibrator, we have to achieve a crystal element size of around 2.4 × 1.7 × 0.42 mm and put it in the ceramic package. In considering the size of the crystal element, it is very important that the AT-cut vibrator works on the condition that the AT plate is infinite. The closer the element area is to the thickness in its dimension, the more the energy of thickness shear mode will weaken and other unwanted modes will increase. As a result, the vibrator will not satisfy the required specification(s). The bevel process is used to concentrate the vibrating energy to the central area of the AT-cut element, but we have not seen the AT-cut 4 MHz vibrator with a 3.2 × 2.5 mm package.

In miniaturizing the quartz crystal vibrators, the River Eletec Corporation has created a few MHz quartz crystal vibrators with a 3.2 × 2.5 mm package by applying Lame mode vibrating. Figures 5.18 and 5.19 illustrate the Lame mode quartz crystal[10] vibration form. From Fig. 5.18, we can see that there are four nodal points in the corners of the unit crystal element. From Fig. 5.19 we can see that the Lame mode vibrator can be achieved with integral numbers of the unit element to the length direction.

Considering a rectangular Y-plate perpendicular to the Y-axis (mechanical axis) and its length to the X-axis $2x_0(= 2z_0)$, length to the z-axis $2z_0(= 2x_0)$, and consistency ρ, the resonant frequency of this Lame mode vibrator will be:

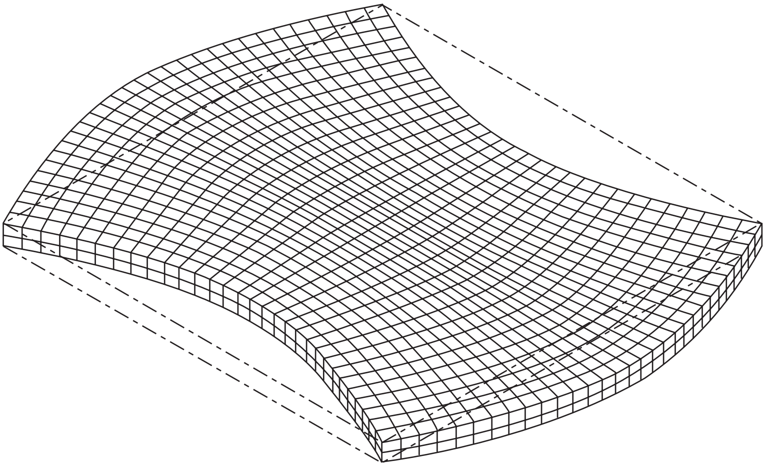

5.18 The fundamental Lame mode quartz crystal.

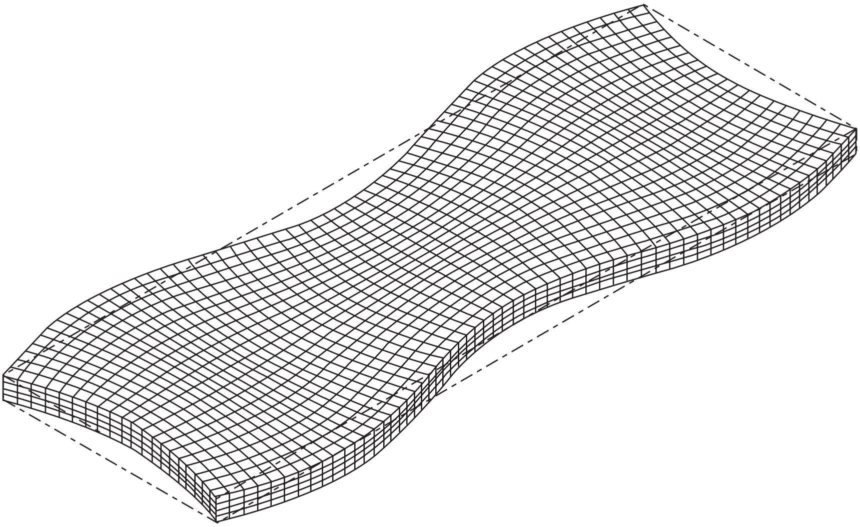

5.19 Integration of the Lame mode quartz crystal.

$$f = \frac{1}{2(2x_0)}\sqrt{\frac{c'_{11} - c'_{13}}{\rho}} = \frac{1}{2(2z_0)}\sqrt{\frac{c'_{33} - c'_{13}}{\rho}} \qquad 5.3$$

where c'_{11}, c'_{13}, c'_{33}, are elastic stiffnesses.

As shown in Fig. 5.14, the Y-plate, rotated $\theta = 36°$ around the X-axis toward the AT-cut direction and again rotated $\phi = 45°$ in the plate, gives LQ1T-cut and its temperature coefficient $\alpha = 0$. The cutting of $\theta = 130°$ and

$\phi = 45°$ gives LQ2T-cut and also its temperature coefficient α will be zero. Comparing second-order temperature coefficient β's shown in Table 5.6, the frequency temperature characteristic LQ2T- cut is superior to the LQ1T-cut, and its second-order temperature coefficient is $-1.7 \times 10^{-8}/°C^2 \cdot S$.

The River Eletec Corporation first developed and commercialized the smallest SMD crystal vibrator, called the LMX-01, which has a resonant frequency range of 3.5–4.5 MHz in the LQ2T-mode. Figure 5.20 shows a comparison of previous AT-cut 4 MHz SMD resonators and the LMX-01 4 MHz SMD resonator. The new resonator has an 87% smaller mounting area, is 96% smaller in volume and is 95% lighter in weight. In spite of this drastic miniaturization, the electric characteristics of LMX-01 compare favorably with previous AT-cut crystal vibrators as shown in Table 5.7 and is compatible with the larger size AT-cut crystal vibrator FCX-01 (already end of life (EOL)).

The shape of crystal element of LMX-01 (LQ2T-cut) is shown in Fig. 5.17 #3, and its dimensions are 2.4 × 1.6 mm with thickness 70 μm. Its cutting angle is shown in Fig. 5.14. In order to satisfy the temperature-frequency characteristic from –10 to +60 °C within +10 to –50 ppm, the cutting angle θ has to be kept 50° ± 30′. Its vibrating frequency is determined mainly by the width of element $2x_0$, and is given from Eq. 5.3 as:

$$f = \frac{K}{2x_0}$$

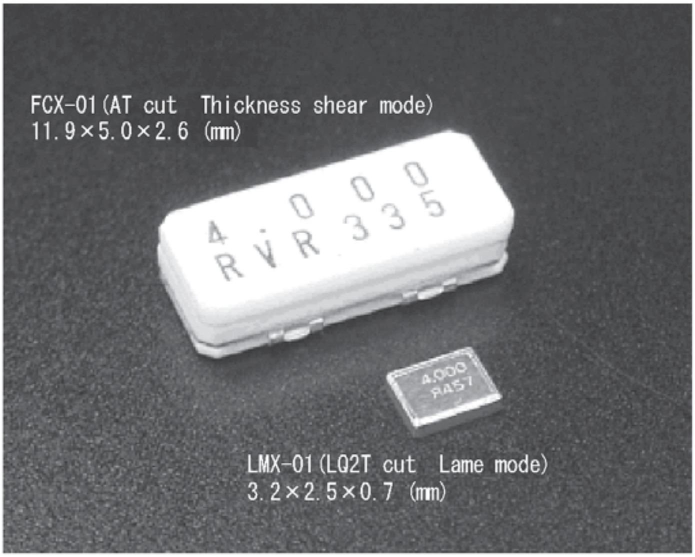
FCX-01 (AT cut Thickness shear mode)
11.9×5.0×2.6 (mm)
4.000
RVR 335
4.000
RA57
LMX-01 (LQ2T cut Lame mode)
3.2×2.5×0.7 (mm)

5.20 Comparison of two packages, LMX-01 and FCX-01, vibrating the same frequency.

Table 5.7 The characteristic compatibility between 4MHz LMX-01 and FCX-01

	LMX-01 (Lame mode)	FCX-01 (Thickness shear mode)
Series resonant frequency, *fr*/MHz	4.00	4.00
Equivalent series resistance, $R1/\Omega$	79	76
Shunt capacitance (include case capacitance), C_0/pF	1.2	1.4
Motional capacitance, C_1/fF	3.5	3.5
Motional inductance, L_1/mH	452	450
Quality factor, *Q*	145,000	149,000
Capacitance ratio (include case capacitance), *r*	400	400

where K is the so-called frequency constant and its value is around 3350 MHz · μm.

At present, only River Eletec Corporation produces and supplies the LMX-01 to the global market. It has very particular applications at this time and several tens of thousands of pieces are produced each month.

5.4 Applications of resonator, oscillator, and filter

5.4.1 Mobile communications

Bluetooth

Bluetooth is a near field communication standard established by the Ericsson Corporation. The industry group Bluetooth-SIG, works mainly to improve this standard and certify applications of the technology. Bluetooth uses the ISM 2.4 GHz band frequency and uses Gaussian frequency shift keying for communication. The communication distance is around 100 m or less.

Bluetooth technology allows wireless communication between electronic devices. The selected profile regulates the flow of information and contains serial, parallel and IP communication as well as IO devices such as keyboards. The same profile must be used for communication between devices. The Bluetooth standard is now frequently used for IO computer devices and wireless headsets for cellular phones. In many cases Bluetooth has all but replaced the need for infrared communication in these devices.

Characteristics of bluetooth

- Standards: Bluetooth Version 1.0b/1.0b+CE/1.1/1.2/2.0/2.1.
- Uses: Near field wireless communication for electronic devices.
- Features: Gaussian frequency shift keying with ISM band.
- Velocity: 3 Mbps maximum (Version 2.1+EDR).

Most devices that use Bluetooth technology integrate the module within the device. This module is driven by the base oscillation of the TCXO/quartz crystal resonator. It is common for cellular phones to use its TCXO for the GSM band processor as the time base. Bluetooth improves these functions and continues to increase its profiles, creating complicated process standards, even with backward compatibility of previous versions. The latest Bluetooth standard, Version 2.1 can reach the full 3 Mbps communication speed by applying the EDR (enhanced data rate) function.

Wireless LAN

The wireless LAN standard, IEEE802.11, was established in 1997. The 802.11 and the 802.11b standards use the 2.4 GHz frequency band and use the Direct Sequence Spread Spectrum Communication System. Their maximum communication speeds are 2 Mbps and 11 Mbps, respectively, and the frequency bandwidth of the channels are arranged partially duplicated to one another. The 802.11a standard uses the 5 GHz frequency band and utilizes the OFDM (orthogonal frequency division multiplexing) applied Direct Sequence Spread Spectrum Communication System with a maximum speed of 54 Mbps. The 802.11g uses the 2.4 GHz frequency band and also has a maximum speed of 54 Mbps. This speed is achieved by using OFDM to the 802.11b base. The 802.11n is a new standard using the frequency band of 5 GHz with a maximum speed of 100 Mbps.

Characteristics of wireless LAN

- Standards: IEEE802.11/11b/11g/11a/11n.
- Uses: Mainly applied for the IP network.
- Features: Spread Spectrum Communication System using ISM band (2.4 GHz/5 GHz).
- Velocity: 2 Mbps to 100 Mbps.

Data volume can be increased proportionally to the quantity of antennas, by simultaneously processing the data based on corresponding information. Based on this, communication speed is expected to be faster using the 5 GHz frequency band. A list of the Wireless LAN standards is shown in Table 5.8.

5.4.2 Cellular phones

One segment/full segment tuners

Digital terrestrial television broadcasting is a digital broadcasting service that uses terrestrial electromagnetic waves. NHK, a leader in digital broadcasting

Table 5.8 List of wireless LAN standards

Standard no.	Frequency band (GHz)	Diffusion/ Modulation	Communication velocity (Mbps)	Note
802.11	2.4	FHSS	2.0	Frequency hopping
802.11b	2.4	DSSS	11	Direct diffusion
802.11a	5.0	DSSS+OFDM	54	Applying OFDM
802.11g	2.4	DSSS+OFDM	54	Expanding .11b and applying OFDM
802.11n	5.0	DSSS+OFDM +MIMO	100	Completed in 2009 and applying MIMO

in Japan, developed the ISDB (integrated services digital broadcasting) standard, based on ISDB-T standard. The frequency range for one channel of analog broadcasting is divided into 13 segments, four of which are used for one channel of standard definition or 12 are used for a channel in high definition. One segment tuners use the one of 13 segments and full segment tuners use the four or 12 segments described above. In Japan, digital TV sets and recording devices contain the digital tuner required to decode the signal. One segment toners are used for smaller displays such as those found in cellular phones and digital media players.

Characteristics of one segment/full segment tuners

- Standard: ISDB-T.
- Uses: Transmitting and receiving digital TV broadcasting.
- Features: Effective use of the limited frequency range and high definition TV transmission.

Quartz crystal vibrators are used for RF receivers and OFDM decoders with the ICs. In most cases, a one crystal vibrator is used that has a commonly required frequency and a recently developed IC chip contains both the RF receiver and OFDM decoder.

The standards of DVB-H, T-DMB and Media FLO are applied in Europe and the USA, while CMMB is applied in China, although not in wide use. Brazil is also planning on adopting Japan's ISDB-T standard for digital terrestrial TV broadcasting. An explanation of frequency occupation with one segment and full segment is shown in Fig. 5.21.

RF module

IEEE 802.15.4 (Zigbee, etc.)

The short range RF communication technology based on IEEE802.15.4 uses the ISM band frequency. The frequency range of 2.4 GHz is allowed for

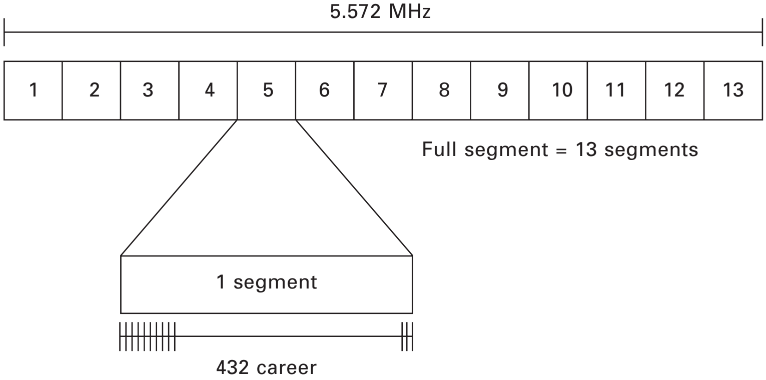

5.21 Explanation of frequency occupation with one segment and full segment.

this technology in Japan and there are other cases using frequency ranges of 800–900 MHz. The RF module, Zigbee contains the protocol which Zigbee alliance certified. This standard settles smaller output power increasing battery life. The Zigbee communication distance is tens of meters and transporting velocity is 250 kbps. To make data relay possible between the clients, not only does the device make direct communication between the two clients but can also use network topology such as star connection, mesh connection, etc. There are 65,535 nodes available for connections and it is possible to sense the position, and communicate between them. Adding a low power consumption CPU or sensor will make it possible for individual data correction from a wide area on an autonomous distributed network.

Characteristics of the RF module

- Standard: IEEE802.15.4.
- Uses: Usually for the near field wireless communications.
- Features: Autonomous distributed networks are available, using the ISM frequency band and low power consumption.
- Velocity: maximum 250 kbps.

There are other similar RF module devices that have protocols not sanctioned by the Zigbee alliance. Some of the devices are used to calculate the data of heart beats, velocity, air pressure, GPS and even some sports goods.

UWB (Ultra wide band)

UWB is a spread spectrum communication technology using a wide frequency band in the 3–4 GHz range. It is best suited for high capacity, fast communication and features low power consumption and strength to external noises. Its communication distance is around ten meters and the quartz crystal vibrator is used as its RF frequency oscillation.

Characteristics of ultra wide band

- Standard: none (abandoned in 2006).
- Uses: Large capacity of data transmitting for very near field.
- Feature: Applied spread spectrum communication using ultra wide band microwave, and used for very near field.
- Velocity: From 100 to 500 Mbps.

In 2006 the ultra wide band standard was abandoned because of various problems and non-conformity. Recently, some of the protocols (transfer-jet, etc.) that were based on UWB have been proposed to make the connections between electronic devices from wired to unwired. This technology has the possibility to popularize the standard if product developers and designers can agree on a common protocol. The serial transfer velocity is from 100 to 500 Mbps, excluding the protocol header.

Secure private cosm (SPC) encryption

Today, various types of personal information are stored on cellular phones, personal digital assistants (PDAs) and other electronic devices, and there is an increasing demand to keep that personal information protected. Secure private cosm is a protection method that permits the device to work only under certain circumstances and become unusable when outside the designated parameters. An example of this technology could use human skin as the encryption key and only function in the hands of certain users. A quartz crystal vibrator would be used for the communication between the key and the device. An image of this action is shown in Fig. 5.22.

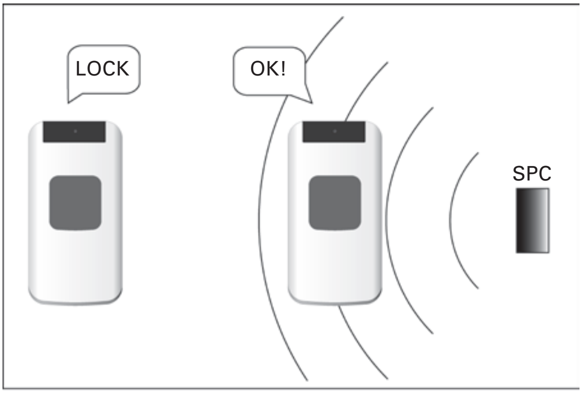

5.22 Image of the SPC action.

Duplexer

Duplexers are commonly used in antennas. They contain a diverging circuit and transmitting/receiving filters that select the required frequency from the widely spread electric wave. While the duplexer separates two waves, a triplexer separates three electric waves. The dielectric resonator and/or SAW (surface acoustic wave) resonator and recently the BAW (bulk acoustic wave) resonator are applications.

IF (intermediate frequency) filter

Cellular phones and other wireless electronic devices such as televisions and radios use a super heterodyne detection system. The electric waves generated in this system are mixed with the aimed/received electric wave and their differential frequency of wave is picked out. This wave (IF) is handled easily with a suitable electric circuit. In order to resolve the noise(s) of the IF wave, quartz crystal, ceramic, and SAW filters are used. Recently, the filters have been used in the IC, and the use of the IF filter has decreased.

Monolithic crystal filter (MCF)

MCF is a filter that has a combined plural quartz crystal resonator and several pairs of electrodes on a single quartz crystal plate. It does not require the winding coil for designing electric circuits. The characteristics of MCF are limited but it can miniaturize and lighten the filter function. Compared with SAW filters, MCF is preferable for narrow band and high Q filters in lower frequency applications. MCF used in band pass filters which have nominal frequency layers from very low MHz to some hundreds of MHz and a bandwidth from tens of KHz to hundreds of KHz similar to RF communication and wired transfer devices. MCF is frequently used in cellular phone applications.

Camera module

The camera modules used in cellular phones consist of smaller sized CCD or CMOS optical lenses. These applications require miniaturization and high definition, auto focus functions. High-end cameras contain optical zoom functions which require special circuits for driving the optical lenses and focus adjustment feedback. A quartz crystal vibrator is used to drive the CCD or CMOS camera and is also used for controlling these circuits.

5.4.3 Automotive applications

Navigation (GPS)

GPS (global positioning system) can locate your exact longitude and latitude position on the ground. It calculates and shows your current location using the time difference of the signals from the orbit of 30 satellites that are controlled by the US army and other commercial companies. The plane point on the ground is calculated by the information from three of the satellites and the 3D point is calculated by the information from four of these satellites. Each satellite has an atomic clock and a very precise time is transmitted to earth. The signals from these satellites are transmitted using pulse diffusion communication technology, received by antenna and then the current position can be calculated. This technology requires very accurate time base and TCXO in the receiving circuit.

Car navigation systems show route information to your destination using GPS information. It can show the shortest and the most suitable way to get to your destination by using the present point data and destination point data on the map. High end car navigation systems also include other functions such as audio, TV, DVD player, outside CCD camera.

Smaller, less expensive, portable car navigation systems that can be used between multiple cars and also as a PND (personal navigation device) for other modes of travel are becoming popular.

Car audio/video system

The staple of the car audio system has been the radio receiver. The media have changed and improved throughout the years from cassette players to CD and MD and now other forms of media. Current systems allow not only audio playing, but also TV and DVD viewing. Many of these systems also contain hard disk drives, providing increased storage for media and navigation systems and provide digital data through the LCD. A quartz crystal vibrator was used for the original radio analog tuner, but these advanced systems now use plural quartz crystal vibrators.

Keyless entry

Keyless entry systems are used to remotely lock, unlock and start your car's engine using RF signals. There are two types of keyless entry systems: active and passive. Active systems send a signal to the receiver in the car, and the system disarms. Passive systems transmit the signal and will receive and require a response signal from the key, before the system disarms. The RF modules are used in both the transmitting and receiving circuits and communication between these circuits are coded. Quartz crystal vibrators are used in these RF modules.

Laser/millimeter wave radar

The next generation of traffic control systems is being developed by many automotive companies throughout the world. These systems will avoid traffic accidents by using laser/millimeter wave radar technology. An applied example of this technology could allow a vehicle to be controlled by markers buried along the road which would receive the reflection of laser or millimeter waves that were being transmitted from the vehicle. The distance between vehicles can also be measured by laser/millimeter wave radar techniques and help prevent collisions. Quartz crystal vibrators are used for the base of these waves and for the information treatment circuit.

Body control module

The body control module (BCM) is the main computer in a vehicle that supervises all of the car's electronic systems. Modern vehicles use electricity for many systems including starting the engine, fuel control, lighting and others that play a critical role in controlling the vehicle. Every electric circuit is required to work under extremely severe conditions and a wide range of temperatures. These systems are required to work reliably for the life of the vehicle.

5.4.4 Other applications

Medical instruments

Capsule endoscopes

Capsule endoscopes are a type of endoscope that are stored and sealed in a 10–30 mm diameter capsule. The patient swallows this capsule and it takes internal pictures of the digestive tract on its way down. This new method reduces the pain over tradition endoscope procedures for the patient. The capsule contains a battery, RF communication circuit, lighting LED and CCD camera and takes a picture every few seconds, resulting in tens of thousand of pictures during the process. These pictures are immediately transmitted by RF to an external receiver. Other than swallowing the capsule, there is no other action required of the patient. Quartz crystal vibrator/oscillators are used in these endoscopes for driving the CCD camera and RF communication circuit.

Capsule endoscopes can take pictures of the small intestine where traditional fiber endoscopes could not reach. Each year, tens of thousands of capsule endoscope procedures are performed in Europe and the US and is increasing in frequency. The Ministry of Welfare in Japan permitted the use of the foreign-made capsule endoscopes in 2008 and some medical facilities could

5.23 Capsule endoscope.

introduce this test in the near future. It is expected to enlarge the market for capsule endoscopes. An image of a capsule endoscope is shown in Fig. 5.23.

Blood sugar level sensors

Blood sugar level sensors allow diabetic patients to know when they require an insulin injection. These devices are direct contact (the sensor has to directly contact blood). Indirect contact devices observe the electromagnetic wave through the blood tube. Scientists are developing a device that would combine the indirect contact sensor and insulin injection mechanism.

Near field communications

Near field communications (NFC) is an international standard for near field RF communication that uses one of the ISM frequency bands around the 13.56 MHz range. NFC consists of two integrated systems called FeliCa and MIFARE. FeliCa was proposed by SONY and is widely supported in Asia. MIFARE was proposed by Philips and has widespread usage in Europe and the US. NFC is used in the no contact-type IC card, set to replace traditional magnetic cards.

Characteristics of near field communications

- Standard: ISO/IEC IS 18092.
- Use: Near field wireless communications between devices.
- Feature: Low power consumption and use 13.56 MHz.
- Velocity: 424 Kbps max.

Many applications are expected to use the NFC compatible standard that require low capacity data communications between electronic devices.

5.5 Acknowledgements

I would like to express my sincere gratitude to Dr Yasuhiko Nakagawa, Professor at Yamanashi University, Mr Katsuya Mizumoto, River Eletec Corporation R&D, and Mr. Kazuki Aoshima, River Eletec Corporation R&D, for their many helpful discussions.

5.6 References

1. Koga, I 1938, *Piezoelectricity and high frequency*, Ohm-sya.
2. Sykes, RA 1946, *Quartz crystal for electrical circuits,* Heising edn., D. Van Nostrand Company Inc.
3. Shinada, T, *Theory and the facts of quartz crystal*.
4. Yanagida, H & Nagai, M 1993, *The Science of ceramic*, Gihodo.
5. QIAJ Technical Committee 2007, 'The explanation of quartz crystal devices and its applications', *The Meiden media front*.
6. Kawashima, H, 'The base of quartz crystal resonator', *The Ultrasonic Techno serialized report*.
7. Maruzen 1999, 'The ultrasonic handbook editing committee' *Ultrasonic Handbook*.
8. Ariga, M 1956, 'Isothermal elastic constants of quartz crystal and its temperature characteristics', *Tokyo Institute of Technology Report*, A–2, pp. 88–182.
9. Bechmann, R, Ballato, AD & Lukaszek, TJ 1962, 'Higher-Order Temperature Coefficients of the Elastic Stiffnesses and Compliances of Alpha-Quartz', *Proceedings of The IRE*, vol. 50, issue 8, pp. 1812–1822.
10. Kawashima, H & Matsuyama, M 1996, 'Analyses of double rotated Lame mode piezoelectric resonator with Energy method', *The Institute of Electronics Information and Communication Engineers Paper A*, vol. J79-A, no. 6.

6

Lithium niobate and lithium tantalate-based piezoelectric materials

V. YA. SHUR, Ural State University, Russia

Abstract: This chapter discusses the influence of the tailored periodical nano- and micro-domain structures on the piezoelectric properties of $LiNbO_3$ and $LiTaO_3$ crystals. The chapter first reviews the main piezoelectric characteristics of $LiNbO_3$ and $LiTaO_3$ crystals and acoustic properties of the crystals with periodic laminar domain structure. The chapter then discusses the physical basis of nano- and micro-domain engineering in $LiNbO_3$ and $LiTaO_3$ crystals and application of the periodically poled $LiNbO_3$ and $LiTaO_3$ for light frequency conversion and generation of terahertz radiation.

Key words: light frequency conversion, tailored periodical domain structure, generation of acoustic waves, nanoscale domains, generation of terahertz radiation.

6.1 Introduction

Lithium niobate ($LiNbO_3$) and lithium tantalate ($LiTaO_3$) crystals are not encountered in nature and are man-made. The single crystals of $LiNbO_3$ and $LiTaO_3$ were synthesized for the first time in Bell Laboratories and their ferroelectric properties were revealed by Matthias and Remeika (1949). Both crystals have an ilmenite structure. Ilmenite ($FeTiO_3$) is a mineral named after its provenance in the Ilmen Mountains, Southern Urals, Russia. It looks like a black crystal with trigonal (rhombohedral) symmetry (space group R3).

It is not easy to recognize that lithium niobate $LiNbO_3$ is being referred to in the first paper, as there it has been called lithium columbite $LiCbO_3$. The element niobium had two names niobium and columbium, for about century after its discovery. Niobium (Nb) was officially adopted as the name of the element in 1949.

Niobium (Nb) has physical and chemical properties similar to those of tantalum (Ta), and the two are therefore difficult to distinguish. The English chemist Charles Hatchett reported a new element similar to tantalum in 1801, and named it columbium. In 1809, the English chemist William Hyde Wollaston wrongly concluded that tantalum and columbium were identical. The German chemist Heinrich Rose determined in 1846 that tantalum ores contain a second element, which he named niobium. In 1864 and 1865, a series of scientific findings clarified that niobium and columbium were the same element, and for a century both names were used interchangeably.

The ferroelectricity of $LiNbO_3$ and $LiTaO_3$ was studied from a theoretical viewpoint by Schweinler (1952) using the Slater method proposed for $BaTiO_3$. The properties of $LiNbO_3$ and $LiTaO_3$ have been studied systematically after a delay of about 15 years when Ballman (1965), Fedulov *et al.* (1965) and Nassau *et al.* (1966) independently succeeded in growing large $LiNbO_3$ single crystals using the Czochralski technique. The results of detailed investigation of their structure and properties were reviewed by Smith and Welsh (1971) and Weis and Gaylord (1985).

Both $LiNbO_3$ and $LiTaO_3$ are well known for their low acoustic losses and are thus excellent materials for surface acoustic wave (SAW) devices, occasioning a commercial growth of several tonnes every year. Nowadays $LiNbO_3$ is widely used in various devices which exploit its superior elastic, piezoelectric, dielectric, acousto-optic, electro-optic, pyroelectric, photoelastic and photovoltaic properties.

$LiNbO_3$ possesses very large electro-mechanical coupling coefficients, which are several times larger than in quartz, and very low acoustic losses. Because of its Curie temperature of 1142 °C, it can be utilized as a high temperature acoustic transducer, such as an accelerometer for jet aircraft. Acoustic wave delay lines and acousto-optic modulators, deflectors and filters now routinely employ $LiNbO_3$ for both shear and longitudinal wave generators because of its high efficiency, broad bandwidth capability, low dielectric constant for all orientations, and consistent repeatability. $LiNbO_3$ possesses a number of useful cuts which are now extensively used in transducer applications. Two longitudinal cuts are popular, the z-cut and the 36° rotated y-cut. The shear mode cuts most commonly used are the x-cut and 163° rotated y-cut.

$LiTaO_3$ also possesses useful cuts for longitudinal and shear wave mode transducers. The two most popular longitudinal cuts are the z-cut and the 47° rotated y-cut, while the x-cut and the 165° rotated y-cut are the most commonly used shear mode cuts. Compared to quartz, $LiTaO_3$ has a much larger electro-mechanical coupling and a number of zero temperature coefficient cuts of resonant frequency. As a result, it finds application in communications for acoustic resonator filters of broad bandwidth.

In recent decades both crystals have become the most important objects of domain engineering. The main target of the domain engineering is the improvement of the characteristics of commercially available ferroelectrics by manufacturing of stable tailored domain patterns (periodic poling). The creation of a stable periodic domain structure allows the introduction of the spatial modulation of the piezoelectric, electro-optic, photorefractive, and nonlinear optical properties thus upgrading the device performance. The low price of these devices achieved under mass production based on periodic poling by electric field will expand this technology into wider markets.

The optimization of the poling process resulted from the fundamental studies of the domain kinetics is expected to enable the fabrication of submicron-pitch gratings and engineered 1D and 2D structures, which could meet the demanding specifications for acoustic and nonlinear optical applications. The ultimate interest is the exploitation of nanoscale domain structures and the precise periodical microscale structures with nanometer accuracy. For example, for achieving high conversion efficiency of laser light the structure has to be precisely reproducible with the period dispersion about 10 nm.

6.2 Piezoelectric properties of lithium niobate and lithium tantalate

$LiNbO_3$ and $LiTaO_3$ are colorless, chemically stable, insoluble in water and organic solvents, ferroelectric crystals which possess very high melting points and Curie temperatures. Both crystals can be grown by the Czochralski technique, thus large, high-quality single crystals in a number of different growth directions are available.

The general properties of $LiNbO_3$ and $LiTaO_3$ not related to piezoelectric effects are given in Table 6.1. Although sometimes several digits for a value are published, a scatter of more than 10% is found in the literature. Therefore, the values should be regarded as examples for the order of magnitude of the respective property (Volk and Woehlecke, 2009).

$LiNbO_3$ and $LiTaO_3$ structures below Curie temperature consist of planar sheets of oxygen atoms in a distorted hexagonal close-packed configuration (see Fig. 6.1). The octahedral interstices formed in this structure are one-third filled by lithium ions, one-third filled by niobium/tantalum ions, and one-third vacant. In the paraelectric phase (above the phase transition point), the Li atoms lie in an oxygen layer that is c/4 away from the Nb/Ta atom, and the Nb/Ta atoms are centered between oxygen layers. These positions make the paraelectric phase non-polar (Weis and Gaylord, 1985) (see Fig. 6.1a). Below the phase transition point, the lithium and niobium ions shift

Table 6.1 Main physical properties of $LiNbO_3$ and $LiTaO_3$

Property/materials	$LiNbO_3$	$LiTaO_3$	Ref.
Melting point (°C)	1255	1650	(Nikogosjan, 2005)
Mohs hardness	~ 5	~ 5.5	(Nikogosjan, 2005)
Lattice constant a_H (pm)	515.0	515.4	(Furukawa *et al.*,1999)
Lattice constant c_H (pm)	1386.4	1378.1	(Furukawa *et al.*,1999)
Density (g cm^{-1})	4.64	7.454	(Smith and Welsh, 1971)
Curie temperature (°C)	1140	605	(Nikogosjan, 2005; Chen *et al.*, 2001)
Spontaneous polarization P_s (μC cm^{-2})	71	60	(Chen *et al.*, 2001; Kitamura *et al.*, 1998)

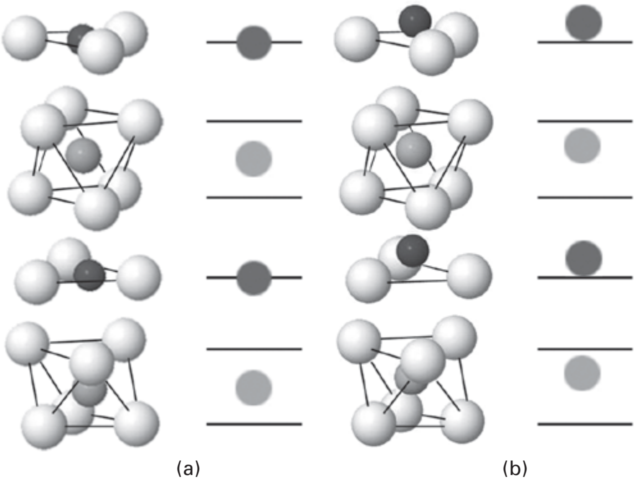

6.1 Positions of the lithium atoms (black circles) and the niobium atoms (gray circles) with respect to the oxygen octahedra of $LiNbO_3$ (a) paraelectric phase ($T > T_c$), (b) ferroelectric phase ($T < T_c$). The horizontal lines in the diagram represent the oxygen layers (Weis and Gaylord, 1985).

into new positions (see Fig. 6.1b). The charge separation resulting from the ions shift relative to the oxygen octahedra leads to exhibition of spontaneous polarization. Thus, $LiNbO_3$ and $LiTaO_3$ belong to a broad class of displacement ferroelectric similar to $BaTiO_3$.

The structures of $LiNbO_3$ and $LiTaO_3$ at room temperature belong to the rhombohedral (trigonal) space group R3c, with point group 3m. Above the phase transition temperature both crystals transform to the centrosymmetric space group R3m. The positions of the lithium and niobium ions in both the paraelectric and ferroelectric phases are shown in Figs 6.2 and 6.3. It is known that the setting of the crystallographic axes for the trigonal symmetry is not unambiguous, thus three types of elementary cells can be chosen, namely, rhombohedral, hexagonal, and orthohexagonal cells (see Figs 6.2 and 6.3). The former two are considered more convenient for crystallographic aims and structure determination (Volk and Woehlecke, 2009).

For most applications, the orthohexagonal setting is preferred and the tensor components of properties are given with respect to these axes. In orthohexagonal setting, all axes are mutually orthogonal. Their directions according to standards of piezoelectric crystals (IRE, 1958) are settled in the following way:

- Z is the threefold axis
- Y axis lies in the mirror plane
- X axis is orthogonal to both of them (see Fig. 6.3a).

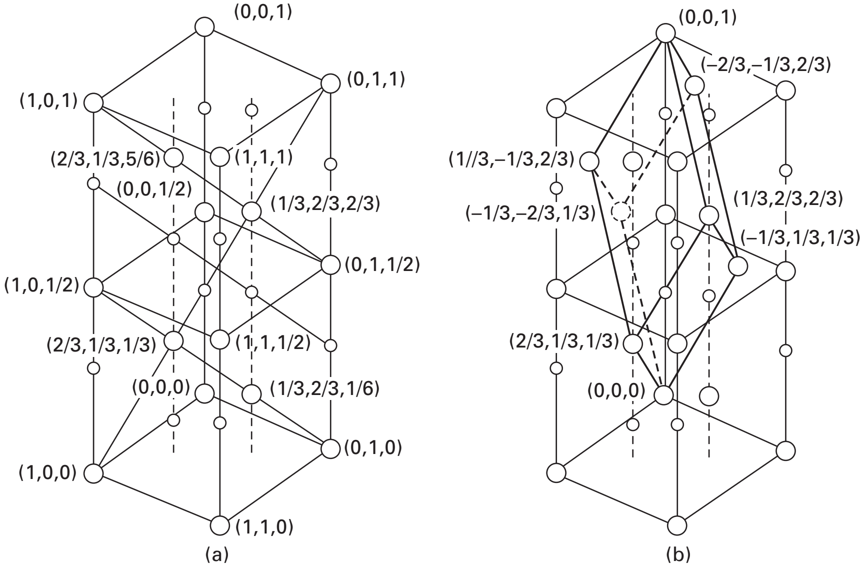

6.2 (a) Hexagonal unit cell of $LiNbO_3$ with positional coordinates of lithium and niobium atoms indicated. (b) Conventional rhombohedral unit cell of $LiNbO_3$ shown with respect to the hexagonal unit cell (Weis and Gaylord, 1985).

Both Z and Y axes are polar (piezoelectric) and by convention their positive ends correspond to the appearance of the negative charge under a uniaxial compression. Additionally, the Z-axis is pyroelectric; by convention its positive end corresponds to the appearance of a positive charge during crystal cooling. The X-axis in this setting is non-polar.

The axes orientations relative to the crystal boule (grown in the Z direction) are shown in the Fig. 6.3b. Additionally, the orientations of the domain walls of the isolated domain for congruent $LiNbO_3$ (CLN) (see Fig. 6.3c) and congruent $LiTaO_3$ (CLT) (see Fig. 6.3d) arising under ‘equilibrium switching conditions’ (Shur, 2006) are presented. Both hexagonal and triangular domain shapes are observed in these crystals during usual slow ‘quasi-equilibrium’ polarization reversal. It must be pointed out that the strict orientation of the domain walls along crystallographic directions is very useful for periodic poling. The domain shape in $LiNbO_3$ and $LiTaO_3$ is strongly dependent on the depolarization field compensation (screening effectiveness) during polarization reversal (Shur *et al.*, 2002b; Shur, 2006; Lobov *et al.*, 2006).

A piezoelectric solid exhibits an induced polarization with applied stress. The linear relationship between induced polarization ΔP_i, the so-called direct piezoelectric effect, can be written as:

$$\Delta P_i = \sum_{jk} d_{ijk}\sigma_{jk} \tag{6.1}$$

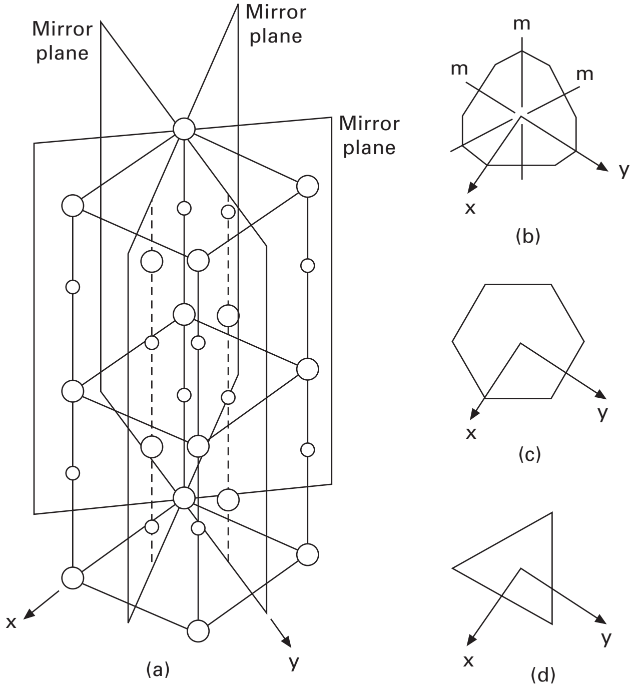

6.3 (a) Standard orientation of the principal axes used to describe tensor physical properties in $LiNbO_3$. Standard orientation of the principle axes relative to: (b) crystal boule, (c) hexagonal domain in congruent $LiNbO_3$, (d) triangular domain in congruent $LiTaO_3$.

where d_{ijk} is the third-rank piezoelectric tensor symmetrical over the last two indices and σ_{jk} is the second-rank stress tensor.

According to standard symmetry considerations, the piezoelectric effect in $LiNbO_3$ and $LiTaO_3$ possessing trigonal symmetry (point group *3m*) is fully described by four independent piezoelectric coefficients (Nye, 1985). In contracted notation:

$$[d_{ijk}] = \begin{bmatrix} 0 & 0 & 0 & 0 & d_{15} & -2d_{22} \\ -d_{22} & d_{22} & 0 & d_{15} & 0 & 0 \\ d_{31} & d_{31} & d_{33} & 0 & 0 & 0 \end{bmatrix} \qquad 6.2$$

If we choose strain as the independent variable, then the induced polarization due to the piezoelectric effect would be proportional to strain magnitude:

$$\Delta P_i = \sum_{jk} e_{ijk} u_{jk} \qquad 6.3$$

where e_{ijk} is the third-rank tensor symmetric over the last two indices and u_{jk} is the second-rank strain tensor.

Accordingly, there exists a converse piezoelectric effect which linearly couples induced strain Δu_{jk} and applied external electric field E_i. It can be shown that the coefficients relating stress and induced polarization in direct piezoelectric effect are the same as the ones relating induced strain and applied electric field in the converse piezoelectric effect.

$$\Delta u_{jk} = \Sigma_i\, d_{ijk} E_i \tag{6.4}$$

This equality is easily understood if we carry out the following 'thought' experiment: let us apply external compressive force to a piezoelectric slab. If the piezoelectric effect were absent, the work of compressive force would be equal to the potential energy of the elastically deformed sample. Due to the piezoelectric effect the charges are induced on the slab surfaces and the electric field is generated in the bulk. It means that the total deformed sample energy increases by the stored energy of the electric field and thus we are to do additional work to compress the piezoelectric, or in other words the additional, forces resisting compression in the sample. These forces are thus the manifestation of the converse piezoelectric effect. It is clear that, if the same charges as in the direct effect are generated on the slab surfaces by external electric field, the sample will stretch out. We can arrive at the same result considering thermodynamics of piezoelectric material under the action of external field and deformations. Choosing electric field E_i and strain u_{ij} as independent variables, the variation of the free energy of piezoelectric δF is given by the expression (Landau and Lifshitz, 1960):

$$\delta F = -\sum_{i} D_i \delta E_i - \sum_{ij} u_{ij} \delta\sigma_{ij} - \sum_{ijk} d_{ijk} \delta E_i \sigma_{jk} \tag{6.5}$$

Using definition $D_i = -\partial F/\partial E_i$ and $u_{ij} = -\partial F/\partial\sigma_{ij}$ we arrive at the stated above result. Alternatively, if the sample is clamped and cannot deform, the converse piezoelectric effect reveals itself as the appearance of additional mechanical stress in the sample under application of external electric field.

It is known that the temperature behavior of ferroelectrics in most cases is fairly well described by the Ginsburg–Landau–Devonshire theory. According to this theory only effects of the second order (electrostrictive coupling between the polarization and strain/stress) exist in the paraelectric proto-phase. It means that in the expansion of free-energy only terms of the type $Q_{ijkl}P_iP_ju_{kl}$ emerge. When structural transition to the ferroelectric phase occurs, the component of polarization along the polar axes P_z 'stiffens' and turns into spontaneous polarization P_s. Thus the third-rank piezoelectric constants appear. It is clear that due to their history the sign of these constants is dependent on spontaneous polarization orientation. In antiparallel domains the relative signs of all piezocoefficients are opposite.

This property is very useful in making it possible to induce required spatial variations in stress/strain by tailored domain structure and also is the basis of high-resolution domain observation by piezo response mode (PRM) of scanning probe microscopy (SPM).

The experimentally obtained values of piezoelectric coefficients for $LiNbO_3$ and $LiTaO_3$ are listed in Table 6.2 (Smith and Welsh, 1971). The measurements of these coefficients present a formidable task (Ogi *et al.*, 2002). One of the experimental methods of obtaining the required data is based on the ultrasonic phase velocity measurements coupled with low-frequency capacitance measurements for dielectric constants (Smith and Welsh, 1971).

It must be understood that piezoelectric properties are interconnected with elastic and dielectric properties of the investigated material. The acoustic experiments yield simultaneously the values of elastic stiffness coefficients C_{ijkl} and compliance coefficients s_{ijkl} (six independent coefficients in crystals with 3m point-group symmetry).

$$[C_{\mathrm{ij}}] = \begin{bmatrix} C_{11} & C_{12} & C_{13} & C_{14} & 0 & 0 \\ C_{12} & C_{11} & C_{13} & -C_{14} & 0 & 0 \\ C_{13} & C_{13} & C_{33} & 0 & 0 & 0 \\ C_{14} & -C_{14} & 0 & C_{44} & 0 & 0 \\ 0 & 0 & 0 & 0 & C_{44} & C_{14} \\ 0 & 0 & 0 & 0 & C_{14} & (C_{11} - C_{12})/2 \end{bmatrix}$$

$$[s_{\mathrm{ij}}] = \begin{bmatrix} s_{11} & s_{12} & s_{13} & s_{14} & 0 & 0 \\ s_{12} & s_{11} & s_{13} & -s_{14} & 0 & 0 \\ s_{13} & s_{13} & s_{33} & 0 & 0 & 0 \\ s_{14} & -s_{14} & 0 & s_{44} & 0 & 0 \\ 0 & 0 & 0 & 0 & s_{44} & 2s_{14} \\ 0 & 0 & 0 & 0 & 2s_{14} & 2(s_{11} - s_{12}) \end{bmatrix}$$

The values of elastic and dielectric constants are listed in Table 6.3.

It must be mentioned that the strong piezoelectric effect leads to a large difference between the resonance frequencies in $LiNbO_3$ and $LiTaO_3$ predicted by elastic theory and those accounting for the piezoelectric effect. This is due to the large contribution of the field produced by the surface charges induced through the piezoelectric effect into the stiffness coefficients.

Table 6.2 Piezoelectric coefficients for $LiNbO_3$ and $LiTaO_3$ (Smith and Welsh, 1971)

Piezoelectric coefficients/materials	$LiNbO_3$	$LiTaO_3$
Piezoelectric strain constants – d_{ij} (pC/N)		
d_{15}	69.2	26.4
d_{22}	20.8	7.5
d_{31}	– 0.85	– 3.0
d_{33}	6.0	5.7
Piezoelectric stress constants – e_{ij} (C/m^2) (at 25 °C),		
e_{15}	3.76	2.72
e_{22}	2.43	1.67
e_{31}	0.23	–0.38
e_{33}	1.33	1.09

Table 6.3 Elastic and dielectric coefficients for $LiNbO_3$ and $LiTaO_3$ (Smith and Welsh, 1971)

Elastic/dielectric coefficients/materials	$LiNbO_3$	$LiTaO_3$
Elastic stiffness constants – c_{ij} (10^{11} N/m^2) (in constant electric field, at 25 °C)		
c_{11}	2.03	2.298
c_{12}	0.573	0.44
c_{13}	0.752	0.812
c_{14}	0.085	–0.104
c_{33}	2.424	2.798
c_{44}	0.595	0.968
Elastic compliance constants – s_{ij} (10^{-12} m^2/N) (in constant electric field, at 25 °C)		
s_{11}	5.831	4.93
s_{12}	–1.15	–0.519
s_{13}	–1.452	–1.28
s_{14}	–1.00	0.588
s_{33}	5.026	4.317
s_{44}	17.1	10.46
Dielectric constants – ε_{ij} (x 10^{-9} F/m)		
$\varepsilon_{11\ (S)}$	0.392	0.377
$\varepsilon_{33\ (S)}$	0.247	0.379
$\varepsilon_{11\ (T)}$	0.754	0.474
$\varepsilon_{33\ (T)}$	0.254	0.384

6.3 The advantages of single crystal ferroelectrics for piezoelectric applications

Most of commercially available piezoelectric actuators are based on ferroelectric ceramics with random orientation of the grains. Nevertheless, single crystal actuators possess higher energy density due to the fact that the crystals can be oriented along proper higher-strain crystallographic directions.

The $LiNbO_3$ and $LiTaO_3$ crystals used for ultrasonic device applications are commonly poled near the Curie temperature into a stable single domain state. As a result, a uniform, highly consistent piezoelectric transducer crystal with 'frozen' single domain state is obtained.

Recently the strong influence of the domain walls on the piezoelectric and acoustic properties presented a problem for creating the periodic domain structures in $LiNbO_3$ and $LiTaO_3$. The production of tailored domain patterns with desirable geometrical parameters is impossible without deep understanding of the physical basis of domain engineering.

In single crystalline $LiNbO_3$ and $LiTaO_3$ all advantages of domain engineering can be realized. It is possible to achieve an extremely high concentration of the domain walls and to control their orientation along crystallographic directions. The important input of the tailored charged domain walls in dielectric permittivity has been observed in $LiNbO_3$ crystals (Shur *et al.*, 2000b). This is the clear demonstration of the reversible hysteresis-free motion of the domain walls as a whole. Such hysteresis-free motion is very important for piezoelectric devices. The field induced shift of the domain walls depends on the spatial distribution of the screening charges which compensate the depolarization field. The existence of the surface intrinsic non-ferroelectric layer leads to incomplete compensation of the depolarization field even in short-circuit ferroelectric capacitor (Shur *et al.*, 2000b). The retardation of the bulk screening of the residual depolarization field leads to spontaneous backswitching in $LiNbO_3$ and $LiTaO_3$ after external field switch-off, which reconstructs the initial domain pattern. This effect is most pronounced in $LiNbO_3$ and $LiTaO_3$ due to the extremely low value of bulk conductivity and the record high value of spontaneous polarization. As a result the hysteresis-free motion of the domain walls is observed in the wide range of the applied electric field magnitudes.

It looks like the tailored periodic 1D and 2D domain structures in congruent $LiNbO_3$ (CLN) and $LiTaO_3$ (CLT) are very stable due to the extremely high value of the coercive field (above 210 kV/cm). However, the domain structures in periodically poled LN (PPLN) and LT (PPLT) are stable at constant temperature only and it is necessary to be careful with heating and cooling. The high value of pyroelectric coefficients produces a high pyroelectric field during heating/cooling which can destroy the tailored domain structure.

6.4 The influence of the periodic domain structure on piezoelectric and acoustic properties

The idea to optimize the piezoelectric properties of ferroelectrics by creation of the stable tailored domain structures was advanced more than thirty years ago by Robert Newnham and Eric Cross with coauthors (Newnham *et al.*, 1975). They wrote about tailored domain patterns in piezoelectric crystals and discussed the possibility of modifying the properties of the crystal by creating ‘domains which are not to be switched during device operation’. The main area of application was related to piezoelectric devices. The authors believed that the domain structure should be added to the list of important factors, which can be manipulated in selecting a desired resonance pattern along with boundary conditions and electrode configurations. They pointed out that the arising of the domain walls (twinning) ‘is generally considered to be a nuisance which detracts from the performance of a piezoelectric oscillator, but this need not be so.’ They claimed that ‘if the domain structure is properly designed, the resonant frequency spectrum can be adjusted to enhance or eliminate certain modes. Normally forbidden modes can be generated in this way, and very high frequency modes become possible’ (Newnham *et al.*, 1975).

It is necessary to mention the independent development of the alternative branch of domain engineering dealing with creation of the periodical domain structures in the nonlinear optical ferroelectric crystals for achievement of the quasi-phase-matching (QPM) for light frequency conversion, in the first place for second harmonic generation (SHG) (Byer, 1997).

The enhancement of piezoelectric properties in the multi-domain state as compared with the single domain one is due in general to two main factors: contribution from the domain walls which are absent in single domain crystals and strong orientation dependence. This leads to the ability to control the acoustic characteristics of single crystals.

The acoustic properties of the $LiNbO_3$ and $LiTaO_3$ crystals with periodic laminar domain structure named ‘acoustic superlattices’ (ASL) were investigated theoretically and experimentally in the series of works by Zhu *et al.* (1988a, 1988b, 1989) and Zhu and Ming (1992). The structures with period in the range of several micrometers can find useful application in high frequency bulk-wave acoustic devices. Two types of 1D laminar periodic structures of 180° domains were considered: ‘in-line system’ aligned along optical axes composed of tail-to-tail and head-to-head domains, and ‘cross-field system’ aligned normal to optical axes (see Fig. 6.4). As already discussed, the adjacent domains possess the opposite sign of the piezoelectric tensor. The spatial discontinuity of piezo-coefficients at the domain walls plays the role of sound sources under application of the external alternating electric field. Neglecting the domain wall width as compared with the excited sound wavelength, these sources can be treated as delta-like. If constructive interference of the waves emitted by these sources can be achieved then the acoustic power emitted by the ASL is proportional to the square of the domain number.

The promising advantages of ASL lie in the fact that the main resonance

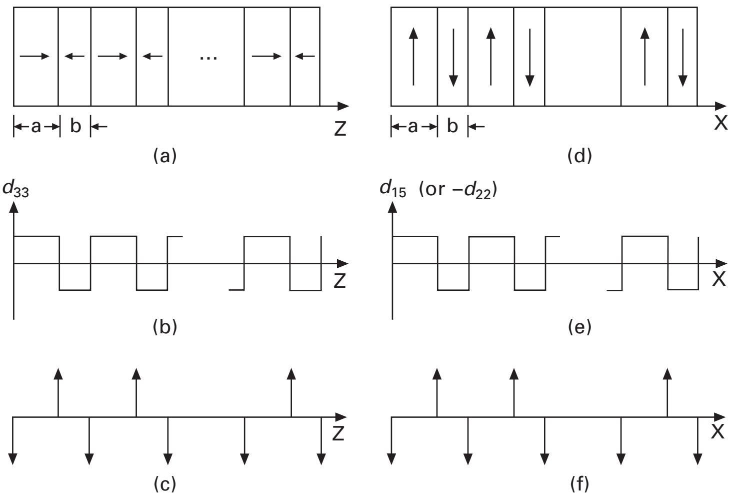

6.4 Acoustic superlattices in $LiNbO_3$: (a)–(c) 'in-line system' aligned along optical axes composed of encountering domains, (d)–(f) 'cross-field system' aligned normal to optical axes: (a), (d) schematic diagram with arrows indicating the directions of the spontaneous polarization; (c), (f) corresponding sound sources; piezoelectric coefficient as a function of (b) z, (e) x.

frequency, determined solely by the period of domain structure, is independent of the sample sizes. In single domain crystal the thickness of the resonator is about acoustic wavelength. Thus the resonators for several hundred MHz have to possess dimensions that are beyond existing common processing techniques (Fig. 6.5) (Wan *et al.*, 2000).

Theoretically main and satellite-like types of resonance are predicted. The main resonance frequency is given by $f_n = nf_a$, where fundamental frequency $f_0 = v/(a + b)$, a and b are the thicknesses of positive and negative domains respectively, and v is the velocity of excited sound wave. The satellite-like resonance frequency is given by $f_m = f_n \pm \frac{m}{2N} f_0$, where N is the number of periods and m is the integral number.

It must be stressed that for successful application of ASL for production of acoustic devices several main requirements concerning engineered domain structures must be fulfilled:

- Regular domain geometry – the planar domain walls must be strictly parallel and the structure period must be held to within sufficient accuracy.
- Wall shift has to be reversible and parallel in the required range of magnitudes and frequencies of the applied electric field.

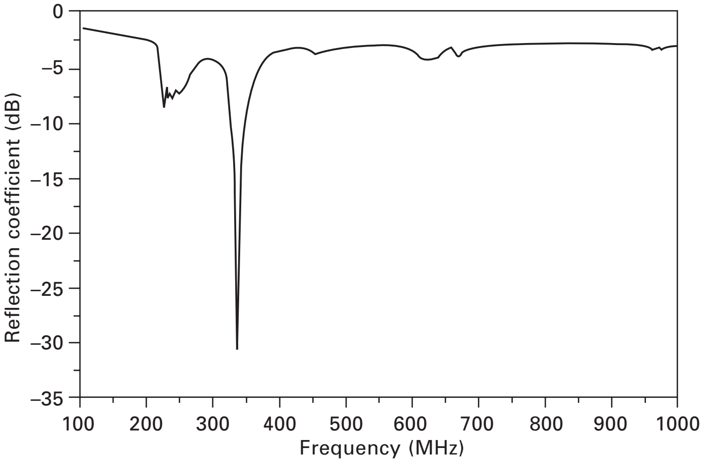

6.5 The measured reflection coefficient of an acoustic superlattice in $LiNbO_3$ with the modulation period of 10.3 mm (Wan *et al.*, 2000).

It is clear that these requirements can be met in $LiNbO_3$ and $LiTaO_3$ with the domain walls parallel to YZ planes. All other orientations are non-equilibrium and can be realized only under special switching conditions (Shur *et al.*, 2002b; Shur, 2006; Lobov *et al.*, 2006).

The piezo-response of the charged domain walls dividing encountering domains needs additional consideration. It was shown that the shape of the charged domain walls in $LiNbO_3$ and $LiTaO_3$ can never be planar and strongly depends on technological conditions such as the cooling regime. The competition between pyroelectric and bulk screening fields during the cooling process determines the final wall shapes (Shur and Rumyantsev, 1998). The ability to control the shape of the periodical charged domain walls is the additional factor in engineering devices with improved piezoelectric properties.

The experimental results of ultrasonic generation and detection in the range of 500–800 MHz using an acoustic superlattice of $LiNbO_3$ crystals were reported by Zhu *et al.* (1988a). Transducers with an insertion loss of nearly 0 dB at 555 MHz and a 5.8% 3 dB bandwidth have been made.

The piezoelectric properties of $LiNbO_3$ and $LiTaO_3$ crystals have been used recently for visualization of the micro- and nanoscale domain structures. The three most popular methods of high resolution study of the nanoscale domains are scanning near-field acoustic microscopy (Soergel, 2005), piezo-response force microscopy (Rodriguez *et al.*, 2005; Kholkin *et al.*, 2007) (Fig. 6.6), and confocal micro-Raman spectroscopy (Hammoum *et al.*, 2008).

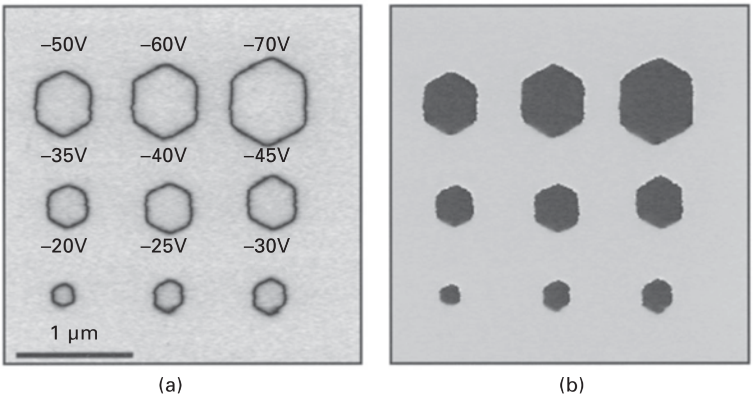

6.6 Piezo-response force microscopy: (a) amplitude and (b) phase images of ferroelectric domains in stoichiometric $LiNbO_3$ (Rodriguez *et al.*, 2005).

6.5 Nano- and micro-domain engineering in lithium niobate and lithium tantalate crystals

$LiNbO_3$ and $LiTaO_3$ possessing record piezoelectric, nonlinear optical and electro-optic properties have been chosen as the most favorable crystals for domain engineering. The advantages of congruent $LiNbO_3$ and $LiTaO_3$ for production of precise periodic domain structures are the stability of tailored domain patterns and the strict orientation of 180° domain walls in the proper crystallographic directions. The disadvantages are the problems with periodic poling under application of external electric field caused by extremely high coercive field (above 200 kV/cm).

The first crystals with periodic domain structure named 'dielectric superlattice' were produced by Feng and Ming (Feng *et al.*, 1980; Ming *et al.*, 1982) by growth of doped $LiNbO_3$ crystals by the Czochralski method in periodically variable temperature field conditions, giving rise to the artificially controlled growth striations, which in turn led to the formation of the periodic domain structure. The melt was doped with 0.5% yttrium and the crystal was grown in an asymmetric temperature field, which was realized by intentionally displacing the rotation axis of the growing crystal from the symmetric axis of the temperature field by means of a fine screw to adjust the position of the heater relative to the rotation axis (Cheng *et al.*, 1995). The period of the domain structure was controlled by parameters of crystal growth. It was given by $L = (v_{\text{pull}} + v_{\text{dec}})/n_{\text{rot}}$, where v_{pull} is the pulling rate, v_{dec} is the decreasing rate of free surface of melt in the crucible during crystal growth, and n_{rot} is the rotation rate of the pulling crystal. Even periodic domain structures with varied periods have been obtained by gradual change of the pulling rate.

Many other methods were proposed later for the creation of periodic domain structures, such as diffusion, proton exchange, scanning by electron beam, etc. (Rosenman *et al*., 1999), but none of them satisfies the requirements of industrial technology.

The most important step in the development of domain engineering in $LiNbO_3$ and $LiTaO_3$ occurred in 1993, when the poling of CLN at room temperature by application of electric field using the lithographic electrode pattern was realized by Yamada *et al*. (1993), thus opening the way to creation of the periodically-poled $LiNbO_3$ (PPLN) and $LiTaO_3$ (PPLT) crystals. Several scientific groups: Byer and Fejer from Stanford University (Myers *et al*., 1995), Hanna from the University of Southampton (Webjörn *et al*., 1994), Zhu and Ming from Nanjing University (Zhu *et al*., 1995) have developed independently a technology which allows the creation of high-quality PPLN and PPLT by application of the external electric field to lithographically produced electrode pattern in 0.5 mm thick wafers.

In 1997 Byer wrote that ‘the leverage of mass production made possible by lithographic patterning with subsequent domain inversion has led to a rapid transition from nonlinear crystals that cost thousands of dollars to fabricate to nonlinear chips that cost less than one dollar each to fabricate.’ Further activities were directed to the improvement of the electrical poling method, a decrease in threshold fields, and the struggle with optical damage. Nevertheless, low cost mass production remains an issue. It is believed that the essential progress in domain engineering requires an understanding of the physical mechanisms governing the formation of the domain structure from micro- to nano-scale. The kinetic nature of the engineered domain patterns has been clearly shown in a series of recent papers (Shur, 1996, 2005, 2006, 2008).

We will restrict ourselves to the polarization reversal through arising and growth of the 180° domains as $LiNbO_3$ and $LiTaO_3$ belong to uniaxial ferroelectrics. The domain evolution during polarization reversal of a single-domain state by application of external electric field pulse can be divided into the following main stages (Fatuzzo and Merz, 1967; Shur, 2005; 2008):

(1) ‘nucleation of new domains’
(2) ‘forward growth’
(3) ‘sideways domain growth’
(4) ‘domain coalescence’
(5) ‘spontaneous backswitching’ (see Fig. 6.7).

1. The nucleation of new nano-scale domains is practically impossible to study experimentally. It can be shown only that in high-quality crystals the domains appeared at the surface. This is due to the fact that the intrinsic surface non-ferroelectric dielectric gap leads to incomplete

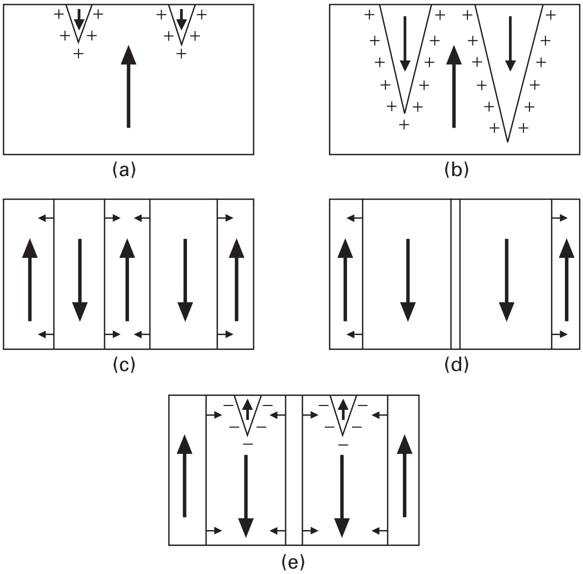

6.7 The main stages of the domain kinetics during polarization reversal in ferroelectrics.

compensation of the depolarization field in the vicinity of the electrodes (see Fig. 6.7a) (Janovec, 1959; Shur, 1996).

2. The ‘forward growth’ (domain tip propagation) represents a fast expansion of the formed ‘nuclei’ in the polar direction (see Fig. 6.7b). The depolarization fields produced by bound charges result in pronounced optical contrast due to electro-optical effect in $LiNbO_3$ and $LiTaO_3$.
3. The ‘sideways domain growth’ (domain spreading) represents the domains expansion normal to the polar direction (see Fig. 6.7c). Usually in $LiNbO_3$ and $LiTaO_3$ the anisotropic sideways domain wall motion results in the formation of regular shaped polygon domains oriented along crystallographic directions (see Fig. 6.3c,d). It was revealed that the domain shape depends crucially on the switching conditions (Shur, 2005, 2006). The variation of the field pulse parameters and modification of the dielectric gap properties allow control of the domain shape (Shur *et al.*, 1984, 1985, 2002b; Shur, 2006).
4. The ‘coalescence of residual domains’ (merging) is observed when the switching process is close to completion (see Fig. 6.7d). During this stage jump-like switching behavior is observed (Shur *et al.*, 2002a).
5. The ‘spontaneous backswitching’ (flip-back) represents full or partial reconstruction of the initial domain pattern after the external electric field switch-off. The shrinkage of the arisen domains through the backward wall motion and the nucleation of the domains with the initial

orientation of spontaneous polarization are observed (see Fig. 6.7e). The backswitching takes place under the action of the abnormally high field and can be used for creation of self-assembled nano-domain structures (Shur *et al.*, 2000a).

All stages of the domain structure evolution can be considered from the unified point of view as a manifestation of the various nucleation processes driving the first-order phase transformations (Fatuzzo and Merz, 1967; Miller and Weinreich, 1960). Within this approach the coexisting domains with opposite orientation of the spontaneous polarization are considered as the volumes of different phases, while the domain walls represent the phase boundaries. The domain kinetics is to be considered a result of elementary processes of thermally activated generation of one-, two- and three-dimensional nuclei with preferred orientation of the spontaneous polarization. In analogy with the heterogeneous nucleation during first-order phase transformation the nucleation sites during polarization reversal are situated mostly at imperfections and point defects.

The domain growth by wall motion is achieved through 1D- and 2D-nucleation. The elementary one unit cell thick steps are generated at the domain wall by 2D-nucleation. The subsequent motion along the wall is a result of 1D-nucleation. The nucleation probability determining the switching rate is governed by electric field averaged over the volume of the order of the nucleus size ('local field', E_{loc}) (Shur, 1996). E_{loc} is spatially inhomogeneous and can undergo essential changes during polarization reversal. In a ferroelectric capacitor, E_{loc} is the sum of:

- the external field applied by electrodes pattern,
- the depolarization field produced by bound charges,
- the external screening field originating from the redistribution of the charges at the electrodes,
- the bulk screening field governed by various processes.

The singularities of external field exist in the surface layer near the boundaries of the electrode pattern used for engineering of PPLN structures due to the fringe effect. Thus new domains appear under the edges and tips of the stripe electrodes. Such field concentration must be accounted for while creating the tailored domain structures (Shur, 2005).

The bound charges at the polar surfaces and at the charged walls of the encountering domains ('head to head' or 'tail to tail') are the sources of depolarization field E_{dep}, which is proportional to the spontaneous polarization P_S. E_{dep} usually exceeds by far the experimentally observed threshold fields and leads to fragmentation of the domain structure into narrow domains. The effect of E_{dep} on polarization reversal during manufacturing of PPLN and PPLT is crucial for $LiNbO_3$ and $LiTaO_3$ which possess the record P_S value.

E_{dep} is compensated by screening processes. The incomplete screening leads to the partial or full reconstruction of the initial domain state after the external field switch-off (spontaneous back-switching). External and bulk screening processes must be distinguished. The fast external screening with characteristic times ranging from nanoseconds to microseconds is achieved through charge redistribution in the electrodes. This process never compensates E_{dep} completely due to existence of the intrinsic dielectric surface layer (Fridkin, 1980; Shur, 1996). The bulk residual depolarization field E_{rd} remains in the switched areas after complete external screening. E_{rd} is by several orders of magnitude less than E_{dep}, but is about experimentally observed threshold field. Thus, the further compensation of E_{rd} by slow bulk screening is necessary. That is why retardation of bulk screening plays the key role in the evolution of the domain structure.

Three groups of bulk screening mechanisms are considered:

1. redistribution of the bulk charges (Fridkin, 1980; Shur, 1996),
2. reorientation of the defect dipoles (Lambeck and Jonker, 1986),
3. injection of carriers from the electrode through the dielectric gap (Tagantsev *et al.*, 2001).

All bulk screening mechanisms are slow with time constants ranging from milliseconds to days and months. According to the above discussed considerations, E_{loc} being the driving force of all nucleation processes is spatially inhomogeneous and time dependent.

The application of the short field pulse, for which the bulk screening of the new domain state is ineffective, does not allow modification of the domain pattern. After external field switch-off the complete spontaneous back-switching will be observed. The stable tailored domain configuration can be created only if the field pulse duration is sufficient for effective bulk screening. The slow switching when the redistribution of the bulk screening charges is fast enough to keep pace with changes in the domain structure corresponds to quasi-equilibrium switching. Any retardation of the bulk screening leads to non-equilibrium switching.

The domain shape is strongly dependent on the spatial distribution of the nucleation sites at the domain walls. The hexagon domain shape that is in $LiNbO_3$ with walls oriented along Y directions can be understood, if we assume the predetermined nucleation with inhomogeneous step generation. The nucleation must be realized at polygon domain vertices (Fig. 6.8). The crystal symmetry restricts the step growth directions, which leads to the experimentally observed step propagation mostly along three allowed Y directions (Shur, 2005) and growth of the steps generated at three non-adjacent vertices (Fig. 6.8). As a result the domain shape is determined by ratio between step generation and step growth rates. It was shown experimentally that qualitatively different domain shapes can be produced at the same place

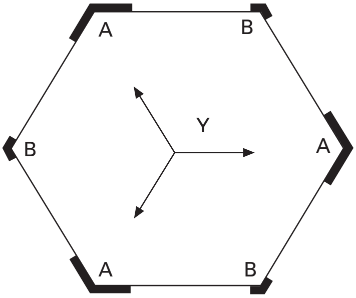

6.8 Predetermined nucleation: step generation at vertices and step growth along three Y directions.

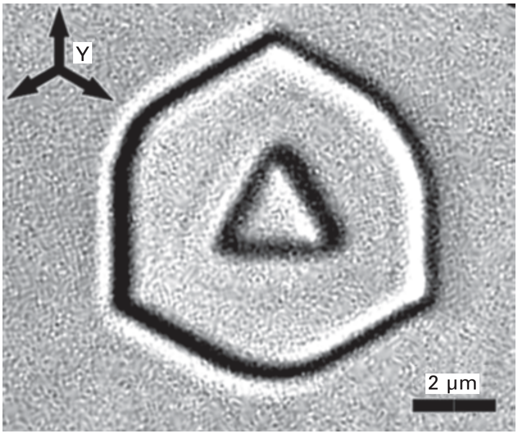

6.9 The domain shapes formed by pulse switching and subsequent spontaneous back-switching in congruent $LiNbO_3$. Switching by single short pulse. Z+ view. Optical images of domains revealed by etching.

of CLN wafer (Fig. 6.9). In this case the hexagon has been produced during switching, while the triangular domain appears within freshly switched hexagon during back-switching.

The effects of loss of the domain wall shape stability are observed under highly non-equilibrium switching. The loss of stability is caused by self-assembled nucleation and oriented growth of domain rays. The non-equilibrium switching is obtained due to essential role of the screening retardation effect. It is possible to accelerate the polarization reversal by application of 'super-strong' external field or to increase the input of residual depolarization field by deposition of artificial surface dielectric layer. The last situation is realized during conventional production of the PPLN using periodical electrode pattern (Yamada *et al.*, 1993; Webjörn *et al.*, 1994; Zhu *et al.*, 1995; Myers *et al.*, 1995; Batchko *et al.*, 1999; Rosenman *et al.*, 1999). The area between the stripe electrodes is covered by photoresist, and domain 'broadening' out of the electrodes is frequently accompanied by the loss of the regular wall shape (Shur, 2005, 2006). The formation of the domain shape instabilities ('fingers') was revealed (Fig. 6.10a) (Shur, 2005, 2006). The backward wall motion after external field switch-off (back-switching) is realized frequently through formation and propagation of the quasi-regular 'dendrite' structures (Fig. 6.10b) (Shur, 2005).

The recent study reveals 'discrete switching' – the formation of nano-scale domain structures under highly non-equilibrium switching in $LiNbO_3$. The self-assembled structures usually demonstrate quasi-regular spatial distribution of the isolated nano-domains. The typical structure produced in congruent $LiNbO_3$ covered by artificial dielectric layer (photoresist) as a result of back-switching is shown in Fig. 6.11. This domain pattern is stable (frozen-in) and does not undergo any evident changes for years.

The back-switching process is always considered undesirable, because it destroys the tailored domain structure, but its detailed study is useful. We have proposed an original poling method for creation of short-pitch periodical domain structures in $LiNbO_3$ and $LiTaO_3$, so-called 'back-switched poling' (Batchko *et al.*, 1999, 2003; Shur *et al.*, 2000a). The unique feature of the back-switching process is that the polarization reversal occurs without application of any external electric field. The domain kinetics is activated by an internal source – E_{rd} existing after abrupt external field switch-off

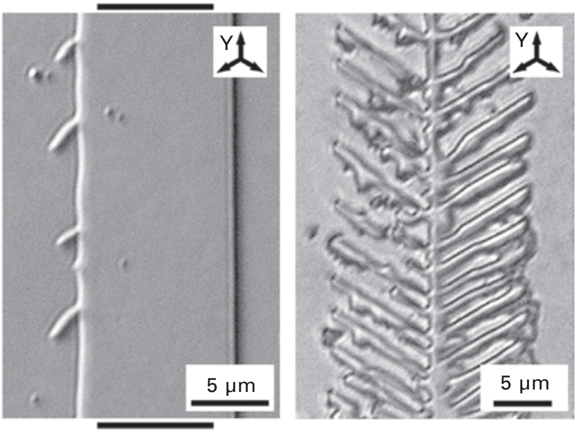

(a) (b)

6.10 (a) Finger domain structure formed during periodical poling in congruent $LiNbO_3$. (b) Dendrite structure formed during back-switching in MgO:LN. Z+ view. Strip electrode oriented along Y direction covers the area between the black lines. Optical images of domains revealed by etching.

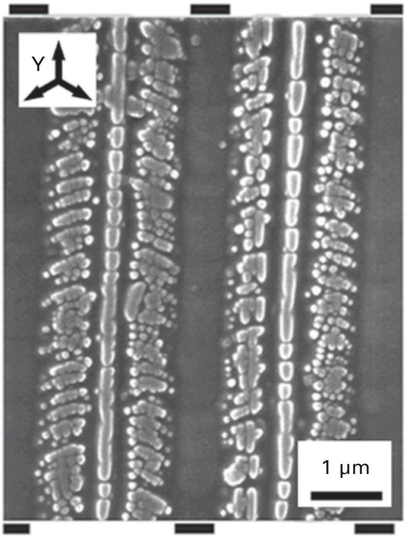

6.11 Stable nano-domain array in congruent $LiNbO_3$ formed as a result of back-switching during periodical poling. Strip electrode oriented along Y direction covers the area between the black lines. Domain patterns revealed by etching and visualized by scanning electron microscopy. Z+ view.

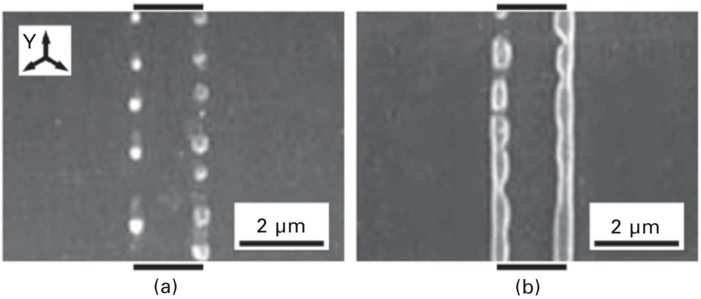

(a) (b)

6.12 Formation of the nano-domain rays along the electrode edges during back-switching in congruent $LiNbO_3$. Strip electrode oriented along Y direction covers the area between the black lines. Domain patterns revealed by etching and visualized by scanning electron microscopy. Z+ view.

due to retardation of the bulk screening. The process starts with nucleation of chains of the new needle-like nano-domains along the electrode edges at the Z+ surface due to the field singularities (Fig. 6.12a). The nano-domains merge and propagate through the wafer forming the lamellar domains (with the initial orientation of P_s) along the electrode edges (see Fig. 6.12b). The back-switch poling allows the undesirable effect of domain broadening to be overcome leading to difference between the electrode pattern and the produced periodical domain structure, whereas the domains enlarged during the poling stage shrink by the backward wall motion. The back-switch poling has been applied for 2.6 μm periodic poling of the $LiNbO_3$ and $LiTaO_3$ 0.5 mm thick wafers (Shur, 2008).

It has been shown recently that illumination of the polar surface of congruent $LiNbO_3$ crystal by pulsed ultraviolet laser leads to the formation of the surface domain structure with a depth of about a few microns (Valdivia *et al.*, 2005). The process of formation of the nano-scale domain structure as a result of pulse laser irradiation has been studied in detail (Kuznetsov *et al.*, 2008; Shur *et al.*, 2008). Three types of domain patterns have been revealed on the Z+ surface:

- 'dots' – isolated domain patterns in the narrow region along the boundary of the irradiated area (Fig. 6.13a)
- 'lines' – quasi-periodic nano-domain patterns, consisting of parallel rays inside the irradiated area (Fig. 6.13b)
- 'fractals' – self-similar domain patterns formed inside the irradiated area as a result of ray 'reflection' (Fig. 6.13c).

The detailed study of the nano-domain structures by piezo-responce force microscopy demonstrates that all structures represent the chains of isolated nano-domains (Kuznetsov *et al.*, 2008; Shur *et al.*, 2008). It was considered that the driving force of the polarization reversal is the pyroelectric field appearing during cooling after pulse laser irradiation (Miyazawa, 1979; Nakamura and Tourlog, 1993; Zhu *et al.*, 1994; Shur, 2008; Shur *et al.*, 2008). The 'discrete switching' can be attributed to highly non-equilibrium switching conditions caused by ineffective screening of the depolarization field while switching without electrodes when the residual depolarization field is abnormally high (Shur, 2005).

The self-assembled formation of the nano-scale domain chains is caused by electrostatic domain–domain interaction, which is very strong for ineffective

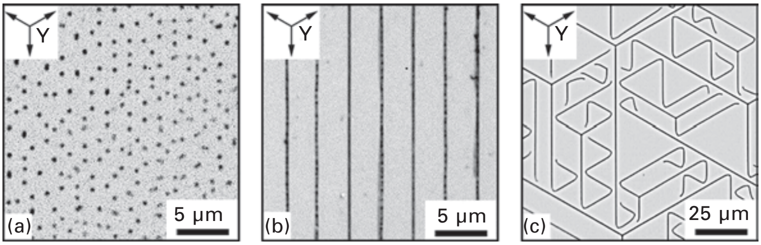

6.13 Nano-domain patterns formed in congruent $LiNbO_3$ as a result of pulsed laser irradiation on Z+ face: (a) dots, (b) lines, (c) fractal structure. Optical images of nano-domains revealed by etching.

screening. The reflection effect can be understood as a result of suppression of the nucleation in initial direction due to electrostatic domain–domain interaction. The tailored self-similar nano-scale structures with typical width about 200–300 nm and depth up to 300–400 μm can be produced by spatially non-uniform illumination (Fig. 6.14). The production of the stable bulk nano-domain patterns with sub-micron periods can be realized in this way.

6.6 Applications of domain engineered lithium niobate and lithium tantalate crystals for light frequency conversion

Domain engineering in $LiNbO_3$ and $LiTaO_3$ has revolutionized their use in nonlinear optical applications (Byer, 1997; Myers *et al.*, 1995). The performance of $LiNbO_3$ and $LiTaO_3$ as electro-optic, photorefractive, piezoelectric, and nonlinear optical crystals, makes them useful for various applications. It has been shown that $LiNbO_3$ and $LiTaO_3$ with periodic 1D- and 2D-domain structures possessing an efficient quasi-phase-matching open up a wide range of possibilities for bulk and waveguide nonlinear optical devices (Myers *et al.*, 1995; Ross *et al.*, 1998; Broderick *et al.*, 2000) (Fig. 6.15). For 15 years since the first electrical poling of bulk $LiNbO_3$ samples (Yamada *et al.*, 1993), research on periodically-poled $LiNbO_3$ and $LiTaO_3$ has aroused intense interest around the world resulting in production of photonic devices.

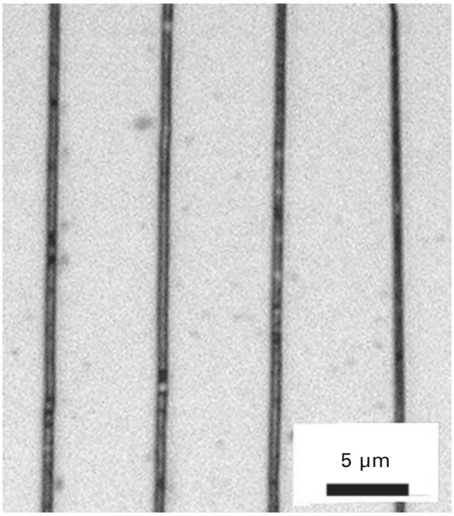

6.14 Periodical nano-domain structure produced by pulse laser irradiation in congruent $LiNbO_3$.

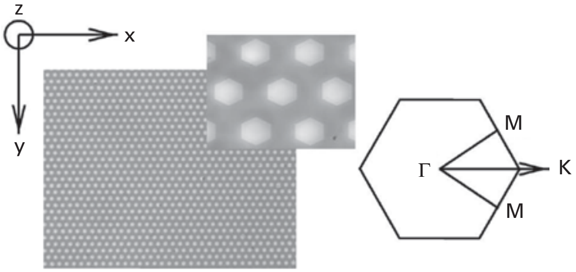

6.15 Two-dimensional (2D) nonlinear photonic crystal. The 2D nonlinear periodic domain structure with hexagonal symmetry in $LiNbO_3$. The structure period is 18.05 μm (Broderick *et al.*, 2000).

It is well known that efficient quadratic nonlinear optical interactions require constant relative phase shift between the interacting light waves. The phase drift which results from the difference in phase velocities due to material dispersion must be compensated by some phase-matching methods (Hum and Fejer, 2007). For the first 25 years of nonlinear optics, the dominant employed method was birefringent phase-matching (BPM), in which the difference in phase velocity of orthogonally polarized waves was used to compensate the difference caused by dispersion. BPM has been demonstrated by Maker *et al.* (1962) and Giordmaine (1962), independently. Subsequently PFM has been very well developed and has shown to be practical in a wide variety of commercial applications.

An alternative approach, quasi-phase-matching (QPM), uses a periodic modification of the properties of the nonlinear medium to correct the relative phase at regular intervals without matching phase velocities. Armstrong *et al.* (1962), and independently Franken and Ward (1963), proposed the original method of phase-matching by reversing the sign of the nonlinear coefficient every coherence length (l_c), which is the distance over which an accumulated phase difference between the interacting waves is equal to π. This idea was applied experimentally to an array of ferroelectric domains by Miller (1964), who claimed that 'the optimum domain array for SHG is one where the crystal consists of sheets of antiparallel domains, each l_c thick, with the wall normal parallel to the beam direction'. He has shown that an SHG intensity enhancement is proportional to $(1 + 2N)$, where N is the number of 180° properly placed domain walls in array. While QPM was invented at the same time as BPM, it has not seen widespread use due to difficulties in fabricating suitable crystals with the required micron-scale periodical domain structures.

The crystals of the $LiNbO_3$ and $LiTaO_3$ family are the first and still the most widely exploited periodically poled ferroelectrics. Both are readily available in three- and four-inch diameter substrates, convenient for lithographic patterning and processing, and have established waveguide technologies compatible with periodic domain structures. Quasi-phase-matched SHG to wavelengths as short as 386 and 325 nm has been demonstrated in $LiNbO_3$ and $LiTaO_3$ (White *et al.*, 2003; Meyn and Fejer, 1997). In the mid-IR, multi-phonon absorption in both materials rises steeply at 4–5 μm, limiting high average power operation to wavelengths shorter than 4 μm, through CW interactions out to 6.6 μm, and short-pulse operation (enabling the use of short crystals) to wavelengths as long as 7.25 μm (Watson *et al.*, 2002).

Efficient frequency conversion has been shown to cover the range from 460 nm to 2.8 microns in device lengths about 4 cm. In MgO-doped $LiNbO_3$ periods as small as 1.4 microns have been achieved in bulk devices. The large coercive field of these materials has limited conventional poling to 1 mm thick substrates and imposes a limit to the available aperture for high energy and peak power applications. Efforts to extend this thickness by diffusion bonding (Nakamura *et al.*, 2001) and pulsed poling (Ishizuki and Taira, 2005) techniques have increased usable thicknesses to 5 mm.

6.7 Generation of terahertz radiation in periodically poled lithium niobate crystal

One of the most promising applications of PPLN that is in great demand is the development of new devices for generation, propagation and detection of terahertz (THz) bandwidth electromagnetic radiation (Lee *et al.*, 2000, 2001; Ding and Kurgin, 1998; Sasaki *et al.*, 2002, 2006; Suizu *et al.*, 2006). Radiation in the THz region has attracted special attention due to its potential advantages for various applications. THz radiation covers the frequency range from 100 GHz to 30 THz filling the frequency gap between microwave and infrared bandwidths. The absorption of the photons with THz energies leads to the excitation of bending and stretching vibration modes of molecules. Thus applications of THz technology are expected in the fields of medicine, biology, physics, telecommunications, etc. The possible applications range from quality control of food and global environment monitoring to ultrafast computing (Tonouchi, 2007). For detailed information on achievements and basic principles of THz technology, readers are referred to numerous reviews (Ferguson and Zhang, 2002; Siegel, 2004; Mittleman, 2003; Sakai, 2005; Tonouchi, 2006).

The method of THz wave generation by PPLN is based on the above discussed effect of frequency conversion in nonlinear optical materials (Lee *et al.*, 2000, 2001; Ding and Kurgin *et al.*, 1998; Sasaki *et al.*, 2002, 2006; Suizu *et al.*, 2006). Frequency conversion is achieved through excitation in the media second-order nonlinear polarization under the action of external ‘pump’ electromagnetic fields. The effect is described by second-order nonlinear susceptibility which accounts for the presence of three waves:

two pump and one response. Second-order nonlinear susceptibility is third-rank tensor symmetrical over the last two indices: $\chi_{\mathrm{ijk}} = \chi_{\mathrm{ikj}}$. As regards its symmetrical properties, they coincide formally with those of piezoelectric tensor d_{ijk}. Thus, the components of this tensor also reverse sign between neighboring domains. The three waves involved in the nonlinear process must satisfy k-vector requirement or so-called phase-matching condition: $k_2 \pm k_2 = k$, and for the frequencies ω_1, ω_2, ω of these waves the following equality holds due to conservation of energy ω_1, $\pm\ \omega_2$, ω.

One of the most popular methods of generating THz radiation based on difference frequency generation (DFG) is capable of producing tunable, highly coherent THz radiation. Several DFG schemes were proposed and realized. The 'direct' one was based on the output of the laser oscillating at two wavelengths (Avetisyan *et al.*, 2001). The drawback of this method is the large absorption loss in $LiNbO_3$ in the THz frequency range (Shall *et al.*, 1999).

The special method of surface-emitting (SE) DFG using PPLN structures, when generated THz radiation propagates perpendicular to the optical beam was proposed to overcome this difficulty. The PPLN period Λ_{SE} was chosen to be: $\frac{2\pi}{\Lambda_{\mathrm{SE}}} = k_1 - k_2$, where k_1 and k_2 are wavenumbers at corresponding optical frequencies ω_1 and ω_2. The modifications of this method using slant-stripe-type and two-dimensional PPLN crystals were proposed (Sasaki *et al.*, 2002) (see Figs 6.16 and 6.17).

The phase-matching condition discussed above is the important prerequisite for efficient energy conversion from external pump fields via such second-order processes into the desired spectral range. The physical essence of this condition consists in the requirement that the phase of induced signal wave of quadratic polarization in the given place must interfere constructively with the waves generated at every other point. Only in this case is the energy conversion from the pump fields efficient. This condition is violated due to the wavelength dependence of refractive index (Bakker *et al.*, 1994).

At the passage of optical beam, a DC potential difference across the crystal can appear. This effect, called optical rectification (also electrooptical rectification (EOR)), was reported for the first time by Bass *et al.* (1962). EOR can be easily understood taking into account the retardation of induced polarization. The quadratic polarization induced by external laser electromagnetic field does not reverse completely when the sign of the field is reversed. EOR is observed only in the low symmetry crystals which provide preferred internal direction. It is clear that $LiNbO_3$ and $LiTaO_3$ just fulfill this condition. If we assume the sinusoidal time variation of the pump field, the time average polarization develops in full analogy with arising of DC currents in congenial electronic rectificators (Bass *et al.*, 1962).

The modification of the EOR effect was used for generation of THz

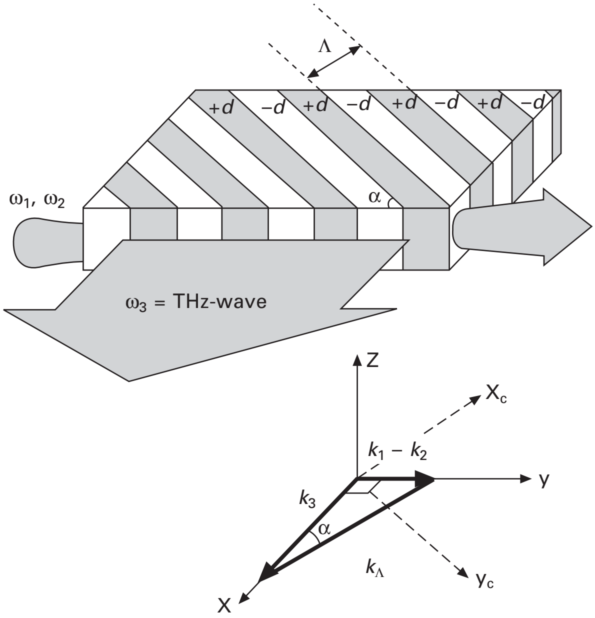

6.16 Schematic illustration of THz generation in slant-stripe-type periodically poled $LiNbO_3$ (upper) and the wave-vector diagram (lower), *d*–nonlinear optical coefficient (Sasaki *et al.*, 2002).

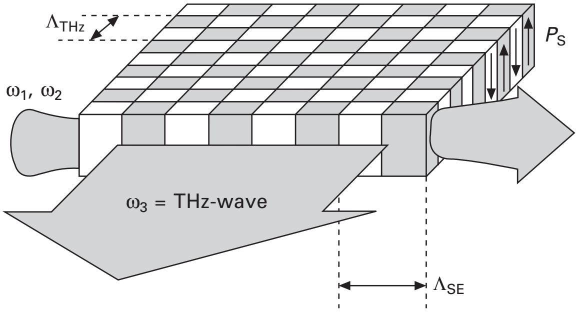

6.17 Schematic illustration of THz generation in two-dimensional periodically poled $LiNbO_3$ (Sasaki *et al.*, 2005).

radiation. The distinction with 'classical' EOR, which leads to arising of DC second-order polarization, is due to the fact that in these experiments the crystal is illuminated by ultrashort (femto- or pico-second) optical pulses. When an intense optical pulse propagates in the crystal with non-zero second-order nonlinear susceptibility χ_{ijk} the time dependence of induced quadratic polarization $P^q_i(t)$ is determined by time dependence of the optical pulse intensity $|E^{\mathrm{opt}}(t)|^2$. Fourier decomposition of a short pulse contains broad frequency spectrum, which leads to generation of far infrared radiation as a result of beating between frequency components.

The only obstacle for obtaining intense THz radiation while illuminating a single crystal is due to the existing mismatch between group velocities of optical and THz waves. The destructive interference occurs due to the walk off of THz pulses generated in different parts of the crystal. As a result only the regions in the vicinity of front and back surfaces of the crystal contribute to the observed THz radiation. The promising technique for generating of narrow-band THz radiation overcoming this problem is based on the EOR of femto-second pulses in PPLN. When the pump wave is propagating across PPLN, the crystal response is periodically modulated as far as adjacent domains having opposite sign of second-order susceptibility.

The period of engineered PPLN is matched to the walk-off length between the optical and THz pulses. In each domain the nonlinear polarization is generated by EOR and contributes half-cycle to the emitted THz radiation. The frequency of the generated THz radiation is given by $f = c/[2l_d(n_{\mathrm{opt}} – n_{\mathrm{THz}})]$, where l_d is domain width, and n_{opt} and n_{THz} are refractive indices at optical and THz frequencies, respectively.

It is seen that obtained THz radiation frequency is dependent only on the period of PPLN and respective refractive indices. This means that by engineering proper PPLN structures the THz radiation of desirable wave length can be obtained.

6.8 Conclusions and future trends

In this chapter, we have discussed the influence of the tailored periodic nano- and micro-domain structures on the piezoelectric properties of $LiNbO_3$ and $LiTaO_3$ crystals. First, the main piezoelectric characteristics of both crystals have been reviewed. It was pointed out that $LiNbO_3$ and $LiTaO_3$ are among the most popular commercially produced ferroelectric crystals.

It was pointed out that in recent decades both crystals have become the most important objects of domain engineering. The main target of the domain engineering is the improvement of the characteristics of commercially available ferroelectrics by manufacturing of stable tailored domain patterns (periodic poling). The periodic domain structures introduce the spatial modulation of the piezoelectric, electro-optic, photorefractive, and nonlinear optical properties thus upgrading device performance.

The tailored domain patterns in piezoelectric crystals which are not switched during device operation and allow modification of the piezoelectric properties were discussed. The domain structure has been included in the list of factors that can be manipulated in selecting a desired resonance along with boundary conditions and electrode configurations. It was shown that the properly designed domain pattern can be adjusted to enhance or eliminate certain modes and very high frequency modes become possible.

It was shown that the spatial discontinuity of piezo-coefficients at the domain walls plays the role of delta-like sound sources under application of an external alternating electric field. If constructive interference of the waves emitted by these sources can be achieved then the acoustic power emitted by crystal with periodic domain structure will be proportional to the square of the domain number. It was stressed that the main resonance frequency is determined solely by the period of domain structure and is independent of the sample sizes.

The independent development of the alternative branch of domain engineering dealing with creation of the periodical domain structures in the nonlinear optical ferroelectric crystals for achievement of the quasi-phase-matching for light frequency conversion, in the first place for second harmonic generation has been considered. The applications of the periodically poled $LiNbO_3$ and $LiTaO_3$ for light frequency conversion and generation of terahertz radiation have been discussed. The main achievements in this area have been demonstrated.

The strong influence of the domain walls on the piezoelectric and acoustic properties presented a problem of creation of the periodical domain structures in $LiNbO_3$ and $LiTaO_3$. It was stressed that the production of the tailored domain patterns with desirable geometrical parameters is impossible without a thorough understanding of the physical basis of domain engineering.

The unified approach to the domain kinetics based on the nucleation mechanism of the polarization reversal allows an understanding of the variety of experimentally observed domain evolution scenarios in $LiNbO_3$ and $LiTaO_3$ crystals. We have proved that the domain kinetics essentially depends upon the effectiveness of the bulk screening. Original scenarios of the domain structure evolution were revealed and discussed within an approach accounting for the decisive role of the retardation of the screening process. It has been shown that in $LiNbO_3$ and $LiTaO_3$ the predetermined nucleation effect plays the key role in domain growth. The formation of the self-assembled nano-scale domain structures has been studied for different non-equilibrium switching conditions: spontaneous back-switching, switching with artificial surface layer, and switching as a result of pulse laser irradiation.

The recent achievements in studying the domain kinetics with nano-scale spatial resolution allow prediction that the future of domain engineering lies in the production of tailored nano-domain structure and structures possessing the nano-scale period accuracy. The structures can be produced as a result of the local switching of the single domain using application of the inhomogeneous electric field by nano-scale electrode pattern, conductive tip of SPM or electron beam. The periodic nano-scale modification of the surface layer looks very promising. It is proposed that the effective methods are based on formation of self-assembled structures.

The piezo-response of the charged domain walls dividing encountering domains needs additional study. It was shown that the cogged shape of the charged domain walls in $LiNbO_3$ and $LiTaO_3$ strongly depends on technological conditions such as the cooling regime. The ability to control the shape of the periodical charged domain walls is the additional factor in engineering of the devices with improved piezoelectric properties.

It is clear that future development of nano-scale engineering requires deep investigations of the polarization kinetics in $LiNbO_3$ and $LiTaO_3$ using modern sophisticated experimental methods with nano-scale resolution including elaborate modes of SPM and scanning electron microscopy. The development of a reliable technology for domain engineering at the submicron scale would be a major breakthrough, leading to new generation of devices.

6.9 References

Armstrong J A, Bloembergen N, Ducuing J and Perhsan P S (1962), 'Interactions between light waves in a nonlinear dielectric', *Phys Rev*, 127 (6), 1918–1939.

Avetisyan Y, Sasaki Y and Ito H (2001), 'Analysis of THz-wave surface-emitted difference-frequency generation in periodically poled lithium niobate waveguide', *Appl Phys B*, 73, 511–514.

Bakker H J, Hunsche S and Kurz H (1994), 'Investigation of anharmonic lattice vibrations with coherent phonon polaritons', *Phys Rev B*, 50, 914–920.

Ballman A A (1965), 'Growth of piezoelectric and ferroelectric materials by the Czochralski technique', *J Am Ceramic Soc*, 48 (2), 112–113.

Bass M, Franken P A, Ward J F and Weinreich G (1962), 'Optical rectification', *Phys Rev Lett*, 9, 446–448.

Batchko R G, Shur V Ya, Fejer M M and Byer R L (1999), 'Backswitch poling in lithium niobate for high-fidelity domain patterning and efficient blue light generation', *Appl Phys Lett*, 75 (12), 1673–1675.

Batchko R, Miller G, Byer R, Shur V and Fejer M (2003), 'Backswitch poling method for domain patterning of ferroelectric materials', US Patent No. 6,542,285 B1, April 1.

Broderick N G R, Ross G W, Offerhaus H L, Richardson D J and Hanna D C (2000), 'Hexagonally poled lithium niobate: a two-dimensional nonlinear photonic crystal', *Phys Rev Lett*, 84, 4345–4348.

Byer R L (1997), 'Quasi-phasematched nonlinear interactions and devices', *J Nonl Opt Phys Mats*, 6, 549–592.

Chen Y L, Xu J J, Chen X J, Kong Y F and Zhang G Y (2001), 'Domain reversion process in near-stoichiometric $LiNbO_3$ crystals', *Opt Commun*, 188, 359–364.

Cheng S D, Zhu Y Y, Lu Y L and Ming N B (1995), 'Growth and transducer properties of an acoustic superlattice with its periods varying gradually', *Appl Phys Lett*, 66, 291–292.

Ding Y J and Kurgin J B (1998), 'A new scheme for generation of coherent and incoherent submillimeter to THz waves in periodically poled lithium niobate', *Optic Comm*, 148, 105–109.

Fatuzzo E and Merz W J (1967), *Ferroelectricity*, Amsterdam, North-Holland.

Fedulov S A, Shapiro I and Ladyzhenski P B (1965), 'Application of Czochralski method for growth of $LiNbO_3$, $LiTaO_3$, and $NaNbO_3$ single crystals', *Kristallografiya*, 10 (2), 268–269.

Feng D, Ming N B, Hong J F, Yang Y S, Zhu J S, Yang Z and Wang Y N (1980), 'Enhancement of second-harmonic generation in $LiNbO_3$ crystals with periodic laminar ferroelectric domains', *Appl Phys Lett*, 37, 607–609.

Ferguson B and Zhang X-C (2002), 'Materials for terahertz science and technology', *Nature Mater*, 1, 26–33.

Franken P A and Ward J F (1963), 'Optical harmonics and nonlinear phenomena', *Rev Mod Phys*, 35 (1), 23–39.

Fridkin V M (1980), *Ferroelectrics Semiconductors*, New York, Consultants Bureau.

Furukawa Y, Kitamura K, Niwa K, Hatano H, Bernasconi P, Montemezzani G and Gunter P (1999), 'Stoichiometric $LiTaO_3$ for dynamic holography in near UV wavelength range', *Jpn J Appl Phys*, 38, 1816–1819.

Giordmaine J A (1962), 'Mixing of light beams in crystals', *Phys Rev Lett*, 8 (1), 19–20.

Hammoum R, Fontana M D, Bourson P and Shur V Ya (2008), 'Characterization of PPLN-microstructures by means of Raman spectroscopy', *Appl Phys A. Mater Sci Process*, 91, 65–67.

Hum D S and Fejer M M (2007), 'Quasi-phasematching', *C R Physique*, 8, 180–198.

IRE (1958), 'IRE standards on piezoelectric crystals: the electromechanical coupling factor', *Proc IRE*, 46, 764–778.

Ishizuki H and Taira T (2005), 'High-energy quasi-phase-matched optical parametric oscillation in a periodically poled MgO:$LiNbO_3$ device with a 5 mm × 5 mm aperture', *Opt Lett*, 30, 2918–2920.

Janovec V (1959), 'Anti-parallel ferroelectric domain in surface space-charge layers of $BaTiO_3$', *Czechosl J Phys*, 9, 468–480.

Kholkin A L, Kalinin S V, Roelofs A and Gruverman A (2007), 'Review of ferroelectric domain imaging by piezoresponse force microscopy', in Kalinin S and Gruverman A, *Scanning probe microscopy. Electrical and electromechanical phenomena at the nanoscale*, Berlin, Springer, 173–214.

Kitamura K, Furukawa Y, Niwa K, Gopalan V and Mitchell T E (1998), 'Crystal growth and low coercive field 180° domain switching characteristics of stoichiometric $LiTaO_3$', *Appl Phys Lett*, 73, 3073–3075.

Kuznetsov D K, Shur V Ya, Negashev S A, Lobov A I, Pelegov D V, Shishkin E I, Zelenovskiy P S, Platonov V V, Ivanov M G and Osipov V V (2008), 'Formation of nano-scale domain structures in lithium niobate using high-intensity laser irradiation', *Ferroelectrics*, 373, 133–138.

Lambeck P V and Jonker G H (1986), 'The nature of domain stabilization in ferroelectric perovskites', *J Phys Chem Solids*, 47, 453–461.

Landau L D and Lifshitz E M (1960), *Electrodynamics of Continuous Media. Course of Theoretical Physics*, Oxford, Pergamon Press.

Lee Y-S, Meade T, Perlin V, Winful H and Norris T B (2000), 'Generation of narrow-band teraherz radiation via optical rectification of femtosecond pulses in periodically poled lithium niobate', *Appl Phys Lett*, 76, 2505–2507.

Lee Y-S, Meade T, Norris T B and Galvanauskas A (2001), 'Tunable narrow-band terahertz generation from periodically poled lithium niobate', *Appl Phys Lett*, 78, 3583–3585.

Lobov A I, Shur V Ya, Baturin I S, Shishkin E I, Kuznetsov D K, Shur A G, Dolbilov M A and Gallo K (2006), 'Field induced evolution of regular and random 2D domain structures and shape of isolated domains in $LiNbO_3$ and $LiTaO_3$', *Ferroelectrics*, 341, 109–116.

Maker P D, Terhune R W, Nisenoff M and Savage C M (1962), 'Effects of dispersion and focusing on the production of the optical harmonics', *Phys Rev Lett*, 8 (1), 21–23.

Matthias B T and Remeika J P (1949), 'Ferroelectricity in the ilmenite structure', *Phys Rev*, 76, 1886–1887.

Meyn J P and Fejer M M (1997), 'Tunable ultraviolet radiation by second-harmonic generation in periodically poled lithium tantalate', *Opt Lett*, 22, 1214–1216.

Miller R C (1964), 'Optical harmonic generation in single crystal $BaTiO_3$', *Phys Rev*, 134, A1313–A1319.

Miller R C and Weinreich G (1960), 'Mechanism for the sidewise motion of 180° domain walls in barium titanate', *Phys Rev*, 117, 1460–1466.

Ming N B, Hong J F and Feng D (1982), 'The growth striations and ferroelectric domain structures in Czochralski-grown $LiNbO_3$ single crystals', *J Mater Sci*, 17 (6), 1663–1670.

Mittleman D (2003), *Sensing with Terahertz Radiation*, Berlin, Springer.

Miyazawa S (1979), 'Ferroelectric domain inversion in Ti-diffused $LiNbO_3$ optical waveguide', *J Appl Phys*, 50, 4599–4603.

Myers L E, Eckardt R C, Fejer M M, Byer R L, Bosenberg W R and Pierce J W (1995), 'Quasi-phase-matched optical parametric oscillators in bulk periodically poled $LiNbO_3$', *J Opt Soc Am B*, 12 (11), 2102–2116.

Nakamura K and Tourlog A (1993), 'Single-domain surface layers formed by heat treatment of proton-exchanged multidomain $LiTaO_3$ crystals', *Appl Phys Lett*, 63, 2065–2066.

Nakamura K, Hatanaka T and Ito H (2001), 'High output energy quasi-phase-matched optical parametric oscillators using diffusion-bonded periodically poled and single domain $LiNbO_3$', *Jpn J Appl Phys*, 40, L337–L339.

Nassau K, Levinstein H J and Lociacono G M (1966), 'Ferroelectric lithium niobate. 1. Growth, domain structure, dislocations and etching', *J Phys Chem Sol*, 27 (6–7), 983–988.

Newnham R E, Miller C S, Cross L E and Cline T W (1975), 'Tailored domain patterns in piezoelectric crystals', *Phys Stat Sol (a)*, 32, 69–78.

Nikogosjan D N (2005), *Nonlinear Optical Crystals: A Complete Survey*, New York, Springer.

Nye J (1985), *Physical Properties of Crystals,* London, Oxford University Press.

Ogi H, Kavasaki Y, Hirao M and Ledbetter H (2002), 'Acoustic spectroscopy of lithium niobate: elastic and piezoelectric coefficients', *J Appl Phys,* 92, 2451–2456.

Rodriguez B J, Nemanich R J, Kingon A, Gruverman A, Kalinin S V, Terabe K, Liu X Y and Kitamura K (2005), 'Domain growth kinetics in lithium niobate single crystals studied by piezoresponse force microscopy', *Appl Phys Lett*, 86, 012906.

Rosenman G, Skliar A and Arie A (1999), 'Ferroelectric domain engineering for quasi-phasematched nonlinear optical devices', *Ferroelectrics Review*, 1, 263–326.

Ross G W, Pollnau M, Smith P G R, Clarkson W A, Britton P E and Hanna D C (1998), 'Generation of high-power blue light in periodically poled $LiNbO_3$', *Opt Lett*, 23, 171–173.

Sakai K (2005), *Terahertz Optoelectronics*, Berlin, Springer.

Sasaki Y, Avetisyan Y, Kawase K and Ito H (2002), 'Terahertz-wave surface-emitted difference frequency generation in slant-stripe-type periodically poled $LiNbO_3$ crystal', *Appl Phys Lett*, 81, 3323–3325.

Sasaki Y, Avetisyan Y, Yokoyama H and Ito H (2005), 'Surface-emitted terahertz-wave difference-frequency generation in two-dimensional periodically poled lithium niobate', *Optics Lett*, 30, 2927–2929.

Sasaki Y, Suzuki Y, Suizu K, Ito H, Yamaguchi S and Imaeda M (2006), 'Surface-emitted terahertz-wave difference-frequency generation in periodically poled lithium niobate ridge-type waveguide', *Jpn J Appl Phys*, 45, L367–369.

Schweinler H C (1952), 'Ferroelectricity in the ilmenite structure', *Phys Rev*, 87, 5–11.

Shall M, Helm H and Keiding S R (1999), 'Far infrared properties of electro-optic crystals measured by THz time-domain spectroscopy', *Int J Infrared Millim Waves*, 20, 595–604.

Shur V Ya (1996), 'Fast polarization reversal process: evolution of ferroelectric domain structure in thin films', in Paz de Araujo C A, Scott J F and Taylor G W, *Ferroelectric Thin Films: Synthesis and Basic Properties*, New York, Gordon and Breach, 153–192.

Shur V Ya (2005), 'Correlated nucleation and self-organized kinetics of ferroelectric domains', in Schmelzer J W P, *Nucleation theory and applications*, Weinheim, WILEY-VCH, 178–214.

Shur V Ya (2006), 'Kinetics of ferroelectric domains: application of general approach to $LiNbO_3$ and $LiTaO_3$', *J Mat Sc*, 41 (1), 199–210.

Shur V Ya (2008), 'Nano- and micro-domain engineering in normal and relaxor ferroelectrics', in Ye Z G, *Advanced Dielectric, Piezoelectric and Ferroelectric Materials – Synthesis, Characterization and Applications*, Cambridge, Woodhead, 622–669.

Shur V Ya and Rumyantsev E L (1998), 'Arising and evolution of the domain structure in ferroelectrics', *J Korean Phys Soc*, 32, S727–S732.

Shur V Ya, Letuchev V V and Rumyantsev E L (1984), 'Field dependence of the polarization switching parameters and shape of domains in lead germanate', *Sov Phys Solid State*, 26, 1521–1522.

Shur V Ya, Letuchev V V, Rumyantsev E L and Ovechkina I V (1985), 'Triangular domains in lead germanate', *Sov Phys Solid State*, 27, 959–960.

Shur V Ya, Rumyantsev E L, Nikolaeva E V, Shishkin E I, Fursov D V, Batchko R G, Eyres L A, Fejer M M and Byer R L (2000a), 'Nanoscale backswitched domain patterning in lithium niobate', *Appl Phys Lett*, 76 (2) 143–145.

Shur V Ya, Rumyantsev E L, Nikolaeva E V and Shishkin E I (2000b), 'Formation and evolution of charged domain walls in congruent lithium niobate', *Appl Phys Lett*, 77 (22), 3636–3638.

Shur V Ya, Rumyantsev E L, Pelegov D V, Kozhevnikov V L, Nikolaeva E V, Shishkin E I, Chernykh A P and Ivanov R K (2002a), 'Barkhausen jumps during domain wall motion in ferroelectrics', *Ferroelectrics*, 267, 347–353.

Shur V Ya, Nikolaeva E V, Shishkin E I, Chernykh A P, Terabe K, Kitamura K, Ito H and Nakamura K (2002b), 'Domain shape in congruent and stoichiometric lithium tantalate', *Ferroelectrics*, 269, 195–200.

Shur V Ya, Kuznetsov D K, Lobov A I, Pelegov D V, Pelegova E V, Osipov V V, Ivanov M G and Orlov A N (2008), 'Self-similar surface nanodomain structures induced by laser irradiation in lithium niobate', *Phys Solid State*, 50 (4), 717–723.

Siegel P H (2004), 'Terahertz technology in biology and medicine', *IEEE Trans. Microwave Theory Tech*, 52, 2438–2446.

Smith R T and Welsh F S (1971), 'Temperature dependence of the elastic, piezoelectric, and dielectric constant of lithium tantalate and lithium niobate', *J Appl Phys,* 42, 2219–2230.

Soergel E (2005), 'Visualization of ferroelectric domains in bulk single crystals', *Appl Phys B*, 81, 729–752.

Suizu K, Suzuki Y, Sasaki Y, Ito H and Avetisyan Y (2006), 'Surface-emitted terahertz-wave generation by ridged periodically poled lithium niobate and enhancement by mixing of two terahertz waves', *Opt Lett*, 31(7), 957–959.

Tagantsev A K, Stolichnov I, Colla E L and Setter N (2001), 'Polarization fatigue in ferroelectric films: basic experimental findings, phenomenological scenarios, and microscopic features', *J Appl Phys*, 90, 1387–1402.

Tonouchi M (2006), *Terahertz Technology*, Tokyo, Ohmsha.

Tonouchi M (2007), 'Cutting-edge terahertz technology', *Nature Photonics*, 1, 97–105.

Valdivia C E, Sones C L, Scott J G, Mailis S, Eason R W, Scrymgeour D A, Gopalan V, Jungk T, Soergel E and Clark I (2005), 'Nanoscale surface domain formation on the +z face of lithium niobate by pulsed ultraviolet laser illumination', *Appl Phys Lett*, 86, 022906.

Volk T R and Woehlecke M (2009), *Lithium Niobate. Defects, Potorefraction and Ferroelectric Switching*, Berlin, Springer.

Wan Z l, Wang Q, Xi Y X, Lu Y Q, Zhu Y Y and Ming N B (2000), 'Fabrication of acoustic superlattice $LiNbO_3$ by pulsed current induction and its application for crossed field ultrasonic excitation', *Appl Phys Lett*, 77, 1891–1893.

Watson M A, O'Connor M V, Lloyd P S, Shepherd D P, Hanna D C, Gawith C B E, Ming L, Smith P G R and Balachninaite O (2002), 'Extended operation of synchronously pumped optical parametric oscillators to longer idler wavelengths', *Opt Lett*, 27, 2106–2108.

Webjörn J, Pruneri V, Russell P St J, Barr J R M and Hanna D C (1994), 'Quasi-phase-matched blue light generation in bulk lithium niobate, electrically poled via periodic liquid electrodes', *Electron Lett*, 30 (11), 894–895.

Weis R S and Gaylord T K (1985), 'Lithium niobate: summary of physical properties and crystal structure', *Appl Phys A*, 37 (4), 191–203.

White R, McKinnie I, Butterworth S, Baxter G, Warrington D, Smith P, Ross G and Hanna D (2003), 'Tunable single-frequency ultraviolet generation from a continuous-wave Ti: sapphire laser with an intracavity PPLN frequency doubler', *Appl Phys B: Lasers and Optics*, 77, 547–550.

Yamada M, Nada N, Saitoh M and Watanabe K (1993), 'First-order quasi-phase matched $LiNbO_3$ waveguide periodically poled by applying an external field for efficient blue second-harmonic generation', *Appl Phys Lett*, 62, 435–436.

Zhu S N, Zhu Y Y, Zhang Z Y, Shu H, Wang H F, Hong J F, Ge C Z and Ming N B (1995), '$LiTaO_3$ crystal periodically poled by applying an external pulsed field', *J Appl Phys*, 77 (10), 5481–5483.

Zhu Y Y and Ming N B, (1992) 'Ultrasonic excitation and propagation in an acoustic superlattice', *J Appl Phys,* 72, 904–914.

Zhu Y Y, Ming N B, Jiang W H and Shui Y A (1988a), 'Acoustic superlattice of $LiNbO_3$ crystals and its applications to bulk-wave transducers for ultrasonic generation and detection up to 800 MHz', *Appl Phys Lett*, 53, 1381–1383.

Zhu Y Y, Ming N B, Jiang W H and Shui Y A (1988b), 'High-frequency resonance in acoustic superlattice of $LiNbO_3$ crystals', *Appl Phys Lett*, 53, 2278–2280.

Zhu Y Y, Ming N B and Jiang W H (1989) 'Ultrasonic spectrum in Fibonacci acoustic superlattices', *Phys Rev B,* 40, 8536–8540.

Zhu Y Y, Zhu S N, Hong J F and Ming N B (1994), 'Domain inversion in $LiNbO_3$ by proton exchange and quick heat treatment', *Appl Phys Lett*, 65, 558–560.

7

Single crystal PZN–PT, PMN–PT, PSN–PT and PIN–PT-based piezoelectric materials

---

L. LUO, X. ZHAO and H. LUO, Shanghai Institute of Ceramics, China

Abstract: This chapter reviews the investigation of several relaxor-PT single crystals with perovskite structure. First, this chapter introduces several milestones during the development of relaxor-PT complex solid solutions, and then discusses the PMN–PT, PZN–PT, PSN–PT and PIN–PT in separate sections, focusing on their growth, phase structure and performance. We then introduce two theoretical models to explain the excellent piezoelectric properties of relaxor-based crystals and the application of relaxor ferroelectric single crystals in piezoelectric actuators and medical transducers. Finally, the challenges and future trends in relaxor-based crystals are discussed.

Key words: relaxor single crystals, crystal growth, Bridgman method, flux method, ferroelectrics, piezoelectric performance, dielectric constant.

7.1 Introduction

Novel relaxor ferroelectric single crystals refer to $Pb(Mg_{1/3}Nb_{2/3})O_3$ (PMN) or $Pb(Zn_{1/3}Nb_{2/3})O_3$ (PZN) and ferroelectric $PbTiO_3$ (PT), namely (1-x) PMN–xPT and (1-x)PZN–xPT, which are a kind of single crystal of solid solution with perovskite structure. They are solid solutions synthesized with relaxor ferroelectric $A(B'B'')O_3$ and normal ferroelectric PT, and their general chemical formulas are written as $A(B'B'')O_3$-$PbTiO_3$, in which, the A site is usually occupied by Pb; the B′ site is occupied by Mg, Zn, Sc, Ni, etc., and the B″ site is occupied by Nb, Ta or W. It can form lots of ferroelectrics due to the variation of B site element; however, most of the compounds are unable to be applicable at present, with only several kinds of solid solution that can in practice. The crystal growths, performance, structure, and device applications of PZN–PT, PMN–PT, $Pb(Sc_{1/2}Nb_{1/2})$–$PbTiO_3$ (PSN–PT), $Pb(In_{1/2}Nb_{1/2})$–$PbTiO_3$ (PIN–PT), $Pb(Yb_{1/2}Nb_{1/2})$–$PbTiO_3$ (PYN–PT) have been investigated intensively during the past two decades.

Among the family of relaxor ferroelectric single crystals, PZN–PT, PMN–PT PIN–PT and PSN–PT are the most important representatives of relaxor-based perovskite. So this chapter is mainly about these four kinds of crystals in terms of their growth, structure, performance and applications.

Intensive research into relaxor ferroelectrics crystals has been carried out, mainly concerning crystal growth, their properties (including piezoelectric, ferroelectric, pyroelectric and optic performance) and microstructures, their applications in transducers and actuators. In this chapter, we will discuss some of the most important results. Following this introduction, Section 7.2 presents the development history of relaxor ferroelectrics. PZN–PT and PMN–PT single crystals posses the largest piezoelectric performance in piezoelectric materials, and they have been commercialized in medical ultrasonic probes. So in Sections 7.3 and 7.4, we discuss in detail some of the results about PZN–PT and PMN–PT, respectively. In Sections 7.5 and 7.6, we present results for PSN–PT and PIN–PT, which can make up for the deficiency of PMN–PT and PZN–PT in temperature stability. Finally, two theoretical models on relaxor crystals, applications of these crystals and a general conclusion are presented.

7.2 The history of relaxor ferroelectrics

In 1959 and 1961, Bokov and Myl'nikova reported the growth of PMN [1] and PZN [2] crystals from a flux of PbO, and they observed their ferroelectric properties successfully. The dielectric relaxation properties of composite perovskite ferroelectrics $A(B'B'')O_3$ were first observed by Smolenskii *et al.* In 1961, they reported the dielectric relaxation behavior of PMN single crystals [3]. In 1967, PMN single crystals were grown by Bonner and Uiter [4] using the Kyropoulos method. After that, many scientists grew PZN and PZN–PT single crystals using the flux method [5–8]. The growth method of PMN–PT and PZN–PT crystals was mainly using a flux of PbO or B_2O_3. During this time, the properties of these crystals were difficult to characterize due to the small size of grown crystals. In the following years, no great progress was achieved in the growth of PZN–PT and PMN–PT crystal.

The research into relaxor ferroelectric single crystals got a large boost in the early 1980s, because of obtaining a large size sample (size of one side not less than 6 mm) to measure its piezoelectric performance, which was achieved by Kuwata, Uchino and Nomura [9,10]. They used the flux method to grow PZN–PT with compositions near the morphotropic phase boundary (MPB). The d_{33} and k_{33} of 0.91PZN–0.09PT achieved 1500–1570 pC/N and 90–92%, respectively; however, piezoelectric properties of tetragonal PZN–PT was relatively low ($d_{33} < 800$ pC/N, $k_{33} < 85\%$). At the same time, they also found that the orientation of rhombohedral PZN–PT with optimized d_{33} was along the <001> direction, not along its spontaneous polarization <111> direction. After that, the growth of relaxor ferroelectric single crystals made little further progress during the 1980s, partly because not enough attention was paid to Kuwata *et al.* study and partly because the growth of these single crystals was too difficult. Towards the end of the 1980s, further studies were carried out on relaxor ferroelectric single crystals. In 1989 and 1990, Shrout *et al.* from Pennsylvania State University grew PMN–PT crystal by the flux method, and the d_{33} of the sample reached 1500 pC/N [11]. In 1990, Ye *et al.* grew PMN single crystal using the same method, and the largest size reached 13 mm [12]. Yamashita and Saitoh from Toshiba Co. repeated Kuwata *et al.* study, and got similar results to the original study. In 1994 and 1995, they were granted several patents for ultrasonic probes based on relaxor ferroelectric crystal [13–15]. From then on, investigation of growth of the ferroelectric single crystals and their properties became the focus in ferroelectrics. PZN–PT crystals with size larger than 20 mm were grown successfully by Mulvihill *et al.* [16]. The size of their crystals met the size requirement for some kinds of ultrasonic probe. At the same time, the piezoelectric performance of the crystals was improved considerably: the d_{33} and k_{33} achieved 2500 pC/N and 94%, respectively; it achieved a strain of 1.7% with a hysteresis of 0.6%. Figure 7.1 presents the high piezoelectric performance of these kinds of crystals, as reported by Park and Shrout [17]. Compared with PZT ceramics, their piezoelectric performance is much superior to that of PZT. A piezoelectric materials expert at Penn State, Eric Cross, described it as ‘an exciting breakthrough’. The journal *sciences* reported their

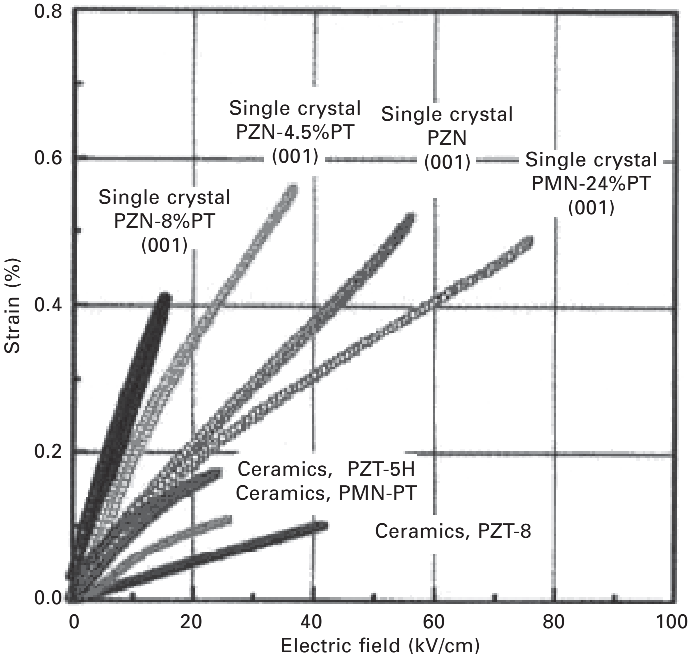

7.1 Strain vs E-field behavior for <001> oriented rhombohedral crystals of PZN–PT and PMN–PT and for various electromechanical ceramics [17].

investigation [18]. These excellent performances make relaxor-based single crystal a promising candidate for the next generation of transducers.

In 1997, Kobayashi *et al.* used improved flux method to grow PZN–PT crystal, and the size of the as-grown crystal reached $43 \times 42 \times 40$ mm^3, the largest size reported at that time [19]. In 1998, Shimanuki *et al.* used the Bridgman method to grow PZN–PT crystal; the size reached a diameter of 30 mm and a length of 20 mm [20]. In 1997, Luo *et al.* used a modified Bridgman method to grow PMN–PT single crystals successfully directly from their melt, the size reaching dimensions of $\phi 40 \times 80$ mm^3 [21, 22]. The Bridgman method is now widely adapted to make PMN–PT, which are promising candidates for the practical applications of the next generation of high performance devices.

7.3 PZN–PT crystal

PZN is rhombohedral phase, and PT is tetragonal phase; the structure of (1-x) PZN–xPT crystal depends on the composition x at room temperature. The MPB in (1-x) PZN–xPT occurs near $x = 0.09$. (1-x)PZN–xPT is rhombohedral if PT content is lower than MPB composition, and it becomes tetragonal phase at PT content larger than MPB composition. At MPB composition, rhombohedral and tetragonal phases coexist in PZN–PT; some ferroelectric experts think that monoclinic and orthorhombic phases also exist at the MPB. Figure 7.2(a) shows a simple phase diagram of PZN–PT at low temperature. PZN–PT crystal near MPB is very unstable: on the one hand, the existence of MPB in PZN–PT enables it to possess excellent performance characteristics, such as very high electromechanical coefficient, piezoelectric constant and strain induced by electric field; on the other hand, the instability of PZN–PT make the crystal very difficult to grow, especially in controlling homogeneity and composition of the crystal [23]. The piezoelectric performance of PZN–PT crystal depends not only on its composition, but also on its orientation, as shown in Fig. 7.2(b). Rhombohedral PZN–PT crystal near its MPB has the largest d_{33}, reaching ~2500 pC/N; furthermore, its optimized orientation for high piezoelectric performance is along the <001> direction, not along its spontaneous polarization direction <111>. In the rhombohedal region, d_{33} increases sharply with PT content when approaching the MPB. PZN–PT with 9% PT content has the largest d_{33}, and then d_{33} decreases sharply in the tetragonal region. Compared with in the rhombohedral phase, d_{33} is relatively low in the tetragonal phase.

7.3.1 Growth of PZN–PT

PZN–PT is not stable at high temperature; it decomposes from perovskite structure to pyrochlore phase. It is not easy to fabricate high-quality and

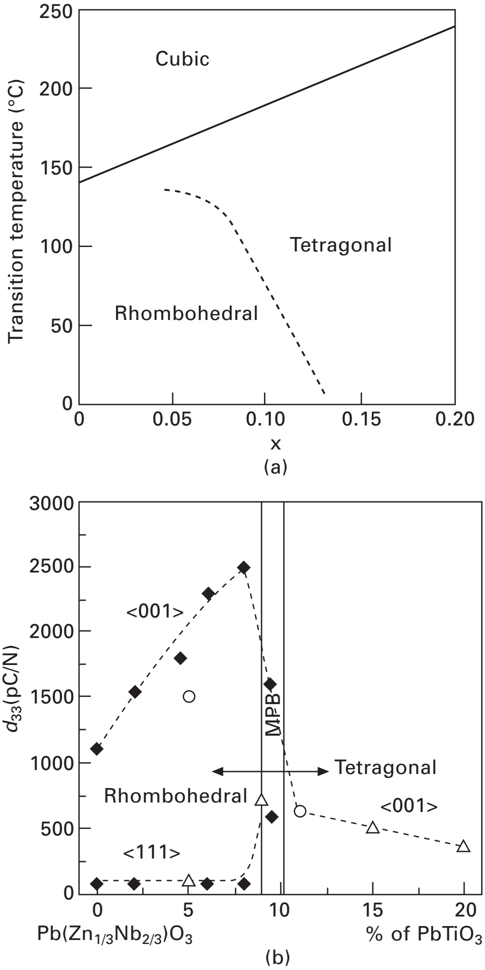

7.2 (a) Phase diagram of the (1-x)$Pb(Zn_{1/3}Nb_{2/3})O_3$–$x$$PbTiO_3$ solid solution system near MPB [9, 10], (b) d_{33} as a function of crystal composition and orientation for PZN–PT [17].

large-size single crystals in a pure phase, a result of the high volatility of lead oxide and instability of PZN–PT at high temperature. Until now, many methods have been used to grow this crystal. At the prophase during the investigation of PZN–PT, scientists mainly used the fluxing method to grow PZN–PT, though the grown crystal is not large enough for application in practice. In terms of synthetic process, PZN–PT crystals were mainly grown by the flux method [16, 24, 25] and by a modified Bridgman technique [20, 26, 27]. The fluxing method is usually unsuitable for the growth of large crystals because of the occurrence of spontaneous nucleation. The as-grown crystals produced by fluxing are liable to contain inclusions of PbO flux and a pyrochlore phase. The Bridgman method allows for the manufacture of crystals with controlled dimension and good reproducibility. The perovskite phase of PZN–PT is not very stable; it decomposes from perovskite phase to pyrochlore phase. The decomposition from perovskite to pyrochlore phase is one of the main reasons that the crystal is difficult to grow. It partially decomposes into a pyrochlore phase above 1148 °C and undergoes an incongruent melting at 1226 °C [28]. PZN–PT single crystals need to be grown in sealed platinum crucibles to suppress the volatilization of PbO and occurrence of spontaneous nucleation. We have developed a modified Bridgman technique to grow 0.91PZN–0.09PT single crystals with 0.69PMN–0.31PT seed crystal oriented along <111> direction. Figure 7.3(a) is a sketch of the furnace used to grow PZN–PT.

High purity raw powders of PbO, ZnO, Nb_2O_5 and TiO_2 are dried before weighing. The mixture of these powders is maintained in the ratios of PZN:PT = 91:9 and PZN–PT:PbO = 45:55 in mole percentage. PbO acts as flux. The raw materials are precalcined by B-site precursor synthesis, which can prevent, to some extent, the formation of the pyrochlore phase [26]. B-site precursor synthesis of raw materials can effectively reduce the formation of pyrochlore phase during crystal growth. 0.91PZN–0.09PT crystals are grown in sealed platinum crucibles to prevent the evaporation of PbO during crystal growth. PZN–PT crystals are grown at about 1250 °C. It is possible to obtain four 0.91PZN–0.09PT crystal boules simultaneously by this method. Temperature gradient is an important consideration for the Bridgman technique [27]. Fig. 7.3(b) shows the temperature gradient of the Bridgman furnace. The temperature gradient could be dominated at around 30–50 °C/cm at the solid–liquid interface by this method, which is ideal for crystal growth. 0.91PZN–0.09PT single crystals with diameter 28 mm and length 30 mm can be obtained, as shown in Fig. 7.4(a). The as-grown crystals exhibit dark-brown color on their surface due to a thin coat of PbO flux. After flux removal by boiling acetic acid, the obtained crystals reveal three faces, as shown in Fig. 7.4(b).

7.3.2 Properties of PZN–PT

Ranjan *et al.* [25] investigated the relation between the T_c and PT content of PZN–PT; Fig. 7.5 indicates a nearly linear function between T_c and PT. If PZN–PT single crystal is heated to a temperature higher than T_c, the tetragonal phase transforms to a cubic phase. The PT content of the PZN–PT can be inferred according to the wafer's T_c. Figure 7.6 shows the temperature dependence of the dielectric constants of poled wafers of 0.93PZN–0.07PT and 0.91PZN–0.09PT single crystal. Between 70 and 100 °C, there are two dielectric peaks, which relate to the phase transition temperature T_{rt}, responding

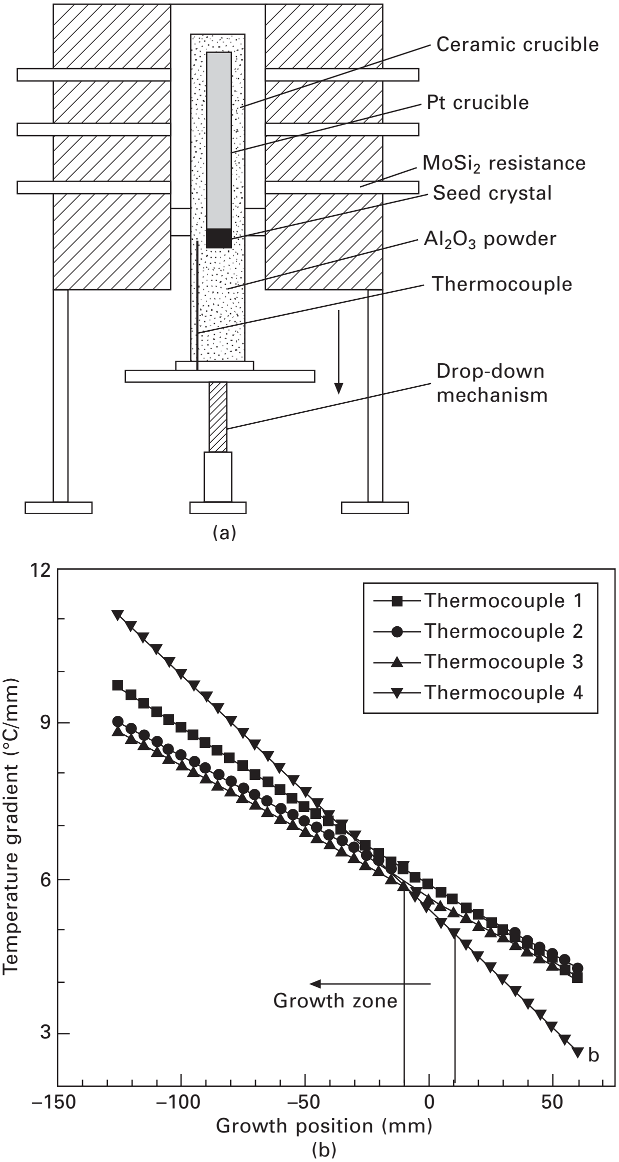
Ceramic crucible
Pt crucible
$MoSi_2$ resistance
Seed crystal
Al_2O_3 powder
Thermocouple
Drop-down mechanism
(a)
12
9
6
3
Temperature gradient (°C/mm)
Thermocouple 1
Thermocouple 2
Thermocouple 3
Thermocouple 4
Growth zone
b
–150
–100
–50
0
50
Growth position (mm)
(b)

7.3 (a) Schematic diagram of the modified Bridgman furnace used for the growth of PZN–PT single crystal from flux. (b) Axial temperature gradient profile of the Bridgman furnace for the growth of 0.91PZN–0.09PT single crystals [29].

to the phase transition from rhombohedral to tetragonal. The existence of T_{rt} makes piezoelectric performances of PZN–PT unstable with temperature, which limits its application in some transducers to some extent. The T_{rt} of

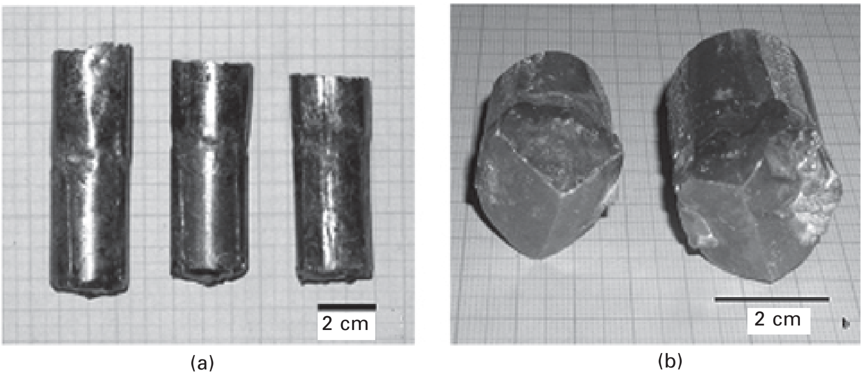

7.4 (a) As-grown 0.91PZN–0.09PT crystal boules grown by a modified flux Bridgman method. (b) Morphology of 0.91PZN–0.09PT crystals grown by a modified flux Bridgman method [29].

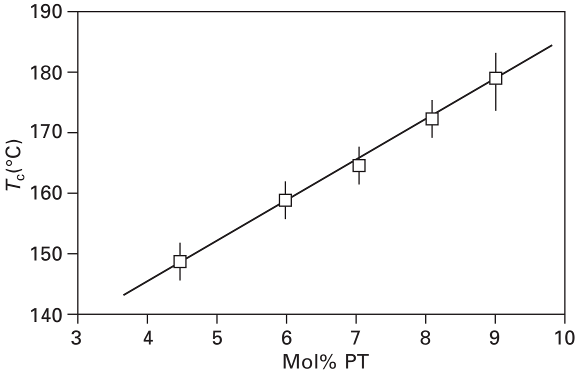

7.5 T_c of PZN–PT as a function of PT content [25].

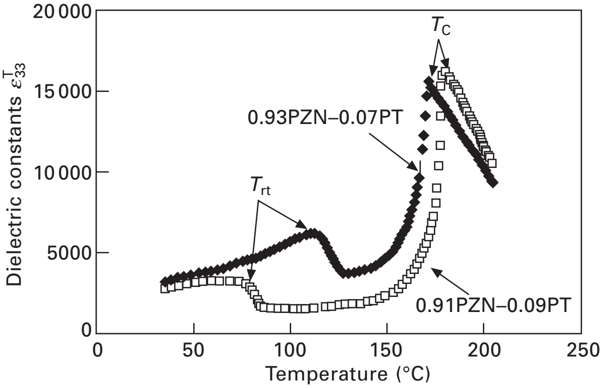

7.6 Temperature dependence of the dielectric constants of poled 0.93PZN–0.07PT and 0.91PZN–0.09PT crystal measured at 1 kHz [30].

0.93PZN–0.07PT and 0.91PZN–0.09PT single crystal occur at about 110 °C and 72 °C, respectively. The T_{rt} of 0.93PZN–0.07PT single crystal is about 40 °C higher than that of 0.91PZN–0.09PT, while the T_c of 0.93PZN–0.07PT single crystal is about 10 °C lower than that of 0.91PZN–0.09PT. Although the piezoelectric performance of 0.93PZN–0.07PT is lower than that of 0.91PZN–0.09PT, the stability of 0.93PZN–0.07PT is higher than that of 0.91PZN–0.09PT, due to its higher T_{rt} [30]. So 0.93PZN–0.07PT is more practical in piezoelectric devices.

A stable multidomain state and correspondingly high level of piezoelectric activity can be achieved in nonpolar <001>-oriented crystals. A complete set of elastic, piezoelectric and dielectric constants has been reported for 0.955PZN–0.045PT, 0.93PZN–0.07PT and 0.92PZN–0.08PT single crystal systems [31, 32, 33]. It is helpful to list the complete set of matrix properties for those crystals for both fundamental study and device design purposes; the data is presented in Table 7.1. The elastic constant of the three crystals is very close to each other. Compared with the other two crystals, the 0.955PZN–0.045PT single crystal system represents relatively lower electromechanical capability of this solid solution system, because it is further away from the MPB composition. 0.92PZN–0.08PT single crystal system possesses much better piezoelectric performance than that of 0.955PZN–0.045PT. The electromechanical coupling coefficient k_{33} of 0.92PZN–0.08PT can reach 0.94. PZN–PT single crystal systems near the MPB composition exhibit strong property fluctuations because of their complex domain structure. Among the domain engineered PZN–PT single crystal systems, the 0.93PZN–0.07PT single crystal system might be the best candidate for device applications since its properties are comparable to that of 0.92PZN–0.08PT and it is much more stable, because it is a little further away from the MPB composition. It has been reported that the properties of 0.92PZN–0.08PT vary greatly [33]: the measured value of d_{33} varies from 2000 to 4000 pC/N and the value of ε_{33}^{T} varies from 5000 to 8000, which makes 0.92PZN–0.08PT single crystal unsuitable for many practical device applications. Furthermore, the T_{rt} of 0.93PZN–0.07PT is higher than that of 0.92PZN–0.08PT, which makes 0.93PZN–0.07PT more stable with temperature.

The piezoelectric properties of PZN–PT crystal have strong anisotropy. PZN–PT is a complicated solid solution; its properties are sensitive not only to its composition but also to its orientations, as shown in Table 7.2. Although PZN–PT crystals with the same composition are grown from their high-temperature melt, their properties are much different from each other due to different growth techniques and post-treatment processes. Even a different position of one wafer produces different properties due to its complex domain structure and phase structure, so the reported results in the literature are different.

Table 7.1 Measured and derived material properties of 0.955PZN–0.045PT, 0.93PZN–0.07PT, 0.92PZN–0.08PT single crystal poled along <001> [31,32,33]

Density: ρ(kg/mm^3)

0.93PZN–0.07PT	0.92PZN–0.08PT	0.955PZN–0.045PT
8350	8315	8310

Elastic stiffness constants: c_{ij} (10^{10} N/m^2)

PT (%)	c^E_{11}	c^E_{12}	c^E_{13}	c^E_{33}	c^E_{44}	c^E_{66}	c^D_{11}	c^D_{12}	c^D_{13}	c^D_{33}	c^D_{44}	c^D_{66}
7.0	11.30	10.3	10.5	10.91	6.30	7.10	11.37	10.37	10.00	14.00	6.80	7.10
8.0	11.50	10.50	10.90	11.51	6.34	6.50	11.80	10.80	10.00	14.30	6.76	6.50
4.5	11.10	10.20	10.10	10.50	6.40	6.30	11.30	10.40	9.50	13.50	6.70	6.30

Elastic compliance constants: (10^{-12}m^2/N)

PT (%)	s^E_{11}	s^E_{12}	s^E_{13}	s^E_{33}	s^E_{44}	s^E_{66}	s^D_{11}	s^D_{12}	s^D_{13}	s^D_{33}	s^D_{44}	s^D_{66}
7.0	85.90	–14.10	–69.0	142	15.9	14.1	56.7	–43.3	–9.6	20.9	14.7	14.1
8.0	87.0	–13.1	–70.0	141	15.8	15.4	55.8	–44.2	–8.2	18.5	14.8	15.4
4.5	82.0	–28.5	–51.0	108	15.6	15.9	61.5	–49.0	–9.0	20.6	14.9	15.9

Piezoelectric constants: $e_{i\lambda}$ (C/m^2) $d_{i\lambda}$ (10^{-12} C/N) $g_{i\lambda}$ (10^{-3}Vm/N) $h_{i\lambda}$ (10^8 V/m)

PT (%)	e_{15}	e_{31}	e_{33}	d_{15}	d_{31}	d_{33}	g_{15}	g_{31}	g_{33}	h_{15}	h_{31}	h_{33}
7.0	11.1	–2.3	15.1	176	–1204	2455	6.6	–24.2	49.3	4.5	–3.1	20.7
8.0	10.1	–5.1	15.4	159	–1455	2890	6.2	–21.3	42.4	4.2	–5.8	17.7
4.5	8.9	–3.7	15.0	140	–970	2000	5.0	–21.0	44	3.4	–4.3	17

Dielectric constants: $\varepsilon(\varepsilon_0)$ $\beta(10^{-4}/\varepsilon_0)$

PT (%)	ε^s_{11}	ε^s_{33}	ε^T_{11}	ε^T_{33}	β^s_{11}	β^s_{33}	β^T_{11}	β^T_{33}	k_{15}	k_{31}	k_{33}	k_t
7.0	2779	823	3000	5622	3.60	12.2	3.33	1.78	0.27	0.58	0.92	0.47
8.0	2720	984	2900	7700	3.68	10.2	3.45	1.30	0.25	0.60	0.94	0.45
4.5	3000	1000	3100	5200	3.4	10.0	3.2	1.9	0.23	0.50	0.91	0.50

Table 7.2 The main piezoelectric properties of PZN–PT crystal with different compositions and orientations [23]

Composition	Direction	k_{33} (%)	k_{31} (%)	ε	tanδ (%)	d_{33} (pC/N)	d_{31} (pC/N)	Reference
0.91PZN–0.09PT	(001)	95.3	80.8	4600	0.9	2500	–1700	34
	(110)	/	59	3512	2.09	530	–715	35
	(111)	/	18.9	1606	0.89	190	–167	35
0.92PZN–0.08PT	(001)	94	60	5000	1	2500	–1250	17
	(110)	/	31	3745	/	580	331	36
	(111)	39	/	1000	1.2	84	/	17
0.93PZN–0.07PT	(001)	92	58	5622	<1	2455	–1024	32
0.955PZN–0.045PT	(001)	92	57	5000	0.3	2280	–1015	37
	(110)	73	56	2675	/	900	611	36
	(111)	41	17	640	0.2	92	–47	37

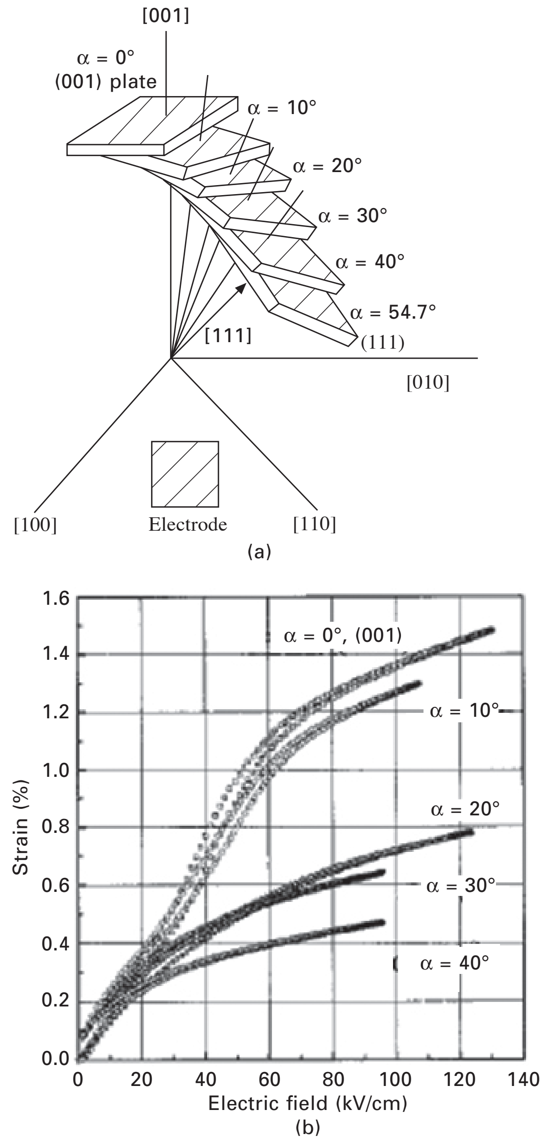

7.7 (a) Schematic diagram of sample preparation for investigating optimum crystallographic orientation. (b) Strain vs *E*-field curve of PZN–4.5%PT crystals oriented along <001>, where α is the degree of deviation from <001> toward <111> [17].

To find the optimal orientation for high piezoelectric performance, Park and Shrout [17] have investigated 0.955PZN–0.045PT samples whose orientation deviates from <001> to <111>. The dice method and result are presented in Fig. 7.7, the results of which are consistent with Table 7.2. Strain saturation becomes more significant as α increases from <001> to <111> direction. At high fields, strain level decreases with increased α; however, crystals oriented close to <001> (α <20°) exhibit no saturation and low hysteresis. So the <001> orientation is the optimal direction for high piezoelectric coefficient.

P-E hysteresis loops are measured for <001>, <011> and <111> oriented crystals at room temperature under electric field level of 10 kV/cm [38], as shown in Fig. 7.8. The data clearly show the ferroelectric state of the PZN–PT and anisotropy in the three orientations. At room temperature, the value of P_s and P_r for the <001> orientation are 35 and 25 μC/cm^2, 35 and 30 μC/cm^2 for <110> orientation, while those for the <111> orientation are 35 and 33 μC/cm^2, respectively. These results show that in each orientation the room temperature polarization state (*P*s) is equivalent along all of the three directions. Furthermore, there are significant differences in the magnitude of the P_r, area of the hysteresis loops and in the coercive field (E_c). The coercive field at room temperature is found to increase from 2.2 kV/cm for the <001> to 4.5 kV/cm for the <110> to 6 kV/cm for the <111> orientations [38].

7.4 PMN–PT crystal

7.4.1 Phase diagram and crystal growth

(1-x)PMN–xPT crystal is also a kind of complex solid solution of relaxor ferroelectric PMN and normal ferroelectric PT. PMN is rhombohedral phase, and its T_c is –10 °C. The structural characterization of (1-x)PMN–xPT crystal is similar to PZN–PT, its structure also depends on the composition x at room temperature. The structure of (1-x) PMN–xPT transforms from rhombohedral to tetragonal phase with x increment. MPB exists in (1-x) PMN–xPT system near $x = 0.33$. However, the exact MPB position of x is not consistent in the literature [39, 40]. Generally speaking, the PT content of the MPB region is located at $x = 0.30$–0.35, which means that the MPB region is not a line but an area. Investigation shows that there is not only rhombohedral and tetragonal phases but also a monoclinic phase in PMN–PT at the MPB region [41, 42]. Figure 7.9(a) is a simple phase diagram of PMN–PT at low temperature, which suggests that the MPB region lies at $x = 0.33$ [43]. Figure 7.9(b) is a modified phase diagram: MPB exists within a range of 0.30–0.38, in which a monoclinic phase also exists. MPB separates a trigonal from a tetragonal phase [44].

PMN–PT also undergoes an incongruent melting at high temperature; however, it is more stable than PZN–PT, so it is easier to grow PMN–PT than PZN–PT. There are mainly two processes to grow PMN–PT crystal: the flux method and the Bridgman method. In terms of synthesis process, PMN–PT

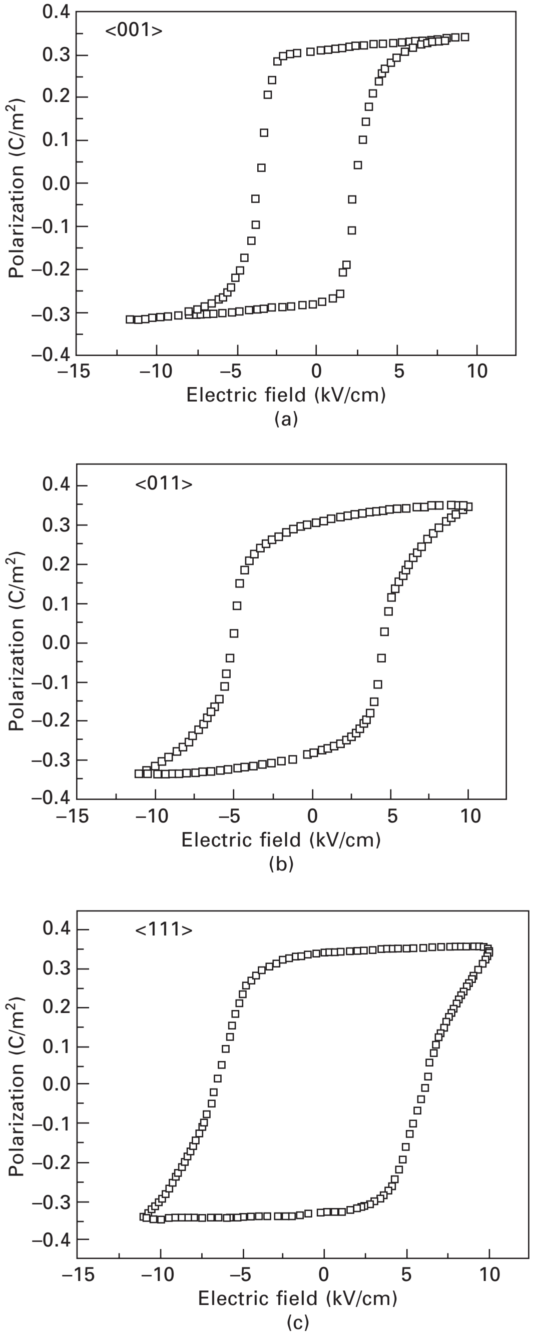

7.8 Polarization-electric field measurements on 0.92PZN–0.08PT single crystals oriented along (a) <001>, (b) <011> and (c) <111> [38].

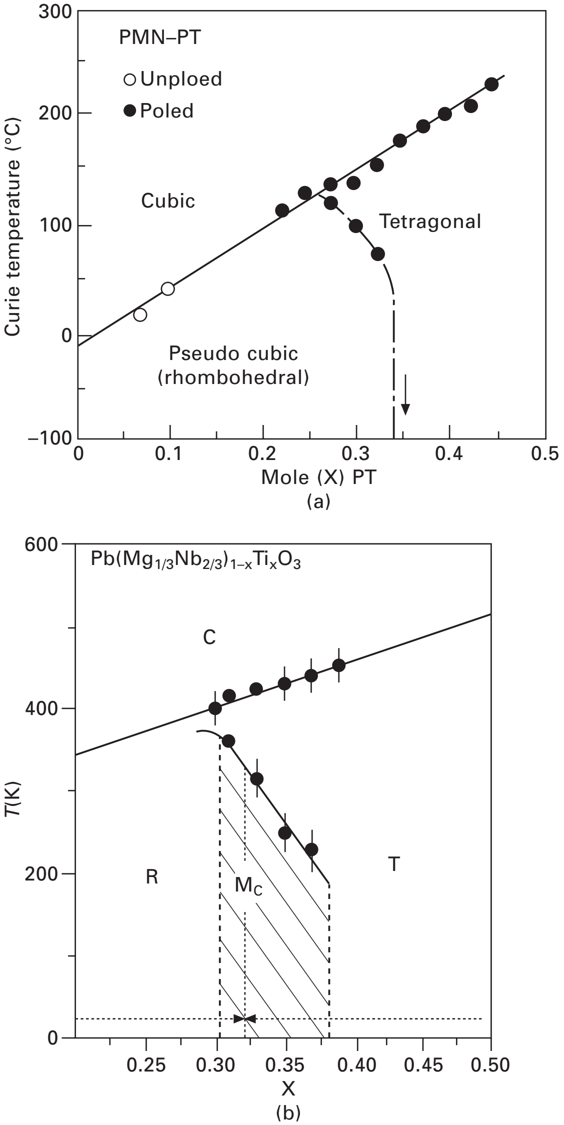

7.9 (a) Phase diagram of (1-*x*)PMN–*x*PT at low temperature [43]. (b) Modified phase diagram in (1-*x*)PMN–*x*PT around the MPB by Noheda *et al.* [44].

crystals are mainly grown by the flux method [45, 46, 47]. The modified Bridgman technique was developed for the growth of large size crystals for device applications [20, 21, 48]. The control of spontaneous nucleation has been a major concern both for the flux and the Bridgman growth. We have established a technique to grow PMN–PT single crystals directly from its melt on the basis of investigation of the phase stability of PMN–PT at high temperature. The PMN–PT crystal with pure perovskite structure is grown directly from its melt in an isolated Pt crucible. The furnace used here is the same as that used for the growth of PZN–PT, as mentioned in Section 7.3.1. The seed crystals can be used either along <001>, <110> or <111> direction. The furnace is kept at about 1380 °C during crystal growth, and the temperature gradient is about 40–100 °C at the solid–liquid interface. After the accomplishment of growth, the furnace is cooled down to room temperature at a rate of 25 °C/h. Using this method, large sizes over $\phi 50 \times 80$ mm^3 PMN–PT can be grown. Figure 7.10 shows the as-grown crystals with composition near the MPB. The PMN–PT can be diced into different shapes to be used in different devices.

By replacing the flux technique with the Bridgman method, crystal size increases and cost reduces. However, it brings a problem for the PMN–PT crystal: Ti content varies along the boule axis, which results in property variation along the axis. Figure 7.11 shows Park and Hackenberger's result, in which the T_c of the boule varies with boule axis [49]. By using a combination of zone melting technique with Bridgman method, the Ti distribution can be manipulated to some degree. H.C. Materials Corp. has improved the composition uniformity by using a combination of zone melting technique with Bridgman method [50].

7.4.2 Dielectric properties

The Curie points of the pure $PbTiO_3$ and pure $Pb(Mg_{1/3}Nb_{2/3})O_3$ crystals are 490 °C and –10 °C, respectively. The T_c of the PMN–PT increases with

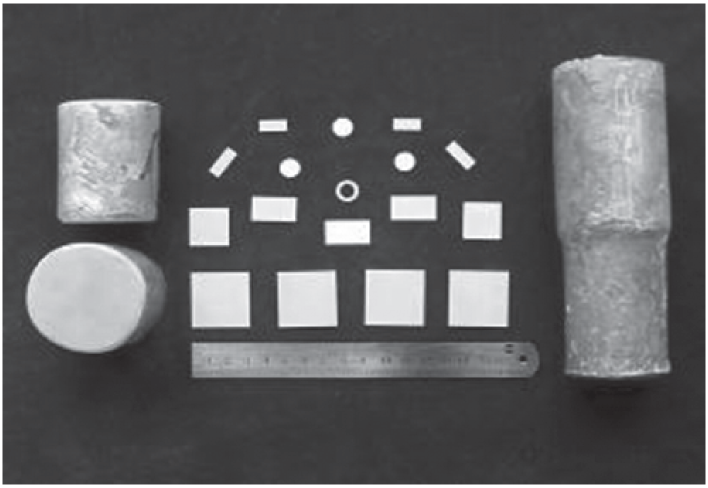

7.10 The as-grown PMN–PT crystals with composition near the MPB.

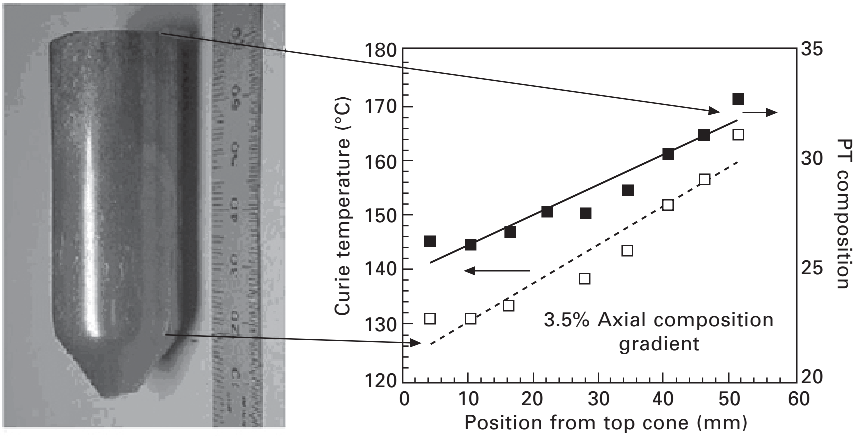

7.11 PMN–PT crystals grown by the Bridgman method and PT content along the growth direction [49].

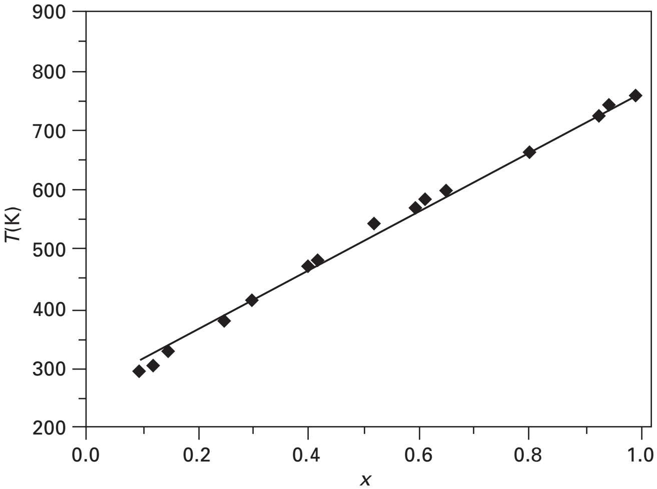

7.12 The compositional dependence of T_c fitted with one line [51].

PT content. Segregation will occur during the growth of PMN–PT single crystals, it is necessary to determine the composition of the grown crystal. Zekria *et al*. [51] have investigated the relation between composition and the T_c of PMN–PT crystal. The local compositions of the PMN–PT were determined by electron probe microanalysis. The Curie temperature was measured by an optical method. The compositional dependence of T_c is shown in Fig. 7.12.

One line can fit the relation between T_c and PT content [51]:

$$T_c = 268 + 494x \quad \text{for } x < 0.50 \tag{7.1}$$

By this relation, we can calculate the PT content (x) by measuring the T_c. The content of PT and the orientation influence the dielectric properties of PMN–PT greatly. Zhao *et al.* [52] have investigated the dielectric behavior of the <001>-oriented unpoled (1-x)PMN–xPT single crystals with different composition. The temperature corresponding to the maximum of the dielectric constant is called the temperature T_m (or T_c). For the rhombohedral PMN–PT crystals, only one dielectric peak is obtained at T_m, indicating a phase transition from the FE_r phase to paraelectric cubic phase near the T_m [53, 54]. For the tetragonal PMN–PT crystal, there is also one dielectric peak at the T_m, indicating a phase transition from the FE_t phase to paraelectric cubic phase. (1-x)PMN–xPT crystals with $x \leq 0.31$ is a dominant relaxor state for the evident frequency dispersion of dielectric constant in the ferroelectric phases [52]. However, with the increment of PT, the frequency dispersion behavior is not obvious and could be observed only near T_m.

For the poled rhombohedral PMN–PT near the MPB, its phase transition is very complex. As shown in Fig. 7.13(a), upon heating from room temperature along the <111>-direction of 0.70PMN–0.30PT, rhombohedral macrodomain begins to transit to microdomain near T_{rd} at 100 °C; then rhombohedral microdomain transitions to tetragonal microdomain near T_{rt} at 105 °C [55]. Near the temperature T_m at 135 °C, ferroelectric tetragonal (FE_t) phase transforms to paraelectric cubic phase. Three temperatures (T_{rd}, T_{rt}, T_m) correspond to three discharging current peaks. As presented in Fig. 7.13(b), upon heating from room temperature along the <110> direction, two small permittivity peaks can be observed at T_{ro} (89 °C) and T_{ot} (100 °C), respectively. The first small peak T_{ro} coincides with a phase transition from the FE_r to a ferroelectric orthorhombic FE_o state, and the second small peak T_{ot} indicates the transition from the FE_o to FE_t state [56, 57]. For <001> poled 0.70PMN–0.30PT crystals shown in Fig. 7.13(c), there are also two small permittivity peaks at T_{rm} and T_{mt}, respectively, a monoclinic ferroelectric FE_m phase being a metastable state between the lower temperature FE_r phase and the higher temperature FE_t phase [42, 58]. Corresponding to the permittivity versus temperature curve, there are also three discharging current peaks in the discharging current curve. Two broad small permittivity peaks and two broad discharging current peaks indicate three ferroelectric phases (FE_r, FE_m, and FE_t) coexisting in a large temperature range. For the poled <111> PMN–PT, it transmits to tetragonal ferroelectric phase at about 100 °C; for the <110> poled PMN–PT, the orthorhombic ferroelectric and tetragonal phase can be easily induced during the heating process; for the <001> poled PMN–PT, monoclinic and tetragonal phase transition occur, all the phase transitions are mentioned as above.

The piezoelectric response can be greatly affected due to phase transition happening. So the practical application of the poled PMN–PT is limited by the first phase transition temperature. Figure 7.14 presents the composition

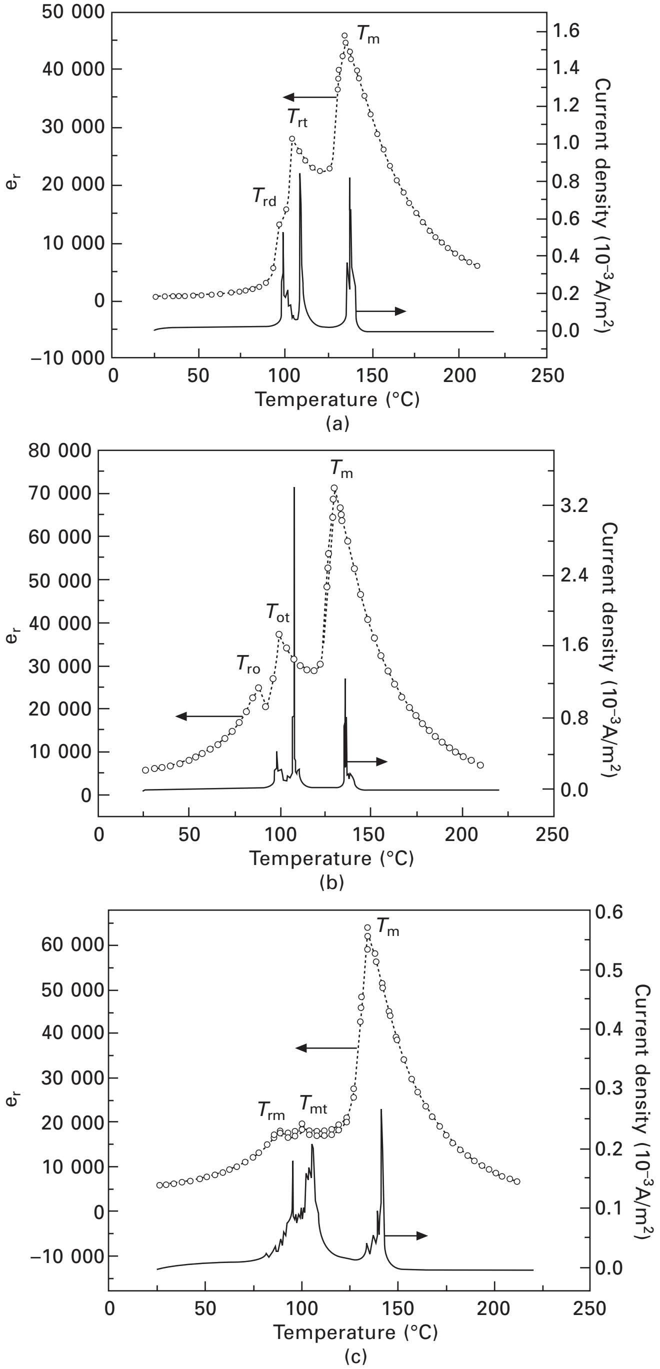

7.13 Temperature and orientation dependence of the dielectric constant and discharging current density for the poled 0.70PMN–0.30PT single crystals: (a) <111>, (b) <110> and (c) <001>.

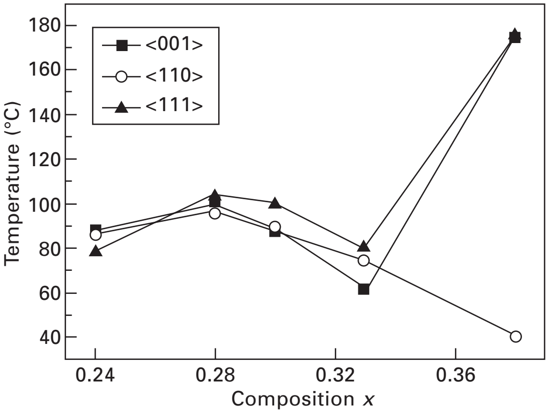

7.14 Composition and orientation dependence of the first structure transformation temperature for the poled (1-*x*)PMN–*x*PT crystal.

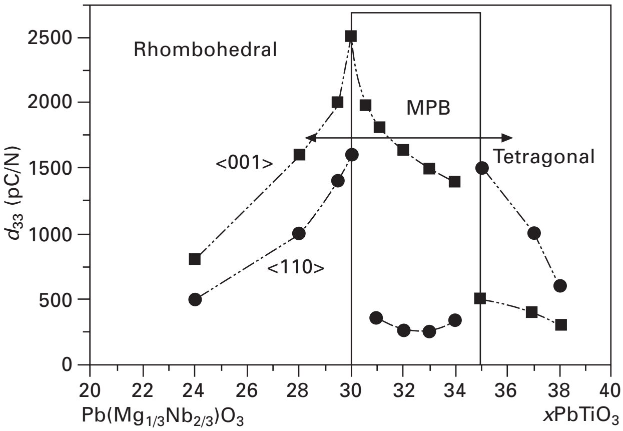

7.15 Piezoelectric coefficient d_{33} as a function of composition and orientation dependence for PMN–PT single crystals.

and orientation dependence of the first structure transformation temperature of the poled PMN–PT. In order to keep high response in a broad temperature range, these <001> poled crystals with *x* from 0.28 to 0.30, whose first phase transformation temperature is between 80 °C and 100 °C and piezoelectric performance is very high, should be some of the preferred materials for practical applications in transducers, sensors, and actuators.

7.4.3 Piezoelectric properties

Piezoelectric coefficients as a function of composition and crystal orientation for PMN–PT are presented in Fig. 7.15. As shown, large piezoelectric coefficients (d_{33} ~ 2500 pC/N) were found for PMN–PT single crystals with the MPB composition (0.7PMN–0.3PT). This is in perfect accord with that reported by Singh and Pandey [59]. As shown, crystals poled along the pseudocubic <001> direction exhibit large piezoelectric coefficients and d_{33} increases with $PbTiO_3$ content for <001>-oriented rhombohedral crystals. However, piezoelectric coefficients d_{33} and electromechanical coefficients k_{33} for <111>-oriented rhombohedral PMN–PT single crystals are only 100 pC/N and 35%. For <110> poled PMN–PT single crystals, piezoelectric coefficient also has a strong dependence on the PT content. As shown in Fig. 7.15, in the rhombohedral region, piezoelectric coefficient d_{33} has a similar trend to <001> poled crystals. Two abnormal points (or rather, almost certainly two narrow regions) of the piezoelectric constant appear clearly for <110>-oriented crystals, the piezoelectric coefficients for the composition region $0.30 < x < 0.35$ are very low. It can be concluded that the equivalent domain configuration is indispensable for a strong piezoelectric response in ferroelectric perovskite crystals. In the MPB region, orthorhombic phase can be easily induced which leads to low piezoelectric properties.

<001>-oriented PMN-PT crystals near the MPB exhibit very high strain and low hysteresis, as reported by Park and Shrout [17]. We also have calculated the strain behavior of PMN–PT as a function of composition and orientation. Figure 7.16 is an *E*-field-induced strain as a function of composition for <001>-oriented PMN–PT crystals. Due to the complexity of the domain configuration and phase composition near the MPB in PMN–PT crystals, domain motion and phase transformation can easily be induced by an *E*-field, which can cause unusually high strain and large hysteresis.

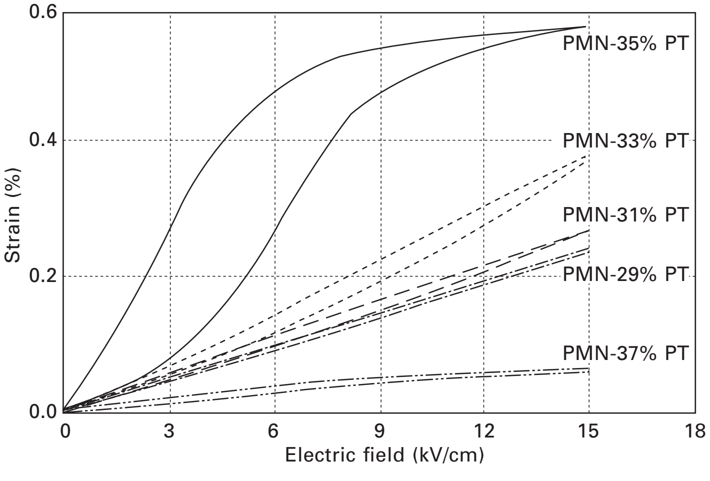

7.16 Strain versus *E*-field curve for <001>-oriented PMN–PT crystals [60].

In the rhombohedral ferroelectric phase such as 0.71PMN–0.29PT and 0.69PMN–0.31PT, high strain values and small hysteresis can be achieved with the engineered domain stability. The <001>-oriented PMN–PT with engineered domain structure is suitable for high strain actuators due to its high strain and little hysteresis.

Viehland *et al.* [61] have carried out temperature dependent electromechanical investigations of <110>, <001>, and <111>-oriented MPB compositions of PMN–PT crystals. Figure 7.17(a) reveals that the values of d_{33} along the <001> and <011> directions are nearly equivalent over the temperature range of 25–80 °C. d_{33} increases from 1200 to 4000 pC/N sharply with temperature

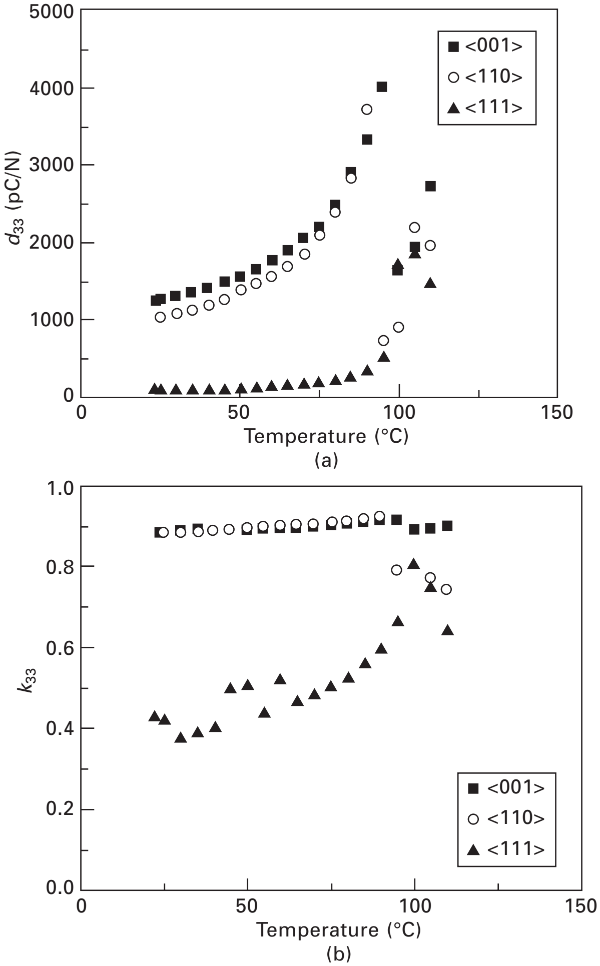

7.17 (a) d_{33} and (b) k_{33} as a function of temperature for <001>, <011> and <111> oriented PMN–PT crystals [61].

over this temperature range. The results are consistent with Fig. 7.15, which shows that <011>-oriented PMN–PT with MPB composition also has high d_{33}. Although <111> direction is the spontaneous direction of rhombohedral PMN–PT, the value of d_{33} for the <111>-oriented crystal is much lower. The piezoelectric constant increment of <001>, <011>, and <111>-oriented PMN–PT with temperature may be due to the phase transition, softening of Young's modulus and the increased mobility of domain with temperature. Figure 7.17(b) shows the longitudinal electromechanical coupling coefficient (k_{33}) as a function of temperature for poled <001>, <111>, and <011> orientations. The data reveal that the values of k_{33} along the <001> and <011> directions are also nearly equivalent over the temperature range from 25 to 80 °C, However, it is almost temperature independent, which is different from the behavior of d_{33}. Furthermore, the value for the <111> orientation is much lower. At room temperature, only a k_{33} of 0.38 is obtained; however, it increases with temperature reaching 0.8 at 100 °C.

The properties of PMN–PT crystals are influenced greatly by their orientation, composition, process of growth, post-processing and so on. So the properties of PMN–PT reported by different researchers are different. Table 7.3 shows the piezoelectric performance of <001>-oriented PMN–PT obtained by different research groups. <001>-poled 0.7PMN–0.3PT crystals exhibit 4 mm symmetry in macroscopic material properties because of stable engineered domain structure. There are a total of 11 independent physical constants describing the elasto-piezo-dielectric matrices for this symmetry. Because of its high piezoelectric performance, it is necessary to determine the complete set of elastic, piezoelectric, and dielectric constants of these crystals for device design. Peng *et al.* [62] used a resonant method to determine the entire set of constants for these crystals according to the IEEE standard on piezoelectricity. The data are presented in Table 7.4. Wang *et al.* [63] have also determined the complete set of <011>-poled 0.7PMN–0.3PT crystals. Zhang *et al.* [64] used a hybrid method combining the advantages of ultrasonic and resonance techniques to determine the complete set of constants of <111>-oriented 0.67PMN–0.33PT with single domain, which can minimize the propagation of measurement errors and improve the consistency of the complete data set. The complete set of constants of PMN–PT with single domain is very useful to calculate the optimal orientation for piezoelectric, dielectric, and other properties; furthermore, it is helpful in understanding the origin of the excellent performance. Using these data, Damjanovic *et al.* [65] demonstrated that the multi-domain configuration contributes relatively little to the piezoelectric response of 0.67PMN–0.33PT single crystals; the dominant contribution to the large piezoelectric response in this composition appears to be intrinsic lattice effects (such as the large shear piezoelectric coefficients).

Table 7.3 Properties of PMN–PT reported by different research groups

Composition	d_{33} (pC/N)	d_{31} (pC/N)	ε^T	k_{33}/k_{31}	T_c (°C)	tan δ	Reference
<001>-oriented							
0.7PMN–0.3PT	2200–2500	–900	7500–9000	0.92–0.94	130–140	<0.1	66
0.67PMN–0.33PT	2200	–	8000	0.94	166	0.01	49
PMN–PT (PT=0.30–0.33)	2000–3500	–	5500–6500	0.90–0.94	–	< 0.008	50
0.7PMN–0.3PT	1600–2000	–800	5100	0.90	150	–	67
0.7PMN–0.3PT	2280	–1015	4030–7070	–	140–150	<0.01	68
0.7PMN–0.3PT	1500–2500	–(700–1300)	~5000	0.90–0.95	~140	~0.005	ours
<011>-oriented (<100>-length cut)							
0.7PMN–0.3PT	–	–(2100–2600)	5500–6000	0.90–0.94	–	<0.01	69
0.69PMN–0.31PT	–	–(1600–2000)	4000–5000	0.88–0.92	140–145	<0.01	70
PMN–PT	–	–1750	–	–	–	–	71
0.7PMN–0.3PT	900–1600	–(1500–2500)	~6000	0.90–0.95	~140	~0.005	ours

Table 7.4 Measured and derived elastic, piezoelectric, dielectric constants and electromechanical coupling factors of engineered domain 0.7PMN–0.3PT single crystals at room temperature [68]

Elastic stiff constants: c_{ij} (10^{10} N/m^2)

c_{11}^E	c_{12}^E	c_{13}^E	c_{33}^E	c_{44}^E	c_{66}^E	c_{11}^D	c_{12}^D	c_{13}^D	c_{33}^D	c_{44}^D	c_{66}^D
16.04	14.96	12.4	12.0	5.38	2.87	16.3	15.1	6.22	19.6	7.69	2.87

Elastic compliance constants: s_{ij} (10^{-12} m^2/N)

s_{11}^E	s_{12}^E	s_{13}^E	s_{33}^E	s_{44}^E	s_{66}^E	s_{11}^D	s_{12}^D	s_{13}^D	s_{33}^D	s_{44}^D	s_{66}^D
57.3	–34.7	–23.6	57.7	18.6	34.8	11.4	–80.5	–16.7	10.96	13.0	34.8

Piezoelectric constants: e (C/m^2), d (10^{-12} C/N), g (10^{-3} Vm/N), h (10^8 V/m)

e_{15}	e_{31}	e_{33}	d_{15}	d_{31}	d_{33}	g_{15}	g_{31}	g_{33}	h_{15}	h_{31}	h_{33}
31.84	–5.22	30.4	592	–1395	2000	9.4	–23.8	34.2	7.25	–4.26	24.8

Dielectric constants: ε (ε_0), β ($10^{-4}/\varepsilon_0$) and coupling coefficients

ε_{11}^S	ε_{33}^S	ε_{11}^T	ε_{33}^T	β_{11}^S	β_{33}^S	β_{11}^T	β_{33}^T	k_{15}	k_{31}	k_{33}	k_t
4963	1386	7093	6610	2.01	10.9	1.41	1.51	0.55	0.895	0.92	0.62

7.4.4 Solid state crystal growth

Solid state crystal growth (SSCG) or templated grain growth of PMN–PT crystals has been studied for many years due to its comparatively low cost [45, 72, 73]. This technique can convert ceramics with random orientation into single crystal without melting, and its principle is simple: bury an external single crystal seed in fine grain matrix grains; the seed grows by consuming the fine matrix grains without melting the major constituents. SSCG can develop PMN–PT with properties similar to single crystals grown by the melt method using only conventional powder processing techniques at relatively low cost. This technique is an effective method for mass production of large single crystals. PMN–PT crystal can grow from a $BaTiO_3$, PMN–PT and other crystal seed with perovskite structure [70, 74]. Ceracomp Co. can manufacture commercialized PMN–PT by SSCG method; its d_{33} can reach 1500 pC/N [75]. SSCG possesses two advantages over conventional crystal growth. Compared with conventional crystal growth, including Bridgman growth, this process is believed to be more cost-effective. Second, significant compositional variation exists for relaxor-PT crystals such as PMN–PT and PZN–PT during the growth process. In contrast, for SSCG, the compositional variation is small, which leads to the consistency of performance of different parts of a wafer. However, the piezoelectric performance of PMN–PT synthesized by SSCG is comparatively lower. As far as we know, using the SSCG method to synthesize PZN–PT is reported little. Table 7.5 shows the performance of PMN–PT with composition near the MPB, manufactured using the SSCG (Ceracomp Co.), Bridgman (H.C. Materials Corp.) and flux (Microfine Materials Technologies Pte Ltd) methods.

7.5 PSN–PT crystal

Relaxor-based single crystals PZN–PT and PMN–PT offer ultrahigh piezoelectric properties, which make them promising candidates for medical ultrasound transducers. However, their relatively low Curie temperature and their substantially lower ferroelectric (rhombohedral to tetragonal) phase transition temperature limit their application in some piezoelectric transducers, in which thermal stability is desired in terms of dielectric and piezoelectric property variation [63, 76]. Some transducers such as ultrasonic motor, high intensity focused ultrasound (HIFU) and sound-guided therapy probes, require piezoelectric materials with high piezoelectric properties and Curie temperature. Among all the relaxor-PT systems, PSN–PT, PYN–PT and PIN–PT binary systems possess relative high Curie temperatures near the MPB composition, with T_c in the range of 260–350 °C, which is close to that of commercial PZT ceramics. The crystal growth of novel MPB compositions in the $Bi(Me)O_3$–$PbTiO_3$ (Me = Sc^{3+}, In^{3+}, Yb^{3+}) family has been shown

Table 7.5 Main performance of PMN–PT crystal grown by SSCG, flux and Bridgman methods

Composition	T_c (°C)	T_{rt} (°C)	k_{33} (%)	ε	tan δ	d_{33} (pC/N)	Method	Cost
0.7PMN–0.30PT by SSCG [75]	130	90	0.90	5500	0.01	1500	SSCG	Relative high
PMN–PT (PT=0.30–0.33) [70]	140–155	>75	0.90–0.94	5500–6500	< 0.008	2000–3500	Bridgman	High
PMN–30% PT [62]	130–140	~85	0.92–0.94	7500–9000	<0.01	2200–2500	Flux	Very high

to exhibit $T_c > 450\,°C$ in polycrystalline ceramics [77]. PSN–PT exhibits excellent piezoelectric properties, with a Curie temperature much higher than that of either PMN–PT or PZN–PT, which provides many advantages in some applications. In this section, we introduce PSN–PT growth and its properties.

7.5.1 Growth of PSN–PT

Smolenskii was the first to investigate ferroelectric PSN. He used PbO as flux to grow PSN in 1959. PSN is a typical relaxor ferroelectric, having a Curie temperature of ~90 °C [78]. PSN–PT possesses MPB at compositions of 0.60PSN–0.40PT and 0.575PSN–0.425PT, respectively, [79, 80]. It is very hard to grow PSN–PT directly from its melt because of the very high melting point (>1425 °C). Yamashita and Harada have grown PSN–PT using 75mol%PbO–25mol%B_2O_3 flux, the melt solution being cooled from 1200 °C to 880 °C at a rate of 1 °C /h. The as-grown crystals were 2–15 mm in length. Chemical analysis and X-ray studies reveal that the crystals are perovskite structure with $x = 0.33$–0.35, which is slightly away from the charged MPB composition. They measured the electromechanical coupling factor k_{33} (0.72) of <001>-oriented crystal [81]. Bing and Ye used an improved high-temperature solution method to grow PSN–PT near MPB composition. Using mixtures of PbO and B_2O_3 as flux, the results showed that the variations of chemical compositions, such as the ratios of PSN–PT vs. flux and PbO vs. B_2O_3, influenced the morphology and quality of the grown crystals [82]. The primary growth of the perovskite PSN–PT crystals takes place in the composition range of PSN–PT/flux = 15/85–25/75 within a certain temperature interval, as indicated by the dashed area in Fig. 7.18, in which T_{s1} and T_{s1}' represent the upper limit of the solidification temperature range for the perovskite phase, and T_{s2} and T_{s2}' indicate the upper limit of the temperature range in which the pyrochlore phase starts to form. They drew a conclusion that the optimum chemical compositions in mole ratio should be PSN–PT/flux = 25/75 and PbO/B_2O_3 = 70/30.

Recently, Rajasekaran *et al.* have investigated the growth and morphology of $Pb[(Sc_{1/2}\,Nb_{1/2})_{0.58}Ti_{0.42}]O_3$ by slow-cooling technique [83]. The size of the crystals varies from 1 to 4 mm, as show in Fig. 7.19. From above, we know that, the size of PSN–PT grown by the flux method is too small to be used in practical applications, even for piezoelectric measurement. Guo *et al.* used a modified Bridgman method to grow large size PMN–PSN–PT ternary single crystal; the size reached 28 mm in diameter [84]. Hosono *et al.* also used a flux method to grow PMN–PSN–PT by a Bridgman technique [85].

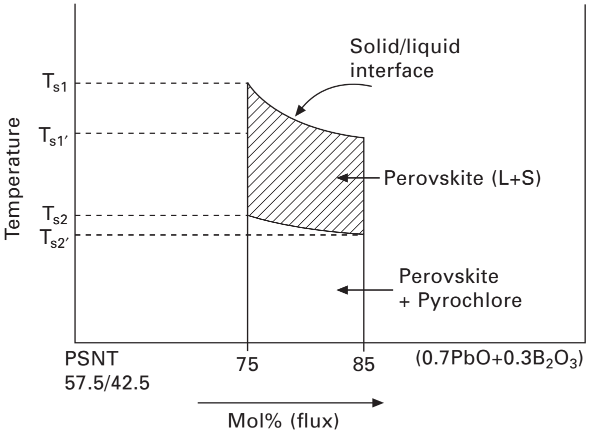
Temperature
T_{s1}
$T_{s1'}$
T_{s2}
$T_{s2'}$
Solid/liquid interface
Perovskite (L+S)
Perovskite + Pyrochlore
PSNT 57.5/42.5
75
85
$(0.7PbO+0.3B_2O_3)$
Mol% (flux)

7.18 Schematic diagram showing the formation of the perovskite crystals in the pseudo-binary system of PSN–PT–$(0.7PbO+0.3B_2O_3)$ [82].

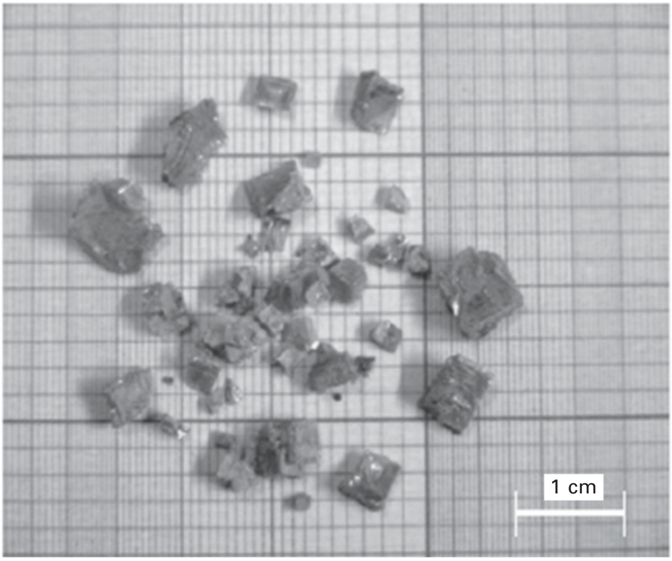

7.19 Photograph of PSN–PT crystals grown by Rajasekaran *et al.* [83].

7.5.2 Properties of PSN–PT

There have been few studies reported of the characterization of PSN–PT single crystal near MPB compositions. Yamashita and Harada have characterized the $(1\text{-}x)$PSN–xPT crystal with $x = 0.33$–0.35. The crystals have a remnant polarization $P_r = 26\ \mu C/cm^2$, a coercive field $E_c = 6$ kV/cm, a room temperature dielectric constant after poling $\varepsilon^T_{33}/\varepsilon_0 = 960$, a dielectric loss of 0.5%, and an electromechanical coupling factor $k_{33} = 72\%$ [81]. Bing and Ye characterized the properties of <001>-oriented (1-x)PSN–xPT with nominal compositions of $x = 0.425$ [82]. Figure 7.20 shows the variation of the real part and loss of dielectric permittivity at various frequencies (10, 50, 100 and 500 kHz) measured on a (001) platelet upon heating [83]. The result shows that the maximum permittivity at various frequencies occurs nearly at the same temperature, which is in contrast to the typical relaxor ferroelectric behavior in pure PSN. This indicates that the long-range ferroelectric order is enhanced in PSN–PT by the substitution of Ti^{4+} for $(Sc_{1/2}Nb_{1/2})^{4+}$ in PSN [83]. The Curie temperature (T_m) was obtained around 234 °C at all frequencies. The typical relaxor behavior was observed at and around the temperature of the dielectric maximum, which indicates that the relaxor behavior is retained to some extent. The temperature of the maximum dielectric constant obtained for this crystal with the same nominal composition as that used by Bing and Ye, was around 240 °C [86], the curve for dielectric constant vs. temperature is sharper than the present result observed by Rajasekaran. The T_c of this crystal measured by the two groups is consistent with each other. The T_c for pure PSN is 90 °C, and for pure $PbTiO_3$ is 490 °C. If we consider T_c to be linear with x for the (1-x)PSN–xPT solid solution, then the T_c near 230 °C obtained by the two groups shows that the content of PT in PSN–PT is around 36–37% in mole content. Severe composition segregation occurs during the crystallization of the solid solution of PSN–PT, so the actual PT content differs significantly from nominal composition.

The ferroelectric property of the <001>-oriented 0.575PSN–0.425PT (nominal composition) sample is displayed by the polarization-electric

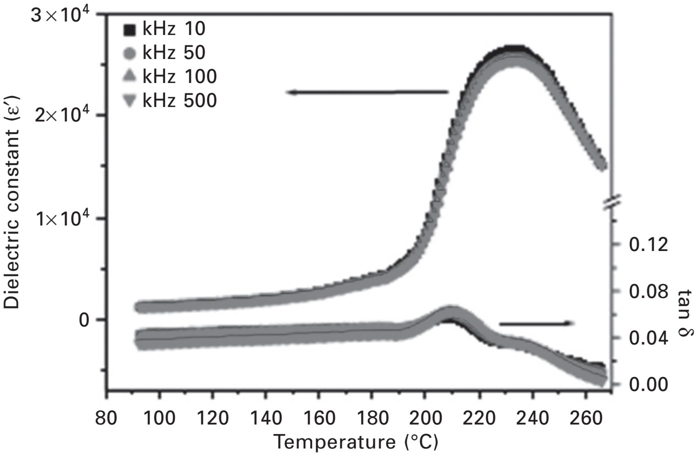

7.20 Dielectric properties of 0.575PSN–0.425PT single crystal as a function of temperature, measured along <001 > direction at various frequencies [83].

field hysteresis loops measured at room temperature, as presented in Fig. 7.21 [82]. The polarization saturates at a field of ~7.10 kV/cm. The almost vertical lines of the loop indicate sharp switching of the domains. Only slight depolarization occurs after the removal of the electric field. The remnant polarization (P_r) reaches ~25 μC/cm^2 under a field of 12 kV/cm with a coercive electric field E_c ~ 4 kV/cm. The crystal possesses a longitudinal electromechanical coupling factor k_{33} = 78%.

7.6 PIN–PT crystal

PIN–PT crystal is also a relaxor-based single crystal with high Curie temperature and piezoelectric properties. Kodama *et al.* have investigated its piezoelectric properties and phase transition, and found that its MPB composition is located at $x = 0.37$, responding to a T_c of 320 °C [87]. The melting point of PIN–PT is higher than PMN–PT and PZN–PT, and it is more difficult to grow PIN–PT than PMN–PT and PZN–PT. Most crystal growers grow PIN–PT by a flux method [88, 89]; the as-grown crystal is not large enough for device application. Guo *et al.* and Duan *et al.* [90, 91] used a Bridgman technique to grow PIN–PT with the allomeric PMN–PT seed crystals. Using this method, crystals with size over $\phi 20 \times 50$ mm^3 are obtained.

Single crystals with starting composition 0.66PIN–0.34PT can be grown directly from their melt by the modified Bridgman technique. Allomeric seed crystals PMN–PT can be used and come into operation in the control of the spontaneous nucleation and parasitic growth. Chemicals comprising PbO,

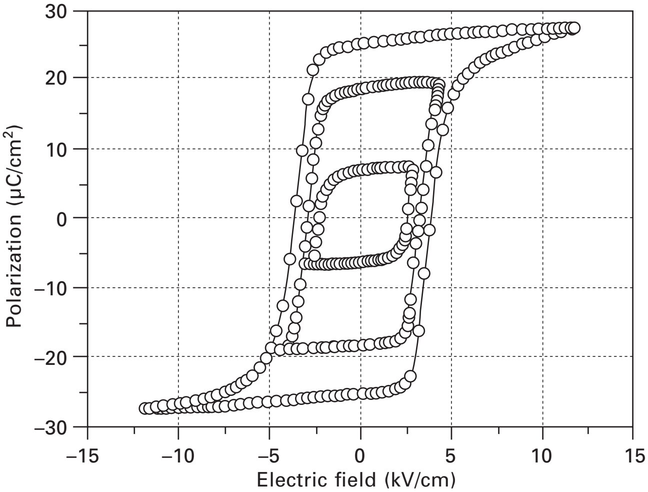

7.21 P-E loops for the <001>-oriented rhombohedral 0.575PSN–0.425PT (nominal composition) single crystal [82].

In_2O_3, TiO_2, and Nb_2O_5 with high purity are used as the starting materials. To prevent the sublimation of In_2O_3 and the formation of a pyrochlore phase during crystal growth, Wolframite phase oxide $InNbO_4$ was formed by reacting In_2O_3 with Nb_2O_5 for 24 h at 1000 °C. Then PbO, $InNbO_4$, and TiO_2 are mixed, and put into an 80 cm^3 platinum crucible. The growth technique is similar to that of PMN–PT. Figure 7.22 shows the as-grown 0.66PIN–0.34PT (nominal composition).

Segregation will occur during the growth of PIN–PT single crystals, which is similar to PMN–PT single crystals. X-ray fluorescence analysis (XRFA) was carried out to reveal the uniformity in composition of the single crystals. The result shows that the $PbTiO_3$ content increases during the growth of PIN–PT single crystals. In addition, it was observed that MgO was also present in the crystals, which reveals the Mg^{2+} diffuse into the PIN–PT single crystal during the crystal growth. The results of XRFA show that the composition of the crystals cutting from the seed end and the boule end of a boule are 0.23PMN–0.46PIN–0.31PT and 0.19PMN–0.46PIN–0.35PT, respectively.

For the poled-(001) plates, the temperature dependence of the relative permittivity and the dielectric loss for different samples are shown in Fig. 7.23. It is seen that the curves have peaks T_c (200 °C for sample no. 1 and 218 °C for sample no. 2) and then a shoulder at the phase transition temperature T_{rt} (113 °C for sample no. 1 and 82 °C for sample no. 2). Such temperature dependence of the permittivity indicates the sequence of transition of cubic–tetragonal–rhombohedral phases in the system. On the other hand, it exhibits an abnormal high permittivity of more than 4000 at room temperature; while the permittivity of binary PIN–PT system after poling is lower than 2000 [92, 93]. Piezoelectric performances were also measured; the results show that the piezoelectric coefficient d_{33} is higher than 2000 pC/N, and electromechanical coupling factor $k_{33} < 92\%$ for the longitudinal

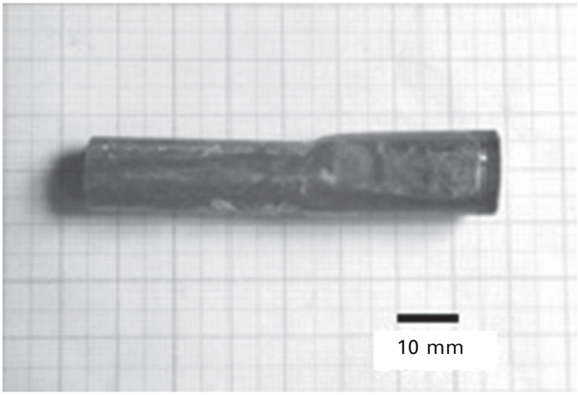

7.22 The as-grown PIN–PT by the Bridgman method.

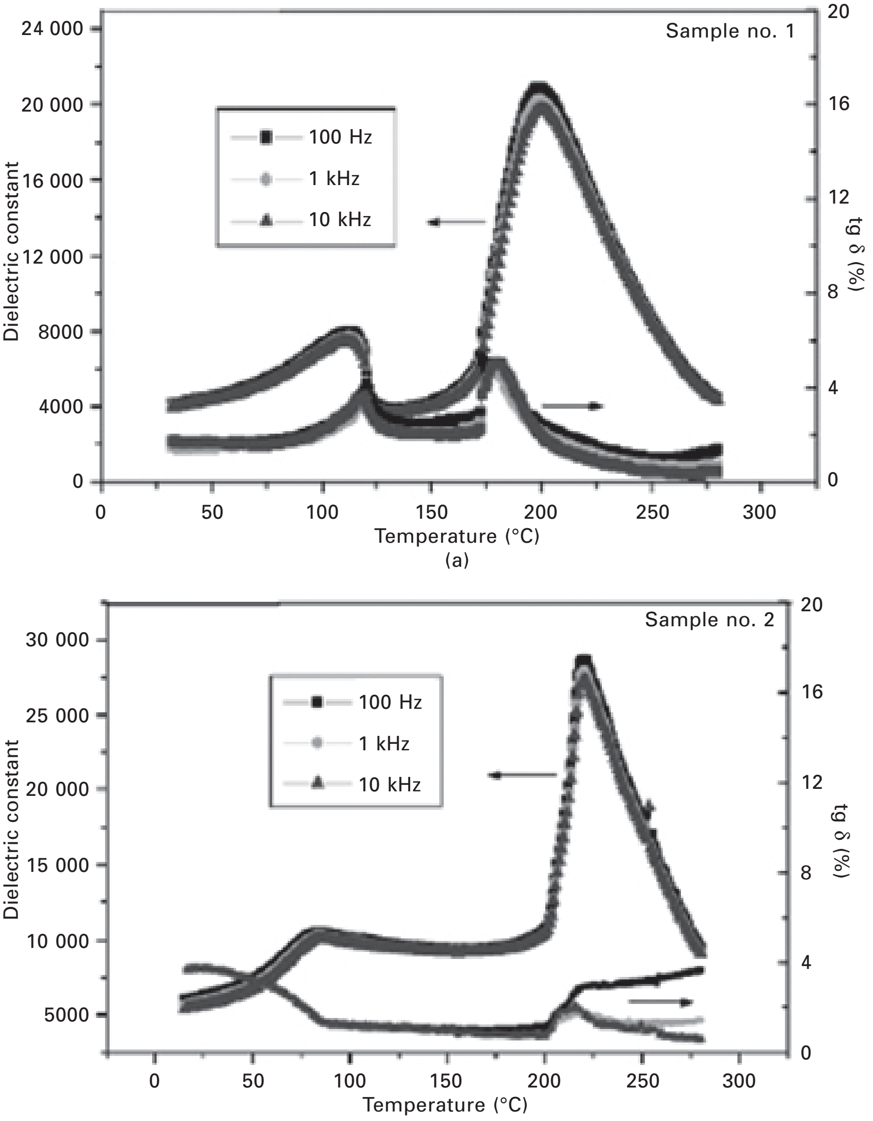

(a)

(b)

7.23 Temperature frequency dependence of the dielectric constant and dielectric loss of poled plates cut from the seed end (a) and boule end (b) of a boule along [100] direction [72].

bar mode, $k_t < 59.2\%$ for the thickness mode, which are comparable to that of 0.67PMN–0.33PT and 0.91PZN–0.09PT single crystals. The coercive field of the <001>-oriented crystal reaches ~6 kV/mm, which is much higher than PMN–PT and PZN–PT near the MPB. The results mentioned above show that the diffuseness of magnesium ion into the PIN–PT single crystal is favorable for dielectric and piezoelectric properties.

Duan *et al*. have also grown 0.66PIN–0.34PT crystals with the Bridgman method using PMN–PT as seed crystal [89]. T_c of the as-grown crystal varies from 265 to 269 °C because of the composition variation, and the T_c is similar to the polycrystalline form; furthermore, T_{rt} is located at 134 °C. Both T_c and T_{rt} are higher than those of PMN–PT and PZN–PT. In particular, T_{rt}, which directly determines the operating temperature range of these piezoelectric materials, is much higher than that of PMN–PT and PZN–PT single crystals. They also measured the piezoelectric performance of 0.66PIN–0.34PT. Table 7.6 shows the comparison of properties of PMN–PT, PZN–PT, PSN–PT, and PIN–PT single crystals. The piezoelectric performance of PIN–PT is comparable with that of PMN–PT and PZN–PT single crystals, with a much higher T_c and E_c. However, the cost of PIN–PT is much higher than those of PMN–PT and PZN–PT because of the expensive raw material In_2O_3 and the difficulty in growing large size PIN–PT.

7.7 Theoretical models for relaxor-based crystals

The optimal piezoelectric performance of relaxor crystals is not along its spontaneous direction <111>, but along its <001> direction. The origin of the high piezoelectric behavior of relaxor crystals has been attributed to many factors. The FE_r phase has a much smaller c/a ratio than the FE_t one; accordingly under field the large c/a ratio change results in a high electrically-induced strain. For PMN–PT and PZN–PT, investigations have also demonstrated the stable engineered domain results in a high piezoelectric response. The origin of the high piezoelectric performance may also be attributed to the presence of monoclinic (FE_m) and orthorhombic (FE_o) ferroelectric states in between the FE_r and FE_t phases. In PMN–PT and PZN–PT, first principles calculations have shown that these intermediate states (FE_m, FE_o, FE_r, FE_t) can be induced by outer field, and have indicated that the transformation induced by an electric field between FE_r and FE_t proceeds by a rotation of the polarization between <111> and <001>. Experimentation and theory to explain these phenomena remain a focus in the field of ferroelectrics. Here, we introduce two theoretical models in PMN–PT and PZN–PT crystals.

7.7.1 Domain engineering and engineered domain configurations

In 1997, Park and Shrout proposed a model to explain the high field-induced strain and piezoelectric performance of <001>-oriented relaxor crystal, as presented in Fig. 7.24. Figure 7.24 schematically presents engineered domain states and their piezoelectric response under high field for rhombohedral crystals

Table 7.6 Comparison of the properties of PMN–PT, PZN–PT, PSN–PT, PIN–PT single crystals

Materials	T_c (°C)	T_{rt} (°C)	E_c (kV/mm)	ε	tan δ	d_{33} (pC/N)	k_t
0.67PSN–0.33PT [81]	206	—	6	960	<0.01	–	–
PMN–PT (PT=0.30–0.33) [50]	–	>75	0.3	5500–6500	<0.008	2000–3500	–
0.7PMN–0.3PT [ours]	141	70–90	0.25–0.3	–5000	–0.005	1500–2500	~0.62
0.955PZN–0.045PT [49]	155	120	0.32	4400	–	2200	–
0.93PZN–0.07PT [30]	172	110	–	4450	0.012	2500	0.48
0.66PIN–0.34PT [89]	269	134	–	>3000	~0.012	~2000	0.59
0.24PIN–0.42PMN–0.34PT [94]	187	52	0.68	~4900	–	2200	0.56

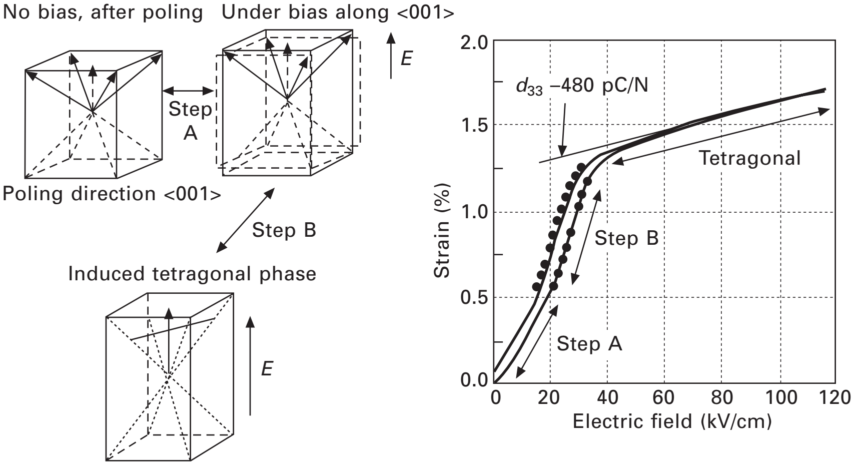

(a) (b)

7.24 (a) Schematic diagram of domain configurations in <001>-oriented rhombohedral ferroelectric crystals under bias (step A – piezoelectricity, step B – induced rhombohedral to tetragonal phase transition); (b) strain vs *E*-field behavior for <001>-oriented PZN–8%PT crystal (corresponding to (a)) [17].

oriented and poled along <001>. It can be divided into three steps with the outer field varying from low field to high field. When strain is induced by a low *E* field along <001>, the polar direction of each domain inclines close to the outer *E*-field direction, which is responding to step A, as shown in Fig. 7.24. In this procedure, it results in an increased rhombohedral lattice distortion and domain reorientation is not necessary during this step. In this step, hysteresis-free or low hysteresis strain behavior for <001>-oriented rhombohedral crystals is observed. During step B, far from saturation, the strain abruptly increases with outer *E*-field. The observed strain behavior is related to an *E*-field induced rhombohedral–tetragonal phase transition. Polarization inclination towards <001> finally results in collapse of all polarizations into the <001> direction. In step B, larger hysteresis and slope of strain versus *E* field are observed. In step C, the strain continues to increase with outer *E*-field, due to lattice extension by *E*-field. During this step, a much lower piezoelectric performance can be obtained, as shown in Fig. 7.24(b) where a d_{33} of only ~480 is obtained for 0.92PZN–0.08PT.

Wada *et al.* [95] and Park *et al.* extended [96] this model to $BaTiO_3$ single crystal, and proposed engineered domain configuration. This concept includes three main aspects:

(a) the *E*-field-induced strain is hysteresis-free or low hysteresis due to inhibition of movement of domain wall;

(b) piezoelectric properties along non-spontaneous polarization direction is higher than along polarization;
(c) the macroscopic symmetry of the crystal is changed by the engineered domain configuration; for example, the rhombohedral crystal before step B owns 4 mm symmetry, as shown in Fig. 7.24(a).

This theory explains many phenomena in relaxor crystals successfully. However, it is difficult to explain why the relaxor crystal exhibits optimal properties near the MPB.

7.7.2 Polarization rotation and mesophase

In 2000, Fu and Cohen reported a first principles study of the ferroelectric perovskite, $BaTiO_3$, which is similar to relaxor single crystal, but is a simpler system to analyze [97]. The result shows that a large piezoelectric response can be driven by polarization rotation induced by an external electric field. They proposed a polarization rotation mechanism, as shown in Fig. 7.25. Figure 7.25(a) is the rotation path for polarization from <001> to <111> direction, which polarization might take when driven by outer field: one path is along *a f g e*; the other along *a b c d e*. Figure 7.25(b) shows free

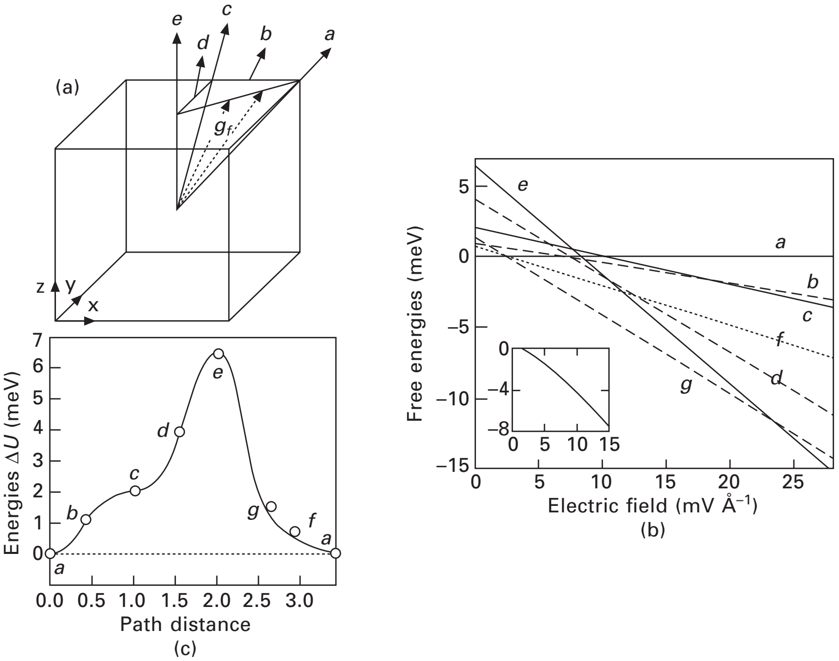

7.25 Polarization rotation paths from [111] to [001] under applied electric field [97].

energies as a function of field strength for different polarization directions. Figure 7.25(c) shows the internal energies ΔU ($\Delta U = U - U_{\mathrm{rhom}}$) relative to the rhombohedral phase along the closed path *a b c d e g f a*. It is easier to rotate through path *a f g e* than *a b c d e* due to lower free energy according to their calculations, Furthermore, the piezoelectric constant along path *a f g e* is closer to experimental results than along path *a b c d e*. Polarization at *a* site corresponds to the <111> direction of the rhombohedral phase; *c* site corresponding to the <110> direction of the orthorhombic phase; and the *e* site corresponding to the <001> direction of the tetragonal phase. The monoclinic mesophase will appear when the polarization rotation path is along *a f g e*; and the orthorhombic mesophase will appear when path *a f g e* is taken by polarization rotation. The polarization rotation mechanism presents the phase transition induced by the electrical field and the possible path of polarization rotation; the result is consistent with the monoclinic and orthorhombic phase found in relaxor crystal near the MPB. This theory has pushed forward the microstructure and polarization rotation research for relaxor crystals.

7.8 Application in piezoelectric actuators and medical transducers

7.8.1 Application in piezoelectric actuators

Piezoelectric actuators are used as critical elements in various electromechanical systems. Relaxor-based rhombohedral PMN–PT and PZN–PT exhibit ultrahigh electric-field-induced strain and low hysteresis [17, 60], which is very suitable for piezoelectric actuators. Feng *et al.* have manufactured different size <001>-oriented PMN–PT actuators [60, 98]. Actuators based on PZT–SF ceramics with the same size and fabricating process have also been manufactured. Under free-load conditions, 48 μm displacements can be achieved in PMN–PT actuators with electric fields ranging from –1.5 to 10 kV/cm, which is more than twice the displacement of the PZT–SF actuators driven from –10 to 10 kV/cm. Under 4 kg loading, the displacements in PMN–PT actuators are decreased to 42.5 mm.

Jiang *et al.* [99] have investigated the relationship between electromechanical coupling coefficient of PMN–PT crystals and the crystal thickness. It is found that the electromechanical coupling coefficient of PMN–PT single crystal thin plates are slightly lower than that of bulk single crystal. Single crystal actuators are then assembled using crystal plates with thickness ranging from 150 to 200 μm. A 5 mm × 5 mm × 12 mm single crystal actuator exhibits 13.5 μm stroke at room temperature under 150 V, and 6 μm stroke at 77 K under 150 V. Ko *et al.* [100] have proposed a new optical pick-up bimorph actuator for slim and small form factor optical disk drives using PMN–PT.

Woody *et al.* [101] have discussed the relative merits and limitations of using PMN–PT actuator material for adaptive structures and a case study is presented for a high bandwidth steering mirror using ultra-high-strain single crystals. KCF technologies have designed a motor based on PMN–PT layer actuator [102]. The motor achieves a speed of 330 rpm under free load and a stall torque of 0.11 N·m. If an optimal external load is applied by appropriate motion amplification, the single-crystal stack can deliver five to ten times as much work per cycle compared to a piezoceramic actuator. The power density for the piezocrystal stack reaches over 10 000 W/kg when the drive frequency is in the kHz range. The power density of the piezocrystal stack motor can be over 1000 W/kg, which compares favorably with even the highest-performing electromagnetic actuators.

The results of actuators based on relaxor single crystal show that single crystal actuators hold promise for space precise positioning and adaptive structures and cryogenic applications. The major limitation to bringing single crystal multilayer devices to mass production is assembly cost.

7.8.2 Application in medical transducers

Many company such as Toshiba, GE and Philips have investigated the application of an ultrasonic imaging system based on relaxor-based single crystals PMN–PT or PZN–PT, due to their ultrahigh piezoelectric performance. Theoretically, ultrasound transducer models indicate a dramatic bandwidth increment when using PMN–PT or PZN–PT crystals to replace PZT ceramics. The extended transducer bandwidth and sensitivity offer significant performance advantages, particularly in penetration and imaging resolution. Philips has released iE 33 ultrasound systems with pure wave single crystal technology, and have received excellent market acceptance [103]. The processing of fabrication of transducers based on relaxor single crystal is similar to that of PZT ceramics, and the difference is the modification of design parameters due to using different piezoelectric materials. It is necessary to modify the size of the materials used in the devices and matching materials and so on.

Saitoh *et al.* [104] from Toshiba Corp. have developed a 40-channel phased array ultrasonic probe using $0.91\text{Pb}(\text{Zn}_{1/3}\text{Nb}_{2/3})\text{O}_3\text{–}0.09\text{PbTiO}_3$ single crystal. The 40-channel phased array ultrasonic probe exhibits greater sensitivity and broader bandwidth than conventional probes. The echo amplitude of the PZN–PT single-crystal probe is 8 and 5 dB higher than that of one- and two-matching-layer PZT probes, respectively. Moreover, the fractional bandwidth of the single-matching-layer PZN–PT probe is broader than that of the two-matching-layer PZT probes. The PZN–PT single crystals provide great increment in the sensitivity and bandwidth of phased array probes. Also they have fabricated a 20 MHz single-element ultrasonic probe using PZN–PT single crystal [105]. The bandwidth of the PZN–PT probe is 13–26 MHz, which is 4 MHz broader than that of the conventional PZT probe. Cheng *et al*. have used PMN–PT to fabricate PMN–PT/epoxy 1–3 composites with different volume fractions of PMN–PT. It was demonstrated that the thickness electromechanical coupling coefficients of the composites could reach as high as 0.8. A 2.4 MHz plane ultrasonic transducer was fabricated using a PMN–PT/epoxy 1–3 composite with 0.37 volume fraction of PMN–PT. It shows a –6 dB bandwidth of ~61% and an insertion loss of –14 dB [106]. Sung *et al*. [107] have developed multilayer PMN–PT single crystal transducers for medical application. The performance of a multilayer 64-channel 3.5 MHz phased array ultrasonic probe has been investigated. Ritter *et al*. [108] have investigated PZN–PT for potential application in ultrasound transducers. Modeling of 1–3 composites and experimental results have demonstrated that thickness coupling greater than 0.80 could be achieved with a 40–70% volume fraction of PZN–PT. Ultrasonic transducers fabricated using PZN–PT 1–3 composites achieve experimental bandwidths as high as 141%.

Medical transducers based on single crystal were developed more than two decades ago, but commercialization was started only a few years ago. The performance of single crystal medical transducers is much better than that of conventional PZT transducers, and single crystal transducers have increasingly replaced conventional PZT transducers especially in high end medical products, which require high penetration imaging resolution.

7.9 Conclusion and future trends

This chapter has discussed four kinds of crystal: PZN–PT, PMN–PT, PSN–PT and PIN–PT, which are typically representative of relaxor-PT crystals. In this chapter, we have introduced a modified Bridgman method to grow PMN–PT and PZN–PT crystal based on the complete investigation of the feasibility of relaxor-PT crystal. PZN–PT is not stable at high temperature; it decomposes from perovskite structure to pyrochlore phase. It is not easy to fabricate high-quality and large-size single crystals in a pure phase; we established a novel method to grow PZN–PT from a flux of PbO with an allomeric PMN–PT as seed crystal. Pure perovskite PZN–PT with size over 28 mm in diameter can be obtained. The growth method of PMN–PT crystal is similar to that of PZN–PT, PMN–PT is more stable than PZN–PT at high temperature, and it is less difficult to grow PMN–PT than PZN–PT. The size of as-grown PMN–PT can reach $\phi 50 \times 80$ mm^3, which meets the size requirements for most ultrasonic transducers. Currently, PZN–PT and PMN–PT exhibit the highest piezoelectric performance of all piezoelectric materials. There is a MPB in PMN–PT and PZN–PT, near to which the relaxor crystals exhibit very high piezoelectric response ($d_{33} > 2000$ pC/N,

$k_{33} > 0.90$, $S \sim 1.7\%$) along the <001> direction, but not along its spontaneous direction <111>. The T_c of PZN–PT and PMN–PT near the MPB is around 170–190 °C and 140–165 °C, respectively. The phase structure of PMN–PT and PZN–PT is very complex; FE_r, FE_t, FE_m and FE_o exist or coexist in these crystals. Also the complete elastic, piezoelectric, dielectric constants of PZN–PT and PMN–PT are discussed in this chapter for both fundamental research and device design.

The T_c of PSN–PT crystal near the MPB is much higher than for PMN–PT and PZN–PT. The melting point of PSN–PT is over 1425 °C, which makes this crystal difficult to grow directly from its melt. The size of PSN–PT grown from a flux of PbO–B_2O_3 is very small, and the composition of the as-grown crystal deviates from the nominal composition. PSN–PT possesses a MPB at compositions of 0.60PSN–0.40PT and 0.575PSN–0.425PT, respectively. The piezoelectric and ferroelectric properties of PSN–PT single crystal near the MPB has still not been investigated fully. The difficulty in growing PSN–PT limits its research. Pure PIN–PT crystal is also very difficult to grow in large sizes. In this chapter, we use a Bridgman method using PMN–PT as seed crystal to grow large size PIN–PT crystal. The piezoelectric properties of the as-grown crystal is comparable with that of PMN–PT and PZN–PT near the MPB, but with a much higher T_{rt} and T_c, which give the PIN–PT crystal good temperature stability.

Perovskite oxide piezoelectric materials are of great fundamental and technological importance since the discovery of ferroelectric PZT ceramics. Among them, single crystals PZN–PT and PMN–PT have been the focus for recent decades because of their ultrahigh piezoelectric coefficients and electromechanical coupling factors. They are promising materials for the next generation of ultrasonic transducers and high strain actuators. Now many research studies on piezoelectric devices based on PMN–PT and PZN–PT crystal have been carried out. However, there are still a number of technical challenges to overcome before PMN–PT and PZN–PT can be widely applied in commercial piezoelectric devices. These technical challenges include the facts that PZN–PT and PMN–PT single crystals are difficult to grow in large sizes by flux, and the crystals are very expensive. To minimize this and reduce the cost, the Bridgman method should replace the flux technique. However, due to the compositional gradient associated with Bridgman growth, single crystal properties vary along the growing axis which causes variation of properties from wafer to wafer, and even within one wafer. From an application point of view, the property variations between wafers make the single crystal difficult to use and more expensive. The variation of properties of the crystals in manufacturing is the most serious issue. To solve this problem, crystal growers should use a combination of zone melting technique with the Bridgman technique. Also solid state crystal growth techniques to grow PMN–PT crystals or aligned polycrystalline materials is an effective method. Commercial crystal could be realized for PZN–PT or PMN–PT at commercial sources: TRS Ceramics, JFE Mineral Company, Morgan Electro Ceramics, H.C. Materials Corporation, Kawatetsu Mining Co. Ltd. Research Lab., Shanghai Institute of Ceramics, etc.

A further technical challenge is that the relatively low elastic stiffness and phase transition temperature make the crystals susceptible to outer mechanical condition and temperature. Their piezoelectric performance degrades in bonded condition or under high compressive preloads. Also the low T_{rt} limits their application in piezoelectric devices and the temperature range of operation. Low coercive electric field is another disadvantage. To broaden the application field for relaxor crystal, crystal with high Curie temperature, phase transition and coercive field should be paid much more attention. Large size PSN–PT, PYN–PT, PIN–PT and Bi(Me)O_3–$PbTiO_3$ (Me = Sc^{3+}, In^{3+}, Yb^{3+}) binary systems should be grown by an improved method. To reduce the growth difficulty of high Curie crystal, ternary system complex with PMN such as PMN–PIN–PT, PMN–PSN–PT should also be developed. In summary, relaxor-PT single crystals have a bright future in the next generation of piezoelectric devices.

7.10 References

1. Myl'nikova I E and Bokov V A (1959), *Growth of Crystals*, New York, Consultants Bureau.
2. Bokov V A and Myl'nikova I E (1961), 'Electrical and optical properties of single crystals of ferroelectrics with a diffused phase', *Sov Phys Solid State*, 2, 2428–2430.
3. Smolenskii G A, Isupov V A, Agranovskaya V A and Popov S N (1961) 'New ferroelectrics of complex composition', *Sov Phys Solid State*, 2, 2584.
4. Bonner W A and Uiter L G V (1967), 'Growth of single crystals of $Pb_3MgNb_2O_9$ by the Kyropoulos technique', *Mat Res Bull*, 2, 131–134.
5. Adachi M, Sankar S G, Bhalla A S, Chang Z P and Cross L E (1986), 'Growth and dielectric properties of lead barium niobate single crystals and morphotropic phase boundary', *6th Proc. IEEE int Symp Appl Ferroelectrics*, 168–171.
6. Shrout T R and Halliyal A (1987), 'Preparation of lead-based ferroelectric relaxors for capacitors', *Am Ceram Soc Bull*, 66, 704–711.
7. Yokomizo Y, Takahashi T and Nomura S (1970), 'Ferroelectric properties of $Pb(Zn_{1/3} Nb_{2/3})O_3$', *J Phys Soc Jpn*, 28, 1278–1284.
8. Kuwata J, Uchino K and Nomura S (1979), 'Diffuse phase transition in lead zinc niobate', *Ferroelectrics*, 22, 863–866.
9. Kuwata J, Uchino K and Nomura S (1981), 'Phase transitions in the $Pb(Zn_{1/3}Nb_{2/3})O_3$-$PbTiO_3$ system', *Ferroelectrics*, 37, 579–582.
10. Kuwata J, Uchino K and Nomura S (1982), 'Dielectric and piezoelectric properties of $0.91Pb(Zn_{1/3}Nb_{2/3})O_3$-$0.09PbTiO_3$ single crystals', *Jpn J Apl Phys*, 21, 1298–1302.
11. Shrout T R, Chang Z P, Kim N and Markgraf S (1990), 'Dielecreic behavior of single crystals near the $(1\text{-}x)Pb(Mg_{1/3}Nb_{2/3})O_3$-$xPbTiO_3$ morphotropic phase boundary', *Ferroelect Lett*, 12, 63–69.

12. Ye Z G, Tissot P and Schmid H (1990), 'Pseudo-binary $Pb(Mg_{1/3}Nb_{2/3})O_3$-PbO_3 phase diagram and crystal growth of $Pb(Mg_{1/3}Nb_{2/3})O_3$ [PMN]', *Mater Res Bull*, 25, 739–748.
13. Yamashita Y and Saitoh S (1995), 'Piezoelectric material and ultrasonic probe', US Patent, No. 5 410 209.
14. Saitoh S, Izumi M, Shimanuki S, Hashimoto S and Yamashita Y (1994), 'Ultrasonic probe', US Patent, No. 5 295 487.
15. Saitoh S, Izumi M, Yamashita Y *et al.* (1995). 'Piezoelectric single crystal, ultrasonic probe, and array-type ultrasonic probe', US Patent, No. 5 402 791.
16. Mulvihill M L, Park S-E, Risch G *et al.* (1996), 'The role of processing variables in the flux growth of lead zinc niobate-lead titanate relaxor ferroelectric single crystals', *Jpn J Appl Phys*, 35, 51–57.
17. Park S-E and Shrout T R (1997), 'Ultrahigh strain and piezoelectric behavior in relaxor based ferroelectric single crystals', *J Appl Phys*, 82, 1804.
18. Service R E (1997), 'Shape-changing crystals get shiftier', *Science*, 275, 1878.
19. Kobayashi T, Shimanuki S, Saitoh S *et al.* (1997), 'Improved growth of large lead zinc titanate piezoelectric single crystals for medical ultrasonic transducers', *Jpn J Appl Phys*, 36, 272–275.
20. Shimanuki S, Saito S and Yamashita Y (1998), 'Single crystal of the $Pb(Zn_{1/3}Nb_{2/3})O_3$-$PbTiO_3$ system grown by the vertical Bridgman method and its characterization', *Jpn J Appl Phys*, 37, 3382–3385.
21. Luo H, Xu G, Xu H, Wang P and Yin Z (2000), 'Compositional homogeneity and electric properties of lead magnesium niobate titanate single crystals grown by a modified Bridgman technique', *Jpn J Appl Phys*, 39, 558.
22. Luo H, Shen G, Wang P, *et al.* (1997), 'Study of new piezoelectric materials – relaxor ferroelectric single crystals', *J Inorgan Mater,* 12, 768 (in Chinese).
23. Xue J and Jing M (2007), *Novel Relaxor Ferroelectric Crystals – Growth*, Performance and Application, Chemical Industry Press, Beijing (in Chinese).
24. Saitoh S, Kobayashi R, Harada K, Shimanuki S and Yamashita Y (1998), 'Simulation and fabrication process for a medical phased array ultrasonic probe using a $0.91Pb(Zn_{1/3}Nb_{2/3})O_3$–$0.09PbTiO_3$ single crystal', *Jpn J Appl Phys*, 37, 3053–3057.
25. Ranjan K, Zhang J and Lim L (2005), 'Optimum compositions for $Pb(Zn_{1/3}Nb_{2/3})O_3$–$PbTiO_3$ single crystal for high-performance applications', *Jpn J Appl Phy*, 44, 264–266.
26. Fang B, Shan Y, Xue H, Luo H and Yin Z (2004), 'On the feasibility of growing $Pb[(Zn_{1/3}Nb_{2/3})_{0.91}Ti_{0.09}]O_3$ single crystals', *Adv Funct Mater*, 14, 169–173.
27. Fang B, Xue H, He T, Luo H and Yin Z (2004), 'Growth of $Pb((Zn_{1/3}Nb_{2/3})_{0.91}Ti_{0.09})O_3$ single crystals using an allomeric seed crystal and their electrical properties', *J Am Ceram Soc,* 87, 991–995.
28. Ye Z G, Dong M and Yamashita Y (2000), 'Thermal stability of the $Pb(Zn_{1/3}Nb_{2/3})O_3$–$PbTiO_3$ [PZNT91/9] and $Pb(Mg_{1/3}Nb_{2/3})O_3$–$PbTiO_3$ [PMNT68/32] single crystals', *J Crystal Growth*, 211, 247–251.
29. Fang B, Xue H, He T, Luo H and Yin Z (2002), 'Growth mechanism and electrical properties of $Pb[(Zn_{1/3}Nb_{2/3})_{0.91}Ti_{0.09}]O_3$ single crystals by a modified Bridgman method', *J Crystal Growth*, 244, 318–326.
30. Hoson Y, Harada K, Kobayashi T, Itsumi K, *et al.* (2002), 'Dielectric and piezoelectric properties of $0.93Pb(Zn_{1/3}Nb_{2/3})O_3$–$0.07PbTiO_3$ piezoelectric single crystals for medical array transducers', *Jpn J Appl Phys*, 41, 7084–7088.

31. Yin J, Jiang B and Cao W (2000), 'Elastic, piezoelectric, and dielectric properties of 0.955PZN–0.045PT single crystal with designed multidomains', *IEEE Trans Ultraso, Freq, Cont*, 47, 285–291.
32. Zhang R, Jiang B and Cao W (2002), 'Complete set of material constants of $0.93Pb(Zn_{1/3}Nb_{2/3})O_3$–$0.07PbTiO_3$ domain engineered single crystal', *J Mater Scien Lett*, 21, 1877–1879.
33. Zhang R, Jiang B, Jiang W and Cao W (2003), 'Complete set of properties of $0.92Pb(Zn_{1/3}Nb_{2/3})O_3$–$0.08PbTiO_3$ single crystal with engineered domains', *Mater Lett*, 57, 1305–1308.
34. Ogawa T and Numamoto Y (2002), 'Origin of giant electromechanical coupling factor of k_{31} mode and piezoelectric d_{31} constant in $Pb[(Zn_{1/3}Nb_{2/3})0.91Ti_{0.09}]O_3$ single crystal', *Jpn J Appl Phys*, 41, 7108–7112.
35. Ogawa T and Numamoto Y (2004), 'Origin of giant piezoelectricity in $Pb[(Zn_{1/3}Nb_{2/3})_{0.91}Ti_{0.09}]O_3$ single crystals', *Integrated Ferroelectrics*, 63, 21–26.
36. Zhang R, Jiang B and Cao W (2004), 'Superior d_{32}^* and k_{32}^* coefficients in $0.955Pb(Zn_{1/3}Nb_{2/3})O_3$–$0.045PbTiO_3$ and $0.92Pb(Zn_{1/3}Nb_{2/3})O_3$–$0.08PbTiO_3$ single crystals poled along [011]', *J Physics and Chemistry of Solids*, 65, 1083–1086.
37. Liu S, Park S, Shrout T and Cross L (1999), 'Electric field dependence of piezoelectric properties for rhombohedral $0.955Pb(Zn_{1/3}Nb_{2/3})O_3$–$0.045PbTiO_3$ single crystals', *J Appl Phys*, 85, 2810.
38. Priya S and Uchino K (2003), 'Estimation of polarocaloric contribution to dielectric loss in oriented $0.92Pb(Zn_{1/3}Nb_{2/3})O_3$–$0.08PbTiO_3$ single crystals', *Jpn J Appl Phys*, 42, 5158–5164.
39. Tu C, Tsai C, Chen J and Schmidt V (2002), 'Orientation dependence and electric-field effect in the relaxor-based ferroelectric crystal $(PbMg_{1/3}Nb_{2/3}O_3)_{0.68}(PbTiO_3)_{0.32}$', *Phys Rev B*, 65, 104113.
40. Topolov V and Ye Z (2004), 'Coexistence of morphotropic phases in (1–x) $Pb(Mg_{1/3}Nb_{2/3})O_3$–$xPbTiO_3$ solid solutions', *Phys Rev B*, 70, 094113.
41. Kiat J, Uesu Y, Dkhil B, Matsuda M, Malibert C and Calvarin G (2002), 'Monoclinic structure of unpoled morphotropic high piezoelectric PMN-PT and PZN-PT compounds', *Phys Rev B*, 65, 064106.
42. Ye Z, Noheda B, Dong M, Cox D and Shirane G (2001), 'Monoclinic phase in the relaxor-based piezoelectric/ferroelectric $Pb(Mg_{1/3}Nb_{2/3})O_3$–$PbTiO_3$ system', *Phys Rev B*, 64, 184114.
43. Choi S W, Shrout T R, Jang S J and Bhalla A S (1989), 'Morphotropic phase boundary in $Pb(Mg_{1/3}Nb_{2/3})O_3$–$PbTiO_3$ system', *Mater Lett*, 8, 253–255.
44. Noheda B, Cox D E, Shirane G, *et al.* (2002), 'Phase diagram of ferroelectric-relaxor $(1\text{-}x)Pb(Mg_{1/3}Nb_{2/3})O_3$–$xPbTiO_3$', *Phys Rev B*, 66, 054104.
45. Dong M and Ye Z-G (2000), 'High-temperature solution growth and characterization of the piezo-/ferroelectric $(1\text{-}x)Pb(Mg_{1/3}Nb_{2/3})O_3$–$xPbTiO_3$ [PMN–PT] single crystals', *J Crystal Growth*, 209, 81–90.
46. Fan H, Zhao L, Tang B, Tian C and Kim H (2003), 'Growth and characterization of PMNT relaxor-based ferroelectric single crystals by flux method', *Mater Sci Eng B*, 99, 183–186.
47. Zawilski K T, Custodio M C C, DeMattei R C, Lee S, Monteiro R G, Odagawa H and Feigelson R S (2003), 'Segregation during the vertical Bridgman growth of lead magnesium niobate–lead titanate single crystals' *J Crystal Growth*, 258, 353–367.

48. http://www.trsceramics.com/.
49. Park S E and Hackenberger W (2002), 'High performance single crystal piezoelectrics: applications and issues', *Curr Opin Solid St M*, 6, 11–18.
50. http://www.hcmat.com/.
51. Zekria D, Shuvaeva V A and Glazer A M (2005), 'Birefringence imaging measurements on the phase diagram of $Pb(Mg_{1/3}Nb_{2/3})O_3$–$PbTiO_3$', *J Phys: Condens Matter*, 17, 1593–1600.
52. Zhao X, Wang J, Chew K H, Chan H L W, *et al.* (2004), 'Composition dependence of piezoelectric constant and dielectric constant tunability in the <001>-oriented $Pb(Mg_{1/3}Nb_{2/3})O_3$–$PbTiO_3$ single crystals', *Mater Lett*, 58, 2053.
53. Xu G, Luo H, Wang P, Qi Z and Yin Z (2000), 'Ferroelectric and piezoelectric properties of novel relaxor ferroelectric single crystals $Pb(Mg_{1/3}Nb_{2/3})O_3$–$PbTiO_3$', *Chin Sci Bull*, 45, 1380.
54. Cross L E (1987), 'Relaxor ferroelectrics', *Ferroelectrics*, 76, 241.
55. Zhao X, Wang J, Chan H L W, Choy C L and Luo H (2003), 'Effect of a bias field on the dielectric properties of $0.69Pb(Mg_{1/3}Nb_{2/3})O_3$–$0.31PbTiO_3$ single crystals with different orientations', *J Phys: Condens Matter*, 15, 6899–6908.
56. Lu Y, Jeong D-Y, Cheng Z-Y, *et al.* (2001), 'Phase transitional behavior and piezoelectric properties of the orthorhombic phase of $Pb(Mg_{1/3}Nb_{2/3})O_3$–$PbTiO_3$ single crystals', *Appl Phys Lett*, 78, 3109–3111
57. Feng Z, Zhao X and Luo H (2006), 'Composition and orientation dependence of dielectric and piezoelectric properties in poled $Pb(Mg_{1/3}Nb_{2/3})O_3$–$PbTiO_3$ crystals', *J Appl Phys*, 100, 024104.
58. Durbin K, Hicks J C, Park S E and Shrout T R (2000), 'X-ray diffraction and phenomenological studies of the engineered monoclinic crystal domains in single crystal relaxor ferroelectrics', *J Appl Phys*, 87, 8159–8164.
59. Singh A K and Pandey D (2001), 'Structure and the location of the morphotropic phase boundary region in $(1\text{-}x)[Pb(Mg_{1/3}Nb_{2/3})O_3]$–$xPbTiO_3$' *J Phys: Condens Matter*, 13, L931–L936.
60. Feng Z, He T, Xu H, Luo H and Yin Z (2004), 'High electric-field-induced strain of $Pb(Mg_{1/3}Nb_{2/3})O_3$–$PbTiO_3$ crystals in multilayer actuators', *Solid State Commu*, 130, 557–562.
61. Viehland D, Li J F and Amin A (2002), 'Electromechanical and elastic isotropy in the <011>-plane of $0.7Pb(Mg_{1/3}Nb_{2/3})O_3$–$0.3PbTiO_3$ crystals: Inhomogeneous shearing of polarization', *J Appl Phys*, 92, 3985–3989.
62. Peng J, Luo H, He T, Xu H and Lin D (2005), 'Elastic, dielectric, and piezoelectric characterization of $0.70Pb(Mg_{1/3}Nb_{2/3})O_3$–$0.30PbTiO_3$ single crystals', *Mater Lett*, 59, 640–643.
63. Wang F, Luo L, Zhou D, Zhao X and Luo H (2007), 'Complete set of elastic, dielectric, and piezoelectric constants of orthorhombic $0.71Pb(Mg_{1/3}Nb_{2/3})O_3$–$0.29PbTiO_3$ single crystal', *Appl Phys Lett*, 90, 212903.
64. Zhang R, Jiang B and Cao W (2003), 'Single-domain properties of $0.67Pb(Mg_{1/3}Nb_{2/3})O_3$–$0.33PbTiO_3$ single crystals under electric field bias', *Appl Phys Lett*, 82, 787.
65. Damjanovic D, Budimir M, Davis M and Setter N (2003), 'Monodomain versus polydomain piezoelectric response of $0.67Pb(Mg_{1/3}Nb_{2/3})O_3$–$0.33PbTiO_3$ single crystals along nonpolar directions', *Appl Phys Lett*, 83, 527.
66. http://www.microfine-piezo.com/.
67. Zhang S, Randall C A and Shrout T R (2005), 'Recent developments in high

Curie temperature perovskite single crystals', *IEEE Trans Ultraso, Freq, Cont*, 52, 564–569.

68. Karaki T, Adachi M, Hosono Y and Yamashita Y (2002), 'Distribution of piezoelectric properties in $Pb[(Mg_{1/3}Nb_{2/3})_{0.7}Ti_{0.3}]O_3$ single crystal', *Jpn J Appl Phys*, 41, L402–L404.
69. Rajan K, Shanthi M, Chang W, Jin J and Lim L (2007), 'Dielectric and piezoelectric properties of [001] and [011]-poled relaxor ferroelectric PZN–PT and PMN–PT single crystals', *Sensors and Actuators A: Physical*, 133, 110–116.
70. Shanthi M, Chia S and Lim L (2005), 'Overpoling resistance of [011]-poled $Pb(Mg_{1/3}Nb_{2/3})O_3$–$PbTiO_3$ single crystals', *Appl Phys Lett*, 87, 202902.
71. Han P, Yan W, Tian J, Huang X and Pan H (2005), 'Cut directions for the optimization of piezoelectric coefficients of lead magnesium niobate–lead titanate ferroelectric crystals', *Appl Phys Lett*, 86, 052902.
72. Li T, Scotch A M, Chan H, Harmer M, Park S, Shrout T and Michael J (1998), 'Single crystals of $Pb(Mg_{1/3}Nb_{2/3})O_3$–35mol%$PbTiO_3$ from polycrystalline precursors', *J Am Ceram Soc*, 81, 244.
73. Messing G, Trolier-McKinstry S, Sabolsky E, Duran C, Kwon S, Brahmaroutu B, Park P, Yilmaz H, Rehrig P, Eitel K, Suvaci E, Seabaugh M, and Oh K (2004), 'Templated grain growth of textured piezoelectric ceramics', *Crit Rev Solid State Mater Sci*, 29, 45.
74. Kim M, Fisher J and Kang S (2006), 'Grain growth control and solid-state crystal growth by Li_2O/PbO addition and dislocation introduction in the PMN–35PT system', *J Am Ceram Soc*, 89, 1237–1243.
75. http://www.ceracomp.com/.
76. Zhang S, Ru X, Lebrun L, Anderson D and Shrout T R (2005), 'Piezoelectric materials for high power, high temperature applications', *Mater Lett*, 59, 3471–3475.
77. Eitel R, Randall C A, Shrout T R, Rehrig P, Hackenberger W and Park S-E (2001), 'New high temperature morphotropic phase boundary piezoelectrics based on $Bi(Me)O_3$–$PbTiO_3$ ceramics', *Jpn J Appl Phys*, 40, 5999–6002.
78. Smolenskii G A, Isupov V A and Agranovskaya A I (1959) 'New ferroelectrics of complex composition of the type A_2^{+2} $(B_I^{3+}B_{II}^{5+})O_6$', *Sov Phys Solid State*, 1, 150–151.
79. Edward F A and Bhalla A S (1968), 'High strain and low mechanical quality factor piezoelectric $Pb[(Sc_{1/2}\ Nb_{1/2})_{0.575}Ti_{0.425}]O_3$ ceramics', *Mater Lett*, 35 199–201.
80. Tennery V J, Huang K W and Novak R E (1968), 'Ferroelectric and structural properties of the $Pb(Sc_{1/2}Nb_{1/2})_{1-x}Ti_xO_3$ system', *J Am Ceram Soc*, 51, 671–674.
81. Yamashita Y and Harada K (1997), 'Crystal growth and electrical properties of lead scandium niobate-lead titanate binary single crystals', *Jpn J Appl Phys* 36, 6039–6042.
82. Bing Y H and Ye Z-G (2003), 'Effects of chemical compositions on the growth of relaxor ferroelectric-$Pb(Sc_{1/2}Nb_{1/2})_{1-x}Ti_xO_3$ single crystals', *J Crystal Growth*, 250, 118–125.
83. Rajasekaran S V, Singh A K and Jayavel R (2008), 'Growth and morphological aspects of $Pb[(Sc_{1/2}\ Nb_{1/2})_{0.58}Ti_{0.42}]O_3$ single crystals by slow-cooling technique', *J Crystal Growth*, 310, 1093–1098.
84. Guo Y, Xu H, Luo H, Xu G and Yin Z (2001), 'Growth and electrical properties of $Pb(Sc_{1/2}Nb_{1/2})O_3$–$Pb(Mg_{1/3}Nb_{2/3})O_3$–$PbTiO_3$ ternary single crystals by a modified Bridgman technique', *J Crystal Growth*, 226, 111–116.
85. Hosono Y, Harada K, Yamashita Y, Dong M and Ye Z-G (2000), 'Growth, electric

and thermal properties of lead scandium niobate-lead magnesium niobate-lead titanate ternary single crystals', *Jpn J Appl Phys*, 39, 5589–5592.

86. Bing Y-H and Ye Z-G (2002), 'Growth and characterization of relaxor ferroelectric (1-x)Pb($Sc_{1/2}Nb_{1/2}$)O_3–xPbTiO_3 single crystals,' *Proceedings of the 13th IEEE International Symposium on Applications of Ferroelectrics*.
87. Kodama U, Osada M, Kumon O, *et al.* (1969), 'Piezoelectric properties and phase transition of Pb($In_{1/2}Nb_{1/2}$)O_3–PbTiO_3 solid solution ceramics', *Amer Ceram Soc Bull*, 48, 1122–1124.
88. Yasuda N, Ohwa H, Hasegawa D, Hayashi K, Hosono Y and Yamashita Y (2000), 'Temperature dependence of piezoelectric properties of a high Curie temperature Pb($In_{1/2}Nb_{1/2}$)O_3-PbTiO_3 binary system single crystal near morphotropic phase boundary', *Jpn J Appl Phys*, 39, 5586–5588.
89. Duan Z, Xu G, Wang X and Yang D (2004), 'Growth and electrical properties of Pb($In_{0.5}Nb_{0.5}$)O_3–PbTiO_3 crystals by the solution Bridgman method', *J Crystal Growth*, 275, 1907–1911.
90. Guo Y, Luo H, He T and Yin Z (2002), 'Peculiar properties of a high Curie temperature Pb($In_{1/2}Nb_{1/2}$)O_3–PbTiO_3 single crystal grown by the modified Bridgman technique', *Solid State Commun*, 123, 417–420.
91. Duan Z, Xu G, Wang X, Yang D, Pan X and Wang P (2005), 'Electrical properties of high Curie temperature (1–x)Pb($In_{1/2}Nb_{1/2}$)O_3–xPbTiO_3 single crystals grown by the solution Bridgman technique', *Solid State Commun*, 134, 559–563.
92. Yasuda N, Hidehiro O, Kume M and Yamashita Y (2000), 'Piezoelectric properties of a high Curie temperature Pb($In_{1/2}Nb_{1/2}$)O_3–PbTiO_3 binary system single crystal near a morphotropic phase boundary', *Jpn J Appl Phys*, 39, L66–L68.
93. Guo Y, Luo H, He T, Pan X and Yin Z (2003), 'Electric-field-induced strain and piezoelectric properties of a high Curie temperature Pb($In_{1/2}Nb_{1/2}$)O_3–PbTiO_3 single crystal', *Mater Res Bull*, 38, 857–864.
94. Yasuharu H, Yohachi Y, Kentaro H and Nobory I (2005), 'Dielectric and piezoelectric properties of Pb[$(In_{1/2}Nb_{1/2})_{0.24}(Mg_{1/3}Nb_{2/3})_{0.42}Ti_{0.34}$]$O_3$ single crystals', *Jpn J Appl Phys*, 44, 7037–7041.
95. Wada S, Suzuki S, Noma T, *et al.* (1999), 'Enhanced piezoelectric property of barium titanate single crystals with engineered domain configurations', *Jpn J Appl Phys*, 38, 5505–5511.
96. Park S-E, Wada S, Cross L E and Shrout T R (1999), 'Crystallographically engineered BaTiO_3 single crystals for high-performance piezoelectrics', *J Appl Phys*, 86, 2746–2750.
97. Fu H and Cohen R E (2000), 'Polarization rotation mechanism for ultrahigh electromechanical response in single-crystal piezoelectrics', *Nature*, 403, 281–283.
98. Feng Z, Luo H, Yin Z, Guang C and Ling N (2005), 'High electric-field-induced strain of Pb($Mg_{1/3}Nb_{2/3}$)O_3–PbTiO_3 crystals and their application in multilayer actuators', *Appl Phys A*, 81, 1245–1248.
99. Jiang X, Rehrig P W, Hackenberger W S *et al.* (2005) 'Advanced piezoelectric single crystal based actuators', *Proceedings of the SPIE*, 5761, 253.
100. Ko B, Jung J and Lee S (2006), 'Design of a slim-type optical pick-up actuator using PMN-PT bimorphs', *Smart Mater Struct*, 15, 1912–1918.
101. Woody S, Smith S, Jiang X and Rehrig P (2005), 'Performance of single-crystal Pb($Mg_{1/3}Nb_{2/3}$)–32%PbTiO_3 stacked actuators with application to adaptive structures', *Review of Scientific Instruments*, 76, 075112.

102. http://www.kcftech.com.
103. Chen J and Panda R (2005), 'Review: commercialization of piezoelectric single crystals for medical imaging applications', *Ultrasonics Symposium, 2005 IEEE*, 1, 235–240.
104. Saitoh S, Kobayashi T, Harada K, Shimanuki S and Yamashita Y (1999), 'Forty-channel phased array ultrasonic probe using $0.91Pb(Zn_{1/3}Nb_{2/3})O_3$–$0.09PbTiO_3$ single crystal', *Ultrasonics, Ferroelectrics and Frequency Control, IEEE Transactions*, 46, 152–157.
105. Saitoh S, Kobayashi T, Harada K, Shimanuki S and Yamashita Y (1998), 'A 20 MHz single-element ultrasonic probe using $0.91Pb(Zn_{1/3}Nb_{2/3})O_3$–$0.09PbTiO_3$ single crystal', *Ultrasonics, Ferroelectrics and Frequency Control, IEEE Transactions*, 45, 1071–1076.
106. Cheng K, Chan H, Choy C, Yin Q, Luo H and Yin Z (2003), 'Single crystal PMN-0.33PT/epoxy 1-3 composites for ultrasonic transducer applications', *Ultrasonics, Ferroelectrics and Frequency Control, IEEE Transactions*, 50, 1177–1183.
107. Sung M, Jung H and Lee K (2004), 'Multilayer PMN-PT single crystal transducer for medical application', *Ultrasonics Symposium, 2004 IEEE*, 2, 1021–1024.
108. Ritter T, Geng X, Shung K, Lopath K, Park S and Shrout T (2000), 'Single crystal PZN/PT-polymer composites for ultrasound transducer applications', *Ultrasonics, Ferroelectrics and Frequency Control, IEEE Transactions*, 47, 792–800.

8

Electroactive polymers as actuators

Y. BAR-COHEN, Jet Propulsion Lab, USA

Abstract: Electroactive polymers (EAP) are actuators that most closely emulate biological muscles compared to any other actuators that are human-made and therefore they earned the moniker 'artificial muscles'. The materials that were developed in the early days of this field generated limited actuation strain and therefore received relatively little attention. However, over the last 20 years a series of EAP materials has emerged that exhibits a significant shape change in response to electrical stimulation. Their capability allowed producing and demonstrating various exciting and novel mechanisms including robot fish, catheter steering element, miniature gripper, loudspeaker, fishlike blimp, and dust-wiper. The impressive advances in improving their actuation strain are attracting the attention of many engineers and scientists from many different disciplines. These materials are particularly attractive to biomimetic applications since they can be used to make biologically inspired intelligent robots and other mechanisms. Increasingly, EAP actuated mechanisms are being engineered that were previously considered science fiction. This chapter reviews the state-of-the-art challenges and potential applications of EAP materials.

Key words: EAP, electroactive polymers, polymer actuators, robotics, artificial muscles, biomimetics, biologically inspired technologies.

8.1 Introduction

Polymers are inherently lightweight, easy to process and to mass produce, as well as mechanically flexible making them highly attractive for numerous applications. In response to stimulation, some polymers sustain change in properties adding significant advantages to their use. For many years, mechanically responsive polymers were known to vary their shape or size when subjected to electric, chemical, pneumatic, optical, or magnetic field. Electrical excitation is one of the most sought after stimulation methods for causing elastic deformation in polymers. The convenience and practicality of their electrical stimulation and recent response improvements made electroactive polymers (EAP) the most preferred among the activatable polymers (Bar-Cohen, 2004). An added benefit of EAP materials is that some of these polymers also exhibit the reverse effect of converting mechanical strain to electrical signal. This makes them useful for sensors and energy harvesting mechanisms. Today, there are many known EAP materials and, according to their activation mechanism, they were divided by the author into two groups: *electronic* (also known as the *field activated*) and *ionic* (Bar-Cohen, 2004). One of the main applications of EAP materials is their use for biologically inspired applications, a field known as biomimetics (Bar-Cohen, 2005; Bar-Cohen and Hanson, 2009). Some of the biomimetic applications were previously imaginable only in science fiction.

Being new materials, there is a need to establish the scientific and engineering foundations of the field of EAP to allow turning them into actuators-of-choice. This involves improving the understanding of the basic principles that drive them. Some of the necessary scientific foundations involve having effective computational chemistry models, comprehensive material science, electro-mechanics analytical tools and material processing techniques. The development of the foundations requires gaining better understanding of the parameters that control their electro-activation behavior. In order to maximize the actuation capability and operational durability, effective processing techniques are being developed for their fabrication, shaping, and electroding. Methods of reliably characterizing the response of EAP materials are being developed and efforts are underway to create databases with documented material properties (http://www.actuatorweb.org/). To bring these materials to the level of application in daily use products will necessitate finding niches that address critical needs.

8.2 Historical review

The first documented study of EAP materials was conducted in 1880 by Roentgen. In his experiment he used a rubber-band subjected to an electric field across the fixed end and a mass attached to the free end (Roentgen, 1880). This experiment was followed by Sacerdote (1899) who formulated the strain response to electric field activation. A subsequent progress milestone was recorded by Eguchi (1925) who discovered a piezoelectric polymer called electret when carnauba wax, rosin, and beeswax were cooled to solidify while being subjected to a DC bias field. Electrets are insulation materials (mostly polymers) that can hold electric charges after being polarized in an electric field. They generate voltage when subject to stress and also have the reverse behavior of being deformed under an electric field. However, their output strain is generally very low for application as actuators and therefore their use has been limited to sensors. Only about 40 years later another breakthrough was reported, when Kawai (1969) observed a substantial piezoelectric activity in uniaxially-drawn and poled polyvinylidene fluoride (PVDF) (Bergman *et al.*, 1971). This breakthrough was preceded by Fukada's work on piezoelectric biopolymers (Fukada, 1955). Subsequent investigations of PVDF and its copolymers have shown that some noncrystalline polymers with very large dielectric relaxations exhibit strong electromechanical activity due to the orientation of molecular dipoles (e.g., Wada, 1976; Kepler, 1978). Extensive research and development efforts related to PVDF took place mostly during the 1970s and 1980s where, in parallel to the efforts to improve the performance of the materials, applications in many areas were considered (Furukawa, 1989). The limited strain that can be produced by PVDF led to its use mostly for sensors and transducers of ultrasonic waves (Bauer and Bauer, 2008).

The success in developing PVDF as an electroactive polymer was followed with extensive search for other polymer systems that exhibit significant electroactive response. These efforts led to the discovery and development of many effective materials as reported for example in Lovinger (1983), Oguro *et al*. (1992), Nalwa (1995), Baughman (1996), Zhang *et al*. (1998) and Baughman *et al*. (1999). In the dielectric elastomer EAP materials the generated strain levels have even exceeded 100% with a relatively fast response speed (<0.1 sec) (Pelrine *et al*., 2000).

After working in the field since 1995, the author recognized that it is critical to have international cooperation for the field in order to accelerate the development of EAP materials. For this purpose, he initiated and organized through SPIE the first EAP Actuators and Devices (EAPAD) Conference in March 1999, as part of the Smart Structures and Materials Symposium (Bar-Cohen, 1999). This EAPAD conference marked an important milestone for the field, bringing EAP materials to the attention of scientists and engineers worldwide. The SPIE's EAPAD conference is now organized annually with a growing number of presentations and attendees. In recent years, an increasing number of organizations and technical societies have started organizing related workshops, meetings and conferences with sessions on EAP. As forums of information exchange, a website was created called the WorldWide EAP (WW-EAP) Webhub that archives EAP related information and links (http://eap.jpl.nasa.gov). Also, since June 1999, the semi-annual WW-EAP Newsletter has been published with short synopses from authors worldwide providing a snapshot of their advances. This Newsletter is published electronically and its issues are accessible from the above mentioned WW-EAP webhub. For a documented reference book, the author edited and co-authored a reference book on EAP that was published in 2001 and its 2nd edition was published in 2004 (Bar-Cohen, 2004). This book provides a comprehensive text on the subject covering the capabilities, potentials and challenges to the field including description of the available materials, analytical models, processing techniques, and characterization methods.

8.3 The two electroactive polymers (EAP) groups

As mentioned earlier, the author divided the EAP materials into two major groups (Bar-Cohen, 2004) as follows:

Ionic EAP

The mechanism of activation of these materials involves transport or diffusion of ions (Park *et al.*, 2008). These materials consist of two electrodes and electrolyte. Examples of these materials include ionic polymer–metal composites (IPMC), conductive polymers, carbon nanotubes, and ionic polymer gels. Their advantages include the large bending under low activation voltage (1–2 V). However, their disadvantages are the need to maintain electrolytes wetness, having a relatively low efficiency in the range of ~1%, and they have difficulty sustaining constant displacement under activation of a DC voltage (except for conductive polymers). The diffusion or macroscopic motion of ions is responsible for the actuation slow speed of these materials that is the range of tens to a fraction of a second.

Electronic (also known as field-activated) EAP

This group is activated by Coulomb force that is produced by an electric field between the electrodes on a film shaped polymer material. The piezoelectric polymers, such as PVDF, exhibit linear relation between the electric field and the generated stain but produce low strain at a fraction of percent level (Ohigashi, 1976; Wada, 1976; Tasaka and Miyata, 1981; Sessler, 1981; Furukawa and Wen, 1984; Furukawa, 1989; Bauer and Bauer, 2008). On the other hand, the EAP materials with electrostrictive behavior exhibit quadratic relation between the field and the strain that reaches as high as several to hundreds of percent (Pelrine *et al.*, 2000). The electrostrictive polymers are used for actuators while the piezoelectric types are used for such applications as sensors and transducers to generate ultrasonic waves. In some of these materials the Coulomb field directly causes strains while in others it causes the change through an internal polarization with molecular alignment (Cheng and Zhang, 2008). Generally, high voltage levels (>10 V/μm) are required, which may be close to the breakdown level. The required high activation field is the result of the low dielectric constant in polymers that, typically, is below 10. To address this issue two different approaches are used:

- making multilayered structures of thin films that are stacked to reach the required thickness (this is a method that is commonly used in piezoelectric ceramic actuators); and
- increasing the dielectric constant by forming a composite.

Since the actuation does not involve diffusion of charge species, these EAP materials respond fast in the range of milli-seconds. Examples of these materials include electrostrictive, electrostatic, piezoelectric, and ferroelectric materials. Generally, the electronic EAP materials can be made to hold the induced displacement while operated under a DC voltage, allowing them to be considered for robotic applications with high efficiency. The electronic EAP materials have a greater mechanical energy density and they can be activated in air with no major constraints. However, as mentioned above, they require high activation field that may be close to the electric breakdown level.

The generated displacement in both the electronic and ionic EAP materials can be designed geometrically to bend, stretch or contract. For example, in the case of linear strain an EAP material bonded to a passive film acts as a bimorph that bends in response to electric stimulation. Generally, the bending that is produced by EAP materials involves low force and due to their low modulus they generate low moments and torques.

8.3.1 Producing EAP materials

So far, the progress in advancing the field of EAP has been hampered by the unavailability of commercial sources for related materials and actuators. While efforts are underway to establish production capabilities, EAP materials are still custom made mostly by researchers and they are not available in commercial quantities. New researchers who are seeking to start working on these materials have been encountering difficulties obtaining samples and some had to learn how to make the materials themselves. To help in making these materials widely available, the author established a website that provides fabrication procedures for the leading types of EAP materials (http://ndeaa.jpl.nasa.gov/nasa-nde/lommas/eap/EAP-recipe.htm). These fabrication procedures were contributed by related leading EAP researchers who were willing to share the information about their material preparation procedure. In preparing these materials, especially the ionic EAP, it is critical to pay attention to safety issues that are related to the specific materials. In parallel, as more companies are starting to be established with focus on making EAP materials and products, the author also formed a website that lists the sources where custom made materials and samples can be obtained (http://ndeaa.jpl.nasa.gov/nasa-nde/lommas/eap/EAP-material-n-products.htm).

8.3.2 Electronic (also known as field-activated) EAP

Ferroelectric polymers

The property of piezoelectricity is found in non-centro-symmetric materials. The phenomenon is called ferroelectricity when a non-conducting crystal or dielectric material exhibits spontaneous electric polarization. Piezoelectricity was discovered in 1880 by Pierre and Paul-Jacques Curie, who found that a voltage is produced on the surface of the crystal when certain types of crystals, such as quartz, tourmaline, and Rochelle salt, are compressed along certain axes. The Curie brothers followed this discovery a year later with the observation of the reverse effect that, upon application of an electric voltage, these crystals sustain an elongation. There are also polymers with ferroelectric behavior and the most widely exploited one is poly(vinylidene fluoride), which is also known as PVDF or PVF2 (Ohigashi, 1976; Sessler, 1981; Furukawa, 1989; Bar-Cohen *et al.*, 1996), and its copolymers (Cheng and Zhang, 2008). These polymers are partly crystalline, with an inactive amorphous phase, having a Young's modulus near 1–10 GPa. While, as mentioned earlier, PVDF exhibits piezoelectric behavior with the strain related linearly to the electric field that generates it, the strain response of electrostrictive materials is quadratic with the field (Sessler, 1981). This relatively high elastic modulus provides a high mechanical energy density. Generally, PVDF generates strain levels of about 0.1% and a pressure level of about 5 MPa, where under large electric field (~200 V/μm) its copolymers can generate a strain that is nearly 2% (Zhang *et al.*, 2004). However, this level of field is dangerously close to dielectric breakdown, and the dielectric hysteresis is very large. In 1998, Zhang and his coinvestigators introduced defects into the crystalline structure using electron radiation to increase the dielectric constant of the copolymer P(VDF-TrFE). The resulting material generates strains as large as 5% and levels of pressure of about 45 MPa under voltages of about 150 V/μm. The drawback to the irradiation is the introduction of many undesirable defects including the formation of crosslinkings and chain scission (Mabboux and Gleason, 2002). This issue was addressed by producing terpolymers via molecular design that enhances the degree of conformational changes at the molecular level in the polymer. The resulting terpolymer generates higher electro-mechanical response than the high energy electron irradiated copolymer (Cheng and Zhang, 2008; Zhang *et al.*, 2004).

The formation of a composite as an approach for increasing the dielectric constant was proposed by the author (Bar-Cohen, 2004). For this purpose, Zhang and his co-investigators (2004) used an all-organic composite that consists of particulates having high dielectric constant (K > 10 000). For a CuPc-PVDF-based terpolymer composite having elastic modulus of 750 MPa, the particulates increased the dielectric constant from single digits to the range from 300 to 1000 (at 1 Hz) and under a field of 13 V/μm generated strain of ~2% and pressure level of 7.5 MPa. Photographs of such a composite ferroelectric EAP in passive and activated states are shown in Fig. 8.1.

Dielectric electroactive polymers (DEAP)

Low elastic stiffness polymers with high dielectric breakdown strength that are subjected to an electrostatic field generate a large strain and act as EAP

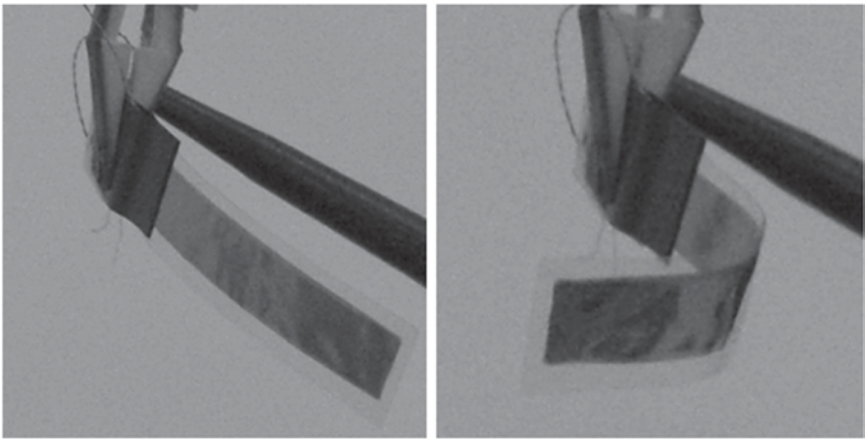

8.1 Photographs of a composite ferroelectric EAP in passive (left) and activated states (right). This EAP material was provided to the author courtesy of Qiming Zhang, Penn State University.

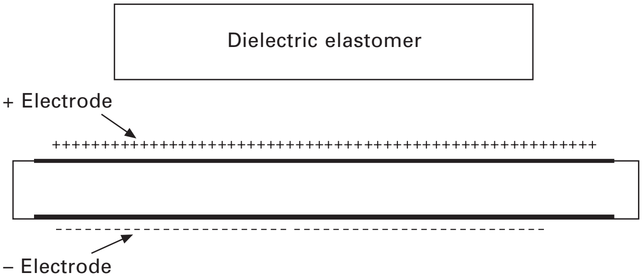

8.2 Under electroactivation, a dielectric elastomer with compliant electrodes on both surfaces expands laterally and can be made to operate longitudinally.

materials. These materials are known as dielectric elastomer EAP and can be represented by a parallel plate capacitor as shown schematically in Fig. 8.2. To avoid impeding the generated high strain it is necessary to use highly compliant electrodes such as conductive carbon grease.

A 1992–1993 study by Pelrine and his co-investigators (Pelrine and Joseph, 1993, 1994; Pelrine and Kornbluh, 2009) led to the first observation of the fact that dielectric elastomers sustain large strain (23% in silicone films) when subjected to high electric field. In their reports they suggested the use of dielectric EAP materials for actuation mechanisms. Independently, in 1994, Zhenyi and his co-investigators reported that they measured 3% strain in polyurethane when subjected to a 20 V/μm electric field (Zhenyi *et al.*, 1994). Significant levels of strain started to be observed in the years that followed where in 1998 a level of strain of 30% was reported being measured in silicone (Pelrine *et al.*, 1998). A major milestone in the development was documented in 2000, when using acrylic as an elastomer and preload Pelrine and his co-investigators reported strains that are much higher than 100% (Pelrine *et al.*, 2000). Today, there are many researchers who are using dielectric elastomers as EAP materials and significant progress has been made towards making practical actuators (Kornbluh *et al.*, 2004; Cheng and Zhang, 2008; Carpi *et al.*, 2008).

Application of an electric field results in a strain that is proportional to the square of the electric field and to the dielectric constant while inversely proportional to the elastic modulus. Practically, to apply the required electric field at the levels of 100 V/μm and above necessitates using thin films. Dielectric elastomer EAP actuators can generate significant levels reaching more than 100% strain. The applied field causes thickness contraction and lateral expansion. To produce linear actuators using dielectric elastomer films, scientists at SRI International rolled two elastomer layers with carbon-based electrodes on both sides of one of the layers forming a cylindrical actuator (Kornbluh *et al.*, 2004). Further modifications of their actuator design led to the development of the multifunctional electroelastomer roll (MER). In this actuator (Fig. 8.3) highly prestrained dielectric elastomer are rolled around a

8.3 A dielectric elastomer EAP-based multifunctional electroelastomer roll (MER) spring roll. Courtesy of Qibing Pei, UCLA, Roy Kornbluh, SRI International, and SPIE (adapted from Pei *et al.*, 2002; and Kornbluh *et al.*, 2002).

compression spring (Pei *et al.*, 2004). By selectively actuating only certain regions of electrodes around the periphery of the actuator, the actuator can be made to bend as well as elongate.

The required voltages for the activation of dielectric elastomers are close to the breakdown strength of the material, and a safety factor that lowers the actuator potential is used. Another concern associated with the use of such EAP materials is the required prestraining that over time is released due to creep degrading the actuator performance. Researchers at Sungkyunkwan University, Korea, (Jung *et al.*, 2004) and at UCLA, USA, (Ha *et al.*, 2006) developed a method that has shown promise with regard to eliminating the need for prestrain. Ha and his co-investigators (2006) used an interpenetrating polymer network (IPN) where tension in the network is balanced by compression. To form IPN thermally crosslinkable liquid additives were used including a difunctional acrylate (e.g., HDDA) and a trifunctional acrylate (e.g., TMPTMA). Alternatively, using folded film structure, scientists at the University of Pisa, Italy, produced a contractile actuator that does not require prestrain (Fig. 8.4). Also, recently investigators at EMPA, Switzerland, developed a method of stacking thousands of thin layers of a dielectric elastomer to form an effective actuator that generates contraction and does not require preload (Fig. 8.5). Using this design, levels of 40% strain were measured using up to 40 mm diameter, 100 mm long actuator and generated as high as 250 N contractile force (Kovacs and Düring, 2009). Recent development at PolyPower, Danfoss, Denmark, using a dielectric elastomer film that was designed in wavy configuration along the thickness, led to a process that is easy to mass produce and with actuators

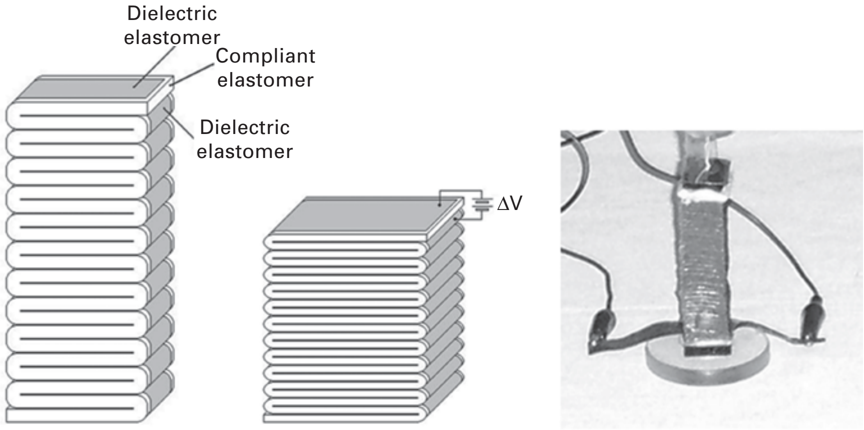

8.4 A contractile EAP actuator using a folded film structure. Courtesy of Federico Carpi, University of Pisa, Italy.

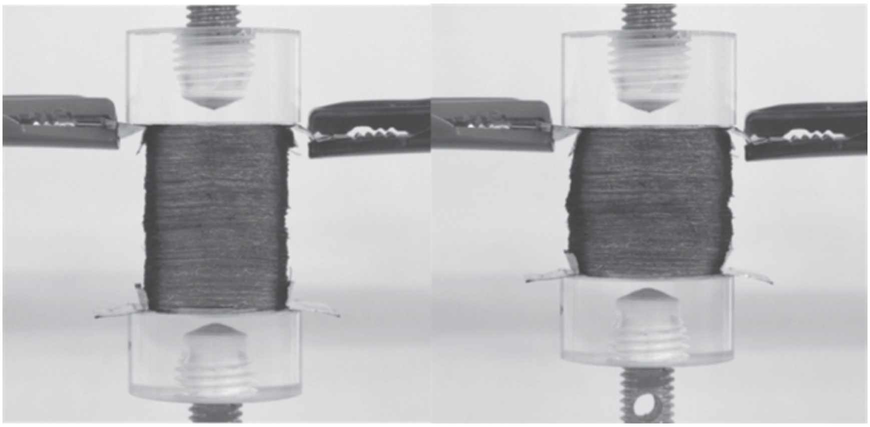

8.5 Photographs of multilayered dielectric elastomer in passive (left) and activated states (right). Courtesy of Gabor Kovacs, EMPA Dübendorf, Switzerland.

that are capable of lifting and pushing levels of kilograms (Fig. 8.6) (Kiil and Benslimane, 2009).

Electrostrictive graft elastomers

Graft-elastomer EAP is a polymer that exhibits electrostriction behavior when subjected to a large electric field and it can generate strain levels of about 4% and stress levels of about 24 MPa (Su *et al.*, 1999; Zhang *et al.*, 2004). This electronic EAP material offers relatively high electromechanical power density and is relatively easy to process compared to the ferroelectric EAP. Grafted-elastomer EAP was developed at NASA Langley Research Center by Su and his co-investigators (Su *et al.*, 1999). It consists of two components, a flexible backbone macromolecule and a grafted polymer that can form a crystalline structure (see Fig. 8.7). The grafted crystalline polar phase provides moieties in response to an applied electric field and cross-linking sites for the elastomer system. A combination of the electrostrictive-grafted elastomer with a piezoelectric poly(vinylidene fluoride-trifluoroethylene) copolymer yields several compositions of a ferroelectric-electrostrictive molecular composite system. Such a combination can be operated both as piezoelectric sensor and electrostrictive actuator. Careful selection of the polymer composition allows for the creation and optimization of a molecular composite system with respect to its electrical, mechanical, and electromechanical properties. A photographic view of an activated grafted elastomer-based bimorph actuator is shown in Fig. 8.8 where on the left an unexcited state is shown while on the right it is shown in an excited state.

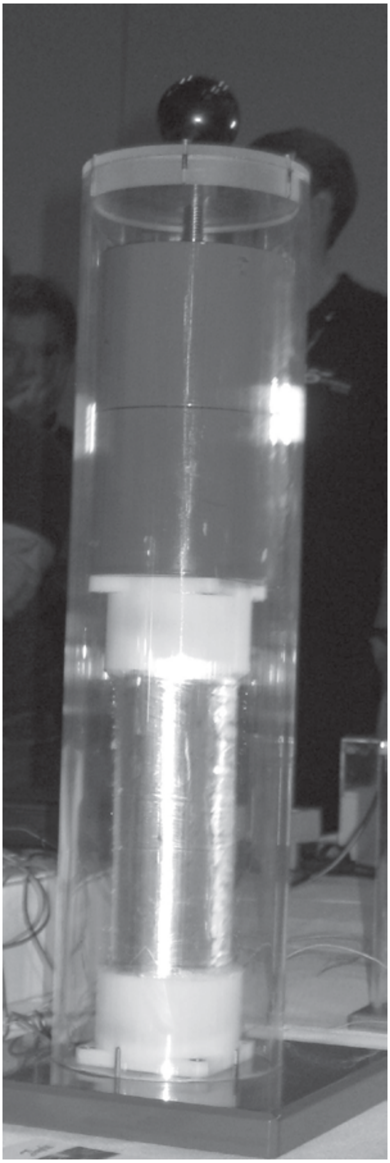

8.6 A dielectric elastomer with wavy shape film made by PolyPower, Danfoss, Denmark, is shown lifting 10 kg (the cylinders).

8.3.3 Ionic EAP

Ionomeric polymer–metal composite (IPMC)

Ionomeric polymer–metal composite (IPMC) is an ionic EAP that bends in response to an electrical activation (Fig. 8.9) as a result of mobility of

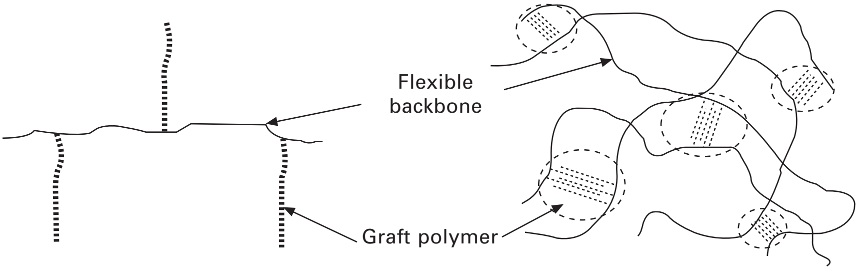

8.7 Structure and morphology of the graft elastomer EAP. Courtesy of Ji Su, NASA LaRC, VA.

8.8 An electrostrictive grafted elastomer-based bimorph actuator in an unexcited state (left) and in one of the two directions of the excited state (right). Courtesy of Ji Su, NASA LaRC, VA.

cations in its polymer network (Nemat-Nasser and Thomas, 2004; Park *et al*., 2008). In 1992, this electroactive characteristic of IPMC was realized independently by three different groups of researchers: Oguro *et al*. (1992) in Japan, as well as Shahinpoor (2000) and Sadeghipour *et al*. (1992) in the United States. A relatively low voltage stimulates the bending of IPMC, where the base polymer provides channels for mobility of positive ions in a fixed network of negative ions on interconnected clusters. Electrodes on the surface are used to supply the required electrical field and the polarity determines the direction of bending and even a fraction of a volt leads to a response. Two types of base polymers are widely used to produce an IPMC: perfluorosulfonate that is also known as Nafion® (DuPont, USA) and perfluorocarboxylate, which is also known as Flemion® (Asahi Glass, Japan). An illustration of the principle of activation of a Nafion-based IPMC

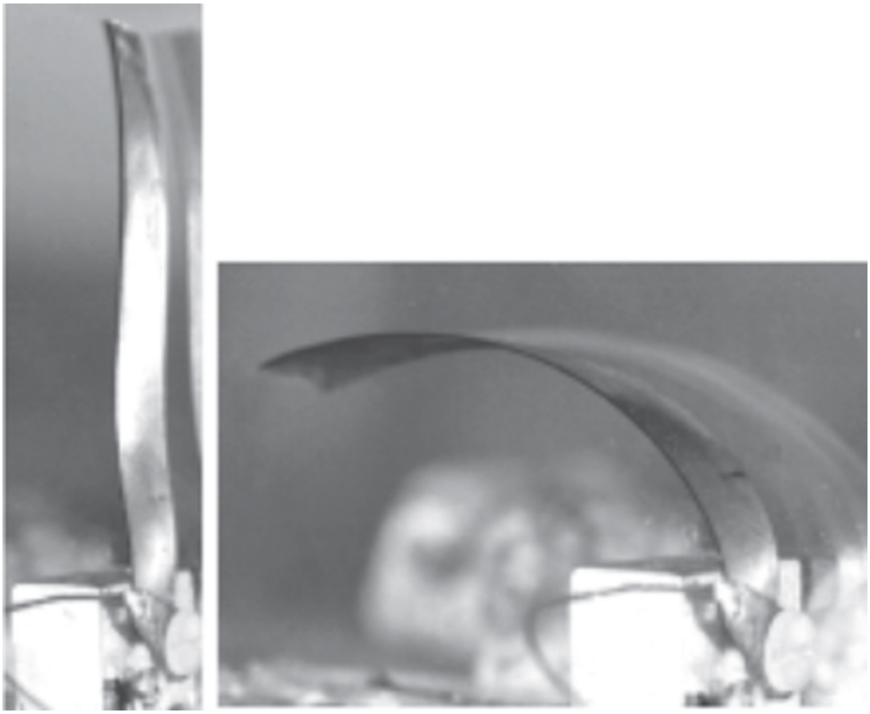

8.9 IPMC in passive (left) and activated states (right).

is shown in Fig. 8.10. In order to electrode the polymer films, metal ions (platinum, gold, etc.) are dispersed throughout the hydrophilic regions of the polymer surface and are subsequently reduced to zero-valence metal atoms. The ionic content of IPMC determines its electromechanical response (Bar-Cohen 1999; Nemat-Nasser and Thomas, 2004). The response of IPMC is relatively slow (<10 Hz) because the ions need to physically travel though the polymer material. Using Li+ cations that are small offers higher mobility and therefore faster bending response. Using gold electrodes, the displacement of IPMC was further increased as a result of the higher electric conductivity.

Conductive polymers (CP)

As EAP materials, conductive polymers typically function via reversible counter-ion insertion and expulsion that occurs during redox cycling (Otero *et al*., 1995; Anquetil *et al*., 2002; Sansiñena and Olazabal, 2004; Smela, 2008). Oxidation and reduction take place at the interface with the electrodes, inducing volume change due mainly to exchange of ions with an electrolyte (Fig. 8.11). A sandwich of two conductive polymer electrodes

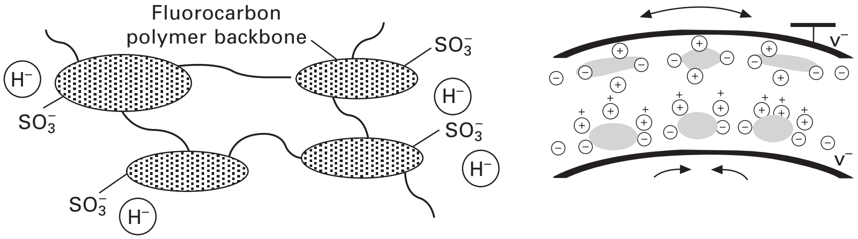
Fluorocarbon polymer backbone
SO_3^-
H^-
SO_3^-
H^-
SO_3^-
H^-
SO_3^-
H^-
v⁻
v⁻

(a) Structure model of Nafion™ polymer chain

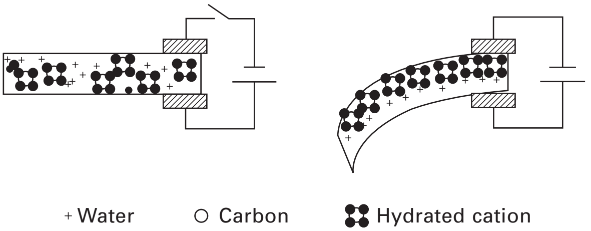
+ Water
○ Carbon
Hydrated cation

8.10 Illustrations of the actuation principle in IPMC. Courtesy of Kwang Kim, University of Nevada, Reno, NV.

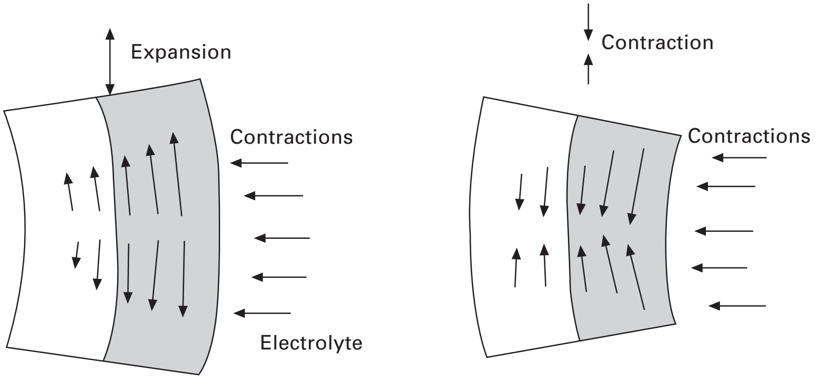
Expansion
Contractions
Electrolyte
Contraction
Contractions

(a) Oxidation (b) Reduction

8.11 Illustration of the oxidation and reduction in conductive polymers as the principle for the actuation mechanism.

(e.g., polypyrrole) with an electrolyte between them forms an EAP actuator. Voltage applied between the electrodes causes oxidation at the anode and reduction at the cathode. The electric charge is balanced by migration of ions between the electrolyte and the electrodes. The added ions cause swelling of the polymer while their removal results in shrinkage leading to the bending of the sandwich. The layer thickness determines the speed of the response where thinner layers are faster reaching as high as 40 Hz (Madden *et al.*, 2001) but generate lower force. Conductive polymer actuators require voltages in the range of 1–5 V (Fig. 8.12) and the speed increases with the voltage. Conductive polymer EAP materials offer relatively high mechanical energy densities of over 20 J/cm^3 but with low efficiencies at the level of 1% if no electrical energy is recovered (Madden *et al.*, 2001). The shear forces that act on the electrolyte layer cause premature failure after as short as several tens of cycles.

Carbon nanotubes (CNT)

The use of carbon nanotubes as EAP was first reported in 1999 (Baughman *et al.*, 1999; Spinks *et al.*, 2004; Qu *et al.*, 2008). The carbon–carbon bonds in nanotubes (NT), which are suspended in an electrolyte and the change in bond length are responsible for the actuation mechanism. A network of conjugated bonds connects all carbons and provides a path for the flow of electrons along the bonds. The electrolyte forms an electric double layer with the nanotubes and allows injection of large charges that affect the ionic charge balance between the NT and the electrolyte (Fig. 8.13). The more charges are injected into the bond the larger the dimension changes. Removal of electrons causes the nanotubes to carry a net positive charge, which is spread across all the carbon nuclei causing repulsion between

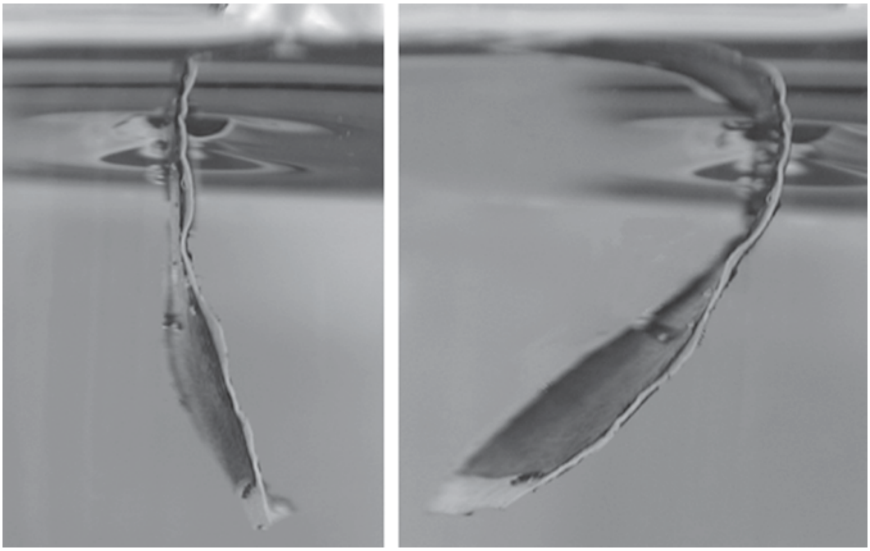

8.12 Conductive polymer in reference and activated states (about 1.5 V).

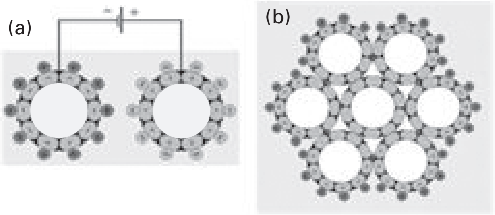

Applied potential injects opposite sign charge in the two nanotube electrodes that are immersed in an electrolyte (light grey background).

Charge injected ion at the surface of a nanotube bundle is illustrated, which is balanced by the pictured surface layer of electrolyte cations.

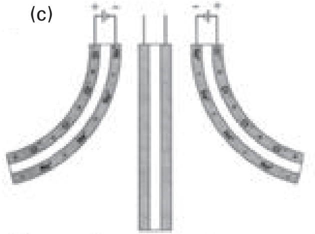

Schematic edge-view of a cantilever-based actuator operated in aqueous NaCl at ±1V

8.13 Schematic illustration of the charge injection in a nanotube-based EAP actuator. Courtesy of Ray Baughman, University of Texas at Dallas, TX.

adjacent carbon nuclei and increasing the C–C bond length. Injection of electrons into the bond also causes lengthening of the bond resulting in an increase in nanotube diameter and length. These changes in dimension are translated into macroscopic movement in the network element of entangled nanotubes and the net result is extension of the CNT.

CNT consists of nanometer-size tubes that can induce strains in the range of 1% along the length. A carbon nanotube actuator can be constructed by laminating two narrow strips of carbon nanotube sheet with an electronically insulated intermediate adhesive layer. The resulting three-layer strip is then immersed in an electrolyte. Application of ~1 V is sufficient to cause bending, and the direction depends on the polarity of the field with a response that is approximately quadratic between the strain and charge. CNT actuators have the potential to produce a very high work per cycle compared to other types of actuators. However, such energy densities and forces have not been realized yet in macro-scale devices.

Ionic polymer gels (IPG)

Ionic polymer gels (e.g., poly-acrylonitrile) are generally activated by a chemical reaction where changing from an acid to an alkaline environment causes the gel to become dense or swollen, respectively. This chemo-mechanical mechanism was first reported in 1955 by Katchalsky and his co-investigators (Katchalsky and Zwick, 1955; Kuhn *et al*., 1955). The related mechanical change results either from the displacement of water out of the gel, or the redistribution of water within the gel (Osada and Hasebe, 1985). The chemo-mechanical reaction was stimulated electrically by researchers at the University of Arizona, USA (Liu and Calvert, 2000; Calvert, 2004, 2008). When activated, these gels bend as the cathode side becomes more alkaline and the anode side more acidic. However, just like other ionic EAP materials, because of the need to migrate ions through the gel, the response of this multilayered gel structure is relatively slow. A significant amount of research and development efforts and application considerations using ionic gel polymers were explored at Hokkaido University, Japan (Osada and Kishi, 1989). Further, Schreyer and his co-investigators at the University of New Mexico, Albuquerque, used a combination of ionic gel and conductive polymer electrodes to demonstrate an effective EAP actuator (Schreyer *et al*., 2000).

8.4 Current and under consideration applications

Increasingly, there is significant progress toward making practical EAP actuators, and commercial products are starting to emerge. A growing number of organizations are exploring potential applications for EAP materials, and cooperation among experts from various disciplines is helping to overcome related challenges. The mechanisms and devices that are being considered or developed are applicable to many fields. Eamax, Japan, is credited with developing the first EAP-related commercial product, when at the end of 2002 it announced the marketing of a biomimetic device in the form of a fish robot (Bar-Cohen, 2004). Today, various prototypes of potential commercial products are being developed for a range of applications including zoom lens of cellular phones, valves, energy harvesting, pumps and many others.

8.4.1 Medical applications

One of the application areas that is attracting a great deal of effort is the field of medicine. The potential use of EAP materials as artificial muscles for driving devices with biomimetic characteristics is being explored. Some of the applications that are considered include catheter steering mechanism (Della Santa *et al*., 1996), vein connectors for repair after surgery, smart prosthetics (Herr and Kornbluh, 2004), Braille displays (Bar-Cohen, 2004) and others. Research at Sungkyunkwan University, Korea, is seeking to develop such devices as a smart pill, which is made as a tube-like structure, designed to travel like an inchworm inside the gastrointestinal tract (Jung *et al*., 2004).

Also, the development of a Braille reading interface for the visually impaired is being investigated (Fig. 8.14). Blind patients are given display patterns of letters and symbols and they are asked to recognize them. The use of dielectric elastomer EAP for Braille display has also been a subject of study at SRI (Heydt and Chhokar, 2003; Kornbluh *et al*., 2004) where individually addressable diaphragm actuators were developed at the small scale of Braille dots of 1.5 mm diameter and 2.3 mm center-to-center spacing.

8.4.2 Dust wiper for the JPL's Nanorover

Between 1995 and 1999, under the author's lead, a NASA study took place with the objective of improving the understanding and practicality of EAP materials towards identifying planetary applications. One of the applications that was investigated includes a miniature dust wiper. The wiper was intended for dust removal from the Nanorover's optical/IR window of the MUSES-CN mission. The MUSES-CN mission itself was cancelled due to budget constraints but it gave the field of EAP an important recognition and brought the field to the public spotlight. An IPMC actuator was designed to wipe the window with the aid of a novel 104 mg blade having a gold-plated fiberglass brush (Fig. 8.15), which was developed by ESLI (San Diego,

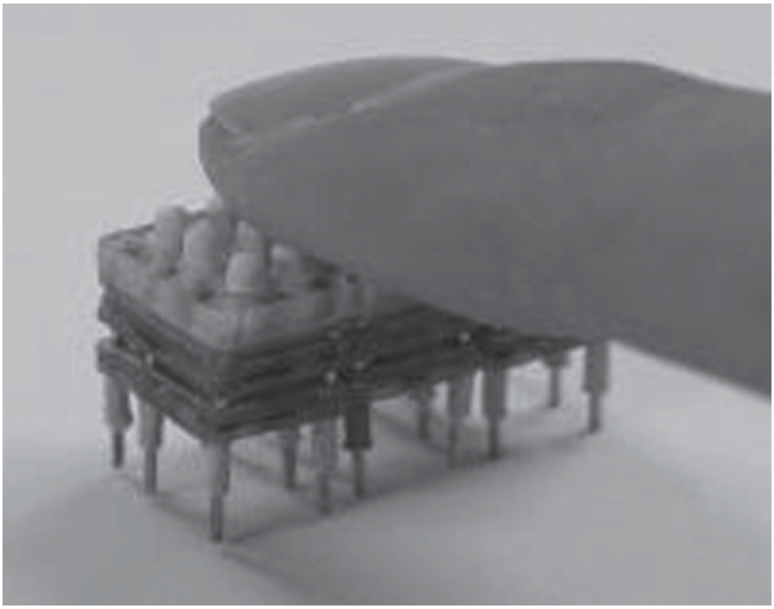

8.14 Braille display for visually impaired. Courtesy of H.R. Choi, Sungkyunkwan University, Korea.

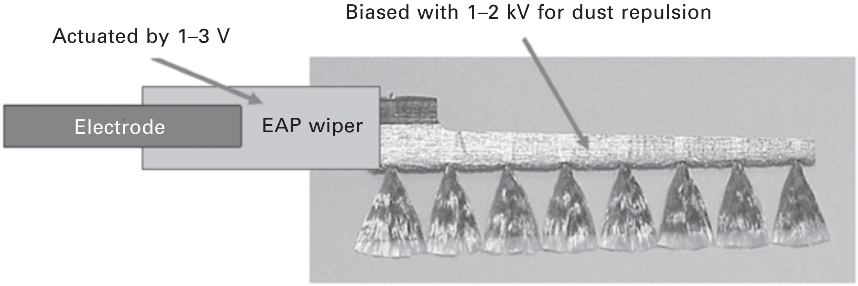

8.15 Combined schematic and photographic view of the EAP dust wiper.

CA). To repel dust the blade was subjected to high voltage (1–2 KV) while wiping the surface.

8.4.3 Biomimetic robotics

EAP actuators offer many important capabilities for the engineering of biomimetic devices (Bar-Cohen, 2004). Using EAP actuators, biologically inspired devices and robots may be developed with capabilities that are far superior to natural creatures since they are not constrained by evolution and survival needs. Flight is an example of the success of taking biologically inspired technology and making aircraft that can fly faster, far higher, carry more weight, and operate in significantly more difficult environmental conditions than any flying creature is capable. One may produce such devices as artificial bugs that may walk, swim, hop, crawl and dig while reconfiguring themselves as needed. Mimicking nature would immensely expand the collection and functionality of robots allowing performance of tasks that are impossible with existing capabilities (Bar-Cohen and Breazeal, 2003; Bar-Cohen, 2005; Bar-Cohen and Hanson, 2009). For example, the author and his co-investigators constructed a miniature robotic arm that was lifted by a rolled dielectric elastomer EAP as a linear actuator and with four IPMC-based fingers as bending actuators (Bar-Cohen, 2004). The linear actuator was used to raise and drop a graphite/epoxy rod that served as a simplistic representation of a robotic arm. To produce an end-effector for the arm, the gripper was developed (Fig. 8.16) where IPMC strips acted as fingers, and hooks at the bottom of the strips allowed emulating fingernails. This gripper grabbed rocks in a very similar way to the human hand. Other recently reported robotic applications include a 6-legged skitter that was developed by SRI International (Fig. 8.17), as well as a blimp (made by EMPA, Switzerland) having fins that are activated by Dielectric Elastomer EAP for steering (Fig. 8.18)

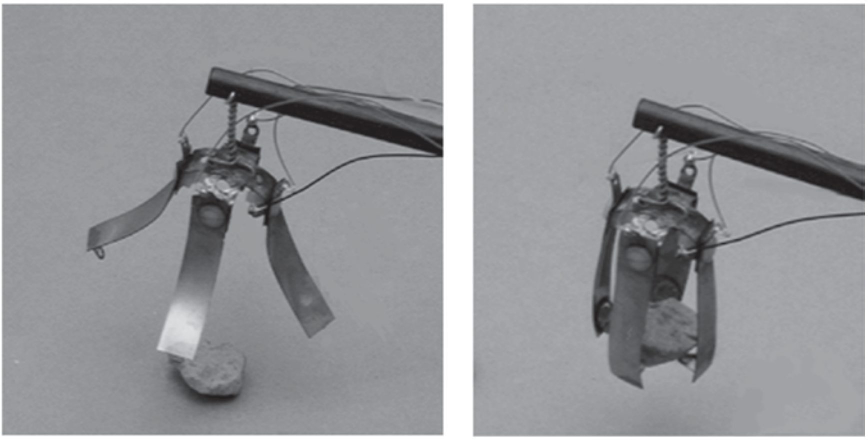

8.16 4-finger EAP gripper lifting a rock.

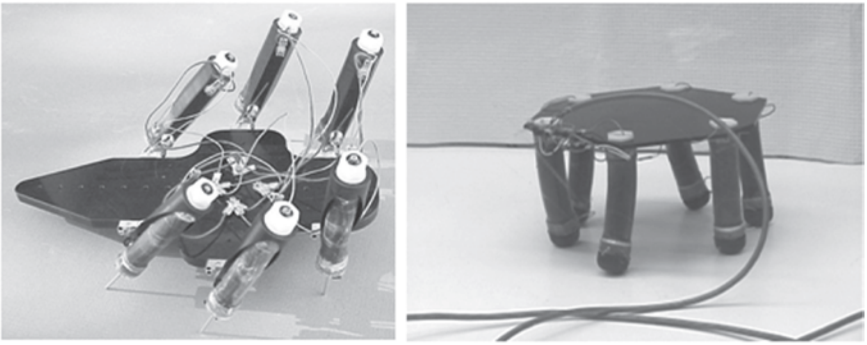

8.17 A skitter with 6 legs using spring roll actuators based on dielectric elastomer EAP. These two images are published with the permission of SPIE where the left image is courtesy of Ron Pelrine, SRI International (adapted from Pelrine *et al.*, 2002) and the image on the right is courtesy of Qibing Pei, UCLA (adapted from Pei *et al.*, 2003).

8.5 The armwrestling challenge – as a state-of-the-art indicator

In an effort to promote worldwide development towards the realization of the potential of EAP materials, in 1999 the author posed an armwrestling challenge (http://ndeaa.jpl.nasa.gov/nasa-nde/lommas/eap/EAP-armwrestling.htm). In posing this challenge, the author is seeking to see an EAP activated robotic arm win against a human in a wrestling match and a graphic rendering of the challenge icon is illustrated in Fig. 8.19. The emphasis on armwrestling with humans was carried out in order to have our muscles as a baseline for

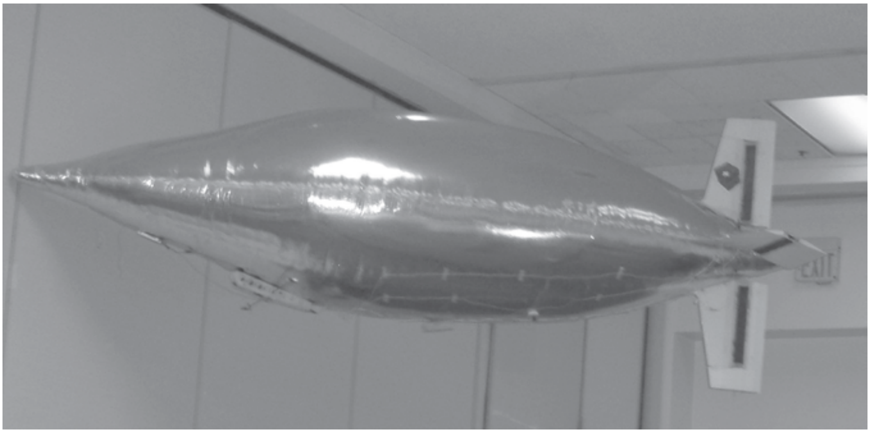

8.18 Blimp with fin steering (made by EMPA) demonstrated at the EAP-in-Action Session of the SPIE's EAPAD 2008 in San Diego, CA.

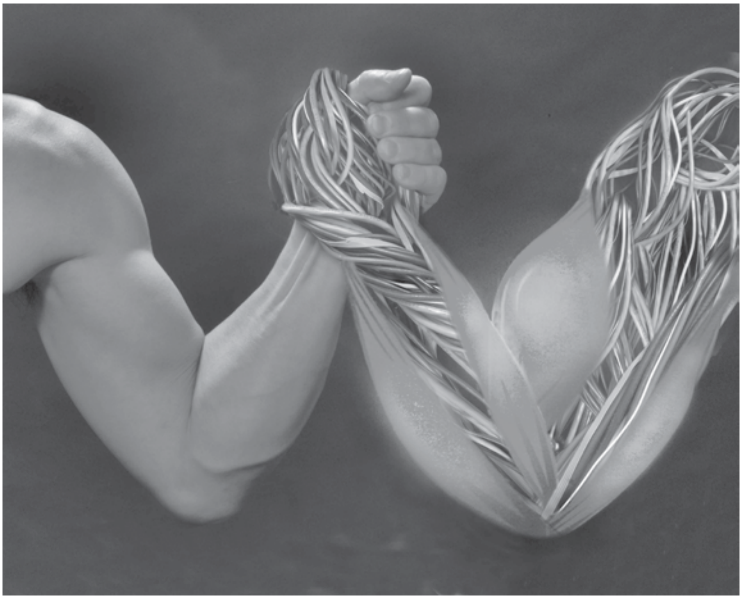

8.19 Grand challenge for the development of EAP actuated robotics.

performance comparison. Success will allow applying EAP materials to improve many aspects of our life where some of the possibilities include effective implants and prosthetics, active clothing, realistic biologically inspired robots as well as fabricating products with unmatched capabilities and dexterity.

The first arm-wrestling match with humans was held on March 7, 2005 as part of the EAP-in-Action Session of the SPIE's EAPAD Conference. Three robotic arms participated in the contest against a 17-year-old high school female student and the student won against all these arms (see Fig. 8.20). The 2nd Artificial Muscles Armwrestling Contest was held on Feb. 27, 2006. However, rather than wrestling with a human opponent, the contest consisted of measuring the arms, performance and comparing the results. A measuring fixture was developed jointly by individuals from UCLA and members of the author's group at JPL. The fixture was strapped to the contest table and the EAP actuated arms were tested for speed and pulling force. Each competing arm pulled on the fixture cable that has a force gauge on its other end. To simulate a wrestling action a 0.5 kg weight was mounted on the pulling cable and had to be lifted to the top of the fixture while stretching the cable. The time to reach the top was measured to determine the wrestling speed. To establish a baseline for performance comparison, the capability of the student, who was the same human wrestler in 2005, was measured first and then the three participating robotic arms were tested. The results have shown two orders of magnitude lower performance of the arms compared to the student. Due to the significant weakness of the state of the art of the current arms there are no current plans to hold in the near future another wrestling match against humans. However, if improvements reach a level that would allow the potential of winning, a professional wrestler will be invited to the next human/machine wrestling match.

8.20 An EAP driven arm made by students from Virginia Tech and the human opponent, a 17-year-old student.

8.6 Challenges, trends and potential developments

For many years, EAP materials received relatively little attention due to their limited actuation capability at the level of a fraction of percent strain and the small number of available materials. Since the early 1990s, new materials have emerged that generate large strain reaching above 100% and this development brought great attention to these materials. EAP materials offer attractive characteristics of operational similarity to biological muscles, including resilience, damage tolerance, and ability to induce large actuation strains (stretching, contracting or bending). Even though EAP actuators still have limited capability, as described in this chapter there has already been a series of reported successes in driving novel mechanisms. Most of the considered applications are still far from being practical for daily applications. If EAP materials are developed to operate internal organs inside a human body, this technology can make a tremendously positive impact on many human lives.

Using EAP materials to produce actuators involves various challenges that need to be addressed (Bar-Cohen, 2004). These challenges range from fundamental issues to repeatable fabrication capability. Advancing the materials to a mature state necessitates overcoming the related challenges. Some of the challenges include the need to increase their actuation force, electromechanical conversion efficiency, and lifetime. The electronic (i.e., *field-activated*) EAP materials require reduction of the activation voltage, which may be achieved by increasing the polymer dielectric constant possibly using fillers, or through the use of stacks of many thin layers as reported by EMPA, Switzerland. Further, the *ionic* EAP materials require increasing their response speed and lifetime as well as making them operational in 'dry' environments over extended time. The latter necessitates developing effective protective coating and/or working with solvents that have near zero vapor pressure. Addressing these challenges requires improving the understanding of operating mechanism of EAP materials, as well as their fabrication and characterization techniques. Effective sensors and control algorithms are needed to address the unique and challenging requirements of testing practical EAP actuators. To compete with other actuation mechanisms, it is essential to identify niche applications for these materials so that they will be used in spite of their limitations. Namely, it is necessary to develop devices that take advantage of the unique characteristics of EAP with performance that is within their current capability.

Space applications are among the most demanding in terms of the harshness of the operating conditions (extreme temperatures, high pressure or vacuum) and they require a very high reliability and durability. Today's available materials are not applicable to handle the related challenges. Space applications are of great need for effective actuation materials that can operate in temperatures down to as low as single digit degrees of Kelvin or as high as hundreds of degrees Celsius as on Venus. Another challenge is the need for large-scale EAP in the form of films, fibers, etc. The required dimensions can be as large as several meters or kilometers and in such dimensions they are needed to produce large gossamer structures such as antennas, solar sails, and various large optical components. Making biomimetic capabilities using EAP material will potentially allow NASA and other space agencies to conduct missions on other planets using human-like robots that will emulate the operation of humans before sending real humans.

Addressing the challenges to EAP materials requires continuing growth in multidisciplinary cooperative efforts among experts in various fields including the participation of more chemists, materials scientists, roboticists, computer and electronic engineers, etc. It is quite encouraging to see the growing number of researchers and engineers who are pursuing a career in EAP-related disciplines.

8.7 Conclusions

Nature offers a great model for imitation and inspiration of methods, designs and processes for the improvement of our lives and the tools we use. Using EAP materials as artificial muscles is enabling novel biomimetic applications that are unimaginable otherwise. Polymers that can be stimulated via electric, chemical, pneumatic, optical, and/or magnetic fields to change shape or size have been known for many years. Electrical excitation is one of the most attractive stimulators for generating elastic deformation, where the convenience and the practicality made EAP materials one of the most attractive among the activatable polymers. As polymers, EAP materials offer many appealing characteristics that include low weight, fracture tolerance, and pliability. Further, they can be configured into almost any conceivable shape and their properties can be tailored to suit a broad range of requirements. These capabilities and the significant electrical stimulated shape change while being able to endure many cycles of actuation are inspiring many potential possibilities among engineers and scientists in many different disciplines. Generally, the various EAP materials have characteristics that are associated with their related group and mechanism of operation. A summary of the principle of operation as well as the advantages and disadvantages of the various EAP materials for the electronic EAP materials are listed in Table 8.1 and for the ionic EAP in Table 8.2.

Turning EAP materials to actuators-of-choice requires well established scientific and engineering foundations, i.e., field's infrastructure. This involves improving the understanding of the basic principles that drive the various EAP materials. Also, it is necessary to develop a comprehensive material

Table 8.1 Summary of the leading electronic EAP materials

EAP type	Principle	Advantages	Disadvantages
Ferroelectric polymers	Polymers that exhibit non-centro-symmetric sustained shape change in response to electric field. Some of these polymers have spontaneous electric polarization making them ferroelectric.	• Induce relatively large strain (~5%). • Offer high mechanical energy density resulting from the relatively high elastic modulus. • Permit ac switching with little generated heat. • Rapid response (msec levels).	• Require high voltage (~150 MV/m). • Difficult to mass produce. • Making thin multilayers is still a challenge.
Dielectric elastomer EAP	Coulomb forces between the electrodes squeeze the material, causing it to expand in the plane of the electrodes.	• Very large strain reaching levels of 380%. • Rapid response (msec levels). • Inexpensive to produce.	• Require high voltage (~150 MV/m). • Obtaining large displacements compromises the actuation force.
Graft elastomers	Electric field causes molecular alignment of the pendant group made of graft crystalline elastomers that are attached to the backbone.	• Strain levels of 5%. • Relatively large force. • Cheaper to produce. • Rapid response (msec levels).	• Require high voltage (~150 MV/m).

science, as well as effective electromechanics analytical tools and material processing techniques. Researchers are continually making improvements in the various related areas including a better understanding of the operation mechanism of the various EAP material types. The processes of synthesizing, fabricating, electroding, shaping and handling are being refined to maximize the actuation capability and robustness. Methods of reliably characterizing the response of these materials are being developed and efforts are being made to establish databases with documented material properties in order to support design engineers that are considering the use of these materials.

The application of these materials as actuators to drive various manipulation, mobility, and robotic devices involves multidisciplines including materials, chemistry, electromechanics, computers, and electronics. Even though the force of actuation of existing EAP materials and their robustness require further improvement, there has already been a series of reported successes

Table 8.2 Summary of the leading ionic EAP materials

EAP type	Principle	Advantages	Disadvantages
Ionomeric polymer–metal composites (IPMC)	The base polymer provides channels for mobility of positive ions in a fixed network of negative ions on interconnected clusters. Electrostatic forces and mobile cation are responsible for the bending.	• Require low voltage. • Produce significant bending.	• Low frequency response (effectively below 1 Hz). • Extremely sensitive to dehydration. • dc causes permanent deformation. • Subject to hydrolysis above 1.23 V. • Displacement drift.
Conductive polymers (CP)	Materials that swell in response to an applied voltage as a result of oxidation or reduction, depending on the polarity causing insertion or de-insertion of (possibly solvated) ions.	• Require relatively low voltage. • Induce relatively large force. • Extensive body of knowledge. • Biologically compatible.	• Sensitive to dehydration. • Suffer fatigue after repeated activation. • Slow response (<40 Hz).
Carbon nanotubes (CNT)	The carbon–carbon bond of nanotubes (NT) suspended in an electrolyte changes length as a result of charge injection that affects the ionic charge balance between the NT and the electrolyte.	• Potentially provide superior work/cycle and mechanical stresses. • Carbon offers high thermal stability at high temperatures <1000 °C.	• Expensive to produce. • Difficult to mass produce.
Ionic gels	Application of voltage causes movement of hydrogen ions in or out of the gel.	• Require low voltage. • Potentially capable of matching the force and energy density of biological muscles.	Operate very slowly.

in the development of EAP-actuated mechanisms. Using EAP to replace existing actuators may be a difficult challenge and therefore it is highly desirable to identify a niche application where EAP materials would not need to compete with existing technologies.

8.8 Acknowledgements

Some of the research reported in this chapter was conducted at the Jet Propulsion Laboratory (JPL), California Institute of Technology, under a contract with the National Aeronautics and Space Administration (NASA).

8.9 References

Anquetil P. A., Yu H.-H., Madden P. G., Madden J. D., Swager T. M. and Hunter I. W., 'Thiophene-based molecular actuators', *Proceedings of SPIE 9th Annual Symposium on Smart Structures and Materials: Electroactive Polymer Actuators and Devices*, Y. Bar-Cohen (ed.), SPIE Press, March 2002, pp. 424–434.

Bar-Cohen Y. (ed.), *Proceedings of 1st SPIE's Electroactive Polymer Actuators and Devices (EAPAD) Conf., Smart Structures and Materials Symposium*, Volume 3669, 1999.

Bar-Cohen Y. (ed.), *Electroactive Polymer (EAP) Actuators as Artificial Muscles – Reality, Potential and Challenges*, 2nd edn, SPIE Press, Bellingham, Washington, Vol. PM136, 2004.

Bar-Cohen Y., (ed.), *Biomimetics – Biologically Inspired Technologies*, CRC Press, Boca Raton, FL, 2005.

Bar-Cohen Y. and Breazeal C. (eds), *Biologically-Inspired Intelligent Robots*, SPIE Press, Bellingham, Washington, Vol. PM122, 2003.

Bar-Cohen Y. and Hanson D., *The Coming Robot Revolution – Expectations and Fears About Emerging Intelligent, Humanlike Machines*, Springer, New York 2009.

Bar-Cohen Y., Xue T. and Lih S.-S., 'Polymer piezoelectric transducers for ultrasonic NDE', *1st International Internet Workshop on Ultrasonic NDE, Subject: Transducers*, organized by R. Diederichs, UTonline J., Germany, http://www.ndt.net/article/yosi/yosi.htm 1996.

Bauer S. and Bauer F., 'Piezoelectric polymers and their applications', *Piezoelectricity Evolution and Future of a Technology Series: Springer Series in Materials Science*, Vol. 114, W. Heywang, K. Lubitz and W. Wersing (eds.), Springer, New York, pp. 157–177, 2008.

Baughman R. H., 'Conducting polymer artificial muscles', *Synthetic Metals*, 78, 339–353, 1996.

Baughman R. H., Cui C., Zakhidov A. A., Iqbal Z., Basrisci J. N., Spinks G. M., Wallace G. G., Mazzoldi A., de Rossi D., Rinzler A. G., Jaschinski O., Roth S. and Kertesz M., 'Carbon nanotune actuators', *Science*, 284, 1340–1344, 1999.

Bergman J. G., McFee J. H. and Crane G. R., 'Pyroelectricity and optical second harmonic generation in polyvinylidene fluoride,' *Appl. Phys. Lett.*, 18, 203–205, 1971.

Calvert P., 'Electroactive polymer gels', in *Electroactive Polymer (EAP) Actuators as Artificial Muscles – Reality, Potential and Challenges*, 2nd edn, Y. Bar-Cohen (ed.), SPIE Press, Bellingham, Washington, Vol. PM136 (2004), pp. 95–148.

Calvert P., 'Gel sensors and actuators', Special Issue dedicated to EAP, *Materials Research Society (MRS) Bulletin*, 33(3), 207–212, 2008.

Carpi F., De Rossi D., Kornbluh R., Pelrine R. and Sommer-Larsen P., *Dielectric Elastomers as Electromechanical Transducers: Fundamentals, Materials, Devices, Models and Applications of an Emerging Electroactive Polymer Technology*, Elsevier, San Diego, CA 2008.

Cheng Z. and Zhang Q., 'Field-activated electroactive polymers', Special Issue dedicated to EAP, *Materials Research Society (MRS) Bulletin*, 33 (3), 190–195, 2008.

Della Santa A., Mazzoldi A. and De Rossi D., 'Steerable microcatheters actuated by embedded conducting polymer structures', *Journal of Intelligent Material Systems and Structures*, 7(3), 292–301, 1996.

Eguchi M., 'On the permanent electret', *Philosophical Magazine*, 49, 178, 1925.

Fukada E., 'Piezoelectricity of wood', *J. Phys. Soc. Japan*, 10, 149–154, 1955.

Furukawa T., 'Piezoelectricity and pyroelectricity in polymers', *IEEE Transactions on Electrical Insulation*, 24(3), 375–394, 1989.

Furukawa T. and Wen J. X., 'Electrostriction and piezoelectricity in ferroelectric polymers', *Japan J. Appl. Phys.*, 23, L677–L679, 1984.

Ha S. M., Yuan W., Pei Q., Pelrine R. and Stanford S., 'Interpenetrating polymer networks for high-performance electroelastomer artificial muscles', *Advanced Materials*, 18, 887–891, 2006.

Herr H. M. and Kornbluh R. D. 'New horizons for orthotic and prosthetic technology: artificial muscle for ambulation', *Proceedings of SPIE's Smart Structures and Materials 2004: Electroactive Polymer Actuators and Devices (EAPAD)*, Y. Bar-Cohen (Ed.), Vol. 5385, pp. 1–9, 2004.

Heydt R. and Chhokar S., 'Refreshable Braille display based on electroactive polymers', *Record of the 23rd Intl. Display Research Conference*, sponsored by the Society for Information Display, Phoenix, Arizona (16–18 Sept. 2003), pp. 111–114.

Jung K., Nam J., Lee Y. and Choi H., 'Micro-inchworm robot actuated by artificial muscle actuator based on dielectric elastomer', *Proceedings of the 2004 SPIE's EAP Actuators and Devices (EAPAD)*, paper number 5385-47, Volume 5385, San Diego, CA, March 14–18, 2004.

Katchalsky A. and Zwick M., 'Mechanochemistry and ion exchange', *Journal of Polymer Science*, 16(82), 221–234, 1955.

Kawai H., 'Piezoelectricity of poly(viny1idene fluoride)', *Japan J. Appl. Phys.*, 8, 975–976, 1969.

Kepler R. G., 'Piezoelectricity, pyroelectricity and ferroelectricity in organic materials', *Annual Review of Physical Chemistry*, 29, 497–518, 1978.

Kiil H. E. and Benslimane M., 'Scalable industrial manufacturing of DEAP', *Proceedings of SPIE EAPAD Conference XI, Smart Structures symposium*, Volume 7287, SPIE Electronic Library Paper 7287–26, 2009.

Kornbluh R. D., Pelrine R. E., Pei Q., Heydt R., Stanford S. E., Oh S. and Eckerle J., 'Electroelastomers: applications of dielectric elastomer transducers for actuation, generation and smart structures', *Proceedings of the SPIE's Smart Structures and Materials 2002*, Vol. 4698, San Diego, CA 2002.

Kornbluh R., Pelrine R., Pei Q. and Shastri V. 'Application of dielectric EAP actuators', in *Electroactive Polymer (EAP) Actuators as Artificial Muscles – Reality, Potential and Challenges*, 2nd edn, Y. Bar-Cohen (ed.), SPIE Press, Bellingham, Washington, Vol. PM136 2004, pp. 529–581.

Kovacs G. M. and Düring L., 'Contractive tension force stack actuator based on soft dielectric EAP', Paper 7287-8, *Proceedings of the 11th SPIE Annual Electroactive Polymer Actuators and Devices (EAPAD) Conf.*, Y. Bar-Cohen (Ed.), SPIE Press 2009.

Kuhn W., Hargitay B., Katchalsky A. and Eisenberg H., *Nature*, 165, 514–516, 1955.

Liu Z. and Calvert P., ‘Multilayer hydrogels and muscle-like actuators’, *Advanced Materials*, 12(4), 288–291, 2000.

Lovinger A., ‘Ferroelectric polymers’, *Science*, 220, 1115–1121, 1983.

Mabboux P. and Gleason K., ‘F-19 NMR characterization of electron beam irradiated vinyllidene fluoride-trifluoroethylene copolymers’, *J. Fluorine Chemistry*, 113, 27, 2002.

Madden J. D. W., Madden P. G. A. and Hunter I. W., ‘Characterization of polypyrrole actuators: modeling and performance’, *Proceedings of 3th Annual SPIE Electroactive Polymer Actuators and Devices (EAPAD) Conf.*, Y. Bar-Cohen (ed.), SPIE Press, 2001, pp. 72–83.

Nalwa H. S. (ed.), *Ferroelectric Polymers – Chemistry, Physics, and Applications*, Marcel Dekker, New York 1995.

Nemat-Nasser S. and Thomas C. W., ‘Ionomeric polymer-metal composites’, in *Electroactive Polymer (EAP) Actuators as Artificial Muscles – Reality, Potential and Challenges*, 2nd edn, Y. Bar-Cohen (ed.), SPIE Press, Bellingham, Washington, Vol. PM136 2004, pp. 171–230.

Oguro K., Kawami Y. and Takenaka H., ‘Bending of an ion-conducting polymer film-electrode composite by an electric stimulus at low voltage’, *Trans. J. Micromachine Society*, 5, 27–30, 1992.

Ohigashi H., ‘Electromechanical properties of polarized polyvinylidene fluoride films as studied by the piezoelectric resonance method’, *J. Appl. Phys*, 47(3), 949, 1976.

Osada Y. and Hasebe M., ‘Electrically activated mechanochemical devices using polyelectrolyte gels’, *Chem Lett.*, 14, (9), 1285–1288, 1985.

Osada Y. and Kishi R., ‘Reversible volume change of microparticles in an electric field’, *J. Chem. Soc.*, 85, 655–662, 1989.

Otero T. F., Grande H. and Rodriguez J. ‘A new model for electrochemical oxidation of polypyrrole under conformational relaxation control’, *J. Electroanal. Chem.*, 394, 211–216, 1995.

Park I.-S., Jung K., Kim D. Kim S.-M. and Kim K. J., ‘Physical principles of ionic polymer-metal composites as electroactive actuators and sensors’, Special Issue dedicated to EAP, *Materials Research Society (MRS) Bulletin*, 33(3), 190–195, 2008.

Pei Q., Pelrine R. E., Stanford S. E., Kornbluh R. D., Rosenthal M., Meijer K. and Full R. J., ‘Multifunctional electroelastomer rolls and their application for biomimetic robots’, *Proc. SPIE, Smart Structures and Materials 2002: Industrial and Commercial Applications of Smart Structures Technologies*, Y. Bar-Cohen (ed.), Vol. 4698, San Diego, CA 2002.

Pei Q., Rosenthal M. A., Pelrine R., Stanford S. and Kornbluh R. D., ‘Multifunctional electroelastomer roll actuators and their application for biomimetic walking robots’, *Proceedings of the 1SPIE’s Electroactive Polymer Actuators and Devices (EAPAD). Smart Structures and Materials 2003*, Y. Bar-Cohen (ed.), Volume 5051, 2003, pp. 281–290.

Pei Q., Pelrine R., Rosenthal M., Stanford S., Prahlad H. and Kornbluh R., ‘Recent progress on electroelastomer artificial muscles and their application for biomimetic robots’, *Proc. SPIE EAPAD Conf.*, Y. Bar-Cohen (ed.) Vol. 5385, 2004, pp. 41–50.

Pelrine R. and Joseph J., *FY 1992 Final Report on Artificial Muscle for Small Robots*, ITAD-3393-FR-93-063, SRI International, Menlo Park, CA 1993.

Pelrine R. and Joseph J., *FY 1993 Final Report on Artificial Muscle for Small Robots*, ITAD-4570-FR-94-076, SRI International, Menlo Park, CA (1994).

Pelrine R. and Kornbluh R., Personal communication (April 2009).

Pelrine R., Kornbluh R. and Joseph J. P., 'Electrostriction of polymer dielectrics with compliant electrodes as a means of actuation', *Sensor and Actuators A: Physical*, 64, 77–85, 1998.

Pelrine R., Kornbluh R., Pei Q. and Joseph J., 'High-speed electrically actuated elastomers with strain greater than 100%', *Science*, 287(5454), 836–839, 2000.

Pelrine R. E., Kornbluh R. D., Pei Q., Stanford S. E., Oh S., Eckerle J., Full R. J. and Meijer R. J., 'Dielectric elastomer artificial muscle actuators: toward biomimetic motion', *Proc. SPIE, Smart Structures and Materials 2002: Electroactive Polymer Actuators and Devices (EAPAD)*, Y. Bar-Cohen (ed.), Vol. 4695, San Diego, CA 2002.

Qu L., Peng Q., Dai L., Spinks G. M., Wallace G. G. and Baughman R. H., 'Carbon nanotube electroactive polymers: opportunities and challenges', Special Issue dedicated to EAP, *Materials Research Society (MRS) Bulletin*, 33(3), 215–234, 2008.

Roentgen W. C., 'About the changes in shape and volume of dielectrics caused by electricity', Section III in G. Wiedemann (ed.), *Annual Physics and Chemistry Series*, Vol. 11, John Ambrosius Barth Publisher, Leipzig, Germany (1880), pp. 771–786 (in German).

Sacerdote M. P., 'On the electrical deformation of isotropic dielectric solids', *J. Physics*, 3 Series, t, VIII, 31 (1899), 282–285 (in French).

Sadeghipour K., Salomon R. and Neogi S., 'Development of a Novel Electrochemically Active Membrane and 'Smart' Material Based Vibration Sensor/Damper', *J. Smart Materials and Structures*, 1(1), 172–179, 1992.

Sansiñena J. M. and Olazabal V., 'Conductive Polymers', in *Electroactive Polymer (EAP) Actuators as Artificial Muscles – Reality, Potential and Challenges*, 2nd edn, Y. Bar-Cohen (ed.), SPIE Press, Bellingham, Washington, Vol. PM136 (2004), pp. 231–259.

Schreyer H. B., Gebhart N., Kim K. J. and Shahinpoor M., 'Electric activation of artificial muscles containing polyacrylonitrile gel fibers', *Biomacromolecules J.*, 1, 642–647, 2000.

Sessler G. M., 'Piezoelectricity in polyvinylidenefluoride', *J. Acoustic Society of America*, 70(6), 1596–1608, 1981.

Shahinpoor M., 'Elastically-activated artificial muscles made with liquid crystal elastomers', *Proceedings of the SPIE's 7th Annual International Symposium on Smart Structures and Materials*, Y. Bar-Cohen (ed.), EAPAD Conf. Vol. 3987, (2000) pp. 187–192.

Smela E., 'Conjugated polymer actuators', Special Issue dedicated to EAP, *Materials Research Society (MRS) Bulletin*, 33(3), 197–204, 2008.

Spinks G. M., Wallace G. G., Baughman R. H. and Dai L., 'Carbon nanotube actuators: synthesis, properties and performance', in *Electroactive Polymer (EAP) Actuators as Artificial Muscles – Reality, Potential and Challenges*, 2nd edn, Y. Bar-Cohen (ed.), SPIE Press, Bellingham, Washington, Vol. PM136 (2004), pp. 261–295.

Su J., Harrison J. S., St. Clair T., Bar-Cohen Y. and Leary S., 'Electrostrictive graft elastomers and applications', *MRS Symp. Proceedings*, Vol. 600, Warrendale, PA, (1999) pp. 131–136.

Tasaka S. and Miyata S., 'The origin of piezoelectricity in poly(viny1idene fluoride)', *Ferroelectrics*, 32, 17–23, 1981.

Wada Y., 'Piezoelectricity and pyroelectricity of polymers', *Japanese J. Appl. Phys.*, 15, 2041–2057, 1976.

Zhang Q. M., Bharti V. and Zhao X., 'Giant electrostriction and relaxor ferroelectric behavior in electron-irradiated poly(vinylidene fluoride-trifluorethylene) copolymer', *Science*, 280, 2101–2104, 1998.

Zhang Q., Huang C. and Xia F., in ‘Electric field activated EAP’, in *Electroactive Polymer (EAP) Actuators as Artificial Muscles – Reality, Potential and Challenges*, 2nd edn, Y. Bar-Cohen (ed.), SPIE Press, Bellingham, Washington, Vol. PM136 (2004), pp. 95–148.

Zhenyi M., Scheinbeim J. I., Lee J. W. and Newman B. A., ‘High field electrostrictive response of polymers’, *J. Polym. Sci. B: Polym. Phys.*, 32(16), 2721–2731, 1994.

9

Piezoelectric composite materials

K. UCHINO, The Pennsylvania State University, USA

Abstract: Piezo-composites composed of a piezoelectric ceramic and a polymer are promising materials because of their excellent tailorable properties. The geometry for two-phase composites can be classified according to the connectivity of each phase (1, 2 or 3 dimensionally) into 10 structures; 0-0, 0-1, 0-2, 0-3, 1-1, 1-2, 1-3, 2-2, 2-3 and 3-3. In particular, a 1-3 piezo-composite, or PZT-rod/polymer-matrix composite is considered most useful. The advantages of this composite are high coupling factors, low acoustic impedance, good matching to water or human tissue, mechanical flexibility, broad bandwidth in combination with a low mechanical quality factor and the possibility of making undiced arrays by simply patterning the electrodes. The acoustic match to tissue or water of the typical piezoceramics is significantly improved when it is incorporated into such a composite structure, that is, by replacing some of the dense and stiff ceramic with a less dense, more pliant polymer. Piezoelectric composite materials are especially useful for underwater sonar and medical diagnostic ultrasonic transducer applications. Other types of composites based on piezoelectric ceramics are also introduced in this chapter. Piezo-passive-dampers comprise a piezoelectric ceramic particle, polymer, and a carbon black, which suppress the noise vibration more effectively than traditional rubbers. A composite with a magnetostrictive ceramic and a piezoelectric ceramic produces an intriguing product effect, the magnetoelectric effect in which an electric field is produced in the material in response to an applied magnetic field.

Key words: piezoelectric composite, phase connectivity, sum effect, combination effect, product effect, magnetoelectric effect, PZT-polymer composite, piezoelectric damping, piezoelectric energy harvesting.

9.1 Introduction

Piezo-composites composed of a piezoelectric ceramic and a polymer are promising materials because of their excellent tailorable properties. The geometry for two-phase composites can be classified according to the connectivity of each phase (1, 2 or 3 dimensionally) into 10 structures; 0-0, 0-1, 0-2, 0-3, 1-1, 1-2, 1-3, 2-2, 2-3 and 3-3. In particular, a 1-3 piezo-composite, or PZT-rod/polymer-matrix composite is considered most useful. The advantages of this composite are high coupling factors, low acoustic impedance, good matching to water or human tissue, mechanical flexibility, broad bandwidth in combination with a low mechanical quality factor and the possibility of making undiced arrays by simply patterning the electrodes. The acoustic match to tissue or water (1.5 Mrayls) of the typical piezoceramics (20–30 Mrayls) is significantly improved when it is incorporated into such a composite structure, that is, by replacing some of the dense and stiff ceramic with a less dense, more pliant polymer. Piezoelectric composite materials are especially useful for underwater sonar and medical diagnostic ultrasonic transducer applications.

In this chapter, other types of composites based on piezoelectric ceramics are also introduced. Piezo-passive-dampers comprise piezoelectric ceramic particle, polymer, and a carbon black, which suppress the noise vibration more effectively than traditional rubbers. Another type of composite with a magnetostrictive ceramic and a piezoelectric ceramic produces an intriguing product effect, the magnetoelectric effect, in which an electric field is produced in the material in response to an applied magnetic field.

9.2 Connectivity

Newnham *et al*. introduced the concept of '*connectivity*' for classifying the various PZT:polymer composite structures.[1] When considering a two-phase composite, the connectivity of each phase is identified: e.g., if a phase is self-connected in all x, y and z directions, it is called '3'; if a phase is self-connected only in the z direction, it is called '1'. A di-phasic composite is identified with this notation with two numbers '*m-n*', where *m* stands for the connectivity of an active phase (such as PZT) and *n* for an inactive phase (such as a polymer). In general, there are 10 types of diphasic composites: 0-0, 1-0, 2-0, …, 3-2, 3-3, as illustrated in Fig. 9.1 (Note that there are two different configurations for 3-2 and 3-3.)

A 0-0 composite, for example, is depicted as two alternating hatched and unhatched cubes, while a 1-0 composite has Phase 1 connected along the z direction. A 1-3 composite has a structure in which PZT rods (one-dimensionally connected) are arranged in a three-dimensionally connected polymer matrix, and in a 3-1 composite, a honeycomb-shaped PZT contains the one-dimensionally connected polymer phase. A 2-2 indicates a structure in which ceramic and polymer sheets are stacked alternately, and a 3-3 is composed of a jungle-gym-like PZT frame embedded in a 3-D connecting polymer.

9.3 Composite effects

There are three types of composite effects (Fig. 9.2): the *sum effect*, the *combination effect* and the *product effect*.

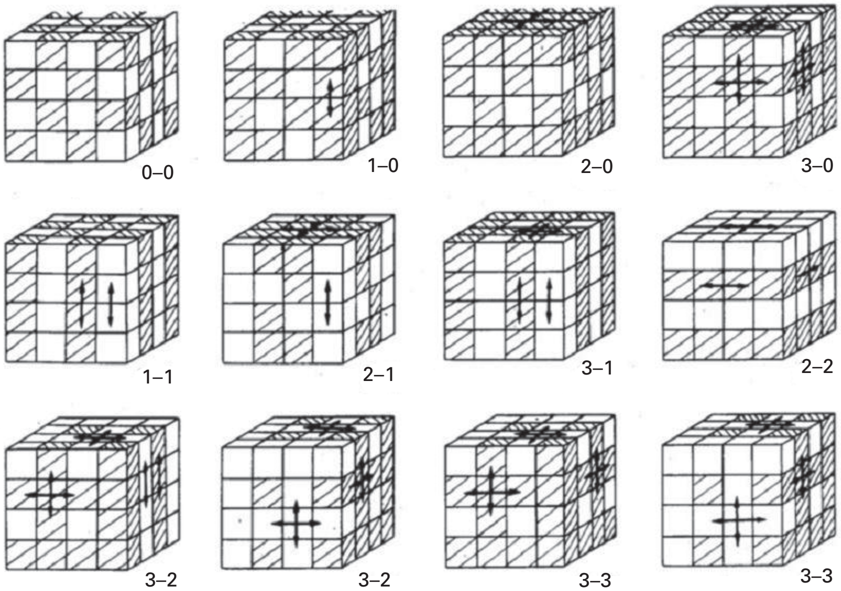

9.1 Classification of two-phase composites with respect to connectivity.[1] Two configurations are shown for 3-2 and 3-3.

9.3.1 Sum effects

Let us discuss a composite function in a diphasic system to convert an input parameter X to an output parameter Y. Assuming Y_1 and Y_2 are the outputs from Phase 1 and 2, respectively, responding to the input X, the output Y* of a composite of Phase 1 and 2 could be an intermediate value between Y_1 and Y_2. Figure 9.2(a) shows the Y* variation with volume fraction of Phase 2 for a case of $Y_1 > Y_2$. The variation may exhibit a concave or a convex shape, but the averaged value in a composite does not exceed Y_1, nor is it less than Y_2. This effect is called a '*sum effect*'.

An example is a fishing rod, i.e., a light-weight/tough material, where carbon fibers are mixed in a polymer matrix (between 3-1 and 3-0). The density of a composite should be an average value with respect to volume fraction, if no chemical reaction occurs at the interface between the carbon fibers and the polymer, following the linear trend depicted in Fig. 9.2(a). A dramatic enhancement in the mechanical strength of the rod is achieved by adding carbon fibers in a special orientation, i.e., along a rod (showing a convex relation as depicted in Fig. 9.2(a)).

Another interesting example is an NTC-PTC material.[2] V_2O_3 powders are mixed in epoxy with a relatively high packing rate (3-3), as illustrated in Fig. 9.3. Since V_2O_3 exhibits a semiconductor-metal phase transition at 160 K, a drastic resistivity change is observed with increasing temperature.

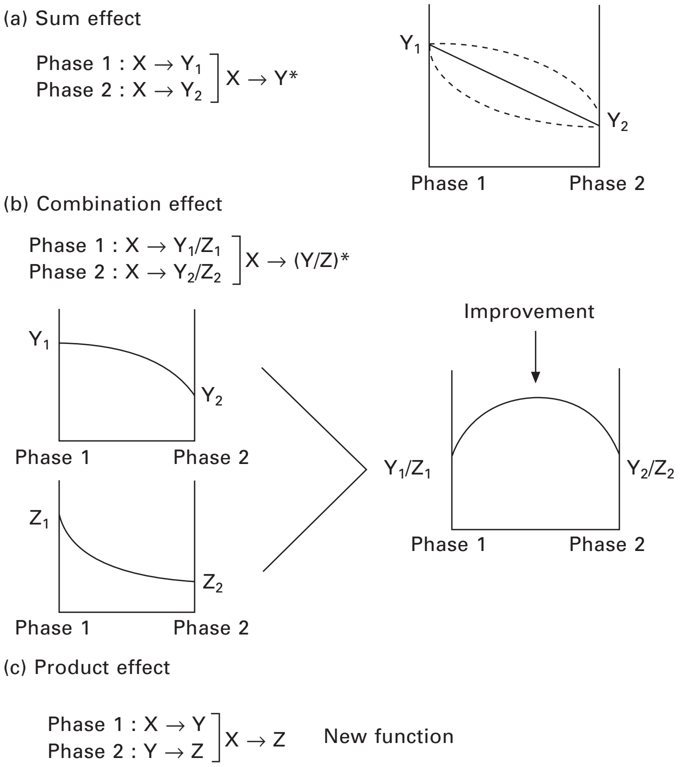
(a) Sum effect
Phase 1 : X → Y1
Phase 2 : X → Y2
X → Y*
Y1
Y2
Phase 1
Phase 2
(b) Combination effect
Phase 1 : X → Y1/Z1
Phase 2 : X → Y2/Z2
X → (Y/Z)*
Y1
Y2
Phase 1
Phase 2
Z1
Z2
Phase 1
Phase 2
Improvement
Y1/Z1
Y2/Z2
Phase 1
Phase 2
(c) Product effect
Phase 1 : X → Y
Phase 2 : Y → Z
X → Z
New function

9.2 Composite effects: sum, combination and product effect.

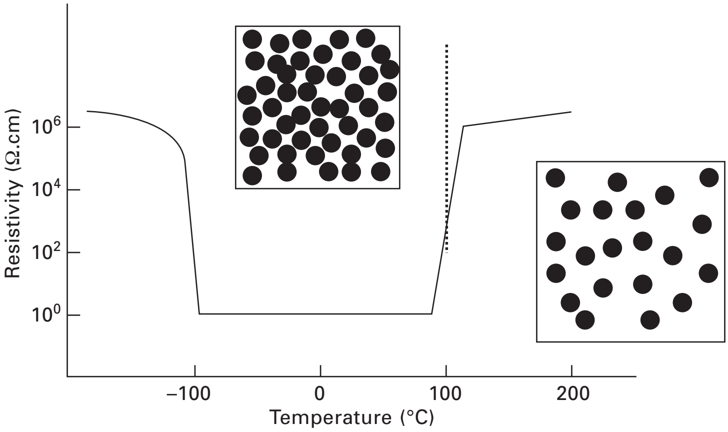

9.3 NTC-PTC effect observed in a V_2O_3:epoxy composite.[2]

A further increase in temperature results in a larger thermal expansion for epoxy than for the ceramic, leading to a separation of each particle, and the structure becomes a 0-3 composite. The V_2O_3 particle separation increases the resistivity significantly at around 100 °C. Thus, the conductivity of this composite is rather high only over a limited temperature range (around –100 to 100 °C), which is sometimes called the '*conductivity window*'.

9.3.2 Combination effects

In certain cases, the averaged value of the output, Y^*, of a composite does exceed Y_1 and Y_2. This enhanced output refers to an effect Y/Z which depends on two parameters Y and Z. Suppose that Y and Z, follow convex and concave type sum effects, respectively, as illustrated in Fig. 9.2(b), the combination value Y/Z will exhibit a maximum at an intermediate ratio of phases. This is called a '*combination effect*'.

Certain piezoelectric ceramic:polymer composites exhibit a combination property of g (the *piezoelectric voltage constant*) which is provided by d/ε (d: piezoelectric strain constant, and ε: permittivity). The details of these materials will be described in the next section.

9.3.3 Product effects

When Phase 1 exhibits an output Y with an input X, and Phase 2 exhibits an output Z with an input Y, we can expect for the composite an output Z with an input X. A completely new function is created for the composite structure, called a '*product effect.*'

Philips developed a *magnetoelectric material* based on this concept.[2] This material was composed of magnetostrictive $CoFe_2O_4$ and piezoelectric $BaTiO_3$ mixed and sintered together. Figure 9.4 shows a micrograph of a transverse section of a uni-directionally solidified rod of the materials with an excess of TiO_2 (1.5 wt%). Four finned spinel dendrites $CoFe_2O_4$ are observed in cells (× 100). Figure 9.5 shows the magnetic field dependence of the magnetoelectric effect in an arbitrary unit measured at room temperature. When a magnetic field is applied on this composite, cobalt ferrite generates magnetostriction, which is transferred to barium titanate as stress, finally leading to the generation of a charge/voltage via the piezoelectric effect in $BaTiO_3$.

Since the magnetoelectric effect in a single phase material, such as Cr_2O_3, can be observed only at a very low temperature (liquid He temperature), observation of this effect at room temperature is really a breakthrough. Inexpensive sensors for monitoring magnetic field at room temperature or at elevated temperature can be produced from these composite materials. Recent developments will be discussed in Section 9.6.

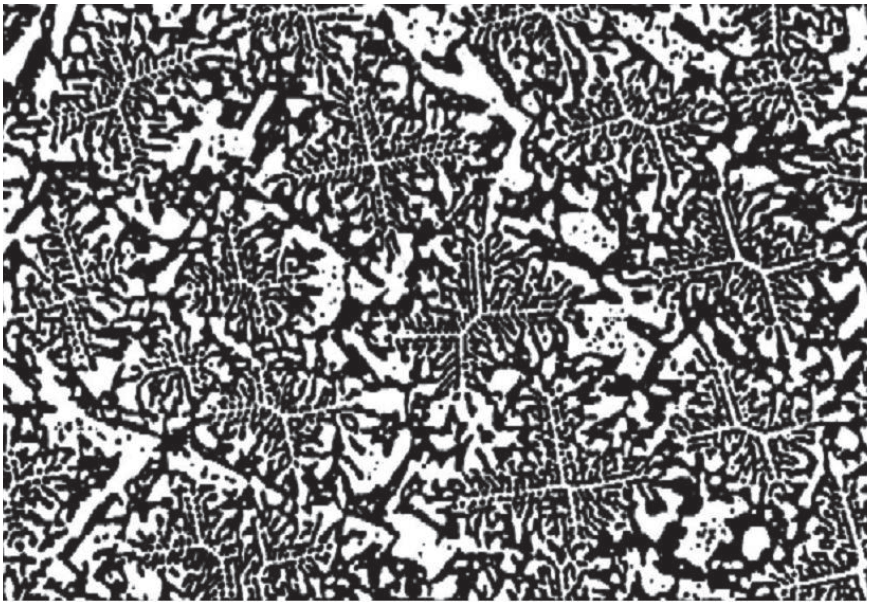

9.4 Micrograph of a transverse section of a uni-directionally solidified rod of mixture of magnetostrictive $CoFe_2O_4$ and piezoelectric $BaTiO_3$, with an excess of TiO_2 (1.5 wt%).[2]

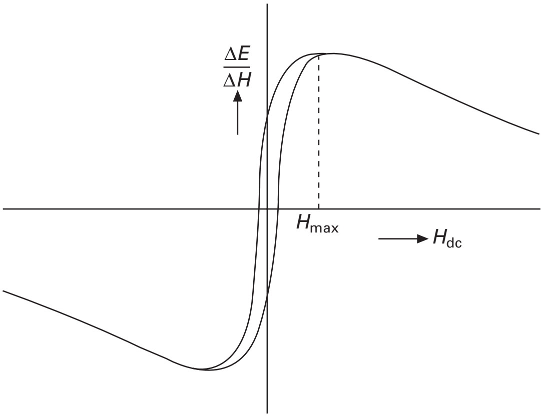

9.5 Magnetic field dependence of the magnetoelectric effect in a $CoFe_2O_4$: $BaTiO_3$ composite (arbitrary unit measured at room temperature).

9.4 PZT:polymer composites

9.4.1 Piezoelectric composite materials

Polymer piezoelectric materials such as PVDF are very suitable for sensor applications. However, because of its small piezoelectric *d* constants and very small elastic stiffness, PVDF cannot be used by itself in fabricating actuators or high power transducers. PZT:polymer composites, however, play a key role in the design of transducers, for applications such as sonar, which have both actuator and sensor functions.[3]

The piezoceramic:polymer composite was first reported by Kitayama and Sugawara on the 0-3 type in 1972.[3] Since then, various piezo-composites have been investigated, as summarized in Table 9.1. Representative data for several composite piezoelectric materials are listed in Table 9.2,[4] with data for some single phase piezoelectric polymer and PZT materials. The piezoelectric *d* constant of PVDF, which indicates the strain per unit electric field (in actuator applications), is 1/10 smaller than that of PZT; however, because of its small dielectric constant, the piezoelectric *g* constant of PVDF, which indicates the voltage per unit stress (in sensor applications), is 10 times larger than that of PZT. PZT:polymer composites exhibit a wide range of piezoelectric response, but in general *d* is slightly smaller than PZT and *g* is slightly smaller than PVDF. Thus, particularly for underwater transducers, which perform both actuation and sensing and have a figure of merit of $d_h \cdot g_h$, the composite materials are found to be far superior to single phase materials, like PZT or PVDF.

9.4.2 Principle of PZT:polymer composites

Here, in order to illustrate the principle, let us take a 1-3 composite which is composed of PZT fibers embedded in a polymer matrix, as shown in Fig. 9.6. The original fabrication process involves the injection of epoxy resin into an array of PZT fibers assembled with a special rack.[5] After the epoxy

Table 9.1 Piezoceramic composite development history

Year	Researchers	Piezo-composite
1971	Kitayama (NTT, Japan)	PZT powder:PVDF
1973	Powell (Gould)	PZT powder:Polyurethane
1976	Furukawa (Riken, Japan)	Spherical model
1978	Newnham (Penn State)	Coral replica PZT:Silicone rubber and connectivity concept
1978	Seo (Mitsubishi Chemical, Japan)	PZT powder:Poly acetal
1980	Harrison (Honeywell)	PZT powder:Silicone rubber
1980	Newnham (Penn State)	1:3, 3:1, 3:2 Types
1983	Banno (NTK, Japan)	PT:Polymer 0-3 type
1990	Uchino (Sophia Univ, Japan)	PZT:Carbon:Polymer piezo-damper
1990	Newnham (Penn State)	Moonie/Cymbal
2000	Uchino (Penn State)	PZT:Terfenol magnetoelectric composites
2004	Uchino (Penn State)	Composite piezo-energy harvesting

Table 9.2 Comparison of the piezoelectric response of PZT:polymer composites, with the single phase materials, PVDF and PZT

Connectivity	Material	Density ρ (10^3 kgm^{-3})	Elastic constant c_{33} (GPa)	Dielectric constant ε_3	Piezoelectric constants		
					d_{33} (10^{-12} CN^{-1})	g_{33} (10^{-3} mVN^{-1})	gh (10^{-3} mVN^{-1})
–	**PZT(501A) single phase**	**7.9**	**81**	**2000**	**400**	**20**	**3**
3-1	PZT:Epoxy	3.0	19	400	300	75	40
3-3	PZT:Silicone rubber (Replica type)	3.3	3	40	110	280	80
	PZT:Silicone rubber (Ladder type)	4.5	19	400	250	60	–
3-0	PZT:PVDF	5.5	2.6	120	90	85	–
	PZT:Rubber	6.2	0.08	73	52	140	30
	PZT:Chloroprene rubber	–	–	40	–	–	90
–	**Extended PVDF**	**1.8**	**3**	**13**	**20**	**160**	**80**

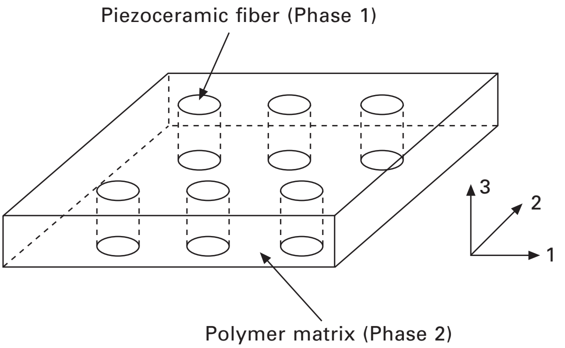

9.6 A 1-3 composite of PZT rods and polymer. The top and bottom plates are rigid electrodes.

is cured, the sample is cut, polished, electroded on the top and bottom, and finally electrically poled. The die casting technique has also been employed to make rod arrays from a PZT slurry.[6]

The effective piezoelectric coefficients d^* and g^* of the composite can be interpreted as follows. When an electric field E_3 is applied to this composite, the piezo-ceramic rods extend easily because the polymer is elastically very soft (assuming the electrode plates which are bonded to its top and bottom are rigid enough). Thus, d_{33}^* is almost the same as ${}^1d_{33}$ of the PZT itself,

$$d_{33}^* = {}^1d_{33}. \qquad 9.1$$

Similarly,

$$d_{33}^* = {}^1V\,{}^1d_{33}, \qquad 9.2$$

where ${}^1V$ is the volume fraction of phase 1 (piezoelectric). On the other hand, when an external stress is applied to the composite, the elastically stiff piezo-ceramic rods will support most of the load, and the effective stress is drastically enhanced and inversely proportional to the volume fraction. Thus, larger induced electric fields and larger g^* constants are expected:

$$\begin{aligned} g_{33}^* &= d_{33}^*/\varepsilon_0\,\varepsilon_3^* = {}^1d_{33}/{}^1V\,\varepsilon_0\,{}^1\varepsilon_3 \\ &= {}^1g_{33}/{}^1V. \end{aligned} \qquad 9.3$$

Figure 9.7 shows the piezoelectric coefficients for a PZT–Spurrs epoxy composite with 1-3 connectivity, measured with a Berlincourt d_{33} meter. As predicted by the model for this composite, the measured d_{33}^* values are almost independent of volume fraction, but are only about 75% of the d_{33} value of the PZT 501A ceramic. This discrepancy may be due to incomplete poling of the rods. A linear relation between the permittivity and the volume fraction ${}^1V$ is satisfied, resulting in a dramatic increase in g_{33}^* with decreasing fraction of PZT. The piezoelectric coefficients for the 1-3 composite are

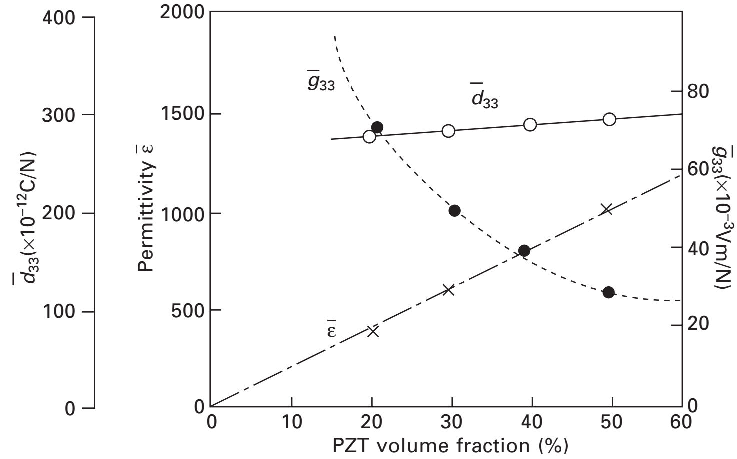

9.7 Volume fraction dependence of the permittivity ε and the piezoelectric constants d_{33} and g_{33} in a 1-3 PZT:polymer composite.

listed in Table 9.2, together with those of a PZT-silicone composite with 3-3 connectivity. In conclusion, for the composites, the piezoelectric *g* coefficient can be enhanced by two orders of magnitude with decreasing volume fraction of PZT, while the *d* coefficient remains constant.

The advantages of this composite are high coupling factors, low acoustic impedance, good matching to water or human tissue (more than 90% of a human body is water!), mechanical flexibility, broad bandwidth in combination with a low mechanical quality factor and the possibility of making undiced arrays by simply patterning the electrodes. The thickness-mode electromechanical coupling of the composite can exceed the k_t (0.40–0.50) of the constituent ceramic, almost approaching the value of the rod-mode electromechanical coupling, k_{33} (0.70–0.80) of that ceramic.[7] The acoustic match to tissue or water (1.5 Mrayls) of the typical piezo-ceramics (20–30 Mrayls) is significantly improved when they are incorporated in forming a composite structure, that is, by replacing the dense, stiff ceramic with a low density, soft polymer. Piezoelectric composite materials are especially useful for underwater sonar and medical diagnostic ultrasonic transducer applications.

Although the PZT composites are very useful for acoustic transducer applications, care must be taken when using them in actuator applications. Under an applied DC field, the field induced strain exhibits large hysteresis and creep due to the viscoelastic property of the polymer matrix. More serious problems are found when they are driven under a high AC field, related to the generation of heat. The heat generated by ferroelectric hysteresis in the piezo-ceramic cannot be dissipated easily due to the very low thermal conductivity of the polymer matrix, which results in rapid degradation of piezoelectricity.

A composite consists of two piezoelectric phases, 1 and 2, poled along the 3-axis and arranged in a parallel configuration as shown in Fig. 9.8(a). Analogous to the terminology used in electronic circuit analysis, the structures shown in Figs 9.8(a) and 9.8(b) are designed as 'parallel' and 'series' connections, respectively. The volume fraction is ${}^1V : {}^2V$ (${}^1V + {}^2V = 1$). Assuming that the top and bottom electrodes are rigid enough to prevent surface bending, and that the transverse piezoelectric coupling between Phases 1 and 2 is negligibly small in the parallel connection, let us calculate the following physical properties of this composite:

- effective dielectric constant $\varepsilon_3{}^*$,
- effective piezoelectric $d_{33}{}^*$ coefficient,
- effective piezoelectric voltage coefficient $g_{33}{}^*$.

We use the parameters $D_3, E_3, X_3, x_3, s_{33}{}^E$ which are the dielectric displacement, electric field, stress, strain, and the elastic compliance along the 3-axis (poling direction), respectively.

Since the electrodes are common and E_3 is common to Phases 1 and 2,

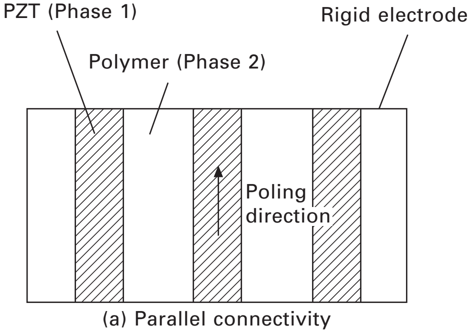

(a) Parallel connectivity

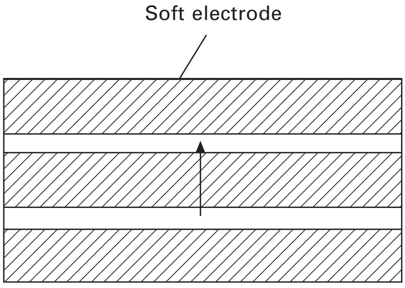

(b) Series connectivity

9.8 Diphasic composites arranged in parallel (a) and series (b) configurations.

$$D_3 = {}^1V\,{}^1\varepsilon_3\varepsilon_0\,E_3 + {}^2V\,{}^2\varepsilon_3\varepsilon_0\,E_3$$

$$= \varepsilon_3{}^*\varepsilon_0\,E_3. \qquad 9.4$$

Therefore,

$$\varepsilon_3{}^* = {}^1V\,{}^1\varepsilon_3 + {}^2V\,{}^2\varepsilon_3. \qquad 9.5$$

If Phases 1 and 2 are independently free (no interaction):

$${}^1x_3 = {}^1d_{33}\,E_3,$$

$${}^2x_3 = {}^2d_{33}\,E_3.$$

However, when we assume that the top and bottom electrodes are rigid, the strain x_3 must be common to both Phases 1 and 2, and the average strain $x_3{}^*$ is given by:

$${}^1V\,({}^1x_3 - x_3{}^*)/{}^1s_{33} = {}^2V\,(x_3{}^* - {}^2x_3)/{}^2s_{33}.$$

Therefore,

$$x_3{}^* = [({}^1V\,{}^2s_{33}\,{}^1d_{33} + {}^2V\,{}^1s_{33}\,{}^2d_{33})/({}^1V\,{}^2s_{33} + {}^2V\,{}^1s_{33})]\,E_3,$$

and consequently, the effective piezoelectric constant is given by

$$d_{33}{}^* = ({}^1V\,{}^2s_{33}\,{}^1d_{33} + {}^2V\,{}^1s_{33}\,{}^2d_{33})/({}^1V\,{}^2s_{33} + {}^2V\,{}^1s_{33}). \qquad 9.6$$

Since $g_{33}{}^* = d_{33}{}^*/\varepsilon_0\varepsilon_3{}^*$,

$$g_{33}{}^* = ({}^1V^2s_{33}{}^1d_{33} + {}^2V^1s_{33}{}^2d_{33})/$$
$$[({}^1V^2s_{33} + {}^2V^1s_{33})\varepsilon_0({}^1V^1\varepsilon_3 + {}^2V^2\varepsilon_3)]. \qquad 9.7$$

9.4.3 Theoretical models for 0-3 composites

Various models have been proposed to predict the electromechanical properties of a composite material. Pauer developed a 0-3 composite material comprised of PZT powder and polyurethane rubber, and predicted its permittivity values by means of a cubes model.[8] Figure 9.9 shows the relative permittivity plotted as a function of volume fraction of PZT powder, in comparison with theoretical values calculated on the basis of the cubes model (cubic PZT particles), the sphere model (spherical PZT particles), and the parallel and series models. Note that none of the models provided a close fit to the experimental data.

Banno then proposed a 'modified cubes model', which took into account the anisotropic distribution of cubes in x, y and z directions.[9] The unit cell of this model is shown in Fig. 9.10. The following formulas can be derived for a uniaxially anisotropic case (i.e., $l = m = 1$, $n \neq 1$):

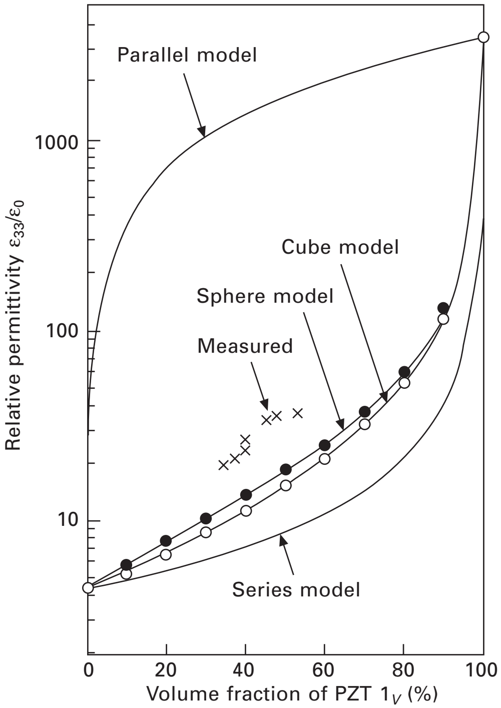

9.9 Relative permittivity plotted as a function of volume fraction of PZT in PZT powder:polyurethane rubber composites. Comparisons were made for the cube model, sphere model, parallel and series models.

$$\varepsilon_{33}^* = [a^2(a + (1 - a)n)^2 \cdot {}^1\varepsilon_{33} \cdot {}^2\varepsilon_{33}]/[a \cdot {}^2\varepsilon_{33} + (1 - a)n \cdot {}^1\varepsilon_{33}] + [(1 - a^2)/(a + (1 - a)n)] \cdot {}^2\varepsilon_{33}, \quad 9.8$$

$$d_{33}^* = {}^1d_{33}\ [a^3(a + (1 - a)n)]/[a + (1 - a)n({}^1\varepsilon_{33}/{}^2\varepsilon_{33})]/ [(1 - a)n/(a + (1 - a)n) + a^3], \quad 9.9$$

$$d_{31}^* = {}^1d_{31}\ [a^2(a + (1 - a)n)]/[a + (1 - a)n({}^1\varepsilon_{33}/{}^2\varepsilon_{33})] \cdot a/[1 - a\ (a + (1 - a)n)^{1/2} + a^3]. \quad 9.10$$

The volume fraction of Phase 1 is given by

$$ {}^1V = a^3/(a + (1 - a)n). \quad 9.11$$

The case $n = 1$ corresponds to the cubes model, and a general case $0 < n < 1$ corresponds to a configuration more dense along the z direction. Figure 9.11 shows the experimentally determined permittivity and piezoelectric d_h^* ($= d_{33}^* + 2d_{31}^*$) coefficient for $PbTiO_3$:chloroprene rubber composites, with the theoretical curves.[10] When the volume fraction of $PbTiO_3$ (${}^1V$)

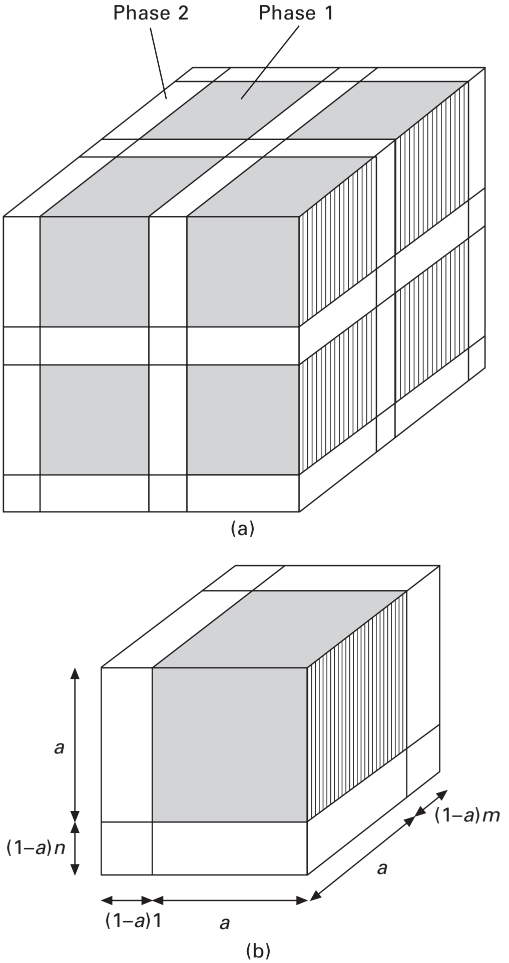

9.10 Unit cell configuration for a 0-3 composite, according to Banno's modified cubes model.

is small, *n* seems to be less than 1 (that is, the rubber thickness around a $PbTiO_3$ ceramic cube is thinner along the z direction and thicker along the x and y directions) and with increasing the volume fraction, *n* approaches 1 (that is, the rubber thickness becomes equal in all three dimensions). This configuration change may be caused by the method of fabrication, which typically involves rolling and calendering.

Figure 9.12 shows a structure of piezoelectric–rubber composite co-axial cables developed by NTK/NGK, Japan, which were applied for the pick-up of electric pianos and guitars, and automobile speed monitoring on the highway.

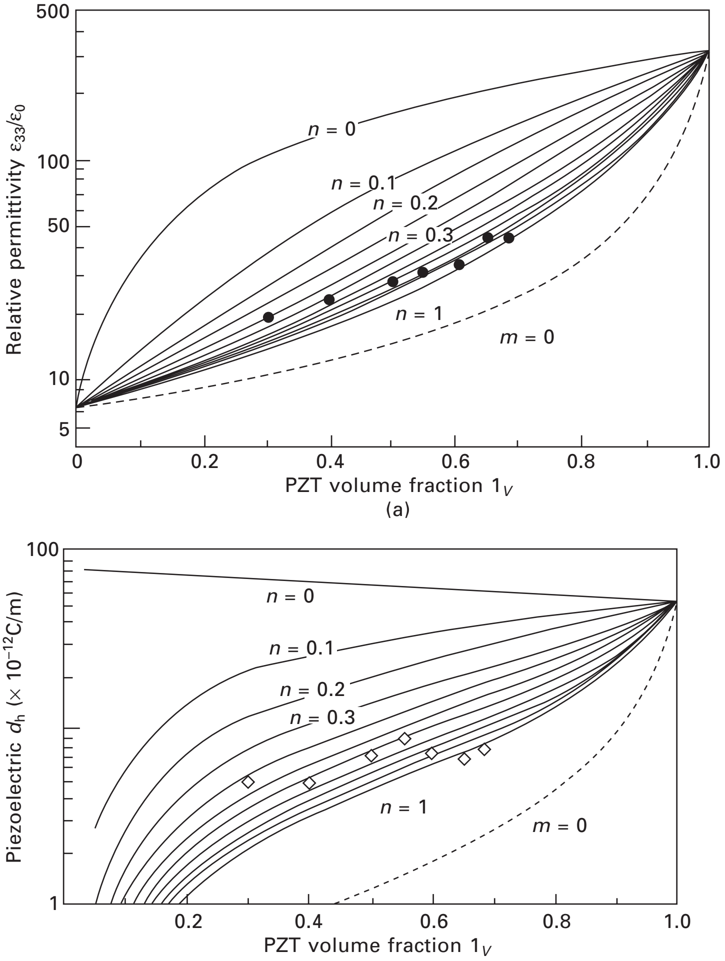

(a)

(b)

9.11 Experimental values of the permittivity (a) and the piezoelectric d_h^* (= d_{33}^* + $2d_{31}^*$) coefficient (b) for $PbTiO_3$:chloroprene rubber 0-3 composites, shown with theoretical curves based on Banno's modified cubes model.

9.4.4 Advanced PZT:polymer composites

3-3 composites were first fabricated by the *replamine method*. A negative replica of a natural coral structure with 3-3 connectivity was made of wax. Then, a positive replica of the negative structure was prepared by introducing a PZT slurry into the porous network of the negative template, drying, burning out the wax, and finally sintering the PZT ceramic.[11] In order to make highly porous PZT skeletons, the BURPS (BURned-out Plastic Spheres) method was proposed,[12] where PZT powders and plastic spheres

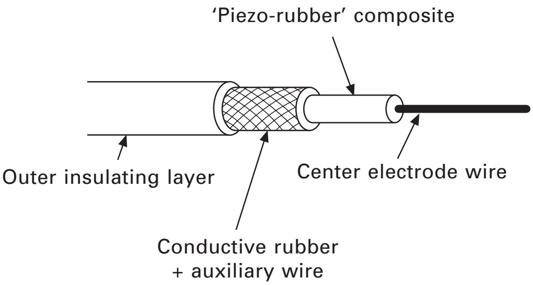

9.12 Structure of piezoelectric–rubber composite co-axial cables developed by NTK/NGK, Japan.

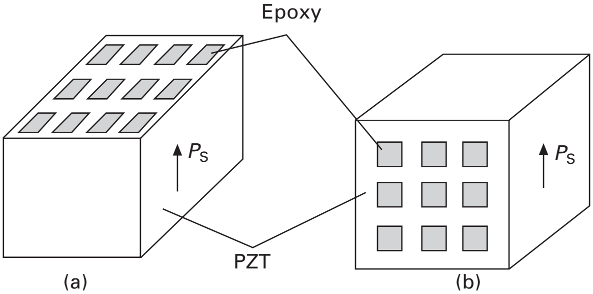

9.13 3-1 composites with (a) parallel and (b) series electrode configurations.

are mixed in a binder solution, and the mixture is sintered. Miyashita *et al.* reported an alternative method that involves piling up thin PZT rods in a three-dimensionally connected array.[13]

3-1 and 3-2 composites can be fabricated by drilling holes in a PZT block, and backfilled with epoxy. In addition to this drilling method, an extrusion method has also been used to fabricate a PZT honeycomb. The 3-1 and 3-2 composites show large d_h and g_h values.[14] As shown in Fig. 9.13, there are two types of electrode configurations commonly applied to these composites: parallel (P) and series (S). In general, S types exhibit larger d_h and g_h values than P types.

Materials Systems Inc. developed a mass-production process for the 1-3 piezo-composites by using injection molding, as illustrated in Fig. 9.14(a) and 9.14(b).[15] The piezo-composites are shown in Fig. 9.15, alongside a US quarter coin for size comparison.

9.5 Composite dampers and energy harvesters

In this section we review piezoelectric dampers and energy harvesting devices from the viewpoint of composite application.

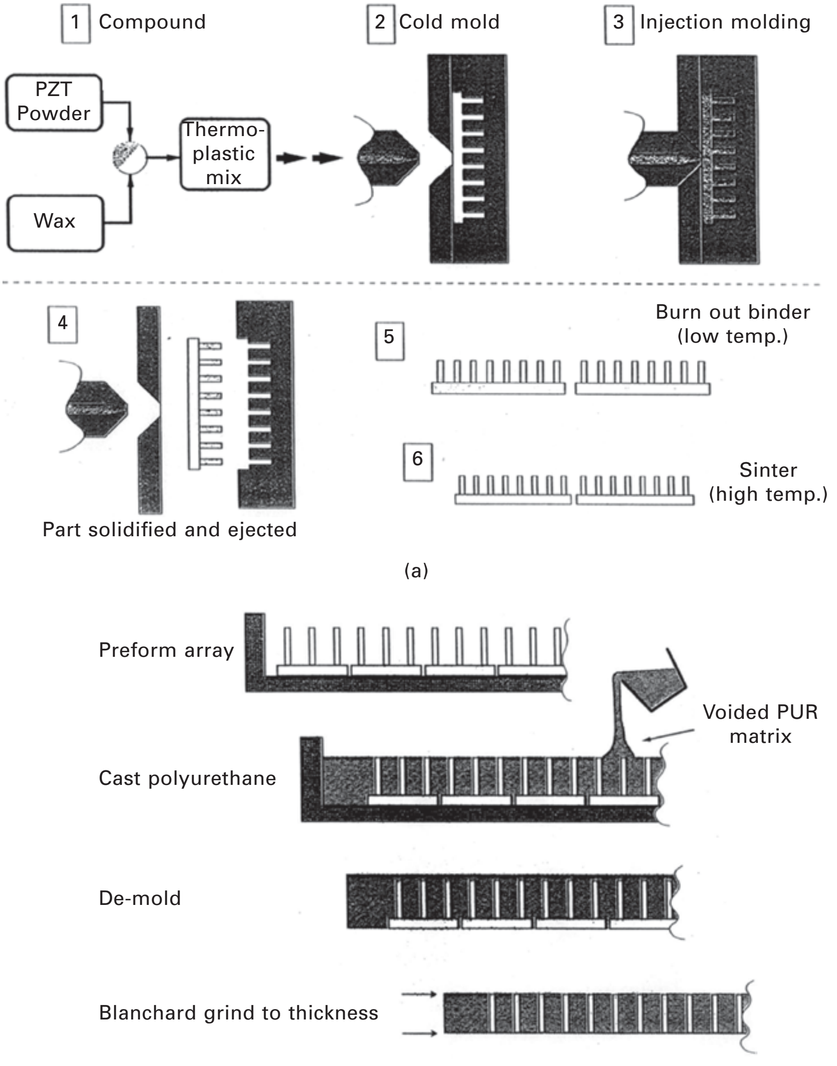
1 Compound
2 Cold mold
3 Injection molding
PZT Powder
Wax
Thermo-plastic mix
4
Part solidified and ejected
5
Burn out binder (low temp.)
6
Sinter (high temp.)
Preform array
Cast polyurethane
Voided PUR matrix
De-mold
Blanchard grind to thickness

(a)

(b)

9.14 (a) Manufacturing process of the ceramic preform, and (b) 1-3 composite fabrication steps, developed by Materials Systems Inc.[15]

9.5.1 Piezoelectric composite dampers

An intriguing application of PZT composites is as a passive mechanical damper. Consider a piezoelectric material attached to an object whose vibration is to be damped. When vibration is transmitted to the piezoelectric material, the vibration energy is converted into electrical energy by the piezoelectric

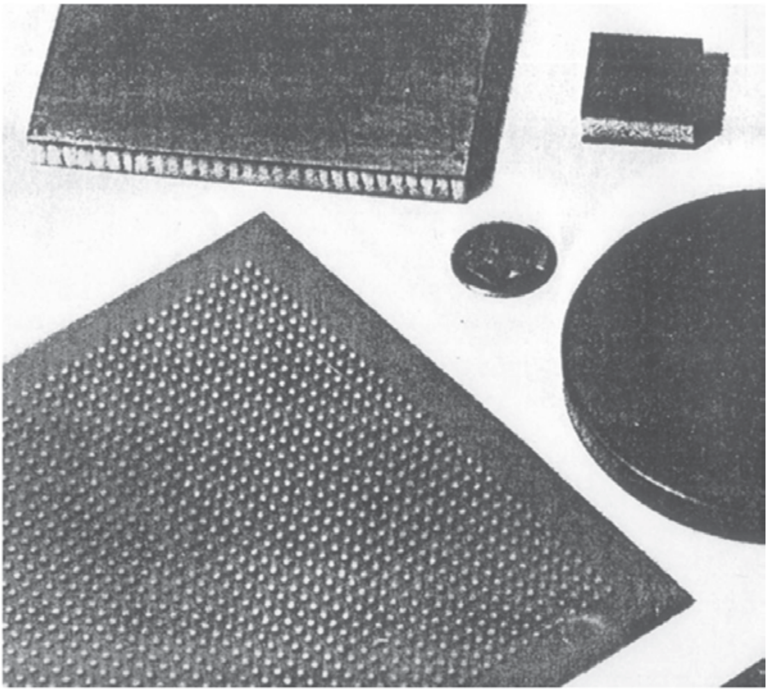

9.15 1-3 piezo-composites developed by Materials Systems Inc.

effect, and an AC voltage is generated. If the piezoelectric material is in an open- or short-circuit condition, the generated electrical energy changes back into vibration energy without loss. The repetition of this process provides continuous vibration. If a proper resistor is connected, however, the energy converted into electricity is consumed in Joule heating of the resistor, and the amount of energy converted back into mechanical energy is reduced, so that the vibration can be rapidly damped. Taking the series resistance as R, the capacitance of the piezoelectric material as C, the vibration frequency as f, damping takes place most rapidly when the series resistor is selected in such a manner that the *impedance matching* condition, $R = 1/2\pi f C$, is satisfied.[16] Figure 9.16(b) shows a mechanical damping difference for a unimorph-type beam (Fig. 9.16(a)) under various resistive shunt conditions. Notice that the resistance 6.6 kΩ (i.e., empedance matching condition) realized the minimum period of the vibration.

Using this technique, in collaboration with ACX Company, K2 developed ski blades with PZT patches to suppress unnecessary vibration during sliding.[17] The integrated damping module in Fig. 9.17 measures 6.62 × 1.66 × 0.07 inches, and includes piezoelectric wafers, energy dissipating resistive shunt, and an LED function indicator. This module is located around a quarter of the ski blade length from the tip (i.e., the nodal point region).

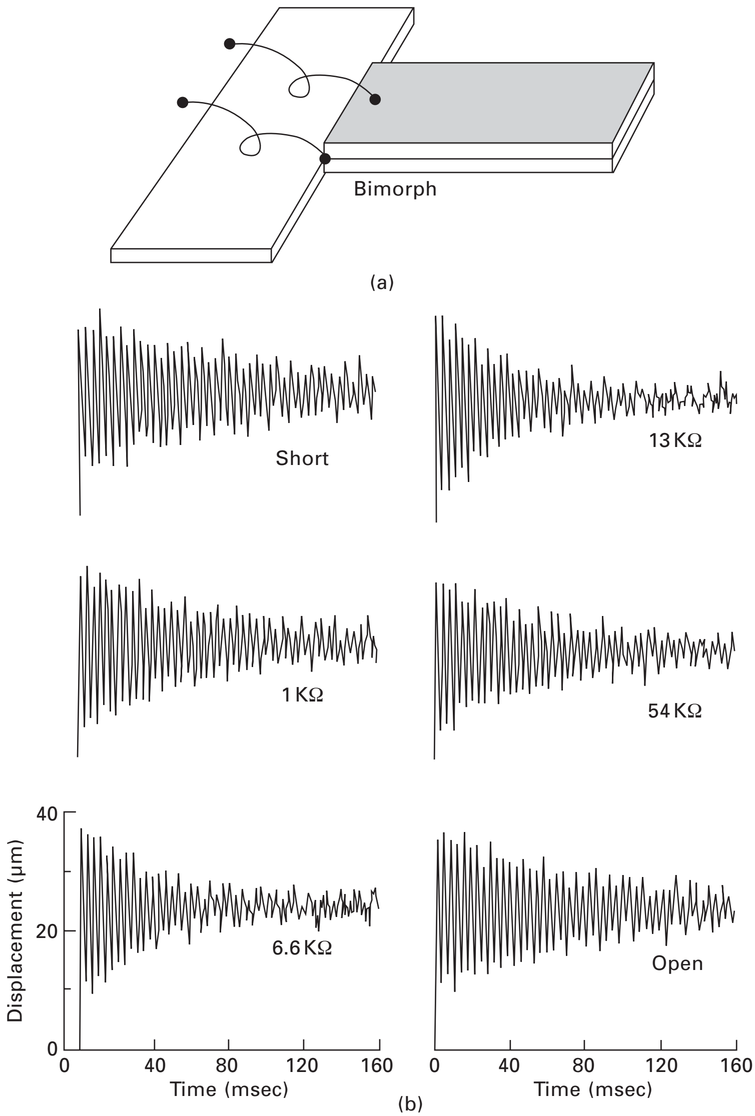

9.16 Mechanical damping difference for a unimorph-type beam. (a) Unimorph beam structure, and (b) damping performance under various resistive shunt conditions.

The electric energy U_E generated can be expressed by using the electromechanical coupling factor k and the mechanical energy U_M:

$$U_E = U_M \times k^2 \qquad 9.12$$

The piezoelectric damper transforms electrical energy into heat energy when a resistor is connected, and the transforming rate of the damper can be raised

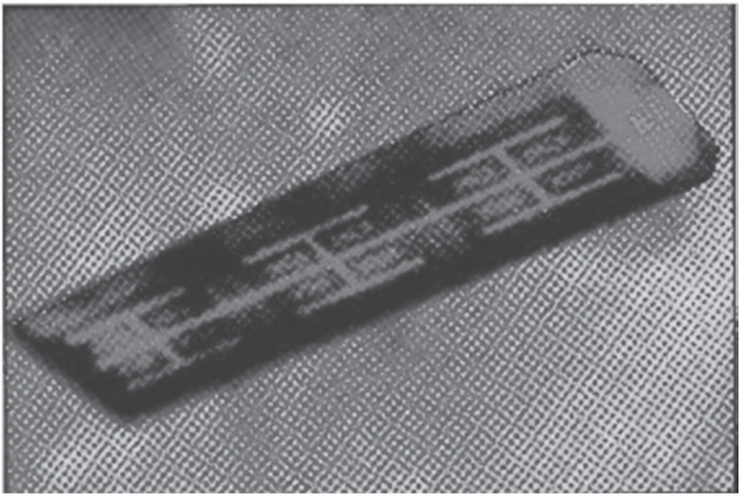

9.17 Piezoelectric damper patch (6.62 × 1.66 × 0.07 inches) with piezoelectric wafers, energy dissipating resistive shunt, and an LED function indicator, developed by ACX and K2.

to a level of up to 50% (under the electrical impedance matching condition). Accordingly, the vibration energy is decreased at a rate of $(1 - k^2/2)$ times for a vibration cycle, since $k^2/2$ multiplied by the amount of mechanical vibration energy is dissipated as heat energy. As the square of the amplitude is equivalent to the amount of vibration energy, the amplitude decreases at a rate of $(1 - k^2/2)^{1/2}$ times with every vibration cycle. If the resonance period is taken to be T_0, the number of vibrations for t sec is $2t/T_0$. Consequently, the amplitude in t sec is $(1 - k^2/2)^{t/T_0}$. Thus, the damping in the amplitude of vibration in t sec can be expressed as follows:

$$(1 - k^2/2)^{t/T_0} = \exp(-t/\tau) \tag{9.13}$$

or

$$\tau = -T_0 \ln(1 - k^2/2). \tag{9.14}$$

In conclusion, the higher the k value is, the quicker the vibration suppression is.

Being brittle and hard, ceramics are difficult to assemble directly into a mechanical system. Hence, flexible composites can be useful in practice. When a composite of polymer, piezo-ceramic powder and carbon black is fabricated (Fig. 9.18), the electrical conductivity of the composite is greatly changed by the addition of small amounts of carbon black.[18] Figure 9.19 illustrates the fabrication process of the damper composite. By properly selecting the electrical conductivity of the composite (i.e., electrical impedance matching),

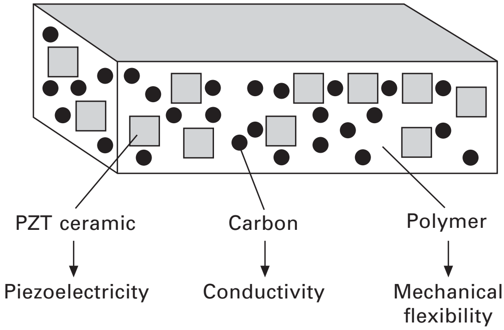
PZT ceramic
Carbon
Polymer
Piezoelectricity
Conductivity
Mechanical flexibility

9.18 Piezoceramic:polymer:carbon black composite for vibration damping.

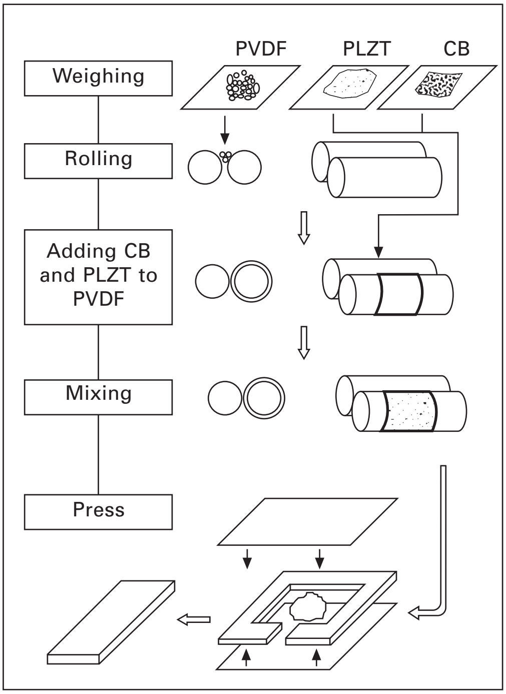
PVDF
PLZT
CB
Weighing
Rolling
Adding CB and PLZT to PVDF
Mixing
Press

9.19 Fabrication process of carbon black contained PLZT:PVDF composites.

the ceramic powder effectively forms a series circuit with the carbon black, so that the vibration energy is dissipated effectively. The conductivity of the composite changes by more than 10 orders of magnitude around a certain carbon fraction called the ‘percolation threshold’, where the carbon powder link starts to be generated. This eliminates the use of external resistors.

Note that the damper material exhibits a selective damping performance for a certain vibration frequency, depending on the selected resistivity of the composite, which can be derived from the electrical impedance matching between the permittivity and resistivity.

Figure 9.20 shows the relation between the damping time constant and the volume percentage of carbon black in the PLZT:PVDF and PZT:PVDF composites. A volume percentage of about 7% carbon black exhibited the minimum damping time constant, and therefore the most rapid vibration damping. Note that the PLZT with a higher electromechanical coupling *k* shows a larger dip (more effective) in the damping time constant curve, which can be expected from Eq. (9.14).

Passive damping systems of carbon-fiber-reinforced plastic (CFRP)/PZT beams were developed.[19] Figure 9.21(a) and (b) shows two configurations; a pair of PZT plates were bonded on the tip part of the CFRP plate, and on the bottom part of the CFRP with a bimorph configuration, respectively. When we considered the initial three vibration modes (1st, 2nd, and 3rd bending modes) shown in Fig. 9.22, we studied which bimorph configuration (a) or (b) is effective on which modes.

Taking into account that the mechanical energy concentrated nodal range should overlap with the bimorph part to effectively damp the vibration, we concluded that type (a) bimorph is effective on the 2nd and 3rd modes.

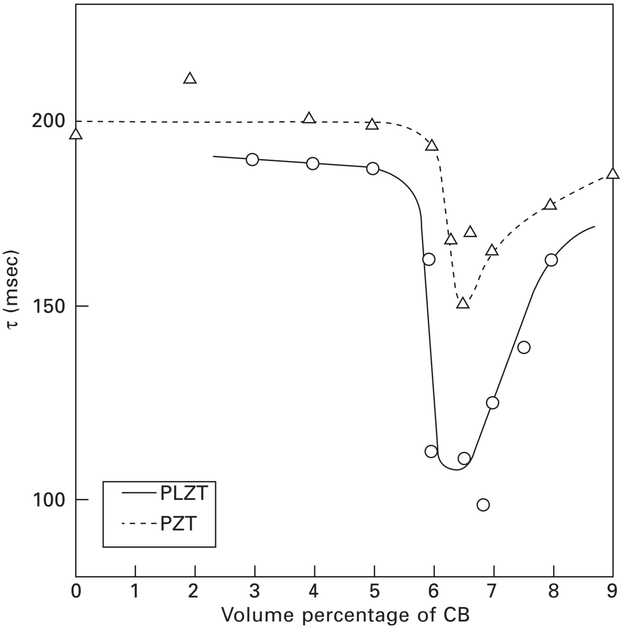

9.20 Damping time constant vs. volume percentage of carbon black in the PLZT:PVDF composite.[18]

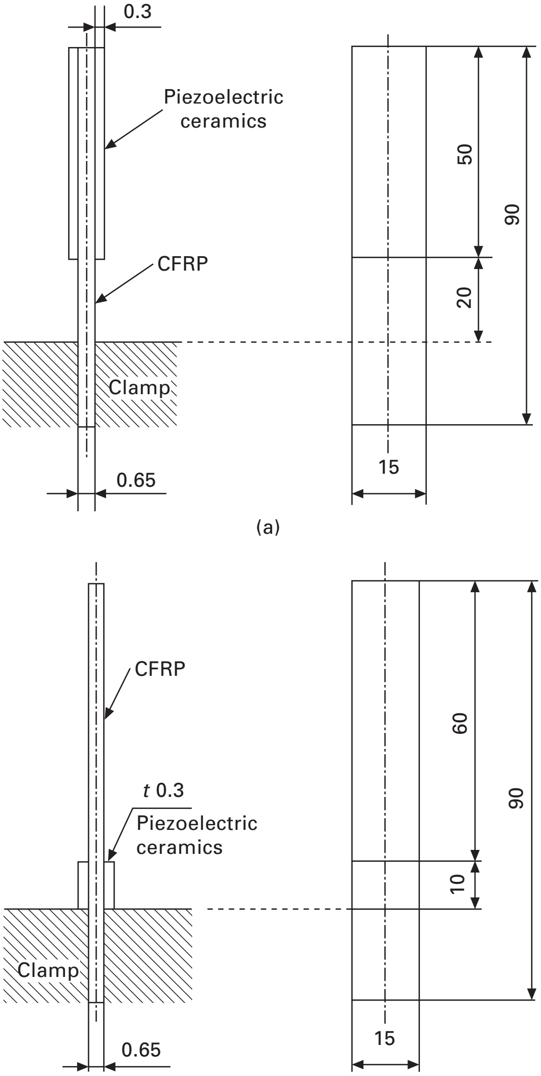
0.3
Piezoelectric ceramics
CFRP
Clamp
0.65
50
20
90
15
CFRP
t 0.3
Piezoelectric ceramics
Clamp
0.65
60
10
90
15

(a)

(b)

9.21 Two configurations of CFRP/PZT cantilever beams: (a) a pair of PZT plates are bonded on the tip part of the CFRP plate, and (b) on the bottom part of the CFRP with a bimorph configuration.

9.5.2 Piezoelectric composite energy harvesting

Energy recovery from wasted or unused power has been a topic of discussion for a long time. Unused power exists in various forms such as vibration, flowing water, wind, human motion and shock wave. Flexible piezoelectric composites such as macro fiber composite (MFC) were employed to the small

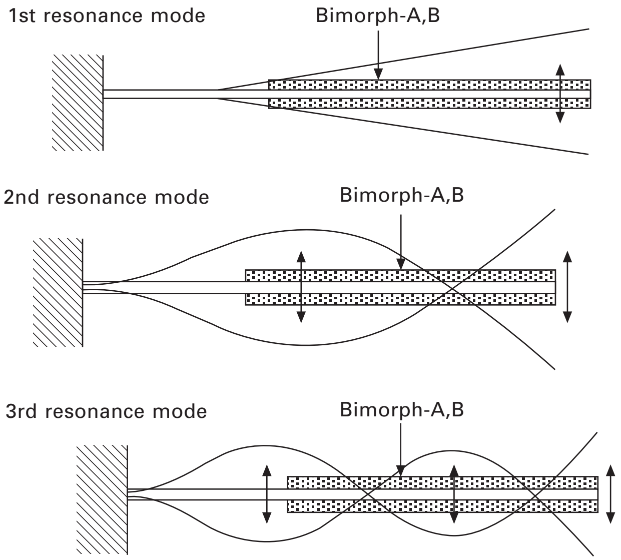

9.22 Three initial bending modes of the beam.

force vibration sources where flexibility was necessary. The flexibility of the PZT element can generate the mechanical stress easily. In addition, it is easy to handle and shape. Previously, a PVDF film was used for implantable physiological power supply,[20] and inserted for recovering some of the power in the process of walking.[21] As an alternative, the advanced piezo fiber composite (PFC) was experimentally demonstrated and confirmed recently for the energy conversion component by the Penn State group.

Several flexible PZT composites such as active fiber composite (AFC) and MFC (Fig. 9.23) are commercially available, and used for high displacement actuators and transducers for energy conversion. The major advantages of those fiber composites over conventional piezoelectric elements are their flexibility and toughness, both far superior compared with monolithic PZT wafers. Furthermore, due to their thin, planar geometry the fiber composites can be easily integrated into composite laminates.[22]

The MFC is a revolutionary actuator which was developed at the NASA Langley Research Center. The piezoelectric fibers manufactured by computer controlled dicing saw and embedded in the matrix were sandwiched between two layers of polyimide film that had a conductive interdigitated electrode pattern printed on the inner surface. There are two types of MFC depending on the poling direction. The poling direction of d_{33} type is parallel along the fiber length and each segment has opposite poling direction by interdigitated electrodes as shown in Fig. 9.23. For the d_{31} type, the poling direction is from the top to the bottom along the fiber thickness. The MFC is extremely

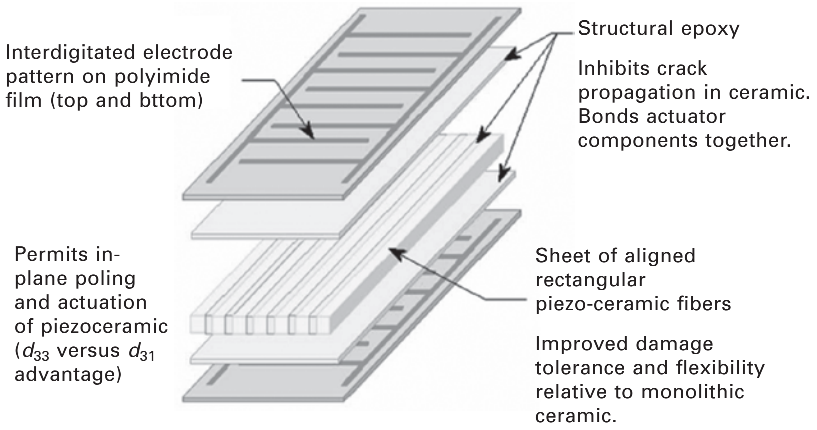
Interdigitated electrode pattern on polyimide film (top and bttom)
Structural epoxy
Inhibits crack propagation in ceramic. Bonds actuator components together.
Permits in-plane poling and actuation of piezoceramic (d_{33} versus d_{31} advantage)
Sheet of aligned rectangular piezo-ceramic fibers
Improved damage tolerance and flexibility relative to monolithic ceramic.

9.23 Macro fiber composite (MFC) by Smart Material Corporation.

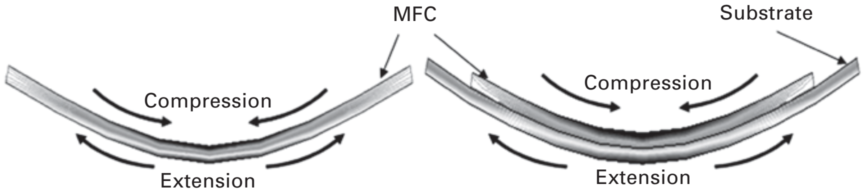
MFC
Substrate
Compression
Extension
Compression
Extension

9.24 Stress distribution in the MFC: (a) without a substrate, and (b) with an aluminum foil substrate (0.17 mm in thickness).

flexible, durable and has the advantage of higher electromechanical coupling coefficients granted through the interdigitated electrodes.

Previously, the d_{33} mode type of the MFC was tested to charge a battery, but Sodano *et al.*[23] claimed that the MFC did not produce high current because of its construction. The interdigitated electrodes of the d_{33} type made the small segments connect in series. Therefore the voltage was added to generate high value but the current was not sufficient. Uchino *et al.* tested the d_{31} mode type of MFC under small mechanical vibration source to generate enough current for battery charging.[24] The d_{31} mode type of MFC (M8528 P2) was fabricated by Smart Material Corp. The piezo-ceramic fibers in the MFC were cut to 350 μm width and 170 μm thickness from piezoelectric wafer by computer-controlled dicing saw. The total dimensions of the MFC are 85 mm length, 28 mm width, and 0.3 mm thickness. Figure 9.24 shows the stress distribution of MFC when the mechanical force is applied. As shown in Fig. 9.24(a), without any substrate, the extensive stress and compressive stress occur on the top and the bottom of the MFC. In this case, the neutral line of the stress distribution is in the middle of the MFC. For this reason the electrical output will be very small. But in Fig. 9.24(b), when the additional substrate is bonded on the bottom of the MFC, the neutral line will move down in the substrate. Therefore, the electrical output will be increased because the MFC will have only a compressive stress or extensive stress in the whole volume. In addition, the thickness and material of the substrate should be carefully considered to maintain the flexibility of the MFC. The minimum thickness of the substrate can be calculated by FEM simulation software, depending on the material to escape the neutral line from the MFC. For this calculation, the dimensions of MFC are 85 mm × 28 mm × 0.17 mm, and the thickness of a substrate is 0.17 mm. The aluminum foil was selected to be used as the substrate in the experiment, even though the neutral line is located slightly above the adjacent line.

The MFC was excited to generate a big bending motion by a small force at the frequency of 1–5 Hz. Note that the small mechanical force used in the experiment means the minimum force that can generate maximum strain in the flexible element without cracking. The voltage signal of the MFC is shown in Fig. 9.25(a). The voltage of MFC is considerably increased by bonding an aluminum substrate. This signal was generated by a small mechanical force with a frequency of 5 Hz, and monitored by oscilloscope (TDS 420A). The aluminum substrate gave a lower flexibility to the MFC, but the output voltage from MFC with small bending showed a much higher voltage signal. The output voltage signal from the MFC was passed through the rectifier and charged to the capacitor, and successively discharged through a resistive load. The rectified voltage and output power were shown in Fig. 9.25(b). The generated electric power from a small mechanical force at 5 Hz was around 1.5 mW at 200 kΩ.

The MFC shows the potential for use in intelligent clothing (IC) with flexible piezoelectric energy harvesting system, aiming at a general power source for charging up portable equipment such as cellular phones, health monitoring units or medical drug delivery devices.

9.6 Magnetoelectric sensors

Similar to nuclear radiation, magnetic irradiation cannot be easily felt by humans. Some reports mention that brain cancer may be triggered by frequent use of a mobile phone, though there is no strong scientific evidence. The problem is that we cannot even purchase a magnetic field detector for a low frequency (50 or 60 Hz). Penn State, in collaboration with Seoul National University, developed a simple and handy magnetic noise sensor for environmental monitoring.[25] Figure 9.26(a) shows a schematic structure of the device, in which a PZT disk is sandwiched between two terfenol-D (magnetostrictor) disks. When a magnetic field is applied to this composite, the terfenol metal expands, which is mechanically transferred to the PZT, leading to an electric charge generation from the PZT. By monitoring the

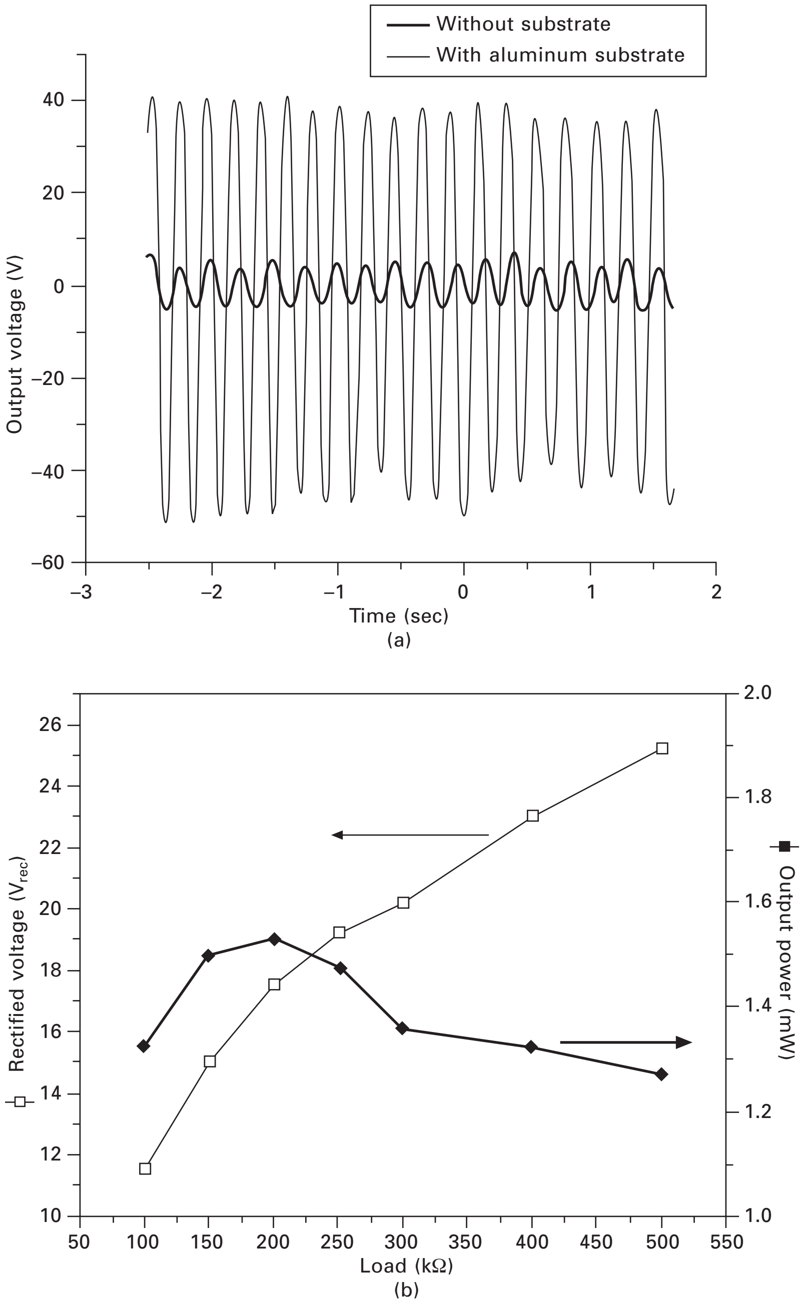

(a)

(b)

9.25 Output of the MFC by around 5 Hz: (a) output voltage signal of the MFC, and (b) rectified voltage and output power with a resistive load.[24]

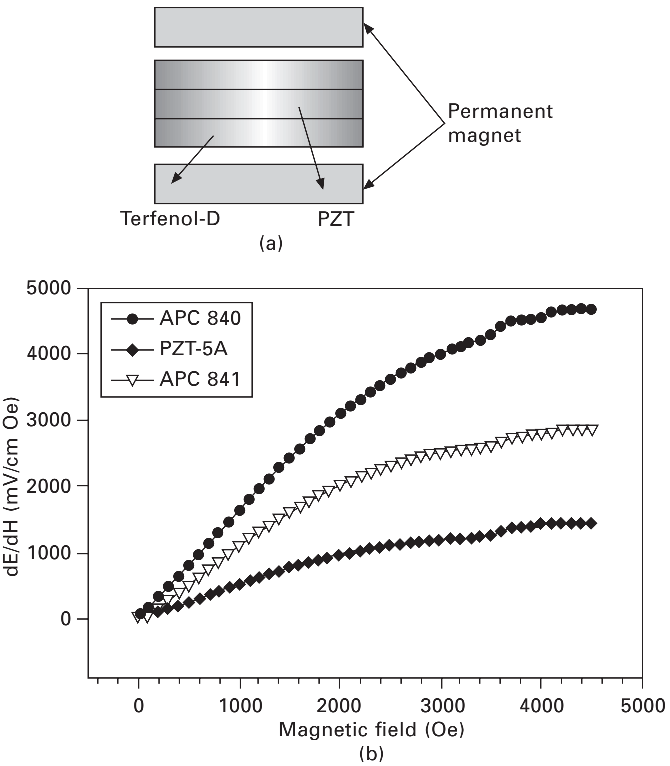

9.26 (a) Schematic structure of the magneto-electric device, in which a PZT disk is sandwiched between two terfenol-D (magnetostrictor) disks. (b) Comparison of the magnetic field monitoring performance of the electromagnetic devices with different PZT materials.

voltage generated in the PZT, we can detect the magnetic field. Figure 9.26(b) compares the experimental results of the magnetic field monitoring performance of the devices with different PZT materials, which indicates that a high piezoelectric g constant material (APC 840) exhibits the best performance. The key point of this device is that it is highly effective at low frequencies.

9.7 References

1. R. E. Newnham *et al.*: *Mater. Res. Bull.* 13, 525 (1978).
2. K. Uchino: *Solid State Phys.* 21, 27 (1986).
3. T. Kitayama and S. Sugawara: *Study Comm. Electronic Circuit Components & Mater.*, Ref. No. CPM72-17 (1972).
4. K. Uchino, S. Nomura and R. E. Newnham: *Sensor Technology* 2, 81 (1982).
5. K. A. Klicker, J. V. Biggers and R. E. Newnham: *J. Amer. Ceram. Soc.* 64, 5 (1981).

6. http://www.matsysinc.com/, U.S. Patent 5,340,510.
7. W. A. Smith: *Proc. IEEE Ultrasonic Symp. '89*, p. 755 (1989).
8. L. A. Pauer: *IEEE Int'l Convention Record*, 1–5 (1973).
9. H. Banno: *Proc. 6th Int'l Meeting on Ferroelectricity* (IMF-6, Kobe, 1985), *Jpn. J. Appl. Phys.* 24, Suppl. 24–2, 445 (1985).
10. H. Banno and T. Tsunooka: *Ceramic Data Book '87*, Industrial Product Technology Soc., p. 328 (1987).
11. D. P. Skinner, R. E. Newnham and L. E. Cross: *Mater. Res. Bull.* 13, 599 (1978).
12. T. R. Shrout, W. A. Schulze and J. V. Biggers: *Mater. Res. Bull.* 14, 1553 (1979).
13. M. Miyashita *et al.*: *Ferroelectrics* 27, 397 (1980).
14. A. Safari, R. E. Newnham, L. E. Cross and W. A. Schulze: *Ferroelectrics* 41, 197 (1982).
15. http://www.matsysinc.com/, US Patent 5,340,510.
16. K. Uchino and T. Ishii: *J. Ceram. Soc. Jpn.* 96, 863 (1988).
17. ACX Company catalogue: Passive Damping Ski.
18. Y. Suzuki, K. Uchino, H. Gouda, M. Sumita, R. E. Newnham and A. R. Ramachandran: *J. Ceram. Soc. Jpn., Int'l Edition* 99, 1096 (1991).
19. T. Tanimoto, K. Horiuchi and K. Uchino: *Japan. J. Appl. Phys.*, 36 Part 1 (No. 9B), p. 6110–6113 (1997).
20. E. Hausler, L. Stein and G. Harbauer: *Ferroelectrics*, 60, 277 (1984).
21. J. Kymissis, C. Kendall, J. Paradiso and N. Gershenfield: *Digest of Papers, Second IEEE International Symposium on Wearable Computers*, 132 (1998).
22. L. J. Nelson: *Material Science and Technology*, 18, 1245 (2002).
23. H. A. Sodano, G. Park, D. J. Leo and D. J. Inman: *Smart Structure and Materials: Smart Sensor Technology and Measurement Systems, Proc. of SPIE, 5050*, 101 (2003).
24. K. Uchino *et al.*: *Proc. 9th Japan Int'l SAMPE Symp.*, pp. 11–14, Nov. 18–21, Tokyo (2005).
25. J. Ryu, A.Vazquez Carazo, K. Uchino and H. E. Kim: *Jpn. J. Appl. Phys.*, 40, 4948–4951 (2001).

Part II

Preparation methods and applications

10

Manufacturing methods for piezoelectric ceramic materials

K. UCHINO, The Pennsylvania State University, USA

Abstract: After the material designing such as solid solution compositions and dopants, we need to consider material fabrication processes. The fabrication of piezoelectric ceramic devices generally involves two steps: preparation of the ceramic powders and sintering of the shaped structures. Wet chemical preparation methods are utilized for producing the ceramic powders in order to ensure reproducibility of the advanced characteristics of the devices. Popular device designs include multilayers, bimorphs and other composite types. Necessary basic knowledge of particle size and film thickness effect on ferroelectricity will also be discussed in conjunction with micro/nano technologies in this chapter.

Key words: solid solution, dopant, sintering, calcination, bimorph, multilayer, composite, particle size.

10.1 Material designing

10.1.1 Composition selection

The first strategy for designing ferroelectric materials is to select a material with a suitable Curie temperature. Piezoelectric materials are used as sensors and actuators, where the T_C should be much above room temperature. Though the piezoelectric coefficient is high around T_C, this selection is related for the following two reasons: (1) temperature stability of the performance, and (2) reliability under an elevated temperature (aging effect is significant due to depoling for a low T_C material).

Let us consider an example of a piezoelectric application. In general, $Pb(Zr,Ti)O_3$ (PZT), $PbTiO_3$ (PT), $(Pb,La)(Zr,Ti)O_3$ (PLZT) and PZT-based ternary ceramics are utilized for piezoelectric applications. The reader can refer to the international data book summarizing various piezoelectric coefficients.[1]

Figure 10.1 shows the composition dependence of the permittivity and the electromechanical coupling factor k_p for the PZT system.[2] If we do not have this sort of comprehensive experimental data, how can we estimate the values for the solid solutions? In general, physical properties of a solid solution between A and B, (1–x)A–xB, can be estimated by a *phenomenological theory*.[3,4] Expanding the theories, the Gibbs elastic energy of a solid solution

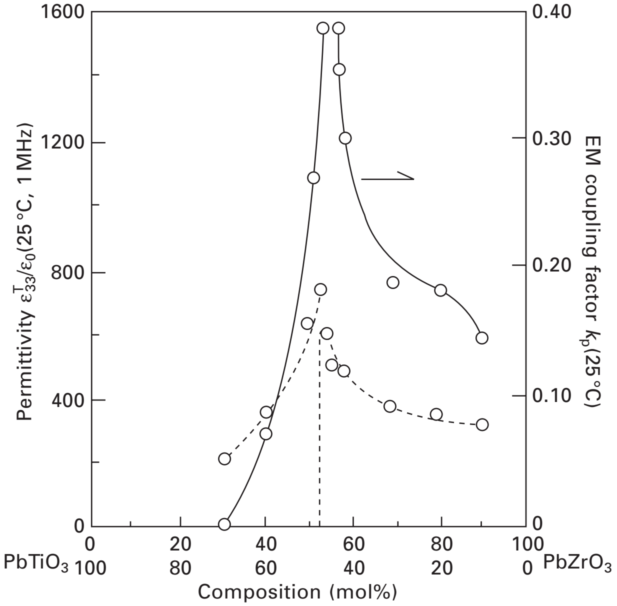

10.1 Composition dependence of the permittivity and the electromechanical coupling factor *k*p in the PZT system.[2]

is assumed to be a linear combination of the Gibbs elastic energy of each component:

$$G_1(P, X, T) = (1/2)[(1-x)\alpha_A + x\alpha_B]\,P^2 + (1/4)[(1-x)\beta_A + x\beta_B]\,P^4$$
$$+ (1/6)[(1-x)\gamma_A + x\gamma_B]\,P^6 - (1/2)[(1-x)s_A + xs_B]\,X^2$$
$$- [(1-x)Q_A + xQ_B]\,P^2\,X.$$
$$(\alpha_A = (T - T_{0,A})/\varepsilon_0 C_A,\ \alpha_B = (T - T_{0,B})/\varepsilon_0 C_B) \qquad 10.1$$

The solution provides reasonable first-order estimates of the Curie temperature, spontaneous polarization and strain, permittivity, piezoelectric constant and electromechanical coupling. Abe *et al.* reported a good example of theoretical fitting to experimental results for the solid solution $Pb(Zn_{1/3}Nb_{2/3})O_3$–$PbTiO_3$.[4] By expanding Eq. (10.1) into the three-dimensional expression with P_1, P_2, P_3, X_{11}, X_{33}, X_{44}, etc., for realizing cubic, tetragonal and rhombohedral symmetry phases, the Gibbs energy is calculated for a certain composition x and temperature T. Then, the lower energy phase is taken as a stable phase at that particular point (x, T). Figures 10.2–10.5 show these fittings calculated on the basis of the data presented in Table 10.1. The transition temperature from the tetragonal to cubic phase (Curie temperature) changes linearly with the composition x, as the reader can imagine, while the transition temperature

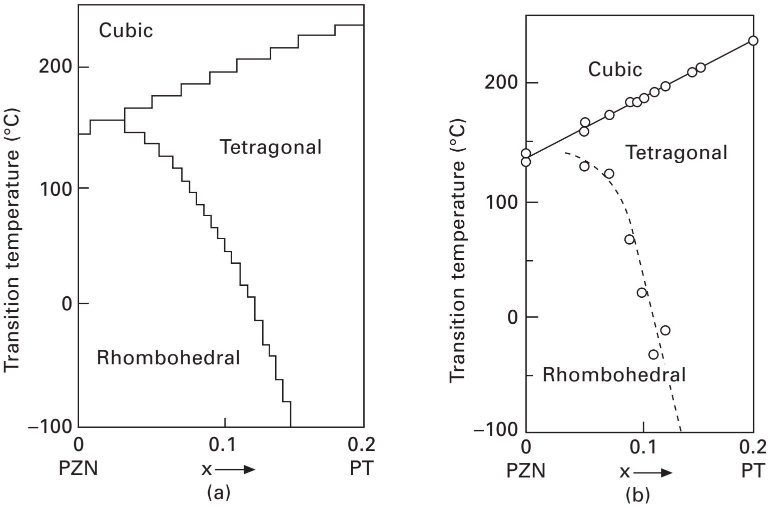

(a)

(b)

10.2 Phase diagram for (1 - x)Pb($Zn_{1/3}Nb_{2/3}$)O_3–$x$$PbTiO_3$; (a) calculated and (b) experimental.

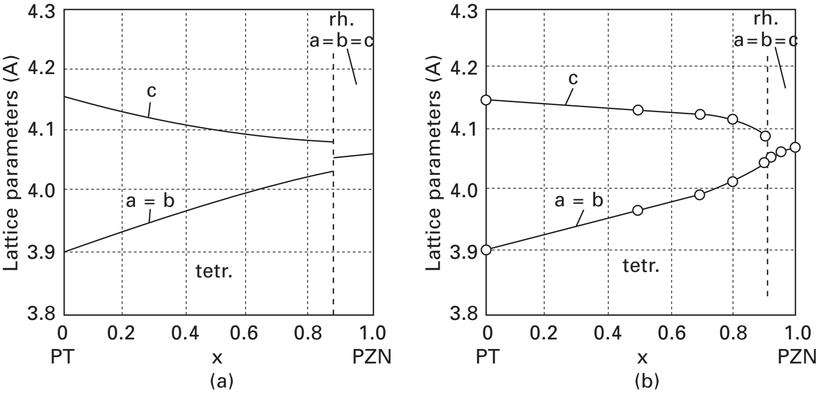

(a)

(b)

10.3 Lattice parameters for (1 - x)Pb($Zn_{1/3}Nb_{2/3}$)O_3–$x$$PbTiO_3$; (a) calculated and (b) experimental.

from the rhombohedral to tetragonal phase is calculated by comparing the G_1 for both phases.

10.1.2 Dopant effects on piezoelectricity

Small amounts of dopants sometimes drastically change the dielectric and electromechanical performances in ceramics. In this section we consider the 'hard' and 'soft' piezoelectric PZT properties. Hard or soft property is defined by the coercive electric field of the PZT sample. Figure 10.6 depicts soft and

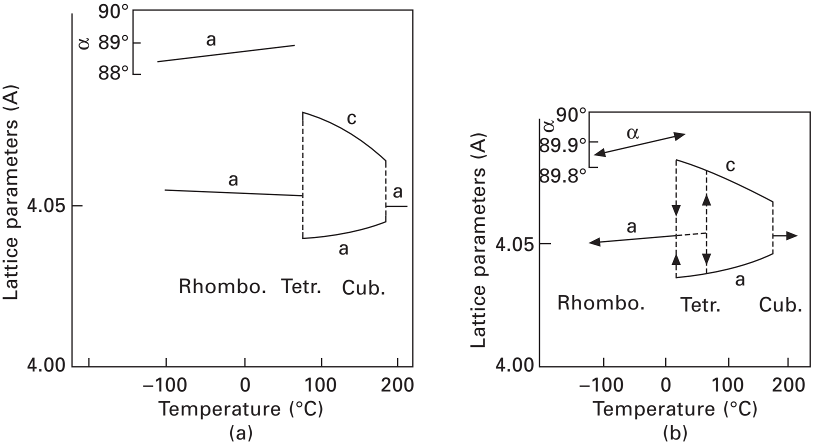

(a)
(b)

10.4 Temperature dependence of lattice parameters for 0.91PZN–0.09PT; (a) calculated and (b) experimental.

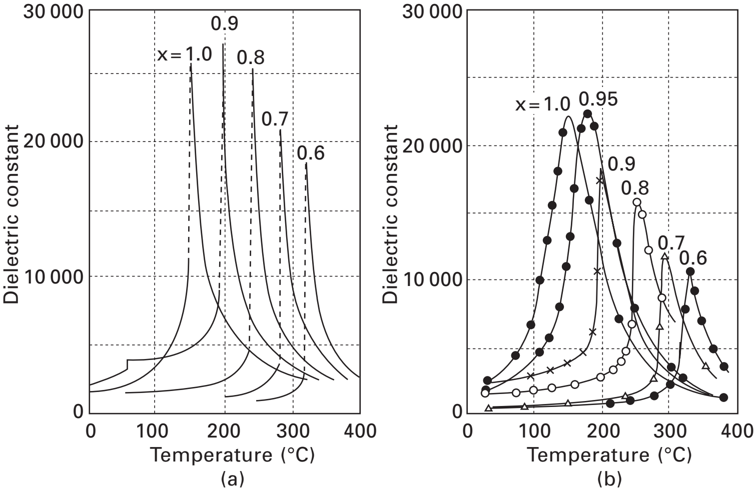

(a)
(b)

10.5 Temperature dependence of dielectric constant for *x*PZN–(1 – *x*) PT; (a) calculated and (b) experimental.

hard properties in the strain curve. When the coercive field is higher than 1 kV/mm, the PZT is called 'hard'; while when the coercive field is less than 100 V/mm, it is called 'soft'. When the coercive field is in between, it is called 'semi-hard'. Note that both samples have the same base composition PZT 52/48 with only 1 at% (atomic percent) different dopants.

The difference in piezoelectric properties among PMN-based electrostrictor, PZT-based soft and hard piezoelectrics is compared in Table 10.2.[5]

Table 10.1 Coefficients for PZN ($Pb(Zn_{1/3}Nb_{2/3})O_3$) and PT($PbTiO_3$) used in calculating the transition temperature and lattice parameters in (1-x) PZN-xPT

Constants	PZN	PT
T_0 (°C)	130	478.8
C (10^5°C)	4.7	1.5
ξ_{11} (10^7 m^5C^{-2} F^{-1})	–13.7	–29.0
ξ_{12} (10^8 m^5C^{-2} F^{-1})	–1.0	15.0
ζ_{111} (10^8 m^9C^{-4} F^{-1})	10.3	15.6
ζ_{112} (10^8 m^9C^{-4} F^{-1})	6.8	12.2
Q_{11} (10^{-2} m^4C^{-2})	2.4	8.9
Q_{12} (10^{-2} m^4C^{-2})	–0.86	–2.6
Q_{44} (10^{-2} m^4C^{-2})	1.6	6.75
a_c (Å)	4.058	3.957

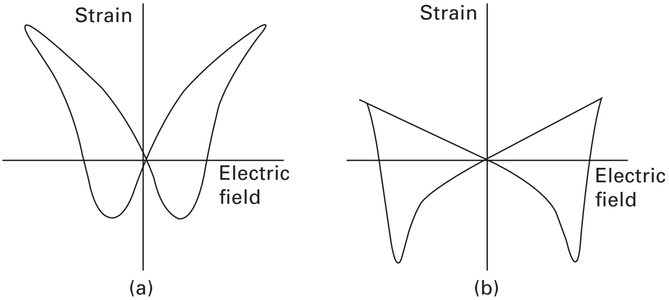

10.6 Soft (a) and hard (b) properties of PZT samples in the strain curve.

Table 10.2 Comparison among electrostrictor, soft and hard piezoelectrics

	d	*k*	Q_m	Off-resonance application	Resonance application
Electrostrictor (PMN)	High *(under DC bias)	High	Low	High displacement No hysteresis	Wide band
Soft piezo (PZT-5H)	High	High	Low	High displacement ($\Delta L = dEL$)	*Heat generation
Hard piezo (PZT- 8)	Low	Low	High	*Low strain	High AC displacement ($\Delta L \propto Q_m\ dEL$)

* Demerit

Domain wall stability

First, the ‘soft’ and ‘hard’ characteristics are a reflection of the coercive field E_C, in other words, the stability of the domain walls. Consider the transient state of a 180° domain reversal, which reveals a domain wall front with a head-to-head polarization configuration (see Fig. 10.7). From Gauss's law,

$$\text{div}\, \mathbf{P} = \rho, \quad (\rho\text{: charge density}) \qquad 10.2$$

the domain wall front is very unstable in a highly insulating material (Fig. 10.7(a) with no space charge), leading to quick disappearance of this domain wall, i.e., a low coercive field. However, if the material has movable space charges (Fig. 10.7(b)) in the crystal lattice, the head-to-head polarization configuration is stabilized, leading to a high coercive field. This is called '*domain wall pinning*' model.

Crystallographic deficiencies

We consider possible crystallographic deficiencies due to impurity doping in a perovskite crystal. Acceptor ions, such as Fe^{3+}, introduce oxygen deficiencies (□) in the PZT lattice as follows:

$$Pb(Zr_y\, Ti_{1\text{-}y\text{-}x}\, Fe_x)(O_{3\text{-}x/2}\, \square_{x/2}).$$

This acceptor doping causes the easy reorientation of deficiency-related dipoles. These dipoles are generated by an Fe^{3+} ion (effectively negative charge) and an oxygen vacancy site (effectively positive charge). The deficiencies are produced at a high temperature (> 1000 °C) during sintering; however, the oxygen ions are still movable even below the Curie temperature (e.g., at room temperature), because the oxygen and the vacancy are adjacent (only 2.8 A!) and hopping easily occurs (see Fig. 10.8(a)). The movable oxygen ion is considered to stabilize the domain motion, i.e., 'hard' PZT.

In the case of donor ions, e.g., Nb^{5+}, Pb deficiency is introduced because of the charge neutrality requirement in the crystal:

$$(Pb_{1\text{-}x/2}\, \square_{x/2})(Zr_y\, Ti_{1\text{-}y\text{-}x}\, Nb_x)O_3.$$

Donor doping is not very effective for generating movable dipoles, because

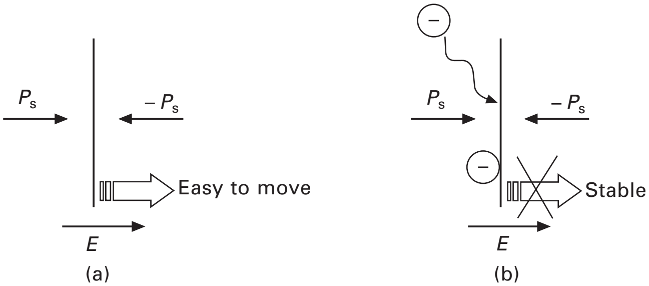

10.7 Domain wall stability, in consideration of Gauss's law (a) without space charge and (b) with movable charge in the crystal.

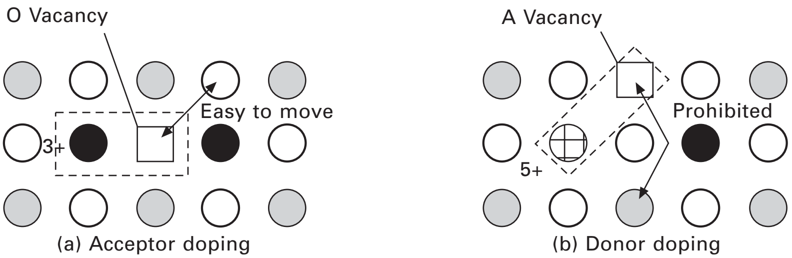

10.8 Crystal deficiencies in PZT for acceptor (a) and donor (b) dopants.

the Pb ion cannot easily hop to an adjacent A-site vacancy due to the close oxygen (large ionic size) surroundings (Fig. 10.8(b)).

Moreover, it is noteworthy that lead-containing ceramics such as PZT tend to be p-type semiconductors due to Pb evaporation during sintering. Hence, donor-type ion doping is considered to compensate the original acceptor type or p-type deficiencies. Thus, donor-doped piezo-ceramics facilitate the domain wall motion, i.e., ‘soft’ PZT, exhibiting large piezoelectric *d* constants, but also easy depoling under usage.

The above ‘oxygen deficiency’ and ‘domain-wall pinning’ model is popularly used to explain the origin of ‘hard’ PZT. However, in Chapter 16. Uchino *et al*. are proposing a different model to explain the ‘hardening’ mechanism of PZT, i.e., ‘internal bias’ model originated from ‘oxygen diffusion’.

The previously mentioned crystal deficiency model helps us to understand various ferroelectric property changes with doping. Hagimura and Uchino[6] studied the effect of impurity doping on field-induced strains using a base composition of $(Pb_{0.73}Ba_{0.27})(Zr_{0.75}Ti_{0.25})O_3$ (soft piezoelectric). Figure 10.9(a) shows the definitions of the *maximum strain* x_{max}, and the *degree of hysteresis* $\Delta x/x_{max}$ (%). The degree of hysteresis is calculated from the strain deviation during the rise and fall of the field Δx at half of the maximum electric field (1 kV/mm) divided by the maximum strain x_{max} at 1 kV/mm. Figure 10.9(b) shows the dopant effect on the strain characteristics, in which the doping concentration is fixed at 2 at%. It is seen that materials incorporating donor-type ions on the B-site with a large valence +4–+6 ion (Ta^{5+}, Nb^{5+}, W^{6+}) exhibit excellent characteristics as positioning actuators; namely, enhancement of the strain magnitude and reduction of the hysteresis.

In contrast, the acceptor-type ions with a small valence +1–+3 suppress the strain and increase the hysteresis and the coercive field. Although acceptor-type ions must be avoided in designing actuator ceramics used for positioner applications (off-resonance applications under high electric field), acceptor doping is very necessary for preparing ‘hard’ piezo-ceramics which are particularly suitable for ultrasonic motor applications (resonance applications under lower electric field).

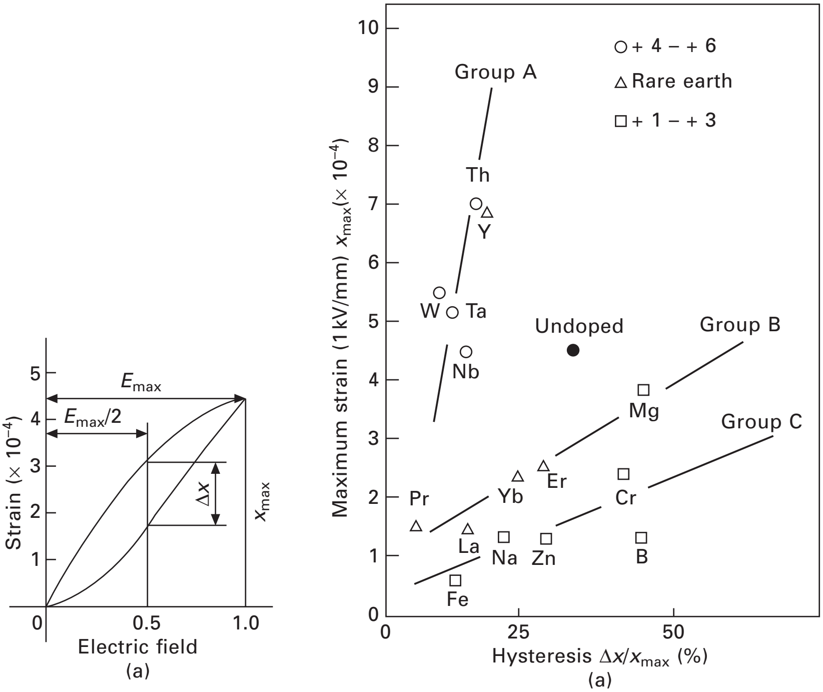

10.9 Dopant effect on the field-induced strain. Maximum strain and hysteresis in $(Pb_{0.73}Ba_{0.27})(Zr_{0.75}Ti_{0.25})O_3$-based ceramics. (a) Definition of the maximum strain x_{max} and the degree of hysteresis $\Delta x/x_{max}$ (%), and (b) dopant effect on the actuator parameters.

10.1.3 High power characteristics

The power density of a piezoelectric is measured by different figures of merit (FOM) for different applications:

- Off-resonance actuator applications – positioners:

  FOM = d (piezoelectric constant)

- Resonance actuator applications – ultrasonic motors:

  FOM = v (vibration velocity) ≈ $Q_m \cdot d$ (for a low level excitation)

- Resonance transducer applications – piezoelectric transformers, sonars (transmitters and receivers):

  FOM = $k \cdot v$ (k: electromechanical coupling factor)

We will focus on high power piezoelectric ceramics for ultrasonic (AC drive) applications in this section. In order to obtain a large output power, the ceramics are driven under a high vibration level, namely under a relatively large AC electric field. This causes heat generation as well as a drastic degradation in piezoelectric properties. Therefore, the high-power device such as an ultrasonic motor requires a very 'hard' piezoelectric with a high *mechanical quality factor* Q_m in order to suppress heat generation. The Q_m is defined as an inverse value of the elastic loss factor, tan ϕ'. It is also notable that the actual mechanical vibration amplitude at the resonance frequency is directly proportional to this Q_m value (i.e., displacement amplification factor).

The *vibration velocity* dependence of the piezoelectric constant, permittivity, elastic compliance and electromechanical coupling factor was obtained for PZT-based samples.[7] Figure 10.10 shows the mechanical quality factor Q_m and the actual temperature rise plotted as a function of the average vibration velocity. Notice a significant decrease in Q_m above a certain critical vibration level, which is the limit of the output vibration energy. Even if the input electrical energy is increased further, the additional energy will be converted only into heat. We define the *maximum vibration velocity* when the temperature rise at the nodal point (maximum temperature point) reaches 20 °C higher than the room temperature.

Figure 10.11 shows the temperature rise versus vibration velocity for undoped, Nb-doped and Fe-doped PZT samples. In comparison with the sample doped with Nb (donor) ion, which generates heat just around 0.05 m/s (rms value), the suppression of heat generation is significant in the Fe (acceptor) doped ceramic. Note that commercially available hard PZTs exhibit 0.3 m/s as the maximum vibration velocity v_{max}.

Figure 10.12 shows mechanical Q_m versus mole fraction of Zr (x) at effective

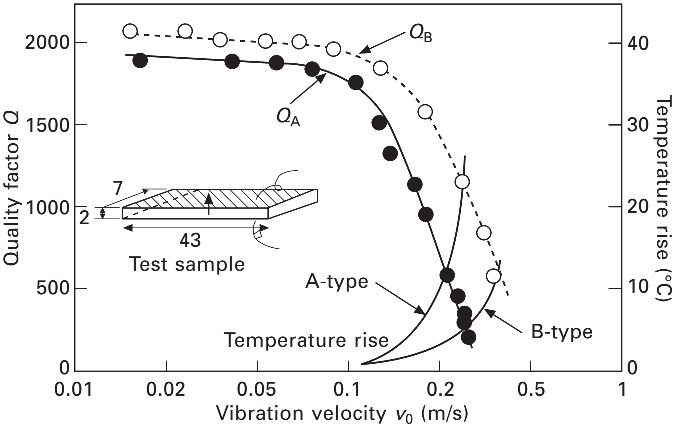

10.10 Vibration velocity (at the sample edge) dependence of the quality factor Q_m and temperature rise for both A (resonance) and B (anti-resonance) type resonances of a longitudinally vibrating PZT ceramic transducer through d_{31}. The test sample size is shown in the figure.

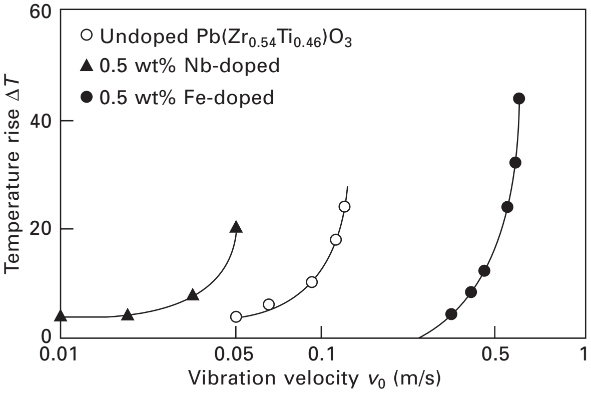

10.11 Temperature rise ΔT vs. effective vibration velocity v for PZT samples.

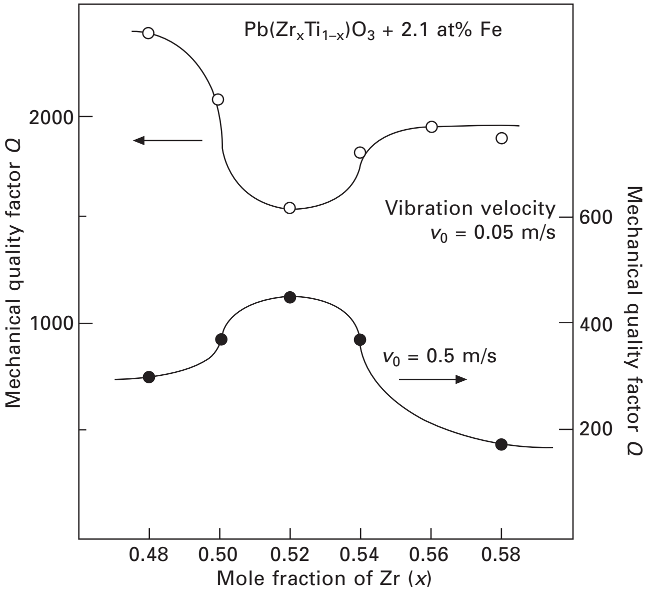

10.12 Mechanical quality factor Q_m vs. mole fraction of Zr (x) at effective vibration velocities v_0 = 0.05 and 0.5 m/s for $Pb(Zr_xTi_{1-x})O_3$ + 2.1 at% Fe^{3+} ceramics.

vibration velocities $v_0 = 0.05$ m/s and 0.5 m/s for $Pb(Zr_xTi_{1-x})O_3$ doped with 2.1 at% of Fe^{3+}.[8] The decrease in mechanical Q_m with increase in vibration level is minimum around the rhombohedral-tetragonal morphotropic phase boundary (52/48). In other words, the worst material at a small vibration level becomes the best at a large vibration level, and data obtained from a conventional impedance analyzer are not relevant to search high power materials.

10.2 Fabrication processes of ceramics

Ferroelectric devices are typically fabricated from polycrystalline ceramics. This involves two steps: preparation of the ceramic powders and sintering of the shaped structures. Single crystals are expanding their applications because of superior performance in comparison with polycrystalline forms. Template grain growth techniques are also used to obtain inexpensive single crystal-like performance.

10.2.1 Preparation of ceramic powders

Particle shape, particle size distribution and compositional uniformity are the key factors to be controlled in the raw powder in order to realize reproducibility of the piezoelectric characteristics. The usual method is the *oxide-mixing technique*, in which a desired chemical composition is made by firing raw oxide powders (calcination), then crushing them into fine powders. Since the oxide-mixing method results in difficulties in achieving microscopic compositional uniformity, wet chemical methods (coprecipitation, alkoxide) have been employed more recently in manufacturing ceramic devices. In this section, processes for fabricating barium titanate (BT), lead zirconate titanate (PZT) and lead magnesium niobate (PMN) ceramics are reviewed.[9]

Solid state reaction

Let us consider the preparation of $Pb(Zr_xTi_{1-x})O_3$ powders. The raw powders PbO, ZrO_2 and TiO_2 are weighed in an appropriate proportion, mixed, and calcined at around 800–900 °C for 1–2 hours. Then the sample is crushed and milled into fine powder. Figure 10.13 illustrates the preparation process of $Pb(Zr_{0.5}Ti_{0.5})O_3$. The drawbacks here are that the milling process does not efficiently give particles of size less than 1 μm, and that the contamination of the sample by milling media is unavoidable. On the other hand, the accidental 'Fe' contamination was a trigger for discovering 'hard' PZT; conventionally steel (Fe) balls were used for ball-milling of PZT powders.

$BaTiO_3$ is prepared in principle from equi-molar quantities of raw powders of BaO and TiO_2. In general, $BaCO_3$ powder is recommended instead of BaO, because high purity BaO is expensive and chemically less reactive.

A similar calcination process starting from PbO, MgO, Nb_2O_5 and TiO_2 can be used for $Pb((Mg_{1/3}Nb_{2/3})_{1-x}Ti_x)O_3$. However, this simple process generates a second phase (pyrochlore) in addition to the perovskite phase. To suppress this second phase several mol% excess PbO doped in the final

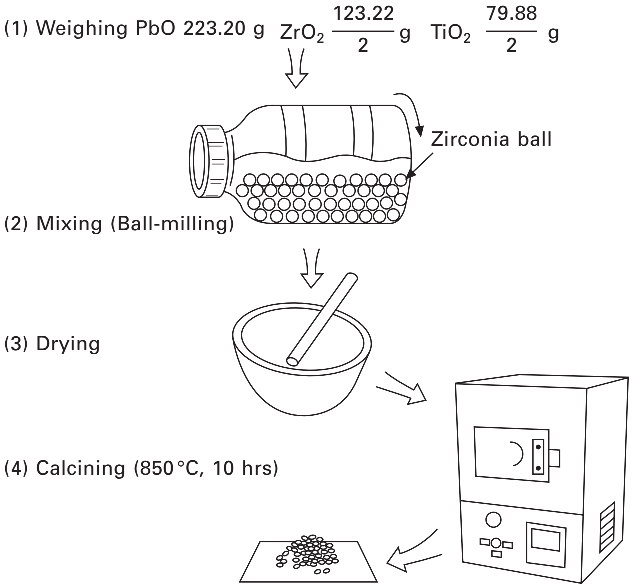
(1) Weighing PbO 223.20 g ZrO_2 $\frac{123.22}{2}$ g TiO_2 $\frac{79.88}{2}$ g
Zirconia ball
(2) Mixing (Ball-milling)
(3) Drying
(4) Calcining (850 °C, 10 hrs)

10.13 Powder preparation process of 1 mole $Pb(Zr_{0.5}Ti_{0.5})O_3$.

sintering stage is effective.[10] Swartz *et al.* reported a unique method taking account of the chemical reaction process.[11] They demonstrated that the perfect perovskite phase can be obtained by the reaction starting from columbite $MgNb_2O_6$ and PbO:

$$3PbO + MgNb_2O_6 \rightarrow 3Pb(Mg_{1/3}Nb_{2/3})O_3$$

For PMN-PT, MgO, Nb_2O_5 and TiO_2 are mixed and fired at 1000 °C initially. Then PbO is added to the columbite, and the sample is calcined at 800–900 °C. Several mol% excess MgO is particularly effective in obtaining the perfect perovskite phase.

Coprecipitation

Since practical piezoelectric/electrostrictive ceramics are from complex solid solution systems, the compositional fluctuation among ceramic particles is very important, as well as the purity. The above method, involving a combination of solid state reaction and mechanical mixing, is inevitably accompanied by this problem. The coprecipitation method is employed to realize enhanced homogeneity. Adding a precipitant into the liquid solution of mixed metal salts produces a homogeneous precipitate. Thermal dissolution makes homogeneous powders from the precipitate.

For example, $BaTiO(C_2\,H_4)_2 \cdot 4H_2O$ with the Ba/Ti ratio exactly equal to 1:1, on an atomic scale, can be precipitated from an aqueous solution of $BaCl_2$ and $TiCl_4$ by dripping in oxalic acid. Thermal dissolution of this precipitate provides fine stoichiometric $BaTiO_3$ powders with good sintering characteristics. For PLZT, $Pb(NO_3)_2$, $La(NO_3)_3 \cdot 6H_2O$, $ZrO(NO_3)_2 \cdot 2H_2O$ and $TiO(NO_3)_2$ are used as the starting materials.[12] First, the water solutions of each nitrate are mixed in the desired proportion, then a half volume of ethanol is added. Oxalic acid diluted with ethanol is dripped slowly into the nitric solution, leading to the precipitation of the PLZT oxalate. Thermal dissolution is carried out at 800 °C.

In the above coprecipitation methods, thermal dissolution of the precipitate is finally required to obtain the desired powder. However, the oxide powder can be obtained directly through the precipitation process in special cases. A direct precipitation method for $BaTiO_3$ is introduced here. By dripping $Ti(OR)_4$ (R: propyl) into $Ba(OH)_2$ water solution, fine high-purity stoichiometric BT powders with an average particle size of 10 nm can be obtained directly.

Alkoxide hydrolysis

When metal alkoxides $M(OR)_n$ (M: metal atom, R: alkyl) are mixed in alcohol in an appropriate proportion, and water is added, the hydrolytic reaction produces alcohol and the metal oxide or metal hydrate. This is sometimes called the sol-gel method. The alkoxide method can produce very fine and very high purity powders. Since metal alkoxides are evaporative, purification is easily accomplished through distillation. Also high purity can be sustained during the hydrolic reaction because no other ion doping is necessary. The mechanisms of hydrolysis and condensation can be summarized as follows:

- *Hydrolysis*

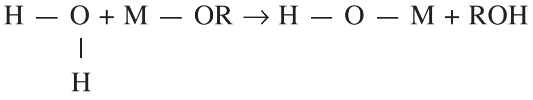

$$H - \underset{\substack{| \\ H}}{O} + M - OR \rightarrow H - O - M + ROH$$

- *Alkoxylation* (removal of H as an alcohol)

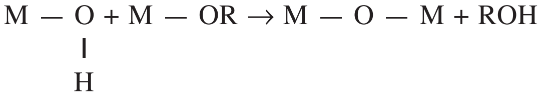

$$M - \underset{\substack{| \\ H}}{O} + M - OR \rightarrow M - O - M + ROH$$

- *Oxolation* (removal of H as water)

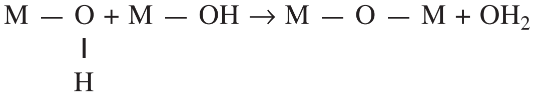

$$M - \underset{\substack{| \\ H}}{O} + M - OH \rightarrow M - O - M + OH_2$$

In order to obtain BT powders, $Ba(OC_3H_7)_2$ and $Ti(OC_5H_{11})_4$ are diluted with isopropyl alcohol (or benzene). Choosing an appropriate hydrolysis condition (pH), very fine stoichiometric BT powders with good crystallinity and a particle size of 10–100 Å can be obtained (agglomerate size = 1 μm). Also the hydrolytic process gives a specimen powder with purity more than 99.98%, leading to a remarkable increase in the permittivity of the sintered ceramic in comparison with samples prepared by oxide-mixing.[13] Table 10.3 lists examples of ferroelectric ceramic powders synthesized by alkoxide hydrolysis.

In the case of PZT preparation, Pb alkoxide is relatively difficult to obtain compared to Ti and Zr alkoxides. Thus, one way is to employ a two-stage method for convenience: $(Zr,Ti)O_2$ is prepared by the alkoxide method, and PbO is added later for use in the solid state reaction.[14] A partial sol-gel method combined with inexpensive ready-made nano size powders will be a promising direction to achieve reduction in production costs. Of course, the other way is to use Pb alkoxide; zirconium n-butoxide $Zr[O(CH_2)_3CH_3]_4$ and titanium isopropoxide $Ti[OCH(CH_3)_2]_4$ are added into lead acetyl acetonate $Pb(CH_3COCHCOCH_3)$ to obtain PZT precursor.

10.2.2 Sintering process

After being molded into a desired shape, the agglomerated powder body is fired at a high temperature (lower than the melting temperature). Accelerated diffusion of the constituent atoms on the fine particle surfaces due to the surface energy (surface tension) promotes crystal bonding at the contact interface between the two adjacent particles and provides sufficient mechanical strength to the ceramic without significant distortion from the initial molded shape. This firing process is called '*sintering*', which primarily eliminates pores and increases the ceramic density (see Fig. 10.14). Notice that the physical properties of the sintered body depend not only on the property of each fine crystalline particle, but also on the grain boundary and the pores. An example is found in the mechanical strength: mechanical fracture in ceramic bodies occasionally occurs at the grain boundary (intergranular type). In contrast, when the crystal itself has a strong cleavage character, the polycrystalline material shows higher mechanical strength.

Table 10.3 Ferroelectric powders synthesized by hydrolysis of alkoxides

Crystalline	$BaTiO_3$ $Ba(Zr,Ti)O_3$ $(Ba,Sr)TiO_3$
Amorphous	$Pb(Mg1/3Nb2/3)O_3$ $Ba(Zn1/3Nb2/3)O_3$ $Pb(Zr,Ti)O_3$ $(Pb,La)(Zr,Ti)O_3$

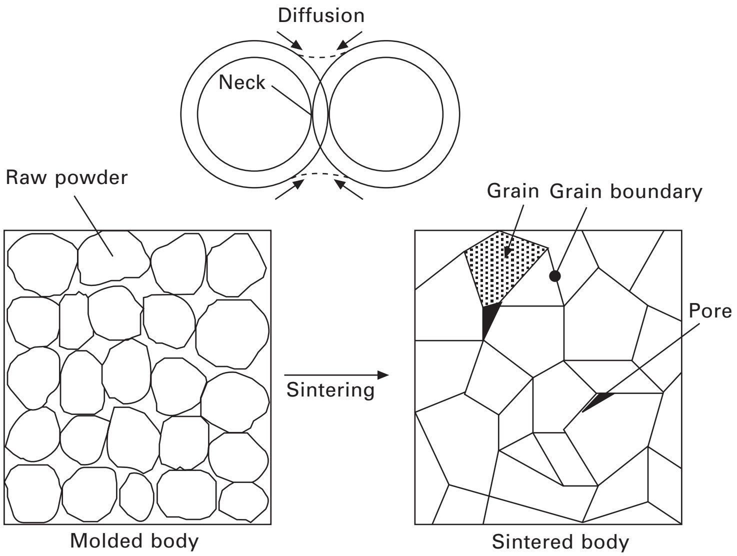

10.14 Schematic diagram of sintering process.

During sintering, the grains grow and the grain shape also changes significantly. However, it is well recognized that the raw powder characteristics strongly affect the manufacturing conditions and the final product characteristics. In general, sintering is accelerated with decreasing particle size of the raw powder (i.e., with increased specific surface area), because the driving force of sintering is related to the surface energy of the particles. Moreover, for fine powders, the necessary diffusion length of the atoms for sintering becomes shorter, which accelerates pore diffusion. This results in high density ceramics.

There have been many studies on grain growth. Reference 15 is recommended for further study. The following relationship between the grain size *D* and the sintering period *t* is generally used:

$$D^{\beta} - D_0^{\beta} \propto t. \qquad 10.3$$

In the case of normal grain growth, $\beta = 2$, and for abnormal grain growth, $\beta = 3$. Figure 10.15 shows the microphotographs of a PLZT 9/65/35 surface sintered at 1200 °C for 1 and 16 hours, starting from the oxalic acid/ethanol method.[16] Figure 10.16 shows a good linear relation between the sintering period and the square of the grain size.

Doping must also be considered. The main role of dopants is to decrease the sintering temperature, but additional effects such as suppression or enhancement of grain growth are sometimes observed. Excess PbO or Bi_2O_3 in Pb-based perovskites (PZT) inhibits grain growth. Dry doping (0.8 at%) is very effective in suppressing the grain size to less than 1 μm in $BaTiO_3$.[17]

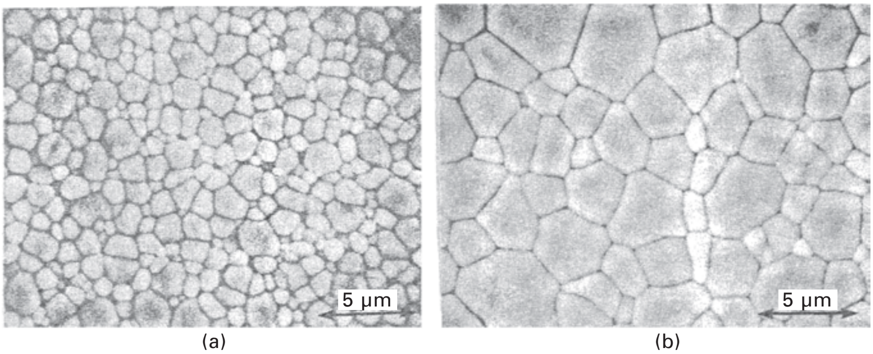

10.15 Grain growth in the PLZT ceramic 9/65/35 sintered for (a) 1 hour and (b) 16 hours.

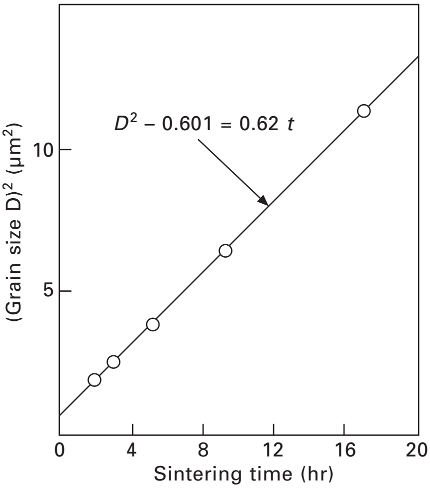

10.16 Grain growth in PLZT as a function of sintering time.

10.2.3 Single crystal growth

Since a detailed explanation of single crystal growth is given in Chapter 12, only a brief summary is provided here.

Quartz, LN, LT

The popular single crystals are quartz, grown by hydrothermal synthesis, and $LiNbO_3$ and $LiTaO_3$, by the Czochralski method. Recently, Nakamura *et al.* reported on a monomorph bending actuator fabricated from a thin plate of $LiNbO_3$ crystal, in which half of the thickness is reverse polarized to function like a bimorph.[18] Although this device is fragile and the bending displacement is not large, linearity in the displacement curve without hysteresis is attractive for some special applications such as scanning tunneling microscopes.

PZN–PT, PMN–PT, PZT

Since single crystal growth of PZT was rather difficult with a composition near the morphotropic phase boundary, $Pb(Zn_{1/3}Nb_{2/3})O_3$–$PbTiO_3$ (PZN–PT) and $Pb(Mg_{1/3}Nb_{2/3})O_3$–$PbTiO_3$ (PMN–PT) have been the focus of medical acoustic transducer applications, because large single crystals more than 1 cm^3 can be easily grown by a simple flux method, and enormously high electromechanical coupling factors (95%) and piezoelectric *d* constants (1570×10^{-12} C/N) can be obtained when they are poled in a special crystal direction.[19,20]

Rather than using the rather expensive Czochralski, hydrothermal or flux methods, inexpensive 'template grain growth' methods have been introduced for preparing BT, PZN–PT, PMN–PT, PZT, and Pb-free piezoelectric crystals. Figure 10.17 shows a large PMN–PT single crystal prepared from a seed $BaTiO_3$ crystal with solid-state single crystal growth (SSCG) (Ceracomp, Korea).[21]

10.2.4 Templated grain growth

Crystallographic texturing of polycrystalline ferroelectric ceramics exhibits significant enhancements in the piezoelectric response. Templated grain

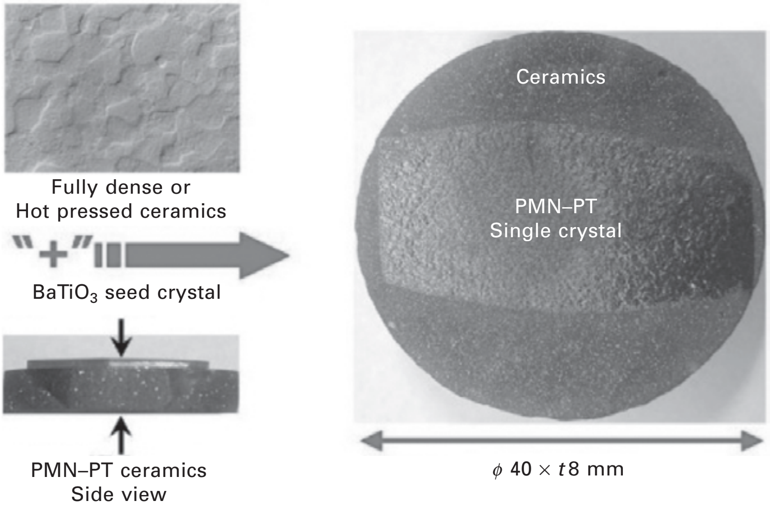

10.17 Growth of PMN–PT single crystals using SSCG (courtesy of Ho-Yong Lee).[21]

growth (TGG) is a technique for textured ceramics with single crystal-like properties. In TGG, nucleation and growth of the desired crystal on aligned single crystal template particles with heating results in an oriented material. To facilitate alignment during forming, template particles are anisometric in shape. To serve as the preferred sites for epitaxy and subsequent oriented growth of the matrix, the template particles need to be single crystal and chemically stable up to the growth temperature. Messing *et al.* reported that the resulting ceramics show texture levels up to 90%, and significant enhancements in the piezoelectric properties, in comparison with randomly-oriented ceramics.[22] For example, the piezoelectric *d* coefficient of textured PMN–32.5PT piezoelectrics was about 1150 pC/N, 2–3 times higher than randomly-oriented ceramics, and as high as 90% of the single crystal values.

Toyota Central Research Laboratory is using reactive-templated grain growth (RTGG) as a key processing technique for preparing textured Pb-free piezoelectric ceramics. Bismuth layer structured ferroelectric $ABi_4Ti_4O_{15}$ (A = $Na_{0\cdot5}Bi_{0\cdot5}$, Ca, Sr) ceramics with a highly preferred [001] orientation were fabricated with enhanced piezoelectric properties using $Bi_4Ti_3O_{12}$ platelets. Textured simple perovskite type ceramics were also prepared in $Bi_{0\cdot5}Na_{0\cdot5}TiO_3$ (BNT), $BaTiO_3$ and $K_{0\cdot5}Na_{0\cdot5}NbO_3$ (KNN)-based compositions with Lotgering's factor higher than 0.8, which exhibited enhanced electromechanical coupling coefficients and piezoelectric constants when compared with their randomly-oriented counterparts.[23] Figure 10.18(a) and (b) shows the strain versus electric field curves and the displacement change with temperature for textured and randomly-oriented piezo-ceramics, (K,Na,Li)(Nb,Ta,Sb)O_3.[24] Note the significant enhancement in the strain level in the textured ceramic, which is almost comparable with the PZT ceramic strain.

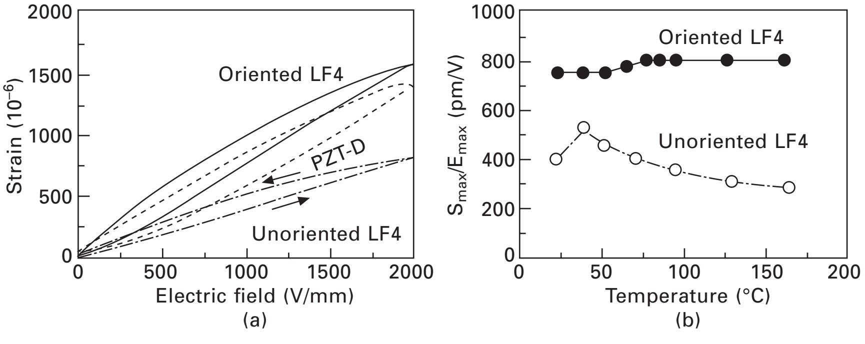

10.18 Strain versus electric field curves (a), and the displacement change with temperature (b), for textured and randomly-oriented piezo-ceramics, (K,Na,Li)(Nb,Ta,Sb)O_3.[24]

10.3 Device designing

We introduce several device designs in this section, including single disks, multilayers, composites and thin/thick films.

10.3.1 Single disks

Single disk devices are not practically found these days because of low efficiency in (performance/space). However, they are still important for laboratory experiments.

10.3.2 Multilayers

To achieve a low driving voltage, miniaturization and hybridization of the devices, ferroelectric ceramic multilayer structures have been investigated intensively for capacitor, actuator and electrooptic applications. Key words for future trends will be 'finer' and 'hybridization'. Layers thinner than 3 μm, which is currently used in multilayer capacitors, can also be introduced in actuator devices technologically instead of the present 60–80 μm thick sheets. A typical actuator with 10 mm length exhibits 10 μm displacement (strain of 0.1%) with a fundamental resonance frequency around 100 kHz. Non-uniform configurations or hetero-structures of the materials, layer thickness or the electrode pattern can be adopted for practical devices.

There are two techniques for making multilayered ceramic devices: the cut-and-bond method and the tape-casting method. The tape-casting method has been widely used for multilayer capacitor fabrication, and requires expensive fabrication facilities and sophisticated techniques, but is suitable for mass production of more than 100 000 pieces per month.

As shown in Fig. 10.19, a multilayer structure is composed of alternate ferroelectric ceramic and internal electrode layers fabricated by cofiring. An adjacent pair of electrodes composes a unit displacement element, which is connected in parallel by the external electrode up to hundreds of layers. Figure 10.20 shows a flowchart of the manufacturing process of multilayer ceramic actuators. Green sheets are prepared in two steps: slip preparation of the ceramic powder and a doctor blade process. The slip is made by mixing the ceramic powder with solvent, deflocculant, binder and plasticizer. The slip is cast into a film under a special straight blade, a 'doctor blade', whose distance above the carrier determines the film thickness. After drying, the film, called a green sheet, has the elastic flexibility of synthetic leather. The volume fraction of the ceramic in the polymer matrix at this point is about 50%. The green sheet is then cut into an appropriate size, and internal electrodes are printed using Ni (for BT-based capacitors), silver-paladium, platinum or Cu ink (for PZT-based transducers). Several tens to hundreds of

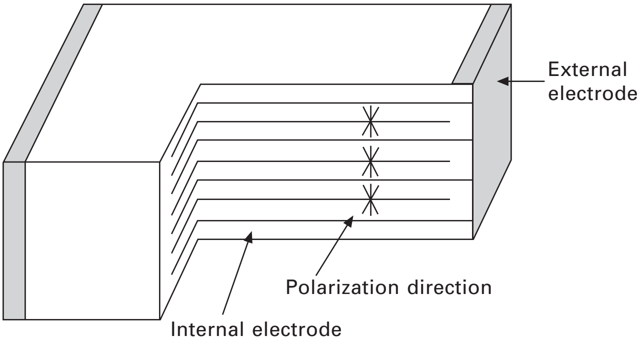
External electrode
Polarization direction
Internal electrode

10.19 Structure of a multilayer actuator.

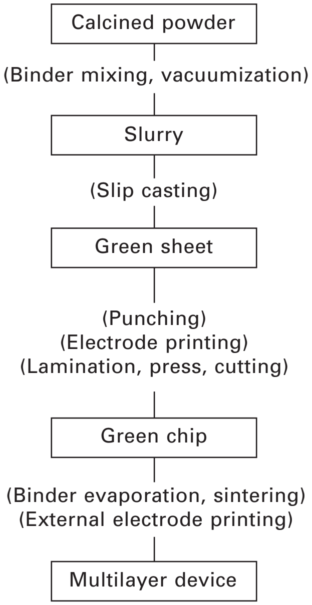
Calcined powder
(Binder mixing, vacuumization)
Slurry
(Slip casting)
Green sheet
(Punching)
(Electrode printing)
(Lamination, press, cutting)
Green chip
(Binder evaporation, sintering)
(External electrode printing)
Multilayer device

10.20 Fabrication process for a multilayer ceramic actuator.

such layers are then laminated and pressed using a hot press. After cutting into small chips, the green bodies are sintered at around 1200 °C in a furnace, taking special care to control binder evaporation around 500 °C. The sintered chips are then polished, externally electroded, lead wires are attached, and finally the chips are coated with a waterproof spray.

Zheng *et al*. reported on the heat generation from multilayer piezoelectric ceramic actuators of various sizes.[25] The temperature change was monitored in actuators driven at 3 kV/mm and 300 Hz. Figure 10.21 shows the saturated temperature plotted as a function of V_e/A, where V_e is the effective volume

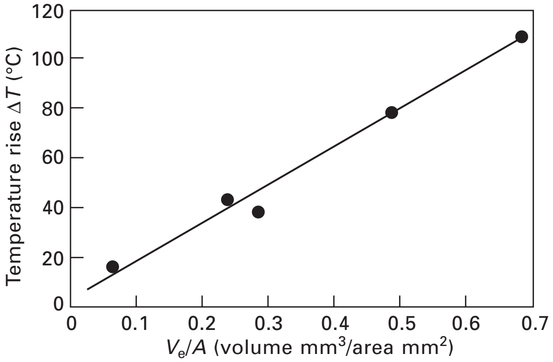

10.21 Temperature rise vs. V_e/A (3 kV/mm, 300 Hz), where V_e is the effective volume generating the heat and A is the surface area dissipating the heat.

(electroded portion of the actuator) and A is the surface area. This linear relation is reasonable because the volume V_e generates the heat and this heat is dissipated through the area A. Thus, if you need to suppress the heat, a small V_e/A (flat and cylinder shapes are better than cube and solid rod structures, respectively) is preferred.

10.3.3 Unimorphs/bimorphs

Unimorph and *bimorph* devices are defined by the number of piezoelectric ceramic plates: only one ceramic plate is bonded onto an elastic shim, or two ceramic plates are bonded together, respectively. Mainly the bimorphs are considered here. The bimorph causes bending deformation because two piezoelectric plates are bonded together and each plate produces extension or contraction under an electric field. This effect is employed for various speakers. The bimorph induces voltage for a bending deformation, which can be used for accelerometers. Since the fabrication process is simple (two ceramic plates are just bonded using a resin) and large magnification of the displacement is easily obtained, this structure has been widely used. However, the drawbacks include a low response speed (1 kHz) and low generative force due to the bending mode (tensile stress concentrates on the top of the piezo-plate). A metallic sheet (called the shim) is occasionally sandwiched between the two piezo-ceramic plates to increase the reliability, that is, the structure is maintained even if the ceramic fractures (Fig. 10.22). Also notice the tapering of the bimorph, which increases the response frequency by maintaining the tip displacement magnitude.

There have been many reports on equations describing the tip displacement and the resonance frequency. Summaries are provided here. Figure 10.23

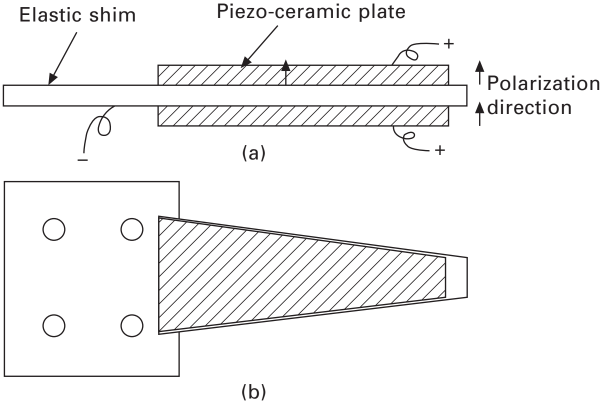

10.22 Fundamental structure of a piezoelectric bimorph.

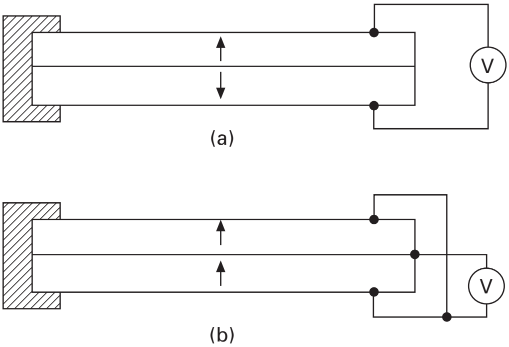

10.23 Two types of piezoelectric bimorphs: (a) the non-parallel polarization type and (b) the parallel polarization type.

illustrates two bimorph designs without shims. Two poled piezo-ceramic plates, $t/2$ in thickness (i.e., t is the total thickness) and L in length, are bonded with their polarization directions opposite to each other (a) or parallel to each other (b). According to the configuration, the tip displacement δ under a voltage V is provided as follows when one end is clamped (cantilever condition):

$$\delta = (3/2)\, d_{31}\, (L^2/t^2)\, V, \qquad 10.4a$$

$$\delta = 3d_{31}\, (L^2/t^2)\, V. \qquad 10.4b$$

Notice that this difference comes from the electrode gap difference: t in (a) and $t/2$ in (b), leading to the double electric field in (b). For both cases the fundamental resonance frequency is determined by the total thickness t as,[26]

$$f = 0.161\, (t/L^2)\, (\rho\, s^E_{11})^{-1/2}. \qquad 10.5$$

As can be anticipated, the bimorph drive is inevitably accompanied by a rotational motion. To obtain a perfect parallel motion a special mechanism must be employed. Figure 10.24 shows such a bimorph structure. A complex bimorph proposed by Ampex has divided electrodes electrically connected oppositely at the tip and bottom (supporting) parts so as to compensate the canting angle at the bottom by the opposite bend at the tip.[27] The bimorph also included a sensor function: the sensor electrode can detect the voltage generated in proportion to the magnitude of bend.

10.3.4 Flextension/hinge lever amplification mechanisms

Market research conducted by the author in the late 1990s suggested that the target specifications for actuators required by the market will be:

- Stroke = 100 μm
- Force = 100 N
- Response time = 100 μ sec

Neither multilayer nor bimorph actuators can satisfy the above specifications directly. A multilayer needs a displacement amplification mechanism, while a bimorph is required to improve its force and response speed.

Hinge-lever and flextension type displacement amplification mechanisms are adopted for the multilayer actuators. The most famous hinge-type design is the one utilized in a dot-matrix printer developed by NEC, as depicted in Fig. 10.25(a).[28] Figure 10.25(b) shows a flextensional type developed by Cedrat.[29]

A composite actuator structure called the 'moonie' or 'cymbal' has been developed to amplify the pressure sensitivity and the small displacements induced in a piezoelectric ceramic.[30] The moonie/cymbal has intermediate characteristics between the conventional multilayer and bimorph actuators;

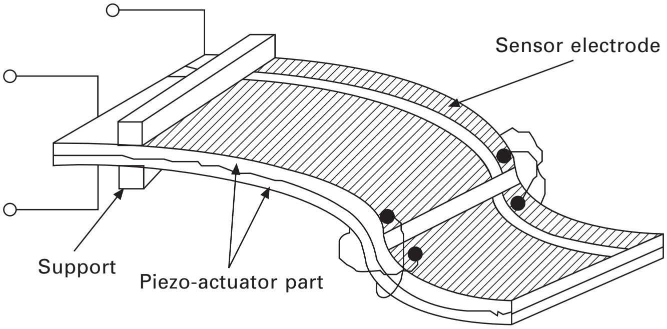

10.24 Bimorph structure for a perfectly parallel motion with a position sensing feedback function (Ampex).

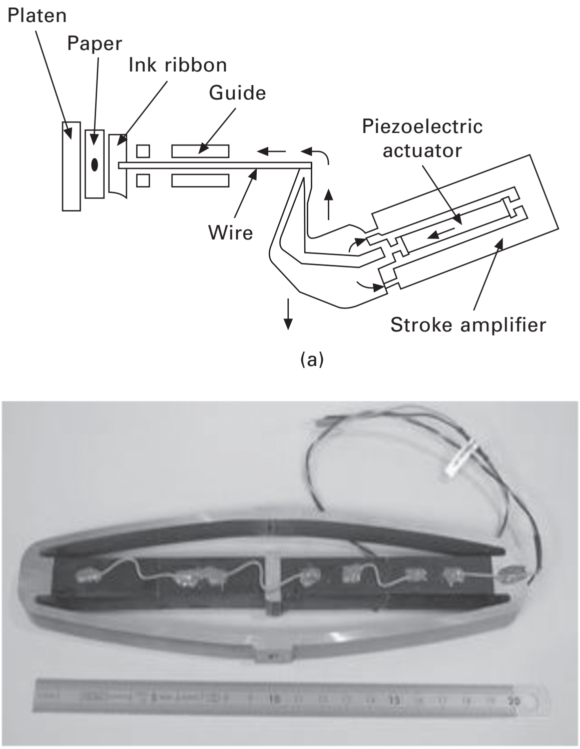
Platen
Paper
Ink ribbon
Guide
Piezoelectric actuator
Wire
Stroke amplifier

(a)

(b)

10.25 (a) A hinge-lever type displacement amplification mechanism (NEC), and (b) a flextensional amplified piezoelectric actuator (Cedrat).

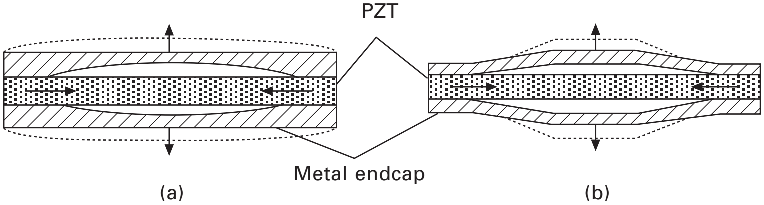
PZT
Metal endcap

(a) (b)

10.26 Structures of a moonie (a) and a modified design cymbal (b).

it exhibits an order of magnitude larger displacement (100 μm) than the multilayer, and much larger generative force (10 kg · *f*) with quicker response (100 μsec) than the bimorph. The moonie device consists of a thin multilayer ceramic element and two metal plates with a narrow moon-shaped cavity bonded together (Fig. 10.26(a)). The moonie with a size of 5 mm × 5 mm × 2.5 mm can generate a 20 μm displacement under

60 V, which is eight times as large as the generative displacement of a multilayer of the same size. By modifying the endcap design (cymbal type) as shown in Fig. 10.26(b), twice the displacement can be obtained.[31] Also the generative displacement is rather uniform, independent of the position from the center of the endcap. Another advantage of the cymbal over the moonie is its easy fabrication process. One-step punching can make endcaps from a metal plate.[32]

10.3.5 Flexible composites

When needle or plate-shaped piezoelectric ceramic bodies are arranged and embedded in a polymer matrix, functional composites can be fabricated that provide enhanced sensitivity by keeping the actuation function. Figure 10.27(a) shows such a 1-3 composite device, where PZT rods are arranged in a polymer in a two-dimensional array. The simplest composite from a fabrication viewpoint is a 0-3 connectivity type, which is made by dispersing piezoelectric ceramic powders uniformly in a polymer matrix (Fig. 10.27(b)). The fabrication processes are classified into a melting and a rolling method.[33] Figure 10.28 shows a flowchart for the fabrication processes. The powders are mixed with molten polymer in the first method, while the powders are rolled into a polymer using a hot-roller in the second method. The connectivity concept, fabrication processes, and the performance for 1-3 composites are detailed in Chapter 9.

10.3.6 Thin/thick films

Film manufacturing techniques

Techniques for fabrication of oxide thin films are classified into physical and chemical processes:

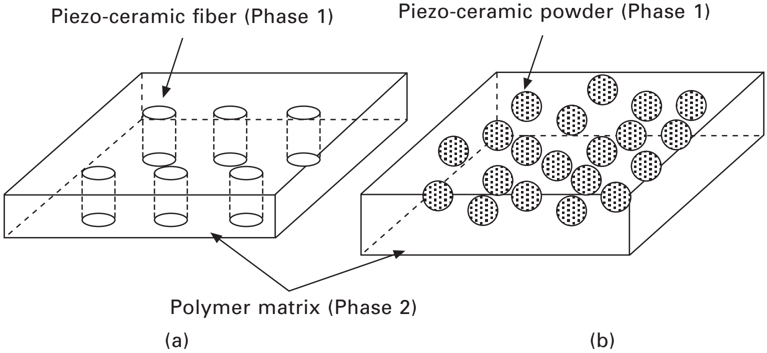

10.27 PZT:polymer composites: (a) 1-3 connectivity and (b) 0-3 connectivity.

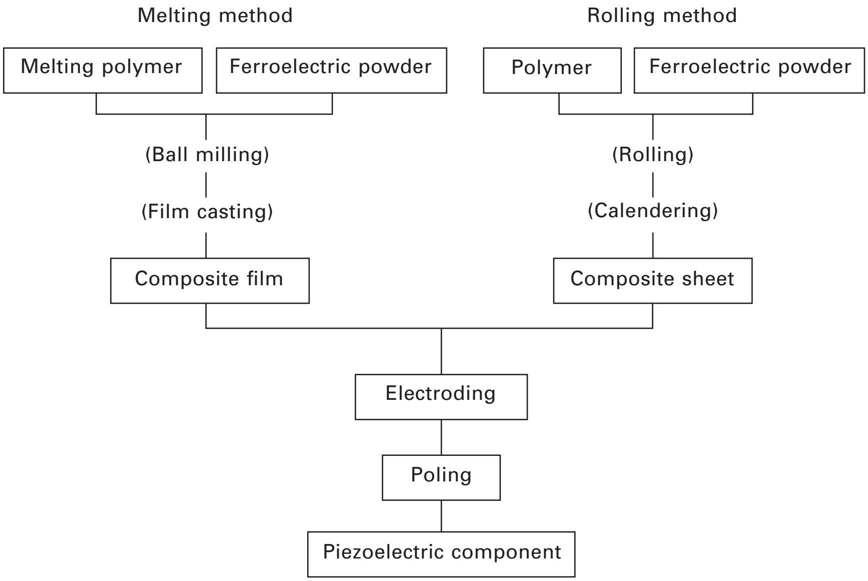
Melting method
Rolling method
Melting polymer
Ferroelectric powder
Polymer
Ferroelectric powder
(Ball milling)
(Film casting)
(Rolling)
(Calendering)
Composite film
Composite sheet
Electroding
Poling
Piezoelectric component

10.28 Fabrication process for PZT:polymer composites.

- Physical processes
  - Electron beam evaporation
  - RF sputtering, DC sputtering
  - Ion beam sputtering
  - Ion plating
- Chemical processes
  - Sol-gel method (dipping, spin coating, etc.)
  - Chemical vapor deposition (CVD)
  - MOCVD
  - Liquid phase epitaxy, melting epitaxy, capillary epitaxy, etc.

Sputtering has been most commonly used for ferroelectric thin films such as $LiNbO_3$, PLZT,[34] and $PbTiO_3$.[35] In a magnetron sputtering apparatus, heavy Ar plasma ions bombard the cathode (target) and eject its atoms. These atoms are deposited uniformly on the substrate in an evacuated enclosure. Choosing a suitable substrate and deposition condition, single crystal-like epitaxially deposited films can be obtained. The sol-gel technique has also been employed for processing PZT films.[36] Applications of thin film ferroelectrics include memories, surface acoustic wave devices, piezo-sensors and micro-mechatronic or MEMS (micro electro-mechanical system) devices. Chapter 13 provides the details on thin film piezoelectrics.

Uchino's group at Penn State University proposed that (001) epitaxially-oriented PZT rhombohedral composition films are most suitable from the application viewpoint. Kalpat *et al*. demonstrated (001) and (111)-oriented films on the same Pt-coated Si substrate by changing the rapid thermal annealing profile.[37] Figure 10.29(a) and (b) shows the PZT (70/30) films with (001) and (111) orientations.

MEMS application

The micromachining process used to fabricate the PZT micropump is illustrated in Fig. 10.30. The etching process for the silicon:PZT unit is shown on the left-hand side of the figure and that for the glass plate on the right side. A schematic of the micropump for a blood tester is shown in Fig. 10.31. The

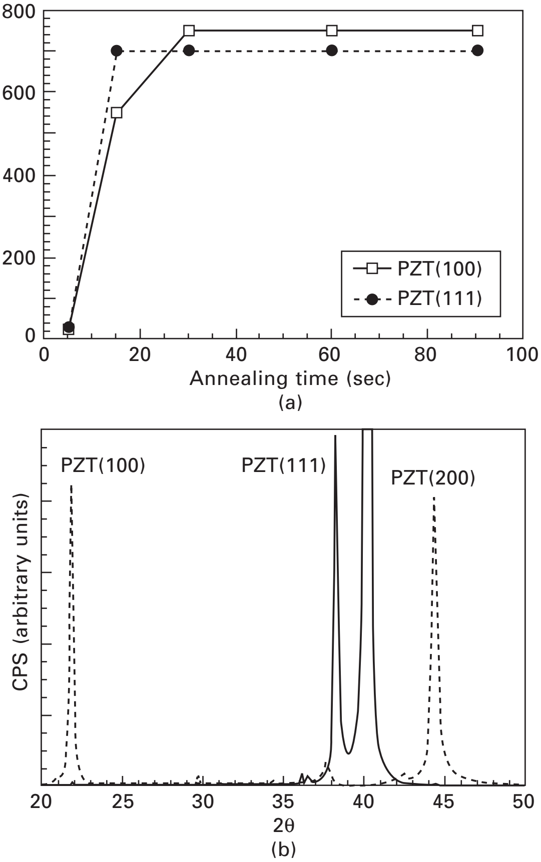

10.29 Epitaxially grown rhombohedral (70/30) PZT films with (001) and (111) orientations: (a) optimum rapid thermal annealing profiles, and (b) x-ray diffraction patterns for films grown according to these profiles.[37]

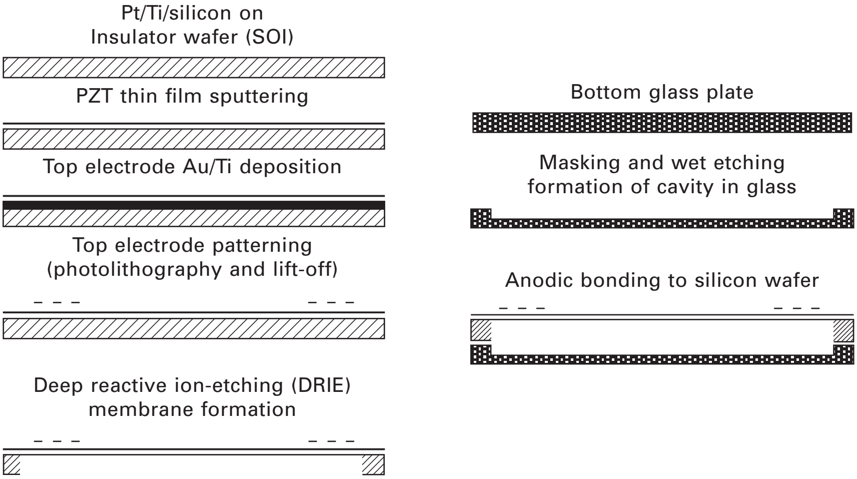
Pt/Ti/silicon on
Insulator wafer (SOI)
PZT thin film sputtering
Top electrode Au/Ti deposition
Top electrode patterning
(photolithography and lift-off)
Deep reactive ion-etching (DRIE)
membrane formation
Bottom glass plate
Masking and wet etching
formation of cavity in glass
Anodic bonding to silicon wafer

10.30 The micromachining process used to fabricate a PZT micropump.[37]

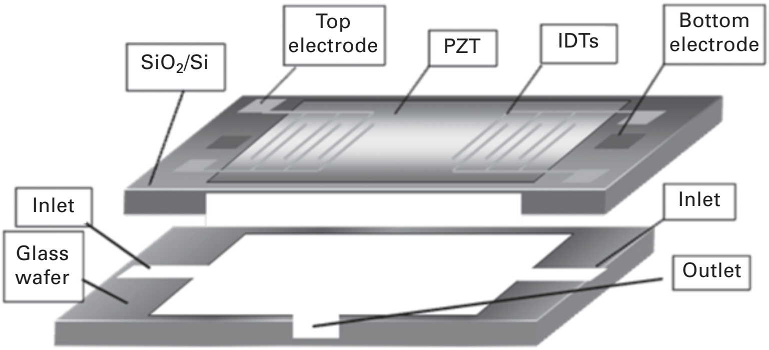
Top
electrode
PZT
IDTs
Bottom
electrode
SiO_2/Si
Inlet
Glass
wafer
Inlet
Outlet

10.31 A schematic diagram of the structure of a PZT micropump.[37] Actual size: 4.5 mm × 4.5 mm × 2 mm.

blood sample and test chemicals enter the system through the two inlets, identified in Fig. 10.31, are mixed in the central cavity, and finally are passed through the outlet for analysis. The movement of the liquids through the system occurs through the bulk bending of the PZT diaphragm in response to the drive potential provided by the interdigital surface electrodes.

Constraints in thin/thick films

The thin film structure is inevitably affected by four significant parameters:

1. *Size constraints*: Similar to a powder sample, there may exist a critical film thickness below which the ferroelectricity would disappear. No research has yet been conducted to investigate this (see Section 10.4).
2. *Stress from the substrate*: Tensile or compressive stress is generated due to thermal expansion mismatch between the film and the substrate, sometimes leading to a higher coercive field for domain reorientation. Curie temperature is also modified at a rate of 50 °C per 1 GPa.
3. *Epitaxial growth*: Crystal orientation dependence should also be considered, similar to the case in single crystals. An example can be found in a rhombohedral composition PZT, which is supposed to exhibit the maximum performance when the P_s direction is arranged 57° cant from the film normal direction (i.e., (001) crystallographic orientation).
4. *Preparation constraint*: Si substrate requires low sintering temperature of the PZT film. Typically, 800 °C for a short period is the maximum for preparing the PZT, which may limit the crystallization of the film, leading to the reduction of the properties. A metal electrode on a Si wafer such as Pt also limits the crystallinity of the PZT film.

Siemens group reported intriguing grain/domain texture generated by the internal stress, when decreasing the layer thickness of multilayer devices. Two types of multilayer PZT actuators were prepared with their layer thicknesses of 280 and 17 μm, as shown in Figs 10.32(a) and (b).[38] This PZT composition has tetragonal symmetry, and when the x-ray diffraction pattern was taken for both samples from the top surface, Fig. 10.33(a) was obtained. The sample with 280 μm layer thickness seemed to have no texture by showing the x-ray intensity ratio roughly 1:2 for the (001) and (100) reflections, while the intensity of the (001) reflection was very high for the sample with 17 μm layer thickness. The high intensity of the (001)

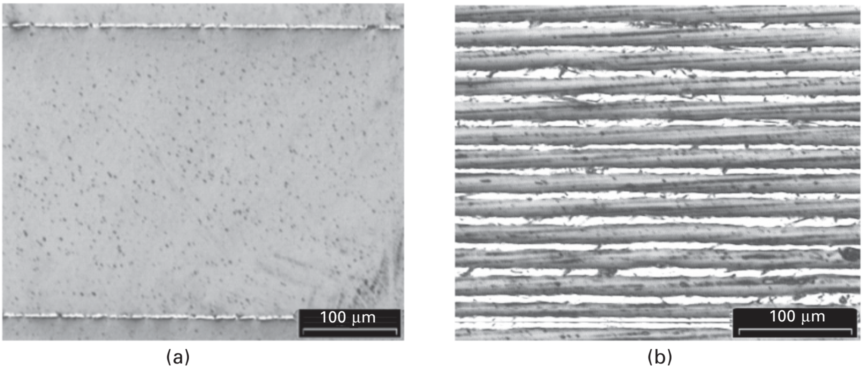

(a) (b)

10.32 PZT multilayer actuators with their layer thicknesses of (a) 280 and (b) 17 μm.[38]

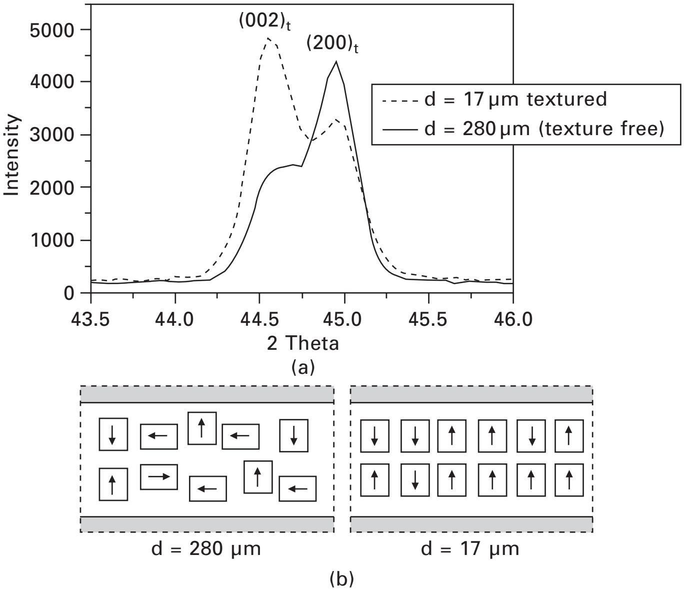

10.33 (a) Two x-ray diffraction patterns for the multilayer actuators with 280 and 17 μm layer thicknesses. (b) Two domain texture models for the multilayer actuators with 280 and 17 μm layer thicknesses.[38]

reflection for the sample with 17 μm layer thickness indicates the polarization direction aligned normal to the layer plane, as schematically shown in Fig. 10.33(b).

If this domain texture was induced by the mechanical stress through the manufacturing process, the thermal expansion difference between the PZT and metal electrode may be the origin. Because the metal electrode shrinkage is larger than the PZT during the cooling-down process, the PZT layer will experience compressive stress (the thinner layer sample will experience larger compressive stress), leading to domain alignment normal to the layer surface (Fig. 10.34).

10.4 Size effect on ferroelectricity

So-called 'fine ceramic' used in the 1980s has been rephrased as 'nano technology' in the 2000s; that is, manufacturing ceramics which possess controlled-grain size or very fine grains (note that 'nano' does not mean a real nano-meter range, but a micron range). In parallel, so-called 'amorphous ferroelectric' was studied in the 1980s. Lines theoretically suggested that significantly large permittivity might be realized when a ferroelectric ceramic

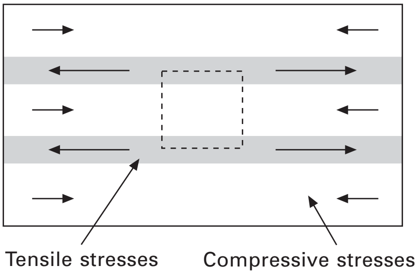

10.34 Domain texture creation model for the multilayer actuators with 17 μm layer thickness.[38]

is prepared in an amorphous form.[39] Note that he was not suggesting that the amorphous form of this material exhibits 'ferroelectric' properties. All results reported during the 1980s concluded that there is little possibility to realize 'amorphous' ferroelectrics. Unlike 'ferro-magnetics' which originated from short-range spin-exchange coupling, 'ferro-electrics' originated from a cooperative phenomenon based on rather long-range Coulombic coupling. In conclusion, relatively large crystalline size (sub-micron meter) seems to be required to realize 'ferroelectricity', by annealing amorphous ferroelectrics to increase the crystallinity.[40]

Small particle 'nano' technology seems to eliminate the ferroelectric functionality, unfortunately. However, thin film technology with nanometer thickness seems to be able to realize good ferroelectricity. Further experimental and theoretical studies are required to clarify the following:

- 3D problem: What is a critical particle size below which ferroelectricity will disappear?
- 2D problem (1D connectivity): What is a critical fiber diameter below which ferroelectricity will disappear?
- 1D problem (2D connectivity): What is a critical film thickness below which ferroelectricity/piezoelectricity will disappear?

10.4.1 Grain size effect on ferroelectricity

To understand the grain size dependence of the dielectric properties, we must consider two size regions: the μm range in which a multiple domain state becomes a mono-domain state, and sub-μm range in which the ferroelectricity becomes destabilized.

Figure 10.35 shows the transverse field-induced strains of 0.8 at% Dy-doped fine grain ceramic $BaTiO_3$ (grain diameter around 1.5 μm) and of the undoped coarse grain ceramic (50 μm), as reported by Yamaji *et al.*[17] As the grains become finer, under the same electric field, the absolute value of the strain decreases and the hysteresis becomes smaller. This is explained by the

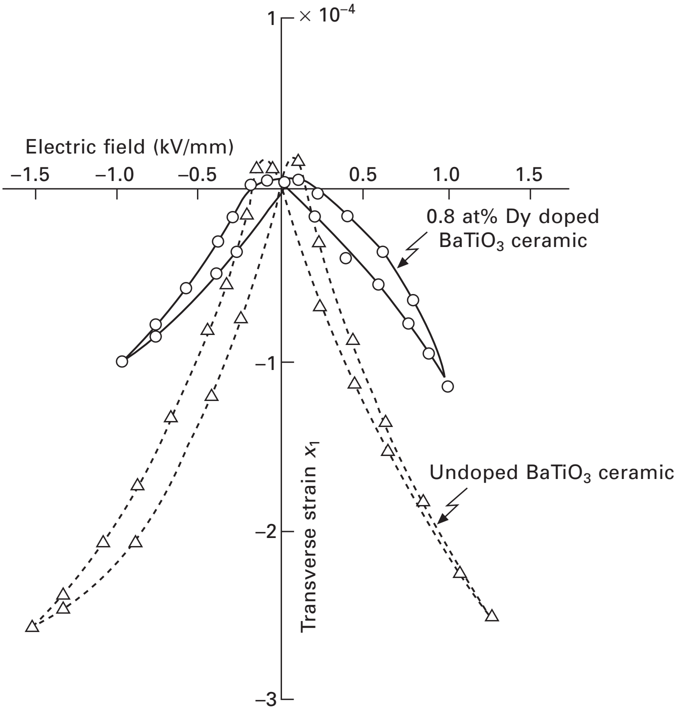

10.35 Electric field induced strain curves in Dy-doped and undoped $BaTiO_3$ ceramic samples.[17]

increase in coercive field for 90° domain rotation with decreasing grain size. The grain boundaries (with many dislocations on the grain boundary) 'pin' the domain walls and do not allow them to move easily. Also the decrease of grain size seems to make the phase transition of the crystal much more diffuse. Figure 10.36 shows the temperature dependence of the piezoelectric coefficient d_{33}. Although the absolute value of d_{33} decreases in the Dy-doped sample, the temperature dependence is remarkably improved for practical applications. It should be noted that Yamaji *et al.* experiment cannot separate the effect due to intrinsic grain size from that due to dopants.

Uchino and Takasu studied the effects of grain size on PLZT.[16] They obtained PLZT (9/65/35) powders by coprecipitation. Various grain sizes were prepared by hot-pressing and by changing sintering periods, without using any dopants. PLZT (9/65/35) shows significant dielectric relaxation (frequency dependence of the permittivity) below the Curie point of about 80 °C, and the dielectric constant tends to be higher at lower frequency. Figure 10.37 shows the dependence of the peak dielectric constant on grain size. For grain size larger than 1.7 μm, the dielectric constant decreases with decreasing grain size. Below 1.7 μm, the dielectric constant increases rapidly.

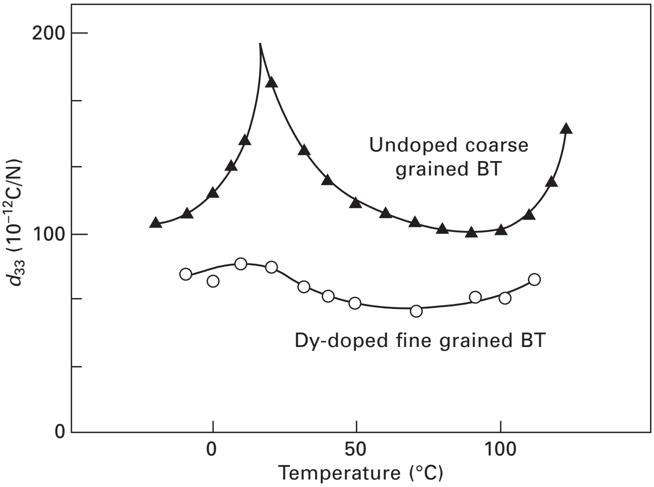

10.36 Temperature dependence of the piezoelectric d_{33} in Dy-doped and undoped $BaTiO_3$ ceramics.[17]

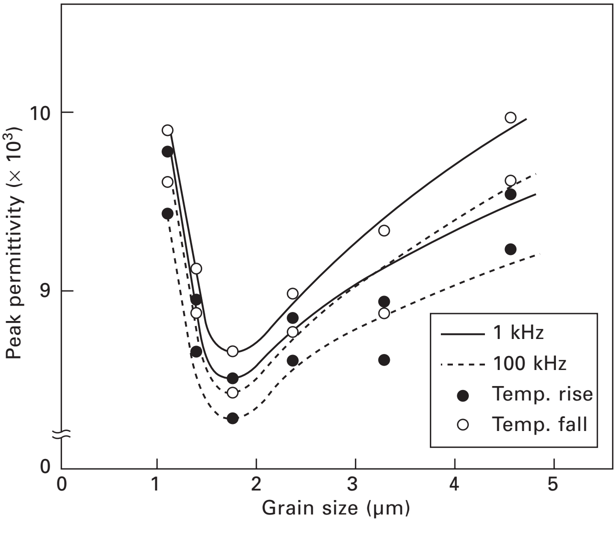

10.37 Grain size dependence of the peak permittivity in PLZT 9/65/35.[16]

Figure 10.38 shows the dependence of the longitudinal field-induced strain on the grain size. As the grain size becomes smaller, the maximum strain decreases monotonically. However, when the grain size becomes less than 1.7 μm, the hysteresis is reduced. This behavior can be explained as follows: with decreasing grain size, (anti)ferroelectric (ferroelastic) domain walls

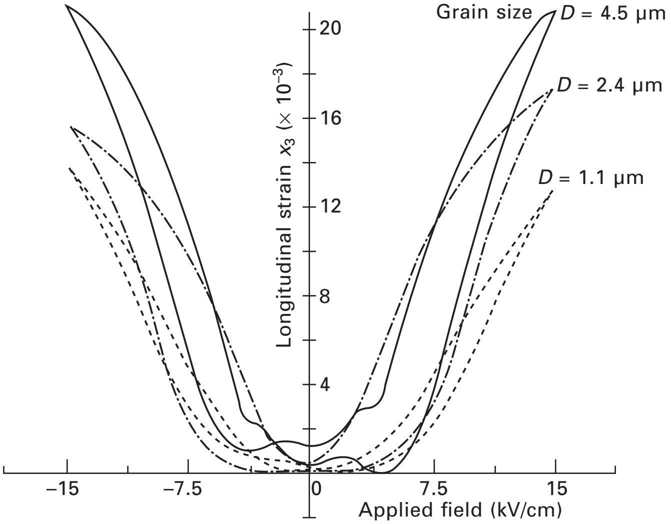

10.38 Grain size dependence of the induced strain in PLZT ceramics.[16]

become difficult to form in the grain, and the domain rotation contribution to the strain becomes smaller (multidomain–monodomain transition model). The critical size is about 1.7 μm. However, note that the domain size is not constant, but is dependent on the grain size, and that in general the domain size decreases with decreasing grain size.

10.4.2 3D particle size effect on ferroelectricity

Regarding the much smaller grain/particle size range, Uchino *et al.* reported a number of informative experiments. Figure 10.39 shows the most cited figure in recent nanotechnology papers. The degree of tetragonality (i.e., *c*/*a* ratio) is plotted as a function of particle size in pure $BaTiO_3$ at room temperature.[41] The *c*/*a* value decreases dramatically below 0.2 μm and becomes 1 (i.e., cubic!) at 0.12 μm, defined as a critical particle size. Figure 10.40 shows the temperature dependence of the *c*/*a* ratio for various particle size powders. This demonstrates the correlation between the critical particle size and the Curie temperature, which decreases with decreasing particle size. This paper clearly indicated that the ferroelectricity disappears when reducing the three-dimensional particle size. It is interesting to note that the tetragonality between 1 and 1.0025 was not observed experimentally, suggesting that the first-order phase transition seems to be sustained regardless of the crystalline size. The tetragonality change curve is simply shifted to lower temperature with reducing particle size.

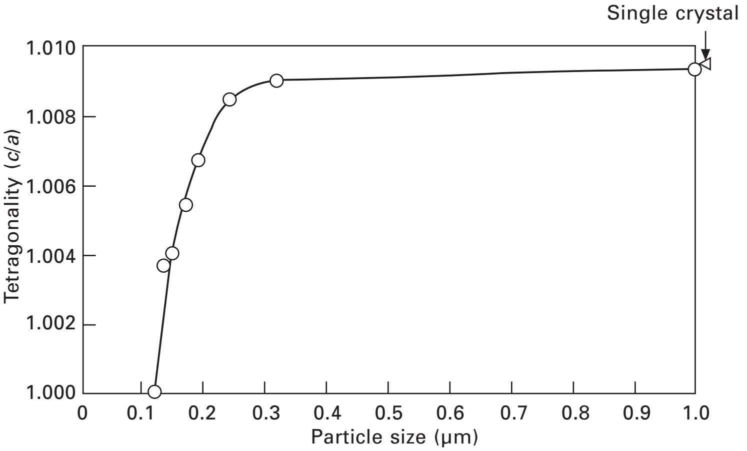

10.39 Particle size dependence of the tetragonality in $BaTiO_3$ at room temperature. Note that the tetragonal crystal distortion disappears below a critical particle size around 0.1 μm.[41]

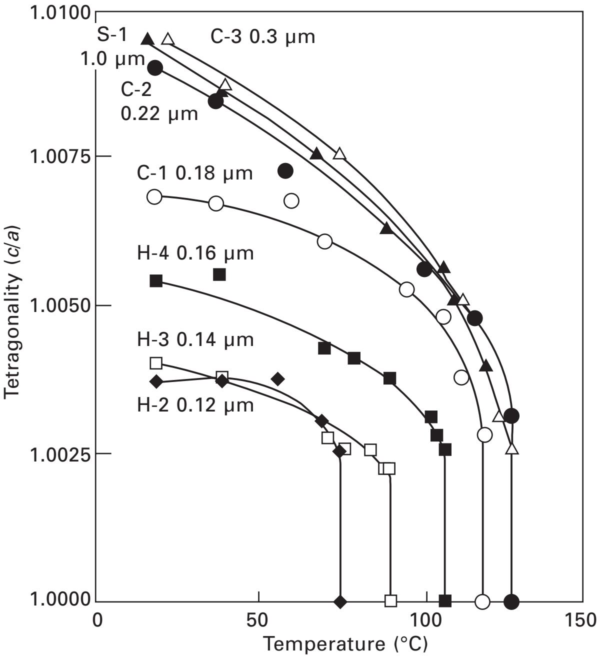

10.40 Temperature dependence of the tetragonality in $BaTiO_3$ for various particle size samples.[41]

Though multiple recent papers discussed whether the critical particle size of 0.12 μm is too small or too large, experimentally, it is not the key point, because there is a big ambiguity in determining the average particle size as Ref. 41 explicitly explained. Specific surface area, X-ray diffraction, electron microscope, or optical microscope provides a large deviation in the particle size of more than several times.

A similar critical particle size was also reported in $(Ba,Sr)TiO_3$,[42] $(Ba,Pb)TiO_3$[43] and for antiferroelectric $PbZrO_3$.[44] Figure 10.41 shows the relationship between the critical particle size D_{crit} and the Curie (or Neel) temperature T_C for these materials. An important empirical rule was obtained:

$$D_{crit} \times (T_C - \text{Room Temp.}) = \text{Constant.} \qquad 10.6$$

Although there have been many reports on the critical grain/particle size, it seems to be true that there is a kind of critical size below which the ferroelectricity disappears (i.e., the crystal becomes cubic). No satisfactory explanation has yet been presented so far. One possible explanation is based on a hydrostatic pressure model. In general, the ferroelectric transition temperature decreases sharply (50 °C/MPa) with increasing hydrostatic pressure. Systematic data can be found in Samara's papers, who used external hydrostatic oil pressure.[44] The effective surface tension γ on a fine particle causes a hydrostatic pressure p intrinsically:[45]

$$p = 2\gamma/R \quad (R\text{: particle radius}) \qquad 10.7$$

From the critical particle size D_{crit} (= $2R_{crit}$) and the critical hydrostatic pressure p_{crit}, above which the cubic structure is realized at room temperature, we can calculate the effective surface tension γ as listed in Table 10.4. The γ value is almost constant for all perovskite ferroelectrics. The γ value, 50

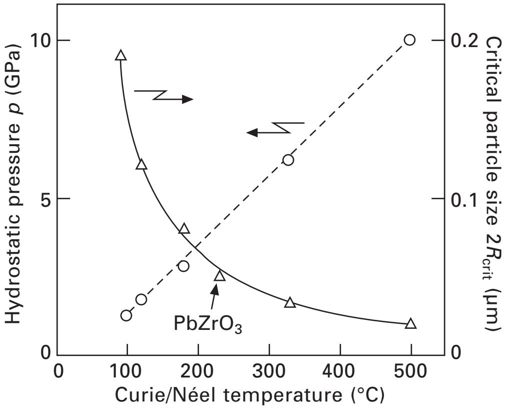

10.41 Relationship between the critical particle size D_{crit} or the critical hydrostatic pressure and the phase transition temperature.

Table 10.4 Critical particle size, critical hydrostatic pressure and the surface tension energy for various perovskites. ($p = 2\gamma/R$)[45]

Material	Curie Temp. (°C)	$2R_{crit}$ (μm)	p_{crit} (GPa)	γ (N/m)
$Ba_{0.9}Sr_{0.1}TiO_3$	95	0.19	1.2	57
$BaTiO_3$	125	0.12	1.8	54
$Ba_{0.85}Pb_{0.15}TiO_3$	180	0.08	2.9	58
$Ba_{0.5}Pb_{0.5}TiO_3$	330	0.032	6.2	50
$PbTiO_3$	500	0.02	10	50

times larger than that of non-polar oxides (such as MgO), may be due to the additional energy from the surface charge contribution, and/or from a crystallographically different skin-phase on the particle surface (i.e., core-shell model).

In conclusion, the reader needs to understand that there seems to be a critical particle size for a ferroelectric ceramic, below which the ferroelectricity and piezoelectricity will disappear.

10.5 References

1. K.-H. Hellwege and A. M. Hellwege (eds): *Landolt-Börnstein: Numerical Data and Functional Relationships in Science and Technology*. Group III, Volume 11. Springer-Verlag, New York (1979).
2. B. Jaffe, W. R. Cook and H. Jaffe: *Piezoelectric Ceramics*, Academic Press, New York (1971).
3. K. Uchino and S. Nomura: *Jpn. J. Appl. Phys.* **18**, 1493 (1979).
4. K. Abe, O. Furukawa and H. Inagawa: *Ferroelectrics* **87**, 55 (1988).
5. K. Uchino: *Ferroelectric Devices*, Marcel Dekker/CRC Press, New York (2000).
6. A. Hagimura and K. Uchino: *Ferroelectrics* **93**, 373 (1989).
7. S. Takahashi and S. Hirose: *Jpn. J. Appl. Phys.* **32**, Pt. 1, No. 5B, 2422 (1993).
8. K. Uchino, J. Zheng, A. Joshi, Y. H. Chen, S. Yoshikawa, S. Hirose, S. Takahashi and J. W. C. de Vries: *J. Electroceramics* **2**, 33 (1998).
9. T. Kato: *Fine Ceramics Technology*, Vol. 3 *Fabrication Technology of Ceramic Powder and Its Future*, Industry Research Center, Japan (1983).
10. M. Lejeune and J. P. Boilot: *Ferroelectrics* **54**, 191 (1984).
11. S. L. Swartz, T. R. Shrout, W. A. Schulze and L. E. Cross: *J. Amer. Ceram. Soc.* **67**, 311 (1984).
12. M. Tanada, H. Yamamura and S. Shirasaki: *Abstract 22nd Jpn. Ceram. Soc. Fundamental Div.* 3B5, 81 (1984).
13. Y. Ozaki: *Electronic Ceramics* **13**, Summer, 26 (1982).
14. K. Kakegawa, J. Mohri, M. Imai, S. Shirasaki and K. Tekahashi: *Abstract 21st Jpn. Ceram. Soc. Fundamental Div.* 2C6, 100 (1983).
15. H. Abe: *Recrystallization*, Mater. Sci. Series 2, Kyoritsu Pub., Tokyo (1969).
16. K. Uchino and T. Takasu: *Inspec.* **10**, 29 (1986).
17. A. Yamaji, Y. Enomoto, E. Kinoshita and T. Tanaka: *Proc. 1st Mtg. Ferroelectric Mater. & Appl.* p. 269, Kyoto (1977).

18. K. Nakamura, H. Ando and H. Shimizu: *Jpn. J. Appl. Phys.* **26**, Suppl. 26–2, 198 (1987).
19. J. Kuwata, K. Uchino and S. Nomura: *Ferroelectrics* **37**, 579 (1981).
20. J. Kuwata, K. Uchino and S. Nomura: *Jpn. J. Appl. Phys.* **21**(9), 1298 (1982).
21. http://www.ceracomp.com/
22. G. Messing, S. Trolier-McKinstry, E. Sabolsky, C. Duran, S. Kwon, B. Brahmaroutu, P. Park, H. Yilmaz, P. Rehrig, K. Eitel, E. Suvaci, M. Seabaugh and K. Oh: *Crit. Rev. Solid State Mater. Sci.* **29**(2), 45 (2004).
23. T. Tani and T. Kimura: *Adv. Appl. Ceram.* **105**(1) 55 (2006).
24. Y. Saito, H. Takao, T. Tani, T. Nonoyama, K. Takatori, T. Homma, T. Nagaya and M. Nakamura, *Nature*, **432**(4), 84–7 (2004).
25. J. Zheng, S. Takahashi, S. Yoshikawa, K. Uchino and J. W. C. de Vries: *J. Amer. Ceram. Soc.* 79, 3193 (1996).
26. K. Nagai and T. Konno (eds): *Electromechanical Vibrators and their Applications*, Corona, Tokyo. (1974).
27. K. Uchino: *Piezoelectric Actuators and Ultrasonic Motors*, Kluwer Academic Publishers, Boston, MA, (1997).
28. T. Yano, E. Sato, I. Fukui and S. Hori: *Proc. Int'l Symp. Soc. Information Display*, p. 180 (1989).
29. http://www.cedrat.com/en/mechatronic-products.html
30. A. Dogan: Ph. D. Thesis, Penn State University (1994).
31. Y. Sugawara, K. Onitsuka, S. Yoshikawa, Q. C. Xu, R. E. Newnham and K. Uchino: *J. Amer. Ceram. Soc.* **75**, 996 (1992).
32. H. Goto, K. Imanaka and K. Uchino: *Ultrasonic Techno* **5**, 48 (1992).
33. M. Kitayama: *Ceramics* **14**, 209 (1979).
34. M. Ishida *et al.*: *Appl. Phys. Lett.* **31**, 433 (1977).
35. M. Okuyama *et al.*: *Ferroelectrics* **33**, 235 (1981).
36. S. K. Dey and R. Zuleeg: *Ferroelectrics* **108**, 37 (1990).
37. S. Kalpat, X. Du, I. R. Abothu, A. Akiba, H. Goto and K. Uchino: *Jpn. J. Appl. Phys.* **40**, 158 (2001).
38. M. Laurent, H. Bödinger, T. Steinkopff, K. Lubitz, C. Schuh, S. Wagner, M. J. Hoffmann, H. Murmann-Biesenecker, A. J. Schmid: *Proc. 14th IEEE Int. Symp. Appl. of Ferroelectrics '04*, IEEE-UFFC-S, Montreal, Canada, Aug. 23–27 (2004).
39. M. E. Lines: *Phys. Rev. B* **15**, 497 (1980).
40. T. Nakamura: *Solid State Physics* **20**(8), 660 (1985).
41. K. Uchino, E. Sadanaga and T. Hirose: *J. Amer. Ceram. Soc.* **72**, 1555 (1989).
42. T. Yamakawa and K. Uchino: *Proc. Int'l. Symp. Appl. Ferroelectrics '90*, p. 610 (1991).
43. K. Saegusa *et al.*: *Amer. Ceram. Soc., 91th Ann. Mtg.* (1989).
44. G. A. Samara: *Ferroelectrics* **2**, 277 (1971).
45. K. Uchino, E. Sadanaga, K. Oonishi and H. Yamamura: Ceramic Dielectrics – *Ceramic Trans.*, **8**, 107 (1990).

11
Multilayer technologies for piezo-ceramic materials

K. UCHINO, The Pennsylvania State University, USA

Abstract: Multilayer structures have been introduced in the piezoelectric actuator primarily to introduce the following advantages: much lower drive voltage, making them safer to use, and with a cheaper power supply, and higher capacitance/lower impedance – n^2 times for the n-layer device. However, the following problems are also involved: more expensive manufacturing cost, both processing cost and the electrode material cost (typically rare-metal), and they are mechanically weak due to the electrode insertion.

Key words: multilayer capacitor, multilayer actuator, green sheet, tape casting, cut-and-bond method, interdigital electrode, plate-through electrode, crack propagation, ceramic electrode, base metal electrode.

11.1 Introduction

Ferroelectric ceramic multilayer (ML) devices have been investigated intensively for capacitor and actuator applications, because they have low driving voltages and they are highly suitable for miniaturization and integration onto hybrid structures. According to Dr. Kikuo Wakino, Murata Manufacturing (private communication), the ML capacitor with a barium titanate-based composition seems to have been invented by researchers at Sandia National Laboratory in the Manhattan Project during World War II; that is, this ML device was used for triggering the nuclear bombs targeting Hiroshima and Nagasaki, Japan. On the contrary, ML actuators were first co-fired by Kenji Uchino at Penn State University in 1979, the technology of which was transferred to NEC, Japan, who started mass production for their dot-matrix printer applications after 1983.

Miniaturization and hybridization are key concepts in the development of modern micromechatronic systems. The goal for multilayer actuators is to eventually incorporate layers thinner than 10 μm, which is the current standard for multilayer capacitors, in order to reduce the driving voltage below the 10 V provided by a regular battery. However, the typical layer thickness for multilayer actuators at this time is about 60 μm, primarily due to the minimization of the total cost of ML manufacturing and the required power supply. For the reader's information, a multilayer structure typically exhibits a field-induced strain of 0.1% along its length, l (for example, a 1 cm long sample will exhibit a 10 μm displacement) and the generative (i.e., blocking) stress 40 MPa (~100 kg·weight per 5 × 5 mm^2). Regarding the response speed, since the fundamental resonance frequency is given by:

$$f_r = \frac{1}{2l\sqrt{\rho s_{33}^{D}}}, \qquad 11.1$$

where ρ is the density and s_{33}^{D} is the elastic compliance (for example, a 1 cm long sample will have a ~100 kHz resonance frequency), the quickest response is provided by $1/f_r$ (10 μs for a 1 cm sample). Note that the mechanical response should not exceed the material's sound velocity.

New multilayer configurations or heterostructures comprising electromechanical materials and modified electrode patterns are anticipated and will be incorporated into ever more sophisticated smart systems. In comparison with a single rod sample, ML samples have the following advantages and disadvantages:

- Much lower drive voltage, making them safe to use, and with a cheaper power supply
- More expensive manufacturing cost, both processing cost and the electrode material cost (typically rare-metal)
- Mechanically weak due to the electrode insertion
- Higher capacitance/lower impedance – n^2 times for the n-layer device.

11.2 Multilayer (ML) manufacturing processes

There are two general methods for fabricating multilayer ceramic devices: (1) the cut-and-bond method and (2) the tape-casting method.

11.2.1 Cut-and-bond method

A schematic diagram of a commercially manufactured piezopile from NTK-NGK is shown in Fig. 11.1.[1] It consists of one hundred cut and polished PZT ceramic discs, each 1 mm thick, which are stacked and interleaved with metal foils that serve as electrodes within the device. A 100 μm displacement is generated by the pile with an applied voltage of 1.6 kV, and the maximum generative force is about 3 tons. Since the entire device is clamped by bolts and mechanically biased, delamination and mechanical fracture do not occur readily. Although devices such as this offer substantial displacements and generative forces, the cut-and-bond method in general has its disadvantages. One major drawback is the labor-intensive process itself, which is not at all well suited to mass production. The devices also tend to require rather

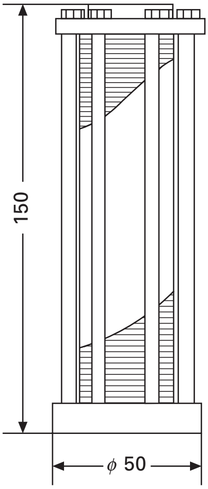

11.1 Schematic diagram of a piezopile manufactured by NTK-NGK.[1]

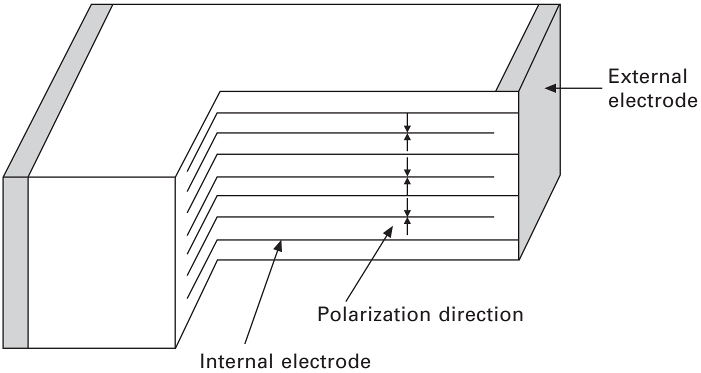

11.2 The structure of a multilayer actuator.

high drive voltages because the minimum layer thickness possible for stacks prepared in this way is only about 0.2 mm.

11.2.2 Tape-casting method

The tape-casting method, in which ceramic green sheets with printed electrodes are laminated and co-fired with compatible internal electrodes, is far more conducive to mass production and produces devices with much thinner layers so that low drive voltages may be employed.

The multilayer structure essentially comprises alternating ferroelectric and conducting layers, which are co-fired to produce a dense, cohesive unit as shown in Fig. 11.2. A ferroelectric layer sandwiched between a pair of electrodes constitutes a single displacement element. Hundreds of these units may be connected in parallel to the potential difference supplied by the external electrodes, which are connected to the many interleaved internal electrodes of the stack as shown in Fig. 11.2. A flowchart for the manufacturing process is shown in Fig. 11.3. Green sheets are prepared in two steps. First, the ceramic powder is combined with an appropriate liquid solution to form a slip. The slip mixture generally includes the ceramic powder and a liquid consisting of a solvent, a deflocculant, a binder and a plasticizer. During the second part of the process, the slip is cast into a film under a special straight blade, called a 'doctor blade', whose distance above the carrier determines the film thickness. Once dried, the resulting film, called a green sheet, has the elastic flexibility of synthetic leather. The volume fraction of the ceramic in the now polymerized matrix at this point is about 50–60%. The green sheet is cut into an appropriate size, and internal electrodes are printed using silver, palladium or platinum ink. Several tens to hundreds of these layers are then laminated, and pressed using a hot uni-axial press. After the stacks are cut into small chips, the green bodies are sintered at around 1100 °C in a furnace (lower than bulk sintering temperature), with special care taken to control the initial binder evaporation at 500 °C. The sintered chips are polished, externally electroded, lead wires are attached, and finally the chips are coated with a waterproof spray.

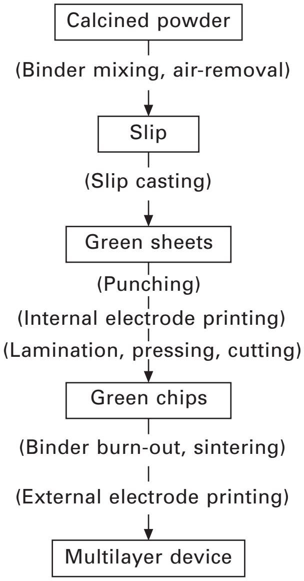
Calcined powder
(Binder mixing, air-removal)
Slip
(Slip casting)
Green sheets
(Punching)
(Internal electrode printing)
(Lamination, pressing, cutting)
Green chips
(Binder burn-out, sintering)
(External electrode printing)
Multilayer device

11.3 A tape-casting flowchart for the fabrication of a multilayer ceramic actuator.

11.3 Internal electrode design

11.3.1 Internal electrode configuration

Interdigital-type electrode

A cross-sectional view of a conventional interdigital electrode configuration is shown in Fig. 11.4(a).[2] The area of the internal electrode is slightly smaller than the cross-sectional area of the device. Notice that every two layers of the internal electrodes extend to one side of the device and connect with the external electrode on that side so that all active layers of the device are effectively connected in parallel. The small segments in each layer that are not addressed by the internal electrodes remain inactive, thereby restricting the overall generative displacement and leading to detrimental stress concentrations in the device. A multilayer structure is represented in Fig. 11.5(a) and the strain distribution measured in a test device is shown in Fig. 11.5(b). The derivative of the displacement distribution provides an estimate of the stress concentration in the device.[3] The internal stress distribution was also predicted using the finite element method. The results of this analysis are summarized in Fig. 11.6. The maximum tensile and compressive stresses are 1×10^8 N/m^2 and 1.2×10^8 N/m^2, respectively, which are very close to the critical strength of the ceramic.[3]

Crack propagation has been investigated in a variety of multilayer systems.[4] A crack pattern commonly observed in $Pb(Ni_{1/3}Nb_{2/3})O_3$–$Pb(Zr,Ti)O_3$ (PNNZT) piezoelectric actuators under bipolar drive is shown in Fig. 11.7(a). It occurs much as predicted in the theoretical treatment of these systems.[3] The crack originates at the edge of an internal electrode and propagates toward the adjacent electrode. Delamination between the electrode and the ceramic occurs simultaneously, leading to a Y-shaped crack. An interesting difference was observed in the case of the antiferroelectric $Pb(Nb,Zr,Sn,Ti)O_3$ (PNZST) system shown in Fig. 11.7(b). Here a Y-shaped crack is again produced, but it originates in the ceramic between the electrodes.[5] This is probably due to the combination of two distinct induced strains in the ceramic: the

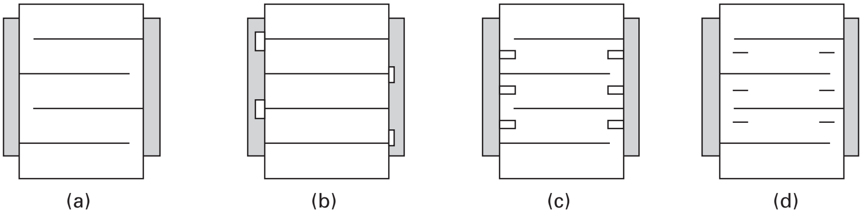

11.4 Various internal electrode configurations for multilayer actuators: (a) interdigital, (b) plate-through, (c) slit-insert, and (d) interdigital with float electrode.

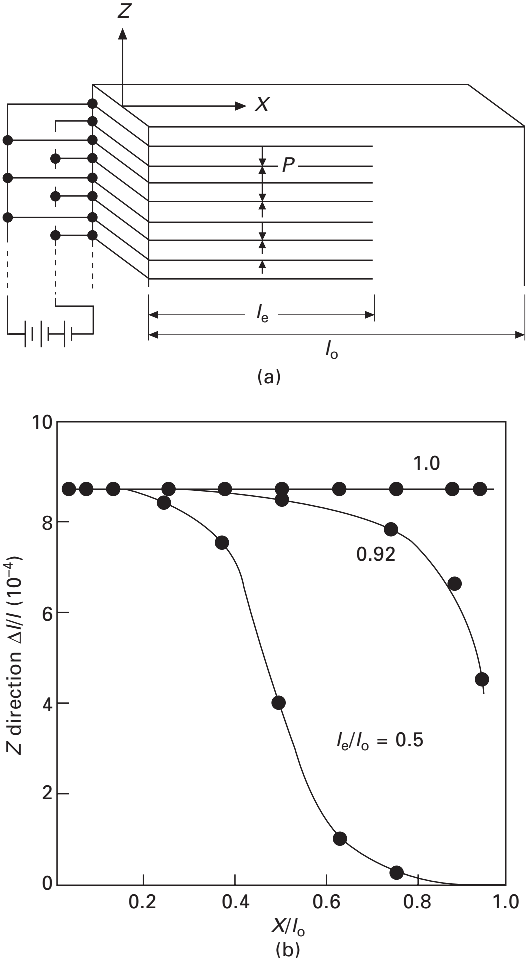

11.5 A multilayer structure: (a) a schematic depiction and (b) the induced strain distribution measured in a test device.[3]

anisotropic piezoelectric strain and the more isotropic strain (i.e., 'negative' Poisson's ratio) associated with the antiferroelectric response to the applied field.

Plate-through internal electrode

A modified electrode configuration, called the plate-through design (see Fig. 11.4(b)), was developed by NEC as a solution to this particular mechanical problem.[6] The electrode in this modified configuration extends over the entire surface of the ceramic so that the stress concentration cannot develop. This

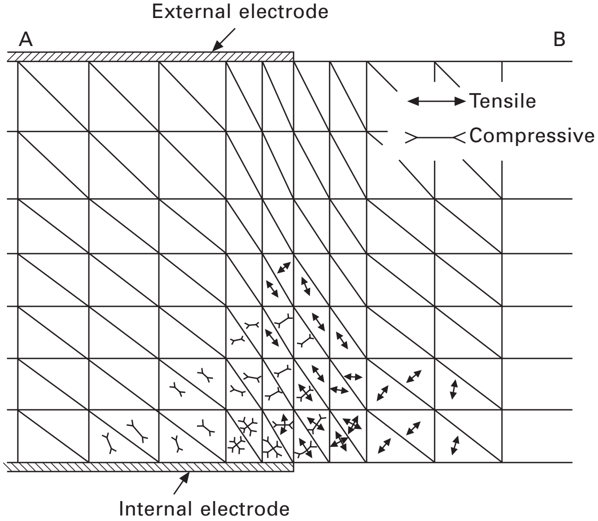

11.6 The internal stress distribution for a multilayer actuator as predicted by finite element analysis.[3]

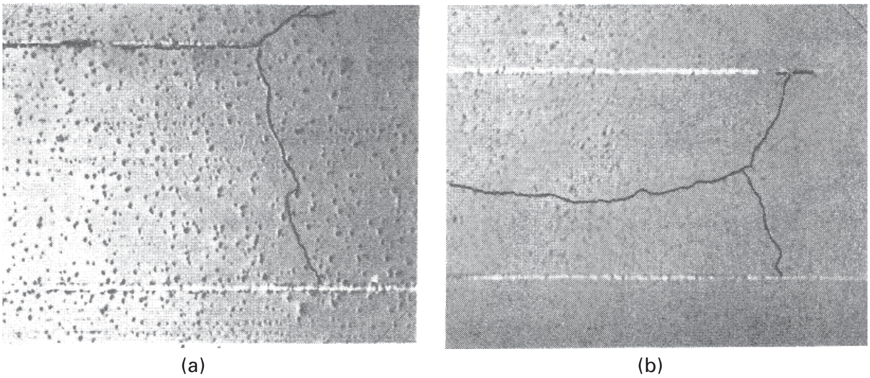

11.7 Crack generation in multilayer ceramic actuators under bipolar drive: (a) piezoelectric PNNZT, and (b) antiferroelectric PNZST.[4,5]

modification requires that an insulating tab terminate every two electrode layers on the sides of the device where the external electrodes are painted. Key issues in producing reliable devices with this alternative electrode design are concerned with the precise application of the insulating terminations and improvement of the adhesion between the ceramic and internal electrode layers. The designers of NEC addressed the first of these issues by developing an electrophoretic technique for applying glass terminators to the device.

The problem of adhesion due to no ceramic connection point between the adjacent layers was resolved by making use of a special electrode paste containing powders of both the Ag–Pd electrode material and the ceramic phase. The displacement curve for a (0.65)PMN–(0.35)PT multilayer actuator with 99 layers of 100 μm thick sheets ($2 \times 3 \times 10$ mm^3) is shown in Fig. 11.8(a).[7] We see from these data that a 8.7 μm displacement is generated by an applied voltage of 100 V, accompanied by a slight hysteresis. This curve is consistent with the typical response of a bulk disk specimen. The transient

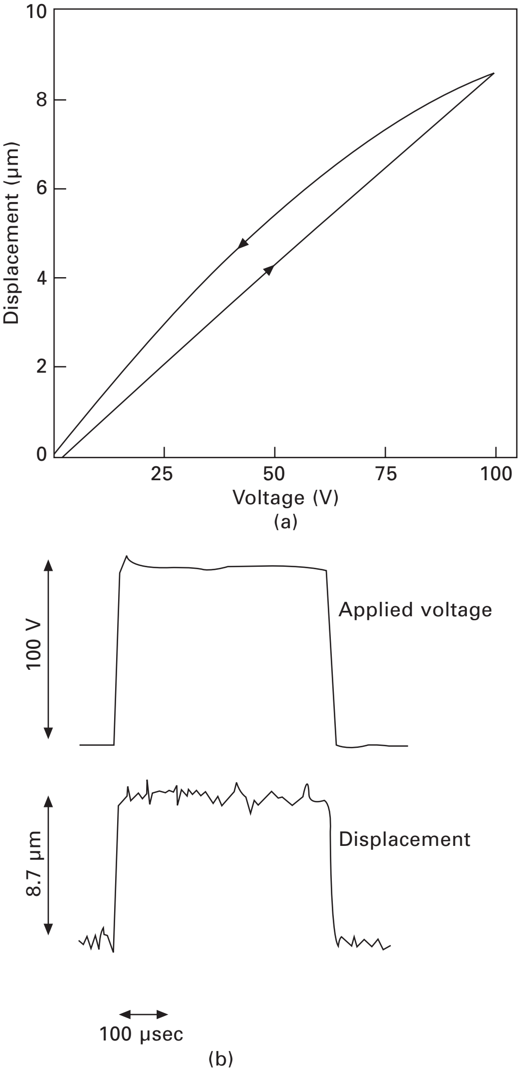

11.8 The response of a (0.65)PMN–(0.35)PT multilayer actuator (100 μm layer, $2 \times 3 \times 10$ mm^3): (a) the displacement as a function of applied voltage and (b) the displacement response to a step voltage.[7]

response of the induced displacement after the application of a rectangular voltage is shown in Fig. 11.8(b). Rising and falling responses as quick as 10 μsec are observed.

Slit-insert design/interdigital with float electrode

The slit-insert design and the interdigital with float electrode are shown in Fig. 11.4(c) and 11.4(d), respectively. The induced stress concentration is relieved in the slit-insert design while the electric field concentration is avoided using the interdigital with float electrode configuration.[8]

11.3.2 Printing pattern of electrode

As already mentioned, one of the major problems with ML structures is weak adhesion at the internal electrode portion due to lack of ceramic–ceramic connection point between the adjacent PZT layers. The most popular solution is to use a special electrode paste containing powders of both the Ag–Pd electrode material and the ceramic phase. Another solution can be found by taking a special printing pattern of the electrode. Figure 11.9(a) shows a pattern for large area ML actuators, designed by Uchino *et al.* (private information). Notice eight small electrode holes on the internal electrode pattern, which make the ceramic–ceramic conjunction strengthen the adhesion, in addition to the circumference connection. In order to realize the external electric lead connection with every two layers, without losing the active PZT volume portion, a tab-shape electrode removal is popularly used (see Figs 11.9(a) and 11.9(b)).

11.3.3 Layer-thickness effect

Siemens group reported an intriguing self-poling effect of ML piezo-actuators with very thin layer thickness (17 μm).[9] Two types of multilayer PZT actuators were prepared with their layer thicknesses of 280 and 17 μm, as shown in Figs 11.10(a) and 11.10(b).[9]

This PZT composition has tetragonal symmetry, and when the x-ray diffraction pattern was taken for both samples from the top surface, Fig. 11.11 was obtained. The sample with 280 μm layer thickness seemed to have no texture by showing the x-ray intensity ratio roughly 1:2 for the (001) and (100) reflections, while the intensity of the (001) reflection was very high for the sample with 17 μm layer thickness. In contrast, the x-ray pattern for the multilayer actuator with 17 μm thickness exhibited high intensity of the (001) reflection, indicating the polarization direction (elongated c axis) aligned normal to the layer plane, as schematically shown in Fig. 11.12.[9]

If this domain texture was induced by the mechanical stress through the

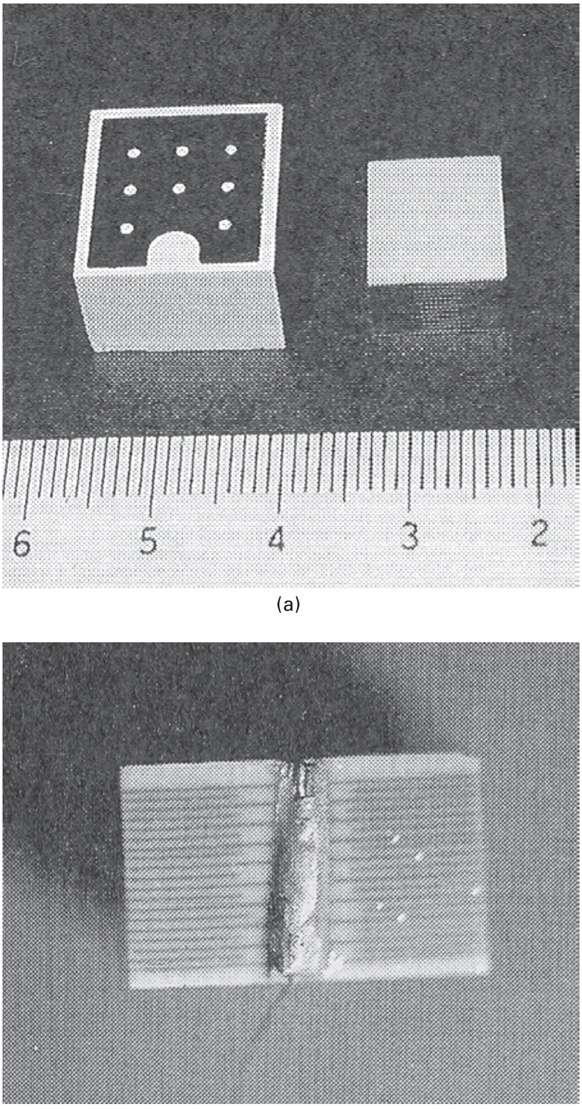

(a)

(b)

11.9 (a) Printing pattern for large area ML actuators (left: before sintering, right: after sintering). (b) Side view of the ML actuator (private data).

manufacturing process, the thermal expansion difference between the PZT and metal electrode may be the origin. Because the metal electrode shrinkage is larger than the PZT during the cooling-down process, the PZT layer will experience compressive stress (the thinner layer sample will experience larger compressive stress), leading to the domain alignment normal to the

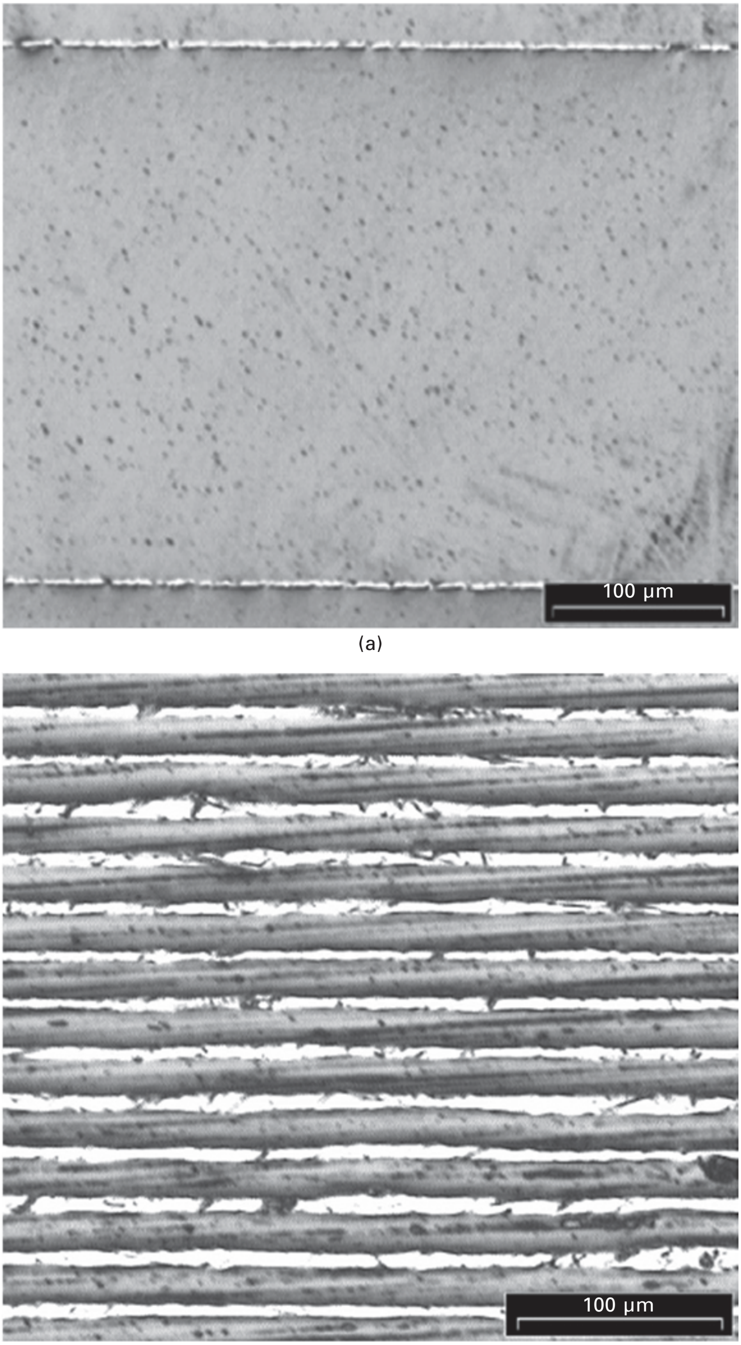

11.10 PZT multilayer actuators with their layer thicknesses of (a) 280 and (b) 17 μm.

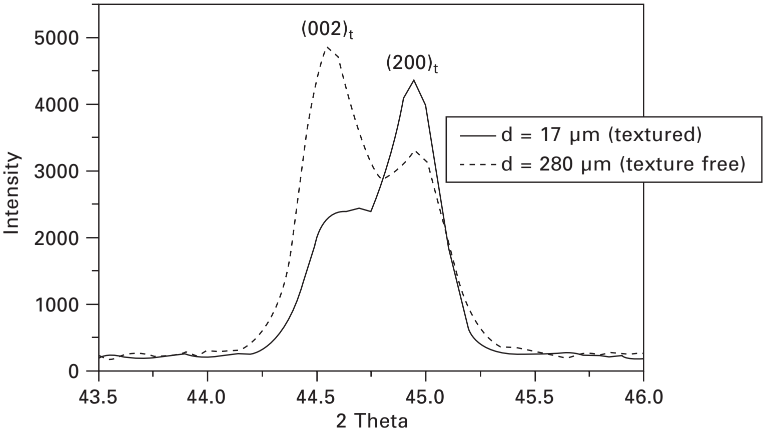

11.11 Two x-ray diffraction patterns for the multilayer actuators with 280 and 17 μm layer thicknesses.[9]

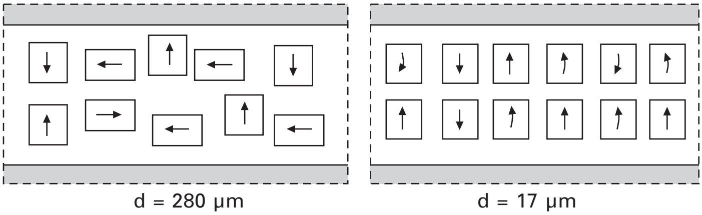

11.12 Two domain texture models for the multilayer actuators with 280 and 17 μm layer thicknesses.[9]

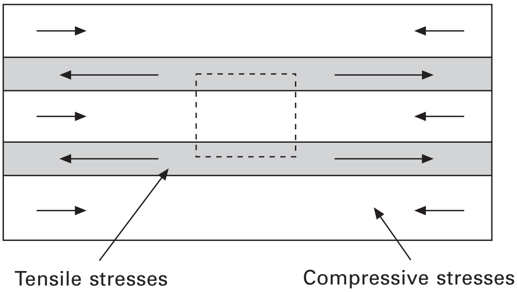

11.13 Domain texture creation model for the multilayer actuators with 17 μm layer thickness.[9]

layer surface (see Fig. 11.13). The electromechanical performance of the ML components deteriorates in general with reducing layer thickness, because an increase in relative volumetric fraction of the electrode material suppresses the deformation under the electric field. However, because of the highly-aligned domain texture discussed above, the deterioration was unexpectedly relieved.

11.3.4 Vertical crack

Non-uniform stress distribution in the interdigital electrode configuration of ML actuators, and the associating Y-shape crack propagation pattern were discussed in Section 11.3.1. Another common crack pattern is the vertical crack, which occasionally occurs in the layer just adjacent to the top or bottom inactive layer. The inactive layer serves as an interface between the device and the object to which the actuator is attached. A crack occurring in the layer adjacent to the inactive bottom layer of a multilayer device is shown in Fig. 11.14.[4] It originated from a transverse tensile stress produced in this layer due to clamping from the adjacent thick inactive layer. One solution that has been proposed for this problem is to pre-pole the top and bottom layers of the device.

11.4 Electrode materials

11.4.1 Actuator electrodes: an overview

The major problem with the most commonly used electrode material, silver (Ag), is that it tends to migrate into ceramics under high electric fields. Another problem is its ease of oxidation during sintering. One solution to this problem has been to use alloys such as silver-palladium (Ag–Pd). PZT-based ML actuators usually adopt Ag–Pd electrode with a Pd fraction higher than 30%.

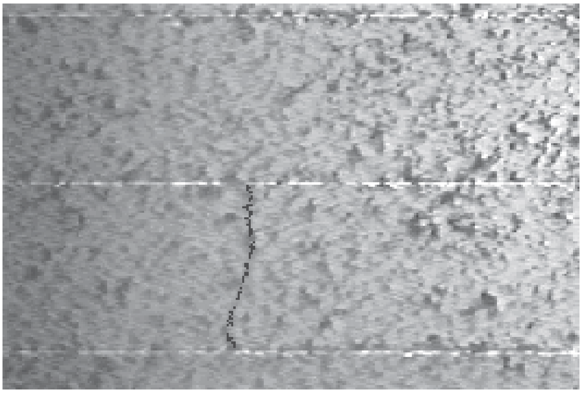

11.14 A vertical crack observed in the layer just adjacent to the bottom inactive layer in a multilayer actuator.[4]

However, as the reader can easily imagine, precious metals such as gold (Au), platinum (Pt), and silver-palladium (Ag–Pd) are expensive, thus not very suitable for inexpensive products. This cost problem was accelerated at the end of the 1990s, when Russia, the major Pd production country, experienced serious economic recession, and reduced Pd supply dramatically, leading to a sudden tenfold increase in worldwide Pd prices.

Another important issue to be pointed out here is the electric conductivity of electrode materials. In comparison with Ag and copper (Cu), the electric conductivity of Pt and Pd is poor, 1/10 of Cu's value, which creates deteriorated loss problems, such as heat generation and decreased efficiency of piezoelectric transducers and transformers under a resonance drive.

The above two problems (i.e., cost and performance) with Pd alloys initiated the adoption of base-metals for the internal electrode of ML devices. However, base-metal electrode materials such as copper (Cu) and nickel (Ni) are easily oxidized during sintering. Careful preparation techniques in terms of (1) sintering temperature (lower than 900 °C) and (2) sintering atmosphere (reduced condition) are required for successful base-metal electrode ML devices.

11.4.2 Pure-silver ML actuators

The cut-and-bond method developed for pure-Ag ML actuators by Ohnishi and Morohashi[10] is an interesting method. The structure fabricated by this method is a multilayer stack of 22 layers comprising 0.3 mm thick sintered ceramic disks arranged alternately with 10 μm thick silver (Ag) foils. The multilayer structure is hot-pressed at 900 °C for 4 hours. A device of this type with dimensions $5 \times 5 \times 9$ mm^3 demonstrates a bending strength of approximately 100 MPa, 10 times higher than usual ML devices. The cost of manufacturing multilayer devices by the bonding method is thus significantly cheaper than conventional methods, because inexpensive metal foils are used for the internal electrodes.

11.4.3 Cu-embedded co-fired ML actuators

An innovative fabrication technique has been developed by Morgan Electroceramics, which involves incorporating a copper internal electrode in a PZT multilayer actuator.[11] The PZT and Cu electrode materials are co-fired. Ordinarily the sintering temperature of PZT is too high to allow for co-firing with a Cu electrode. The sintering temperature of the PZT used in these structures is reduced to 1015 ºC by adding excess PbO. Special measures are taken to optimize the co-firing process. The oxygen pressure is precisely regulated by sintering in a nitrogen atmosphere (10^{-10} atm). The pieces are also fired in a special sintering sand, which is essentially a mixture of the Cu and PZT powders. This helps to inhibit the oxidation of the Cu electrode during firing. A four-layer PZT actuator (with layer thickness of 25 μm) fabricated by this method is shown in Fig. 11.15.

The Penn State group developed Cu and pure-Ag embedded multilayer piezo-transformers (Fig. 11.16(b)), which were sintered at 900 °C in a reduced atmosphere with N_2, as illustrated in Fig. 11.16(a).[12] Ring-dot disk multilayer types (OD = 27, center dot D = 14 mm) with Cu and Ag/Pd (or Ag/Pt) (as references) revealed the maximum power density (at 20 °C temperature rise) of 42 W/cm^3 and 30 W/cm^3, respectively. This big difference comes from the poor electrical conductivity of Pd or Pt, compared to Cu or pure Ag. Note that the power density depends not only on the piezo-ceramic composition, but also on the choice of electrode material in a ML design.

11.4.4 ML actuators with ceramic electrodes

Mechanical weakness at the junction between the ceramic and the electrode metal often gives rise to delamination problems. One solution to this problem has been to make a more rigid electrode by mixing ceramic powder of the composition used for the actuator material with the metal electrode paste. Abe *et al.* examined some of the more popular conducting ceramic materials as electrodes in ML ceramic actuators.[13]

Ceramic electrodes

The most attractive ceramic electrode materials are conducting or semiconducting perovskite oxides because of their compatibility with the crystal structure of the actuator ceramics. Among the conducting ceramics $Sr(Fe,Mo)O_3$, $(La,Ca)MnO_3$ and $Ba(Pb,Bi)O_3$ (which is actually a superconductor) are considered the best, but their conductivity is dramatically reduced when they are sandwiched between the lead-based ceramic layers and sintered. One of the few successful structures utilizing a ceramic conductor is a

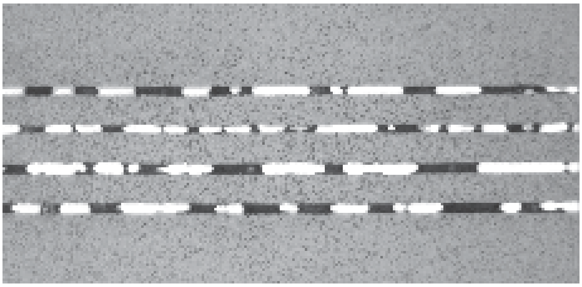

11.15 A PZT multilayer actuator with Cu internal electrodes co-fired at 1015 °C.[11]

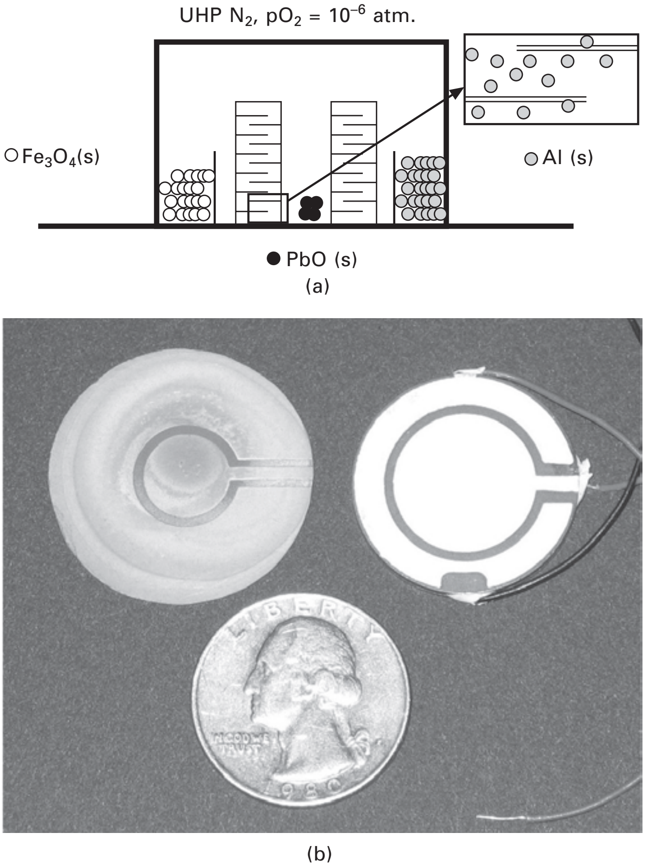

11.16 (a) Experimental setup for sintering Cu-electrode-embedded multilayer transformers in a reduced N_2 atmosphere. (b) Multilayer co-fired transformer with hard PZT and Cu (left) or pure Ag (right) electrode, sintered at 900 °C (Penn State trial products).[12]

unimorph device comprising a piezo-ceramic and a $Ba(Pb,Bi)O_3$ fabricated by hot-pressing. Semiconducting $BaTiO_3$-based ceramics with a positive temperature coefficient of resistivity (PTCR) also appear to be promising alternative electrode materials for these structures.

In general, good ceramic electrode materials should possess the following characteristics:

- high conductivity
- sintering temperature and shrinkage similar to that of the piezoelectric ceramic
- good adhesion with the piezoelectric ceramic
- slow diffusion into the piezoelectric ceramic during sintering.

The last characteristic is perhaps the most critical and the ultimate success of the structure will depend on a well-defined interface between the electrode and piezoelectric layers.

Barium titanate-based ML actuator

Barium titanate ($BaTiO_3$), which is a ferroelectric with a Curie temperature of 120 °C, is known to become electrically conductive when polycrystalline samples are doped with rare-earth ions.[13,14] The resistivity of some $BaTiO_3$-based ceramics (with 5 mol% SiO_2 and 2 mol% Al_2O_3) is plotted in Fig. 11.17 as a function of La_2O_3 concentration. We see from these data that relatively small concentrations of La in the range of 0.1 to 0.25 at% lead to a change in the resistivity of more than 10 orders of magnitude. Multilayer actuators consisting of alternating layers of undoped resistive $BaTiO_3$ and the $BaTiO_3$-based semiconducting composition doped with 0.15 at% La have been fabricated by the tape-casting process. The main advantage in using these materials is that atomic diffusion across the interface between layers during the sintering process tends to be suppressed because the layers are compositionally similar, resulting in a well-defined interface between the actuator and electrode layers. Another beneficial feature of this combination is that the sintering temperature and shrinkage of both materials are almost the same, so that no residual stress is present in the sample after sintering. The fabrication of this structure is also somewhat simpler since it requires no binder burn-out process, which is a time consuming step required in

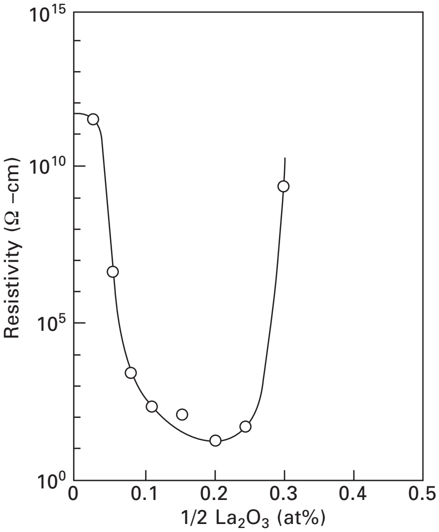

11.17 The resistivity of $BaTiO_3$-based ceramics (with 5 mol% SiO_2 and 2 mol% Al_2O_3) plotted as a function of La_2O_3 concentration.[13,14]

the fabrication of devices with metal electrodes. A prototype device of this type has been produced with eight 0.5 mm thick actuator layers of 0.5 mm thickness, sandwiched between 0.25 mm thick electrode layers.[13]

The mechanical strength of multilayer samples having an overall plate-like shape with their piezoelectric and ceramic electrode layers perpendicular to the plate as shown in Fig. 11.18(a) has been tested by a three-point bend method.[13] Data were also collected for samples of this configuration having the same piezoelectric ceramic as the test specimens and Pd electrode layers, which served as a reference. Weibull plots for both are shown in Fig. 11.18(b). The mechanical strength of the ceramic electrode device is observed to be about 50 MN/m^2, which is approximately three to four times higher than that observed for the metal electrode actuator. It is also noteworthy that the Weibull coefficient is generally much larger when the ceramic electrodes are used, indicating that the deviation in fracture strength is much smaller. Fracture was observed to occur mainly at the ceramic–electrode interface for the structures with the metal electrodes, while no such tendency was observed for the ceramic electrode device.

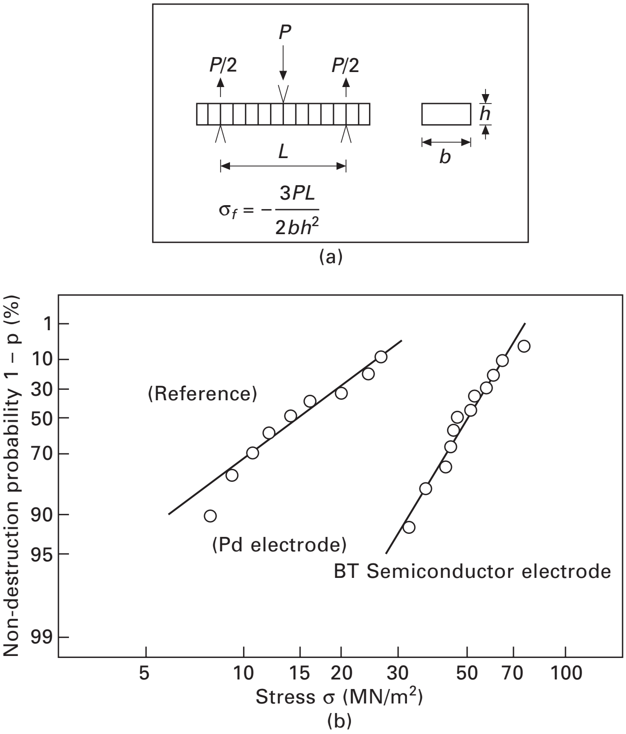

11.18 Three-point bend testing of multilayer actuators: (a) sample configuration and experimental setup, and (b) the Weibull plots for the ceramic electrode and metal electrode (reference) structures.[13]

The electric field-induced strains measured in the prototype ceramic electrode device are shown in Fig. 11.19(a). It was determined in the study of this structure that the longitudinal strain induced in the actuator layers was $x_3 = 5 \times 10^{-4}$ and the transverse strain $x_1 = -1.2 \times 10^{-4}$. The measured strains are 30% and 60% smaller than the predicted values for the longitudinal and transverse strains, respectively. The clamping effect associated with this strain anisotropy can be reduced by decreasing the thickness of the electrode layers.

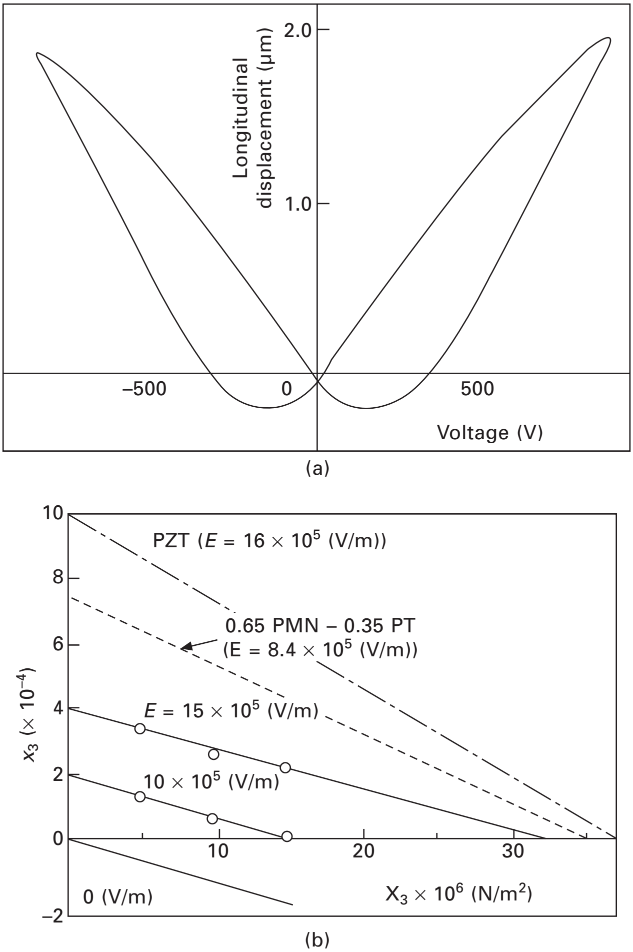

11.19 (a) Displacement curve for a $BaTiO_3$-based multilayer actuator with ceramic electrodes.[13] (b) Uniaxial stress dependence of the strain induced in $BaTiO_3$ for several applied electric field strengths. The typical strain responses of PZT and PMN–PT specimens are also shown for comparison.[15]

The uniaxial stress dependence of the strain induced in $BaTiO_3$ for several applied electric field strengths is shown in Fig. 11.19(b). The typical strain responses of PZT and PMN–PT specimens are also shown in the figure for comparison.[15] The magnitude of the induced strain in $BaTiO_3$ is not as large as that generated in the lead-based materials, but the generative stress (320 kgf/cm^2) level is comparable with those of the PZT and PMN–PT samples mainly due to the relatively small elastic compliance ($s_{33} = 13 \times 10^{-12}$ (m^2/N)) of $BaTiO_3$.

11.5 Innovative multilayer (ML) structures

11.5.1 Super-long ML design

A multilayer actuator incorporating a new interdigital internal electrode pattern has been developed by NEC-Tokin.[16] In contrast to devices with the conventional interdigital electrode structure, line electrodes are printed for this modified design on the piezoelectric green sheets (i.e., the printing pattern has an interdigital type), which are stacked so that alternate electrode lines are displaced by one-half pitch. This actuator produces displacements normal to the stacking direction through the longitudinal piezoelectric effect. ML actuators up to 74 mm in length have been manufactured, which can generate longitudinal displacements up to 55 μm.

11.5.2 3D positioning stage

A three-dimensional positioning actuator with a stacked structure has been proposed by PI Ceramic, Germany, in which both longitudinal and shear strains are induced to generate displacements.[17] As shown in Fig. 11.20(a), this actuator consists of three parts: the top 10 mm long Z-stack generates the displacement along the z direction, while the second and the bottom 10 mm long X and Y stacks provide the x and y displacements through shear deformation, the principle of which is illustrated in Fig. 11.20(b). The device can produce 10 μm displacements in all three directions (3D) when 500 V is applied to the 1 mm thick layers.

11.6 Reliability/lifetime of multilayer (ML) actuators

11.6.1 Heat generation in ML actuators

The Penn State group reported on the heat generation from ‘soft’ PZT-based multilayer piezoelectric ceramic actuators of various sizes under off-resonance (slow) drive.[18] The temperature change was monitored in actuators driven by a large field 3 kV/mm and at 300 Hz. Figure 11.21 shows the saturated temperature plotted as a function of V_e/A, where V_e is the effective volume

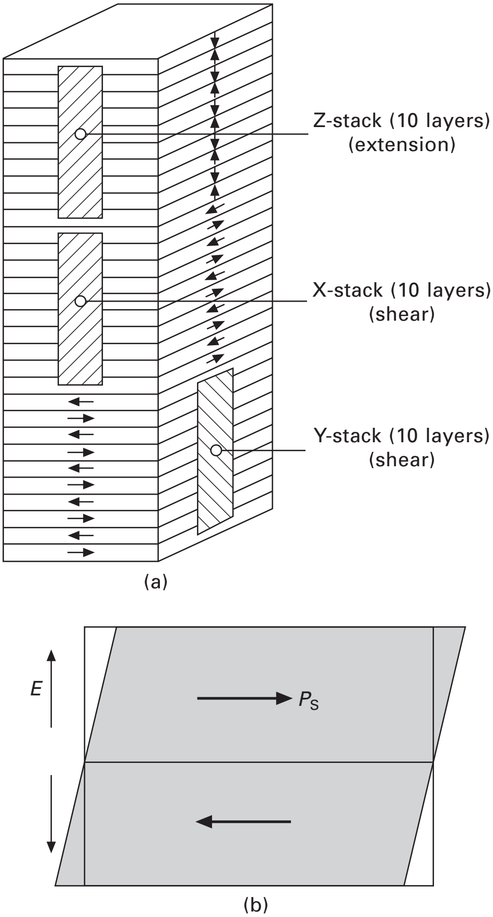

11.20 A three-dimensional positioning actuator with a stacked structure proposed by PI Ceramic: (a) a schematic diagram of the structure and (b) an illustration of the shear deformation.[17]

(electroded portion of the actuator, excluding non-active PZT volume) and A is the surface area. This linear relation is reasonable because the volume V_e generates the heat through the material's loss and this heat is dissipated through the area A. Thus, if you need to suppress the heat, a small V_e/A is preferred, i.e., flat and cylinder shapes are better than cube and solid rod structures, respectively.

11.6.2 Lifetime test

The effect of aging in multilayer actuators is manifested clearly by the gradual decrease in its resistance with the number of drive electric field cycles, as

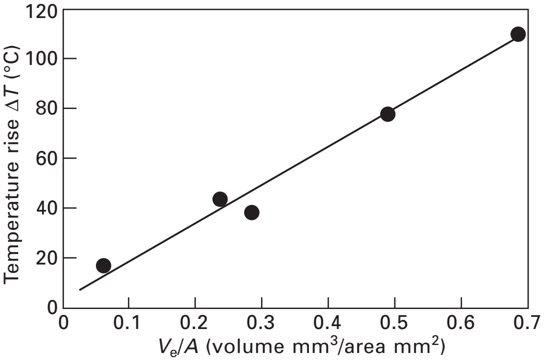

11.21 Temperature rise in ML actuators versus V_e/A (under 3 kV/mm, 300 Hz), where V_e is the effective volume and A is the surface area.

demonstrated in a piezoelectric ML actuator in Fig. 11.24(a). Ceramic aging is an extremely important factor to consider in the design of a reliable actuator device, although there have been relatively few investigations carried out to better understand and control it. Aging is associated with two types of degradation: (1) depoling and (2) mechanical failure. Creep and zero-point drift in the actuator displacement are caused by depoling of the ceramic. The strain response is also seriously impaired when the device is operated under conditions of very high electric field, elevated temperature, high humidity, and high mechanical stress. According to Nagata,[19] the lifetime of a multilayer piezoelectric actuator operated under a DC bias voltage can be described by the empirical relationship:

$$t_{DC} = AE^{-n} \exp(W_{DC}/kT), \qquad 11.2$$

where W_{DC} is an activation energy ranging from 0.99 to 1.04 eV.

11.6.3 Health monitoring

Various failure detection techniques have been proposed for implementation in smart actuator devices to essentially monitor their own 'health'.[20] One such 'intelligent' actuator system that utilizes acoustic emission (AE) detection is shown in Fig. 11.22. The actuator is controlled by two feedback mechanisms: position feedback, which can compensate for positional drift and hysteresis, and breakdown detection feedback, which can shut down the actuator system safely in the event of an imminent failure. Acoustic emission from a piezoelectric actuator driven by a cyclic electric field is a good indicator of mechanical failure. The emissions are most pronounced when a crack propagates in the ceramic at the maximum speed. A portion of this smart piezoelectric actuator is therefore dedicated to sensing and responding to acoustic emissions. The AE rate in a piezoelectric device can increase by

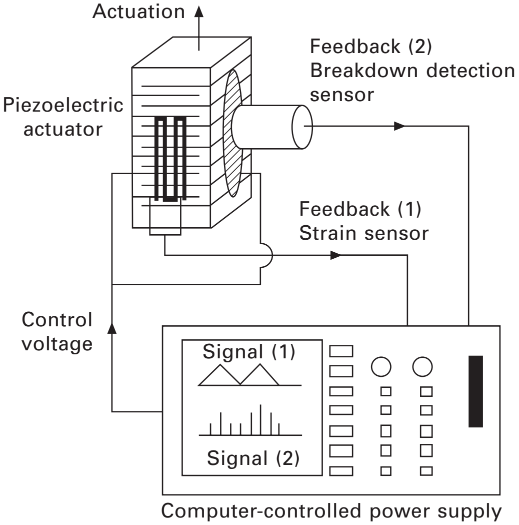
Actuation
Feedback (2)
Breakdown detection
sensor
Piezoelectric
actuator
Feedback (1)
Strain sensor
Control
voltage
Signal (1)
Signal (2)
Computer-controlled power supply

11.22 An intelligent actuator system with both position and breakdown detection feedback mechanisms.[20]

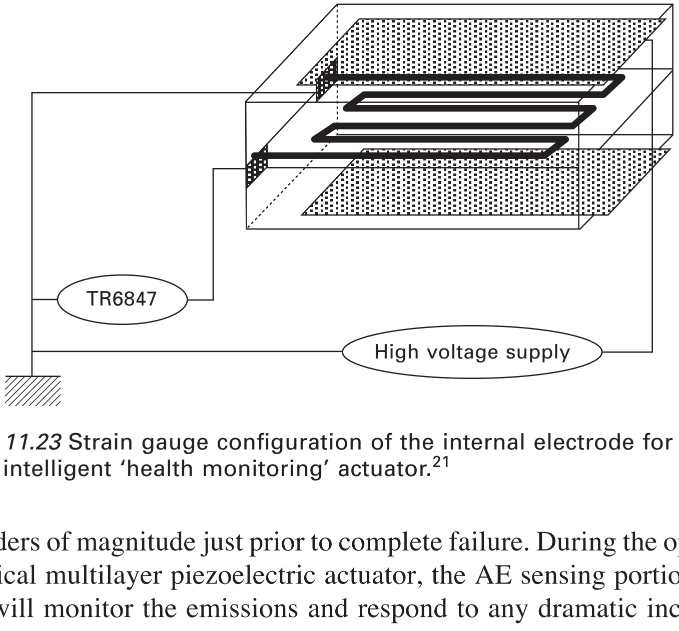
TR6847
High voltage supply

11.23 Strain gauge configuration of the internal electrode for an intelligent 'health monitoring' actuator.[21]

three orders of magnitude just prior to complete failure. During the operation of a typical multilayer piezoelectric actuator, the AE sensing portion of the device will monitor the emissions and respond to any dramatic increase in the emission rate by initiating a complete shut-down of the system.

Another development by the Penn State group on ML device failure self-monitoring is based on a strain gauge type electrode configuration as shown in Fig. 11.23.[21] Both the electric field-induced strain and the occurrence of cracks in the ceramic can be detected by closely monitoring the resistance

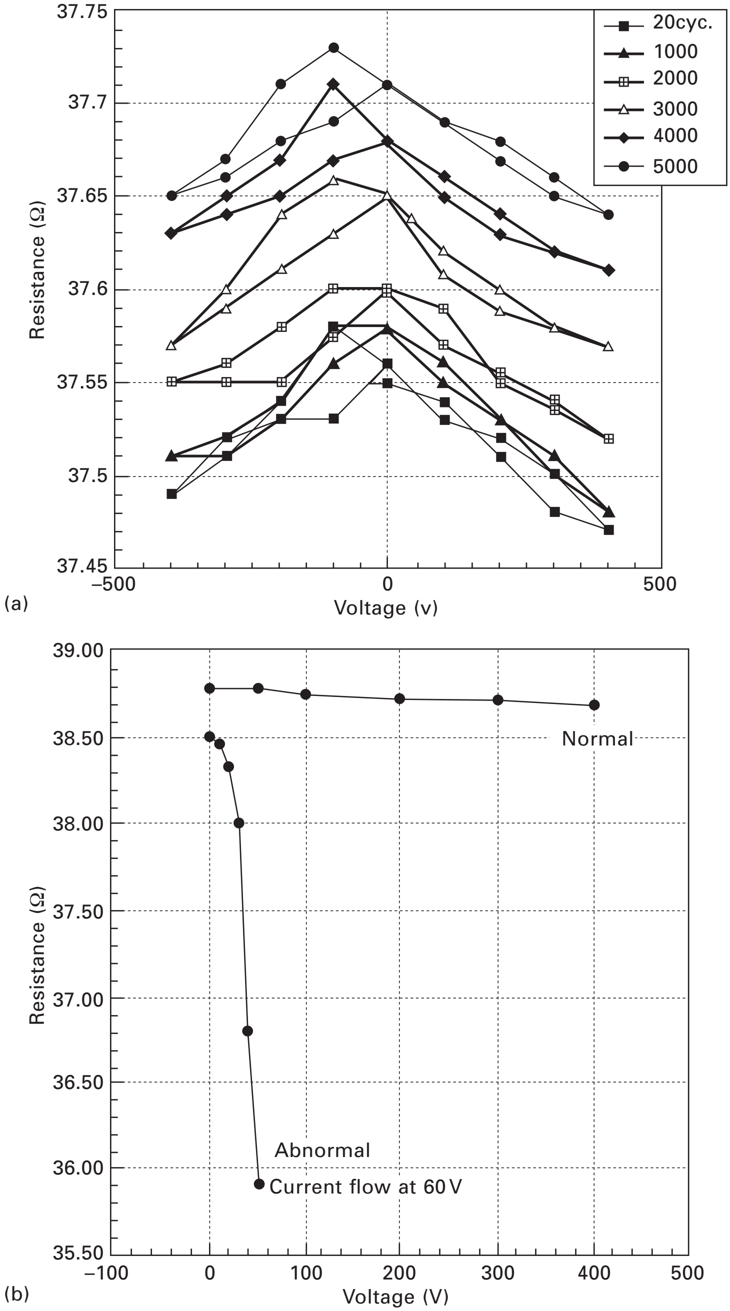

11.24 Resistance change with applied electric field for a smart actuator with a strain gauge type internal electrode for self-monitoring of potential failure: (a) the electric field-induced strain response of a 'healthy' device and (b) the response of a failing device.[2]

of a strain gauge shaped electrode embedded in a ceramic actuator. The resistance of such a smart device is plotted as a function of applied electric field in Fig. 11.24. The field-induced strain of a 'healthy' device is represented by the series of curves depicted in Fig. 11.24(a). Each curve corresponds to a distinct number of drive cycles. A sudden decrease in the resistance as shown in Fig. 11.24(b) is a typical symptom of device failure.

11.7 References

1. S. Yamashita: *Jpn. J. Appl. Phys.* **20**, Suppl. 20-4, 93 (1981).
2. K. Uchino, S. Nomura, L. E. Cross, R. E. Newnham and S. J. Jang: *J. Mater. Sci.* **16**, 569 (1981).
3. S. Takahashi, A. Ochi, M. Yonezawa, T. Yano, T. Hamatsuki and I. Fukui: *Jpn. J. Appl. Phys.* **22**, Suppl. 22-2, 157 (1983).
4. A. Furuta and K. Uchino: *J. Amer. Ceram. Soc.* **76**, 1615 (1993).
5. A. Furuta and K. Uchino: *Ferroelectrics* **160**, 277 (1994).
6. S. Takahashi: *Fabrication and Application of Piezoelectric Materials* (T. Shiosaki, ed.), Chapter 14 'Actuators', CMC Pub. (1984).
7. S. Takahashi: *Sensor Technology* **3**, No.12, 31 (1983).
8. H. Aburatani, K. Uchino, A. Furuta and Y. Fuda: *Proc. 9th Int'l Symp. Appl. Ferroelectrics*, p. 750 (1995).
9. M. Laurent, H. Bödinger, T. Steinkopff, K. Lubitz, C. Schuh, S. Wagner, M.J. Hoffmann, H. Murmann-Biesenecker, A.J. Schmid: *Proc. 14th IEEE Int. Symp. Appl. of Ferroelectrics '04*, IEEE-UFFC-S, Montreal, Canada, Aug. 23–27 (2004).
10. K. Ohnishi and T. Morohashi: *J. Jpn. Ceram. Soc.* **98**, 895 (1990).
11. W. A. Groen, D. Hennings and M. Thomas: *Proc. 33rd Int'l Smart Actuator Symp.*, State College, PA (April, 2001).
12. S. Ural, S.-H. Park, S. Priya and K. Uchino: *Proc. 10th Int'l Conf. New Actuators*, Bremen, Germany, June 14–16, 2006, pp. 556–558 (2006).
13. K. Abe, K. Uchino and S. Nomura: *Ferroelectrics* **68**, 215 (1986).
14. O. Saburi: *J. Phys. Soc. Jpn.* **14**, 1159 (1959).
15. K. Uchino and J. R. Giniewicz: *Micromechatronics*, CRC/Marcel Dekker, New York (2003).
16. J. Ohashi, Y. Fuda and T. Ohno: *Jpn. J. Appl. Phys.* **32**, 2412 (1993).
17. A. Banner and F. Moller: *Proc. 4th Int'l Conf. New Actuators*, AXON Tech. Consult. GmbH, p. 128 (1995).
18. J. Zheng, S. Takahashi, S. Yoshikawa, K. Uchino and J. W. C. de Vries: *J. Amer. Ceram. Soc.* **79**, 3193 (1996).
19. K. Nagata: *Proc. 49th Solid State Actuator Study Committee*, JTTAS, Japan (1995).
20. K. Uchino and H. Aburatani: *Proc. 2nd Int'l Conf. Intelligent Mater.*, p. 1248 (1994).
21. H. Aburatani and K. Uchino: *Amer. Ceram. Soc. Annual Mtg. Proc.*, SXIX-37-96, Indianapolis, April (1996).

12

Single crystal preparation techniques for manufacturing piezoelectric materials

L.-C. LIM, National University of Singapore, Singapore

Abstract: Recent progresses in high-temperature flux growth of relaxor-PT ferroelectric single crystals with PbO-based fluxes are reviewed. The PT content of the grown crystals, and hence the solution, plays a significant role in the growth mechanism and result. For crystals of low PT contents, such as PZN–PT, the solution is composed of simple ions. By engineering the solution isotherms and the growth conditions to promote near-equilibrium layer growth of the crystal, large crystals of relatively uniform compositions can be readily grown by the flux technique with PbO flux. In contrast, for crystals of high PT content for which ionic complexes are present in the solution (such as PMN-PT–PbO solution), careful control of the flux composition to break up such ionic complexes into simpler ones (e.g., with suitable amounts of B_2O_3) and the growth conditions is essential to promote layer growth of the crystal for a good growth result. In addition to the solution chemistry, typical problems encountered in the flux growth of relaxor-PT single crystals are described and their causes and remedies briefly discussed.

Key words: relaxor-PT single crystal, PZN–PT, PMN–PT, flux growth, flux compositions, typical growth problems.

12.1 Introduction

Due to their excellent dielectric and piezoelectric properties, the growth and property characterization of lead-based relaxor-PT single crystals, notably lead zinc niobate–lead titanate ($Pb(Zn_{1/3}Nb_{2/3})O_3$–$PbTiO_3$ or PZN–PT) and lead magnesium niobate–lead titanate ($Pb(Mg_{1/3}Nb_{2/3})O_3$–$PbTiO_3$ or PMN–PT) solid solutions, have been pursued aggressively over the past 15 years. These single crystals display much superior dielectric and piezoelectric properties to state-of-the-art lead zirconate titanate (PZT) ceramics. For instance, while [001]-poled PZN–(6–7)%PT single crystals exhibit $k_{33} \approx 0.92$ and $d_{33} \approx 2800$ pC/N, PMN–28%PT single crystals give $k_{33} \approx 0.90$ and $d_{33} \approx 2000$ pC/N.[1–8] Very high transverse piezoelectric properties were also reported for [011]-poled crystals, giving $k_{32} \approx 0.92$ and $d_{32} \approx -(3200–4000)$ pC/N for PZN–(6–7)%PT and $k_{32} \approx 0.90$ and $d_{32} \approx -2200$ pC/N for PMN–28%PT single crystals.[7–15] Furthermore, these single crystals have relatively high elastic compliances[16–21] and hence low sound velocities.[22,23] They are thus candidate materials for future high-performance piezoelectric devices.

Unlike PZT materials, most lead-based relaxor-PT single crystals can be grown readily using the high-temperature flux techniques from PbO-based fluxes. However, there have been many technological hurdles in growing large-size relaxor-PT single crystals for commercial exploitation. This chapter reviews the recent developments in the flux growth of lead-based relaxor-PT single crystals, focusing on the growth of large-size high-quality PZN–PT and PMN–PT single crystals.

The flux growth of relaxor single crystals was pioneered by Myl'nikova and Bokov[24–26] in the late 1950s. They successfully synthesized monocrystals of $PbMg_{1/3}Nb_{2/3}O_3$ (PMN), $PbZn_{1/3}Nb_{2/3}O_3$ (PZN), $PbNi_{1/3}Nb_{2/3}O_3$ (PNiN), $PbCo_{1/3}Nb_{2/3}O_3$ (PCoN), $PbMg_{1/3}Ta_{2/3}O_3$ (PMT), $PbNi_{1/3}Ta_{2/3}O_3$ (PNiT) and $PbCo_{1/3}Ta_{2/3}O_3$ (PCoT) by the solution growth technique with PbO flux. About a decade later, Nomura *et al.*[27,28] succeeded in growing single crystals of $PbZn_{1/3}Nb_{2/3}O_3$–$PbTiO_3$ (PZN–PT) solid solution over the whole composition range by the same technique. In 1982, Kuwata *et al.*[1] investigated the dielectric and piezoelectric properties of single crystals of PZN–9%PT and reported that samples poled along the [001] crystal axis exhibited anomalously high piezoelectric coefficients and electromechanical factors ($d_{33} = 1500$ pC/N and $k_{33} = 0.92$). In 1990, Shrout *et al.*[2] successfully synthesized $PbMg_{1/3}Nb_{2/3}O_3$–$PbTiO_3$ (PMN–PT) solid solution single crystals from high temperature solution with PbO–B_2O_3 fluxes.

By the mid 1990s, systematic studies on the growth of PZN–PT and PMN–PT single crystals had been performed by Saitoh *et al.*,[29] Park *et al.*,[30–32] and Kobayashi *et al.*[33,34], respectively. By then, the size of the crystals obtained was sufficiently large to enable detailed property evaluation of the material. In 1997, Park and Shrout[3–5] published a series of papers detailing the superior dielectric and piezoelectric properties of single crystals of PZN–PT and PMN–PT of near-morphotropic phase boundary compositions. Their work has created a renewed interest worldwide in growing large-size relaxor-PT single crystals as well as in their applications in high-performance piezoelectric devices such as ultrasound medical imaging probes, sonar for underwater communications and imaging, high-power-density and high-sensitivity sensors and actuators, etc.

Tables 12.1–12.3 list the earlier developments in the flux growth of PZN–PT, PMN–PT and other lead-based relaxor-PT single crystals, respectively. Since 1998, the present author has been involved in relaxor crystal growth, focusing on the growth of large-size high-homogeneity PZN–PT and PMN–PT single crystals using the high-temperature flux technique. In what follows, typical flux growth processes for PZN–PT and PMN–PT single crystals are presented and discussed. Various commonly encountered problems concerning the subject matter are described.

Table 12.1 Growth of PZN and PZN–PT single crystals with PbO-based fluxes

Technique	Materials	Activities – approx. largest size of crystals grown
Flux-growth via spontaneous nucleation with or without local cooling arrangement	PZN and PZN–PT	Bokov and Myl'nikova (1961)[25]; few mm (edge length)
		Nomura *et al.* (1969)[27,28]; 10 mm
		Saitoh *et al.* (1995)[29]
		Park *et al.* (1996/97)[30-32]; 20 mm
		Kobayashi *et al.* (1997/98)[33,34]; 43 mm
		Park *et al.* (1998)[35]; 10 mm
		Saitoh *et al.* (1999)[36,37]; 40 mm
		Zheng *et al.* (2000)[38]; 17 mm
		Gentil *et al.* (2000)[39]; few mm
		Kumar *et al.* (2000/01)[40,41]; 30 mm
		Xiao *et al.* (2002)[42]; 26 mm
		Santailler *et al.* (2002/03)[43,44]; 30 mm
		Lim *et al.* (2004/05)[6,45]; 35 mm
		Dabkowski *et al.* (2004)[46]; 30 mm
		Benayad *et al.* (2004)[47]; 35 mm
		Babu *et al.* (2006)[48]; 15 mm
Solution (flux) Bridgman growth with or without seed	PZN–PT	Shimanuki *et al.* (1998)[49]; $\phi 30 \times 20$ mm^3
		Harada *et al.* (1998/99)[50-52]; $\phi 40 \times 20$ mm^3
		Harada *et al.* (2001/02)[53,54]; $\phi 50 \times 12$ mm^3
		Matsushita *et al.* (2002)[55]; $\phi 75 \times 55$ mm^3
		Xu *et al.* (2002/03)[56,57]; <111> seed; $\phi 338 \times 20$ mm^3
		Fang *et al.* (2002)[58]; <111> seed; $\phi 28 \times 30$ mm^3
		Benayad *et al.* (2004)[47]; $\phi 25 \times 40$ mm^3
		Xu *et al.* (2005)[59]; $\phi 50 \times 15$ mm^3
Top-seeded solution growth (TSSG)	PZN–PT	Chen and Ye (2001)[60]; <111> seed; $\phi 30 \times 10$ mm^3
		Karaki *et al.* (2002)[61]; <111> seed; $\phi 16 \times 12$ mm^3
		Bertram *et al.* (2003)[62]; pointed Pt rod; $\phi 10 \times 20$ mm^3
		Ye and Chen (2003)[63]
Flux-growth via spontaneous nucleation	Fe-doped PZN–PT	Priya *et al.* (2002)[64]
		Zhang *et al.* (2003)[65]; 24 mm
		Sato *et al.* (2004)[66]
	Mn-doped PZN–PT	Priya *et al.* (2001)[67]
		Zhang *et al.* (2004)[68]; 30 mm [(Mn,F)-co-doped]
		Kobor *et al.* (2005/07)[69,70]; few mm
	Co-doped PZN–PT	Priya and Uchino (2004)[71]

12.2 Flux growth of PZN–PT single crystals (i.e. relaxor-PT crystals of low PT contents)

Flux growth is an efficient self-purification process. The use of high purity charge is thus not a necessity in that 99.9% purity starting powders generally suffice.

PZN–xPT system has a morphotropic phase boundary at $x = 0.09$–0.11.[124] Flux growth of PZN–PT single crystals of near morphotropic phase boundary compositions using PbO self-flux has been well documented (see Table

Table 12.2 Growth of PMN and PMN–PT single crystals with PbO-based fluxes

Technique	Materials	Activities – approx. largest size of crystals grown
Flux-growth via spontaneous nucleation with or without local cooling arrangement	PMN and PMN–PT	Myl'nikova and Bokov (1940)[24,26]; few mm Afanas'ev *et al.* (1977)[72] Setter and Cross (1980)[73]; 3 mm Petrovskii *et al.* (1984)[74] Ye *et al.* (1990)[75]; 13 mm Shrout *et al.* (1990)[2]; 10 mm Park *et al.* (1996)[30]; 20 mm Park *et al.* (1998)[35]; 10 mm Dong and Ye (2000)[76]; 10 mm Jiang *et al.* (2001)[77]; 4 mm Fan *et al.* (2003)[78]; 5 mm Lim *et al.* (2003/05)[79,80]; 35 mm Kania *et al.* (2005)[81]; <10 mm Tang *et al.* (2006)[82] (Mn-doped PMN–PT)
Top-seeded solution growth (TSSG)	PMN and PMN–PT	Bonner and Van Uitert (1967)[83]; 16 mm Park *et al.* (1998)[35] Ye and Chen (2001/03)[63,84]; <111> seed; ϕ35 mm
Flux-growth via spontaneous nucleation	PMN–PSN; PMN–PSN–PT; PMN–PIN–PT	Hosono *et al.* (2000)[85] 3mm (PMN–PSN–PT) Honoso *et al.* (2001)[86] 20 mm (PMN–PIN–PT) Raevskii *et al.* (2003)[87]; 6 mm (PMN–PSN)

12.1). Other than having a reasonably low viscosity and high solubility for complex oxides, being an end element of the final compound, the use of PbO flux is advantageous in that introduction of foreign ions can be avoided. However, its major drawbacks include its toxicity, volatility above 1100 °C and a tendency to corrode platinum above 1300 °C.

A schematic of the typical setup for high temperature flux growth of lead-based relaxor-PT single crystals is provided in Fig. 12.1(a). For the growth of PZN–PT, the starting precursor powders are PbO, ZnO, Nb_2O_5 and TiO_2, all of 99.95% or higher in purity. The component powders, weighed to desired proportions, are first mixed thoroughly for more than 24 hours. Depending on the PT content, typical solute-to-flux mole ratio used varies from 0.45:0.55 to 0.50:0.50. After mixing, the charge is loaded directly into the Pt crucible. Then, the Pt crucible is covered with the lid and further placed in a sealed alumina crucible assembly, as shown in Fig. 12.1(a). This serves to contain potential PbO loss during the crystal growth run. The assembly is then placed in the crystal growth furnace, which is equipped with a local cooling arrangement to eliminate unwanted nucleation. Various techniques have been used for local point cooling including the use of a thin metal rod,[55–59,62] metal wire,[60,61] controlled stream of gas flow[33,34,36,37,41,47] and their combination.[46]

The crucible assembly with the charge is heated to high temperatures, typically between 1150 °C and 1250 °C, and held for a period to melt and

Table 12.3 Growth of other relaxor and relaxor-PT single crystals with PbO-based fluxes

Technique	Materials	Activities – approx. largest size of crystals grown
Flux-growth via spontaneous nucleation with or without local cooling arrangement	PSN; PSN–PT; PSN–PST; PSN–BSN; PMN–PSN; PMN–PSN–PT;	Fesenko *et al.* (1971)[88] (PSN)
		Smotrakov *et al.* (1983)[89] (PSN)
		Caranoni *et al.* (1992)[90–92]; few mm (PSN; PSN–PT)
		Yamashita *et al.* (1996)[93-95]; few mm (PSN–PT)
		Eremkin *et al.* (1999)[96,97]; (PSN–PST)
		Raevskii *et al.* (2000)[98] (PSN–BSN)
		Hosono *et al.* (2000)[85] 3mm (PMN–PSN–PT)
		Bing and Ye (2002)[99,100]; 5 mm (PSN–PT)
		Raevskii *et al.* (2003)[87]; 6 mm (PMN–PSN)
		Rajasekaran *et al.* (2008)[101]; few mm (PSN–PT)
	PIN; PIN–PT;	Grove (1986)[102] (PIN)
		Kania and Rowinski (1991)[103](PIN)
		Yasuda *et al.* (2000)[104]; 10 mm (PIN–PT)
		Honoso *et al.* (2001)[86] 20 mm (PMN–PIN–PT)
		Kania (2008)[105]; few mm (PIN)
	PYN; PYN–PT	Topolov *et al.* (1995)[106] ; (PYN)
		Yasuda *et al.* (2001)[107]; 2 mm (PYN–PT)
		Yasuda *et al.* (2002)[108]; $\phi 15 \times 10$ mm^3 (PYN–PY–SB)
		Zhang *et al.* (2002)[109]; 6 mm (PYN–PT)
		Kania (2008)[105]; few mm (PYN)
	PNiN; PCoN; PMnN; PCdN; PFN	Myl'nikova and Bokov (1959)[24–26] (PNiN; PCoN)
		Ichinose *et al.* (1971)[110]; (PCdN)
		Brunskill *et al.* (1981)[111,112]; 40 mm (PFN); few mm (PMnN)
Flux-growth via spontaneous nucleation	PMT; PMT–PT; PST;PSN–PST; PIT; PYT; PNiT; PCoT	Myl'nikova and Bokov (1959)[24–26]; (PMT; PNiT; PCoT;)
		Galasso and Darby (1965)[113]; (PST)
		Afanas'ev *et al.* (1977)[72]; (PMT)
		Setter and Cross (1980)[73]; 3 mm (PST)
		Kania (1990)[114]; (PIT)
		Bokov *et al.* (1991)[115]; (PIT)
		Caranoni *et al.* (1992)[87–89]; few mm (PST; PSN–PST)
		Gagarina *et al.* (1998)[116]; (PYT)
		Eremkin *et al.* (1999)[96,97]; (PSN–PST)
		Kania *et al.* (2007)[117]; (PYT)
		Kania (2007)[118]; 10 mm (PMT)
		Kania *et al.* (2008)[119]; few mm (PMT; PT)
	PCoW; PFW; PMW	Sun *et al.* (1991)[120]; 8 mm (PCoW)
		Ye *et al.* (1996)[121,122]; 3 mm (PFW)
		Kania *et al.* (1996)[123]; (PMW)

Key: PSN: $Pb(Sc_{1/2}Nb_{1/2})O_3$; PIN: $Pb(In_{1/2}Nb_{1/2})O_3$; PYN: $Pb(Yb_{1/2}Nb_{1/2})O_3$; PCdN: $Pb(Cd_{1/3}Nb_{2/3})O_3$; PCoN: $Pb(Co_{1/3}Nb_{2/3})O_3$; PMnN: $Pb(Mn_{1/3}Nb_{2/3})O_3$; PNiN: $Pb(Ni_{1/3}Nb_{2/3})O_3$; PFN: $Pb(Fe_{1/2}Nb_{1/2})O_3$; PMT: $Pb(Mg_{1/3}Ta_{2/3})O_3$; PCoT: $Pb(Co_{1/3}Ta_{2/3})O3$; PYT: $Pb(Yb_{1/2}Ta_{1/2})O_3$; PIT: $Pb(In_{1/2}Ta_{1/2})O_3$; PFT: $Pb(Fe_{1/2}Ta_{/1/2})O_3$; PMW: $Pb(Mg_{1/2}W_{1/2})O_3$; PCoW: $Pb(Co_{1/2}W_{1/2})O_3$; PFW: $Pb(Fe_{2/3}W_{1/3})O_3$; PT: $PbTiO_3$.

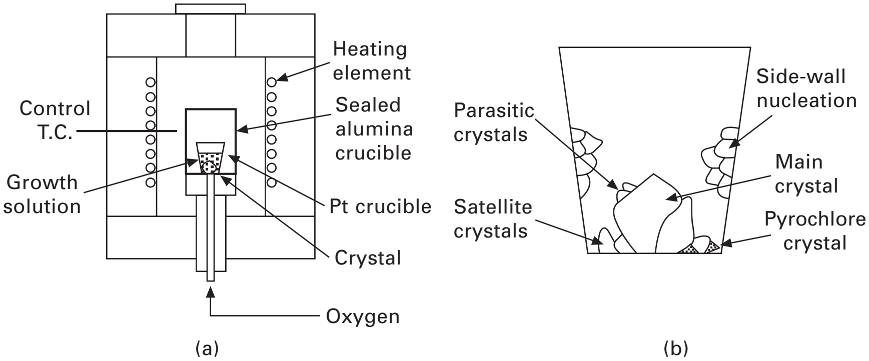

12.1 Schematics showing (a) the setup used for high-temperature flux growth of lead-based relaxor-PT single crystals via bottom point cooling arrangement and (b) typical growth results.

homogenize the solution. Then, the assembly is cooled at a controlled rate, typically in the range of 0.5–2.0 °C/h, to start the crystal growth process. It has also been common practice to use a gradually increasing cooling rate in the slow cooling stage,[37,38,75,76] in order to achieve a more constant crystal growth rate. This, however, requires knowledge of the ternary phase diagram of the material system concerned. Although relevant ternary phase diagrams remain unavailable to-date, binary phase diagrams for PMN–PbO, PZN–PbO and PMN–PT systems have been reported by Ye *et al.*[63,75,125]

As-grown PZN–PT single crystals generally exhibit prominent (001) facets. At low degree of supersaturation (i.e., at a low cooling rate), the growth of a PZN–PT single crystal starts by nucleation at <111> corners followed by spreading down adjacent <001> edges and (001) crystal faces, as evident in Fig. 12.2. This is typical of crystal growth from a solution of simple ionic salts,[126] suggesting that PZN–PT–PbO solutions must be composed of simple ions. This holds even when the PT content in the solution is near the morphotropic phase boundary compositions, i.e., about 9–10 mol%PT.

With an increased degree of supersaturation in the solution, growth of respective single crystals via nucleation at <001> edges and on {001} faces becomes feasible. Examples of such are shown in Fig. 12.3(a) and (b). The growth remains very much crystallographic in nature until the supersaturation is sufficiently high to promote profuse nucleation and growth on {001} faces. Should this occur, {001} growth faces are gradually replaced with smooth, non-crystallographic crystal faces. An example of such is shown in Fig. 12.3(c).

Small, newly nucleated PZN–PT single crystals are cubic in shape.[39,40] With favourable isotherms in the solution, preferential nucleation at certain <111> corners is promoted such that the corner nucleation rate outpaces the spreading rate onto adjacent {001} crystal faces. As a result, the small

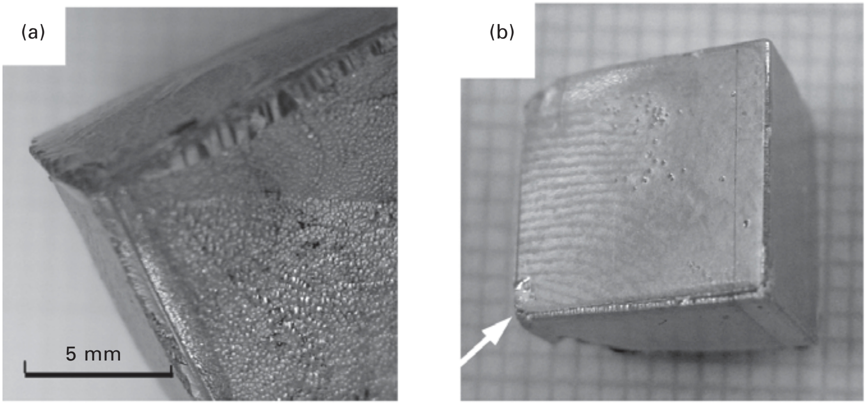

12.2 Natural (001) growth facets in flux-grown (a) PZN–9%PT and (b) PMN–30%PT single crystals. Note evidence of <111> corner nucleation (arrowed) followed by <001> edge and (001) layer growth in (b).

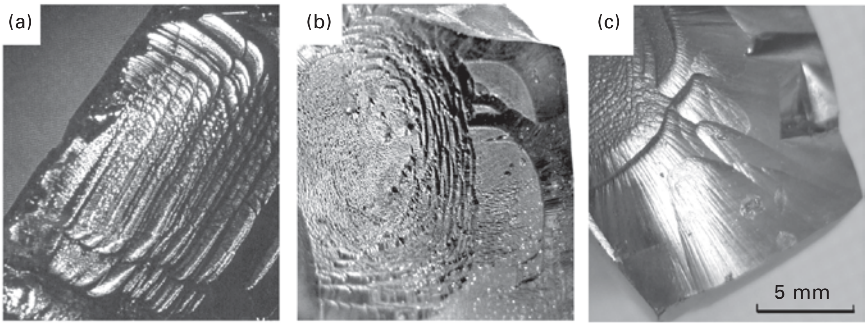

12.3 (a) Nucleation of (001) layer growth at (a) <001> edge and (b) (001) face in PZN–9%PT. (c) shows non-crystallographic crystal faces at higher cooling rates.

cube-shaped crystals would evolve into various shapes as they grow in size, as shown in Fig. 12.4.

With the above knowledge, one may engineer the isotherms in the solution such that upon nucleation in the middle of the Pt crucible bottom, subsequent <111> corner nucleation and {001} layer growth of the crystal occur preferentially across the base of the Pt crucible. In other words, for growing large-size relaxor-PT single crystals by the spontaneous nucleation technique, it is imperative that the isotherms in the solution be appropriately engineered such that the sideward growth rate of the crystal outpaces its vertical growth rate into the solution. Since the growing crystal is totally surrounded by the PbO-rich solution, it will grow in a stress-free near-equilibrium condition.

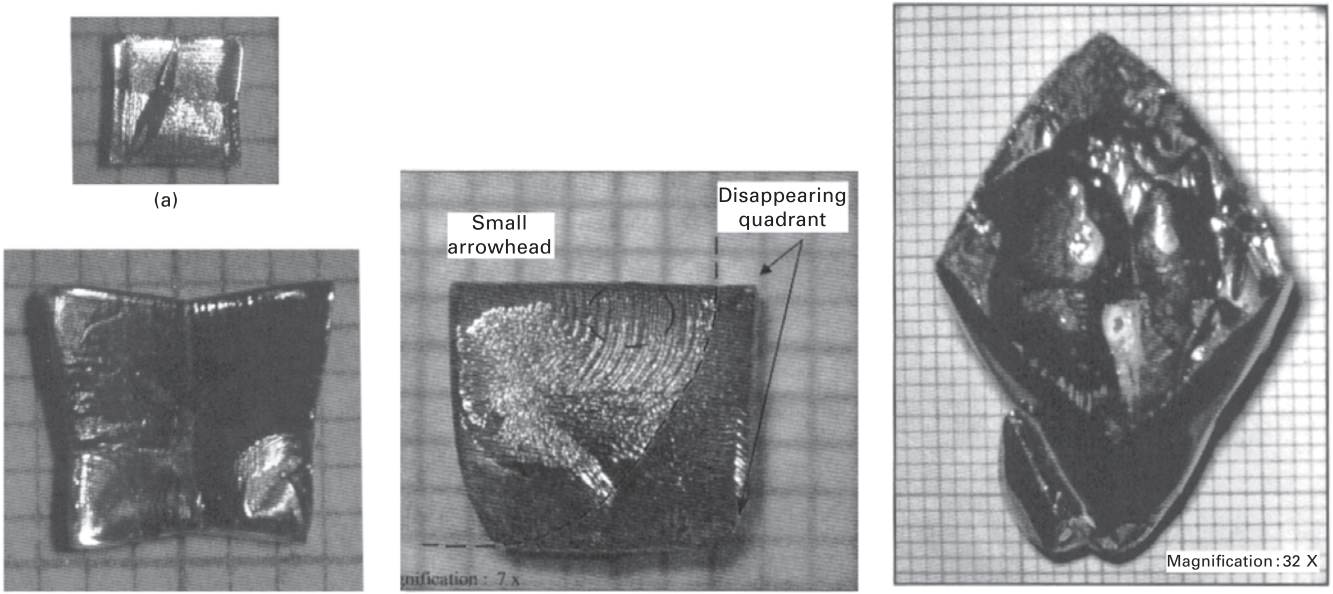
(a)
Small arrowhead
Disappearing quadrant
gnification : 7 x
Magnification : 32 X

(b) (c) (d)

12.4 Evolution from (a) near-cubic, to (b) star-shaped, (c) arrowhead-shaped, and finally (d) spearhead-shaped crystal as a result of increased growth rate along certain <111> directions promoted by favorable isotherms in the solution.

A PbO-rich solution environment is important for PZN–PT crystal growth. This is because PZN–PT is unstable at high temperatures even in PbO-rich vapor environments.[127–129]

The entire crystal growth run may last for one to several weeks. Depending on the crystal composition, slow cooling is stopped after the growth temperature reaches about 800–1000 °C, whereupon the assembly is cooled at a faster rate to room conditions. At the conclusion of the crystal growth run, the crystal is retrieved from the solidified flux by leaching in boiling concentrated nitric acid.

Pictures of typical flux-grown PZN–PT single crystals are provided in Fig. 12.5. They measure about 30–35 mm in edge length and up to 20 mm in height, extending to the bottom edge of the Pt crucible. As-grown PZN–*x*PT crystals, $x = 0.045$–0.09, are light brownish-yellow in color. Good quality crystals are translucent when viewed against the light and are relatively clear except for the shadowing effects produced by diffraction of light due to domains and inclined crystal surfaces. Figure 12.5 further shows that the growth direction of the crystals can be engineered with a certain degree of success by exploiting the <111> fast growth direction with respect to the isotherms in the solution.

The compositional uniformity of as-grown PZN–PT crystals was examined by slicing the entire crystal into 0.5 mm thick wafers parallel to the largest (001) growth facet and measuring the distribution of Curie temperature (T_c) over the entire wafer area using the array dot electrode technique.[130] The results showed that under optimum growth conditions, a large part (i.e., 80–90% of

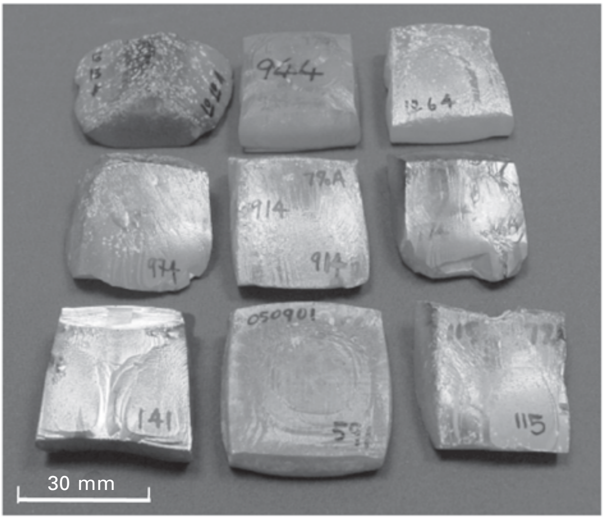

12.5 Pictures of PZN–PT single crystals grown from PbO flux.

the crystal boule) of as-grown PZN–xPT single crystals with $x \leq 0.07$ exhibit good compositional uniformity with $\Delta T_c \leq \pm 2.5\,°C$, corresponding to $\Delta x \leq \pm 0.005$.[6,45] The last part is typically higher in PT content. For PZN–xPT single crystals with $x \leq 0.07$, this part is comparatively small, giving a high crystal yield.

12.3 Flux growth of PMN–PT single crystals (i.e. relaxor-PT Crystals of high PT contents)

PMN–yPT system has a morphotropic phase boundary at $y = 0.33$–0.35.[131,132] The setup, charge preparation and growth procedure for flux growth of PMN–PT single crystals are similar to those for PZN–PT crystals described in the previous section. To determine the optimum flux composition, the following charge compositions were studied (in mode fraction): 0.4(PMN–yPT)–(0.6–z) PbO–$z$$B_2O_3$, with $y = 0.30$–0.32 and $z = 0.00$–0.20.

Small PMN–PT single crystals (of a few millimetres edge length) can be readily grown from PbO-based fluxes. They generally exhibit clear (001) growth facets, as shown in Fig. 12.2(b). However, it may not be as straightforward when growing large PMN–PT single crystals, because the high PT content of the system produces significant complications to the flux growth of this material.[79,80] Thus, PbO+B_2O_3 complex fluxes were used instead. Even so, the growth results depended sensitively on the B_2O_3 content in the PbO solution, as will be shown below.

Figure 12.6(a) shows the effect of charge composition on the growth result of PMN–PT single crystals. With nil or insufficient B_2O_3 in the solution, the starting charge has a high liquidus. In this case, the initially grown crystal falls within the 'liquid + $(PMN + PT)_{SS}$' two-phase field of the flux-free binary relaxor-PT system. When this happens, the initially formed phase is actually a mixture of a crystalline phase of PMN–PT solid solution of lower PT content and a liquid phase of higher PT content. Under limited convection conditions, as in the flux growth of most relaxor-PT crystals, the newly separated liquid phase may become trapped between the solidifying PMN–PT crystallites, leading to the 'hollow-crystal' feature shown in Fig. 12.6(b). Flux inclusions are thus an expected feature when the liquidus of the precursor powder mixture is high, i.e., when it falls within the 'liquid + $(PMN + PT)_{SS}$' phase field of the flux-free binary relaxor-PT system. The problem of phase-separated flux inclusions, or hollow crystals, can be avoided by increasing the B_2O_3 in the PbO flux, and hence the starting charge, such that crystal growth takes place predominantly below the solidus of the corresponding binary relaxor-PT system. This is shown schematically in Fig. 12.6(a). No phase-separation problem occurs in this case and the grown PMN–PT single crystals are free of flux inclusions and fully dense, as shown in Fig. 12.6(c).

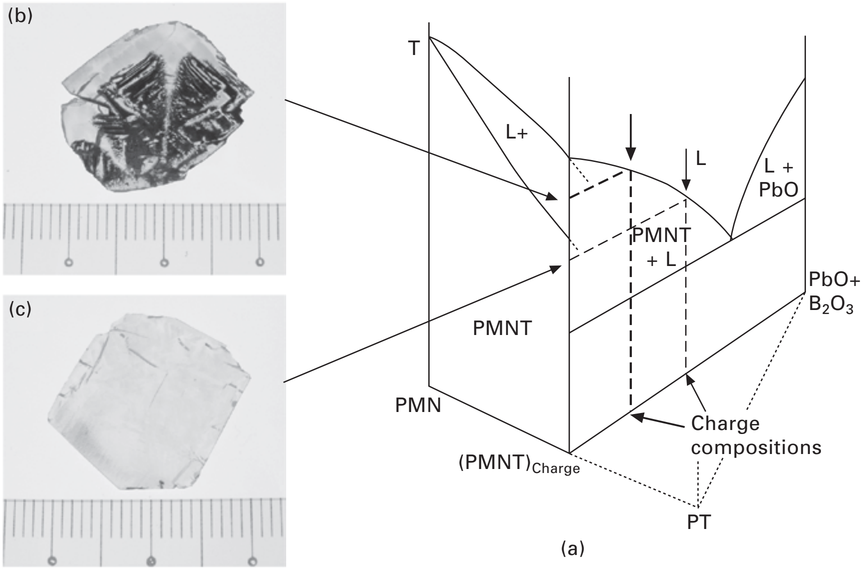

12.6 (a) A hypothetical phase diagram of the PMN–PT–($PbO+B_2O_3$) system. The vertical sections of PMN–PT single crystals grown with insufficient B_2O_3 and sufficient B_2O_3 in PbO-based fluxes are given in (b) and (c), respectively.

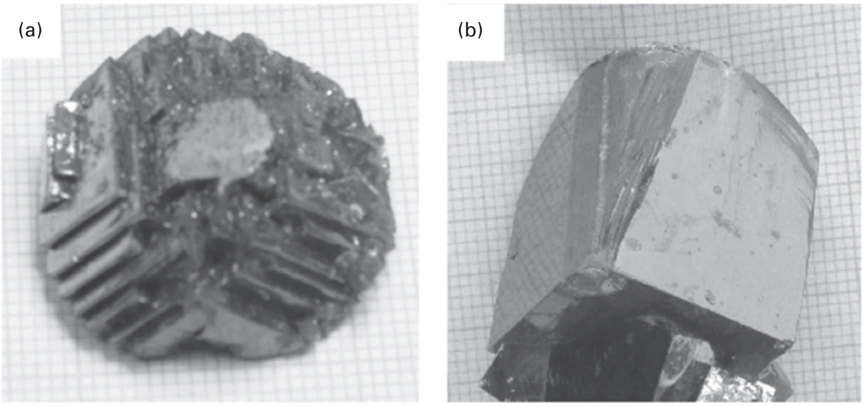

12.7 Different (001) growth morphologies in flux-grown PMN–30%PT single crystals: (a) (001) platelet growth in the absence of B_2O_3 in PbO flux; (b) microscopic (001) layer growth with >5 mol%B_2O_3 addition to PbO flux.

The amount of B_2O_3 in PbO flux also affects the growth mechanism of PMN–PT single crystals. Figure 12.7(a) and (b) shows the general morphologies of large-size PMN–PT single crystals (i.e., those ≥ 20 mm edge length) grown in the author's laboratory. Although all crystals exhibit apparent (001) growth facets, those grown with or without sufficient B_2O_3 in PbO flux have a platelet morphology (Fig. 12.7a). An obvious change from (001) platelet growth to microscopic (001) layer growth is evident even with a few mol% of B_2O_3 (i.e., about 5 mol%) added to the PbO flux (Fig. 12.7b).

Figure 12.8 shows the change in nucleation mechanism during growth from solution with increasing B_2O_3 content, revealed by deliberately increasing the cooling rate at the later stage of the crystal growth run. Apparently, with a low B_2O_3 content in the PbO flux, the (001) layer growth is initiated via the nucleation and growth of (001)-oriented crystal blocks on the (001) growth facets (Fig. 12.8a). On the other hand, with sufficient B_2O_3 addition, (001) layer growth occurs through <111> corner nucleation followed by spreading down the adjacent <001> edges and (001) faces (Fig. 12.8b).

The above observations suggest that ionic complexes formed in the high temperature solution of the PMN–PT–PbO(B_2O_3) system play an important role in the growth of PMN–PT single crystals. Owing to the strong affinity between Ti^{4+} and O^{2-} ions and the substantial amount of PT present in the PMN–yPT system studied ($y = 0.28$–0.34), it is likely that Ti^{4+} and O^{2-} ions may form various large ionic complexes or clusters (possibly with some covalent nature) in the solution. The growth of PMN–PT with insufficient B_2O_3 addition is thus controlled by cluster growth of Ti^{4+}–O^{2-}-based complexes, leading to a significant increase in the PT content of successively grown layers as the crystal grows in size.

On the other hand, owing to the strong B^{3+}–O^{2-} bonds and the valency difference, addition of B_2O_3 helps modify the nature of the Ti^{4+}–O^{2-}-based

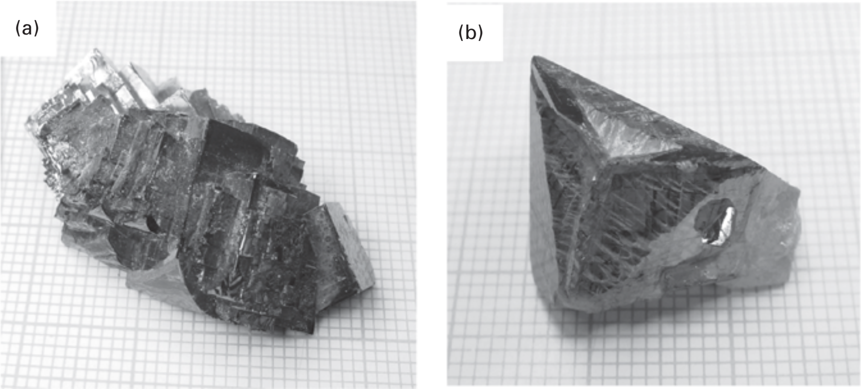

12.8 Different nucleation mechanisms revealed by higher cooling rates near the end of the growth runs: (a) cluster nucleation on (001) facets with less-than-optimum amounts of B_2O_3 in PbO flux: (b) <111> corner and <001> edge nucleation and growth with near-optimum amounts of B_2O_3 in PbO flux.

complexes in the solution. With sufficient B_2O_3 in the PbO flux, a change from the cluster nucleation on (001) faces (Fig. 12.8a) followed by platelet growth (Fig. 12.7a), to <111> corner and <001> edge nucleation (Fig. 12.8b) followed by microscopic (001) layer growth (Fig. 12.7b) takes place.

Since the corner and edge nucleation mechanisms are favoured in the growth of ionic crystals from solutions of simple ions,[126] the addition of B_2O_3 must have broken up existing Ti^{4+}–O^{2-}-based complexes into simpler or smaller ones comprising, possibly, Ti^{4+}, B^{3+} and O^{2-} ions. When this occurs, the diffusivity of the simpler or smaller ionic complexes in the solution is substantially enhanced. This, in turn, would lead to reduced compositional gradients in the grown crystal.

Figure 12.9 shows two large PMN–PT single crystals grown from optimal fluxes of PbO + zB_2O_3, where $z \geq 0.10$. The color of as-grown PMN–PT crystals varies from brownish-to-greenish yellow. High quality crystals are translucent when viewed against the light. Unlike PZN–PT single crystals, the surfaces of as-grown PMN–PT crystals often show characteristic <001> domain wall traces criss-crossing one another at right angles (see also Section 12.4.9).

Even with successful growth of large-size PMN–PT single crystal, the amount of B_2O_3 was found to play a significant role in the extent of compositional segregation in the crystal. For instance, measurements of T_c distributions from wafers cut parallel to the largest (001) growth facet from as-grown PMN–PT crystals showed that with less-than-optimum amounts of B_2O_3 in PbO flux, the variations within wafers were acceptable (i.e., $\Delta T_c \leq \pm 3.0\,°C$) but were too large even between adjacent cuts of wafers (of about

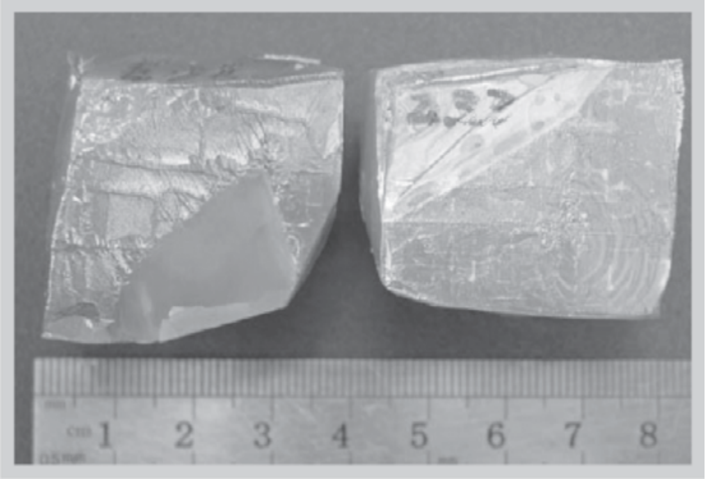

12.9 Two large PMN–PT single crystals grown from PbO+B_2O_3 complex fluxes.

0.5 mm thickness).[79,80] On the other hand, the reverse was observed when the amount of B_2O_3 in the PbO flux is higher than the optimum.

For PMN–32%PT single crystals grown with optimum B_2O_3 in the PbO flux, the initial part of the grown crystal (of 60–70% of the entire crystal) has a relatively uniform PT content (i.e., with $\Delta T_c \leq \pm 3.0\,°C$ typically). The outer part, however, shows a fairly steep increase in PT content. The same observation was made for crystals grown at two different growth rates of 0.8 and 0.2 °C/h, respectively.[80] Since the composition remains relatively uniform over a large initial portion of the grown crystals which is independent of the growth rate, flux growth of PMN–PT crystals from optimum PbO–B_2O_3 fluxes is likely to occur under equilibrium or near-equilibrium conditions, at least during the initial to intermediate stage of the growth. Furthermore, since the difference between the PT content in the initial charge and the grown crystal is not affected by the growth rate used, it is likely that this difference, i.e., about 2.0 mol% PT, is retained in the solution to maintain the equilibrium of the complex flux formation reaction. This being the case, one can anticipate that the grown crystal always has a lower PT content than the charge, regardless of the initial charge composition and the growth rate. This holds as long as equilibrium is attained for the complex flux reaction. The above hypothesis was confirmed with the successful growths of PMN–28%PT ($T_c \approx 125\,°C$) and PMN–30%PT ($T_c \approx 135\,°C$) by using starting charges of PMN–30%PT and PMN–32%PT instead. The T_c values of the flux-grown PMN–PT single crystals agree reasonably well with those obtained by Choi *et al.*[131] and Noblanc *et al.*[132] from PMN–PT ceramics of controlled compositions.

The above result confirms that the actual fluxes for the growth of PMN–PT are indeed complex fluxes of $PbO+z(B_2O_3+\delta PT)$, where δ is a function of B_2O_3 content in the flux. Furthermore, it suggests that with the established complex flux, the growth path is nearly vertical under equilibrium or near-equilibrium growth conditions. This is illustrated schematically in Fig. 12.10. The actual flux should be $PbO + z(B_2O_3 + \delta PT)$, because a fixed amount of PT, determined by the amount of B_2O_3 in the flux, is needed to maintain the equilibrium of the complex flux formation reaction in the solution (marked ‘1’ in the figure). The growth path is relatively vertical at sufficiently high growth temperatures under near-equilibrium growth conditions (marked ‘2’). As a result, the composition of the initial part of the grown crystal is about 2 mol%PT less than that of the initial charge (marked ‘3’). The growth path deviates from the vertical line at low growth temperatures when the growth becomes kinetics controlled, as indicated by the dashed curve (marked ‘4’).

Our finding has shown that with optimum B_2O_3 content in the flux, such that the large ionic complexes are broken up into simpler ions, high uniformity PMN–PT single crystals can be grown with PbO-based fluxes when the

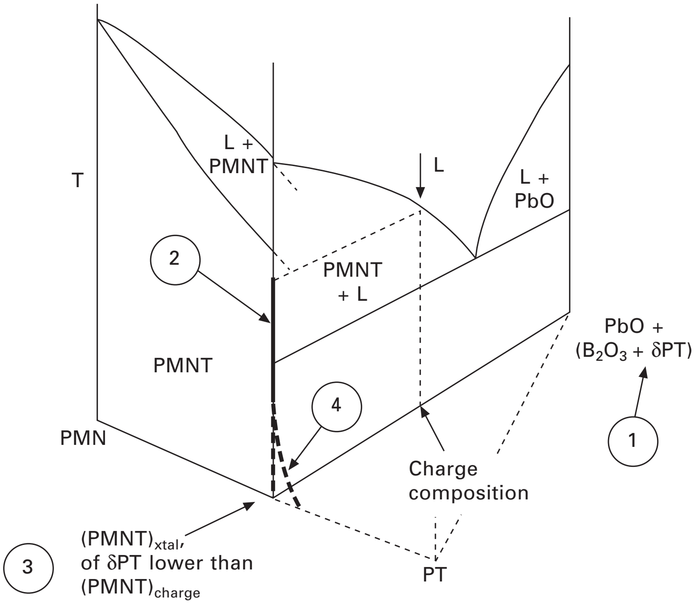

12.10 Modified phase diagram and growth path for flux growth of PMN–PT single crystals from PbO–B_2O_3 based fluxes.

growth is allowed to proceed in a near-equilibrium manner. However, as the growth temperature reduces, the ratio of B_2O_3-to-PT in the solution increases appreciably and the B^{3+}-based ionic complexes may reform in the solution. When this happens, the viscosity of the solution would increase considerably. The (001) layer growth may then become kinetics-controlled. As a result, the uniformity in the crystal composition degrades accordingly, leading to an appreciable increase in PT content in the last part of the crystal.

12.4 Other commonly encountered phenomena

Despite being a convenient means, the flux growth technique via spontaneous nucleation is often plagued with formidable technical problems. Such problems become more pronounced when the technique is used to grow large-size relaxor-PT single crystals for commercial exploitation. The various problems encountered can be grouped into those pertaining to nucleation of crystals and those pertaining to growth of crystals. Multiple nucleation at the cooling point, formation of satellite and parasitic crystals and size-wall nucleation are problems related to the first group (see Fig. 12.1b), while flux inclusions, cracks, solute segregation and fragile domain walls are problems related to the second group. They are briefly described below.

12.4.1 Multiple nucleation and satellite crystals

The use of local point cooling arrangement in flux growth does not always guarantee single crystal nucleation and growth. Instead, multiple crystal nucleation at the intended cooling point is common. Even if single nucleation is successful, satellite crystals may nucleate later in the course of slow cooling, destroying an otherwise perfect crystal growth run. Under less controlled conditions, the situation could be a lot worse and the end result is many mm-size crystals. The problem of satellite crystal formation has been traced to limited convection in the solution coupled with a high cooling and hence growth rate. Such problems can be eradicated, to a large degree, by improving the point cooling arrangement and lowering the cooling rate used.

12.4.2 Parasitic crystals

Unlike satellite crystals which nucleate at the periphery of the main crystal at the base of the Pt crucible, parasitic crystals nucleate and grow onto the main growing crystal. The cause for the formation of parasitic crystals is the same as that for satellite crystals except that a higher degree of supersaturation is required for their formation. Small parasitic crystals are a common feature when the remaining solution is cooled too quickly after the end of the crystal growth run. Similar to satellite crystals, the formation of parasitic crystals can be suppressed by lowering the cooling rate.

12.4.3 Side-wall nucleation

In flux growth of relaxor-PT single crystals, profuse spontaneous nucleation often occurs at the Pt crucible wall along the meniscus ring. Although this may not affect the quality of the main crystal growing from the base of the Pt crucible, it deprives the latter of needed solute to feed its growth. Suppression of side-wall nucleation is crucial for the growth of large-size relaxor-PT single crystals by the flux growth technique. This can be achieved by carefully engineering the temperature gradient of the growth setup such that the meniscus region is of higher isotherms than the solution below.

12.4.4 Pyrochlore crystals

Pyrochlore crystals could form in the early stage of the crystal growth run when the starting solution is far from homogenized. They also appear when the crystal growth run is allowed to proceed to a much lower temperature, say, <850 °C. Under the latter condition, the solution becomes exceedingly enriched in PbO flux, a conducive condition for their formation. Ending the crystal growth run at a higher temperature helps in this regard. Pyrochlore crystals are also common when point nucleation has failed such that a pool of solution is trapped inside the inner periphery of a ring of interconnected satellite crystals. Pyrochlore crystals will form eventually when the pool of solution is deprived sufficiently of the solute. Pyrochlore crystal formation seldom occurs when the crystal growth conditions are not far from ideal and satellite crystal formation has been avoided. The use of B_2O_3 in PbO flux should be avoided in the growth of PZN–PT as several works have noted that B_2O_3 promotes the formation of the pyrochlore phase.[25,38–40,45]

12.4.5 Flux inclusions/trappings

An as-grown single crystal may appear fine on the outside but may contain abundant fluxes and/or is hollow inside. An example of such is shown in Fig. 12.6(b). This figure shows that the bottom, initially grown part of the crystal is porous and full of flux inclusions, while the top, latter grown part is dense and free of flux inclusions. Such a problem is more acute in the growth of relaxor-PT singe crystals of high PT contents, such as PMN–32%PT.

The cause of formation of 'hollow crystals' has been discussed in Section 12.3. Their formation can be avoided by optimizing the flux ingredient in the starting charge such that crystal growth takes place predominantly below the solidus of the corresponding flux-free binary relaxor-PT system. This is shown schematically in Fig. 12.6(a). A vertical section of a PMN–30%PT single crystal grown under such a condition is shown in Fig. 12.6(c). It is evident that the crystal obtained is free of flux inclusions and fully dense.

Under normal growth conditions, multiple growth sectors often operate concurrently in a given crystal. The boundaries where such growth sectors meet are potential sites for flux trapping. An example of such is given in Fig. 12.11(a). At sufficiently high growth rates such that uncontrolled nucleation and growth occur on (001) crystal faces, the flux can be easily trapped at the growth front of the solidifying solid. A vivid example of such is given in Fig. 12.11(b).

12.4.6 Cracks

Lead-based relaxor-PT single crystals are brittle and crack easily when subjected to mild thermal shocks across the rhombohedral-to-tetragonal phase transformation temperature. A large as-grown relaxor-PT single crystal may crack along its periphery if it experiences such thermal shocks during the crystal growth or retrieval processes. When satellite and/or parasitic crystals are present, the stress concentrations associated with anisotropic thermal expansion produced by cooling may also induce cracking of the larger crystal, which often initiates at the apex of the smaller embedded crystals. The presence of pyrochlore crystals is another main cause for

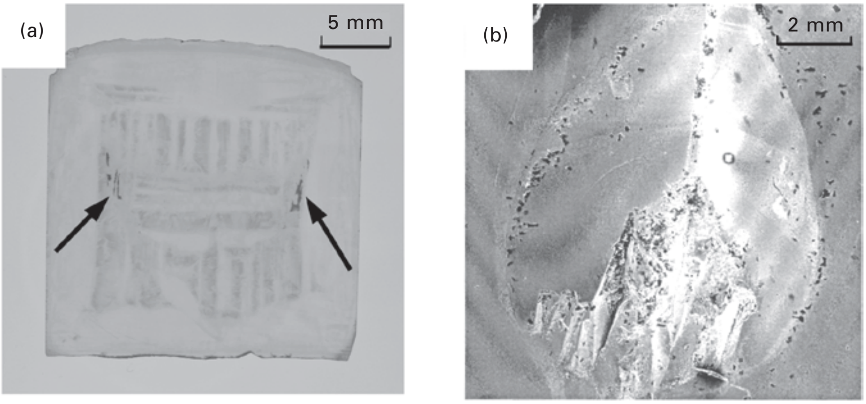

12.11 Trapping of flux (a) at growth sector boundary (arrowed) and (b) at the growth front with increasing growth rates in PZN–9%PT.

crack formation. Cracks in relaxor-PT single crystals may or may not be crystallographic especially for periphery cracks, which at times can assume a smooth hemi-spherical profile. Crystal cracking problems can be largely eliminated by avoiding the pyrochlore phase and the formation of satellite and parasitic crystals during crystal growth, and by handling the crystal with care to avoid unnecessary thermal and/or mechanical shocks.

12.4.7 Pt inclusions

Although not always, Pt inclusions were at times observed in flux-grown PMN–PT single crystals produced in the author's laboratory. They often manifested as a shining deposit layer on the surface of internal cracks and/or growth sector boundaries. Their presence may be attributed to the presence of B_2O_3 in the solution and the higher growth solution temperature used in this case. In contrast, Pt inclusions were seldom detected in the growth of PZN–PT single crystals when pure PbO flux and a significantly lower solution temperature were employed.

12.4.8 Compositional segregation

Even when the grown crystals are free from flux and cracks, under less than ideal growth conditions, compositional segregations are common in as-grown crystals. This is especially so for relaxor-PT crystals of increased PT content. For instance, while flux-grown PZN–xPT single crystals with $x \leq 0.07$ show good compositional homogeneity (with $\Delta T_c \leq \pm 2.5\,°C$ corresponding to $\Delta x \leq \pm 0.005$; see Ref. 130 for details of the measurement technique used), those of $x \geq 0.08$ exhibit $\Delta T_c \geq \pm 3.0\,°C$ or higher.[45] And, as discussed in Section

12.3, compositional segregation could be quite severe when growing relaxor-PT single crystals of high PT content, such as PMN–(30–32)%PT.[79,80,133–136] Compositional segregations in relaxor-PT crystals translate to variations in dielectric and piezoelectric properties of the materials.[133,134,136] They should thus be minimized as far as possible.

12.4.9 PT-rich surface layer and fragile domain walls

At high temperature, the relaxor-PT single crystal is paraelectric with a cubic structure.[124,131,132] On cooling to room conditions, a transition from paraelectric cubic to a ferroelectric rhombohedral or a ferroelectric tetragonal crystal structure occurs depending on the actual PT content in the crystal. As-grown relaxor-PT single crystals thus contain abundant ferroelectric domains, each being the regions within which all spontaneous polarizations are aligned. Ferroelectric domains are visible with the naked eye in grown and polished PZN–PT and PMN–PT single crystal plates when viewed against the light (see, e.g. Fig. 12.11a). They are expected features and are usually harmless.

However, in as-grown PMN–PT single crystals of near-morphotropic phase boundary compositions, certain domain walls are very prominent. Such domain walls generally lie on (001) crystallographic planes criss-crossing one another at right angles and are largely located in the surface layer only. As described in Section 12.3, severe segregation occurs at the later stage of flux growth of relaxor-PT crystals, notably for those of high PT contents. When growing PMN–PT single crystals of near-morphotropic phase boundary compositions, this may lead to the formation of a tetragonal-rich surface layer and associated domains, as shown in Fig. 12.12. When viewed against the light, some of these domain walls are highly reflective, suggesting that they may be cracked. Those intact walls remain fairly fragile and are potential sites of cracking during subsequent crystal cutting, polishing and electrical poling. Such surface layers and domain walls were seldom observed in flux-grown PZN–PT single crystals when the starting charge composition was kept below 8 mol% PT.

12.5 Conclusions

While the solutions of relaxor-PT single crystals of low PT content, such as PZN–xPT with $x \leq 0.08$, are made of simple ions, those of high PT content, such as PMN–yPT with $y \geq 0.25$, contain large ionic complexes.

Due to the large ionic complexes in the solution, as-grown PMN–yPT single crystals of near morphotropic phase boundary compositions ($0.28 < y < 0.34$) exhibit fairly severe compositional variations and are often covered by a PT-rich outer layer. Despite this, with optimum PbO–B_2O_3 fluxes to break

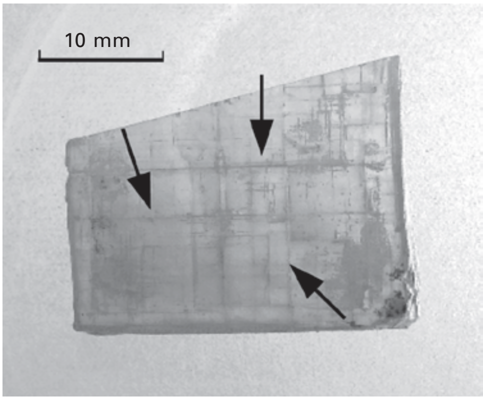

12.12 PT-rich surface layer with prominent but fragile (001) domain walls (arrowed) in an as-grown PMN–30%PT single crystal.

up the ionic complexes and by carefully engineering the growth condition to attain near-equilibrium growth, high uniformity PMN–PT single crystals (with $\Delta y \leq \pm 0.01$) can be produced which may occupy up to 65–75% of the crystal boule.

In contrast, due to the simpler ions in the solution, large (>30 mm edge length), high-homogeneity PZN–PT single crystals can be reproducibly grown by the high-temperature flux technique, by implementing appropriate measures to induce single-point nucleation, applying a slow cooling rate to ensure near-equilibrium growth conditions, and engineering the isotherms in the solution to promote controlled (001) layer growth. Under optimum growth conditions, as-grown PZN–xPT single crystals with $x \leq 0.07$ exhibit good compositional uniformity with $\Delta x \leq \pm 0.005$ over 80–90% of the crystal boule. Flux growth of PZN–xPT single crystals with $x \leq 0.07$ thus shows promise for large-scale growth for commercial exploitation. In addition to improved compositional homogeneity, and hence higher crystal yield in terms of larger usable boule, other advantages of the flux growth technique include lower charge cost, reusable Pt crucibles and ease of crystal growth process.

12.6 Acknowledgements

The author wishes to acknowledge the financial support received from the following organizations over the past six years under which the present research has been made possible: Defense Science and Technology Agency (Singapore), Temasek Defence Science Institute (Singapore), Ministry of Education (Singapore), Maritime and Port Authority (Singapore), National University of Singapore, Office of Naval Research (USA)/NICOP (USA), and

Microfine Materials Technologies Pte. Ltd. (Singapore). The author is also indebted to the staff of the Department of Mechanical Engineering, NUS, and of MMT for the technical support and assistance rendered.

12.7 References

1. J. Kuwata, K. Uchino and S. Nomura, 'Dielectric and piezoelectric properties of $0.91Pb(Zn_{1/3}Nb_{2/3})O_3$–$0.09PbTiO_3$ single crystals', *Japanese Journal of Applied Physics*, vol. 21 (1982), 1298–1302.
2. T.R. Shrout, Z.P. Chang, N. Kim and S. Markgraf, 'Dielectric behaviour of single crystals near the $(1–x)Pb(Mg_{1/3}Nb_{2/3})O_3$–$(x)PbTiO_3$ morphotropic phase boundary', *Ferroelectrics Letters*, vol. 12 (1990), 63–69.
3. S.E. Park and T.R. Shrout, 'Ultrahigh strain and piezoelectric behavior in relaxor based ferroelectric single crystals', *Journal of Applied Physics*, vol. 82 (1997), 1804–1811.
4. S.E. Park and T.R. Shrout, 'Characteristics of relaxor-based piezoelectric single crystals for ultrasonic transducers', *IEEE Transactions on Ultrasonics, Ferroelectrics and Frequency Control*, vol. 44 (1997), 1140–1147.
5. S.E. Park and T.R. Shrout, 'Relaxor based ferroelectric single crystals for electromechanical actuators', *Materials Research and Innovations*, vol. 1 (1997), 20–25.
6. K.K. Rajan, M.J. Zhang and L.C. Lim, 'Optimum compositions for $Pb(Zn_{1/3}Nb_{2/3})O_3$–$PbTiO_3$ single crystals for high-performance applications', *Japanese Journal of Applied Physics*, vol. 44 (2005), 264–266.
7. L.C. Lim, K.K. Rajan and J. Jin, 'Characterization of flux-grown PZN–PT single crystals for high-performance piezo devices', *IEEE Transactions on Ultrasonics, Ferroelectrics and Frequency Control*, vol. 54 (2007), 2474–2478.
8. K.K. Rajan, M. Shanthi, W.S. Chang, J. Jin and L.C. Lim, 'Dielectric and piezoelectric properties of [001] and [011]-poled relaxor ferroelectric PZN–PT and PMN–PT single crystals', *Sensors and Actuators A*, vol. 133 (2007), 110–116.
9. Y. Guo, H. Luo, H. Xu, X. Zhou, X. Pan and Z. Yin, 'Ultra-high piezoelectric response in <110>-oriented polydomain $Pb(Mg_{1/3}Nb_{2/3})O_3$–$PbTiO_3$ single crystals', *Applied Physics A*, vol. 77 (2003), 707–709.
10. J. Peng, H. Luo, D. Lin, H. Xu, T. He and W. Jin, 'Orientation dependence of transverse piezoelectric properties of $0.70Pb(Mg_{1/3}Nb_{2/3})O_3$–$0.30PbTiO_3$ single crystals', *Applied Physics Letters*, vol. 85 (2004), 6221–6223.
11. T. Liu and C.S. Lynch, 'Ferroelectric properties of [110], [001] and [111] poled relaxor single crystals: measurements and modelling', *Acta Materialia*, vol. 51 (2004), 407–416.
12. R. Zhang, B. Jiang and W. Cao, 'Superior d_{32}^* and k_{32}^* coefficients in $0.955Pb(Zn_{1/3}Nb_{2/3})O_3$–$0.045PbTiO_3$ and $0.92Pb(Zn_{1/3}Nb_{2/3})O_3$–$0.08PbTiO_3$ single crystals poled along [011]', *Journal of Physics and Chemistry of Solids*, vol. 65 (2004), 1083–1086.
13. E.A. McLaughlin, T. Liu and C.S. Lynch, 'Relaxor ferroelectric PMN–32%PT crystals under stress and electric field loading: I–32 mode measurements', *Acta Materialia*, vol. 52 (2004), 3849–3857.
14. P. Han, W. Yan, J. Tian, X. Huang and H. Pan, 'Cut directions for the optimisation of piezoelectric coefficients of lead magnesium niobate-lead titanate ferroelectric crystals', *Applied Physics Letters*, vol. 86 (2005), 052902.

15. K.K. Rajan, J. Jin, W.S. Chang and L.C. Lim, 'Transverse-mode properties of [011]-poled $Pb(Zn_{1/3}Nb_{2/3})O_3$–$PbTiO_3$ single crystals: effects of compositions, length orientation, and poling conditions', *Japanese Journal of Applied Physics*, vol. 46 (2007), 681–685.
16. R. Zhang, B. Jiang and W. Cao, 'Elastic, piezoelectric and dielectric properties of multidomain $0.67Pb(Mg_{1/3}Nb_{2/3})O_3$–$0.33PbTiO_3$ single crystals', *Journal of Applied Physics*, vol. 90 (2001), 3471–3473.
17. R. Zhang, B. Jiang, W. Cao and A. Amin, 'Complete set of materials constants of $0.93Pb(Zn_{1/3}Nb_{2/3})O_3$–$0.07PbTiO_3$ domain engineered single crystal', *Journal of Materials Science Letters*, vol. 21 (2002), 1877–1879.
18. R. Zhang, B. Jiang, W. Jiang and W. Cao, 'Complete set of elastic, dielectric, and piezoelectric coefficients of $0.93Pb(Zn_{1/3}Nb_{2/3})O_3$–$0.07PbTiO_3$ single crystal poled along [011]', *Applied Physics Letters*, vol. 89 (2006), 242908.
19. F. Wang, L. Luo, D. Zhou, X. Zhao and H. Luo, 'Complete set of elastic, dielectric, and piezoelectric constants of orthorhombic $0.71Pb(Mg_{1/3}Nb_{2/3})O_3$–$0.29PbTiO_3$ single crystal', *Applied Physics Letters*, vol. 90 (2007), 212903.
20. R. Shukla, K.K. Rajan, P. Gandhi and L.C. Lim, 'Complete sets of elastic, dielectric, and piezoelectric properties of [001]-poled $Pb(Zn_{1/3}Nb_{2/3})O_3$–(6–7)%$PbTiO_3$ single crystals of [110] length cut', *Applied Physics Letters*, vol. 91 (2008), 212907.
21. M. Shanthi, L.C. Lim, K.K. Rajan and J. Jin, 'Complete set of elastic, dielectric, and piezoelectric properties of flux-grown [011]-poled $Pb(Mg_{1/3}Nb_{2/3})O_3$–(28–32)%$PbTiO_3$ single crystals', *Applied Physics Letters*, vol. 92 (2008), 142906.
22. R. Zhang, W. Jiang and W. Cao, 'Frequency dispersion of ultrasonic velocity and attenuation of longitudinal waves propagating in $0.68Pb(Mg_{1/3}Nb_{2/3})O_3$–$0.32PbTiO_3$ single crystals', *Applied Physics Letters*, vol. 87 (2005), 182903.
23. L.C. Lim, J. Jin and K.K. Rajan, 'Transverse-mode properties of PZN–PT single crystals and devices', presented at the *2006 US Navy Workshop on Acoustic Transduction Materials and Devices*, May 9–11, 2006, State College, PA (Abstract VI.2).
24. I.E. Myl'nikova and V.A. Bokov, *Kristallografiya*, vol. 4 (1959), 433 (in Russian).
25. V.A. Bokov and I.E. Myl'nikova, 'Ferroelectric properties of monocrystals of new perovskite compounds', *Journal of Applied Physics*, vol. *Soviet Physics – Solid State*, vol. 2 (1961), 2428–2432.
26. I.E. Myl'nikova and V.A. Bokov, 'Growth and electrical properties of monocrystals of $Pb_3NiNb_2O_9$ and $Pb_3MgNb_2O_9$', in *Growth of Crystals* (ed. A.V. Shubnikov and N.N. Sheftal), Consultants Bureau, New York, vol. 3 (1962), 309–315.
27. S. Nomura, T. Takahashi and Y. Yokomizo, 'Ferroelectric properties in the system $Pb(Zn_{1/3}Nb_{2/3})O_3$–$PbTiO_3$', *Japanese Journal of Applied Physics*, vol. 27 (1969), 262.
28. Y. Yokomizo, T. Takahashi and S. Nomura, 'Ferroelectric properties of $Pb(Zn_{1/3}Nb_{2/3})O_3$', *Journal of the Physical Society of Japan*, vol. 28 (1969), 1278–1284.
29. S. Saitoh, M. Izumi, Y. Yamashita, S. Shimanuki, M. Kawachi and T. Kobayashi, 'Piezoelectric single crystal, ultrasonic probe, and array-type ultrasonic', US Patent, No. 5,402,891 (1995).
30. S.E. Park, M.L. Mulvihill, P.D. Lopath, M. Zippara and T.R. Shrout, 'Crystal growth and ferroelectric related properties of (1-x)$Pb(A_{1/3}B_{2/3})O_3$–x$PbTiO_3$ (A = Zn^{2+},Mg^{2+})', *Proceedings of the 1996 International Symposium of Applications of Ferroelectrics (ISAF'96)* (edited by B.M. Kulwichi, A. Amin and A. Safari), IEEE, Piscataway, N.J., vol. 1, pp.79–82 (1996).

31. M.L. Mulvihill, S.E. Park, G. Risch, Z. Li, K. Uchino and T.R. Shrout, ‘The role of processing variables in the flux growth of lead zinc niobate-lead titanate relaxor ferroelectric single crystals’, *Japanese Journal of Applied Physics*, vol. 36 (1997), 1154–1158.
32. S.E. Park, M.L. Mulvihill, G. Risch and T.R. Shrout, ‘The effect of growth condition on dielectric properties of $Pb(Zn_{1/3}Nb_{2/3})O_3$ crystal’, *Japanese Journal of Applied Physics*, vol. 36 (1997), 1154–1158.
33. T. Kobayashi, S. Shimanuki, S. Saitoh and Y. Yamashita, ‘Improved growth of large lead zinc niobate titanate piezoelectric single crystals for medical ultrasonic transducers’, *Japanese Journal of Applied Physics*, vol. 36 (1997), 6035–6038.
34. T. Kobayashi, S. Saitoh, K. Harada, S. Shimanuki and Y. Yamashita, ‘Growth of large and homogeneous PZN–PT single crystals for medical ultrasonic array transducers’, *Proceedings of the 1998 International Symposium of Applications of Ferroelectrics (ISAF’98)* (edited by E. Colla, D. Damjanovic and N. Setter), IEEE, Piscataway, N.J., pp. 235–238 (1998).
35. C.S. Park, K.Y. Lim, D.Y. Choi and S.J. Chung, ‘Crystal growth of $PbMg_{1/3}Nb_{2/3}O_3$ and $PbZn_{1/3}Nb_{2/3}O_3$ and structural studies on the ordering’, *Journal of Korean Physical Society*, vol. 32 (1998), S974–S977.
36. S. Saitoh, T. Takeuchi, T. Kobayashi, K. Harada, S. Shimanuki and Y. Yamashita, ‘An improved phased array ultrasonic probe using $0.91Pb(Zn_{/3}Nb_{2/3})O_3$–$0.09PbTiO_3$ single crystal’, *IEEE Transactions on Ultrasonics, Ferroelectrics and Frequency Control*, vol. 46 (1999), 414–421.
37. S. Saitoh, T. Takeuchi, T. Kobayashi, K. Harada, S. Shimanuki and Y. Yamashita, ‘A 3.7 MHz phased array probe using $0.91Pb(Zn_{/3}Nb_{2/3})O_3$–$0.09PbTiO_3$ single crystal’, *Japanese Journal of Applied Physics,* vol. 38 (1999), 3380–3384.
38. L. Zheng, M. Dong and Z.-G. Ye, ‘Flux growth and characterization of the relaxor-based $Pb[(Zn_{1/3}Nb_{2/3})_{1-x}Ti_x]O_3$ [PZNT] piezocrystals’, *Materials Science and Engineering B*, vol. 78 (2000), 96–104.
39. S. Gentil, G. Robert, N. Setter, P. Tissot and J.-P. Rivera, ‘Growth mechanism and electrical properties of $Pb(Zn_{/3}Nb_{2/3})O_3$–$PbTiO_3$ single crystals with a cubic habitus’, *Japanese Journal of Applied Physics*, vol. 39 (2000), 2732–2735.
40. J.F. Kumar, L.C. Lim, C. Chilong and M.J. Tan, ‘Morphological aspects of flux grown $0.91Pb(Zn_{1/3}Nb_{2/3})O_3$–$0.09PbTiO_3$ crystals’, *Journal of Crystal Growth*, vol. 216 (2000), 311–316.
41. L.C. Lim and F.J. Kumar, ‘Growth of large-size inclusion-free 0.91PZN–0.09PT single crystals’, presented at the *2001 US Navy Workshop on Acoustic Transduction Materials and Devices*, 14–16 May, 2001, Baltimore, MA.
42. J. Xiao, Y. Hang, S. Wan, X. Zhu, S. Zhou, W. Huang, Y. Tian and S. Yin, ‘Characterization of $0.92Pb(Zn_{1/3}Nb_{2/3})O_3$–$0.08PbTiO_3$ crystals grown from high-temperature solutions’, *Journal of Crystal Growth*, vol. 242 (2002), 255–361.
43. J.L. Santailler, B. Ferrand, D. Damjanovic, M. Couchaud, P. Dusserre, M. Budimir, S. Mibord and T. Abad, ‘Growth and characterization of piezoelectric PZN–PT 89/11 and PMN–PT 66/34 single crystals for ultrasonic transducers’, *Proceedings of the 2002 International Symposium of Applications of Ferroelectrics (ISAF’02)* (edited by G. White and T. Tsurumi), IEEE, Piscataway, NJ, vol. 1, 443–446 (2002).
44. J.L. Santailler, B. Ferrand, M. Couchaud, A. Renault, P. Dusserre, C. Calvat, G. Basset, D. Damjanovic and M. Budimir, ‘Growth of ferroelectric single crystals – application to PZN–PT 91/9 and PMN–PT 66/34’, presented at the *15th American*

Conference on Crystal Growth and Epitaxy (ACCGE15), July, 2003, Keystone, CO.

45. L.C. Lim and K.K. Rajan, ‘High-homogeneity high-performance flux-grown $Pb(Zn_{1/3}Nb_{2/3})O_3$–$PbTiO_3$ single crystals’, *Journal of Crystal Growth*, vol. 271 (2004), 435–444.
46. A. Dabkowski, H.A. Dabkowdka, J.E. Greedan, W. Ren and B.K. Mukherjee, ‘Growth and properties of single crystals of relaxor PZN–PT materials obtained from high-temperature solution’, *Journal of Crystal Growth*, vol. 265 (2004), 204–213.
47. A. Benayad, D. Kobor, L. Lebrun, B. Guiffard and D. Guyomar, ‘Characteristics of $Pb[(Zn_{1/3}Nb_{2/3})_{0.955}Ti_{0.045}]O_3$ single crystals versus growth method’, *Journal of Crystal Growth*, vol. 270 (2004), 137–144.
48. J.B. Babu, G. Madeswaran, C. Prakash and R. Dhanasekaran, ‘Growth, structural phase transition and ferroelectric properties of $Pb[(Zn_{1/3}Nb_{2/3})_{0.91}Ti_{0.09}]O_3$ single crystals’, *Journal of Crystal Growth*, vol. 292 (2006), 399–403.
49. S. Shimanuki, S. Saitoh and Y. Yamashita, ‘Single crystal of the $Pb(Zn_{1/3}Nb_{2/3})O_3$–$PbTiO_3$ system grown by the vertical Bridgman method and its characterization’, *Japanese Journal of Applied Physics*, vol. 37 (1998), 3382–3385.
50. K. Harada, S. Shimanuki, T. Kobayashi, S. Saitoh and Y. Yamashita, ‘Crystal growth and electrical properties of $Pb[(Zn_{1/3}Nb_{2/3})_{0.91}Ti_{0.09}]O_3$ single crystals produced by solution Bridgman method’, *Journal of the American Ceramic Society*, vol. 81 (1998), 2785–2788.
51. K. Harada, S. Shimanuki, T. Kobayshi, S. Saitoh and Y. Yamashita, ‘Growth of $Pb[(Zn_{1/3}Nb_{2/3})_{0.91}Ti_{0.09}]O_3$ single crystal of ultrasonic transducer for medical application’, *Journal of Intelligent Materials Systems and Structures*, vol. 10 (1999), 493–497.
52. K. Harada, S. Shimanuki, T. Kobayashi, S. Saitoh and Y. Yamashita, ‘Dielectric and piezoelectric properties of $Pb[(Zn_{1/3}Nb_{2/3})_{0.91}Ti_{0.09}]O_3$ single crystal grown by solution Bridgman method’, *Key Engineering Materials*, vol. 157–158 (1999), 95–102.
53. K. Harada, Y. Hosono, T. Kobayashi, Y. Yamashita and K. Miwa, ‘Piezoelectric $Pb[(Zn_{1/3}Nb_{2/3})_{0.91}Ti_{0.09}]O_3$ single crystals with a diameter of 2 inches by the solution Bridgman method supported on the bottom of a crucible’, *Journal of Crystal Growth*, vol. 229 (2001), 294–298.
54. K. Harada, Y. Hosono, T. Kobayashi, Y. Yamashita, S. Wada and T. Tsurumi, ‘Piezoelectric single crystal $Pb[(Zn_{1/3}Nb_{2/3})_{0.93}Ti_{0.07}]O_3$ (PZNT 93/7) for ultrasonic transducers’, *Journal of Crystal Growth*, vol. 237–239 (2002), 844–852.
55. M. Matsushita, T. Tachi and K. Echizenya, ‘Growth of 3-in single crystals of $Pb[(Zn_{1/3}Nb_{2/3})_{0.91}Ti_{0.09}]O_3$ by the supported solution Bridgman method’, *Journal of Crystal Growth*, vol. 237–239 (2002), 853–857.
56. J. Xu, S. Fan, B. Lu, J. Tong and A. Zhang, ‘Seeded growth of relaxor ferroelectric single crystals $Pb[(Zn_{1/3}Nb_{2/3})_{0.91}Ti_{0.09}]O_3$ by the vertical Bridgman method’, *Japanese Journal of Applied Physics*, vol. 41 (2002), 7000–7002.
57. J. Xu, J. Tong, M. Shi, A. Wu and S. Fan, ‘Flux Bridgman growth of $Pb[(Zn_{1/3}Nb_{2/3})_{0.93}Ti_{0.07}]O_3$ piezocrystals’, *Journal of Crystal Growth*, vol. 253 (2003), 274–279.
58. B.J. Fang, H.Q. Xu, T.-H. He, H.S. Luo and Z.-W. Yin, ‘Growth mechanism and electrical properties of $Pb[(Zn_{1/3}Nb_{2/3})_{0.91}Ti_{0.09}]O_3$ single crystals by a modified Bridgman method’, *Journal of Crystal Growth*, vol. 244 (2002), 318–326.

59. J. Xu, X. Wu, J. Tong, M. Shi and G. Qian, 'Two-step Bridgman growth of $0.91Pb(Zn_{1/3}Nb_{2/3})O_3$–$0.09PbTiO_3$ single crystals', *Journal of Crystal Growth*, vol. 280 (2005), 107–112.
60. W. Chen and Z.-G. Ye, 'Top-cooling-solution-growth and characterization of piezoelectric $0.955Pb(Zn_{1/3}Nb_{2/3})O_3$–$0.045PbTiO_3$ [PZNT] single crystals', *Journal of Materials Science*, vol. 36 (2001), 4393–4399.
61. T. Karaki, M. Nakamoto and M. Adachi, 'Top-seeded solution growth of $Pb[(Zn_{1/3}Nb_{2/3})_{0.93}Ti_{0.07}]O_3$ single crystals', *Japanese Journal of Applied Physics*, vol. 41 (2002), 6997–6999.
62. R. Bertram, G. Reck and R. Uecker, 'Growth and correlation between composition and structure of $(1\text{-}x)Pb(Zn_{1/3}Nb_{2/3})O_3$–$xPbTiO_3$ near the morphotropic phase boundary', *Journal of Crystal Growth*, vol. 253 (2003), 212–220.
63. Z.-G. Ye and W. Chen, 'Top-seeded solution growth and characterization of PMN–PT and PZN–PT single crystals', presented at the *15th American Conference on Crystal Growth and Epitaxy (ACCGE15)*, July, 2003, Keystone, CO.
64. S. Priya, K. Uchino and D. Viehland, 'Fe-substituted $0.92Pb(Zn_{1/3}Nb_{2/3})O_3$–$0.08PbTiO_3$ single crystals – a hard piezocrystal', *Applied Physics Lett*ers, vol. 81 (2002), 2430–2432.
65. S. Zhang, L. Lebrun, D.-Y. Jeong, C.A. Randall and Q. Zhang, 'Growth and characterization of Fe-doped $Pb(Zn_{1/3}Nb_{2/3})O_3$–$PbTiO_3$ single crystals', *Journal of Applied Physics*, vol. 93 (2003), 9257–9262.
66. Y. Sato, S. Abe, R. Fujimura, H. Ono, K. Oda, T. Shimura and K. Kuroda, 'Photorefractive effect and photochromism in the Fe-doped relaxor ferroelectric crystal $Pb(Zn_{1/3}Nb_{2/3})O_3$–$PbTiO_3$', *Journal of Applied Physics*, vol. 96 (2004), 4852–4855.
67. S. Priya, K. Uchino and D. Viehland, 'Crystal growth and piezoelectric properties of Mn-substituted $Pb(Zn_{1/3}Nb_{2/3})O_3$ single crystal', *Japanese Journal of Applied Physics*, vol. 40 (2001), L1044–L1047.
68. S. Zhang, L. Lebrun, C.A. Randall and T.R. Shrout, 'Growth and electrical properties of (Mn,F) co-doped $0.92Pb(Zn_{1/3}Nb_{2/3})O_3$–$0.08PbTiO_3$ single crystal', *Journal of Crystal Growth*, vol. 267 (2004), 204–212.
69. D. Kobor, L. Lebrun, G. Sebald and D. Guyomar, 'Characterization of pure and substituted $0.955Pb(Zn_{1/3}Nb_{2/3})O_3$–$0.045PbTiO_3$', *Journal of Crystal Growth*, vol. 275 (2005), 580–588.
70. D. Kobor, B. Guiffard, L. Lebrun, A. Hajjaji and D. Guyomar, 'Oxygen vacancies effect on ionic conductivity and relaxation phenomenon in undoped and Mn doped PZN–4.5PT single crystals', *Journal of Physics D: Applied Physics,* vol. 40 (2007), 2920–2926.
71. S. Priya and K. Uchino, 'High power resonance characteristics and dielectric properties of Co-substituted $0.92Pb(Zn_{1/3}Nb_{2/3})O_3$–$0.08PbTiO_3$ single crystal', *Japanese Journal of Applied Physics*, vol. 42 (2003), 531–534.
72. I.I. Afanas'ev, A.A. Berezhnoi, T.S. Bushneva and S.V. Prokof'ev, 'Growing crystals of lead magnoniobate and magnotantalate', *Soviet Journal of Optical Technol*ogy, vol. 44 (1977), 613–615.
73. N. Setter and L.E. Cross, 'Flux growth of lead scandium tantalite $Pb(Sc_{0.5}Ta_{0.5})O_3$ and lead magnesium niobate $Pb(Mg_{1/3}Nb_{2/3})O_3$ single crystals', *Journal of Crystal Growth*, vol. 50 (1980), 555–556.
74. G.T. Petrovskii, I.A. Bonder, E.M. Andreev and N. Keroleva, 'Formation of single crystals of the perovskite like ferroelectrics PMN', *Inorganic Materials*, vol. 20 (1984), 924–928.

75. Z.-G. Ye, P. Tissor and H. Schmid, ‘Pseudo-binary $Pb(Mg_{1/3}Nb_{2/3})O_3$–PbO phase diagram and crystal growth of $Pb(Mg_{1/3}Nb_{2/3})O_3$ [PMN]’, *Materials Research Bulletin*, vol. 25 (1990), 739–748.
76. M. Dong and Z.-G. Ye, ‘High-temperature solution growth and characterization of the piezo-/ferroelectric (1-x)$Pb(Mg_{/3}Nb_{2/3})O_3$–$x$$PbTiO_3$ [PMNT] single crystals’, *Journal of Crystal Growth*, vol. 209 (2000), 81–90.
77. X. Jiang, F. Tang, J.T. Wang and T.P. Chen, ‘Growth and properties of PMN–PT single crystals’, *Physica C*, vol. 364–365 (2001), 678–683.
78. H. Fan, L. Zhao, B. Tang, C. Tian and H.-E. Kim, ‘Growth and characterization of PMNT relaxor-based ferroelectric single crystals by flux method’, *Materials Science and Engineering B*, vol. 99 (2003), 183–186.
79. L.C. Lim, ‘Flux growth of large-size high-homogeneity PMN–PT single crystals’, presented at the *2003 US Navy Workshop on Acoustic Transduction Materials and Devices*, 6–8 May, 2003, State College, PA, and at the 15th American Conference on *Crystal Growth and Epitaxy (ACCGE15)*, July, 2003, Keystone, CO.
80. L.C. Lim, M. Shanthi, K.K. Rajan and C.Y.H. Lim, ‘Flux growth of high-homogeneity PMN–PT single crystals and their property characterization’, *Journal of Crystal Growth*, vol. 282 (2005), 330–342.
81. A. Kania, A. Slodczyk and Z. Ujma, ‘Flux growth and characterization of (1-x) $PbMg_{1/3}Nb_{2/3}O_3$–$x$$PbTiO_3$ single crystals’, *Journal of Crystal Growth*, vol. 29 (2005), 134–139.
82. Y. Tang, L. Luo, Y. Jia, H. Luo, X. Zhao, H. Xu, D. Lin, J. Sun, X. Meng, J. Zhu and M. Es-Souni, ‘Mn-doped $0.71Pb(Mg_{1/3}Nb_{2/3})O_3$–$0.29PbTiO_3$ pyroelectric crystals for uncooled infrared focal plane arrays applications’, *Applied Physics Lett*ers, vol. 89 (2006), 162906.
83. W.A. Bonner and L.G. Van Uitert, ‘Growth of single crystals of Pb_3MgNbO_9 by Kyrpoulos technique’, *Materials Research Bulletin*, vol. 2 (1967), 131–134.
84. W. Chen and Z.-G. Ye, ‘Top seeded solution growth and characterization of piezo/ferroelectric (1–x)$Pb(Mg_{/3}Nb_{2/3})O_3$–$x$$PbTiO_3$ single crystals’, *Journal of Crystal Growth*, vol. 233 (2001), 503–511.
85. Y. Hosono, K. Harada, Y. Yamashita, M. Dong and Z.–G. Ye, ‘Growth, electric and thermal properties of lead scandium niobate-lead magnesium niobate-lead titanate ternary single crystals’, *Japanese Journal of Applied Physics*, vol. 39 (2000), 5589–5592.
86. Y. Hosono, Y. Yamashita, H. Sakamoto and N. Ichinose, ‘Growth of single crystals of high-Curie-temperature $Pb(In_{1/2}Nb_{1/2})O_3$–$Pb(Mg_{1/3}Nb_{2/3})O_3$–$PbTiO_3$ ternary system near morphotropic phase boundary’, *Japanese Journal of Applied Physics*, vol. 40 (2001), 5664–5667.
87. I.P. Raevskii, S.M. Emel’yanov, F.I. Savenko, I.N. Zakharchenko, O.A. Bunina, M.A. Malitskaya, A.S. Bogatin and E.V. Sakhkar, ‘Growth and study of single crystals of solid solutions of ferroelectric-relaxor (1-x)$PbMg_{1/3}Nb_{2/3}O_3$–(x)$PbSc_{1/2}Nb_{1/2}O_3$ with different degrees of compositional order’, *Crystallography Report*, vol. 48 (2003), 461–465.
88. E.G. Fesenko, E.A. Grigor, A. Ya Dantsiger, Yu. I. Golovko and S.I. Dudkina, ‘Synthesis and study of $PbNb_{0.5}Sc_{0.5}O_3$ single crystals’, *Bulletin of the Academy of Science USSR Physics,* Series 33 (1971), 2287–2289.
89. I.J. Smotrakov, I.P. Raevskii, M.A. Malitskaya, S.M. Zaitsev, Yu M. Popov and N.A. Strekneva, ‘Preparation and properties of single crystals of Pb_2ScNbO_6’, *Inorganic Materials*, vol. 19 (1983), 105–109.

90. C. Caranoni, P. Lampin, I. Siny, J.G. Zheng, Q. Li, Z.C. Kang and C. Boulesteix 'Comparative study of the ordering of B-site cations in Pb_2ScTaO_6 and Pb_2ScNbO_6 perovskites', *Physica State Solidus A*, vol. 130 (1992), 25–37.
91. J. Wolak, B. Hilczer, C. Caranoni, P. Lampin and C. Boulesteix, 'Dielectric studies of PSNT single crystals', *Ferroelectrics*, vol. 158 (1994), 399–404.
92. P. Lampin, N. Menguy and C. Caranoni, 'Microstructure of $PbSc_{0.5}(Nb,Ta)_{0.5}O_3$ – a highly ordered solid-solution of complex perovskite compounds', *Philosophical Magazine Letters*, vol. 72 (1995), 215–222.
93. Y. Yamashita and S. Shimanuki, 'Synthesis of lead scandium niobate-lead titanate pseudo binary system single crystals', *Materials Research Bulletin*, vol. 31 (1996), 887–895.
94. Y. Yamashita and K. Harada, 'Crystal growth and electrical properties of lead scandium niobate-lead titanate binary single crystals', *Japanese Journal of Applied Physics*, vol. 36 (1997), 6039–6042.
95. Y. Yanagisawa, J.C. Rendon-Angeles, H. Kanai and Y. Yamashita, 'Stability and single crystal growth of dielectric materials containing lead under hydrothermal conditions', *Journal of the European Ceramic Society*, vol. 19 (1999), 1033–1036.
96. V.V. Eremkin, V.G. Smotrakov, E.S. Gagarina, S.NM. Zaitsev and S.I. Shevtsova, 'Growth and study of the crystals of the $PbSc_{1/2}Nb_{1/2}O_3$–$PbSc_{1/2}Ta_{1/2}O_3$ solid solutions', *Crystallography Reports*, vol. 44 (1999), 818–820.
97. I.P. Raevski, M.A. Malitskaya, E.S. Gagarina, V.G. Smotrakov and V.V. Eremkin, 'T-x-s phase diagram of compositionally orderable $(1\text{-}x)PbSc_{1/2}NBb_{1/2}O_3$–$xPbSc_{1/2}Ta_{1/2}O_3$ solid solution', *Ferroelectrics*, vol. 235 (1999), 221–230.
98. I.P. Raevskii, V.G. Smotrakov, V.V. Eremkin, E.S. Gagarina and M.A. Malitskaya, 'The growth and study of $PbSc_{0.5}Nb_{0.5}O_3$–$BaSc_{0/5}Nb_{0.5}O_3$ solid solution crystals', *Ferroelectrics*, vol. 247 (2000), 27–36.
99. Y.-H. Bing and Z.-G. Ye, 'Growth and characterization of relaxor ferroelectric (1-x) $Pb(Sc_{1/2}Nb_{1/2})O_3$–$xPbTiO_3$ single crystals', *Proceedings of the 2002 International Symposium of Applications of Ferroelectrics (ISAF'02)* (edited by G. White and T. Tsurumi), IEEE, Piscataway, NJ, pp. 447–450 (2002).
100. Y.H. Bing and Z.-G. Ye, 'Effect of chemical compositions on the growth of relaxor ferroelectric $Pb(Sc_{1/2}Nb_{1/2})_{1-x}Ti_xO_3$ single crystals', *Journal of Crystal Growth*, vol. 250 (2003), 118–125.
101. S.V. Rajasekaran, A.K. Singh and R. Jayavel, 'Growth and morphological aspects of $Pb[(Sc_{1/2}Nb_{1/2})_{0.58}Ti_{0.42}]O_3$ single crystals by slow-cooling technique', *Journal of Crystal Growth*, vol. 310 (2008), 1093–1098.
102. P. Grove, 'Structural phase transitions and long-range order in ferroelectric perovskite lead indium niobate', *Journal of Physics C – Solid State Physics*, vol. 19 (1986), 111–128.
103. A. Kania and E. Rowinski, 'Dielectric properties for differently quenched $PbIn_{0.5}Nb_{0.5}O_3$ crystals', *Ferroelectrics*, vol. 124 (1991), 265–270.
104. N. Yasuda, H. Ohwa, D. Hasegawa, K. Hayashi, Y. Hosono, Y. Yamashita, M. Iwata and Y. Ishibashi, 'Temperature dependence of piezoelectric properties of a high Curie temperature $Pb(In_{1/2}Nb_{1/2})O_3$–$PbTiO_3$ binary system single crystal near a morphotropic phase boundary', *Japanese Journal of Applied Physics*, vol. 39 (2000), 5586–5588.
105. A. Kania, 'Crystallographic and dielectric properties of flux grown $PbB'_{1/2}B''_{1/2}O_3$ ($B'B''$: InNb, InTa, YbNb, YbTa and MgW) single crystals', *Journal of Crystal Growth*, vol. 310 (2008), 2767–2773.

106. V. Yu. Topolov, E.S. Gagarina and V.V. Demidova, 'Domain structure and related phenomena in $PbYb_{0.5}Nb_{0.5}O_3$ crystals', *Ferroelectrics*, vol. 172 (1995), 373–376.
107. N. Yasuda, H. Ohwa, M. Kume, Y. Hosono, Y. Yamashita, S. Ishino, H. Terauchi, M. Iwata and Y. Ishibashi, 'Crystal growth and dielectric properties of solid solutions of $Pb(Yb_{1/2}Nb_{1/2})O_3$–$PbTiO_3$ with a high Curie temperature near a morphotropic phase boundary', *Japanese Journal of Applied Physics*, vol. 40 (2001), 5664–5667.
108. N. Yasuda, N. Mori, H. Ohwa, Y. Hosono, Y. Yamashita, M. Iwata, M. Maeda, I. Suzuki and Y. Ishibashi, 'Crystal growth and some properties of lead indium niobate-lead titanate single crystals produced by solution Bridgman method', *Japanese Journal of Applied Physics*, vol. 41 (2002), 7007–7010.
109. S.J. Zhang, P.W. Rehring, C.A. Randall and T.R. Shrout, 'Crystal growth and electrical properties of $Pb(Yb_{1/2}Nb_{1/2})O_3$–$PbTiO_3$ perovskite single crystals', *Journal of Crystal Growth*, vol. 234 (2002), 415–420.
110. N. Ichinose, T. Takahashi and Y. Yokomizo, 'Crystal growth of $Pb(Cd_{1/3}Nb_{2/3})O_3$ and its dielectric properties', *Journal of Physical Society of Japan*, vol. 31 (1971), 1848–1850.
111. I.H. Brunskill, P. Tissot and H. Schmid, 'Determination of the phase diagrams, PbO–$Pb(Fe_{1/2}Nb_{1/2})O_3$ and PbO–$Pb(Mn_{1/2}Nb_{1/2})O_3$', *Thermochimica Acta*, vol. 49 (1981), 351–355.
112. I.H. Brunskill, R. Boutellier, W. Depmeier and H. Schmid, 'High-temperature solution growth of $Pb(Fe_{0.5}Nb_{0.5})O_3$ and $Pb(Mn_{0.5}Nb_{0.5})O_3$ crystals', *Journal of Crystal Growth*, vol. 56 (1982), 541–546.
113. F. Galasso and W. Darby, 'Preparation of single crystals of complex perovskite ferroelectric and semiconducting compounds', *Inorganic Chemistry*, vol. 4 (1965), 71–73.
114. A. Kania, 'A new perovskite $PbIn_{1/2}Ta_{1/2}O_3$ (PIT)', *Ferroelectrics Letters*, vol. 11 (1990), 107–110.
115. A.A. Bokov, I.P. Rayevsky, V.V. Neprin and V.G. Smotrakov, 'Investigation of phase transitions in $Pb(In_{0.5}Ta_{0.5})O_3$ crystals', *Ferroelectrics*, vol. 124 (1991), 271–273.
116. E.S. Gagarina, S.M. Zaitsev, V.Y. Topolov, V.V. Demidova, S.V. Titov and E.S. Tsikhotskii, 'X-ray diffraction studies of the domain structure in $PbYb_{0.5}Ta_{0.5}O_3$ crystals', *Crystallography Reports*, vol. 43, (1998), 415–418.
117. A. Kania, A. Majda, S. Miga and A. Slodczyk, 'Anisotropic dielectric properties of $PbYb_{1/2}Ta_{1/2}O_3$ single crystals', *Physica B*, vol. 400 (2007), 42–46.
118. A. Kania, 'Flux growth of $PbMg_{1/3}Ta_{2/3}O_3$ single crystals', *Journal of Crystal Growth*, vol. 300 (2007), 343–346.
119. A. Kania, A. Leonarska and Z. Ujma, 'Growth and characterization of (1-x) $PbMg_{1/3}Ta_{2/3}O_3$–$xPbTiO_3$ single crystals', *Journal of Crystal Growth*, vol. 310 (2008), 594–598.
120. B.N. Sun, R. Boutellier, Ph. Sciau, E. Burkhardt, V. Rodriguez and H. Schmid, 'High temperature solution growth of perovskite Pb_2CoWO_6 single crystals', *Journal of Crystal Growth*, vol. 112 (1991), 71–83.
121. Z.-G. Ye and H. Schmid, 'Growth from high temperature solution and characterization of $Pb(Fe_{2/3}W_{1/3})O_3$ singe crystals', *Journal of Crystal Growth*, vol. 167 (1996), 628–637.
122. Z.G. Ye, K. Toda, M. Sato, E. Kita and H. Schmid, 'Synthesis, structure and

properties of magnetic relaxor ferroelectric Pb($Fe_{2/3}W_{1/3}$)O_3', *Journal of Korean Physical Society*, vol. 32 (1998), S1028–S1031.

123. A. Kania, E. Jahfel, G.E. Kugel, K. Roleder and M. Hafid, 'A Raman investigation of the ordered complex perovskite $PbMg_{0.5}W_{0.5}O_3$', *Journal of Physics: Condensed Matter*, vol. 8 (1996), 4441–4453.
124. J. Kuwata, K. Uchino and S. Nomura, 'Phase transitions in the Pb($Zn_{1/3}Nb_{2/3}$)O_3–$PbTiO_3$ systems', *Ferroelectrics*, vol. 37 (1981), 579–582.
125. M. Dong and Z.-G. Ye, 'High-temperature thermodynamic properties and pseudo-binary phase diagram of the Pb($Zn_{1/3}Nb_{2/3}$)$_{0.91}Ti_{0.09}O_3$–PbO system', *Japanese Journal of Applied Physics*, vol. 40 (2001), 4604–4610.
126. A. Van Hook, *Crystallization: Theory and Practice*, Reinhold Publishing Corp., New York, 1961, p. 73.
127. H.M. Jang, S.H. Oh and J.H. Moon, 'Thermodynamic stability and mechanisms of formation and decomposition of perovskite Pb($Zn_{1/3}Nb_{2/3}$)O_3 prepared by the PbO flux method', *Journal of the American Ceramic Society*, vol. 75 (1992), 82–85.
128. N. Wakiya, N. Ishizawa, K. Shinozaki and N. Mizutani, 'Thermal stability of Pb($Zn_{1/3}Nb_{2/3}$)O_3(PZN) and consideration of stabilization conditions of perovskite type compounds', *Materials Research Bulletin*, vol. 30 (1995), 1121–1131.
129. L.C. Lim, R. Liu and F.J. Kumar, 'Surface breakaway decomposition of perovskite 0.91PZN–0.09PT during high-temperature annealing', *Journal of the American Ceramic Society*, vol. 85 (2002), 2817–2826.
130. F.J. Kumar, L.C. Lim, S.P. Lim and K.H. Lee, 'Nondestructive evaluation of large-area PZN–8%PT single crystal wafers for medical ultrasound imaging probe applications', *IEEE Transactions on Ultrasonics, Ferroelectrics and Frequency Control*, vol. 44 (1997), 1140–1147.
131. S.W. Choi, T.R. Shrout, S.J. Jang and A.S. Bhalla, 'Dielectric and pyroelectric properties in the Pb($Mg_{1/3}Nb_{2/3}$)O_3–$PbTiO_3$ systems', *Ferroelectrics*, vol. 100 (1989), 29–38.
132. O. Noblanc, P. Gaucher and G. Galvarin, 'Structural and dielectric studies of Pb($Mg_{1/3}Nb_{2/3}$)O_3–$PbTiO_3$ ferroelectric solid solutions around the morphotropic boundary', *Journal of Applied Physics*, vol. 79 (1996), 4291–4297.
133. H. Luo, G. Xu, H. Xu, P. Wang and Z. Yin, 'Compositional homogeneity and electrical properties of lead magnesium niobate titanate single crystals grown by a modified Bridgman technique', *Japanese Journal of Applied Physics*, vol. 39 (1999), 5581–5585.
134. T. Karaki, M. Adachi, Y. Hosono and Y. Yamashita, 'Distribution of piezoelectric properties in Pb[($Mg_{1/3}Nb_{2/3}$)$_{0.7}Ti_{0.3}$]O_3 single crystals', *Japanese Journal of Applied Physics*, vol. 41 (2002), L402–L404.
135. K.T. Zawilski, M.C.C. Custodio, R.C. DeMattei, S.-G. Lee, R.G. Monteiro, H. Odagawa and R.S. Feigelson, 'Segregation during the vertical Bridgman growth of lead magnesium niobate-lead titanate single crystals', *Journal of Crystal Growth*, vol. 258 (2003), 353–367.
136. M. Shanthi, S.M. Chia and L.C. Lim, 'Overpoling-induced property degradation in Pb($Mg_{1/3}Nb_{2/3}$)O_3–$PbTiO_3$ single crystals of near-morphotropic phase boundary compositions', *Applied Physics Letters*, vol. 86 (2005), 262908.

13

Thin film technologies for manufacturing piezoelectric materials

K. WASA, Kyoto University, Japan

Abstract: Over the past 20 years, research work has been carried out on the thin films of the ferroelectric ceramics including $Pb(Zr,Ti)O_3$ (PZT) in relation to their applications for infrared sensors, micro-electromechanical systems (MEMS), and ferroelectric dynamic random access memory (FEDRAM). This chapter is not intended to be a comprehensive review of these works. In this chapter, principles and technologies of deposition of ferroelectric thin films are described in relation to their application for fabrication of PZT-based MEMS based on the author's research since 1967. The differences between bulk PZT ceramics and PZT thin films are discussed in relation to their piezoelectric properties. It has been shown that thin film processing is environmentally benign.

Key words: thin film PZT, thin film process, PZT thin film actuators, thin film MEMS.

13.1 Introduction: bulk and thin film materials

Since the discovery of bulk ferroelectric perovskite $BaTiO_3$(BT) ceramics in 1943, varieties of perovskite ferroelectric materials such as $PbTiO_3$(PT), binary compound $Pb(Zr,Ti)O_3$(PZT), and ternary compound $Pb(Mg,Nb)O_3$–PT(PMNT) have been developed (Cross 1993). These ferroelectric functional materials are used in practice mostly in the form of bulk ceramics.

Current interest has been paid to thin film dielectric and piezoelectric devices in relation to their application for micro-electromechanical systems (MEMS). The minimum thickness of the bulk ceramic materials in production is typically 100–300 microns, while the thickness of thin film materials is typically less than several microns. The thin film materials are not created by thinning bulk materials but by depositing source materials on a substrate. Thin film growth exhibits the following features:

- The birth of thin films of all materials created by any deposition technique starts with a random nucleation process followed by nucleation and growth stages.
- Nucleation and growth stages are dependent upon various deposition conditions, such as growth temperature, growth rate, and substrate chemistry.

- The nucleation stage can be modified significantly by external agencies, such as electron or ion bombardment.
- Film microstructure, associated defect structure, and film stress depend on the deposition conditions at the nucleation stage.
- The crystal phase and the orientation of the films are governed by the deposition conditions.

The basic properties of thin films, such as film composition, crystal phase and orientation, film thickness, and microstructure, are controlled by the deposition conditions. Thin films exhibit unique properties that cannot be observed in bulk materials:

- Unique material properties resulting from the depositing process.
- Size effects, including quantum size effects, characterized by the thickness, crystalline orientation, and multi-layer aspects.

It is expected that thin film piezoelectric materials lower the working voltage of piezoelectric actuators by one order in magnitude. This thin film material process is based on the thin film technology established for a variety of industries, first and foremost, the semiconductor industry.

Thin films of ferroelectric perovskite materials have been grown for more than 40 years. Initially thin films of BT were prepared by thermal evaporation in the 1950s (Gerstenberg 1970). In the 1960s, the thin films of PT were deposited by sputtering (Wasa and Hayakawa 1969). However, the ferroelectric properties of these thin films were poor and not well characterized. In the past 20 years, a variety of the fabrication process of the perovskite materials has been extensively studied in relation to the development of high T_c superconductors (Wasa and Hayakawa 1992) and ferroelectric random access memory (FERAM) (Auciello *et al.* 1998). At present, thin films of perovskite materials are widely fabricated by a magnetron sputtering, laser ablation, sol-gel, and/or metal organic chemical vapor deposition (MOCVD). The PZT-based thin films are used in practice for the sensors and high precision actuators including gyro-sensors and printer heads (Fujii *et al.* 2007). An excellent review of thin film piezoelectric materials has been published in relation to MEMS applications (Trolier-McKinstry and Muralt 2004).

Ferroelectric ceramics have been studied in the past half century and a large amount of basic material data on them has been accumulated. Novel functional devices including nano-scale engineered connectivity originally proposed by Newnham *et al.* in 1978 is provided by the combination of the thin film technology and the bulk ceramic technology. It is also noted that environmental restrictions may terminate the usage of the present toxic bulk Pb-based piezo-ceramics in the 2010s. Thin films are environmentally benign materials due to the minimization of the usage of the Pb-based materials (Wasa 1995). The thin films of the Pb-based piezo-ceramics could be used forever, since the thin film device technology could further reduce the toxic Pb consumption (Wasa *et al*. 2004a, p. 1).

13.2 Fundamentals of thin film deposition

13.2.1 Classification of deposition process

The thin film deposition technologies and the related nanotechnologies are described in several textbooks (Elshabini-Riad and Barlow 1998, Bunshah 1993, Vossen and Kern 1991, Timp 1999). Typical deposition processes for the PZT-based thin films are shown in Table 13.1. Among these deposition processes sputtering, plasma enhanced metal organic chemical vapor deposition (PE-MOCVD), and sol-gel processes are mostly used for the deposition of PZT-based thin films. These deposition processes are defined as follows:

- *Sputtering deposition*. Source materials of sintered PZT disk are sputtered by the impingement of high energy ions in an oxidizing atmosphere. Sputtered source materials are deposited on a heated substrate in an oxidizing atmosphere resulting in the growth of PZT thin films. Multi-source materials of Pb, Zr, and Ti metal disks and/or multi-source materials of PbO, ZrO_2, and TiO_2 sintered disks are also used for the deposition of PZT thin films.
- *PE-MOCVD*. This process is based on a chemical reaction of metal-organic precursors of PZT in the gas phase, which includes Pb, Zr, and Ti

Table 13.1 Classification of the deposition system for PZT-based thin films

Classification	Deposition system	Source materials
PVD^a	Thermal evaporation	Individual metals
	Electron beam	Individual oxides
	Crucible	Multi-source
	MBE	
		PZT compounds
	Laser ablation	Individual oxides
		Multi-target
		PZT compounds
	Sputtering	Individual metals
		Individual oxides
		Multi-target
CVD^b	Low pressure CVD	Individual halide
	MOCVD	Metal organic gas
	PE-MOCVD	
CSD^c	MOD	Metal organic gas
	Sol-gel deposition	Metal alkoxide

^{a}Physical vapor deposition, ^{b}Chemical vapor deposition

^{c}Chemical solution deposition

metal elements, followed by diffusion of reactants to a heated substrate. The diffused reactants create a chemical reaction on the heated substrate in an oxidizing atmosphere resulting in the growth of PZT thin films. The high energy electrons in plasma enhance the chemical reaction of metal-organic complexes.

- *Sol-gel deposition*. Chemical solutions of PZT precursor complexes are spin-coated on a substrate followed by drying, pyrolysis, and sintering.

13.2.2 Key deposition conditions of PZT-based thin films

The PZT thin films of perovskite phase are fabricated by two different deposition conditions as shown in Table 13.2. One is deposition at room temperature followed by post-annealing at crystallizing temperature of perovskite phase (mode 1, low temperature process), the other is deposition at crystallizing temperature of perovskite phase (mode 2, high temperature process). The sintering process of the bulk ceramics is also shown in Table 13.2.

The low temperature process, mode 1, is similar to the bulk sintering process. The mixing process at the bulk ceramic sintering corresponds to the deposition at room temperature. The post annealing process corresponds to the bulk sintering process. The high temperature process, mode 2, creates the perovskite PZT thin films without the post-annealing.

Many kinds of the deposition conditions of PZT thin films are reported in the literature. The important factors for the deposition of the PZT thin films are control of chemical compositions, control of crystal phase, and control of micro-structure.

Control of chemical compositions

The important factors that influence the chemical compositions are as follows:

Table 13.2 Basic fabrication processes for PZT-based thin films

		Composition	Crystallization	Structure
Ceramics	mixing	sintering (800–1200 °C)	polycrystal	
Thin films	low temp. mode 1	deposition (non-heated)	post annealing (700–800 °C)[a]	polycrystal
	high temp. mode 2		deposition (600–700 °C)	polycrystal single crystal[b]

[a] Rapid thermal annealing (RTA)

[b] Heteroepitaxial growth on single crystal substrates

- Sputtering process: target composition, deposition temperature, and oxygen partial pressure of sputtering atmosphere.
- Sol-gel process: chemical compositions of PZT precursors and sintering temperature.
- MOCVD process: Ar carrier gas flow ratios of each metal precursor and deposition temperature.

Control of crystal phase

The important factors that influence the crystal phase are deposition temperature and chemical compositions of the deposited thin films.

The crystal phase of the deposited perovskite thin films is governed chiefly by the substrate temperature during film growth. PT is a base composition of PZT. Here, the effects of the deposition temperature on the crystal phase of PT thin films are described.

The PT is a base material of the PZT. Thin films of the PT were deposited by a planar sputtering system and the crystal phases of the sputtered thin films were studied for various substrate temperature. Sapphire (0001) single crystals were used for the substrates. The XRD analyses show that the sputtered PT thin films at cooled substrates (at liquid nitrogen temperature) comprise amorphous PT phase with Pb crystallites (Kitabatake *et al.* 1982). Heating the substrate activates the surface migration of the Pb adatoms on the substrates and the Pb crystallites will transfer into amorphous PT resulting in the formation of Pb crystallite-free amorphous PT thin films.

Figure 13.1 shows XRD patterns of sputtered PT thin films on (0001) sapphire substrates for different substrate temperatures. The sputtered PT thin films at 200 °C are amorphous phase and free from the Pb crystallites as shown in the XRD patterns of Fig. 13.1(a). Further activation of the surface migration causes the formation of crystalline phase. The sputtered thin films deposited at 500 °C show the pyrochlore phase as shown in the XRD patterns of Fig. 13.1 (b). The PT thin films deposited at 600 °C show perovskite PT phase as shown in Fig. 13.1 (c). The figure shows the sputtered films are epitaxially grown on the (0001) sapphire, and the epitaxial relation is (111) PT/(0001) sapphire. These experiments suggest the epitaxial temperature and the crystallizing temperature of perovskite PT is around 600 °C and the crystallizing temperature of pyrochlore phase is around 500 °C.

Figure 13.2 (a) and (b) shows the XRD patterns of the sputtered PT amorphous thin films annealed at 480 °C and 600 °C, respectively. It is seen the PT thin films annealed at the crystallizing temperature of perovskite PT show the perovskite PT structure as expected. Figure 13.3 shows the temperature variations of crystal phase for the sputtered PT thin films. A conventional planar magnetron sputtering system was used for the measurement of the crystal phase shown in Fig. 13.3. In the conventional planar magnetron

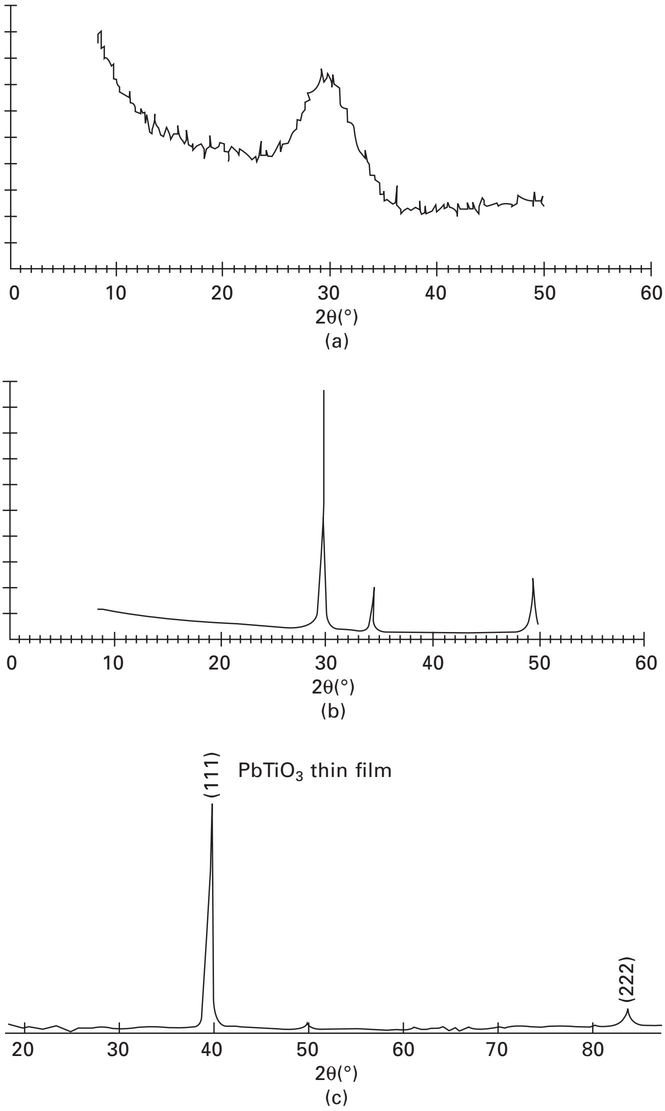

13.1 X-ray diffraction patterns of sputtered PbTiO$_3$ thin films on (0001) sapphire: (a) deposited at 200 °C, (b) deposited at 500 °C, and (c) deposited at 600 °C.

sputtering system, the energy of the sputtered particles was thermallized and the effect of high-energy sputtered particles on the crystallizing temperature was removed. Therefore, the crystallizing temperature of sol-gel and/or MOCVD PZT thin films is possibly similar to the sputtered PZT thin films.

The crystal phase is also governed by the chemical composition. Figure

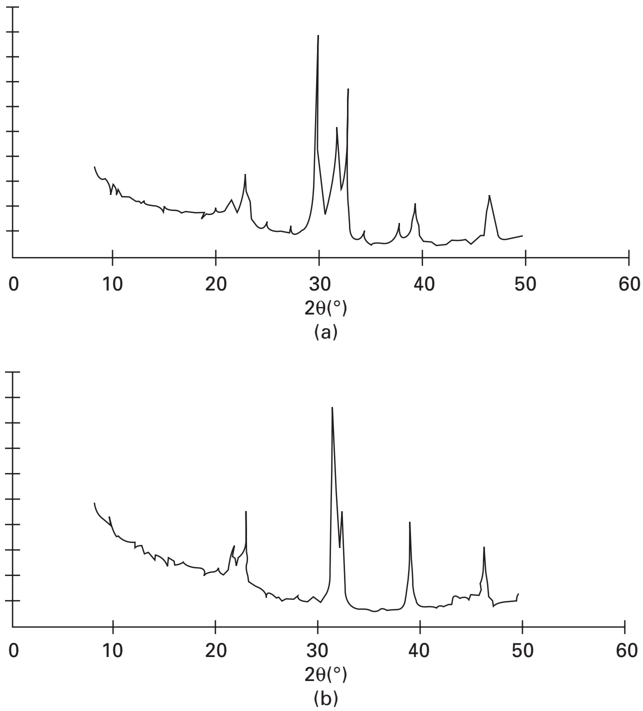

13.2 X-ray diffraction patterns of sputtered $PbTiO_3$ thin films on (0001) sapphire at room temperature: (a) post annealed at 480 °C, (b) post annealed at 600 °C.

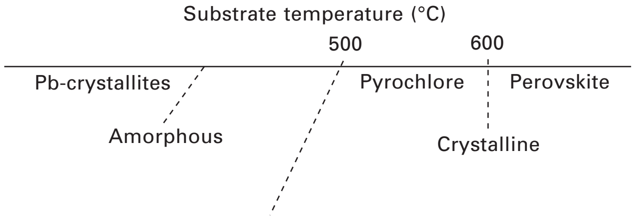

13.3 Schematic phase diagram of sputter-deposited $PbTiO_3$.

13.4 shows the crystal phases of sputtered PT thin films for various deposition temperatures and chemical compositions. The growth condition of the perovskite structure is a narrow zone of deposition temperature and Pb/Ti ratios. It is noted the ceramic data are useful for the estimation of the crystal phase of the PT/PZT thin films. Typical ceramic data are shown in Fig. 13.5 (Ouchi 1976). The growth temperature of perovskite PT is above 500 °C. Higher temperatures will be necessary for the growth of PZT. These bulk data are almost the same as those of the deposition process. In the case of

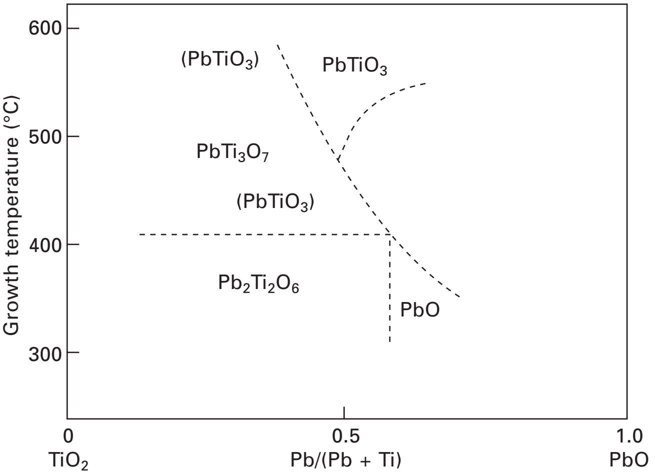

13.4 Crystal phase of sputtered Pb–Ti–O thin films on (001)MgO substrates showing chemical composition of thin films vs. growth temperature.

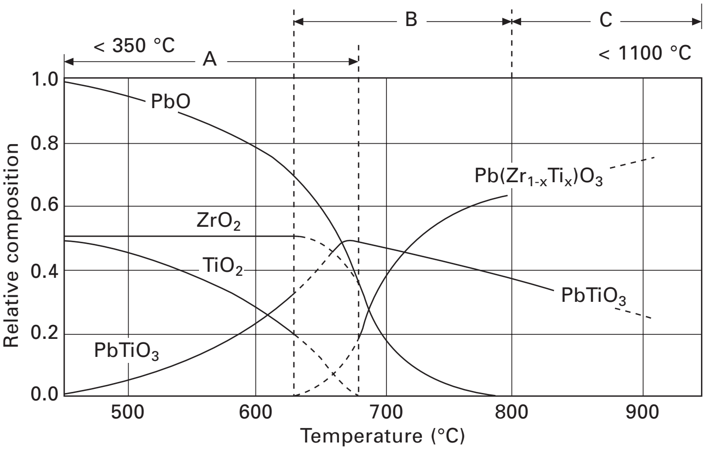

13.5 Crystal phase of PbO–TiO_2 binary systems for various sintering temperatures.

high energetic sputtering process, the growth temperature of the perovskite PT/PZT thin films is as low as room temperature (Kusao *et al.* 1969, Hayashi *et al.* 1992).

Control of microstructure

The micro-structures of the resultant PZT thin films are governed by a surface (growing surface) structure of substrates as well as the deposition conditions.

The substrates are usually hetero-structure, i.e. buffer layer/base metal electrode/base substrate materials. Highly oriented thin films and/or single crystal thin films of perovskite structure are obtained by a suitable material selection of the substrate hetero-structure. For the selection of the buffer layers, thermodynamic stability should be considered (Hubbard and Schlom 1996). The buffer layers show a variety of functions including nucleation centers, stress control, diffusion barriers, and conductive electrodes. One of the reliable buffer layers is $SrRuO_3$ (Eom *et al*. 1992). Table 13.3 shows a summary of the substrate materials and the buffer layers for the ferroelectric perovskite thin films.

13.2.3 Film characterizations

Film structure

Dielectric and/or piezoelectric properties of PZT-based thin films are governed by their structural properties. Surface and thin film analysis methods are

Table 13.3 Lattice parameters of PZT-based ferroelectric materials and single crystal substrates

	Crystal system	Structure	Lattice constant (nm)	Thermal expansion (10^{-6}/K)	Dielectric constant
Ferroelectric materials					
$PbTiO_3$	tetragonal	perovskite	$a = 0.3889$ $c = 0.41532$	12	$51(\varepsilon_{33})$ $115(\varepsilon_{11})$
$PbTiO_3$	cubic		$a = 0.3961$		
PZT(50/50)	tetragonal	perovskite	$a = 0.40311$ $c = 0.41393$		
PZT(60/40)	rhombo	perovskite	$a = 0.40818$		
Substrates					
Sapphire	trigonal	corundum	$a = 0.4763$	5.3(c//)4.5(c⊥)	11.5(c//)9.3(c⊥)
$SrTiO_3$	cubic	perovskite	$a = 0.3905$	10.8	
MgO	cubic	NaCl	$a = 0.4203$	9.65	17
$LaAlO_3$	pseudo cubic	perovskite	$a = 0.3792$	10	16
$KTaO_3$	cubic	perovskite	$a = 0.3989$	6.7	
Si	cubic	diamond	$a = 0.5431$	2.6	11.7
GaAs	cubic		$a = 0.5654$	6.9	13
Buffer layer					
YSZ	cubic	fluorite	$a = 0.516$	10	27
$SrRuO_3$	pseudo cubic	$GFeO_3$	$a = 0.393$		

Epitaxial relations:
(111)PT//(0001)sapphire, (001)PT//(001)$LaAlO_3$, (001)PT//(001)ST, (001)PT//SRO//(001)ST
(001)PT//(001)MgO, (001)PT//SRO//(001)MgO, (111)PT//YSZ//(100)Si

available for the evaluation of the structural properties of thin films. Typical analysis methods are summarized in Table 13.4.

Piezoelectric properties

Piezoelectric properties of the ferroelectric thin films are estimated by the measurement of direct piezoelectric (dp) or inverse piezoelectric (ip) effects. Figure 13.6 shows the basic measurement systems. The d_{33} (ip) values are evaluated by the measurements of electric-field-induced displacement by atomic force microscopy (AFM) or interferometry based on the inverse piezoelectric effect measurements (Yamamoto *et al.* 2007, Kholkin *et al.* 1996). The d_{33} (dp) values are also estimated by the stress-induced charge based on direct piezoelectric effects. The measured d_{33} (ip) values of PZT thin films measured by AFM or interferometry are much smaller than real values partially due to the in-plane clamping by the substrates and/or continuous

Table 13.4 Evaluation methods of thin films

Film properties	Evaluation methods	Remarks
Thickness	Mechanical stylus	~ 2 nm, step required, simple
	AFM	~ 1 nm, simple
	Cross-sectional SEM	~ 2 nm, conducting coating for dielectric films
Surface roughness	Mechanical stylus	~ 1 nm, simple.
	AFM	~ 0.1 nm, simple
	Cross-sectional SEM	~ 1 nm, conducting coating for dielectric films
	STM	~ 0.1 nm, conducting coating for dielectric films
Chemical composition	ICP, SIMS RBS AES XPS EPMA	High sensitivity by ICP and SIMS; detection limit ~0.1 ppm. Non-destructive, quantitative analysis; by RBS and EPMA. Depth profile; by RBS, SIMS and AES. Simple analysis; by ICP and EPMA.
Structure	Electron/X-ray diffraction XPS EELS	Crystal structure by electron/X-ray diffraction analysis. Amorphous films by infrared absorption and/or EXAFS. Electronic states and valence states by EELS and XPS.

AFM: Atomic force microscope. SEM: Scanning electron microscope. STM: Scanning tunneling microscope. ICP: Inductively coupled plasma optical emission spectroscopy. SIMS: Secondary ion mass spectroscopy. RBS: Rutherford back scattering. AES: Auger electron spectroscopy. XPS: X-ray photo-electron spectroscopy. EELS: Electron energy loss spectroscopy. EXAFS: Extended X-ray absorption fine structure. EPMA: Electron microprobe microanalysis.

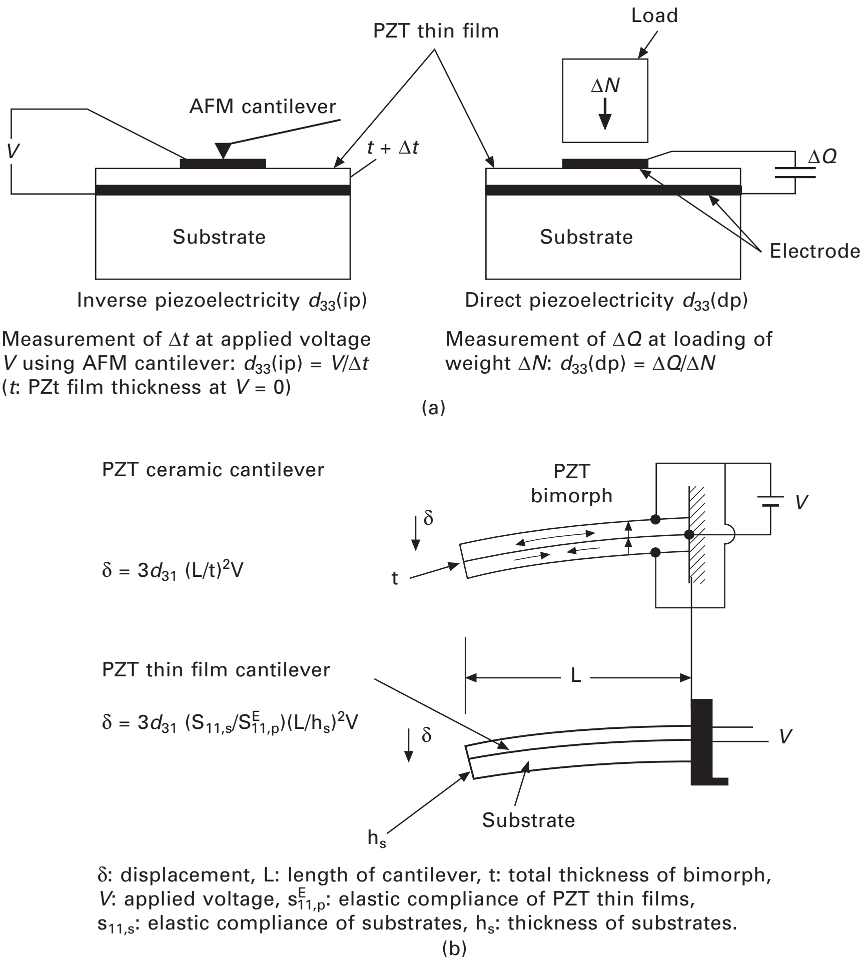
PZT thin film
Load
ΔN
AFM cantilever
V
$t + \Delta t$
ΔQ
Substrate
Substrate
Electrode
Inverse piezoelectricity d_{33}(ip)
Direct piezoelectricity d_{33}(dp)
Measurement of Δt at applied voltage V using AFM cantilever: $d_{33}(\text{ip}) = V/\Delta t$
(t: PZt film thickness at $V = 0$)
Measurement of ΔQ at loading of weight ΔN: $d_{33}(\text{dp}) = \Delta Q/\Delta N$
(a)
PZT ceramic cantilever
PZT bimorph
V
δ
$\delta = 3d_{31}\,(L/t)^2V$
t
PZT thin film cantilever
L
$\delta = 3d_{31}\,(S_{11,s}/S^E_{11,p})(L/h_s)^2V$
δ
V
Substrate
h_s
δ: displacement, L: length of cantilever, t: total thickness of bimorph,
V: applied voltage, $s^E_{11,p}$: elastic compliance of PZT thin films,
$s_{11,s}$: elastic compliance of substrates, h_s: thickness of substrates.
(b)

13.6 (a) Measurements of piezoelectric constant d_{33} for thickness mode; (b) measurements of piezoelectric constant d_{31} for transverse mode.

films. The effective d_{33} (ip) is expressed by the following equation (Lefki and Dormans 1994):

$$d_{33}\,(\text{ip}) = d_{33} - [2s^E_{13}/(s^E_{11} + s^E_{12})]\,d_{31}, \qquad 13.1$$

where s_{13}, s_{12}, and s_{11} are the mechanical compliances of the piezoelectric thin films and d_{31} is the transverse piezoelectric constant. Since d_{31}, s_{12}, and s_{13} are usually negative and s_{11} is positive and larger than s_{12}, d_{33}(ip) is smaller than real d_{33}. In order to achieve the direct measurement of the the real d_{33} without the effect of the in-plane clamping, the diameter of the top electrode Φ_{TE} should be equal to or less than PZT film thickness $t_{PZT,}$ t_{PZT}

$> \Phi_{TE}$ (Yamamoto *et al.* 2007).

The d_{33} (dp) values evaluated by the direct piezoelectric measurement are almost the same as the real d_{33} values. The d_{33} (dp) is measured according to the following equation:

$$d_{33}\ (\mathrm{dp}) = \Delta Q/\Delta N, \qquad 13.2$$

where ΔQ is the induced charge by loading of weight ΔN. The response of stress-induced charge is measured by an accurate charge integrator. The d_{33} (dp) is expressed by:

$$d_{33}(\mathrm{dp}) = d_{33} - 2d_{31}(s_{13}^{\mathrm{E}} + \sigma/Y)/(s_{11}^{\mathrm{E}} + s_{12}^{\mathrm{E}}), \qquad 13.3$$

where Y and σ are the Young's modulus and the Poisson's ratio of the substrate (Lefki and Dormans 1994). As s_{13} and the ratio σ/Y are comparable but of opposite sign for most materials, the d_{33} (dp) will be much closer to the real d_{33}.

The transverse piezoelectric constant d_{31} is evaluated by the tip displacement of the unimorph cantilever. The tip displacement increases proportionally with increasing magnitude of the applied voltage. The transverse piezoelectric coefficient d_{31} is calculated from the tip displacement of the cantilever (Kanno *et al.* 2003a):

$$d_{31} = -\frac{\delta K}{3s_{11,p}^{E} s_{11,s} h_s (h_s + h_p) V L^2} \qquad 13.4$$

$$K = 4s_{11,p}^{E} s_{11,s} h_s (h_p)^3 + 4s_{11,p}^{E} s_{11,s} (h_s)^3 h_p + (s_{11,p}^{E})^2 (h_s)^4 + (s_{11,s})^2 (h_p)^4 + 6s_{11,p}^{E} s_{11,s} (h_s)^2 (h_p)^2$$

where δ, V, L, h, s_{11} are the tip displacement, applied voltage between top and bottom electrodes, length of the cantilever, thickness, and the elastic compliance, respectively. The subscripts '*s*' and '*p*' denote the substrate and the piezoelectric film, respectively. When $h_\mathrm{s} >> h_\mathrm{p}$, Eq. (13.4) can be simplified as:

$$d_{31} \cong -\frac{h_s^2}{3L^2} \frac{s_{11,p}^{E}}{s_{11,s}} \frac{\delta}{V} \qquad 13.5$$

Although the mechanical properties of substrates are stable and easy to measure because of the large volume of the materials, those of thin films are difficult to estimate because the small volume of the thin films as well as the existence of the substrate makes precise mechanical measurements difficult. In this study, to eliminate the ambiguity of the mechanical properties of the piezoelectric thin films, we define the transverse piezoelectric coefficient e_{31}^{*} as follows:

$$e_{31}^{*} = \frac{d_{31}}{s_{11,p}^{E}} \cong -\frac{h_s^2}{3s_{11,s}L^2}\frac{\delta}{V} \qquad 13.6$$

This equation is equivalent with the following equation:

$$e_{31}^{*} = e_{31,f}\,\frac{s_{11,p}^{E} + s_{12,p}^{E}}{s_{11,p}^{E}} = \left(e_{31} - \frac{c_{13}^{E}}{c_{33}^{E}}\,e_{33}\right)\left(1 + \frac{s_{12,p}^{E}}{s_{11,p}^{E}}\right) \qquad 13.7$$

where c_{ij} is the elastic stiffness of the piezoelectric thin films, and e_{31} and $e_{31,f}$ are transverse piezoelectric coefficient and intrinsic effective transverse piezoelectric coefficient for thin films, respectively (Ouyang *et al.* 2005). Equation (13.6) means that the e_{31}^{*} neglects the effects of the deformation along thickness and width of the cantilever. However, we could evaluate transverse piezoelectric properties of the thin film by a simple calculation. The $e_{31},_f$ is obtained from Eq. (13.7). Taking $s_{11,p}^{E} = 13.8 \times 10^{-12}\mathrm{m}^2\mathrm{N}^{-1}$, $s_{12,p}^{E} = -4.07 \times 10^{-12}\mathrm{m}^2\mathrm{N}^{-1}$ for PZT, we have $e_{31,f} = 1.3 \times {}^{*}e_{31}$.

Apart from these piezoelectric measurements, the traditional thickness resonance techniques in GHz frequency range are also used for the evaluation of k_t and mechanical quality factor Q_m (Zhang *et al.* 1999, Chen and Wang 2005). The transverse piezoelectric measurement of d_{31} is simple and reliable for the evaluation of the piezoelectric properties, although the measurement frequency is lower than the MHz range.

13.3 Deposition of PZT-based thin films

13.3.1 Sputtering

Figure 13.7 shows a typical sputtering system. The sputtering system comprises an rf-diode glow discharge system in a vacuum chamber having a cathode target disk. A stainless vacuum chamber acts as an anode. The substrate holder is settled above the cathode disk. The cathode target disk comprises source materials for perovskite ferroelectric thin films. The cathode target materials are typically sintered disks of PZT. Typical sputtering conditions and the crystal structure of sputtered PZT-based thin films are shown in Table 13.5. The deposition rates are governed by sputtering yields (Behrisch 1981, Sigmund 1969). In the low temperature process the sputtered thin films are post-annealed at crystallizing temperature of around 600–700 °C. In the high temperature process the thin films are deposited on a heated substrate at the crystallizing temperature of around 600–700 °C.

The cathode electrode consists of a planar rf-magnetron structure (Wasa 2004a, p. 141). Mixed discharge gas of Ar and O_2 is introduced into the vacuum chamber. The pressure of the discharge gas in the chamber is kept at 0.5–1 Pa. The glow discharge is initiated by the application of 500–1000

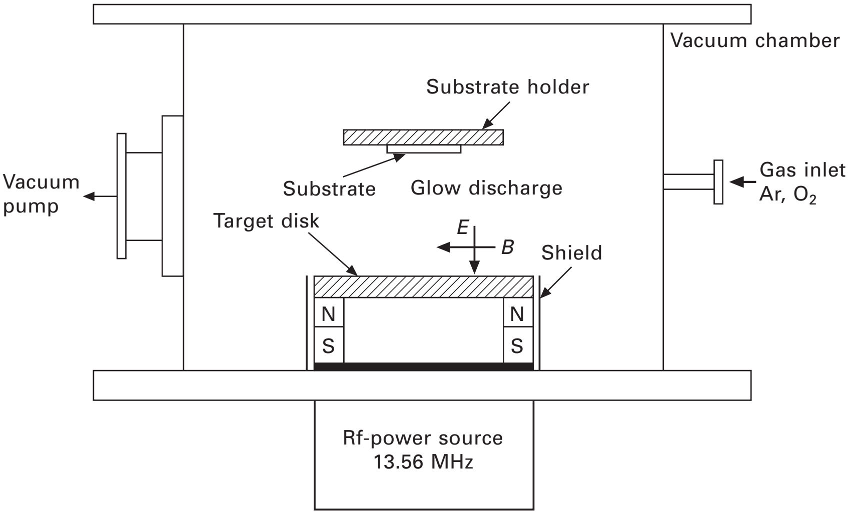

13.7 Construction of rf-magnetron diode sputtering system.

Table 13.5 Typical sputtering conditions for PZT thin films

Sputtering system	RF-planar magnetron
Target	PZT ceramic disk (100 mm$^{\phi}$)
Sputtering gas	Ar + O_2 (Ar/O_2 = 1, 0.5 Pa)
Substrates	Glass, sapphire, MgO, $SrTiO_3$
Substrate temperature	500–700 °C
RF power	100–200 W
Deposition rates	300–600 nm/hr
Film structure	Polycrystal (glass) Single crystal (sapphire, MgO, $SrTiO_3$)

V at the cathode current density of 1–5 mA/cm^2. An rf-power source, 13.56 MHz, is used for the initiation of the glow discharge at the dielectric target materials. High energy Ar ions created in the glow discharge strike the surface of the cathode target and remove the surface atoms of target materials. This phenomenon is called sputtering and the removed atoms are called sputtered atoms. The sputtered atoms are deposited on the substrates resulting in the formation of PZT thin films.

In the magnetron configuration the electrons near the cathode surface show cycloid motion due to ***ExB*** field configuration. The cycloid motion of electrons enhances the grow discharge due to the increase of electron impact ionization resulting in the increase of the sputtering currents at low working pressure. The energy of the sputtered atoms is around 1–10 eV (Stuart and Wehner 1964). The energy is much higher than the energy of thermally evaporated atoms. The high energy sputtered atoms will be thermallized due to the collisions with discharge gas molecules in transit (Wasa and Hayakawa 1977).

A multi-target sputtering system is also used for the deposition of complex perovskite thin films. A typical multi-target sputtering system is shown in Fig. 13.8. The multi-target sputtering system is convenient for adjusting the chemical composition of binary perovskite thin films of PZT using $PbTiO_3$ and $PbZrO_3$ targets. Ternary perovskite thin films of PMN–PZT are also provided for a variety of chemical compositions using PT, PZ, and PMN targets. The cathode target disk for the deposition of perovskite ferroelectric thin films is commercialized. The chemical composition of the Pb-based perovskite cathode target is usually Pb-rich composition, 10–20% rich, in order to compensate for the Pb reduction during deposition.

13.3.2 MOCVD/sol-gel processes

A typical PE-MOCVD system for PZT thin films is shown in Fig. 13.9. Three different precursors for Pb, Zr, and Ti are transported to the reaction chamber in a gas phase. Organic metals, alkyls (C–M bonds), alkoxides (O–M bonds), and/or chelates (organic metal complex) are used as the precursors. Their chemical structures are shown in Fig. 13.10 (Keijser *et al.* 1996). The diffused reactants comprising Pb, Zr, and Ti elements are absorbed on a heated substrate surface in an oxidizing atmosphere resulting in the formation of

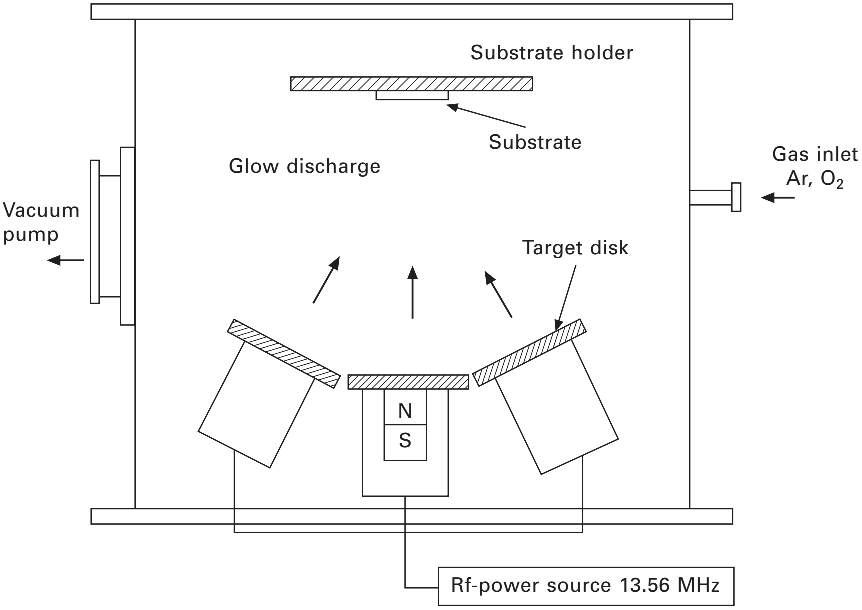

13.8 Construction of multi-target sputtering system.

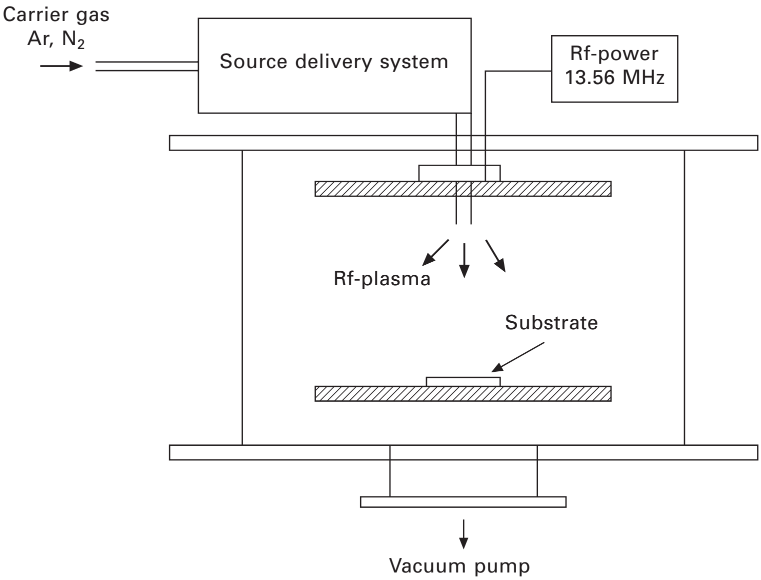
Carrier gas
Ar, N2
Source delivery system
Rf-power
13.56 MHz
Rf-plasma
Substrate
Vacuum pump

13.9 Construction of plasma-enhanced MOCVD system.

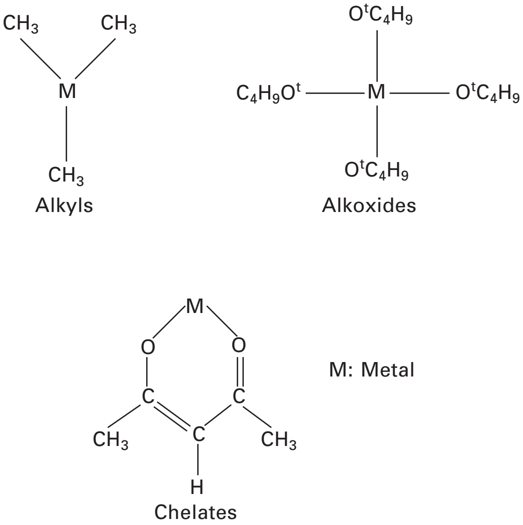
CH3
CH3
M
CH3
Alkyls
OtC4H9
C4H9Ot
M
OtC4H9
OtC4H9
Alkoxides
M
O
O
C
C
C
CH3
CH3
H
Chelates
M: Metal

13.10 Chemical structures of precursors for a deposition of PZT-based thin films.

PZT thin films. In the reaction chamber plasma enhances the decomposition and/or chemical reactions of the precursors. The source material vapor is delivered to the deposition chamber using Ar carrier gas.

These source materials are solid and/or liquid. Solid precursors are vaporized by a sublimation process and liquid precursors are vaporized by a bubbling process. In the past alkyls $Pb(C_2H_5)_4$ of liquid precursors were used as the Pb source (Li *et al.* 1994), because the liquid system was more convenient than the solid one for a stable supply of precursors. The lead alkyls are highly toxic. At present solid precursors such as organic metal complexes are dispersed into the organic solvent and used as liquid-like precursors. Table 13.6 shows typical deposition conditions of PZT thin films using the MOCVD process (Shimizu *et al.* 1993, Hendrics *et al.* 1993).

The sol-gel process is a chemical solvent deposition process called a wet process (Dey 1996). The deposition process includes preparation of the initial solution of precursors, hydrolysis, drying, and thermal treatments. In the sol-gel deposition metal alkoxides are commonly used as the precursors. PZT precursor complexes are made by the mixing and hydration of metal alkoxides of Pb, Zr, Ti. The PZT precursors are saluted into solvent, i.e. propanol and thin layers are deposited by spin coating followed by sintering. Mixing of PT and PZ precursors is also used for making PZT precursors. Typical deposition processes are shown in Fig. 13.11 (Iijima *et al.* 2007). Their thin film growth mechanisms are not based on the deposition of evaporated atoms on a substrate surface in a vacuum. The sol-gel method is based on a wet process comprising the deposition of the precursors in solvent. It is noted the chemical composition of perovskite thin films is controlled only by the chemical composition of the precursors if the reduction of lead is neglected during the sintering process. Conventionally the reduction of lead during the sintering process is compensated by the addition of excess lead. The control of chemical compositions is easy. Typical precursors for the MOCVD and sol-gel processes are shown in Table 13.7.

Table 13.6 Typical deposition conditions for PZT thin films using MOCVD

Substrates	Sapphire, Pt/Ti/SiO2/Si, RuOx/SiO2/Si	
Substrate temperature	550 °C	
Precursor temperature	$Pb(C_{11}H_{19}O_2)_2$, $Zr(C_{11}H_{19}O_2)_4$ $Ti(C_2H_5O)_4$	145–165 °C 210–230 °C 90–115 °C
Precursor flow rate (N_2)	$Pb(C_{11}H_{19}O_2)_2$, $Zr(C_{11}H_{19}O_2)_4$ $Ti(C_2H_5O)_4$	20–30 sccm 15–30 sccm 5 sccm
Dilute gas (O_2)		500–1000 sccm
Total pressure		6 Torr
Deposition rate		3–20 nm/min

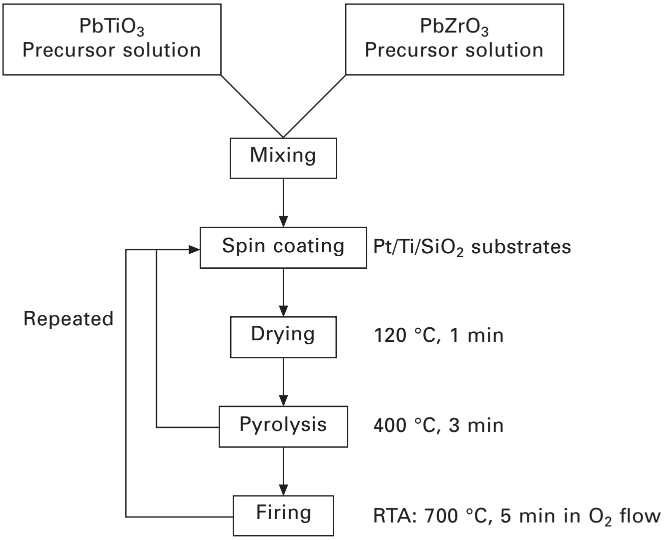
$PbTiO_3$ Precursor solution
$PbZrO_3$ Precursor solution
Mixing
Spin coating
Pt/Ti/SiO_2 substrates
Repeated
Drying
120 °C, 1 min
Pyrolysis
400 °C, 3 min
Firing
RTA: 700 °C, 5 min in O_2 flow

13.11 Typical sol-gel deposition process for PZT-based thin films.

Table 13.7 Typical precursors for the deposition of PZT thin films in the MOCVD and sol-gel processes

Materials	Mp (°C)	Phase (RT)	Bp(°C)/ P(Torr)	Vapor pressure (Torr)/temp.	Remarks
$Pb(CH_3)_4$	–28	Liq.	110	10/6 °C	Toxic
$Pb(C_2H_5)_4$	–130	Liq.	83/13		Toxic
$Pb(CH_3COOH)_2$					
$Pb(dpm)_2$	130	Solid	58-64/3	log P = –7800/T(K) +18.42	
$Zr(O\text{-}iC_3H_7)_4$	185	Solid			SC
$Zr(O\text{-}tC_4H_9)_4$	3	Liq.	45.5/0.2	70/2.0	SC
$Zr(dpm)_4$	182	Solid		110–162/1.0 logP = –3687/T(K) + 7.659	SC
$Ti\ (O\text{-}iC_3H_7)_4$	20	Liq.	116/10	logP = –3425/T(K) + 10.12	SC
$Ti(O\text{-}iC_3H_7)_2(dpm)_2$	160	Solid	100/0.1	logP = –5435/T(K) + 12.73	
$TiO(dpm)_2$	176	Solid			
$Ti(dpm)_2(OCH_3)_2$	80	Solid			

dpm: $C_{11}H_{19}O_2$: dipivaloylmethan = $Pb[(C_3HO_2)\text{-}C(CH_3)_3]_2$ SC: Spontaneous combustion

13.4 Dielectric and piezoelectric properties of PZT-based thin films

13.4.1 Sol-gel/MOCVD

Figure 13.12 shows typical structural properties of sol-gel derived polycrystalline PZT thin films. The PZT thin films are deposited by the sol-gel

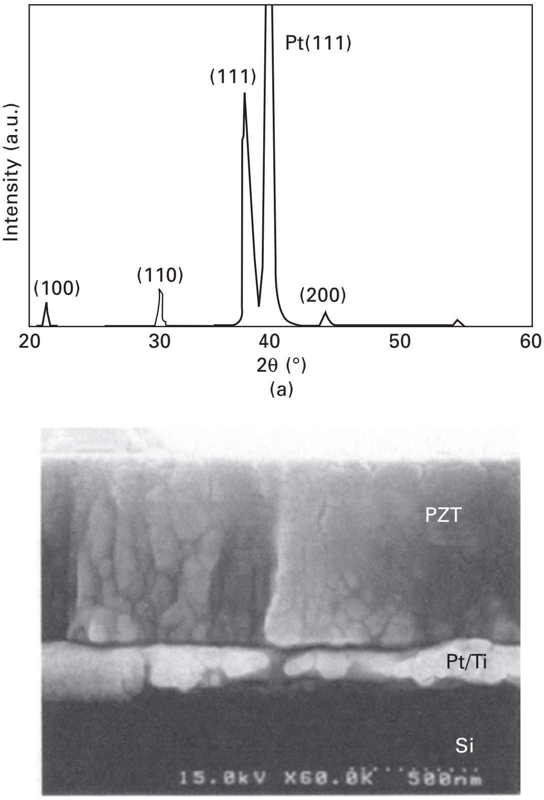

(a)

(b)

13.12 Structural properties of PZT thin films prepared by sol-gel deposition on Pt/Ti/SiO_2/Si substrates. (a) XRD pattern and (b) cross-sectional SEM image.

process as follows (Xiong *et al.* 2008). The precursor solution of PZT (52/48) at MPB composition was used for the deposition. The precursor solution includes 15% excess lead. First, a single layer of PZT film was deposited on (111)Pt/Ti-coated SiO_2/Si wafers by spin-coating followed by annealing at 350 °C for 10 min. Second, three additional single layers were deposited on the first single layer to make a four multi-layered structure. Finally, the multi-layered PZT thin films were annealed at 650 °C for 10 min using RTA furnace in oxygen atmosphere. The total film thickness was around 0.7 µm. The resultant thin films show (111) highly oriented PZT. The cross-sectional SEM image (Fig. 13.12(b)) indicates the PZT thin films have a fine-grained structure. The *P-E* hysteresis curves show their remnant and spontaneous polarization are $P_r = 16$ µC/cm^2 and $P_s = 25$ µC/cm^2, respectively, as shown in Fig. 13.13. The coercive force E_c is around 35 kV/cm.

Figure 13.14 shows typical tip edge displacement of the cantilever for

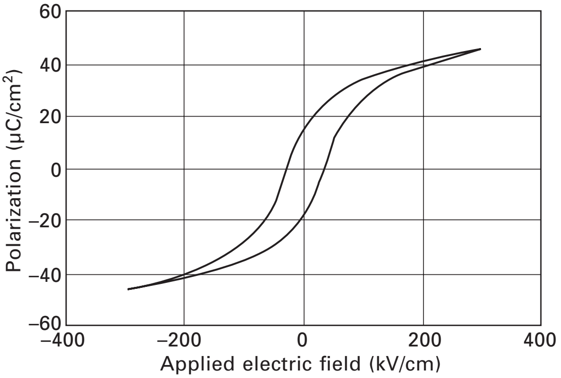

13.13 P-E hysteresis curve of the sol-gel-derived PZT thin films.

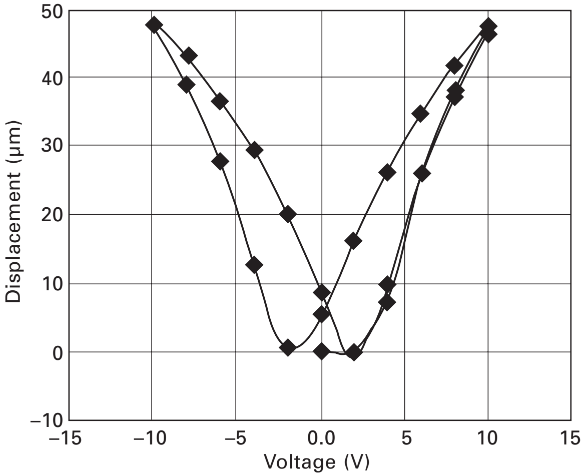

13.14 Tip displacements of the cantilever under bipolar voltage at quasi-static frequency.

applied AC voltage at quasi-static frequency. From the tip displacement curves, the $e_{31,f}$ and d_{31} values are $e_{31,f}$ = –16.5 C/m^2 and d_{31} = –172 pC/N. It is noted that the piezoelectricity d_{31} measured by the cantilever is higher than the bulk PZT ceramic values of –93.5 pC/N. The P_r values are almost the same as the bulk values. The E_c values are slightly higher than the bulk PZT ceramic values (around two times bulk data), probably due to the presence of the interfacial structure and/or the effect of the constraint on the substrates. These observed piezoelectric constants are obtained by skilled engineers. Most of the reported values are smaller than these observed ones. But, this example shows the possibility of production of high coupling PZT thin films by the wet process.

It is noted that the sintering temperature is further lowered by adjusting the film composition (lowering of Zr/Ti ratio and/or increase of excess Pb), the use of seeding layers (PT and/or TiO_2), and choosing a suitable preparation process, and the choice of the preparation methods of the chemical solution. The sintering temperature is lowered from 700 °C to 435 °C by the improvement of the sol-gel solution (diol-based solution) and modified film preparation process (multiple annealing) (Maki *et al*. 2001). The orientation of PZT thin films is controlled not only by the selection of the substrates but the selection of pyrolysis condition of precursors after spin-coating (Park *et al*. 2005).

Bulk PZT materials show their crystal structures and dielectric/piezoelectric properties are sensitive to the Zr/Ti ratios. Figure 13.15 shows the compositional dependence of piezoelectric constants and dielectric constants of the bulk PZT phenomenologically calculated for the compositions near the MPB (Du *et al*. 1998). It is shown that the crystal structure of the PZT comprises the tetragonal and rhombohedral phases, and the PZT transit from tetragonal to rhombohedral around Zr/Ti~1 at the MPB condition. Maximum values of the piezoelectricity and dielectric constants are expected near the MPB composition.

Variations of crystal structures and piezoelectric properties of sol-gel derived PZT thin films were studied for various Zr/Ti ratios. It is seen that the phase transition from tetragonal to rhombohedral is observed near the Zr/Ti ≅ 1 at the bulk MPB composition. The maximum values of the dielectric constants are also observed near the MPB composition similar to bulk PZT (Robert *et al*. 1993, Ledermann *et al*. 2003, Iijima *et al*. 2007). Interestingly, the orientation dependence on piezoelectricity for the sol-gel-derived thin films is also almost the same as bulk PZT (Ouyang *et al*. 2004).

Heteroepitaxial single crystal PT and/or PZT thin films are deposited by the MOCVD process on (100)MgO using the high temperature deposition process (Foster *et al*. 1996, 1997). The crystallizing temperature is around 700 °C. The thin films show strained structure at the film thickness less than critical values. It is reported that thick films include 90° domains, *c*/*a*/*c*/*a*/*c* periodic structure, at the interface caused by strain-accommodating processes (Gao *et al*. 1993). The lattice constants of the PZT thin films show very similar compositional dependence to that of bulk PZT near the MPB composition. The phase transition from tetragonal to rhombohedral is clearly observed near the MPB composition. Their P_r and E_c show compositional dependence similar to bulk PZT. For Pb $(Zr_xT_{i-x})O_3$ at $0.4 < x < 0.6$, P_r values are in the range of 40–90 μC/cm^2 and E_c values are 20–80 kV/cm. These P_r and E_c values are larger than those of sol-gel-derived PZT thin films (Shimizu *et al*. 1993).

Figure 13.15 suggests that there is a strong orientation dependence on the piezoelectric properties for the bulk PZT. The piezoelectric constants

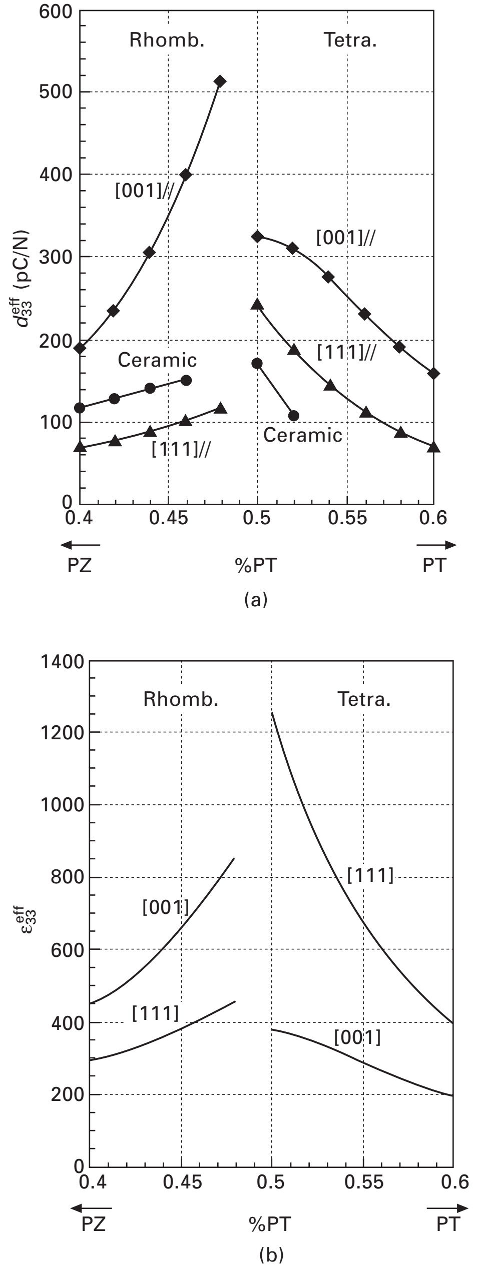

13.15 Phenomenologically calculated dielectric and piezoelectric properties of PZT with various compositions: (a) effective piezoelectric constants d_{33} and (b) dielectric constants.

of (001) PZT are higher than those of (111) PZT. However, the orientation dependence of the dielectric constants for these PZT thin films is not the same as the bulk properties. The orientation dependence of dielectric and/or piezoelectric properties is governed by the thin film micro-structures and/or the ferroelectric domain wall motion. The orientation dependence still includes ambiguity (Trolier-McKinstry and Muralt 2004).

13.4.2 Sputtered PZT thin films

Figure 13.16 shows typical cross-sectional SEM images of PZT (53/47) thin films near the MPB composition deposited by a conventional planar diode sputtering. The sputtered PZT thin films are heteroepitaxially grown on the (001)Pt/(001)MgO substrates. The resultant thin films show a high density and bulk single crystal-like structure as shown in Fig. 13.16(a). The PZT thin films show (001) oriented single crystal structure. The densities of the sputtered thin films are much higher than those of sol-gel-derived PZT thin films. The sputtered PZT thin films on (111)Pt/Ti/Si substrates show a columnar structure as shown in Fig. 13.16(b). The sputtered PZT thin films

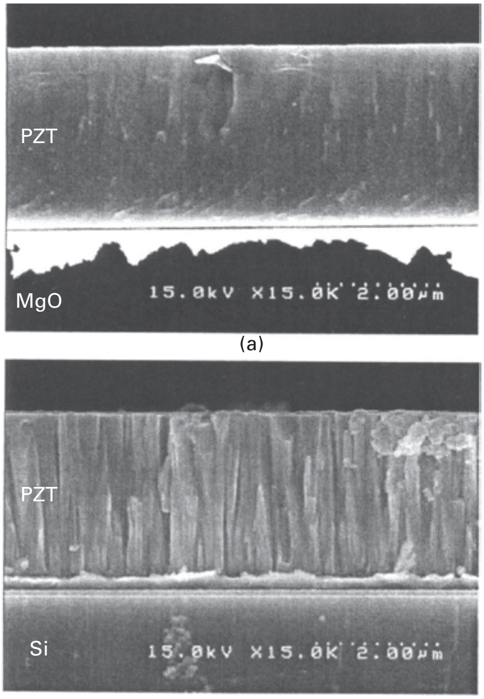

13.16 SEM images of the PZT thin films deposited on (a) (001)Pt/(001) MgO, and (b) (111)Pt/Ti/Si.

show a highly (111) oriented polycrystalline structure. Their P-E hysteresis curves are shown in Fig. 13.17. The *P-E* curve of heteroepitaxial PZT thin films on MgO show square-like properties with high P_r, $2P_r$ = 120 μC/cm^2 and high E_c, $2E_c$ = 200 kV/cm, while the polycrystalline PZT thin films show small P_r, $2P_r$ = 70 μC/cm^2 and small E_c, $2E_c$ = 100 kV/cm. Their properties were evaluated by the tip displacements of the PZT thin film cantilevers. Figure 13.18 shows typical tip deflections of the cantilevers. The transverse piezoelectric constant $e_{31,f}$ and d_{31} is estimated from Eq. (13.5): $e_{31,f} = -6.11$ to -6.37C/m^2 and $d_{31} = -64.9$ to -67.6×10^{-12}m/V for heteroepitaxial (001)PZT (53/47) thin films, and $e_{31,f} = -5.6$ to -10.1C/m^2 and $d_{31} = -59.5$ to -107.2×10^{-12}m/V for (111) oriented polycrystalline PZT(53/47) thin films. These values are slightly smaller than those of sol-gel-derived PZT thin films.

The lattice constants of the sol-gel-derived PZT thin films show very similar compositional dependence to those of bulk materials. However, these phase

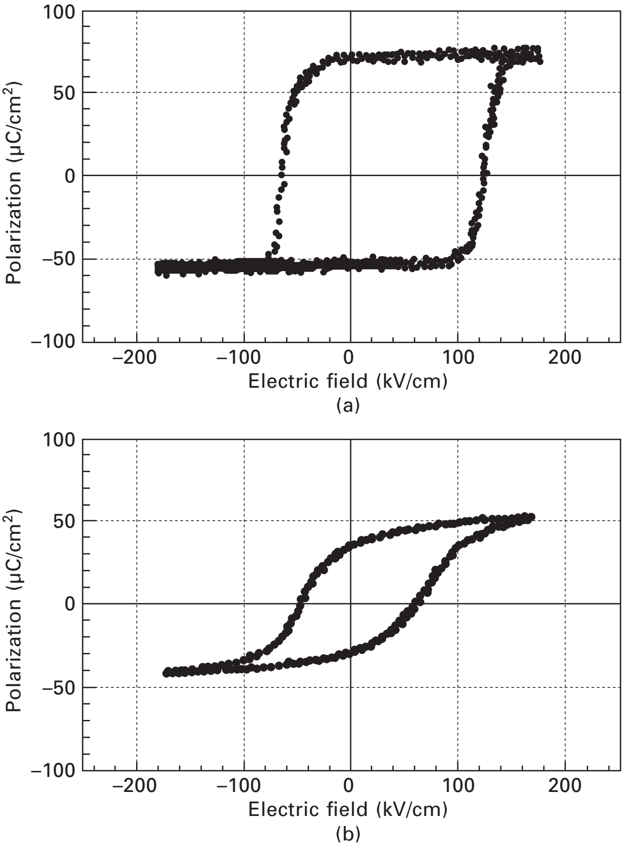

13.17 P-E hysteresis curves of the sputtered PZT thin films deposited on (a) Pt/MgO and (b) Pt/Ti/Si.

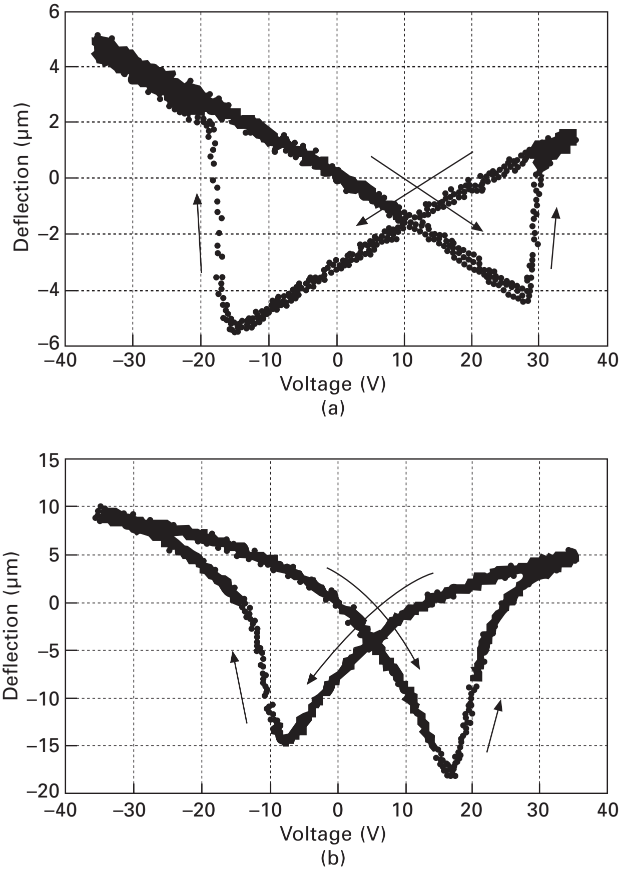

13.18 Tip deflection of the cantilevers: (a) PZT thin films on Pt/MgO, (b) PZT thin films on Pt/Ti/Si.

transitions could not be observed for the sputtered thin films as shown in Fig. 13.19 (Kanno 1998, Kanno *et al.* 2003b), because of differences in the microstructure. In the high temperature process, the PZT thin films are epitaxially grown on the substrates and the interface between thin films and the substrates are coherent. The PZT thin films are constrained to the substrates. The crystal structure of the substrate surface is cubic, so the epitaxial thin films show essentially tetragonal. This results in the ambiguous phase transition in the sputtered thin films. The interface of the sol-gel-derived PZT thin films is not coherent and the films are relaxed. The substrate effects are not so much greater than the sputtered epitaxial thin films. These structural differences between sol-gel thin films and sputtered thin films enhance the difference in their dielectric and piezoelectric properties. The E_c values are sensitive to the domain structure. The domain structure of the sol-gel-derived PZT thin films is almost the same as the bulk structure. Therefore, the E_c values

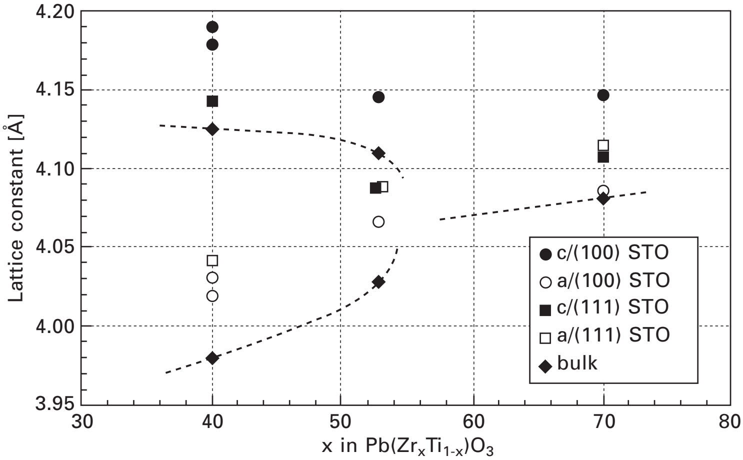

13.19 Lattice constants of PZT thin films as a function of Zr/Ti ratio. ● and ○ represent the *c*- and *a*-lattice constants of PZT thin films grown on (001)Pt/(001)SrTiO$_3$, respectively. ■ and □ represent the *c*- and *a*-lattice constants of PZT grown on (111)Pt/(111)SrTiO$_3$, respectively. ◆ and dashed line indicate the bulk data.

are not so different from the bulk values for sol-gel-derived PZT thin films, $E_c < 100$ kV/cm. However, the sputtered high density PZT thin films show high E_c values, $E_c > 100$ kV/cm. The E_c values increase with the decrease of film thickness. If the sputtered PZT thin films comprise a mixed orientation, their compositional dependence of crystal structure and dielectric constant is similar to bulk PZT properties (Takayama and Tomita 1989).

13.5 PZT-based thin films for micro-electromechanical systems (MEMS)

Thin films of intrinsic PZT are widely used for the fabrication of PZT-based thin film MEMS devices. However, the thin films of the Pb-based ternary perovskite compounds, i.e. Pb(Mg,Nb)O$_3$(PMN) and PT (PMNT), PMN–PZT and/or Pb(Mn,Nb)O$_3$ (PMnN)–PZT, will be much more useful for the fabrication of MEMS devices, since a variety of ferroelectric properties will be realized by the selection of the chemical compositions. In this section, the deposition and the ferroelectric properties of the Pb-based ternary ferroelectric thin films are described in relation to their application for MEMS devices.

13.5.1 PMNT thin films

The PMNT, (1-*x*)PMN–*x*PT, is a solid solution of a relaxor ferroelectric material PMN and a normal ferroelectric material PT and exhibits a very high dielectric permittivity and an exceptionally high coefficient of electromechanical coupling (Uchino 1998). The PMNT shows a morphotropic phase boundary (MPB) at about $x = 0.33$ for the bulk single crystals. Several deposition processes are reported including a sputtering (Jang and Wu, 1994), MOCVD (Takaeshima *et al.* 1995), PLD (Tantigate *et al.* 1995), and sol-gel method (Wakiya *et al.* 1999). These PMNT thin films often include the isometric compound of the pyrochlore, $Pb_2(Mg,Nb)_2O_7$, and include grains and/or interfacial dislocated layers. The structure looks like polycrystalline ceramics with a large porosity and a poor crystal orientation. The reliable deposition process of the single crystal-like PMNT thin films is necessary for the development of the thin film MEMS devices but also for the understanding of the ferroelectric thin films. Among these deposition processes, sputtering is the most promising process for the deposition of the bulk single crystal-like thin films (Wasa *et al.* 2004a, p. 71).

The PMNT thin films are directly sputtered from PMNT powder target on (001)$SrTiO_3$ and/or (001)MgO single crystal substrates. The target powder is composed of the mixture of PT, PbO, MgO, Nb_2O_5, and TiO_2 powder. The epitaxial temperature is 500–550 °C. The Pb-reduced structure, $Pb(Mg_{1/3},Nb_{2/3})_3O_{7,}$ is grown at a temperature higher than 600 °C. The typical sputtering conditions are shown in Table 13.8. The optimum growth temperatures showed a narrow window of 500–550 °C. The sputtered thin films were quenched after the deposition in order to suppress the growth of the pyrochlore phase during the cooling down stage. The quenching process is essential for the deposition of high quality thin films with a high reproducibility.

Figure 13.20 shows a typical XRD pattern of the sputtered PMNT thin films on the (001)MgO substrate. The XRD Θ–2Θ pattern showed the sputtered film was highly (001) orientated (Fig. 13.20a). The pole figure of the (110) direction showed a strong four-fold intensity describing three-dimensional epitaxy (Fig. 13.20b). The similar epitaxial properties were also

Table 13.8 Sputtering conditions for PMNT thin films

Sputtering system	Planar rf-magnetron
Target[a]	mixed powder: PbO, MgO, Nb_2O_5, PT
Substrates[b]	La-0.75wt% doped(001)ST, (001)MgO
Buffer layer	(110)SRO, (001)PLT
Sputtering gas	0.5 Pa (Ar/O_2=20/1)
Growth temperature	480–600 °C
Sputtering power	1.3 W/cm^2
Growth rate	200 nm/hr
Film thickness	20–8000 nm
Quenching rate	100 °C/min. in air

[a] Typical composition: stoichiometric + 10%PbO
[b] Conductive base electrode: (001)Pt for (001)MgO

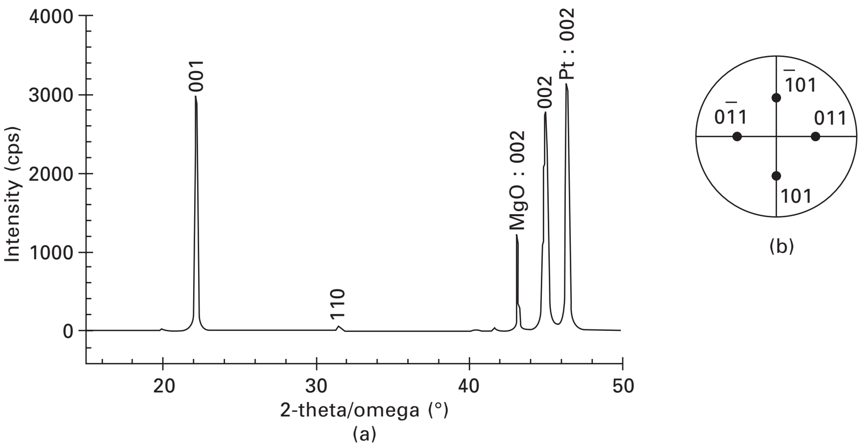

13.20 Typical XRD patterns of the sputtered PMN–33PT thin films on (001)MgO substrates. Film thickness: 230 nm.

Table 13.9 Lattice parameters of sputtered PMNT thin films for different substrates

	Bulk PMN a = 0.405 nm	c = 0.405 nm
Substrates	PMN thin films	
(001)MgO	a = 0.405 nm	c = 0.406 nm
(001)Pt/(001)MgO	0.405	0.406
(001)SrTiO3	0.405	0.406

MgO a = 0.420 nm, $SrTiO_3$ a = 0.3905 nm

observed for the different substrates. The lattice parameters of the sputtered PMNT thin films are shown in Table 13.9. It is noted that the in-plane lattice parameters of the PMNT thin films are almost the same as the bulk lattice values independent of the substrate lattice parameters. The c-axis is slightly prolonged probably due to the inclusion of the high energy particles during the sputtering deposition.

The cross-sectional SEM and TEM images in Fig. 13.21 show that the sputtered PMNT thin films exhibit continuous single crystal-like structure without grains and/or interfacial dislocated layer between the PMNT thin films and the substrates. These structural analyses show that the sputtered PMNT thin films comprise bulk-like single crystal structure without in-plane stress. The point and/or line defects are found in the interface between the thin films and the substrates. However, the dislocated interfacial layer is absent (Seo 2004).

Typical P-E curves are shown in Fig. 13.22. The P_r increases with the addition of the PT into the PMN similar to the bulk materials. Figure 13.23

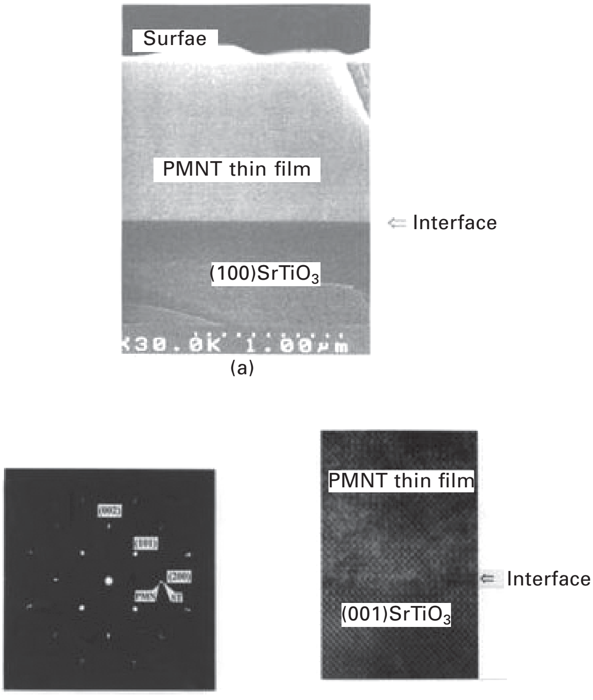
Surfae
PMNT thin film
Interface
(100)SrTiO$_3$
x30.0K 1.00µm
PMNT thin film
Interface
(001)SrTiO$_3$

(a)

(b)

13.21 Cross-sectional SEM and TEM images of (001)PMNT thin films on (001)ST: (a) SEM image. Film thickness: 1170 nm, (b) TEM lattice image with SAD patterns at interface. Film thickness: 300 nm.

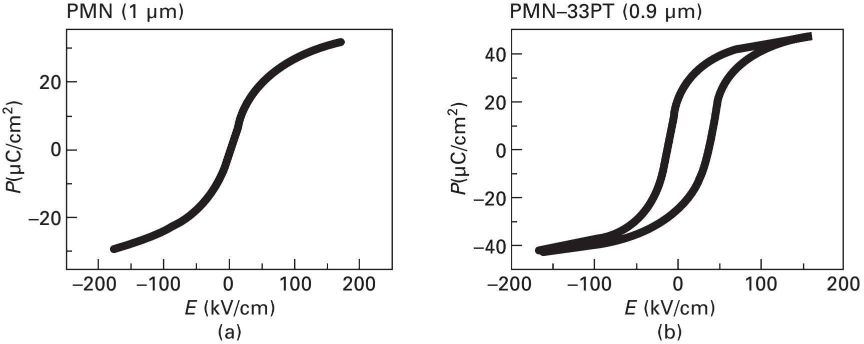

(a)

(b)

13.22 Typical *P–E* curves for PMNT thin films on (001)MgO substrates: (a) PMN thin films, (b) PMN–33PT thin films. Film thickness: 300 nm.

shows a typical temperature variation of the dielectric constants of the sputtered PMNT thin films. A broad peak near the phase transition temperature is observed. The figure shows frequency dependence of the dielectric properties

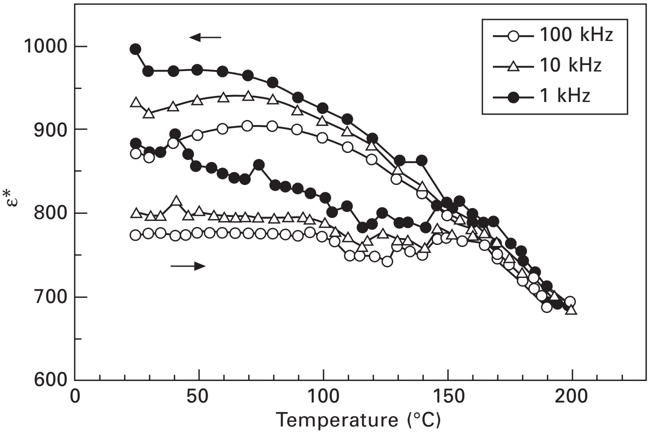

13.23 Temperature variations of the dielectric constants for sputtered PMNT thin films. Film thickness: 300 nm.

similar to the bulk PMNT. The transition temperature is slightly higher than bulk values. The shift of the transition temperature suggests that the sputtered PMNT thin films are almost relaxed according to the XRD analyses; however, the sputtered PMNT thin films are still constrained to substrate (Nagarajan *et al.* 2000). The temperature shift decreases with the increase in the film thickness (Nagarajan *et al.* 1999).

The piezoelectric properties have been evaluated by a deflection of cantilever beam. A typical deflection of the cantilever beams for the sputtered PMNT thin films of different compositions is shown in Fig. 13.24. The cantilever comprises the PMNT thin film capacitor deposited on metallized MgO substrate beam. The length, width, and thickness of the MgO beam are 7–10 mm, 1–3 mm, and 0.3 mm, respectively. The tip displacements show a parabolic change with the applied electric field for PMN thin films, while the displacements show linear dependence with the electric field for PMN–33PT thin films similar to the bulk PMNT. Their transverse piezoelectric constants, $d_{31,}$ were $d_{31} = -73$ pC/N for PMN and –104 pC/N for PMN–33PT.

The frequency range of the piezoelectric properties evaluated by the cantilever beam is lower than 100–500 kHz. Planar PMNT thin film BAW resonator is useful for the evaluation of GHz piezoelectric properties (Ito *et al.* 2005). Figure 13.25 shows the typical structure of the PMNT thin film BAW resonator for the measurement of the resonant spectrum (Wasa *et al.* 2006).

A typical resonant spectrum for the PMN–33PT thin films of 2.3 μm film thickness is shown in Fig. 13.26. The resonance was observed at about 1.3 GHz indicating the longitudinal phase velocity of 5500–6000 m/s. The multi-reflection mode was superposed on the main spectrum. This mode

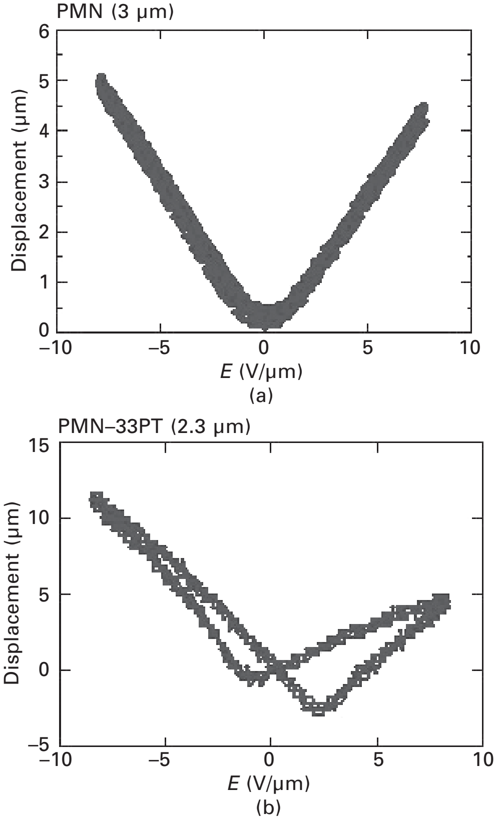

13.24 Tip deflection of cantilever with applied voltage for PMNT thin film cantilevers. Film thickness: (a) 3.0 µm, PMN thin films; (b) 2.3 µm, PMN–33PT thin films.

was caused by the acoustic multi-reflection of a longitudinal standing wave excited in the MgO substrate. The electromechanical coupling k_t evaluated by Mason's equivalent circuit was about 45% at the resonant frequency of 1.3 GHz with $\varepsilon_{33}^{s} = 500$, $Q_{ms} = 2000$, $Q_{mp} = 20$, where Q_{ms} and Q_{mp} are mechanical Q values of the MgO substrate and PMNT thin films. The observed coupling values are almost the same as the single crystal values as expected (Zhang and Cao 2004).

The structure of the sputtered PMN thin films is almost the same as the bulk PMN except for a small enlargement of the *c*-axis. A complex composition with a small additive is used for the bulk ceramics piezoelectric materials. The present sputtering process easily achieves the complex composition by using a powder target. Figure 13.27 shows an example of ferroelectric properties of complex compound PMN–PT–PZ thin films with addition of Sr

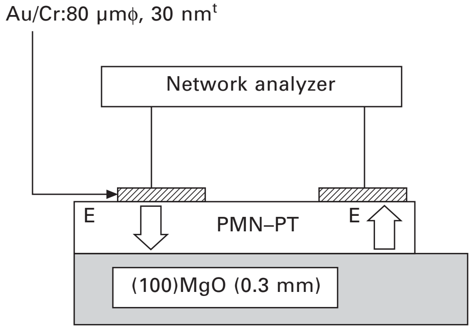
Au/Cr:80 μmφ, 30 nm^t
Network analyzer
E
PMN–PT
E
(100)MgO (0.3 mm)

13.25 Construction of PMNT thin film FBAR for measurement of resonant properties.

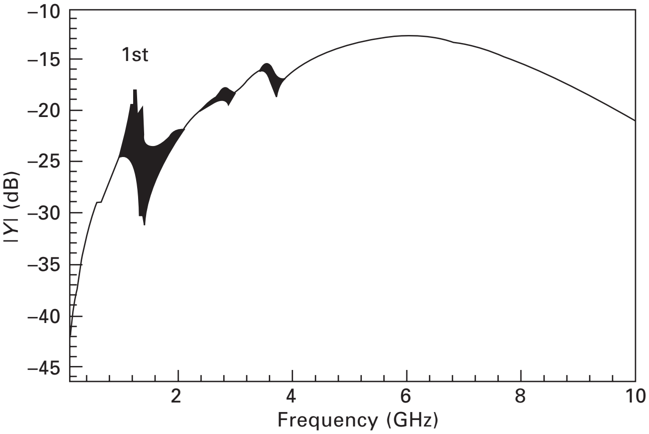

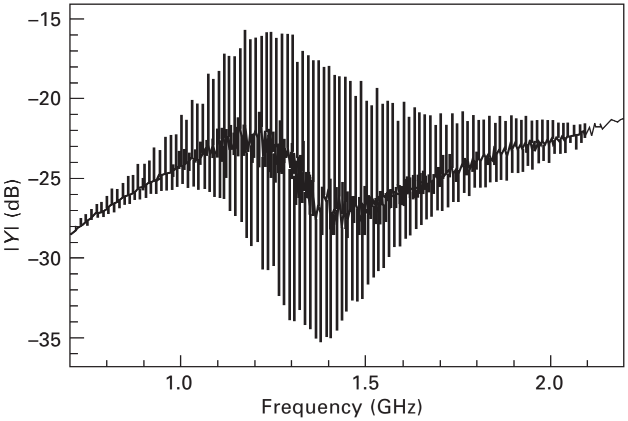

13.26 Typical resonant spectrum of PMN–33PT thin film FBAR. Film thickness: 2.3 μm.

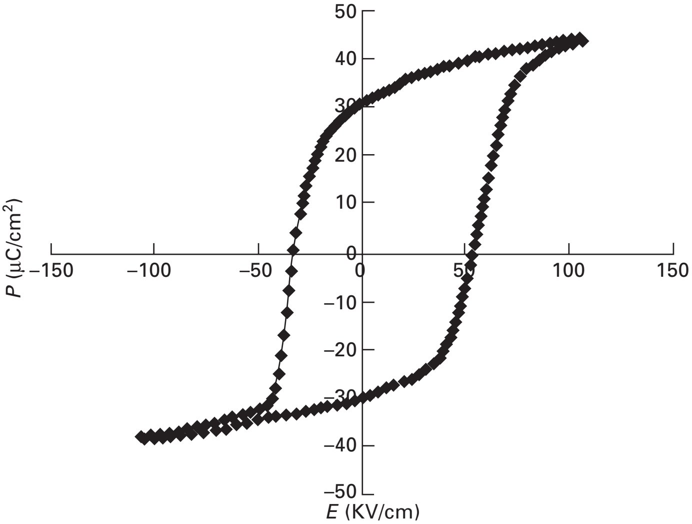

13.27 P–E hysteresis curve of Sr-doped PMN–PT–PZ thin films on SRO/Pt/(001)MgO. Film thickness: 1.9 μm.

(Wasa *et al.* 2004b). The PMN–PT–PZ ceramic composition was developed by Ouchi (1976).

Excellent ferroelectric *P-E* curves with a large P_r was observed. In the bulk ceramics, the addition of the Sr increases the dielectric constant. In the present sputtered PMN–PZT films, the addition of the Sr also increases the dielectric constants similar to the bulk ceramics. These experiments suggest that the sputtering with the quenching is useful for the deposition of Pb-based ferroelectric perovskite thin films. The selection of the chemical composition with a variety of the small additive will achieve the well-designed ferroelectric thin films including dielectric properties, piezoelectric properties, and mechanical properties for the fabrication piezoelectric thin film devices. The traditional material design for the perovskite ferroelectric ceramics including doping effects is applicable for the material design of the perovskite ferroelectric thin films.

13.5.2 PMnN–PZT thin films

Based on the understanding of the deposition mechanism of PMNT thin films by using the sputtering process, the thin films of the ternary compounds PMnN–PZT were deposited using the sputtering process and their ferroelectric properties were evaluated.

The PMnN–PZT ternary ceramics comprise PZT with a donor additive Nb and an acceptor additive Mn. However, it is known that the ternary ceramics show hard ferroelectric response (Takahashi *et al.* 1971). The single crystal

PMnN–PZT thin films are provided by the sputtering deposition similar to the deposition of PMNT thin films. The target powder was composed of the mixture of PT, PZT, PbO, Nb_2O_5, MnO_2, ZrO_2, and TiO_2 (Zhang *et al*. 2008). Figure 13.28 shows a typical *P-E* hysteresis curve for the single *c*-domain/single crystal thin films of 0.06PMnN–0.94PZT(45/55) (Wasa *et al*. 2008). The hysteresis curve shows typical hard ferroelectric properties of the square shaped loops with high E_c and large P_r values ($2E_c \cong 230$ kV/cm and $P_r \cong 60$ μC/cm^2). The PMnN–PZT thin films showed the dielectric anomaly at $T_c = 560$ °C as shown in Fig. 13.29. The T_c was higher than the bulk PMnN–PZT ceramic value. The observed relative dielectric constants were 150–200 with tan $\delta = 0.01$–0.02 at 1 kHz. The dielectric constants were much lower than the bulk non-doped intrinsic PZT ceramics (bulk ceramic values ≅ 700).

The transverse piezoelectric coefficients of the (001)PMnN–PZT thin films epitaxiallly grown on (001)MgO were $e_{31f} = -10.8$ C/m^2, $d_{31} = -83 \times 10^{-12}$m/V, respectively. The observed transverse piezoelectric constants were almost the same as the bulk PZT ceramic values at the MPB compositions. The doping effects of the PMnN into the PZT on the piezoelectric constants were not large. However, it is known that the bulk PMnN–PZT ceramics show that the doping of the PMnN into the intrinsic PZT remarkably enhances the mechanical quality factor Q_m. In order to confirm the effect of the PMnN doping on the Q_m, the PMnN thin film FBAR structure was fabricated and their Q_m values were evaluated. Figure 13.30 shows typical variations of the

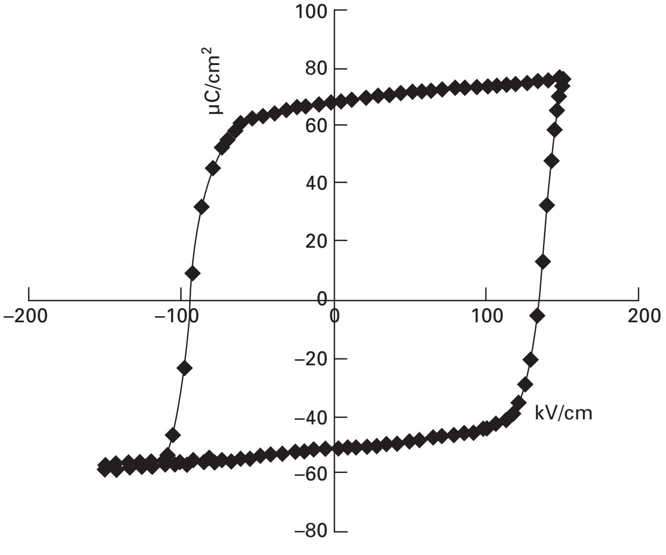

13.28 Typical *P-E* hysteresis curve for the single *c*-domain/single crystal thin films of 0.06 PMN–0.94PZT(45/55). Film thickness: 1.9 μm.

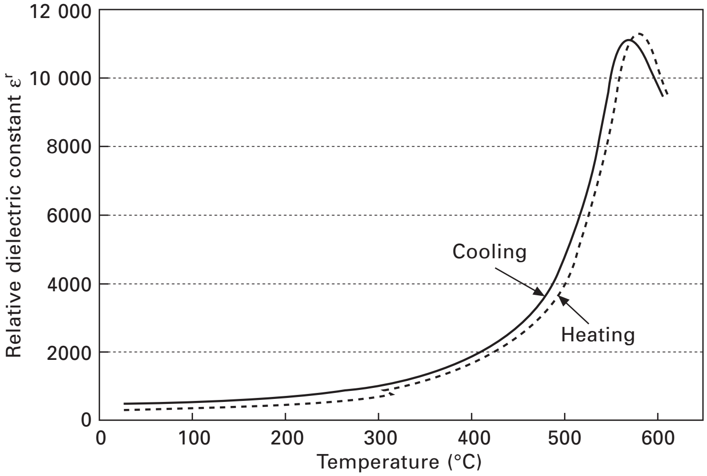

13.29 Temperature variations of dielectric constant for the single *c*-domain/single crystal thin films of 0.06PMnN–0.9PZT(45/55). Film thickness: 1.9 μm.

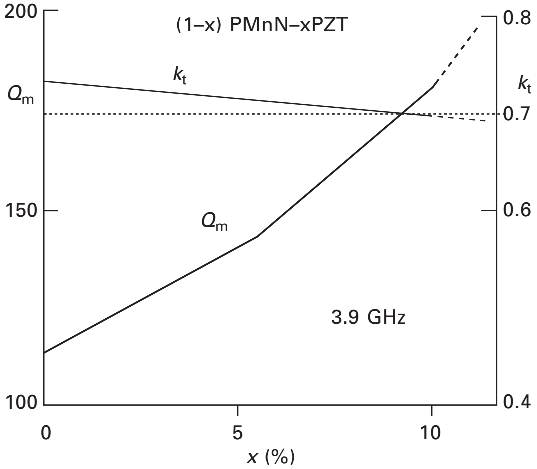

13.30 Typical variations of the Q_m and the coupling factor k_t for the different amounts of PMnN doping to PZT.

Q_m and the coupling factor k_t for the different amounts of PMnN doping. In the figure it is seen that the Q_m and the k_t for the intrinsic PZT thin films are 100 and 70%, respectively. The Q_m values increase with the doping of the PMnN to the PZT. The k_t decreases with the doping of PMnN. However, the decrease of the k_t is around 10% for the doping of PMnN of 10%, while the Q_m increases almost two times. Therefore, the doping is effective for the improvement of Q_m for intrinsic PZT thin films.

Typical thin films of PMnN–PZT, 0.1PMnN–0.9PZT(55/45), 300 nm in film thickness showed *f*s = 3.373 GHz and *f*p = 3.870 GHz. Taking the observed *f*p and *f*s values, the k_{eff} = 0.487 and the k_{t} = 0.689. From the phase properties, Q_{m} = 185. Thin films of intrinsic PZT (48/52) showed *f*s = 3724 MHz and *f*p = 4451 MHz. Their k_{eff} = 0.547 and k_{t} = 0.726. The Q_{m} was 114. So, it is found that the doping of the PMnN into the PZT does not remarkably affect the k_{t} values. The k_{t} of the intrinsic PZT thin films was slightly higher than the PMnN-doped PZT thin films. The doping increases the Q_{m} almost two times in magnitude (Yamauchi *et al*. 2009).

13.6 PZT-based thin film micro-electromechanical systems (MEMS)

13.6.1 PZT-based thin film piezoelectric actuators

Several types of actuators are proposed for fabrication of MEMS as shown in Fig. 13.31. Among these actuators the piezoelectric actuators show low voltage operation and fast response. Thin films of PZT-based piezoelectric materials are useful for the fabrication of the piezoelectric actuators. A basic construction of PZT-based thin film piezoelectric actuators is shown in Fig. 13.32. Thin film piezoelectric actuators comprise piezoelectric thin films deposited on a substrate such as a Si wafer. Since a displacement of the thin film longitudinal actuators is small, the cantilever and/or diaphragm type actuators are used in practice.

From Eqs (13.5) and (13.6), the deflection of the cantilevers δ and the resonance frequency f_0 are given by the following relations:

Electrostatic	Magnetic	Thermal	Piezoelectric
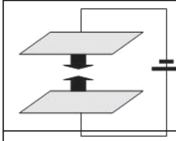	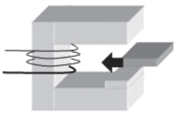	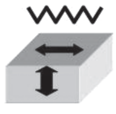	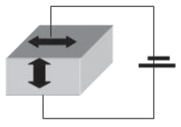
$F(x) = \frac{1}{2}\frac{\varepsilon_0 S}{(d-x)^2} V^2$	$F = \frac{n^2 I^2}{2x_0} \frac{\mu_0 A}{g_\mu + \frac{\mu_0 L_m}{\mu}}$	$F = \alpha \cdot \Delta T \cdot E$	$T_3 = E \cdot d_{33} \cdot \frac{V}{t}$ $T_1 = E \cdot d_{31} \cdot \frac{V}{t} L$
Easy microfabrication Fast response	Conventional and traditional actuators Remote operation	Large force Simple structure	Fast response Low voltage Large force
Small force (high voltage)	Microfabrication Generation of heat	Cross talk Slow response	Thin film growth Microfabrication

13.31 Classifications of micro-actuators.

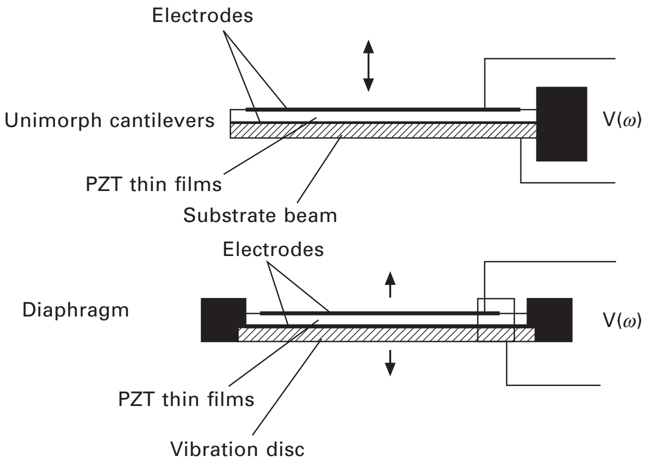

13.32 Constructions of thin film piezoelectric actuators.

$$\delta = -\,3(L/h_s)^2(s_{11s}/s^{\mathrm{E}}_{11p})V, \qquad 13.8$$

$$= -\,3(L/h_s)^2\,(s_{11s})\ {}^{*}e_{31}V, \qquad 13.9$$

$$f_0 = 0.161[h_s/L^2\,(\rho\ s_{11s})]^{1/2}, \qquad 13.10$$

where V denotes the applied voltage between top and bottom electrodes, L, h_s, s_{11s}, ρ are, length, thickness, elastic compliance, and density of cantilever substrates, respectively. A blocking force F is given by the following relation:

$$F = (1/s_{11\mathrm{s}})w(h_s)^3\delta/4L^3, \qquad 13.11$$

where w denotes the width of cantilevers (Uchino 2000, Duval *et al.* 2007). The deflection of the thin film cantilevers is governed by the combination of piezoelectric properties of PZT thin films and the dimension and the elastic properties of the substrate beam. The resonant frequency is determined by the dimension and the elastic constants of the substrate beam.

The resonant frequency and the vibration modes of the thin film diaphragms are also governed by the dimension and the elastic properties of the substrates. The resonant frequency of the diaphragms is expressed by the relation:

$$f_0 = (0.932t/D^2)[(E/\rho)(1-\sigma^2)]^{1/2}, \qquad 13.12$$

where D, t, E, ρ, and σ denote the diameter, thickness, density, Young's modulus, and Poisson's ratios of the substrate materials (Terada *et al.* 2007).

For the PZT thin film cantilevers deposited on the Si beam, taking $L = 10$ mm, $h_s = 0.3$ mm, $s_{11s} = 5.95 \times 10^{-12}$ m^2/N (Si), ${}^{*}e_{31} = -5$ C/m^2, $\rho = 2.33$ g/cm^3, the deflection δ becomes $\delta = 1$ μm at the applied voltage $V = 10$ V and the resonant frequency f_0 becomes $f_0 = 4.1$ kHz.

Table 13.10 shows the deflection properties of the PZT-based piezoelectric thin film cantilevers for different substrate materials. The piezoelectric properties are governed by the domain structure and/or orientation of the PZT thin films. The PMnN–PZT thin films with Si substrates show the maximum deflections probably due to their domain motions (Zhang *et al.* 2009).

The tip displacements of these thin film unimorph cantilevers are almost the same as those of the bulk PZT-based ceramic bimorph cantilevers, if we compare the tip displacements of thin film cantilevers with the ceramic bimorph cantilevers under the same dimension. A suitable selection of substrates could further improve their piezoelectric properties (Suzuki *et al.* 2006, Kanda *et al.* 2009). Figure 13.33 shows a photograph of a typical PZT-based thin film cantilever fabricated on a Si beam.

Figure 13.34 shows the construction of the PZT-based thin film cantilevers without the substrate (Kanno *et al.* 1997). The length of the cantilevers is 100–500 μm. The thickness of the PZT thin films is 2–5 μm. Since the wavelength of the fundamental transverse oscillation mode λ is $4L$, and the longitudinal elastic wave velocity v_s for the piezoelectric thin films is given by the relation:

$$v_s = f_0 \lambda, \tag{13.13}$$

and the resonant frequency f_n are expressed by

$$(2n + 1) f_0 = (1/4L)(1/\rho\, s_{11}^{E})^{1/2} \tag{13.14}$$

$$n = 0, 1, 2, 3.$$

Figure 13.35 shows typical resonant properties of the (001)PZT (53/47) thin film resonators. The resonant frequency is three orders of magnitude higher than the PZT-based thin films with Si cantilever beam. From the measurements of resonant properties, the s_{11}^{E} values and v_s for PZT thin films are estimated. The v_s and s_{11}^{E} values for the PZT thin films are 3520 m/sec and 10.8×10^{-12} m^2/N, respectively. These values are the same as the bulk PZT values. This suggests that the elastic constants of the bulk PZT could be used for the design of the PZT-based thin film actuators.

13.6.2 Some examples of the PZT-based piezoelectric thin film MEMS and related devices

Several kinds of thin film MEMS and MEMS sensors are fabricated using the piezoelectric thin film actuators. The PZT thin film cantilever beams and diaphragms are used for the fabrication of the optical MEMS, RF-MEMS, power MEMS, bio-MEMS, and/or MEMS sensors. Table 13.11 shows a summary of the piezoelectric thin film MEMS and thin film MEMS sensors. The optical MEMS devices are useful for fabrication of the optical switch,

Table 13.10 Piezoelectric properties of PZT-based thin film unimorph cantilevers

PZT composition	Substrates	Displacements δ^a (μm)	Piezoelectric $e_{31,f}$ (C/m^2)	Constants d_{31} (pC/N)	Deposition method	Reference
(001)PZT (52/48)	MgO	1.13	–11.3	–91.3	Sputter	Wasa *et al*. (2008)
(111)PZT (53/47)	Si	1.33	–10.1	–107.2	Sputter	Kanno *et al*. (2003a)
(111) PZT(53/47)	Si	2.13	–16.5	–172	Sol-gel	Xiong *et al*. (2008)
(001)PMnN-PZT	MgO	1.03	–10.1	–83.1	Sputter	Zhang *et al*. (2008)
(111)PMnN-PZT	Si	1.95	–14.9	–158	Sputter	Zhang, *et al*. (2009)
(001)/(101)PZT(53/47)	Ti	0.5	–5.6	–47.7	Sputter	Kanda *et al*. (2009)

δ^{*1}: Tip displacement for thin film cantilevers, $\delta = 3d_{31}(L/hs)^2 V$ at $V = 10$V.$L = 10$ mm, and $hs = 0.3$ mm. Bulk PZT ceramic bimorph cantilever: $\delta = 3d_{31}(L/2t)^2$V, $\delta = 0.75$ μm for PZT (52/48) at $V = 10$V, $L = 10$ mm, $2t = 0.3$ mm, and $d_{31} = -93 \times 10^{-12}$C/N; $\delta = 2.2$ μm for PZT-5H at $V = 10$ V, $L = 10$ mm, $2t = 0.3$ mm, and $d_{31} = -274 \times 10^{-12}$C/N.

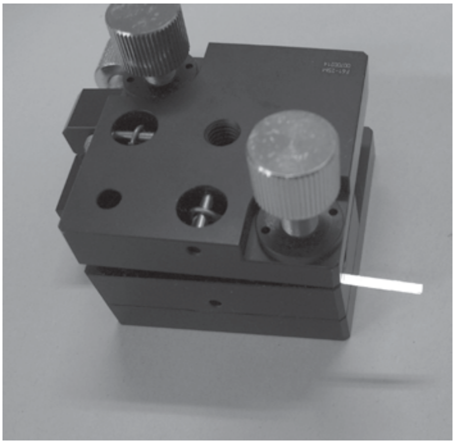

13.33 Photograph of PZT thin film cantilever on Si beam.

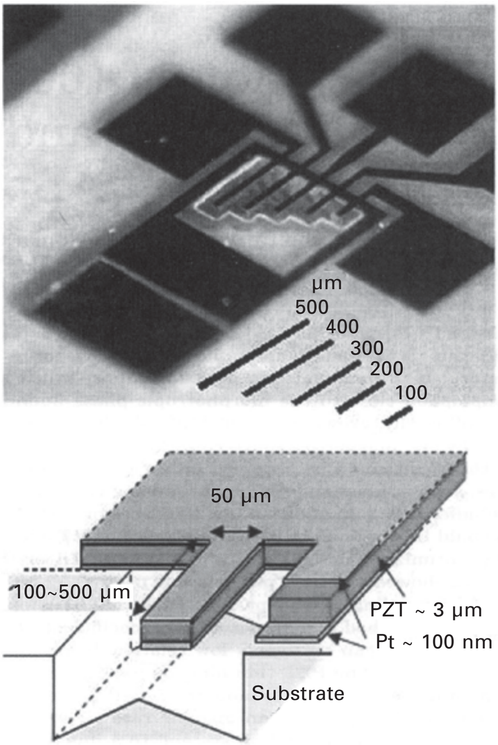
µm
500
400
300
200
100
50 µm
100~500 µm
PZT ~ 3 µm
Pt ~ 100 nm
Substrate

13.34 Photographs of PZT thin film cantilevers without substrate Si beam.

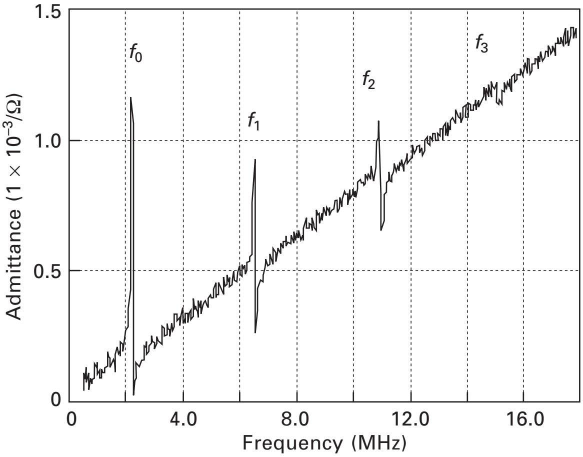

13.35 Typical resonant properties of the PZT thin film micro-cantilevers.

Table 13.11 Summary of thin film piezoelectric MEMS devices

MEMS devices	Typical devices	Constructions
Optical MEMS	Micro-mirror Scanner Display Deformable mirrors	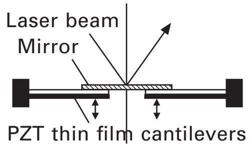 Laser beam Mirror PZT thin film cantilevers Micro-optical scanner
RF MEMS	Microwave switches Antennas Resonators Varactors Phase shifters (FBAR)	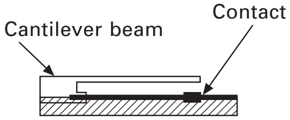 Contact Cantilever beam Micro-strip line
Power MEMS	Piezoelectric generators (Micro fuel cells) (Micro-gas turbine)	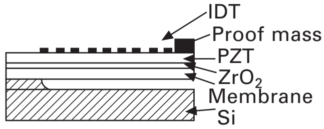 IDT Proof mass PZT ZrO$_2$ Membrane Si Micro-power generators (Jeon *et al.* 2005)
Micro-fluid devices	Bio-MEMS μ-TAS Micro-chemical reactors	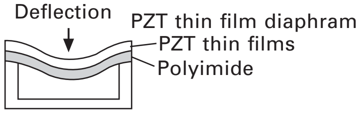 Deflection PZT thin film diaphram PZT thin films Polyimide
MEMS sensors	Gyro-sensors Force sensors Pressure sensors IR sensors Gas sensors	Micro-pump for micro-fluid devices (Terada *et al.* 2007)

1D or 2D optical scanners, and the display system. The deformable mirrors are useful in medical applications (Kanno *et al.* 2007). The RF-MEMS devices are useful for a mobile communication system due to the small power consumption with low voltage operations (Rebeiz *et al.* 2003, Kanno *et al.* 2003c). The GHz PZT piezoelectric thin film resonators, FBAR (film bulk acoustic resonators), are also promising devices in the near future. The power MEMS comprises the micro-fuel cells and/or micro-power generators by using the piezoelectric effect (Jeon *et al.* 2005). In the micro-fuel cells, the PZT thin film pumps will be applicable. The piezoelectric micro-power generators have been developed for energy harvesting from the environment. Most of all, mechanical vibration is a potential power source. The micro-power will be used in wireless applications. In the micro-fluid devices, the cantilever and/or the diaphragm type pump is used for the operation of micro-fluid devices. Bio-MEMS devices comprise a micro-fluid device (Zahn 2007). The thin film pump is a key device for the stable operation of micro-fluid devices. Among these thin film MEMS devices, some of them, such as a gyro-sensor and an inkjet printer head, are used in practice. In this section, the construction and operations of the gyro-sensors, the inkjet printer head, and the GHz -FBAR are described.

Gyro-sensors

The PZT thin films deposited on (111)Pt/Ti/Si substrates are used in practice for fabrication of a tuning fork type angular rate sensor in a car navigation system (Fujii *et al.* 2007). A construction of the tuning fork type angular rate sensors is shown in Fig. 13.36. The tuning fork-type angular rate sensor, when an angular rate is applied to its vibrating tuning fork element, detects the Coriolis force exerted perpendicularly to its direction of vibration. The PZT thin films play two roles: generation of the tuning fork vibration and detection of the Coriolis force. The Si tuning forks with high aspect ratio were

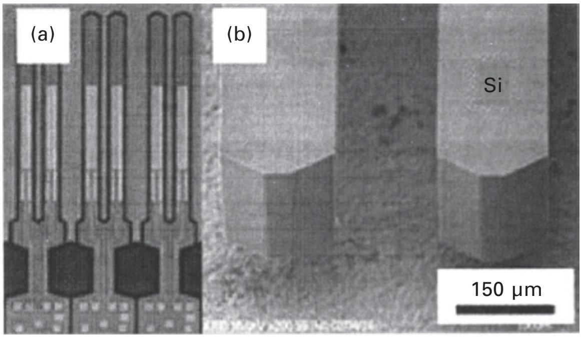

13.36 Construction of PZT thin film angular rate sensor.

fabricated by Si deep etching. Table 13.12 shows the operating properties of the Si tuning fork type angular rate sensor.

Inkjet printers

The other example of piezoelectric PZT thin film MEMS used in practice is an inkjet printer head (see Fig. 13.37). The inkjet head consists of PZT thin film actuators, pressure chambers, ink canals and nozzle plates with water-repellent films. Each inkjet head has 400 nozzles and 400 pressure chambers. Typical operating properties of the inkjet head are shown in Table 13.13 (Fujii *et al*. 2007).

FBAR

The thin film bulk acoustic wave resonator (FBAR) is currently of interest for key micro-devices in a GHz range for a mobile communication system (Lakin 1999). The bulk acoustic resonators use a longitudinal oscillation excited in the piezoelectric disc. The resonant frequency f_0 is basically expressed by $f_0 = v_s/2d$, where v_s and d denote the phase velocity of longitudinal elastic wave and thickness of the piezoelectric disc. Conventional piezoelectric thin films are ZnO and AlN (Lobl *et al*. 2001). Their phase velocities are v_s = 6400 m/s for ZnO and v_s = 11000 m/s for AlN. Assume d = 100 nm f_0 = 3.2 GHz for ZnO and f_0 = 5.5 GHz for AlN. Although the mechanical quality factor Q_m is high, the coupling coefficient k_t is not sufficient for fabrication of wide band filters. PZT thin films have been tried in making the FBAR, since the k_t of PZT ceramics is higher than ZnO and AlN. However, the Q_m of PZT thin films is too small for fabrication of the FBAR. For fabrication of PZT-based FBAR, the ternary PZT-based thin films, PMnN–PZT thin films, will be useful. Figure 13.38 shows a typical construction of the PMnN–PZT thin film FBAR (Wasa *et al*. 2008). The FBAR comprises the high Q_m thin films of the PMnN–PZT. The 0.3 mm thick (001)MgO substrates were used for fabrication of the FBAR structure. The FBAR structure comprised the PMnN–PZT thin films, 280 to 320 nm thick, SRO/Pt base conductive electrodes, and Al top electrodes. The thickness of the SRO, Pt, and Al

Table 13.12 Operating properties of Si tuning fork type thin film angular rate sensors

Operating temperature range	–40 to +85 °C
Power supply voltage range	5± 0.25 °C
Sensitivity	25 mV(°/S)
Frequency response (7 kHz)	> –7 dB
Output voltage range	0.3–4.7 V
Output noise	< 10 mVp-p

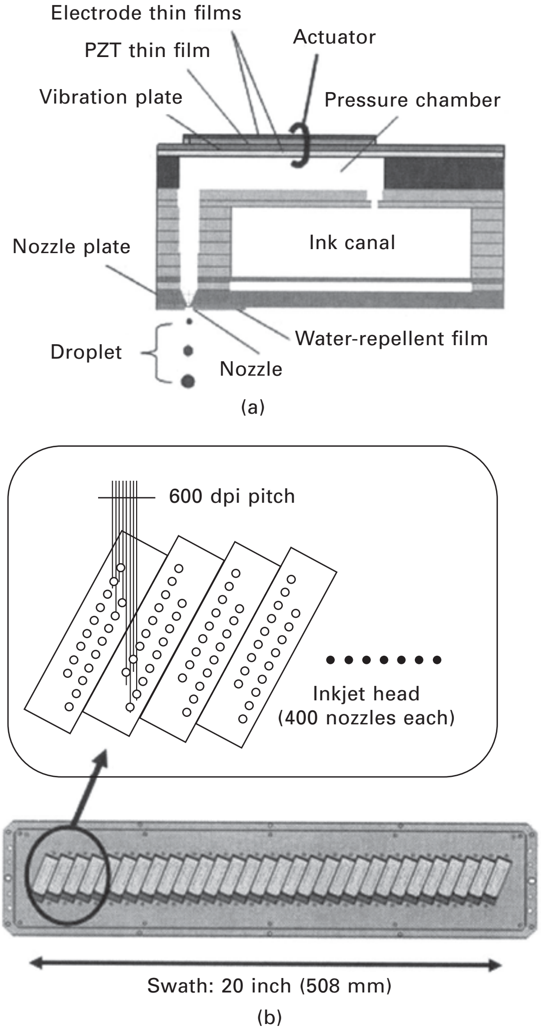
Electrode thin films
PZT thin film
Actuator
Vibration plate
Pressure chamber
Ink canal
Nozzle plate
Droplet
Nozzle
Water-repellent film
(a)
600 dpi pitch
Inkjet head
(400 nozzles each)
Swath: 20 inch (508 mm)
(b)

13.37 Photographs of inkjet printer head using PZT thin film actuators: (a) cross-sectional illustration of an inkjet head corresponding to one nozzle; (b) schematic illustration of the line head devices.

electrodes were typically 50 nm, 60 nm, and 100 nm, respectively. The surface roughness of the PMnN–PZT thin films was 3 to 4 nm. The size of the Al top electrodes was 50 μm × 50 μm. The outside of the Al electrode was covered by a layer of SiO_2 100 nm thick. The back side of the MgO substrate was removed by chemical etching (Yamauchi *et al*. 2009).

The effective coupling factor k_{eff} was evaluated by the relation $k_{\mathrm{eff}} = [(f_{\mathrm{p}}^2 - f_{\mathrm{s}}^2)/f_{\mathrm{p}}^2]^{1/2}$, where f_{p} and f_{s} denote the parallel and the series resonant frequency,

Table 13.13 Operating properties of PZT thin film inkjet printer head

Type of printer head	Line head devices
Nozzle number	12 000 nozzles/line 400 nozzles/head
Printer resolution	600 dpi
Printer width	500 mm
Printer speed	60 m/min
Drop volume	0.5–20 pL
Drop speed	8–10 m/s
Lifetime	> 10^{10} drops/nozzle

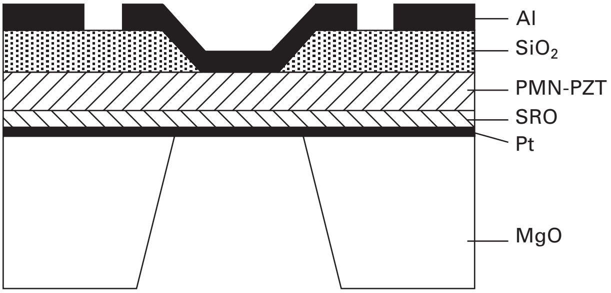

13.38 Construction of PMnN–PZT thin film for FBAR.

respectively. The k_t was evaluated by the relation $k_t^2 = (\pi/8)^2(k_{eff}^2)/(1\text{-}k_{eff}^2)$. The Q_m was obtained by the phase change of the impedance at the anti-resonant frequency f_p using the relation $Q_m = 1/2\omega(d\Phi/d\omega)$. These impedance properties were evaluated by a network analyzer. Their typical impedance properties are shown in Fig. 13.39 for the PMnN–PZT thin film FBAR. From these impedance measurements, the doping effects of PMnN on k_t and Q_m were clarified. Table 13.14 provides a summary of the k_t and Q_m of the present sputtered thin films in comparison with reported values. The doping of PMnN into PZT increases the Q_m. The sputtered PMnN–PZT thin films show the highest k_t. The doping does not affect the k_t. The high values of figure of merit, $k_t^2 \text{x} Q_m$, are observed. This suggests that the PMnN–PZT thin films have a potential to alternate with AlN piezoelectric thin film which is widely studied for making FBAR (Muralt *et al*. 2005). Since the PMnN–PZT thin films show high k_t, the PMnN–PZT thin films will be very useful for making wide band planar filters. From the impedance analyses of the PMnN–PZT thin film FBAR using BVD model, the capacitance of C_0 is found to be 6.5 pF, which shows the relative dielectric constant of PMnN–PZT thin films is 88 at 4 GHz. The dielectric constants are by one order of magnitude smaller than bulk values. The small dielectric constant is useful for the operation of the GHz- FBAR. The high Curie temperature of 580 °C observed in the

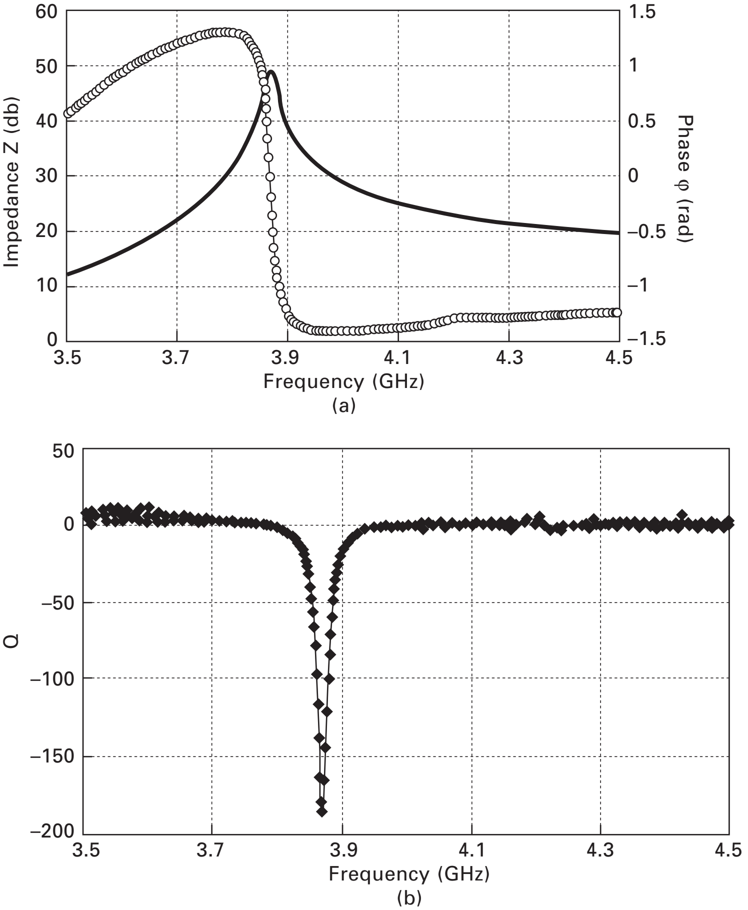

13.39 Typical impedance properties of PMnN–PZT thin film FBAR.

Table 13.14 Figure of merits of PZT-based thin films for FBAR

Deposition	Composition	Freq. (GHz)	kt^2 (%)	Q_m	$kt^2 \times Q_m$
Sputter	(111)PZT(58/42)	2	9	220	19.8[a]
MOCVD	(111)PZT(30/70)	2.1	22	30	6.6[a]
Sputter	(001)PZT(45/55)	3.9	52	110	57[b]
Sputter	0.1PMnN-PZT(55/45)	3.9	49	185	90.6[b]

[a] Muralt *et al.* (2005) [b] Wasa *et al.* (2008)

PMnN–PZT thin films is also essential for the stable operation of the planar thin film filters. One of the reasons why high k_t and high Q_m values are observed in present sputtered thin films is their in-plane relaxed structure.

The relaxed structure was achieved by the sputtering deposition followed by the quenching after the deposition. The second reason is the doping of the PMnN into the intrinsic PZT. The small doping of the PMnN, similar to the bulk ceramics, improves the Q_m. The excess addition of the PMnN induces the growth of the pyrochlore phase resulting in the decrease in k_t. Further improvement of composition will further increase the Q_m (Hwang *et al*. 2002).

13.7 Conclusions

This chapter describes the fundamentals of the thin film process of the PZT-based ferroelectric materials. The PZT-based ferroelectric thin films have been studied over the past 20 years. Production of these thin films has only just started, but environmental restrictions may terminate the usage of Pb-based bulk piezo-ceramics in the near future. Several processes are proposed for production of the Pb-based piezoelectric thin films. It should be remembered that each fabrication process has its own advantages and disadvantages. The sol-gel process is simple and the sol-gel-derived PZT thin films exhibit a high coupling value. However, their mechanical quality factor Q_m is low. The piezoelectric properties of MOCVD-derived PZT thin films are similar to the sol-gel derived ones. The PZT-based piezoelectric thin films with high Q_m and high coupling are obtained by the sputtering process. A suitable selection of deposition process is essential for the production of PZT-based ferroelectric thin film devices. We should also create an environmentally benign production system for PZT-based ferroelectric ceramics. In order to achieve this the key factors will be pollution prevention, waste minimization, and energy saving. Thin film material processing essentially meets these requirements. The PZT materials include toxic lead elements. However, the amount of lead in thin film PZT actuators is less than 0.3% of bulk PZT actuators, if we consider the thickness of PZT is 1 μm for thin film actuators and 300 μm for bulk actuators. The amount of lead in thin film actuators will be further reduced in multilayer and/or nano-composites. Therefore, it would still be possible to use PZT-based piezoelectric materials in the form of thin films.

13.8 Acknowledgements

The author thanks R.E. Newnham, L.E. Cross, K. Uchino, S. Trolier-McKinstry, and T. Yamamoto for their helpful discussions, and H. Adachi, K. Nakamura, I. Kanno, T. Matsushima, and T. Matsunaga for their measurements of PZT-based thin films.

13.9 References

Auciello O, Scott J F, and Ramesh R (1998), 'The physics of ferroelectric memories', *Physics Today*, July, 22–27.

Behrisch R, ed. (1981), *Sputtering by Particle Bombardment* I, New York, Springer, p. 2.

Bunshah R F, ed. (1993), *Handbook of Deposition Technologies for Films and Coatings*, New York, Noyes.

Chen Q and Wang Q-M (2005), 'The effective electromechanical coupling coefficient of piezoelectric thin-film resonators', *Appl. Phys. Lett.*, 86, 022904.

Cross L E (1993), 'Ferroelectric ceramics: tailoring properties for specific applications', in Setter N and Colla E L, eds, *Ferroelectric Ceramics*, Basel, Birkhäuser-Verlag, pp. 1–85.

Dey S K (1996), 'Sol-gel science and PE-MOCVD of dielectric perovskite films', in de Araujo C P, Scott J F, and Taylor G W eds, *Ferroelectric Thin Films: Synthesis and Basic Properties*, Amsterdam, Gordon and Breach, p. 329.

Du X-H, Zheng J, Belegundu U, and Uchino K (1998), 'Crystal orientation dependence of piezoelectric properties of lead zirconate titanate near the morphotropic phase boundary', *Appl. Phys. Lett.*, 72, 2421–2423.

Duval F C, Wilson S A, Ensell G, Markys N, Cain G, and Whatmore R W (2007), 'Characterisation of PZT thin film micro-actuators using a silicon micro-force sensor', *Sensor & Actuators*, A, 133, 35–44.

Eom C B, Cava R J, Fleming R M, Phillips J M, van Dover R B, Marshall J H, Hsu J W P, Krajewski J J, and Peck Jr W F (1992), 'Single-crystal epitaxial thin films of the isotropic metallic oxides $Sr_{1-x}Ca_xRuO_3$', *Science*, 258, 1766–1769.

Elshabini-Riad A A R and Barlow III F D (1998), *Thin Film Technology Handbook*, New York, McGraw-Hill.

Foster M, Bai G R, Li Z, Jammy R, Wills L A, and Hiskes R (1996), 'Properties variations with composition of single-crystal films $Pb(Zr_x,Ti_{1-x})O_3$ thin films prepared by MOCVD', *Mater. Res. Soc. Symp. Proc.,* 401, 139–149.

Foster M, Bai G R, Csencsits R, Vetrone J, Jammy R, Wills L A, Carr E, and Amano J (1997), 'Single-crystal films $Pb(Zr_x,Ti_{1-x})O_3$ thin films prepared by metal-organic chemical vapor deposition: systematic compositional variation of electronic and optical properties', *J. Appl. Phys.*, 81, 2349–2357.

Fujii E, Takayama R, Nomura K, Murata A, Hirasawa T, Tomozawa A, Fujii S, Kamada T, and Torii H (2007), 'Preparation of (001)-oriented $Pb(Zr,Ti)O_3$ thin films and their piezoelectric applications', *IEEE Trans. on UFFC*, 54, 2431–2438.

Gao Y, Merkle K L, Chang H L M, and Lam D J (1993), 'MOCVD growth and structure of $PbTiO_3$ thin films', *Mater. Res. Soc. Symp. Proc.,* 310, 235–240.

Gerstenberg D (1970), 'Thin film capacitors', in Maissel L I and Glang R, *Handbook of Thin Film Technology*, New York, McGraw-Hill, pp. 19–24.

Hayashi S, Iijima K, and Hirao T (1992), 'Prepapration of Pb-based ferroelectric thin films byion-and photo-assisted deposition', *Mater. Res. Soc. Symp. Proc.*, 243, 155–165.

Hendrics W C, Desu S B, Si J, and Peng C H (1993), 'Metallorganic chemical vapor deposition (MOCVD) of titanium-based ferroelectric thin films', *Mater. Res. Symp. Proc.*, 310, 241–247.

Hubbard K J and Schlom D G (1996), 'Thermodynamic stability of binary oxides in contact with silicon', *Mat. Res. Soc. Symp. Proc.*, 401, 33–38.

Hwang S M, Yoo J H, Hwang L H, Hong J I, Ryu S R, Lee S I, and Lee M S (2002), *Proc. of 13th IEEE ISAF*, pp. 367–370.

Iijima T, Osone S, Brinkman K, and Shimojo Y (2007), 'Piezoelectric response of Pb(ZrxTi)1-xO3 thick films prepared using a chemical solution deposition process', *Extended Abstarct.13th US–Japan Seminar on Dielectric and Piezoelectric Ceramics*, pp. 292.

Ito S, Nakamura K, and Ishikawa K (2005), 'Piezoelectric properties of $BaTiO_3$ thin films grown by ECR-PLD', *Proc. 2005 IEEE International Ultrasonics Symp.* (Rotterdam, 2005), P1L–7.

Jang M C and Wu T B (1994), 'The effect of electrode composition on rf magnetron sputtering deposition of $Pb[Mg_{1/3}Nb_{2/3}]_{0.7}$–$Ti_{0.3}O_3$', *J. Mater. Res.,* 9, 1879–1885.

Jeon Y B, Sood R, Jeong J-H, and Kim S-G (2005), 'MEMS power generator with transverse mode thin film PZT', *Sensor and Actuators* A, 122, 16–22.

Kanda K, Kanno I, Kotera H, and Wasa K (2009), 'Simple fabrication of metal-based piezoelectric MEMS by direct deposition of $Pb(Zr,Ti)O_3$ thin films on titanium substrates', *J. Microelectromechanical Systems*, 18, 610–615.

Kanno I (1998), 'Preparation of Pb-based ferroelectric thin films by using ion-beam sputtering and their application to functional devices,' PhD. Thesis, Osaka University.

Kanno I, Fujii S, Kamada T, and Takayama R (1997), 'Piezoelectric characteristics of c-axis oriented $Pb(Zr,Ti)O_3$ thin films', *Appl. Phys. Lett.*, 70, 1378–1380.

Kanno I, Kotera H, and Wasa K (2003a), 'Measurement of transverse piezoelectric properties of PZT thin films', *Sensors and Actuators A*, 107, 68–74.

Kanno I, Kotera H, Wasa K, Matsunaga T, Kamada T, and Takayama R (2003b), 'Crystallographic characterization of epitaxial $Pb(Zr,Ti)O_3$ films with different Zr/Ti ratio grown by radio-frequency-magnetron sputtering', *J. Appl. Phys.*, 93, 4091–4096.

Kanno I, Endo H, and Kotera H (2003c), 'Low-voltage actuation of RF-MEMS switching using piezoelectric PZT thin films', in Reich H, ed., *Micro System Technologies 2003*, Berlin, Springer-Verlag, pp. 529–531.

Kanno I, Kunisawa T, Suzuki T, and Kotera H (2007), 'Development of deformable mirror composed of piezoelectric thin films for adaptive optics', *IEEE J. Selected Topics in Quantum Electronics*, 13, 155.

Keijser M, Dormans G J M, and Larsen P K (1996), 'Synthesis of ferroelectric thin films by organometallic chemical vapor deposition', in de Araujo C P, Scott, J F, and Taylor G W, eds, *Ferroelectric Thin Films: Synthesis and basic properties*, Amsterdam, Gordon and Breach, p. 485.

Kholkin A L, Wütchrich Ch, Taylor D V, and Setter N (1996), 'Interferometric measurements of electric field-induced displacements in piezoelectric thin films', *Rev. Sci. Instrum.*, 67, 1935–1941.

Kitabatake M, Mitsuyu T, and Wasa K (1982), 'Structure and electrical properties of amorphous $PbTiO_3$ thin films sputtered on cooled substrates', *J. Non-Crystalline Solids*, 53, 1–10.

Kusao K, Wasa K, and Hayakawa S (1969), 'Electrical properties of mixed oxide films of PbO and TiO_2', *Jpn. J. Appl. Phys.*, 8, 278.

Lakin K M (1999), 'Thin film resonators and filters', *Proc. 1999 IEEE Ultrason. Symp.*, Lake Tahoe, pp. 895–907.

Ledermann N, Muralt P, Baborowski J, Gentil S, Mukati K, Cantoni M, Seifert A, and Setter N (2003), '{100}-Textured, piezoelectric $Pb(Zrx,Ti1–x)O_3$ thin films for MEMS:integration, deposition and properties', *Sensors and Actuators A*, 105, 162–170.

Lefki K and Dormans J.M (1994), 'Measurement of piezoelectric coefficients of ferroelectric thin films', *J. Appl. Phys.*, 76, 1764–1767.

Li Z, Foster M, Guo D, Zhang H, Bai G R, Baldo P M, and Rehn L E (1994) , 'Growth of high quality single-domain single crystal films of $PbTiO_3$', *Appl. Phys. Lett.*, 65, 1106–1108.

Lobl H P, Klee M, Milsom R, Dekker R, Metzmacher C, Brand W, and Lok P (2001), 'Materials for bulk acoustic wave (BAW) resonators and filters', *J. European Ceramic Society*, 21, 2633–2640.

Maki K, Soyama N, Nagamine K, Mori S, and Ogi K (2001), 'Low-temperature crystallization of sol-gel derived $Pb(Zr_{0.4},Ti_{0.6})O_3$ thin films', *Jpn. J. Appl. Phys.* 40, 5533–5538.

Muralt P, Antifakos J, Cantoni M, Lane R, and Martin F (2005), 'Is there a better material for thin film BAW applications than AlN', *Proc. 2005 IEEE Ultrasonic Symp.*, 1, 315–320.

Nagarajan V, Ganpule C S, Nagaraj B K, Aggarwal S, Alpay S P, Roytburd A L, Williams E D, and Ramesh R (1999), 'Effect of mechanical constraint on the dielectric and piezoelectric behavior of epitaxial $Pb(Mg_{1/3}Nb_{2/3})O_3$(90%)-$PbTiO_3$(10%),' *Appl. Phys. Lett.*, 75, 4183–4185.

Nagarajan V, Alpay S, Ganpule C S, Nagaraj B K, Aggarwal S P, Williams E D, Roytburd A L, and Ramesh R (2000), 'Role of substrate on the dielectric and piezoelectric behavior of epitaxial lead magnesium niobate-lead titanate relaxor thin films', *Appl. Phys. Lett.*, 77, 438–440.

Newnham R E, Skinner D P, and Cross L E (1978), *Mat. Res. Bull.,* 13, 525.

Ouchi H (1976), 'Piezoelectric ceramic mataerials', *National Tech. Rept.*, 22, 720–740.

Ouyang J, Yang S Y, Chen L, Ramesh R, and Roytburd A L (2004), 'Orientation dependence of the converse piezoelectric constants for epitaxial single domain ferroelectric films', *Appl. Phys. Lett.*, 85, 278–280.

Ouyang J, Ramesh R, and Roytburd AL (2005), 'Intrinsic effective piezoelectric coefficient $e_{31,f}$ for ferroelectric thin films', *Appl. Phys. Lett.*, 86, 152901.

Park G-T, Park C-S, Choi J-J, and Kim H-E (2005), 'Orientation control of sol-gel-derived lead titanate film by addition of polyvinylpyrrolidone', *J. Mater. Res.*, 20, 882–888.

Rebeiz G M, Muldavin J B, and Tan G-L (2003), 'MEMS switch library', in Rebeiz G M, ed., *RF MEMS – Theory Design, and Technology*, New York, Wiley, p. 151.

Robert W S, Dimos D, Lockwood S J, and Torres V M (1993), 'Electrical properties of sol-gel PZT thin films for decoupling capacitor application', *Mat. Res. Soc. Symp. Proc.*, 310, 59–64.

Seo S H (2004), PhD Thesis, Kwangju Institute of Science and Technology, p. 109.

Shimizu M, Fujimoto M, Katayama T, Shiosaki T, Nakaya K, Fukagawa M, and Tanikawa E (1993), 'Growth and characterization of ferroelectric $Pb(Zr,Ti)O_3$ thin films by MOCVD using 6 inch single wafer CVD system', *Mater. Res. Soc. Symp. Proc.*, 310, 255–260.

Sigmund P (1969), 'Theory of sputtering. I. Sputtering yield of amorphous and polycrystalline targets', *Phys. Rev.*, 184, 382–416.

Stuart R V and Wehner G K (1964), 'Energy distribution of sputtered Cu atoms', *J. Appl. Phys.*, 35, 1819–1824.

Suzuki T, Kanno I, Loverich J J, Kotera H, and Wasa K (2006), 'Characterization of $Pb(Zr,Ti)O_3$ thin films deposited on stainless steel substrates by RF-magnetron sputtering for MEMS applications', *Sensors and Actuators A*, 125, 382–386.

Takaeshima Y, Shiratsuyu K, Takagi H, and Tomono K (1995), 'Preparation of lead magnesium niobate titanate thinfilms by chemical vapor deposition,' *Jpn. J. Appl. Phys.*, 34 (Part 1), 5083–5085.

Takahashi M, Tsubouchi N, and Ohno T (1971), 'Piezoelectric properties of the ternary and quaternary systems containing $PbTiO_3$–$PbZrO_3$', *IEC Report Japan,* CPM71–22, 1–17.

Takayama R and Tomita Y (1989), 'Preparation of epitaxial $Pb(Zr_xTi_{1-x})O_3$ thin films and their crystallographic, pyroelectric, and ferroelectric properties', *J. Appl. Phys.*, 65, 1666–1670.

Tantigate C, Lee J, and Safari A (1995), 'Processing and properties of Pb $(Mg_{1/3}Nb_{2/3})$ O_3–$PbTiO_3$ thin films by pulsed laser deposition', *Appl. Phys. Lett.*, 66, 1611–1613.

Terada K, Suzuki T, Kanno I, and Kotera H (2007), 'Fabrication of single crystal PZT thin films on glass substrates', *Vacuum*, 81, 571–578.

Timp G, ed. (1999), *Nanotechnology*, New York, Spring-Verlag.

Trolier-McKinstry and Muralt P (2004), 'Thin film piezoelectric for MEMS', *J. Electroceramics,* 12, 7–17.

Uchino K (1998), 'High electromechanical coupling piezoelectrics: relaxor and normal ferroelectric solid solutions', *Solid State Ionics*, 108, 43–52.

Uchino K (2000), *Ferroelectric Devices*, New York, Marcel Dekker, p. 78.

Vossen J. L and Kern W, eds (1991), *Thin Film Processes II*, San Diego, CA, Academic Press.

Wakiya N, Shiihara J, Shinozaki K, and Mizutani N (1999), 'Raman spectroscopic determination of pyrochlore-type compound on the synthesis and decomposition of sol-gel-derived $Pb(Mg_{1/3}Nb_{2/3})O_3$ (PMN)', *J. Sold State Chem.*, 142, 344–348.

Wasa K (1995), 'Materials engineering for a better global environment', *Bull. Mater. Sci.*, India, 18, 937–953.

Wasa K and Hayakawa S (1969), 'Low pressure sputtering system of the magnetron type', *Rev. Sci. Instr.*, 40, 693–697.

Wasa K and Hayakawa S (1977), 'Some features of magnetron sputtering', *Thin Solid Films*, 52, 31–43.

Wasa K and Hayakawa S (1992), *Handbook of Sputter Deposition Technology*, New York, Noyes, pp. 193–226.

Wasa K, Adachi H, and Kitabatake M (2004a), *Thin Film Materials Technology*, New York, William Andrew, and Heidelberg, Springer.

Wasa K, Kanno I, Suzuki T, Seo S H, Noh D Y, Okino H, and Yamamoto T (2004b), 'Structure and ferroelectric properties of sputtered PMNT thin films,' *Proc. 2004 IEEE UFFC 50th Anniversary Joint Conf.* (Montreal, 2004), FE1A–5.

Wasa K, Nakamura K, Matsunaga T, Kanno I, Suzuki T, Okino H, Yamamoto T, Seo S H, and Noh D Y (2006), 'Electromechanical coupling factors of single-domain 0.67Pb $(Mg_{1/3}Nb_{2/3})_3$–0.33$PbTiO_3$ single-crystal thin films', *Appl. Phys. Lett.*, 88, 122903.

Wasa K, Kanno I, Kotera H, Yamauchi N, and Matsushima T (2008), 'Thin films of PZT-based ternary perovskite compounds for MEMS', *Proc. 2008 IEEE International Ultrasonics Symp.* (Beijing, 2008), pp. 213–216.

Xiong S, Kawada H, Yamanaka H, and Matsushima T (2008), 'Piezoelectric properties of PZT films prepared by the sol-gel method and their application in MEMS', *Thin Solid Films*, 516, 5309–5312.

Yamamoto T, Nishida K, Nakamura K, Matsunaga S, Motomura T, Funakubo H, and Iijima T (2007), 'Electric-field-induced displacements in ferroelectric films investigated by finite element method (FEM)', *Proc. 113th US–Japan Seminar, Awaji 2007*, pp. 276–279.

Yamauchi N, Shirai T, Matsushima T, Matsunaga T, Wasa K, Kanno I, and Kotera H (2009), 'High coupling piezoelectric thin films of PZT-based ternary perovskite compounds for GHz FBAR', *Appl. Phys. Lett.*, 94, 172903.

Zahn J D (2007), 'Micropump applications in bio-MEMS', Wang W and Soper S A, eds, in *Bio-MEMS-Technologies and Applications,* Boca Raton, FL, CRC Press, p. 151.

Zhang R and Cao W (2004), 'Transformed material coefficients for single domain $0.67Pb(Mg_{1/3}Nb_{2/3})$–$0.33PbTiO_3$ single crystal under differently defined coordinate system', *Appl. Phys. Lett.*, 85, 6380–6382.

Zhang T, Wasa K, Kanno I, and Zhang S-Y (2008), 'Ferroelectric properties of $Pb(Mn_{1/3}Nb_{2/3})O_3$–$Pb(Zr,Ti)O_3$ thin films epitaxially grown on (001)MgO substrates', *J. Vac. Sci. Technol.,* A26(4), 985–990.

Zhang T, Wasa K, Zhang S-Y, Chen Z J, Zhou F, Zhang Z, and Yang Y (2009), 'High piezoelectricity of $Pb(Zr,Ti)O_3$-based ternary compound thin films on silicon substrates', *Appl. Phys. Lett.*, 94, 122909.

Zhang Y, Wang Z, Cheeke J D N, and Hickernell F S (1999), 'Direct characterization of ZnO films in composite resonators by the resonance spectrum method', *Proc. 1999 IEEE Ultrasonic Symp.*, 991–994.

14
Aerosol techniques for manufacturing piezoelectric materials

J. AKEDO, National Institute of Advanced Industrial
Science and Technology, Japan

Abstract: Aerosol deposition (AD) is a unique approach for depositing ceramic films, where submicron ceramics particles (both oxide and non-oxide) are accelerated by gas flow up to 100–500 m/s and then impacted on a substrate. It can rapidly form a thick, dense, uniform and hard ceramic layer at room temperature without additional heating for solidifying ceramic powders, even in low vacuums, using relatively cheap and simple production facilities. It is expected to reduce energy and costs, ease the fabrication of thin or thick film with complicated material compositions, and reduce the number of processes during fabrication of electronic devices, as well as to improve substantially their performance. This technique is particularly useful for fabricating piezoelectric thick films and producing micro-actuator devices. This chapter deals with the mechanism and features of the AD process first, followed by its application for piezoelectric materials and devices.

Key words: aerosol deposition, RTIC, consolidation, ceramic powder, piezoelectric, ferroelectric, MEMS, actuator, optical scanner, ultrasonic motor.

14.1 Introduction

Manufacturing ceramics usually requires sintering at temperatures higher than 1000 °C, which makes it difficult to compound or integrate ceramics with low-melting point, metals, glass, or plastics. This is a major problem for upgrading electro-ceramic components and optical components. For example, an effective and reliable technology is required to fabricate micro-actuators made of piezoelectric thick films for optical scanners, micro-motors, [1, 2] scanning force microscopy, [3] micro-pumps, ultrasonic mixers [4, 5] and micro manipulators for medical applications in micro-electromechanical systems (MEMS). Improvements in manufacturing process will be very important in the near future to produce ink-jet printer heads that will reduce printing time, and to produce flapper-actuators that will control the high speed positioning of recording heads for high-density storage drives. [6] For these applications, piezoelectric or electrostrictive materials with large strain and high-speed response often require dense and thick micro-patterned films with thickness exceeding 1 μm in many cases. [2,7,8] However, thick layers prepared by conventional thin or thick film methods usually exhibit cracks and may easily be peeled from the substrates. With these methods it is also difficult to produce complicated material compositions, or fabrication can be time-consuming and costly in actual mass production.

Figure 14.1 summarizes the conventional methods used to fabricate PZT films on substrates and the applications of these films. There are many reports on the fabrication of lead-zirconate-titanate ($Pb(Zr_{0.52},Ti_{0.48})O_3$)(PZT) films of thicknesses ranging from 0.08 μm to 5 μm by sol-gel, [9,10] sputtering, [11, 12] metal organic chemical vapor deposition (MO-CVD), [13] pulse laser ablation, [14] electron beam evaporation [15] and ion-beam deposition. [16] In these methods, dense PZT film can be formed and oriented on a Pt/Ti/SiO_2/Si substrate. However, fabrication of PZT films with a thickness of over 1–3 μm with these methods requires much care because there are many problems to overcome in terms of film quality or deposition. Hydrothermal synthesis [17, 18] has the advantage of a low process temperature at 150 °C and the poling procedure is not required. However, the surface roughness and the density of the films are poor. PZT thick films fabricated by the screen-printing method [19, 20] have a low density and PZT/Pt/Si structures can be damaged because of the long firing time at temperatures higher than 800 °C. An improved screen-printing method with a low-temperature sintering and a high-resistance electrode has been reported, [21] but the piezoelectric properties of films produced by this method were not reported. For sputtered and sol-gel-derived PZT thin films, a post deposition rapid thermal annealing treatment [22] was introduced to reduce the damage to the substrate or structure, and to improve the electrical properties. However, for thick films, with a thickness over 1 μm, this process was not so effective. The etching

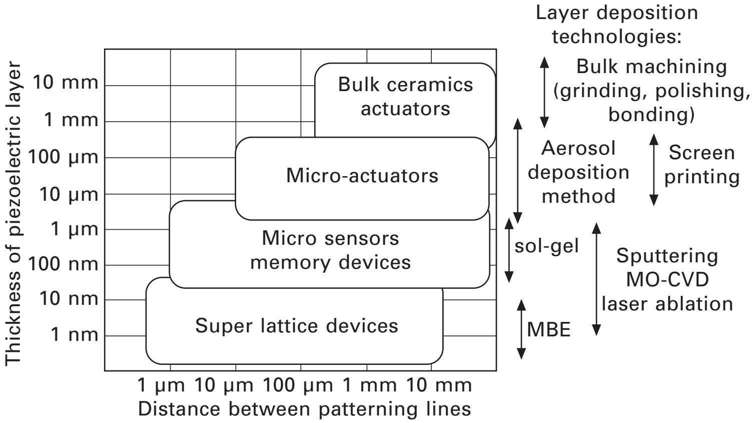
Layer deposition technologies:
Bulk machining (grinding, polishing, bonding)
Aerosol deposition method
Screen printing
sol-gel
Sputtering MO-CVD laser ablation
MBE
Thickness of piezoelectric layer
10 mm
1 mm
100 μm
10 μm
1 μm
100 nm
10 nm
1 nm
Bulk ceramics actuators
Micro-actuators
Micro sensors memory devices
Super lattice devices
1 μm 10 μm 100 μm 1 mm 10 mm
Distance between patterning lines

14.1 Fabrication method for PZT layer in various thickness ranges.

of thick ceramic films by plasma etching, [23] inductively coupling plasma etching, [24, 25] or reactive ion etching [26] is also difficult. For bulk PZT adhered to a Si membrane, it is difficult to ensure an adequate mechanical and electrical coupling between the films and to assemble complex structure. Thus, it can be concluded that, by conventional methods, fine patterning of thick (over 1 μm) PZT films on Si-based substrates is still difficult to realize.

To reduce costs and fabrication time and to avoid damage to circuitry already present on the substrate, it is very important to have a high-speed deposition rate, low process temperature, and fine patterning. Until now, a number of studies have been aimed at reducing the sintering temperature for the purpose of reducing energy consumption, and implementing innovative functional components through the integration with metal or glass materials. Several deposition methods based on the principle of particle collisions have already been investigated. Recently, cold spraying method (CSM) for metal materials has attracted much attention. However, for ceramic materials this method is not successful.

For these reasons, a new deposition technique based on collision adhesion of fine particles for fabrication and micro-patterning of thick ceramic layers has been developed, named the aerosol deposition (AD) method. AD [27–31] is a novel and very attractive coating method for ceramic integration. Submicrometer ceramic powder is mixed with a carrier gas to form an aerosol flow, ejected through a micro-orifice nozzle and deposited onto a substrate in the deposition chamber kept under vacuum during the deposition. Special attention is paid to the character of primary powder particles and the deposition conditions. Using this method, ceramic layers of $Pb(Zr,Ti)O_3$, α-Al_2O_3, Y_2O_3, YSZ, AlN, MgB_2 and other ceramic materials with nanocrystalline structure, high transparency, high hardness, and high breakdown voltage were formed at room temperature. It is suggested that during impact of the fine particles with the substrate, part of the particle's kinetic energy is converted into bonding energy between the substrate and the fine particles and between the fine particles themselves. In fabrication of thick films with thickness range of 1–100 μm, AD has many advantages in comparison with conventional thin or thick film methods.

14.2 Aerosol deposition process

The AD method is based on shock-loading solidification due to the impact of ultrafine ceramic particles with a surface. [27, 28] First, particles are mixed with a gas to generate an aerosol. This aerosol is ejected through a nozzle at low pressure and impacted onto a substrate to form a thin/thick film. During the impact with the substrate, part of the particle's kinetic energy is converted into thermal energy causing increase in temperature at the point-of-impact and promoting bonding between the substrate and the particles and also between multiple particles. However, the detailed mechanism occurring during the particle impingement with a surface in the AD process has not yet been fully clarified.

Figure 14.2 shows the deposition apparatus and Table 14.1 gives the deposition conditions for the AD process. The AD apparatus consists of two vacuum chambers connected by a tube. The first chamber is an aerosol-generation chamber and the second chamber is a deposition chamber. The deposition chamber is used for the formation and patterning of films. The aerosol-generation chamber has a carrier gas system and a vibration system to mix the powder with the carrier gas. The aerosol generated in this chamber is delivered to the deposition chamber by a pressure difference between the two chambers. The deposition chamber contains a nozzle, a substrate

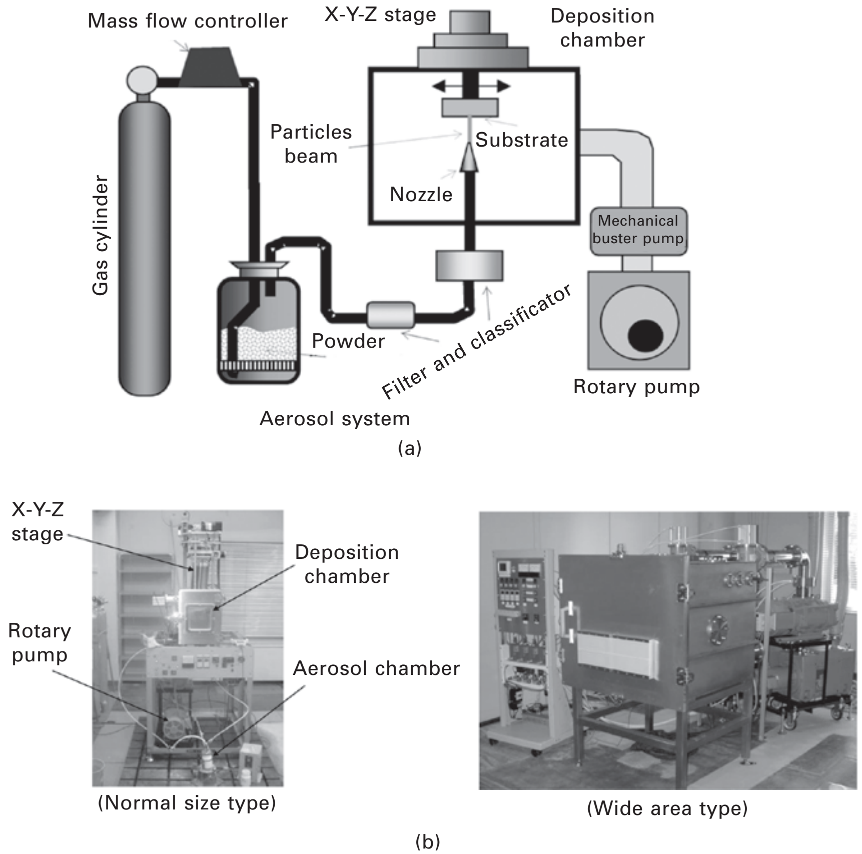
Mass flow controller
X-Y-Z stage
Deposition chamber
Particles beam
Substrate
Nozzle
Gas cylinder
Mechanical buster pump
Powder
Filter and classificator
Rotary pump
Aerosol system
(a)
X-Y-Z stage
Deposition chamber
Rotary pump
Aerosol chamber
(b)

(Normal size type)

(Wide area type)

14.2 Schematic (a) and prototype photograph (b) of aerosol deposition (AD) apparatus.

Table 14.1 Typical deposition conditions (experimental parameters)

Pressure in deposition chamber	0.05 ~ 2 kPa
Pressure in aerosol chamber	10 ~ 80 kPa
Size of nozzle orifice	5×0.3 mm^2 ; 10×0.4 mm^2
Accelerating gas	He, N_2, air,
Consumption of accelerating gas	1 ~ 10 l/min
Maintained substrate temperature during deposition	300 K
Scanning area (area of deposition)	40×40 mm^2, 400×400 mm^2
Scanning speed of the nozzle motion along substrate	0.125 ~ 10 mm/sec
Distance between the nozzle and substrate	1 mm ~ 40 mm

holder with a heating system, and a mask alignment system used for making patterned films. A rotary vacuum pump coupled to a mechanical booster pump is used to vacuum this chamber to a pressure of about 50–2000 Pa during deposition. Figure 14.2(b) shows various size deposition machines.

Sintered ceramic powders with a particle size range of about 0.08–2 μm are typically used as the deposition particles. After suspension in the carrier gas to form an aerosol, the aerosol is accelerated to several hundred m/sec through a rectangular orifice with width less than 1 mm. Not all the aerosol particles are deposited onto the substrate. The ratio of deposited to non-deposited particles strongly depends on particle size and the degree of aggregation of the particles. To form films with an acceptable density and material properties, particles with a particular size and morphology must be used. To generate a jet of particles with acceptable size and morphology, a de-agglomeration device and a filter are used between the aerosol-generation and deposition chamber to break the particles apart as much as possible and to select particles in a prescribed size range.

14.3 Room temperature impact consolidation (RTIC)

14.3.1 Consolidation of ceramic powders at room temperature

For the AD process, the high-speed film formation of ceramic films at room temperature with a high density and a high transparency is possible by optimizing the particle diameter and deposition conditions. The result is a process that yields an acceptable consolidation at room temperature without the need for a thermal treatment. This process is called room temperature impact consolidation (RTIC).[28,29,32]

Figures 14.3 and 14.4 show micrographs of typical RTIC ceramic layers, a cross-sectional scanning electron microscope (SEM) image of an as-deposited α-Al_2O_3 layer at room temperature, comparison of its XRD

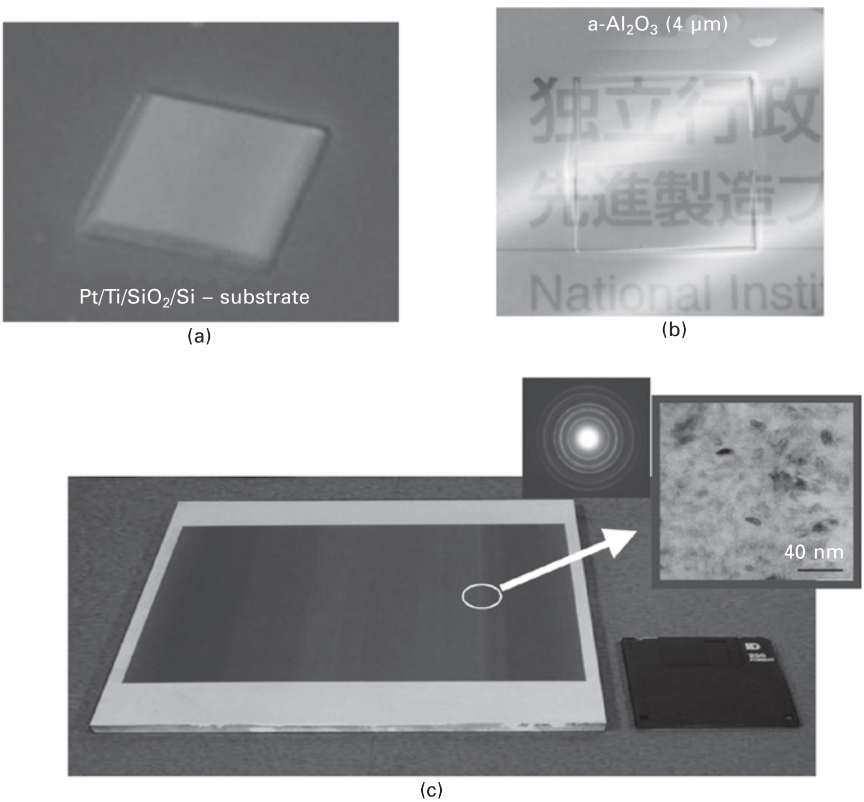

14.3 Photograph of AD-ceramic layer deposited at room temperature using RTIC phenomenon: (a) thick ceramic layer: over 500 mm, (b) transparent ceramic layer: 99% @ 400–900 nm, (c) wide area coating: 200 x 200 mm^2.

profile with the profiles obtained for the raw powder and bulk material, and transmission electron microscope (TEM) images of as-deposited layer and starting powder. The formation of thick films with a thickness over 100 μm having high transparency was confirmed, as shown in Fig. 14.3(a) and (b). Using a multi-nozzle system, the coating area could be enlarged as shown in Fig. 14.3(c). The aerosol deposited films showed a relatively good thickness uniformity of 1.4%. The surface roughness (R_a) was less than 100 nm. The deposited film has a high density and randomly oriented polycrystalline nanostructure with crystal grains smaller than 20 nm in length. TEM and electron diffraction imaging did not show either amorphous layers or hetero-structures at the boundary of the crystal grains. XRD profiles confirmed that the spectral phases of the α-Al$_2$O$_3$ particles were retained in the deposited layer. However, a broadening of the spectral peaks and a slight shift in peak angle positions were observed. The reason for the change between the spectra

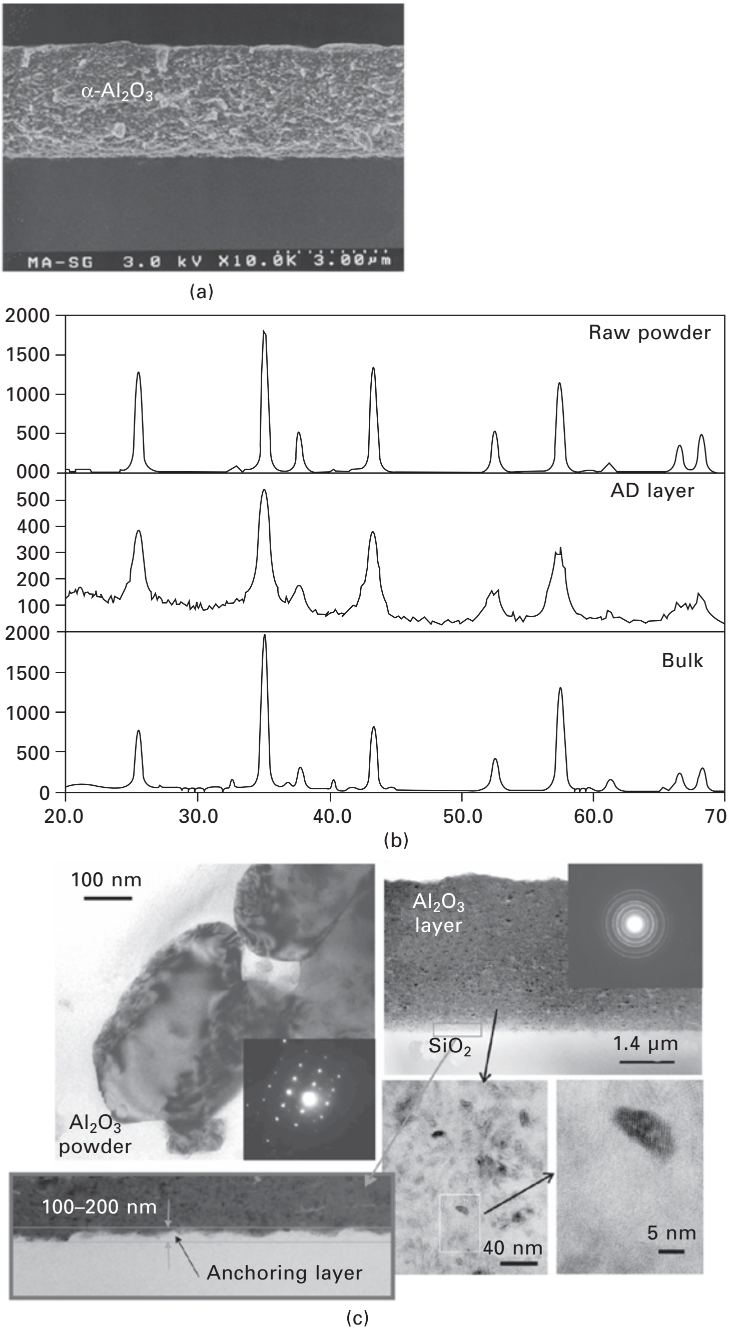

14.4 Microstructure of α-Al_2O_3 layer deposited at room temperature by AD method: (a) cross-sectional SEM image of as-deposited layer at room temperature; (b) comparison of XRD profiles; (c) TEM images of starting powder and as-deposited layer at room temperature.

of the raw particles and the deposited layer is the reduction of the film crystal size and/or the distortion during deposition. Clear lattice images in crystal grains less than 10 nm were observed, as well as uniform microstructures at the boundary between the substrate and the deposited layer. For α-Al_2O_3 layers deposited at room temperature, the film density was over 95% of the theoretical density and Vickers hardness was 1600 HV. [27] Such α-Al_2O_3 layers are acceptable for use as abrasion-resistant coatings. [30] The crystal grain size of the as-deposited films was smaller than that of the starting particles because the starting particles break down during collisions.

Table 14.2 shows the relationship between micro-Vickers hardness, the crystallite size and particle impact velocity in various AD deposited materials. The layer hardness increased with increasing particle-impact velocity, and sometimes was higher than that of the bulk material, which was sintered at a high temperature. Critical particle velocities for an acceptable RTIC ranged from 150–500 m/sec, and the velocity needed to create films with acceptable hardness tended to increase with increasing sintering temperature for a particular ceramic material.

Although distortions were included inside the films, a rise of the substrate temperature due to particle collisions was not observed. Consolidation of ceramic powders was possible at room temperature without the use of binders. Even if the formation of thin films using RTIC does not require sintering, it produces high-density films. Acceptable room-temperature deposition was observed not only for oxide materials such as α-Al_2O_3, lead zirconate titanate (PZT : $Pb(Zr_{52},Ti_{48})O_3$) and Ni–Zn–Fe_3O_4, but also for non-oxide materials such as AlN and MgB_2. In either case, particles with diameter greater than 80 nm are needed to make films having an acceptable hardness.

Table 14.2 Mechanical properties of AD deposited layers

Material	Hardness (Hv)		Average crystallite size of the layer (nm)	Particle velocity at the collision (m/sec)
	Layer (deposited at room temperature)	Bulk*		
Oxide				
Al_2O_3	1200 ~ 2100	1900±100	13 ~ 20	150 500
PZT	400 ~ 550	350±50	10 ~ 30	100 300
$(Ni,Zn)Fe_2O_3$	700 ~ 750	1040±80	5 ~ 20	250 600
Non-oxide				
AlN	1100 ~ 1470	1180±90	5 ~ 15	200 600
MgB_2	700		5 ~ 20	300 550

* Bulk samples were prepared from the same starting powder as layers, by conventional sintering procedure (at temperature over 1200 °C)

14.3.2 Impact particle velocity and local temperature increase during AD process

The particle's velocity during the AD process was measured by a time-of-flight method, in which some part of the particle's flow was mechanically cut from the total flow and deposited onto a moving substrate. The deflection of the deposited pattern from the center axis, the geometrical dimensions and the moving substrate speed provide data to determine the particle flow velocity. [31] The merit of this method is that the impact particle velocity is measured directly. This is a more accurate method than the conventional measurement using a high-speed camera that can only estimate particle flow velocity. Figure 14.5 shows the relationship between the impact particle velocity and gas consumption in controlling the particle velocity. The particle impact velocities were estimated as varying from 150 to 500 m/s. The critical velocity for RTIC of α-Al_2O_3 was 150 m/s. This implies a very small kinetic energy compared to that obtained in the conventional shock compaction process. Using the values measured for particle impact velocity, the local rise in temperature and the shock pressure at the point of impact between the particle and the substrate were simulated by finite element method (FEM) computational simulations using AUTODYNs-2D (CRC Solutions Co., Tokyo, Japan) with Johnson–Holmquist material model. [29,33,34] In the simulation, the particle diameter was set to 0.3 μm, which was the same as the average diameter of the starting α-Al_2O_3 powder. Bulk material constants of α-Al_2O_3 [35] were used for these simulations. The

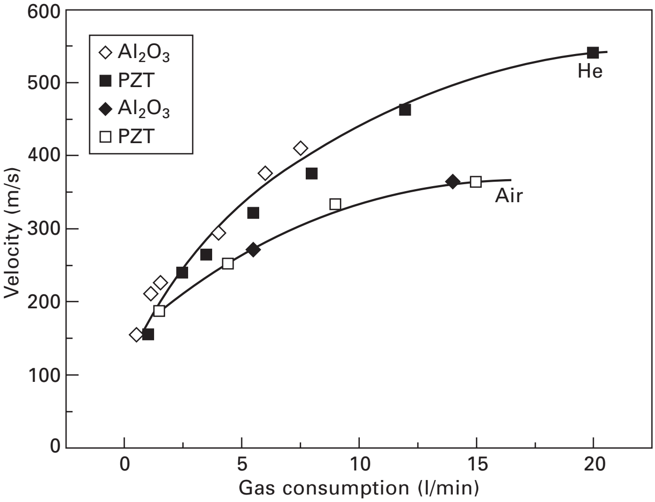

14.5 Relationship between impact particle velocity and gas consumption to control the particle velocity for different gases (nozzle of 10 × 0.4 mm^2).

maximum local temperature rise and the shock pressure at the point of impact during layer formation do not exceed 500 °C and 2.5 GPa, as shown in Figs 14.6(a) and (b). This local increase in temperature is too small to induce any ceramic sintering. Consolidation features of ceramic material fabricated using the AD process are fundamentally similar to those in the case of the shock compaction method. However, the local rise in temperature and the compact pressure for brittle materials such as ceramics and glasses were less than those of over 1000 °C and 10 GPa that are typical for conventional shock wave synthesis. [36, 37]

14.3.3 Densification mechanism of ceramic layers in AD process

From the simulation and experimental results, it may be concluded that particle partial or total melting does not occur during collision. Then, how can the reduction of the crystallite size for the starting particle and the production of dense structures during deposition be explained? There are two possible explanations:

- first, only small particles less than 20 nm in the jet flow will actually take part at the deposition to form the layer, and/or
- second, fracture and deformation of starting particles are obtained during the impact with the substrate to fill up the gaps between the deposited particles.

In order to clarify this, a mixed aerosol of α-Al_2O_3 and PZT powders was deposited to form a composite layer. The cross-section of this layer was observed by HR-TEM to investigate the densification and bonding mechanism of ceramic particles. Figure 14.7(a) and (b) shows TEM images of the

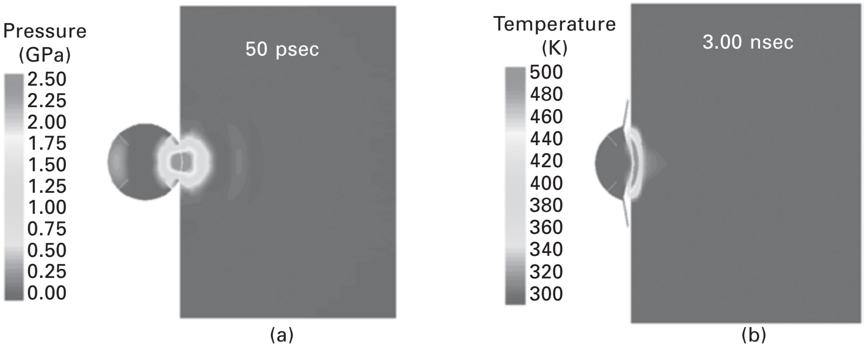

14.6 FEM simulation of the local rise in temperature and shock pressure during impact of particle with the substrate for AD deposition. Impact particle velocity was 300 m/sec [29].

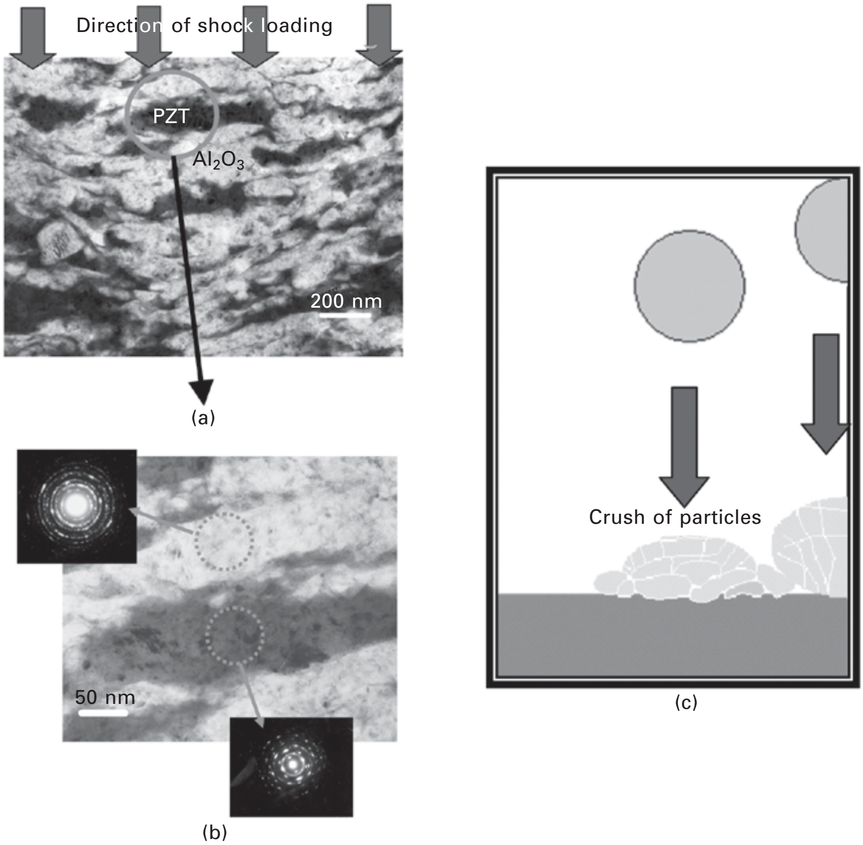

14.7 TEM image α-Al_2O_3/PZT composite layer and densification mechanism: (a) cross-sectional TEM image; (b) zoom-up image; (c) densification image [29].

α-Al_2O_3/PZT composite layers. Selected area diffraction (SAD) for both starting particles indicates that these particles have a single crystal structure. Black and white regions indicate PZT and α-Al_2O_3, respectively, because lead elements are much heavier than aluminum elements and the electron absorption for each element depends on their mass. A laminar structure along the substrate plane was only observed in the cross-section TEM image. Inside black and white regions, electron diffraction patterns with an 80 nm electron beam irradiating diameter indicate a typical net-pattern image, as shown in Fig. 14.7(b), and randomly oriented small crystallites less than 20 nm were observed in a zoom-up image. These crystallites were almost the same in size as those in the as-deposited α-Al_2O_3 films (shown in Fig. 14.4(c)). The volume of the black part, assuming an oval shape, was close to that of starting particles of PZT. The fracture toughness of the α-Al_2O_3

starting particle was estimated as 3–6.5 GPa by the special nano-indentation system. [38] This value was close to the value obtained for maximum impact pressure in the simulation meaning that the α-Al_2O_3 starting particle is most likely to be fractured during impaction. From these results, it was concluded that the dense structure occurs due to the reduction of crystallite size by fracture or plastic deformation at room temperature during the AD process. This explanation for densification of ceramic particles during the AD process is different from that of conventional shock compaction. The plastic deformation of ceramic particles at room temperature can be assumed not only for α-Al_2O_3 case and may be a general phenomenon because AD layers for a large variety of ceramic material could be easily formed.

By comparison, the cold spray method [39],[40] for metal coating requires particle velocities over 500 m/sec to fabricate high-density layers, being much higher than the ones required for the AD process. Also, melting points of ceramic materials are higher than those of metal materials, and ceramics are more difficult to deform. Therefore, the bonding mechanism in the case of AD cannot be explained as for the case of CSM. To date, the bonding mechanism between the fine particles themselves and between the substrate and the fine particles has not been clarified. There are still some questions to be answered regarding the AD process. Does the generation of a clean and active layer of starting particles make the particle bonding at a low temperature possible? Is some kind of chemical reaction induced during impaction? To answer these questions further studies are needed on the bonding mechanism of ceramic particles during the AD deposition.

14.4 Deposition properties and film patterning

14.4.1 Deposition ratio and influence of starting powder properties

High deposition rates can be achieved easily with AD because the source material is already in particle state form. These deposition rates are at least 30 times higher than other conventional thin film formation methods. Therefore, AD is an attractive manufacturing process due to high throughput. The particle velocity and concentration in the aerosol jet at the nozzle increase with increasing carrier gas flow rate, resulting in increased deposition efficiency. Starting particle properties, such as the average particle size and the size distribution, mechanical and surface properties can also strongly affect the deposition efficiency. [41]

The deposition rates for PZT AD layers using powders subjected to various milling procedures are indicated in Fig. 14.8. It can be seen that, by increasing the milling time, the deposition rate of the PZT layer significantly increased and reached a maximum of 73 μm/min for a 5 mm^2 deposition

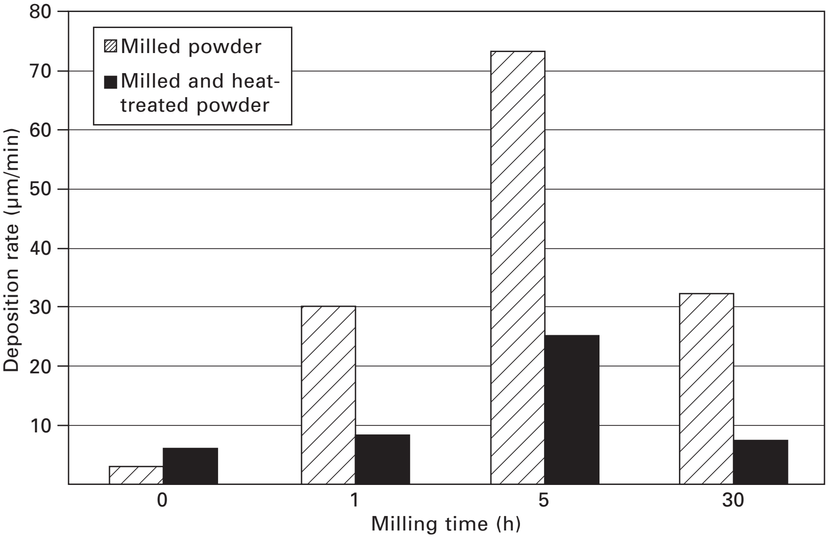

14.8 Deposition rate for PZT film formation at room temperature using powder milled for different duration times with (black bar) / without (hatched bar) heat-treatment procedure at 800 °C for 4 h in air [41].

area when powder was milled for 5 h. This value is 30 times higher than that for a starting powder without the milling procedure. An interesting fact is that the deposition rate decreased as a result of further milling to 30 h. It is assumed that particle surface properties (for example, surface activation, defects, gas absorption) will change by longtime milling making them less probable to be deposited in the same conditions.

The milling procedure is also strongly influenced by the film density. The cross-sectional SEM images of the deposited layers vs. the milling time are shown in Fig. 14.9. With the increase of powder milling time, density and hardness of the deposited layer decreased. On the other hand, for 5 h and 30 h milling procedures, grain images of starting powders with the diameters from 100 to 300 nm and porous structures were distinct in the deposited layer images. At the same time, color and transmittance of layers were markedly changed from yellow to white due to the increase of optical scattering. [41] Thus the milling procedure is applicable to control the porosity of ceramic layers deposited by the AD process.

The starting powder particle size and shape strongly influence the RTIC phenomenon in the AD process. If spherical α-Al_2O_3 ultra-fine particles with average particle size around 50 nm were used, after AD deposition the films have a pressed-like structure and the RTIC phenomenon could not be observed even if the ejecting particle velocity from the nozzle was over

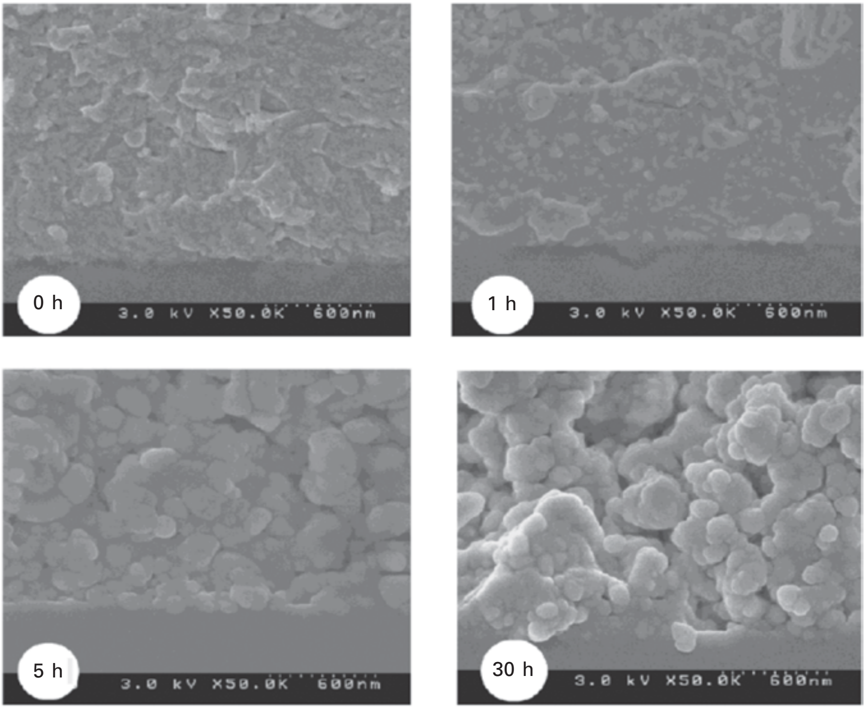

14.9 SEM images of PZT films deposited on glass substrates at room temperature using powders milled for different duration times [41].

400 m/sec and particle size was very small (Fig. 14.10(a)). In contrast, if non-spherical α-Al_2O_3 fine powder with average particle size around 1 µm was used, the deposited particles on the substrate were consolidated at room temperature and RTIC phenomenon was observed even for particle velocities around 200 m/sec, as shown in Fig. 14.10(b). As a result, high density and transparent ceramic layers were obtained. These results are explained by aerodynamic properties of the particle jet flow near the substrate. If particle size and weight are too small, the particle follows the carrier gas flow as shown schematically in Fig. 14.11. Therefore the particle velocity normal to the substrate is largely decreased and is not high enough to obtain RTIC phenomenon. Detailed further investigation about the particles' aerodynamic properties in the AD process still needs to be conducted.

An advantage of AD over conventional thin film and thermal spray coating methods is that substrate surface does not need pre-cleaning to achieve good deposition. During the initial deposition stage, the particles impacting the substrate will act as cleaning agents in a similar way as in sand-blasting processes. Surface contaminants such as dirt and oils are removed by the initial particle collisions. The deposition automatically begins when the surface

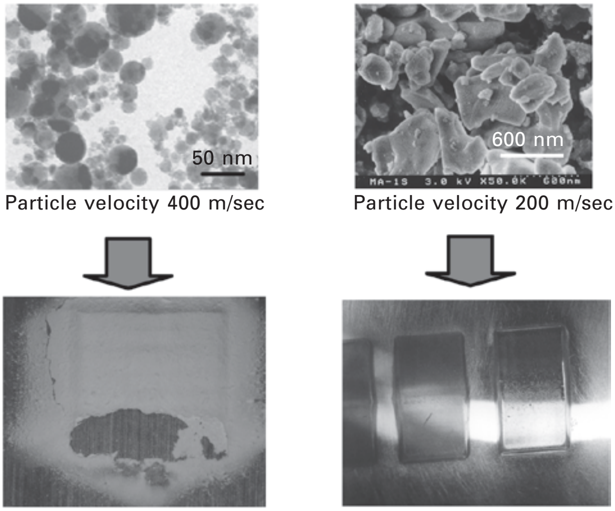
50 nm
600 nm
Particle velocity 400 m/sec
Particle velocity 200 m/sec

Pressed compact
(a)

(Consolidation in ADM)
(b)

14.10 Influence of starting particle diameter for RTIC phenomenon on AD method: (a) average diameter: 50 nm, (b) average diameter: 700 nm.

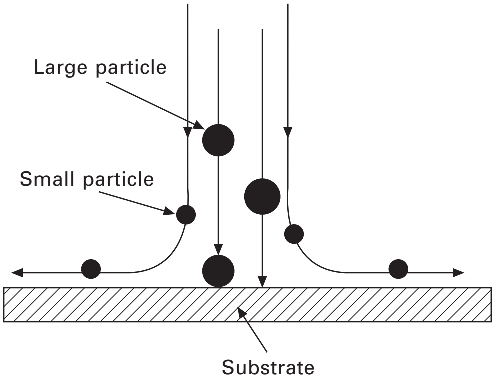
Large particle
Small particle
Substrate

14.11 Particles' trajectories in an aerosol jet flow near substrate in AD method.

becomes sufficiently clean. The film adhesive strength to glass and metal substrates may be in excess of 30 MPa, because an anchoring layer having a thickness of about 100–200 nm was formed in the interface between the substrate and the deposited layer. To obtain maximum adhesive strength, a substrate with suitable hardness and elasticity is needed to allow the formation of the anchoring layer. A substrate that is very soft will be etched by the particle jet flow and the deposition will not occur. On the other hand, when a substrate with large hardness value is used, the adhesion strength between the deposited layer and substrate is weak and the film may easily peel off.

14.4.2 Patterning properties of ceramic film

Ceramic film patterning can be achieved by using a mask deposition method, in which a particle jet is impacted onto the substrate through a defined pattern mask that contains openings with width of at least 50 μm. In this case, it is important to consider the aerosol jet flow in the deposition chamber and through the mask orifices. If the pressure in the deposition chamber is not sufficiently low, the particle jet is scattered by the edge of the openings in the mask and the resulting mask pattern is not preserved on the substrate.

The effect of the ceramic particles sprayed onto a substrate changes from deposition to erosion, [42] as shown in Fig. 14.12, depending on the particle diameter, velocity, and angle of incidence, β, of the particle jet to the substrate. In the figure, β_c is the angle of incidence when deposition rate and abrasion rate have the same value, and the normalized thickness is the thickness of the PZT layer after AD deposition relative to the initial value of PZT thickness. These factors also influence the layer density and surface roughness. However, to achieve acceptable patterns through a mask with acceptable detail the angle of incidence of the particle jet must be kept within a specified range. This is because the angle of incidence affects the flow patterns on the downstream side of the mask, which in turn affects the deposition efficiency and the degree to which the mask profile is distorted. Figure 14.13 shows a thick, patterned PZT layer deposited under optimum deposition conditions onto Si, SUS, and Pt/Si substrates. [43] A ceramic microstructure with a 50 μm line width and aspect ratio (line height/line width) greater than 1 can be patterned by controlling the substrate heating temperature and starting particle properties. The AD process is useful for making piezoelectric films more than 10 μm thick, for applications such as ultrasonic devices. However, pattern widths less than 50 μm were difficult to obtain. Recently, the production of ceramic fine patterns using AD and lift-off was tried. The hardness and thickness of the photo resist layer were chosen carefully. As a result, a minimum pattern width less than 10 μm for a 2 μm thick PZT and α-Al_2O_3 layers were obtained, as shown in Fig. 14.14.[44]

14.5 Electrical properties of aerosol deposition (AD) films and improvements by heat treatment

14.5.1 High breakdown voltage of AD layer

Fundamentally, the above-mentioned coating methods are based on the shock loading consolidation of solid state particles with or without thermal

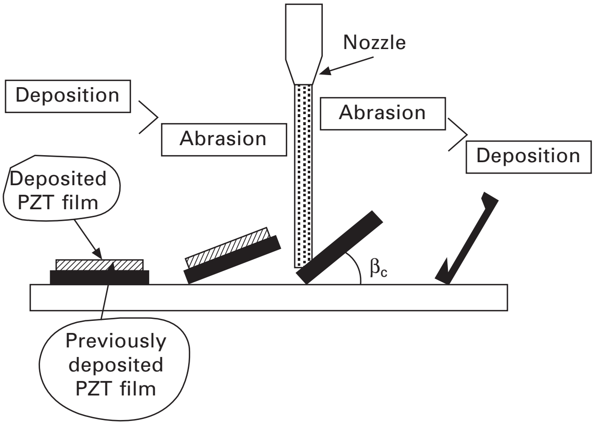
Nozzle
Deposition
Abrasion
Abrasion
Deposition
Deposited PZT film
β_c
Previously deposited PZT film

Experimental set up

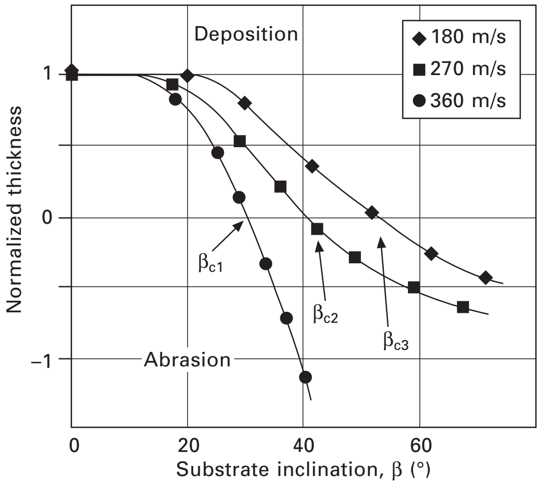

14.12 Incidence angle effect of particle jet flow on deposition properties [43].

or plasma energy assistance. The microstructures of the films produced by these methods are completely different from those of the films made by typical spray coating methods, because the primary powders used are not melted before impact with the substrate and particles are bonded directly in their solid state. The expected features for these methods are a dense film formation at a low temperature and the retaining of the primary material composition and crystal structure. However, there is no report about applications of these methods to electrical and functional materials. It should be mentioned that, if the crystal structure of the ceramic particles is retained

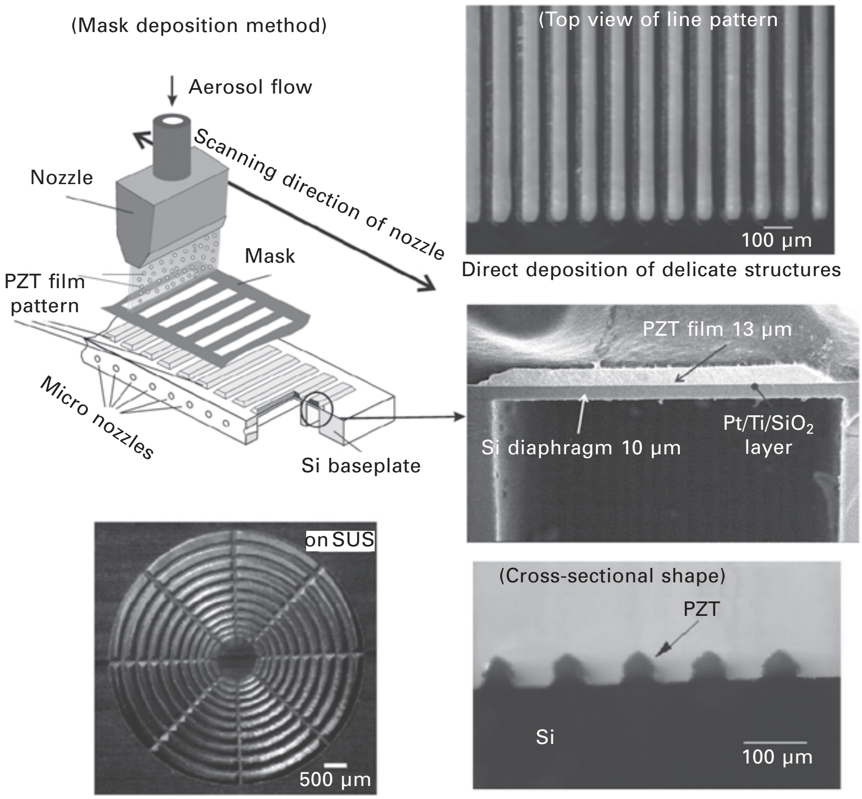
(Mask deposition method)
Aerosol flow
Scanning direction of nozzle
Nozzle
Mask
PZT film pattern
Micro nozzles
Si baseplate
(Top view of line pattern)
100 μm
Direct deposition of delicate structures
PZT film 13 μm
Si diaphragm 10 μm
Pt/Ti/SiO₂ layer
on SUS
500 μm
(Cross-sectional shape)
PZT
Si
100 μm

14.13 Patterning properties of thick ceramic layers on AD method using mask deposition method.

during the deposition, the processes temperature might be decreased and the application of these methods is expected to spread to electro-ceramics materials.

AD layers deposited at room temperature generally have high electrical insulation and electrical breakdown characteristics that exceed that of the bulk material. For example, the electrical breakdown of α-Al_2O_3 and Y_2O_3 exceeded 3 MV/cm and for PZT it was found to exceed 500 kV/cm. [27,45,46] The volume resistivity, the dielectric constant and the dielectric loss of α-Al_2O_3 layer formed by AD were 1.5×10^{15} Ω cm, 9.8 at 1 kHz and 0.2%, respectively. [47] Those values are almost the same as those of the bulk material. Such electrical characteristics can be useful for developing devices such as electrostatic chucks, [48] electrical insulation layers with a good thermal conductivity for high power electric devices.

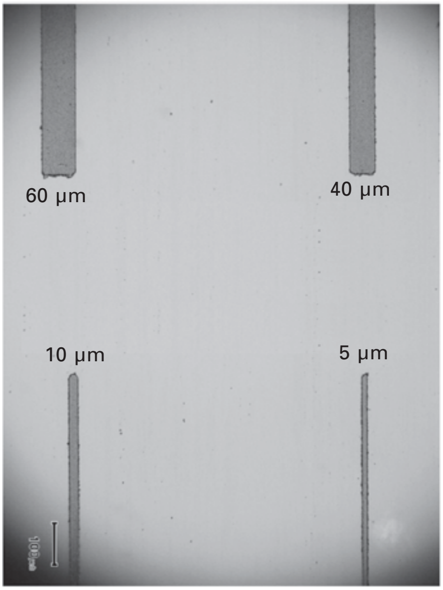

14.14 Fine patterning of ceramic layers deposited by AD method using lift-off process with photo-resist [44].

14.5.2 Annealing effect for electrical properties of AD–PZT layer

PZT layers deposited at room temperature exhibit the polarization switching at high external field over 1 MV/cm as shown in Fig. 14.15(a). The remanent polarization (P_r) and coercive fields (E_c) were 13 µC/cm^2 and 300 kV/cm. These results indicate that as-deposited AD–PZT layers have very high electrical resistance and breakdown voltage by high density structuring, and also have spontaneous polarizations in spite of the structural defects introduced and the reduction of the crystallite size during the AD process. However, their properties are unacceptable for practical applications.

By post-annealing in air at temperatures ranging from 500 to 600 °C for 10 min to 1 h (depending on layer thickness), a grain growth of fine crystals and a defect recovery in AD layers were observed, which dramatically improved the ferroelectric properties. The grain size of AD–PZT layer after annealing was 80–120 nm. Figure 14.15(b) shows the *P–E* hysteresis loop of 5 µm thick PZT thin film annealed at 600 °C for 15 min with a variety of particle impact velocities. The best values of P_r and E_c, 36 µC/cm^2 and 89 kV/cm, respectively, were achieved using He carrier gas for the particle impact velocity of 150 m/s. The breakdown voltage of the 5 µm thick films after annealing was about 600 kV/cm and was more than 1 MV/cm for 2 µm thick PZT thin film. According to conventional understanding of shock

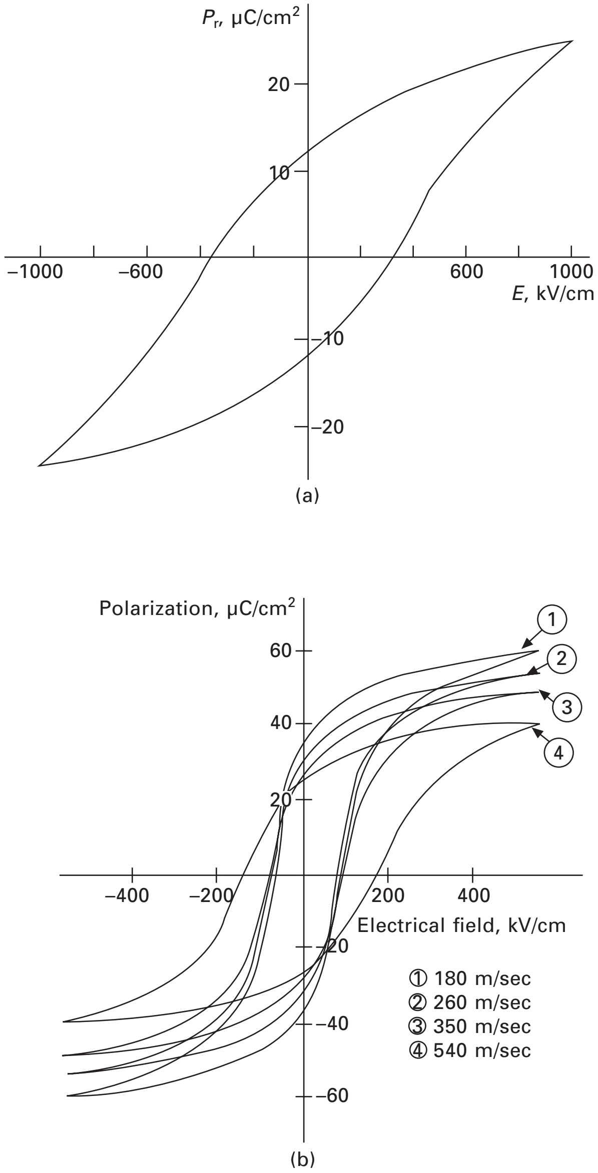

14.15 Hysteresis loops of 5 mm thick PZT films deposited at room temperature (a), and after post annealing at 600 °C (b) with a variety of particle impact velocities [32].

loading consolidation, the defect density and residual strain of as-deposited PZT thin films might be increased by increasing the impact force during the deposition. Even after the annealing procedure that reduced defects, influence of the particle impact velocity remained.[32] The dielectric constant (ε) and the piezoelectric constant (d_{31}) of post-annealed layers formed at 600 °C in Fig. 14.16 were 800–1200 and –100 pm/V, [49] respectively, which are comparable to the values of the specimens obtained with conventional thin-film formation methods. Moreover, the electrical breakdown (< 1 MV/cm) and the Young's modulus (>80 GPa) of the AD films exceeded those obtained with conventional thick film formation technologies. By post-annealing at temperatures up to 850 °C, a remanent polarization (P_r) of 38 μC/cm^2 and a coercive field strengths (E_c) of 30 kV/cm were obtained in the PZT films. [28], [50].

Figure 14.17 shows the changing of the hysteresis loop under application of a 170 kV/cm external electrical field for various pre-process conditions. [41] The thickness of all the PZT layers was 20 μm. All the PZT layers were deposited on stainless steel at room temperature and annealed at 600 °C for 1 h. Only the dry-milling procedure of starting powder induced reduction of ferroelectric properties as shown in Fig. 14.17(a). Remanent polarization (P_r) and coercive field (E_c) of the PZT layer without the milling procedure were 20 μC/cm^2 and 50 kV/cm, respectively, which were the same as those of the previous report. [51, 52] The pre-process for a starting powder with heat treatment significantly improved the ferroelectric properties as shown in Fig. 14.17(b). P_r and E_c of the PZT layer deposited using even a powder with the milling procedure conducted for 5 h, and with the heat treatment procedure were 32 μC/cm^2 and 45 kV/cm, respectively.

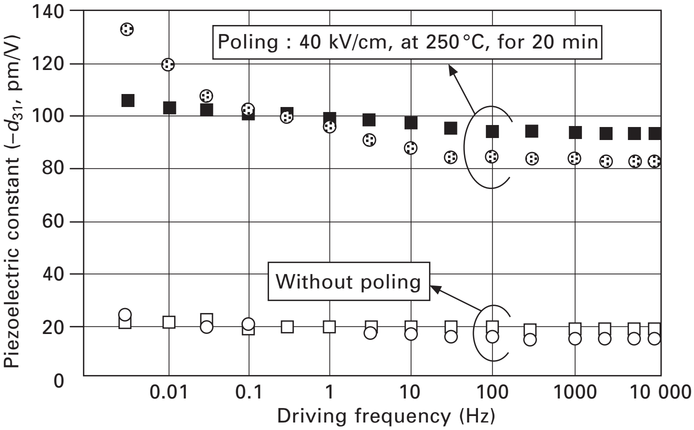

14.16 Frequency dependence of the piezoelectric coefficient (-d_{31}) of the unimorph cantilever sample. □, PZT on the Si cantilever; ○, PZT on stainless steel. Applied electrical field was 40 kV/cm. The resonance frequency of the sample was 80 kHz [49].

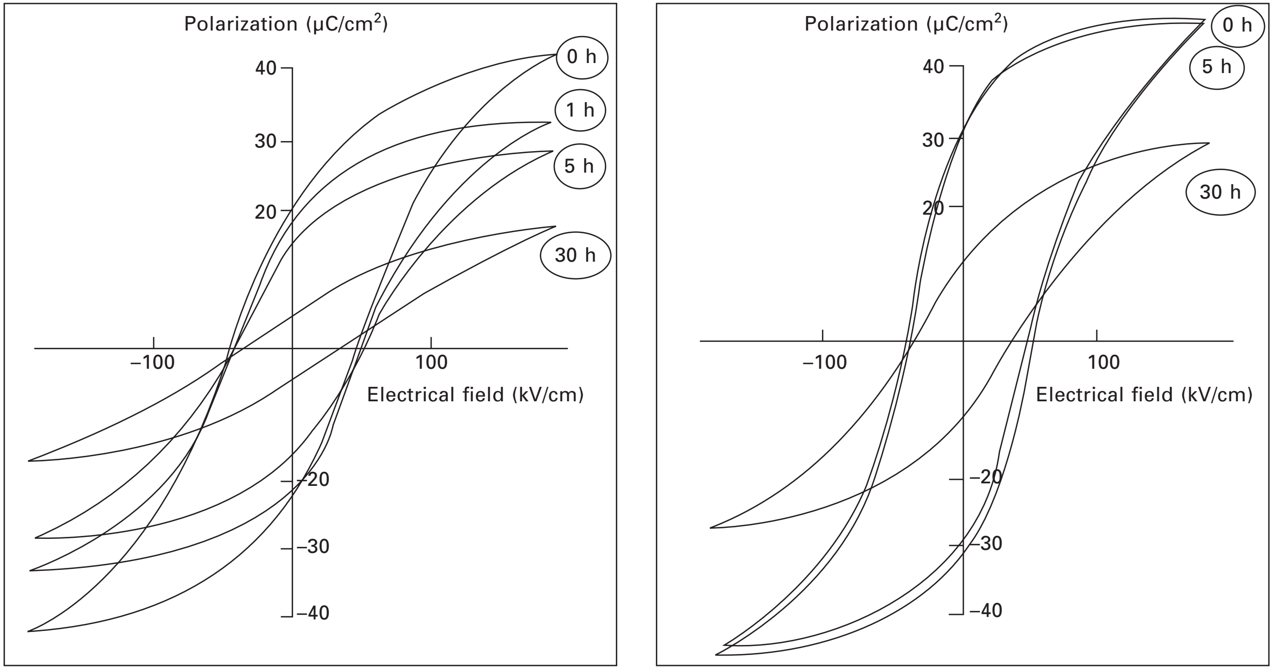

Using milled powder
(a)

Using milled and heat-treated powder
(b)

14.17 Hysteresis loop of PZT film deposited on stainless steel substrate using: (a) powder subjected to milling for 0 h, 1 h, 5 h and 30 h; (b) milled powders (for 0 h, 5 h and 30 h) heat treated at 800 °C for 4 h in air. 20 μm thick samples were deposited at room temperature and annealed at 600 °C for 1 h in air [41].

14.5.3 Relaxor type piezoelectric AD layer

A PNN–PZT (with the composition $0.5Pb(Ni_{1/3}Nb_{2/3})O_3$–$0.5Pb(Zr_{0.3}Ti_{0.7})O_3$) thick film was deposited on a Pt-coated YSZ (3mol% Y_2O_3-stabilized ZrO_2) and Pt-Al_2O_3 coated stainless steel (SS) substrate at room temperature by AD process. [53,54] α-Al_2O_3 used as barrier layer for chemical diffusion, was formed on stainless steel substrate deposited at room temperature by the AD process. To make piezoelectric unimorph cantilevers, 10 μm thick PNN–PZT films were also deposited on these substrates at room temperature.

The prepared films were annealed at temperatures ranging from 600 to 950 °C to investigate the annealing effect. The PNN–PZT film showed a pure perovskite phase without pyrochlore. SEM and TEM observations revealed mean grain sizes of films annealed at 600 and 950 °C to be 83 and 1150 nm, respectively. [54]

The dielectric properties and *P-E* hysteresis of annealed films on YSZ substrate are shown in Fig. 14.18. The dielectric constant of the films increases with annealing temperature and reaches a maximum value of 2530. This value was about four times larger than that of the film annealed at 600 °C. Dielectric loss @ 1 KHz was almost 0.05 with samples annealed at temperatures ranging from 600 to 950 °C. Remanent polarization (P_r) and coercive field (E_c) of the PNN–PZT AD layer annealed at 950 °C were 52 μC/cm^2 and 6.5 kV/cm, respectively. [55]

The piezoelectric constant d_{31} of the PNN–PZT films annealed at 850, 900 and 950 °C on YSZ substrate was estimated to be –164, –240 and –360 pm/V, respectively. The piezoelectric constant d_{31} of PNN–PZT film annealed at 950 °C on Pt-Al_2O_3 coated SS substrate was estimated to be –158 pm/V. The large absolute values of piezoelectric constant d_{31} for PNN–PZT films formed by AD process on Pt/YSZ and Pt/Al_2O_3/SS were confirmed for over 10 samples. [55]

The relationship between the piezoelectric properties and grain size of PNN–PZT film is shown in Fig. 14.19. Hayashi and co-workers [56] reported that the electro-mechanical coupling factor of PNN–PZT ceramics increases with increasing grain size. A similar result was obtained by Hackenberger and co-workers. [57]

Therefore, the recovery of electric properties of PNN–PZT AD film may be mainly due to grain growth as a result of annealing. And the porosity of the PNN–PZT films also increased by increasing annealing temperature. This factor may also influence the improvement in electric properties because of reduction of stress at the near grain boundary. Piezoelectric constant after annealing at 950 °C was still smaller than that of sintered bulk material. P. Muralt [58] and Akedo and Lebedev [50] reported the relationship between the piezoelectric constant and clamping from the substrate. They indicated that the piezoelectric constant of PZT film released from a substrate was

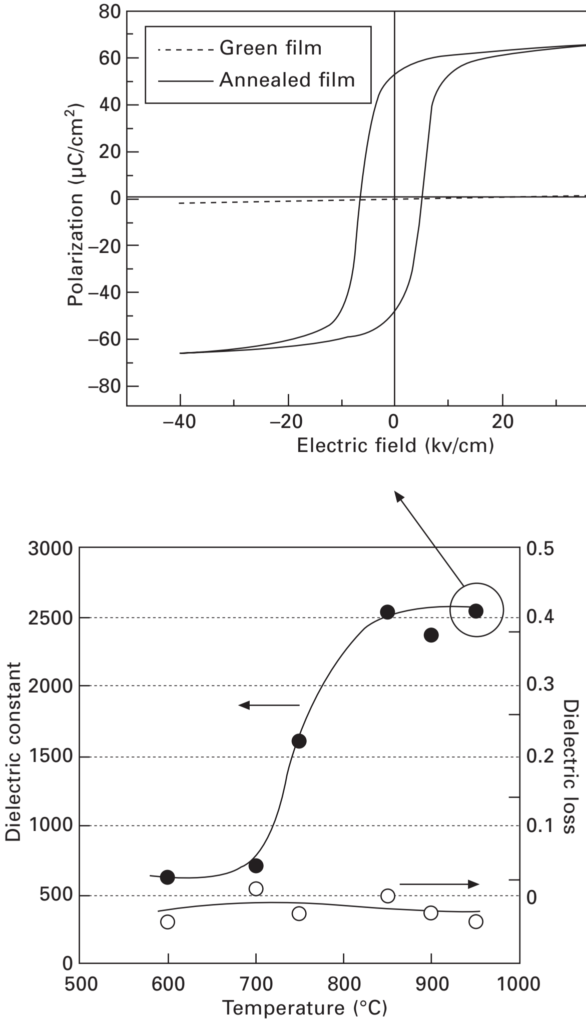

14.18 Dielectric property and *P–E* hysteresis of annealed film on YSZ substrate at various annealing temperatures.

almost two times that of film clamped from the substrate. It seems that a smaller value of piezoelectric constant of PNN–PZT film compared with that of bulk ceramics was caused due to stress from the substrate.

Figure 14.20 shows the comparison of the piezoelectric d_{31} constants with conventional deposition methods. [59] It is confirmed that the piezoelectric constant of PNN–PZT AD film was larger than that of the conventional thick film. In addition, even though PNN–PZT films were annealed without additives, their piezoelectric constant is superior to that of the conventional thick film.

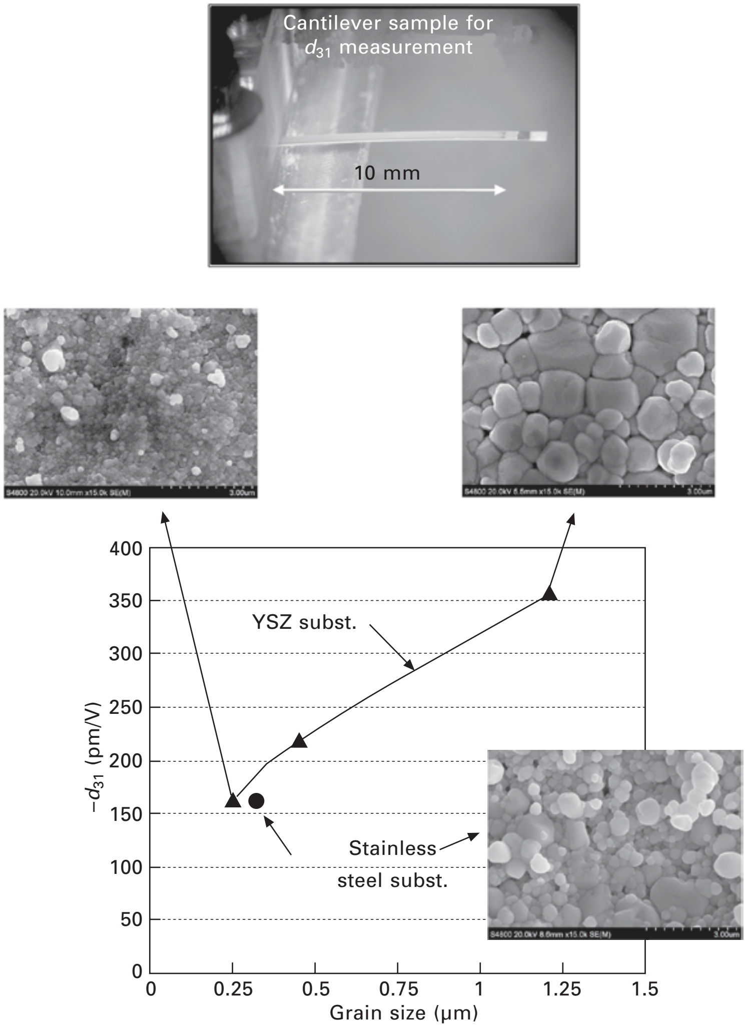

14.19 Relationship between the piezoelectric constant and grain size of PNN–PZT film.

The most important characteristic of the AD process, in comparison with conventional thin or thick film methods, is easily getting a high dense and crystallized structure in the as-deposited film for complicated material compositions without the influence of substrate materials.

14.5.4 Application to lead-free piezoelectric materials

$(K_{0.44}Na_{0.52}Li_{0.04})(Nb_{0.86}Ta_{0.10}Sb_{0.04})O_3$ (LF4) thick films were prepared directly on glass, stainless steel and Pt/Ti/ZrO$_2$ substrates at room temperature

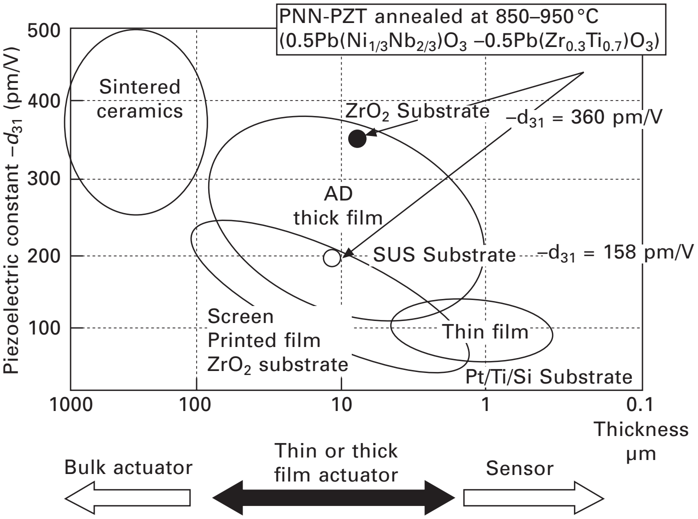

14.20 Comparison of piezoelectric constants and film thickness between AD and conventional thick films [59].

by the AD process. [60] The effects of moisture content in the starting powder and post-annealing temperature on the dielectric properties of LF4 film were investigated. The LF4 powders (a) without preheating, and (b) with preheating at 600 °C and (c) at 1100 °C for 3 h were prepared. From SEM images, non-preheated powders are strongly agglomerated, whereas preheated powders (600 and 1100 °C for 3 h) have well-dispersed states. The average particle sizes of each powder were 0.24, 0.24 and 0.29 μm, respectively. The sizes of all the powders were almost equal. Also, the moisture contents contained in the powders were 0.21%, 0.006%, and 0.005%, respectively. Using these powders, as-deposited films on glass substrates were prepared by AD. The as-deposited film prepared using preheated powder (1100 °C for 3 h) was almost transparent, whereas the one prepared using non-preheated powder was not transparent and had a compacted powder form. It is thought that agglomerated particles play a role in the absorption of kinetic energy, resulting in the formation of compacted powders by AD. [42,46,61]

The LF4 film prepared using preheated powder (moisture content of 0.006%) has dielectric properties with high stability at increasing frequencies, whereas the LF4 film prepared with non-preheated powders (0.21%) has a dielectric constant that decreases abruptly at higher frequencies. When the post-annealing temperature of the film was 600 °C, the dielectric constant increased from 200 to 343 at 1 MHz with increasing preheating temperature from 150 to 1100 °C. Also, the dielectric constant of the film increased from 231 to 559 with increasing annealing temperature from 400 to 1000 °C. These results strongly indicate that moisture elimination in starting powders through preheating and post-annealing for AD plays an important role in realizing good dielectric properties of LF4 film for practical application as lead-free piezoelectric ceramics. Also, the Curie temperature (T_c) of the deposited LF4 film was 250 °C. Figure 14.21 shows *D–E* hysteresis loops for LF4 thick films deposited on YSZ substrates at various post-annealing temperatures. The remanent polarization (P_r) and coercive field (E_c) of LF4 film with a thickness of 4–5 μm were increased with increasing annealing temperature and their values reached 5 μC/cm^2 and 42.4 kV/cm, respectively, at 1000 °C. For comparison with the characteristics of LF4 film, the *D–E* hysteresis loop for LF4 bulk, which was sintered in air at 1100 °C for 5 h, is also shown in the inset of Fig. 14.21. The P_r value of the bulk (3.6 μC/cm^2) was about three times higher than that of the film (1.3 μC/cm^2) in the same electrical field (90 kV/cm). It is thought that the P_r values are related to the grain size in samples and also to annealing temperature and holding time.

Recently, Ryu and Park's group presented several papers about the improvement of lead-free piezoelectric AD layers using the KNN system. [60–62] They reported that the AD process was found to be very effective for the formation of dense lead-free piezoelectric KNN films. The higher density and slight crystal orientation were suggested as being the main reasons for the improved properties.

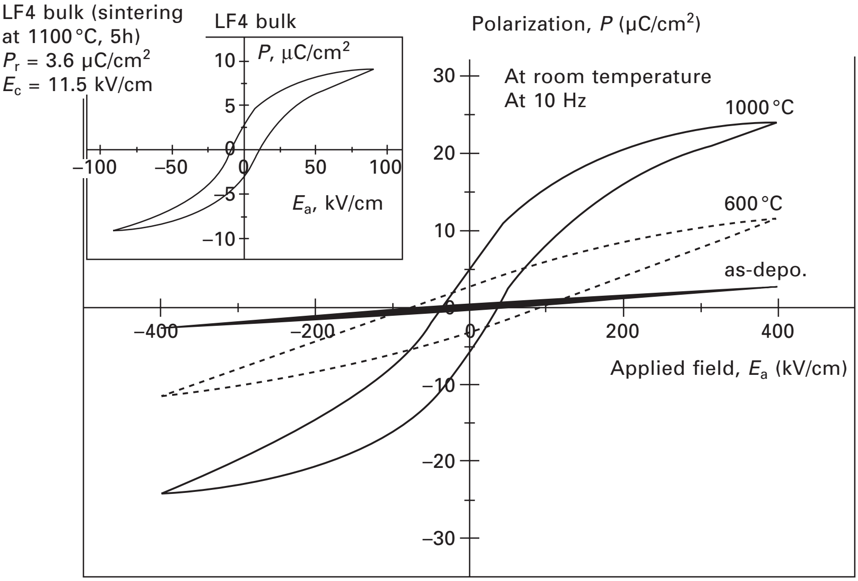

14.21 D–E hysteresis loops for as-deposited LF4 thick films and films deposited at various annealing temperatures. The inset shows *P–E* hysteresis loops for LF4 bulk sintered in air at 1100 °C for 5 h [60].

Ferroelectric properties have been investigated for $(Bi_{0.5}Na_{0.5})TiO_3$ (BNT) dense ceramic films with 25 μm of thickness prepared by an AD method at room temperature. Although BNT is expected for a lead-free piezoelectric material because of their large remanent polarization, [63, 64] remanent polarization is decreased by a large leakage current density and lattice defects in BNT. [65] To obtain BNT dense ceramics fabricated by solid-phase reaction, it is necessary to be sintered at high temperature (at around 1200 °C) which induces Bi vaporization. Nagata and Takenaka reported a P_r of 33.7 $\mu C/cm^2$ and coercive field (E_c) of 57.9 kV for the BNT ceramics fabricated by solid-phase reaction using high-purity materials. [66]

Figure 14.22 indicates polarization properties for the BNT ceramic films annealed at 1000 °C for 1 h. [67] Since bismuth vaporization, which creates lattice defects and oxygen vacancies, is suppressed up to 1000 °C and AD allows a possible deposition of dense ceramic films at room temperature, BNT ceramic films annealed at 1000 °C represent saturated polarization properties (P_r of 27 $\mu C/cm^2$ and E_c of 40 kV/cm).

14.5.5 Leaser annealing

To improve the piezoelectric property of the AD–PZT layer and to reduce the damage to the substrate, laser annealing to the as-deposited AD layer was introduced.

A CO_2 laser (CL) can be used to heat treat thick films without damaging the metal sheet by adjusting the laser power density, because it consists of a beam of thermal energy with low photon energy. It is well known that the most advanced ceramics can absorb infrared radiation very well. Because

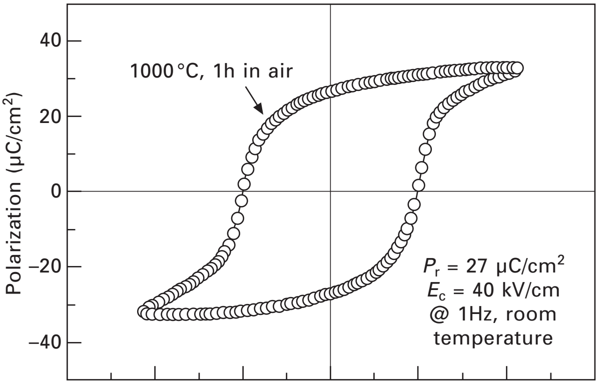

14.22 Polarization properties for the BNT lead-free ceramic film prepared by AD.

this is the wavelength range covered by CLs, they can clearly be used to heat thin films [68–70] and also for the sintering of ceramics. [71] In this section, improvements in the electrical properties of PZT thick films deposited directly onto stainless steel (SS) sheets and subsequently annealed using CL radiation were investigated. [72]

The surface brilliance of the stainless steel (SS) sheets was not influenced by thermal heating by CL and the temperature of the reverse side of the film (i.e., the SS sheet) in Fig. 14.23 was measured at 150 °C or less. The remanent polarization, coercive field values, and the dielectric constant are 34 μC/cm^2, 25 kV/cm, and 1500–1800, respectively. Figure 14.24 shows cross-sectional TEM images and the results of EDX analysis of PZT/SS annealed by CL radiation. We speculate that the hetero-phase is chromium oxide. It is interesting that the diffusion characteristics of Fe and Cr show the opposite behavior. Moreover, E_c for PZT films annealed by CL radiation is 31.6 kV/cm, although Fe and Cr generally behave as acceptors in PZT. [73] This leads us to suggest that Fe and Cr are not diffused as acceptors within the PZT films annealed by CL radiation. It is considered that CL could also be a powerful tool for the annealing of PZT films deposited by other processes, such as the sol-gel method, as well as by the AD process.

Recently, in order to improve the piezoelectric properties and reduce thermal damage to the substrate, a fiber laser (FL) with laser spot size of 50 μm was introduced for the annealing procedure. [74] The results show

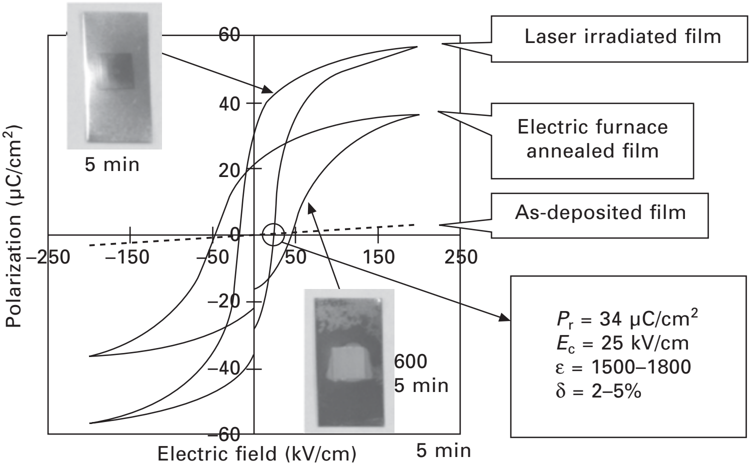

14.23 (a) Dielectric properties and (b) ferroelectric hysteresis loops of 10 mm thick AD–PZT films deposited directly on an SUS substrate and annealed using CO$_2$ laser at 600 °C (CL-annealed PZT/SUS), and annealed using an electric furnace at 600 °C (EF-annealed PZT/SUS) [72].

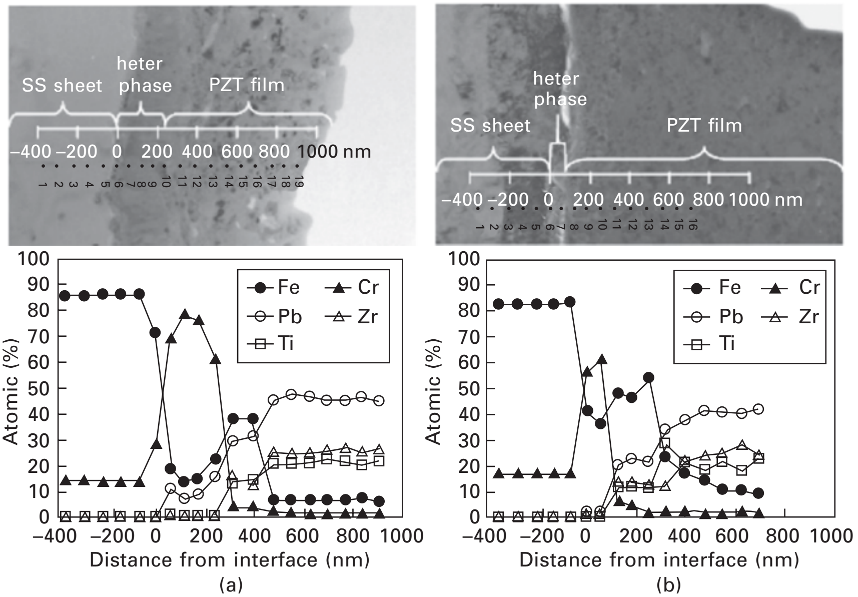

14.24 Cross-sectional TEM–EDX analysis of Pb(Zr,Ti)O_3 (PZT)/stainless steel (SS) annealed by (a) electric furnace at 600 °C for 1 h and (b) CO_2 laser radiation [72].

that fiber laser annealing can effectively improve the grain growth of PZT/SUS by suppressing thermal damage to the SUS substrate.

14.6 Piezoelectric device applications

14.6.1 Thickness of the piezoelectric layer for micro-actuators [75]

Piezoelectric-type actuators as compared with electromagnetic ones have some advantages such as low cost, small size, low energy consumption, and the possibility of realizing a multi-array arrangement of actuators. During the actuator design process many parameters such as piezoelectric constant of the piezoelectric layer, length, thickness of each layer and so on are taken into account. The value of the breakdown electrical field of the piezoelectric material mainly determines the thickness of the piezoelectric layer. Although there are many theoretical and experimental reports about investigations of macro-scale unimorph actuators fabricated from bulk piezoelectric ceramics (for example, in refs. [76–80]), there appears to be no discussion on micro-actuator design taking into account the parameter of breakdown voltage of the piezoelectric layer. But for micro-actuators, this parameter is significant. In this section, we discuss the influence of the breakdown electrical field on micro-actuator design, and show the results of cantilever type actuator fabrications using the AD process

The typical schematic of a unimorph actuator is shown in Fig. 14.25. The performance of a unimorph-type cantilever actuator, which consists of a piezoelectric layer (thickness t_p), which was bound on the top of the non-piezoelectric material (thickness t_{np}), has been investigated by many authors. [76–78, 80] The piezoelectric layer is sandwiched between two electrodes (the non-piezoelectric layer may be one of the electrodes). If some external voltage (V) is applied across the electrodes, the piezoelectric material will either expand or contract. Because the layer t_{np} is not piezoelectric, the movement of the piezoelectric layer t_p is restricted along the interface of the two materials, which results in bending of the free tip of the actuator. The displacement of the free tip, total energy of the bender as well as fundamental

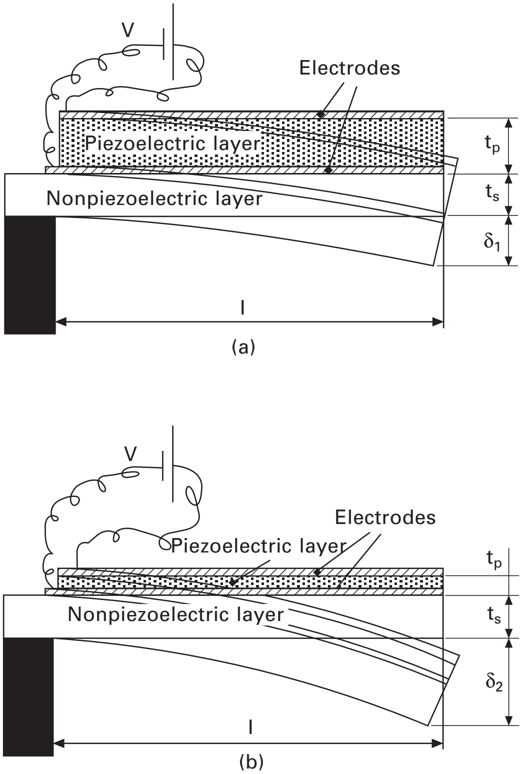
V
Electrodes
Piezoelectric layer
Nonpiezoelectric layer
t_p
t_s
δ_1
l
(a)
V
Electrodes
Piezoelectric layer
Nonpiezoelectric layer
t_p
t_s
δ_2
l
(b)

14.25 Schematic of unimorph actuator. (a) thickness of piezoelectric layer is equal to that of non-piezoelectric layer ($t_p = t_{np}$); (b) thickness of piezoelectric layer is smaller than that of non-piezoelectric layer ($t_p < t_{np}$). For PZT/stainless steel actuator, if applied voltage (V) in both (a) and (b) is the same, the displacement (δ) in (b) is more ($\delta_2 > \delta_1$) [75].

resonance frequency of the actuator are important characteristics of such devices. The displacement of the free tip (δ) if some voltage V is applied across the piezoelectric layer, can be calculated as: [78]

$$\delta = \frac{3}{2}\frac{l^2}{t_p^2}\frac{2xy(1+x)}{1+4xy+6x^2y+4x^3y+x^4y^2}d_{31}V \qquad 14.1$$

where, l, t_p, t_{np} are described in Fig. 14.25, $x = t_{np}/t_p$, $y = Y_{np}/Y_p$ (Y_{np} and Y_p are the Young's modulus of the substrate and piezoelectric, respectively), and d_{31} is a piezoelectric constant. For micro-actuators, the geometrical dimensions of each element are very important to reduce the total device size. If an external applied voltage to the micro-actuator is determined and a piezoelectric layer is fabricated from the bulk material, the two factors restricting the minimum thickness of piezoelectric layer are (a) the slicing and grinding process from bulk piezoelectric (it is difficult to fabricate piezoelectric layers thinner than 30 μm); and (b) breakdown electrical voltage of the piezoelectric. Thus, in a conventional design of an actuator, the thickness of the piezoelectric layer is determined first. After that the non-piezoelectric layer thickness is optimized from the point of view of maximum displacement (for example, see ref. [81]). For this procedure, the maximum displacement calculated using Eq. 14.1 should be found as a function of parameter x. As a result of optimization (curve 2 in Fig. 14.26), for various piezoelectric (PZT, PLZT, etc.) and non-piezoelectric (metal, glass, etc.) layers, the maximum displacement of the actuator will occur if the thickness of the piezoelectric layer is approximately 0.3–1.0 of that of the non-piezoelectric layer (x = 1–3). Let us consider the case when the piezoelectric layer is fabricated from the film (deposited on the substrate). The displacement of the unimorph actuator free tip for various thicknesses of the piezoelectric layer while the thickness of the non-piezoelectric is constant as calculated by Eq. (14.1) is presented in Fig. 14.26. In this case for fixed applied external voltage the maximum displacement of the actuator will occur if the piezoelectric layer is as thin as possible. Curve 1 in Fig. 14.26 presents the results of such calculations. This result is completely different from that of optimization using the conventional concept (curve 2 in Fig. 14.26). Thus only the breakdown electrical field of the piezoelectric layer restricts the selection of the piezoelectric layer thickness. Additionally, only the limitation of the breakdown voltage of the piezoelectric layer will limit the displacement performance of the actuator. Thus, if there are some limitations on maximum applied voltage and the piezoelectric layer has high breakdown electrical voltage properties, it is better to make piezoelectric layers as thin as possible. (It is important to note that the results in this and the above paragraphs are valid only if the Young's modulus of piezoelectric layers is not more than five times less than that of non-piezoelectric layers, i.e.

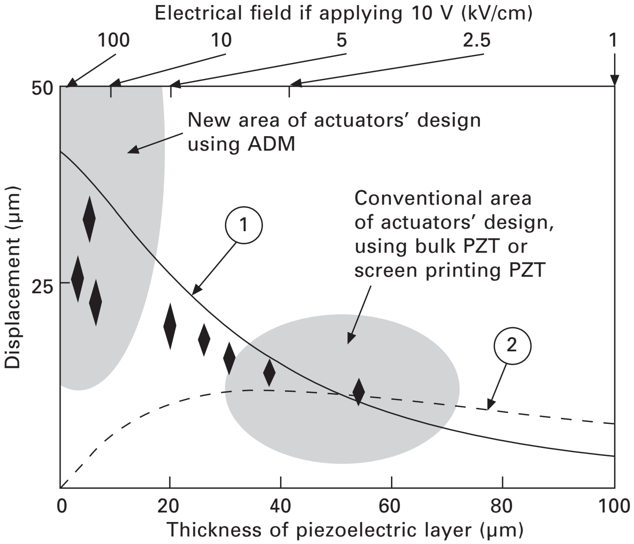

14.26 Displacement (δ, Fig. 14.25) of PZT/stainless steel (SUS-304) cantilever for various thicknesses of PZT layer. Calculations: 1 – Applying 10 V, DC; 2 – Applying DC electrical field of 2 kV/cm for each thickness of PZT layer; calculations were performed for d_{31} of PZT layer of –80 pm/V, Young's modules of PZT and stainless steel (Y_{np}, Y_p) are 80 GPa and169 GPa, respectively. [10] Length of cantilever is 10 mm, thickness of stainless steel (t_{np}) is 50 μm. ◆, experimental results [75].

$Y_p > Y_{np}/5$, according to the analysis of Eq. 14.1.) Thus we should fabricate a PZT film with high breakdown electrical field properties.

To estimate electrical consumption of the actuator, a sine wave unipolar voltage was applied continuously to poled cantilevers with various thicknesses of PZT layer. The amplitude was selected to provide the same free tip displacement of cantilevers at low frequency (static) for both cantilevers. The deflection of a 10 mm cantilever used in this study strongly depends on the driving frequency because many deflection modes of the cantilever exist at different frequencies. However, according to our previous reports, [49, 52] the piezoelectric coefficient d_{31} of PZT on stainless steel was constant in the frequency range from 10 Hz to 10 kHz and displacement of the Si diaphragm driven by the PZT layer was constant up to first resonance (22.4 kHz). Taking into account that for membranous type piezoelectric actuators, actual efficiency (ratio of 'real mechanical work' to 'electrical consumed energy') is small, we can assume that electrical energy consumption is determined mainly by losses (both active-to-bend layer, or passive losses in dielectric) in the piezoelectric layer. Thus we can measure electrical energy consumption for a non-real device. For this purpose, we applied 'low' (+10V (28 kV/cm) and +22.5V (7 kV/cm)) and 'high' (+100V (280 kV/cm) and +225V (70 kV/cm)) voltage to a PZT/stainless steel cantilever with 3.5 μm and 32 μm thick PZT, respectively. Under these conditions, the free tip of the 10 mm long cantilever was deflected by 14 μm and 140 μm (in low frequency under 300 Hz), respectively. The AC electrical current and applied voltage was monitored. The results of measurement are shown in Fig. 14.27. No significant difference in energy consumption between 32 μm thick and 3.5 μm thick PZT layers under a low driving voltage or high driving voltage was observed. The values of energy consumption are close to calculation results using data of permittivity and dielectric losses. However, under high electrical field driving (case 2 in Fig. 14.27) a small difference between calculation and experimental results is obvious at low frequency, which may be explained by the increasing leakage current in the piezoelectric layer.

Thus, from the point of view of energy consumption, a thinner PZT layer has no disadvantages compared with a thicker one. Moreover decreasing the thickness of the PZT layer approximately tenfold (from 32 to 3.5 μm) enabled a twofold decrease in the applied voltage (remaining displacement requirements) and thus decreased the cost of the driving circuit. Production cost of PZT films (under 10 μm thick) using AD is also expected to be cheaper than for PZT films over 30 μm thickness.

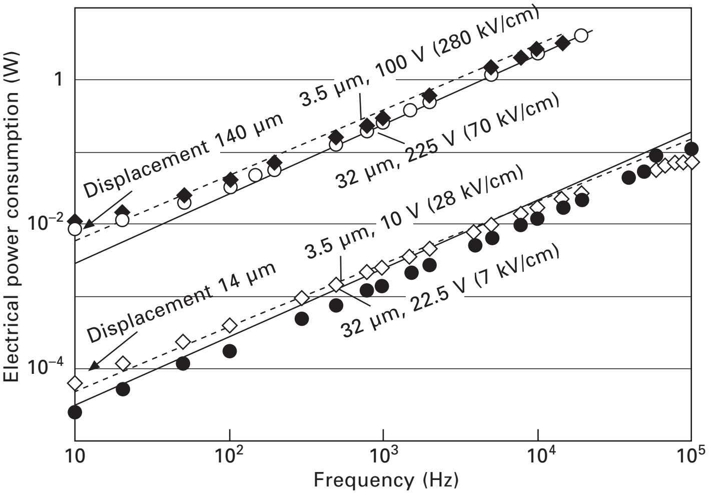

14.27 Total electrical power consumption of PZT/SUS actuator, for various thicknesses: circuit 3.5 μm thick; rhomb 32 μm thick PZT layers; thickness of stainless steel is 50 μm; area of upper electrode 10 mm^2. After annealing at 600 °C for 1 h in air. Lines – simulation of electric power consumptions: solid 32 μm thick; dotted 3.5 μm thick PZT layer [75].

14.6.2 Si-MEMS optical micro-scanner [82]

High-speed resonance optical scanners have many applications in bar-code readers, laser displays, laser printers, and as the key components in various optical sensors. The application to display devices with an enormous market required high performance horizontal scanners, which have high frequencies (exceeding 20 kHz), large scan-angles of over 20° and large mirror sizes (>1 mmφ) to achieve good display quality. [83–85] Micro-electromechanical systems (MEMS) technology has been used to realize optical scanners with special requirements of compact size, low power consumption and high scanning speed. [85–89]

Using the AD process, a high-performance optical micro-scanner with a scanning speed at a resonance frequency over 30 kHz and a scan angle (peak-to-peak value) over 30° in atmospheric environment was successfully fabricated by the deposition of the piezoelectric materials at a high rate onto the scanner structure fabricated by Si-micromachining, as shown in Fig. 14.28. [69, 82] This optical scanner with a high scanning speed is expected to be a key component for various types of sensor for the next generation of projection display devices.

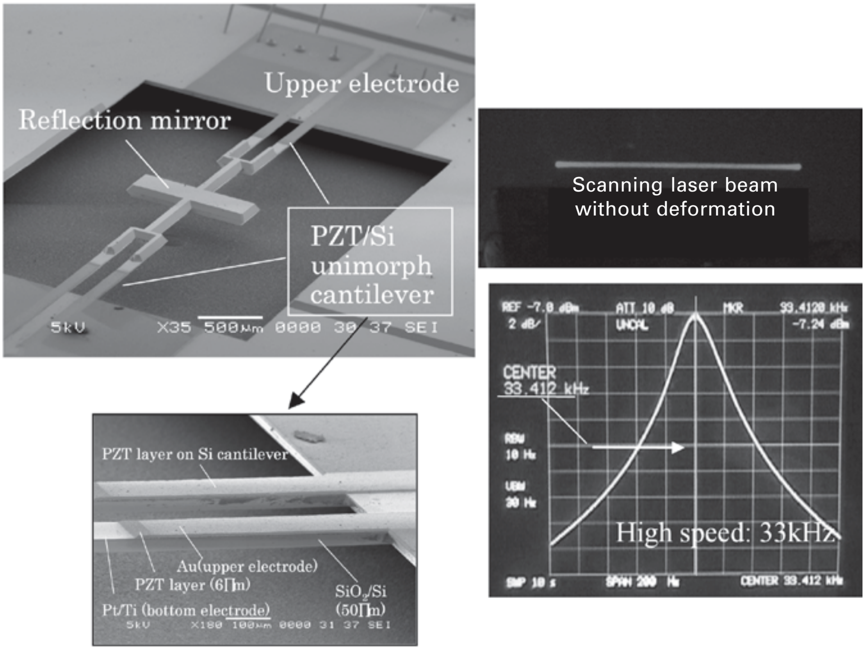
Upper electrode
Reflection mirror
PZT/Si
unimorph
cantilever
5kV X35 500μm 0000 30 37 SEI
Scanning laser beam
without deformation
PZT layer on Si cantilever
Au(upper electrode)
PZT layer (6Γm)
Pt/Ti (bottom electrode)
SiO2/Si
(50Γm)
5kV X180 100μm 0000 31 37 SEI
REF -7.0 dBm
2 dB/
ATT 10 dB
UNCAL
MKR 33.4120 kHz
-7.24 dBm
CENTER
33.412 kHz
RBW
10 Hz
VBW
30 Hz
High speed: 33kHz
SWP 10 s
SPAN 200 Hz
CENTER 33.412 kHz

14.28 Optical micro-scanner driven with PZT thick layer deposited on Si-MEMS structure by AD method. Scanning speed: over 30 kHz, scanning angle: over 30 degree [82].

14.6.3 Metal-based optical micro-scanner[90]

However, MEMS technology has several problems: processes are complicated, products are costly and many facilities are needed. In addition, Si-based optical micro-scanners are made from silicon and can be easily broken due to mechanical shock and high stress concentration near the mirror. It is very attractive to use a metal substrate instead of silicon in optical micro-scanner devices because of a reduction of the device cost and an improvement in the ambient durability by changing brittle silicon to ductile stainless steel. At the same time, stainless steel and silicon have approximately the same Young's modulus (Y), about 200 GPa, and the densities of the materials (ρ), 7.81 g/cm^3 for steel and 2.33 g/cm^3 for silicon, make the ratio of $(Y/\rho)^{1/2}$ that determines the mechanical resonance for this material different by factor of only 2. Such a difference in resonance characteristics can be accommodated by appropriate device design. Thus, silicon can be replaced by stainless steel in MEMS structures.

Figure 14.29(a) shows a schematic and an optical image of a metal-based optical micro-scanner. An optical mirror was attached using two narrow torsion hinges from both sides at the center of gravity of the mirror (symmetrical mirror structure). The other sides of these hinges were connected to the scanner frame and one edge of the scanner frame was clamped and fixed with a heavy block. A piezoelectric layer was deposited directly on the stainless steel scanner frame beside the mirror. The d_{31} actuation mode of the piezoelectric layer bends the scanner frame and induces the vibration of a 'Lamb wave' in the scanner frame. Lamb waves are two-dimensionally guided and concentrate at the narrow torsion hinges holding the mirror through the specially designed metal scanner structure. The waves change with the torsion vibrations of the mirror caused by the vertical difference in the direction between progressing waves and the torsion hinge. The torsional vibration vertically scans the mirror axis. Figure 14.29(b) shows frequency properties of the optical micro-scanner (mirror size: 1 mm × 0.25 mm, hinge width and length: 0.1 and 1.35 mm, respectively) driven by a PZT thick film at a driving voltage of 60 V (peak-to-peak). A large optical scanning angle (41°) was achieved at a high resonance frequency (28.24 kHz) in ambient air using the prototype scanner device. [91] The torsional resonance frequency of our metal-based optical micro-scanner showed no hysteresis because of the symmetrical standing mirror. Moreover, the image of the scanned laser beam exhibited no beam distortion. The quality factor of the metal-based scanner was estimated to be 330. This is lower than that of a Si-MEMS scanner (600) [82]. This low quality factor is effective in reducing the temperature dependence of scanner operation since the quality factor of the optical scanner was dominated by the mechanical dumping factor of the scanner frame, electrical dumping factor of the PZT films

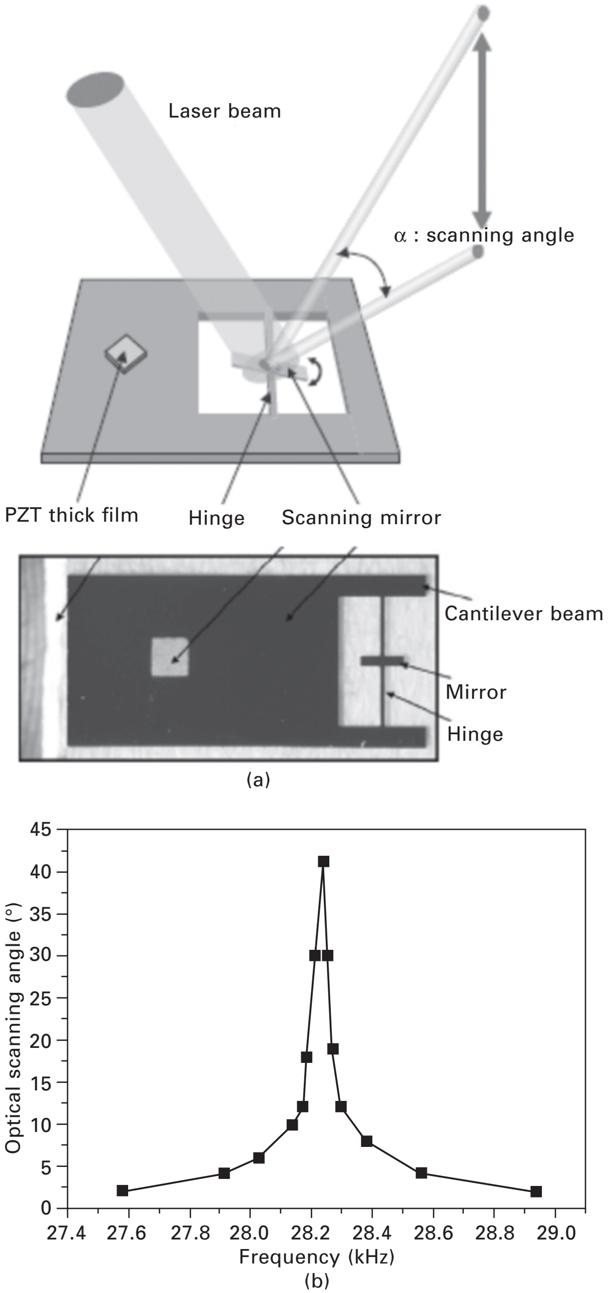

14.29 (a) Novel design of 1 D optical micro-scanner based on metal structure and Lamb wave resonation for raster scanning laser display. (b) Frequency properties of optical micro-scanner driven by PZT thick film at a driving voltage of 60 V (peak-to-peak) [91].

and the aerodynamic dumping of scanning mirror motion under ambient atmosphere.

14.6.4 Optical modulator [92]

Further research is still under way targeting the realization of 3D displays and holographic data storage and the development of fast response spatial light modulators aiming to replace the liquid crystal technology. APZT-MOSLM (PZT-based magneto-optic spatial light modulators) prototype, shown in Fig. 14.30, has been fabricated by incorporating a piezoelectric thick film into magneto-optic materials. [93] In MOSLMs, the high switching speed results from the fact that the pixel switching is achieved by switching the direction of magnetization, up or down within 1 nanosecond. The novel MOSLM driven by an electric field instead of a magnetic field was first achieved using the

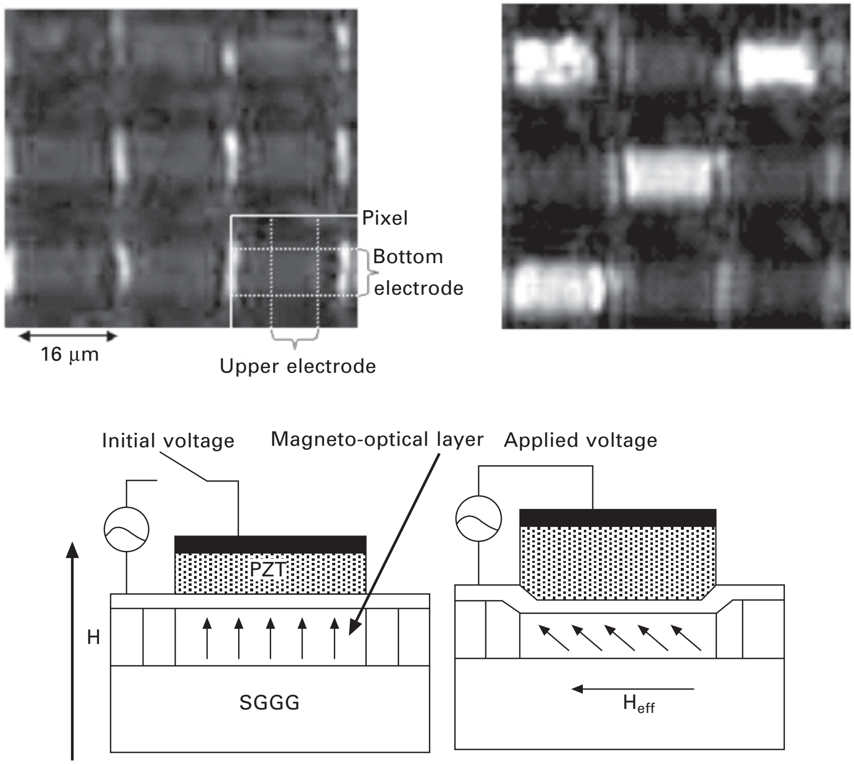
Pixel
Bottom electrode
16 μm
Upper electrode
Initial voltage
Magneto-optical layer
Applied voltage
PZT
H
SGGG
H_{eff}

Cross section of v-MOSLM

14.30 PZT-based magneto-optic spatial light modulators driven with PZT thick layer deposited on Bi–YIG single crystal structure by AD method [92].

piezoelectric effect of AD–PZT thick films, which reduces the anisotropic energy of the structured garnet film. The pixels could be easily switched in the presence of a small external bias field. As a result, the power consumption of such MOSLM was drastically reduced, being 10 times smaller than that of a conventional current driven one. Successful pixel switching at 20 MHz has already been achieved with an 8 V drive voltage.

14.6.5 Ultrasonic motor

Tube typed ultrasonic micro-motors, shown in Fig. 14.31, were also fabricated as the prototype for an application of the AD process. [59] In this device, a 10 μm PZT thick layer was deposited on a stainless steel tube having a 2 mm diameter by using another advantage of the AD process that consists in successful deposition onto curved surfaces. The rotation speed of this ultrasonic motor ranged between 1200 and 1500 rpm for a 7–15 V drive voltage.

14.7 Conclusions

In this chapter, the high potential of aerosol deposition on the fabrication of electro-ceramic thick films for micro-device applications has been highlighted. Through the overview of deposition mechanism, fundamental properties

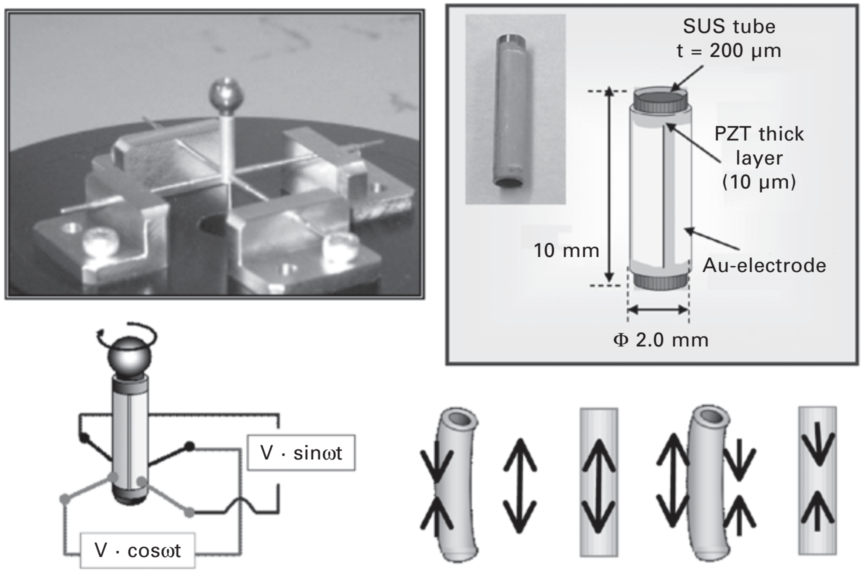

14.31 Tube typed ultrasonic motor driven with PZT thick layer deposited on SUS tube by AD method [59].

and the comparison with conventional thin film technology, the AD process shows important advantages such as:

- high deposition rate,
- low process temperature,
- dense film formation at a low temperature and
- primary material composition and crystal structure are retained in the deposited films due to room temperature impact consolidation (RTIC).

For AD, the following topics have been discussed:

1. Dense consolidation of ceramic particles at room temperature (RTIC phenomenon) was obtained using AD.
2. Reduction of crystallite size was observed and nano-crystalline ceramic layers were formed by AD.
3. Densification mechanism of the AD layer was explained by the plastic deformation of collision particles.
4. AD is applicable to complicated piezoelectric materials such as PNN–PZT and lead-free KNN, BNT system.
5. AD has great potential for integration of functional ceramic materials and application to micro-actuators.

The essential point of the AD process is the RTIC phenomenon of ceramic fine powder. As-deposited AD film at room temperature can be an ultra high density ceramic green body without binder. It is a kind of novel powder molding process different from conventional thin film technology which is based on crystal growth on the substrate. Resulting from this particular feature, low process temperature and high speed deposition (which is one to two orders higher than that of conventional thin film technology) are obtained simultaneously. The aerosol deposition technique has the advantage of offering the possibility to deposit on any kind of substrate materials an array of materials in solid form. However, to use the AD process in practical production, the control of aerosol density and the mono-dispersion of ceramic fine particles in aerosol jet flow for long periods should be further improved to obtain the uniformity and reliability of deposited layers.

For piezoelectric materials, the AD process requires medium temperature (500–950 °C) annealing to obtain sufficient piezoelectric properties for actuator applications. The change in microstructure in the AD layer during annealing was completely different from that in bulk material during the conventional sintering process. The grain growth and the densification of the layer structure are independent. Piezoelectric properties were very sensitive to grain size and residual stress. Therefore, we should investigate more the relationship between grain growth and residual stress on the AD layer to optimize device fabrication.

To date, the bonding mechanism between the fine particles themselves and between the substrate and the fine particles have not been clarified. Does the generation of a clean and active surface of starting particles make bonding of particles at a low temperature possible? Is some kind of chemical reaction induced during impaction? We need further studies on the bonding mechanism of ceramic particles in the AD method. These issues are also important for structuring of nano-composite and gradient material layers.

14.8 References

1. P. Muralt, A. Kholkin, M. Kohli, T. Maeder, K.G. Brooks and R. Luthier, 'Fabrication and Characterization of PZT Thin Films for Micromotors', *Integrated Ferroelectrics*, 11, pp. 213–220 (1995).
2. S. Akamine, T.R. Albrecht, M.J. Zdeblick and C.F. Quate, 'A Planar Process for Microfabrication of a Scanning Tunneling Microscope', *Sens. & Actuators A*, 23, pp. 964–970 (1990).
3. T.-A. Massood, *Microactuators: Electrical, Magnetic, Thermal, Optical, Mechanical, Chemical and Smart Structures*, Kluwer Academic Publishers, New York (1998).
4. A. Manz, N. Graber and H.M. Widmer, 'Miniaturized Total Chemical Analysis Systems: A Novel Concept for Chemical Sensing', *Sens. & Actuators B*, 1990, 1, pp. 244–248.; P. Bergveld, *Proc. Micro Total Analysis Systems Workshop* μ*-TAS'94*, p. 1–4 (1994).
5. S. Koganezawa, Y. Uematsu, T. Yamada, H. Nakano, J. Inoue and T. Suzuki, 'Dual-stage Actuator System for Magnetic Disk Drives Using a Shear Mode Piezoelectric Microactuator', *IEEE Trans. Magn.*, 35(2), pp. 988–992 (1999).
6. J. Akedo and M. Lebedev, 'Ceramics Coating Technology based on Impact Adhesion Phenomenon with Ultrafine Particles – Aerosol Deposition Method for High Speed Coating at Low Temperature', *Materia*, 41 (7), pp. 459–466 (2002) (in Japanese).
7. M. Sayer and K. Sreenivas, 'Ceramic Thin Films: Fabrication and Applications', *Science*, 247, pp. 1056–1060 (1990).
8. I.R. Abothu, Y. Ito, P. Poosanaas, S. Kalpat, S. Komarneni and K. Uchino, 'Sol-gel Processing of Piezoelectric Thin Films', *Ferroelectrics*, 232, pp. 191–195 (1999).
9. H.D. Chen, K.R. Udayakumar, C.J. Gaskey, L.E. Cross, J.J. Bernstein and L.C. Niles, 'Fabrication and Electrical Properties of Lead Zirconate Titanate Thick Films', *J. Am. Ceram. Soc.*, 79, pp. 2189–2192 (1996).
10. Ph. Luginbuhl, G.-A. Racine, Ph. Lerch, B. Romanowicz, K.G. Brooks, N.F. de Rooij, Ph. Renaud and N. Setter, 'Piezoelectric Cantilever Beams Actuated by PZT Sol-gel Thin Film', *Sens. & Actuat.* A, 54, pp. 530–535 (1996).
11. S. Watanabe, T. Fujiu and T. Fujii, 'Effect of Poling on Piezoelectric Properties of Lead Zirconate Titanate Thin Films Formed by Sputtering', *Appl. Phys. Lett.*, 66, pp. 1481–1483 (1995).
12. M. Sakata, S. Wakabayashi, M. Ikeda, H. Goto, M. Takeuchi and T. Yada, 'Pb-based Ferroelectric Thin Film Actuator for Optical Applications', *J. Microsystem Technologies*, 2, pp. 26–31 (1995).
13. Y. Sakashita, T. Ono, H. Segawa, K. Tominaga and M. Okada, 'Preparation and Electrical Properties of MOCVD-deposited PZT Thin Films', *J. Appl. Phys.*, 69, pp. 8352–8357 (1991).
14. H. Kidoh, T. Ogawa, A. Morimoto and T. Shimizu, 'Ferroelectric Properties of

Lead-Zirconate-Titanate Films Prepared by Laser Ablation', *Appl. Phys. Lett.*, 58 (25), pp. 2910–2912 (1991).

15. M. Oikawa and K. Toda, 'Preparation of Pb(Zr,Ti)O_3 Thin Films by an Electron Beam Evaporation Technique', *Appl. Phys. Lett.*, 29 (8), pp. 491–492 (1976).
16. R.N. Castellano and L.G. Feinstein, 'Ion-beam Deposition of Thin Films of Ferroelectric Lead Zirconate Titanate (PZT)', *J. Appl. Phys.*, 50 (6), pp. 4406–4411 (1979).
17. Y. Ohba, M. Miyauchi, T. Tsurumi and M. Daimon, 'Analysis of Bending Displacement of Lead Zirconate Titanate Thin Film Synthesized by Hydrothermal Method', *Jpn. J. Appl. Phys.*, 32 (9B), pp. 4095–4098 (1993).
18. K. Shimomura, T. Tsurumi, Y. Ohba and M. Daimon, 'Preparation of Lead Zirconate Titanate Thin Film by Hydrothermal Method', *Jpn. J. Appl. Phys.*, 30, pp. 2174–2177(1997).
19. B. Morten, G. De. Cicco, A. Gandolfi and C. Tonelli, 'PZT-based Thick Films and the Development of a Piezoelectric Pressure Sensor', *Hybrid Circuits*, 28, pp. 25–28 (1992).
20. H.D. Chen, K.R. Udayakumar, L.E. Cross, J.J. Bernstein and L.C. Niles, 'Dielectric, Ferroelectric, and Piezoelectric Properties of Lead Zirconate Titanate Thick Films on Silicon Substrates', *J. Appl. Phys.*, 77, pp. 3349–3353 (1995).
21. Y. Akiyama, K. Yamanaka, E. Fujisawa and Y. Kowata, 'Development of Lead Zirconate Titanate Family Thick Films on Various Substrates', *Jpn. J. Appl. Phys.*, 38 (9B), pp. 5524–5527 (1999).
22. C.V.R. Vasant Kumar, M. Sayer, R. Pascual, D.T. Amm and Z. Wu, 'Lead Zirconate Titanate Films by Rapid Thermal Processing', *Appl. Phys. Lett.*, 58 (11), pp. 1161–1163 (1991).
23. M.R. Poor and C.B. Fledderman, 'Measurements of Etch Rate and Film Stoichiometry Variations During Plasma Etching of Lead-Lanthanum-Zirconium-Titanate Thin Films', *J. Appl. Phys.*, 70, pp. 3385–3387 (1991).
24. C. W. Chung, 'Reactive Ion Etching of $Pb(Zr_xTi_{1-x})O_3$ Thin Films in an Inductively Coupled Plasma', *J. Vac. Sci. & Technol. B*, 16, pp. 1894–1900 (1998).
25. X. Li, T. Abe and M. Esashi, 'Deep Reactive Ion Etching of Pyrex Glass', *Proc. IEEE MEMS'2000*, p. 271, Miyazaki, Japan (2000).
26. K. Saito, J.H. Choi, T. Fukuda and M. Ohue, 'Reactive Ion Etching of Sputtered $PbZr_{1-x}Ti_xO_3$ Thin Films', *Jpn. J. Appl. Phys.*, 31, pp. L1260–L1262 (1992).
27. J. Akedo, 'Aerosol Deposition Method for Fabrication of Nano Crystal Ceramic Layer – Novel Ceramics Coating with Collision of Fine Powder at Room Temperature', *Material Science Form*, 449–452, pp. 43–48 (2004).
28. J. Akedo and M. Lebedev, 'Microstructure and Electrical Properties of Lead Zirconate Titanate ($Pb(Zr_{52}/Ti_{48})O_3$) Thick Film Deposited with Aerosol Deposition Method', *Jpn. J. Appl. Phys.*, 38 (9B), pp. 5397–5401 (1999).
29. J. Akedo, 'Aerosol Deposition of Ceramic Thick Films at Room Temperature – Densification Mechanism of Ceramic Layer', *J. Am. Ceram. Soc.*, 89 (6), pp. 1834–1839 (2006).
30. M. Kiyohara, Y. Tsujimichi, K. Mori, H. Hatono, J. Migita, T. Kusunoki, N. Minami, M. Lebedev and J. Akedo, *Proc. of 15th Ceram. Soc. Jpn. Autumn Symp.*, 228 (2002).
31. M. Levedev, J. Akedo, K. Mori and T. Eiju, 'Simple Self-selective Method of Velocity Measurement for Particles in Impact-based Deposition', *J. Vac. Sci. & Tech. A*, 18 (2), pp. 563–566 (2000).
32. J. Akedo and M. Lebedev, 'Influence of Carrier Gas Conditions on Electrical and

Optical Properties of $Pb(Zr,Ti)O_3$ Thin Films Prepared by Aerosol Deposition Method', *Jpn. J. Appl. Phys.*, 40 (9B), pp. 5528–5532 (2001).

33. G.R. Johnson and T.J. Holmquist, 'An Improved Computational Constitutive Model for Brittle Materials', *High Pressure Science and Technology – 1993*, Vol. 2, edited by S.C. Schmidt, J.W. Shaner, G.A. Samara and M. Ross, AIP Press, New York, pp. 981–984 (1994).
34. T.J. Holmquist, G.R. Johnson, D.E. Grady, C.M. Lopatin and E.S. Hertel, 'High Strain Rate Properties and Constitutive Modeling of Glass', *Proc. 15th Int. Symp. Ballistics*, pp. 237–244, TB31, Jerusalem, Israel, May 21–24 (1995).
35. C.E. Anderson, G.R. Johnson and T.J. Holmquist, 'Ballistic Experiments and Computations of Confined 99.5% Al_2O_3 Ceramic Tiles', *Proc. 15th Int. Symp. Ballistics*, pp. 65–72, G6, Jerusalem, Israel, May 21–24 (1995).
36. H. Hirai and K. Kondo, 'Shock–Compacted Si_3N_4 Nanocrystalline Ceramics: Mechanisms of Consolidation and of Transition from α- to β-form', *J. Am. Ceram. Soc.*, 77 (2), pp. 487–492 (1994).
37. J.J. Petrovic, B.W. Olinger and R.B. Roof, 'Explosive Shock Loading on Alpha-Si_3N_4 Powder', *J. Mater. Sci.*, 20, pp. 391–398 (1985).
38. M. Yoshida, H. Ogiso, S. Nakano and J. Akedo, 'Compression Test System for a Single Submicron Particle', *Rev. Sci. Instr.*, 76, 093905 (2005).
39. R.C. Dykhuizen, M.F. Smith, D.L. Gilmore, R.A. Neiser, X. Jiang and S. Sampath, 'Impact of High Velocity Cold Spray Particle', *J. of Thermal Spray Technology*, 8, pp. 559–564 (1999).
40. J. Vlcek, H. Huber and H. Voggenreiter, 'Kinetic Powder Compaction Applying the Cold Spray Process – A Study on Parameter', *Proc. of ITSC2001*, pp. 417–420 (2001).
41. J. Akedo and M. Lebedev, 'Powder Preparation for Lead Zirconate Titanate Thick Films in Aerosol Deposition Method', *Jpn. J. Appl. Phys.*, 41 (10B), pp. 6980–6984 (2002).
42. M. Lebedev and J. Akedo, 'Patterning Properties of Lead Zirconate Titanate (PZT) Thick Films Made by Aerosol Deposition', *IEEJ Trans. Sens. & Micromach.*, 120-E (12), pp. 600–601 (2000).
43. J. Akedo, 'Study on Rapid Micro-structuring using Jet-molding: Present status and structuring subjects toward HARMST', *Microsystem Technologies*, 6 (11), pp. 205–209 (2000).
44. J. Akedo, J-H. Park and H. Tsuda, 'Aerosol Deposition – Film Formation, Fine Patterning of Piezoelectric Materials and Its Applications', *J. Electroceram.*, 22, pp. 319–326 (2009).
45. J. Akedo and M. Kiyohara, 'Nanostructuring and Shock Compaction using Fine Particle Beam – Aerosol Deposition for Forming of Nanocrystal Layer and Powder Technology', *J. Soc. Powder Tech.*, 43 (5), pp. 376–384 (2006) (in Japanese).
46. J. Iwasawa, R. Nishimizu, M. Tokita, M. Kiyohara and K. Uematsu, 'Dense Yttrium Oxide Film Prepared by Aerosol Deposition Procee at Room Temperature', *J. Ceram. Soc. Jpn.*, 114 (3), pp. 272–276 (2006) (in Japanese).
47. S.-M. Nam, M. Momotani, N. Mori, H. Kakemoto, S. Wada, J. Akedo and T. Tsurumi, 'Microstrip Band Pass Filter of GHz Region Employing Aerosol-Deposited Alumina Thick Films', *Integrated Ferroelectrics*, 66, pp. 301–310 (2004).
48. J. Akedo, 'Aerosol Deposition for Coating of Transparent and High Resistive Ceramic Layer', *Metal, AGNE Gijutsu Center*, 75 (3), pp. 16–23 (2005) (in Japanese)
49. J. Akedo and M. Lebedev, 'Piezoelectric Properties and Poling Effect of Pb(Zr,Ti)

O_3 Thick Films Prepared for Microactuators by Aerosol Deposition', *Appl. Phys. Lett.*, 77 (11), pp. 1710–1712 (2000).

50. J. Akedo and M. Lebedev, 'Effects of Annealing and Poling Conditions on Piezoelectric Properties of $Pb(Zr_{0.52},Ti_{0.48})O_3$ Thick Films Formed by Aerosol Deposition Method', *J. Cryst. Growth*, 235, pp. 397–402 (2002).
51. J. Akedo, N. Minami, K. Fukuda, M. Ichiki, and R. Maeda, 'Electrical Properties of Direct Deposited Piezoelectric Thick Film Formed by Gas Deposition Method – Annealing Effect of the Deposited Films', *Ferroelectrics*, 231 (7) pp. 285–292 (1999).
52. M. Lebedev, J. Akedo, and Y. Akiyama, 'Actuation Properties of Lead Zirconate Titanate Thick Films Structured on Si Membrane by the Aerosol Deposition Method', *Jpn. J. Appl. Phys.*, 39 (9B), pp. 5600–5603 (2000).
53. Y. Kawakami, H. Yoshikawa, Y. Hiroshi, K. Komagata and J. Akedo, 'Microstructure and Electric Properties of $Pb(Ni,Nb)O_3$–$PbZrTiO_3$ Thin Films Deposited by Aerosol Deposition Method', *J. Cryst. Growth*, 275 (2), pp. e1295–e1300 (2005).
54. Y. Kawakami and J. Akedo, 'Annealing Effect on $0.5Pb(Ni_{1/3}Nb_{2/3})O_3$–$0.5Pb(Zr_{0.3}Ti_{0.7})O_3$ Thick Film Deposited by Aerosol Deposition Method', *Jpn. J. Appl. Phys.*, 44 (9B), pp. 6934–6937 (2005).
55. Y. Kawakami and J. Akedo, 'Piezoelectric Properties of $0.5Pb(Ni_{1/3}Nb_{2/3})O_3$–$0.5Pb(Zr_{0.3}Ti_{0.7})O_3$ Thick Film Prepared by Aerosol Deposition Process' (to be submitted).
56. T. Hayashi, J. Tomizawa, T. Hasegawa and Y. Akiyama, 'Low-temperature Fabrication of $Pb(Ni_{1/3}Nb_{2/3})O_3$–$Pb(Zr_{0.3}Ti_{0.7})O_3$ Ceramics with $LiBiO_2$ as a Sintering Aid', *J. Europ. Ceram. Soc.*, 24, pp. 1037–1039 (2004).
57. W. Hackenberger, M. Pan, V. Veducla, P. Pertsch, W. Cao, C. Randall, and T. Shrout, *SPIE Conference on Smart Materials Tech.*, SPIE vol. 3324, pp. 28–36, (1998).
58. P. Muralt, 'PZT Thin Films for Microsensors and Actuators: Where Do We Stand?', *IEEE Trans. Ultrason. Ferroelect. Freq. Control*, 47, pp. 903–915 (2000).
59. Nanotech2007 NEDO project on 'Nanostructure Forming for Advanced Ceramic Integration Technology in Japan: Nanotechnology Program', pamphlet, 2/21 (2007).
60. S.-W. Oh, J. Akedo, J.-H. Park and Y. Kawakami, 'Fabrication and Evaluation of Lead-Free Piezoelectric Ceramic LF4 Thick Film Deposited by Aerosol Deposition Method', *Jpn. J. Appl. Phys.*, 45 (9B), pp. 7465–7470 (2006).
61. S.M. Nam, N. Mori, H. Kakemoto, S. Wada, J. Akedo and T. Tsurumi, 'Alumina Thick Films as Integral Substrates Using Aerosol Deposition Method', *Jpn. J. Appl. Phys.*, 43, pp. 5414–5417 (2004).
62. J. Ryu, J.-J. Choi, B.-D. Hahn, D.-S. Park, W.-H. Yoon and K.-H. Kim, 'Fabrication and Ferroelectric Properties of Highly Dense Lead-free Piezoelectric $(K_{0.5}Na_{0.5})NbO_3$ Thick Films by Aerosol Deposition', *Appl. Phys. Lett.*, 90, e-152901–152903 (2007).
63. T. Takenaka, K. Maruyama and K. Sakata, '$(Bi_{1/2}Na_{1/2})TiO_3$-$BaTiO_3$ System for Lead-Free Piezoelectric Ceramics', *Jpn. J. Appl. Phys.*, 30 (9B), pp. 2236–2239 (1991).
64. G.A. Smolenskii, V.A. Isupov, A.I. Agranovskaya and N.N. Krainik, 'New Ferroelectrics of Complex Composition.IV', *Sov. Phys.-Solid State*, 2, p. 2651 (1961).
65. S.E. Park, S.-J. Chung, I.-T. Kim and K.S. Hong, 'Nonstoichiometry and the Long-Range Cation Ordering in Crystals of $(Na_{1/2}Bi_{1/2})TiO_3$', *J. Am. Ceram. Soc.*, 77 (10), pp. 2641–2647 (1994).

66. H. Nagata and T. Takenaka, 'Effects of Substitution on Electrical Properties of $(Bi_{1/2}Na_{1/2})TiO_3$-based Lead-free Ferroelectrics', Proc. 2001 12th IEEE Int. Symp. Applications of Ferroelectrics, 1 and 2, 45 (2001).
67. M. Suzuki, J. Akedo, Y. Noguchi and M. Miyayama, 'Polarization Properties of $(Bi_{0.5}Na_{0.5})TiO_3$ Ceramic Films Prepared by Aerosol Deposition Process', *22nd Fall Meeting of The Ceramics Society of Japan in Ehime Univ.*, Extended Abstracts 1P-A13, p. 31 (2009).
68. C.-F. Chou, H.-C. Pan and C.-C. Chou, 'Electrical Properties and Microstructures of $PbZrTiO_3$ Thin Films Prepared by Laser Annealing Techniques', *Jpn. J. Appl. Phys.*, 41 (11B) pp. 6679–6681 (2002).
69. H.-C. Pan, C.-C. Chou and H.-L. Tsai, 'Low-Temperature Processing of Sol-Gel Derived $La_{0.5}Sr_{0.5}MnO_3$ Buffer Electrode and $PbZr_{0.52}Ti_{0.48}O_3$ Films Using CO_2 Laser Annealing', *Appl. Phys. Lett.*, 83 (15), pp. 3156–3158 (2003).
70. M. Knite, G. Mezinskis, L. Shebanovs, I. Pedaja and A. Sternbergs, 'CO_2 Laser-Induced Structure Changes in Lead Zirconate Titanate $Pb(Zr_{0.58},Ti_{0.42})O_3$ Sol–Gel Films', *Appl. Surf. Sci.*, 208–209, pp. 378–381 (2003).
71. S. Sugihara, 'Sintering of Piezoelectric Ceramics with CO_2 Laser', *Jpn. J. Appl. Phys.*, 31 (9B), pp. 3037–3040 (1992).
72. S. Baba, and J. Akedo, 'Damage-free and Short Annealing of $Pb(Zr,Ti)O_3$ Thick Films Directly Deposited on Stainless Steel Sheet by Aerosol Deposition with CO_2 Laser Radiation', *J. Am. Ceram. Soc.*, 88 (6), pp. 1407–1410 (2005).
73. C. Prakash and O.P. Thakur, 'Effects of Samarium Modification on the Structural and Dielectric Properties of PLZT Ceramics', *Mater. Lett.*, 57, pp. 2310–2314 (2003).
74. S. Baba, and J. Akedo, 'Fiber Laser Annealing of Nanocrystalline PZT Thick Film Prepared by Aerosol Deposition', *Appl. Surf. Sci.*, 255 (24), pp. 9791–9795 (2009).
75. M. Lebedev and J. Akedo, 'What Thickness of Piezoelectric Layer with High Breakdown Voltage is Required for Microactuator?', *Jpn. J. Appl. Phys.*, 41 (5B), pp. 3344–3347 (2002).
76. J.G. Smits and W. Choi, 'The Constituent Equations of Piezoelectric Heterogeneous Bimorphs', *IEEE Trans. Ultrason. Ferroelect. Freq. Control*, 38, pp. 256–270 (1991).
77. Q. Wang and L.E. Cross, 'Constitutive Equations of Symmetrical Triple Layer Piezoelectric Benders', *IEEE Trans. Ultrason. Ferroelect. Freq. Control.*, 46, pp. 1343–1351 (1999).
78. L.L. Ries and S.W. Smith, 'Finite Element Analysis of a Deformable Array Transducer', *IEEE Trans. Ultrason. Ferroelect. Freq. Control*, 46, pp. 1352–1363 (1999).
79. D.E. Daush, 'Ferroelectric Polarization Fatigue in PZT-Based RAINBOWs and Bulk Ceramics', *J. Am. Ceram. Soc.*, 80 (9), pp. 2355–2360 (1997).
80. Q. Wang and L.E. Cross, 'Tip Deflection and Blocking Force of Soft PZT-Based Cantilever RAINBOW Actuators', *J. Am. Ceram. Soc.*, 82 (1), pp. 103–110 (1999).
81. X. Li, W.Y. Shin, I.A. Aksay and W.H. Shin, 'Electromechanical Behavior of PZT-Brass Unimorphs', *J. Am. Ceram. Soc.*, 82 (7), pp. 1733–1740 (1999).
82. N. Asai, R. Matsuda, M. Watanabe, H. Takayama, S. Yamada, A. Mase, M. Shikida, K. Sato, M. Lebedev and J. Akedo, 'A Novel High Resolution Optical Scanner Actuated by Aerosol Deposited PZT Films', *Proc. MEMS 2003*, Kyoto, Japan, pp. 247–250 (2003).

83. M. Bayer, 'Retinal Scanning Display – a Novel HMD Approach to Army Aviation', *Proc. SPIE*, 4711, p. 4557 (2002).
84. H. Urey, 'Torsional MEMS scanner design for high-resolution display systems', *Proc. SPIE*, 4773, pp. 27–37 (2002).
85. H. Schenk, P. Durr, D. Kunze, H. Lakner and H. Kuck, 'A Resonantly Excited 2D Micro-scanning Mirror with Large Deflection', *Proc. IEEE 13th Annual Int. Conf. Micro Electro Mechanical Systems (MEMS)*, pp. 473–476 (2000).
86. D. Dickensheets and G. KiNo, 'Microfabricated Biaxial Electrostatic Torsional Scanning Mirror', *Proc. SPIE*, 3009, pp. 141–150 (1997).
87. K. Yamada and T. Kuriyama, 'A Novel Asymmetric Silicon Micro-mirror for Optical Beam Scanning Display', *Proc. MEMS 98*, pp. 110–115 (1998).
88. F. Filhol, E. Defay, C. Divoux, C. Zinck and M.-T. Delaye, 'Resonant Micro-mirror Excited by a Thin-film Piezoelectric Actuator for Fast Optical Beam Scanning', *Sensors and Actuators A*, 123–124, pp. 483–489 (2005).
89. R. Conant, J. Nee, K. Lau and R. Muller, 'A Flat High Frequency Scanning Micromirror', Solid-State Sensor and Actuator Workshop, Hilton Head, South Carolina, June 2000, pp. 6–9 (2000).
90. J. Akedo, M. Lebedev, H. Sato and J.H. Park, 'High-Speed Optical Microscanner Driven with Resonation of Lambda Waves Using Pb(Zr,Ti)O_3 Thick Films Formed by Aerosol Deposition', *Jpn. J. Appl. Phys.*, 44 (9B), pp. 7072–7077 (2005).
91. J.-H. Park, J. Akedo and H. Sato, 'High-speed Metal-based Optical Microscanners using Stainless-steel Substrate and Piezoelectric Thick Films Prepared by Aerosol Deposition Method', *Sensors and Actuators A*, 135 (1), pp. 86–91 (2007).
92. H. Takagi, M. Mizoguchi, J.H. Park, K. Nishimura, H. Uchida, M. Lebedev, J. Akedo and M. Inoue, 'PZT-Driven Micromagnetic Optical Devices', *Mat. Res. Soc. Symp. Proc.*, 785, pp. D6.10.1–D6.10.6 (2004).

15

Manufacturing technologies for piezoelectric transducers

K. UCHINO, The Pennsylvania State University, USA

Abstract: This chapter deals with ultrasonic transducers used underwater, such as Langenvin types and cymbals. Ultrasonic washers, ultrasonic microphones and sonars for short-distance remote control, underwater detection, fish finding, and non-destructive testers are typical applications. Ultrasonic scanning detectors are useful in medical electronics for clinical applications ranging from diagnosis to therapy and surgery.

Key words: Langevin transducer, cymbal, underwater acoustics, acoustic imaging.

15.1 Introduction

Ultrasonic waves are now used in various fields. The sound source is made from piezoelectric ceramics, as well as magnetostrictive materials. Piezoceramics are generally superior in efficiency and in size to magnetostrictive materials. In particular, hard piezoelectric materials with a high Q_M are preferable because of high-power generation without heat generation. A liquid medium is usually used for sound energy transfer. Typical applications include ultrasonic washers, ultrasonic microphones and sonars for short-distance remote control, underwater detection, fish locating, and non-destructive testers. Ultrasonic scanning detectors are useful in medical devices for clinical applications ranging from diagnosis to therapy and surgery. This chapter reviews how to design and manufacture transducers with a particular focus on Langevin types, cymbals, acoustic lenses, horns and impedance matching layers. Most of the contents and figures have been referred to previously in Refs 1–3.

15.2 Transducer designs

15.2.1 Langevin transducer

Paul Langevin succeeded in transmitting an ultrasonic pulse into the sea off the south of France in 1917. We learn most of the practical development approaches from this original transducer design (Fig. 15.1). First, 40 kHz was chosen for the sound wave frequency. Increasing the frequency (shorter

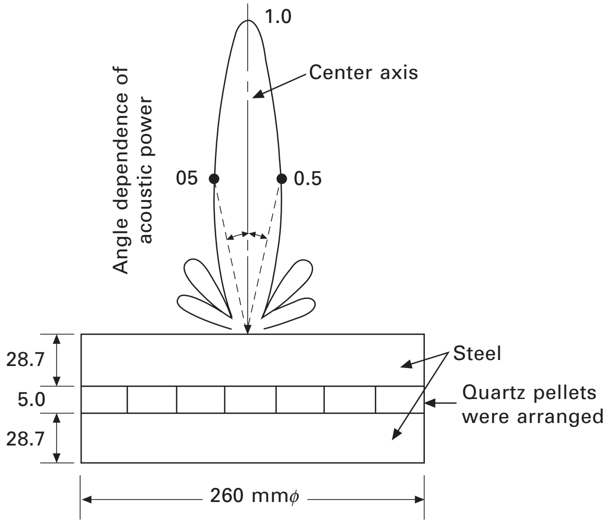
1.0
Center axis
Angle dependence of acoustic power
05
0.5
28.7
5.0
28.7
Steel
Quartz pellets were arranged
260 mmϕ

15.1 Original design of the Langevin underwater transducer and its acoustic power directivity.

wavelength) leads to better monitoring resolution of the objective, but also leads to a rapid decrease in the reachable distance. Notice that quartz single crystals were the only available piezoelectric material in the early twentieth century. Since the sound velocity in quartz is about 5 km/s, 40 kHz corresponds to the wavelength of 12.5 cm in quartz. If we use a mechanical resonance in the piezoelectric material, a 12.5/2 = 6.25 cm thick quartz single crystal piece is required. However, in that period, it was not possible to produce such large single crystals.

In order to overcome this dilemma, Langevin invented a new transducer construction; small quartz crystals arranged in a mosaic were sandwiched by two steel plates. Since the sound velocity in steel is in a similar range to quartz, taking 6.25 cm in the total thickness, he succeeded to set the thickness resonance frequency around 40 kHz. This sandwich structure is called 'Langevin type', which remains in common use today. Notice that quartz is located at the center, which corresponds to the nodal plane of the thickness vibration mode, where the maximum stress/strain (or the minimum displacement) is generated.

Further, in order to provide a sharp directivity for the sound wave, Langevin used a sound radiation surface with a diameter of 26 cm (more than double of the wavelength). Since the half-maximum-power angle ϕ can be evaluated as

$$\phi = 30 \times (\lambda/2a)\ [^\circ], \tag{15.1}$$

where λ is the wavelength in the transmission medium (not in steel) and a

is the radiation surface radius, if we use λ = 1500 [m/s]/40 [kHz] = 3.75 cm, a = 13 cm, we obtain ϕ = 4.3° for this original design. He succeeded in practice in detecting a submarine 3000 m away. Furthermore, Langevin also observed many bubbles generated during his experiments, which seems to be the 'cavitation' effect.

15.2.2 Cymbal transducer

Single 'cymbal'

A composite actuator structure called the 'moonie' has been developed to amplify the pressure sensitivity and the small displacements induced in a piezoelectric ceramic.[4] The moonie has characteristics intermediate between the conventional multilayer and bimorph actuators; it exhibits an order of magnitude larger displacement (100 μm) than the multilayer, and a much larger generative force (10 kgf) with a quicker response (100 μsec) than the bimorph. This device consists of a thin multilayer ceramic element and two metal plates with a narrow moon-shaped cavity bonded together as shown in Fig. 15.2(a). A moonie with dimensions 5 mm × 5 mm × 2.5 mm can generate a 20 μm displacement under an applied voltage of 60 V, which is eight times as large as the generative displacement of a multilayer of similar dimensions.[5] A displacement twice that of the moonie can be obtained with the 'cymbal' design pictured in Fig. 15.2(b) and (c). The generative

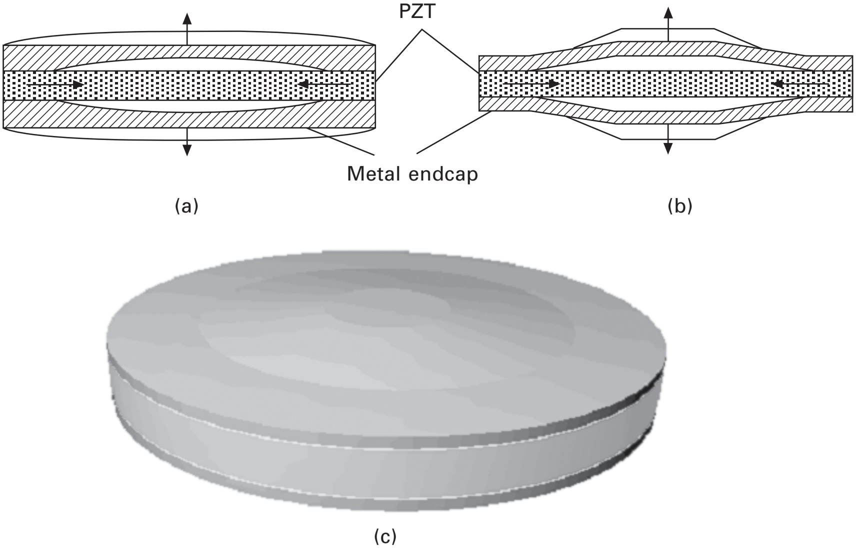

15.2 Flextensional structures: (a) the moonie, (b) the cymbal, and (c) cymbal appearance.

displacement of this device is quite uniform, showing negligible variation for points extending out from the center of the endcap.[5] Another advantage the cymbal has over the moonie is its relatively simple fabrication. The endcaps for this device are made in a single-step punching process that is both simpler and more reproducible than the process involved in making the endcaps for the moonie structure.

A ‘cymbal’ is a sort of displacement amplifier, and also fits well with water in view of its relatively low acoustic impedance. Compared to the Langevin type, the cymbal has very thin profile, is light-weight, and is easy to assemble into an array. Figures 15.3 and 15.4 compare the ATILA simulation and the experimental result in terms of transmitting voltage response (TVR) as functions of beam directivity and operating frequency, respectively. Note first that a single cymbal under water works as an almost-uniform mono-pole sound source. The TVR response is relatively flat from 20 to 60 kHz.

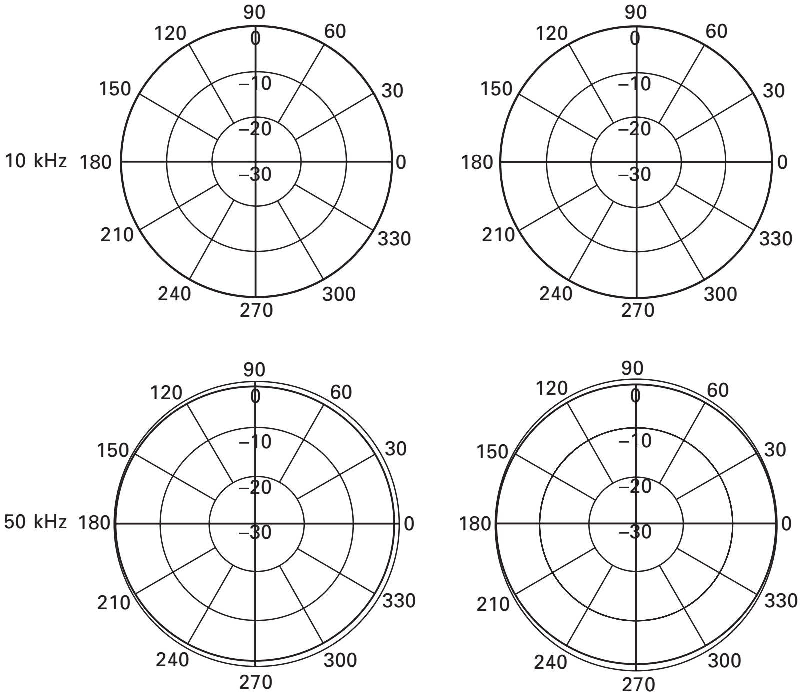

Measured (potted in polyurethane)

Calculated

15.3 Beam patterns of a single cymbal under different conditions. The cymbal symmetric axis is along the horizontal axis.

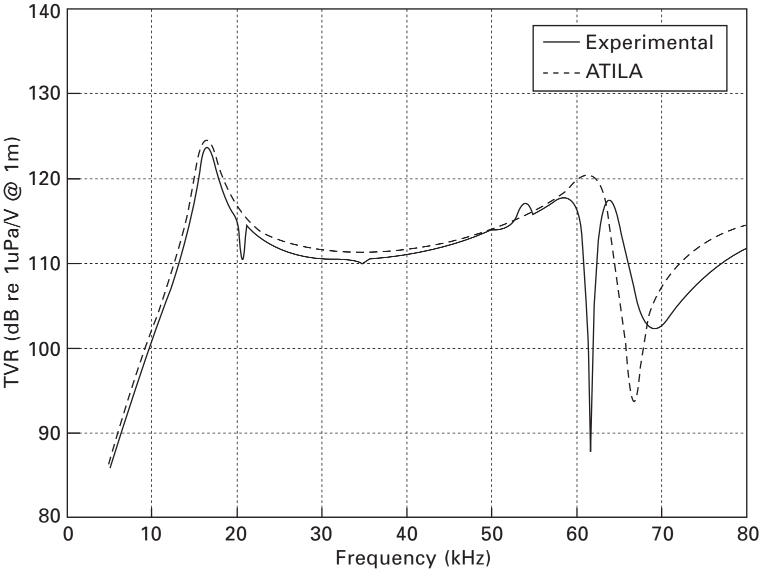

15.4 Comparison of the ATILA simulation and the experimental result in terms of transmitting voltage response (TVR) as a function of frequency.

Cymbal array

A 3 × 3 cymbal array shown in Fig. 15.5(a) was developed for underwater sonar application at The Penn State University, and analyzed by ATILA simulation and experimentally measured.[6] The resonance frequency of the unit cymbal was 17 kHz.

When all the cymbals are identical and driven at 17 kHz under water, the displacements of the center, edge and corner cymbals are calculated as in Fig. 15.6(a). The definitions of the center, edge and corner transducers are illustrated in Fig. 15.5(b). Interestingly, the center cymbal excites a significant magnitude, while the corner cymbal does not generate a displacement. Thus, experimentally, the center cymbal collapse was observed occasionally during operation. This peculiar non-uniform distribution of the displacement originates from the mutual interaction of these three (center, edge and corner) cymbals through the water.

This problem can be solved by slightly modifying the cymbal performance; that is, when the resonance frequencies of the center, edge and corner cymbals are adjusted to 17 kHz, 16 kHz and 18 kHz, respectively, as shown in Fig. 15.6(b), rather uniform displacements are obtained for these cymbal transducers. In conclusion, the significant interaction originates from the totally identical cymbal transducer choice, and this may not be observed in practice, due to a slight deviation in transducer performance of each

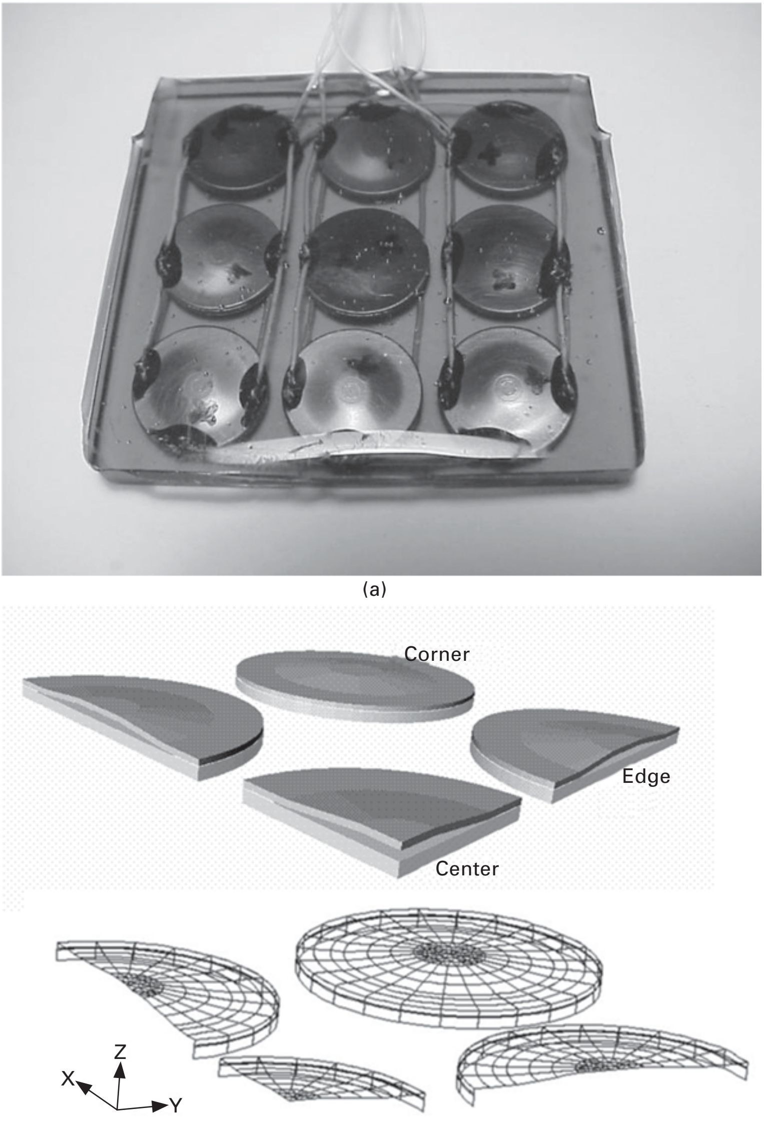

(a)

(b)

15.5 (a) A 3 × 3 cymbal array, and (b) ATILA simulation model of the cymbal array.

cymbal. A slight deviation of performance helps with decoupling the mutual interaction between these cymbals.

Figure 15.7 shows the measured and calculated (point source model) beam patterns of the 3 × 3 cymbal array. Unlike the situation of a single cymbal, the array increased the sound beam directivity dramatically with

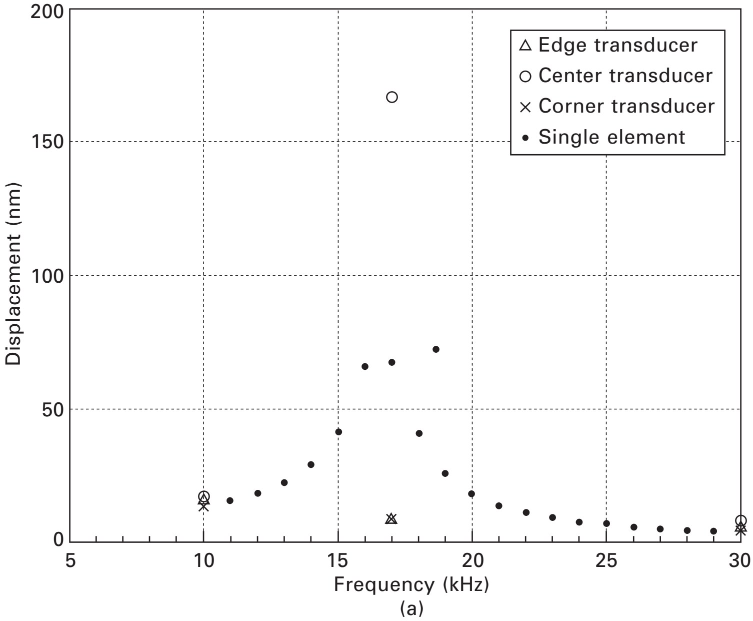

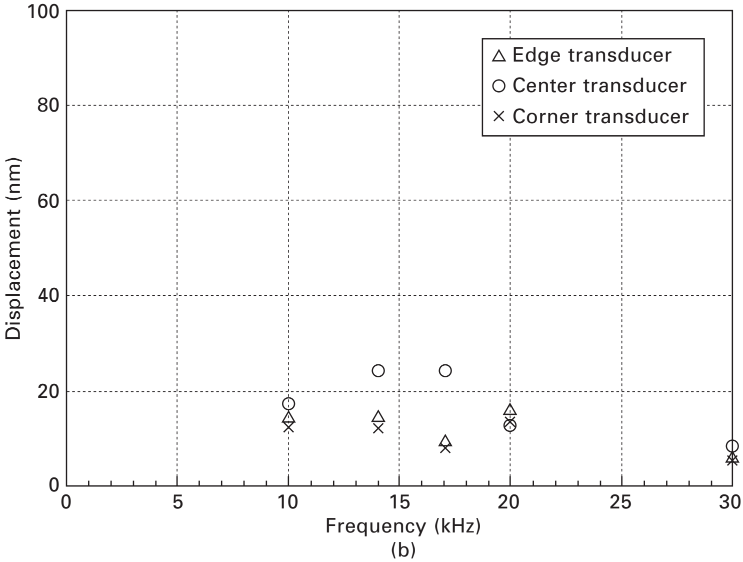

15.6 (a) The displacements of the center, edge and corner identical cymbals in a 3 × 3 array driven at 17 kHz under water. Note that the center cymbal generates a significant magnitude. (b) The displacements of the center, edge and corner identical cymbals in a 3 × 3 array driven at 17 kHz under water. Three slightly deviated cymbals are arrayed in this structure (center 17 kHz, edge 16 kHz and corner 18 kHz).

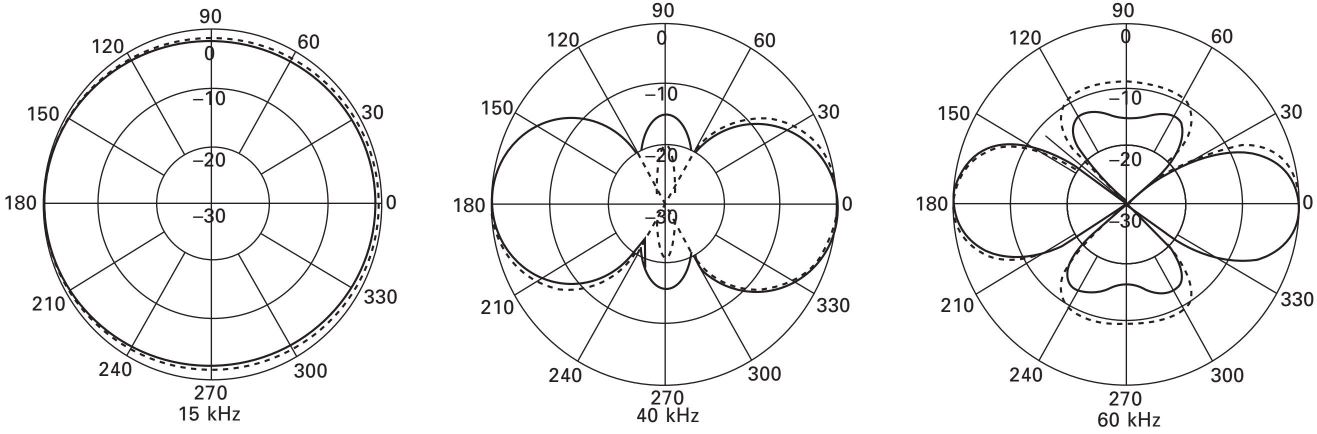

15.7 Measured and calculated (point source model) beam patterns of the 3 × 3 array. The cymbal array plane vector is along the horizontal axis.

changing the drive frequency. In general, the multiple cymbal array provides the following benefits:

- Transmitting voltage response increases with the number of cymbals.
- Beam maneuverability is improved; 15 kHz is used for wide-angle surveillance, and 60 kHz can be used for narrow-angle detailed surveillance.

15.3 Acoustic lens and horn

15.3.1 Acoustic lens

A dolphin is one of the best animals to explain the ideal acoustic transducer systems. Dolphins and whales do not have vocal chords, but a breathing hole on the head, as shown in Fig. 15.8. By breathing strongly through this hole, a dolphin can generate sound like a human whistle. Though this breathing hole is a point sound source, because of additional physical structures, the sound beam can be focused quite sharply toward the front direction (Fig. 15.8 bottom). The cranium shape seems to be a parabola antenna, which reflects the radial propagating sound into a rather parallel frontward beam. Further, ‘melon’ made of soft tissue like paraffin (with a sound velocity lower than water) behaves as a convex acoustic lens, and focuses the sound beam more sharply. It is notable that if we use a glass lens with a sound velocity higher than water, a convex shape acoustic lens diverges the sound beam (like an optical concave lens). This is the initial sound transmitting process.

In order to receive the returned sound signal reflected from some object, if the strong original transmitting signal transfers directly to the receiving organ (ear), a serious blackout problem occurs. In order to overcome this problem, the dolphin has an acoustic impedance mismatch layer (air), which behaves like a double-glazed window for shutting out the noise.

The dolphin’s receiver is its bottom jaws, through which the sound is transferred to the ear. Notice that the highly sensitive ear is isolated from the cranium bones to protect it from direct sound penetration. This situation is rather different from the human ear, which is connected directly to the bones (in fact, we have a head set that uses direct bone transmission of sound for a hearing aid). Since the dolphin has completely separated right and left jaws, the two ears can detect the right and left sound signals independently, like a 3D stereo system.

15.3.2 Acoustic horn

The original steel portion of the Langevin transducer can be modified with a ‘horn’ concept to increase the displacement amplitude. By tapering the steel tip portion as shown in Fig. 15.9, we can significantly amplify the

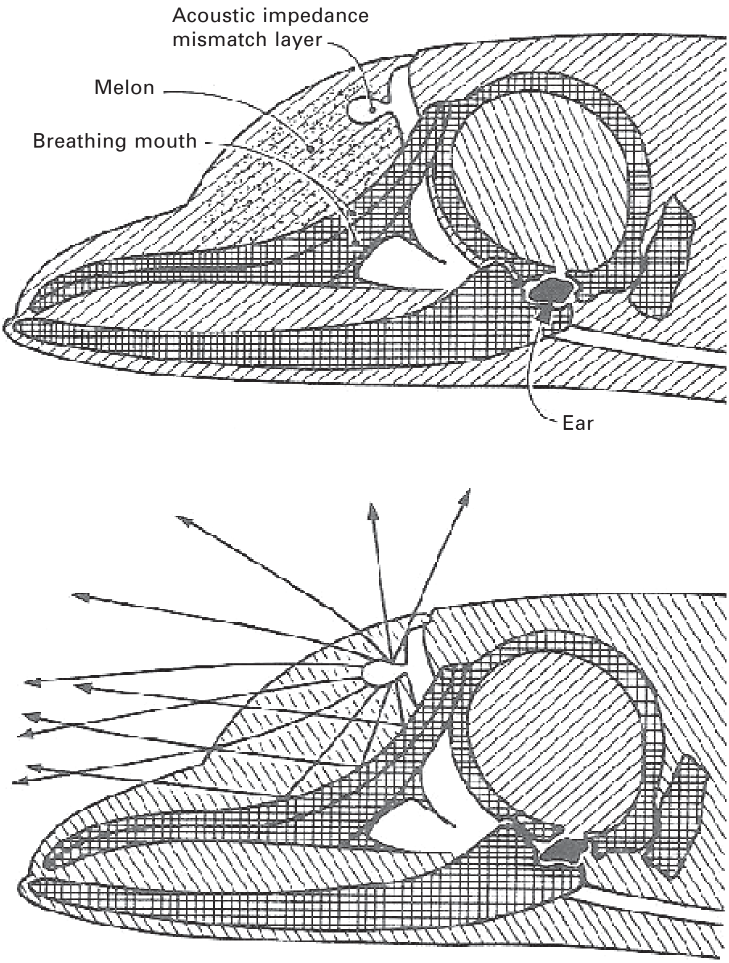

15.8 Dolphin head: mesh portion = bone, hatched portion = soft tissue, white portion = air, black portion = ear. Top figure exhibits the biological names, and the bottom illustrates the acoustic beam radiation situation.

displacement level, which can be utilized for ultrasonic cutters and cavitation instruments.

For a resonance mode, the most popular displacement amplification mechanism is a horn. Figure 15.10 illustrates some of the horn configurations. The axial displacement is increased in inverse proportion to the radius of the vibrator. These three samples exhibit the following features:

- Exponential taper: highest efficiency, but costly to manufacture.
- Straight taper: cheaper to manufacture, with a reasonable efficiency.
- Step type: cheapest, but some mechanical energy is bounced back.

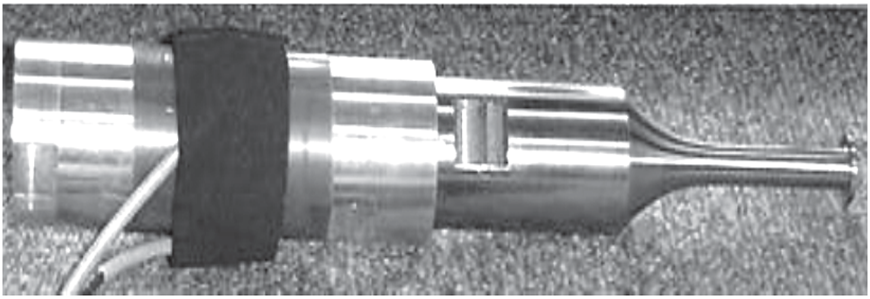

15.9 Langevin transducer with a horn (courtesy of Honda Electronics, Japan).

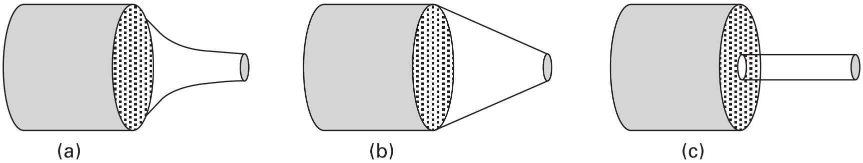

15.10 Three example configurations of the horn: (a) exponential taper; (b) straight taper; (c) step type.

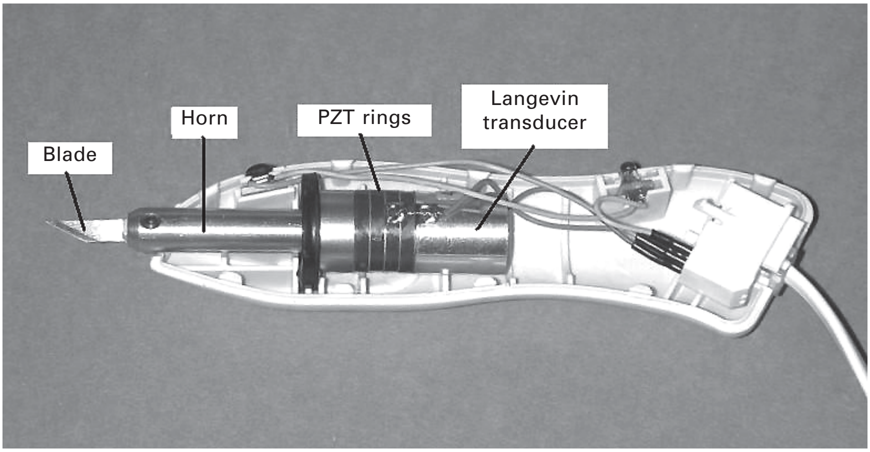

15.11 Ultrasonic cutter with a Langevin type transducer and a step-type horn at the tip (Courtesy of Honda Electronics, Japan).

Figure 15.11 shows a commercialized ultrasonic cutter with a Langevin type transducer. Note the step-type horn at the tip.

When we use a concave radiation surface for a high frequency wave (GHz) at the tip of the horn, as illustrated in Fig. 15.12, we can focus the acoustic beam into 0.1 mm range, which can be used as an acoustic microscope.

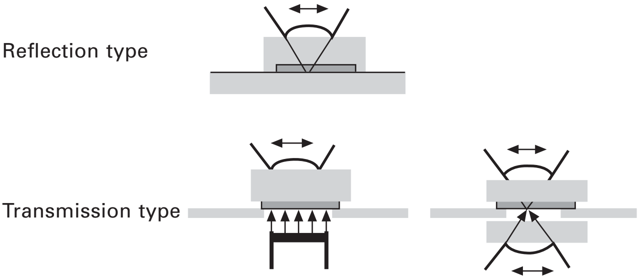
Reflection type
Transmission type

15.12 Classification of mechanical scan acoustic microscopes (SAM).

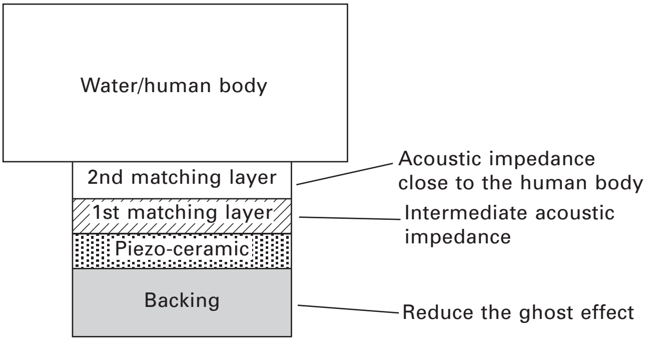
Water/human body
2nd matching layer
1st matching layer
Piezo-ceramic
Backing
Acoustic impedance close to the human body
Intermediate acoustic impedance
Reduce the ghost effect

15.13 Acoustic transducer design for medical imaging applications.

There are two acoustic microscope types: reflection type and transmission type. This acoustic microscope is helpful for detecting a cancer portion with a harder elasticity than a normal portion in a patient tissue.

15.4 Acoustic impedance matching

If we increase the driving frequency of the fish-finder by 70 times (50 kHz), that is, 3.5 MHz, we can increase the resolution by 70 times, and this can be used to detect the infant situation in the human body. However, the practical situation is not so easy. Since the piezoelectric ceramic (such as PZT) has very large acoustic impedance in comparison with the human body (like water), most high power ultrasonic sound is reflected at the interface, and the transmitted sound power is very low. In order to transmit the sound energy effectively, we need to suitably design the acoustic impedance matching layer. When the acoustic impedances of PZT and water are Z_1 and Z_2, the recommended matching impedance of the matching layer is $\sqrt{(Z_1 Z_2)}$. As shown in Fig. 15.13, we sometimes use multiple matching layers. Also like a dolphin, the backing layer is used for reducing the ghost effect. Soft rubber is commonly used as a backing material.

15.5 Ultrasonic imaging application

One of the most important applications is based on ultrasonic echo field.[7,8] Ultrasonic transducers convert electrical energy into mechanical form when generating an acoustic pulse and convert mechanical energy into an electrical signal when detecting its echo. The transmitted waves propagate into a body and echoes are generated which travel back to be received by the same transducer. These echoes vary in intensity according to the type of tissue or body structure, thereby creating images. An ultrasonic image represents the mechanical properties of the tissue, such as *density* and *elasticity*. We can recognize anatomical structures in an ultrasonic image since the organ boundaries and fluid-to-tissue interfaces are easily discerned. The ultrasonic imaging process can also be performed in real time. This means we can follow rapidly moving structures such as the heart without motion distortion. In addition, ultrasound is one of the safest diagnostic imaging techniques. Unlike X-rays, it does not use ionizing radiation and thus is routinely used for fetal and obstetrical imaging. Useful areas for ultrasonic imaging include cardiac structures, the vascular systems, the fetus and abdominal organs such as liver and kidney. In brief, it is possible to see inside the human body without breaking the skin by using a beam of ultrasound.

Figure 15.14 shows the basic ultrasonic transducer geometry. The transducer is mainly composed of matching piezoelectric material and backing layers.[9] One or more matching layers are used to increase sound transmissions into tissues. The backing is added to the rear of the transducer in order to damp the acoustic backwave and to reduce the pulse duration. Piezoelectric materials are used to generate and detect ultrasound. In general, broadband transducers should be used for medical ultrasonic imaging. The broad bandwidth response corresponds to a short pulse length, resulting in better axial resolution. Three

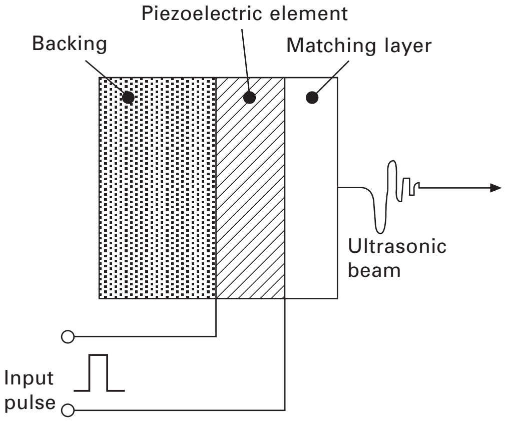

15.14 Basic transducer geometry for acoustic imaging applications.

factors are important in designing broad bandwidth transducers; *acoustic impedance matching*, a *high electromechanical coupling coefficient* of the transducer, and *electrical impedance matching*. These pulse echo transducers operate based on thickness mode resonance of the piezoelectric thin plate. Further, a low planar mode coupling coefficient, k_p, is beneficial for limiting energies being expended in non-productive lateral mode. A large dielectric constant is necessary to enable a good electrical impedance match to the system, especially with tiny piezoelectric sizes.

There are various types of transducers used in ultrasonic imaging. Mechanical sector transducers consist of single, relatively large resonators and can provide images by mechanical scanning such as wobbling. Multiple element array transducers permit discrete elements to be individually accessed by the imaging system and enable electronic focusing in the scanning plane to various adjustable penetration depths through the use of phase delays. Two basic types of array transducers are linear and phased (or sector). A linear array is a collection of elements arranged in one direction, producing a rectangular display (see Fig. 15.15). A curved linear (or convex) array is a modified linear array whose elements are arranged along an arc to permit

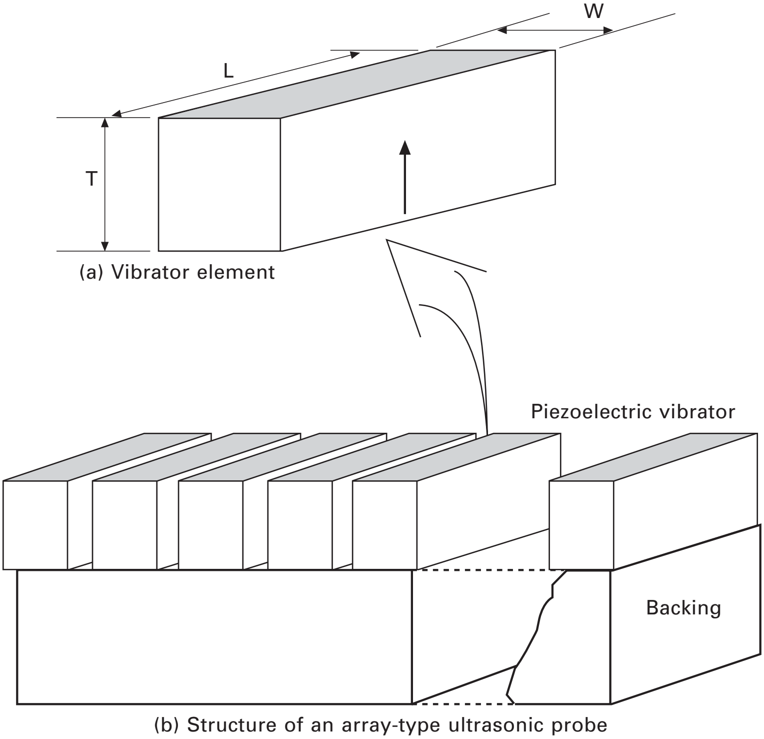

15.15 Linear array type ultrasonic probe.

an enlarged trapezoidal field of view (see Fig. 15.16). The elements of these linear type array transducers are excited sequentially group by group with the sweep of the beam in one direction. These linear array transducers are used for radiological and obstetrical examinations. On the other hand, in a phased array transducer the acoustic beam is steered by signals that are applied to the elements with delays, creating a sector display. This transducer is useful for cardiology applications where positioning between the ribs is necessary.

Figure 15.17 demonstrates the superiority of the PZN–PT single crystal to the PZT ceramic for the medical imaging transducer application, developed

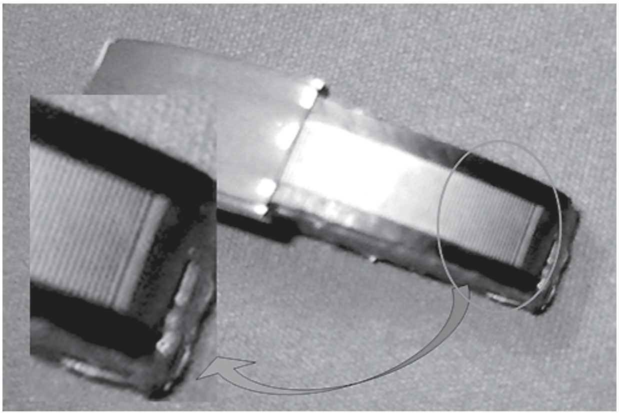

15.16 Curved linear (or convex) array whose elements are arranged along an arc to permit an enlarged trapezoidal field of view (courtesy of Honda Electronics, Japan).

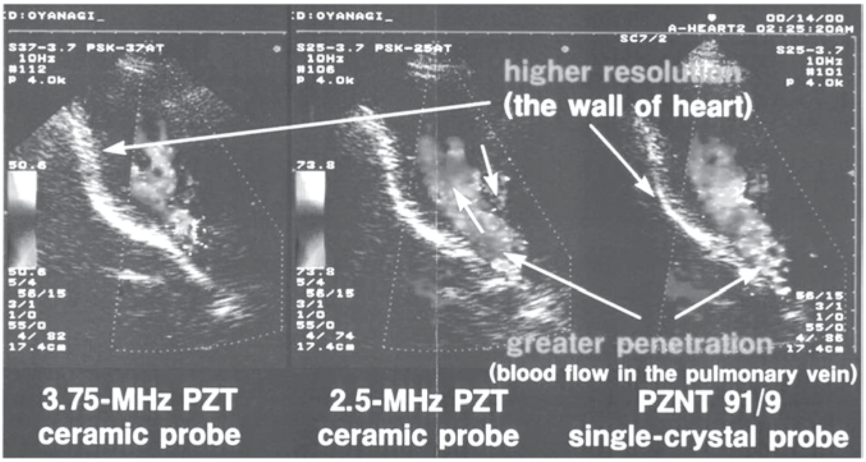
D:OYANAGI_
S37-3.7 PSK-37AT
10Hz
#112
P 4.0k
50.6
50.6
5/4
56/15
3/1
1/0
55/0
4/ 82
17.4cm
D:OYANAGI_
S25-3.7 PSK-25AT
10Hz
#106
P 4.0k
73.8
73.8
5/4
56/15
3/1
1/0
55/0
4/ 74
17.4cm
00/14/00
A-HEART2 02:25:20AM
SC7/2
S25-3.7
10Hz
#101
P 4.0k
56/15
3/1
1/0
55/0
4/ 86
17.4cm
higher resolution
(the wall of heart)
greater penetration
(blood flow in the pulmonary vein)
3.75-MHz PZT
ceramic probe
2.5-MHz PZT
ceramic probe
PZNT 91/9
single-crystal probe

15.17 Ultrasonic imaging with the two PZT ceramic probes (left) and with the PZN–PT single crystal probe (right) (courtesy of Toshiba).

by Toshiba Corporation.[10] Conventionally, the medical doctor needs to use two different frequency PZT probes, one is 2.5 MHz for checking wider and deeper areas, and the other is 3.75 MHz for monitoring the specified area with a better resolution. The PZN–PT single crystal (with very high k_{33} and k_t) probe provides two additional merits: wide bandwidth – without changing the probe, the doctor can just switch the drive frequency from 2.5 to 3.75 MHz, and strong signal – because of the high electromechanical coupling, the receiving signal level is enhanced more than double compared with the PZT probe.

15.6 Sono-chemistry

Fundamental research on 'sono-chemistry' is now ongoing very rapidly. Using the 'cavitation' effect, toxic materials such as dioxin and trichloroethylene can be easily transformed into innocuous materials at room temperature. Ultrasonic distillation is also possible at room temperature for obtaining highly concentrated Japanese 'Sake'. Unlike the regular boiling distillation, this new method makes 'Sake' with much higher alcohol content while keeping the gorgeous taste and fragrance. Figure 15.18(a) shows the alcoholic concentration in the base solution and mist. Note that the higher alcoholic concentration is obtained from a low concentration solution at the lower ambient temperature. Figure 15.18(b) shows an arrayed Langevin transducer system for the 'Sake' distillation application. This high-quality Sake product is now commercially available.[11]

High power ultrasonics can also be used in transdermal drug delivery. Desktop types have been commercialized as shown in Fig. 15.19(a). The Penn State researchers are now working on a 'needle-free' injection system for insulin by using cymbal piezo-actuators in a portable fashion (see Fig. 15.19(b)).[12]

15.7 Acknowledgements

The author owes a great debt of gratitude to Dr Nagaya Okada at Honda Electronics, Japan for his help with providing Honda's products that have been used in this article. Also much of the content and figures have been taken from the author's textbooks (Refs. 1–3), published by CRC Press, New York.

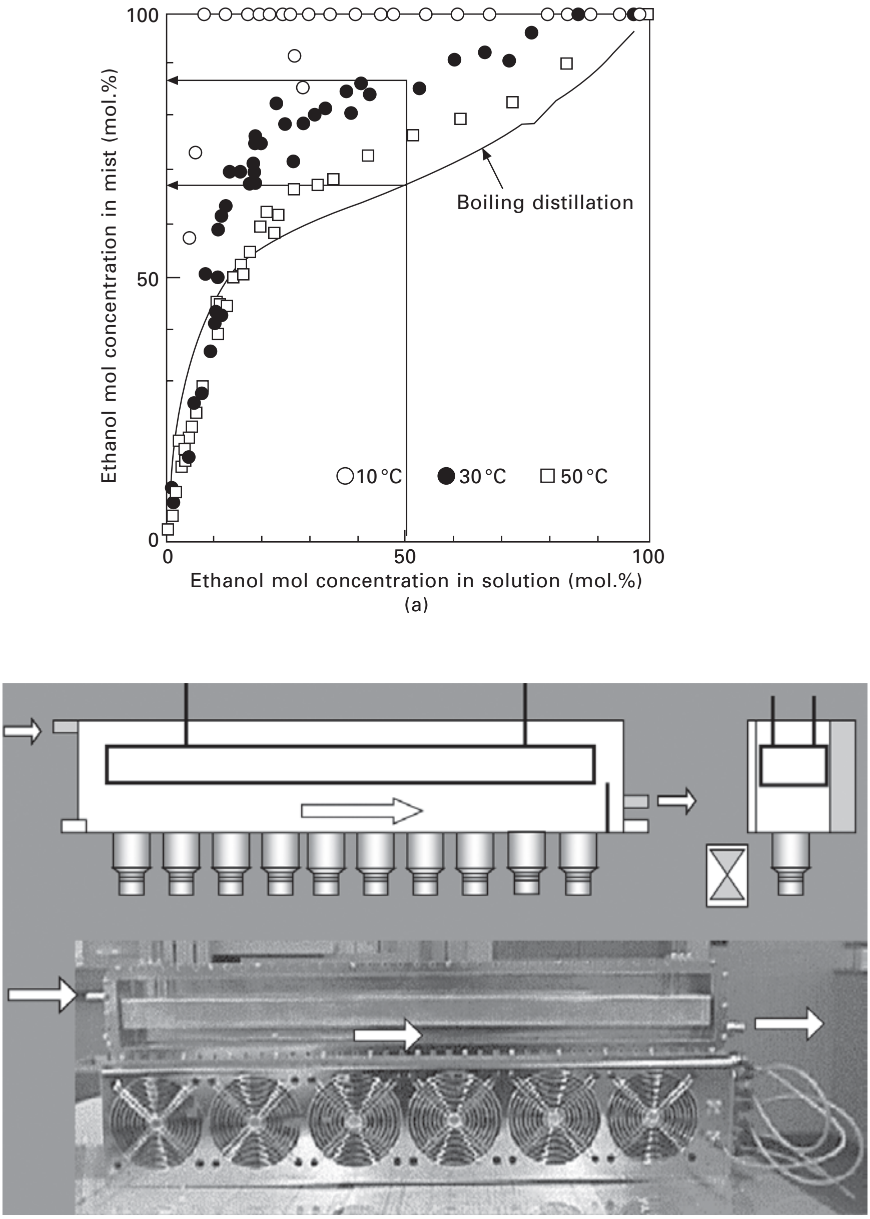

(a)

(b)

15.18 (a) Low temperature distillation with high power ultrasonic (courtesy by Matsuura Brewer, Japan), and (b) arrayed Langevin transducer system for the 'Sake' distillation application (courtesy of Honda Electronics, Japan).

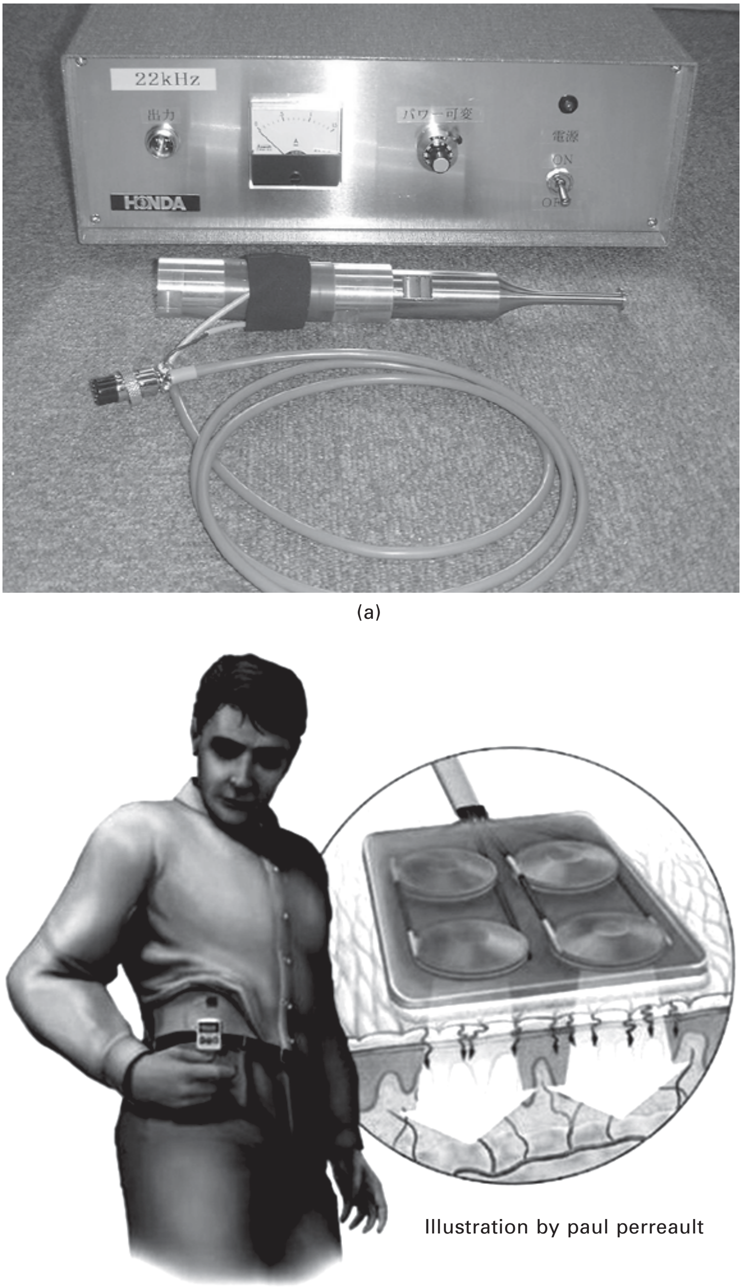

(a)

Illustration by paul perreault

(b)

15.19 (a) Desktop 'Sonicater' for drug delivery (courtesy of Honda Electronics, Japan), and (b) portable transdermal insulin drug delivery system using cymbal transducers (cited from *Popular Mechanics*).

15.8 References

1. K. Uchino and J. R. Giniewics, *Micromechatronics*, CRC Press, New York (2003).
2. K. Uchino, *FEM and Micromechatronics with ATILA Software*, CRC Press, New York (2008).
3. K. Uchino, *Ferroelectric Devices*, 2nd edn, CRC Press, New York, (2009).
4. H. Goto, K. Imanaka and K. Uchino, *Ultrasonic Techno*, **5**, 48 (1992).
5. A. Dogan, Ph.D. Thesis, Penn State University (1994).
6. J. Zhang, W. J. Hughes, P. Bouchilloux, R. J. Meyer Jr., K. Uchino and R. E. Newnham, *Ultrasonics*, **37**, 387–393 (1999).
7. B. A. Auld, *Acoustic Fields and Waves in Solids*, 2nd edn., Melbourne: Robert E. Krieger (1990).
8. G. S. Kino, *Acoustic Waves: Device Imaging and Analog Signal Processing*, Englewood Cliffs, NJ: Prentice-Hall (1987).
9. C. S. Desilets, J. D. Fraser and G. S. Kino, *IEEE Trans. Sonics Ultrason.*, SU-25, 115 (1978).
10. S. Saitoh, T. Takeuchi, T. Kobayashi, K. Harada, S. Shimanuki and Y. Yamashita, *Jpn. J. Appl. Phys.*, **38** (5B), 3380–3384 (1999).
11. http://www.shumurie.co.jp
12. *Popular Mechanics*, **180** (3), p. 20 (2003).

Part III

Application oriented materials development

16

High power piezoelectric materials

K. UCHINO, The Pennsylvania State University, USA

Abstract: Heat generation is one of the significant problems in piezoelectrics for high power density applications. In this chapter, we review first the loss mechanisms in piezoelectrics, followed by the experimental techniques to measure dielectric, elastic and piezoelectric losses separately. Second, heat generation processes for various drive conditions are discussed. Heat generation at off-resonance is attributed mainly to intensive dielectric loss $\tan \delta'$ (i.e., Polarization (P) – Field (E) hysteresis loss), not to mechanical loss, while the heat generation at resonance originates mainly from the intensive mechanical loss $\tan \phi'$. Third, the maximum vibration velocity and the mechanical quality factor (an amplification factor of the impedance or displacement of a piezoelectric at its resonant status) are discussed in terms of driving voltage level. Fourth, practical high power 'hard' $Pb(Zr,Ti)O_3$ (PZT)-based materials are introduced, which exhibit vibration velocities more than 1 m/s, leading to the power density capability 10 times that of commercially available 'hard' PZTs. We propose an internal bias field model to explain the low loss and high power origin of these materials, which are suitable for actuator (ultrasonic motor) applications. We also describe 'semi-hard' materials based on PZT–$Pb(Zn,Nb)O_3$–$Pb(Ni, Nb)O_3$, with reasonable electromechanical coupling k factors, which are suitable for piezoelectric transducers. Finally, using a low temperature sinterable 'semi-hard' PZT, we demonstrate high power multilayer piezoelectric transformers with Cu or Ag internal electrodes.

Key words: high power piezoelectrics, heat generation, loss mechanism, mechanical quality factor, vibration velocity, hard PZT.

16.1 Introduction

Loss or hysteresis in piezoelectrics exhibits both merits and demerits. For positioning actuator applications, hysteresis in the field-induced strain causes a serious problem, and for resonance actuation such as ultrasonic motors, loss generates significant heat in the piezoelectric materials. Further, in consideration of the resonant strain amplified in proportion to a mechanical quality factor, low (intensive) mechanical loss materials are preferred for ultrasonic motors. In contrast, for force sensors and acoustic transducers, a low mechanical quality factor Q_m (which corresponds to high mechanical loss) is essential to widen the frequency range for receiving signals.

Haerdtl wrote a review article on electrical and mechanical losses in ferroelectric ceramics.[1] Losses are considered to consist of four portions:

- domain wall motion,
- fundamental lattice portion, which should also occur in domain-free monocrystals,
- microstructure portion, which occurs typically in polycrystalline samples, and
- conductivity portion in highly-ohmic samples.

However, in the typical piezoelectric ceramic case, the loss due to the domain wall motion exceeds the other three contributions significantly. Haerdtl reported interesting experimental results on the relationship between electrical and mechanical losses in piezoceramics, $Pb_{0.9}La_{0.1}(Zr_{0.5}Ti_{0.5})_{1-x}Me_xO_3$, where Me represents the dopant ions Mn, Fe, or Al and x varies between 0 and 0.09. However, Haerdtl measured the mechanical losses on poled ceramic samples, while the electrical losses were measured on unpoled samples, i.e., in a different polarization state, which lead to an ambiguity in the discussion.

Few systematic studies of the loss mechanisms in piezoelectrics have been reported, particularly in high electric field and high power density ranges. Although some of the formulas in this chapter were described by Ikeda in his textbook,[2] the piezoelectric losses, which have been found in our investigations to play an important role, were totally neglected. In this chapter, we review first the loss mechanisms in piezoelectrics, followed by the experimental techniques to measure dielectric, elastic and piezoelectric losses separately. Second, heat generation processes for various drive conditions are discussed. Third, the maximum vibration velocity and the mechanical quality factor (an amplification factor of the impedance or displacement of a piezoelectric at its resonant status) are discussed in terms of driving voltage level. Fourth, practical high power 'hard' $Pb(Zr,Ti)O_3$ (PZT)-based materials are introduced, which exhibit a vibration velocity of more than 1 m/s. The power density of these materials is 10 times that of commercially available 'hard' PZTs, which is suitable to actuator (ultrasonic motor) applications. We also describe 'semi-hard' materials based on $PZT–Pb(Zn,Nb)O_3–Pb(Ni,Nb)O_3$, with reasonable electromechanical coupling k factors, which are suitable for piezoelectric transducers. Finally, using a low temperature sinterable 'semi-hard' PZT, we demonstrate high power multilayer piezoelectric transformers with Cu or Ag internal electrodes.

The terminologies, 'intensive' and 'extensive' losses are introduced in relation to 'intensive' and 'extensive' parameters in the phenomenology. These are not directly related to the 'intrinsic' and 'extrinsic' losses which were introduced to explain the loss contribution from the mono-domain single crystal state, among others.[3] In this chapter, our discussion is focused on the 'extrinsic' losses, in particular, domain-reorientation originated losses.

16.2 General consideration of loss and hysteresis in piezoelectrics

16.2.1 Theoretical formulas

Since the detailed mathematical treatment has been described in a previous paper,[4] we just summarize the results in this section. We start from the following two piezoelectric equations:

$$x = s^{E} X + \mathrm{d}E, \tag{16.1}$$

$$D = \mathrm{d}\, X + \varepsilon^{X} \varepsilon_0 E, \tag{16.2}$$

where x is strain, X, stress, D, electric displacement, E, electric field. Equations 16.1 and 16.2 are expressed in terms of intensive (i.e., externally controllable) physical parameters X and E. The elastic compliance s^E, the dielectric constant ε^X and the piezoelectric constant d are temperature-dependent. Note that, in general, the piezoelectric equations cannot yield a delay-time-related loss without taking into account irreversible thermodynamic equations or dissipation functions. However, the latter considerations are mathematically equivalent to the introduction of complex physical constants into the phenomenological equations, if the loss is small and can be treated as a perturbation.

Therefore, we will introduce complex parameters ε^{X*}, s^{E*} and d^* in order to consider the hysteresis losses in dielectric, elastic and piezoelectric coupling energy:

$$\varepsilon^{X*} = \varepsilon^{X} (1 - j \tan \delta'), \tag{16.3}$$

$$s^{E*} = s^{E} (1 - j \tan \phi'), \tag{16.4}$$

$$d^{*} = d\, (1 - j \tan \theta'). \tag{16.5}$$

θ' is the phase delay of the strain under an applied electric field, or the phase delay of the electric displacement under an applied stress. Both delay phases should be exactly the same if we introduce the same complex piezoelectric constant d^* into Eqs 16.1 and 16.2. δ' is the phase delay of the electric displacement to an applied electric field under a constant stress (e.g., zero stress) condition, and ϕ' is the phase delay of the strain to an applied stress under a constant electric field (e.g., short-circuit) condition. We will consider these phase delays as ‘intensive’ losses.

Figure 16.1(a)–(d) corresponds to the model hysteresis curves for practical experiments: D vs. E curve under a stress-free condition, x vs. X under a short-circuit condition, x vs. E under a stress-free condition and D vs. X under a short-circuit condition for measuring current, respectively. Note that these measurements are easily conducted in practice.

Since the area on the D-E and x-X domains exhibits directly the electrical and mechanical energies, respectively (see Fig. 16.1(a) and (b)), the stored

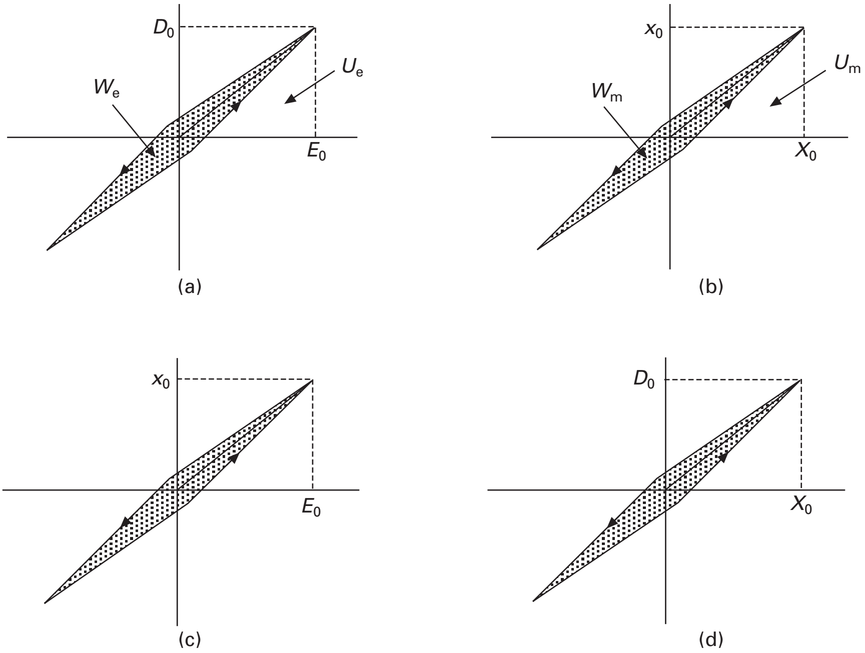

16.1 (a) *D* vs. *E* (stress free), (b) *x* vs. *X* (short-circuit), (c) *x* vs. *E* (stress free) and (d) *D* vs. *X* (short-circuit) curves with a slight hysteresis in each relation.

energies and hysteresis losses for pure dielectric and elastic energies can be calculated as:

$$U_e = (1/2)\, \varepsilon^X \varepsilon_0\, E_0^2, \tag{16.6}$$

$$W_e = \pi\, \varepsilon^X \varepsilon_0\, E_0^2 \tan \delta', \tag{16.7}$$

$$U_m = (1/2)\, s^E\, X_0^2, \tag{16.8}$$

$$W_m = \pi\, s^E\, X_0^2 \tan \phi'. \tag{16.9}$$

The electromechanical hysteresis losses are more complicated, since the area on the *x*-*E* or *P*-*X* domain does not directly provide energy. The area on these domains can be calculated as follows, depending on the method of measurement; when measuring the induced strain under an electric field,

$$U_{em} = (1/2)\, (d^2/s^E)\, E_0^2, \tag{16.10}$$

and

$$w_{em} = \pi\, (d^2/s^E)\, E_0^2\, (2 \tan \theta' - \tan \phi'). \tag{16.11}$$

Note that the strain vs. electric field measurement should provide the combination of piezoelectric loss tan θ′ and elastic loss tan ϕ′. When we measure the induced charge under stress, the stored energy U_{me} and the hysteresis loss w_{me} during a quarter and a full stress cycle, respectively, are obtained as

$$U_{me} = (1/2)\ (d^2/\varepsilon_0\varepsilon^X)\ X_0^2, \qquad 16.12$$

$$W_{me} = \pi\ (d^2/\varepsilon_0\varepsilon^X)\ X_0^2\ (2 \tan \theta' - \tan \delta'). \qquad 16.13$$

Hence, from the measurements of D vs. E and x vs. X, we obtain tan δ' and tan ϕ', respectively, and either the piezoelectric (D vs. X) or converse piezoelectric measurement (x vs. E) provides tan θ' through a numerical subtraction.

So far, we have discussed the 'intensive' dielectric, mechanical and piezoelectric losses in terms of 'intensive' parameters X and E. In order to consider real physical meanings of the losses in the material, we will introduce the 'extensive' losses[4] in terms of 'extensive' parameters x and D. In practice, intensive losses are easily measurable, but extensive losses are not, but they are obtainable from the intensive losses. The extensive losses are essential when we consider a physical microscopic or semi-macroscopic model. When we start from the piezoelectric equations in terms of extensive physical parameters x and D,

$$X = c^D\ x - h\ D, \qquad 16.14$$

$$E = -\ h\ x + \kappa^x\kappa_0\ D, \qquad 16.15$$

we introduce the extensive dielectric, elastic and piezoelectric losses as

$$\kappa^{x*} = \kappa^x\ (1 + j \tan \delta), \qquad 16.16$$

$$c^{D*} = c^D\ (1 + j \tan \phi), \qquad 16.17$$

$$h^* = h\ (1 + j \tan \theta). \qquad 16.18$$

It is notable that the permittivity under a constant strain (e.g., zero strain or completely clamped) condition, ε^{x*} and the elastic compliance under a constant electric displacement (e.g., open-circuit) condition, s^{D*} can be provided as an inverse value of κ^{x*} and c^{D*}, respectively, in this simplest one-dimensional expression (in the case of a general 3-D expression, this part must be translated as 'inverse matrix components of κ^{x*} and c^{D*} tensors'). Thus, using exactly the same losses in Eqs 16.16 and 16.17:

$$\varepsilon^{x*} = \varepsilon^x(1 - j \tan \delta), \qquad 16.19$$

$$s^{D*} = s^D(1 - j \tan \phi), \qquad 16.20$$

we will consider these phase delays again as 'extensive' losses.

Here, we consider the physical property difference between the boundary conditions: E constant and D constant, or X constant and x constant in a simple 1D model. When an electric field is applied on a piezoelectric sample as illustrated at the top of Fig. 16.2, this state will be equivalent to the superposition of the following two steps: first, the sample is completely clamped and the field E_0 is applied (pure electrical energy (1/2) $\varepsilon^x\varepsilon_0 E_0^2$ is input); second, keeping the field at E_0, the mechanical constraint is released (additional mechanical energy (1/2) $(d^2/s^E) E_0^2$ is necessary). The total energy should correspond to the total input electrical energy (1/2) $\varepsilon^X\varepsilon_0 E_0^2$. Similar energy calculation can be obtained from the bottom part of Fig. 16.2, leading to the following equations:

$$\varepsilon^x/\varepsilon^X = (1 - k^2), \tag{16.21}$$

$$s^D/s^E = (1 - k^2), \tag{16.22}$$

$$\kappa^X/\kappa^x = (1 - k^2), \tag{16.23}$$

$$c^E/c^D = (1 - k^2), \tag{16.24}$$

where

$$k^2 = d^2/(s^E\ \varepsilon_0\varepsilon^X) = h^2/(c^D\ \kappa^x\kappa_0). \tag{16.25}$$

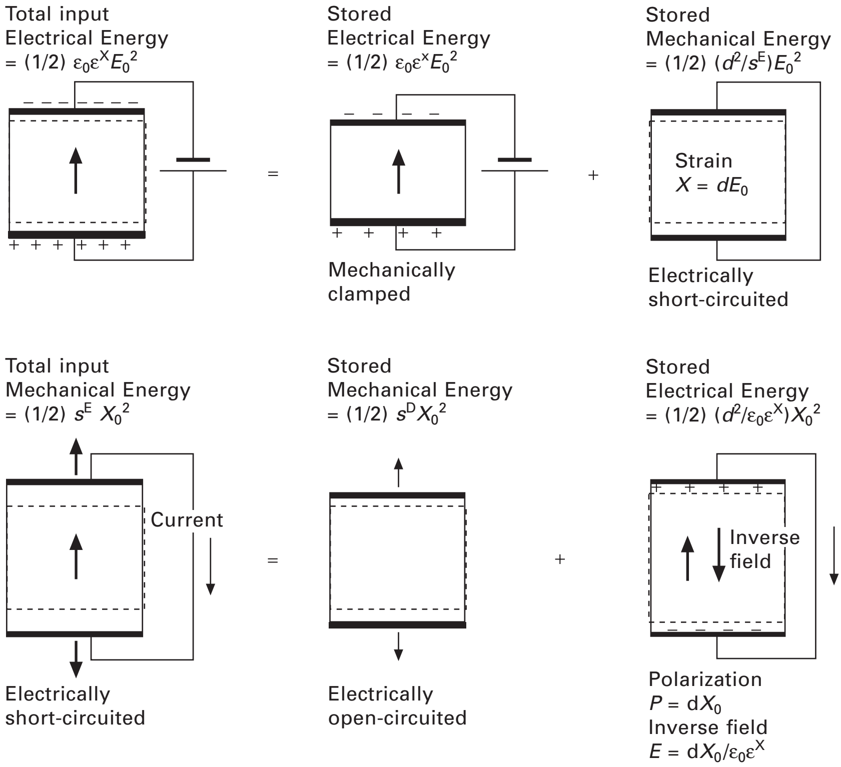
Total input
Electrical Energy
= (1/2) $\varepsilon_0\varepsilon^X E_0^2$
=
Stored
Electrical Energy
= (1/2) $\varepsilon_0\varepsilon^x E_0^2$
Mechanically
clamped
+
Stored
Mechanical Energy
= (1/2) $(d^2/s^E)E_0^2$
Strain
$X = dE_0$
Electrically
short-circuited
Total input
Mechanical Energy
= (1/2) $s^E X_0^2$
Current
Electrically
short-circuited
=
Stored
Mechanical Energy
= (1/2) $s^D X_0^2$
Electrically
open-circuited
+
Stored
Electrical Energy
= (1/2) $(d^2/\varepsilon_0\varepsilon^X)X_0^2$
Inverse
field
Polarization
$P = dX_0$
Inverse field
$E = dX_0/\varepsilon_0\varepsilon^X$

16.2 Conceptual figure for explaining the relation between ε^X and ε^x, s^E and s^D.

This k is called the *electromechanical coupling factor*, which is defined here as a real number.

In order to obtain the relationships between the intensive and extensive losses, the following three equations are essential:

$$\varepsilon_0\varepsilon^X = [\kappa^x\kappa_0\,(1 - h^2/(c^D\,\kappa^x\kappa_0))]^{-1}, \qquad 16.26$$

$$s^E = [c^D\,(1 - h^2/(c^D\,\kappa^x\kappa_0))]^{-1}, \qquad 16.27$$

$$d = [h^2/(c^D\,\kappa^x\kappa_0)]\,[h\,(1 - h^2/(c^D\,\kappa^x\kappa_0))]^{-1}. \qquad 16.28$$

Replacing the parameters in Eqs 16.26–16.28 by the complex parameters in Eqs 16.3–16.5 and 16.16–16.18, we obtain the relationships between the intensive and extensive losses:

$$\tan\delta' = (1/(1 - k^2))[\tan\delta + k^2(\tan\phi - 2\tan\theta)], \qquad 16.29$$

$$\tan\phi' = (1/(1 - k^2))[\tan\phi + k^2(\tan\delta - 2\tan\theta)], \qquad 16.30$$

$$\tan\theta' = (1/(1 - k^2))[\tan\delta + \tan\phi - (1 + k^2)\tan\theta], \qquad 16.31$$

where k is the electromechanical coupling factor defined by Eq. 16.25, and here as a real number. It is important that the intensive dielectric and elastic losses are mutually correlated with the extensive dielectric, elastic and piezoelectric losses through the electromechanical coupling k^2, and that the denominator $(1 - k^2)$ comes basically from the ratios, $\varepsilon^x/\varepsilon^X = (1 - k^2)$ and $s^D/s^E = (1 - k^2)$, and this real part reflects to the dissipation factor when the imaginary part is divided by the real part. The author emphasizes that the extensive losses are more important for considering the physical micro/macroscopic models, and can be obtained mathematically from a set of intensive losses, which can be obtained more easily experimentally.

Expanding the discussion above, we introduce various loss formulas, as summarized in Fig. 16.3, where the relationship between the vibration mode and the corresponding elastic loss formula is provided.

16.2.2 Loss measuring technique I – pseudo-static method

We determined 'intensive' dissipation factors, $\tan\delta'$, $\tan\phi'$, and $\tan\theta'$, separately from (a) D vs. E (stress free), (b) x vs. X (short-circuit), (c) x vs. E (stress free) and (d) D vs. X (short-circuit) curves for a soft PZT-based multilayer actuator.[5] Using a stress applying jig shown in Fig. 16.4, we measured the x vs. X and D vs. X relationships. Figure 16.5 summarizes intensive loss factors, $\tan\delta'$, $\tan\phi'$ and $\tan\theta'$ as a function of electric field or compressive stress, measured for a 'soft' PZT-based actuator. Note first that the piezoelectric loss $\tan\theta'$ is not negligibly small as believed by previous researchers, but rather large, comparable to the dielectric and elastic losses;

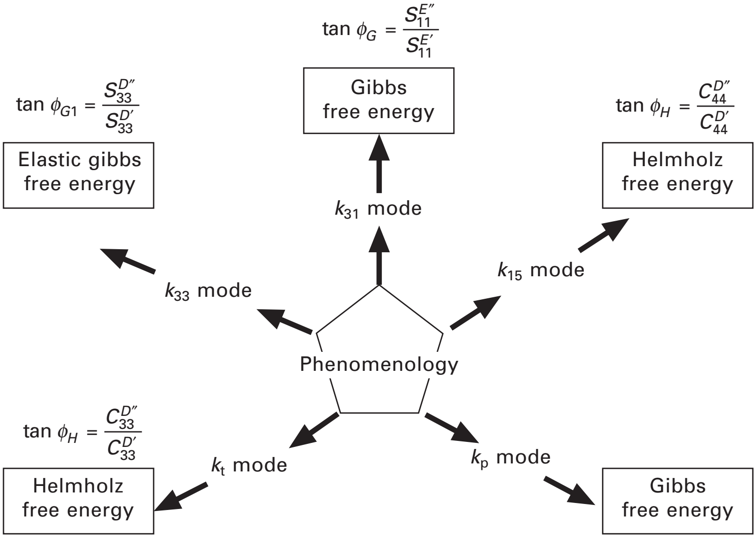
$\tan\phi_G = \frac{S_{11}^{E''}}{S_{11}^{E'}}$
Gibbs free energy
$\tan\phi_{G1} = \frac{S_{33}^{D''}}{S_{33}^{D'}}$
Elastic gibbs free energy
$\tan\phi_H = \frac{C_{44}^{D''}}{C_{44}^{D'}}$
Helmholz free energy
k_{31} mode
k_{15} mode
k_{33} mode
Phenomenology
$\tan\phi_H = \frac{C_{33}^{D''}}{C_{33}^{D'}}$
k_t mode
k_p mode
Helmholz free energy
Gibbs free energy

16.3 Relationship between the vibration mode and the corresponding elastic loss.

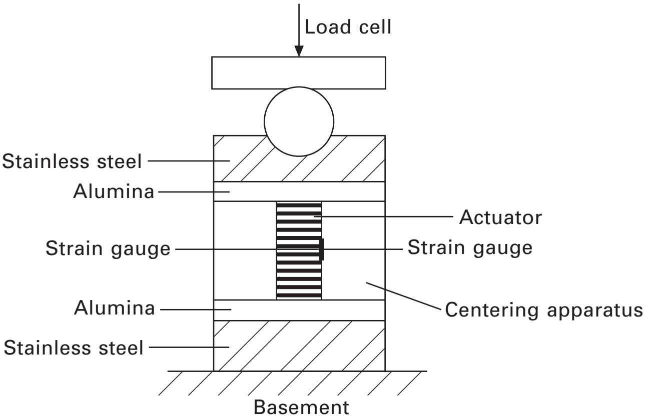
Load cell
Stainless steel
Alumina
Actuator
Strain gauge
Strain gauge
Alumina
Centering apparatus
Stainless steel
Basement

16.4 Stress applying jig construction for a multilayer piezoelectric sample.

tan θ′ (= 0.08) > (1/2)[tan δ′ (= 0.06) + tan ϕ′ (= 0.08)]. This relationship will be used in Section 16.2.4.

Then, we calculated the 'extensive' losses as shown in Fig. 16.6. Note again that the magnitude of the piezoelectric loss tan θ is comparable to the dielectric and elastic losses, and increases gradually with the field or stress; now tan θ (= 0.05) < (1/2) [tan δ (= 0.05) + tan ϕ (= 0.07)]. Also it is noteworthy that the extensive dielectric loss tan δ increases significantly

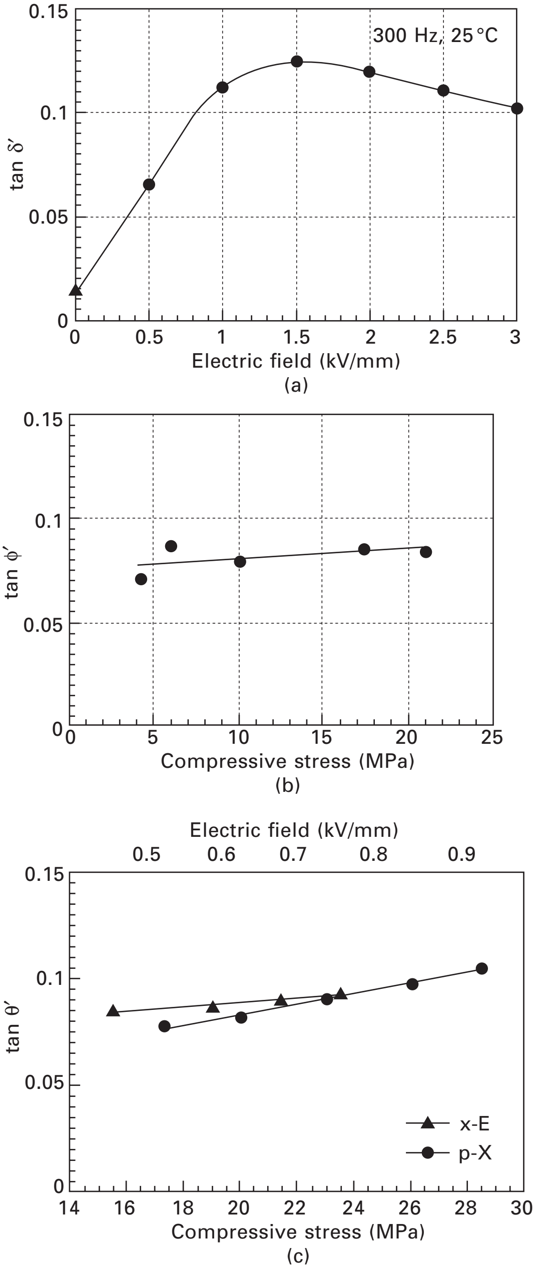

(a)

(b)

(c)

16.5 Intensive loss factors, tan δ′ (a), tan ϕ′ (b) and tan θ′(c) as a function of electric field or compressive stress, measured for a PZT-based actuator.

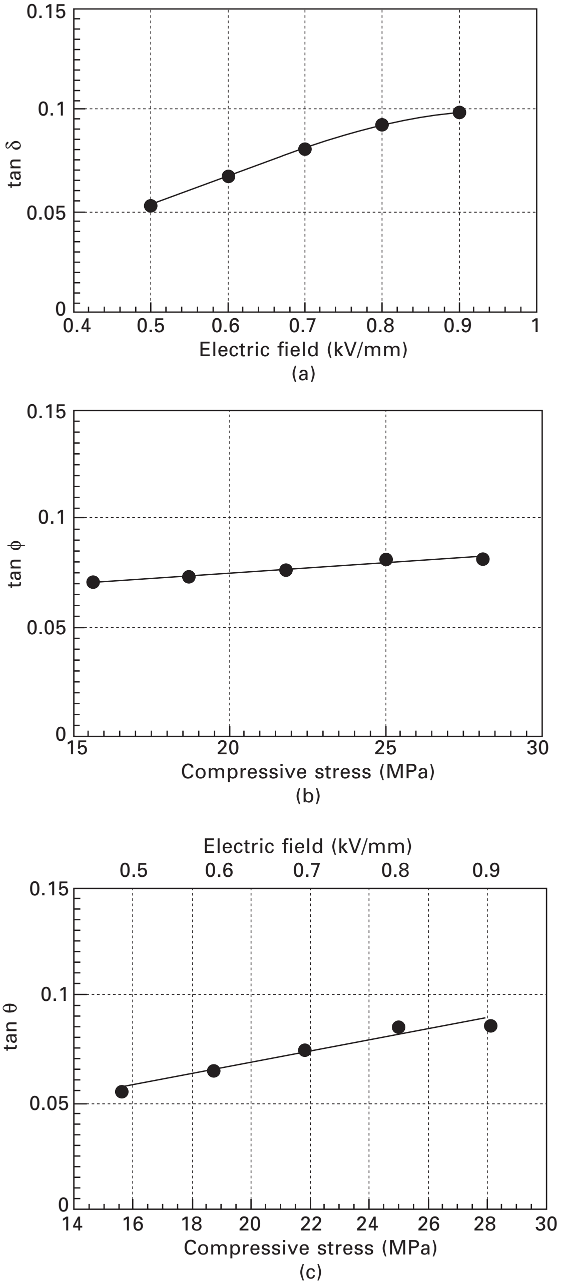

16.6 Extensive loss factors, tan δ (a), tan ϕ (b) and tan θ (c) as a function of electric field or compressive stress, measured for a PZT-based actuator.

with an increase in the intensive parameter, i.e., the applied electric field, while the extensive elastic loss tan ϕ is rather insensitive to the intensive parameter, i.e., the applied compressive stress. With similar measurements to Figs 16.1(a) and 16.1(b), but under constrained conditions; that is, D vs. E under a completely clamped state, and x vs. X under an open-circuit state, respectively, we can expect smaller hystereses, that is, extensive losses, tan δ and tan ϕ. These measurements seem to be alternative methods to determine the three losses separately. However, they are rather difficult in practice.

16.2.3 Loss measuring technique II – pulse drive method

The pulse drive method is an alternative, simpler method for measuring high voltage piezoelectric characteristics. By applying a step electric field to a piezoelectric sample, the transient vibration displacement corresponding to the desired mode (extensional, bending, etc.) is measured (see Fig. 16.7). The resonance period, stabilized displacement and damping constant are obtained experimentally, from which the elastic compliance, piezoelectric constant, mechanical quality factor and electromechanical coupling factor can be calculated. Using a rectangular piezoelectric ceramic plate (length: L; width: w; and thickness: b; poled along the thickness; Fig. 16.8), we explain how to determine the electromechanical coupling parameters k_{31}, d_{31} and Q_M. The density ρ, permittivity ε^X_{33}, and size (L, w, b) of the ceramic plate must be known prior to the experiments.

1. From the stabilized displacement, we obtain the piezoelectric coefficient d_{33}:

$$D_s = d_{31} EL \qquad 16.32$$

2. From the ringing period, we obtain the elastic compliance s^E_{11}:

$$T_0 = 2L/v = 2L(\rho s^E_{11})^{1/2} \qquad 16.33$$

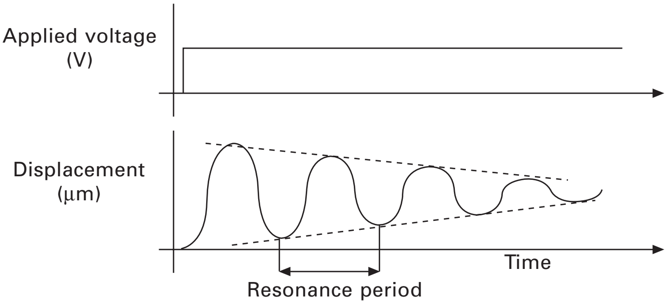

16.7 Pulse drive technique for measuring the electromechanical parameters.

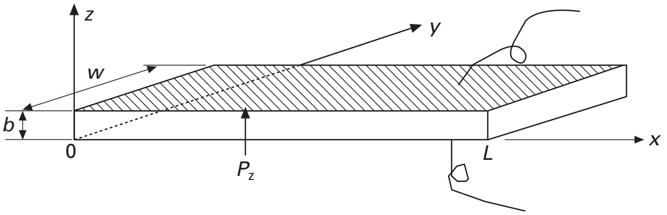

16.8 A rectangular piezo-ceramic plate ($L \gg w \gg b$) for a longitudinal mode through the transverse piezoelectric effect (d_{31}).

3. From the damping constant τ, which is determined by the time interval to decrease the displacement amplitude by $1/e$, we obtain the mechanical quality factor Q_M:

   $$Q_M = (1/2)\,\omega_0\tau, \qquad 16.34$$

   where the resonance angular frequency $\omega_0 = 2\pi/T_0$.
4. From the piezoelectric coefficient d_{31}, elastic compliance s^E_{11}, and permittivity ε_3, we obtain the electromechanical coupling factor k_{33}:

   $$k_{31} = d_{31}/(\varepsilon_0\varepsilon_3 s^E_{11})^{1/2} \qquad 16.35$$

Although the experimental accuracy is not high, the simple setup is attractive especially for its low cost. Moreover, unlike the resonance/antiresonance methods in the next section, this technique requires only one voltage pulse during the measurement, and thus does not generate heat (i.e., temperature effect can be eliminated). Thus, the electric field dependence of piezoelectricity can be measured.

16.2.4 Loss measuring technique III – piezoelectric resonance method

Mathematical formulation: resonance/antiresonance

So far, we have considered the loss measurement with a quasi-static or a pulse drive method. We introduce here a piezoelectric resonance method for measuring three losses separately.

Let us derive the necessary formulas for the longitudinal mechanical vibration of a piezo-ceramic plate through the transverse piezoelectric effect (d_{31}) as shown in Fig. 16.8. Assuming that the polarization is in the z-direction and the x-y planes are the planes of the electrodes, the extensional vibration in the x direction is represented by the following dynamic equation:

$$(\partial^2u/\partial t^2) = F = (\partial X_{11}/\partial x) + (\partial X_{12}/\partial y) + (\partial X_{13}/\partial z), \qquad 16.36$$

where u is the displacement of the small volume element in the ceramic plate in the x-direction. When the plate is very long and thin, X_2 and X_3

may be set equal to zero through the plate, and the following solutions can be obtained:

$$\text{(strain)} \quad \partial u/\partial x = x_1 = d_{31}Ez\,[\sin \omega(L\text{-}x)/v + \sin(\omega x/v)]/\sin(\omega L/v), \qquad 16.37$$

$$\text{(total displacement)} \quad \Delta L = \int_0^L x_1 dx = d_{31}E_z L\,(2v/\omega L)\tan(\omega L/2v). \qquad 16.38$$

Here, v is the sound velocity in the piezoceramic which is given by

$$v = 1/\sqrt{\rho s_{11}^{\mathrm{E}}}\,. \qquad 16.39$$

The admittance Y for the mechanically free sample is calculated to be:

$$\begin{aligned} Y &= (1/Z) = (i/V) = (i/E_z\,t) \\ &= (j\omega wL/t)\,\varepsilon_0\varepsilon_{33}^{\mathrm{LC}}\,[1 + (d_{31}^2/\varepsilon_{33}^{\mathrm{LC}}\,s_{11}^{\mathrm{E}})(\tan(\omega L/2v)/(\omega L/2v)], \end{aligned} \qquad 16.40$$

where w is the width, L the length, t the thickness of the rectangular piezo-sample, and V is the applied voltage. $\varepsilon_{33}^{\mathrm{LC}}$ is the permittivity in a longitudinally clamped sample, which is given by:

$$\varepsilon_0\varepsilon_{33}^{\mathrm{LC}} = \varepsilon_0\,\varepsilon_{33}^{\mathrm{X}} - \left(\frac{d_{31}^2}{s_{11}^{\mathrm{E}}}\right) = \varepsilon_0\varepsilon_3^{\mathrm{X}}(1 - k_{31})^2 \qquad 16.41$$

Note that $\varepsilon_3^{\mathrm{LC}} \equiv \varepsilon_3^{\mathrm{X}}$ from Eq. 16.21.

The piezoelectric resonance (A-type resonance) is achieved where the admittance becomes infinite or the impedance is zero. The resonance frequency f_{R} is calculated from Eq. 16.40 (by putting $\omega L/2v = \pi/2$), and the fundamental frequency is given by:

$$f_{\mathrm{R}} = \omega_{\mathrm{R}}/2\pi = v/2L = 1/(2L\sqrt{\rho s_{11}^{\mathrm{E}}}). \qquad 16.42$$

On the other hand, the antiresonance state (B-type resonance) is generated for zero admittance or infinite impedance:

$$(\omega_{\mathrm{A}}L/2v)\cot(\omega_{\mathrm{A}}L/2v) = -d_{31}^2/\varepsilon_0\varepsilon_{33}^{\mathrm{LC}}\,s_{11}^{\mathrm{E}} = -k_{31}^2/(1-k_{31}^2). \qquad 16.43$$

The final transformation is provided by the definition,

$$k_{31} = d_{31}/\sqrt{s_{11}^{\mathrm{E}} \cdot \varepsilon_0\varepsilon_{33}^{\mathrm{X}}}.$$

The resonance and antiresonance states are both mechanical resonance states with amplified strain/displacement states, but they are very different from the driving viewpoints. The mode difference is described by the following intuitive model. In a hypothetically high electromechanical coupling material with k almost equal to 1, the resonance or antiresonance states appear for tan $(\omega L/2v) = \infty$ or 0 (i.e., $\omega L/2v = (m-1/2)\pi$ or $m\pi$ (m: integer)), respectively. The strain amplitude x_1 distribution for each state (calculated using Eq. 16.37) is illustrated in Fig. 16.9. In the resonance state, large strain amplitudes and large capacitance changes (called *motional capaci*tance) are induced, and the current can easily flow into the device (i.e., Y is infinite). In contrast, at the antiresonance, the strain induced in the device compensates completely (i.e., half extends and half shrinks), resulting in no motional capacitance change, and the current cannot flow easily into the sample (i.e., Y is zero). Thus, for a high k material the first antiresonance frequency f_A should be twice as large as the first resonance frequency f_R.[6]

In a typical case, where $k_{31} = 0.3$, the antiresonance state varies from the previously mentioned double f_R mode and becomes closer to the resonance mode (top-center in Fig. 16.9). The low-coupling material exhibits an antiresonance mode where the capacitance change due to the size change (*motional capaci*tance) is compensated completely by the current required to charge up the static capacitance (called *damped capaci*tance). Thus, the antiresonance frequency f_A will approach the resonance frequency f_R.

Mathematical formulation: loss and mechanical quality factor

Now, we introduce the complex parameters into the admittance curve around the resonance frequency, in a similar way to the previous section:[4] $\varepsilon_3^{X}{}^* = \varepsilon^X_3\,(1 - j \tan \delta')$, $s_{11}^{E}{}^* = s^E_{11}\,(1 - j \tan \phi')$, and $d_{31}{}^* = d(1 - j \tan \theta')$ into Eq. 16.40:

$$\begin{aligned} Y &= Y_d + Y_m \\ &= j\omega C_d\,(1 - j \tan \delta) + j\omega C_d\, K_{31}^2\,[(1 - j\,(2\tan \theta' - \tan \phi')] \\ &\quad [(\tan(\omega L/2v^*)/(\omega L/2v^*)], \end{aligned} \qquad 16.44$$

where

$$C_0 = (wL/t)\,\varepsilon_0\,\varepsilon^X_3, \quad \text{(free electrostatic capacitance)} \qquad 16.45$$

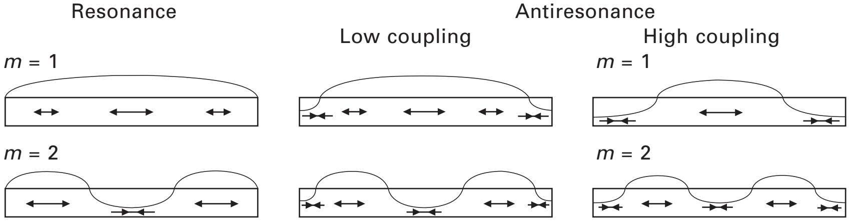

16.9 Strain distribution in the resonant or antiresonant state. Longitudinal vibration through the transverse piezoelectric effect (d_{31}) in a rectangular plate.

$$C_d = (1 - k_{31}^2)\, C_0. \quad \text{(damped/clamped capacitance)} \tag{16.46}$$

Note that the loss for the first term (damped conductance) is represented by the 'extensive' dielectric loss tan δ, not by the intensive loss tan δ′. We further calculate $1/[\tan(\omega L/2v^*)]$ with an expansion-series approximation around the resonance frequency $(\omega_a L/2v) = \pi/2$, taking into account that the resonance state is defined in this case for the maximum admittance point. Using new frequency parameters,

$$\Omega = \omega L/2v, \Delta\Omega = \Omega - \pi/2 \ (<<1), \tag{16.47}$$

and $K_{31}^2 = k_{31}^2/(1 - k_{31}^2)$, the motional admittance Y_m is approximated around the first resonance frequency by:

$$Y_m = j(8/\pi^2)\, \omega_a C_d\, K_{31}^2\, [(1 + j((3/2)\tan\phi' - 2\tan\theta')]/$$

$$[-(4/\pi)\Delta\Omega + j\tan\phi']. \tag{16.48}$$

The maximum Y_m is obtained at $\Delta\Omega = 0$:

$$Y_m^{max} = (8/\pi^2)\, \omega_a\, C_d\, K_{31}^2\, (\tan\phi')^{-1} = (8/\pi^2)\, \omega_a\, C_0\, k_{31}^2\, Q_a, \tag{16.49}$$

where the mechanical quality factor for A-type resonance $Q_a = (\tan\phi')^{-1}$. Similarly, the maximum displacement u_{max} is obtained at $\Delta\Omega = 0$:

$$u_{max} = (8/\pi^2)\, d_{31}\, E_Z\, L\, Q_a. \tag{16.50}$$

The maximum displacement at the resonance frequency is $(8/\pi^2) Q_a$ times larger than that at a non-resonance frequency, $d_{31}E_Z L$. In a brief summary, when we observe the admittance or displacement spectrum as a function of drive frequency, and obtain the mechanical quality factor for A-type resonance Q_a estimated from $Q_a = \omega_a/2\Delta\omega$, where $2\Delta\omega$ is a full width of the 3 dB down (i.e., $1/\sqrt{2}$) of the maximum value at $\omega = \omega_a$, we can obtain the intensive mechanical loss tan ϕ′.

Now we derive the mechanical quality factor Q_b for B-type resonance (i.e., antiresonance). Introducing frequency parameters:

$$\Omega = \omega L/2\,v, \Delta\Omega = \Omega - \Omega_b \ (<< 1),\ \Omega_b = \omega_b L/2v, \tag{16.51}$$

we consider an expansion-series approximation around the antiresonance (B-type) frequency $(\omega_b L/2v)$.[7] Finally, the mechanical quality factor Q_b is obtained as

$$\frac{1}{Q_B} = \frac{1}{Q_A} + \frac{2}{1 + \left(\frac{1}{k_{31}} - k_{31}\right)^2 \Omega_b^2} (\tan\delta' + \tan\phi' - 2\tan\theta') \tag{16.52}$$

In this section summary, we proposed a simple, easy and friendly method to determine the piezoelectric loss factor tan θ′ in k_{31} mode through admittance/impedance spectrum analysis:

1. Obtain $\tan\delta'$ from a capacitance meter at a frequency far from the resonance or antiresonance range;
2. Obtain the following parameters experimentally from an impedance spectrum analyzer: ω_a, ω_b, Q_A, Q_B (from the 3 dB bandwidth method), and the normalized frequency $\Omega_b = \omega_b l/2v$;
3. Obtain $\tan\phi'$ from the inverse value of Q_A (quality factor at the resonance);
4. Calculate k_{31} from the ω_a and ω_b with the following equation:[8]

$$\frac{k_{31}^2}{1-k_{31}^2} = \frac{\pi}{2}\frac{\omega_b}{\omega_a}\tan\left[\frac{\pi(\omega_b-\omega_a)}{2\omega_a}\right] \qquad 16.53$$

5. Finally obtain $\tan\theta'$ by:

$$\tan\theta' = \frac{\tan\delta' + \tan\phi'}{2} + \frac{1}{4}\left(\frac{1}{Q_A} - \frac{1}{Q_B}\right)\left[1 + \left(\frac{1}{k_{31}} - k_{31})^2\Omega_b^2\right)\right]. \qquad 16.54$$

Constant voltage drive versus constant current drive

Though the above-mentioned measurement technique is simple yet sophisticated, there have been problems in heat generation in the sample, and also in significant distortion of the admittance frequency spectrum when the sample is driven by a constant voltage, due to the nonlinear behavior of elastic compliance at high vibration amplitude. Figure 16.10(a) exemplifies the problem, where the admittance spectrum is skewed with a jump around the maximum admittance point. Thus, we cannot determine the resonance frequency or the mechanical quality factor precisely from these skewed spectra.

In order to escape from the problem with a constant voltage measurement, we proposed a constant current measurement technique.[9] Since the vibration amplitude is primarily proportional to the driving current (not the voltage), a constant current condition guarantees almost constant vibration amplitude through the resonance frequency region, escaping the spectrum distortion due to the elastic nonlinearity. As demonstrated in Fig. 16.10(b), the spectra exhibit symmetric curves, from which we can determine the resonance frequency and the mechanical quality factor Q_a precisely.

Although the traditional constant voltage measurement was improved by using a constant current measurement method, the conventional technique was still limited to the vicinity of the resonance. In order to identify a full set of high power electromechanical coupling parameters and the loss factors of a piezoelectric, both resonance and antiresonance vibration performance (in particular, Q_a and Q_b) should be precisely measured simultaneously. Basically, Q_a can be determined by the constant current method around the resonance (A-type), while Q_b should be determined by the constant voltage method

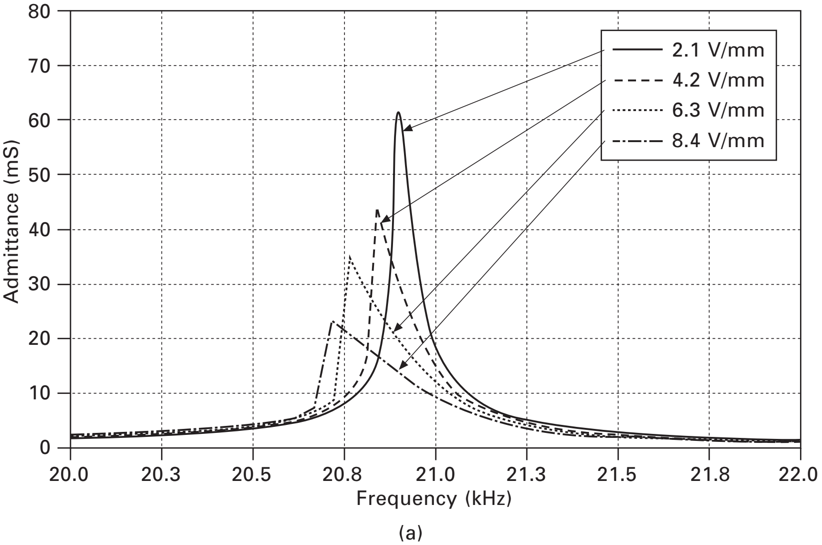

(a)

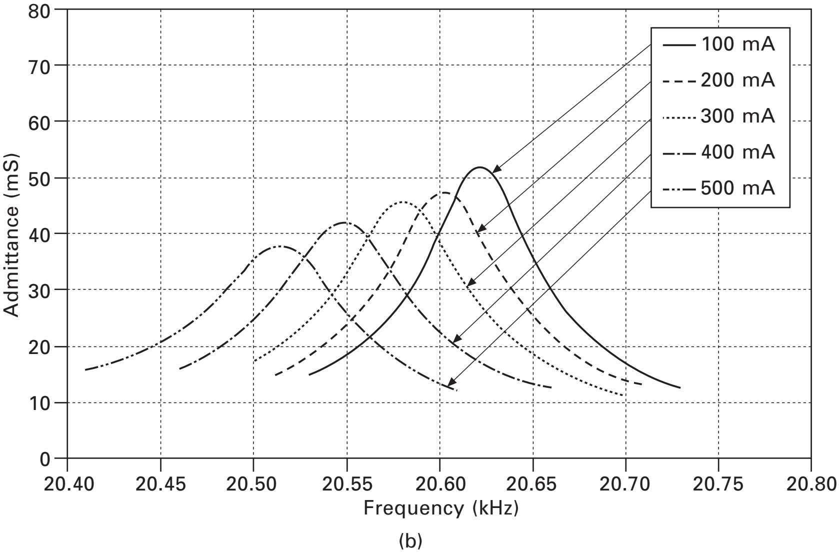

(b)

16.10 Experimentally obtained admittance frequency spectra under (a) constant voltage, and (b) constant current condition. Note the skew-distorted spectrum with a jump under a constant voltage condition (data taken by Michael R. Thibeault, The Penn State Univ.).

around the antiresonance (B-type). Thus, we developed recently a new high power characterization system (HiPoCS), which is capable of measuring the impedance/admittance curves by keeping the following conditions:

- constant voltage,

- constant current,
- constant vibration velocity of a piezoelectric sample, and
- constant input power.[10]

In addition, the system is equipped with an infrared image sensor to monitor the heat generation distributed in the test sample. We demonstrated the usefulness of the new system in a rectangular piezoelectric plate in the whole frequency range including the resonance and antiresonance frequencies. The results will be described in Section 16.4.2.

16.3 Heat generation in piezoelectrics

Heat generation in various types of PZT-based actuators has been studied under a large electric field (1 kV/mm or higher) applied at an off-resonance frequency and under a relatively small electric field (100 V/mm) applied at a resonance frequency.

16.3.1 Heat generation at off-resonance

Zheng *et al*. reported the heat generation at an off-resonance frequency from various sizes of multilayer type piezoelectric ceramic (soft PZT) actuators.[5] The temperature change with time in the actuators was monitored when driven at 3 kV/mm (high electric field) and 300 Hz (low frequency), and Fig. 16.11 plots the saturated temperature as a function of V_e/A, where V_e is the effective volume (electrode overlapped part) and A is the surface area. The

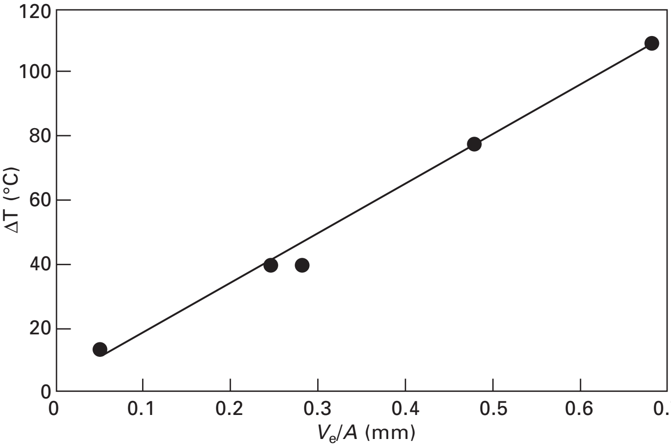

16.11 Temperature rise at off-resonance versus V_e/A (3 kV/mm, 300 Hz) in various size soft PZT multilayer actuators, where V_e is the effective volume generating the heat and A is the surface area dissipating the heat.

temperature was uniformly generated in a bulk sample. This linear relation is reasonable because the volume V_e generates the heat and this heat is dissipated through the area A. Thus, if we need to suppress the temperature rise, a small V_e/A design is preferred. From these experimental results, we calculated the total loss u of the piezoelectric, which is summarized in Table 16.1. The experimental data of P-E hysteresis losses under a stress-free condition are also listed for comparison. It is very important that the P-E hysteresis or intensive dielectric loss agrees well with the total loss contributing to the heat generation under an off-resonance drive.

16.3.2 Heat generation at resonance

Tashiro *et al.* observed the heat generation in a rectangular piezoelectric plate during a resonating drive.[11] Even though the electric field is not large, considerable heat is generated due to the large induced strain/stress at the resonance. Figure 16.12 depicts an infrared image taken for a resonating rectangular 'hard' PZT plate at its second resonance (or third harmonic) mode

Table 16.1 Loss and overall heat transfer coefficient for PZT multilayer samples (E = 3 kV/mm, f = 300 Hz). The effective heat transfer coefficient here is the sum of the rates of heat flow by radiation and convection, neglecting the conduction effect

Actuator	4.5 ×3.5 ×2 mm	7 × 7 × 2 mm	17 × 3.5 × 1 mm
Total loss (x10^3 J/m^3) $u = \frac{\rho c v}{f v_e}\left(\frac{dT}{dt}\right) t > 0$	19.2	19.9	19.7
P-E hysteresis loss (×10^3 J/m^3)	18.5	17.8	17.4
$k(T)$ (W/m^2K)	38.4	39.2	34.1

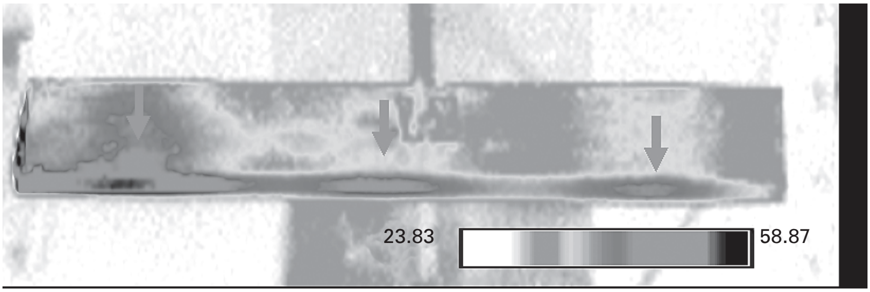

16.12 An infrared image of a PZT rectangular plate driven at the second resonance (or third harmonic) mode. Note the three hot points which correspond to the nodal points for this vibration mode.

in our laboratory. The maximum heat generation was observed at the nodal points/lines of the resonance vibration (note the three hot spots), where the maximum strain/stress is generated. This observation supports that the heat generation in a resonating sample is attributed to the intensive elastic loss tan ϕ'. This is not contradictory to the result in the previous paragraph, where a high-voltage was applied at an off-resonance frequency. We concluded there that the heat originates from the intensive dielectric loss tan δ'. Taking into account that both the 'intensive' dielectric and mechanical losses are composed of the 'extensive' dielectric and mechanical losses, and that the extensive dielectric loss tan δ changes significantly with the external electric field and stress (see Fig. 16.6), the major contribution to the heat generation seems to come from the 'extensive' dielectric loss (i.e., 180° domain wall motion), not from the 'extensive' elastic loss (i.e., non-180° domain wall motion). We discuss the microscopic origin again in Section 16.4.3. However, since this is still our speculative model, it is possible that there can be different domain reorientation models, and further investigations are expected for the actual microscopic observation of this phenomenon.

16.4 Loss mechanisms in piezoelectrics

16.4.1 Mechanical quality factors at resonance and antiresonance

The resonance and antiresonance are both electro-mechanical resonance, and both generate large displacement amplitude, which can be used for actuator/transducer applications. The major difference is the driving electrical admittance/impedance; low voltage and high current drive vs. high voltage and low current drive. Another difference can be found in the mechanical quality factor Q_m; in most of the PZT materials, Q_b is higher than Q_a, or the antiresonance mode has a higher efficiency.

Table 16.2 shows two examples of the electromechanical parameters (in particular Q_A and Q_B).[7] The Q_A and Q_B values were determined with HP Impedance Analyzer (HP4192) under an electric voltage level of 0.5 V_{rms}. In the experiment, we used a hard PZT-based ceramic sample (17 × 3 × 1 mm^3) APC 841 (American Piezo Ceramic International Ltd., Mackeyville, PA, USA), and a manganese-doped $Pb(Mg_{1/3}Nb_{2/3})O_3$–$PbTiO_3$ (Mn–PMN–PT)

Table 16.2 Electromechanical parameters of PZT ceramic APC 841 and Mn–PMN–PT single crystal (k_{31} mode)

Material	Q_A (1/tan ϕ')	tan ϕ'	Q_B	tan δ'	k_{31}	tan θ'
APC 841	1183	0.00085	1986	0.0035	0.31	0.0042
Mn–PMN–PT	240	0.0042	445	0.0070	0.50	0.0094

single crystal (Ceracomp Co., Ltd., Cheonan, South Korea) with a size of 17 × 3 × 1 mm^3. By applying Eq. 16.54, the piezoelectric loss factor $\tan\theta'$ was obtained. It is notable that the piezoelectric loss is comparable to, and even larger than, the other two losses.

The difference between Q_B and Q_A is determined mainly by the term $(\tan\delta' + \tan\phi' - 2\tan\theta')$. According to Eq. 16.52, if $2\tan\theta' > (\tan\delta' + \tan\phi')$, then $Q_B > Q_A$, which is consistent with the above experimental observations. Otherwise, if $2\tan\theta' < (\tan\delta' + \tan\phi')$, then $Q_A > Q_B$ which has not been observed experimentally so far. The condition $2\tan\theta' = (\tan\delta' + \tan\phi')$ sets $Q_B = Q_A$. The argument is in exact agreement with the results in Fig. 16.6, which were obtained by a quasi-static hysteresis measurement method.

It is noteworthy that the condition for the intensive loss factors $2\tan\theta' > (\tan\delta' + \tan\phi')$ for explaining the experimental results $Q_B > Q_A$ automatically derives the condition for the extensive loss factors $2\tan\theta < (\tan\delta + \tan\phi)$ from the conversion relations Eqs 16.29–16.31. In summary, the 'intensive' piezoelectric loss factor is larger than the average of dielectric and elastic losses, while the 'extensive' piezoelectric loss factor is smaller than the average of dielectric elastic losses.

16.4.2 Vibration velocity dependence of losses

Let us consider here the degradation mechanism of the mechanical quality factor Q_m with increasing electric field and vibration velocity. Figure 16.13

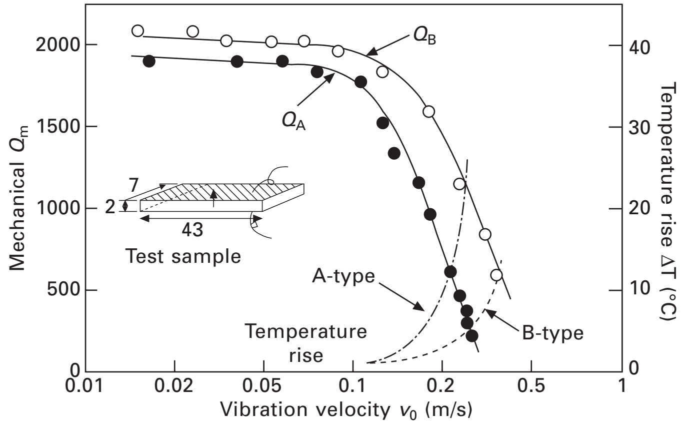

16.13 Vibration velocity dependence of the mechanical quality factors Q_A and Q_B, and corresponding temperature rise for A (resonance) and B (antiresonance) type resonances of a longitudinally vibrating PZT ceramic transducer through the transverse piezoelectric effect d_{31} (the sample size is inserted).

shows the vibration velocity dependence of the mechanical quality factors Q_A and Q_B, and corresponding temperature rise for A (resonance) and B (antiresonance) type resonances of a longitudinally vibrating PZT ceramic transducer through the transverse piezoelectric effect d_{31} (the sample size is inserted).[12] Q_m is almost constant for a small electric field/vibration velocity, but above a certain vibration level Q_m degrades dramatically, where temperature rise starts to be observed.[12] In order to evaluate the mechanical vibration level, we introduced the vibration velocity at the rectangular plate tip, rather than the vibration displacement, because the displacement is a function of size, while the velocity is not. The maximum vibration velocity is defined at the velocity where a 20 °C temperature rise at the nodal point from room temperature occurs. Note that even if we increase the driving voltage/field, additional energy will merely convert to heat (i.e., PZT becomes a ceramic heater!) without increasing the vibration amplitude. Thus, the reader can understand that the maximum vibration velocity is a sort of material's constant which ranks the high power performance. Note that most of the commercially available hard PZTs exhibit the maximum vibration velocity around 0.3 m/sec, which corresponds to roughly 5 W/cm^3 (i.e., 1 cm^3 PZT can generate a maximum 5 W mechanical energy).

When we compare the change trends in Q_A and Q_B, Q_B is higher than Q_A in all vibration levels. The same result was already discussed for a small vibration level in the previous Section. Accordingly, the heat generation in the B-type (antiresonance) mode is superior to the A-type (resonance) mode under the same vibration velocity level (in other words, the maximum vibration velocity is higher for Q_B than for Q_A).

Figure 16.14(b) depicts an important notion on heat generation from the piezoelectric material, where the damped and motional resistances, R_d and R_m, in the equivalent electrical circuit of a PZT sample (Fig. 16.14(a)) are plotted separately as a function of vibration velocity. Note that R_m, which we speculate to be related mainly to the extensive mechanical loss (90° domain wall motion), is insensitive to the vibration velocity, while R_d, related to the extensive dielectric loss (180° domain wall motion), increases significantly around a certain critical vibration velocity. Thus, the resonance loss at a small vibration velocity is determined mainly by the extensive mechanical loss which provides a high mechanical quality factor Q_m, and with increasing vibration velocity, the extensive dielectric loss contribution significantly increases. This is consistent with our discussion of Fig. 16.6. After R_d exceeds R_m, we started to observe heat generation.

The equivalent circuit for the piezoelectric resonator is represented by a combination of L, C and R. Figure 16.14(a) shows an equivalent circuit for the resonance state, which has very low impedance. Taking into account Eq. 16.44, we can understand that C_d and R_d correspond to the electrostatic capacitance (for a longitudinally clamped sample in the previous case, not a

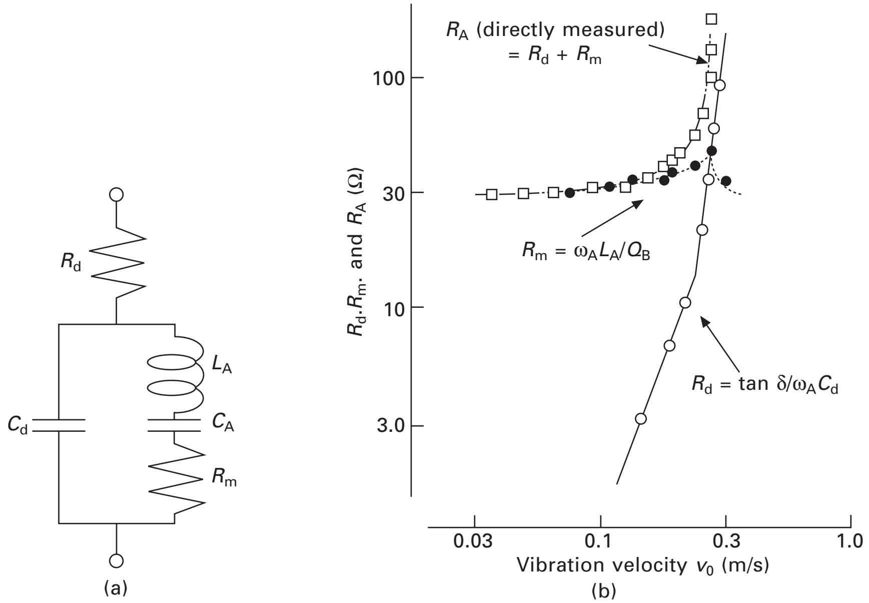

16.14 (a) Equivalent circuit of a piezoelectric sample for the resonance under high power drive. (b) Vibration velocity dependence of the resistances R_d and R_m in the equivalent electric circuit for a longitudinally vibrating PZT ceramic plate through the transverse piezoelectric effect d_{31}.

free sample) and the clamped (or 'extensive') dielectric loss tan δ, respectively, and the components L_A and C_A in a series resonance circuit are related to the piezoelectric motion. For example, in the case of the longitudinal vibration of the above rectangular plate through d_{31}, these components are represented approximately by

$$L_A = (\rho/8)(Lb/w)[(s^E_{11})^2/d^2_{31}], \qquad 16.55$$

$$C_A = (8/\pi^2)(Lw/b)(d^2_{31}/s^E_{11}). \qquad 16.56$$

The total resistance R_A (= $R_d + R_m$) may correspond to the loss tan φ′, which is composed of the extensive mechanical loss tan φ and dielectric/piezoelectric coupled loss (tan δ – 2 tan θ) (see Eq. 16.30). Thus, intuitively speaking, R_d and R_m correspond to the extensive dielectric and mechanical losses, respectively. Note that we have introduced an additional resistance R_d to explain a large contribution of the dielectric loss when a vibration velocity is relatively large. There are, of course, different ways to introduce R_d in an equivalent circuit.[13]

The Penn State group developed a new high power characterization system

(HiPoCS), which is capable of measuring the impedance/admittance curves by keeping the following various conditions:

- constant voltage,
- constant current,
- constant vibration velocity of a piezoelectric sample, and
- constant input power.[10]

In addition, the system is equipped with an infrared image sensor to monitor the heat generation distributed in the test sample. Figure 16.15 plots the frequency spectra of power under constant vibration velocity conducted across the resonance and antiresonance frequencies. It is obvious that the power required for generating the same tip vibration velocity of the rectangular plate is smaller for the antiresonance mode than for the resonance mode. This is the first experimental evidence of the higher efficiency at the antiresonance than at the resonance. Figure 16.16 depicts heat generation/distribution contours from the rectangular PZT8 plate driven under the same vibration velocity (0.3 m/sec) for the resonance (type A) and for the antiresonance (type B) mode. Note the key issues:

1. Heat generation is smaller for the antiresonance mode than for the resonance mode to generate the same vibration velocity (mechanical output), as supported by a higher Q_M value.
2. Heat distribution is more dispersive for the antiresonance mode than for the resonance mode, as expected by the superposition of the uniform heat generation contributed from the dielectric loss.

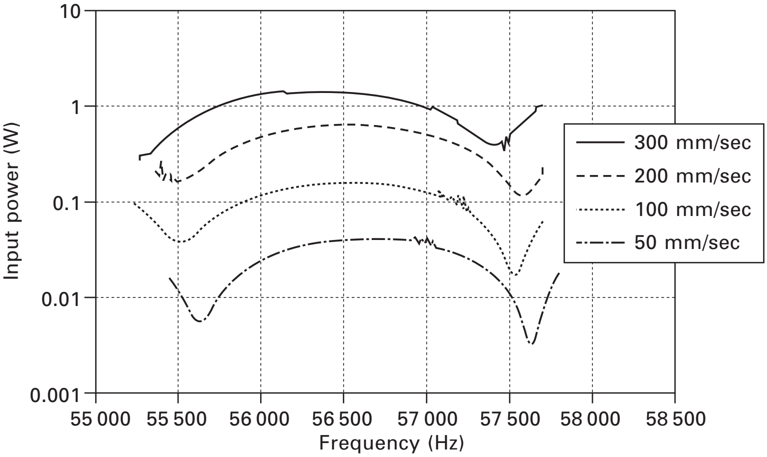

16.15 Frequency spectra of power under constant vibration velocity, conducted across the resonance and antiresonance frequencies.

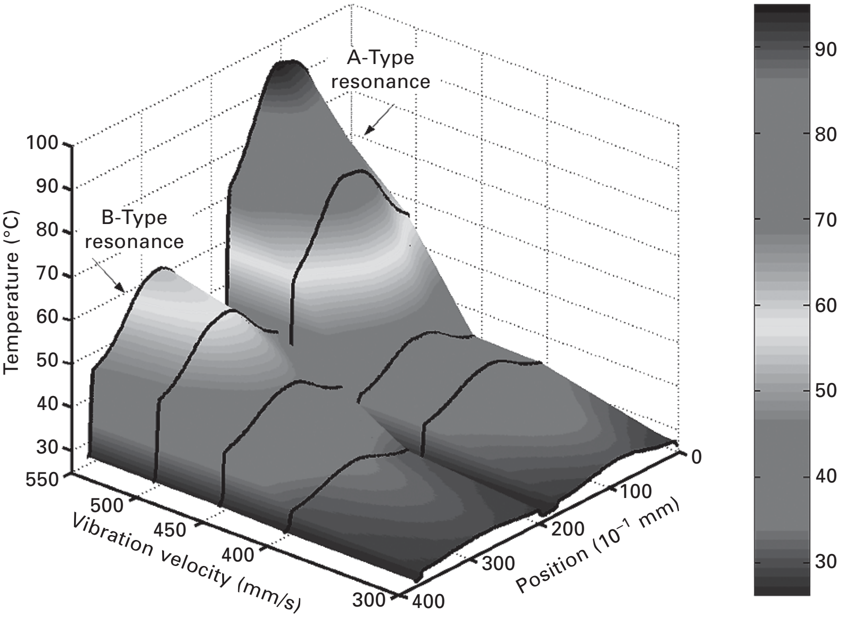

16.16 Heat generation from the rectangular PZT8 plate driven under the same vibration velocity (0.3 m/sec) for the resonance (type A) mode and for the antiresonance (type B).

16.4.3 Microscopic origins of extensive losses

We have discussed so far the macroscopic phenomenology of losses in piezoelectrics. We discuss here the relationship of the loss phenomenology with the microscopic origins. To make the situation simplest, we consider here only the domain wall motion-related losses. Taking into account the fact that the polarization change is primarily attributed to 180° domain wall motion, while the strain is attributed to 90° (or non-180°) domain wall motion, we suppose that the extensive dielectric and mechanical losses originate from 180° and 90° domain wall motions, respectively, as illustrated in Fig. 16.17. The dielectric loss comes from the hysteresis during the 180° polarization reversal under E, while the elastic loss comes from the hysteresis during the 90° polarization reorientation under X. In this model, the intensive (observable) piezoelectric loss is explained by the 90° polarization reorientation under E, which can be realized by superimposing the 90° polarization reorientation under X and the 180° polarization reversal under E. This is the primary reason why Eq. 16.11 includes a combination term as $(2 \tan \theta' - \tan \phi')$.

If we adopt the Uchida–Ikeda polarization reversal/reorientation model,[14] we can explain the loss change with intensive parameter (externally controllable parameter). By finding the polarization P and the field-induced

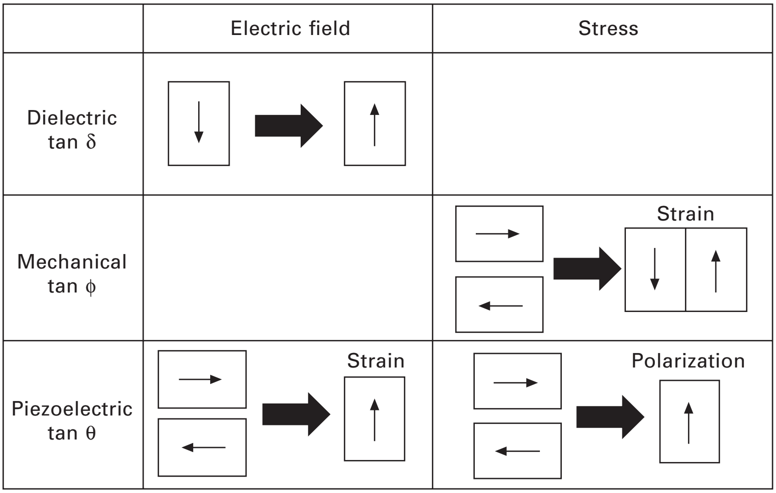
Electric field
Stress
Dielectric
tan δ
Mechanical
tan ϕ
Strain
Piezoelectric
tan θ
Strain
Polarization

16.17 Polarization reversal/reorientation model for explaining ‘extensive’ dielectric, elastic and piezoelectric losses.

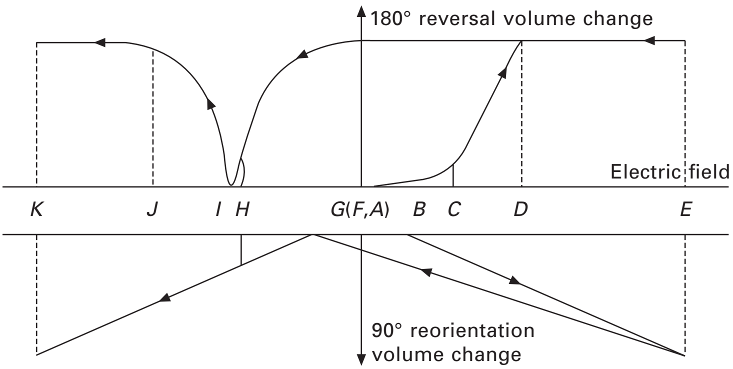
180° reversal volume change
Electric field
K
J
I
H
G(F,A)
B
C
D
E
90° reorientation
volume change

16.18 Polarization reversal/reorientation model for explaining the loss change with electric field.

strain *x* as a function of the electric field *E*, it is possible to estimate the volume in which 180° reversal or 90° rotation occurred. This is because the 180° domain reversal does not contribute to the induced strain, only the 90° rotation does, whereas the 180° domain reversal contributes mainly to the polarization. The volume change of the domains with external electric field is shown schematically in Fig. 16.18. It can be seen that with the application of an electric field the 180° reversal occurs rapidly at a certain *E*, whereas the 90° rotation occurs gradually from a low field. It is notable that at *G* in the figure, there remains some polarization while the induced strain is zero, at *H* the polarizations from the 180° and 90° reorientations cancel each other out and become zero, but the strain is not at its minimum. Due to a sudden change in the 180° reversal above a certain electric field, we can expect a sudden increase in the polarization hysteresis and in the dielectric loss (this may reflect the extensive dielectric loss measurement in Fig. 16.6(a)); while the slope of 90° reorientation is almost constant, we can expect a constant extensive elastic loss with changing the external parameter, E or X (extensive elastic loss in Fig. 16.6(b)). This drastic increase in 180° domain wall motion (i.e., the extensive dielectric loss) seems to be the origin of the apparent Q_m degradation and heat generation above the maximum vibration velocity.

16.5 High power piezoelectric ceramics

16.5.1 Very hard PZT-based ceramics

'High power' in this chapter stands for 'high power density' in mechanical output energy converted from the maximum input electrical energy under the drive condition with 20 °C temperature rise. For an off-resonance drive condition, the figure of merit of piezo-actuators is given by the piezoelectric d constant ($\Delta L = d \cdot EL$). Heat generation can be evaluated by the intensive dielectric loss tan δ' (i.e., P-E hysteresis). On the other hand, for a resonance drive condition, the figure of merit is the vibration velocity v_0, which is roughly proportional to $Q_m \cdot dEL$. Q_m can be considered as an amplification factor of the vibration amplitude/velocity. Heat generation originates from the intensive elastic loss tan ϕ' (inverse value of Q_m). The mechanical power density can be evaluated by the square of the maximum vibration velocity (v_0^2), which is a sort of material's constant. Remember that there exists a maximum mechanical energy density, above which level the piezoelectric material becomes a mere ceramic heater. High vibration velocity materials are suitable for actuator applications such as ultrasonic motors. Our primary target for the high power materials is set around $v_0 = 0.6$ m/sec or 20 W/cm^2, in comparison with the commercially available $v_0 = 0.3$ m/sec or 5 W/cm^2. Further, when we consider transformers and transducers, where both transmitting and receiving functions are required, the figure of merit will be the product of $v_0 \cdot k$ (k: electromechanical coupling factor).

Let us first discuss high vibration velocity materials. Figure 16.19 shows the mechanical Q_m versus basic composition x at two effective vibration velocities $v_0 = 0.05$ m/s and 0.5 m/s for $Pb(Zr_xTi_{1-x})O_3$ doped with 2.1 at% of Fe.[15] The decrease in mechanical Q_m with an increase of vibration level is minimum around the rhombohedral–tetragonal morphotropic phase boundary (52/48). In other words, the smallest Q_m material under a small vibration level becomes the highest Q_m material under a large vibration level, which is very suggestive. The data obtained by a conventional impedance analyzer with a small voltage/power do not provide any information relevant to high power

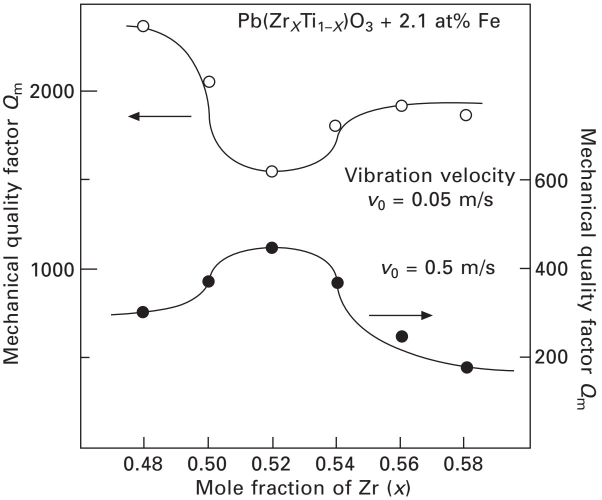

16.19 Mechanical Q_m versus basic composition x at two effective vibration velocities v_0 = 0.05 m/s and 0.5 m/s for Pb(Zr$_x$Ti$_{1-x}$)O$_3$ doped with 2.1 at% of Fe.

characteristics. The reader should notice that most of the materials with Q_m > 1200 in a company catalog are degraded dramatically at an elevated power measurement. Thus, the Penn State group has developed various measuring techniques of high power piezoelectricity, including 'pulse drive', 'constant current', and 'constant vibration velocity' methods, as we introduced in Section 16.2.

The conventional piezo-ceramics have the limitation of a maximum vibration velocity (v_{max}), since the additional input electrical energy is converted into heat, rather than into mechanical energy. The typical rms value of v_{max} for commercially available materials, defined by the temperature rise of 20 °C from room temperature, is around 0.3 m/sec for rectangular samples operating in the k_{31} mode (like a Rosen-type transformer).[12] Pb(Mn,Sb)O$_3$ (PMS)–lead zirconate tatanate (PZT) ceramics with a v_{max} of 0.62 m/sec are currently used for NEC transformers.[15] By doping the PMS–PZT or Pb(Mn,Nb)O$_3$–PZT with rare-earth ions such as Yb, Eu and Ce, we further developed high power piezoelectrics, which can operate with v_{max} up to 1.0 m/sec.[16,17] Compared with commercially available piezoelectrics, 10 times (square of 3.3 times of v_0) higher input electrical energy and output mechanical energy can be expected from these new materials without generating significant temperature rise, which corresponds to 50 W/cm^2. Figure 16.20 shows the dependence of the maximum vibration velocity v_0 (20 °C temperature rise) on the at% of rare-earth ion, Yb, Eu or Ce in the Pb(Mn,Sb)O$_3$ (PMS)–PZT-based ceramics. Enhancement in the v_0 value is significant by the addition of a small amount of the rare-earth ion.[17]

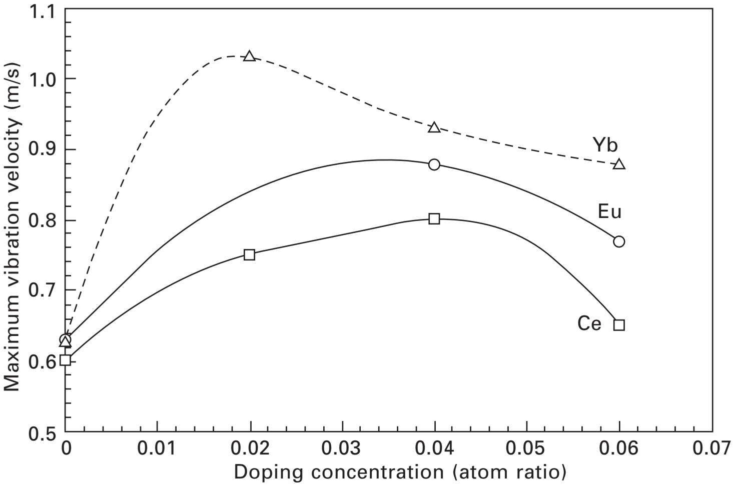

16.20 Dependence of the maximum vibration velocity v_0 (20 °C temperature rise) on the at% of rare-earth ion, Yb, Eu or Ce in the $Pb(Mn,Sb)O_3$ (PMS)–PZT-based ceramics.

16.5.2 Origin of the high power piezoelectrics

'Hard' PZT is usually used for high power piezoelectric applications, because of its high coercive field, in other words, the stability of the domain walls. Acceptor ions, such as Fe^{3+}, introduce oxygen deficiencies in the PZT crystal (in the case of donor ions, such as Nb^{5+}, Pb deficiency is introduced). Thus, in the conventional model, the acceptor doping causes 'domain wall pinning' through the easy reorientation of deficiency-related dipoles, leading to 'hard' characteristics (Domain Wall Pinning Model; Ref. 6). Our group explored the origin of our high power piezoelectric ceramics, and found that the 'internal bias field model' seems to be better for explaining our material's characteristics.

High mechanical Q_m is essential in order to obtain a high power material with a large maximum vibration velocity. Figure 16.21 exhibits suggestive results in the mechanical Q_m increase with time lapse (minute) after the electric poling, measured for various commercial soft and hard PZTs, PSM–PZT, and PSM–PZT doped with Yb.[18,19] It is notable that the Q_m values for commercial hard PZT and our high power piezoelectrics were almost the same, slightly higher than soft PZTs, and around 200–300 immediately after the poling. After a couple of hours passed, the Q_m values increased by more than 1000 for the 'hard' materials, while no change was observed in the 'soft' material. The increasing slope is the maximum for the Yb-doped PSM–PZT. We also found a contradiction that this gradual increase (in a couple of hours) in the Q_m cannot be explained by the above-mentioned

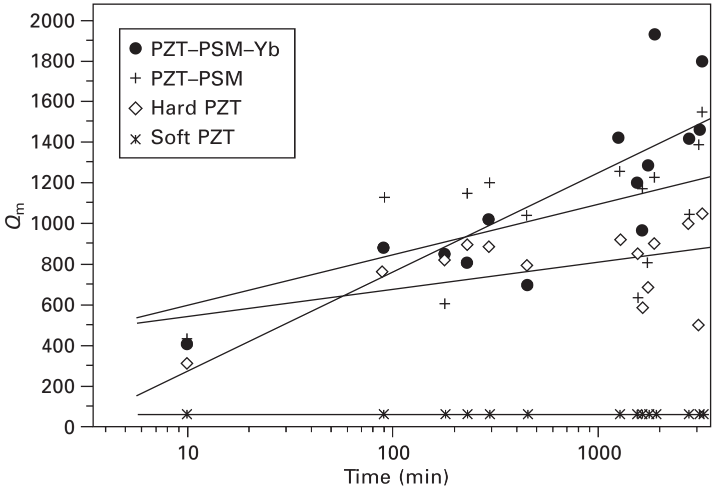

16.21 Change in the mechanical Q_m with time lapse (minute) just after the electric poling, measured for various commercial soft and hard PZTs, PSM–PZT, and PSM–PZT doped with Yb.

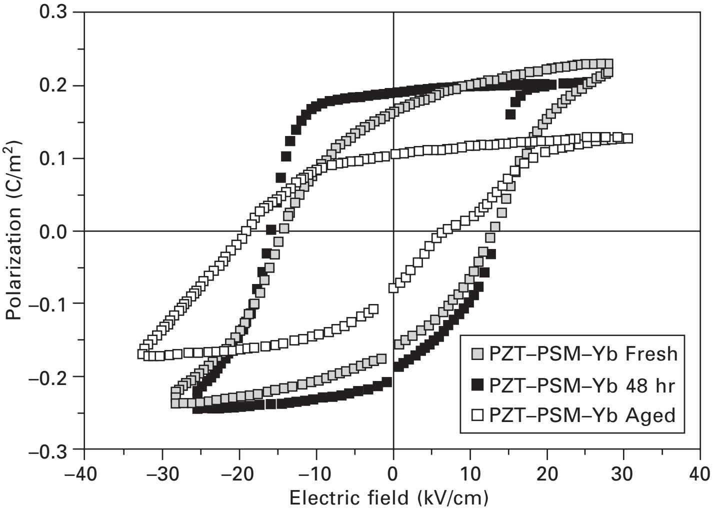

16.22 Polarization vs. electric field hysteresis curves measured for the Yb-doped Pb(Mn,Sb)O_3–PZT sample just after poling (fresh), 48 hours after, and a week after (aged).

'domain wall pinning' model, which hypothesizes that the oxygen-deficit-related dipole should move rather quickly in milli-second scale.

Figure 16.22 shows the polarization vs. electric field hysteresis curves measured for the Yb-doped Pb(Mn,Sb)O_3–PZT sample immediately after poling (fresh), 48 hours after, and a week after (aged).[20,21] Remarkable aging effects could be observed: (a) in the decrease in magnitude of the remanent polarization, and (b) in the positive internal bias electric field growth (i.e., the hysteresis curve shifts leftwards in terms of the external electric field axis). The first phenomenon can be explained by the local domain wall pinning effect, but the large internal bias (close to 1 kV/mm) growth seems to be the origin of the high power characteristics. Suppose that the vertical axis in Fig. 16.18 shifts rightwards (according to 1 kV/mm positive internal bias field), the larger negative electric field is required for realizing the 180° polarization reversal, leading to the resistance enhancement against generating the hysteresis or heat with increasing the applied AC voltage.

Finally, let us propose the origin of this 'internal bias field' growth. Based on the presence of the oxygen deficiencies and the relatively slow (a couple of hours) growth rate, we assume here the oxygen deficiency diffusion model, which is illustrated in Fig. 16.23.[20,21] Under the electric poling process, the defect dipole P_{defect} (a pair of acceptor ions and oxygen deficiency) will be arranged parallel to the external electric field. After removing the field, the oxygen diffusion occurs, which can be estimated on a scale of hours at room temperature. Taking into account slightly different atomic distances between the A and B ions in the perovskite crystal in a ferroelectric (asymmetric) phase, the oxygen diffusion probability will be slightly downward, as shown in the figure schematically, leading to the increase in the defect dipole with time. This may be the origin of the internal bias electric field.

16.5.3 Semi-hard PZT-based ceramics

Though the rare-earth doped PZT–Pb(Mn,Sb)O_3 system with the highest vibration velocity satisfies actuator applications, due to relatively smaller piezoelectric d constants, it cannot replace transducer or transformer

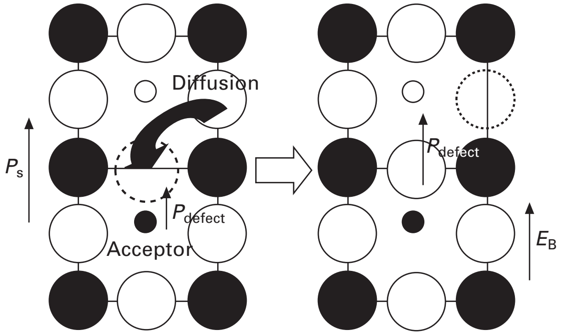

16.23 Oxygen deficiency diffusion model for explaining the internal bias electric field growth.

materials, where direct piezoelectric effect is successively utilized to convert the mechanical energy into final electrical energy. In this sort of electric-mechanical-electric conversion application, since the figure of merit is $v_0 \cdot k$, we modified the composition to improve the high Q_m by sustaining the high d and k, starting from originally soft $Pb(Zn_{1/3}Nb_{2/3})O_3$–$Pb(Ni_{1/3}Nb_{2/3})O_3$–$Pb(Zr_{0.5}Ti_{0.5})O_3$. Sb, Li and Mn were substituted to the $0.8Pb(Zr_{0.5}Ti_{0.5})O_3$–$0.16Pb(Zn_{1/3}Nb_{2/3})O_3$–$0.04Pb(Ni_{1/3}Nb_{2/3})O_3$ ceramics.[22] The composition $0.8Pb(Zr_dTi_{1-d})O_3$–$0.2Pb[(1 - c)\{(1 - b)\ (Zn_{0.8}\ Ni_{0.2})_{1/3}\ (Nb_{1-a}\ Sb_a)_{2/3} - b\ (Li_{1/4}\ (Nb_{1-a}\ Sb_a)_{3/4})\} - c\ (Mn_{1/3}\ (Nb_{1-a}\ Sb_a)_{2/3})]O_3$ ($a = 0.1$, $b = 0.3$, $c = 0.3$ and $d = 0.5$) showed the value of $k_p = 0.56$, $Q_m = 1951$ (planar mode), $d_{33} = 239$ pC/N, $\varepsilon^T_3/\varepsilon_0 = 739$ and the maximum vibration velocity = 0.6 m/s at 31-mode. By adjusting the Zr/Ti ratio, compromised properties of $k_p = 0.57$, $Q_m = 1502$ (planar mode), $d_{33} = 330$ pC/N, $\varepsilon^T_3/\varepsilon_0 = 1653$ and the maximum 31-mode vibration velocity = 0.58 m/s were obtained when Zr/Ti = 0.48/0.52 (see Table 16.3). These compositions are suitable for piezoelectric transformers and transducers.

16.6 High power piezoelectric components

16.6.1 Low temperature sinterable 'hard' PZT

Though we have developed 'high power density' piezoelectric ceramics, multilayer and/or co-firing are the key to develop actual 'high power' components from the device design viewpoint. However, the present Ag–Pd electrode structure has two problems: pd is expensive, and although Ag migration during sintering and under applied electric field can be suppressed by Pd, the electrode conductance is significantly decreased with Pd content. The latter is the major problem in designing multilayer ultrasonic motors and transformers, because the electrode loss appears to be large, leading to heat generation and low efficiency. In order to solve these problems, pure Cu (or pure Ag) electrode will be a key. But, the multilayer samples need to be sintered at a relatively low temperature (900 °C or lower) in a reduced

Table 16.3 Piezoelectric properties of semi-hard piezoelectric ceramics based on $Pb(Zn_{1/3}Nb_{2/3})O_3$–$Pb(Ni_{1/3}Nb_{2/3})O_3$–$Pb(Zr_{0.5}Ti_{0.5})O_3$

Composition	Sintering condition	Q_m (planar)	Q_m (31-mode)	$\varepsilon^T_3/\varepsilon_0$	d_{33}	k_p	k_{31}	T_c(°C)	v_o (m/s)
HP-HT-6-2	1200/2h	1951	1815	739	239	0.56	0.3	285.6	0.6
HP-HT-12-4	1200/2h	1502	1404	1653	330	0.573	0.33	289.58	0.58
HP-LT-17-3	900/2h	1282	*	1326	294	0.56	*	*	0.41

HT: high temperature sintering; LT: low temperature sintering.
HP-HT-6-2: Pb(Zr,Ti)-Pb(Zn,Ni)Nb with Sb, Li and Mn substitution.
HP-HT-12-4: Further modification on the HP-HT-6-2.
HP-LT-17-3: Low temperature sintering of the HP-HT-12-4 with CuO and Bi_2O_3.

atmosphere, when utilizing Cu-embedded electrodes. Thus, low temperature sintering of 'hard' type PZTs is a necessary technology to be developed. Unlike soft PZTs, most of the conventional dopants to decrease the sintering temperature have not been used, because these dopants also degrade the Q_m value significantly.

Based on our high power piezoelectric ceramics, the Sb, Li, and Mn-substituted $0.8Pb(Zr_{0.5}Ti_{0.5})O_3$–$0.16Pb(Zn_{1/3}Nb_{2/3})O_3$–$0.04Pb(Ni_{1/3}Nb_{2/3})O_3$, we further modified them by adding CuO and Bi_2O_3 in order to lower the sintering temperature of the ceramics.[22,23] Table 16.3 summarizes piezoelectric properties of semi-hard piezoelectric ceramics based on $Pb(Zn_{1/3}Nb_{2/3})O_3$–$Pb(Ni_{1/3}Nb_{2/3})O_3$–$Pb(Zr_{0.5}Ti_{0.5})O_3$, sinterable at 900 °C. Under a sintering condition of 900 °C for 2 h, the properties were: $k_p = 0.56$, Q_m (31-mode) = 1023, d_{33} = 294 pC/N, $\varepsilon_{33}/\varepsilon_o$ = 1282 and tan δ = 0.59%, when 0.5wt% CuO and Bi_2O_3 each were added. The maximum vibration velocity of this composition was 0.41 m/s. Figure 16.24 shows the maximum vibration velocity vs. applied field change with various amounts of CuO. Note that with increasing CuO content (0.4 wt% or higher) only 6–8 V_{rms}/mm is required to obtain v_0 = 0.48 m/s.

16.6.2 New high power piezoelectric applications

Using the above new low-temperature-sinterable 'hard' PZT, the Penn State developed an optical fiber alignment device, consisting of a Δ-shaped bimorph

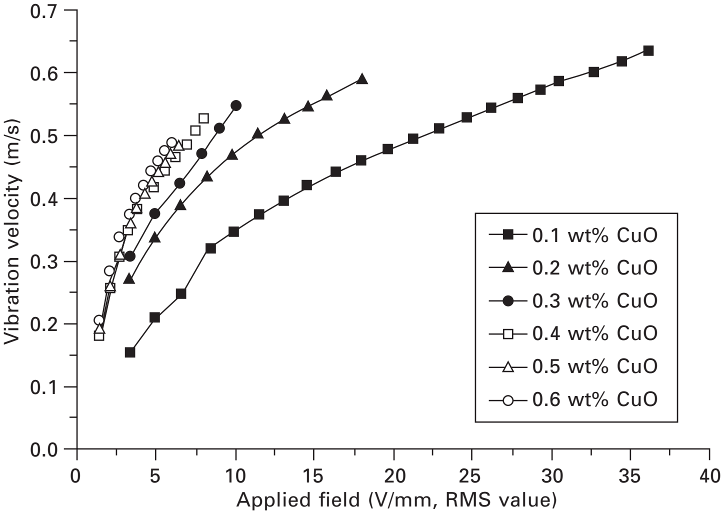

16.24 Vibration velocity variation with applied field in $0.8Pb(Zr,Ti)O_3$–$0.2Pb[0.7\{0.7(Zn,Ni)_{1/3}$–$(Nb, Sb)_{2/3}$–$0.3Li_{1/4}(Nb,Sb)_{3/4}\}$–$0.3Mn_{1/3}(Nb,Sb)_{2/3}]O_3$ for various *x* wt% of CuO added to the ceramic.

piezo-ultrasonic 2D freedom motor, which can be co-fired with packaging material at 900 °C, having mass production capability (Fig. 16.25).[23] The motor was designed around the two orthogonal resonance modes of the Δ-shape bimorph that enabled an elliptical motion of the tip (Fig. 16.25(a)), which then permitted the possibility of 2 degrees of freedom. One of the important goals was to co-fire the ultrasonic motor at 900 °C with commercial LTCC green tapes in order to create a reliable housing structure with low fabrication costs and facilitate mass production.

We also developed Cu and pure Ag embedded multilayer piezo-transformers (Fig. 16.26(b)), which were sintered at 900 °C in a reduced atmosphere with N_2, as illustrated in Fig. 16.26(a).[24] Ring-dot disk multilayer types (OD = 27, center dot $D = 14$ mm) with Cu and Ag/Pd (or Ag/Pt) (as references) revealed the maximum power density (at 20 °C temperature rise) of 42 W/cm^3 and 30 W/cm^3, respectively. This big difference comes from the poor electrical conductivity of Pd or Pt, compared to Cu or pure Ag. Note that the power density depends not only on the piezo-ceramic composition, but also on the electrode species.

16.7 Summary and conclusions

(1) There are three loss origins in piezoelectrics: the dielectric, elastic, and piezoelectric losses. The 180° and non-180° domain wall motions contribute primarily to the extensive dielectric and elastic losses, respectively.

(2) We introduced three loss measurement techniques for separately measuring dielectric, elastic, and piezoelectric losses: quasi-DC, pulse drive, and resonance drive methods.

(3) Heat generation occurs in the sample uniformly under an off-resonance mainly due to the 'intensive dielectric' loss, while heat is generated primarily at the vibration nodal points via the 'intensive elastic' loss under a resonance. In both cases, the loss increase originates from the 'extensive' dielectric loss change with electric field and/or stress.

(4) In a 'hard' piezoelectric PZT, the mechanical quality factor Q_B for the antiresonance (B-type) mode is higher than Q_A for the resonance (A-type) mode. Since the maximum vibration velocity is also higher for the antiresonance mode than for the resonance mode, we propose antiresonance usage for motor and transducer applications.

(5) Actuator materials: doping rare-earth ions into PZT–$Pb(Mn,X)O_3$ (X = Sb, Nb) ceramics increases the maximum vibration velocity up to 1 m/s, which corresponds to one order of magnitude higher energy density than conventionally commercialized piezo-ceramics. To obtain high power density/high vibration velocity materials, domain wall immobility/stabilization via the positive internal bias field seems to be essential, rather than the local domain wall pinning effect.

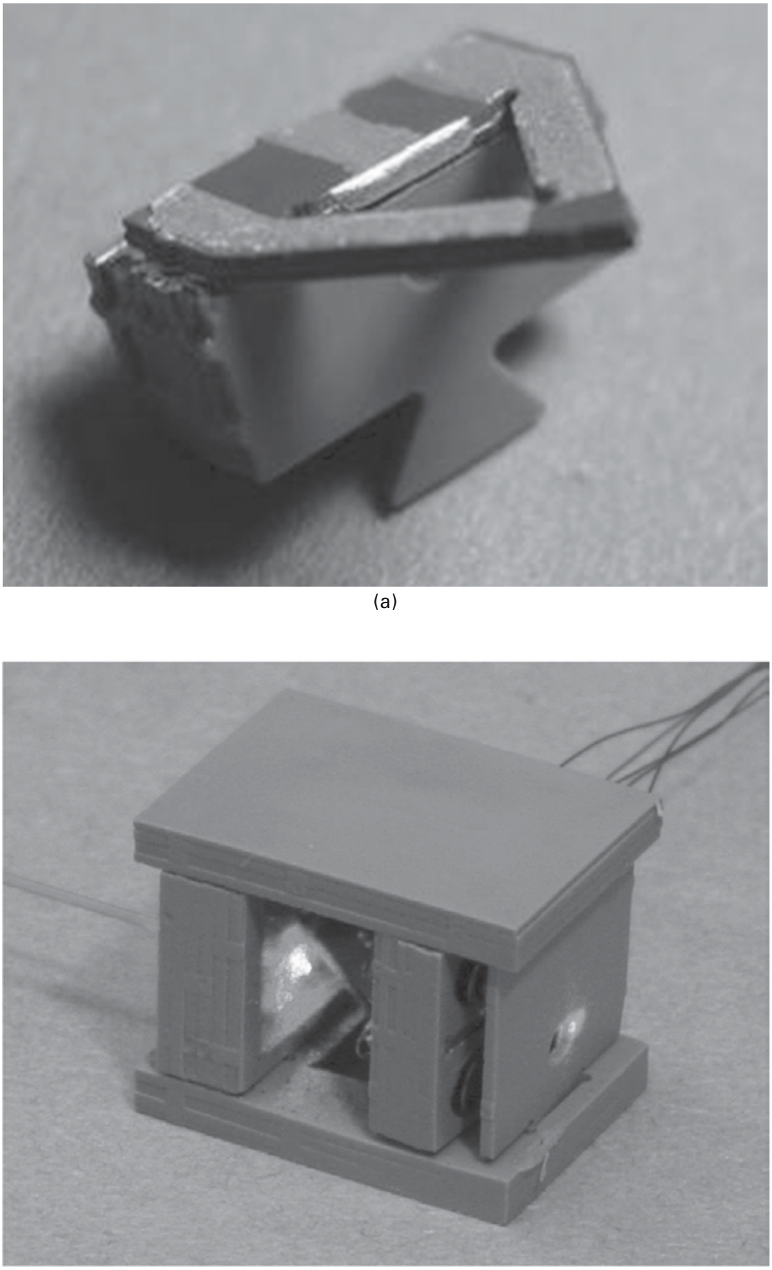

(a)

(b)

16.25 (a) D-shape co-fired motor stator, and (b) integrated optical fiber alignment package.

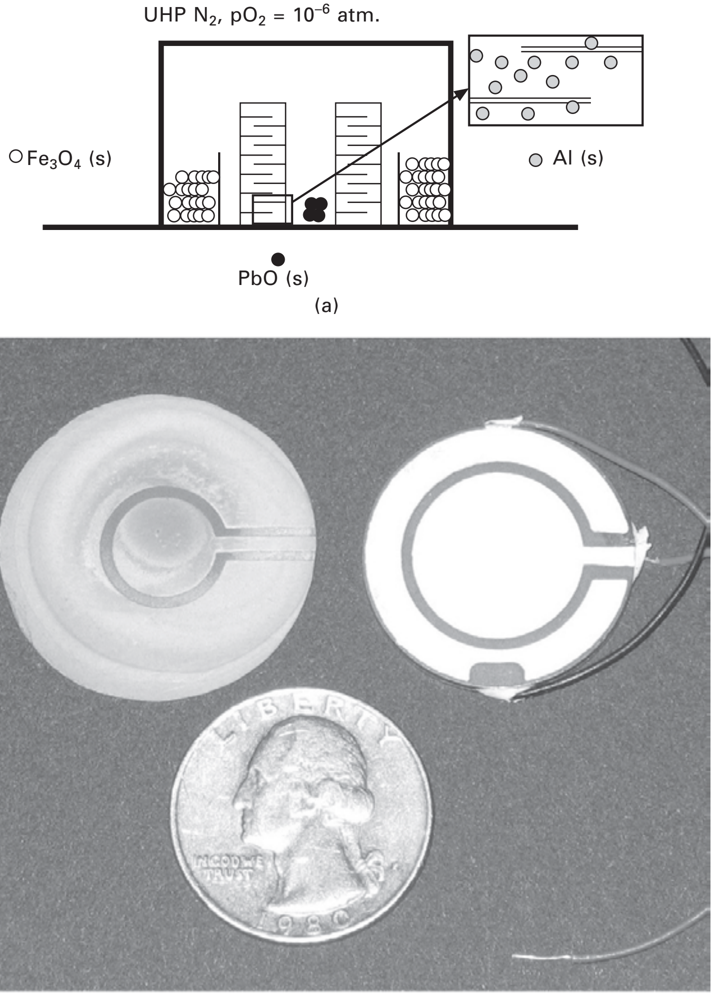

16.26 (a) Experimental setup for sintering Cu-electrode-embedded multilayer transformers in a reduced N$_2$ atmosphere. (b) Multilayer co-fired transformer with hard PZT and Cu (left) or pure Ag (right) electrode, sintered at 900 °C (Penn State trial products).

(6) Transducer materials: the Sb, Li and Mn-substituted $0.8Pb(Zr_{0.48}Ti_{0.52})O_3$–$0.16Pb(Zn_{1/3}Nb_{2/3})O_3$–$0.04Pb(Ni_{1/3}Nb_{2/3})O_3$ ceramics showed the value of $k_p = 0.57$, $Q_m = 1502$ (planar mode), $d_{33} = 330$ pC/N, $\varepsilon^T{}_3/\varepsilon_0 = 1653$ and the maximum vibration velocity = 0.58 m/s at 31-mode. Low-temperature sinterable ‘hard’ piezoelectrics were also synthesized based on the Sb, Li and Mn-substituted ceramics of $0.8Pb(Zr_{0.5}Ti_{0.5})O_3$–$0.16Pb(Zn_{1/3}Nb_{2/3})O_3$–$0.04Pb(Ni_{1/3}Nb_{2/3})O_3$, by adding CuO and

Bi_2O_3, giving rise to $k_p = 0.56$, Q_m (31-mode) = 1023, $d_{33} = 294$ pC/N, $\varepsilon_{33}/\varepsilon_0 = 1282$ and tan $\delta = 0.59\%$, and vibration velocity = 0.41m/s.

(7) Integrated Optical Fiber Alignment package (IFAP) was developed by co-firing the ultrasonic motor at 900 °C with commercial LTCC green tapes in order to create a reliable housing structure at low fabrication cost and to facilitate mass production. Cu embedded multilayer piezo-transformers were also trial manufactured under a low temperature sintering process (900 °C for 2 h) in reduced atmosphere.

16.8 Acknowledgement

Part of this research was supported by the Office of Naval Research through the grant no. N00014-96-1-1173, N00014-99-1-0754, and N00014-08-1-0912.

16.9 References

1. K. H. Haerdtl, *Ceram. Int'l.*, **8**, 121–127 (1982).
2. T. Ikeda, *Fundamentals of Piezoelectric Materials Science* (Ohm Publication Co., Tokyo, 1984), p. 83.
3. N. Setter, ed., *Piezoelectric Materials in Devices* (EPFL, Lausanne, 2002).
4. K. Uchino and S. Hirose, *IEEE-UFFC Trans.*, **48**, 307–321 (2001).
5. J. Zheng, S. Takahashi, S. Yoshikawa, K. Uchino and J. W. C. de Vries, *J. Amer. Ceram. Soc.*, **79**, 3193–3198 (1996).
6. K. Uchino, *Ferroelectric Devices*, CRC Press/Marcel Dekker, New York (2000).
7. Y. Zhuang, S. O. Ural, A. Rajapurkar, S. Tuncdemir, A. Amin and K. Uchino, *Jpn. J. Appl. Phys.*, **48** 041401 (2009).
8. *IEEE Standard on Piezoelectricity*, Std. **176**, p. 54 (1987).
9. K. Uchino, J. Zheng, A. Joshi, Y. H. Chen, S. Yoshikawa, S. Hirose, S. Takahashi and J. W. C. de Vries, *J. Electroceramics*, **2**, 33–40 (1998).
10. S. O. Ural, S. Tuncdemir, Y. Zhuang and K. Uchino, *Jpn. J. Appl. Phys.*, **48** 056509 (2009).
11. S. Tashiro, M. Ikehiro and H. Igarashi, *Jpn. J. Appl. Phys.*, **36**, 3004–3009 (1997).
12. S. Hirose, M. Aoyagi, Y. Tomikawa, S. Takahashi and K. Uchino, *Proc. Ultrasonics Int'l '95*, Edinburgh, pp. 184–187 (1995).
13. M. Umeda, K. Nakamura and S. Ueha, *Jpn. J. Appl. Phys.*, **38**, 3327–3330 (1999).
14. N. Uchida and T. Ikeda, *Jpn. J. Appl. Phys.*, **6**, 1079 (1967).
15. S. Takahashi and S. Hirose, *Jpn. J. Appl. Phys.*, **32**, 2422–2425 (1993).
16. J. Ryu, H. W. Kim, K. Uchino and J. Lee, *Jpn. J. Appl. Phys.*, **42**(3), 1307–1310 (2003).
17. Y. Gao, K. Uchino and D. Viehland, *J. Appl. Phys.*, **92**, 2094–2099 (2002).
18. Y. Gao and K. Uchino, *J. Materials Tech.*, **19**(2), 90–98 (2004).
19. Y. Gao, K. Uchino and D. Viehland, *Jpn. J. Appl. Phys.*, **45**(12), 9119–9124 (2006).
20. Y. Gao, K. Uchino and D. Viehland, *J. Appl. Phys.*, **101** (11), 114110 (2007).
21. Y. Gao, K. Uchino and D. Viehland, *J. Appl. Phys.*, **101**(5), 054109 (2007).

22. S.-H. Park, S. Ural, C.-W. Ahn, S. Nahm and K. Uchino, *Jpn. J. Appl. Phys.*, **45**, 2667–2673 (2006).
23. S.-H. Park, Y.-D. Kim, J. Harris, S. Tuncdemir, R. Eitel, A. Baker, C. Randall and K. Uchino, *Proc. 10th Int'l Conf. New Actuators*, Bremen, Germany, June 14–16, 2006, B7.3, pp. 432–435 (2006).
24. S. Ural, S.-H. Park, S. Priya and K. Uchino, *Proc. 10th Int'l Conf. New Actuators*, Bremen, Germany, June 14–16, 2006, P23, pp. 556–558 (2006).

17
Photostrictive actuators using piezoelectric materials

K. UCHINO, The Pennsylvania State University, USA

Abstract: Photostrictive materials, exhibiting light-induced strains, are of interest for future generation wireless remote control photo-actuators, micro-actuators, and micro-sensor applications. The photostrictive effect arises from a superposition of the 'bulk' photovoltaic effect, i.e. generation of large voltage from the irradiation of light, and the converse piezoelectric effect, i.e. expansion or contraction under the voltage applied. (Pb,La)(Zr,Ti) O_3 (PLZT) ceramics doped with WO_3 exhibit large photostriction under uniform illumination of near-ultraviolet light. Using a bimorph configuration, a photo-driven relay and a micro walking device have been demonstrated. However, for the fabrication of these devices, higher response speed must be achieved. This chapter first reviews the theoretical background of the photostrictive effect, then discusses enhanced performance through composition modification and sample preparation techniques (thickness and surface characteristics of the sample). Future applications of photostrictive actuators are briefly described.

Key words: photovoltaic effect, photostriction, actuator, surface characteristics, PLZT ceramics.

17.1 Introduction

The continuing thrust towards greater miniaturization and integration of microrobotics and microelectronics has resulted in significant work towards development of piezoelectric actuators. One of the bottlenecks of the piezo-actuator is the need for an electric lead wire, which is too heavy for a miniaturized self-propelling robot less than 1 cm^3. The important reason is a drastic reduction of the propelling friction force due to the increase in specific area; that is, surface area/volume or weight ratio. 'What if you, an expert on actuators, could produce a remote-controlled actuator that could bypass the electrical lead?' To many people, 'remote control' equals control by radio waves, light waves, or sound. Light-controlled actuators require that light energy be transduced twice: first from light energy to electrical energy, and second from electrical energy to mechanical energy. These are 'photovoltaic' and 'piezoelectric' effects. A solar cell is a well-known photovoltaic device, but it does not generate sufficient voltage to drive a piezoelectric device; in other words, this combination fails due to the electric impedance mismatch.

The key to success is to adopt a high-impedance photovoltaic effect (so-called ‘anomalous’ or ‘bulk’ photovoltaic effect in piezoelectrics), which is totally different from the p-n junction-based solar cell.

In the recent years, photostrictive actuators – which converts the photonic energy to mechanical motion directly – have drawn significant attention for their potential usage in microactuation and microsensing applications. Optical actuators are also anticipated to be used as the driving component in optically controlled electromagnetic noise-free systems. The photostrictive effect will also be used in fabricating a photophonic device, where light is transformed directly into sound from the mechanical vibration induced by intermittent illumination at a human-audible frequency.

The photostrictive effect has been studied mainly in ferroelectric polycrystalline materials for potential commercial applications. Lanthanum-modified lead zirconate titanate (PLZT) ceramic is one of the most promising photostrictive materials due to its relatively high piezoelectric coefficient and ease of fabrication. However, previous studies have shown that for commercial applications, improvements in photovoltaic efficiency and response speed of PLZT ceramics are still essential. The improvement in photostrictive properties requires consideration of several parameters, such as material parameters, processing condition and microstructure, and sample configuration and performance testing conditions.

This chapter first reviews the theoretical background of the photostrictive effect before going on to discuss enhanced performance through composition modification and sample preparation techniques (thickness and surface characteristics of the sample). Future applications of photostrictive materials are briefly described.

17.2 Photovoltaic effect

The photostriction phenomenon was discovered by Dr. P. S. Brody and the author independently almost at the same time in 1981.[1] In principle, the photostrictive effect arises from a superposition of the ‘bulk’ photovoltaic effect, i.e. generation of large voltage from the irradiation of light, and the converse piezoelectric effect, i.e. expansion or contraction under the voltage applied.[2] The photostrictive phenomenon has been observed in certain ferroelectric/piezoelectric materials. By doping suitable ionic species, the photovoltaic effect is introduced in the material. The figure of merit (FOM) for photostriction magnitude is generally expressed as the product of photovoltage (electric field), E_{ph}, and the piezoelectric constant, d_{33}, while the FOM for response speed is determined by the photocurrent (current density), I_{ph}, as $d_{33}I_{ph}/C$ (C: capacitance of the photostrictive device). Therefore, for application purposes, enhancement and/or optimization of photostrictive properties requires consideration of both the terms in the figure of merit; that is, photovoltaic voltage and current, as well as its piezoelectric *d* constant. Recently, PLZT ceramics have gained considerable attention due to their excellent photovoltaic properties, high d_{33}, and ease of fabrication. We will review the background of the photovoltaic effect first in this section.

17.2.1 Principle of the bulk photovoltatic effect

'Bulk' photovoltaic effect

When a non-centrosymmetric piezoelectric material (with some dopants) is illuminated with uniform light having a wavelength corresponding to the absorption edge of the material, a steady photovoltage/photocurrent is generated.[3] The distinction between the photovoltaic effect and the pyroelectric effect (i.e., voltage/charge generation due to the temperature change) may not be obvious. Figure 17.1 demonstrates the difference, where illumination responses of photovoltaic current are plotted under two different external resistances in 1.5 mol% MnO_2-doped $0.895PbTiO_3$–$0.105La(Zn_{2/3}Nb_{1/3})O_3$ ceramic.[4] Mercury lamp illumination on this ceramic sample slightly increased the sample temperature, leading to the initial voltage peak (up to 8 mV through 10 MΩ resistor) for a couple of tens of seconds. However, note that the output voltage stabilized around 4 mV after temperature stability was obtained. The magnitude of the steady current is independent of the externally connected resistance. When the illumination was shut off, the negative pyrocurrent was observed due to a slight temperature decrease again for a period of tens of seconds. But, the output voltage became completely zero after the saturation, which verified that there was no junction

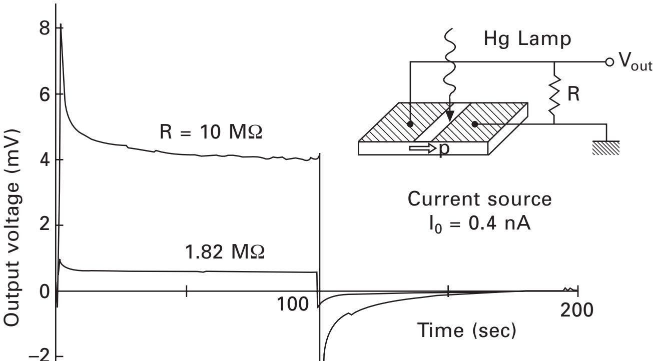

17.1 Illumination responses of photovoltaic current for 1.5 mol% MnO_2-doped $0.895\ PbTiO_3$–$0.105\ La(Zn_{2/3}Nb_{1/3})O_3$ ceramic.

(piezoelectric ceramic–metal electrode) effect. The reader can now clearly understand the difference between the photovoltaic and pyroelectric effects from this demonstration. Note that we can eliminate the pyroelectric effect when we use an IR blocking filter for cutting the longer wavelength light intensity (see Fig. 17.2).

In some materials, the photovoltage generated is greater than the band-gap energy, and can be of the order of several kV/cm. This phenomenon, thus referred to as the ‘bulk’ or ‘anomalous’ photovoltaic effect (APV), seems to be totally different from the corresponding phenomenon in the p-n junction of semiconductors (e.g., solar battery).[5,6] The APV effect is observed primarily in the direction of the spontaneous polarization (P_S) in the ferroelectric material, and the generated photovoltage is proportional to the sample length along the P_S direction.

The origin of the photovoltaic effect is not yet clear, even though several models have been proposed on a possible mechanism. The key features of the APV effect are summarized as follows:

- This effect is observed in a uniform crystal or ceramic having non-centrosymmetry, and is entirely different in nature from the p-n junction effect observed in semiconductors.
- A steady photovoltage/current is generated under uniform illumination.
- The magnitude of the induced voltage is greater than the band gap of the crystal.

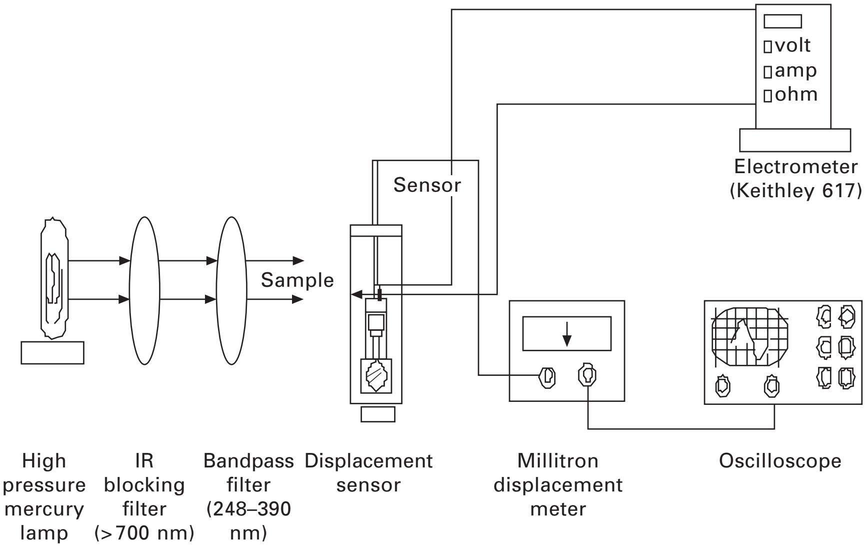
volt
amp
ohm
Electrometer (Keithley 617)
Sensor
Sample
High pressure mercury lamp
IR blocking filter (>700 nm)
Bandpass filter (248–390 nm)
Displacement sensor
Millitron displacement meter
Oscilloscope

17.2 Experimental setup for measuring photovoltaic and photostrictive effects.

Two models proposed previously by the author's group were the current source model and the voltage source model.

Experimental setup

Prior to the detailed discussion, the measuring setup is described here (see Fig. 17.2). PLZT ceramic samples are cut into standard sizes of 5 × 5 mm^2 and polished to 1 mm thickness. The samples are poled along the length (5 mm) under a field of 2 kV/mm at 120 °C for 10 min. The ceramic preparation methods are described in Sections 17.2.3 and 17.3.3.

Radiation from a high-pressure mercury lamp (Ushio Electric USH-500D) is passed through infrared-cut optical filters in order to minimize the thermal/pyroelectric effect. The light with the wavelength peak around 366 nm, where the maximum photovoltaic effect of PLZT is obtained, is then applied to the sample. A xenon lamp is alternatively used to measure the wavelength dependence of the photovoltaic effect. The light source is monochromated by a monochromator to 6 nm HWHM.

The photovoltaic voltage under illumination generally reaches several kV/cm, and the current is in the order of nA. The induced current is recorded as a function of the applied voltage over a range –100 V to 100 V, by means of a high-input impedance electrometer (Keithley 617). The photovoltaic voltage and current are determined from the intercepts of the horizontal and the vertical axes, respectively. An example measurement is shown in Fig. 17.3. The photovoltage (typically kV) is estimated by the linear extrapolation method. Photostriction is measured directly by a differential transformer or an eddy current displacement sensor.

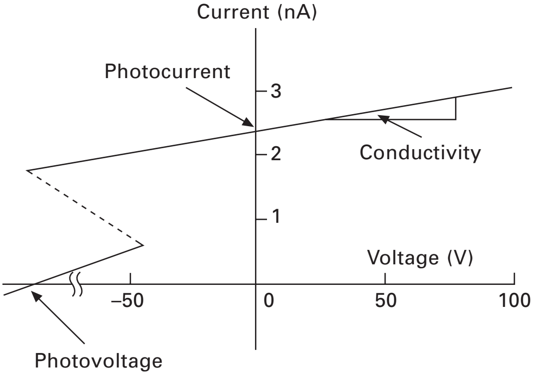

17.3 Photocurrent measured as a function of applied voltage under illumination.

Current source model

Taking into account the necessity of both doping and crystal asymmetry, we proposed a current source model, as illustrated in Fig. 17.4, which is based on the electron energy band model for (Pb,La)(Zr,Ti)O_3 (PLZT).[7,8] The energy band is basically generated by the hybridized orbit of p-orbit of oxygen and d-orbit of Ti/Zr. The donor impurity levels induced in accordance with La doping (or other dopants) are present slightly above the valence band. The transition from these levels with an asymmetric potential due to the crystallographic anisotropy may provide the 'preferred' momentum to the electron. Electromotive force is generated when electrons excited by light move in a certain direction of the ferroelectric/piezoelectric crystal, which may arise along the spontaneous polarization direction. The asymmetric crystal exhibiting a photovoltaic response is also piezoelectric in principle, and therefore a photostriction effect is expected as a coupling of the bulk photovoltaic voltage (E_{ph}) with the piezoelectric constant (d).

The photocurrent J_{ph} varies in proportion to the illumination intensity I:

$$J_{ph} = \kappa\alpha I, \qquad 17.1$$

where α denotes the absorption coefficient and κ is a Glass constant (named according to Glass's contribution to the APV effect).[9] On the other hand, the photovoltage E_{ph} shows saturation caused by a large photoconductive effect, represented by

$$E_{ph} = \kappa\alpha I/(\sigma_d + \beta I), \qquad 17.2$$

where σ_d is the dark conductivity and β is a constant relating to the photoconductivity.

This model is validated as follows:

(1) The photovoltaic current is constant in Fig. 17.1, regardless of the externally connected resistance.

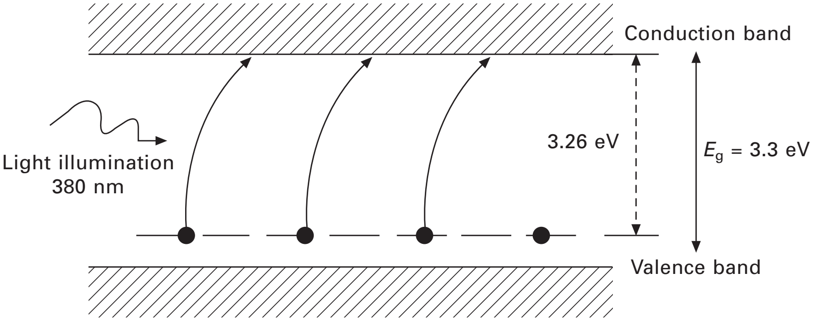

17.4 Energy band gap model of excited electron transition from deep donor impurity level in PLZT.

(2) The photocurrent J_{ph} is strongly dependent on the wavelength under constant intensity of illumination, suggesting a sort of band gap, as is shown in Fig. 17.5. A sharp peak is observed at 384 nm or 372 nm near the absorption edge for 0.895PT–0.105LZN or PLZT (3/52/48), respectively. The donor level seems to be rather deep, close to the valence band level.

(3) The linear relationship of the photocurrent with light intensity (Eq. 17.1 above) is experimentally verified in Fig. 17.6, where photo-induced short-circuit current J_{ph} (a) and the open-circuit electric field E_{ph} (b) are plotted as a function of illumination intensity I for pure and MnO_2-doped 0.895PT–0.105LZN.[4]

Voltage source model

In this model, the photovoltaic properties are attributed to the photocarriers and internal electric fields generated by near-UV illumination. The optical nonlinearity of the second order, which is popularly introduced in ferroelectrics, is proposed as the origin of photo-induced DC field generation.[10] The expression for the polarization of dielectrics, considering the nonlinear effect up to the second order is given by:[11]

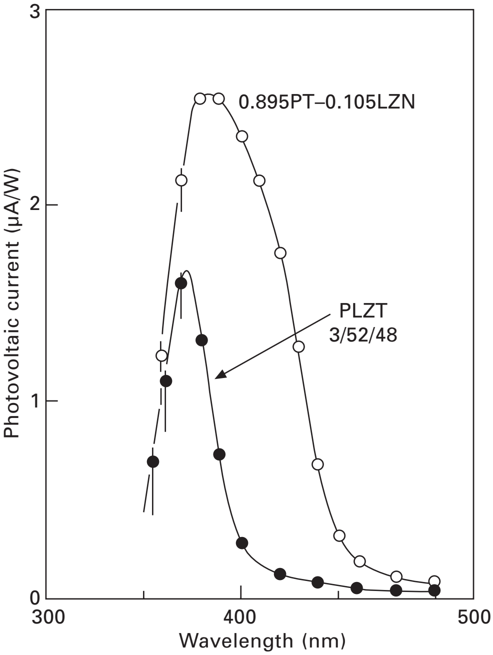

17.5 Wavelength dependence of photovoltaic current in 0.895PT–0.105LZN and PLZT (3/52/48).

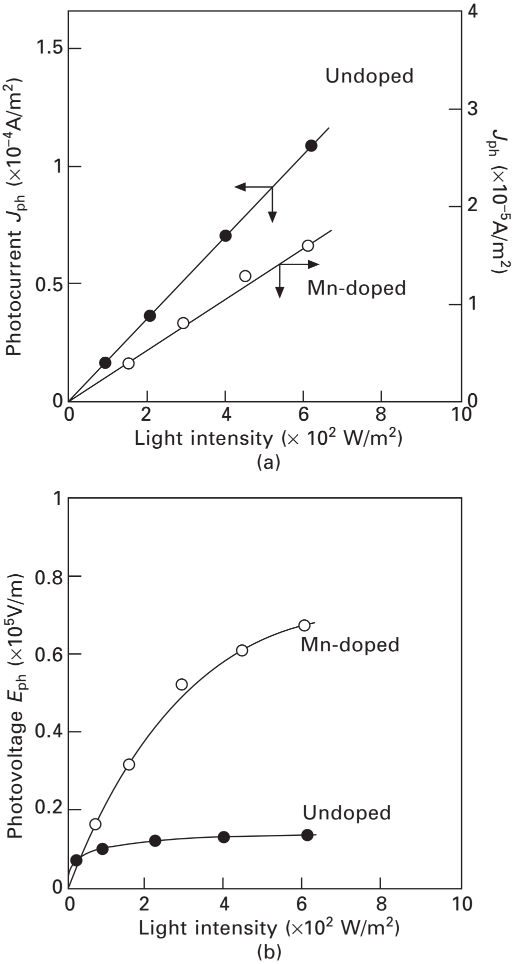

(a)

(b)

17.6 Short-circuit current J_{ph} (a) and open-circuit electric field E_{ph} (b) as a function of illumination intensity *I*for pure and MnO$_2$-doped 0.895PT–0.105LZN.

$$P = \varepsilon_0(\chi_1 E_{op} + \chi_2 E_{op}^2), \tag{17.3}$$

where ε_0 is the permittivity of vacuum, χ_1 is the linear susceptibility, χ_2 is the nonlinear susceptibility of the second order, and E_{op} is the electric field of the illumination beam at an optical frequency (THz).

In dielectrics, the value of the local electric field is different from the value of the external electric field. For simplicity, the local field in dielectrics has been approximated using the Lorentz relation for a ferroelectric material (as Ref 12):

$$E_{\text{local}} = E + \frac{\gamma P}{3\varepsilon_0} \tag{17.4}$$

where E is the external electric field and γ is the Lorentz factor. When an alternating electric field at an optical frequency is applied (i.e., light illumination), the average of the local electric field E_{local} is not zero, but can be calculated as:

$$\overline{E_{\text{local}}} = \frac{1}{6}\gamma\chi_2 E_{\text{op}}^2 \tag{17.5}$$

It must be noted that Eq. 17.5 has been derived for a coherent propagation of the light wave at a single frequency. However, the condition of coherent illumination may not be satisfied in our experimental conditions, where a mercury lamp is used as a light source. The nonlinear effect will be affected by the degree of coherence. Therefore, considering the depression of nonlinear effect due to the incoherency, the expression for the effective DC field induced by incoherent light source may be modified as:

$$\overline{E_{\text{local}}} = c_1\,\gamma\chi_2 (E_{\text{op}}^2)^{\beta} \tag{17.6}$$

where c_1 is a constant and β is a parameter expressing the depression effect. The value of parameter β is expected to lie between 0 and 1. Replacing the variable E_{op}^2 with the intensity (I_{op}) [Ref. 11], the following expression for the average induced (DC) field due to the incoherent light can be obtained:

$$E_{\text{dc}} = \overline{E_{\text{local}}} = c_2\,\gamma\chi_2 (I_{\text{op}})^{\beta} \tag{17.7}$$

where c_2 is a constant and E_{dc} is the effective DC field for photo-induced carriers. Note that the induced field, E_{dc}, is proportional to the nonlinear susceptibility as well as the Lorentz factor, γ.

The photoconductivity can be obtained as a function of light intensity, I_{op}:

$$\sigma_{\text{op}} = c_3 q\mu\sqrt{\frac{I_{\text{op}}}{R}} \tag{17.8}$$

where q is the charge of the photocarrier, μ, the carrier mobility, R, the recombination rate of the carrier, and c_3 is a constant. Since the photo-current is provided by the product of the photoconductivity and the photo-induced DC field ($j_{\text{ph}} = \sigma_{\text{op}} E_{\text{dc}}$), we finally obtain:

$$J_{\text{ph}} = c_4\, q\mu\gamma\chi_2\sqrt{\frac{1}{R}}(I_{\text{op}})^{\beta+\frac{1}{2}} \tag{17.9}$$

where c_4 is another constant. Equations 17.8 and 17.9 provide a correlation for the photovoltaic response of ferroelectrics on the basis of optical nonlinearity.

The model validation and analysis are made by the light intensity dependence of photovoltaic properties. The experiments were made on PLZT 3/52/48 samples 1 mm and 140 μm in thickness. Figure 17.7(a) shows the plot of photoconductivity (σ_{op}) as a function of light intensity (I_{op}). The exponent relating the photo-conductivity and the light intensity was calculated to be 0.54. This is in good agreement with the value of 0.5 derived for the recombination process of the carriers (Eq. 17.8). Note the difference from Eq. 17.2, where we assume the photoconductivity directly in proportion to the intensity (see Fig. 17.6). Figure 17.7(b) shows the experimental results of the open-circuit photovoltage (E_{ph}) as a function of light intensity. The photovoltage was found to be proportional to the square root of the light intensity, leading to $\beta = 0.5$ (Eq. 17.7). Figure 17.7(c) shows the results of short-circuit photocurrent (J_{ph}) as a function of I_{ph}. The parameter β based on Eq. 17.9 was calculated to be 0.46, which is very close to the β value above. The depression in β value can be attributed to the incoherent illumination of the mercury lamp. Note again that J_{ph} is almost directly proportional to I_{ph}, in accordance with Eq. 17.1 (Fig. 17.6).

Investigation was further made in terms of the illumination coherency. Since a partial coherence of light can be achieved in a very small area, an increase in β is expected in thinner photovoltaic samples. The photocurrent measured as a function of light intensity in a very thin (140 μm) PLZT sample (Fig. 17.7(d)) resulted in the parameter β (Eq. 17.9) being 0.80, which is higher than the β value of 0.46 in the thicker sample (1 mm thickness). These results suggest that the parameter β increases with a decrease in the thickness of photovoltaic sample, due to higher coherency of illumination in thinner samples. This suggests that an enhancement in the photovoltaic properties may be achieved in a very thin sample or by using coherent illumination. As suggested already, we cannot conclude at present which of the two models better fits the experimental results.

17.2.2 Effect of light polarization direction

The effect of the light polarization direction on the photovoltaic phenomenon also helps with understanding the mechanism. Figure 17.8 shows the measuring system of the dependence of photovoltaic effect on light polarization direction (a), and the photovoltaic voltage and current as a function of the rotation angle measured for the PLZT (3/52/48) polycrystalline sample (b). The rotation angle θ was taken from the vertical spontaneous polarization direction. Even in a polycrystalline sample, both the photovoltatic voltage and current provide the maximum at $\theta = 0$ and 180° and the minimum at $\theta = 90°$; this also indicates that the contributing electron orbit may be the p-d hybridized orbit mentioned

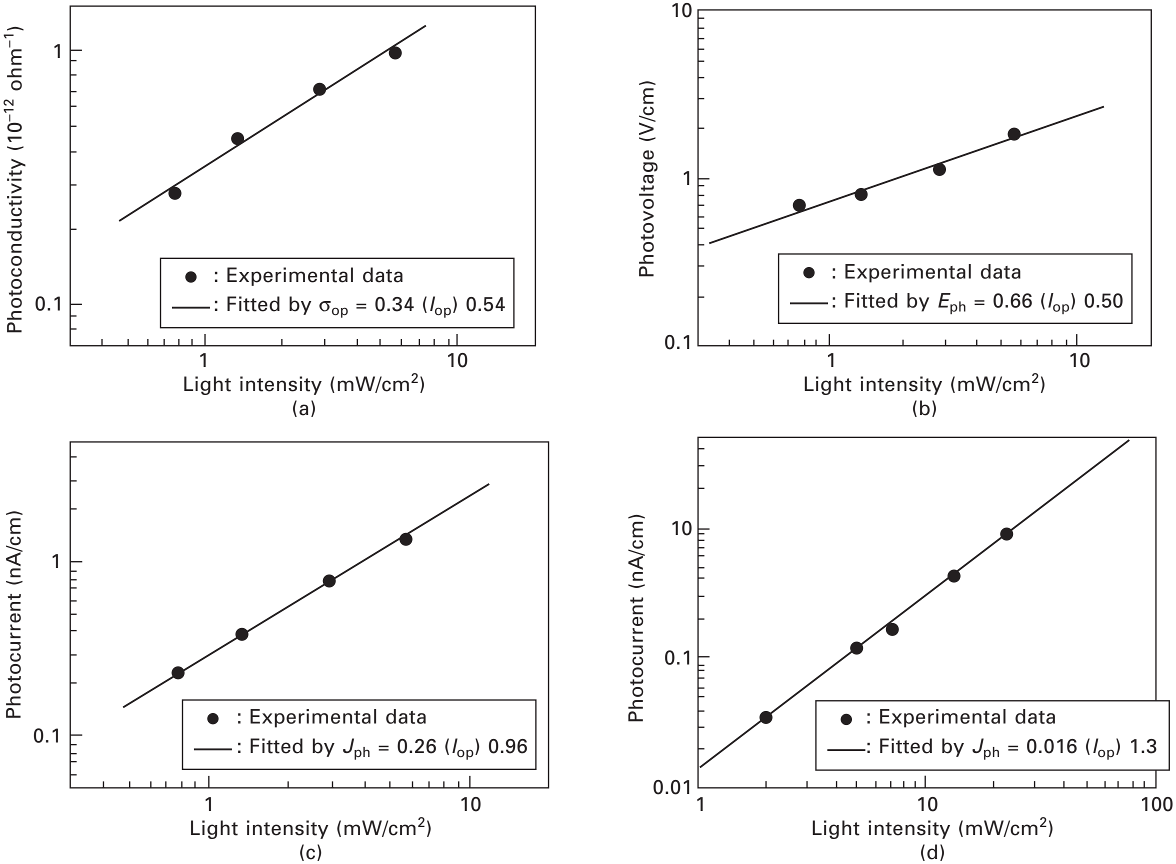

17.7 Dependence of (a) photoconductivity, (b) photovoltage, and (c) photocurrent on illumination intensity in a PLZT 3/52/48 sample 1 mm in thickness; (d) the result for a sample 140 μm in thickness.

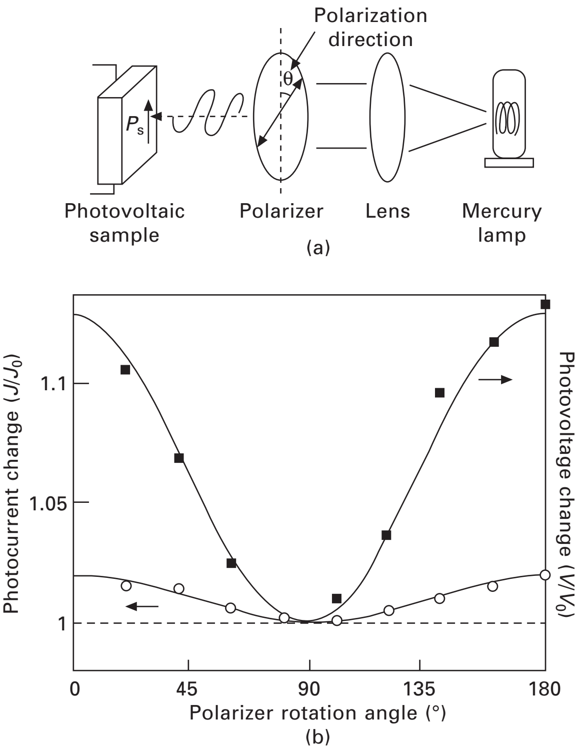

17.8 (a) Measuring system of the dependence of photovoltaic effect on light polarization direction. (b) Photovoltaic voltage and current as a function of the rotation angle.

above (i.e., the perovskite Zr/Ti-O direction). This experiment is also important when the photostriction is employed in ‘photophones’, where the sample is illuminated with the polarized light traveling through an optical fiber.

17.2.3 PLZT composition research

Since the FOM of the photostriction is evaluatated by the product of the photovoltatic voltage and the piezoelectric constant; i.e., $d \cdot E_{ph}$, $Pb(Zr,Ti)O_3$ (PZT)-based ceramics are focused on primarily because of their excellent piezoelectric properties, i.e., high *d* values. Lanthanum-doped PZT (PLZT) is one such material with La^{3+} donor doping in the A-site, which is also well known as a transparent ceramic (good sinterability) applicable to electro-optic devices.

PLZT (x/y/z) samples were prepared in accordance with the following composition formula:

$$Pb_{1-x}La_x(Zr_yTi_z)_{1-x/4}O_3. \ (y + z = 1)$$

As discussed in Section 17.3.2, the piezoelectric *d* coefficient exhibits the maximum around the morphotropic phase boundary (MPB) between the tetragonal and rhombohedral phases, SO our composition search was also focused around the MPB compositions. Figure 17.9 shows the photocurrent J_{ph} for various PLZT compositions with tetragonal and rhombohedral phases, plotted as a function of their remanent polarization P_r.

1. Significantly large photocurrent is observed for the tetragonal composition PLZT (3/52/48).[13] This is the major reason why many data in this chapter were taken from this composition. The details will be discussed in Section 17.3.2.
2. The relation $J_{ph} \propto P_r$ first proposed by Brody[14,15] appears valid for the PLZT system. Further, it is worth noting that the P_r value capable of producing a certain magnitude of J_{ph} is generally larger in the rhombohedral symmetry group than in the tetragonal group. The average remanent polarization exhibiting the same magnitude of photocurrent differs by 1.7 times between the tetragonal and rhombohedral phases, which is nearly equal to $\sqrt{3}$, the inverse of the direction cosine of the [111] axis in the perovskite structure. This suggests the photo-induced electron excitation is related to the (001) axis-oriented orbit, i.e., the hybridized orbit of p-orbit of oxygen and d-orbit of Ti/Zr.[16]

17.2.4 Dopant research

The photovoltaic effect is caused by the dopant in a ferroelectric/piezoelectric crystal, as discussed in Section 17.2.1. La^{3+} seems to be the primary dopant

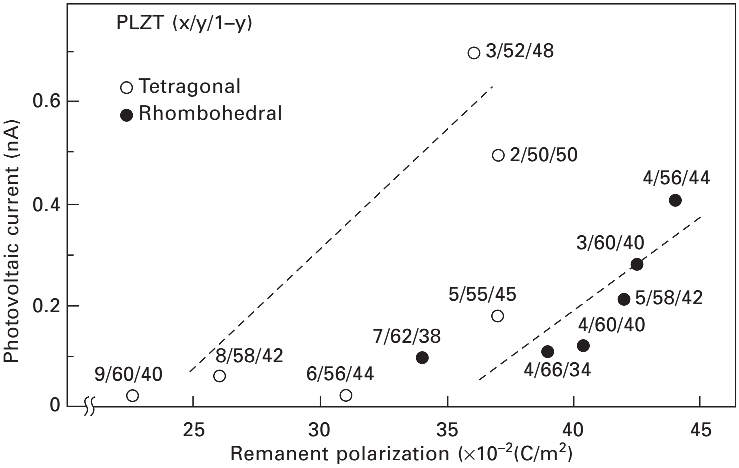

17.9 Interrelation of photovoltaic current with remanent polarization in PLZT family.

in $Pb(Zr,Ti)O_3$. Additional impurity doping on PLZT also affects the photovoltaic response significantly. Figure 17.10 shows the photovoltatic response for various dopants with the same concentration of 1 at% into the base PLZT (3/52/48) under an illumination intensity of 4 mW/cm^2 at 366 nm.[8] The dashed line in Fig. 17.10 represents the constant power curve corresponding to the non-doped PLZT (3/52/48). Photovoltaic power is enhanced by donor doping onto the B-site (Nb^{5+}, Ta^{5+}, W^{6+}). In contrast, impurity ions substituting at the A-site and/or acceptor ions substituting at the B-site, whose ionic valences are small (1 to 4), degrade the effect on performance. Figure 17.11 shows the photovoltaic response plotted as a function of at% of WO_3 doping concentration.[6] Note that the maximum power is obtained at 0.4 at% of the dopant, due to a significant enhancement in the current density.

17.3 Photostrictive effect

17.3.1 Figures of merit

The figures of merit for photostriction are derived here. The photostriction is induced as a function of time, t, as

$$x_{\mathrm{ph}} = d_{33}E_{\mathrm{ph}}\left(1 - \exp\left(\frac{-t}{RC}\right)\right), \qquad 17.10$$

where x_{ph} is the photo-induced strain, d_{33}, the piezoelectric constant of the

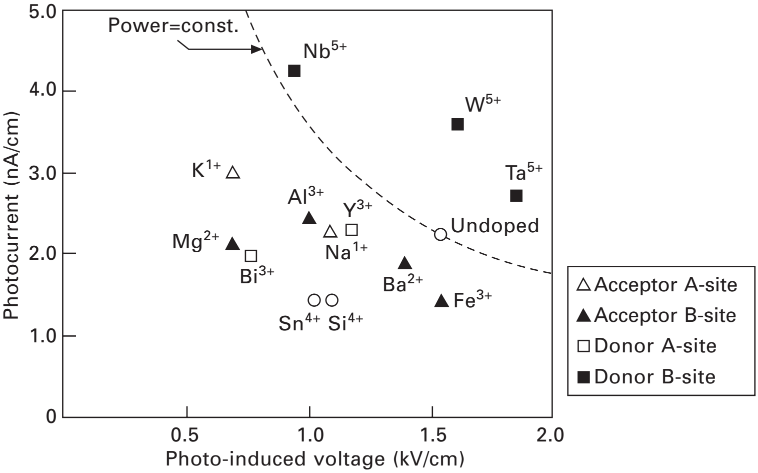

17.10 Photovoltaic response of PLZT (3/52/48) for various impurity dopants (illumination intensity: 4 mW/cm^2).

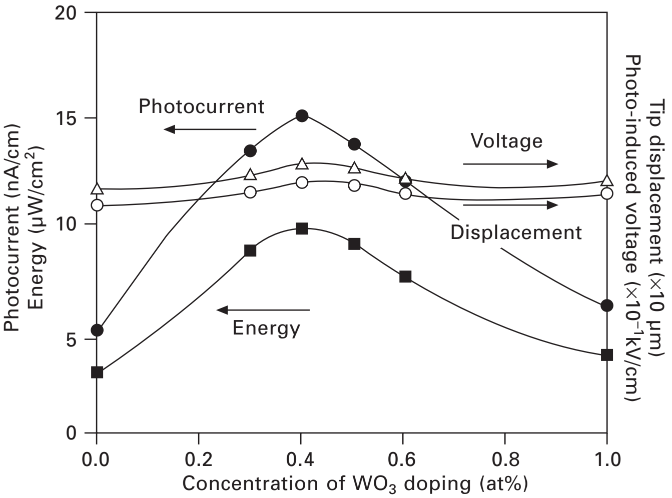

17.11 Photovoltaic current, voltage, power, and tip displacement of a bimorph specimen as a function of dopant concentration in WO_3-doped PLZT (3/52/48).

materials, E_{ph}, photovoltage, I_{ph}, photocurrent, t, time, R and C are resistance and capacitance of the material, respectively.

For $t << 1$, we obtain:

$$x_{ph} = d_{33}E_{ph}\left(\frac{t}{RC}\right). \qquad 17.11$$

Thus, the figure of merit for response speed should be provided by $d_{33}E_{ph}\left(\frac{1}{RC}\right)$.

Taking account of the relation $I_{ph} = \frac{E_{ph}}{R}$ this figure of merit is transformed to $\frac{d_{33}I_{ph}}{C}$ Or, it can be given by $\frac{d_{33}I_{ph}}{\varepsilon}$ (ε: permittivity).

On the other hand, for $t >> 1$, the saturated strain is provided by:

$$x_{ph} = d_{33}E_{ph}. \qquad 17.12$$

Thus, the figure of merit for the magnitude of strain is defined by $d_{33}E_{ph}$. In order to obtain high photo-induced strain, materials with high d_{33} and E_{ph} are needed. On the other hand, for high response speed such as photophonic applications, materials with high d_{33}, I_{ph} and low dielectric constant ε are required.

17.3.2 Materials considerations

We reconsider the optimum compositions in the PLZT system from the photostrictive actuator's viewpoint. Figure 17.12(a), (b) and (c) shows contour maps of photovoltaic voltage E_{ph}, photocurrent I_{ph}, and piezoelectric

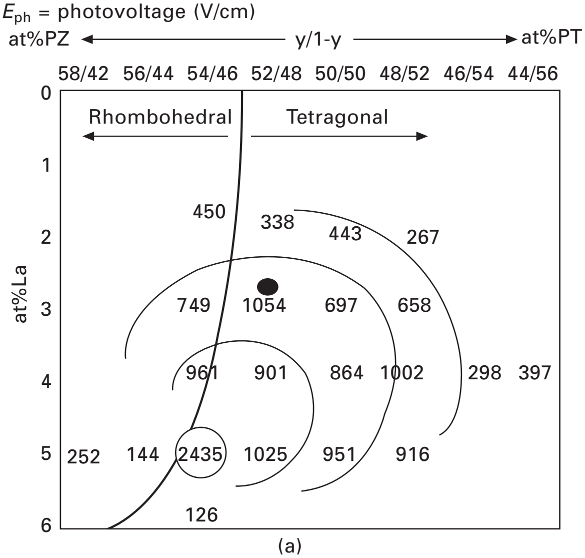

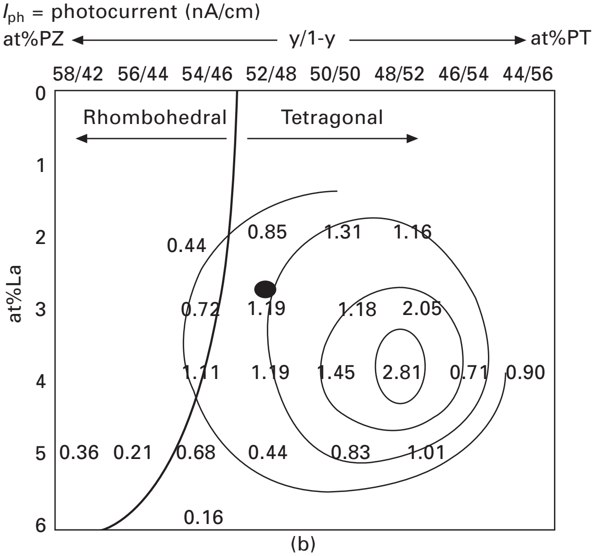

17.12 Contour maps of (a) photovoltaic voltage E_{ph}, (b) photocurrent I_{ph}, and (c) piezoelectric constant d_{33} in the PLZT (x/y/1–y) system.

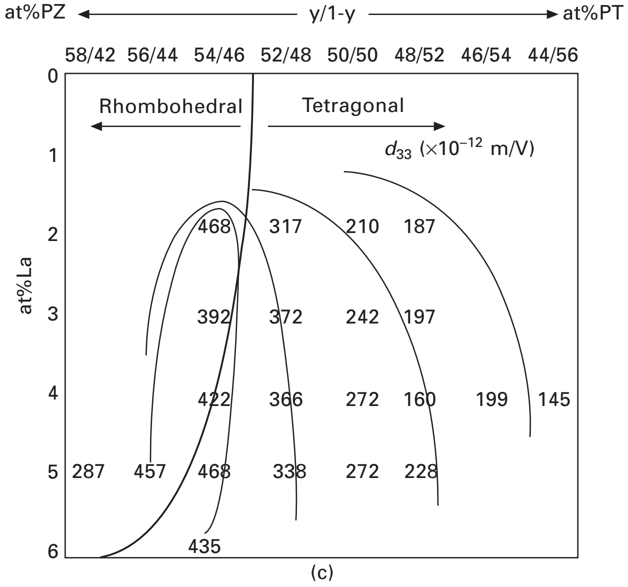

17.12 Continued

constant d_{33} on the PLZT (x/y/1−y) phase diagram, respectively.[17] The morphotropic phase boundary (MPB) appears between the rhombohedral and tetragonal phases around 52–56% of Zr concentration y. As is well known, the piezoelectric coefficient exhibits the maximum along the MPB. The photovoltaic effect is also excited around the MPB. However, precisely speaking, the photovoltage was found to be maximum at PLZT 5/54/46, while the maximum photocurrent was found at PLZT 4/48/52. In Fig. 17.12(a) and (b), the solid circles indicate the location of PLZT 3/52/48 which had been reported earlier to exhibit the maximum photovoltage and current. In the finer measurement, the maximum photovoltage and current have been found at different compositions of the PLZT system, both still being in the tetragonal phase. In conclusion, the FOM $d_{33}E_{ph}$ shows maximum for PLZT 5/54/46, while the maximum of the FOM $d_{33}I_{ph}/C$ is for PLZT 4/48/52. A similar composition study is reported by Nonaka *et al.*[18]

17.3.3 Ceramic preparation method effect

Processing method

Fabrication and processing methods have been reported to profoundly influence the photovoltaic properties and strain responses of PLZT ceramics.[16,19,20] This effect comes through the influence of processing methods on the microstructure, and other physical properties such as density, porosity, and chemical composition. Ceramic materials with high density, low porosity, better homogeneity and a good control of stoichiometry are desired for enhanced photovoltaic and photostrictive properties. Coprecipitation and sol-gel techniques are two of the chemical routes which have the inherent advantage in producing high density homogeneous ceramics with a greater control of stoichiometry. Therefore, processes to fabricate photostrictive ceramics via chemical routes with suitable non-oxide precursors are attractive. PLZT ceramics prepared by sol-gel and coprecipitated techniques exhibit better photovoltaic and photostrictive properties as compared to the oxide mixing process.[19,20] Ceramics prepared by solid state reaction have compositional variation and inhomogeneous distribution of impurities whereas the ceramics prepared by chemical synthesis exhibited high purity with good chemical homogeneity at the nanometer scale.

Grain size effect

Even when the composition is fixed, the photostriction still depends strongly on the sintering condition, or in particular, grain size.[16,21] Figure 17.13 shows the dependence of the photostrictive characteristics on the grain size. As is well known, the piezoelectric coefficient d_{33} gradually decreases with decreasing grain size down to the 1 μm range. On the other hand, photovoltage increases dramatically with a decrease in grain size, and the photocurrent seems to exhibit the maximum at around 1 μm. Thus, the photostriction exhibits a dramatic increase similar to the photovoltage change. The smaller grain sample is preferable, if it is sintered to a high density.

Surface/geometry dependence

Since the photostrictive effect is excited by the absorption of illumination in the surface layer of ceramics, it is apparent that the surface geometry of the photostrictive material will have a strong bearing on the generation of photocurrent and photovoltage. Using a sample thickness closer to the penetration depth will ensure that the entire film will be active and efficiently utilized. We also discussed the light coherency for the 'thin' sample in Fig. 17.7. Therefore, investigation of photovoltaic response as a function of sample thickness is desired in determining the optimal thickness range with maximum photovoltaic effect. In addition, studying the effect of surface roughness will provide an insight into the absorption dependence of photostriction.

In order to determine the optimum sample thickness, dependence of photovoltaic effect on sample thickness of PLZT (3/52/48) ceramics doped with 0.5 at.% WO_3 was examined.[22] Photovoltaic response was found to increase with a decrease in sample thickness in PLZT ceramics (see Fig. 17.14).

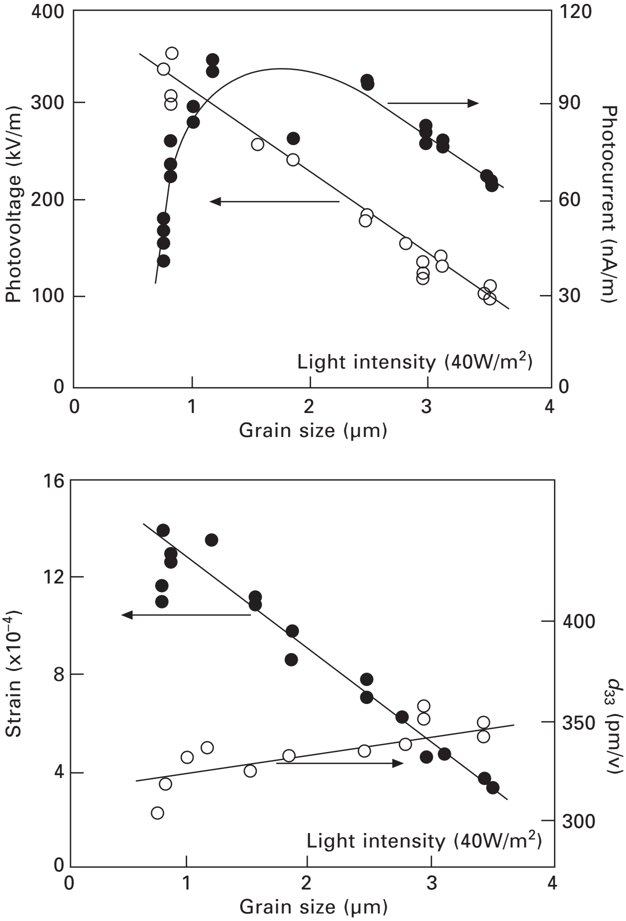

17.13 Grain size dependence of photostrictive characteristics in PLZT (3/52/48).

A model was proposed in Fig. 17.15 to explain and quantify the observed influence of sample thickness on photovoltaic response,[22] where the absorption coefficient is assumed to be independent of light intensity and the photocurrent density is taken to be proportional to light intensity. The sample is assumed to comprise thin slices along the thickness direction of the sample. Figure 17.14 shows the plot between the normalized photocurrent (i_m) and sample thickness calculated for the external resistance (R_m = 200 TΩ). The computed result shows good agreement with the experimental data (☐ is for the measured photocurrent, and ● for the computed results from the proposed model). With increasing sample thickness, i_m increases, reaches a maximum, and subsequently decreases with sample thickness. The decrease

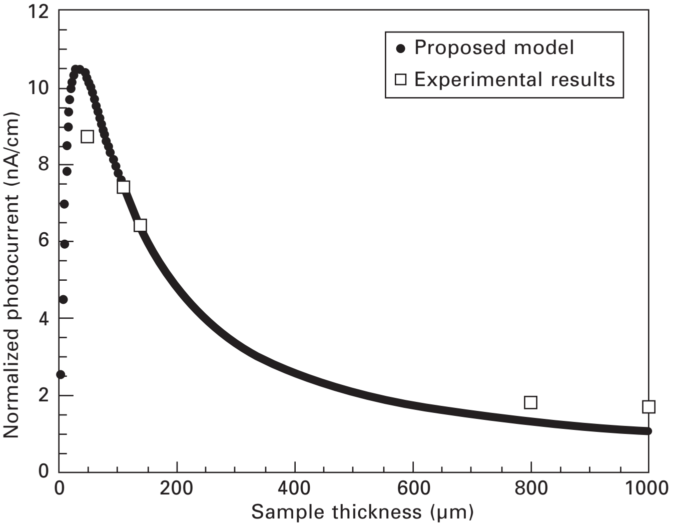

17.14 Comparison of measured and computed normalized photocurrent with photovoltaic coefficient (i_m/k) in 0.5 at% WO_3-doped PLZT (3/52/48).

in i_m can be attributed mainly to the dark conductivity (σ_d). The optimum thickness (for the present set of samples) which yields maximum photocurrent is found at 33 μm, which is close to the light (366 nm) penetration depth of the PLZT (absorption coefficient α of PLZT (3/52/48) = 0.0252 μm^{-1} at 366 nm; the inverse of α = 39 μm). The relatively low value of optimum thickness implies that the lower sample thickness will be expected to give better photovoltaic response.

The effect of surface roughness on photovoltaic and photostrictive properties was also examined in the PLZT sample, with different surface roughness obtained by polishing to different surface finishes. The surface roughness was measured by a profilometer (Tencor, Alpha-Step 200) and the average surface roughness was determined using the graphical center line method. The variation of photovoltaic current with surface roughness is plotted in Fig. 17.16.[10] The photocurrent increases exponentially with decreasing surface roughness. This is due to the fact that with an increase in surface roughness, the penetration depth of the illumination decreases, while contributions from multiple reflections increase. A model based on the effect of multi-reflection has been proposed for two different shapes, a sine profile and a 'V' profile roughness. In both these shapes, half of the up-down amplitude was taken as a roughness (r) and the cyclic distance period as a roughness pitch (g). The normalized photocurrents (i_m) computed for the above two surface profiles are also plotted in Fig. 17.16 as a function of surface roughness. A distance

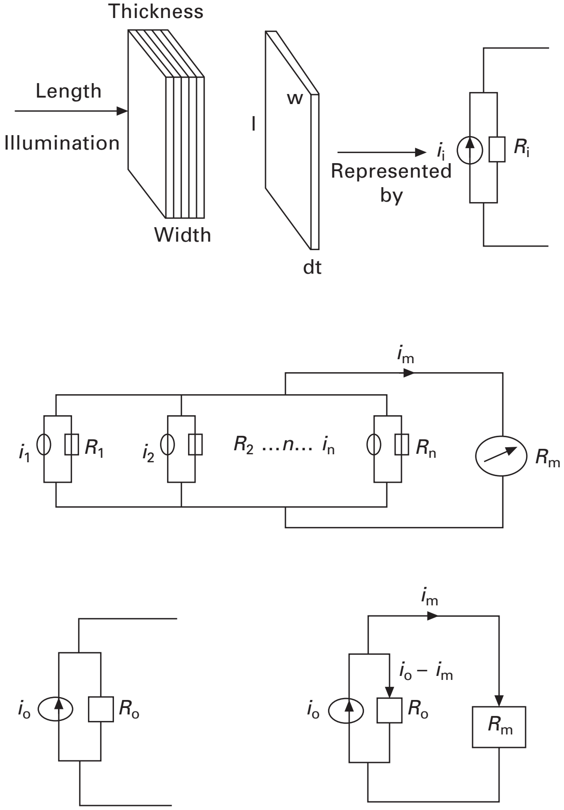
Thickness
Length
Illumination
Width
w
l
dt
Represented by
i_i
R_i
i_m
i_1
R_1
i_2
R_2 ...n... i_n
R_n
R_m
i_o
R_o
i_m
$i_\mathrm{o} - i_\mathrm{m}$
i_o
R_o
R_m

17.15 Model to compute the dependence of photocurrent on sample thickness. The sample was modeled as thin slices along the thickness direction and the corresponding circuit diagrams are also shown.

pitch (wavelength) of roughness at 1 μm gave the best fit to the experimental results, which is close to the size of the grain of this PLZT sample.

In conclusion, the optimum profile of the photostictive PLZT actuator is a film shape with thickness around 30 μm and surface roughness less than 0.2 μm.

17.4 Photostrictive device applications

In this section, we introduce the possible applications of photostriction to photo-driven relay, a micro walking machine, a photo-phone, and the micro propelling robot, which are designed to function as a result of light irradiation, having neither lead wires nor electric circuits. See Ref 23 for details of applications of photostrictive devices.

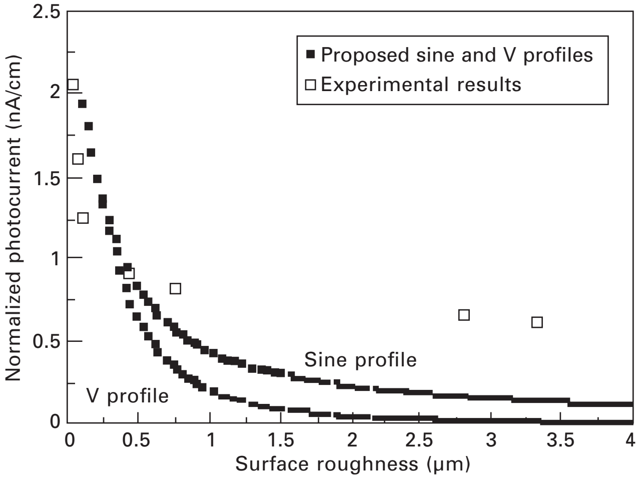

17.16 Variation of photocurrent with surface roughness in 0.5 at% WO_3-doped PLZT. Comparison with the normalized computed photocurrent for the two surface profiles is also made.

17.4.1 Displacement amplification mechanism

Since the maximum strain level of the photostriction is only 0.01% (one order of magnitude smaller than the electrically induced piezostriction, and this corresponds to 1 μm displacement from a 10 mm sample), we need to consider a sophisticated amplification mechanism for the displacement. We employed a bimorph structure, which is analogous to a bi-metal consisting of two metallic plates with different thermal expansion coefficients bonded together to generate a bending deformation according to a temperature change.

Two PLZT plates were pasted back to back, but were placed in opposite polarization, then connected on the edges electrically, as shown in Fig. 17.17.[8] A purple light (366 mn) was shone to one side, which generated a photovoltaic voltage of 7 kV across the length (along the polarization direction). This caused the PLZT plate on that side to expand by nearly 0.01% of its length, while the plate on the other (unlit) side contracted due to the piezoelectric effect through the photovoltage. Since the two plates were bonded together, the whole device bent away from the light. Figure 17.18 demonstrates the tip deflection of the bimorph device made from WO_3 0.5 at% doped PLZT under a dual beam control (illumination intensity: 10 mW/cm^2). For this 20 mm long and 0.35 mm thick bi-plate, the displacement at the edge was ±150 μm, and the response speed was a couple of seconds.

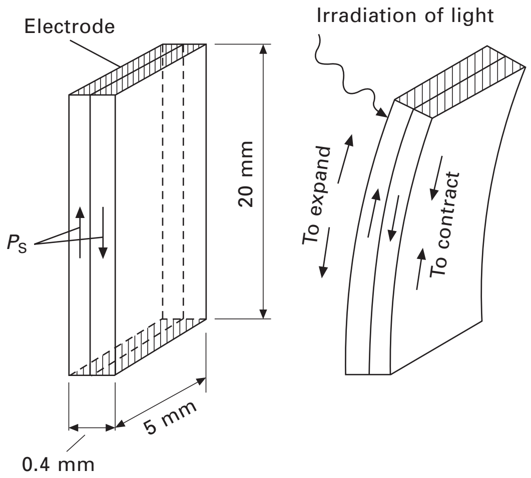

17.17 Structure of the photo-driven bimorph and its driving principle.

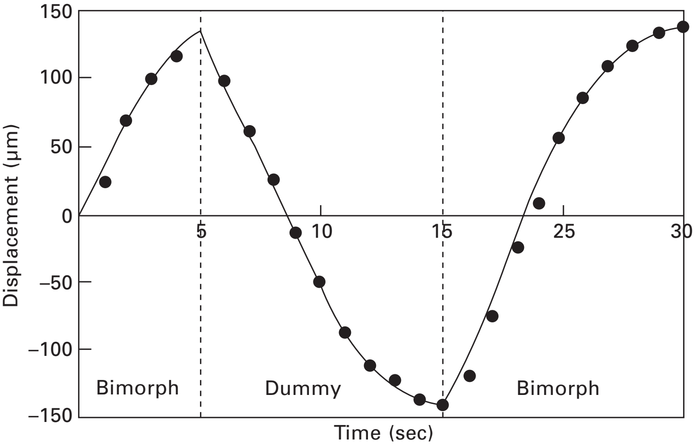

17.18 Tip deflection of the bimorph device made from WO_3 0.5 at% doped PLZT under a dual beam control (illumination intensity: 10 mW/cm^2).

17.4.2 Photo-driven relay

A photo-driven relay was constructed using a PLZT photostrictive bimorph as a driver which consists of two ceramic plates bonded together with their polarization directions opposing each other (Fig. 17.19).[8] A dummy PLZT plate was positioned adjacent to the bimorph to cancel the photovoltaic voltage generated on the bimorph. Utilizing a dual beam method, switching was controlled by alternately irradiating the bimorph and the dummy. Using

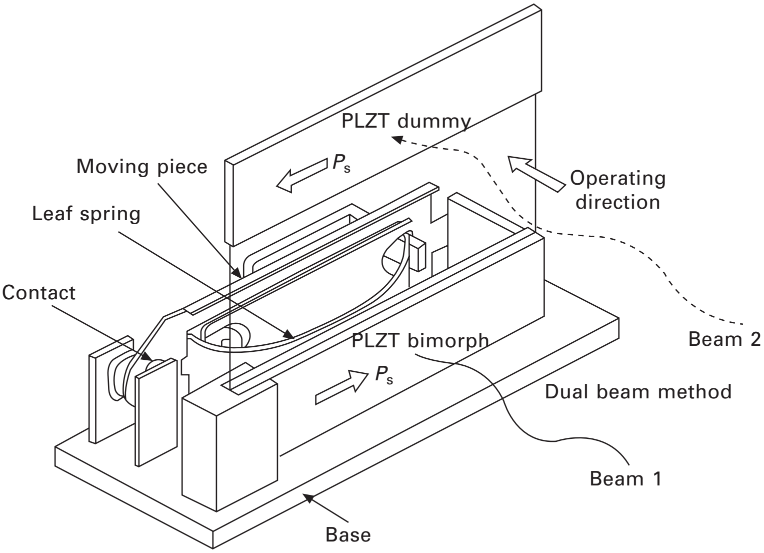

17.19 Structure of the photo-driven relay.

this dual beam method, the time delay of the bimorph that ordinarily occurs in the off process due to a low dark conductivity could be avoided, ± 150 μm displacement was transferred to a snap action switch, with which on/off switching was possible. The on/off response of the photo-driven relay was demonstrated with a typical delay time of 1–2 seconds.

17.4.3 Micro walking machine

A photo-driven micro walking machine was also developed using the photostrictive bimorph.[24] It was simple in structure, having only two PLZT bimorph legs (5 mm × 20 mm × 0.35 mm) fixed to a plastic board, as shown in Fig. 17.20. When the two legs were irradiated with purple light alternately, the device moved like an inchworm. The photostrictive bimorph as a whole was caused to bend by ± 150 μm as if it averted the radiation of light. The inchworm built on a trial basis exhibited rather slow walking speed (several tens μm/min), since slip occurred between the contacting surface of its leg and the floor. The walking speed can be increased to approximately 1 mm/min by providing some contrivances such as the use of a foothold having microgrooves fitted to the steps of the legs.

17.4.4 'Photophone'

The technology to transmit voice data (i.e., a phone call) at the speed of light through lasers and fiber optics has been advancing rapidly. However,

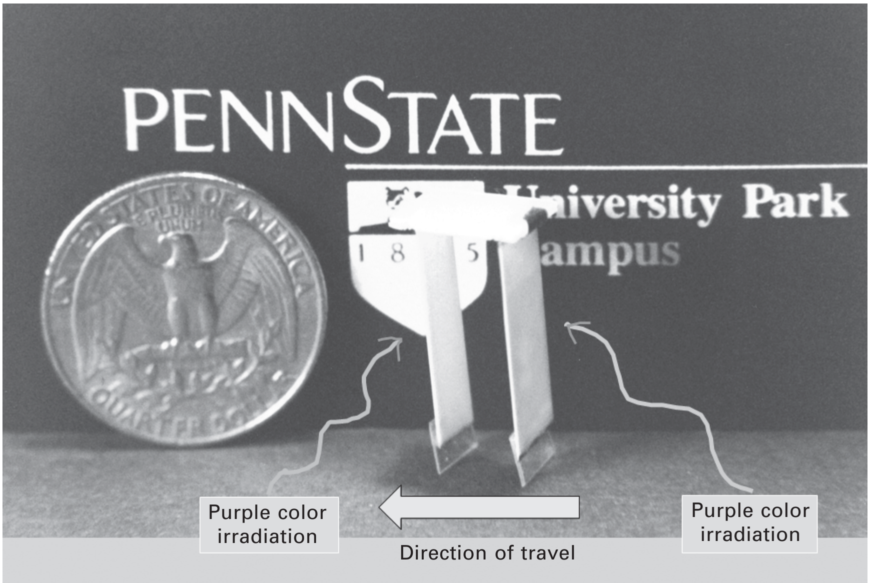

17.20 Photo-driven micro walking machine made of two photostrictive bimorphs. Alternating irradiation provides a walking motion.

the end of the line – the interface speaker – limits the technology, since optical phone signals must be converted from light energy to mechanical sound via electrical energy at present. The photostriction may provide new photo-acoustic devices.

Photo-mechanical resonance of a PLZT ceramic bimorph has been successfully induced using chopped near-ultraviolet irradiation, having neither electric lead wires nor electric circuits.[25] A thin cover glass was attached on the photostrictive bimorph structure to decrease the resonance frequency so as to easily observe the photo-induced resonance. A dual-beam method was used to irradiate the two sides of the bimorph alternately with an optical chopper intermittently with a 180° phase difference. The mechanical resonance was then monitored by changing the chopper frequency. Figure 17.21 shows the tip displacement of the thin-plate-attached sample as a function of chopper frequency. Photo-induced mechanical resonance was successfully observed. The resonance frequency was about 75 Hz with a mechanical quality factor Q_m of about 30. The maximum tip displacement of this photostrictive sample was about 5 μm at the resonance point. Though the sound level is low, the experiment suggests the promise of photostrictive PLZT bimorphs as photo-acoustic components, or ‘photophones’, for the next optical communication age.

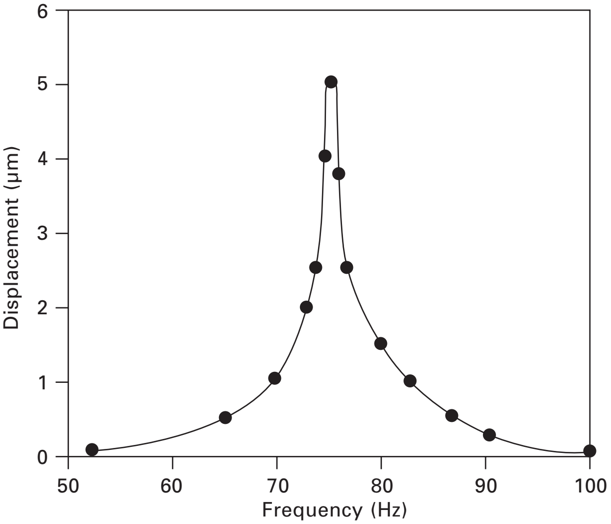

17.21 Frequency dependence of the tip deflection of the bimorph device made from WO_3 0.5 at% doped PLZT under a dual beam control (illumination intensity: 10 mW/cm^2).

17.4.5 Micro propelling robot

A new application of highly efficient, photostrictive PLZT films on flexible substrates has been conceived for usage in the new class of small vehicles for future space missions.[26] A micro propelling robot can be designed into arch-shaped photo-actuating composite films (unimorph type) with a triangular top (Fig. 17.22). In order to maximize the photostrictive properties of the sample, the sample thickness was determined as 30 μm. This device is driven at their resonance mode under an intermittent illumination. Photo-actuating films may be fabricated from PLZT solutions and coated on one side of a suitable flexible substrate which will then be designed to have a curvature of 1 cm^{-1}. A slight difference in length/width between the right and left legs is designed in order to provide a slight difference between their resonance frequencies. This facilitates controlling the device in both clockwise and counterclockwise rotations (i.e., right and left steering). A light chopper operating at a frequency close to resonance can be used to illuminate the device, in order to maximize the vibration of the bimorph which will then provide the capability to turn by applying different resonance frequencies to the two legs.

17.5 Conclusions

Photostrictive actuators can be driven only by the irradiation of light, so they will be suitable for use in actuators to which lead wires can hardly be

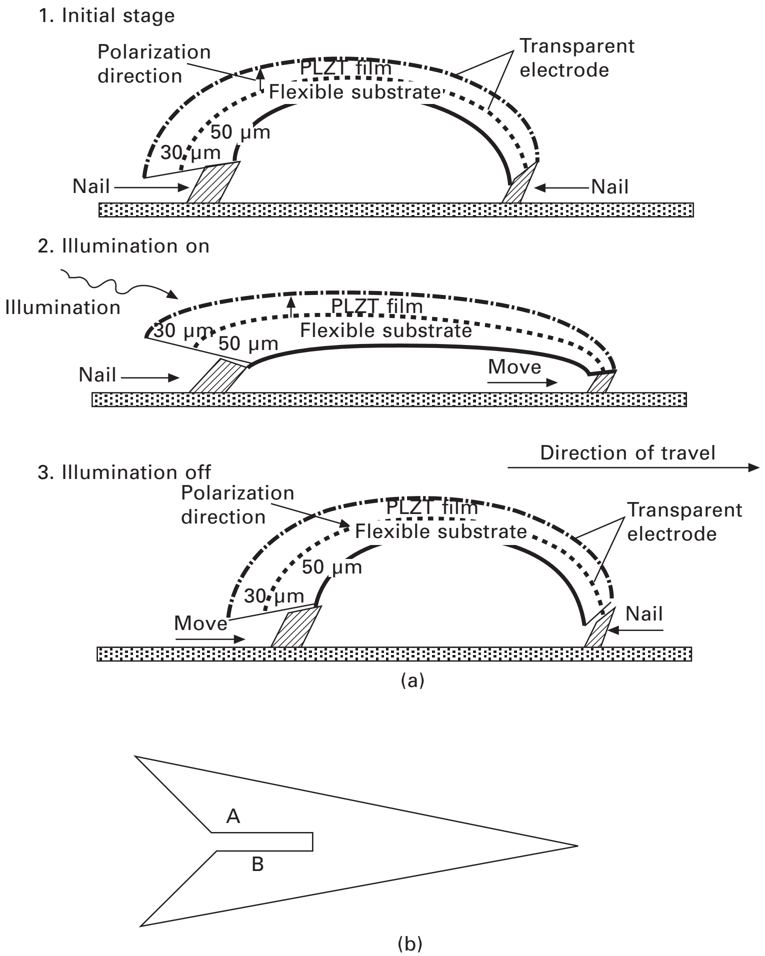
1. Initial stage
Polarization direction
PLZT film
Flexible substrate
Transparent electrode
50 μm
30 μm
Nail
Nail
2. Illumination on
Illumination
PLZT film
Flexible substrate
30 μm
50 μm
Nail
Move
3. Illumination off
Direction of travel
Polarization direction
PLZT film
Flexible substrate
Transparent electrode
50 μm
30 μm
Move
Nail
(a)
A
B
(b)

17.22 (a) Schematic diagram of an arch-shaped photo-actuating film device, and (b) its triangular top shape.

connected because of their ultra-small size or the conditions in which they are employed, such as ultra-high vacuum or outer space. The photostrictive bimorphs will also be applicable to 'photophones'. Note also their remote control capability without being interfered with by electromagnetic noise. Figure 17.23 summarizes the improvement in response speed of photostrictive bulk ceramics and of devices in the sequence of year and key technological developments. Compared to the speed of 1 hour at the point of discovery of PZT, two-orders-of-magnitude improvement (up to 10 seconds) has been achieved in materials, and even photo-induced resonance has been realized in devices. The new principle actuators will have a considerable effect upon the future of micro-mechatronics.

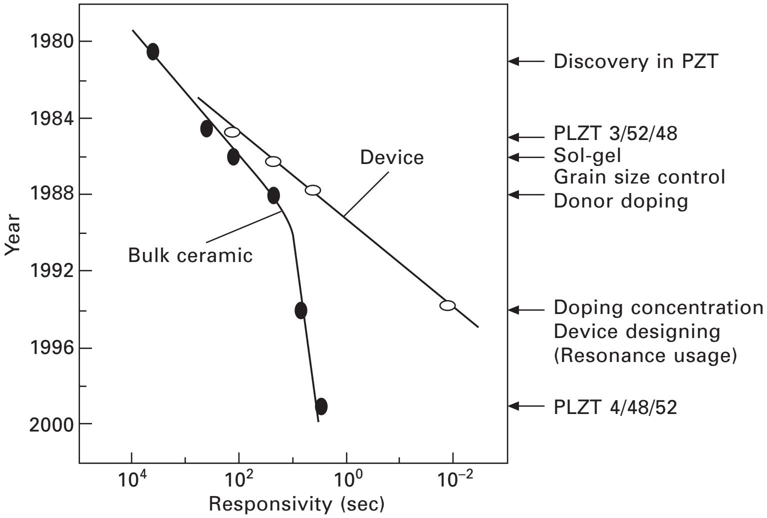

17.23 Response speed improvement of the photostrictive bulk ceramic and of the device in the sequence of year and key technological developments.

17.6 References

1. Brody, P. S., *Ferroelectrics*, **50**, 27 (1983).
2. Uchino, K. and Aizawa, M., 'Photostrictive Actuators Using PLZT Ceramics', *Jpn. J. Appl. Phys. Suppl.*, **24**, 139–141 (1985).
3. Fridkin, V. M., in Photoferroelectrics, edited by M. Cardona, P. Fulde, and H.-J. Queisser, Solid-State Sciences 9 (Springer-Verlag, New York), pp. 85–113 (1979).
4. Uchino, K., Miyazawa, Y. and Nomura, S., 'High-Voltage Photovoltaic Effect in $PbTiO_3$-Based Ceramics', *Jpn. J. Appl. Phys.*, **21**(12), 1671–1674 (1982).
5. Uchino, K., 'New Applications of Photostriction', *Innovations Mater. Res.*, **1**(1), 11–22 (1996).
6. Chu, S. Y. and Uchino, K., 'Impurity Doping Effect on Photostriction in PLZT Ceramics', *J. Adv. Performance Mater.*, **1**, 129–143 (1994).
7. Uchino, K., Aizawa, M. and Nomura, S., 'Photostrictive Effect in (Pb,La)(Zr,Ti)O_3', *Ferroelectrics*, **64**, 199 (1985).
8. Tanimura, M. and Uchino, K., 'Effect of Impurity Doping on Photo-strictive in Ferroelectrics', *Sensors and Materials*, **1**, 47–56 (1988).
9. Glass, A. M., von der Linde, D. and Negran, T. J., *Appl. Phys. Lett.*, **25**, 233 (1974).
10. Poosanaas, P., Tonooka, K. and Uchino, K., 'Photostrictive Actuators', *Mechatronics*, **10**, 467–487 (2000).
11. Hecht, E., in *Optics,* with contributions by Alfred Zajac, 2nd edn. (Addison-Wesley Publishing, Massachusetts), pp. 44, 81–104, 610–616 (1987).
12. Kittel, C., in *Introduction to Solid States Physics*, 7th edn. (John Wiley & Sons, New York), p. 388 (1996).

13. Uchino, K., Miyazawa, Y. and Nomura, S., ‘Photovoltaic Effect in Ferroelectric Ceramics and Its Applications’, *Jpn. J. Appl. Phys.*, **22**, 102 (1983).
14. Brody, P. S., *Solid State Commun.*, **12**, 673 (1973).
15. Brody, P. S., *J. Solid State Chem.*, **12**, 193 (1975).
16. Sada, T., Inoue, M. and Uchino, K., ‘Photostriction in PLZT Ceramics’, *J. Ceram. Soc. Jpn. Inter. Edn*, **95**, 499–504 (1987).
17. Poosanaas, P. and Uchino, K., ‘Photostrictive Effect in Lanthanum-Modified Lead Zirconate Titanate Ceramics Near the Morphotropic Phase Boundary’, *Mater. Chem. & Phys.*, **61**, 31–41 (1999).
18. Nonaka, K., Akiyama, M., Takase, A., Baba, T., Yamamoto, K. and Ito, H., ‘Nonstoichiometry Effects and Their Additivity on Anomalous Photovoltaic Efficiency in Lead Lanthanum Zirconate Titanate Ceramics’, *Jpn. J. Appl. Phys.*, **34**, 5380–5383 (1995).
19. Poosanaas, P., Dogan, A., Prasadarao, A. V., Komarneni, S. and Uchino, K., ‘Effect of Ceramic Processing Methods on Photostrictive Ceramics’, *Adv. Performance Mater.*, **6**, 57–69 (1999).
20. Poosanaas, P., Dogan, A., Prasadarao, A. V., Komarneni, S. and Uchino, K., ‘Photostriction of Sol-Gel Processed PLZT Ceramics’, *J. Electroceramics*, **1**, 105–111 (1997).
21. Sada, T., Inoue, M. and Uchino, K., ‘Photostrictive Effect in PLZT Ceramics’, *J. Ceram. Soc. Japan*, **5**, 545–550 (1987).
22. Poosanaas, P., Dogan, A., Thakoor, S. and Uchino, K., ‘Influence of Sample Thickness on the Performance of Photostrictive Ceramics’, *J. Appl. Phys.*, **84** (3), 1508–1512 (1998).
23. Uchino, K., ‘New Applications of Photostrictive Ferroics’, *Mat. Res. Innovt.*, **1**, 163–168 (1997).
24. Uchino, K., ‘Micro Walking Machine Using Piezoelectric Actuators’, *J. Rob. Mech.*, **124**, 44–47 (1989).
25. Chu, S. Y. and Uchino, K., *Proc. 9th Int’l Symp. Appl. Ferroelectrics*, State College, PA, p. 743 (1995).
26. Thakoor, S., Morookian, J. M. and Cutts, J. A., ‘The Role of Piezoceramics Microactuation for Advanced Mobility’, *Conf. Proc. 10th IEEE Int’l Symp. on Appl. Ferroelectrics*, **1**, 205–211 (1996).

18

The performance of piezoelectric materials under stress

C. S. LYNCH, University of California, Los Angeles, USA

Abstract: The mechanics of coupled large field behavior of ferroelectric materials is discussed in this chapter. The models are multiaxial in both stress and electric field, and thus are suitable for implementation in finite element analysis. The material behavior is described in terms of fundamental behavior that takes place at multiple length scales from the atomic level to the macroscopic level. The crystal structure and an example of a lattice defect are introduced at the atomic scale. A simplified model of the unit cell behavior is introduced at the scale of tens of atoms. This leads to domain structures at the single crystal length scale and an explanation of compatibility issues across domain boundaries, phase boundaries, and grain boundaries. The macroscopic behavior is described as a volume average of the behavior at smaller length scales.

Key words: ferroelectric, piezoelectric, crystal, constitutive behavior, domains, polarization, perovskite, PZT, relaxor, electrostrictive.

18.1 Introduction

The need for models that can be used to simulate large field behavior beyond the butterfly shaped strain–electric field and the ‘D’ shaped electric displacement–electric field hysteresis loops first arose with attempts to perform a computational analysis of internal electrodes in co-fired stack actuators and to perform a computational fracture mechanics analysis to understand and improve the reliability of ferroelectric devices. The problem is that in ferroelectric materials, even in the absence of mechanical loading, discontinuities in material properties lead to electric field concentrations. The electro-mechanical coupling results in local stresses that can crack the material and lead to failure. Models were needed that could accurately simulate polarization reorientation in response to stress, and electric field components that could change direction and amplitude during the loading process. Micromechanical techniques provided the necessary constitutive laws with polarization reorientation, but this only led to the next problem. These material models could not be implemented in commercially available codes such as ABAQUS or ANSYS as a user defined material as there was no mechanism in these codes to pass an irreversible polarization increment back to the main code. The solution was to develop a specialized code solely for this purpose [1]. Since that time, other researchers have developed similar specialized codes using various approaches to modeling the material behavior [2–6]. This chapter addresses the large field electro-mechanical properties of ferroelectric materials that are related to polarization reorientation and phase transformations.

Without the ability to reorient polarization, ferroelectric ceramics and single crystals could not be poled and many applications would not be possible. The source of this behavior is a polar crystal structure with multiple stable polarization states. The polarization can be reoriented to other stable states through the process of domain wall motion. The driving forces for polarization reorientation are stress and electric field, and the energy barrier to this reorientation is a function of temperature. In some ferroelectric materials, unstable polarization states can become stable in the presence of stress or electric field. Stress and electric field can thus drive both domain wall motion and phase boundary motion.

Domain wall motion and phase boundary motion in ferroelectric materials are hysteretic processes. Under small field cyclic loading of a poled ferroelectric ceramic, domain walls move back and forth a small amount about an average position. This process involves local polarization reorientation that makes a contribution to the macroscopically observed piezoelectric effect referred to as an extrinsic contribution. The distortion of the unit cells about a stable polarization state is referred to as an intrinsic contribution [7]. Hysteresis resulting from this process is typically characterized in terms of a loss tangent, an approximation in which the macroscopically observed behavior is modeled as a phase lag between a sinusoidal driving force (stress, electric field) and a sinusoidal response (strain, electric displacement) [8]. Although this simple description can be used to predict heating in many device applications, the loss tangent depends on the magnitude and frequency of the driving force and the phase lag approximation loses validity under large field loading.

Although it is well known that there is symmetry in the electro-mechanical coupling equations, i.e. the same set of piezoelectric coefficients appears in two equations, it is less well known that this same symmetry appears during large field driven polarization reorientation. Measurements of stress/strain/electric-field/electric-displacement under large field loading at various temperatures have been shown to display this symmetry in the major hysteresis loops [9]. Constitutive models have been developed to describe this behavior.

Large field ferroelectric constitutive behavior is a multiscale phenomenon. This chapter begins with a description of ferroelasticity and ferroelectricity at the length scale of the unit cell. Next, the behavior of groups of unit cells is described. This includes examples of electronic defect structures associated with substitution of different ions into the crystal, followed by the conditions of energy minimization that lead to the formation of domains. The formation of domains is explained in terms of a global energy minimization. This leads to an explanation of field driven phase transformations in single crystals in terms of energy minimization in the presence of stress and electric field. A ceramic comprises many single crystal grains, each subdivided into many domains. The behavior of the ceramic is described in terms of the volume average of the behavior at each of the smaller length scales. This chapter closes with a discussion of a micromechanical modeling approach that makes the connection between the orientation distribution of grains and the observed macro-scale nonlinear and hysteretic behavior of ferroelectric ceramics.

18.2 The unit cell, ferroelectricity, and ferroelasticity

Many technologically important ferroelectric materials have the perovskite type crystal structure. This structure is described in terms of distortions of the high temperature cubic parent phase of barium titanate (BT) shown in Fig. 18.1. The ions in this structure are closely packed together, but have been sketched spaced apart to assist in describing the structure. Barium titanate is used in the description of the structure. In this structure the barium ions carry a charge of +2, the oxygen ions a charge of –2 and the titanium ions a charge of +4. The unit cell is thus charge neutral, with the one titanium contributing +4, the six oxygen ions contributing –6 (each –2 oxygen ion charge is shared between two neighboring unit cells), and the eight barium ions contributing +2 (each +2 barium ion charge is shared between eight corner unit cells).

Lattice vibrations of the ions about an average position maintain the structure in the cubic configuration above the Curie temperature, T_c. As the temperature is reduced below T_c, the vibration amplitude decreases, the ions require less space, and the structure settles down into a slightly distorted

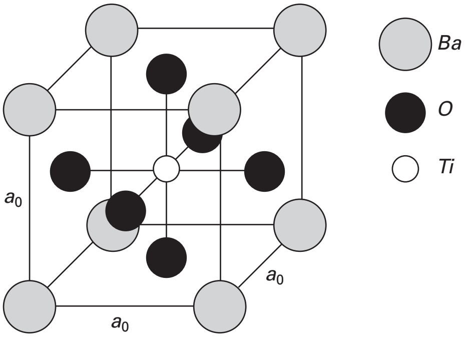

18.1 The cubic parent phase of barium titanate with a titanium ion at the center of the unit cell, an oxygen ion at the center of each face of the unit cell, and barium ion at each corner of the unit cell.

configuration through a displacive transformation. In bariun titanate the transformation is from cubic to tetragonal. The polar tetragonal phase is shown schematically in Fig. 18.2. In the polar phase the center of negative charge has shifted in one direction and the center of positive charge has shifted in the other, resulting in a dipole moment within each unit cell. The dipole moment vector $\underline{p}$ is given by Eq. 18.1:

$$\underline{p} = Q\underline{d} \qquad 18.1$$

where Q is the charge and $\underline{d}$ is the vector with magnitude equal to the distance between the positive and negative charge centers pointing from negative to positive. The spontaneous polarization $\underline{P}^s$ is the dipole moment per unit volume, and is given by:

$$\underline{P}^s = \underline{p}/V \qquad 18.2$$

The spontaneous strain describes the distortion of the unit cell relative to the high temperature cubic configuration as shown in Fig. 18.2. The strain is the symmetric part of the displacement gradient and the displacement is defined with respect to a cubic configuration. If x_3 is taken as the polarization direction, the components of the spontaneous strain tensor $\underline{\underline{\varepsilon}}$ in matrix form are given by Equation 18.3. In this matrix of coefficients of the strain tensor, the extensional strain component corresponds to the polarization direction:

$$[\varepsilon] = \begin{bmatrix} \frac{a - a_0}{a_0} & 0 & 0 \\ 0 & \frac{a - a_0}{a_0} & 0 \\ 0 & 0 & \frac{c - a_0}{a_0} \end{bmatrix} \qquad 18.3$$

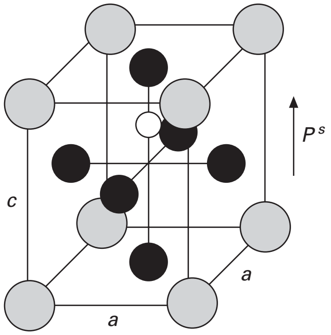

18.2 The tetragonal phase of barium titanate is shown schematically. This phase displays a spontaneous polarization and a spontaneous strain.

Phase transformations from cubic to structures other than tetragonal also occur. The distortion that takes place depends on composition. In the lead zirconate–lead titanate solid solution, zirconium-rich compositions distort into a rhombohedral phase. In the rhombohedral phase the spontaneous polarization direction is across the body diagonal of the unit cell. This is a principal strain direction and corresponds to an elongation (positive) strain component. The strain components perpendicular to this direction are contraction (negative). Figure 18.3 shows the polarization direction (also the direction of elongation) of the tetragonal, rhombohedral, orthorhombic, and monoclinic phases. Miller indices are used to identify cubic referenced crystallographic directions. Polarization of the tetragonal structure is in one of the six possible <001> directions, polarization of the rhombohedral structure is in one of the eight possible <111> directions and polarization of the orthorhombic structure is in one of the 12 possible <111> directions. The polarization directions of three possible monoclinic structures are also indicated. An antiferroelectric phase is also possible. In the antiferroelectric phase, alternate unit cells are polarized in opposite directions and thus the polarization vectors cancel each other out, resulting in zero macroscale (volume average) polarization. Below the Curie point, solid solutions of lead zirconate titanate with greater than 95% lead zirconate form the antiferroelectric non-polar phase.

After the initial processing of a ferroelectric oxide at high temperature and cooling through the Curie temperature, the material does not display

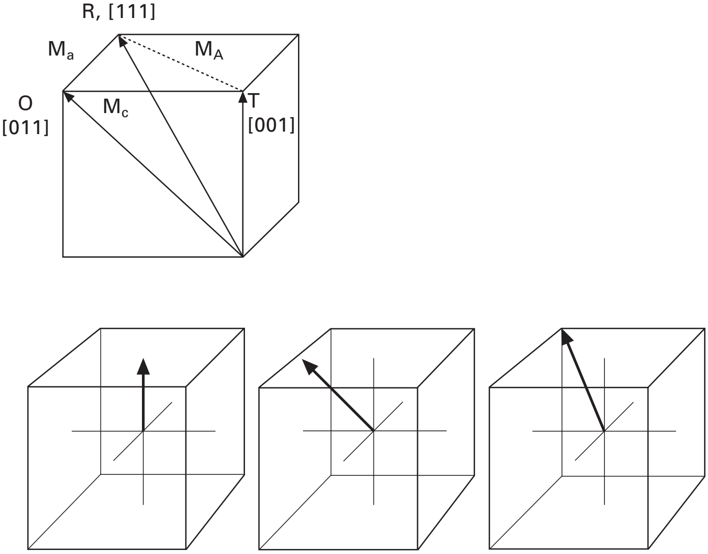

Tetragonal (6) Orthorhombic (12) Rhombohedral (8)

18.3 The polarization direction (also the direction of elongation) of the various phases that occur in the perovskite type crystal structure.

piezoelectric properties. The reason is the polarization vectors of unit cells within the bulk material lie in different directions and thus cancel out at the macroscopic scale. The poling process, in which a large electric field is applied, aligns the polarization vectors as closely as possible with the field and produces macroscale piezoelectricity in the material. This process involves field driven variant changes and phase changes.

Field driven variant changes (polarization reorientation within the same crystal structure) are driven by a combination of stress and electric field. A switch from one tetragonal variant to another is shown schematically in Fig. 18.4. The top row shows a 180° switch driven by electric field and the bottom row shows a 90° switch driven by stress. In this example, the cell is initially polarized upward (top left). This initial state has a positive spontaneous strain component in the polarization direction and a positive spontaneous polarization. Three idealized plots are shown at the right. The top plot is strain vs. electric field, the center plot is electric displacement vs. electric field, and the bottom plot is stress vs. strain.

The 180° switch (top row of figures) is driven by electric field. The process is explained in terms of a hypothetical parallel plate capacitor fabricated with one of these unit cells by placing a metallic electrode on the top and bottom.

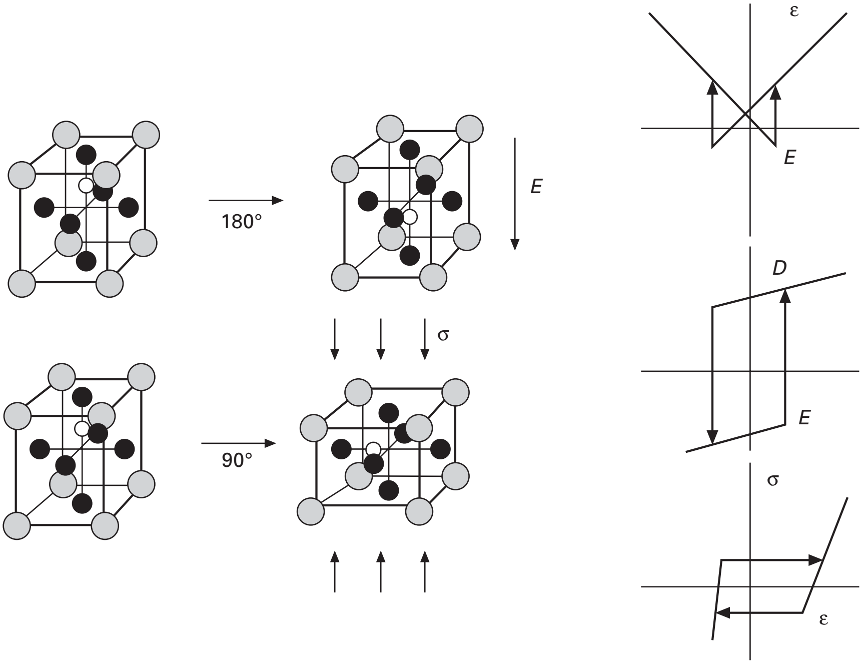

18.4 A schematic illustration of 180° switching and 90° switching of an idealized tetragonal cell structure.

An electric field is produced by removing a small amount of negative charge from the bottom electrode and placing it on the top electrode (this is done with a battery or otherwise applied potential). The excess negative charge on the top electrode attracts the positive ions and repels the negative ions and the excess positive charge at the bottom electrode attracts the negative ions and repels the positive ions within the crystal. The result is that the crystal structure stretches out (elongates). The strain increases, moving up the branch of the strain vs. electric field curve that has positive slope. The slope of this curve is the piezoelectric coefficient. The electric displacement also increases (this is a measure of the charge per unit area on the electrodes), moving up the top branch of the electric displacement vs. electric field curve. The slope of the electric displacement/electric field curve is the dielectric permittivity.

Now consider the opposite case in which a negative charge is moved from the top electrode to the bottom electrode. The positive center ion is repelled toward the center of the unit cell. The associated distortion is toward the cubic state and the strain is a contraction. The associated reduction of polarization results in motion down the top branch of the electric displacement vs. electric field curve and the contraction results in motion down the positive slope branch of the strain vs. electric field curve. As more charge is added (increasing the negative electric field), a point is reached where the central ion pops into a new equilibrium position. This field level is the coercive field. The result of this switch from an upward poled variant to a downward poled variant is a jump in the strain vs. electric field and the electric displacement vs. electric field plots. The strain jumps from negative to positive as the center ion goes from being pushed toward the center in the upward configuration to being pulled away from the center in the downward configuration. The piezoelectric coefficient (slope of the strain/electric field curve) changes sign and the remanent polarization changes sign.

A 90° switch can be driven by either stress or electric field. The stress driven variant change is illustrated in the bottom row of Fig. 18.4. As stress is applied to the cell, it is compressed toward the cubic shape. This results in the central ion moving toward the center of the cell (all other ions are similarly rearranged). The change toward cubic reduces the dipole moment and thus reduces the polarization of the cell. The result is shown schematically on the stress vs. strain curve shown at the bottom right. The initial remanent strain is positive, and the slope is the elastic modulus. At a critical stress level, the coercive stress, the central ion will pop out toward one of the four sides and the remanent strain will switch to a negative value. The slope of the stress vs. strain curve will change because the force is now applied to the a-axis rather than to the c-axis of the cell.

18.3 Driving forces for polarization reorientation

A mathematical description of the polarization reorientation process is developed next. The driving forces for variant transformations are stress and electric field, with the energy barrier to these transformations being temperature dependent. In the following description, the driving force for the transformation is described in terms of the availability of external forces to do positive work during the transformation.

Electrical work is done by moving a positive charge up a potential gradient. It takes one Newton-meter of work to move one Coulomb of charge through one volt of potential, thus 1V = 1 N-m/C. The work can be thought of in terms of physically taking a charge and applying a force to move it up the potential gradient to a new location near the body. This typically involves moving a charge from one electrode to another electrode at a different potential. The work done is thus given by:

$$W^E = \int \phi dQ \qquad 18.4$$

where the electric potential is denoted ϕ.

If the charge is not uniformly distributed over the surface of the body, the work done by establishing a charge configuration on the surface is found as a surface integral:

$$W^E = \int_\gamma \left(\int \phi d\omega\right) d\gamma \qquad 18.5$$

where ω is the surface charge density.

If this charge accumulates on a surface (typically a metallic electrode) with boundary conditions such that the electric displacement outside of the body is zero (no electric field outside of the body or fringing fields small enough that they can be neglected), the normal component of electric displacement just inside the surface is equal to the surface charge density:

$$\underline{D} \cdot \hat{n} = -\omega \qquad 18.6$$

The electric field is defined as the negative of the gradient of ϕ:

$$\underline{E} = -\nabla\phi \qquad 18.7$$

The gradient points in the direction of maximum increasing potential. The negative sign points the electric field in the direction of decreasing potential such that a positive electric field produces a force on a positive charge in the direction of the field.

Electrical work per unit volume done on a material by external forces can be expressed in terms of electric field and electric displacement within the material. Electrical work is done by physically rearranging charges on the surface of the volume (or in the vicinity of the volume). An example is a parallel plate capacitor in which charge is physically removed from one electrode and placed on another electrode. This changes the electric displacement and the electric field in the material between the electrodes. Electric displacement has units of charge per unit area. The dot product of electric field with an incremental change of electric displacement gives an incremental work per unit volume.

The electrical work per unit volume is thus given by an integral:

$$w^E = \int \underline{E} \cdot d\underline{D} \qquad 18.8$$

Mechanical work is done on a volume of material by applying forces to the surface of the volume. These forces induce displacement associated with deformation of the volume. The increment of mechanical work done is the force multiplied by the increment of displacement. The relative displacement field $\underline{u}(\underline{x})$ within the volume is a vector field that is dependent on position. The gradient of this vector field describes the strain and the rigid body rotation of the body. The strain field $\underline{\underline{\varepsilon}}(\underline{x})$, is a function of position. It describes the distortion of the body. For small strain, the strain is given by the symmetric part of the displacement gradient:

$$\underline{\varepsilon} = \frac{1}{2}(\underline{u}\overleftarrow{\nabla} + \overrightarrow{\nabla}\underline{u}) \qquad 18.9$$

The mechanical work done on the body is given by the expression $W^M = \int \underline{F} \cdot d\underline{x}$. If the forces are not uniformly distributed, the dot product of the traction vector $\underline{t}$ (force per unit area on the surface) with the displacement vector $\underline{u}$ must be integrated over the surface to obtain the mechanical work.

The traction vector on the surface is related to certain stress components just below the surface by Eq. 18.10:

$$\underline{t} = \hat{n} \cdot \underline{\underline{\sigma}} \qquad 18.10$$

The equation of mechanical equilibrium is given by Eq. 18.11

$$\nabla \cdot \underline{\underline{\sigma}} + \underline{f} = \rho\underline{\ddot{u}} \qquad 18.11$$

which, in the absence of body forces and accelerations becomes $\nabla \cdot \underline{\underline{\sigma}} = 0$ This leads to Eq. 18.12 for the mechanical work per unit volume:

$$w^M = \int (\underline{\underline{\sigma}} \circlearrowright d\underline{\underline{\varepsilon}}) \qquad 18.12$$

The total external work per unit volume done during a transformation from one variant to another is thus given by Eq. 18.13:

$$w^T = w^E + w^M \tag{18.13}$$

For a transformation that takes place at constant stress and constant electric field, these terms come outside of the integrals:

$$w^T = \underline{\underline{\sigma}} \bullet \int d\underline{\underline{\varepsilon}} + \underline{E} \cdot \int d\underline{D} \tag{18.14}$$

which integrates to give:

$$w^{T(\alpha\to\beta)} = \underline{\underline{\sigma}} \bullet (\underline{\underline{\varepsilon}}^{\beta} - \underline{\underline{\varepsilon}}^{a}) + \underline{E} \cdot (\underline{D}^{\beta} - \underline{D}^{\alpha}) \tag{18.15}$$

If the material behavior is linear piezoelectric before and after the transformation, the strain and electric displacement are given by linear constitutive laws:

$$\underline{\underline{\varepsilon}} = \underline{\underline{\underline{\underline{s}}}}^{E} \bullet \underline{\underline{\sigma}} + \underline{\underline{\underline{d}}} \cdot \underline{E} + \underline{\underline{\varepsilon}}^{0} \tag{18.16}$$

$$\underline{D} = \underline{\underline{\kappa}}^{\sigma} \cdot \underline{E} + \underline{\underline{\underline{d}}} \bullet \underline{\underline{\sigma}} + \underline{D}^{0}$$

Ferroelectric materials typically have symmetry about the polar axis, thus when the polar axis switches the elastic, dielectric, and piezoelectric tensors also switch. The elastic contributions can be a significant fraction of the strain change associated with the switching and thus the contribution of the reorientation of the material tensors can be included to give:

$$\begin{aligned} w^{T(\alpha\to\beta)} &= \underline{\underline{\sigma}} \bullet ((\underline{\underline{\underline{\underline{s}}}}^{E\beta} - \underline{\underline{\underline{\underline{s}}}}^{E\alpha}) \bullet \underline{\underline{\sigma}} + (\underline{\underline{\underline{d}}}^{\beta} - \underline{\underline{\underline{d}}}^{\alpha}) \cdot \underline{E} + (\underline{\underline{\varepsilon}}^{0\beta} - \underline{\underline{\varepsilon}}^{0\alpha})) \\ &+ \underline{E} \cdot ((\underline{\underline{\kappa}}^{\sigma\beta} - \underline{\underline{\kappa}}^{\sigma\alpha}) \cdot \underline{E} + (\underline{\underline{\underline{d}}}^{\beta} - \underline{\underline{\underline{d}}}^{\alpha}) \bullet \underline{\underline{\sigma}} + (\underline{D}^{0\beta} - \underline{D}^{0\alpha})) \end{aligned} \tag{18.17}$$

where the superscripts α and β refer to the variant or phase before and after the transformation. The terms in the first set of parentheses are the strain associated with the change of elastic constants, the strain associated with the change of piezoelectric constants, and the change of spontaneous strain. The terms in the second set of parentheses are the polarization change associated with the change of dielectric constants, the polarization change associated with the change of piezoelectric constants, and the change of spontaneous polarization.

The total work done during a virtual transformation from α to β (the available work) is the driving force for the transformation. The criterion for the transformation to occur is that the driving force should exceed an energy barrier:

$$w^T \geq E^b \tag{18.18}$$

The energy barrier will likely be a function of the type of transformation, i.e. a 90° or 180° switch in the tetragonal system.

18.4 Polarization as an order parameter

Discussions of using polarization as an order parameter can be found in many papers on phase field modeling [10–13].

The geometry of the perovskite type crystal structure leads to the coupling between strain and polarization. Each is associated with relative shifts of the ions within the unit cell. For the portion of the strain that is coupled to polarization, the geometry leads to a relation betweens strain and polarization that is quadratic:

$$\underline{\underline{\varepsilon}} = \underline{\underline{\underline{\underline{Q}}}} \bullet (\underline{P} \otimes \underline{P}) \qquad 18.19$$

where the '⊗' represents the tensor product of the vectors.

Writing the strain in terms of the polarization enables using the polarization as a single parameter that describes the energy of the crystal structure. Consider the free energy to be a function of the polarization only at a fixed temperature:

$$\phi = \phi\ (\underline{P}) \qquad 18.20$$

Constructing an energy function that has the properties of minima at finite polarization values (spontaneous polarization) is instructive and can be accomplished using a negative quadratic function and a positive fourth-order function in polarization. Consider the function given by Eq. 18.21:

$$\phi = -\underline{\underline{a}} \bullet (\underline{P} \otimes \underline{P}) + (\underline{P} \otimes \underline{P}) \bullet \underline{\underline{\underline{\underline{b}}}} \bullet (\underline{P} \otimes \underline{P}) \qquad 18.21$$

which can be expressed in indicial form as:

$$\phi = -a_{ij}P_iP_j + b_{ijkl}P_iP_jP_kP_l \qquad 18.22$$

Taking the quadratic tensor to have isotropic symmetry and the fourth-order tensor to have cubic symmetry produces the desired function. In 2-D this gives:

$$\phi = -a_{11}(P_x^2 + P_y^2) + b_{1111}(P_x^4 + P_y^4) + b_{1122}(P_x^2 P_y^2) \qquad 18.23$$

This energy function is plotted as a function of polarization in Fig. 18.5. The energy wells correspond to the spontaneous polarization. The coefficients can be selected to give the spontaneous polarization a magnitude that matches that of a particular tetragonal material. The addition of a sixth-order term and careful selection of coefficients can be used to create energy functions with minima in [011] and [111] directions.

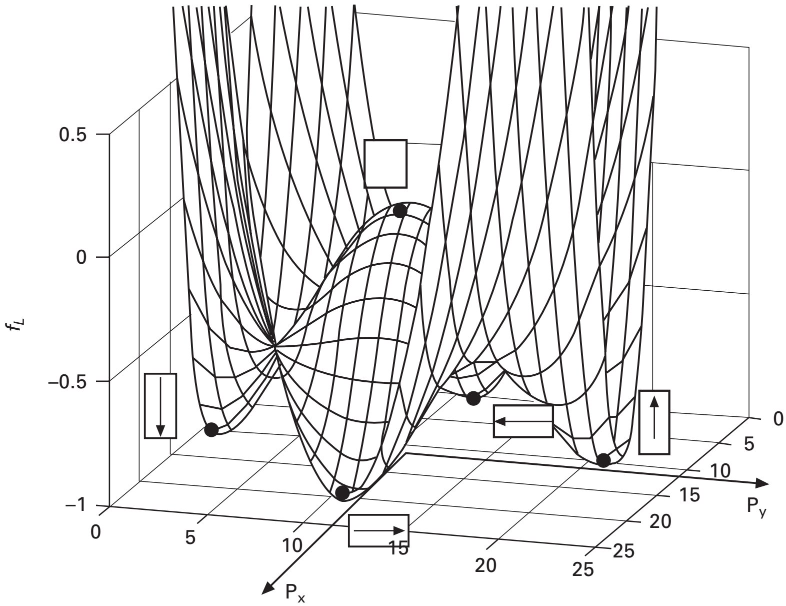

18.5 An energy function based on polarization as a single order parameter uses a negative quadratic term and a positive fourth-order term to create minima corresponding to the spontaneous polarization.

Stress and electric field change the shape of the energy surface. The switching criterion that was discussed above is based on the availability of the external forces to do positive work. Consider the zero strain state to be the cubic state (the top of the hump in the center of the energy surface). If a constant electric field is present, how much work is done if the polarization changes to any other value? The answer is that the work done is the dot product of the constant electric field with the polarization vector:

$$w^E = \underline{E} \cdot \underline{P} \tag{18.24}$$

A modified energy surface can be constructed that subtracts the available work from the structure energy:

$$\psi = \phi - w^E - w^M \tag{18.25}$$

This new function is plotted for a constant electric field in the y-direction in Fig. 18.6. It is clear that the polarization in the upward direction becomes the lowest energy state. The criterion for evolution of the polarization from an initial state to this lower energy state is that the path must be downhill. This does not occur until the electric field reaches a threshold value.

A similar approach can be used to account for the presence of stress. With the strain given in terms of the polarization squared, a strain tensor can be

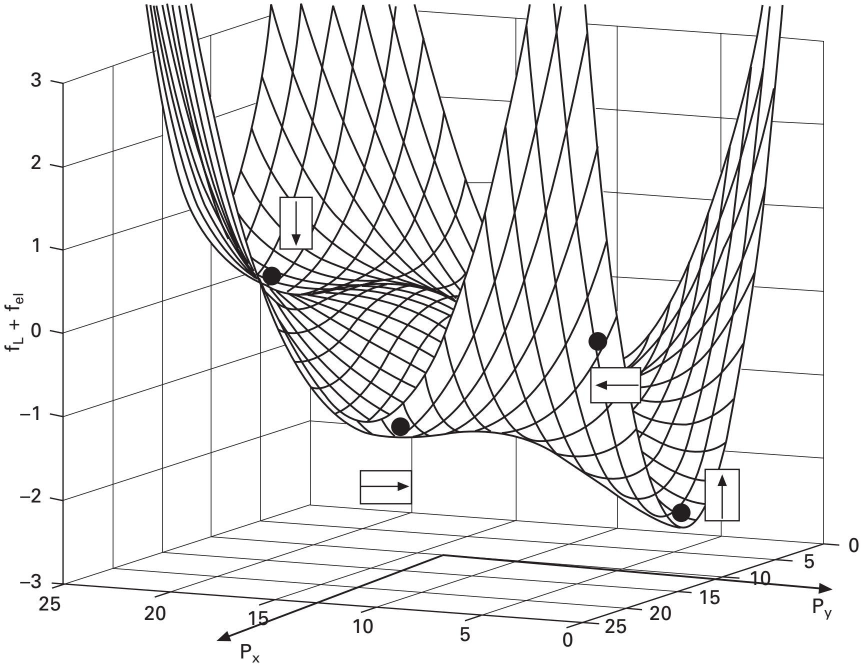

18.6 The energy function plotted in Fig. 18.5 has been modified by subtracting the available work of a constant electric field in the y-direction, rendering the y-polarization state the lowest energy state.

constructed for each possible polarization value. The work done to achieve this polarization value in the presence of a constant stress is given by:

$$w^M = \underline{\underline{\sigma}} \bullet \underline{\underline{\varepsilon}} = \underline{\underline{\sigma}} \bullet \underline{\underline{\underline{\underline{Q}}}} \bullet (\underline{P} \otimes \underline{P}) \tag{18.26}$$

The values of the coefficients of the fourth-order *Q* tensor are selected to give a strain tensor that is positive along the polar direction and negative in the two transverse directions. The sum of the normal strain coefficients can be set to be zero, i.e. ε_{kk}, giving a constant volume process. The energy function is next modified by subtracting the availability of mechanical forces to do work and plotted in Fig. 18.7. When the compressive stress is sufficiently large, the path from poled up or down to poled sideways will be downhill on the energy surface and the reorientation will take place when the stress is sufficiently large.

The energy surfaces presented in Figs 18.5–18.7 offer some insight into how the stress and electric field drive the polarization in a manner that minimizes the energy of the structure in the presence of external driving forces. The homogeneous process just described does not address the effects of defects

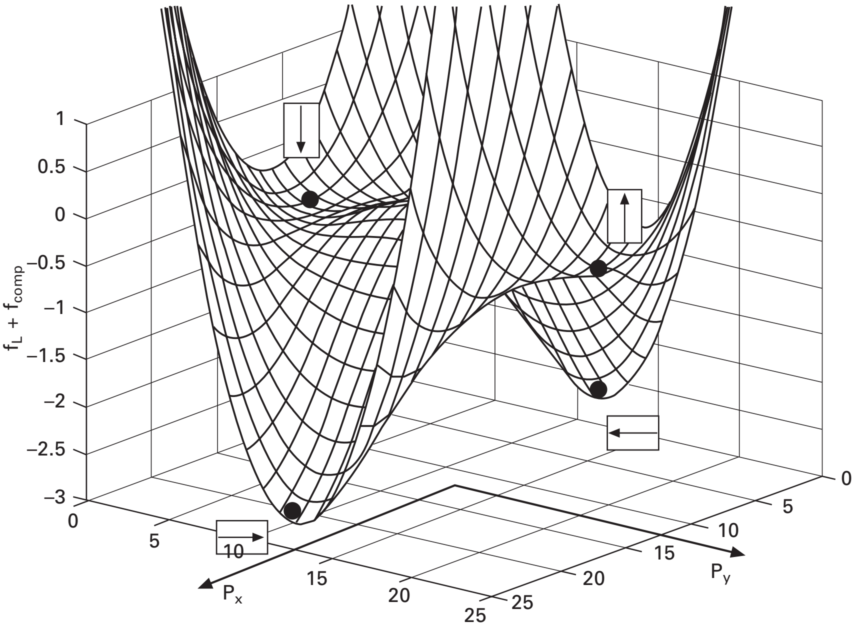

18.7 The energy function is modified by subtracting the availability of a constant stress to do work when the polarization changes. A compressive stress yields minima in the sideways polarized states.

in the crystal structure. These tend to be in the form of point defects, sessile dislocations, domain walls, phase boundaries, and macroscale defects such as porosity and second phase particles.

18.5 Groups of unit cells, defects, and domains

The idealized polarization reorientation process just described gives a conceptual framework for understanding the behavior of the material, but in the real material the process is significantly more complex than a sudden homogeneous switch of a crystal. The process is analogous to slip systems in metals. In a metal, dislocations move on slip planes resulting in a heterogeneous plastic deformation. This significantly reduces the stress required to produce yield in a metal. When dislocation densities are large, they tangle and pin resulting in hardening. In a ferroelectric/ferroelastic system domains (regions of like polarization) are separated by domain walls [14, 15]. In the presence of a driving force, domain walls will propagate through the structure transforming material from one crystal variant to another. This heterogeneous deformation significantly reduces the energy barrier to polarization reorientation. When two domain walls intersect, they can pin at the intersection and require an increased driving force to break free, a hardening mechanism. Figure 18.8 depicts 180° and 90° domain walls in a tetragonal structure.

Domain walls tend to be straight and lie only on certain crystallographic planes such that their orientation minimizes both the local electrical energy and the local mechanical energy. In the absence of free charge, the electrical energy is minimized when the normal component of polarization is continuous across the wall. Equation 18.27 from electrostatics

$$\nabla \cdot \underline{D} = \rho \tag{18.27}$$

where ρ is the free charge density, leads to this condition. If Equation 18.27 is integrated about a volume and the volume reduced to enclose a boundary surface, the result is that the jump in the normal component of electric displacement across the boundary is equal to the free charge per unit area on that boundary:

$$\|D_n\| = Q/A \tag{18.28}$$

In the case of a domain wall with no free charge, the jump in the normal component of electric displacement across the wall is zero. The electric displacement is related to the polarization by:

$$\underline{D} = \varepsilon_0\, \underline{E} + \underline{P} \tag{18.29}$$

Thus if the jump in normal component of polarization across a domain wall is non-zero and the jump in electric displacement must be zero, there will be a large local electric field. This is the source of high electrical energy if the domain walls are not on specific planes. In tetragonal structures the walls that separate 180° domains are parallel to the polarization vectors, and the walls that separate 90° domains are at 45° to the polarization direction with the polarization vectors in a head-to-tail configuration across the wall. Note

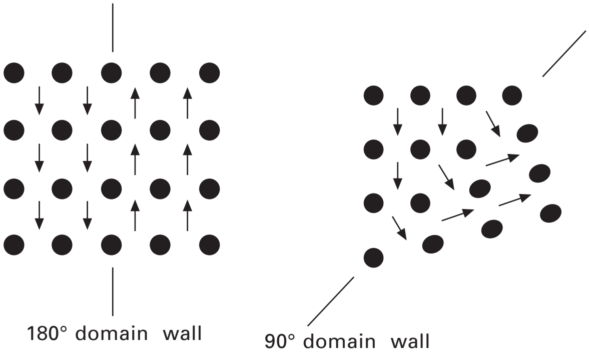

18.8 Groups of like poled unit cells form domains separated by domain walls. The type of wall is identified by the angle change of polarization on the two sides.

that the ‘90°’ wall is somewhat less than 90° due to the geometry. This can be seen if one considers slicing two rectangles across their face diagonals, rotate and flip one, and paste them together. The pasted together corners are no longer 90°.

Equation 18.29 also leads to a description of the ‘depolarization’ field. If we consider the case of a single domain single crystal with no free charge on the surface, the jump in normal component of polarization across the boundary is not zero, yet the jump of electric displacement across the boundary must be zero. Equation 18.29 leads to a large internal electric field in the opposite direction of the polarization. This field can well exceed the coercive field and cause the polarization to re-orient in a way that reduces the net polarization of the crystal. This is referred to as a depolarization field.

The mechanical energy associated with a domain wall is a little easier to visualize. If there is a jump in the tangential component of spontaneous strain across the wall, then there must be a local stress, i.e. mechanical stretching must be present in order to fit the two sides together. This is the source of strain energy. It is clear from Fig. 18.4 that in the tetragonal structure both the 90° and 180° domain walls shown simultaneously eliminate the mechanical and the electrical energy associated with the wall.

Donor doping increases the piezoelectric coefficient while increasing material loss coefficients. This is the result of enhanced domain wall motion. Acceptor doping reduces piezoelectric coefficients and reduces material loss coefficients through stabilization of domains. An example of donor doping is discussed. Lanthanum is a donor dopant in PZT with La^{3+} substitution on Pb^{2+} sites giving rise to defects of the type $LA^{\bullet}_{Pb}$, where the dot indicates a single positive excess charge and the subscript indicates the site that the substitution ion occupies. Each two positive charges are compensated by a lead site vacancy V_{Pb}'', where the two primes indicate two negative charge associated with the vacancy [16]. Figure 18.9 shows an example of the defect structure in PZT with a small volume fraction of La doping.

18.6 The large field behavior of relaxor single crystals

The development of crystal growth techniques for large size single crystals of the binary solid solutions PMN–xPT and PZN–xPT has led to the identification of many interesting and technologically important properties [17–21]. These crystals have very low phase stability (the energy wells are not very deep) and thus have large piezoelectric, compliance, and dielectric coefficients (these coefficients are the curvatures of the wells). These crystals display anisotropic elastic, dielectric, and piezoelectric properties, a relatively low Curie temperature, a relatively low coercive field, and high dielectric loss associated with domain wall motion and phase boundary motion. Domain

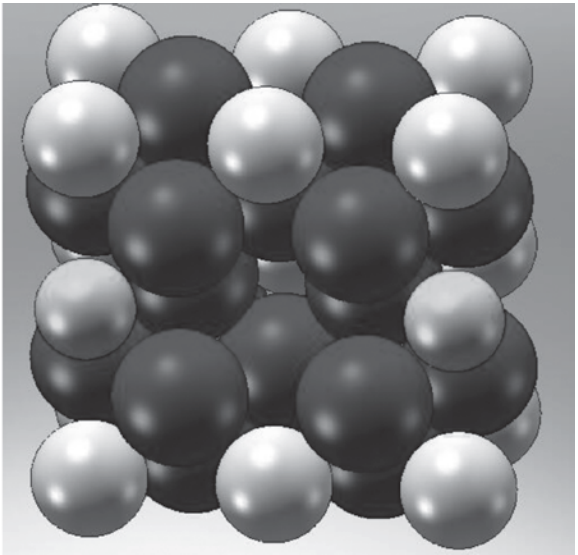

18.9 The smaller La ions substituted on the Pb sites (center sides) require a lead site vacancy (center) to maintain charge neutrality.

wall motion can be reduced or eliminated through the selection of crystal cuts in which there is no driving force. This results in crystals with very low loss. Although field induced phase transformations limit the range of linear behavior, and the energy barrier to these transformations displays strong temperature dependence, these crystals have provided considerable insight into the large field behavior of ferroelectric materials and are being used in a number of applications. The development of ternary compounds and the addition of dopants may lead to improved phase stability.

'Domain engineering' is a term that refers to selecting crystal cuts that produce stable domain configurations, i.e. there is no driving force for domain wall motion. This can be shown through geometric arguments or mathematically through orthogonal transformation equations. A schematic of the crystal variant configurations is shown in Fig. 18.10. Consider the rhombohedral structure in which the polarization is toward the corner of the unit cell. The crystal can be cut into plates and electroded. If it is cut on a (111) plane and these surfaces electroded, application of an electric field will result in a single variant single crystal as shown schematically in Fig. 18.10 (a). If it is cut on a (001) plane and poled in a [001] direction, four crystal variants may occur, Fig. 18.10(b). If it is cut on a (110) plane and poled in a [110] direction, two crystal variants may occur, Fig. 18.10(c). Once a domain configuration has been established by poling the material, there is no driving force for further domain switching. Going back to the switching criterion of Eq. 18.17 it is clear that switching from one variant

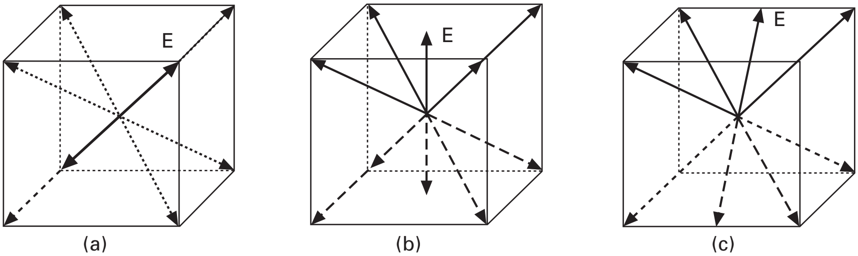

18.10 Domain states in different crystal cuts of rhombohedral single crystals.

to another results in no electrical work being done. In sensor and actuator applications, the material is often under a pre-load with a compressive stress along a single axis that is typically either parallel or perpendicular to the polarization direction. If the [111] poled crystal is mechanically compressed in the polarization direction, the strain will be decreased by a switch to one of the other variants. This stress component drives switching (drives domain wall motion). If the [001] poled crystal is subjected to a compressive stress parallel to the polarization direction, there is no strain change if one variant switches to another. There is thus zero driving force for domain wall motion. Crystals cut and loaded in the [001] direction display a linear response with very low loss. This is a 'domain engineered' structure. Crystals cut and poled in the [110] direction are typically mechanically loaded in the transverse [001] direction. This takes advantage of a large d_{32} coefficient and the stress again does not produce a driving force for domain wall motion.

18.7 Calculation of 'domain engineered' properties

The piezoelectric, elastic, and dielectric properties of domain engineered single crystals can be expressed in terms of the tensor properties of the single domain single crystal, an orthogonal transformation of these properties into a coordinate system aligned with the crystal cut, and a volume average [22]. Figure 18.11 shows three coordinate systems, and below each a direction cosine matrix giving the direction cosines of the shown coordinate axes relative to a cubic referenced coordinate system. The direction cosines are readily found by normalizing the Miller indices of the three coordinate axes. The first coordinate system shown in Fig. 18.11 has the x_1, x_2, and x_3 axes in the [–1 1 0], [–1 –1 2] and [1 1 1] directions, the second in the [1 0 0], [0 1 0] and [0 0 1] directions and the third in the [1 0 –1], [0 1 0], and [1 0 1]. The matrix of direction cosines is constructed by normalizing these indices such that they represent the components of a unit vector in the cubic referenced coordinate system, and then placing them in the rows of the direction cosine matrices as shown below each coordinate system in Fig.

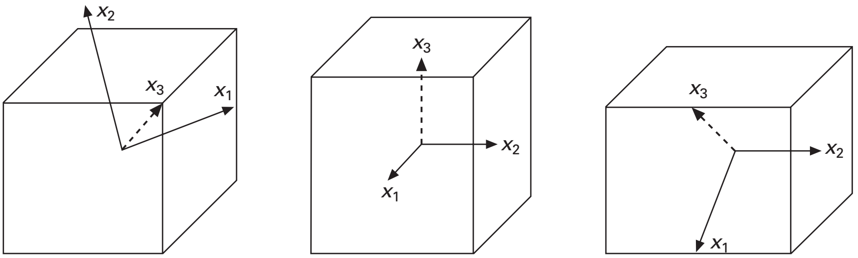

$$A^{111} = \begin{bmatrix} -\frac{1}{\sqrt{2}} & \frac{1}{\sqrt{2}} & 0 \\ -\frac{1}{\sqrt{6}} & -\frac{1}{\sqrt{6}} & \frac{2}{\sqrt{6}} \\ \frac{1}{\sqrt{3}} & \frac{1}{\sqrt{3}} & \frac{1}{\sqrt{3}} \end{bmatrix} \qquad A^{001} = \begin{bmatrix} 1 & 0 & 0 \\ 0 & 1 & 0 \\ 0 & 0 & 1 \end{bmatrix} \qquad A^{101} = \begin{bmatrix} \frac{1}{\sqrt{2}} & 0 & -\frac{1}{\sqrt{2}} \\ 0 & 1 & 0 \\ \frac{1}{\sqrt{2}} & 0 & \frac{1}{\sqrt{2}} \end{bmatrix}$$

18.11 Three coordinate systems are shown, and beneath each is the direction cosine matrix with respect to a cubic referenced coordinate system (center).

18.11. Note that the center sketch in Fig. 18.11 shows the cubic referenced coordinate system.

If a set of properties is known for the single domain rhombohedral single crystal and described in the coordinate system with x_3 in the [1 1 1] direction, the properties can be expressed in the cubic coordinate system using an orthogonal transformation. This is most easily expressed using indicial notation. Consider the second-order dielectric permittivity tensor $\underline{\underline{\kappa}}$, the third-order piezoelectricity tensor $\underline{\underline{\underline{d}}}$, and the fourth-order elasticity tensor $\underline{\underline{\underline{\underline{s}}}}$. For the rhombohedral single domain single crystal with the polarization direction aligned with the [1 1 1] or x_3 direction, the properties can be described in the cubic referenced X_1, X_2, X_3 coordinate system shown in Fig. 18.12 using Eqs 18.30:

$$\begin{aligned} \kappa_{ij}^{(2)} &= a_{ir}\,a_{js}\kappa_{rs}^{(1)} \\ d_{ijk}^{(2)} &= a_{ir}\,a_{js}a_{kt}d_{rst}^{(1)} \\ s_{ijkl}^{(2)} &= a_{ir}\,a_{js}a_{kt}a_{lu}s_{rstu}^{(1)} \end{aligned} \qquad 18.30$$

The eight rhombohedral variants each have a different set of direction cosines with respect to the cubic referenced coordinate system. If the domain walls are fixed and inter domain clamping effects can be neglected, the properties of the crystal will be the volume average of the properties of the domains. This can be expressed as an integral or, if the volume fraction of each variant is known, as a sum:

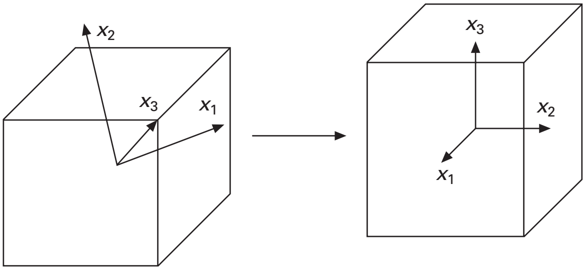

18.12 Tensor components expressed in one coordinate can be expressed in any other coordinate system using the direction cosines.

$$\bar{\kappa}_{ij} = \frac{1}{v}\int_v \kappa_{ij}dv = \sum_{a=1}^{n} f^{(n)}\kappa_{ij}^{(n)}$$

$$\bar{d}_{ijk} = \frac{1}{v}\int_v d_{ijk}\,dv = \sum_{a=1}^{n} f^{(n)}d_{ijk}^{(n)} \qquad 18.31$$

$$\bar{s}_{ijkl} = \frac{1}{v}\int_v s_{ijkl}\,dv = \sum_{a=1}^{n} f^{(n)}s_{ijkl}^{(n)}$$

where the coefficients of the tensors of each variant are expressed in a single coordinate system.

The summation approach can be applied to determining the properties of the domain engineered crystals poled in the [001] or the [110] orientation. The [001] poled crystal, by symmetry arguments, likely has equal volume fractions of four variants, and the [110] cut and poled crystal likely has equal volume fractions of two variants. This leads to Eqs 18.32 and 18.33 for the properties of the domain engineered single crystals in terms of the single variant properties:

$$d_{31}^{001} = d_{32}^{001} = 0.385\,d_{31}^{111} + 0.192d_{33}^{111} - 0.192\,d_{15}^{111} + 0.136\,d_{16}^{111}$$

$$d_{33}^{001} = 0.385\,d_{31}^{111} + 0.192d_{33}^{111} + 0.385\,d_{15}^{111} - 0.272\,d_{16}^{111} \qquad 18.32$$

$$d_{24}^{001} = d_{15}^{001} = -0.192\,d_{31}^{111} + 0.192d_{33}^{111} + 0.096\,d_{15}^{111} + 0.136\,d_{16}^{111}$$

and

$$d_{31}^{110} = 0.816\,d_{31}^{111} - 0.289\,d_{16}^{111}$$

$$d_{32}^{110} = 0.544\,d_{31}^{111} + 0.272\,d_{33}^{111} - 0.272d_{15}^{111} + 0.192d_{16}^{111}$$

$$\begin{aligned} d_{33}^{110} &= 0.272\, d_{31}^{111} + 0.544\, d_{33}^{111} + 0.272 d_{15}^{111} + 0.096 d_{16}^{111} \\ d_{24}^{110} &= -0.272\, d_{31}^{111} + 0.272\, d_{33}^{111} + 0.136 d_{15}^{111} + 0.192 d_{16}^{111} \\ d_{15}^{110} &= 0.408 d_{15}^{111} - 0.289 d_{16}^{111} \end{aligned} \qquad 18.33$$

The piezoelectric coefficients listed in Table 18.1 for the [110] crystal cut are the slopes of the strain vs. electric field curves shown in Fig. 18.13(a). The electric field is applied in the [110] direction. The strain is measured in each of the [110], [1 –1 0], and [001] directions. These slopes are constant through a range of electric field values, but undergo jumps when the electric field exceeds a threshold. These jumps are associated with field driven phase transformations [23].

18.8 Field driven phase transformations

Field driven phase transformations are similar to the field driven variant transformations discussed above [24]. Phase transformations occur when the energy surfaces have absolute minima in certain directions and relative minima in other directions. As stress or electric field tilt the energy surfaces toward relative minima, a point is reached where the polarization 'falls' into the well associated with the relative minimum of the new phase.

In the [110] cut and poled crystal the largest piezoelectric strain occurs in the transverse [001] direction, i.e. the d_{32} coefficient is the largest. This is the typical direction of a stress pre-load on the crystal. Figure 18.14 shows the loading directions for stress and electric field. The stress and electric field each act to drive the crystal into the orthorhombic phase.

The [001] cut and poled crystal displays two different field driven phase transformations. Compressive stress drives the structure from rhombohedral to an orthorhombic phase with polarization transverse to the stress direction, and electric field drives the structure from rhombohedral to tetragonal with the polarization in the direction of the electric field vector. This is shown schematically in Fig. 18.15.

Table 18.1 Properties of single variant and domain engineered PZN 0.045PT single crystals

Poling direction	d_{31} (pC/N)	d_{32} (pC/N)	d_{33} (pC/N)	d_{15} (pC/N)	d_{16} (pC/N)	D_3^r (C/m^2)
<111>	(–35)	(–35)	(125)	3824	–1902	0.44
<001>	–984	–984	(2000)	(140)	0	0.25
<110>	734	(–1670)	(980)	2527 d_{14} = 123	0	0.36

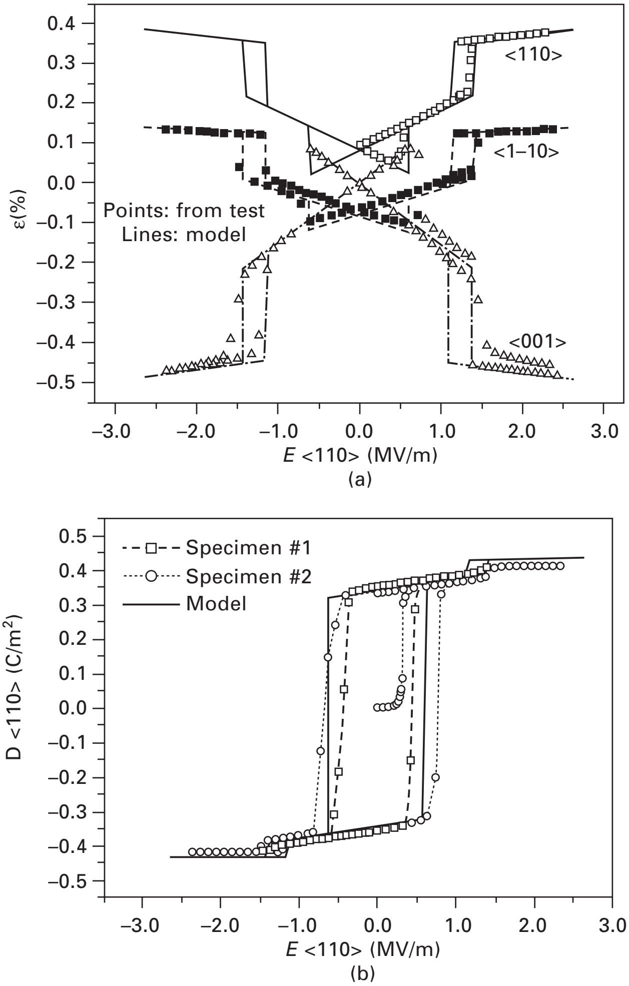

18.13 Strain vs. electric field (a) and electric displacement vs. electric field (b) for [110] cut PZN 4.5%PT. The strain vs. electric field curves for three orthogonal directions display the material anisotropy. The jumps are associated with a field driven phase transformation.

The driving force for field driven phase transformations is the same as the driving force for crystal variant switching. It is the availability of the stress and electric field to do positive work on the change of strain and electric displacement associated with the phase transformation. This process is also represented by Eq. 18.17. The identification and characterization of field driven phase transformations have led to a deeper understanding of the large field behavior of ferroelectric ceramics.

Characterization of the behavior of domain engineered single crystals

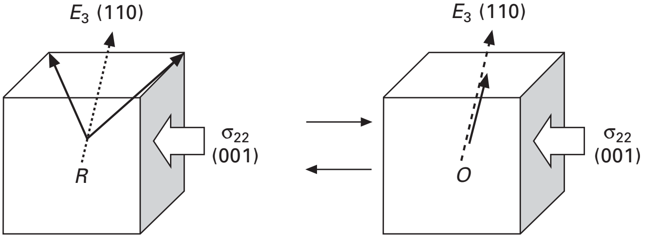

18.14 In the [110] cut and poled crystal with electric field in the [110] direction and compressive stress in the [001] direction, both the stress and electric field provide a positive driving force for the field driven rhombohedral to orthorhombic phase transformation.

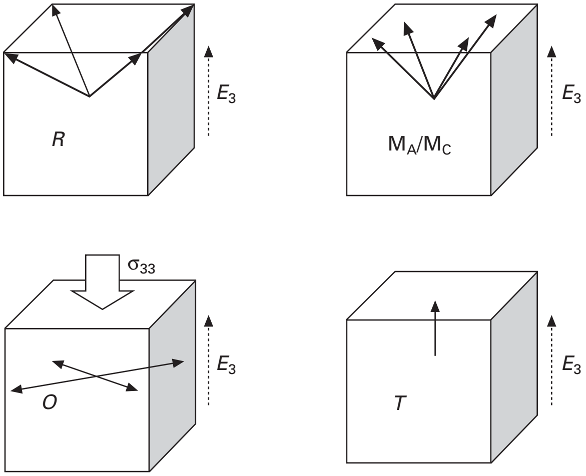

18.15 Working clockwise from the lower left: a compressive stress can drive the structure into a transverse poled orthorhombic phase, a small electric field results in linear response from the [001] poled crystal, an intermediate electric field rotates the polarization into an effective monoclinic phase, and a large electric field drives the structure to the tetragonal phase.

has enabled the isolation of intrinsic and extrinsic effects. The intrinsic behavior is a term used to describe the contributions of single variants to ferroelectricity (no domain wall motion). There are no loss mechanisms associated with ideal intrinsic ferroelectricity. The losses that are present in domain engineered single crystals are associated with defects in the lattice structure (possibly conduction losses) and with limited domain wall motion. The extrinsic behavior is that associated with domain wall motion and phase boundary motion. If stress and electric field are applied to crystals in directions that do produce a driving force for domain wall motion, the propagation of domain walls results in losses (the generation of heat).

18.9 The large field behavior of ferroelectric ceramics

Micromechanical models can give considerable insight into the behavior of ferroelectric ceramics [25–30]. A ceramic comprises many single crystal grains that are mechanically connected at grain boundaries. If we consider a volume of ceramic and establish a global coordinate system to the ceramic, the cubic referenced crystallographic axes of each grain will have a different orientation relative to the global coordinate system. Figure 18.16 shows a micrograph of a polished specimen of PZT. The composition is close to the morphotropic phase boundary. The micrograph was taken using electron back scatter diffraction. This micrograph shows the typical structure of a ferroelectric ceramic, with grains separated by grain boundaries, domain structure within the grains, and porosity at some of the grain boundaries.

The large field behavior of ceramics is a multiscale phenomenon that results from the volume average of all of the behavior at smaller length scales. The behavior of unit cells, groups of unit cells forming domains, and driving forces for the evolution of domain and phase structures in the single crystal have been discussed. A substantial contribution to nonlinear behavior in ceramics is the orientation of the grains. This effect will be described in terms of a Preisach type model that greatly simplifies the behavior of the grain sub-structure and isolates the contributions of grain orientation to the ferroelectric behavior. This gives considerable insight into the response of the ceramic to combined stress and electric field loading.

The discussion from this point will focus on a donor-doped PZT that displays relaxor behavior, 8/65/35 PLZT [9]. This notation means a composition of 65% lead zirconate, 35% lead titanate, with an 8% lanthanum substitution, predominantly on lead sites. Figure 18.17 shows several measured response

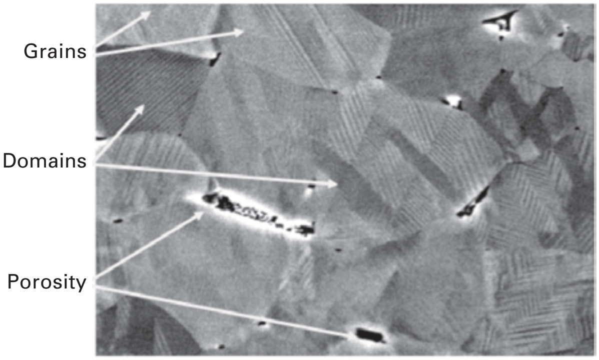

Work with Ed Kennik at ORNL, SHARE program, EBSD

18.16 A micrograph of MPB composition PZT taken using electron back scatter diffraction. Grain size is approximately 5 microns.

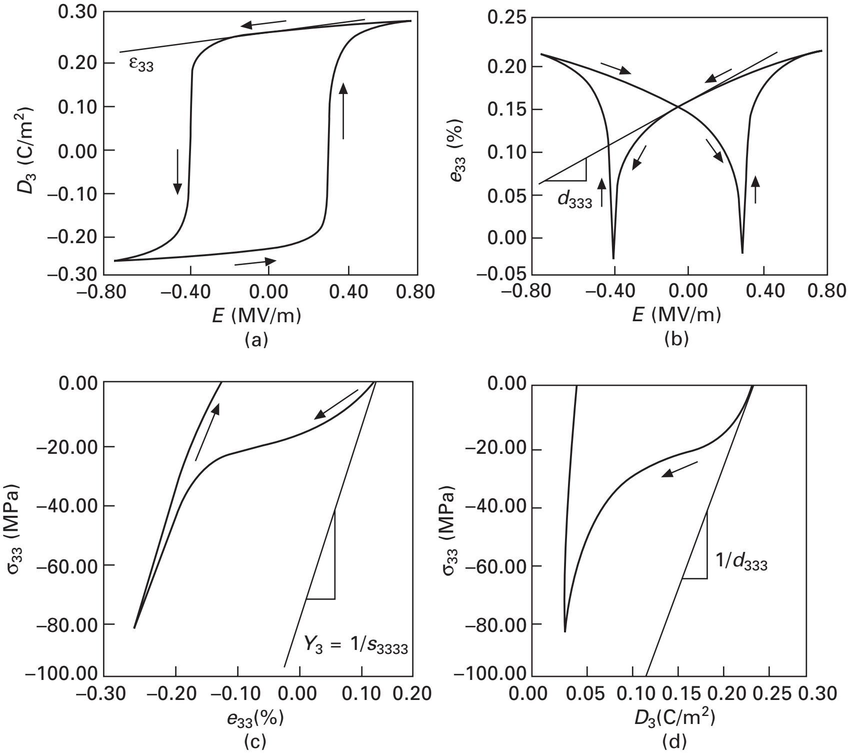

18.17 The response of 8/65/35 PLZT is shown in (a) the electric displacement vs. electric field, (b) strain vs. electric field, (c) stress vs. strain, and (d) stress vs. electric displacement.

curves for 8/65/35 PLZT. The slope of the electric displacement vs. electric field curve is the dielectric permittivity, the slope of the strain vs. electric field curve is the piezoelectric coefficient, the slope of the stress vs. strain curve is the elastic modulus, and the slope of the stress vs. electric displacement curve is the inverse of the piezoelectric coefficient. These slopes correspond to the linear constitutive coefficients. It is clear from this figure that these coefficients only describe a small range of the overall material behavior, and this figure represents only a fraction of the overall large field behavior.

18.10 Preisach modelling

The model used to isolate the contribution of grain orientation to the nonlinearity observed in Fig. 18.17 is based on the simplified switching behavior described in Fig. 18.4. Each grain in the ceramic is assumed to undergo a complete switch from one crystal variant to another crystal variant when the availability of externally applied stress and electric field to do positive work during a virtual switch is sufficient to overcome the energy barrier to that switch. The ceramic is modelled as a collection of non-interacting grains, each with a different orientation relative to the global coordinate system. The response of the ceramic is taken as the volume average of the response of the individual grains.

The ceramic is modeled as consisting of *n*-grains. The orientation of each grain is described by introducing a local coordinate system for each grain. The orientation of each local coordinate system is defined relative to the global coordinate system by a direction cosine matrix. The direction cosine matrices can be obtained by generating a set of three Euler angles for each grain. Random generation of Euler angles for each grain does not generate a random distribution of grain orientations. It produces a texture. A quasi-random grain orientation can be achieved by generating two random sets of Euler angles for each grain, obtaining two rotation matrices, and multiplying them together. The resulting set of rotation matrices whose components are the direction cosines between the grain coordinate systems and the global coordinate system produce a system of grains with no discernable texture (preferential orientation). Next an initial polarization direction is assigned to each grain. This fully defines the spontaneous polarization, the spontaneous strain, and the orientation of the elastic, piezoelectric, and dielectric tensors of each grain.

The macroscopic strain and polarization are computed as the volume average of the strain and polarization of the grains. First the strain and polarization components are expressed in the global coordinate system, then the strain components of each grain are added and divided by the number of grains:

$$P_I = \frac{1}{n} \sum_{r=1}^{n} a_{ip}^{(r)} P_p^{(r)} \qquad 18.34$$

$$\varepsilon_{IJ} = \frac{1}{n} \sum_{r=1}^{n} a_{ip}^{(r)} a_{jq}^{(r)} \varepsilon_{pq}^{(r)}$$

where the upper case indices indicate components expressed in the global coordinate system and the lower case indices indicate components expressed in the local (cubic referenced grain) coordinate system.

The components of the applied stress and electric field are described in the global coordinate system, $\underline{X}$. To assess whether a grain should switch from one variant to another, the stress and electric field must first be expressed in each of the (*n*) local coordinate systems:

$$\sigma_{pq}^{(n)} = a_{ip}^{(n)} a_{jq}^{(n)} \sigma_{IJ} \qquad 18.35$$

$$E_p^{(n)} = a_{ip}^{(n)} E_I$$

The availability of the stress and electric field to do work for each possible switch is calculated next using Eq. 18.36:

$$w = \sigma_{pq}^{(n)} (\varepsilon_{pq}^{\beta} - \varepsilon_{pq}^{\alpha})^{(n)} + E_p^{(n)} (D_p^{\beta} - D_p^{\alpha})^{(n)} \qquad 18.36$$

where the work calculation is performed for each possible switch (five possibilities for a tetragonal system). The switch with the largest positive work is identified as the potential switch. If the available work to drive this switch exceeds the energy barrier, the switch is allowed to take place.

Equation 18.36 indicates an equivalency between stress as a driving force and electric field as a driving force for polarization reorientation. If we consider the example of a 90° switch, a compressive stress in the original polarization direction drives the switch, and an electric field in the new polarization direction drives the switch. It is the sum of the work done by the stress and the electric field that provides the driving force for the switch. There is thus an equivalence between stress as a driving force and electric field as a driving force for polarization reorientation.

This simulation is used to generate curves of the type shown in Fig. 18.17. Certain parameters must be identified to compare the simulated results with measured data. The parameters matched are the elastic moduli (this is simplified by using an isotropic elastic symmetry), the piezoelectric moduli, and the dielectric moduli (this is again simplified by using an isotropic dielectric symmetry). The model gives insight into the contribution of grain orientation to the rounding of the hysteresis loops, and also results in some predictive capability that support the use of Equation 18.36 as a switching criterion. The model predicts the downward shift and the shape change of the strain vs. electric field hysteresis loops in the presence of a constant compressive stress as shown in Fig. 18.18. The rounding of the bottom of the strain – electric field hysteresis loops is the result of the compressive stress driving non-180° switching and thus aligning the polarization in the horizontal direction with the negative strain component in the vertical direction. The electric field in the vertical direction is competing with this. When the electric field is large enough, it overcomes the ability of the stress to drive the polarization to the horizontal orientation and pulls it to the vertical orientation.

This type of micromechanical model has been extended considerably from the version described here. It has been used to simulate tetragonal structures, rhombohedral structures, and antiferroelectric to ferroelectric phase transformations. Additional levels of complexity have been added to incorporate the evolution of volume fractions of crystal variants within each grain, and to incorporate intergranular interactions using a back stress and back electric field.

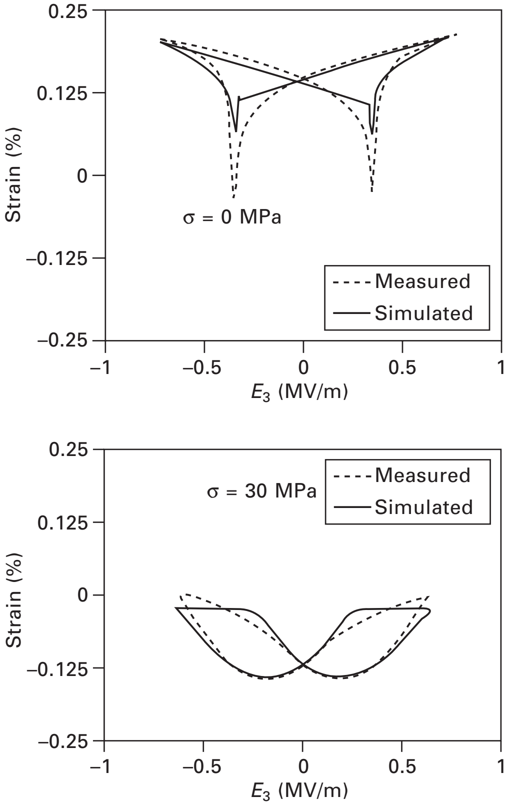

18.18 The Preisach model gives insight into the contribution of grain orientation to nonlinearities in the large field response of ferroelectric ceramics.

18.11 Future trends

Large field behavior of feroelectric materials, including both polarization reorientation and field driven phase transformations, will continue to be of significant technological importance. This behavior is exploited in numerous applications that include poling ceramics and single crystals to obtain a bulk piezoelectric effect, using switching behavior in non-volatile memory, using field driven transformations to electronically control dielectric properties of electronically steerable antennas, and using stress driven phase transformations to generate large electro-magnetic pulses. Although not well addressed in the technical literature, field driven polarization reorientation and field driven phase transformations likely contribute to the behavior of morphotropic boundary compositions of PZT, and likely have a large effect on thin films where the film stresses can be large.

The discussion in this chapter was based on quasi-static assumptions. This is an assumption that leaves out some very important properties of ferroelectric material behavior. These materials are time dependent and temperature dependent. This gives rise to mechanical creep under constant stress, stress relaxation under constant strain, and similar relaxation effects in the electrical and field coupled properties.

Reliability of ferroelectric materials will continue to be an important subject. Field concentrations such as cracks, pores, and inhomogeneities can lead to electrical breakdown. The polarization induced anisotropy of fracture behavior initially identified using indentations [31–35] has been extended to include the application of electric fields across the indentations [36–42]. The indentation work is semi-qualitative in that the technique of using crack length induced by a Vicker's indentation developed by Anstis *et al.* [43] relies on the material properties being isotropic. The elastic properties of a ferroelectric become anisotropic when it is poled, and this is compounded by differences between open and short circuit conditions (s^E and s^D). Recent work has resulted in more quantitative measurements of fracture toughness in ferroelectric materials and has identified time dependent mechanisms in the fracture process [44–55].

Accurate constitutive laws for ferroelectric materials that include the effects of polarization reorientation and field driven phase transformations are needed. Once developed, they must be implemented in finite element codes for a full analysis of field concentrations. This problem is further complicated when the effects of diffusion of charge carriers in the presence of electric fields are considered. Although considerable efforts have been directed at the development of an understanding of ferroelectric constitutive behavior and the development of constitutive laws governing that behavior, considerable research remains to be carried out.

18.12 References

1. Chen, W. and Lynch, C.S., Finite element analysis of cracks in ferroelectric ceramic materials. *Engineering Fracture Mechanics*, 1999. **64**(5): 539–562.
2. Steinkopff, T., Finite-element modelling of ferroic domain switching in piezoelectric ceramics. *Journal of the European Ceramic Society*, 1999. **19**(6–7): 1247–1249.
3. Landis, C.M. and McMeeking, R.M., Phenomenological constitutive law for ferroelastic switching and a resulting asymptotic crack tip solution. *Journal of Intelligent Material Systems and Structures*, 2000. **10**(2): 155–163.
4. Kamlah, M. and Bohle, U., Finite element analysis of piezoceramic components taking into account ferroelectric hysteresis behavior. *International Journal of Solids and Structures*, 2001. **38**(4): 605–633.
5. Landis, C.M., A new finite-element formulation for electromechanical boundary value problems. *International Journal for Numerical Methods in Engineering*, 2002. **55**(5): 613–628.

6. Li, F.X. and Rajapakse, R., Nonlinear finite element modeling of polycrystalline ferroelectrics based on constrained domain switching. *Computational Materials Science*, 2008. **44**(2): 322–329.
7. Randall, C.A., *et al.*, Intrinsic and extrinsic size effects in fine-grained morphotropic-phase-boundary lead zirconate titanate ceramics. *Journal of the American Ceramic Society*, 1998. **81**(3): 677–688.
8. Uchino, K. and Hirose, S., Loss mechanisms in piezoelectrics: How to measure different losses separately. *IEEE Transactions on Ultrasonics, Ferroelectrics and Frequency Control*, 2001. **48**(1): 307–321.
9. Lynch, C.S., The effect of uniaxial stress on the electro-mechanical response of 8/65/35 PLZT. *Acta Materialia*, 1996. **44**(10): 4137–4148.
10. Long-Qing, C. and Khachaturyan, A.G., Computer simulation of structural transformations during precipitation of an ordered intermetallic phase. *Acta Metallurgica et Materialia*, 1991. **39**(11): 2533.
11. Long-Qing, C. and Khachaturyan, A.G., Kinetics of decomposition reactions accompanied by a congruent ordering of the first kind. *Scripta Metallurgica et Materialia*, 1991. **25**(1): 67.
12. Oates, W.S., *et al.*, Phase field modeling of domain structures in ferroelectric materials. 2004. San Diego, CA: International Society for Optical Engineering, Bellingham, WA.
13. Wang, J., *et al.*, Phase field simulations of ferroelectric/ferroelastic polarization switching. *Acta Materialia*, 2004. **52**(3): 749–764.
14. Merz, W.J., Domain formation and domain wall motions in ferroelectric BaTiO single crystals. *Physical Review*, 1954. **95**(3): 690–698.
15. Hooton, J.A. and Merz, W.J., Etch patterns and ferroelectric domains in BaTiO single crystals. *Physical Review*, 1955. **98**(2): 409–413.
16. Moulson, A.J., Herbert, J. M., Electroceramics: materials, properties, applications 1990.
17. Kuwata, J., Uchino, K. and Nomura, S., Phase transitions in the $Pb(Zn_{1/3}Nb_{2/3})\ O_3 - PbTiO_3$ system. *Ferroelectrics*, 1981. **37**(1–4): 579–582.
18. Kuwata, J., Uchino, K. and Nomura, S., Dielectric and piezoelectric properties of $0.91Pb(Zn_{1/3}\ Nb_{2/3})O_3 - 0.09PbTiO_3$ single crystals *Japanese Journal of Applied Physics*, 1982. **21**(9): 1298–1302.
19. Park, S.E. and Shrout, T.R., Ultrahigh strain and piezoelectric behavior in relaxor based ferroelectric single crystals. *Journal of Applied Physics*, 1997. **82**(4): 1804–1811.
20. Park, S.E. and Shrout, T.R., Characteristics of relaxor-based piezoelectric single crystals for ultrasonic transducers. *IEEE Transactions on Ultrasonics, Ferroelectrics and Frequency Control*, 1997. **44**(5): 1140–1147.
21. Park, S.E., *et al.*, Electric field induced anisotropy in electrostrictive $Pb(Mg_{1/3}Nb_{2/3}O_3PbTiO_3$ crystals. *Ferroelectrics*, 1998. **207**(3–4): 519–526.
22. Liu, T. and Lynch, C.S., Domain engineered relaxor ferroelectric single crystals. *Continuum Mechanics and Thermodynamics*, 2006. **18**(1–2): 119–135.
23. Liu, T. and Lynch, C.S., Ferroelectric properties of [110], [001] and [111] poled relaxor single crystals: measurements and modeling. *Acta Materialia*, 2003. **51**(2): 407–416.
24. Tieqi, L., Lynch, C.S. and McLaughlin, E.A., Thermodynamics of stress and electric field induced phase transition in relaxor ferroelectric crystals. *Journal of Intelligent Material Systems and Structures*, 2007. **18**(4): 409–415.
25. Hwang, S.C., Lynch, C.S. and McMeeking, R.M., Ferroelectric/ferroelastic interactions

and a polarization switching model. *Acta Metallurgica et Materialia*, 1995. **43**(5): 2073–2084.

26. McMeeking, R.M. and Hwang, S.C., On the potential energy of a piezoelectric inclusion and the criterion for ferroelectric switching. *Ferroelectrics*, 1997. **200**(1–4): 151–173.
27. Huber, J.E., *et al.*, Constitutive model for ferroelectric polycrystals. *Journal of the Mechanics and Physics of Solids*, 1999. **47**(8): 1663–1697.
28. Landis, C.M. and McMeeking, R.M., Self consistent model for switching in polycrystalline ferroelectrics electrical polarization only. *Proceedings of SPIE – The International Society for Optical Engineering*, 1999. **3667**: 172–180.
29. Kessler, H., Drescher, J. and Balke, H., *Constitutive modeling of repolarization for the ferroelectric process zone of a crack*. 2001. Newport Beach, CA: Society of Photo-Optical Instrumentation Engineers.
30. Landis, C.M., Fully coupled, multi-axial, symmetric constitutive laws for polycrystalline ferroelectric ceramics. *Journal of the Mechanics and Physics of Solids*, 2002. **50**(1): 127–152.
31. Pohanka, R.C., *et al.*, Fracture, Fractography and Internal Stress of $BaTiO_3$ Ceramics. *Ferroelectrics*, 1975. **10**(1–4): 231–235.
32. Cook, R.F., *et al.*, Fracture of Ferroelectric Ceramics. *Ferroelectrics*, 1983. **50**(1–4): 267–272.
33. Megherhi, M.H., *et al.*, Indentation fracture of lead magnesium niobate-based multilayer composite structures. *Journal of Materials Research*, 1990. **5**(3): 515–523.
34. Calderon-Moreno, J.M., *et al.*, Anisotropy in the indentation fracture piezoelectric titanate ceramics. *Ferroelectrics*, 1999. **228**(1): 111–128.
35. Busche, M.J. and Hsia, K.J., Fracture and domain switching by indentation in barium titanate single crystals. *Scripta Materialia*, 2001. **44**(2): 207–212.
36. Lynch, C.S., *et al.*, Electric field induced cracking in ferroelectric ceramics. *Ferroelectrics*, 1995. **166**(1–4): 11–30.
37. Lynch, C.S., Fracture of ferroelectric and relaxor electro-ceramics: influence of electric field. *Acta Materialia*, 1998. **46**(2): 599–608.
38. Chen, W., Lynch, C.S. and Lupascu, D., *Method for measuring short crack R-curve behavior of ferroelectric ceramic*. American Society of Mechanical Engineers, Aerospace Division (Publication) AD, 1999. **59**: 119–124.
39. Schneider, G.A. and Heyer, V., Influence of the electric field on Vickers indentation crack growth in $BaTiO_3$. *Journal of the European Ceramic Society*, 1999. **19**(6–7): 1299–1306.
40. Weitzing, H., *et al.*, Cyclic fatigue due to electric loading in ferroelectric ceramics. *Journal of the European Ceramic Society*, 1999. **19**(6–7): 1333–1337.
41. Fang, F., Li, Y.H. and Yang, W., Effect of poling directions on the electric-field-induced fatigue crack growth in barium titanate ferroelectric single crystals. *Ferroelectrics*, 2005. **322**: 11–21.
42. Huang, H.Y., *et al.*, Anisotropy of indentation cracks propagation of PZT-5H ferroelectric ceramics in air and water under sustained load. *Ferroelectrics*, 2006. **332**: 203–211.
43. Anstis, G.R., *et al.*, Indentation techniques for measuring toughness of ceramics. *Proceedings – Australian Ceramic Conference*, 1980: 32–34.
44. Karastamatis, T., *et al.*, *R-curves in lead zirconate titanate (PZT)*. Honolulu, HI: IEEE.
45. Chen, W., *et al.*, Short crack R-curves in ferroelectric and electrostrictive PLZT. *Journal of the American Ceramic Society*, 2001. **84**(3): 593–597.

46. Dos Santos e Lucato, S.L., *et al.*, Constraint-induced crack initiation at electrode edges in piezoelectric ceramics. *Acta Materialia*, 2001. **49**(14): 2751–2759.
47. Lupascu, D.C., *et al.*, Liquid-crystal display of stress fields in ferroelectrics. *Applied Physics Letters*, 2001. **78**(17): 2554–2556.
48. Dos Santos e Lucato, S.L., *et al.*, Electrically driven cracks in piezoelectric ceramics: Experiments and fracture mechanics analysis. *Journal of the Mechanics and Physics of Solids*, 2002. **50**(11): 2333–2353.
49. Karastamatis, T., *et al.*, R-curves of lead zirconate titanate (PZT). *Journal of the European Ceramic Society*, 2003. **23**(9): 1401–1408.
50. Karastamatis, T., *et al.*, R-curves of lead zirconate titanate (PZT). *Journal of the European Ceramic Society*, 2003. **23**(9): 1401–1408.
51. Oates, W.S., *et al.*, Subcritical crack growth in lead zirconate titanate. *Journal of the American Ceramic Society*, 2004. **87**(7): 1362–1364.
52. Fett, T., Kounga Njiwa, A.B. and Rodel, J., Shielding stresses for soft PZT. *International Journal of Fracture*, 2005. **134**(2): 151–159.
53. Kounga Njiwa, A.B., *et al.*, Effect of geometry and electrical boundary conditions on R-curves for lead zirconate titanate ceramics. *Engineering Fracture Mechanics*, 2006. **73**(3): 309–317.
54. Njiwa, A.B.K., *et al.*, Influence of radial stress on the poling behaviour of lead zirconate titanate ceramics. *Acta Materialia*, 2007. **55**(2): 675–680.
55. Westram, I., *et al.*, Mechanism of electric fatigue crack growth in lead zirconate titanate. *Acta Materialia*, 2007. **55**(1): 301–312.

Index

α-quartz, 174
A-type resonance *see* piezoelectric resonance
abrasion-resistant coatings, 500
AC voltage, 591
accelerometers, 44, 205
acceptor doping, 36, 97
acceptor ions, 589
acoustic emission detection, 408–9
acoustic horn, 547–50
acoustic impedance, 26
acoustic impedance mismatch layer, 547
acoustic lens, 547
acoustic microscope, 549, 550
acoustic superlattices, 214–15
active fibre composite, 341
actuator applications, 591
actuator electrodes, 399–400
ACX Company, 335
AD-PZT
  annealing effect for electrical properties with PZT layer, 511–14
    frequency dependence of PZT coefficient, 513
    PZT film deposited on stainless steel substance, 514
    PZT films deposition at room temperature, 512
  high breakdown voltage, 508–10
  piezoelectric relaxor type, 515–17
    dielectric properties and P-E hysteresis, 516
    PZT constant comparison with conventional deposition methods, 518
    PZT properties and PNN-PZT film relationship, 517
admittance/impedance spectrum analysis, 575
aerosol deposition, 104
  deposition process, 495–7
    apparatus, 496
    conditions, 497
  films electrical properties and heat treatment, 508–22
    AD layer high breakdown voltage, 508–10
    annealing effect for electrical properties of AD-PZT layer, 511–14
    application to lead-free PZT materials, 517–20
    laser annealing, 520–2
    relaxor type piezoelectric AD layer, 515–17
  piezoelectric device applications, 522–31
    metal-based optical micro-scanner, 528–30
    optical modulator, 530–1
    PZT layer thickness for microactuators, 522–6
    Si-MEMS optical micro-scanner, 527
    ultrasonic motor, 531
piezoelectric materials manufacturing, 493–533
properties and film patterning, 504–8
    ceramic film patterning properties, 508
    deposition ratio and influence of powder properties, 504–8
  room temperature impact consolidation, 497–504
    ceramic layers densification mechanism, 502–4
    ceramic powders consolidation, 497–500
    impact partial velocity and local temperature increase, 501–2
AFC *see* active fibre composite
Ag ML actuators, 400
alkoxide hydrolysis, 361–2
  synthesised ferroelectric powders, 362
Alpha-Step 200, 618
aluminium nitride, 40
amorphous ferroelectric, 378–9
Ampex, 371
anomalous photovoltaic effect, 600, 602
antiferroelectric phase, 632
antiresonance state, 573, 582
APC 840, 345
APV effect *see* anomalous photovoltaic effect
array transducers, 552
artificial quartz crystal
  production, 181–3

    - shapes, 183
    - specifications, 182–3
    - vs natural quartz crystal, 181
- ASL *see* acoustic superlattices
- AT-cut, 174
- AT-cut crystal vibrator, 187–90, 191
- ATILA simulation, 542, 543
- AUTODYNs-2D, 501
- automotive applications
  - applications of resonator, oscillator, and filter, 200–1
    - body control module, 201
    - car audio/video system, 200
    - global positioning system, 200
    - keyless entry, 200
    - laser/millimeter wave radar, 201

- B-type resonance *see* antiresonance state
- back-switched poling, 223–5
- back-switching process, 223–5
- backing, 551
- backing material, 550
- $Ba(Mg_{1/3}Ta_{2/3})O_3$, 114
- barium titanate, 35, 92, 144–8, 205, 322, 359, 379, 630–1
  - ceramics, 132
  - discovery, 5–6
  - Dy-doped and undoped samples
    - electric field induced strain curves, 380
    - temperature dependence of piezoelectric d_{33}, 381
  - particle size dependence of tetragonality at room temperature, 383
  - single crystal, 274, 275
  - temperature dependence of tetragonality for various particle size samples, 383
- $BaTiO_3$-based ML actuator, 403–6
- $Ba(Ti,Sn)O_3$, 111
- BCM *see* body control module
- Bell Laboratories, 204
- Berlincourt d_{33} meter, 326
- bimorph devices, 369–71
  - fundamental structure, 370
  - non-parallel and parallel polarisation type, 370
  - structure for perfectly parallel motion with position sensing feedback function, 371
- $(Bi0.5Na0.5)TiO_3$ *see* BNT
- bio-sensor, 54–5
  - principle, 55
- biomimetic robotics, 305
- birefringent phase-matching, 227
- bismuth lithium titanate, 148–58
- bismuth potassium titanate, 144–63
- bismuth sodium titanate, 140–58
- blood sugar level sensors, 202
- bluetooth, 194–5
- Bluetooth-SIG, 194
- BNT, 520
- body control module, 201
- BPM *see* birefringent phase-matching
- Braille reading interface, 304
- Bridgman method, 242, 264, 269, 272, 279
- broadband transducers, 551, 552
- bulk photovoltaic effect, 601–8
  - current source model, 604–5
    - energy band gap model, 604
    - wavelength dependence, 605
  - experimental set-up, 602, 603
    - photocurrent measurement, 603
  - illumination response, 601
  - voltage source model, 605–8
    - photoconductivity dependence, 609
    - short-circuit current and open-circuit electric field, 606
- bulk screening mechanisms, 221
- BURPS (BURned-out Plastic Spheres) method, 332
- butterfly curve, 96

- camera module, 199
- capsule endoscopes, 201–2
- carbon nanotubes, 290, 301–2
- cavitation effect, 541, 554
- cavitation instruments, 548
- Cedrat, 371
- cellular phones
  - applications of resonator, oscillator, and filter, 195–9
    - camera module, 199
    - duplexer, 199
    - intermediate frequency filter, 199
    - monolithic crystal filter, 199
    - one-segment/full segment tuners, 195–6
    - RF module, 196–8
    - secure private cosm encryption, 198
- Ceracomp Co., 264
- ceramic electrodes, 401–3
- ceramic film patterning, 508
  - incidence angle effect of particle jet flow, 509
  - lift-off process, 511
  - mask deposition method, 510
- ceramic heater, 587
- ceramic powders
- consolidation, 497–500
    - α–Al_2O_3 layer SEM image, 499
    - AD-ceramic layer using RTIC phenomenon, 498
    - AD deposited layers mechanical properties, 500
  - powder preparation process, 360
  - preparation, 359–62
    - alkoxide hydrolysis, 361–2
    - coprecipitation, 360–1
    - solid state reaction, 359–60
- ceramics, 651
  - barium titanate-based, 132
  - bismuth potassium titanate-based, 158–63
  - bismuth sodium titanate-based, 140–4
  - fabrication processes, 359–66
    - ceramic powders preparation, 359–62
    - single crystal growth, 364–5
    - sintering process, 362–3
    - templated grain growth, 365–6

    potassium niobate-based, 133–40
    relaxor ferroelectrics-based, 111–28
chemical diffusion, 515
chopped near-ultraviolet irradiation, 623
Clevite corporation, 7–8
CLN *see* congruent lithium niobate
CO_2 laser, 520–1
cobalt ferrite, 322
coherent illumination, 608
cohesive field, 96
cold spraying method, 495, 504
columbite, 360
complex perovskite, 98
1-3 composite device, 373
composite effects, 15–16, 319–22
    combination effects, 322
    product effects, 322
    sum effects, 320–2
0-3 composite material, 329
composites, 15–20, 39–40
    magnetoelectric, 16–19
    piezoelectric dampers, 19–20
    see also piezo-composites
compositional segregation, 429–30
conductive polymers, 290, 299–301
conductivity window, 322
confocal micro-Raman spectroscopy, 216
congruent lithium niobate, 208, 213
congruent lithium tantalate, 208, 213
connectivity, 319
0-3 connectivity, 373
constant current measurement method, 576, 588
constant vibration velocity method, 588
conventional thin film method, 506
converse piezoelectric effect, 2
convex acoustic lens, 547
coprecipitation, 360–1
coprecipitation techniques, 616
cosm, 198
Coulomb force, 290
crack propagation, 391–2
cracks, 428–9
critical particle size, 382
Cr_2O_3, 322
Cu electrode, 400–1
cubes model, 329
Curie point, 119
Curie range, 119
Curie temperature, 205, 213, 255, 264, 268, 269, 280, 349, 350, 519, 630, 632
Curie-Weiss law, 111, 118–19
current density, 600
current source model, 604
curve linear array, 552
cut-and-bond method, 367, 388–9
cymbal, 371, 542
cymbal piezo-actuators, 49, 50, 554
cymbal transducers, 50, 541–7
    cymbal array, 543–7
        3 × 3 cymbal array analysed by ATILA simulation model, 544
        beam patterns of 3 x 3 cymbal array, 546
        cymbals centre, edge, and corner displacements, 545
    single cymbal, 541–3
        ATILA simulation and experimental results comparison in terms of TVR, 543
        beam patterns under different conditions, 542
        flextensional structures, 541
Czochralski process, 205, 206, 217, 364

damped capacitance, 32, 574
DEAP *see* dielectric electroactive polymers
density, 551
depolarisation field, 643
depolarisation temperature, 153
DFG *see* difference frequency generation
dice method, 250
dielectric constant, 552
dielectric elastomer, 305
dielectric electroactive polymers, 292–6
dielectric relaxation, 113, 120–2
dielectric superlattice, 217
difference frequency generation, 229
digital terrestrial television broadcasting, 195–6
dioxin, 554
direct piezoelectric effect, 1, 44, 208–9
direct piezoelectricity, 171
Direct Sequence Spread Spectrum Communication System, 195
Directives on Waste from Electrical and Electronic Equipment, 131
discrete switching, 223, 225
displacement transducers, 10
dolphin, 547, 550
domain engineering, 644
domain spreading, 219
domain tip propagation, 219
domain wall pinning model, 354, 355, 589
donor doping, 36, 98
doping, 363
dot matrix printer, 62
dual-beam method, 621–2, 623
duplexer, 199

Eamax, 303
EAP Actuators and Devices, 289
elasticity, 551
electret, 288
electric axis, 174
electric circuit analysis, 328
electric energy, 336
electric poling process, 591
electrical-electrical energy transfer, 79
electrical excitation, 287, 310
electrical poling method, 218
electrical work, 635–6
electroactive polymers, 287–312

applications, 303–5
    4-finger EAP gripper, 306
    6-legged skitter, 306
    biomimetic robotics, 305
    blimp with fin steering, 307
    Braille display for visually impaired, 304
    dust wiper, 305
    dust wiper for JPL's nanorover, 304–5
    medical applications, 303–4
armwrestling challenge, 306–8
    EAP actuated robotics development challenge, 307
    EAP driven arm, 308
challenges, trends and developments, 309–10
historical review, 288–9
leading electronic EAP materials, 311
leading ionic EAP materials, 312
two electroactive polymers groups, 289–303
    EAP materials production, 291
    electronic EAP, 290–6
    ionic EAP, 290, 297–303
electrode materials, 399–406
    actuator electrodes, 399–400
    Cu-embedded co-fired ML actuators, 400–1
        experimental set-up for sintering, 402
        PZT ML actuator with Cu internal electrodes, 401
    ML actuators with ceramic electrodes, 401–6
        barium titanate-based, 403–6
        $BaTiO_3$-based ceramics resistivity, 403
        ceramic electrodes, 401–3
        displacement curve for $BaTiO_3$-based ceramics, 404
        three point bend testing, 404
    pure-silver ML actuators, 400
electromechanical coupling coefficient, 22–5, 27–8, 33, 93, 94, 106, 163, 336, 567, 587
electromechanical resonance, 580
electromotive force, 604
electronic EAP, 288, 290–6, 309
    dielectric electroactive polymers, 292–6
        contractile EAP actuator using folded film structure, 295
        electroactivation effect, 293
        multifunctional electroelastomer roll, 294
        multilayered dielectric elastomer in passive and activated states, 296
        wavy shape film made by PolyPower, Danfoss, 297
    electrostrictive graft elastomers, 296
        electrostrictive grafted elastomer-based bimorph actuator, 298
        structure and morphology, 298
    ferroelectric polymers, 291–2
        passive and activated states, 293
electrooptic effect, 127–8
electrooptical rectification, 229
electrostatic chucks, 510
electrostatic domain–domain interaction, 225
electrostriction, 10, 125–7
electrostrictive effect, 9, 10
electrostrictive graft elastomers, 296
ELV *see* end-of-life vehicles
end-of-life vehicles, 131
energy transmission coefficient, 23
EOR *see* electrooptical rectification
extensive losses, 565
extrinsic behaviour, 650
extrinsic contribution, 629

Face/PulseSwitch Systems, LC, 81
FBAR *see* film bulk acoustic wave resonator
FCX-01, 193, 194
FeliCa, 202
ferroelectric hysteresis, 327
ferroelectric PE hysteresis curve, 96
ferroelectric perovskite, 275
ferroelectric polymers, 291–2
ferroelectric relaxor *see* relaxor ferroelectrics
ferroelectricity, 9, 291, 379
fetal imaging, 551
field-activated EAP *see* electronic EAP
field driven variant changes, 633
figures of merit, 356, 612–13
film bulk acoustic wave resonator, 483–7
    merits of PZT-based thin films for FBAR, 486
    PMnN–PZT thin film, 485
    typical impedance properties, 486
filters, 51
fine ceramic, 378
finite element method, 501
Flemion, 298
flexible piezoelectric composites, 340
flux growth technique, 426–30
    compositional segregation, 429–30
    cracks, 428–9
    flux inclusions/trappings, 428
        trapping of flux, 429
    multiple nucleation and satellite crystals, 427
    parasitic crystals, 427
    PMN-PT single crystal flux growth, 421–6
        change composition effect on growth, 422
        crystals grown from $PbO+B_2O_3$ complex fluxes, 424
        general morphologies, 422
        modified phase diagram and growth path, 426
        nucleation mechanisms, 423
    Pt inclusions, 429
    PT-rich surface layer and fragile domain walls, 430
        tetragonal-rich surface layer and associated domains, 431
    pyrochlore crystals, 427–8
    PZN-PT single crystal flux growth, 414–21
        evolution of cube-shaped crystals, 419

    - natural (001) growth facets, 418
    - nucleation of (001) layer growth, 418
    - PZN–PT single crystals grown from PbO flux, 420
    - schematic, 417
  - side-wall nucleation, 427
- flux inclusions/trappings, 428
- flux method, 240, 243, 251
- FOM *see* figures of merit
- frequency conversion, 228–9
- fringe effect, 220

- Gauss's law, 354
- GE, 277
- Gibbs elastic energy, 349–50
- Ginsburg–Landau–Devonshire theory, 210
- Glass constant, 604
- global energy minimisation, 629
- global positioning system, 200
- GPS *see* global positioning system
- grain size effect, 616
  - photostrictive characteristics dependence, 617
- green sheets, 367, 390
- gyro-sensors, 482–8
  - operating properties of Si tuning fork, 483
  - PZT thin film angular rate sensor, 482
- gyroscopes, 44, 46

- hard property, 351–2
- hard PZT-based materials, 592–4
  - low temperature sinterable 'hard' PZT, 592–3
    - vibration velocity variation, 593
  - new high power piezoelectric applications, 593–4
    - Cu-electrode-embedded multilayer transformers, 596
    - D-shape motor stator, integrated optical fibre alignment package, 595
- H.C. Materials Corporation, 254, 264, 280
- heat generation processes, 578–7
  - off-resonance, 578–9
    - loss and overall heat transfer coefficient, 579
    - temperature saturation vs effective volume, 578
  - resonance, 579–80
    - PZT rectangular plate infrared image, 579
- HIFU *see* high intensity focused ultrasound
- high-energy harvesting, 79–81
- high frequency wave, 549
- high intensity focused ultrasound, 264
- high power characterisation system, 577, 583–4
- high power density, 587
- high power piezoelectric materials, 561–97
  - general consideration of loss and hysteresis, 563–78
    - piezoelectric resonance method, 572–8
    - pseudo-static method, 567–71
    - pulse drive method, 571–2
    - theoretical formulas, 563–7
  - heat generation, 578–7
    - off-resonance, 578–9
    - resonance, 579–80
  - PZT ceramics, 587–92
    - high power piezoelectrics origin, 589–91
    - semi-hard PZT-based ceramics, 591–2
    - very hard PZT-based ceramics, 587–8
  - PZT components, 592–4
    - low temperature sinterable 'hard' PZT, 592–3
    - new high power piezoelectric applications, 593–4
  - PZT loss mechanisms, 580–7
    - losses vibration velocity dependence, 581–4
    - microscopic origins of extensive losses, 585–7
    - resonance and antiresonance mechanical quality factors, 580–1
- high power ultrasonics, 554
- HiPoCS *see* high power characterisation system
- horn, 547
- hydrothermal synthesis, 364

- iE 33 ultrasound systems, 277
- IEC 60758, 182
- IEEE 802.11, 195
- IEEE 802.15.4, 196–7
- Ilmenite, 204
- impedance matching condition, 335
- impedance spectrum analyser, 576
- infinite impedance, 573
- infrared image sensor, 578, 584
- initial sound transmitting process, 547
- inkjet printer, 63, 64, 483
  - operating properties, 485
  - photograph of printer head, 484
- insulin, 554
- intelligent clothing, 81, 343
- intermediate frequency filter, 199
- internal bias field model, 589
- internal electrode, 391–9
  - electrode configuration, 391–5
    - conventional interdigital electrode configuration, 391
    - crack generation, 393
    - interdigital-type, 391–2
    - internal stress distribution, 393
    - multilayer structure, 392
    - plate-through design, 392–5
    - (0.65)PMN–(0.35)PT multilayer actuator displacement curve, 395
    - slit-insert design/interdigital with float electrode, 395
  - layer-thickness effect, 395–9
    - domain texture models (280 and 17 mm layer thicknesses), 398

    - domain texture models (17 mm layer thicknesses), 398
    - PZT ML actuators, 397
    - X-ray diffraction patterns for ML actuators, 398
  - printing pattern, 395
    - ML actuator, 396
  - vertical crack, 399
    - layer adjacent to the inactive bottom of a ML device, 399
- interpenetrating polymer network, 295
- intrinsic behaviour, 650
- intrinsic contribution, 629
- inverse piezoelectricity, 177, 178
- ionic EAP, 288, 290, 297–303, 309
  - carbon nanotubes, 301–2
    - charge injection in nanotube-based EAP actuator, 302
  - conductive polymers, 299–301
    - oxidation and reduction illustration, 300
    - reference and activated states, 301
  - ionic polymer gels, 302–3
  - ionomeric polymer–metal composites, 297–9
    - actuation principle, 300
    - passive and activated states, 299
- ionic polymer gels, 290, 302–3
- ionomeric polymer–metal composites, 290, 297–9, 304
- IPG *see* ionic polymer gels
- IPMC *see* ionomeric polymer–metal composites
- IPN *see* interpenetrating polymer network
- IR blocking filter, 602

- Japanese Sake, 554
- JFE Mineral Company, 280
- JIS C6704, 183, 184
- Johnson-Holmquist model, 501
- Joule heating, 335

- Känzig region, 116
- Kawatetsu Mining Co. Ltd. Research Lab, 280
- KCF technologies, 277
- keyless entry, 200
- $(K_{0.44}Na_{0.52}Li_{0.04})(Nb_{0.86}Ta_{0.10}Sb_{0.04})O_3$ *see* LF4 film
- Kyropoulos method, 240

- La doping, 604
- Lamb wave, 528
- Lame mode quartz crystal, 191, 192
- Langevin transducer, 539–41
  - original design, 540
- Langevin type, 4
- Langevin vibrator, 71, 173
- lanthanum, 643
- lanthanum-doped lead zirconate titanate, 610
- lanthanum-modified lead zirconate titanate, 600
- lasca, 181
- laser annealing, 520–1
  - dielectric properties and ferroelectric hysteresis loops, 521
  - TEM image and EDX analysis results, 522
- lead-free piezo-ceramics, 130–64
  - barium-titanate-based ceramics, 132
  - bismuth potassium titanate-based ceramics, 158–63
    - coupling factor, 162
    - Curie temperature and secondary phase transition temperature, 162
    - D-E hysteresis loops of HP-BKT, 159
    - dielectric constant and dielectric loss tangent, 159
    - electromechanical coupling factor, 161
    - lattice anisotropy and lattice constants, 161
    - physical and piezoelectric properties, 160
  - bismuth sodium titanate-based ceramics, 140–4
    - dielectric and piezoelectric properties, 144
    - frequency characteristics of impedance, 143
    - resistivity, 143
  - bismuth sodium titanate-bismuth lithium titanate-bismuth potassium titanate system, 148–58
    - coupling factor temperature dependence, 157
    - coupling factors and mechanical quality factors, 156
    - D-E hysteresis loops, 152
    - depolarisation temperature, 154
    - depolarisation temperature, piezoelectric constant and mechanical quality factor relationship, 155
    - field induced strains, 150
    - phase relation, 153
    - phase transition temperatures, 150
    - piezoelectric constant compositional dependence, 151
    - piezoelectric strain constant and mechanical quality factor, 155
    - variations in mechanical quality factor as a function of vibration velocity, 158
  - bismuth sodium titanate-bismuth potassium titanate-barium titanate system, 144–8
    - compositional dependence of piezoelectric constant, 145
    - depolarisation temperature, 147
    - depolarisation temperature and piezoelectric constant, 147
    - depolarisation temperature and piezoelectric properties, 148
    - electromechanical coupling factor, 146
    - phase relation around MPBs, 145
    - piezoelectric properties, 148
    - strain of BNBK2:1, 147
  - patent disclosure statistics, 15

    - potassium niobate-based ceramics, 133–40
        - dielectric constant and loss tangent, 136
        - frequency dependence of impedance, 139, 140
        - P-E hysteresis loops, 137
        - piezoelectric constant and electromechanical coupling factor, 137
        - piezoelectric properties, 141
    - potassium niobate-sodium niobate-lithium niobate system, 132–3
        - dielectric constant and loss tangent, 135
        - electromechanical coupling factors, 136
        - piezoelectric properties of textured LF4T vs PZT4, 135
        - piezoelectric strain constant, 134
- lead-free piezoelectric materials, 14, 517–20
    - BNT lead-free ceramic film polarisation properties, 520
    - D-E hysteresis loops for LF4 thick deposited, 519
- lead magnesium niobate–lead titanate *see* PMN–PT crystals
- lead titanate, 35
- lead zinc niobate–lead titanate *see* PZN–PT crystals
- lead zirconate-lead titanate solid solution, 632
- lead zirconate titanate, 131, 588, 630
    - discovery, 6–9
        - Clevite corporation, 7–8
        - Murata Manufacturing Company, 8
        - ternary system, 8–9
    - epitaxially grown rhombohedral films, 42
    - micropump schematic diagram, 43
    - phase diagram, 36
    - piezo-ceramics, 89–107
        - compositional modifications, 94–100
        - crystalline structure and phase relations, 91–4
        - future trends, 107
        - low temperature sintering, 104–6
        - shaping approach and application trend, 100–4
    - piezoelectric, dielectric, and elastic properties, 37
- LF4 film, 517–19
- lifetime test, 407–8
- lightning switch wireless transmitters, 81–2
- linear array transducers, 48, 553
- linear extrapolation method, 603
- lithium columbite, 204
- lithium niobate, 9, 34, 53, 132–3
    - advantages for piezoelectric applications, 212–13
    - domain engineered crystals applications, 226–8
        - 2D non-linear photonic crystal, 227
    - future trends, 231–3
    - nano- and micro domain engineering, 217–26
        - dendrite structure formed during back-switching, 223
        - different domain shapes formed, 222
        - finger domain structure formed during periodical poling, 223
        - main stages of domain kinetics, 219
        - nano-domain patterns formed in CLN, 225
        - nano-domain rays formation, 224
        - periodical nano-domain structure, 226
        - predetermined nucleation, 222
        - stable nano-domain array in CLN, 224
    - periodic domain structure influence, 213–16
        - acoustic superlattices, 215
        - measured reflection coefficient, 216
        - piezo-response force microscopy, 217
    - piezoelectric materials, 204–33
    - piezoelectric properties, 206–12
        - elastic and dielectric coefficients, 212
        - hexagonal and rhombohedral unit cell, 208
        - physical properties, 206
        - piezoelectric coefficients, 211
        - principal axes standard orientation, 209
        - structures below Curie temperature, 207
    - terahertz radiation generation in PPLN crystal, 228–31
        - 2D periodically poled $LiNbO_3$, 230
        - slant-stripe-type periodically poled $LiNbO_3$, 230
- lithium tantalate, 9, 34, 53
    - advantages for piezoelectric applications, 212–13
    - domain engineered crystals applications, 226–8
    - future trends, 231–3
    - nano- and micro domain engineering, 217–26
        - dendrite structure formed during back-switching, 223
        - different domain shapes formed, 222
        - finger domain structure formed during periodical poling, 223
        - predetermined nucleation, 222
    - periodic domain structure influence, 213–16
    - piezoelectric materials, 204–33
    - piezoelectric properties, 206–12
        - elastic and dielectric coefficients, 212
        - hexagonal and rhombohedral unit cell, 208
        - physical properties, 206
        - piezoelectric coefficients, 211
        - principal axes standard orientation, 209
        - structures below Curie temperature, 207
- lithographic patterning, 218
- LMX-01, 193, 194
- local field, 220
- longitudinal piezoelectricity, 177
- longitudinal vibration, 30

longitudinal vibration mode, 28–33
Lorentz factor, 607
Lotgering's factor, 366
low energy harvesting, 81–2
low temperature sintering, 104–6

macro fibre composite, 81, 340
  made by Smart Material Corporation, 342
  output by around f Hz, 344
  stress distribution, 342
macrodonian, 256
magneto-optic spatial light modulators, 530–1
magnetoelectric effect, 319
magnetoelectric material, 322
magnetoelectric sensors, 343–5
magnetostrictive materials, 539
magnetostrictor disks, 343
magnetron sputtering apparatus, 374
mask deposition method, 508
Materials Systems Inc., 333
Matsushita Electric, 77
maximum strain, 355
maximum vibration velocity, 357, 582
MCF *see* monolithic crystal filter
mechanical axis, 174
mechanical-electrical energy transduction, 79
mechanical energy, 336
mechanical-mechanical energy transfer, 79
mechanical power density, 587
mechanical pulverising, 104
mechanical quality factor, 25, 357
mechanical sector transducers, 552
mechanical work, 636
medical instruments
  applications of resonator, oscillator, and filter, 201–2
    blood sugar level sensors, 202
    capsule endoscopes, 201–2
medical ultrasonic imaging, 551
MEMS *see* microelectromechanical systems
mercury lamp, 601, 607
merging, 219
metal organic chemical vapour deposition, 442, 455–8, 461
MFC *see* macro fibre composite
micro-mass sensor, 54–6
microelectromechanical systems, 41–2, 466–76, 493, 527
  PMnN–PZT thin films, 473–6
  PMNT thin films, 466–73
Microfine Materials Technologies Pte. Ltd, 264
micromachining, 43
micromechanical models, 651
microscopic composition fluctuation model, 116
MIFARE, 202
Miller indices, 632, 645
milling procedure, 505
MLCC *see* multilayer ceramic capacitor
mobile communications
  applications of resonator, oscillator, and filter, 194–5
    bluetooth, 194–5
    wireless LAN, 195
MOCVD *see* metal organic chemical vapour deposition
modified Bridgman method
  PIN–PT, 269
  PMN–PT, 251, 253
  PSN–PT, 266
  PZN–PT crystal, 243–4
modified cubes model, 329
monolithic crystal filter, 199
monomorphs, 20–1
moonie, 371, 541
Morgan Electro Ceramics, 280
morphotropic phase boundary, 7, 35, 90, 92–4, 107, 144, 240–2, 611
MOSLM *see* magneto-optic spatial light modulators
motional capacitance, 31, 32, 574
MPB *see* morphotropic phase boundary
multifunctional electroelastomer roll, 294
multilayer actuators
  innovative structures
    3D positioning stage, 406
    stacked structure proposed by PI Ceramic, 407
    super-long design, 406
  reliability/lifetime, 406–11
    health monitoring, 408–11
    heat generation, 406–7
    lifetime test, 407–8
    position and breakdown detection feedback mechanisms, 409
    resistance change with applied electric field, 410
    strain gauge configuration, 409
    temperature change, 408
multilayer ceramic capacitor, 101
multilayer ceramics, 101
multilayer manufacturing processes, 90, 388–90
  cut-and-bond method, 388–9
    piezopile from NTKNGK, 389
  tape-casting method, 389–90
    flowchart for multilayer ceramic actuator fabrication, 390
    multilayer actuator structure, 389
multiple nucleation, 427
Murata Manufacturing Company, 8
MUSES-CN mission, 304

Nafion, 298
nano technology, 378
nanometer scale, 616
Nanorover's optical/IR window, 304
NASA Langley Research Centre, 341
near field communications, 202
NS-GT cut vibrator, 186
NTC-PTC material, 320
nucleation, 218, 423

obstetrical imaging, 551

OFDM *see* orthogonal frequency division multiplexing
optic axis, 174
optical actuators, 600
optical fibre alignment device, 593
optical frequency, 606
optical micro-scanners, 527, 528
optical phone signals, 623
optical rectification, 229
orthogonal frequency division multiplexing, 195
oxide-mixing technique, 359
oxygen deficiency diffusion model, 591
oxygen deficiency model, 355

parabola antenna, 547
paraffin, 547
parasitic crystals, 427
passive damping systems, 339
Pb, La $(ZrTi)O_3$ *see* PLZT
$Pb(I_{1/2}Nb_{1/2})–PbTiO_3$ *see* PIN–PT
$Pb(Mg_{1/3}Nb_{2/3})O_3$ *see* PMN
$Pb(Mg_{1/3}Nb_{2/3})O_3–PbTiO_3$ *see* PMN–PT
$Pb(Mg_{1/2}W_{1/2})O_3$, 114
$0.5Pb(Ni_{1/3}Nb_{2/3})O_3–0.5Pb(Zr_{0.3}Ti_{0.7})O_3$ *see* PNN–PZT thick film
$Pb(Sc_{1/2}Nb_{1/2})–PbTiO_3$ *see* PSN–PT
$PbTiO_3$:chloroprene rubber composites, 330–1
$Pb(Zn_{1/3}Nb_{2/3})O_3$ (PZN), 111
$Pb(Zn_{1/3}Nb_{2/3})O_3–PbTiO_3$ *see* PZN–PT
$Pb(Zr,Ti)O_3$ *see* PZT
PE-MOCVD, 443–4
Penn State researchers, 554
Penn State University, 543
percolation threshold, 19, 338
perfluorocarboxylate, 298
perfluorosulphonate, 298
periodic poling, 205, 231
periodical electrode pattern, 222
periodically poled lithium niobate, 213, 218
periodically poled lithium tantalate, 213, 218
perovskite crystals, 591
perovskite oxide piezoelectric materials, 279
perovskite type crystal, 638
personal navigation device, 200
pertubation, 563
PFC *see* piezo fibre composite
phase-matching condition, 229
phased array transducers, 48, 553
phenomenological theory, 349
Philips, 277
photo-induced DC field generation, 605
photoconductivity, 607, 608
photocurrent, 600
photomechanical resonance, 623
photostriction, 20, 600
photostrictive applications, 619–24
  displacement amplification mechanism, 620–1
    photo-driven bimorph, 621
    tip deflection of bimorph device, 621
  micro propelling robot, 624
    arch-shaped photo-actuating film device, 625
  micro walking machine, 622
    photo-driven with photostrictive bimorphs, 623
  photo-driven relay, 621–2
    structure, 622
  photophone, 622–3
    frequency dependence of the bimorph device, 624
photostrictive effect, 612–19
  ceramic preparation methods, 615–19
    grain size effect, 616
    processing method, 615–16
    surface/geometry dependence, 616–19
  figures of merit, 612–13
  materials considerations, 614–15
    photovoltaic voltage contour maps, 614–15
photostrictive materials, 20, 599–626
  actuators, 624–6
    photostrictive bulk ceramic response speed improvement, 626
  photostrictive device applications, 619–24
    displacement amplification mechanism, 620–1
    micro propelling robot, 624
    micro walking machine, 622
    photo-driven relay, 621–2
    photophone, 622–3
  photostrictive effect, 612–19
    ceramic preparation method effect, 615–19
    figures of merit, 612–13
    materials considerations, 614–15
  photovoltaic effect, 600–12
    bulk photovoltaic effect principle, 601–8
    dopant research, 611–12
    light polarisation direction effect, 608–10
    PLZT composition research, 610–11
photovoltaic device, 599
photovoltaic effect, 600–12
  bulk photovoltaic effect principle, 601–8
    current source model, 604–5
    experimental set-up, 603
    voltage source model, 605–8
  dopant research, 611–12
    bimorph specimens photovoltaic response, 613
    PLZT photovoltaic response, 612
  light polarisation direction effect, 608–10
    measuring system dependence, 610
  PLZT composition research, 610–11
    photocurrent with PLZT compositions, 611
  theoretical background, 600–1
Pierce circuit, 173
piezo-ceramic plate, 572
piezo-ceramics, 539, 550

    compositional modifications, 94–100
        correlation between electric field and polarisation, 96
        correlation between electric field and strain, 97
        major piezoelectric applications and their required material properties, 95
        PE hysteresis and butterfly curve, 99
    crystalline structure and phase relations, 91–4
        $PbZrO_3$-$PbTiO_3$ solid solutions, 93
        perovskite ABO_3 structure, 91
        piezoelectric properties relationship, 93
    lead zirconate titanate-based, 89–107
        future trends, 107
    low temperature sintering, 104–6
        dependence on density, 106
        dependence on electromechanical coupling coefficient, 106
    shaping approach and application trend, 100–4
        bimorph, moonie, and multilayer structure, 103
        complex perovskite compounds for PZT ternary system, 100
        mechanical power source applications, 102
piezo-composites, 39–40
piezo fibre composite, 341
piezo-passive-dampers, 319
piezo-response force microscopy, 216, 225
piezo response mode, 211
piezo-speaker, 45–6
piezo TEMS, 63–4
piezoelectric actuators, 58–65, 476–87, 522–31
    cantilever with Si beam, 480
    cantilever without substrate Si beam, 480
    classification, 476
    construction, 477
    designs, 58–9
        ceramic actuators, 59
    drive/control techniques, 60–1
        classification, 60
    examples and related devices, 478–87
    MEM devices, 481
    metal-based optical micro-scanner, 528–30
        frequency properties, 529
    optical modulator, 530–1
        APZT-MOSLM prototype, 530
        Si-MEMS optical micro-scanner, 527
    properties of thin film unimorph cantilevers, 479
    pulse drive motors, 62–5
        ACH inkjet printer, 64
        common rail type diesel injector, 66
        dot matrix printer head structure, 63
        Toyota electronic modulated suspension, 65
        walking piezo motor, 66
    PZT layer thickness for microactuators, 522–6
        PZT/SS cantilever displacement, 525
        total electrical power consumption of PZT/SS actuator, 526
        unimorph actuator, 523
    resonant properties, 481
    servo displacement transducers, 62
        bearingless rotor flexbeam with piezoelectric strips, 63
        Hubble telescope using PMN electrostrictive actuators, 62
    Si-MEMS optical micro-scanner, 527
        optical scanner with high scanning speed, 527
    ultrasonic motor, 531
piezoelectric biopolymers, 288
piezoelectric buzzer, 45
piezoelectric ceramic materials
    $(1 - x)Pb(Zn_{1/3}Nb_{2/3})O_3$–$x$ $PbTiO_3$
        lattice parameters, 351
        phase diagram, 351
        PZN and PT coefficients used, 353
    ceramics fabrication processes, 359–66
        ceramic powders preparation, 359–62
        single crystal growth, 364–5
        sintering process, 362–3
        strain vs electric field curves, 366
        templated grain growth, 365–6
    device designing, 367–78
        fabrication process for multilayer ceramic actuator, 368
        flexible composites, 373
        flextension/hinge lever amplification mechanisms, 371–3
        flextensional type developed by Cedrat, 372
        moonie and modified design Cymbal, 372
        multilayer actuator structure, 368
        multilayers, 367–9
        plotted saturated temperature, 369
        single disks, 367
        unimorphs/bimorphs, 369–71
    manufacturing methods, 349–85
    material designing, 349–59
        comparison among electrostrictor, soft and hard piezoelectrics, 353
        composition selection, 349–51
        dopant effect on field-induced strain, 356
        dopant effects on piezoelectricity, 351–5
        high power characteristics, 356–9
        mechanical quality factor and temperature rise dependence on vibration velocity, 357
    size effect on ferroelectricity, 378–85
        critical particle size, critical hydrostatic pressure and surface tension energy for perovskites, 385
        critical particle size and phase transition temperature relationship, 384
        3D particle size effect, 382–5
        grain size effect, 379–82

  - temperature dependence
    - 0.91PZN–0.09PT lattice parameters, 352
    - xPZN–(1 – x)PT dielectric constant, 352
  - thin/thick films, 373–8
    - constraints, 376–8
    - film manufacturing techniques, 373–5
    - MEMS application, 375–6
- piezoelectric ceramics *see* piezo-ceramics
- *Piezoelectric Ceramics*, 8
- piezoelectric coefficient, 616, 634
- piezoelectric composite dampers, 334–9
- piezoelectric composite energy harvesting, 340–3
- piezoelectric composite materials, 318–45
  - composite dampers and energy harvesters, 333–43
    - carbon black contained PLZT:PVDF composites fabrication process, 338
    - CFRP/PZT cantilever beams, 340
    - damping time constant vs volume percentage of carbon black in PLZT:PVDF composite, 339
    - mechanical damping difference for unimorph-type beam, 336
    - piezoceramic:polymer:carbon black composite, 338
    - piezoelectric composite dampers, 334–9
    - piezoelectric composite energy harvesting, 340–3
    - piezoelectric damper patch, 337
    - three initial bending modes of the beam, 341
  - composite effects, 319–22
    - $CoFe_2O_4$:$BaTiO_3$ composite magnetoelectric effect, 323
    - combination effects, 322
    - magnetorestrictive $CoFe_2O_4$ and piezoelectric $BaTiO_3$ mixture with TiO_2 excess, 323
    - NTC-PTC effect in V_2O_3:epoxy composite, 321
    - product effects, 322
    - sum, combination and product effect, 321
    - sum effects, 320–2
  - connectivity, 319
    - two-phase composite classification, 320
  - magnetoelectric sensors, 343–5
    - magnetic field monitoring performance, 345
    - magneto-electric device, 345
  - PZT:polymer composites, 323–33
    - advanced PZT:polymer composites, 332–3
    - piezoelectric composite materials, 323–4
    - principles, 324, 326–9
    - theoretical models for 0-3 composites, 329–31
- piezoelectric dampers, 19–20
- piezoelectric devices, 44–77
- piezoelectric equations, 26–7
- piezoelectric loss mechanisms, 580–7
  - losses vibration velocity dependence, 581–4
    - heat generation from PZT8 plate, 585
    - power frequency spectra, 584
    - PZT equivalent circuit and vibration velocity dependence, 583
    - vibration velocity dependence, 581
  - microscopic origins of extensive losses, 585–7
    - model for dielectric, elastic, PZT losses, 586
    - model for loss change with electric field, 586
  - resonance and antiresonance mechanical quality factors, 580–1
    - electromechanical parameters, 580
- piezoelectric materials, 551
  - aerosol deposition, 493–533
    - AD films electrical properties and heat treatment improvements, 508–22
    - deposition properties and film patterning, 504–8
    - piezoelectric device applications, 522–31
    - process, 495–7
    - PZT layer fabrication method, 494
    - room temperature impact consolidation, 497–504
  - ceramic materials manufacturing methods, 349–85
    - ceramics fabrication processes, 359–66
    - device designing, 367–78
    - material designing, 349–59
    - size effect on ferroelectricity, 378–85
  - composite materials, 318–45
    - composite dampers and energy harvesters, 333–43
    - composite effects, 319–22
    - connectivity, 319
    - magnetoelectric sensors, 343–5
    - PZT:polymer composites, 323–33
  - composites, 15–20
    - composite effects, 15–16
    - first report on piezoelectric composites, 17
    - magnetoelectric composites, 16–19
    - micrograph of uni-directionally solidified rod of materials, 18
    - performance improvement via a combination effect, 17
    - piezoceramic:polymer:carbon black deposit for vibration damping, 19
    - piezoelectric dampers, 19–20
    - strain curves for oriented and unoriented ceramics, 16
  - dawn of piezoelectrics, 1–6
    - discovery of barium titanate, 5–6
    - Langevin underwater transducer original design, 3
    - MgO-TiO_2-BaO system permittivity contour map, 5
    - sinking of Titanic, 2
    - underwater acoustic devices, 2–5
  - development and new perspective, 1–82
    - history of piezoelectrics, 1

  - lithium niobate/tantalate, 9
  - present status, 21
  - PVDF piezoelectricity, 14
- domain engineered properties calculation, 645–8
  - piezoelectric coefficients, 648
  - strain vs electric field curves, 649
  - tensor components, 647
  - three co-ordinate systems, 646
- electroactive polymers, 287–312
  - armwrestling challenge, 306–8
  - challenges, trends and potential developments, 309–10
  - current and under consideration applications, 303–5
  - historical review, 288–9
  - leading electronic EAP materials, 311
  - leading ionic EAP materials, 312
  - two electroactive polymers groups, 289–303
- ferroelectric ceramics, 651–2
  - micrograph of PZT polished specimen, 651
- field driven phase transformations, 648–50
  - compressive stress drives, 650
  - loading directions for stress and electric field, 650
- future trends, 655–6
- lead zirconate titanate discovery, 6–9
  - Clevite corporation, 7–8
  - Murata Manufacturing Co., 8
  - $Pb(Zr,Ti)O_3$ phase diagram, 7
  - PZT, 6–7
  - ternary system, 8–9
- lithium niobate and lithium tantalate-based, 204–33
  - advantages of single crystal ferroelectrics, 212–13
  - domain engineered crystals applications, 226–8
  - future trends, 231–3
  - nano- and micro-domain engineering, 217–26
  - periodic domain structure influence on piezoelectric and acoustic properties, 213–16
  - piezo electric properties, 206–12
  - terahertz radiation generation in PPLN crystal, 228–31
- multilayer technologies, 387–411
  - electrode materials, 399–406
  - innovative structures, 406
  - internal electrode design, 391–9
  - manufacturing processes, 388–90
  - reliability/lifetime of multilayer actuators, 406–11
- other piezoelectric-related materials, 20–1
  - monomorphs, 20–1
  - photo-driven walking machine, 21
  - photostrictive materials, 20
- overview, 34–40
- composites, 39–40
- dependence of piezoelectric constants, 36
  - piezoelectric properties, 34
  - polycrystalline materials, 35–8
  - polymers, 39
  - PZT phase diagram, 36
  - PZT piezoelectric, dielectric, and elastic properties, 37
  - relaxor ferroelectrics, 38
  - single crystals, 34–5
- Pb-free piezoelectrics, 14
  - patent disclosure statistics, 15
- performance under stress, 628–56
- piezoelectric devices applications, 44–77
  - actuators, 58–65
  - basic transducer geometry for acoustic imaging applications, 47
  - bio-sensor principle, 55
  - camera auto zooming/focusing mechanism, 73
  - ceramic actuators, 59
  - cylindrical gyroscope, 46
  - dot-matrix printer head structure, 63
  - linear array type ultrasonic probe, 48
  - linear motor using bending vibration, 75
  - metal tube motor, 72
  - micro-mass sensor, 54–6
  - mixed mode ultrasonic motor, 71
  - p-shaped linear ultrasonic motor, 74
  - piezoelectric/electrostrictive actuators, 60
  - piezoelectric transformers, 56–7
  - piezoelectric vibrators/ultrasonic transducers, 44–51
  - pressure sensors/accelerometers/gyroscopes, 44
  - propagating wave type motor principle, 70
  - room temperature distillation, 50
  - Sashida's motor stator structure, 76
  - SAW material properties, 54
  - surface acoustic wave device structure, 52
  - surface acoustic wave devices, 51–4
  - three-dimensional stress sensor, 45
  - Toyota electronic modulated suspension, 65
  - transient vibration of bimorph, 61
  - trapped-energy filter, 52
  - two-vibration mode coupled type motor, 74
  - ultrasonic imaging with PZT ceramic probes, 49
  - ultrasonic motors, 65–77
  - vibratory coupler type motor, 69
- piezoelectric energy harvesting, 77–82
  - high-energy harvesting, 79–81
  - high power energy harvesting, 80
  - intelligent clothing energy, 81
  - intelligent clothing energy harvesting system, 81–2
  - low energy harvesting, 81–2

- piezoelectric passive damping to energy damping, 77–9
- resistive shunt piezoelectric patch, 79

piezoelectric figures of merit, 21–6
- acoustic impedance, 26
- electromechanical coupling factor k, 22–5
- input electrical and output mechanical energy, 24
- mechanical quality factor, 25–6
- piezoelectric strain constant d, 22
- piezoelectric voltage constant g, 22

piezoelectric resonance, 26–33
- electromechanical coupling factor, 27–8
- impedance curves for reasonable k material, 33
- longitudinal vibration mode, 28–33
- longitudinal vibration through transverse piezoelectric effect, 30
- piezoelectric equations, 26–7
- piezoelectric resonator and electromechanical coupling factors, 29
- strain distribution in resonant or antiresonant state, 32

polarisation as an order parameter, 638–41
- constant electric field in Y-direction, 640
- energy function based on polarisation, 639
- modified energy function, 641

polarisation reorientation, 635–8

Preisach modelling, 652–5
- electric displacement vs electric field, 652
- grain orientation in ferroelectric ceramics, 653

quartz-based materials, 171–80

relaxor ferroelectrics, 9–13
- electromechanical coupling factors changes, 12
- intuitive principle model in understanding piezoelectricity enhancement, 13
- Pb $(Zn_{1/3}Nb_{2/3})O_3$-$PbTiO_3$ phase diagram, 11
- transverse strain in ceramic specimens, 10

relaxor single crystals, 643–5
- crystal variant configurations, 645

single crystal preparation techniques, 412–31
- other technical problems, 426–30
- PMN-PT single crystal flux growth, 421–6
- PZN-PT single crystal flux growth, 414–21

thin film technologies, 441–87
- bulk and thin film materials, 441–3
- deposition of PZT-based thin films, 453–8
- dielectric and piezoelectric properties of PZT-based thin films, 458–66
- film deposition fundamentals, 443–53
- microelectromechanical systems, 466–76
- PZT-based thin films MEMS, 476–87

thin films, 40–4
- constraints in thin/thick films, 43–4
- epitaxially grown rhombohedral PZT films, 42
- magnetron sputtering apparatus principle, 41
- MEMS application, 41–2
- micromachining process, 43
- preparation technique, 40–1
- PZT micropump, 43

unit cell, ferroelectricity, and ferroelectricity, 630–4
- cubic parent phase distortions, 630
- polarisation direction, 632
- schematic illustration of switching, 633
- tetragonal phase of barium titanate, 631

unit cells, defects and domain groups, 641–3
- poled unit cells group, 642
- PZT defect structure, 644

piezoelectric resonance, 26–33, 573, 582
- electromechanical coupling factor, 27–8
- longitudinal vibration mode, 28–33
- piezoelectric equations, 26–7

piezoelectric resonance method, 572–8
- constant voltage drive *vs.* current drive, 576–8
  - admittance spectrum, 577
- loss and mechanical quality factor, 574–6
- resonance/antiresonance, 572–4
  - piezo-ceramic plate vibration through the transverse PZT effect, 572
  - strain distribution, 574

piezoelectric strain, 125

piezoelectric strain constant, 22, 163

piezoelectric transducers, 539–56
- acoustic horn, 547–50
  - horn configurations, 549
  - Langevin transducer with a horn, 549
  - mechanical SAM classification, 550
  - ultrasonic cutter with Langevin type transducer, 549
- acoustic impedance matching, 550
  - transducer design, 550
- acoustic lens, 547
  - dolphin head, 548
- sono-chemistry, 554
  - arrayed Langevin transducer system, 555
  - desktop ‘Sonicater,’ 556
- transducers design, 539–47
  - Cymbal transducer, 541–7
  - Langevin transducer, 539–41
- ultrasonic imaging application, 551–4
  - basic transducer geometry, 551
  - curved linear (or convex) array, 553
  - linear array type, 552
  - ultrasonic imaging with PZT ceramic probes, 553

piezoelectric transformers, 56–7

  - laptop computer adaptor using step-down transformers, 57
  - multilayer type by NEC, 57
  - proposed by Rosen, 56
- piezoelectric vibrators, 44–7
- piezoelectric voltage constant, 15, 22, 322
- piezoelectricity, 1, 10, 291, 327
  - dopant effects, 351–5
    - crystallographic deficiencies, 354–5
    - domain wall front with head-to-head polarisation configuration, 354
    - domain wall stability, 353–4
  - polyvinylidene difluoride, 14
- PIN–PT crystal, 269–72
  - as-grown by Bridgman method, 270
  - temperature frequency dependence of dielectric constant and dielectric loss, 271
- planar magnetron sputtering system, 445–6
- plate-through design, 392–5
- PLZT
  - grain growth in PLZT as function of sintering time, 364
  - grain growth in PLZT ceramic 9/65/35 sintered for 1 hour and 16 hours, 364
  - grain size dependence of induced strain, 382
  - grain size dependence of peak permittivity, 381
  - *see also* Lanthanum-modified lead zirconate titanate
- PMN, 111, 125
- PMN-PbTiO$_3$, 113
- PMnN–PZT thin films, 473–6
  - coupling values for the different PMnN doping to PZT, 475
  - P-E hysteresis curve, 474
  - temperature variations, 475
- PMN–PT crystals, 38, 251, 253–64
  - crystal growth with PbO-based fluxes, 415
  - dielectric properties, 254–8
    - compositional dependence of T$_c$ fitted with one line, 255
    - dielectric constant and discharging current density, 257
    - first structure transformation temperature, 258
  - different growth morphologies, 422
  - growth of single crystals using SSCG, 365
  - hypothetical phase diagram, 422
  - main performance of crystal grown by SSCG, flux and Bridgman methods, 265
  - modified phase diagram and growth path, 426
  - phase diagram and crystal growth, 251, 253–4
    - as-grown crystals with composition near MPB, 254
    - crystals grown by Bridgman method and PT content along the growth direction, 255
    - modified phase diagram, 253
    - phase diagram at low temperature, 253
  - piezoelectric properties, 258–61
    - d$_{33}$ and k$_{33}$ as function of temperature, 260
    - elastic, piezoelectric, dielectric constants and electromechanical coupling factors, 263
    - piezoelectric coefficient, 258
    - properties reported by different research groups, 262
    - strain vs *E*-field curve, 259
  - single crystal flux growth, 421–6
  - solid state crystal growth, 264
- PMNT thin films, 466–73
  - cantilever tip deflection, 471
  - lattice parameters, 468
  - P-E hysteresis curve, 473
  - P–E curves, 469
  - resonant properties measurement, 472
  - SEM and TEM images, 469
  - sputtering conditions, 467
  - temperature variations, 470
  - typical resonant spectrum, 472
  - XRD patterns, 468
- PND *see* personal navigation device
- PNN–PZT thick film, 515–16
- PNNZT piezoelectric actuators, 391
- PNZST system, 391
- polarisation rotation mechanism, 275
- poling, 96
- polycrystalline materials, 35–8
- polycrystals, 179
- polymers, 39, 310
- PolyPower, 295
- polyvinylidene fluoride, 14, 39, 288–9, 292, 323
- polyvinylidene fluoride film, 341
- positive temperature coefficient of resistivity, 402
- potassium di-hydrogen phosphase, 4, 5
- potassium niobate, 132–3
- potassium niobate-sodium niobate-lithium niobate system, 132–3
- potassium niotate-based ceramics, 133–40
  - frequency dependence of impedance
    - Z in (33), (31) and (p) modes, 139
    - Z in (15) mode for sample size of 0.2 × 2 × 8 mm^3, 140
    - Z in (15) mode for sample size of 0.5 × 3 × 8 mm^3, 140
- powder
  - deposition ratio and properties influence, 504–8
    - particle trajectories in an aerosol jet flow, 507
    - PZT AD layers deposition rates, 505
    - PZT film SEM image vs milling time, 506
    - starting particle diameter influence for RTIC phenomenon, 507
  - *see also* ceramic powders
- power generators, 107

PPLN *see* periodically poled lithium niobate
PPLT *see* periodically poled lithium tantalate
Preisach model, 651, 652–5
pressure sensors, 44
PRM *see* piezo response mode
product effect, 16
profilometer, 618
propagating-wave type, 68–9
PSN–PT crystal, 264, 266–9
  growth, 266
    crystal size variation, 267
    perovskite crystals formation in pseudo-binary system, 267
  properties, 267–9
    dielectric properties as function of temperature, 268
    P-E loops for rhombohedral single crystal, 269
Pt inclusions, 429
pulse drive method, 572, 588
pulse drive motors, 62–5
PVDF *see* polyvinylidene fluoride
PVDF-trifluoroethylene, 14
pyrochlore crystals, 427–8, 467
PZN–PT crystal, 242–51
  growth, 242–4
    as-grown crystal boules by modified flux Bridgman method, 246
    modified Bridgman furnace used and its axial temperature gradient profile, 245
    phase diagram at low temperature, 243
  properties, 244–51
    main piezoelectric properties with different compositions and orientations, 249
    measured and derived material properties, 248
    optimum crystallographic orientation, 250
    polarisation-electric field measurements, 252
    T_c as function of PT content, 246
    temperature dependence of dielectric constants of poled crystal, 246
PZN–PT crystals
  crystal growth with PbO-based fluxes, 414, 420
  single crystal flux growth, 414–21
PZT, 180
  crystal deficiencies for acceptor and donor dopants, 355
  epitaxially grown rhombohedral films, 375
  mechanical quality factor vs mole fraction, 358
  multilayer actuators
    domain texture creation model, 379
    layer thickness, 377
    x-ray diffraction patterns and domain texture models, 378
  see also lead zirconate titanate
  permittivity and electrochemical coupling factor composition dependence, 350
  PZT micropump
    micromachining process used, 376
    structure, 376
  soft and hard properties in strain curve, 353
  temperature rise vs effective vibration velocity, 358
PZT 501A ceramic, 326
PZT-based magneto-optic spatial light modulators, 530–1
  prototype, 530
PZT-based thin films
  classification of deposition process, 443–4
    PE-MOCVD, 443–4
    sol-gel deposition, 444
    sputtering, 443
  deposition, 453–8
    chemical structure of precursors, 456
    deposition conditions using MOCVD, 457
    MOCVD/sol-gel processes, 455–8
    multi-target sputtering system, 455
    plasma-enhanced MOCVD system, 456
    rf-magnetron diode sputtering system, 454
    sol-gel deposition process, 458
    sputtering, 453–5
    typical precursors in MOCVD and sol-gel processes, 458
    typical sputtering conditions, 454
  dielectric and piezoelectric properties of PZT-based thin films, 458–66
    cantilever tip displacements, 460, 465
    effective dielectric and piezoelectric constants, 462
    lattice constants, 466
    PZT thin film P-E hysteresis curve, 464
    PZT thin films structural properties, 459
    SEM images, 463
    sol-gel derived film P-E hysteresis curve, 460
    sol-gel/MOCVD, 458–63
    sputtered PZT thin films, 463–6
  film characterisation, 449–53
    piezoelectric properties, 450–3
    structure, 449–50
  key deposition conditions, 444–9
    chemical compositions, 444–5
    crystal phase, 445–8
    microstructure, 448–9
  microelectromechanical systems, 466–76
    PMnN–PZT thin films, 473–6
    PMNT thin films, 466–73
  piezoelectric actuators, 476–87
    cantilever with Si beam, 480
    cantilever without substrate Si beam, 480
    classification, 476
    construction, 477

    - examples and related devices, 478–87
    - MEM devices, 481
    - properties of thin film unimorph cantilevers, 479
    - resonant properties, 481
- PZT ceramics, 587–92
  - high power piezoelectrics origin, 589–91
    - mechanical Q_m results, 590
    - oxygen deficiency diffusion model, 591
    - polarisation vs electric field hysteresis curves, 590
  - semi-hard PZT-based ceramics, 591–2
    - PZT properties, 592
  - very hard PZT-based ceramics, 587–8
    - maximum vibration velocity dependence, 589
    - mechanical Q_m vs basic composition at two vibration velocities, 588
- PZT experimental techniques, 563–78
  - piezoelectric resonance method, 572–8
    - constant voltage drive vs current drive, 576–8
    - loss and mechanical quality factor, 574–6
    - resonance/antiresonance, 572–4
  - pseudo-static method, 567–71
    - extensive loss factor, 570
    - intensive loss factor, 569
    - stress applying jig, 568
  - pulse drive method, 571–2
    - electromechanical parameters measurement, 571
    - piezoelectric ceramic plate, 572
  - theoretical formulas, 563–7
    - electric field, 566
    - hysteresis curves, 564
    - vibration mode and elastic loss, 568
- PZT probe, 554
- PZT ternary system, 98
- PZT:polymer composites, 323–33
  - 1-3 and 0-3 connectivity, 373
  - advanced PZT:polymer composites, 332–3
    - 1-3 piezo-composites, 335
    - ceramic preform manufacturing process, 334
    - composites with parallel and series electrode configurations, 333
  - fabrication process, 374
  - piezoelectric composite materials, 323–4
    - piezoceramic composite development history, 324
    - piezoelectric response comparison with single phase materials, PVDF and PZT, 325
  - principles, 324, 326–9
    - 1-3 composite of PZT rods and polymer, 326
    - diphasic composites in parallel and series configurations, 328
    - permittivity and piezoelectric constants volume fraction dependence, 327
  - theoretical models for 0-3 composites, 329–31
    - permittivity and piezoelectric coefficient, 332
    - piezoelectric–rubber composite co-axial cables structure, 333
    - relative permittivity plotted as function of volume fraction of PZT, 330
    - unit cell configuration, 331

- QPM *see* quasi-phase-matching
- quartz crystal, 171–202
  - artificial quartz crystal production, 181–3
    - autoclave cross section, 182
    - relationship between natural and artificial quartz crystal, 181
    - shapes of grown artificial quartz crystal, 183
    - specifications, 182–3
  - cutting angles and their vibration mode, 184–94
  - compatibility between 4MHz LMX-01 and FCX-01, 194
    - coupling mode, 188
    - developed by River Eletec Corporation, 191–4
    - examples and characteristics, 184–7
    - fundamental Lame mode quartz crystal, 192
    - Lame mode quartz crystal integration, 192
    - LMX-01 and FCX-01, 193
    - major cutting angles and their vibration, 187–91
    - resonant frequency temperature coefficients of resonator, 187
    - vibration modes, 188
  - JIS C6704
    - etch channel density, 184
    - inclusion density, 184
    - infrared absorption constant, 184
  - piezoelectricity, 171–80
    - α-quartz unit cell, 175
    - cross section to Z-axis and cutting angle of crystal plate, 172
    - differences among other piezoelectric materials, 179–80
    - direct longitudinal piezoelectricity, 177
    - direct perpendicular piezoelectricity, 178
    - discovery, 171–4
    - electric and mechanical axis, 175
    - energy change and required characteristics for typical devices, 179
    - inverse piezoelectricity, 178
    - natural quartz crystal external form, 172
    - one unit of Si and O atoms in α-quartz, 176
    - Pierce circuit, 173
    - piezoelectric single crystal and polycrystal constants, 180
    - Si and O atoms arrangement in α-quartz, 176
    - symmetry and its axis, 174–7

    - W.G. Cady experimental device, 173
  - resonator, oscillator, and filter applications, 194–202
    - automotive applications, 200–1
    - capsule endoscope, 202
    - cellular phones, 195–9
    - frequency occupation with one segment and full segment, 197
    - mobile communications, 194–5
    - other applications, 201–2
    - SPC action image, 198
    - wireless LAN standards, 196
- quartz crystal resonators, 173, 180, 190
- quartz crystals vibrators, 184, 196
    - + 1°-X-cut tuning fork, 190–1
    - AT-cut thickness shear mode, 188–90
    - cutting angles, 185
    - shapes and their electrodes, 189
    - temperature frequency characteristics, 186
    - typical vibration modes, 188
- quartz single crystals, 540
- quasi-phase-matching, 214, 227
- quasi-static hysteresis measurement method, 581

- R1-cut, 174
- rare-earth ions, 588
- rattling ion model, 115
- Rayleigh wave *see* surface acoustic wave
- reactive-templated grain growth, 366
- real number, 567
- reflection type, 550
- relaxor ferroelectric based ceramics *see* relaxor ferroelectrics
- relaxor ferroelectrics, 38
  - ceramics, 111–28
    - dependence of reciprocal permittivity, 113
    - temperature dependence of permittivity, 112
    - temperature dependence of spontaneous polarisation, 112
  - ceramics and single crystals, 9–13
    - electromechanical coupling factors changes, 12
    - intuitive principle model in understanding piezoelectricity enhancement, 13
    - Pb $(Zn_{1/3}Nb_{2/3})O_3$-$PbTiO_3$ phase diagram, 11
    - transverse strain in ceramic specimens, 10
  - crystal structures, 114–15
    - B-site ions arrangements in complex perovskites, 114
  - dielectric properties, 115–22
    - computer simulation of composition fluctuation, 118
    - crystal structure models, 117
    - dielectric constant and loss vs temperature, 123–4
    - dielectric relaxation, 120–2
    - diffuse state transition, 116–20
    - multi-potential well model, 122
    - origin of giant permittivity, 115
    - $Pb(Mg_{1/3}Nb_{2/3})O_3$ single crystal sample, 119
    - permittivity vs temperature curves, 121
    - single crystals of $Pb(Sc_{1/2}Ta_{1/2})O_3$, 116
    - temperature dependence of permittivity, 120
  - electrooptic effect, 127–8
    - birefringence vs electric field relation, 128
    - Hubble telescope using electrostrictive actuators, 127
  - electrostriction, 125–7
    - thermal expansion, 126
    - transverse strain in ceramic specimens, 125
  - relaxor single crystals
    - application in piezoelectric actuators and medical transducers, 276–8
    - medical transducers, 277–8
    - piezoelectric actuators, 276–7
  - comparison of properties of PMN–PT, PZN–PT, PSN–PT, PIN–PT single crystals, 273
  - high piezoelectric performance, 241
  - PIN–PT crystal, 269–72
  - PMN–PT crystal, 251, 253–64
    - dielectric properties, 254–8
    - phase diagram and crystal growth, 251, 253–4
    - piezoelectric properties, 258–61
    - solid state crystal growth, 264
  - PSN–PT crystal, 264, 266–9
    - growth, 266
    - properties, 267–9
  - PZN–PT, PMN–PT, PSN–PT and PIN–PT-based piezoelectric materials, 239–80
    - future trends, 278–80
  - PZN–PT crystal, 242–51
    - growth, 242–4
    - properties, 244–51
  - relaxor ferroelectrics history, 240–2
  - theoretical models for relaxor-based crystals, 272, 274–6
    - domain configurations, 274
    - domain engineering and engineered domain configurations, 272, 274–5
    - polarisation rotation and mesophase, 275–6
    - polarisation rotation paths, 275
- remanent polarisation, 96
- remanent strain, 96
- replamine method, 332
- resonance frequency, 543
- resonance optical micro-scanners, 527
- resonant frequency, 187–9
- resonators, 51
- Restriction of Hazardous Substances, 14, 131
- reverse piezoelectricity, 171
- RF module, 196–8

- IEEE 802.15.4, 196–7
- ultrawide band, 197–8

River Eletec Corporation, 191–4
Rochelle salt, 2–5
RoHS *see* Restriction of Hazardous Substances
room temperature impact consolidation, 497–504
  - AD process impact partial velocity and local temperature increase, 501–2
    - FEM simulation, 502
    - impact partial velocity and gas consumption relationship, 501
  - ceramic layers densification mechanism in AD process, 502–4
    - TEM image α–Al_2O_3 /PZT composite layers, 503
  - ceramic powders consolidation, 497–500
    - α–Al_2O_3 layer SEM image, 499
    - AD-ceramic layer using RTIC phenomenon, 498
    - AD deposited layers mechanical properties, 500

Rosen-type transformer, 588
RTGG *see* reactive-templated grain growth
RTIC *see* room temperature impact consolidation

Sake, 49, 554
Sake distillation application, 554
Sashida motor, 76
satellite crystals, 427
SAW *see* surface acoustic wave
scanning near-field acoustic microscopy, 216
scanning probe microscopy, 211
screening retardation effect, 222
secure private cosm encryption, 198
seeded polycrystal conversion, 164
Seiko Instruments, 77
selected area diffraction, 503
semi-hard property, 352
servo displacement transducers, 62
Shanghai Institute of Ceramics, 280
shim, 369
shock compaction method, 502
side-wall nucleation, 427
SIDM *see* smooth impact drive mechanism
single crystal growth, 364–5
  - PZN–PT, PMN–PT, PZT, 365
  - quartz, LN, LT, 364–5

single crystal preparation techniques
  - piezoelectric materials, 412–31
    - PMN and PMN–PT single crystals with PbO-based fluxes, 415
    - PZN and PZN–PT single crystals with PbO-based fluxes, 414
    - relaxor and relaxor-PT single crystals with PbO-based fluxes, 417

single crystals, 34–5, 179
sintering, 104–6, 362
sintering process, 362–3
  - schematic diagram, 363

sintering temperature, 461
Skanavi-type dielectric relaxation, 121
Slater method, 205
slit-insert design, 395
slow-cooling technique, 266
small quartz crystals, 540
Smart Material Corp., 342
smart pill, 303
Smart Structures and Materials Symposium, 289
smooth impact drive mechanism, 77
sodium niobate, 132–3
sodium potassium tartrate, 4
soft property, 351–2
soft rubber, 550
sol-gel deposition, 444
solar cell, 599
sol–gel process, 361, 374, 521, 616
solid state crystal growth, 264, 279
solid state reaction, 359–60, 616
sono-chemistry, 49, 554
  - arrayed Langevin transducer system, 555
  - desktop 'Sonicater,' 556

sound beam, 547
sound-guided therapy probes, 264
sound velocity, 30
sound wave frequency, 539
sphere model, 329
SPM *see* scanning probe microscopy
spontaneous back-switching, 219–20, 221
sputtering, 374, 443, 453–5
SRI International, 305
SSCG *see* solid state crystal growth
stable tailored domain patterns, 205
stainless steel, 515, 517, 521, 526, 528, 531
standing-wave type, 68
stoichiometry, 616
surface acoustic wave, 51–4
  - devices, 51–4, 205
    - fundamental structure, 52
  - filters, 9
  - material properties, 54

surface/geometry dependence, 616–19
  - model to compute the photocurrent dependence, 619
  - photovoltaic response in PLZT ceramics, 618
  - variation of photocurrent with surface roughness, 620

tape-casting method, 367, 389–90
Taylor expansion, 185
TDS 420A, 343
templated grain growth, 164, 365–6
TEMS *see* Toyota electronic modulated suspension
terahertz bandwidth electromagnetic radiation, 228
terfenol-D disks, 343
TGG *see* templated grain growth
thermal spray coating method, 506
thin film technologies, 441–87
  - bulk and thin film materials, 441–3
  - deposition of PZT-based thin films, 453–8

    - MOCVD/sol-gel processes, 455–8
    - sputtering, 453–5
  - dielectric and piezoelectric properties of PZT-based thin films, 458–66
  - film deposition fundamentals, 443–53
    - basic fabrication processes, 444
    - crystal phases of sputtered PT thin films for various temperatures and chemical compositions, 448
    - deposition system classification, 443
    - evaluation methods, 450
    - lattice parameters, 449
    - PbO–TiO_2 binary systems for various sintering temperatures, 448
    - piezoelectric constant for tiredness and transverse mode, 451
    - temperature variations of crystal phase, 447
    - X-ray diffraction patterns of $PbTiO_3$ thin films (200 °C, 500 °C, and 600 °C), 446
    - X-ray diffraction patterns of $PbTiO_3$ thin films (room temp and 480 °C), 447
  - microelectromechanical systems, 466–76
  - PZT-based thin films MEMS, 476–87
- thin films, 40–4
  - constraints in thin/thick films, 43–4
  - MEMS application, 41–2
  - preparation technique, 40–1
- time-of-flight method, 501
- Tita-Con, 5
- Toshiba Corporation, 241, 277, 554
- Toyota Central Research Laboratory, 366
- Toyota electronic modulated suspension, 65
- transdermal drug delivery, 554
- transducers, 587, 591–2
  - design, 539–47
    - Cymbal transducer, 541–7
    - Langevin transducer, 539–41
- transformers, 587, 591–2
- transmission electron microscope images, 498
- transmission type, 550
- transmitting voltage response, 542
- transparent ceramic *see* lanthanum-doped lead zirconate titanate
- transverse piezoelectric constant, 452
- trapped-energy filter, 52
- trapped-energy principle, 51
- trichloroethylene, 554
- TRS Ceramics, 280
- TVR *see* transmitting voltage response
- twinning, 214

- Uchida-Ikeda model, 585
- ultra wide band, 197–8
- ultrasonic cutters, 548
- ultrasonic distillation, 49, 554
- ultrasonic echo field, 551
- ultrasonic imaging, 46–9
- ultrasonic motors, 58, 65–77, 107, 154, 562, 587
  - classification and principles, 68–9
  - fundamental construction, 67
  - propagating-wave type, 73–7
    - linear motor using bending vibration, 75
    - principle, 70
    - stator structure of Sashida motor, 76
  - smooth impact drive mechanism, 77
    - illustration, 78
  - standing wave type motors, 69–72
    - metal tube motor, 72
    - mixed-mode ultrasonic motor, 71
    - p-shaped linear ultrasonic motor, 74
    - two-vibration mode coupled type vibrator, 74
    - vibratory coupler type motor, 69
- ultrasonic probes, 241
- ultrasonic scanning detectors, 539
- ultrasonic transducers, 46, 47, 154
- ultrasound imaging, 551–4
  - basic transducer geometry, 551
  - curved linear (or convex) array, 553
  - linear array type, 552
  - ultrasonic imaging with PZT ceramic probes, 553
- unimorph devices, 369–71
- Ushio Electric USH-500D, 603
- UWB *see* ultra wide band

- vibration energy, 337
- vibration velocity, 357
- Vicker's indentation, 656
- viscosity sensor, 55–6
- V_2O_3 powders, 320
- voltage rise ratio, 56

- wireless LAN, 195
- wobbling, 552
- WorldWide EAP Webhub, 289

- + 1°-X-cut tuning fork, 190–1
- X-ray fluorescence analysis, 270
- X-rays, 551
- xenon lamp, 603

- Young's modulus, 513, 524, 528

- zinc oxide, 40
- zone melting technique, 254, 279
- Zr/Ti ratio, 94